Robert R. Alfano *Editor*
Foreword by Donna Strickland

The Supercontinuum Laser Source

The Ultimate White Light

Fourth Edition

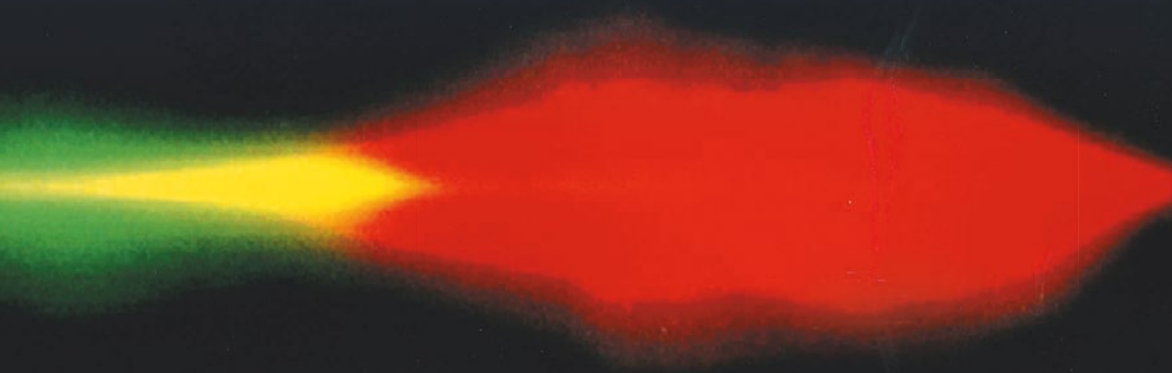

Springer

The Supercontinuum Laser Source

Robert R. Alfano
Editor

The Supercontinuum Laser Source

The Ultimate White Light

Fourth Edition

Springer

Editor
Robert R. Alfano
Departments of Physics and Electrical
Engineering
The City College of New York
New York, NY, USA

The cover image shows the supercontinuum generation of intensity versus wavelength for 1mm of Carbon tetrachloride liquid excited 120 fs 625 nm laser pulses. Photo by Robert Alfano, A Kartz and P.P. Ho

ISBN 978-3-031-06196-7 ISBN 978-3-031-06197-4 (eBook)
https://doi.org/10.1007/978-3-031-06197-4

This Springer imprint is published by the registered company Springer Nature Switzerland AG
The registered company address is: Gewerbestrasse 11, 6330 Cham, Switzerland

Foreword

I highly recommend this most impressive landmark publication on supercontinuum (SC) in the 17 chapters authored by top leading scientists covering various aspects of spectral broadening. The SC gives rise to generation of new frequencies from self-phase modulation, cross-phase modulation, stimulated Raman, modulation instability, 4 wave conical emission, higher harmonic generation (HHG), and attosecond pulse generation. The Kerr index n_2 and dispersion holds the key for temporal pulse expansion and compression to the femtosecond, attosecond, and zeptosecond time scale in order to produce short extreme intense laser pulses in optical regime to interact with and alter matter.

The supercontinuum is an enabling optical process for many diverse applications in metrology, chemistry, biology, solid state physics, WDM communications, microscopy, and extreme laser intensities, and will soon be used in medical applications to advance optical science to new heights. This book helps to further advance the direction towards understanding the use of SC as a coherently driven optical laser electric field to create wide bands of frequencies covering most of E&M spectrum. Undergraduate and graduate students and scientists will find the material expounded in the fourth edition very useful in understanding optical science under extreme laser beam–material interactions.

This book is an excellent up-to-date account of spectral broadening from the temporal responses of the states of laser field to matter to extreme ultrafast laser pulses via Kerr effect arising from different molecular motions: ultrafast – electron cloud; fast – molecular redistribution and plasma formation; and slower – rotation and vibration motions. It is suggested by Alfano in Chap. 17 that HHG can occur from n_2 by electric field by electronic self-phase modulation (ESPM) from gases, liquids, and solids.

Each chapter is well written with comprehensive topics on nonlinear optical process which can be used as a good introduction and advanced research tool to discuss the methods to generate coherent ultrafast pulses covering enabling tools of the supercontinuum to probe and understand ultrafast phenomena in different states of matter in physics, condensed matter, chemistry, biology, and medical applications. It can be used in wide band communication in EE and optical computers.

This book is a must read for students, scientists, engineers, and researchers in optical science. This book is destined to become a classic reference for ultrafast pulse interaction and generation of the ultimate light source to probe nature.

Nobel Prize in Physics 2018.

University of Waterloo, Waterloo, ON, Canada Donna Strickland

Preface

The "supercontinuum" (SC) is generated using ultrafast laser pulses propagating in solids, liquids, gases, and plasmas, and special designs of optical fiber, for example, single-mode, multi-mode, and microstructured. This book is the fourth edition of the classic text on the SC topics of ultrafast nonlinear optical processes responsible for SC from materials. The SC is a most startling and colorful effect. The discovery of white light generation of supercontinuum was borne 52 years ago by Robert Alfano and Stanley Shapiro while at GTE labs (Verzion). The SC light source has become an enabling technology and ultimate source covering an extensive portion of the electromagnetic spectrum, encompassing the XUV, UV, visible, NIR, IR, and THz regions. The SC usage has spread worldwide and has been used to advance ultrafast laser spectroscopy, condensed matter, biology, physics, chemistry, and medicine. Specific applications include high-precision optical frequency and time metrology, precision optical clocks, high-capacity encoding and decoding of information in communications using wavelength division multiplexing, imaging using optical coherence tomography in medicine, light pulse compression and broadening, and extreme high-intensity and ultrafast pulse generation for attosecond pulses and high-harmonic generation (HHG).

The fourth edition is a sequel to *The Supercontinuum Laser Source*, with the third edition being published in 2016. The current edition consists of 17 chapters, with 8 new, and 9 revised and updated chapters, from luminaries and experts in the optical science and nonlinear optics fields. The 17 chapters cover the various underlying processes creating the SC. The SC generation starts with physical process known as self-phase modulation (SPM), induced by the intensity-dependent nonlinear refractive index, referred to as the Kerr effect and represented by n_2 or χ^3, by propagating ultrafast light pulses in different states of matter. A number of other nonlinear processes can simultaneously occur that contribute to broaden the emission spectrum to span bandwidths exceeding well over 10,000 cm^1. These effects include four-wave conical mixing, stimulated Raman scattering, cross-phase modulation, modulation instability, and soliton generation. The effects and their contribution to the SC generation process are highly influenced by the fundamental properties of the medium, including their normal and anomalous dispersive properties. It is possible to cover most of the electromagnetic spectrum, spanning from the XUV to the IR region, and possibly cover from near-DC to the X-ray region, by extreme intense femtosecond pulses from ultrafast table-top laser systems, relying on electronic self-phase modulation (ESPM). The key discussions in the chapters revolve around the various response times of the nonlinear index. Typical experimental configurations rely on milli-joule class lasers with sub-100 fsec optical pulses, focused to a spot size of 10 μm. These parameters are sufficient to alter the envelope and phase of the electric field of the optical pulse to create the SC and HHG.

Various mechanisms are responsible for the intensity-dependent, time-varying index of refraction of matter. The frequency broadening mechanisms are electronic cloud distortion, molecular distribution, plasma generation, liberation, reorientation, and vibration. The influence of these mechanisms on SC generation depends critically on the material's relaxation time with respect to the temporal duration of the excitation pulse. The time varying index $n(t)$ mediated through n_2 can be instantaneous to the driving electric field or averaged over many optical cycles. The salient feature is the relationship of the relaxation time of n_2 to the pulse duration, and the intensity of the optical light pulse. The relevant relaxation time τ_e associated with electronic cloud distortion is about 50 asec, which is ~1/3 of Bohr time of 150 asec. Other key time scales are related to the molecular distribution time, typically on the order of ~100 fs, and time scales associated with the plasmas time, the rocking response, and rotational and vibrational times, which are on the psec scale.

The ESPM follows the ultrafast time of the optical cycle and pulse envelope to create HHG and SC. The ultra supercontinuum (USC), on the other hand, follows the envelope through the time-averaged index <n(t)> and does not produce HHG, while HHG and SC follow both the optical cycle of the carrier envelope phase, and the envelope of the laser pulse.

The following are short overviews of the chapters within this edition. Chapter 1, by Shen and Yang, describes the underlying theory of self-phase modulation and spectral broadening. Chapter 2, by Wang Ho and Alfano, describes SC generation in condensed matter. Chapter 3, by Agrawal, describes the theory of SC in nonlinear dispersive media. Chapter 4, by Baldeck, Ho, and Alfano, describes cross phase modulation. Chapter 5, by Travers and Taylor, describes fiber-based SC generation. Chapter 6, by Alex Heidt et al., describes all normal dispersion fiber SC. Chapter 7, by Corkum and Rolland, describes SC in gases. Chapter 8, by Zhang, Zhano, and Chang, describes attosecond extreme SC. Chapter 9, by Smirnov et al., describes SC in telecommunication applications. Chapter 10, by Mendonca, describes twisted optical angular momentum (OAM) in SC generation. Chapter 11, by Meyer and Alfano, gives an overview of conical four-wave mixing from femtosecond laser pulses. Chapter 12, by Dubietis et al., describes SC in the IR and MIR spectral regions. Chapter 13, by Hu and Menyuk, describes chalcogenide glass fiber for mid-IR SC generation. Chapter 14, by Bolorizadeha and Bezgabadi, provides a quantum mechanical theory of SC. Chapter 15, by Klimczak et al., describes coherent SC from all solid state crystal fiber. Chapter 16, by Wang, Boppart, and Tu, describes SC generation in birefringent all normal dispersion fibers. Chapter 17, by Mazhar and Alfano, describes USC and HHG in various states of matter from intense fs pulses to response times of media following both slow n_2 and fast instanteous n_2 response of the optical fs pulse.

Special thanks to Ms. Sonali Shintre for her untiring and super assistance in the production of the fourth edition and Peter Delfyett for help with the preface.

New York, NY, USA Robert R. Alfano
11/16/2022

Supercontinuum Generated in Different Media

Supercontinuum Light Vector Vortex Beams with OAM (L = 1,2,3) in Air

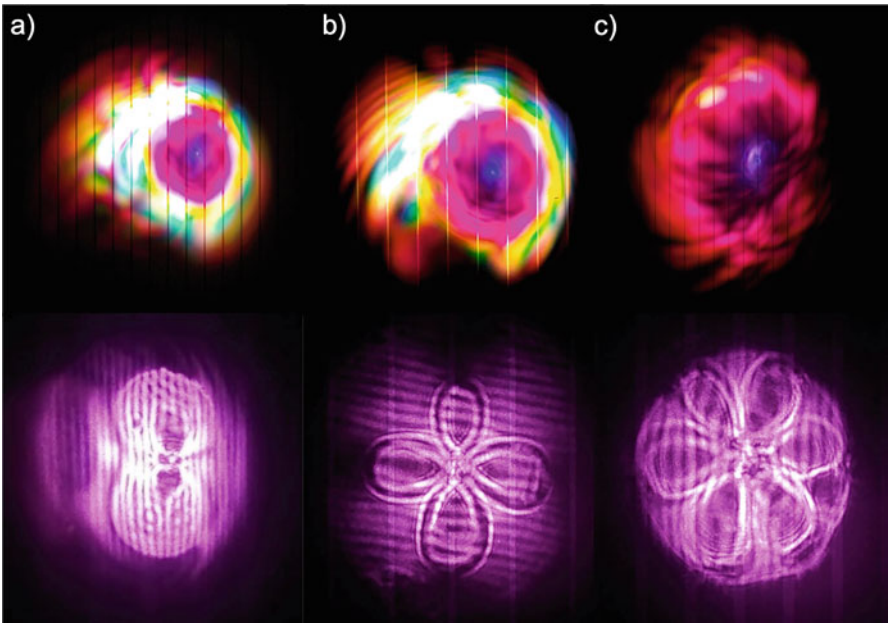

Photographed by Sandra Mamani

Top Row: Supercontinuum light vector vortex beams (Majorana photons) generated in air with an optical vortex retarder with a Spectra Physics Solstice Ace high-energy ultrafast laser with a duration pulse of 90 fs at 800 nm of 4 mJ. The vortex retarder (liquid crystal polymer device) generates Laguerre-Gaussian vortex beams with different orbital angular momentum. a) OAM (L) =1, b) OAM (L) =2, and c) OAM (L) =3. The OAM beam is visible right at the center of the beam (donut profile), which is generated within 5 mm in diameter. Image size is approximately 22 × 22 cm.

Bottom Row: OAM lobes pattern formed due to interference when using a linear polarizer as analyzer after the generation of supercontinuum (SC). The intensity pattern follows the pure multipoles in a spherical symmetry. This process is done to characterize the value of the OAM of SC. The value of the OAM is calculated by dividing the number of petals by two. The pattern observed is generated right at the center where the donut profile is (violet portion of the supercontinuum), which is the section generated within 5 mm in diameter. Image size is approximately 5.5 × 5.5 cm.

Conical Emission and Self-Phase Modulation Light from Vector Vortex Beam with OAM (L = 2) in BK7 Glass

Photographed by Sandra Mamani

Conical emission and supercontinuum light vector vortex beam generated in BK7 glass (2 mm thickness) using an optical vortex retarder to generate orbital angular momentum (OAM) of L = 2 with a Solstice Ace high-energy ultrafast laser with a duration pulse of 90 fs at 800 nm, 4 mJ. This non-linear effect is produced angularly with respect to the wavelength (θ vs. λ). In the image it is observed the order of the colors going from white to violet, red, yellow, green, blue, and violet. The order of colors can be explained by SPM (the first violet/blue about the white center arises from the beam divergence caused by the scattering of the SPM light) followed by four-wave mixing colored rings. See Chap. 11 by Henry Meyer and Robert R Alfano for details.

Image size is approximately 22 x 22cm.

Supercontinuum Light from Calcite

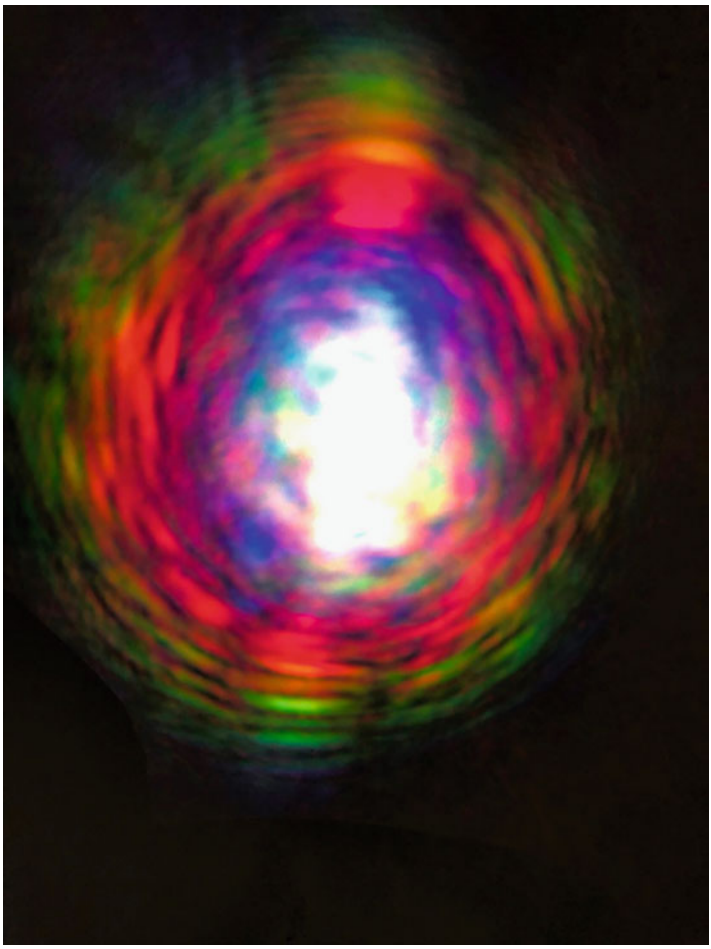

Photographed by Henry J. Meyer

Rings of conical emission surrounding a supercontinuum. The white core arises from self-phase modulation and the outer color arises from four-wave mixing. The first blue and the violet rings about the white center arise from the beam divergence caused by the scattering of the SPM light. The outer rings (red orange, yellow, green, blue, and violet) are produced by the Four-Wave Mixing of Coherent Inc., Monaco + opera-F of 50 fs, 2uJ, at 800 nm laser beam in a 3.5 cm long calcite sample. For more on conical emission, see Chap. 11 by Henry J Meyer and Robert R Alfano.

Supercontinuum Light Generated from Methanol Liquid

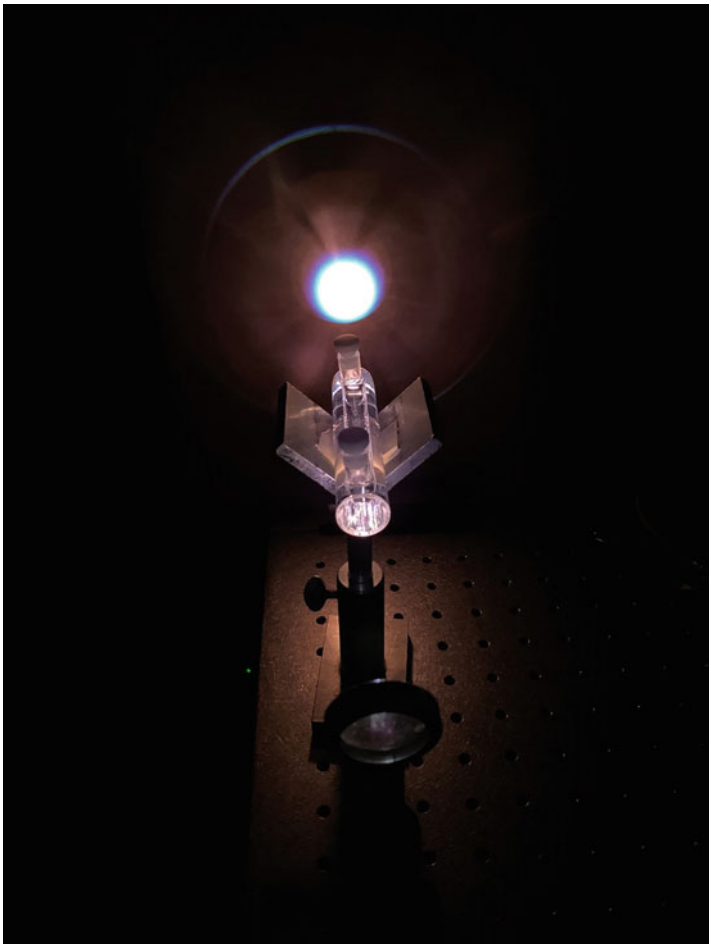

Photographed by Shah Faisal Mazhar

SC generation from Solstice laser 90 fs, 4mj, 800 nm laser pulses propagating through 10 cm long glass cell filled with methanol liquid.

Supercontinuum Light Generated from Plasma Ablation in Air from Copper Foil

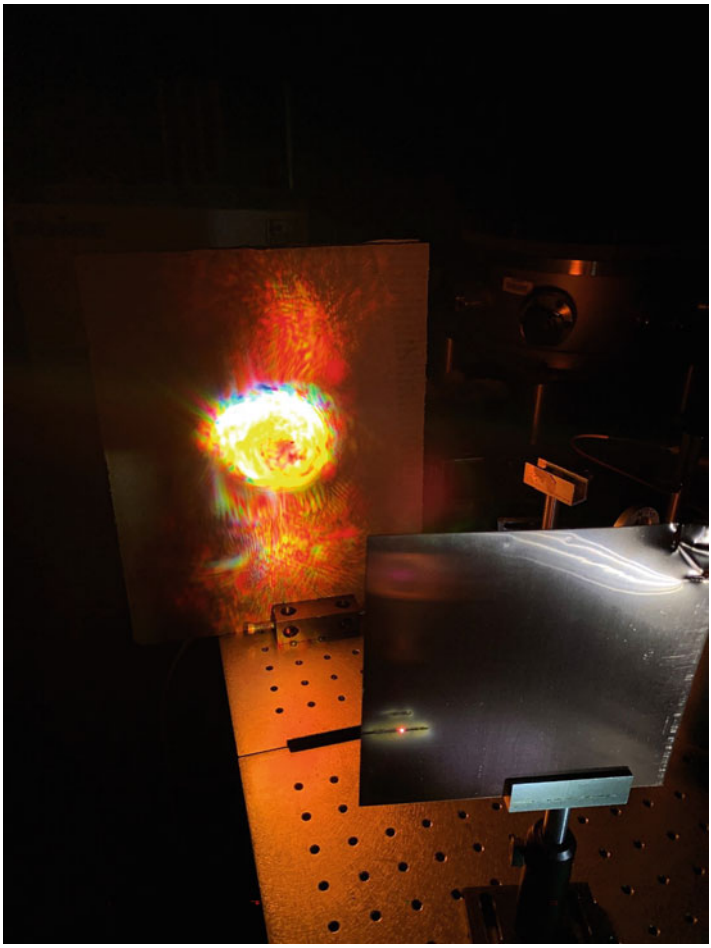

Photographed by Shah Faisal Mazhar

SC generated Solstice laser from 90 fs, 800 nm, 4mj pulses from plasma produced by ablation of thin copper foil in air.

Contents

Contributors

Govind P. Agrawal Institute of Optics, University of Rochester, Rochester, NY, USA

Robert R. Alfano Department of Physics, The City College of the City University of New York, New York, NY, USA

J. D. Ania-Castañón Instituto de Óptica, CSIC, Madrid, Spain

P. L. Baldeck Laboratoire de Spectrométrie Physique, UMR 5588, Université Joseph Fourier/CNRS, 8aint Martin d'Hères, France

Hartmut Bartelt Leibniz-Institute of Photonic Technology, Jena, Germany

A. Safaei Bezgabadib Department of Nanotechnology, Faculty of Sciences and Modern Technologies, Graduate University of Advanced Technology, Kerman, Iran

M. A. Bolorizadeh Department of Photonics, Faculty of Sciences and Modern Technologies, Graduate University of Advanced Technology, Kerman, Iran

Stephen A. Boppart Beckman Institute for Advanced Science and Technology, Department of Electrical and Computer Engineering, University of Illinois at Urbana-Champaign, Urbana, IL, USA

Ryszard Buczyński Faculty of Physics, University of Warsaw, Warsaw, PolandŁukasiewicz Research Network – Institute of Microelectronics and Photonics, Warsaw, Poland

Zenghu Chang Institute for the Frontier of Attosecond Science and Technology (iFAST), CREOL and Department of Physics, University of Central Florida, Orlando, FL, USA

Paul B. Corkum Department of Physics, University of Ottawa, Ottawa, ON, Canada

Arnaud Couairon CPHT, CNRS, Ecole Polytechnique, Institut Polytechnique de Paris, Palaiseau, France

Audrius Dubietis Laser Research Center, Vilnius University, Vilnius, Lithuania

Alexander Hartung Leibniz-Institute of Photonic Technology, Jena, Germany

Alexander M. Heidt Institute of Applied Physics, University of Bern, Benn, Switzerland

P. P. Ho Department of Electrical Engineering, The City College of the City University of New York, New York, NY, USA

Jonathan Hu Baylor University, Waco, TX, USA

Vytautas Jukna Laser Research Center, Vilnius University, Vilnius, Lithuania

Mariusz Klimczak Faculty of Physics, University of Warsaw, Warsaw, Poland

S. Kobtsev Novosibirsk State University, Novosibirsk, Russia

Shah Faisal Mazhar Institute for Ultrafast Spectroscopy and Lasers, City College of New York, City University of New York, New York, NY, USA

J. T. Mendonça Instituto Superior Técnico, Universidade de Lisboa, Lisbon, Portugal

Curtis R. Menyuk University of Maryland Baltimore County, Baltimore, MD, USA

Henry J. Meyer Institute for Ultrafast Spectroscopy and Lasers, Department of Physics, The City College of the City University of New York, New York, NY, USA

Dariusz Pysz Łukasiewicz Research Network – Institute of Microelectronics and Photonics, Warsaw, Poland

Anupamaa Rampur Institute of Applied Physics, University of Bern, Bern, Switzerland

Claude Rolland Division of Physics, National Research Council of Canada, Ottawa, ON, Canada

Y. R. Shen Department of Physics, University of California, Berkeley, CA, USA

S. V. Smirnov Novosibirsk State University, Novosibirsk, Russia

Dirk-Mathys Spangenberg Institute of Applied Physics, Bern, Switzerland

Ryszard Stępień Łukasiewicz Research Network – Institute of Microelectronics and Photonics, Warsaw, Poland

J. R. Taylor Physics Department, Imperial College, London, UK

J. C. Travers Max Planck Institute for the Science of Light, Erlangen, Germany

Haohua Tu Beckman Institute for Advanced Science and Technology, University of Illinois at Urbana-Champaign, Urbana, IL, USA

S. K. Turitsyn Aston Institute of Photonic Technologies, Birmingham, UK

Geng Wang Beckman Institute for Advanced Science and Technology, University of Illinois at Urbana-Champaign, Urbana, IL, USA

Q. Z. Wang United States Patent and Trademark Office, Alexandria, VA, USA

Guo-Zhen Yang Department of Physics, University of California, Berkeley, CA, USA

Qi Zhang Institute for the Frontier of Attosecond Science and Technology (iFAST), CREOL and Department of Physics, University of Central Florida, Orlando, FL, USA

Kim Zhao Institute for the Frontier of Attosecond Science and Technology (iFAST), CREOL and Department of Physics, University of Central Florida, Orlando, FL, USA

Chapter 1
Theory of Self-Phase Modulation and Spectral Broadening

Y. R. Shen and Guo-Zhen Yang

Abstract The chapter focuses on self-phase modulation (SPM) arising from Kerr nonlinear index n2 which leads to spectral broadening from various physical mechanisms depending on temporal responses: ultrafast(electronic), fast (ionization, molecular redistribution), and slow (rotational/vibrational) for n2.

Keywords Self-phase modulation (SPM) · Cross Phase modulation (XPM) · Self-focusing · Transient self-focusing · Kerr index n2 · Frequency broadening · ps laser pulses · fs laser pulses · White light continuum · Self-steepening · Ionizations · n2 response times from electronics clouds · Molecular redistribution · Rotational and vibrational response times

1.1 Introduction

Self-phase modulation refers to the phenomenon in which a laser beam propagating in a medium interacts with the medium and imposes a phase modulation on itself. It is one of those very fascinating effects discovered in the early days of nonlinear optics (Bloembergen & Lallemand, 1966; Brewer, 1967; Cheung et al., 1968; Jones & Stoicheff, 1964; Lallemand, 1996; Shimizu, 1967; Stoicheff, 1963). The physical origin of the phenomenon lies in the fact that the strong field of a laser beam is capable of inducing an appreciable intensity-dependent refractive index change in the medium. The medium then reacts back and inflicts a phase change on the incoming wave, resulting in self-phase modulation (SPM). Since a laser beam has a finite cross section, and hence a transverse intensity profile, SPM on the beam should have a transverse spatial dependence, equivalent to a distortion of the wave front. Consequently, the beam will appear to have self-diffracted. Such a self-diffraction action, resulting from SPM in space, is responsible for the well-known nonlinear

Y. R. Shen (✉) · G.-Z. Yang
Department of Physics, University of California, Berkeley, CA, USA
e-mail: yrshen@berkeley.edu

R. R. Alfano (ed.), *The Supercontinuum Laser Source*,
https://doi.org/10.1007/978-3-031-06197-4_1

optical phenomena of self-focusing and self-defocusing (Marburger, 1975; Shen, 1975). It can give rise to a multiple ring structure in the diffracted beam if the SPM is sufficiently strong (Durbin et al., 1981; Santamato & Shen, 1984). In the case of a pulsed laser input, the temporal variation of the laser intensity leads to an SPM in time. Since the time derivative of the phase of a wave is simply the angular frequency of the wave, SPM also appears as a frequency modulation. Thus, the output beam appears with a self-induced spectral broadening (Cheung et al., 1968; Gustafson et al., 1969; Shimizu, 1967).

In this chapter, we are concerned mainly with SPM that leads to spectral broadening (Bloembergen & Lallemand, 1966; Brewer, 1967; Cheung et al., 1968; Jones & Stoicheff, 1964; Lallemand, 1996; Shimizu, 1967; Stoicheff, 1963). For large spectral broadening, we need a strong SPM in time (i.e., a large time derivative in the phase change). This obviously favors the use of short laser pulses. Consider, for example, a phase change of 6π occurring in 10^{-12} s. Such a phase modulation would yield a spectral broadening of $\sim$100 cm^{-1}. In practice, with sufficiently intense femtosecond laser pulses, a spectral broadening of 20,000 cm^{-1} is readily achievable by SPM in a condensed medium, which is essentially a white continuum (Alfano & Shapiro, 1970). The pulse duration of any frequency component (uncertainty limited) in the continuum is not very different from that of the input pulse (Topp & Rentzepis, 1971). This spectrally superbroadened output from SPM therefore provides a much needed light source in ultrafast spectroscopic studies—tunable femtosecond light pulses (Alfano & Shapiro, 1971; Busch et al., 1973). If the SPM and hence the frequency sweep in time on a laser pulse are known, then it is possible to send the pulse through a properly designed dispersive delay system to compensate the phase modulation and generate a compressed pulse with little phase modulation (Treacy, 1968; Treacy, 1969a, b). Such a scheme has been employed to produce the shortest light pulses ever known (Fork et al., 1987; Ippen & Shank, 1975; Nakatsuka et al., 1981; Nakatsuka & Grischkowsky, 1981; Nikolaus & Grischkowsky, 1983a, b).

Self-phase modulation was first proposed by Shimizu (1967) to explain the observed spectrally broadened output from self-focusing of a Q-switched laser pulse in liquids with large optical Kerr constants (Bloembergen & Lallemand, 1966; Brewer, 1967; Cheung et al., 1968; Jones & Stoicheff, 1964; Lallemand, 1996; Shimizu, 1967; Stoicheff, 1963). In this case, the spectral broadening is generally of the order of a hundred reciprocal centimeters. Alfano and Shapiro (1970) showed that with picosecond laser pulses, it is possible to generate by SPM a spectrally broadened output extending over 10,000 cm^{-1} in almost any transparent condensed medium. Self-focusing is believed to have played an important role in the SPM process in the latter case. In order to study the pure SPM process, one would like to keep the beam cross section constant over the entire propagation distance in the medium. This can be achieved in an optical fiber since the beam cross section of a guided wave should be constant and the self-focusing effect is often negligible. Stolen and Lin (1978) found that indeed the observed spectral broadening of a laser pulse propagating through a long fiber can be well explained by the simple SPM theory. Utilizing a well-defined SPM from an optical fiber, Grischkowsky

and coworkers were then able to design a pulse compression system that could compress a laser pulse to a few hundredths of its original width (Nakatsuka et al., 1981; Nakatsuka & Grischkowsky, 1981; Nikolaus & Grischkowsky, 1983a, b). With femtosecond laser pulses, a strong SPM on the pulses could be generated by simply passing the pulses through a thin film. In this case, the beam cross section is practically unchanged throughout the film, and one could again expect a pure SPM process. Fork et al. (1983) observed the generation of a white continuum by focusing an 80-fs pulse to an intensity of $\sim 10^{14}$ W/cm^2 on a 500-μm ethylene glycol film. Their results can be understood by SPM along with the self-steepening effect (Manassah et al., 1985, 1986; Yang & Shen, 1984).

Among other experiments, Corkum et al. (1985) demonstrated that SPM and spectral broadening can also occur in a medium with infrared laser pulses. More recently, Corkum et al. (1986) and Glownia et al. (1986) have independently shown that with femtosecond pulses it is even possible to generate a white continuum in gas media.

The phase modulation induced by one laser pulse can also be transferred to another pulse at a different wavelength via the induced refractive index change in a medium. A number of such experiments have been carried out by Alfano et al. (1986, 1987). Quantitative experiments on spectral superbroadening are generally difficult. Self-focusing often complicates the observation. Even without self-focusing, quantitative measurements of a spectrum that is generated via a nonlinear effect by a high-power laser pulse and extends from infrared to ultraviolet are not easy. Laser fluctuations could lead to large variations in the output.

The simple theory of SPM considering only the lower-order effect is quite straightforward (Gustafson et al., 1969; Shimizu, 1967). Even the more rigorous theory including the higher-order contribution is not difficult to grasp as long as the dispersive effect can be neglected (Manassah et al., 1985, 1986; Yang & Shen, 1984). Dispersion in the material response, however, could be important in SPM, and resonances in the medium would introduce pronounced resonant structure in the broadened spectrum. The SPM theory with dispersion is generally very complex; one often needs to resort to a numerical solution (Fisher et al., 1983; Fisher & Bischel, 1975). It is possible to describe the spectral broadening phenomenon as resulting from a parametric wave mixing process (in the pump depletion limit) (Bloembergen & Lallemand, 1966; Lallemand, 1996; Penzkofer, 1974; Penzkofer et al., 1973, 1975). In fact, in the studies of spectral broadening with femtosecond pulses, four-wave parametric generation of new frequency components in the phase-matched directions away from the main beam can be observed together with the spectrally broadened main beam. Unfortunately, a quantitative estimate of spectral broadening due to the parametric process is not easy. In the presence of self-focusing, more complication arises. Intermixing of SPM in space and SPM in time makes even numerical solution very difficult to manage, especially since a complete quantitative description of self-focusing is not yet available. No such attempt has ever been reported. Therefore, at present, we can only be satisfied with a qualitative, or at most a semiquantitative, description of the phenomenon (Marburger, 1975; Shen, 1975).

This chapter reviews the theory of SPM and associated spectral broadening. In the following section, we first discuss briefly the various physical mechanisms that can give rise to laser-induced refractive index changes responsible for SPM. Then in Sect. 1.3, we present the simple physical picture and theory of SPM and the associated spectral broadening. SPM in space is considered only briefly. Section 1.4 deals with a more rigorous theory of SPM that takes into account the higher-order effects of the induced refractive index change. Finally, in Sect. 1.5, a qualitative picture of how self-focusing can influence and enhance SPM, and spectral broadening is presented. Some semiquantitative estimates of the spectral broadening are given and compared with experiments, including the recent observations of supercontinuum generation in gases.

1.2 Optical-Field-Induced Refractive Indices

The material response to an applied laser field is often nonlinear. An explicit expression for the response is not readily available in general. Unless specified otherwise, we consider here only the case where the perturbative expansion in terms of the applied field is valid and the nonlocal response can be neglected. We can then express the induced polarization in a medium as (Shen, 1984)

$$\begin{aligned}
\mathbf{P}(t) &= \mathbf{P}^{(1)}(t) + \mathbf{P}^{(2)}(t) + \mathbf{P}^{(3)}(t) + \cdots, \\
\mathbf{P}^{(1)}(t) &= \int \chi^{(1)}\left(t - t'\right) \cdot \mathbf{E}\left(t'\right) dt' \\
&= \int \chi^{(1)}(\omega) \cdot \mathbf{E}(\omega)\, d\omega, \\
\mathbf{P}^{(n)}(t) &= \int \chi^{(n)}(t - t_1, \ldots, t - t_n) : \mathbf{E}(t_1) \ldots \mathbf{E}(t_n)\, dt_1 \ldots dt_n \\
&= \int \chi^{(n)}(\omega = \omega_1 + \omega_2 + \cdots + \omega) : \mathbf{E}(\omega_1) \ldots \mathbf{E}(\omega_n)\, d\omega_1 \ldots d\omega_n,
\end{aligned} \tag{1.1}$$

where the applied field is

$$\mathbf{E}(t) = \int \mathbf{E}(\omega)\, d\omega \quad \text{with } \mathbf{E}(\omega) \propto \exp(-i\omega t) \tag{1.2}$$

and the nth-order susceptibility is

$$\begin{aligned}
\chi^{(n)}(t - t_1, \ldots, t - t_n) = \int \chi^{(n)}(\omega = \omega_1 + \cdots + \omega_n) \exp\Big[& i\omega_1 (t - t_1) \\
& + \cdots + i\omega_n (t - t_n) \Big] d\omega_1 \ldots d\omega_n.
\end{aligned} \tag{1.3}$$

We note that, strictly speaking, only for a set of monochromatic applied fields can we write

$$\mathbf{P}^{(n)} = \chi^{(n)}\left(\omega = \omega_1 + \cdots + \omega_n\right) : \mathbf{E}\left(\omega_1\right) \ldots E\left(\omega_n\right). \tag{1.4}$$

In the case of instantaneous response (corresponding to a dispersionless medium), we have

$$\mathbf{P}^{(n)} = \chi^{(n)} : [E(t)]^n. \tag{1.5}$$

Here, we are interested in the third-order nonlinearity that gives rise to the induced refractive index change. We consider only the self-induced refractive index change; extension to the cross-field-induced change should be straightforward. Thus, we assume a pulsed quasi-monochromatic field $\mathbf{E}_w(t) = \mathscr{E}(t) \exp(-i\omega t)$. The third-order nonlinear polarization in a medium, in general, takes the form

$$\mathbf{P}_{\omega}^{(3)}(t) = \int \Delta\chi\left(t - t'\right) \cdot \mathbf{E}_{\omega}\left(t'\right) dt' \tag{1.6}$$

with $\Delta\chi\left(t - t'\right) = \int \chi^{(3)}\left(t - t', t - t'', t - t'''\right) : \mathbf{E}_{\omega}\left(t''\right)\mathbf{E}_{\omega}^{*}\left(t'''\right) dt''dt'''$. If the optical field is sufficiently far from resonances that the transverse excitations are all virtual and can be considered as instantaneous, we can write

$$\begin{aligned} \mathbf{P}_{\omega}^{(3)}(t) &= \Delta\chi(t) \cdot \mathbf{E}_{\omega}(t), \\ \Delta\chi(t) &= \int \chi^{(3)}\left(t - t'\right) : \left|\mathbf{E}_{\omega}\left(t'\right)\right|^2 dt'. \end{aligned} \tag{1.7}$$

In the dispersionless limit, the latter becomes

$$\Delta\chi(t) = \chi^{(3)} : |E_{\omega}(t)|^2. \tag{1.8}$$

Equation (1.8) is a good approximation when the dispersion of $\Delta\chi$ is negligible within the bandwidth of the field. The optical-field-induced refractive index can be defined as

$$\Delta\mathbf{n} = (2\pi/n_0)\,\Delta\chi, \tag{1.9}$$

where n_0 is the average linear refractive index of the medium. With $\Delta n \equiv n_2|E_{\omega}|^2$, we have $n_2 = (2\pi/n_0)\chi^{(3)}$.

A number of physical mechanisms can give rise to $\Delta\chi$ or $\Delta\mathbf{n}$ (Shen, 1966). They have very different response times and different degrees of importance in different media. We discuss them separately in the following.

1.2.1 Electronic Mechanism

Classically, one can imagine that an applied optical field can distort the electronic distribution in a medium and hence induce a refractive index change. Quantum mechanically, the field can mix the electronic wave functions, shift the energy levels, and redistribute the population; all of these can contribute to the induced refractive index change. For a typical transparent liquid or solid, n_2 falls in the range between 10^{-13} and 10^{-15} esu. For gases at 1 atm pressure, $n_2 \sim 10^{-16}$ to 10^{-18} esu far away from resonances. The response time is of the order of the inverse bandwidth of the major absorption band ($\sim 10^{-14}$ to 10^{-15} s in condensed media) except for the population redistribution part. As the optical frequency approaches an absorption band, n_2 is resonantly enhanced. In particular, when the population redistribution due to resonant excitation is significant, the enhancement of n_2 can be very large, but the time response will then be dominated by the relaxation of the population redistribution. In a strong laser field, saturation in population redistribution and multiphoton resonant excitations can become important. The perturbative expansion in Eq. (1.1) may then cease to be valid. For our discussion of SPM in this chapter, we shall assume that the laser beam is deep in the transparent region, and therefore, all these electronic resonance effects on the induced refractive index are negligible.

1.2.2 Vibrational Contribution

The optical field can also mix the vibrational wave functions, shift the vibrational levels, and redistribute the populations in the vibrational levels. The corresponding induced refractive index change Δn is, however, many orders (~ 5) of magnitude smaller than that from the electronic contribution because of the much weaker vibrational transitions. Therefore, the vibrational contribution to Δn is important only for infrared laser beams close to vibrational resonances. For our discussion of SPM, we shall not consider such cases.

If the laser pulse is very short (10 f. corresponding to a bandwidth of 500 cm^{-1}), the vibrational contribution to Δn can also come in via Raman excitations of modes in the few hundred cm^{-1} range. The Raman transitions are also much weaker than the two-photon electronic transitions, so their contributions to the self-induced Δn are usually not important for the discussion of SPM unless femtosecond pulses are used.

1.2.3 Rotation, Libration, and Reorientation of Molecules

Raman excitations of molecular rotations can, however, contribute effectively to Δn. This is because the rotational frequencies of molecules are usually in the few cm^{-1}

region except for the smaller molecules. Thus, even with a monochromatic field, one can visualize a Raman process (in which absorption and emission are at the same frequency ω) that is nearly resonant. (The difference frequency of absorption and emission is zero, but it is only a few cm^{-1} away from the rotational frequencies.) In condensed media, the rotational motion of molecules is, however, strongly impeded by the presence of neighboring molecules. Instead of simple rotations, the molecules may now librate in a potential well set up by the neighboring molecules. The librational frequencies determined by the potential well are often in the range of a few tens of cm^{-1}. The modes are usually heavily damped. Like the rotational modes, they can also contribute effectively to Δn via the Raman process.

Molecules can also be reoriented by an optical field against rotational diffusion. This can be treated as an overdamped librational motion driven by the optical field. More explicitly, molecular reorientation arises because the field induces a dipole on each molecule and the molecules must then reorient themselves to minimize the energy of the system in the new environment.

All the above mechanisms involving rotations of molecules can contribute appreciably to Δn if the molecules are highly anisotropic. Typically, in liquids, n_2 from such mechanisms falls in the range between 10^{-13} and 10^{-11} esu, with a response time around 10^{-11} s for molecular reorientation and $\sim 10^{-13}$ s for libration. In liquid crystals, because of the correlated molecular motion, n_2 can be much larger, approaching 0.1 to 1, but the response time is much longer, of the order of 1 s. The rotational motion is usually frozen in solids, and therefore, its contribution to Δn in solids can be neglected.

1.2.4 Electrostriction, Molecular Redistribution, and Molecular Collisions

It is well known that the application of a dc or optical field to a local region in a medium will increase the density of the medium in that region. This is because the molecules in the medium must squeeze closer together to minimize the free energy of the system in the new environment. The effect is known as electrostriction. The induced density variation $\Delta\rho$ obeys the driven acoustic wave equation, and from $\Delta n = (\partial n/\partial \rho)\Delta\rho$, the induced refractive index change can be deduced. For liquids, we normally have $n_2 \sim 10^{-11}$ esu with a response time of the order of 100 ns across a transverse beam dimension of $\sim$1 mm.

Molecules will also locally rearrange themselves in a field to minimize the energy of induced dipole–induced dipole interaction between molecules in the system. Whereas electrostriction yields an isotropic Δn, this molecular redistribution mechanism will lead to an anisotropic Δn. Molecular correlation and collisions could also affect molecular redistribution. A rigorous theory of molecular redistribution is therefore extremely difficult (Hellwarth, 1970). Experimentally, molecular redistribution is responsible for the anisotropic Δn observed in liquids

composed of nearly spherical molecules or atoms in cases where the electronic, electrostrictive, and rotational contributions should all be negligible. It yields an n_2 of the order of 10^{-13} esu with a response time in the subpicosecond range. In solids, the molecular motion is more or less frozen, so the contribution of molecular redistribution to Δn is not significant.

1.2.5 Other Mechanisms

A number of other possible mechanisms can contribute to Δn. We have, for instance, laser heating, which increases the temperature of a medium and hence its refractive index; photorefraction, which comes from excitation and redistribution of charged carriers in a medium; and induced concentration variation in a mixture.

We conclude this section by noting that there is an intimate connection between third-order nonlinearities and light scattering (Hellwarth, 1977): Each physical mechanism that contributes to Δn (except the electronic mechanism) is also responsible for a certain type of light scattering. The third-order susceptibility from a given mechanism is directly proportional to the scattering cross section related to the same mechanism, and the response time is inversely proportional to the linewidth of the scattering mode. Thus from the low-frequency light scattering spectrum, one can predict the value of n_2 for the induced refractive index. For example, in most liquids, light scattering shows a Rayleigh wing spectrum with a broad background extending to a few tens of cm^{-1}. This broad background is believed to arise from molecular libration, redistribution, and collisions (Fabellinski, 1967), but the details have not yet been resolved. For our semiquantitative prediction of n_2 and the response time, however, we do not really need to know the details if the Rayleigh wing spectrum of the medium is available. A broad and strong Rayleigh wing spectrum is expected to yield a large n_2 with a fast response.

In Table 1.1, we summarize the results of our discussion of the various physical mechanisms contributing to Δn. It is seen that in nonabsorbing liquid, where all the mechanisms could operate, electrostriction and molecular reorientation may dominate if the laser pulses are longer than 100 ns; molecular reorientation, redistribution, and libration may dominate for pulses shorter than 100 ns and longer than 1 ps; molecular redistribution and libration and electronic contribution may dominate for femtosecond pulses. In transparent solids, usually only electrostriction and electronic contribution are important. Then for short pulses, the latter is the only mechanism contributing to Δn.

Table 1.1 Mechanisms for Kerr n_2 and response times

Physical mechanism	Magnitude of third-order nonlinearity n_2 (esu)	Response time τ(s)
Electronic contribution	10^{-15}–10^{-13}	10^{-14}–10^{-15}
Molecular reorientation	10^{-13}–10^{-11}	$\sim 10^{-11}$
Molecular libration and redistribution	$\sim 10^{-13}$	$\sim 10^{-13}$
Electrostriction	$\sim 10^{-11}$	$\sim 10^{-16}$

1.3 Simple Theory of Self-Phase Modulation and Spectral Broadening

For our discussion of SPM of light, let us first consider the case where the propagation of a laser pulse in an isotropic medium can be described by the wave equation of a plane wave:

$$\left(\frac{\partial^2}{\partial z^2} - \frac{n_0^2}{c^2}\frac{\partial^2}{\partial t^2}\right) E = \frac{4\pi}{c^2}\frac{\partial^2}{\partial t^2} P^{(3)}, \tag{1.10}$$

where

$$E = \mathcal{E}(z,t)\exp(ik_0 z - i\omega_0 t),$$
$$P^{(3)} = \chi^{(3)}|E|^2 E,$$

and n_0 is the linear refractive index of the medium. In the simple theory of SPM (Cheung et al., 1968; Gustafson et al., 1969; Shimizu, 1967), we use the usual slowly varying amplitude approximation by neglecting the $\partial^2\mathscr{E}/\partial t^2$ term on the left and keeping only the $(4\pi/c^2)\chi^{(3)}|\mathscr{E}|^2\mathscr{E}$ term on the right of Eq. (1.10), which then becomes

$$\left(\frac{\partial}{\partial z} + \frac{n_0}{c}\frac{\partial}{\partial t}\right)\mathcal{E} = -\frac{4\pi\omega_0^2}{i2k_0c^2}\chi^{(3)}|\mathcal{E}|^2\mathcal{E}. \tag{1.11}$$

The approximation here also assumes an instantaneous response of $\chi^{(3)}$. Letting $z' \equiv z + ct/n_0$ and $\mathscr{E} = |\mathscr{E}|\exp(i\phi)$, we obtain from the above equation

$$\begin{aligned} \tfrac{\partial|\mathcal{E}|}{\partial z'} &= 0, \\ \tfrac{\partial\phi}{\partial z'} &= \tfrac{2\pi\omega_0^2}{c^2k_0}\chi^{(3)}|\mathcal{E}|^2. \end{aligned} \tag{1.12}$$

They yield immediately the solution

$$|\mathcal{E}| = |\mathcal{E}(t)|, \tag{1.13a}$$

$$\phi(z,t) = \phi_0 + \frac{2\pi\omega_0^2}{c^2 k_0}\chi^{(3)}|\mathcal{E}(t)|^2 z. \tag{1.13b}$$

Equation (1.13a) implies that the laser pulse propagates in the medium without any distortion of the pulse shape, while Eq. (1.13b) shows that the induced phase change $\Delta\phi(t) = \phi(z,t) - \phi_0$ is simply the additional phase shift experienced by the wave in its propagation from 0 to z due to the presence of the induced refractive index $\Delta n = (2\pi/n_0)\chi^{(3)}|\mathscr{E}|^2$, namely $\Delta\phi = (\omega/c)\int_0^z \Delta n\, dz$. Since the frequency of the wave is $\omega = \omega_0(\partial\Delta\phi/\partial t)$, the phase modulation $\Delta\phi(t)$ leads to a frequency modulation

$$\begin{aligned}\Delta\omega(t) &= -\partial(\Delta\phi)/\partial t \\ &= -\frac{2\pi\omega_0^2}{c^2 k_0}\chi^{(3)}\frac{\partial|\mathcal{E}|^2}{\partial t} z.\end{aligned} \tag{1.14}$$

The spectrum of the self-phase-modulated field is, therefore, expected to be broadened. It can be calculated from the Fourier transformation

$$|E(\omega)|^2 = \left|\frac{1}{2\pi}\int_{-\infty}^{\infty}\mathcal{E}(t)e^{-i\omega_0 t + i\omega t}dt\right|^2. \tag{1.15}$$

An example is shown in Fig. 1.1. We assume here a 4.5-ps full width at half-maximum (FWHM) Gaussian laser pulse propagating in a nonlinear medium that yields an SPM output with a maximum phase modulation of $\Delta\phi_{\max} \simeq 72\pi$ rad. The spectrum of the output shows a broadening of several hundred cm^{-1} with a quasiperiodic oscillation. It is symmetric with respect to the incoming laser frequency because the SPM pulse is symmetric. The leading half of the $\Delta\phi$ pulse is responsible for the Stokes broadening and the lagging half for the anti-Stokes broadening. The structure of the spectrum can be understood roughly as follows. As shown in Fig. 1.1, the $\Delta\phi$ curve following the laser pulse takes on a bell shape. For each point on such a curve, one can always find another point with the same slope, except, of course, the inflection points. Since $\partial\phi/\partial t = -\omega$, these two points describe radiated waves of the same frequency but different phases. These two waves will interfere with each other. They interfere constructively if the phase difference $\Delta\phi_{12}$ is an integer of 2π and destructively if $\Delta\phi_{12}$ is an odd integer of π. Such interference then gives rise to the peaks and valleys in the spectrum. The inflection points that have the largest slope on the curve naturally lead to the two outermost peaks with $|\omega_{\max}| \sim |\partial\phi/\partial t|_{\max}$. To find how many peaks we should expect in the spectrum, we need only to know $\phi_{\max}$, as the number of pairs of constructive and destructive interferences is simply $N \sim \phi_{\max}/2\pi$ on each side of the spectrum. The broadened spectrum has Stokes–anti-Stokes symmetry because $\Delta\phi(t)$ is directly proportional to $|E(t)|^2$ and is a symmetric pulse.

With the above qualitative picture in mind, we can now generalize our discussion of SPM somewhat. The response of the medium to the laser pulse is generally not instantaneous. One therefore expects

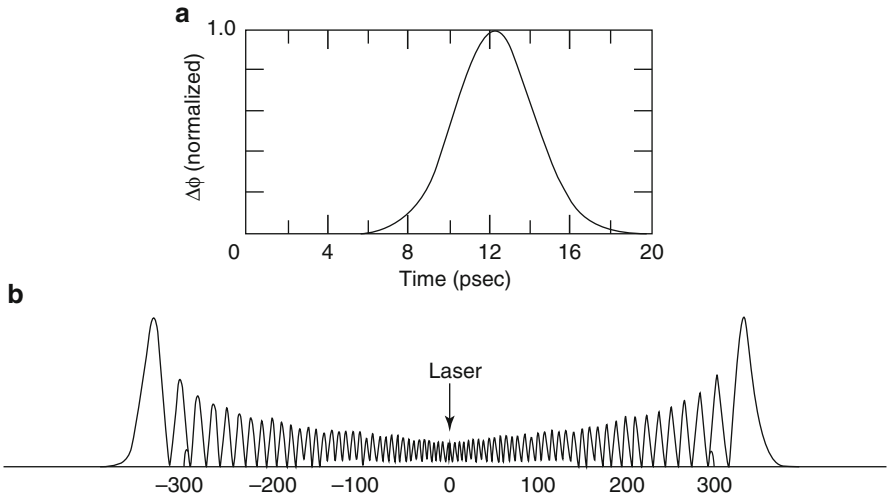

Fig. 1.1 Theoretical power spectrum obtained by assuming an instantaneous response of Δn to the intensity variation $|E(t)|^2$, so that the phase modulation $\Delta\phi(t)$ is proportional to $|E(t)|^2$. (**a**) $\Delta\phi$ versus t and (**b**) power spectrum of the phase-modulated pulse

$$\begin{aligned} \Delta\phi\,(z,t) &= (\omega/c)\int_0^z \Delta n\,(z,t)\,dz, \\ \Delta n\,(z,t) &= \int_{-\infty}^{z} n_2\left(z,t-t'\right)\left|E\left(z,t'\right)\right|^2 dt'. \end{aligned} \tag{1.16}$$

Then, even if $|E(t)|^2$ is symmetric, $\Delta\phi(t)$ is asymmetric and is no longer proportional to $|E(t)|^2$. The consequence is a Stokes–anti-Stokes asymmetry. An example is given in Fig. 1.2. Because of the finite response time of the medium, the leading part of the $\Delta\phi(t)$ curve always sees a larger portion of the intensity pulse $|E(t)|^2$, and therefore, the Stokes side of the spectrum is always stronger. This Stokes–anti-Stokes asymmetry can be drastic if the response time becomes comparable to or smaller than the laser pulse width.

In the more rigorous theory, one should also expect a distortion of the pulse shape as the pulse propagates on in the nonlinear medium. Self-steepening of the pulse, for example, is possible and may also affect the spectral broadening (DeMartini et al., 1967; Gustafson et al., 1969; see Chap. 6). However, the above qualitative discussion still applies since the $\Delta\phi(t)$ curve should still take on an asymmetric bell shape in general.

The experimental situation is usually not as ideal as the simple theory describes. The laser beam has a finite cross section and will diffract. The transverse intensity variation also leads to a $\Delta n(\mathbf{r})$ that varies in the transverse directions. This causes self-focusing of the beam and complicates the simultaneously occurring SPM of the beam (Marburger, 1975; Shen, 1975). Moreover, stimulated light scattering could also occur simultaneously in the medium, in most cases initiated by self-focusing

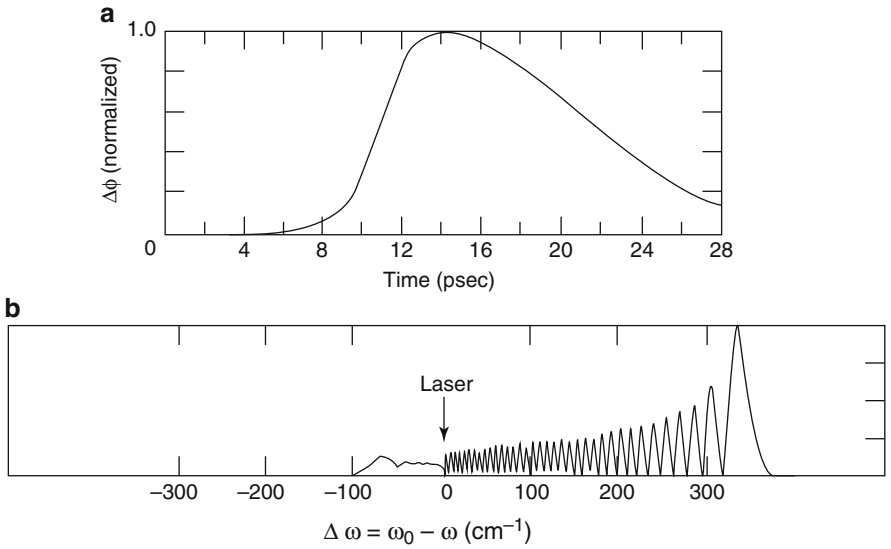

Fig. 1.2 Theoretical power spectrum obtained by assuming a transient response of Δn to the intensity variation $|E(t)|^2$ so that $\Delta\phi(t)$ is no longer proportional to $|E(t)|^2$. (**a**) $\Delta\phi$ versus t and (**b**) power spectrum of the phase-modulated pulse

(Marburger, 1975; Shen, 1975). All these make the analysis of SPM extremely difficult.

One experimental case is, however, close to ideal, namely SPM of a laser pulse in an optical fiber. The transverse beam profile of a guided wave remains unchanged along the fiber. As long as the laser intensity is not too strong, self-focusing and stimulated scattering of light in the fiber can be neglected. For a sufficiently short pulse, the nonlinearity of the fiber is dominated by the electronic contribution and therefore has a nearly instantaneous response. Then if the pulse is not too short and the spectral broadening is not excessive, the slowly varying amplitude approximation is valid and $\partial^2 P^{(3)}/\partial t^2$ in the wave equation can be well approximated by $-\omega_0^2 P^{(3)}$. The only modification of the simple theory of SPM we have discussed is to take into account the fact that we now have a wave in a waveguide with a confined transverse dimension instead of an infinite plane wave in an open space. Thus, the quantitative analysis can easily be worked out. Indeed, Stolen and Lin (1978) found excellent agreement between theory and experiment.

The above discussion of SPM in time can also be used to describe SPM in space. As we already mentioned, the transverse intensity variation of a laser beam can induce a spatial variation of Δn in the transverse directions. Let us consider here, for simplicity, a continuous-wave (cw) laser beam with a Gaussian transverse profile. The phase increment $\Delta\phi(r, z)$ varying with the transverse coordinate r is given by

$$\Delta\phi\,(r, z) = (\omega/c)\,\Delta n(r) z. \tag{1.17}$$

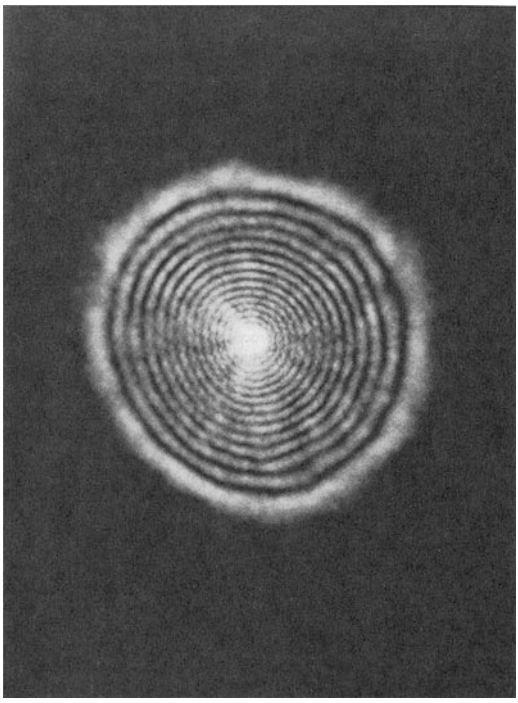

Fig. 1.3 Diffraction ring pattern arising from spatial self-phase modulation of a CW Ar^+ laser beam passing through a 300-μm nematic liquid crystal film. (After Durbin et al., 1981; Santamato & Shen, 1984)

This leads to a distortion of the wave front. Since the beam energy should propagate along the ray path perpendicular to the wave front, this distortion of the wave front would cause the beam to self-focus. If the propagation length is sufficiently long, the beam will actually self-focus and drastically modify the beam cross section. However, if the length of the medium is much shorter than the self-focusing distance, then the self-focusing effect in the medium can be neglected, and we are left with only the SPM effect on the beam. The results of Fig. 1.1 can describe the spatial SPM equally well if we simply replace t by r and ω by $k_\perp$, where $k_\perp$ is the transverse component of the wave vector of the beam. We realize that $k_\perp$ defines the deflection angle θ of a beam by the relation $k_\perp = (\omega n_0/c)\sin\theta$. Therefore, the quasiperiodic spectrum in the $k_\perp$ space actually corresponds to a diffraction pattern with multiple bright and dark rings. This has indeed been observed experimentally (Durbin et al., 1981; Santamato & Shen, 1984). An example is shown in Fig. 1.3. Self-focusing or diffraction in the medium can modify the spatial SPM through its modification of the beam profile. This is analogous to the self-steepening effect on the temporal SPM through its modification of the pulse shape.

We now return to the discussion of temporal SPM and spectral broadening. In the next section, we consider the case where the incoming laser pulse is very short and spectral broadening is very extensive so that the approximations used in the simple theory of SPM need improvement.

1.4 More Rigorous Theory of Self-Phase Modulation and Spectral Superbroadening

Another experimental case of SPM that could avoid complications arising from self-focusing, stimulated scattering, or other nonlinear optical effects involves the propagation of an ultrashort laser pulse through a thin nonlinear medium. In this case, the medium is thin enough so that the self-focusing effect on SPM in the medium can be ignored. The pulse is short enough so that the transient stimulated light-scattering processes are effectively suppressed. Yet, the pulse intensity can still be so high as to induce a very strong SPM, but not high enough to result in appreciable multiphoton absorption or optical breakdown. This is the case first studied by Fork et al. (1987). Using an 80-fs pulse at 627 nm focused to an intensity of 10^{13}–10^{14} W/cm on a 500-μm film of ethylene glycol, they observed in the output a huge spectral broadening that appears as a white continuum. Unlike the spectral broadening discussed in the previous section, the present case shows a Stokes–anti-Stokes asymmetry that emphasizes the anti-Stokes side instead. Such a spectral superbroadening was observed earlier by Alfano and Shapiro (1970) in much longer media with picosecond pulses, but SPM in those cases was definitely affected by self-focusing. Obviously, the results of Fork et al. cannot be explained by the simple theory of SPM. We must resort to a more rigorous analysis.

We first notice that the self-steepening effect on the pulse is not included in the simple theory. This means that the approximations neglecting the $\partial^2\mathscr{E}/\partial t^2$ term and the terms involving the time derivatives of $|P^{(3)}|$ in the wave equation are not quite appropriate. They become worse for shorter pulses. In the more rigorous analysis of SPM, we must improve on these approximations. Let us now go back to Eq. (1.10). Without any approximation, we can transform it into an equation for the field amplitude (Yang & Shen, 1984):

$$\begin{aligned}&\left(\frac{\partial}{\partial z}+\frac{n_0}{c}\frac{\partial}{\partial t}\right)\mathcal{E}+\frac{1}{i2k_0}\left(\frac{\partial^2}{\partial z^2}-\frac{n_0^2}{c^2}\frac{\partial^2}{\partial t^2}\right)\mathcal{E}\\&=-\frac{4\pi\omega_0^2}{i2k_0c^2}\chi^{(3)}|\mathcal{E}|^2\mathcal{E}+\frac{2\pi}{ik_0c^2}\left(-i2\omega_0\frac{\partial}{\partial t}+\frac{\partial^2}{\partial t^2}\right)\chi^{(3)}|\mathcal{E}|^2\mathcal{E}\end{aligned}. \tag{1.18}$$

The last term on both sides of the equation has been neglected in the simple theory of SPM. By defining the differential operators $D_\pm \equiv (\partial/\partial z) \pm (n_0/c)(\partial/\partial t)$, Eq. (1.18) can be written as

$$\begin{aligned}D_+\mathcal{E}+\frac{1}{i2k_0}D_-D_+\mathcal{E}&=\frac{1}{i2k_0}\Pi,\\\Pi&=-\frac{4\pi\omega_0^2}{c^2}\left[1+\frac{2i}{\omega_0}\frac{\partial}{\partial t}-\frac{1}{\omega_0^2}\frac{\partial^2}{\partial t^2}\right]\chi^{(3)}|\mathcal{E}|^2\mathcal{E}.\end{aligned} \tag{1.19}$$

Since $D_- = -(2n_0/c)(\partial/\partial t) + D_+$, we have from Eq. (1.19)

$$\begin{aligned} D_+\mathcal{E} &= \tfrac{1}{i2k_0}\left[\left(-\tfrac{2n_0}{c}\tfrac{\partial}{\partial t} + D_+\right) D_+\mathcal{E} + \Pi\right] \\ &= \tfrac{1}{i2k_0}\sum_{m=0}^{\infty}\left[\left(-\tfrac{2n_0}{c}\tfrac{\partial}{\partial t} + D_+\right)/i2k_0\right]^m \Pi. \end{aligned} \tag{1.20}$$

It is then simply a question of how many terms in the power series expansion we need to include to better describe the SPM.

The zeroth-order approximation corresponds to neglecting all derivatives of $\chi^{(3)}|\mathscr{E}|^2\mathscr{E}$ any yields

$$D_+\mathcal{E} = -\left(2\pi\omega_0^2/ic^2k_0\right)\chi^{(3)}|\mathcal{E}|^2\mathcal{E}, \tag{1.21}$$

which is identical to Eq. (1.11) used as the basis for the simple theory of SPM. We recognize that under this lowest-order approximation,

$$\begin{aligned} &D_+\left(\chi^{(3)}|\mathcal{E}|^2\mathcal{E}\right) \propto \left(\chi^{(3)}|\mathcal{E}|^2\right)^2\mathcal{E} \\ &\ll \chi^{(3)}|\mathcal{E}|^2\mathcal{E} \quad \text{if } \chi^{(3)}|\mathcal{E}|^2 \ll 1. \end{aligned} \tag{1.22}$$

Therefore, we can use D_+ as an expansion parameter in the higher-order calculations. For the first-order approximation, we neglect terms involving $D_+^m\left(\chi^{(3)}|\mathcal{E}|^2\mathcal{E}\right)$ with $m \geq 1$ in Eq. (1.20) and obtain

$$\begin{aligned} D_+\mathcal{E} &= \tfrac{1}{i2k_0}\sum_{m=0}^{\infty}\left[\left(\tfrac{1}{i\omega_0}\tfrac{\partial}{\partial t}\right)^m\Pi\right] \\ &= \left(1 + \tfrac{i}{\omega_0}\tfrac{\partial}{\partial t}\right)\left[-\tfrac{2\pi\omega_0^2}{ik_0c}\chi^{(3)}|\mathcal{E}|^2\mathcal{E}\right]. \end{aligned} \tag{1.23}$$

The calculation here has in a sense used $\chi^{(3)}|\mathscr{E}|^2$ as the expansion parameter. In the above first-order approximation, we have kept the $(\chi^{(3)}|\mathscr{E}|^2)^n\mathscr{E}$ terms with $n \leq 1$ including all their time derivatives. In ordinary cases, this is a very good approximation because usually $\chi^{(3)}|\mathscr{E}|^2 \ll 1$, and therefore, the higher-order terms involving $(\chi^{(3)}|\mathscr{E}|^2)^n\mathscr{E}$ with $n \geq 2$ are not very significant. For example, in the ultrashort pulse case, we have $\chi^{(3)} \sim 10^{-14}$ esu (or $n_2 \sim 10^{-13}$ esu) for a condensed medium; even if the laser pulse intensity is $I \sim 10^{14}$ W/cm^2, we find $\chi^{(3)}|\mathscr{E}|^2 \sim 4 \times 10^3 \ll 1$. For larger $\chi^{(3)}|\mathscr{E}|^2$, one may need to include higher-order terms in the calculations. The next-order correction includes the $D_+(\chi^{(3)}|\mathscr{E}|^2\mathscr{E})$ term and all its time derivatives. They yield additional terms proportional to $(\chi^{(3)}|\mathscr{E}|^2)^2\mathscr{E}$ in the wave equation. If $\chi^{(3)}|\mathscr{E}|^2 \gtrsim 1$, then the approach with series expansion will not be useful, and we have to go back to the original nonlinear wave Eq. (1.19).

In the following discussion, we consider only cases with $\chi^{(3)}|\mathscr{E}|^2 \ll 1$. We are therefore interested in the solution of Eq. (1.23), which, with $n_2 = (2\pi\omega_0/k_0\, c)\chi^{(3)}$, takes the form

$$\frac{\partial \mathcal{E}}{\partial z} + \frac{1}{c}\frac{\partial}{\partial t}\left(n_0\mathcal{E} + n_2|\mathcal{E}|^2\right) = i\frac{n_2\omega_0}{c}|\mathcal{E}|^2\mathcal{E}. \tag{1.24}$$

For simplicity, we now neglect the dispersion of the response of the medium. This, as we mentioned earlier, is equivalent to assuming an instantaneous response. Insertion of $\mathscr{E} = |\mathscr{E}| \exp(i\phi)$ into Eq. (1.24) yields two separate equations for the amplitude and phase:

$$\left[\frac{\partial}{\partial z} + \frac{n_0}{c}\left(1 + \frac{3n_2}{n_0}|\mathcal{E}|^2\right)\frac{\partial}{\partial t}\right]|\mathcal{E}| = 0, \tag{1.25a}$$

$$\left[\frac{\partial}{\partial z} + \frac{n_0}{c}\left(1 + \frac{n_2}{n_0}|\mathcal{E}|^2\right)\frac{\partial}{\partial t}\right]\phi = \frac{n_2\omega_0}{c}|\mathcal{E}|^2. \tag{1.25b}$$

In comparison with Eq. (1.12) for the simple theory of SPM, the only difference is the addition of the $n_2|\mathscr{E}|^2 (= \Delta n)$ terms on the left-hand sides of Eq. (1.25). Its effect is obvious in causing a pulse shape deformation during the pulse propagation. With $\Delta n > 0$, we expect a pulse steepening in the lagging edge. This is because the peak of the pulse then propagates at a lower velocity than either the leading or the lagging part of the pulse (DeMartini et al., 1967).

Let us first neglect the self-steepening effect on the amplitude pulse. Clearly, self-steepening in the lagging part of the ϕ pulse should lead to a spectral broadening with Stokes–anti-Stokes asymmetry emphasizing the anti-Stokes side, because it is the lagging part of the phase modulation that gives rise to the broadening on the anti-Stokes side. To be more quantitative, we assume an input laser pulse with $|\mathscr{E}(0,t)|^2 = A^2/\cosh(t/\tau)$, whose shape remains unchanged in propagating through the medium so that $|\mathscr{E}(z,t)|^2 = A^2/\cosh[(t - n_0/c)/\tau]$. The solution of Eq. (1.25b) can then be found analytically as

$$\phi = \omega_0\tau\left\{x - \sinh^{-1}\left[\sinh\, x - (n_2/c\tau)\, A^2 z\right]\right\} \tag{1.26}$$

with $x = [t - (n_0/c)z]/\tau$. The corresponding frequency modulation is given by

$$\Delta\omega/\omega_0 = \left[1 + \left(Q^2 - 2Q\, \sinh\, x\right)/\cosh\, x\right]^{-1/2} - 1. \tag{1.27}$$

Here, we have defined

$$Q = n_2 A^2 z/c\tau \tag{1.28}$$

as a characteristic parameter for spectral broadening. For $Q \ll 1$, we have

$$\Delta\omega/\omega_0 \simeq -Q \sinh\, x/\cosh^2 x, \tag{1.29}$$

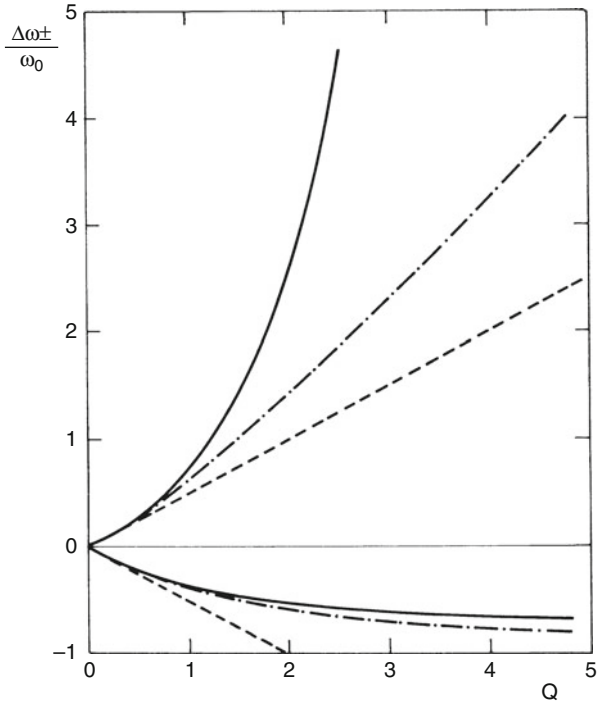

Fig. 1.4 Maximum Stokes ($\Delta\omega_- < 0$) and anti-Stokes ($\Delta\omega_+ > 0$) shifts calculated with different models: simple theory of self-phase modulation (– – –); more rigorous theory without the self-steepening effect on the intensity pulse (–·–); more rigorous theory with the self-steepening effect (—). (After Yang & Shen, 1984)

which is identical to the result one would find from the simple theory of SPM. For $Q \gtrsim 1$, we expect spectral superbroadening with appreciable Stokes–anti-Stokes asymmetry and a maximum anti-Stokes shift $\Delta\omega_+ \gtrsim \omega_0$. The maximum Stokes and anti-Stokes shifts, $\Delta\omega_-$ and $\Delta\omega_+$, respectively, can be directly obtained from Eq. (1.27):

$$\Delta\omega_\pm/\omega_0 = \frac{1}{2}\left[\left(Q^2+4\right)^{1/2} \pm |Q|\right] - 1. \tag{1.30}$$

This is plotted in Fig. 1.4 in comparison with the result calculated from the simple theory of SPM. For $|Q| \ll 1$, we have $\Delta\omega_\pm \simeq \pm(1/2)\omega_0|Q|$, and for $|Q| \gg 1$, we have $\Delta\omega_+ \simeq \omega_0|Q|$ and $\Delta\omega_- \simeq \omega_0(1/|Q| - 1)$. It is seen that Stokes broadening is always limited by $|\Delta\omega_-| < \omega_0$, as it should be.

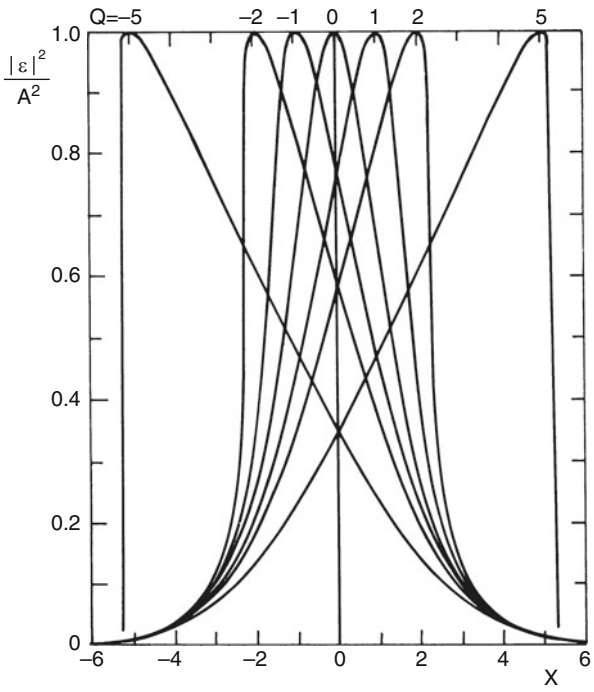

Fig. 1.5 Self-steepening effect on the intensity pulse during its propagation in a nonlinear medium at various values of $Q = n_2 A^2 z c/\tau$, with $x = (t - n_0 z/c)/\tau$. (After Yang & Shen, 1984)

We now include the effect of self-steepening on the amplitude pulse. It can be shown that with $|\mathscr{E}(0,t)|^2 = A^2/\cosh(t/\tau)$, the solution of Eq. (1.25a) must satisfy the implicit algebraic equation

$$|\mathcal{E}(z,t)|^2 = A^2/\cosh\left[x - Q|\mathcal{E}(z,t)|^2/A^2\right]. \tag{1.31}$$

A simple numerical calculation then allows us to find $|\mathscr{E}|^2$ as a function of x for a given Q. The results are shown in Fig. 1.5. For $|Q| \gtrsim 1$, the self-steepening effect is apparent. Knowing $|\mathscr{E}(z,t)|^2$, we can again solve for $\phi(z,t)$ from Eq. (1.25b) and find $\Delta\omega(z,t)$ and $\Delta\omega_\pm$. This can be done numerically; the results are also presented in Fig. 1.4. It is seen that for $Q > 1$, self-steepening of the pulse amplitude has increased the spectral broadening on the anti-Stokes side quite significantly. The additional spectral broadening comes in because the steepening of the amplitude pulse enhances the steepening of the ϕ pulse.

The spectral broadening actually results from frequency chirping since $\partial\phi(t)/\partial t = -\omega(t)$. This is shown in Fig. 1.6 for the numerical example discussed above. As expected, the Stokes and anti-Stokes shifts appear, respectively, in the leading and lagging parts of the self-steepened pulse. The $\Delta\omega = 0$ point appears at larger x for larger values of Q because self-steepening shifts the peak of the pulse to larger x (see Fig. 1.5).

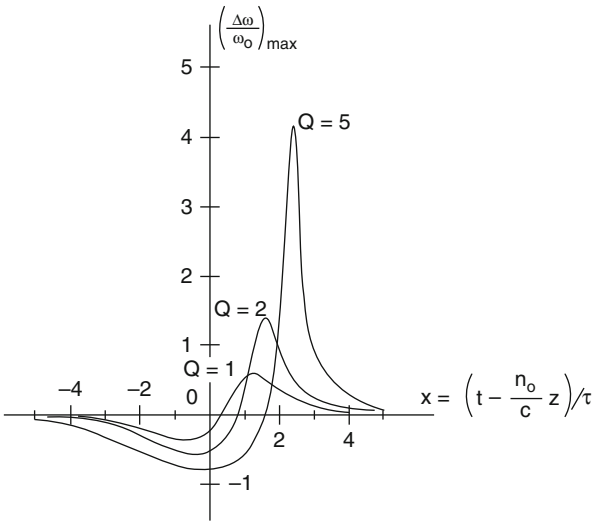

Fig. 1.6 Frequency shift due to phase modulation as a function of $x = (t - n_0 z/c)/\tau$ at various value of $Q = n_2 A^2 z c/\tau$

We can compare the calculation with the experiment of Fork et al. In their experiment, the relevant parameters are $n_2 \simeq 10^{-13}$ esu, $z = 0.05$ cm, $I \sim 10^{14}$ W/cm^2, and τ (pulse width) $\simeq 8 \times 10^{-14}$ s. The corresponding value of Q is about 2.3. They observed a Stokes broadening $\Delta\omega_-/\omega_0 \simeq -0.6$ and an anti-Stokes broadening $\Delta\omega_+/\omega_0 \simeq 2.3$. Our calculation gives $\Delta\omega_-/\omega_0 \simeq -0.54$ and $\Delta\omega_+/\omega_0 \simeq 3.5$. Considering the uncertainty in the experimental parameters, we can regard the agreement between theory and experiment as reasonable.

Manassah et al. (1985, 1986) used the method of multiple scales to solve Eq. (1.18) (neglecting dispersion). They also took $n_2|\mathscr{E}|^2/n_0$ as the expansion parameter in their series expansion and therefore necessarily obtained the same results as we discussed above.[1]

We have neglected in the above calculation the dispersion of the medium response. Normal dispersion may also reshape the pulse (Fisher et al., 1983; Fisher & Bischel, 1975), but in the present case, the length of the medium is so short that this effect is not likely to be important. Anomalous dispersion with resonances in $\chi^{(3)}$ or n_2 could, however, give rise to resonant structure in the broadened spectrum. The calculation including the dispersion of $\chi^{(3)}$ is much more complicated and, in general, must resort to numerical solution (Fisher et al., 1983; Fisher & Bischel, 1975). In obtaining the time-dependent solution of the wave equation with the third-order nonlinearity, we have already taken all the four-wave mixing contributions into account. By adding a noise term with a blackbody spectrum in the nonlinear wave equation, the four-wave parametric generation process proposed by Penzkofer et al. (1973, 1975) could also be included in the calculation.

[1] A factor of 3 in front of n_2 is mistakenly left out in Eq. (1.3a) of Yang and Shen (1984).

1.5 Self-Focusing and Self-Phase Modulation

For pulsed laser beam propagation in a nonlinear medium, SPM in time and SPM in space necessarily appear together. SPM in time causes self-steepening of the pulse, which in turn enhances SPM in time. Similarly, SPM in the transverse beam profile causes self-focusing of the beam, which in turn enhances the transverse SPM. If the propagation distance in the medium is sufficiently long, these effects can build up to a catastrophic stage, namely self-steepening to a shock front and self-focusing to a spot limited in dimensions only by higher-order nonlinear processes and diffraction. SPM in time and SPM in space are then tightly coupled and strongly influenced by each other. In many experiments, the observed strong temporal SPM and extensive spectral broadening are actually initiated by self-focusing. In such cases, the input laser pulse is so weak that without self-focusing in the nonlinear medium, SPM would not be very significant. Self-focusing to a limiting diameter greatly enhances the beam intensity, and hence SPM can appear several orders of magnitude stronger. A quantitative description of such cases is unfortunately very difficult, mainly because the quantitative theory for self-focusing is not yet available. We must therefore restrict ourselves to a more qualitative discussion of the problem.

1.5.1 Self-Phase Modulation with Quasisteady-State Self-Focusing

In the early experiments on self-focusing of single-mode nanosecond laser pulses, it was found that the output of the self-focused light had a spectral broadening of several hundred cm^{-1} (Marburger, 1975; Shen, 1975). This was rather surprising because from the simple theory of SPM, picosecond pulses would be needed to create such a spectral broadening (Cheung et al., 1968; Gustafson et al., 1969; Shimizu, 1967). Later, the observation was explained by SPM of light trailing behind a moving focus (Shen & Loy, 1971; Wong & Shen, 1972). We briefly review the picture here and then use it to interpret the recently observed SPM and spectral superbroadening of ultrashort pulses in gases (Corkum et al., 1986; Glownia et al., 1986).

Figure 1.7 depicts the quasisteady-state self-focusing of a laser pulse leading to a moving focus along the axis ($\hat{z}$) with a U-shaped trajectory described by the equation (Marburger, 1975; Shen, 1975)

$$z_f(t) = \frac{K}{\sqrt{P(t_R)} - \sqrt{P_0}}, \tag{1.32}$$

where P_0 is the critical power for self-focusing, $\sqrt{P(t_R)}$ is the laser power at the retarded time $t_R = t - z_f\, n_0/c$, and K is a constant that can be determined from experiment. This equation assumes instantaneous response of Δn to the applied

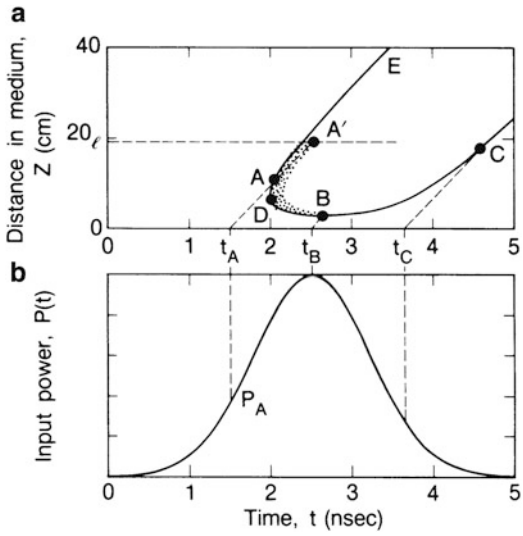

Fig. 1.7 Self-focusing for an input laser pulse in (**a**) leading to the trajectory of a moving focus in the form of U curve in (**b**). The dashed lines in (**b**), with slope equal to the light velocity, depict how light propagates in the medium along the z axis at various times. The shaded region around the U curve has appreciably larger Δn. Light traversing the medium along the dashed lines through the shaded region should acquire a phase increment $\Delta\phi$ that varies with time

field, which is a good approximation as long as the response time τ is much shorter than the laser pulse width. Here, we are interested only in the upper branch of the U curve, along which the focus has a forward velocity faster than light. Because of the high laser intensity in the focal spot, the locally induced Δn should be appreciable and should last for a duration not shorter than the relaxation time τ. Thus one can imagine that the moving focus creates in the medium a channel of Δn at least τ dz_f /dt long trailing after the focus. Consider now the defocused light from a local focal spot. Since it lags behind the moving focus (which travels faster than light), it experiences the Δn dielectric channel created by the focus over a certain distance and will diffract only weakly. In other words, the defocused light from the focus is partially trapped in the Δn channel. This partial trapping of light in turn helps to maintain the Δn channel and make it last longer. The emission from the focal spot at the end of the medium then takes the form of an asymmetric pulse (with a pulse width of the order of a few τ) with a longer trailing edge.

The above picture is also illustrated in Fig. 1.7. We use the shaded area around the U curve to denote the region with appreciable Δn. The laser input at t_A focuses at A, but defocuses more gradually because of the existing Δn channel in front of it. The partially trapped light then propagates along the axis from A to the end of the medium at A', crossing the shaded region with appreciable Δn. It therefore acquires a significant phase increment $\Delta\phi$. From the figure, one may visualize that $\Delta\phi$ can be strongly phase modulated in time, varying from nearly zero to a maximum and back to zero in a few relaxation times. This could yield appreciable spectral broadening in the output of the self-focused light.

To be more quantitative, we realize that the light pulse emitted from a focus in the medium must be asymmetric and must have a pulse width of several τ. The shaded area in Fig. 1.7 has a somewhat larger width since Δn is induced by the focused

light. Knowing the trajectory of the moving focus, the beam intensity in the focal region, and how Δn responds to the intensity, we can calculate $\Delta\phi(t)$ and hence $\Delta\omega(t)$ and the broadened spectrum (Shen & Loy, 1971; Wong & Shen, 1972). As an example, consider the case of a 1.2-ns laser pulse propagating into a 22.5-cm CS_2 cell. The trajectory of the moving focus (focal diameter $\simeq 5\ \mu$m) is described by Eq. (1.32) with $K = 5.7(\text{kW})^{1/2}$-cm and $P_0 = 8$ kW. In this case, Δn is dominated by molecular reorientation; it obeys the dynamic equation

$$\left(\frac{\partial}{\partial t} + \frac{1}{\tau}\right)\Delta n = \frac{n_2}{\tau}|E\,(z,t)|^2. \tag{1.33}$$

For CS_2, $\tau = 2$ ps and $n_2 = 10^{-11}$ esu. The phase increment experienced by light waves traversing the cell along the axis is given by

$$\Delta\phi = \int_0^l (\omega/c)\,\Delta n\left[z, t' = t - (l-z)\,n_0/c\right]dz, \tag{1.34}$$

where l is the cell length. (For this illustrative example, we have neglected the diffraction effect on $\Delta\phi$.) We now simply assume that $|E(z,t)|^2$ in the focal region resulting from self-focusing has a pulse width of $\sim 3\tau$ and a pulse shape as shown in Fig. 1.8a. Equations (1.33) and (1.34) then allow us to find $\Delta n(z,t)$ and $\Delta\phi(t)$. Knowing $\Delta\phi(t)$ and $E(l,t)$, we can then calculate the spectrum of the output from the focal spot at the end of the cell, as shown in Fig. 1.8c. The experimentally observed spectrum has in fact the predicted spectral broadening (Shen & Loy, 1971; Wong & Shen, 1972), but it often has a strong central peak (Fig. 1.9). This is presumably because in the calculation we have neglected a significant portion of the beam that self-focuses from the periphery and experiences little phase modulation. For shorter input pulses of longer cells, self-focusing of the beam toward the end of the cell is more gradual; accordingly, the weakly phase-modulated part is less and the central peak in the spectrum is reduced. We also note that in Figs. 1.8 and 1.9 the anti-Stokes broadening is much weaker. This is because the negatively phase-modulated part of the pulse has little intensity, as seen in Fig. 1.8.

Using the picture sketched in Fig. 1.7, we can actually predict the Stokes broadening with the correct order of magnitude by the following rough estimate. We approximate the upper branch of the U curve toward the end of the medium by a straight line with a slope equal to the end velocity of the moving focus. If Δn is the induced refractive index in the shaded area, then the phase modulation of the emitted light is given by

$$\Delta\phi(t) \simeq \left(\frac{\omega_0}{c}\right)\left(\frac{n_0}{c} - \frac{1}{v}\right)^{-1}\int_{t_0}^{t} n\left(l, t'\right)dt', \tag{1.35}$$

where l is the length of the medium and t_0 is the time when $\Delta n(l,t)$ starts to become appreciable. The extent of Stokes broadening is readily obtained from

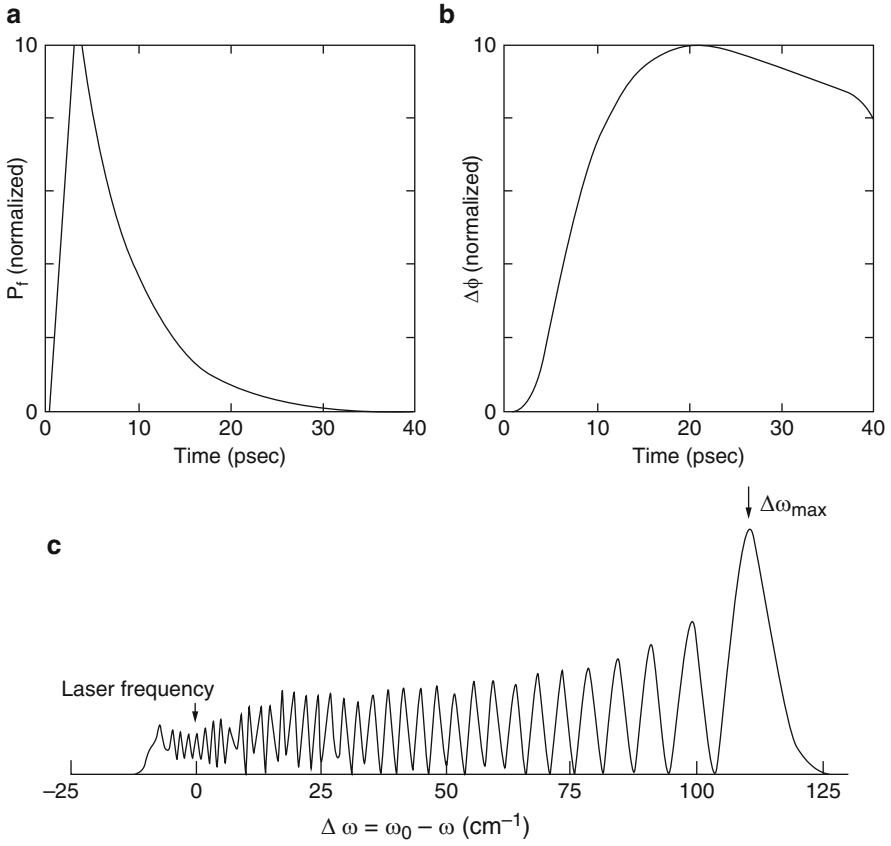

Fig. 1.8 Theoretical power spectrum of a light pulse emitted from the focal region of a moving focus at the end of a CS_2 cell. (**a**) The intensity pulse; (**b**) $\Delta\phi$ versus t; (**c**) the power spectrum (see text for details). (After Shen & Loy, 1971; Wong & Shen, 1972)

$$\Delta\omega_{-} = (\partial\ \Delta\phi/\partial t)_{max} \simeq \omega_0 Q \tag{1.36}$$

with $Q = \Delta n_{\max}\, l_{\text{eff}}/cT$ where $T \sim 2\tau$ and $l_{\text{eff}} = T/[(n_0/c) - (1/v)]$. For the above example with CS_2, we have $\Delta n_{\max} \sim 10^{-3}$, $T \sim 4$ ps, $l_{\text{eff}} \sim 1$ cm, and $Q \sim 0.01$. The resultant Stokes broadening should be $\Delta\omega_{-} \sim 150\ \text{cm}^{-1}$. The experimentally observed broadening is about $120\ \text{cm}^{-1}$.

1.5.2 Spectral Superbroadening of Ultrashort Pulses in Gases

The above discussion can be used to explain qualitatively the recently observed spectral superbroadening of ultrashort pulses in gas media (Corkum et al., 1986;

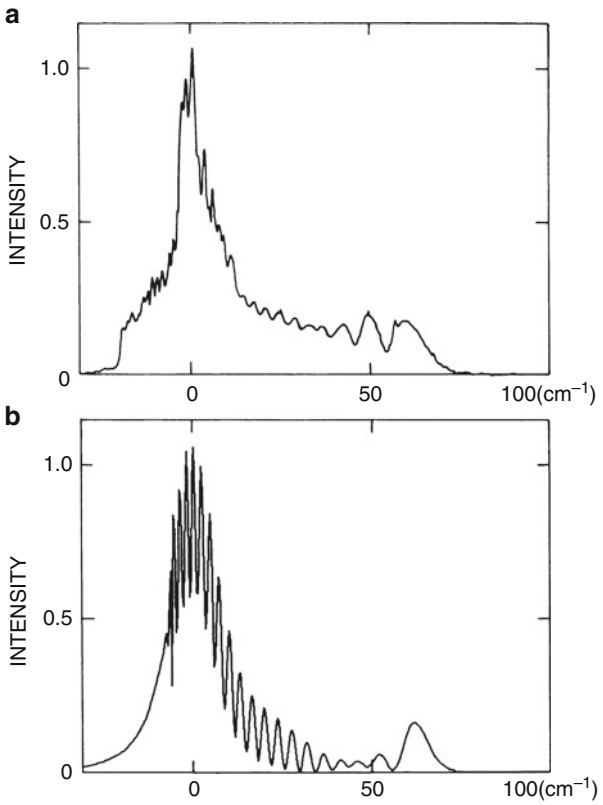

Fig. 1.9 (**a**) Experimentally observed power spectrum of light emitted from the focal region at the end of a 10-cm CS_2 cell; the input pulse has a pulse width of 1.2 ns and a peak power of 27 kW. (**b**) Theoretical power spectrum using the moving focus model (After Shen & Loy, 1971; Wong & Shen, 1972)

Glownia et al., 1986). In those experiments, picosecond or femtosecond laser pulses with energies of several hundred microjoules were weakly focused into a high-pressure gas cell. Spectral superbroadening with $\Delta\omega \sim 10^4$ cm^{-1} was observed. A few examples are shown in Fig. 1.10. Self-focusing was apparently present in the experiment. We therefore use the above simple model for SPM with quasisteady-state self-focusing to estimate the spectral broadening (Loy & Shen, 1973), assuming that Δn from the electronic contribution in the medium has a response time $\tau \sim 10$ fs. In this case, the position of the moving focus is given by (Marburger, 1975; Shen, 1975)

$$\left(z_f^{-1}(t) - f^{-1}\right)^{-1} = \frac{K}{\sqrt{P\,(t_R)} - \sqrt{P_0}} \tag{1.37}$$

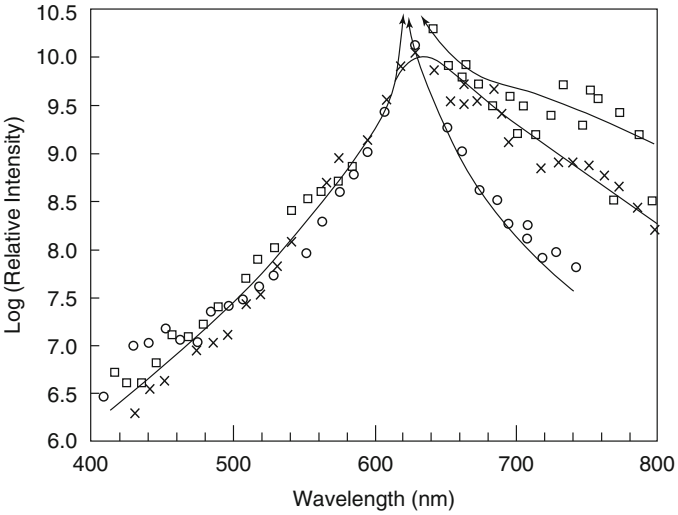

Fig. 1.10 Continuum spectra of self-phase-modulated light from 70-fs pulses in 30-atm xenon (crosses), 2-ps pulses in 15-atm xenon (circles), and 2-ps pulses in 40-atm nitrogen (squares). The cell length is 90 cm. (After Corkum et al., 1986)

instead of Eq. (1.32), where f is the focal length of the external focusing lens. Let us consider, for example, external focusing of a 250-μJ, 100-fs pulse to a nominally 100-μm focal spot in a 3-atm, 100-cm Xe cell. Self-focusing yields a smaller focus, assumed to be 50 μm. We then use the values $n_2 \sim 10^{-16}$ esu, $I \sim 10^{14}$ W/cm^2, $\Delta n_{\max} \sim 4 \times 10^{-5}$, $l_{\text{eff}} \sim 10$ cm, and $T \sim 2\tau \sim 20$ fs; we find $Q \sim 1$ and hence $\Delta\omega_{-} \sim 10^4$ cm^{-1}. The above estimate is admittedly very crude because of uncertainties in the experimental parameters, but it does give a spectral superbroadening in order-of-magnitude agreement with the experiments.

Appreciable anti-Stokes broadening was also observed in the superbroadened spectrum of the SPM light from a gas medium. This seems to be characteristically different from what we have concluded from the discussion in the previous subsection. However, we realize that in the present case the moving focus terminates at $z = f$ instead of the end of the cell, and the total transmitted light is detected and spectrally analyzed. Thus, the detected output pulse has essentially the same intensity envelope as the input pulse if we neglect the self-steepening effect, and the negatively phase-modulated part (the trailing edge) of the $\Delta\phi(t)$ pulse will overlap with the major part of the intensity pulse. Consequently, the spectral intensity of the anti-Stokes side should be nearly as strong as that of the Stokes side. The extent of the anti-Stokes broadening is expected to be somewhat less than that of the Stokes broadening because of the longer trailing edge of the $\Delta\phi$ pulse, unless the self-steepening effect becomes important.

Self-focusing in a gas medium should be more gradual than in a liquid cell. With weak external focusing, the focal dimensions resulting from combined external and

self-focusing may not be very different from those resulting from external focusing alone. Thus, even with self-focusing, the SPM output from the gas medium may not have a much larger diffraction angle than the linearly transmitted output, as was observed in the experiments.

1.5.3 Self-Phase Modulation with Transient Self-Focusing

We have used the picture of a moving focus with a trailing dielectric channel to describe SPM initiated by quasisteady-state self-focusing. For shorter input pulses, the velocity of the forward moving focal spot is closer to the light velocity, and consequently more light is expected to be trapped in the dielectric channel for a longer distance. In fact, when the pulse width is comparable to or shorter than the relaxation time τ, the entire self-focusing process becomes transient, and the input pulse will evolve into a dynamic trapping state (Loy & Shen, 1973).

The dynamic trapping model for transient self-focusing is an extension of the moving focus model for quasisteady-state self-focusing. Consider the case where Δn is governed by Eq. (1.33) or, more explicitly,

$$\Delta n\,(z,\xi) = \frac{1}{\tau}\int_{-\infty}^{\xi} n_2 \left|E\left(z,\xi'\right)\right|^2 \exp\left[-\left(\xi-\xi'\right)/\tau\right] d\xi', \tag{1.38}$$

where $\xi = t - zn_0/c$. Because of this transient response of Δn, the later part of the pulse propagating in the medium may see a larger Δn than the earlier part. As a result, different parts of the pulse will propagate in the medium differently, as sketched in Figure 1.11 (Loy & Shen, 1973). The transient Δn makes the very leading edge of the pulse diffract, the middle part self-focus weakly, and the lagging part self-focus to a limiting diameter. The result is that in propagating through the medium, the pulse is first deformed into a horn-shaped pulse and then the horn-shaped pulse propagates on with only a slight change of the pulse shape due to diffraction of the front edge. In a long medium, the front-edge diffraction finally could blow up the deformed pulse. Note that this picture comes in because in transient self-focusing, both focusing and diffraction are much more gradual, leading to a long longitudinal focal dimension and hence the rather stable horn-shaped propagating pulse. Such a stable form of self-focused pulse propagation is known as dynamic trapping.

Since the various parts of the light pulse see different Δn's along their paths, the phase increments $\Delta\phi$ they acquire are also different. This means phase modulation and hence spectral broadening. As an approximation, we can assume that the overall phase modulation is dominated by that of a stable horn-shaped pulse propagating in the nonlinear medium over a finite length l_{eff}. For illustration, let us take an example in which the horn-shaped pulse can be described by

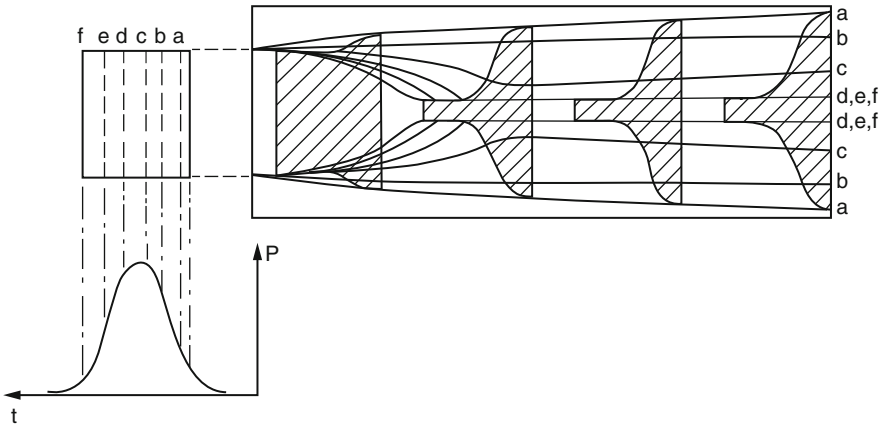

Fig. 1.11 Sketch showing self-focusing of an ultrashort pulse in a medium with a transient response of Δn. Different parts (a, b, c, etc.) of the pulse focus and defocus along different ray paths. The pulse is first deformed into a horn shape and then propagates on without much further change (After Loy & Shen, 1973)

$$|E\,(r,\xi)|^2 = A_0^2 \exp\left[-\xi^2 t_p^2 - 2r^2/r_0^2\,(\xi)\right] \tag{1.39}$$

with

$$\begin{aligned} r_0\,(\xi)\,/a &= 1 && \text{if } \xi \le \xi_1 \\ &= (1-\Delta)\,e^{-(\xi-\xi_1)/\tau_1} + \Delta && \text{if } \xi_1 \le \xi \le \xi_2 \\ &= (1-\Delta)\,e^{-(\xi_2-\xi_1)/\tau_1} + \Delta && \text{if } \xi \ge \xi_2, \end{aligned}$$

where $\xi = t - zn_0/c$. We have picosecond pulse propagation in Kerr liquids in mind and therefore choose $t_p = 1.25\tau, \xi_1 = 2.5\tau, \xi_2 = 2\tau, \tau_1 = \tau, \Delta = 0.05$, and $\tau = 2$ ps (for CS_2). We also choose the pulse intensity as $A_0^2 = 80\,(n_2/n_0)\,k^2a^2$, where k is the wave vector and the effective pulse propagation distance $l_{\text{eff}} = 0.15\,ka^{\,2}$. From the three-dimensional wave equation, it can be shown that the phase modulation obeys the equation

$$\partial\,(\Delta\phi)\,/\partial z = k\,(\Delta n/n_0) - 2/kr_0^2\,(\xi)\,. \tag{1.40}$$

The second term on the right of the equation is the diffractive contribution to $\Delta\phi$, which can be appreciable when r_0 is small. Knowing $|E(r, \xi)|^2$, we can find $\Delta n(z, \xi)$ from Eq. (1.38), and hence $\Delta\phi(z, \xi)$ from Eq. (1.40), and finally the broadened spectrum from $|E(r, \xi)|^2$, and $\Delta\phi(z, \xi)$ for $z = l_{\text{eff}}$, as shown in Figure 1.12.

The main qualitative result of the above calculation is that the spectrum has the quasiperiodic structure with nearly equal Stokes and anti-Stokes broadening, although the Stokes side is more intense. This agrees with the experimental observation (Cubbedu et al., 1971; Cubbedu & Zagara, 1971) and the more

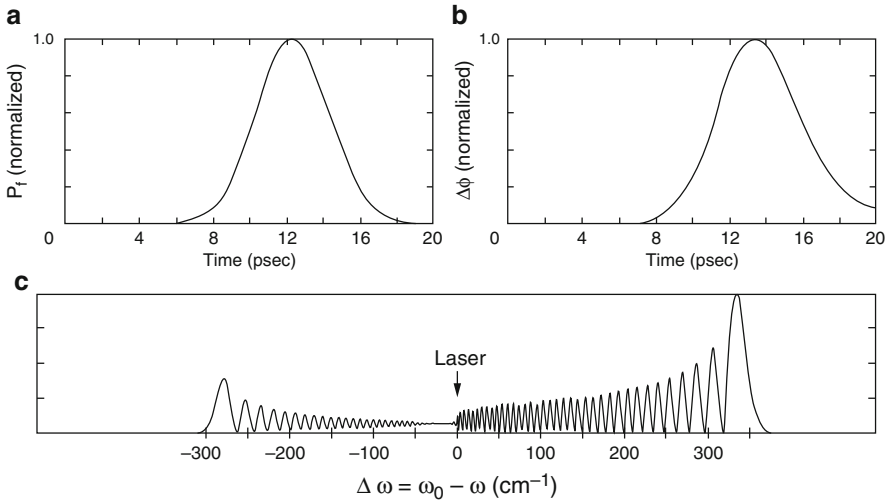

Fig. 1.12 Theoretical power spectrum obtained by assuming a horn-shaped pulse propagating for a certain distance in a nonlinear medium without any change in its shape. (**a**) Normalized intensity output pulse; (**b**) $\Delta\phi$ versus t; (**c**) power spectrum of the output (After Loy & Shen, 1973)

detailed numerical calculation of Shimizu and Courtens (1973). The reason is as follows. The Stokes–anti-Stokes symmetry results from a symmetric $\Delta\phi(t)$ pulse that overlaps well with the intensity pulse. The neck portion of the horn-shaped pulse with $\partial(\Delta\phi)/\partial t < 0$ contributes to the anti-Stokes broadening. As seen in Eq. (1.40), the time dependence of $\Delta\phi$ comes solely from the time dependence in $\left(\Delta n/n_0 - 2/k^2 r_0^2\right)$. Without the diffraction term $\left(-1/k^2 r_0^2\right)$, the $\Delta\phi$ pulse would have a longer trailing edge because of the relaxation of Δn. With the diffraction term, the rapid reduction of r_0 toward the neck makes the $\Delta\phi$ pulse more symmetric. Thus, it appears that the dynamic trapping model explains fairly well the qualitative features of SPM and spectral broadening initiated by transient self-focusing. The broadening is more extensive with more intense input pulses and longer propagation lengths. In a long medium, dynamic trapping may exist only over a limit section of the medium. In that case, the spectrally broadened light may seem to have originated from a source inside the medium. This has also been observed experimentally (Ho et al., 1987).

1.6 Conclusion

We have seen that the temporal SPM and the concomitant spectral broadening of light arise because an intense optical field can induce an appreciable refractive index change Δn in a medium. The theory of pure SPM is, in principle, quite straightforward. If the input pulse intensity is not very strong, the zeroth-order

approximation taking into account only the direct contribution of Δn to the induced phase change $\Delta\phi$ should already give a fairly good description. The next-order approximation including the self-steepening effect on both $\Delta\phi$ and the amplitude pulse should satisfactorily cover the cases of strong SPM with spectral superbroadening.

Unfortunately, the temporal SPM is often complicated by the spatial SPM. The latter can lead to self-focusing, which dramatically alters the intensity distributions of the laser pulse in space and time and therefore drastically modifies the temporal SPM. In fact, in most practical cases, self-focusing occurs long before the temporal SPM becomes appreciable; it is actually self-focusing that increases the beam intensity in the medium and thus initiates a strong SPM in time. Only by using an optical waveguide or a very thin nonlinear medium can self-focusing be avoided. These are then the only experimental cases where a pure temporal SPM has been realized.

In the pure SPM case, the theoretical difficulty is in the description of Δn: it is not easy, in general, to predict quantitatively the nonlinear response of a medium from first principles; one must rely on experimental measurements. Quantitative measurements of $\Delta n(t)$ in the picosecond and femtosecond domains are still rare. In particular, measurements of Δn with femtosecond time resolution are still rather difficult. The various low-frequency resonances could make the time dependence of Δn very complex. Inclusion of the transient response of Δn (or the dispersion of Δn) in the theory complicates the calculation; one may have to resort to numerical solution of the problem. Experimentally, SPM of laser pulses in optical fibers has been well studied; SPM of ultrashort pulses in thin nonlinear media is, however, still not well documented. More careful quantitative measurements are needed in order to have a more detailed comparison with theory.

With self-focusing, the theory of SPM becomes extremely complex. The main difficulty lies in the fact that a quantitative theory capable of describing the details of self-focusing is not yet available. We must then rely on the more qualitative physical pictures for self-focusing. Therefore, the discussion of the subsequently induced SPM can be at most semiquantitative. Thus, we find it quite satisfying that the predicted spectral broadening from such theoretical discussions can give order-of-magnitude agreement with the experimental observations in a number of very different cases: nanosecond pulse propagation in liquids to pico- or femtosecond pulse propagation in gases.

Spectral superbroadening is often observed with the propagation of ultrashort pulses in condensed media and is apparently initiated by self-focusing. In most cases, the details of the self-focusing process have not been measured; in some cases, even the quantitative information on Δn is not available. The measurements on spectral broadening also tend to show strong fluctuations. All these made even an order-of-magnitude comparison between theory and experiment rather difficult.

A complete theory of SPM with self-focusing requires the solution of a time-dependent three-dimensional wave equation. With self-focusing modifying the laser pulse rapidly in both space and time, such a solution, even on the largest computer, is a formidable task. In our opinion, the best way to tackle the problem is to try

to simplify the calculation by reasonable approximations derived from the physical picture that has already been established for self-focusing.

Acknowledgments This work was supported by the Director, Office of Energy Research, Office of Basic Energy Sciences, Materials Sciences Division of the U.S. Department of Energy under Contract No. DE-AC03-76SF00098.

References

Alfano, R. R., & Shapiro, S. L. (1970) Emission in the region 4000–7000 A via four-photon coupling in glass; observation of self-phase modulation and small scale filaments in crystals and glasses; direct distortion of electronic clouds of rare-gas atoms in intense electric fields. Physical Review Letters 24, 584, 592, 1219.

Alfano, R. R., & Shapiro, S. L. (1971). Picosecond spectroscopy using the inverse Raman effect. *Chemical Physics Letters, 8*, 631.

Alfano, R. R., Li, Q., Jimbo, T., Manassah, J. T., & Ho, P. P. (1986). Induced spectral broadening of a weak picosecond pulse in glass produced by an intense picosecond pulse. *Optics Letters, 11*, 626.

Alfano, R. R., Wang, Q., Jimbo, T., & Ho, P. P. (1987). Induced spectral broadening about a second harmonic generated by an intense primary ultrashort laser pulse in ZuSe. *Physical Review A, 35*, 459.

Bloembergen, N., & Lallemand, P. (1966). Complex intensity-dependent index of refraction, frequency broadening of stimulated Raman lines, and stimulated Rayleigh scattering. *Physical Review Letters, 16*, 81.

Brewer, R. G. (1967). Frequency shifts in self-focusing light. *Physical Review Letters, 19*, 8.

Busch, G. E., Jones, R. P., & Rentzepis, P. M. (1973). Picosecond spectroscopy using a picosecond continuum. *Chemical Physics Letters, 18*, 178.

Cheung, A. C., Rank, D. M., Chiao, R. Y., & Townes, C. H. (1968). Phase modulation of Q-switched laser beams in small-scale filaments. *Physical Review Letters, 20*, 786.

Corkum, P. B., Ho, P. P., Alfano, R. R., & Manassah, J. T. (1985). Generation of infrared supercontinuum covering 3–14 μm in dielectrics and semiconductors. *Optics Letters, 10*, 624.

Corkum, P. B., Rolland, C., & Rao, T. (1986). Supercontinuum generation in gases. *Physical Review Letters, 57*, 2268.

Cubbedu, R., & Zagara, F. (1971). Nonlinear refractive index of CS_2 in small-scale filaments. *Optics Communication, 3*, 310.

Cubbedu, R., Polloni, R., Sacchi, C. A., Svelto, O., & Zagara, F. (1971). Study of small-scale filaments of light in CS_2 under picosecond excitation. *Physical Review Letters, 26*, 1009.

DeMartini, F., Townes, C. H., Gustafson, T. K., & Kelley, P. L. (1967). Self-steepening of light pulses. *Physics Review, 164*, 312.

Durbin, S. D., Arakelian, S. M., & Shen, Y. R. (1981). Laser-induced diffraction rings from a nematic liquid crystal film. *Optics Letters, 6*, 411.

Fabellinski, I. L. (1967). *Molecular scattering of light*. Plenum, Chapter VIII.

Fisher, R. A., & Bischel, W. (1975). Numerical studies of the interplay between self-phase modulation and dispersion for intense plane-wave light pulses. *Journal of Applied Physics, 46*, 4921.

Fisher, R. A., Suydam, B., & Yevich, D. (1983). Optical phase conjugation for time domain undoing of dispersive self-phase modulation effects. *Optics Letters, 8*, 611.

Fork, R. L., Shank, C. V., Hirliman, C., & Yen, R. (1983). Femtosecond white-light continuum pulses. *Optics Letters, 8*, 1.

Fork, R. L., Brito Cruz, C. H., Becker, P. C., & Shank, C. V. (1987). Compression of optical pulses to six femtoseconds by using cubic phase compensation. *Optics Letters, 12*, 483.

Glownia, J., Arjavalingam, G., Sorokin, P., & Rothenberg, J. (1986). Amplification of 350-fs pulses in XeCl excimer gain modules. *Optics Letters, 11*, 79.

Gustafson, T. K., Taran, J. P., Haus, H. A., Lifsitz, J. R., & Kelley, P. L. (1969). Self-phase modulation, self steepening, and spectral development of light in small-scale trapped filaments. *Physics Review, 177*, 306.

Hellwarth, R. W. (1970). Theory of molecular light scattering spectra using the linear-dipole approximation. *The Journal of Chemical Physics, 52*, 2128.

Hellwarth, R. W. (1977). Third-order optical susceptibilities of liquids and solids. *Progress in Quantum Electronics, 5*, 1.

Ho, P. P., Li, Q. X., Jimbo, T., Ku, Y. L., & Alfano, R. R. (1987). Supercontinuum pulse generation and propagation in a liquid CCl_4. *Applied Optics, 26*, 2700.

Ippen, E. P., & Shank, C. V. (1975). Dynamic spectroscopy and subpicosecond pulse compression. *Applied Physics Letters, 27*, 488.

Jones, W. J., & Stoicheff, B. P. (1964). Induced absorption at optical frequencies. *Physical Review Letters, 13*, 657.

Lallemand, P. (1996). Temperature variation of the width of stimulated Raman lines in liquids. *Applied Physics Letters, 8*, 276.

Loy, M. M. T., & Shen, Y. R. (1973). Study of self-focusing and small-scale filaments of light in nonlinear media. *IEEE Journal of Quantum Electronics, 9*, 409.

Manassah, J. T., Shapiro, R. R., & Mustafa, M. (1985). Spectral distribution of an ultrashort supercontinuum laser source. *Physics Letters, A107*, 305.

Manassah, J. T., Mustafa, M. A., Alfano, R. R., & Ho, P. P. (1986). Spectral extent and pulse shape of the supercontinuum for ultrashort laser pulse. *IEEE Journal of Quantum Electronics, 22*, 197.

Marburger, J. H. (1975). Self-focusing: Theory. *Progress in Quantum Electronics, 4*, 35.

Nakatsuka, H., & Grischkowsky, D. (1981). Recompression of optical pulses broadened by passage through optical fibers. *Optics Letters, 6*, 13.

Nakatsuka, H., Grischkowsky, D., & Balant, A. C. (1981). Nonlinear picosecond pulse propagation through optical fibers with positive group velocity dispersion. *Physical Review Letters, 47*, 910.

Nikolaus, B., & Grischkowsky, D. (1983a). 12× pulse compression using optical fibers. *Applied Physics Letters, 42*, 1.

Nikolaus, B., & Grischkowsky, D. (1983b). 90-fs tunable optical pulses obtained by two-state pulse compression. *Applied Physics Letters, 43*, 228.

Penzkofer, A. (1974). Parametrically generated spectra and optical breakdown in H_2O and NaCl. *Optics Communication, 11*, 265.

Penzkofer, A., Laubereau, A., & Kaiser, W. (1973). Stimulated short-wave radiation due to single-frequency resonances of $\chi^{(3)}$. *Physical Review Letters, 31*, 863.

Penzkofer, A., Seilmeier, A., & Kaiser, W. (1975). Parametric four-photon generation of picosecond light at high conversion efficiency. *Optics Communication, 14*, 363.

Santamato, E., & Shen, Y. R. (1984). Field curvature effect on the diffraction ring pattern of a laser beam dressed by spatial self-phase modulation in a nematic film. *Optics Letters, 9*, 564.

Shen, Y. R. (1966). Electrostriction, optical Kerr effect, and self-focusing of laser beams. *Physics Letters, 20*, 378.

Shen, Y. R. (1975). Self-focusing: Experimental. *Progress in Quantum Electronics, 4*, 1.

Shen, Y. R. (1984). *The principles of nonlinear optics*. Wiley. Chapters 1 and 16.

Shen, Y. R., & Loy, M. M. T. (1971). Theoretical investigation of small-scale filaments of light originating from moving focal spots. *Physical Review A, 3*, 2099.

Shimizu, F. (1967). Frequency broadening in liquids by a short light pulse. *Physical Review Letters, 19*, 1097.

Shimizu, F., & Courtens, E. (1973). Recent results on self-focusing and trapping. In M. S. Feld, A. Javan, & N. A. Kurnit (Eds.), *Fundamental and applied laser physics* (p. 67). Wiley.

Stoicheff, B. P. (1963). Characteristics of stimulated Raman radiation generated by coherent light. *Physics Letters, 7*, 186.

Stolen, R., & Lin, C. (1978). Self-phase modulation in silica optical fibers. *Physical Review A, 17*, 1448.

Topp, M. R., & Rentzepis, P. M. (1971). Time-resolved absorption spectroscopy in the 10^{-12}-sec range. *Journal of Applied Physics, 42*, 3415.

Treacy, E. P. (1968). Compression of picosecond light pulses. *Physics Letters, 28A*, 34.

Treacy, E. P. (1969a). Measurements of picosecond pulse substructure using compression techniques. *Applied Physics Letters, 14*, 112.

Treacy, E. P. (1969b). Optical pulse compression with diffraction gratings. *IEEE Journal of Quantum Electronics, 5*, 454.

Wong, G. K. L., & Shen, Y. R. (1972). Study of spectral broadening in a filament of light. *Applied Physics Letters, 21*, 163.

Yang, G., & Shen, Y. R. (1984). Spectral broadening of ultrashort pulses in a nonlinear medium. *Optics Letters, 9*, 510.

Chapter 2
Supercontinuum Generation in Condensed Matter

Q. Z. Wang, P. P. Ho, and Robert R. Alfano

Abstract Self-phase modulation (**SPM**), induced-phase modulation (**IPM**), and cross-phase modulation (**XPM**) for supercontinuum generation are presented. Early day experimental measurements of supercontinuum in various materials are reviewed. Recent developments of supercontinuum generation covering from deep ultraviolet to far-infrared spectra are summarized in this chapter.

Keywords SPM · XPM · Supercontinuum · Nonlinear index of refraction · n_2

2.1 Introduction

Supercontinuum generation, the production of intense ultrafast broadband "white light" pulses, arises from the propagation of intense picosecond or shorter laser pulses through condensed or gaseous media. Various processes are responsible for continuum generation. These are called self-, induced-, and cross-phase modulations and four-photon parametric generation. Whenever an intense laser pulse propagates through a medium, it changes the refractive index, which in turn changes the phase, amplitude, and frequency of the incident laser pulse. A phase change can cause a frequency sweep within the pulse envelope. This process has been called *self-phase modulation (**SPM**)* (Alfano & Shapiro, 1970a). Nondegenerate *four-*

Q. Z. Wang (✉)
Technology Center 2600, United States Patent and Trademark Office, Alexandria, VA, USA
e-mail: quan-zhen.wang@uspto.gov

P. P. Ho
Department of Electrical Engineering, The City College of the City University of New York, New York, NY, USA
e-mail: pho@ccny.cuny.edu

R. R. Alfano
Department of Physics, The City College of the City University of New York, New York, NY, USA
e-mail: ralfano@ccny.cuny.edu

R. R. Alfano (ed.), *The Supercontinuum Laser Source*,
https://doi.org/10.1007/978-3-031-06197-4_2

*photon parametric generation (**FPPG**)* usually occurs simultaneously with the **SPM** process (Alfano & Shapiro, 1970a). Photons at the laser frequency parametrically generate photons to be emitted at Stokes and anti-Stokes frequencies in an angular pattern due to the required phase-matching condition. When a coherent vibrational mode is excited by a laser, stimulated Raman scattering (**SRS**) occurs. **SRS** is an important process that competes and couples with **SPM**. The interference between **SRS** and **SPM** causes a change in the emission spectrum resulting in *stimulated Raman scattering cross-**phase** modulation (**SRS-XPM**)* (Gersten et al., 1980). A process similar to **SRS-XPM** occurs when an intense laser pulse propagates through a medium possessing a large second-order χ^2 and third-order χ^3 susceptibility. Both second harmonic generation (**SHG**) and **SPM** occur and can be coupled together. The interference between **SHG** and **SPM** alters the emission spectrum and is called *second harmonic generation cross-phase modulation (**SHG-XPM**)* (Alfano et al., 1987). A process closely related to **XPM**, called *induced phase modulation (**IPM**)* (Alfano, 1986), occurs when a weak pulse at a different frequency propagates through a disrupted medium whose index of refraction is changed by an intense laser pulse. The phase of the weak optical field can be modulated by the time variation of the index of refraction originating from the primary intense pulse.

The first study of the generation and mechanisms of the ultrafast supercontinuum dates back to the years 1968–1972, when Alfano and Shapiro first observed the "white" picosecond continuum in liquids and solids (Alfano & Shapiro, 1970a). Spectra extending over ~6000 cm^{-1} in the visible and infrared wavelength region were observed. Over the years, improvements in the generation of ultrashort pulses from mode-locked lasers led to the production of wider supercontinua in the visible, ultraviolet, and infrared wavelength regions using various materials. Table 2.1 highlights the major accomplishments in this field over the past 20 years.

In this chapter, we focus on the picosecond supercontinuum generation in liquids, solids, and crystals. Supercontinuum generation in gases, **XPM**, and **IPM** is discussed by Corkum and Rolland (Chap. 7), Glownia et al. (Chap. 8), Baldeck et al. (Chap. 4), Agrawal (Chap. 3), and Manassah (Chap. 5), respectively.

2.2 Simplified Model

Before we go further, let us first examine the nonlinear wave equation to describe the self-phase modulation mechanism. A thorough theoretical study of supercontinuum generation has been dealt with in Chaps. 1, 3, and 5.

Table 2.1 Brief history of experimental continuum generation

Investigator	Year	Material	Laser wavelength/pulse width	Spectrum	Frequency (cm^{-1})	Process
Alfano, Shapiro	1968–1973	Liquids and solids	530 nm/8 ps or 1060 nm/8 ps	Visible and near **IR**	6000	**SPM**
Stolen et al.	1974–1976	Fibers	530 nm/ns	Visible UV,	500	**SPM**
Shank, Fork et al.	1983	Glycerol	620 nm/100 fs	visible, near **IR**	10,000	**SPM**
Corkum, Ho, Alfano	1985	Semiconductors Dielectrics	10 μm/6 ps	**IR**	1000	**SPM**
Corkum, Sorokin	1986	Gases	600 nm/2 ps 300 nm/0.5 ps	Visible and UV	5000	**SPM**
Alfano, Ho, Manassah, Jimbo	1986	Glass	1060 nm/530 nm/8 ps	Visible	1000	**IPM** (**XPM**)
Alfano, Ho, Wang, Jimbo	1986	ZnSe	1060 nm/8 ps	Visible	1000	**SHG-XPM** (**ISB**)
Alfano, Ho, Baldeck	1987	Fibers	530 nm/30 ps	Visible	1000	**SRS-XPM**

The optical electromagnetic field of a supercontinuum pulse satisfies Maxwell's equations:

$$\begin{aligned} \nabla \times \mathbf{E} &= -\tfrac{1}{c}\tfrac{\partial \mathbf{B}}{\partial t}, \\ \nabla \times \mathbf{H} &= \tfrac{1}{c}\tfrac{\partial \mathbf{D}}{\partial t} + \tfrac{4\pi}{c}\mathbf{J}, \\ \nabla \cdot \mathbf{D} &= 4\pi\rho \\ \nabla \cdot \mathbf{B} &= 0. \end{aligned} \tag{2.1}$$

Equations (2.1) can be reduced to (see Appendix)

$$\frac{\partial A}{\partial z} + \frac{1}{v_g}\frac{\partial A}{\partial t} = i\frac{\omega_0 n_2}{2c}|A|^2 A, \tag{2.2}$$

where $A(z, t)$ is the complex envelope of the electric field and $v_g = 1/(\partial k/\partial\omega)_{\omega_0}$ is the group velocity. The total refractive index n is defined by $n^2 = n_0^2 + 2n_0 n_2|A(t)|^2$, where n_2 is the key parameter called the nonlinear refractive index. This coefficient is responsible for a host of nonlinear effects: self- and cross-phase modulation, self-focusing, and the optical Kerr effect, to name the important effects. Equation (2.2) was derived using the following approximations: (1) linearly polarized electric field, (2) homogeneous radial fields, (3) slowly varying envelope, (4) isotropic and nonmagnetic medium, (5) negligible Raman effect, (6) frequency-independent nonlinear susceptibility $\chi^{(3)}$, and (7) neglect of group velocity dispersion, absorption, self-steepening, and self-frequency shift.

Denoting by a and α the amplitude and phase of the electric field envelope $A = ae^{i\alpha}$, Eq. (2.2) reduces to

$$\frac{\partial a}{\partial z} + \frac{1}{v_g}\frac{\partial a}{\partial t} = 0 \tag{2.3a}$$

and

$$\frac{\partial \alpha}{\partial z} + \frac{1}{v_g}\frac{\partial \alpha}{\partial t} = \frac{\omega_0 n_2}{2c}a^2. \tag{2.3b}$$

The analytical solutions for the amplitude and phase are

$$a(\tau) = a_0 F(\tau) \tag{2.4a}$$

and

$$\alpha(z, \tau) = \frac{\omega_0 n_2}{2c}\int_0^z a^2 dz' = \frac{\omega_0 n_2}{2c}a_0^2 F^2(\tau)\, z, \tag{2.4b}$$

where a_0 is the amplitude, $F(\tau)$ the pulse envelope, and τ the local time $\tau = t - z/v_g$. For materials whose response time is slower than pure electronic but faster than

molecular orientation (i.e., coupled electronic, molecular redistribution, libratory motion), the envelope is just the optical pulse shape. For a "pure" electronic response, the envelope should also include the optical cycles in the pulse shape.

The electric field envelope solution of Eq. (2.2) is given by

$$A(z,\tau) = a(\tau)\exp\left[i\frac{\omega_0 n_2}{2c}a_0^2 F^2(\tau)\,z\right]. \tag{2.5}$$

The main physics behind the supercontinuum generation by self-phase modulation is contained in Eq. (2.5) and is displayed in Fig. 2.1. As shown in Fig. 2.1a, the index change becomes time dependent, and therefore, the phase of a pulse propagating in a distorted medium becomes time dependent, resulting in self-phase modulation. The electric field frequency is continuously shifted (Fig. 2.1c) in time. This process is most important in the generation of femtosecond pulses (see Chap. 10 by Johnson and Shank).

Since the pulse duration is much larger than the optical period $2\pi/\omega_0$ (slowly varying approximation), the electric field at each position τ within the pulse has a specific *local* and *instantaneous frequency* at given time that is given by

$$\omega(\tau) = \omega_0 + \delta\omega(\tau), \tag{2.6a}$$

where

$$\delta\omega(\tau) = -\frac{\partial\alpha}{\partial\tau} = -\frac{\omega_0}{2c}n_2 a_0^2 z\frac{\partial F^2(\tau)}{\partial\tau}. \tag{2.6b}$$

The $\delta\omega(\tau)$ is the frequency shift generated at a particular time location τ within the pulse shape. This frequency shift is proportional to the derivative of the pulse envelope, which corresponds to the generation of new frequencies resulting in wider spectra.

Pulses shorter than the excitation pulse can be produced at given frequencies. It was suggested by **Y.R.** Shen many years ago that Alfano and Shapiro in 1970 most likely produced femtosecond pulses via supercontinuum generation. Figure 2.1c shows the frequency distribution within the pulse shape. The leading edge, the pulse peak, and the trailing edge are red shifted, nonshifted, and blue shifted, respectively.

The spectrum of **SPM** pulses is obtained by taking the Fourier transform of the complex temporal envelope $A(z, \tau)$:

$$A(\Omega) = \frac{1}{2\pi}\int_{-\infty}^{\infty} A(z,\tau)\exp[i\Omega\tau]\,d\tau, \tag{2.7}$$

Where $\Omega = \omega - \omega_0$. The intensity spectrum is given by

$$S(\Omega z) = \frac{c}{4\pi}|A(\Omega, z)|^2. \tag{2.8}$$

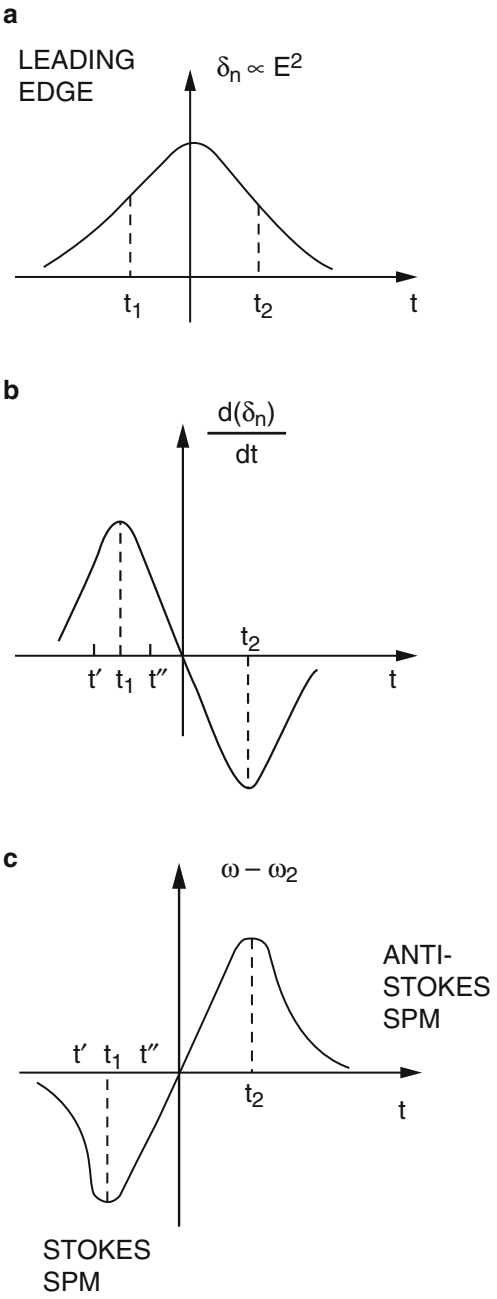

Fig. 2.1 A simple mechanism for **SPM** for a nonlinear index following the envelope of a symmetrical laser pulse: (**a**) time-dependent nonlinear index change; (**b**) time rate of change of index change; (**c**) time distribution of **SPM**-shifted frequencies $\omega(t) - \omega_0$

In practical cases, the phase of $A(z, \tau)$ is large compare with π, and the stationary phase method leads to

$$\omega(z)_{\max} = \frac{\omega_0}{2c} n_2 a_0^2 \left[\left. \frac{\partial F^2}{\partial \tau} \right|_{\tau_1} - \left. \frac{\partial F^2}{\partial \tau} \right|_{\tau_2} \right] z. \tag{2.9}$$

The intensity

$$\begin{aligned} S(\Omega, z) = & \left(\tfrac{c}{4\pi}\right)\left(\tfrac{4\pi c}{\omega_0 n_2 z}\right)\left\{ F^2(\tau') / \left. \tfrac{\partial F^2}{\partial \tau^2} \right|_{\tau'} + F^2(\tau'') / \left. \tfrac{\partial^2 F^2}{\partial \tau^2} \right|_{\tau''} \right. \\ & + 2 \tfrac{F(\tau') F(\tau'')}{\left[\left. \partial^2 F^2 / \partial \tau^2 \right|_{\tau'} \left. \partial^2 F^2 / \partial \tau^2 \right|_{\tau''} \right]^{1/2}} \\ & \left. \times \cos\left[\Omega(\tau' - \tau'') + \tfrac{\omega_0}{2c} n_2 a_0^2 z \left(F^2(\tau') - F^2(\tau'') \right) \right] \right\}, \end{aligned} \tag{2.10}$$

where $\Delta\omega_{\max}$ is the maximum frequency spread, τ_1 and τ_2 are the pulse envelope inflection points, and τ' and τ'' are the points of the pulse shape that have the same frequency.

An estimate of the modulation frequency $\delta\omega_M$ can be made by calculating the maximum number of interference minima and dividing this number into the maximum frequency broadening. A straightforward calculation leads to

$$\delta\omega_M \approx 2\pi \left. \frac{\partial F^2}{\partial \tau} \right|_{\tau_1} / F^2(\tau_1) \approx 2\pi \left. \frac{\partial F^2}{\partial \tau} \right|_{\tau_2} / F^2(\tau_2). \tag{2.11}$$

For a Gaussian laser pulse given by

$$F(\tau) = \exp\left[-\tau^2 / 2\tau_0^2 \right], \tag{2.12}$$

the modulation frequency of the **SPM** spectrum is (Alfano, 1972)

$$\delta\omega_M = \frac{4\pi}{\tau_0} \text{or } \delta\,\overline{v}_M = \frac{2}{\tau_0 c}. \tag{2.13}$$

Using this relation, the average modulation period of 13 cm^{-1} corresponds to an initial pulse duration of 5 ps emitted from mode-locked Nd: glass laser. The maximum frequency extent in this case is (Alfano, 1972)

$$\Delta\omega_{\max} \approx \frac{\omega_0 n_2 a_0^2 z}{c\tau_0}. \tag{2.14}$$

The maximum frequency shift (Eq. 2.14) indicates the following salient points:

- The frequency extent is inversely proportional to the pumping pulse duration. The shorter the incoming pulse, the greater the frequency extent. The first white

light band supercontinuum pulses were generated using picosecond laser pulses (Alfano & Shapiro, 1970a, b).
- The spectral broadening is proportional to n_2. The supercontinuum generation can be enhanced by increasing the nonlinear refractive index. This is discussed in detail in Sect. 2.6.
- The spectral broadening is linearly proportional to amplitude a_0^2. Therefore, multiple-excitation laser beams of different wavelengths may be used to increase the supercontinuum generation. This leads to the basic principle behind **IPM** and **XPM**. These processes are described by Baldeck et al. (Chap. 4) and Manassah (Chap. 5).
- The spectral broadening is proportional to ω_0 and z.

The chirp – the temporal distribution of frequency in the pulse shape – is an important characteristic of **SPM** broadened pulse. In the linear chirp approximation, the chirp coefficient C is usually defined by the phase relation

$$\alpha = C\tau^2. \tag{2.15}$$

For a Gaussian electric field envelope and linear approximation, the envelope reduces to

$$F^2(\tau) = \exp\left[-\tau^2/\tau_0^2\right] \approx 1 - \tau^2/\tau_0^2. \tag{2.16}$$

The linear chirp coefficient derived from Eqs. (2.5) and (2.16) becomes

$$C = \left(\frac{\omega_0}{2c}\right)\left(\frac{n_2 a_0^2 z}{\tau_0^2}\right). \tag{2.17}$$

Typical calculated **SPM** spectra are displayed in Fig. 2.2. The spectral densities of the **SPM** light are normalized, and β is defined as $\beta = \left(n_2 a_0^2 \omega_0 z\right)/2c$, which measures the strength of the broadening process. Figure 2.2a shows the spectrum for a material response time slower than pure electronic but faster than molecular orientation for $\beta = 30$ and $\tau = 0.1$ ps. The extent of the spectrum is about 7000 cm^{-1}. Figure 2.2b shows the **SPM** spectrum for a quasipure electronic response for $\beta = 30$ and $\tau = 0.1$ ps. Typical **SPM** spectral characteristics are apparent in these spectra.

2.3 Experimental Arrangement for SPM Generation

To produce the supercontinuum, an ultrafast laser pulse is essential with a pulse duration in the picosecond and femtosecond time region. A mode-locked laser is used to generate picosecond and femtosecond light pulses. Table 2.2 lists the available mode-locked lasers that can produce picosecond and femtosecond laser

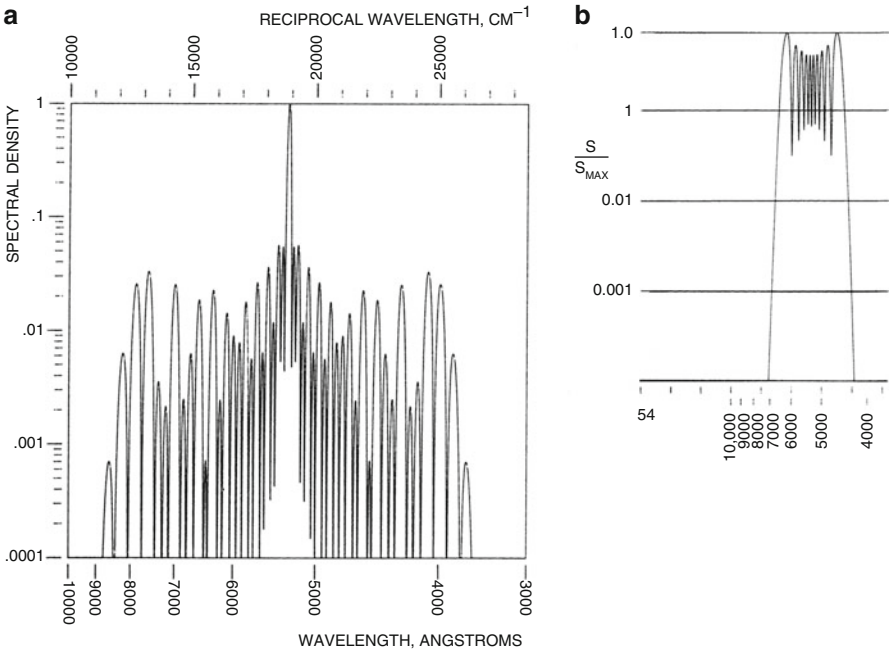

Fig. 2.2 Calculated **SPM** spectrum: (**a**) for response time slower than pure electronic but faster than molecular orientation: $\beta = 30$ and $\tau = 0.1$ ps; (**b**) for pure electronic response: $\beta = 30$ and $\tau = 0.1$ ps. (From Alfano, 1972)

Table 2.2 Available ultrafast mode-locked lasers

Oscillator	Wavelength (nm)	Pulse duration
Ruby	694.3	30 ps
YAG	1064	30 ps
Silicate glass	1060	8 ps
Phosphate glass	1054	6 ps
Dye	Tunable (SYNC or flash lamp)	5–10 ps
Dye + CO_2 + semiconductor switches	9300	1–10 ps
Dye (CPM)	610–630	100 fs
Dye + pulse compression (SYNC)	Tunable	300 fs
Dye + CPM (prisms in cavity)	620	27–60 fs
Dye + SPM + pulse compression (prisms and grating pairs)	620	6–10 fs

pulses. Measurements performed in the 1970s used a mode-locked Nd:glass laser with output at 1.06 μm with power of ~5×10^9 W and the second harmonic (**SHG**) at 530 nm with power of 2×10^8 W. Typically, one needs at least a few microjoules of 100-fs pulse passing through a 1-mm sample to produce continuum.

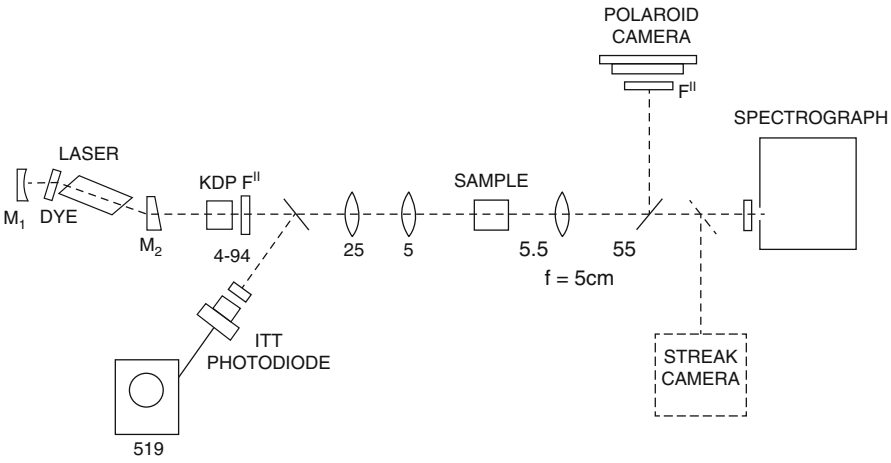

Fig. 2.3 Experimental arrangement for generating and observing supercontinuum and self-focusing. (From Alfano, 1972)

A typical experimental setup for ultrafast supercontinuum generation is shown in Fig. 2.3. Both spectral and spatial distributions are measured. The 8-ps **SHG** pulse of 5 mJ is reduced in size to a collimated 1.2-mm-diameter beam across the sample by an inverted telescope. For weaker excitation pulses, the beam is focused into the sample using a 10- to 25-cm focal lens. The typical sample length used is 10–15 cm for picosecond pulses and 0.1–1 cm for 100-f pulses. The intensity distribution of the light at the exit face of the sample was magnified 10 times and imaged on the slit of a spectrograph. The spectrum of each individual filament within the slit was displayed. Usually, there were 5–20 filaments. A thin quartz-wedge beam splitter was used to photograph filament formation of the Stokes (anti-Stokes) side of the spectra; three type 3–68 and three type 3–67 (two type 5–60) Corning filters were used to prevent the 530-nm direct laser light from entering the spectrograph. To reduce nonfilament light, a wire 2 mm in diameter was sometimes placed at the focal point of the imaging lens. Previously, spectra were taken on Polaroid type 57 film. At present, video systems such as an Silicon-intensified target (**SIT**) camera together with a **PC** computer are commonly used to display the spectra. Today, to obtain temporal information about the supercontinuum, a streak camera is added to the experimental system.

2.4 Generation of Supercontinuum in Solids

In the following sections, we review the experimental measurements of supercontinuum generated in condense matter. Topics discussed include supercontinuum

generation in various kinds of solids and liquids, optical glass fibers, liquid argon, liquid and solid krypton, magnetic crystals, and dielectric crystals.

The mechanisms behind **SPM** are discussed in Chap. 1 by Shen and Yang. In general, various mechanisms are responsible for **SPM** in condensed matter and give rise to the coefficient of the intensity-dependent refractive index n_2. These are the orientational Kerr effect, electrostriction, molecular redistribution, librations, and electronic distribution. In suitably chosen media (central-symmetric molecules), these frequency-broadening mechanisms may be distinguished from the electronic mechanism through their different time responses (Lallemand, 1966). The relation times for these mechanisms are given approximately by (Brewer & Lee, 1968)

$$\tau \text{ (orientation)} = \frac{4\pi}{3}\eta a^3/kT > 10^{-12}s, \tag{2.18}$$

$$\tau \text{ (molecular types)} = \frac{\langle x^2\rangle}{D} = \frac{6\pi\eta a\langle x^2\rangle}{kT} > 10^{-12}s, \tag{2.19}$$

$$\tau \text{ (libration about field)} = \sqrt{\frac{2I}{\alpha E_0^2}} > 10^{-12}s, \tag{2.20}$$

$$\tau \text{ (electronic)} = \frac{2\pi a_0\hbar}{e^2} > 1.5\times 10^{-16}s, \tag{2.21}$$

where η is the viscosity ($\eta = 0.4$ cp for liquids and $\eta = 10^6$ cp for glasses); a is the molecular radius; D is the diffusion coefficient ($\geq 10^{-5}$ cm/s for liquids) and x is the diffusion distance of the clustering, ~10^{-8} cm; I is the moment of inertia, $I_{\text{argon}} = 9.3\times 10^{-38}$ esu and $I_{CC1_4} = 1.75\times 10^{-38}$ esu; α is the polarizability, $\alpha_{\text{argon}} = 1.6\times 10^{-14}$ esu and $a_{CC1_4} = 1.026\times 10^{-24}$ esu; and E_0 is the amplitude of the electric field, taken as 10^5 esu, which is close to the atomic field. The response time for an electron distortion is about the period of a Bohr orbit, ~1.5×10^{-16} s. Thus, typical calculated relaxation time responses for diffusional motions are >10^{-11} s, while the electronic distortion response time is ~150 as.

With picosecond light pulses, Brewer and Lee (1968) showed that the dominant mechanism for filament formation should be electronic in very viscous liquids. Molecular rocking has been suggested as the cause of broadening and self-focusing in CS_2. The molecules are driven by the laser field to rock about the equilibrium position of a potential well that has been set up by the neighboring molecules. This mechanism is characterized by a relaxation time:

$$\tau_1 = \frac{\eta}{G} = 2.3\times 10^{-13}s, \tag{2.22}$$

where G is the shear modulus ~1.5×10^{10} dynes/cm and viscosity $\eta = 3.7\times 10^{-3}$ p for CS_2.

In solids, mechanisms giving rise to the coefficient of the intensity-dependent refractive index n_2 for picosecond pulse excitation are either direct distortion of electronic clouds around nuclei or one of several coupled electronic mechanisms: librational distortion, where electronic structure is distorted as the molecule rocks; electron-lattice distortion, where the electron cloud distorts as the lattice vibrates; and molecular distortion, where electronic shells are altered as the nuclei redistribute spatially. The electrostriction mechanism is rejected because it exhibits a negligible effect for picosecond and femtosecond pulses.

Typical supercontinuum spectra generated in solids and liquids using 8-ps pulses at 530 nm are displayed in Fig. 2.4. All continuum spectra are similar despite the different materials.

2.4.1 Supercontinuum in Glasses

Spectra from the glass samples show modulation (see Fig. 2.4a). The spectral modulation ranged from as small as a few wave numbers to hundreds of wave numbers. The filament size was approximately 5–50 μm. Typically, 5–20 small-scale filaments were observed. Occasionally, some laser output pulses from the samples did not show modulation or had no regular modulation pattern. Typical Stokes sweeps from these filaments were 1100 cm^{-1} in extradense flint glass of length 7.55 cm and 4200 cm^{-1} in both borosilicate crown (**BK**-7) and light barium (**LBC**-1) glass of length 8.9 cm. Sweeps on the anti-Stokes side were typically 7400 cm^{-1} in BK and **LBC** glasses. The sweep is polarized in the direction of the incident laser polarization for unstrained glasses.

2.4.2 Supercontinuum in Quartz

SPM spectra from quartz using an 8-ps pulse at 530 nm are similar to the spectra from glasses displayed in Fig. 2.4a. Typical Stokes sweeps from the filaments were 3900 cm^{-1} in a quartz crystal of length 4.5 cm, and the anti-Stokes sweeps were 5500 cm^{-1}.

2.4.3 Supercontinuum in NaCl

Sweeps of 3900 cm^{-1} in NaCl of length 4.7 cm to the red side of 530 nm were observed. Sweeps on the anti-Stokes side were about 7300 cm^{-1}. Some of the spectra show modulation with ranges from a few wave numbers to hundreds of wave numbers. Some laser shots showed no modulation or no regular modulation pattern. For unstrained NaCl, the supercontinuum light is polarized in the direction of the incident laser polarization.

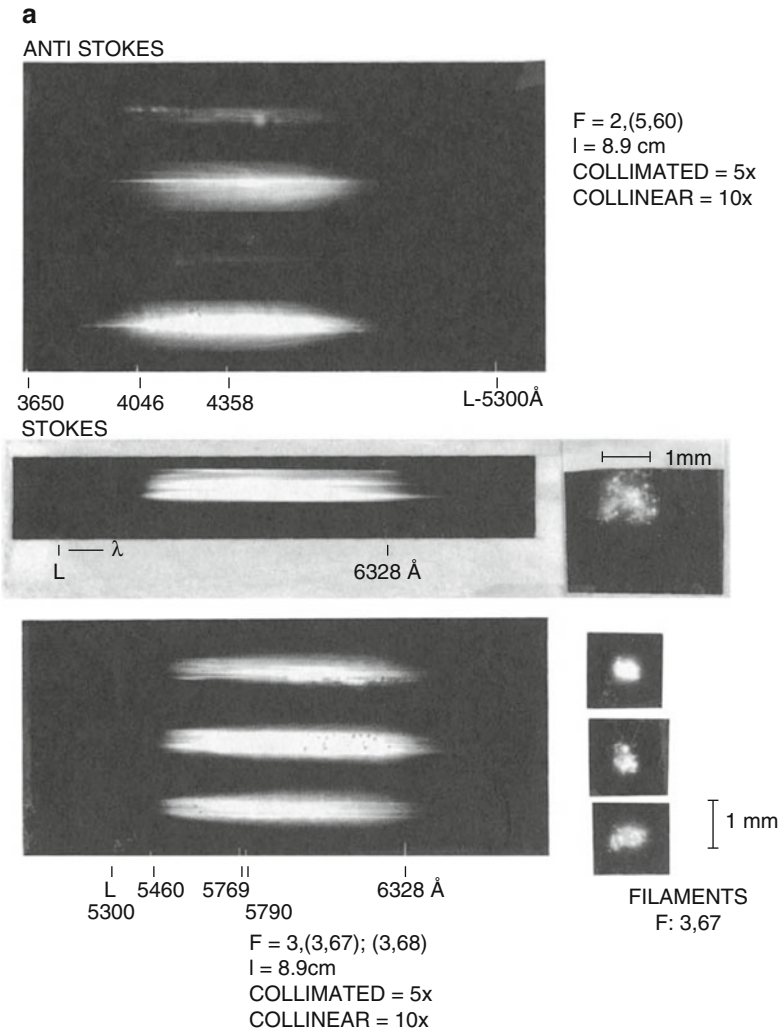

Fig. 2.4 Supercontinuum spectra from various kind of solids and liquids. (**a**) Stokes and anti-Stokes **SPM** from **BK**-7 glass and filament formation for different laser shots. The filaments are viewed through Corning 3–67 filters. (**b**) Stokes and anti-Stokes **SPM** from calcite for different laser shots. The laser beam propagates as an O-wave through the sample. (**c**) Stokes and anti-Stokes **SPM** spectra from calcite for different laser shots. The laser beam propagates as an E-wave. (From Alfano, 1972)

2.4.4 Supercontinuum in Calcite

Sweeps of 4400 cm^{-1} and 6100 cm^{-1} to the Stokes and anti-Stokes sides of 530 nm were observed in a calcite crystal of length 4.5 cm (see Fig. 2.4b). Some

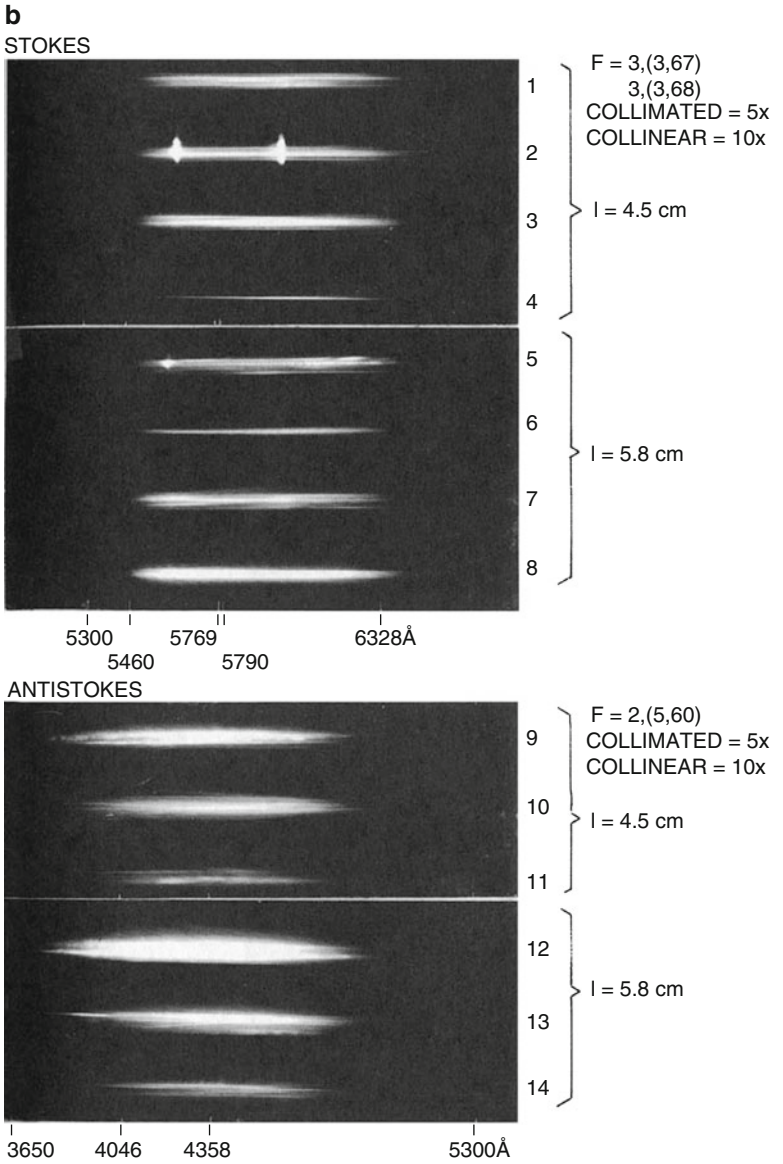

Fig. 2.4 (continued)

spectra showed modulation structure within the broadened spectra; some showed no modulation or no regular modulation pattern. The exit supercontinuum light has same polarization as the incident laser. The **SRS** threshold is lower for laser light traveling as an **O**-wave than an **E**-wave. **SPM** dominates the **E**-wave spectra.

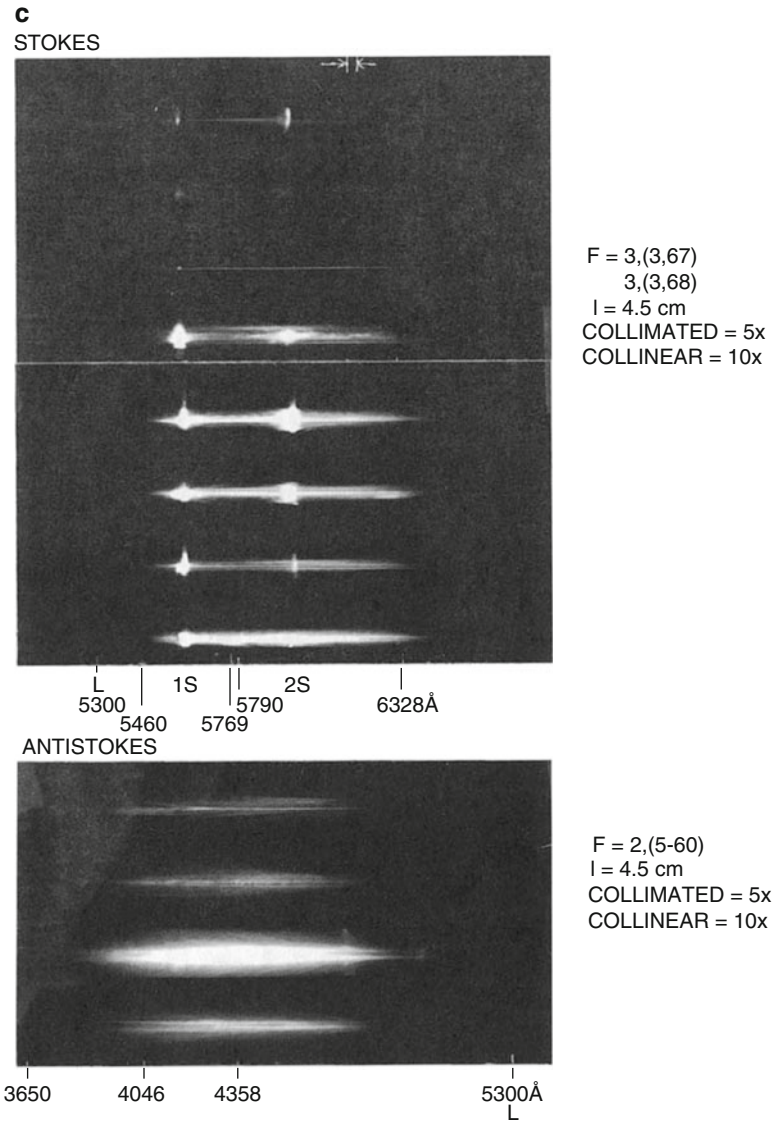

Fig. 2.4 (continued)

2.4.5 Supercontinuum in KBr

A high-power broadband coherent source in the near- and medium-infrared region can be realized by passing an intense 1.06-μm picosecond pulse through a **KBr** crystal. Figure 2.5 shows the spectra from 10-cm-long **KBr** crystal with excitation

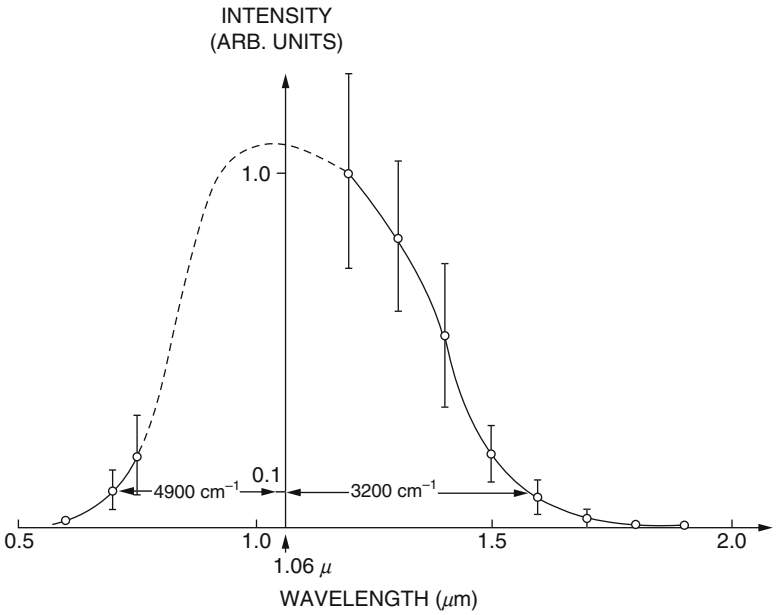

Fig. 2.5 Relative emission intensity versus emission wavelength for **KBr**. Exciting wavelength = 1.06 μm. (From Yu et al., 1975)

of a 9-ps, 10^{11} W/cm^2 pulse at 1.06 μm. On the Stokes side, the maximum intensity occurs at 1.2 μm. When the signal drops to 10^{-1}, the span of the spectral broadening is $\Delta\nu_s = 3200$ cm^{-1} on the Stokes side and $\Delta\nu_a = 4900$ cm^{-1} on the anti-Stokes side. Beyond 1.6 mm, the signal level falls off rapidly. At 1.8 μm, the signal is 10^{-2}, and at 2 mm, no detectable signal can be observed (Yu et al., 1975).

2.4.6 Supercontinuum in Semiconductors

Infrared supercontinuum spanning the range 3–14 μm can be obtained when an intense picosecond pulse generated from a CO_2 laser is passed into GaAs, AgBr, ZnSe, and CdS crystals (Corkum et al., 1985).

The supercontinuum spectra measured from a 6-cm-long Cr-doped GaAs crystal and a 3.8-cm AgBr crystal for different laser pulse durations and intensities and plotted in Figs. 1.6 and 1.7, respectively. The signals were normalized for the input laser energy and the spectral sensitivity of filters, grating, and detectors. Each point represents the average of three shots. The salient feature of the curves displayed in Figs. 2.6 and 2.7 is that the spectral broadening spans the wavelength region from 3 to 14 μm. The wave number spread on the anti-Stokes side is much greater than that on the Stokes side. From data displayed in Fig. 2.6, the maximum

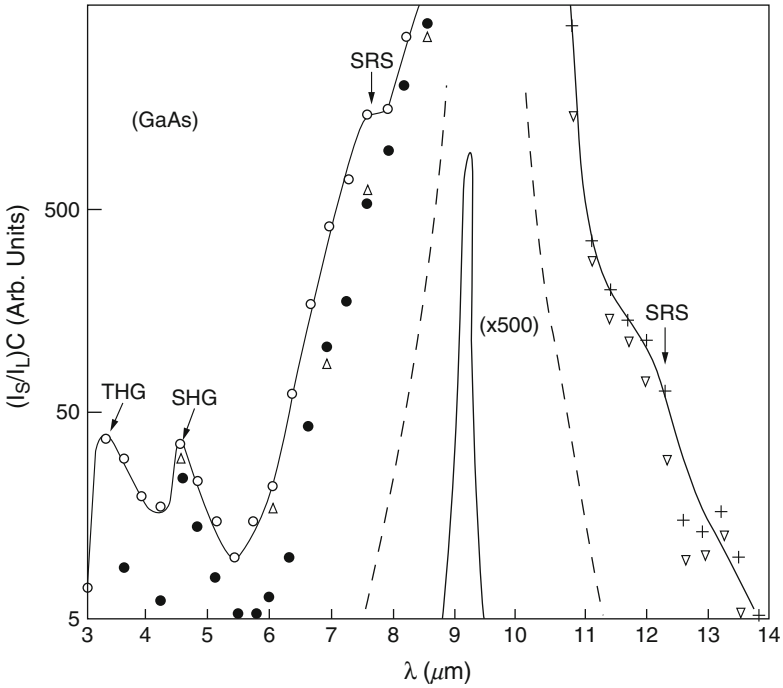

Fig. 2.6 Supercontinuum spectra from a 6-cm-long Cr-doped GaAs crystal. (From Corkum et al., 1985)

anti-Stokes spectral broadening is $\Delta\omega_a = 793\ \text{cm}^{-1}$. Including second and third harmonic generation (**SHG** and **THG**), it spans 2000 cm^{-1}. On the Stokes side, $\Delta\omega_s = 360\ \text{cm}^{-1}$, yielding a value of $\delta\omega_a/\delta\omega_s \sim 2.2$. For AgBr, Fig. 2.7 shows that $\Delta\omega_a = 743\ \text{cm}^{-1}$ and $\Delta\omega_s = 242\ \text{cm}^{-1}$, yielding $\Delta\omega_a/\Delta\omega_s \sim 3$.

The spectral broadening mechanism for the supercontinuum can originate from several nonlinear optical processes. These include self-phase modulation, the four-wave parametric effect, higher-order harmonic generation, and stimulated Raman scattering. In Fig. 2.6, the supercontinuum from the GaAs has two small peaks at 4.5 and 3.3 μm. These arise from the SHG and THG, respectively. Small plateaus are located at 7.5 and 12 μm. These arise from the first-order anti-Stokes and Stokes-stimulated Raman scattering combined with **SPM** about these wavelengths. The **SPM** is attributed to an electronic mechanism.

Summarizing the important experimental aspects of the spectra in condensed matter, the spectra are characterized by very large spectral widths and a nonperiodic or random substructure. Occasionally, a periodic structure interference minimum and maximum are observed. The modulation frequencies range from a few cm^{-1} to hundreds of cm^{-1}, and some modulation progressively increases away from the central frequency. The Stokes and anti-Stokes spectra are approximately equal in intensity and roughly uniform. The extents on the Stokes and anti-Stokes sides are

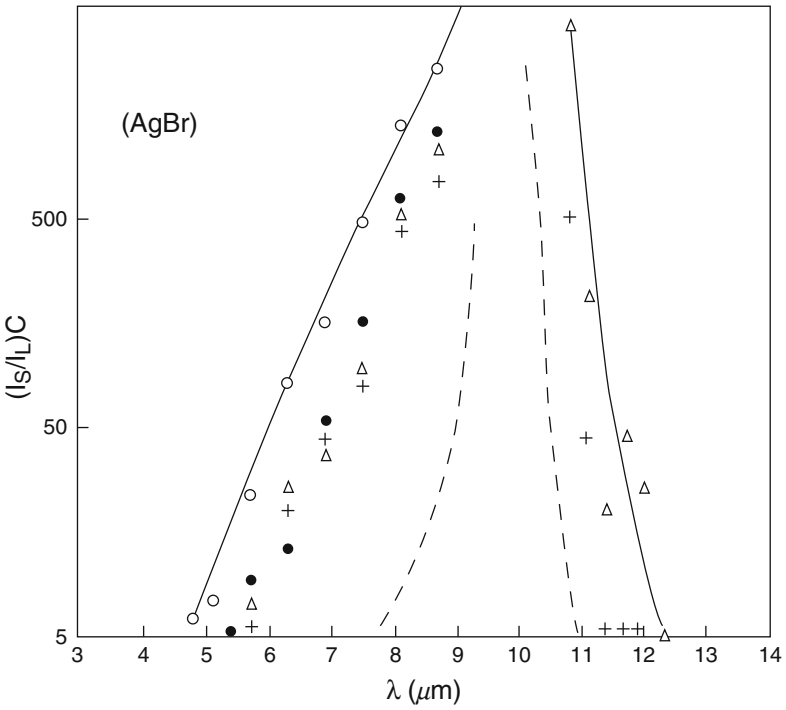

Fig. 2.7 Supercontinuum spectra from a 3.8-cm-long AgBr crystal. (From Corkum et al., 1985)

not symmetric. The peak intensity at the central frequency is 10^2–10^3 the intensity of the **SPM** spectra at a given frequency.

2.5 Generation of Supercontinuum in Liquids

Nonlinear optical effects in solids are very effective; however, damage generated in solid media often limits their usefulness for ultrashort high-power effects. Various kinds of inorganic and organic liquids are useful media for generating picosecond or femtosecond supercontinuum light pulses since they are self-healing media. The supercontinuum spectra produced in liquids (Alfano, 1972) are similar to the spectra displayed in Fig. 2.4 (Alfano, 1972). The following highlights the supercontinuum phenomena in the various favorite liquid media of the authors. These liquids give the most intense and uniform supercontinuum spectral distributions.

2.5.1 Supercontinuum in H_2O and D_2O

The supercontinuum generated in H_2O and D_2O by the second harmonic of a mode-locked neodymium glass laser spanned several thousand wave numbers. The time duration was equal to or less than the picosecond pulse that generated it (Busch et al., 1973). The continuum extended to below 310 nm on the anti-Stokes side and to the near-**IR** region on the Stokes side. There were sharp absorptions at 450 nm in the H_2O continuum and at 470 nm in the D_2O continuum resulting from the inverse Raman effect (Alfano & Shapiro, 1970b; Jones & Stoicheff, 1964). Focusing a 12-mJ, 1060-nm single pulse 14 ps in duration into 25 cm of liquid D_2O resulted in a continuum that showed practically no structure, extending from 380 to at least 800 nm and highly directional and polarized (Sharma et al., 1976). Enhancing the supercontinuum intensity using water with ions is discussed in Sect. 2.10.

2.5.2 Supercontinuum in CCl_4

Another favorite liquid for producing a supercontinuum is CCl_4, in which the spectra produced are similar to the spectra displayed in Fig. 2.4. A typical flat white supercontinuum extending from 430 nm through the visible and near infrared could be produced by focusing an 8-ps pulse at 1060 nm with about 15 mJ pulse energy into a cell containing CCl_4 (Magde & Windsor, 1974).

2.5.3 Supercontinuum in Phosphoric Acid

Orthophosphoric acid was found to be a useful medium for generating picosecond continuum light pulses ranging from the near UV to the near **IR**. By focusing a pulse train from a mode-locked ruby laser into a 10-cm-long cell containing phosphoric acid (60% by weight) solution in water by an 8-cm focal lens, a supercontinuum from near 450 nm to the near **IR** was obtained. The supercontinuum spectra contain structure arising from Raman lines (Kobayashi, 1979).

2.5.4 Supercontinuum in Polyphosphoric Acid

The supercontinuum from polyphosphoric acid was generated by focusing an optical pulse at 694.3 nm with 100 mJ pulse energy and a pulse width of 28 ps into a cell of any length from 2 to 20 cm containing polyphosphoric acid. It reaches 350 nm on the anti-Stokes side, being limited by the absorption of polyphosphoric acid,

and 925 nm on the Stokes side, being cut off by limitations of **IR** film sensitivity (Nakashima & Mataga, 1975).

2.6 Supercontinuum Generated in Optical Fibers

The peak power and the interaction length can be controlled better in optical fibers than in bulk materials. Optical fibers are particularly interesting material for nonlinear optical experiments. In this section, we discuss supercontinuum generation in glass optical fibers. Details of the use of **SPM** for pulse compression are discussed in other chapters.

The generation of continua in glass optical fibers was performed by Stolen et al. in 1974. Continua covering ~500 cm^{-1} were obtained. Shank et al. (1982) compressed 90-fs optical pulses to 30-fs pulses using **SPM** in an optical fiber followed by a grating compressor. Using the **SPM** in an optical fiber with a combination of prisms and diffraction gratings, they were able to compress 30 fs to 6 fs (Fork et al., 1987; also see Chap. 10 by Johnson and Shank).

A typical sequence of spectral broadening versus input peak power using 500-fs pulses (Baldeck et al., 1987b) is shown in Fig. 2.8. The spectra show **SPM** characteristic of heavy modulation. The spectral extent is plotted against the energy in Fig. 2.9 for 500-fs pulses (Baldeck et al., 1987b). The relative energy of each pulse was calculated by integrating its total broadened spectral distribution. The supercontinuum extent increased linearly with the pulse intensity. The fiber length dependence of the spectral broadening is plotted in Fig. 2.10. The broadening was found to be independent of the length of the optical fiber for $l > 10$ cm. This is due to group velocity dispersion. The **SPM** spectral broadening occurs in the first few centimeters of the fiber for such short pulses (Baldeck et al., 1987b).

In multimode optical fibers, the mode dispersion is dominant and causes pulse distortion. Neglecting the detailed transverse distribution of each mode, the light field can be expressed by

$$E(t) = \sum_i a_i A_i(t) \exp\left[i\omega_0 t - ik_i z\right], \tag{2.23}$$

where ω_0 is the incident laser frequency; a_i, $A_i(t)$, and $k = n_i\,\omega_0/c$ are the effective amplitude, electric field envelope function at the local time $\tau = t - z/v_{gi}$, and wave number of mode *i*, respectively; and v_{gi} is the group velocity of mode *i*. The effective refractive index of mode *i* is denoted by n_i and

$$n_i = n_{0i} + n_{2i}|E(t)|^2, \tag{2.24}$$

where n_{0i} and n_{2i} are the linear refractive index and the nonlinear coefficient of the *i*th mode, respectively. The nonlinearities of different modes are assumed to be the

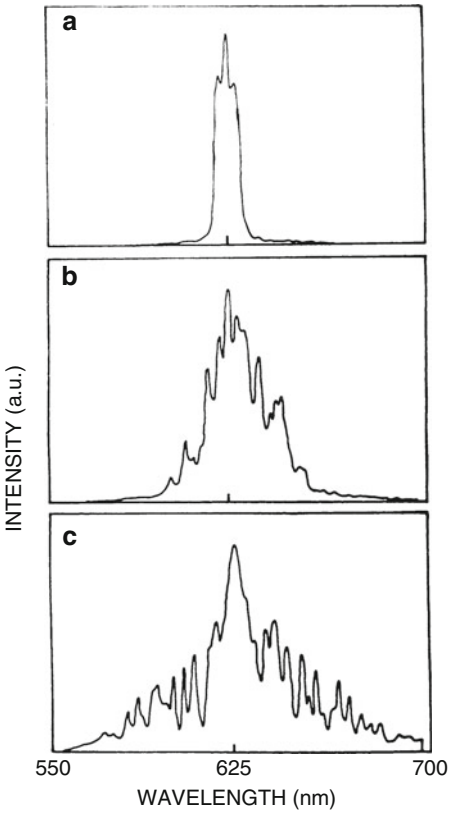

Fig. 2.8 Sequence of spectral broadening versus increasing input energy in a single-mode optical fiber (length = 30 cm). The intensity of the 500-fs pulse was increased from (**a**) to (**c**). (From Baldeck et al., 1987b)

same, that is, $n_{2i} = n_2$. Substituting Eq. (2.21) into Eq. (2.20), we obtain

$$E(t) = \sum a_i A_i(t) \exp\left[i\omega_0 t - i n_{0i}\omega_0 z/c - i\Delta\phi(t)\right], \tag{2.25}$$

where

$$\Delta\phi(t) = (n_2\omega_0 z/c)\,|E(t)|^2. \tag{2.26}$$

After inserting Eq. (2.23) into Eq. (2.26), the time-dependent phase factor $\Delta\phi(t)$ can be expanded in terms of E_i (t):

$$\Delta\phi(t) = \sum_i \sum_j (n_2\omega_0 z/c)\, a_i a_j A_i(t) A_j(t) \exp\left[i\left(n_{0i} - n_{0j}\right)\omega_0 z/c\right]. \tag{2.27}$$

In the picosecond time envelope, the terms of $i \neq j$ oscillate rapidly. Their contributions to the time-dependent phase factor are washed out. The approximate

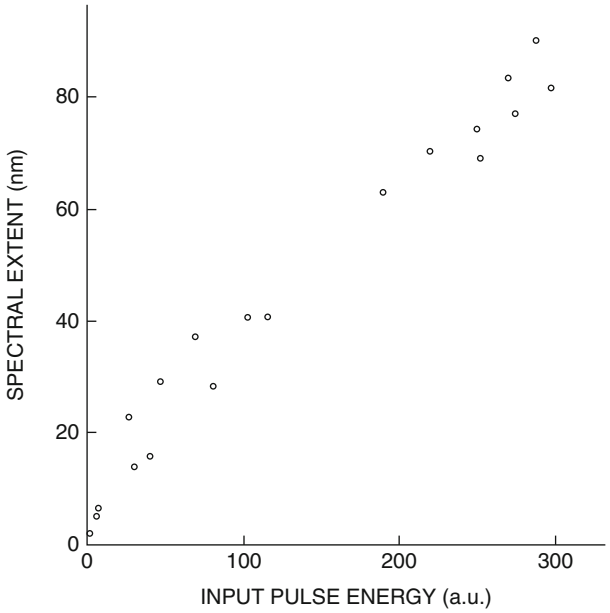

Fig. 2.9 Supercontinuum spectra versus input pulse energy in a single-mode optical fiber (length = 30 cm) for a 500-fs pulse. (From Baldeck et al., 1987b)

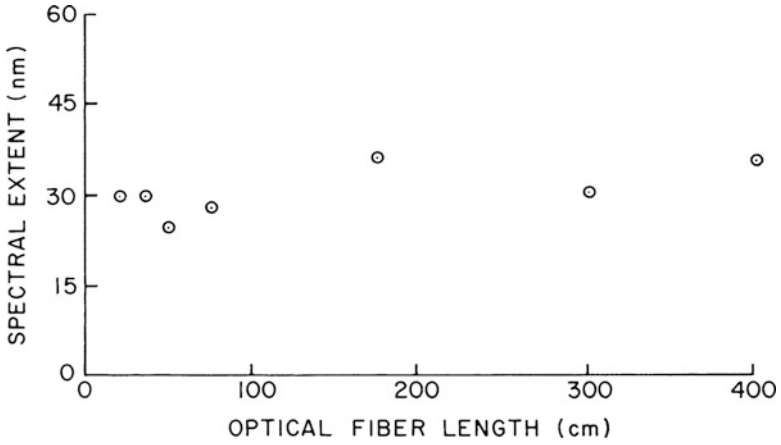

Fig. 2.10 Supercontinuum spectra versus optical fiber length for a 500-fs pulse. (From Baldeck et al., 1987b)

$\Delta\phi(t)$ has the form

$$\Delta\phi = \sum_i (n_2\omega_0 z/c)\, a_i^2 A_i^2(t). \tag{2.28}$$

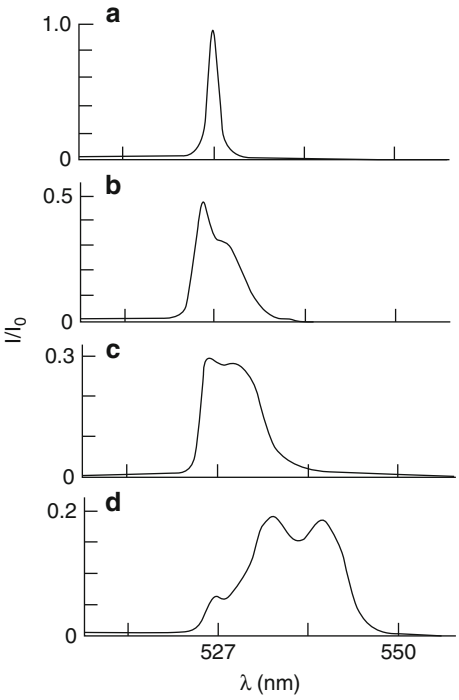

Fig. 2.11 Output spectra for 8-ps laser pulses at 527 nm propagating through different lengths of multimode optical fibers: (**a**) no fiber; (**b**) 22 cm; (**c**) 42 cm; (**d**) 84 cm. (From Wang et al., 1989)

The pulse shape changes due to the different group velocities of various modes. When most of the incident energy is coupled into the lower modes, the pulse will have a fast rising edge and a slow decay tail since the group velocity is faster for lower-order mode. This feature was observed using a streak camera. Therefore, the $\Delta\phi(t, z)$ of Eq. (2.28) will also have a fast rising edge and a slow decay tail. The time derivative of the phase $\Delta\phi(t, z)$ yields an asymmetric frequency broadening.

Figure 2.11 shows the spectral continuum generated from multimode glass optical fibers using 8-ps pulses at 530 nm. The spectral broadening is asymmetric about the incident laser frequency. It is shifted much more to the Stokes side than to the anti-Stokes side. The observed spectra did not show a modulation. This can be explained by the spectral resolution of the measurement system. The calculated modulation period is about 0.13 nm, which is much smaller than the resolution of the measurement system (about 1 nm) (Wang et al., 1989).

2.7 Supercontinuum Generation in Rare-Gas Liquids and Solids

Continuum generation is a general phenomenon that occurs in all states of matter. A system for testing the role of the electronic mechanism is rare-gas liquids and solids

(Alfano & Shapiro, 1970a). Rare-gas liquids are composed of atoms possessing spherical symmetry. Thus, there are no orientational, librational, or electron-lattice contributions to the nonlinear refractive index n_2. However, interrupted rocking of argon can occur in which a distorted atom can rock about an equilibrium value before it collides with other atoms. Contributions to the nonlinear refractive index might be expected from electrostriction, molecular redistribution, interrupted rocking, and a distortion of the electron clouds:

$$n_2 = n_{2\text{ELECTRONIC}} + n_{2\text{MR}} + n_{2\text{LIBRATION}} + n_{2\text{ELECTROSTR}}. \tag{2.29}$$

Electrostriction is ruled out because picosecond exciting pulses are too short. Molecular redistribution arises from fluctuations in the local positional arrangement of molecules and can contribute significantly to n_2. However, n_2 due to all mechanisms except electronic was estimated to be ~2×10^{-14} esu for liquid argon from depolarized inelastic-scattering data. Electronic distortion ($n_2 = 6 \times 10^{-14}$ esu) slightly dominates all nonlinear index contributions (Alfano & Shapiro, 1970a; Alfano, 1972). Furthermore, the depolarized inelastic light-scattering wing vanishes in solid xenon, implying that the molecular redistribution contribution to n_2 vanishes in rare-gas solids. Observations of self-focusing and SPM in rare-gas solids appear to provide a direct proof that atomic electronic shells are distorted from their spherical symmetry under the action of the applied field. However, both pure electronic and molecular redistribution mechanisms contribute to n_2 in rare-gas liquids. The response time of the system for a combination of both of these mechanisms lies between 10^{-15} and 10^{-12} s. For femtosecond and subpicosecond pulses, the dominant mechanism for n_2 and SPM is electronic in origin.

The experimental setup used to generate and detect a supercontinuum in rare-gas liquids and solids is the same as that shown in Fig. 2.3 with the exception that the samples are placed in an optical dewar.

Typical supercontinuum spectra from rare-gas liquids and solids are displayed in Fig. 2.12. Sweeps of 1000–6000 cm^{-1} were observed to both the Stokes and anti-Stokes sides of 530 nm in liquid argon. Modulation ranges from a few cm^{-1} to hundreds of cm^{-1}. Similar spectral sweeps were observed in liquid and solid krypton.

A most important point is that the threshold for observing SPM in liquid krypton is 0.64 ± 0.12 that in liquid argon. The SPM threshold ratio of solid and liquid krypton is 0.86 ± 0.15. In liquid argon, SPM spectra appear at a threshold power of ~0.5 GW focused in a 12-cm sample. The swept light is also collimated, polarized, and modulated. These observations rule out dielectric breakdown.

The refractive index in rare-gas liquids is given by $n_{||} = n_0 + n_2\langle E^2\rangle$, where $n_{||}$ is the refractive index parallel to the field. $\langle E^2\rangle^{1/2}$ is the rms value of the electric field. The electronic nonlinear refractive index in rare-gas liquids is given by

$$n_2 = \left[\left(n_0^2 + 2\right)^4 / 81 n_0\right] \pi N \rho, \tag{2.30}$$

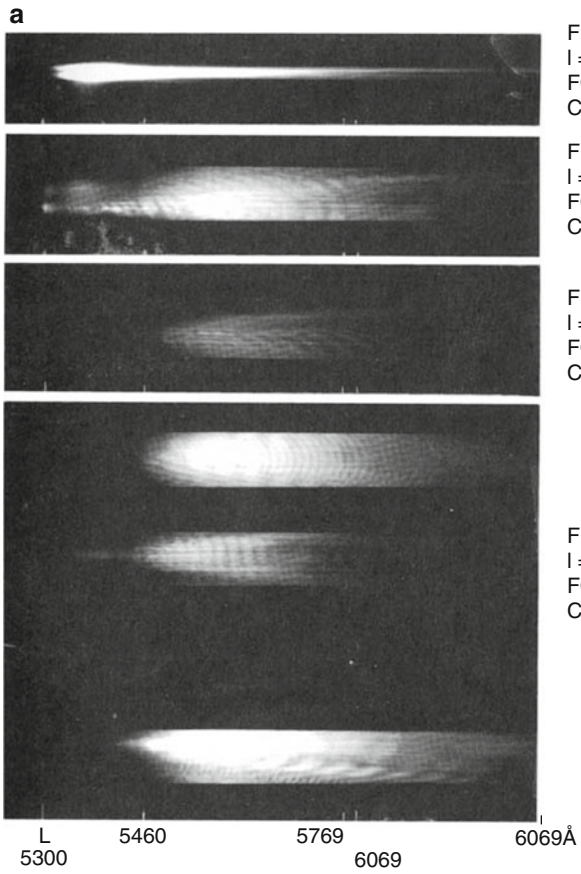

Fig. 2.12 Supercontinuum spectra for picosecond laser pulses at 530 nm passing through rare-gas liquids and solids; (**a**) Stokes SPM from liquid argon for different laser shots; (**b**) anti-Stokes SPM for liquid argon for different laser shots; (**c**) Stokes SPM for liquid and solid krypton for different laser shots. (From Alfano, 1972)

where n_0 is the linear refractive index, ρ is the second-order hyperpolarizability, and N is the number of atoms per unit volume. The term $n_2 = 0.6 \times 10^{-13}$ esu in liquid argon and $\simeq 1.36 \times 10^{-13}$ in liquid krypton. For liquid argon and liquid and solid krypton, the refractive indices are taken as 1.23, 1.30, and 1.35, respectively (McTague et al., 1969). Intense electric fields distort atoms and produce a birefringence. The anisotropy in refractive index between light traveling with the wave vector parallel and perpendicular to the applied electric field is given by (Alfano, 1972)

$$\delta n_{||} - \delta n_{\perp} = \frac{1}{3} n_2 E_0^2, \tag{2.31}$$

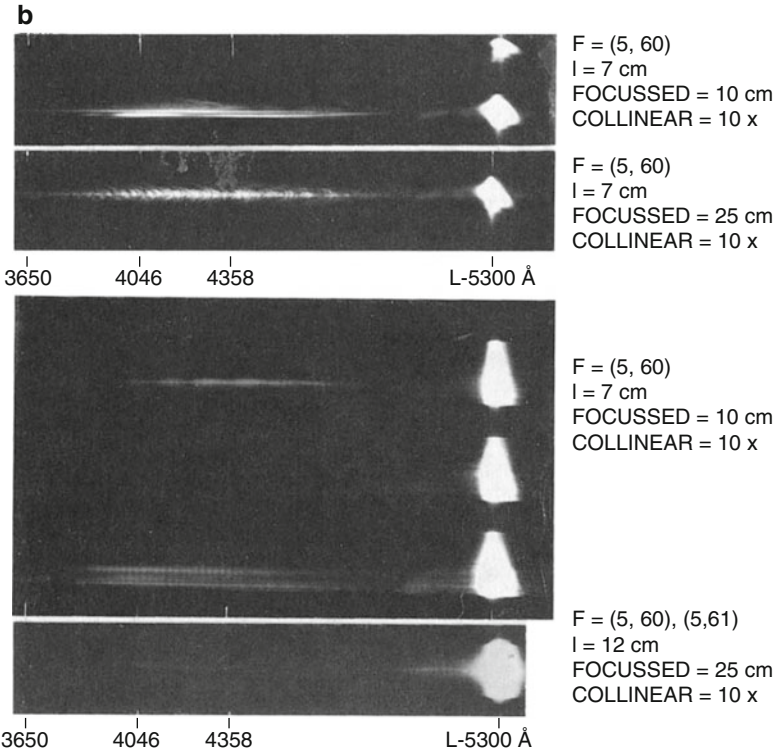

Fig. 2.12 (continued)

where $\delta n_{||}$ and $\delta n_{\perp}$ are the changes in refractive indices parallel and perpendicular to the field. The value of $n_2 E_0^2$ is ~5 × 10^{-5}V/m in liquid argon when E_0~1.5 × 10^7V/m (~4 × 10^{11}W/cm^2). This change in index explains the self-focusing and SPM described above which was observed by Alfano and Shapiro in 1970. Similar SPM effects occur in organic and inorganic liquids, often accompanied by SRS and inverse Raman effects.

2.8 Supercontinuum Generation in Antiferromagnetic $KNiF_3$ Crystals

The influence of magnetic processes on nonlinear optical effects is an interesting topic. In this section, we discuss the supercontinuum generation associated with the onset of magnetic order in a $KNiF_3$ crystal (Alfano et al., 1976). Light at 530 nm is well suited for the excitation pulse because $KNiF_3$ exhibits a broad minimum in its absorption (Knox et al., 1963) between 480 and 610 nm.

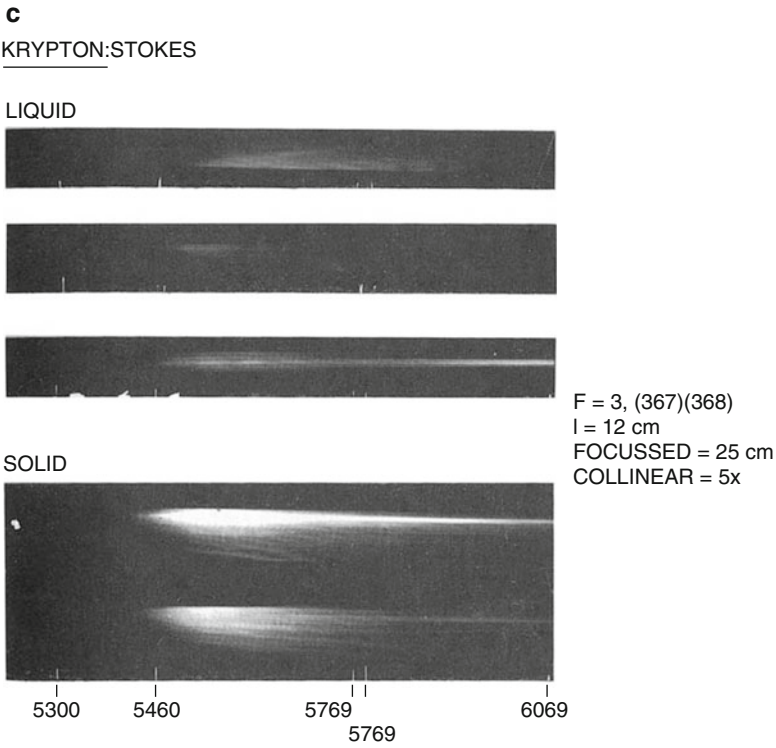

Fig. 2.12 (continued)

Typical spectra from an unoriented 5-cm-long $KNiF_3$ single crystal are displayed in Fig. 2.13 for 530-nm picosecond excitation (Alfano et al., 1976). The spectra are characterized by extensive spectral broadening ranging up to ~3000 cm^{-1} to either side of the laser frequency. The intensity, although not the spectral broadening, of the output exhibited the large temperature dependence illustrated in Fig. 2.14. There is no sharp feature at 552 nm, the position expected for stimulated Raman scattering by the 746-cm^{-1} magnon pair excitation. Usually, the spectra were smooth; however, occasionally structure was observed. A periodic structure with a modulation frequency of tens to hundreds of wave numbers was evident. The frequency broadening light is also polarized in the same direction as the incident 530-nm pulse. This property is the same observed in glass, crystals, and liquids (see Sects. 2.3, 2.4, 2.5, and 2.6). Self-focusing was also observed, usually in the form of 10 to 40 small self-focused spots 5–20 μm in diameter at the exit face of the crystal. Using a focused beam, optical damage could also be produced. It should be emphasized that spectral broadening was always observed even in the absence of self-focusing, damage, or periodic spectral intensity modulation.

Figure 2.15 shows the output intensity at 570 nm as a function of input intensity for two temperatures: above and below the Néel temperature. The output intensity

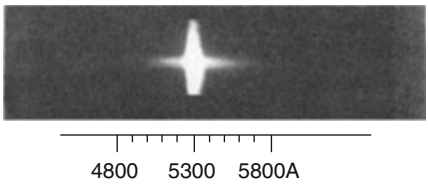

Fig. 2.13 Spectra for picosecond laser pulse at 530 nm passing through 5-cm-long $KNiF_3$. (From Alfano et al., 1976)

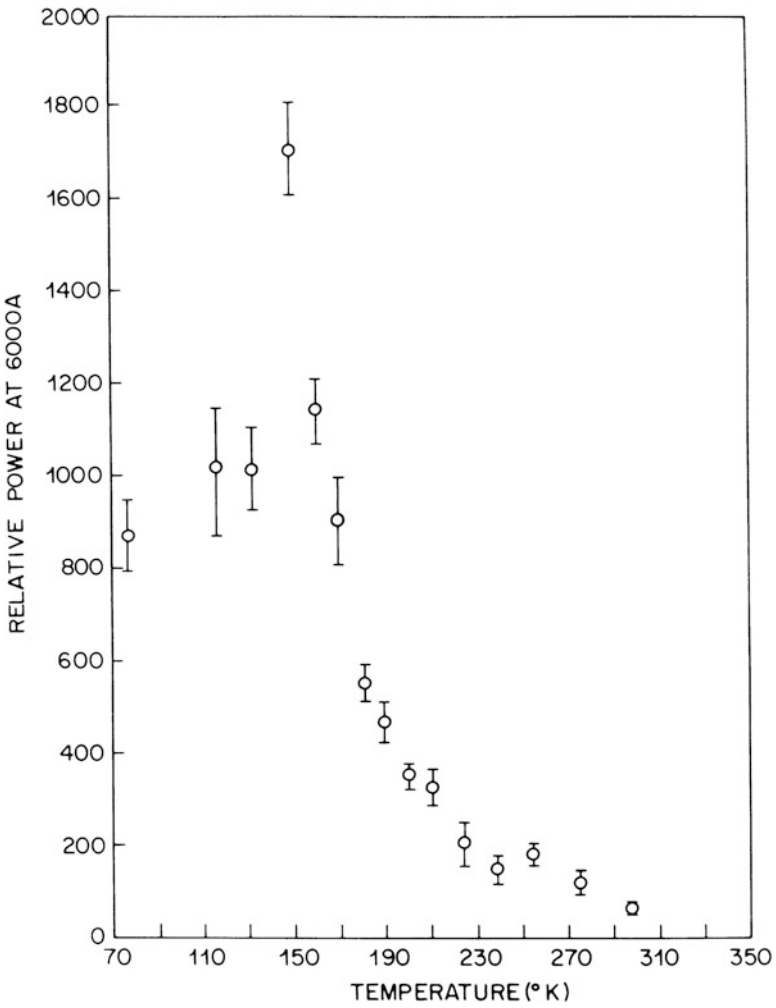

Fig. 2.14 Intensity of the frequency-broadening emission from $KNiF_3$ as a function of temperature at fixed pump intensity at 552 nm. (From Alfano et al., 1976)

is approximately exponential in the input intensity at both temperatures. However, the slope is more than a factor of two larger at 77 K than at 300 K. The rapid rise

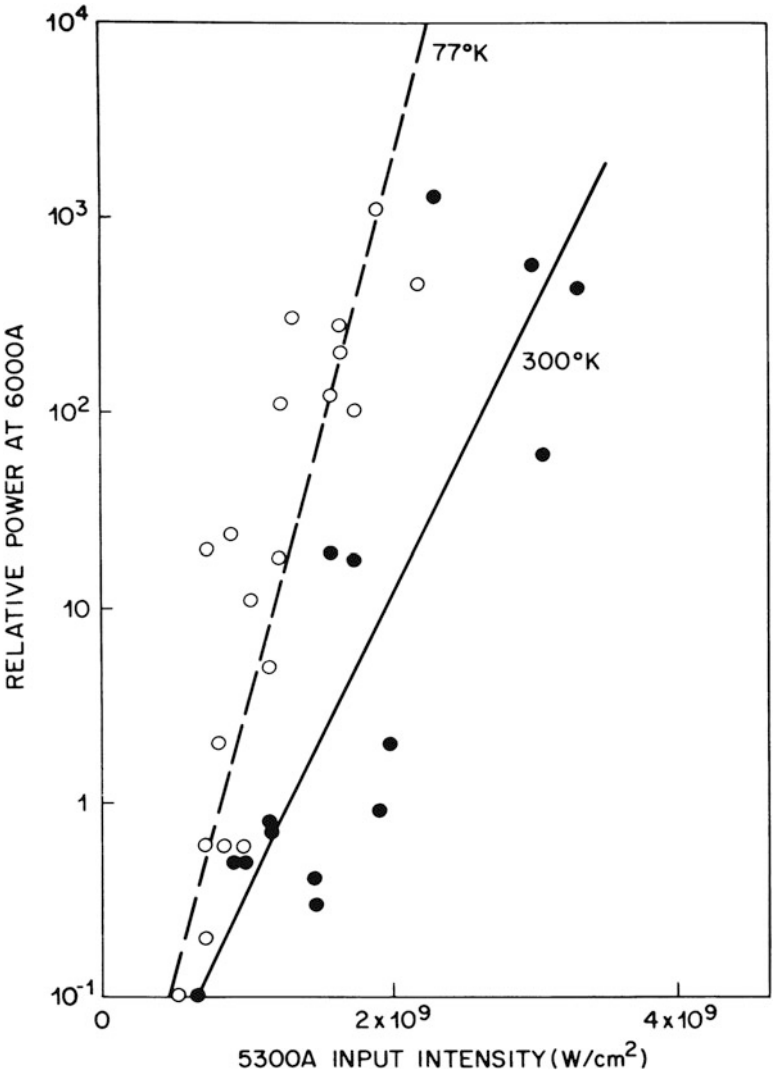

Fig. 2.15 Intensity dependence of continuum spectra at 570 nm from $KNiF_3$ as a function of pumping laser intensity at fixed lattice temperature

in conversion efficiency of four orders of magnitude within a small interval of input intensity is indicative of an amplification process with very large gain. Identical curves were obtained at 551 and 600 nm output wavelengths. The similarity in results for several output frequencies shows that simple stimulated magnon pair scattering is not the dominant process. If it were, one would expect the behavior at 552 nm to differ considerably from that at other wavelengths.

The most novel experimental results in $KNiF_3$ are the large (~20×) intensity increases below T_N. Spectra at 552, 570, and 600 nm behave identically – within experimental error – consistent with the observations in Fig. 2.15. The temperature dependence of the relative **peak** intensity for the spontaneous magnon pair scattering in the $KNiF_3$ sample (using 514.5 nm laser light) was measured and is potted in Fig. 2.14. For $KNiF_3$, the magnon pair scattering accounts for the entire inelastic light scattering and therefore for the non-σ electronic contribution to χ^3 (Hellwarth et al., 1975). The temperature dependence is compelling evidence for the magnetic origin of the low-temperature-enhanced nonlinear optical spectral broadened intensity.

The observation can be semiquantitatively accounted for in terms of a temperature-dependent spin contribution to the overall nonlinear susceptibility $\chi_{ijkl}^{(3)}$ that governs four-photon parametric mixing as the primary process. In general, $\chi^{(3)}$ may be written as a sum of electronic and Raman contributions (Levenson & Bloembergen, 1974). For $KNiF_3$, we may consider the latter to consist solely of the magnon pair Raman scattering contribution (Chinn et al., 1971; Fleury et al., 1975), which we can approximate as a Lorentzian:

$$\chi_{ijkl}^{(3)}(-\omega_3, \omega_1, \omega_1, -\omega_2) = \chi_E^{(3)} + K\frac{\alpha_{ij}^m \alpha_{kl}^m + \alpha_{il}^m \alpha_{jk}^m}{\omega_m - (\omega_1 - \omega_2) + i\Gamma_m}. \tag{2.32}$$

Here, ω_m and Γ_m denote the temperature-dependent frequency and linewidth, respectively, of the magnon pair excitations, a_{ij}^m is the magnon pair polarizability, and $\chi_E^{(3)}$ is the usual nonresonant, temperature-independent "electronic" contribution from nonlinear distortion of the electronic orbits. The second term in Eq. (2.32) is called magnetic $\chi_M^{(3)}$. Since the **integrated intensity** of the spontaneous magnon pair Raman spectrum, which is ~ $|\alpha^m|^2$, has been measured and found to be essentially temperature independent (Chinn et al., 1971; Fleury et al., 1975), the only quantities in Eq. (2.32) that vary significantly with temperature are ω_m and Γ_m. The observed temperature independence of the extent of spectral broadening, $\delta\omega$, may be explained by noting that $\delta\omega \sim 2\Delta\omega n_2 k E_1^2 l$ due to self-phase modulation. Here, $\Delta\omega$ is the spectral width of the input pulse, k is its propagation constant, E_1 is the field amplitude, and l is the path length. n_2 is the nonlinear refractive index, which contains a purely electronic contribution, σ, and a contribution proportional to the integrated Raman scattering cross section (Hellwarth et al., 1975). Since neither σ nor $|\alpha^m|^2$ is temperature dependent in $KNiF_3$, n_2, and therefore, $\Delta\omega$ should not vary either, in agreement with observations.

The observed strong temperature dependence of the intensity of the frequency-broadened spectrum (see Fig. 2.14) arises from the resonant term in Eq. (2.32) through the primary process $2\omega_1 \rightarrow \omega_2 + \omega_3$, which is strongest when $\omega_2 = \omega_1 + \omega_m$ and increases as Γ_m decreases (on cooling below the Néel temperature). That is, the resonant contribution to $\chi^{(3)}$ in Eq. (2.31) varies with temperature in the same way as the peak spontaneous magnon pair cross section: $\Gamma_m^{-1}(T)$. However, the individual contribution to $\chi^{(3)}$ cannot be directly

inferred from the dependence of the broadened spectrum. This is because the latter receives significant contributions from secondary processes of the form $\omega_1 + \omega'_2 \rightarrow \omega'_3 + \omega_4$, etc., in which products of the primary process interact with the pump to smooth the spectral distribution and wash out the sharp features that the resonant spin nonlinearity produces in the primary process. The large values of pump intensity and source spectral width make possible strong amplification in spite of imprecise phase matching in the forward direction. Such behavior (washing out of stimulated Raman features by the spectral broadening process) has frequently been observed in both liquids and crystals. Thus, a full quantitative description of the nonlinear optical processes in $KNiF_3$ is not yet possible.

2.9 Generation of Supercontinuum Near Electronic Resonances in Crystals

Since the active medium of a laser possesses well-defined electronic energy levels, knowledge of SPM near electronic levels is of paramount importance. SPM near electronic levels of a PrF_3 crystal have been investigated experimentally and theoretically to gain additional information on the SPM process – in particular, on the role played by the electronic levels and on how the continuum spectrum evolves through and beyond the electronic absorption levels (Alfano et al., 1974).

Experimentally, the Stokes and anti-Stokes spectrum and filament formation from the PrF_3 crystal are investigated under intense picosecond pulse excitation at the wavelength of 530 nm. The c axis of the crystal is oriented along the optical axis. The intensity distribution at the exit face of the crystal is magnified by $10\times$ and imaged on the slit of a Jarrell-Ash $\frac{1}{2}$-m-grating spectrograph so that the spectrum of each filament can be displayed. The spectra are recorded on Polaroid type 57 film. No visible damage occurred in the PrF_3 crystal.

The PrF_3 crystal was chosen for the experiment because its electronic levels are suitably located on the Stokes and anti-Stokes sides of the 530-nm excitation wavelength. The absorption spectra of a – $\frac{1}{2}$-mm-thick PrF_3 crystal and the energy level scheme of Pr^{3+} ions are shown in Fig. 2.16. The fluorides of Pr have the structure of the naturally occurring mineral tysonite with D^4_{34} symmetry.

Typical spectra of frequency broadening from PrF_3 about 530 nm are shown in Fig. 2.17 for different laser shots. Because of the absorption associated with the electronic level, it is necessary to display the spectrum over different wavelength ranges at different intensity levels. In this manner, the development of the SPM spectrum through the electronic absorption levels can be investigated. Using appropriate filters, different spectral ranges are studied and displayed in the following figures: in Fig. 2.18a, the Stokes side for frequency broadening $\overline{\nu}_B > 100\ \text{cm}^{-1}$ at an intensity level (I_{SPM}) of ~10^{-2} of the laser intensity (I_L), in Fig. 2.18b, the Stokes side for $\overline{\nu}_B > 1500\ \text{cm}^{-1}$ at $I_{\text{SPM}} \sim 10^{-4}\ I_L$, in Fig. 2.18c, the anti-Stokes side for $\overline{\nu}_B > 100\ \text{cm}^{-1}$ at $I_{\text{SPM}} \sim 10^{-2}\ I_L$, and in Fig. 2.18d, the anti-Stokes side

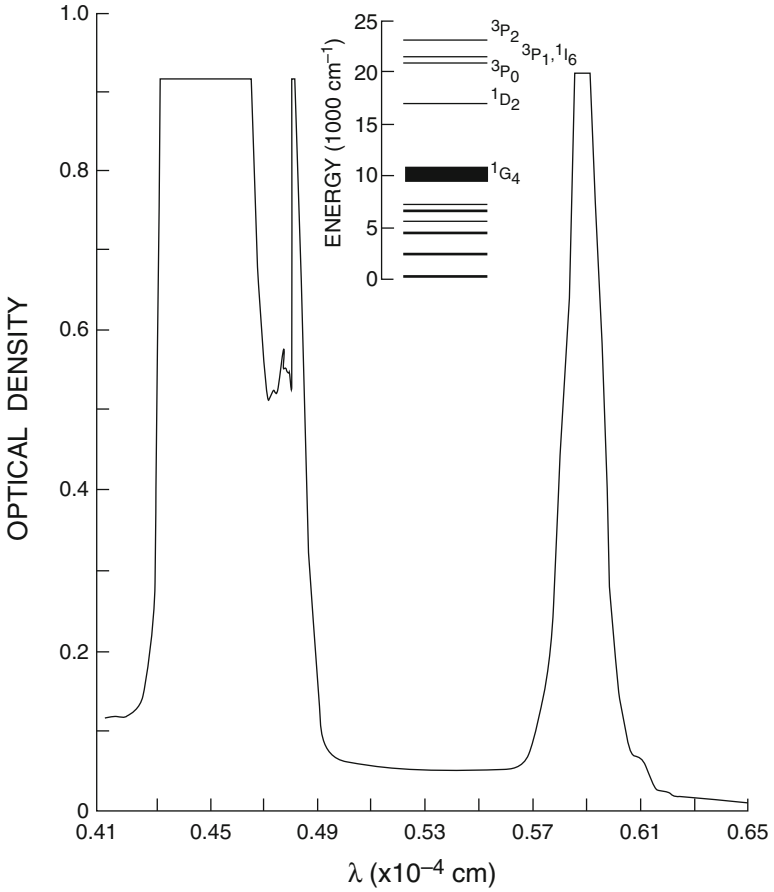

Fig. 2.16 Absorption spectra of 0.5-mm-thick PrF_3 crystal; insert is the level scheme of Pr^{3+} ions. (From Alfano et al., 1974)

for $\overline{v}_B > 1500$ cm^{-1} at $I_{SPM} \sim 10^{-4}\ I_L$. Usually, 50–100 small-scale filaments 5–50 μm in diameter are observed.

Several salient features are evident in the spectra displayed in Figs. 2.17 and 2.18. In Fig. 2.17, the Stokes and anti-Stokes spectra are approximately equal in intensity and frequency extent. The peak intensity at the central frequency is ~100 times the intensity of the SPM at a given frequency. The extent of the frequency broadening is ~1500 cm^{-1}, ending approximately at the absorption lines. Occasionally, a periodic structure of minima and maxima is observed that ranges from a few cm^{-1} to 100 cm^{-1}, and for some observations, no modulation is observed. Occasionally, an absorption band appears on the anti-Stokes side of the 530-nm line whose displacement is 430 cm^{-1}. In Fig. 2.18, the main feature is the presence of a much weaker superbroadband continuum whose frequency extends through and

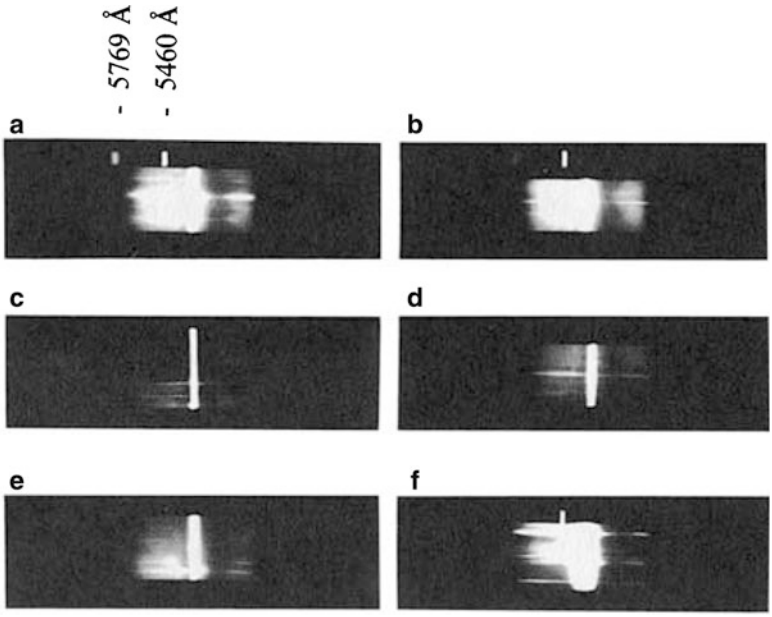

Fig. 2.17 Spectra from PrF_3 excited by 4-ps laser pulses at 530 nm; neutral density (ND) filters: (**a**) ND = 1.5; (**b**) ND = 1.5; (**c**) ND = 2.0; (**d**) ND = 2.0; (**e**) ND = 1.7; (**f**) ND = 1.4. A wire is positioned after the collection lens at the focal length. (From Alfano et al., 1974)

past the well-defined absorption lines of the Pr^{3+} ion to a maximum frequency of >3000 cm^{-1} on the Stokes side (end of film sensitivity) and >6000 cm^{-1} on the anti-Stokes side. The intensity of the continuum at a given frequency outside absorption lines is ~10^{-4} the laser intensity.

The observed absorption lines on the anti-Stokes side of 530 nm are located at 441.5, 465.3, and 484.5 nm and on the Stokes side at 593 and 610.9 nm. These lines correspond within ±0.7 nm to the absorption lines measured with a Cary 14. The absorption lines measured from the Cary spectra are ~3 cm^{-1} at 611.2 nm, 62 cm^{-1} at 5938.8 nm, 46 cm^{-1} at 485.2 nm, and >100 cm^{-1} at 441.2 nm. Figure 2.19 compares the Stokes absorption spectra of a PrF_3 crystal photographed with a $\frac{1}{2}$-m Jarrell-Ash spectrograph with different broadband light sources. Figure 2.19a was obtained with light emitted from a tungsten lamp passing through a $\frac{1}{2}$-mm PrF_3 crystal, Fig. 2.19b was obtained with the Stokes side of the broadband picosecond continuum generated in BK-7 glass passing through a $\frac{1}{2}$-mm PrF_3, and Fig. 2.19c was obtained with the broadband light generated in a 5-cm PrF_3 crystal. Notice that the absorption line at 611.1 nm is very pronounced in the spectra obtained with the continuum generated in PrF_3, whereas with conventional absorption techniques, it is barely visible. The anti-Stokes spectrum obtained with light emitted from a tungsten filament lamp passing through a $\frac{1}{2}$-mm PrF_3 crystal is shown in Fig. 2.20a. This is

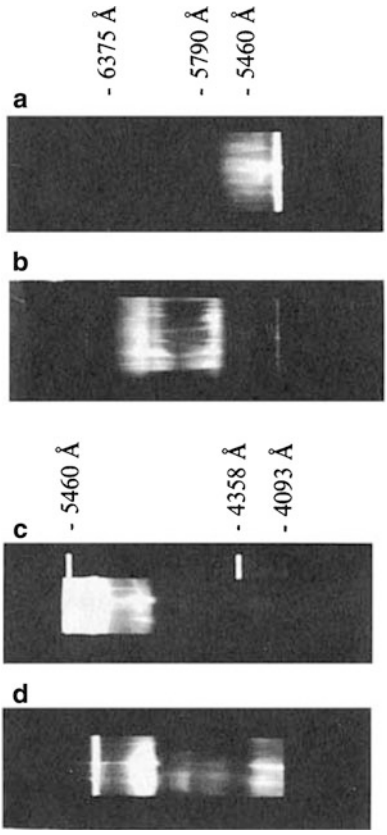

Fig. 2.18 Spectra on the Stokes and anti-Stokes sides of the 530-nm excitation: (**a**) Stokes side, Corning 3–68 filter, wire inserted, ND = 2.0; (**b**) Stokes side, Corning 3–66 filter, wire inserted; (**c**) anti-Stokes side, wire inserted, ND = 1.0; (**d**) anti-Stokes side, Corning 5–61, wire inserted. (From Alfano et al., 1974)

compared with the spectrum obtained with broadband light generated in a 5-cm PrF_3 crystal shown in Fig. 2.20b.

The angular variation of the anti-Stokes and Stokes spectral emission from PrF_3 is displayed in Fig. 2.21. The light emitted from the sample is focused on the slit of a $\frac{1}{2}$-m Jarrell-Ash spectrograph with a 5-cm focal length lens with the laser beam positioned near the bottom of the slit so that only the upper half of the angular spectrum curve is displayed. In this fashion, a larger angular variation of the spectrum is displayed. Emission angles >9° go off slit and are not displayed. This spectrum is similar to four-photon emission patterns observed from glass and liquids under picosecond excitation.

The experimental results show that a discontinuity in intensity occurs when the self-phase modulation frequency extends beyond the absorption line frequency. This is due to almost total suppression of the signal beyond the absorption resonance (Alfano et al., 1974). A similar argument and conclusion hold for the blue side of the laser line. The residual weak intensity that exists beyond the absorption line is not due to SPM. It can arise, however, from three-wave mixing. Since there was a continuum of frequencies created by SPM, it might be possible for three such

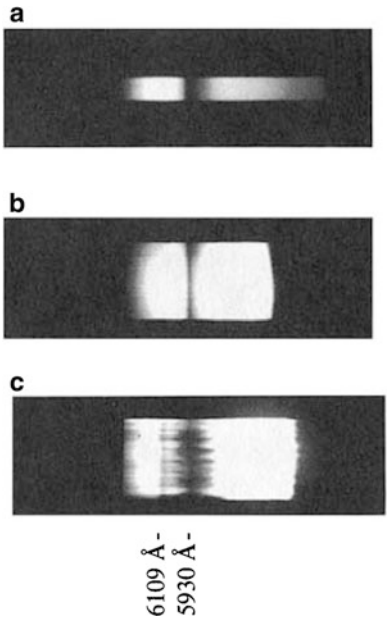

Fig. 2.19 Comparison of the Stokes absorption spectra of PrF_3 photographed with different light sources: (**a**) light emitted from a tungsten lamp is passed through 0.5-cm-thick crystal; (**b**) SPM light emitted from BK-7 glass is passed through 0.5-mm-thick crystal; (**c**) SPM light is generated within the 5-cm PrF_3. (From Alfano et al., 1974)

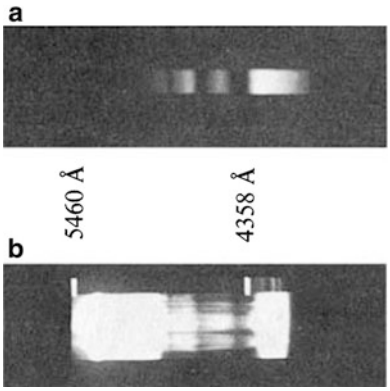

Fig. 2.20 Comparison of the anti-Stokes absorption spectrum of PrF_3 photographed with (**a**) light emitted from a tungsten lamp passing through 0.5-mm-thick crystal and (**b**) SPM light generated within the 5-cm PrF_3. (From Alfano et al., 1974)

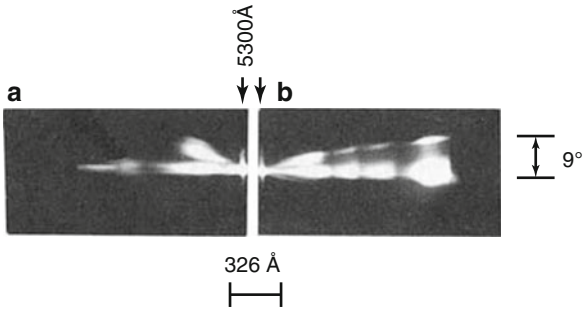

Fig. 2.21 Angular variation of the (**a**) Stokes and (**b**) anti-Stokes spectral patterns emitted from PrF3 crystal: (**a**) Corning 4 (3–67) filters, ND = 1.0; (**b**) Corning 2 (5–60) filters. (From Alfano et al., 1974)

frequencies, ω_1, ω_2, and ω_3, to mix to create a signal at frequency $\omega_1 + \omega_2 - \omega_3$ that lies beyond the absorption line. Since the frequencies are chosen from a continuum, it is also possible for phase matching to be achieved. For the spectrum in the domain between the laser frequency and the absorption line, the extent of self-broadening is proportional to the intensity. Since the energy in the pulse is proportional to the product of the frequency extent and the intensity spectrum, the intensity spectrum remains approximately constant. The observed absorption band in the continuum on the anti-Stokes side about 400 cm^{-1} away from the excitation frequency (see Fig. 2.17) is probably due to the inverse Raman effect (Jones & Stoicheff, 1964). The observed absorption band is located in the vicinity of strong Raman bands: 401, 370, and 311 cm^{-1}.

A curious feature of the associated weak broadband spectrum is the existence of a pronounced absorption line at a position (611.2 nm) where the linear absorption would be expected to be rather weak. A possible explanation for this is as follows: Imagine tracing the spatial development of the phase modulation spectrum. At a short distance, where the bounds of the spectrum have not yet intersected a strong absorption line, the spectrum is reasonably flat. On intersecting the absorption line, the spectrum abruptly drops (Alfano et al., 1974). The mechanism of FFPG is presumably responsible for the appearance of the signal beyond the absorption line limit. This explanation is also supported by the appearance of the angular emission pattern (see Fig. 2.21). As the spectrum continues to develop, one reaches a point where the limit of the regenerated spectrum crosses a weak absorption line. One can again expect a drastic drop in the spectrum at the position of this line. At still greater distances, renewed four-photon parametric regeneration accounts for the feeble signal. A continuum is generated behind absorption bands due to contributions from SPM, three-wave mixing (TWM), and FFPG.

2.10 Enhancement of Supercontinuum in Water by Addition of Ions

The most common liquids used to generate a continuum for various applications are CCl_4, H_2O, and D_2O. In most applications of the ultrafast supercontinuum, it is necessary to increase the conversion efficiency of laser excitation energy to the supercontinuum. One method for accomplishing this is based on the induced- or cross-phase modulation. Another way is to increase n_2 in materials. In this section, chemical means are used to obtain a tenfold enhancement of the ultrafast supercontinuum in water by adding Zn^{2+} or K^+ ions (Jimbo et al., 1987) for 8-ps pulse generation.

The optical Kerr gate (OKG) (Ho & Alfano, 1979) was used to measure the nonlinear refractive index of the salt solutions. The primary and second harmonic light beams were separated by a dichroic mirror and then focused into a 1-cm-long sample cell filled with the same salt solutions that produced the ultrafast

supercontinuum pulse enhancements. The size of the nonlinear index of refraction, n_2, was determined from the transmission of the probe beam through the OKG.

Three different two-component salt solutions of various concentrations were tasted. The solutes were KCl, $ZnCl_2$, and K_2ZnCl_4. All measurements were performed at 20 ± 1 °C. Typical spectra of ultrafast supercontinuum pulses exhibited both SPM and FPPG features. The collinear profile arising from SPM has nearly the same spatial distribution as the incident 8-ps, 530-nm laser pulse. The two wings correspond to FPPG pulse propagation. The angle arises from the phase-matching condition of the generated wavelength emitted at different angles from the incident laser beam direction. FPPG spectra sometimes appear as multiple cones and sometimes show modulated features. SPM spectra also show modulated patterns. These features can be explained by multiple filaments.

Typical ultrafast supercontinuum pulse spectra on the Stokes side for different aqueous solutions and neat water, measured with the optical multichannel analyzer, are shown in Fig. 2.22. The salient features in Fig. 2.22 are a wideband SPM spectrum together with the stimulated Raman scattering of the OH stretching vibration around 645 nm. The addition of salts causes the SRS signal to shift toward the longer-wavelength region and sometimes causes the SRS to be weak (Fig. 2.22a). The SRS signal of pure water and dilute solution appears in the hydrogen-bonded OH stretching region (~3400 cm^{-1}). In a high-concentration solution, it appears in the nonhydrogen-bonded OH stretching region (~3600 cm^{-1}). The latter features of SRS were observed in an aqueous solution of $NaClO_4$ by Walrafen (1972).

To evaluate quantitatively the effect of cations on ultrafast supercontinuum generation, the ultrafast supercontinuum signal intensity for various samples at a fixed wavelength was measured and compared. Figure 2.23 shows the dependence of the supercontinuum (mainly from the SPM contribution) signal intensity on salt concentration for aqueous solutions of K_2ZnCl_4, $ZnCl_2$, and KCl at 570 nm (Fig. 2.23a) and 500 nm (Fig. 2.23b). The data were normalized with respect to the average ultrafast supercontinuum signal intensity obtained from neat water. These data indicated that the supercontinuum pulse intensity was highly dependent on salt concentration and that both the Stokes and the anti-Stokes sides of the supercontinuum signals from a saturated K_2ZnCl_4 solution were about 10 times larger than from neat water. The insets in Fig. 2.23 are the same data plotted as a function of K^+ ion concentration for KCl and K_2ZnCl_4 aqueous solutions. Solutions of KCl and K_2ZnCl_4 generate almost the same amount of supercontinuum if the K^+ cation concentration is same, even though they contain different amounts of Cl^- anions. This indicates that the Cl^- anion has little effect on generation of the supercontinuum. The Zn^{2+} cations also enhanced the supercontinuum, though to a lesser extent than the K^+ cations.

The measurements of the optical Kerr effect and the ultrafast supercontinuum in salt-saturated aqueous solutions are summarized in Table 2.3. The measured n_2 (pure H_2O) is about 220 times smaller than n_2 (CS_2). The value $G_{SPM}(\lambda)$ represents the ratio of the SPM signal intensity from a particular salt solution to that from neat water at wavelength λ. G_{Kerr} is defined as the ratio of the transmitted intensity

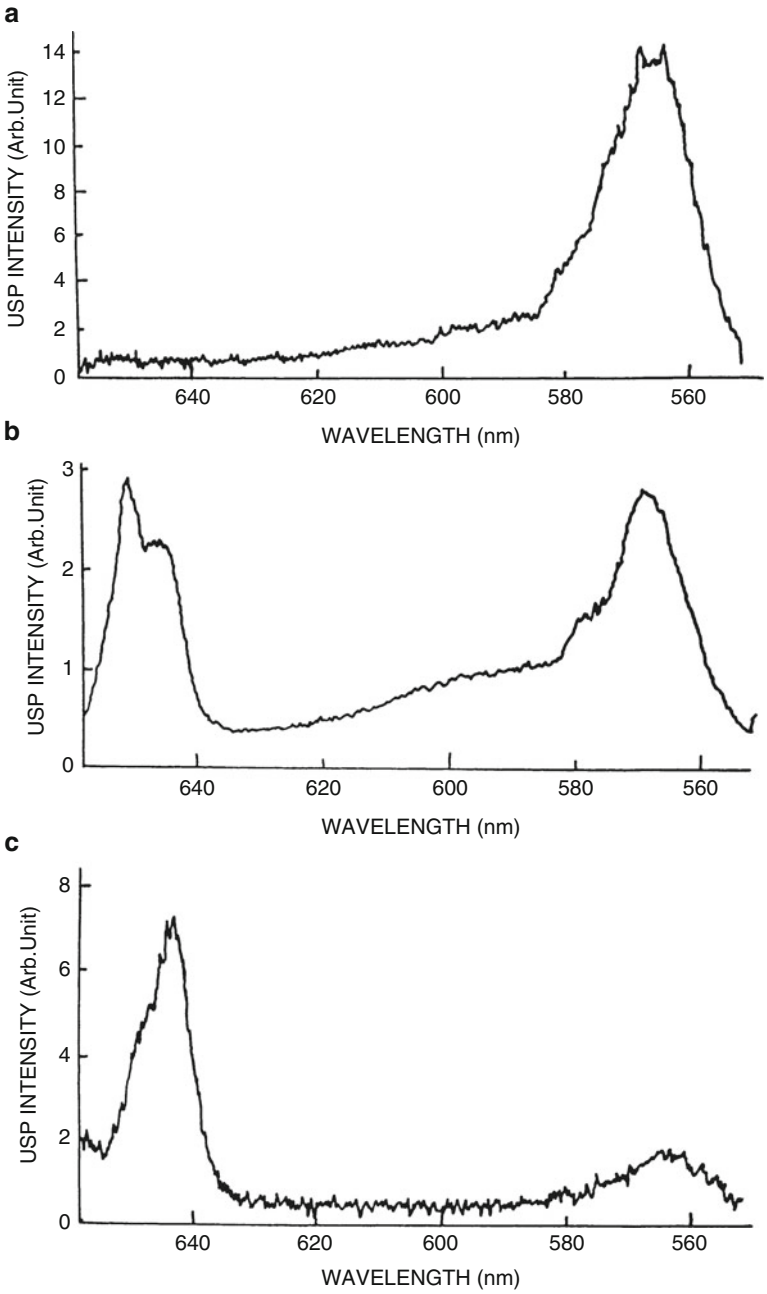

Fig. 2.22 SPM spectrum of (**a**) saturated K_2ZnCl_4 solution, (**b**) 0.6-m K_2ZnCl_4, and (**c**) pure water. The SRS signal (645 nm) is stronger in pure water, and it disappears in high-concentration solution. (From Jimbo et al., 1987)

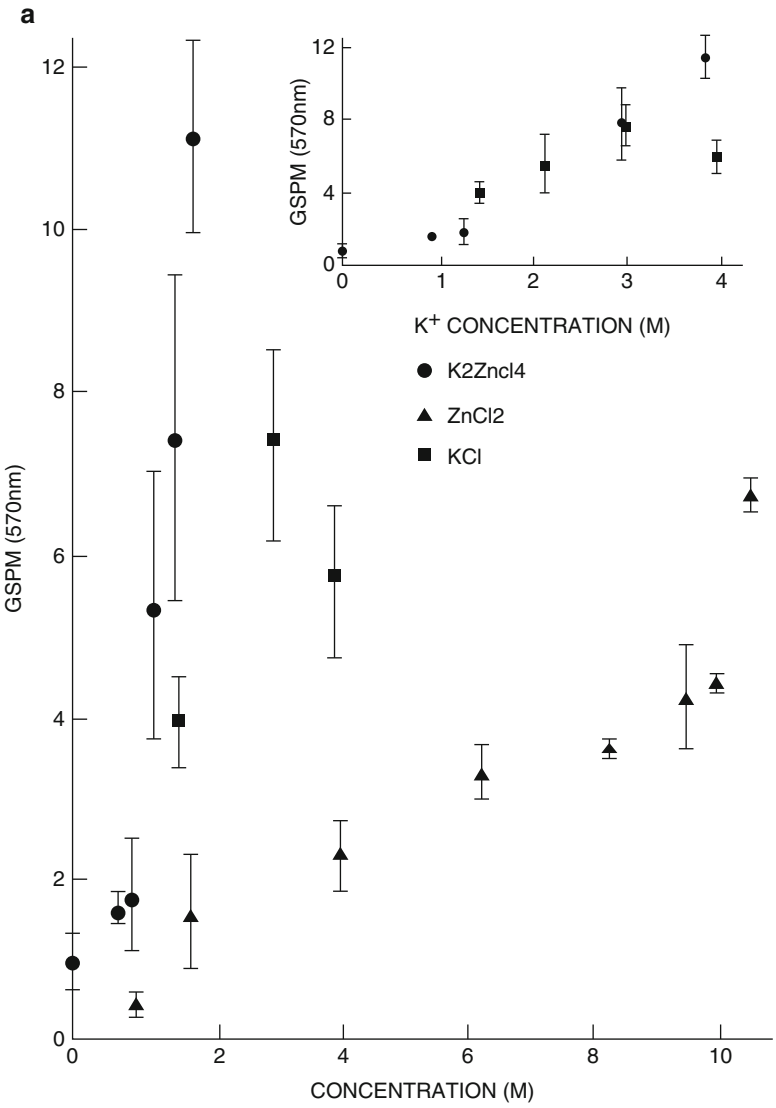

Fig. 2.23 Salt concentration dependence of the SPM signal (**a**) on the Stokes side and (**b**) on the anti-Stokes side 20 °C. Each data point is the average of about 10 laser shots. The inserts are the same data plotted as a function of K^+ ion concentration for KCl and K_2ZnCl_4 aqueous solutions. (From Jimbo et al., 1987)

caused by a polarization change of the probe beam in a particular salt solution to that in neat water; G_{Kerr} is equal to $[n_2$ (particular solution/n_2 (water))$]^2$. Table 2.3 shows that, at saturation, K_2ZnCl_4 produced the greatest increase in the supercontinuum. Although $ZnCl_2$ generated the largest enhancement of the optical Kerr effect, it did

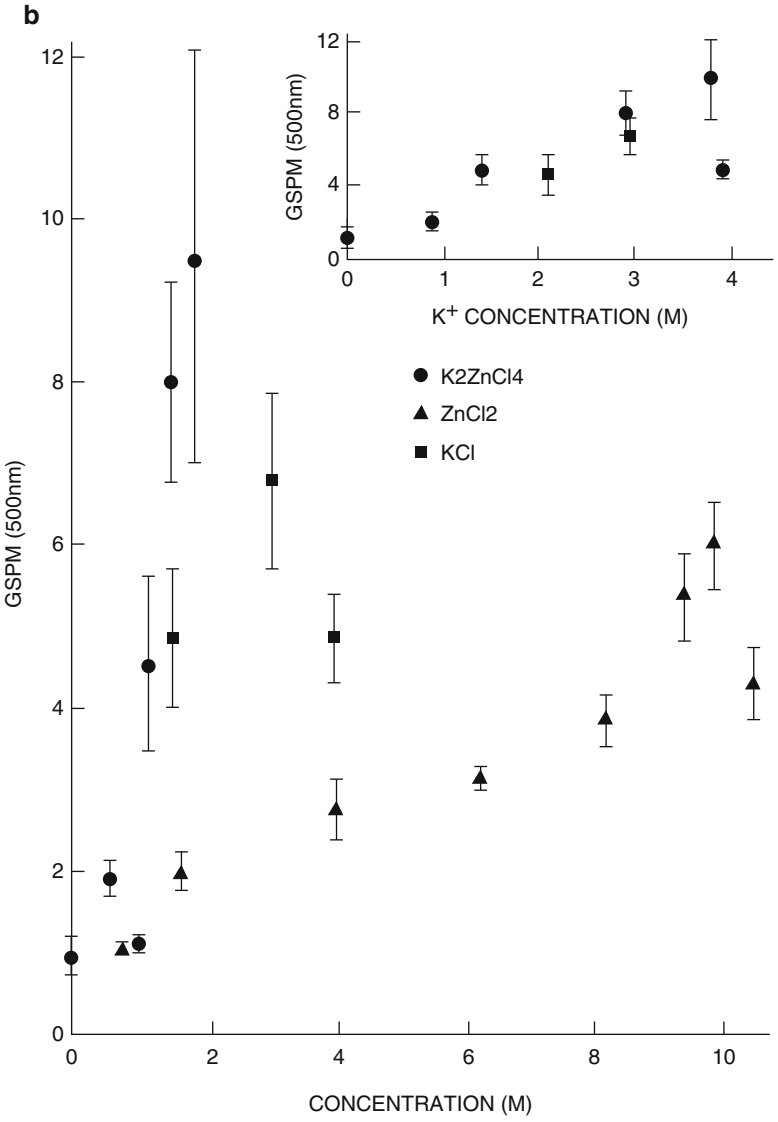

Fig. 2.23 (continued)

not play an important role in the enhancement of the ultrafast supercontinuum (a possible reason for this is discussed below). The optical Kerr effect signal from saturated solutions of $ZnCl_2$ was about 2–3 times greater than that from saturated solutions of K_2ZnCl_4.

The enhancement of the optical nonlinearity of water by the addition of cations can be explained by the cations' disruption of the tetrahedral hydrogen-bonded

Table 2.3 Enhancement of the supercontinuum and optical Kerr effects signals in saturated aqueous solutions at 20 °C[a]

Signal	K_2ZnCl_4 (1.9 M)	KCl (4.0 M)	$ZnCl_2$ (10.6 M)
$G_{SPM}(570)$	11 ± 1	5.6 ± 0.9	6.6 ± 0.4
$G_{SPM}(500)$	9.5 ± 2.5	4.9 ± 0.2	4.3 ± 0.5
G_{Kerr}	16 ± 1	6.1 ± 1.4	35 ± 9

[a] $G_{SPM}(\lambda) = [I_{SPM}(\lambda)/I_{laser}(530\ nm)]_{solution}/[I_{SPM}(\lambda)/I_{laser}(530\ nm)]_{water}$

water structures and their formation of hydrated units (Walrafen, 1972). Since the nonlinear index n_2 is proportional to the number density of molecules, hydration increases the number density of water molecules and thereby increases n_2. The ratio of the hydration numbers of Zn^{2+} and K^+ has been estimated from measurements of G_{Kerr} and compared with their values based on ionic mobility measurements. At the same concentration of KCl and $ZnCl_2$ aqueous solution, (G_{Kerr} generated by $ZnCl_2$ solution)/(G_{Kerr} generated by KCl solution) $= [N(Zn^{2+})/N(K^+)]^2 \sim 2.6$, where $N(Zn^{2+}) \sim 11.2 \pm 1.3$ and $N(K^+) \sim 7 \pm 1$ represent the hydration numbers for the Zn^{2+} and K^+ cations, respectively. The calculation of the hydration number of $N(Zn^{2+})/N(K^+) \sim 1.5$ is in good agreement with the Kerr nonlinearity measurements displayed in Table 2.3.

In addition, from our previous measurements and discussions of nonlinear processes in mixed binary liquids (Ho & Alfano, 1978), the total optical nonlinearity of a mixture modeled from a generalized Langevin equation was determined by the coupled interactions of solute–solute, solute–solvent, and solvent–solvent molecules. The high salt solution concentration may contribute additional optical nonlinearity to the water owing to the distortion from the salt ions and the salt-water molecular interactions.

The finding that Zn^{2+} cations increased G_{Kerr} more than G_{SPM} is consistent with the hydration picture. The transmitted signal of the OKG depends on Δn, while the ultrafast supercontinuum signal is determined by $\partial n/\partial t$. The ultrafast supercontinuum also depends on the response time of the hydrated units. Since the Zn^{2+} hydrated units are larger than those of K^+, the response time will be longer. These effects will be reduced for longer pulses. Two additional factors may contribute to part of the small discrepancy between G_{SPM} and G_{kerr} for $ZnCl_2$. The first one is related to the mechanism of δn generation in which χ_{1111} is involved in the generation of SPM while the difference $\chi_{1111} - \chi_{1112}$ is responsible for the optical Kerr effect. The second is the possible dispersion of n_2 because of the difference in wavelength between the exciting beams of the ultrafast supercontinuum and the optical Kerr effects.

The optical Ker effect is enhanced 35 time by using $ZnCl_2$ as a solute, and the ultrafast supercontinuum is enhanced about 10 times by using K_2ZnCl_4 as a solute. The enhancement of the optical nonlinearity has been attributed to an increase in the number density of water molecules owing to hydration and the coupled interactions of solute and solvent molecules. Addition of ions can be used to increase n_2 for SPM generation and gating.

2.11 Temporal Behavior of SPM

In addition to spectral features, the temporal properties of the supercontinuum light source are important for understanding the generation and compression processes. In this section, the local generation, propagation, and pulse duration reduction of SPM are discussed.

2.11.1 Temporal Distribution of SPM

In Sect. 2.1, using the stationary phase method, it was described theoretically that the Stokes and anti-Stokes frequencies should appear at well-defined locations in time within leading and trailing edges of the pump pulse profile (Alfano, 1972). Theoretical analyses by Stolen and Lin (1978) and Yang and Shen (1984) obtained similar conclusions.

Passing an 80-fs laser pulse through a 500-μm-thick ethylene glycol jet stream, the pulse duration of the spectrum in time was measured by the autocorrelation method (Fork et al., 1983). These results supported the SPM mechanism for supercontinuum generation. In the following, the measurements of the distribution of various wavelengths for the supercontinuum generated in CCl_4 by intense 8-ps laser pulses (Li et al., 1986) are presented. Reduction of the pulse duration using the SPM principle is discussed in Sect. 10.3.

The incident 530-nm laser pulse temporal profile is shown in Fig. 2.24. The pulse shape can be fitted with a Gaussian distribution with duration $\tau(\text{FWHM}) = 8$ ps. The spectral and temporal distributions of the supercontinuum pulse were obtained by measuring the time difference using a streak camera. The measured results are shown as circles in Fig. 2.25. Each data point corresponds to an average of about six laser shots. The observation is consistent with the SPM and group velocity dispersion. To determine the temporal distribution of the wavelengths generated within a supercontinuum, the group velocity dispersion effect (Topp & Orner, 1975) in CCl_4 was corrected. Results corrected for both the optical delay in the added filters and the group velocity are displayed as triangles in Fig. 2.25. The salient feature of Fig. 2.25 indicates that the Stokes wavelengths of the continuum lead the anti-Stokes wavelengths.

Using the stationary phase SPM method [Eqs. 2.6a and 2.6b], the generated instantaneous frequency ω of the supercontinuum can be expressed by

$$\omega(t) - \omega_L = -(\omega_L l/c)\,\partial(\Delta n)/\partial t, \tag{2.33}$$

where ω_L is the incident laser angular frequency, l is the length of the sample, and Δn is the induced nonlinear refractive index n_2E^2. A theoretical calculated curve for the sweep is displayed in Fig. 2.26 by choosing appropriate parameters to fit the experimental data of Fig. 2.25. An excellent fit using a stationary phase model

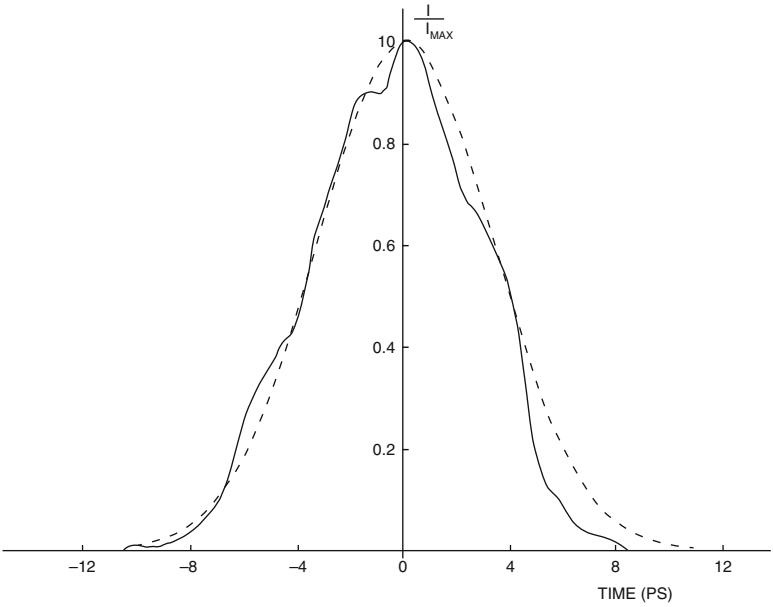

Fig. 2.24 Temporal profile of a 530-nm incident laser pulse measured by a 2-ps-resolution streak camera. The dashed line is a theoretical fit to an 8-ps EWHM Gaussian pulse. (From Li et al., 1986)

up to maximum sweep demonstrates that the generation mechanism of the temporal distribution of the supercontinuum arises from the SPM. During the SPM process, a wavelength occurs at a well-defined time within the pulse. The above analysis will be supported by the additional experimental evidence for SPM described in Sect. 10.3 (see Fig. 2.29).

2.11.2 Local Generation and Propagation

The dominant mechanisms responsible for the generation of the ultrafast supercontinuum as mentioned in Sects. 2.1 and 2.2 are SPM, FPPG, XPM, and SRS. In the SPM process, a newly generated wavelength could have bandwidth-limited duration at a well-defined time location (Alfano, 1972) in the pulse envelope. In the FPPG and SRS processes, the duration of the supercontinuum pulse could be shorter than the pump pulse duration due to the high gain about the peak of the pulse. In either case, the supercontinuum pulse will be shorter than the incident pulse at the local spatial point of generation. These pulses will be broadened in time due to the group velocity dispersion in condensed matter (Ho et al., 1987).

Typical data on the time delay of 10-nm-bandwith pulses centered at 530, 650, and 450 nm wavelengths of the supercontinuum generated from a 20-cm-long cell

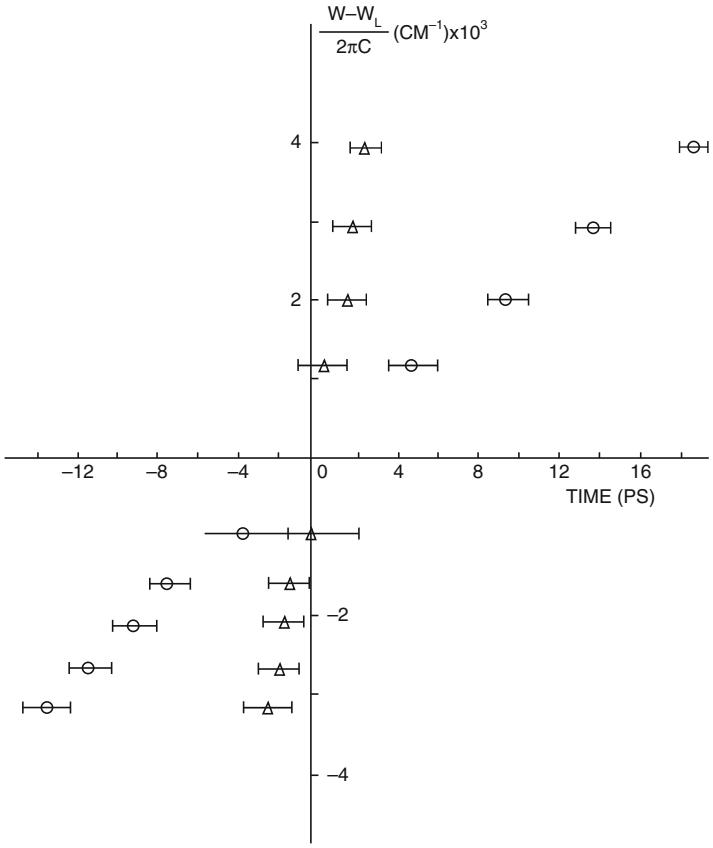

Fig. 2.25 Measured supercontinuum temporal distribution at different wavelengths: (o) data points with correction of the optical path in filters; (Δ) data points with correction of both the optical path in filters and group velocity dispersion in liquid. (From Li et al., 1986)

filled with CCl_4 are displayed in Fig. 2.27. The peak locations of 530, 650, and 450 nm are −49, −63, and −30 ps, respectively. The salient features in Fig. 2.27 (Ho et al., 1987) indicate that the duration of all 10-nm-band supercontinuum pulses is only 6 ps, which is shorter than the incident pulse of 8 ps, the Stokes side (650 nm) of the supercontinuum pulse travels ahead of the pumping 530 nm by 14 ps, and the anti-Stokes side (450 nm) of the supercontinuum pulse lags the 530 nm by 10 ps.

If the supercontinuum could be generated throughout the entire length of the sample, the Stokes side supercontinuum pulse generated by the 530-nm incident laser pulse at $z = 0$ cm of the sample would be ahead of the 530-nm incident pulse after propagating through the length of the sample. Over this path, 530 nm could continuously generate the supercontinuum pulse. Thus, the Stokes side supercontinuum generated at the end of the sample coincides in time with the 530-nm incident pulse. In this manner, a supercontinuum pulse centered at a particular

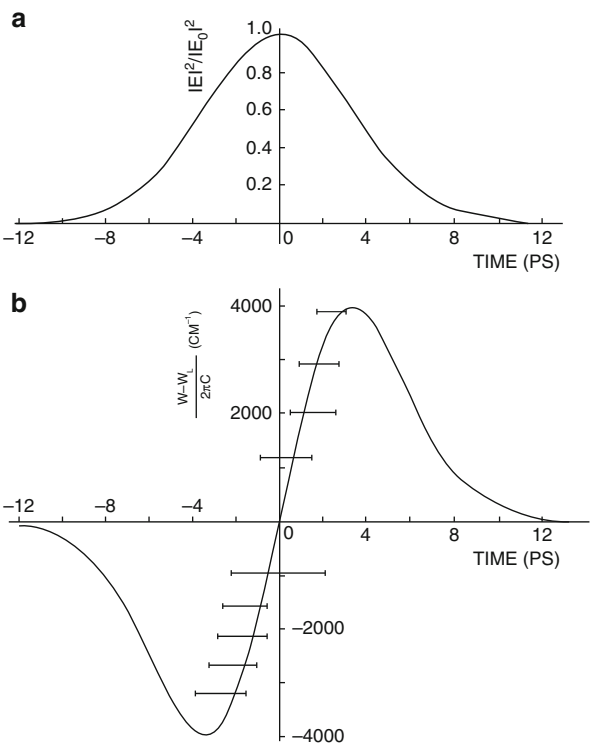

Fig. 2.26 Comparison of the measured temporal distribution of supercontinuum with the SPM model. (From Li et al., 1986)

Stokes frequency could have a pulse greater than the incident pulse extending in time from the energy of the 530-nm pulse to the position where the Stokes frequency was originally produced at $z \sim 0$ cm. From a similar consideration, the anti-Stokes side supercontinuum pulse would also be broadened. However, no slow asymmetric tail for the Stokes pulse or rise for the anti-Stokes pulse is displayed in Fig. 2.27. These observation suggest the local generation of supercontinuum pulses.

A model to describe the generation and propagation features of the supercontinuum pulse has been formulated based on local generation. The time delay of Stokes and anti-Stokes supercontinuum pulses relative to the 530-nm pump pulse is accounted for by the filaments formed ~5 cm from the sample cell entrance window. The 5-cm location is calculated from data in Fig. 2.27 by using the equation

$$T_{530} - T_{\text{supercon.}} = \Delta x \left(\frac{1}{v_{530}} - \frac{1}{v_{\text{supercon.}}} \right), \tag{2.34}$$

where Δx is the total length of supercontinuum pulse travel in CCl_4 after the generation. T_{350} and $T_{\text{supercon.}}$ are the 530-nm and supercontinuum pulse peak time locations in Fig. 2.27, and v_{530} and v_{supercon} are the group velocities of the 530-nm and supercontinuum pulses, respectively.

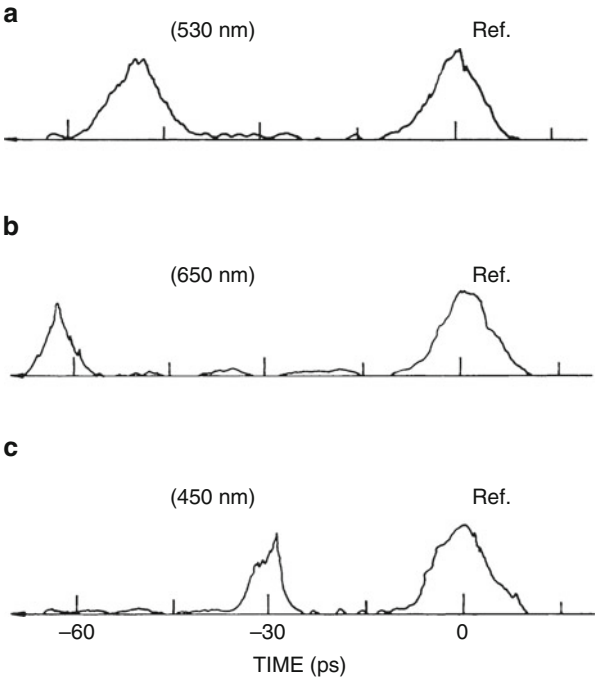

Fig. 2.27 Temporal profiles and pulse locations of a selected 10-nm band of a supercontinuum pulse at different wavelengths propagated through a 20-cm-long CCl4 cell: (**a**) $\lambda = 530$ nm; (**b**) $\lambda = 650$ nm; (**c**) $\lambda = 450$ nm. Filter effects were compensated. (From Ho et al., 1987)

The duration of the supercontinuum pulse right at the generation location is either limited by the bandwidth of the measurement from the SPM process or shortened by the parametric generation process. In either cases, a 10-nm-bandwidth supercontinuum pulse will have a shorter duration than the incident pulse. After being generated, each of these 10-nm-bandwidth supercontinuum pulses will travel through the rest of the sample and will continuously generated by the incident 530 nm over a certain interaction length before these two pulses walk off. The interaction length can be calculated as (Alfano, 1972)

$$l = \tau \frac{v_{530} v_{\text{supercon.}}}{v_{530} - v_{\text{supercon.}}}, \tag{2.35}$$

where l is the interaction length over the pump, and the supercontinuum pulses stay spatially coincident by less than the duration (FWHM) of the incident pump pulse, and τ is the duration of the supercontinuum pulse envelope. From Eq. (2.35), one can estimate the interaction length from the measured τ of the supercontinuum pulse. Using parameters $\tau = 6$ ps, $v_{530} = c/l.4868$, and $v_{\text{supercon.}} = c/l.4656$, the

interaction length $l = 8.45$ cm is calculated. This length agrees well with the measured beam waist length of 8 cm for the pump pulse in CCl4.

Since no long tails were observed from the supercontinuum pulses to the dispersion delay times of the Stokes and anti-Stokes supercontinuum pulses, the supercontinuum was not generated over the entire length of 20 cm but only over 1–9 cm. This length is equivalent to the beam waist length of the laser in CCl4. The length of the local SPM generation over a distance of 8.45 cm yields a possible explanation for the 6-ps supercontinuum pulse duration. In addition, a pulse broadening of 0.3 ps calculated from the group velocity dispersion of a 10-nm band at 650-nm supercontinuum traveling over 20 cm of liquid CCl4 is negligible in this case.

Therefore, the SPM pulses have shorter durations than the pump pulse and were generated over local spatial domains in the liquid cell.

2.11.3 SPM Pulse Duration Reduction

The principle behind the pulse narrowing based on the spectral temporal distribution of the SPM spectrally broadened in time within the pulse is described in Sects. 2.2 and 10.1. At each time t within the pulse, there is a frequency $\omega(t)$. When a pulse undergoes SPM, the changes in the optical carrier frequency within the temporal profile are greatest on the rising and falling edges, where the frequency is decreased and increased, respectively. Near the peak of the profile, and in the far leading and trailing wings, the carrier frequency structure is essentially unchanged. The maximum frequency shift is proportional to the intensity gradient on the sides of the pulse, and this determines the position of the outer lobes of the power spectrum. If these are then attenuated by a spectral window of suitably chosen width, the wings of the profile where the high- and low-frequency components are chiefly concentrated will be depressed, while the central peak will be largely unaffected. The overall effect is to create a pulse that is significantly narrower in time than the original pulse duration. A file can be used to select a narrow portion of the pulse, giving rise to a narrower pulse in time.

A threefold shortening of 80-ps pulses to 30 ps from an Nd:YAG laser broadened from 0.3 to 4 Å after propagation through 125 m of optical fiber with a monochromator as a spectral window was demonstrated using this technique (Gomes et al., 1986). The measurements of pulses at different wavelengths of the frequency sweep of supercontinuum pulses generated by 8-ps laser pulses propagating in CCl_4 show that the continuum pulses have a shorter duration (~6 ps) than the pumping pulses (Li et al., 1986).

A major advance occurred when a 25-ps laser pulse was focused into a 5-cm-long cell filled with D_2O. A continuum was produced. Using 10-nm-bandwidth narrowband filters, tunable pulses of less than 3 ps in the spectral range from 480 to 590 nm (Fig. 2.28) were produced (Dorsinville et al., 1987).

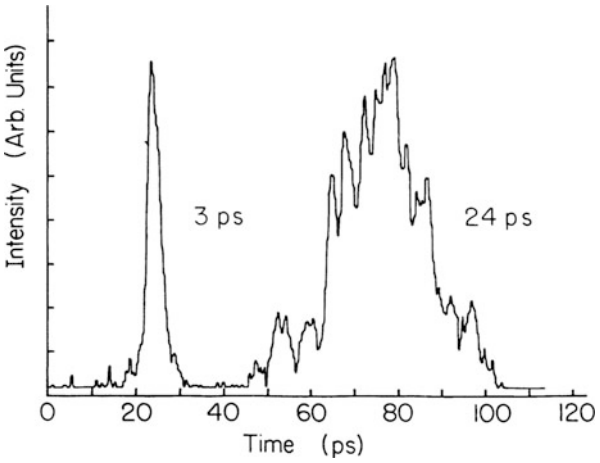

Fig. 2.28 Streak camera temporal profile of the 25-ps, 530-nm incident laser pulse and 10-nm-bandwidth pulse at 580 nm. The 3-ps pulse was obtained by spectral filtering a SPM frequency continuum generated in D_2O. (From Dorsinville et al., 1987)

To identify the SPM generation mechanism, the temporal distribution of the continuum spectrum was determined by measuring the time delay between the continuum and a reference beam at different wavelengths using a streak camera. The results are displayed in Fig. 2.29, which is similar to data displayed in Fig. 2.25. The time delay was ~22 ps for a 140-nm change in wavelength; as predicted by the SPM mechanism, the Stokes wavelength led the anti-Stokes wavelength (Alfano, 1972). The delay due to group velocity over a 5-cm D_2O cell for the 140-nm wavelength change is less than 3 ps.

The remaining 18 ps is well accounted for by the SPM mechanism using a 25-ps (FWHM) pulse and the stationary phase method (Alfano, 1972). Furthermore, a 10-nm selected region in the temporal distribution curve corresponds to an ~2.6-ps width matching the measured pulse duration (Fig. 2.28). This observation suggests that by using narrower bandwidth filters, the pulse duration can be shortened to the uncertainty limit.

2.12 Higher-Order Effects on Self-Phase Modulation

A complete description of SPM-generated spectral broadening should take into account higher-order effects such as self-focusing, group velocity dispersion, self-steepening, and initial pulse chirping. Some of these effects are described by Suydam (Chap. 6), Shen (Chap. 1), and Agrawal (Chap. 3). These effects will influence the observed spectral profiles.

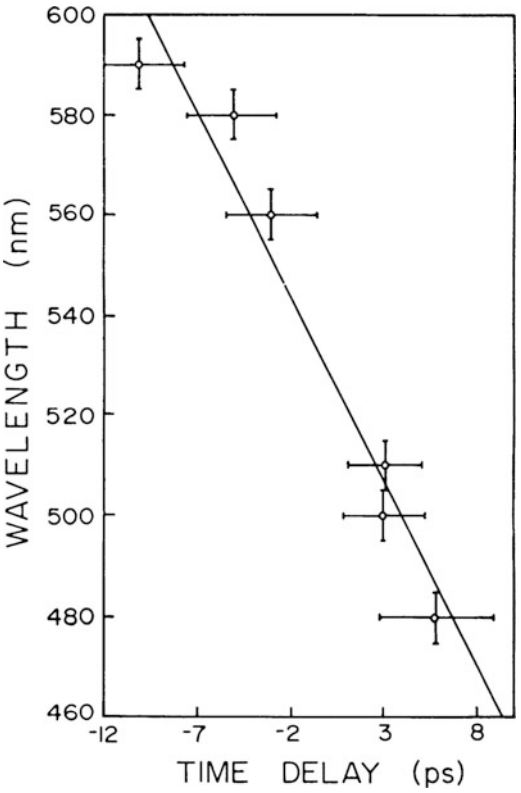

Fig. 2.29 Continuum temporal distribution at different wavelengths. Horizontal error bars correspond to 10-nm bandwidths of the filter. (From Dorsinville et al., 1987)

2.12.1 Self-Focusing

In the earliest experiments using picosecond pulses, the supercontinuum pulses were often generated in small-scale filaments resulting from the self-focusing of intense laser beams (Alfano, 1972). Self-focusing arises from the radial dependence of the nonlinear refractive index $n(r) = n_0 + n_2E^2(r)$ (Shen, 1984; Auston, 1977). It has been observed in many liquids, bulk materials (Shen, 1984), and optical fibers (Baldeck et al., 1987a). Its effects on the continuum pulse generation can be viewed as good and bad. On the one hand, it facilitates the spectral broadening by concentrating the laser beam energy. On the other hand, self-focusing is a random and unstable phenomenon that is not controllable. Femtosecond supercontinua are generated with thinner samples than picosecond supercontinua, so it can reduce but not totally eliminate self-focusing effects.

2.12.2 Dispersion

Group velocity dispersion (GVD) arises from the frequency dependence of the refractive index. These effects are described by Agrawal (Chap. 3). The first-order GVD term leads to a symmetric temporal broadening (Marcuse, 1980). A typical value for the broadening rate arising from $\partial^2 k/\partial\omega^2$ is 500 fs/m-nm (in silica at 532 nm). In the case of supercontinuum generation, spectral widths are generally large (several hundred nanometers), but interaction lengths are usually small (<1 cm). Therefore, the temporal broadening arising from GVD is often negligible for picosecond pulses but is important for femtosecond pulses. Limitations on the spectral extent of supercontinuum generation are also related to GVD. Although the spectral broadening should increase linearly with the medium length (i.e., $\Delta\omega(z)_{\max} = \omega_0\, n_2\, a^2\, z/c\, \Delta\tau$), it quickly reaches a maximum as shown in Fig. 2.10. This is because **GVD**, which is large for pulses having **SPM**-broadened spectra, reduces the pulse peak power a^2 and broadens the pulse duration $\Delta\tau$. As shown in Fig. 2.25, the linear chirp parameter is decreased by the **GVD** chirp in the normal dispersion regime. This effect is used to linearize chirp in the pulse compression technique.

The second-order term $\partial^3 k/\partial\omega^3$ has been found to be responsible for asymmetric distortion of temporal shapes and modulation of pulse propagation in the lower region of the optical fiber (Agrawal & Potasek, 1986). Since the spectra of supercontinuum pulses are exceptionally broad, this term should also lead to asymmetric distortions of temporal and spectral shapes of supercontinuum pulses generated in thick samples. These effects have been observed.

In multimode optical fibers, the mode dispersion dominates and causes distortion of the temporal shapes. This in turn yields asymmetric spectral broadening (Wang et al., 1989).

2.12.3 Self-Steepening

Pulse shapes and spectra of intense supercontinuum pulses have been found to be asymmetric (De Martini et al., 1967). There are two potential sources of asymmetric broadening in supercontinuum generation. The first one is the second-order **GVD** term. The second one is self-steepening, which is intrinsic to the **SPM** process and occurs even in nondispersion media. Details of the effects of self-steepening can be found in Suydam (Chap. 6), Shen and Yang (Chap. 1), and Manassah (Chap. 5).

Because of the intensity and time dependence of the refractive index, $n = n_0 + n_2 E(t)^2$, the supercontinuum pulse peak sees a higher refractive index than its edges. Because $v = c/n$, the pulse peak travels slower than the leading and trailing edges. This results in a sharpened trailing edge. Self-steepening occurs and more blue-shifted frequencies (sharp trailing edge) are generated than red frequencies. Several theoretical approaches have given approximate solutions for the electric

field envelope distorted by self-steepening and asymmetric spectral extent. Actual self-steepening effects have not been observed in the time domain.

2.12.4 Initial Pulse Chirping

Most femtosecond and picosecond pulses are generated with initial chirps. Chirps arise mainly from **GVD** and **SPM** in the laser cavity. As shown in Fig. 2.30, the spectral broadening is reduced for positive chirps and enhanced for negative chirps in the normal dispersion regime. The spectral distribution of SPM is also affected by the initial chirp.

2.13 High-Resolution Spectra of Self-Phase Modulation in Optical Fibers

In bulk materials, self-focusing plays an important role in the SPM process, and the spectral-broadening changes significantly from laser shot to shot. To obtain a stable, repeatable SPM spectrum, one would like to keep the cross section constant over the entire propagation distance in the medium. Optical fibers are ideal materials for this type of investigation because the beam cross section of a guided wave would be constant and the self-focusing effect can be neglected. The spectral features of SPM in optical fibers measured by a piezoelectrically scanned planar Fabry–Perot interferometer with the resolution of approximately one-third of the laser linewidth were pioneered by Stolen and Lin (1978), using a 180-ps laser pulse. Measurements performed on the fine structures of the SPM spectra of picosecond laser pulses by use of a grating spectrometer with a spectral resolution higher than one-tenth of the laser linewidth and comparing the spectral profiles with the results calculated by use of the SPM model are discussed in the following.

2.13.1 Reduced Wave Equation

The optical electromagnetic field of a propagating optical pulse must satisfy Maxwell's equations. From Maxwell's equations, one can obtain the wave equation that describes the amplitudes of light pulses propagating in optical fibers [See Eq. (A.19) in Appendix]:

$$\frac{\partial A}{\partial z} + \frac{1}{v_g}\frac{\partial A}{\partial t} + i\frac{1}{2}k^{(2)}\frac{\partial^2 A}{\partial t^2} = i\frac{\omega_0 n_2}{c}|A|^2 A, \tag{2.36}$$

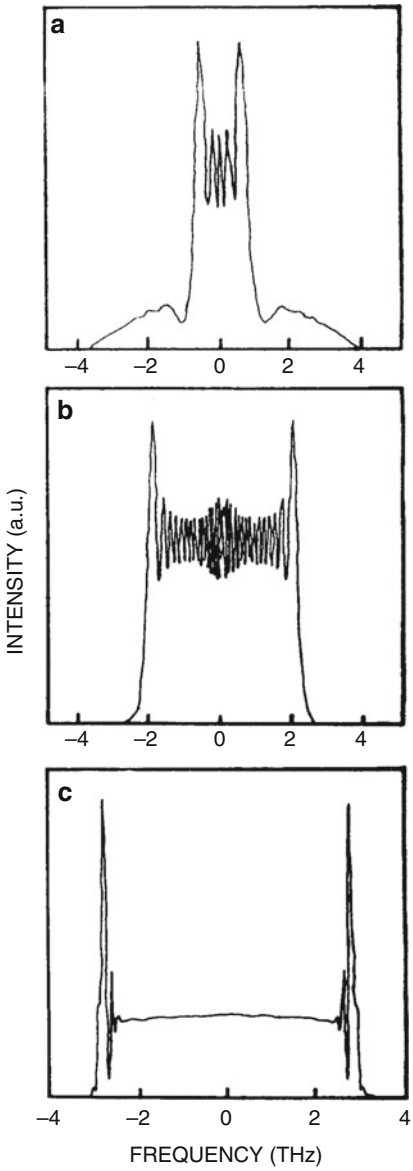

Fig. 2.30 Influence of initial pulse chirping on **SPM**-broadened spectra in optical fibers. Peak power = 1000 W. (**a**) $C = 50$; (**b**) $C = 0$; (**c**) $C = -50$ [see Eq. (2.17)]. (From Baldeck et al., 1987b)

The third term on the left-hand side of this equation is the dispersion term. The absorption of the optical fiber and the higher-order nonlinearities have been neglected in obtaining Eq. (2.36).

Changing the variables

$$\tau = t - \frac{z}{v_g}, \tag{2.37}$$

$$z = z' \tag{2.38}$$

and denoting by a and α the amplitude and the phase of the electric envelope, respectively, A can be expressed as

$$A(z, \tau) = a(z, \tau) \exp[i\alpha(z, \tau)], \tag{2.39}$$

where τ is the local time of the propagating optical pulse.

Because the fiber lengths used in the experiment are much smaller than the dispersion lengths, which can be calculated to be a few kilometers, the dispersion term in Eq. (2.36) can be neglected. Therefore, Eq. (2.36) further reduces to

$$\frac{\partial a}{\partial z} = 0 \tag{2.40}$$

$$\frac{\partial \alpha}{\partial z} = \frac{\omega_0 n_2}{c} a^2 \tag{2.41}$$

The analytical solutions for Eqs. (2.40) and (2.41) can be obtained as

$$a(\tau) = a_0 F(\tau) \tag{2.42}$$

$$\alpha(z, \tau) = \frac{\omega_0 n_2}{c} \int_0^z a^2\left(z', \tau\right) dz' = \frac{\omega_0 n_2}{c} {a_0}^2 F^2(\tau)\, z, \tag{2.43}$$

where a_0 is the amplitude, and $F(t)$ is the pulse envelope of the input optical pulse.

Because the pulse duration is much larger than the optical period $2\pi/\omega_0$, the electric field at each τ within the pulse has a specific local and instantaneous frequency that is given by

$$\omega(\tau) = \omega_0 + \delta\omega(\tau) \tag{2.44}$$

where

$$\delta\omega(\tau) = -\frac{\partial \alpha}{\partial \tau} = -\frac{\omega_0 n_2}{c} {a_0}^2 \frac{\partial F^2(\tau)}{\partial \tau} z \tag{2.45}$$

$\delta\omega(\tau)$ is the frequency shift generated at a particular local time τ within the pulse envelope. This frequency shift is proportional to the derivative of the pulse envelope with respect to τ, the nonlinear refractive index, and the intensity of the pulse.

It can be obtained by the complex-field spectral profiles $E(z, \omega - \omega_0)$ of the optical pulse affected by SPM by computing the Fourier transformation of its temporal pulse distribution as

$$\begin{aligned} E\,(z, \omega - \omega_0) &= \tfrac{1}{2\pi} \int A\,(z, \tau) \exp\left(-i\omega_0\tau\right) \exp\left(i\omega\tau\right) d\tau \\ &= \tfrac{1}{2\pi} \int a\,(z, \tau) \exp\left[\left(i\alpha\left(z, \tau\right)\right]\right] \exp\left[i\,(\omega - \omega_0)\,\tau\right] d\tau \end{aligned} \tag{2.46}$$

The spectral-intensity distribution of the pulse is given by

$$|E\,(z, \omega - \omega_0)|^2. \tag{2.47}$$

Figure 2.31 shows a set of numerical solutions of Eq. (2.47) for laser pulses at 532 nm. The initial pulse shape is Gaussian. The spectrum of the input laser is shown in Fig. 2.31a. The length of the optical fiber used in the calculation is 1 m. As the intensity of the input laser pulse increases, the spectrum of the output signal broadens. Large-intensity oscillations occur at the same time because of the interference. In the same spectrum, the width of the maxima near the input laser frequency is smaller than that farther away from the input laser frequency. The outmost maxima have the largest widths. The salient feature of SPM is the spectral broadening which is accompanied by oscillations structure. The structure in the spectra consists of many maximum peaks (Max) where the outermost peaks are more intense (Also see Agrawal, Chap. 3). These oscillations are caused by interference. The maximum phase $\theta_{\max}$ is given by number of maxima peaks in the SPM spectra by peaks:

$$\text{Phase}_{\text{Max}} = \theta_{\max} = (\text{Max} - 1/2)\,\pi. \tag{2.48}$$

For example, Fig. 2.31e has max phase = 9½π and Fig. 2.31f has max phase = 12½π.

For different spectra, the widths of the maxima at the same wavelength of the spectra of higher-intensity laser pulses are smaller than are those for the lower-intensity pulses. The peak intensities of the outermost maxima for all the different intensities remain the largest, as can be seen in Fig. 2.31b–f. The SPM phase change is $\theta = \omega n_2 I(t) z/c$. The peak of pulse gives rises to 1 radian after propagating a distance given by:

$$L_{\text{spm}} = c/\omega n_2 I_p \tag{2.49}$$

After traveling a distance given by 5π L_{spm}, the phase change at the peak will be 5π.

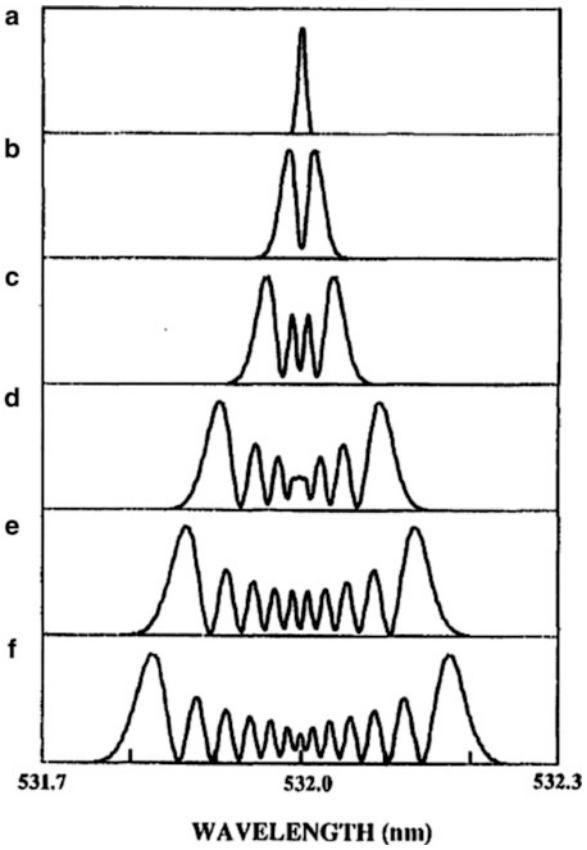

Fig. 2.31 Calculated SPM spectra of 532-nm laser pulses propagating in an optical fiber. The core diameter of the optical fiber was 2.5 μm. $n_2 = 3.2 \times 10^{-16}$ cm^2/W. (**a**) Input laser, (**b**) $P_0 = 110$ W, (**c**) $P_0 = 225$ W, (**d**) $P_0 = 460$ W, (**e**) $P_0 = 630$ W, Max = 10 and Max Phase = 9½π, (**f**) $Po = 790$ W, Max = 13 and Max Phase = 12½π. (From Wang et al., 1994a, b)

The numerical solutions of expression (2.47) for laser pulses at 1064 nm are displayed in Fig. 2.32. The results are similar to those displayed in Fig. 2.31 for laser pulses at 532 nm.

2.13.2 Experiment

The experimental arrangement used to measure high-resolution spectra of self-phase modulation in optical fibers is illustrated in Fig. 2.33. A 10-Hz mode-locked Quantel Nd:YAG laser system was used to generate laser pulses at 1064 nm and pulses at 532 nm. The 1/*e* pulse durations were 39 and 28 ps, respectively, and the pulse energies were approximately 2 μJ and 200 nJ for 1064 and 532 nm, respectively. A set of color filters was used to select the wavelengths of the laser pulses. The laser pulses were coupled into a 1-m optical fiber with a 20× microscope objective lens. A set of neutral-density filters was used in front of the microscope objective lens

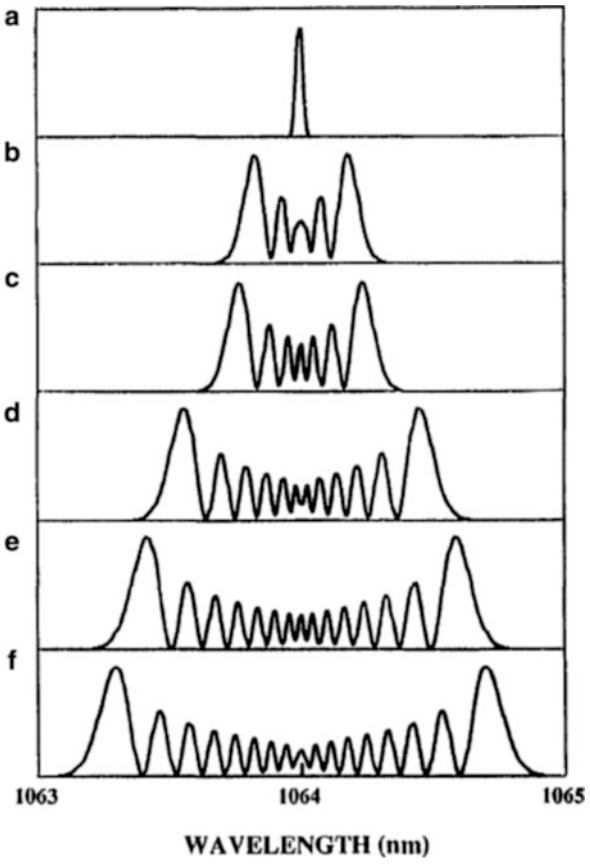

Fig. 2.32 Calculated SPM spectra of 1064-nm laser pulses propagating in an optical fiber. The core diameter of the optical fiber was 4 μm. $n_2 = 2.28 \times 10^{-16}$ cm^2/W. (**a**) Input laser, (**b**) $P_0 = 1800$ W, (**c**) $P_0 = 2300$ W, (**d**) $P_0 = 3900$ W, (**e**) $P_0 = 4900$ W, (**f**) $P_0 = 5700$ W. (From Wang et al., 1994a, b)

to control the pulse energy coupled into the optical fiber. The optical signal pulse was collected with a 20× microscope objective lens. The beam after the collecting lens was split into two. One beam was used to monitor intensities of the pulses coupled into the optical fiber by a photomultiplier tube. The other beam was passed through a spectral analysis system consisting of a 1-m spectrometer combined with a computer controlled CCD camera. The resolution of the spectral analysis system was 0.05 A/pixel for light at the 532-nm region and 0.1 A/pixel at the 1064-nm region.

Optical fibers with a core diameter of 2.5 μm and a cladding diameter of 127 μm were purchased from Corning Inc. The numerical aperture of these fibers is 0.11. Optical fibers with a core diameter of 4 μm and a cladding diameter of 125 μm were purchased from Newport Corporation. Their numerical aperture is 0.1. The optical fibers with a core diameter of 4 μm support a single mode for 1064-nm laser pulses and multimodes for 532-nm laser pulses. The 2.5-μm-core optical fibers support a single mode for 532-nm laser pulses. No detectable 1064-nm laser pulse was coupled into the 2.5-μm-core optical fiber.

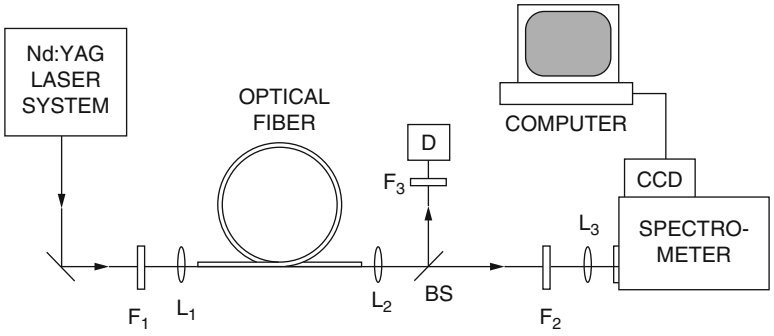

Fig. 2.33 Experimental arrangement. F_1, a set of color and neutral-density filters; F_2, F_3, neutral-density filters; L_1, L_2, 20× microscope objectives; L_3, lens. (From Wang et al., 1994a, b)

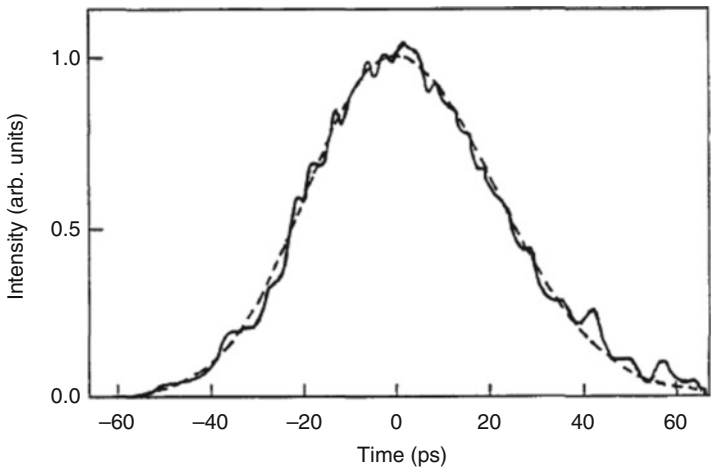

Fig. 2.34 Input laser pulse shape. The laser pulse is slightly asymmetric. The leading edge is shorter than the trailing edge. The dashed curve shows a theoretical fit to the pulse. (From Wang et al., 1994a, b)

Figure 2.34 displays an input laser pulse at 532 nm measured with a Hamamatsu 2-ps streak camera. The laser pulse is slightly asymmetric. The leading edge is shorter than the trailing edge. The dashed curve shows a theoretical fit to the pulse. Because the 532-nm pulse is the second-harmonic generation of the laser pulse at 1064 nm, the pulse width of the 1064-nm pulse is $\sqrt{2}$ times that of the 532 nm pulse, and the pulse shapes are similar.

The output spectra of the laser pulses at 532 nm with different pulse energies propagating in a 1-m optical fiber or core diameter 2.5 μm are displayed in Fig. 2.35. The salient feature of the spectra shown in Fig. 2.35 is that the spectra of the output signal pulses broaden toward both the Stokes and the anti-Stokes sides. The spectral broadening increases as the power of the input pulse increases.

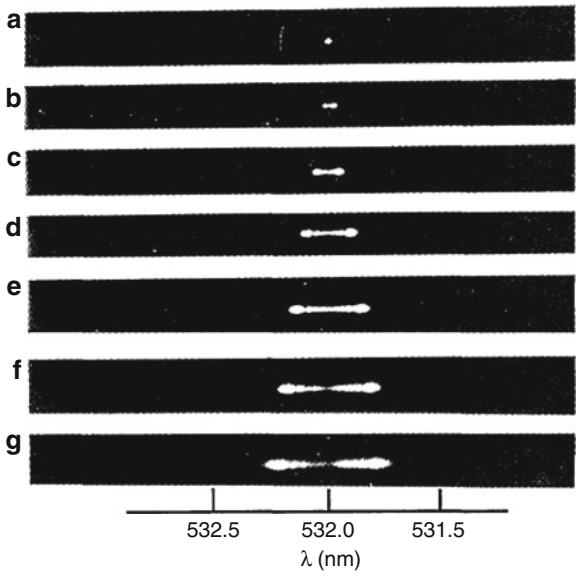

Fig. 2.35 Video display of the spectra of 532-nm laser pulses propagating in a 1-m 2.5−/−Lm-core optical fiber with different peak powers. (**a**) Input laser, (**b**) $P_0 = 110$ W, (**c**) $P_0 = 225$ W, (**d**) $P_0 = 460$ W, (**e**) $P_0 = 630$ W, (**f**) $P_0 = 790$ W, and (**g**) $P_0 = 270$ W. (From Wang et al., 1994a, b)

In addition, the broadened spectra have large intensity oscillations. In the same spectrum, the oscillation period is smaller near the central frequency and larger near both ends of the broadened spectrum. For all the spectra of different input power, the outermost maxima intensities have the largest intensities. The left-hand column of Fig. 2.34 displays some spectral curves of the broadened spectra shown in Fig. 2.35. The outermost maximum intensity on the anti-Stokes side is larger than that on the Stokes side in the same spectral curve. There are two main differences between the experimental observations shown in Figs. 2.35 and 2.36 and the theoretical calculations shown in Fig. 2.31. First, the spectral broadening of calculated spectra are symmetric about the input laser line, whereas the spectral broadening to the Stokes side is larger than that to the anti-Stokes side in the experimental observations. Second, the intensities of the maxima in the calculated spectra are symmetric about the laser line, whereas the intensities of the anti-Stokes-side maxima are larger than the corresponding maxima on the Stokes side. These two differences arise from the asymmetric input laser pulse. A set of numerical solutions of expression (2.47) with the asymmetrical experimental input laser pulse shown in Fig. 2.33 is displayed in the right-hand column of Fig. 2.34. These calculated spectra agree well with the experimental observations.

Note that no fitting parameters were used in the theoretical calculations. All the parameters used in the calculations are deduced from experimental measurements.

Figure 2.37 shows the spectra of the laser pulses at 1064 nm with different pulse energies propagating in a 1-m optical fiber of 4-μm diameter. The spectral curves are displayed in the left-hand column of Fig. 2.38. A set of numerical solutions of expression (2.47) with the asymmetrical experimental input laser pulse is shown in the right-hand column of Fig. 2.38. For the best fit of the experimental spectra, we

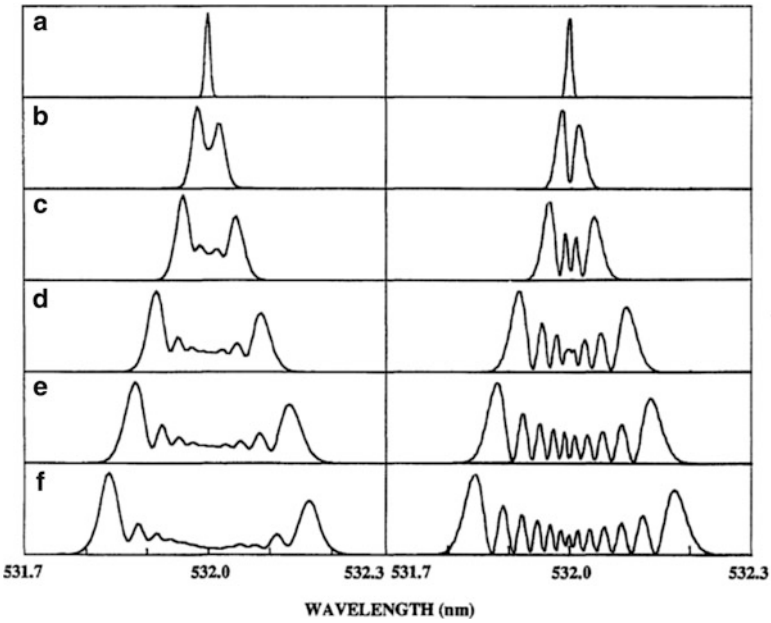

Fig. 2.36 Digital-intensity spectral curves of 532-nm laser pulses propagating in a I-m 2.5-μm-core optical fiber with different peak powers. The left-hand column shows the experimental results, and the right-hand column displays the numerical simulations. (**a**) Input laser, (**b**) $P_0 = 110$ W, (**c**) $P_0 = 225$ W, (**d**) $P_0 = 460$ W, (**e**) $P_0 = 630$ W, (**e**) $P_0 = 790$ W. (From Wang et al., 1994a, b)

used $n_2 = 2.28 \times 10^{-16}$ cm^2/W in the calculations, which is approximately 0.7 times its value for 532 nm.

2.13.3 Discussion

The SPM spectra of laser pulses at wavelengths of 532 and 1064 nm were measured with a high-resolution-grating spectral analysis system. The substructures of the SPM spectra for single-mode operations were observed and were compared with the theoretical results. The measured spectra and those calculated from SPM theory agree well for short pulses propagating in optical fibers. The subspectral structure can be useful in increasing the accuracy of the all-optical information coding. The numerical results also show that the third-order nonlinearity of the optical fibers for 1064 nm is approximately 0.7 times the value for 532 nm.

Whereas the modulation structures of the calculated spectral profiles with the SPM model fit the observed spectra, there is some difference in that the measured spectra always show a weak peak at the input laser frequency. This peak can be qualitatively understood by means of the transverse distribution of the intensity of

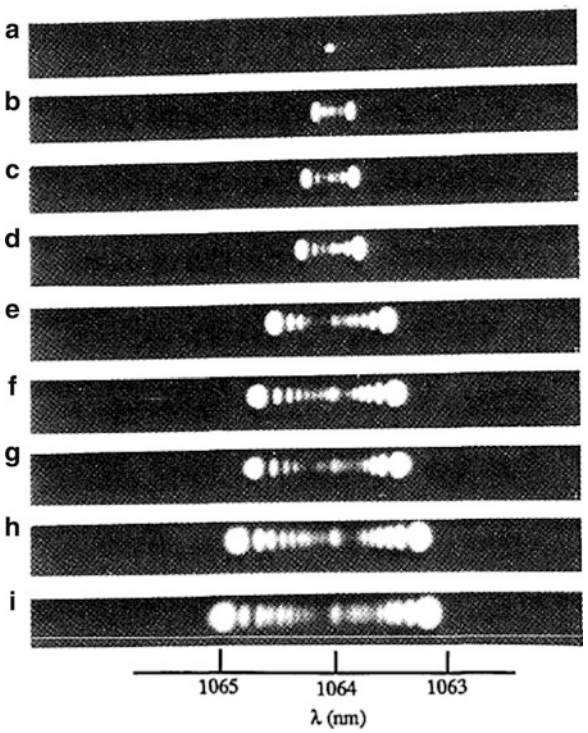

Fig. 2.37 Video display of the spectra of 1064-nm laser pulses propagating in a 1-m 4-μm-core optical fiber with different peak powers. (**a**) Input laser, (**b**) $P_0 = 1800$ W, (**c**) $P_0 = 2300$ W, (**d**) $P_0 = 3100$ W, (**e**) $P_0 = 3920$ W, (**f**) $P_0 = 4900$ W, (**g**) $P_0 = 5700$ W, (**h**) $P_0 = 6900$ W, (**i**) $P_0 = 7800$ W. (From Wang et al., 1994a, b)

the laser pulse in the optical fiber. In the calculations, it is assumed that the intensity of the optical pulse is uniformly distributed over the transverse cross section of the core of the optical fiber, whereas the laser pulse has a Gaussian distribution in the cross section for the lowest mode in practice. The laser light at the outermost area of the fiber core remains at its input wavelength because of the low intensity. The SPM process occurs near the center of the optical fiber core, where the laser pulse has the highest intensity.

Various groups have suggested that the continuum generated by picosecond pulses was not due to SPM because the extent of the spectrum was not in agreement with the SPM mechanism. The measurements and theoretical fittings clearly demonstrate the importance of using a well-defined spatial and temporal beam profile to compare experimental results with theory to confirm the SPM mechanism for continuum generation.

2.13.4 UV Supercontinuum Lower Limit in Holey Fibers

Two of important characteristics of the supercontinuum are (1) short and long wavelength extent from UV to NIR and (2) to keep the pulse structure simple to

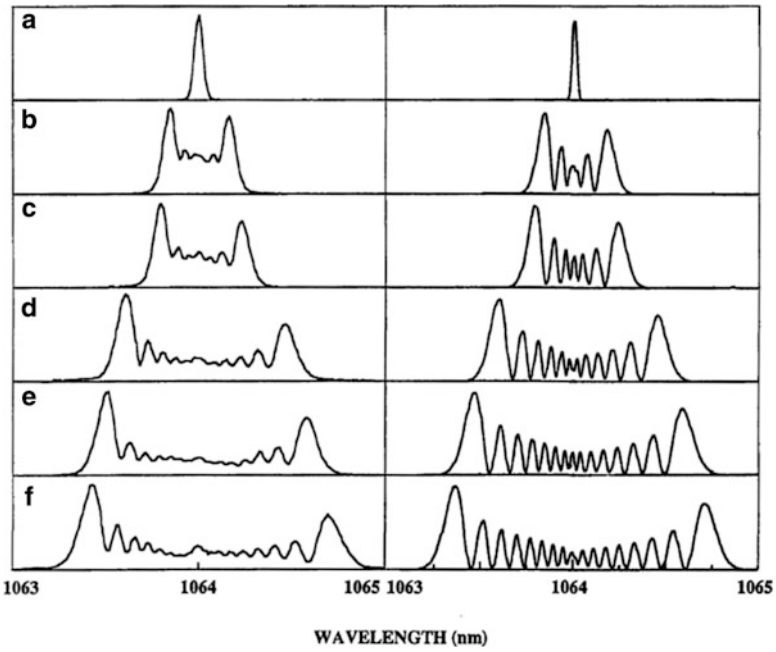

Fig. 2.38 Digital-intensity spectral curves of 1064-nm laser pulses propagating in a 1-m 2.5-μm-core optical fiber with different peak powers. The left-hand column shows the experimental results, and the right-hand column displays the numerical simulations. (**a**) Input laser, (**b**) $P_0 = 1800$ W, (**c**) $P_0 = 2300$ W, (**d**) $P_0 = 3900$ W, (**e**) $P_0 = 4900$ W, (**f**) $P_0 = 5700$ W. (From Wang et al., 1994a, b)

one pulse. It is important to operate in the normal dispersion regime or have all-normal dispersion holey fiber (see Chap. 6 by Alex Heidt) and/or keep the fiber length long enough where self-phase modulation operates.

Typically, the short wavelength limit of SC generation in a 5 μm size holey optical fiber is to about 380–400 nm, and the long wavelength can extend to 2400 nm. The UV SC limit most likely arises from linear (1P) and nonlinear two photon absorption (2PA) process from the IMAG part χ_1 of n_0 and χ_3 of n_2 to about 280 nm using tapered optical PC fibers of 620 nm diameter. The index of refraction: $n = n_0 + n_0 i + (n_2 r + n_2 i)E^2$ has real and imaginary parts for linear and nonlinear parts of the n. The UV SC generation down to $\lambda = 280$ nm (see Stark et al., 2012) is limited by 2PA and is ideal for optically exciting proteins and DNA of biological materials. See the Chap. 5 authored by Taylor and Travers in this SC book for more details on UV cutoff via 2PA and Chap. 6 authored by Heidt et al. in this book.

2.14 High-Resolution Spectra of Cross-Phase Modulation in Optical Fibers

Cross-phase modulation (XPM) is a two-(or more) beam analog or the self-phase modulation (SPM) process. It is similar to SPM, but the phase modulation is caused by the nonlinear refractive index change induced by other more intense optical pulses. When a weak optical pulse is propagating with a strong optical pulse, the phase of the weak optical pulse is modulated by the index change induced by the strong optical pulse to produce spectral broadening. This process is called XPM, which plays an important role in some ultrabroad supercontinuum generations.

XPM in optical fibers can be isolated under certain conditions so that the features of XPM can be observed. In this section, experiments performed on the fine structures of the SPM and XPM of picosecond laser pulses using a grating spectrometer with a spectral resolution higher than one tenth of the laser linewidth will be presented. Measured spectral profiles have been compared and discussed with the calculations of the SPM and XPM model (in Sect. 2.13).

2.14.1 Reduced Wave Equation

Similar to that in Sect. 2.13, from Maxwell's equations, one can obtain the wave equation that describes the amplitudes of light pulses propagating in optical fibers for XPM:

$$\frac{\partial A_1}{\partial z}+\frac{1}{v_{g1}}\frac{\partial A_1}{\partial t}+i\frac{1}{2}k_1^{(2)}\frac{\partial^2 A_1}{\partial t^2}=i\frac{\omega_0 n_2(\omega_1)}{c}\left(|A_1|^2+2|A_2|^2\right)A_1, \tag{2.50a}$$

$$\frac{\partial A_2}{\partial z}+\frac{1}{v_{g2}}\frac{\partial A_2}{\partial t}+i\frac{1}{2}k_2^{(2)}\frac{\partial^2 A_2}{\partial t^2}=i\frac{\omega_0 n_2(\omega_2)}{c}\left(|A_2|^2+2|A_1|^2\right)A_2, \tag{2.50b}$$

where ω_1 and ω_2 are the carrier frequencies of the pump and the probe pulses, and υ_{g1} and υ_{g2} are the group velocities. $k_1^{(2)}$ and $k_2^{(2)}$ are the group-velocity dispersions at ω_1 *and* ω_2, respectively, $n_2(\omega_1) = 3\ \chi^{(3)}_{1111}\ (\omega_1 = \omega_1 + \omega_1 - \omega_1)/8\ n_0\ (\omega_1)$, and $n_2(\omega_2) = 3\ \chi^{(3)}_{1111}\ (\omega_2 = \omega_2 + \omega_2 - \omega_2)/8\ n_0\ (\omega_2)$ are the nonlinear refractive index coefficients, and $n_0(\omega_i)$ is the linear refractive index. Since the fiber length used in the experiment is much smaller than the dispersion length, which can be calculated to be a few kilometers, the dispersion term in Eqs. (2.50a) and (2.50b) can be neglected.

Changing the variables

$$\tau = t - \frac{z}{v_{g1}}, \tag{2.51}$$

$$z = z' \tag{2.52}$$

and denoting by a_i and α_i the amplitude and the phase of the electric envelope, respectively, A_i can be expressed as

$$A_i\,(z,\tau) = a_i\ \ (z,\tau)\exp\left[i\alpha_i\ \ (z,\tau)\right], \tag{2.53}$$

Where $i = 1, 2$ and τ is the local time of the propagating optical pulse.

Considering the fiber lengths used in the experiment are much smaller than the dispersion lengths, which can be calculated to be a few kilometers, the dispersion term in Eq. (2.50a) can be neglected. Therefore, Eq. (2.50b) further reduces to

$$\frac{\partial a_1}{\partial z} = 0, \tag{2.54a}$$

$$\frac{\partial \alpha_1}{\partial z} = \frac{\omega_0 n_2\,(\omega_1)}{c}\left({a_1}^2 + 2{a_2}^2\right), \tag{2.54b}$$

$$\frac{\partial a_2}{\partial z} + \left(\frac{1}{v_{g1}} - \frac{1}{v_{g2}}\right)\frac{\partial a_2}{\partial \tau} = 0, \tag{2.54c}$$

$$\frac{\partial \alpha_2}{\partial z} = \frac{\omega_0 n_2\,(\omega_2)}{c}\left(2{a_1}^2 + {a_2}^2\right). \tag{2.54d}$$

The analytical solutions for Eqs. (2.54a), (2.54b), (2.54c), and (2.54d) can be obtained as

$$a_1(T) = a_{10}F_1(T), \tag{2.55a}$$

$$\alpha_1\,(L,T) = \frac{\omega_0 n_2\,(\omega_1)}{c}L\left[{a_{10}}^2{F_1}^2(T) + \frac{2}{L}{a_{20}}^2\int_0^L {F_2}^2\,(T - z/L_w)\,dz\right], \tag{2.55b}$$

$$a_1(T) = a_{10}F_1(T), \tag{2.55c}$$

$$\alpha_2\,(L,T) = \frac{\omega_0 n_2\,(\omega_2)}{c}L\left[{a_{20}}^2{F_2}^2(T) + \frac{2}{L}{a_{10}}^2\int_0^L {F_1}^2\,(T + z/L_w)\,dz\right]. \tag{2.55d}$$

where a_{i0} are the amplitudes, $F_i(t)$ are the pulse envelopes, $T = \tau/T_0$, $L_w = T_0/\left(\frac{1}{v_{g2}} - \frac{1}{v_{g1}}\right)$ is the walk-off length of the pump and probe pulses, and T_0 is the $1/e$ pulse duration.

One can obtain the field spectral profiles of XPM by computing the Fourier transformation of its temporal pulse distribution as

$$E_i\,(z, \omega - \omega_i) = \frac{1}{2\pi}\int a_i\,(z, \tau)\exp\left[\left(i\alpha_i\left(z, \tau\right)\right]\right]\exp\left[i\,(\omega - \omega_i)\,\tau\right]d\tau. \tag{2.56}$$

The spectral-intensity distribution of the pulse is given by

$$|E_i\,(z, \omega - \omega_i)|^2. \tag{2.57}$$

2.14.2 Experiment

The experimental arrangement is shown in Fig. 2.39. A 10-Hz mode-locked Continuum Nd:YAG laser system was used to generate linearly polarized laser

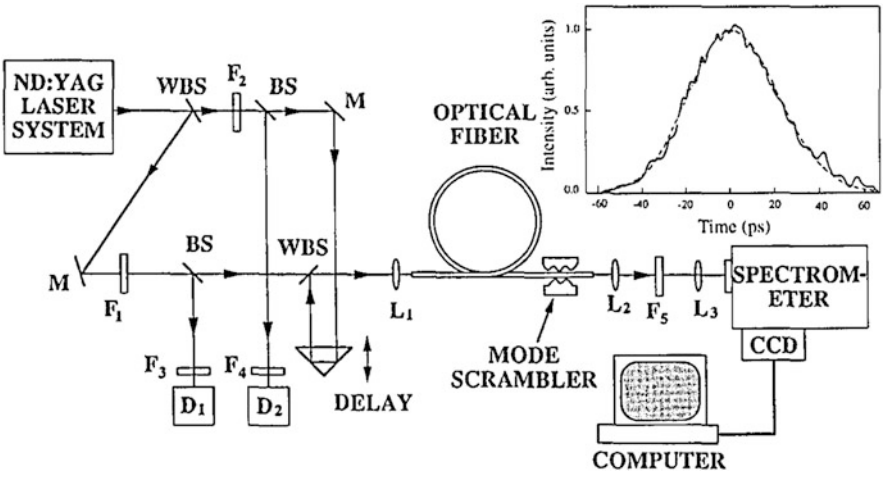

Fig. 2.39 Experimental arrangement: F_1, a set of color and neutral-density filters; F_2–F_3, neutral-density filters; L_1, L_2, 20× microscope objectives; L3, lens; BS's, beam splitters; D_1, D_2, detectors; M's, mirrors. Inset: The pulse shape of the 532-nm laser pulse generated from the laser system. The laser pulse is slightly asymmetric. The leading edge is shorter than the trailing edge. The dashed curve shows a theoretical fit to the pulse. (Reprinted with permission from Wang et al., 1994b © Optical Society of America)

pulses at 1064 and 532 nm. An electronic optical shutter in the laser cavity allows for single-pulse operation. The inset shows an input laser pulse at 532 nm measured with a Hamamatsu 2-ps streak camera. The laser pulse is slightly asymmetrical. The leading edge is shorter than the trailing edge. The dashed curve shows a theoretical fit to the pulse. The leading part of the dashed curve is the front part of a Gaussian pulse with FWHM of 40 ps. The trailing part is the back part of a Gaussian pulse with a FWHM of 50 ps. Because the 532-nm pulse is the second-harmonic generation of the laser pulse at 1064 nm, the pulse width of 1064 nm pulse is approximately $\sqrt{2}$times that of the 532-nm pulse. The pulse shapes are similar. The pulse energies were approximately 2 mJ and 200 nJ for 1064 and 532 nm, respectively. The 1064- and 532-nm laser pulses were separated by a wavelength-selective beam splitter (WBS). These beams were combined by another WBS after propagating along different paths. A polarization rotator was inserted into the 1064-nm beam path to change the polarization to be parallel to that of the 532-nm beam. The optical path of the 532-nm pulse was controlled by variable optical delay. Two sets of filters were used in the two different paths to control the pulse energies. The intensities of the laser pulses were monitored with a photomultiplier tube and a photodiode. The laser pulses were coupled into a 1-m optical fiber with a 20× microscope objective lens. The output signal pulse was collected with a 20× microscope objective lens. An optical fiber with core diameter of 4 μm, a cladding diameter of 125 μm, and a numerical aperture of 0.11 was purchased from Newport. This optical fiber supports a single mode for 1064-nm pulses and multimodes for 532-nm laser pulses. By carefully adjusting the coupling to the optical fiber, we coupled more than 90% of light at 532 nm into the lowest mode of the fiber. The small portion of light at 532 nm coupled into higher modes was removed by a mode scrambler applied 5 cm away from the output end of the optical fiber. The output signal beam was passed through a spectral analysis system consisting of a 1-m spectrometer combined with a computer-controlled CCD camera. A 1200-groove/mm grating blazed at 1000 nm was used in the spectrometer, which enabled us to measure effectively the first-order spectrum of an optical pulse at the 1064-nm region and the second-order spectrum of an optical pulse at the 532-nm region simultaneously. The resolution of the spectral analysis system was 0.01 nm/pixel and 0.005 for the 1064- and 532- nm regions, respectively.

The output XPM spectra of the probe pulse at 532 nm and the SPM spectra of the pump laser pulse at 1064 nm propagating in 1-m optical fiber are shown in Fig. 2.40. The spectrum of the input probe pulse is shown in Fig. 2.40a. The XPM spectra for different initial time delays between the pump and the probe pulses at a constant pump intensity are shown in Fig. 2.40b–d. The SPM spectrum of the pump pulse is shown in Fig. 2.40e. When the pulses coincide at the input end of the fiber, the probe pulse sees only the trailing part of the pump pulse when it propagates in the optical fiber, because of the walk-off effect. The phase of the probe pulse is then modulated by the induced index change caused by the trailing edge of the pump pulse, and the spectrum of the probe pulse is shifted to the anti-Stokes-side only, as shown in Fig. 2.40b. When the probe pulse is 31 ps ahead of the pump pulse at the fiber entrance, the phase of the probe pulse undergoes a symmetric modulation

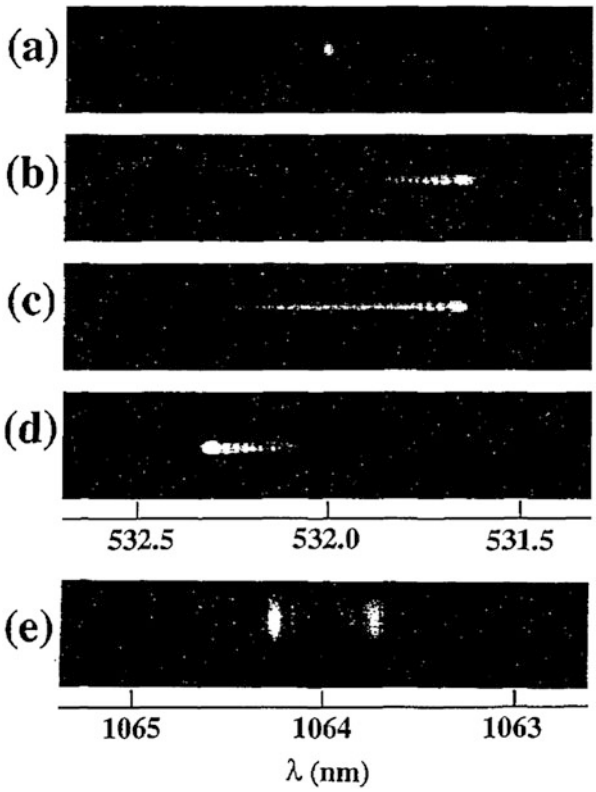

Fig. 2.40 Video display of the SPM spectra of the pump pulse at 1064 nm and the XPM spectra of the probe pulse at 532 nm propagating in 1-m, 4-μm-core optical fiber with different initial time delays between the pump and probe pulses: (**a**) input laser linewidth, (**b**) $t_d = 0$ ps, (**c**) $t_d = 31$ ps, (**d**) $t_d = 63$ ps, (**e**) SPM spectrum of the pump pulse. The peak power of the pump pulse is −2000 W. (Reprinted with permission from Wang et al., 1994b © Optical Society of America)

on both the leading and the trailing edges of the pump pulse in the optical fiber. The XPM spectrum broadens toward both the Stokes and the anti-Stokes sides, as can be seen from Fig. 2.40c. When the probe pulse is initially set approximately 63 ps before the pump pulse, the probe pulse sees only the leading part of the pump pulse in the optical fiber. The spectrum of the probe pulse broadens to the Stokes side only, as displayed in Fig. 2.40d. In addition, the intensity oscillation structures of the XPM and SPM spectra caused by the interference are resolved because of the high spectral resolution of the measurement system. Both the XPM and SPM spectra have large intensity oscillations. In the same spectrum, the oscillation period is smaller near the input frequency and gets larger as the spectrum goes further away from the input frequency. For pump pulses at 1064 nm, Fig. 2.40e shows that the SPM spectral broadening to the Stokes side is larger than that to the anti-Stokes

side. This effect arises from the asymmetric temporal distribution of the input laser pulse. The leading edge of the input laser pulse is shorter than the trailing edge. For all the cases, the spectral broadenings increase as the pump intensity increases.

2.14.3 Discussion

In Fig. 2.41, the digitized experimental spectral curves and the numerical calculations of the changes of the XPM and SPM spectra of the probe and pump pulses are displayed in the left and the right columns, respectively. In the left-hand column of Fig. 2.41, the thick solid curves are the digitized XPM spectral curves of the probe pulse, and the thin solid curves are the experimental SPM spectra of the pump pulse. In the right-hand column, the solid curves are the XPM spectra of the probe pulse, and the dotted curves are the SPM spectra of the pump pulse. The spectra of the input laser pulses are shown in Fig. 2.41a. Figure 2.41b–d show the XPM and SPM spectra for different initial time delays between the probe and the pump pulses at a

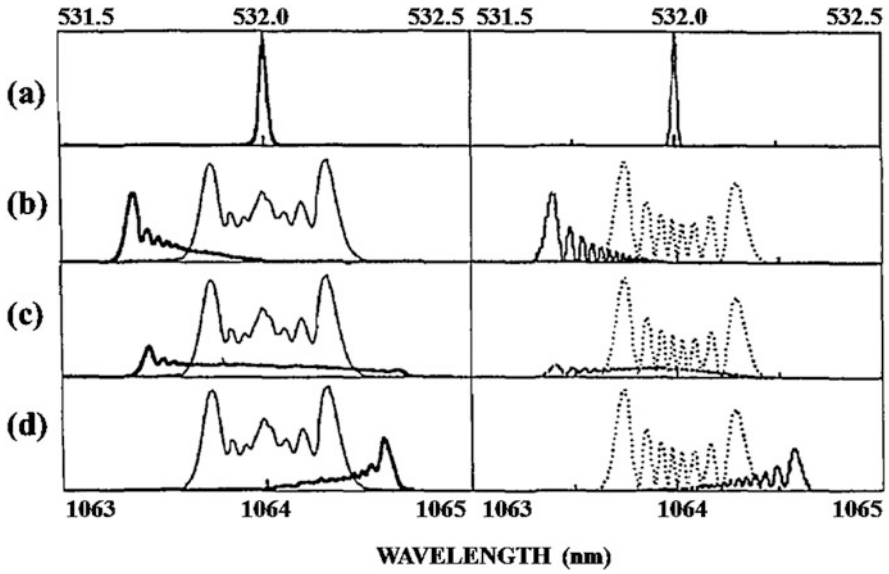

Fig. 2.41 SPM of the pump pulse at 1064 nm and XPM spectra of the probe pulse at 532 nm propagating in an optical fiber with different initial time delays. The left-hand column shows the experimental results, and the right-hand column shows the theoretical calculations. The core diameter of the optical fiber was 4 μm, and $n_2 = 3.2 \times 10^{-16}$ cm^2/W for 532 nm and $n_2 = 1.79 \times 10^{-16}$ cm^2/W for 1064 nm. (**a**) Input laser pulse, (**b**) $t_d = 0$ ps, (**c**) $t_d = 31$ ps, (**d**) $t_d = 63$ ps. The peak power of the pump pulse is 2000 W. (Reprinted with permission from Wang et al., 1994b © Optical Society of America)

constant pump intensity. The theoretical results for $t_d = 0$ and $t_d = 63$ ps reasonably agree with the experimental results shown in Fig. 2.41b–d.

For the best fit of the experimental spectra, $n_2 = 1.79 \times 10^{-16}$ cm^2/W at 1064 nm was used in the calculations, that is ~0.56 times the value for n_2 at 532 rm. Because of the high resolution of the SPM and XPM spectra, small changes of the XPM and SPM spectra caused by the small differences of the nonlinearity can be resolved. By fitting the spectral change, we can measure the small difference between the third-order nonlinearities at the wavelengths of the pump and probe pulses. With our high spectral resolution, depending on the stability of laser pulses, the accuracy of the detected dispersion of the third-order nonlinearity between the pump and the probe wavelengths is estimated to be ~5%.

2.15 Recent Developments of Supercontinuum Generation

Since the discovery made 51 years ago by Alfano and Shapiro (1970a), the supercontinuum generation has been the subject of numerous investigations in a wide variety of nonlinear media and various applications in Physics, Chemistry, Biology, and soon to Medical fields. Over past 24 years, there has been a surge of activity in supercontinuum field using various types of photonic crystal fibers after the first introduction (Russell et al., 1996, 1997). The advancement in the generation of ultrashort laser pulses led to the production of a wider supercontinuum generation that resulted in applications of supercontinuum generation in a diverse range of fields. These applications include optical coherence tomography (Hartl et al., 2001; Hsiung et al., 2004), frequency metrology (Ranka et al., 2000; Jones, 2000; Schnatz & Hollberg, 2003), fluorescence lifetime imaging (Dunsby et al., 2004), optical communications (Takara et al., 2005; Morioka et al., 1993), gas sensing (Sanders, 2002; Ere-Tassou et al., 2003), and many others. The practice of these sources has created a feedback loop whereby the scientists utilizing the supercontinua are demanding better customizable continua to suit their particular applications. This has driven researchers to develop novel methods to produce these continua and to develop theories to understand their formation and aid future development. Rapid progress in supercontinuum generation has been made since 2000. Extremely broad supercontinuum spectra have been produced with various kinds of photonic-crystal optical fibers, optical waveguides, and engineered integrated bulk. Spectrum of supercontinuum generation covers the wider wavelength regions in the deep ultraviolet (DUV), the ultraviolet (UV), the visible, near infrared (NIR), and the infrared (IR).

2.15.1 Nonlinear Refractive Index of Materials Used in Supercontinuum Generation

Buckingham (1955; Boyle et al., 1966; Buckingham & Hibbardas, 1968) expanded on John Kerr's work (Kerr, 1875) by introducing the hyperpolarizability of the first and second kinds. These became most important parameters in nonlinear optics related to the nonlinear index change n_2 as the main mechanism for supercontinuum generation, higher harmonic generation, and attosecond pulse generation. The third-order nonlinearity $\chi^{(3)}$ makes the refractive index to depend on the intensity of light propagating through the medium (Maker et al., 1964; Maker & Terhune, 1965). As optical pulses become shorter and intense, the third-order nonlinearity $\chi^{(3)}$ becomes of increasing interest because its role in Supercontinuum generation via n_2. When optical waves propagate through a medium with the inversion symmetry, third-order nonlinearity can be conveniently described as an intensity dependent index (Yariv, 1975) by average over many optical cycles:

$$n = n_0 + n_2 \left\langle E^2 \right\rangle, \tag{2.58}$$

where n_0 is the linear refractive index, E is the applied optical electric field, and n_2 is the nonlinear refractive index. Buckingham gave the instantaneous index $n(t)$ with the full form of $E(t)$ which forms the response of $n(t)$ to electronic and molecular motions.

Measurements of the nonlinear refractive index were performed for various materials. Tables 2.4a, 2.4b, 2.4c, and 2.4d list measurement results of some optical materials (Bokov, 1974; Milam et al., 1977; Adair et al., 1989; etc.).

The units of that quantity are m^2/W (or cm^2/W) in the SI system, but in older literature, one finds n_2 values in esu units. For the conversion of such units, Eq. (2.59) can be used:

$$\begin{aligned} n_2\left(m^2/W\right) &= \frac{40\pi}{c}\frac{n_2(\text{esu})}{n} \\ &= 4.19 \times 10^{-7} \times \frac{n_2(\text{esu})}{n}\,. \end{aligned} \tag{2.59}$$

where n is the refractive index.

For example, for liquid Kr, $n = 1.30$, $n_2 = 1.36 \times 10^{-13}$ esu

$$\begin{aligned} n_2\left(m^2/W\right) &= 4.19 \times 10^{-7} \times \frac{1.36\times10^{-13}}{1.30}\left(m^2/W\right), \\ &= 4.38 \times 10^{-20}\left(m^2/W\right), \\ &= 4.38 \times 10^{-16}\left(cm^2/W\right). \end{aligned}$$

Table 2.4a Nonlinear index of refraction $n_2 \times 10^{13}$ of several liquids (in cgs esu)

Liquid	$\frac{Z}{(\bar{r})^6} \cdot 10^{-45}$, cm^{-6}	$\gamma \cdot 10^{36}$cgs esu	Onsager Model (9)						K · 10^{13} cgs esu	n_2 ex	theor n_2 Lor(8)
			n_2 hyp	n_2 rad	$n_2^{(0)}$ Kerr	n_2^{int} Kerr	$n_2$qu	(theor)n_2 Ons			
Aragon	3.38	0.59	0.54	1.54				2.08			2.34
Cabon tetrachloride	0.219	9.96	3.66	17.50				21.16	4.76	5.80	27.77
Benzene	0.214	6.46	2.53	21.74	30.00	35.24		59.51	35.00	37.00	87.05
Toluene	0.150	27.20	8.83	25.43	38.84	45.58		79.84	45.40	51.54	116.24
Carbon disulfide	0.262	57.35	37.13	31.50	131.30	157.32	27.64	253.59	194.20	254.95	435.26
Chloroform	0.146	4.80	1.44	4.12	3.59	3.90		9.46	10.00	9.76	17.83
Nitrobenzene	0.219	85.00	23.28	40.07	45.43	73.40		136.75	141.50	144.17	323.70

Recreated according Bokov (1974)

(8) : $n_{2\,\text{Lor}} = 4\pi N L_{\text{Lor}}^4 \alpha_2 / 2n_0$ (9) : $n_{2\,\text{ons}} = \frac{2\pi N}{n_0 G} L_{\text{Ons}}^4 \alpha_2$

Table 2.4b Nonlinear refractive-index coefficients γ of fluoride crystals measured interferometrically using linearly polarized 125 ps, 1064 nm laser pulse and calculated from Eqs. (2.3a and 2.3b)

Material	Structure type	n_D	V	γ (10^{-20}m^2/W)[a]	
				Measured	Calculated
LiF	Cubic (NaCl)	1.392	99	1.05 ± 0.30	1.18
NaF	Cubic (NaCl)	1.326	85	1.37 ± 0.34	1.19
CaF_2	Cubic (fluorite)	1.434	95	1.90 ± 0.26	1.42
SrF_2	Cubic (fluorite)	1.438	92	1.76 ± 0.29	1.51
BaF_2	Cubic (fluorite)	1.475	82	2.85 ± 0.57	1.97
CdF_2	Cubic (fluorite)	1.576	61	3.87 ± 0.54	3.93
PbF_2	Cubic (fluorite)	1.769	34	11.7 ± 2.90	13.97
MgF_2	Tetragonal (rutile)	1.378 (*o*)1.389 (*e*)	108	0.92 ± 0.31	0.99
LaF_3	Hexagonal (tysonite)	1.603 (*o*)1.600 (*e*)	57	3.95 ± 0.72	4.63
CeF_3	Hexagonal (tysonite)	≈1.60	≈55	4.06 ± 0.93	4.85
$LiYF_4$	Tetragonal (scheelite)	1.457 (*o*)1.477 (*e*)	93	1.72 ± 0.20	1.56

From Milam et al. (1977)

[a]To convert to n_2(esu), multiply γ(m^2/W) by $2.39 \pm 10^6 n$

(3) $n_2\left(10^{-13}\text{esu}\right) = K\frac{(n_d-1)\left(n_d^2+2\right)^2}{v\left[1.517+\left(n_d^2+2\right)(n_d+1)v/6n_d\right]^{1/2}}$

2.15.2 *Mid-Infrared Supercontinuum Generation Covering 1.4–13.3 μm*

The mid-infrared spectral region is of great technical and scientific interest because most molecules display fundamental vibrational absorptions in this region, leaving distinctive spectral fingerprints (Schliesser et al., 2012; Allen, 1998).

The interaction of mid-IR radiation with a given sample provides a spectral fingerprint useful for identification of the sample. The mid-IR spectrum results from the absorption of specific frequencies of mid-IR radiation based on the chemical structure of the sample. For this reason, the peaks and troughs in a mid-IR spectrum are very specific to the sample measured. This makes mid-IR spectroscopy well suited for a wide range of applications involving materials identification and characterization for measurements ranging from the analysis of fuels to food safety and detection of counterfeit materials. These applications and many others benefit from the fundamental bands measured with mid-IR, which yield a higher intensity, less convoluted spectra than the overtone and combination bands measured with near-IR and visible radiation.

Mid-IR spectroscopy is widely used by researchers and educators for basic and applied research and for teaching labs in Physics, Chemistry, and Biomedical courses, such as early cancer diagnostics (Seddon, 2011), gas sensing (Allen, 1998; Eggleton et al., 2011), and food quality control (Wegener et al., 1999).

A mid-infrared supercontinuum spanning 1.4–13.3 μm is generated using short pieces of ultrahigh numerical-aperture step-index chalcogenide glass optical fiber by

Table 2.4c Nonlinear- and linear-refractive index of optical crystals (*o* denotes ordinary, *e* extraordinary)

	Linear –index data		Nonlinear-index data	
Sample	n(1.06 μm)	Abbe number v_d	Measured $n_2(10^{-13}$esu)	Calculated $n_2(10^{-13}$esu)
LiF [100]	1. 3866[a]	98.0	0.26	0.40
NaF [100]	1. 3213[a]	85.2	0.34	0.38
KF [100]	1. 3583[a]	97.9	0.75	0.36
NaCl [100]	1. 5312[a]	42.9	1.59	2.28
KC1 [100]	1. 4792[a]	44.1	2.01	1.84
NaBr [100]	1.6228[a]	31.7	3.26	4.74
KBr [100]	1. 5435[a]	33.7	2.93	3.41
MgF_2(*o*)	1. 3735[b]	104.9	0.25	0.34
CaF_2 [100]	1. 4285[c]	95.1	0.43	0.49
SrF_2 [100]	1. 4328[b]	93.9	0.50	0.50
CdF_2 [100]	1. 56[d]	61.0	3.95	1.37
BaF_2 [100]	1. 4682[b]	81.8	0.67	0.70
LaF_3 (*o*)	1.60*	57.0	1.4	1.78
CeF_3 (*o*)	∼1.60[c]		1.3	
AgCl (polycryst.)	2.020[b]	21.2	23.3	23.0
MgO [100]	1. 72[c]	53.4	1.61	2.8
CaO [100]	1. 83[e]		5.20	
SrO [l10]	1. 81[e]		5.07	
ZnO (*e*)	1. 96[c]	11.6	23.0	57.6
ZnO (*o*)	1. 99[c]	12.3	25.0	45.0
$A1_2O_3$(*o*)	1. 75[c]	71.8	1.23	1.9
$A1_2O_3$(*e*)	1. 75[c]	75.2	1.30	1.8
Ga_2O_3	1. 96[b]		5.80	
Y_2O_3	1. 92[a]	37.5	5.33	7.2
Er_2O_3	1. 96[f]		4.53	
SiO_2 (fused)	1. 4496[c]	67.8	0.85	0.83
SiO_2 (quartz) (*o*)	1. 5342[c]	71.6	1.12	1.06
SiO_2 (quartz) (*e*)	1. 5429[c]	70.1	1.16	1.13
TiO_2	2. 48[b]	9.8	55.8	189
ZrO_2	2. 12[b]	35.8	5.8	12.6
$BeAl_2O_4$	1.73[b]	72.5	1.46	1.74
$MgAl_2O_4$	1. 73[b]	60.6	1.50	2.3
$CaMgSi_2O_6$	1. 67[g]		1.73	
$YAIO_3$ (γ)	1. 933[b]	51.2	3.37	4.88
Y_3A15O_{12} (YAG)	1. 822[b]	52.4	2.7	3.6

(continued)

Table 2.4c (continued)

Sample	Linear –index data		Nonlinear-index data	
	n(1.06 μm)	Abbe number v_d	Measured $n_2(10^{-13}$esu)	Calculated $n_2(10^{-13}$esu)
$Gd_3Sc_2Al_3O_{l2}$ (GSAG)	1. 891[h]	48.0	4.0	5.6
$Gd_3Sc_2Ga_3O_{12}$ (GSGG)	1. 943[i]	37.3	5.5	8.0
$Gd_3Ga_5O_{12}$ (GGG)	1. 945[b]	37.6	5.8	8.0
$Y_3Ga_5O_{12}$ (YGG)	1. 912[j]	40.0	5.2	5.8
$La_3Lu_2Ga_3O_{12}$ (LLGG)	1.930[i]	36.4	5.8	8.2
$SrTiO_3$	2. 31[c]	13.6	26.7	83.0
$CaCO_3$ (*o*)	1. 6425[c]	47.6	1.11	2.7
$CaCO_3$ (*e*)	1. 4795[c]	76.8	0.83	0.79

Reprinted with permission from Adair et al. (1989) © The American Physical Society

Table 2.4d Nonlinear refractive index of optical materials

Materials	Wavelength	Nonlinear index (n_2)
Ar (gas)	800 nm	1.08×10^{-19} cm^2/W bar (Wang et al., 2013)
	1800 nm	6.65×10^{-20} cm^2/W bar (Wang et al., 2013)
	1055 nm	10.9×10^{-20} cm^2/W (Bree et al., 2010)
Ar (liquid)	530 nm	2.04×10^{-16} cm^2/W (Alfano, 1972)
Kr (liquid)	530 nm	4.38×10^{-16} cm^2/W (Alfano, 1972)
BK7	810 nm	3.625×10^{-16} cm2/W (Lu et al., 2012)
Methanol (liquid)	1064 nm	1.8×10^{-15} cm^2/W (Rau et al., 2008)
CdS	532 nm	-3.79×10^{-11} cm^2/W (Ganeev et al., 2003)
As_2S_3	1064 nm	5.09×10^{-10} cm^2/W (Ganeev et al., 2003)
GaAs	1060 nm	4×10^{-14} cm^2/W (Hurlbut et al., 2007)
Si	1600 nm	5.5×10^{-14} cm^2/W (Dremetsika et al., 2016)

launching intense ultrashort pulses with a central wavelength of 6.3 μm (Petersen et al., 2014). Typical output spectrum and beam profile are shown in Fig. 2.42.

2.15.3 Enhanced Bandwidth of Supercontinuum Generated in Microstructured Fibers

Coherent octave spanning supercontinuum can be generated in photonic crystal fiber by launching into the fiber femtosecond pulses with a wavelength located near the zero-dispersion wavelength (λ_{ZD}) of the photonic crystal fiber (Holzwarth et al.,

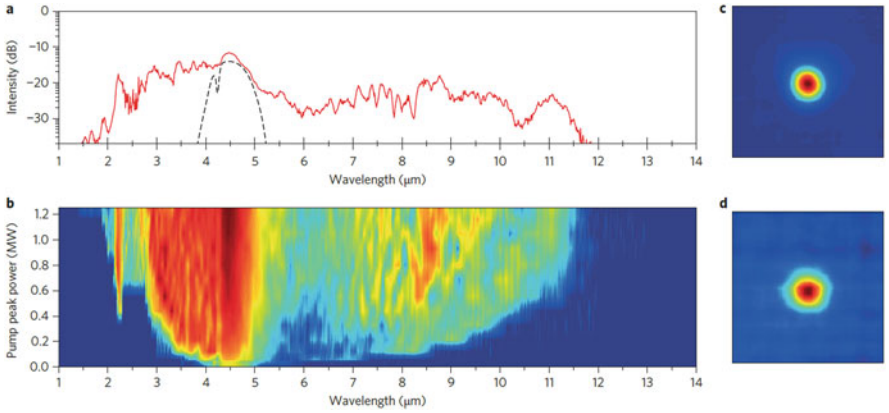

Fig. 2.42 Experimental supercontinuum generation results with the pump centered at 4.5 μm. (**a**) Input pump spectrum (dashed line) and spectral profile at maximum pump power (solid line), showing a relatively flat supercontinuum (2.08–10.29 μm at −20 dB from the signal peak) with distinct soliton peaks above the zero dispersion wavelength of ~5.83 μm, especially at 11 μm. (**b**) Spectral evolution with increasing pump peak power, showing a gradual redshift of distinct soliton peaks above the zero dispersion wavelength, and a combination of SPM and dispersive waves below the pump wavelength. (**c**, **d**) Fiber output near-field beam profile corresponding to the spectrum in a for all wavelengths (**c**) and beam profile for wavelengths above 7.3 μm only (**d**), showing that the long wavelengths are still confined to the core. (Reprinted from Petersen et al., 2014 © Macmillan Publishers Limited)

2000). For a pump wavelength on the anomalous side of λ_{ZD}, it has been shown that the fundamental mechanism leading to the supercontinuum generation mainly involves two distinct physical effects: Amplification of dispersive waves matched in phase with the pump extends the supercontinuum to the blue (Husakou & Hermann, 2002, 2003; Akhemediev & Karlsson, 1995), whereas pulse splitting and multiple soliton self-frequency shifts are responsible for the spreading of the supercontinuum into the infrared (Genty et al., 2002; Dudley et al., 2002).

Designing a photonic crystal fiber so that it has two λ_{ZD}'s, one in the visible (λ_{ZDV}) and another in the vicinity of 1500 nm (λ_{ZDI}), and properly adjust the pump wavelength, a substantial increase of the bandwidth of the supercontinuum in the infrared has been obtained while still efficiently generating the blue wavelength components (Genty et al., 2004a, b). Figure 2.43 shows the typical supercontinuum spectra.

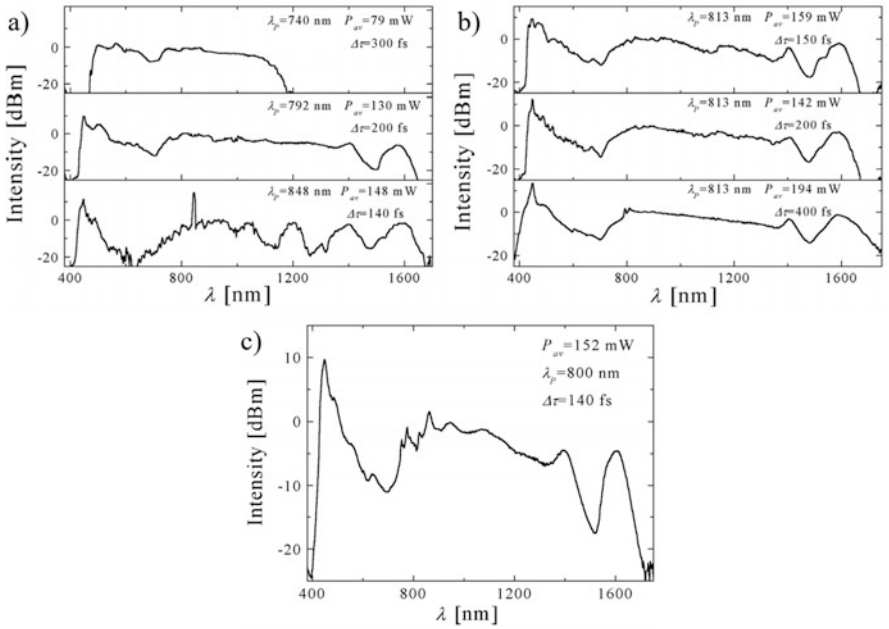

Fig. 2.43 Supercontinuum spectrum recorded when (**a**) tuning the pump wavelength and (**b**) varying the input pulse. (**c**) Supercontinuum generated in 50 cm of fiber with visible $\lambda_{ZDV} = 690$ nm and infrared $\lambda_{ZDI} = 1390$ nm. (Reprinted with permission from Genty et al., 2004b © Optical Society of America)

2.15.4 Deep-Ultraviolet to Mid-Infrared Supercontinuum Generation

Triggered by a tremendous number of applications, such as semiconductor metrology and inspection (Stokowski & Vaez-Iravani, 1998), pump-probe spectroscopy (Riedle et al., 2013; Petersen et al., 2018a), pollution monitoring (Popov et al., 1997), optical coherence tomography, and imaging (Colley et al., 2007; Petersen et al., 2018b), fiber-based laser sources capable of covering the electromagnetic spectrum from DUV (wavelengths <350 nm) up to mi-IR have attracted the scientific attention around the globe. One of the most promising routes toward development of ultrabroad bandwidth sources is supercontinuum generation.

Most reports on supercontinuum generation in the literature are based on solid-core silica photonic crystal fibers (PCF) where the micro-structured cladding of the fiber allows tailoring of the group velocity dispersion (GVD), which is an important property that greatly influences the nonlinear effects (Dudley et al., 2006). Despite silica solid-core PCF-based supercontinuum sources now being commercially available, they can only operate in a limited transmission range around 350–2300 nm due to the limited transparency window of the silica material.

In 2015, Jiang et al. reported for the first time the fabrication of a fluoride (ZBLAN) glass-based solid-core PCF with high air-filing fraction, and they demonstrated a broad supercontinuum spanning more than three octaves in the spectral range of 200–2500 nm (Jiang et al., 2015).

Experimental demonstration of multioctave supercontinuum generation spanning from DUV to mid-IR in a gas-filled HC-ARF pumped directly in the mid-IR region at 2460 nm using a tunable optical parametric amplifier (OPA) system was first reported in 2019 (Adamu et al., 2019). By coupling 100 fs, 20 μJ pulses into a specially designed argon (Ar) filled HC-ARF under 30 bar pressure, soliton self-compression dynamics enabled broadening from 200 to 4000 nm. Furthermore, it was experimentally demonstrated how the pulse energy and the pressure have a crucial role in the mid-IR spectral broadening and emission of DWs in the DUV. Typical spectra are shown in Fig. 2.44.

The supercontinuum embedded in a 4.3-octave-wide spectrum spans from 200 nm up to 4000 nm when 8 μJ, 100 fs pulses are injected into the fiber filled with Ar at a pressure of 30 bar. A total measured average output power of 5 mW (at 1 kHz

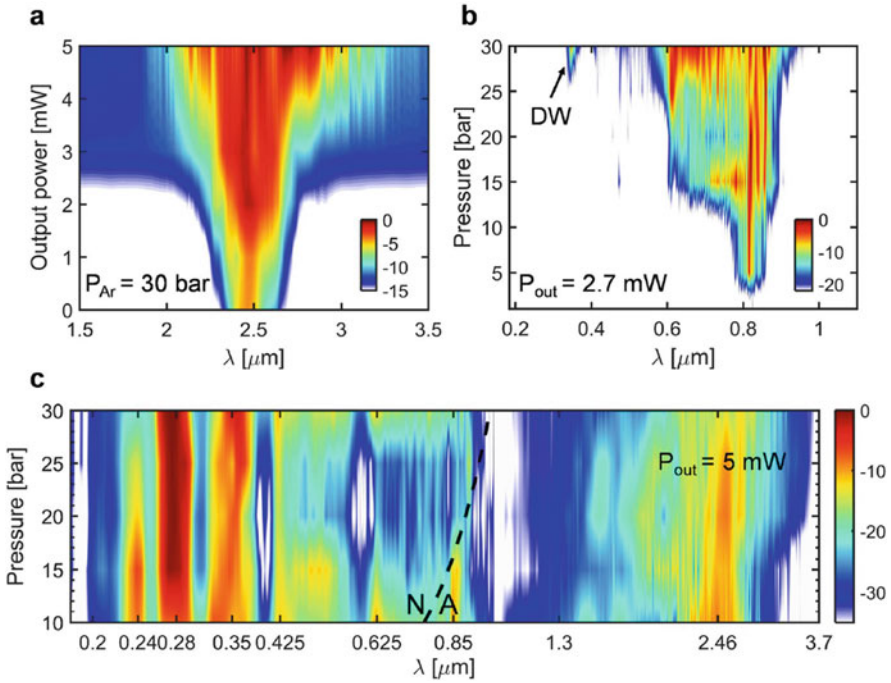

Fig. 2.44 (**a**) Measured spectral evolution and DW formation in the near/mid-IR range indicating the spectrum broadening as a function of measured output power for a fixed pressure of 30 bar. (**b**) Spectral broadening and DW emission as a function of pressure in the DUV/visible. (**c**) Pressure dependent evolution of the spectrum at a fixed low power of 5 mW over the full spectrum from 10 up to 30 bar with a step of 5 bar. (Reprinted from Adamu et al., 2019)

repetition rate) was obtained with a strong resonant DW emission at 275 nm. Finally, it was experimentally demonstrated how the pump energy and pressure increases the nonlinearity resulting in increased mid-IR spectral broadening and efficient DW emission in the DUV range. The current work constitutes an efficient route toward ultrafast source for spectroscopy both in the mid-IR molecular fingerprinting and in the DUV spectral region.

2.15.5 Summary of Selected Supercontinuum Generation Since 2000

Because of its ability to confine light in hollow cores or with confinement characteristics not possible in conventional optical fiber, photonic crystal fiber (PCF) (Knight et al., 1996), the nonlinearity can be increased and the zero dispersion wavelength can be engineered in PCF. These two properties make PCF an excellent medium for supercontinuum generation. There have been a lot of work for supercontinuum generation using PCF (Dudley et al., 2006). There are also other areas of development of supercontinuum generation, including the development of fibers to include new material, production techniques, and tapers, generating supercontinuum in gases, crystal waveguides, and gas-filled hollow-fibers.

An in-depth discussion of these achievements is beyond this chapter. Table 2.5 highlights the major achievements in supercontinuum generation since 2000.

2.16 Overview

Supercontinuum generation is the generation of bursts of E&M which cover wide band of frequency in the so-called "Maxwell Rainbow" most noted as in visible earlier in the "white light," which can be obtained by passing intense picosecond or femtosecond pulses through various materials in gases, liquids, and solids. The supercontinuum is an universal effect and enabling technology. Supercontinuum now covers most of Maxwell Rainbow, the X ray, XUV, UV, Visible, NIR, MIR, IR, THz, and RF spectra zones. The nonlinear response of the medium n_2 and the pulse envelope yield a phase modulation that usually initiates the wide frequency broadening (up to 10,000 cm^{-1}). The extreme femtosecond laser pulse changes the carrier envelope phase (CEP) in time from electronic cloud and molecular changes causing the ultrasuper broadening and higher harmonic generation over large portion of the Maxwell Rainbow. The phase modulation can be generated by the pulse itself, a copropagating pump pulse, or the copropagating stronger pulse in cross-phase modulation (XPM). These different configurations are called self-phase modulation (SPM), induced-phase modulation (IPM), and cross-phase modulation (XPM), respectively. The SPM process for supercontinuum generation in various

Table 2.5 Brief summary of major achievements on supercontinuum generation in condensed matter since 2000

Investigator	Year	Material	Pump wavelength, pulse width, power/energy	Spectrum	Process
Ranka, J. K., R. S. Windeler, and A. J. Stentz	2000	Photonic crystal fiber (air-silica)	790 nm, 100 fs, 800 pJ	390–1600 nm	SPM, Raman scattering
Birks, T. A., W. J. Wadsworth, and P. St. J. Russell	2000	Tapered fiber (1.8 μm)	850 nm, 200 fs, 3.9 nJ	370–1545 nm	SPM, Raman scattering
Husakou, A. V., and J. Herrmann	2001	Photonic crystal fibers	770 nm, 10 fs, 3.3 TW/cm^2	500–1300 nm	Fission of higher-order solutions
Provino, L., J. M. Dudley, H. Maillotte, N. Grossard, R. S. Windeler, and B. J. Eggleton	2001	Photonic crystal fibers	532 nm, 0.8 ns, 400 W (peak)	450–800 nm	Stimulated Raman scattering, FWM
Coen, S., A. H. L. Chau, R. Leonhardt, J. D. Harvey, J. C. Knight, W. J. Wadsworth, and P. St. J. Russell	2001	Photonic crystal fibers	647 nm, 60 ps, 675 W (peak)	400 to >1000 nm	Stimulated Raman scattering, phase-matched parametric process
Genty, G., M. Lehtonen, H. Ludvigsen, J. Broeng, and M. Kaivola	2002	Photonic crystal fibers	804 nm, 100 fs, 45 mW (average, 80 MHz)	400 to >1400 nm	SPM, FWM, Raman scattering, Raman-shifted solitons, soliton self-frequency shifting (SSFS)
Lehtonen, M.; Genty, G.; Ludvigsen, H.; Kaivola, M.	2003	Birefringent photonic crystal fiber	798 nm, 100 fs, 140 mW (average, 80 MHz)	400–1750 nm	Raman scattering, soliton self-frequency shifting (SSFS), perturbation of multiple solutions, FWM

Hundertmark, H., D. Kracht, D. Wandt, C. Fallnich, V. V. R. K. Kumar, A. K. George, J. C. Knight, and P. St. J. Russell	2003	Photonic crystal fibers	1550 nm, 60 fs, 200 pJ	400–1750 nm	Raman scattering, soliton self-frequency shifting (SSFS)
Genty, G., M. Lehtonen, and H. Ludvigsen	2004a	Photonic crystal fibers	790 nm, 27 fs, 118 mW (average, 80 MHz)	450–1600 nm	Soliton formation, dispersive wave generation, XPM
Hilligsøe, K. M., T. V. Andersen, H. N. Paulsen, C. K. Nielsen, K. Mølmer, S. Keiding, R. Kristiansen, K. P. Hansen, and J. J. Larsen	2004	Photonic crystal fibers with two λ_{ZD}'s	790 nm, 80 fs, 700 pJ	Two peaks with inner edges at ~740 nm and ~950 nm, and two outer edges move outward with increasing pulse energy	SPM, phase-matched FWM
Genty, G., M. Lehtonen, H. Ludvigsen, and M. Kaivola,	2004b	Photonic crystal fibers with two λ_{ZD}'s	813 nm, 400 fs, 194 mW (average)	390–1800 nm	Raman scattering, amplification of dispersive wave generations, soliton self-frequency shifting (SSFS)
Hagan, C. L., J.W. Walewski, and S. T. Sanders	2006	ZBLAN fiber	1550 nm, 900 fs, 25 nJ	1800–3400 nm	SPM, FWM, Raman scattering
Domachuk, P., N. A. Wolchover, M. Cronin-Golomb, A. Wang, A. K. George, C.M.B. Cordeiro, J.C. Knight, and F. G. Omenetto	2008	Photonic crystal fibers	1550 nm, 100 fs, 1.9 nJ	789–4870 nm	***
Qin, G., X. Yan, C. Kito, M. Liao, C. Chaudhari, T. Suzuki, and Y. Ohishia	2009	Fluoride fiber	1450 nm, 180 fs, 4 MW (peak)	~350–6280 nm	SPM, Raman scattering, FWM

(continued)

Table 2.5 (continued)

Investigator	Year	Material	Pump wavelength, pulse width, power/energy	Spectrum	Process
Heidt, A. M., A. Hartung, and H. Bartelt	2010	Optical nanofibers	400 nm, 100 fs, 5 nJ	200–580 nm	SPM, OWB, FWM
Stark, S. P., J. C. Travers, and P. St. J. Russell,	2012	Photonic crystal fibers	800 nm, 130 fs, 2 nJ	280–1600 nm	SPM, soliton breathing, stimulated Raman scattering
Halir, R., Y. Okawachi, J. S. Levy, M. A. Foster, M. Lipson, and A. L. Gaeta	2012	Silicon nitride waveguides.	1300 nm, 200 fs, 160 pJ	665–2025 nm	SPM, third-harmonic generation, and self-steepening
Kartashov, D, S. Ališauskas, A. Pugžlys, A, Voronin, A, Zheltikov, M, Petrarca, P, Béjot, J, Kasparian, J.-P, Wolf, and A, Baltuška	2012	Argon (4.5 bars)	3900 nm, 80 fs, 0.1 TW (peak)	350–5000 nm	Filamentation, high-order nonlinear (n_2–n_{10}) SPM, THG, FTH
Petersen, C. R., U. Møller, I. Kubat, B. Zhou, S. Dupont, J. Ramsay, T. Benson, S. Sujecki, N. Abdel-Moneim, Z. Tang, D. Furniss, A. Seddon, and O. Bang,	2014	Step-index chalcogenide glass optical fiber	6300 nm, 100 fs, 2.29 MW (peak)	1400–13,300 nm	Soliton fission, dispersive wave generation, trapping potential, parametric amplification
Safioui, J., F. Leo, B. Kuyken, S.-P. Gorza, S. K. Selvaraja, R. Baets, P. Emplit, G. Roelkens, and S. Massar	2014	Amorphous silicon waveguides	1560 nm, 1 ps, 15.1 W	1470–1770 nm	SPM, MI, FWM

Klimczak, M., B. Siwicki, P. Skibiński, D. Pysz, R. Stępień, A.Heidt, C. Radzewicz, and R. Buczyński	2014	All-solid soft-glass photonic fiber	1550 nm, 75 fs, 200 kW	900–2300 nm	SPM, OWB, FWM
Epping, J. P., T. Hellwig, M. Hoekman, R. Mateman, A. Leinse, R. G. Heideman, A. van Rees, P. J.M. van der Slot, C. J. Lee, C. Fallnich, and K.-J. Boller	2015	High-confinement Si_3N_4 integrated optical waveguides	1064 nm, 115 fs, 590 pJ	470–2130 nm	SPM, XPM, FWM, self-steepening
Jiang, X., N. Y. Joly, M. A. Finger, F. Babic, G. K. L. Wong, J. C. Travers, and P. J. Russell	2015	ZBLAN photonic crystal fibre	1042 nm, 140 fs, 830 nJ	200–2500 nm	SPM, XPM, FWM, soliton fission, dispersive wave generation; THG, XPM from blue-shifted solitons
Belli, F., A. Abdolvand, W. Chang, J. C. Travers, and P. St. J. Russel	2015	Kagomé-PCF filled with hydrogen	805 nm, 30 fs, 2.5 uJ	124 to beyond 1200 nm	SPM, self-steepening, shock formation, Raman-XPM
Boggio, J. M. C., A. O. Moñux, D. Modotto, T. Fremberg, D. Bodenmüller, D. Giannone, M. M. Roth, T. Hansson, S. Wabnitz, E. Silvestre, and L. Zimmermann	2016	Multicladding silicon nitride (Si_xN_y) waveguides	1560 nm, 85 fs, 110 pJ	410–2400 nm	SPM, XPM, self-steepening, dispersive wave generation, phase-matched FWM, THG
Xiang, B, X. Ren, S. Ruan, L. Wang, P. Yan, H. Han, M. Wang, and J. Yin,	2016	Yttrium orthosilicate crystal	800 nm, 100 fs, 6 GW (peak)	380–1100 nm	SPM, XPM, MPE-enhanced SPM

(continued)

Table 2.5 (continued)

Investigator	Year	Material	Pump wavelength, pulse width, power/energy	Spectrum	Process
Wang, N., J.-H. Cai, X. Qi, S.-P. Chen, L.-J. Yang, and J. Hou	2018	Photonic crystal fibers	976 nm, 353 ps, 15.1 W (average, 4.5 MHz)	350–2400 nm	Soliton self-frequency shifting, FWM, dispersive wave generation, XPM
Adamu, A. I., Md. S. Habib, C. R. Petersen, J. E. A. Lopez, B. Zhou, A. Schülzgen, M. Bache, R. Amezcua-Correa, O. Bang, and C. Markos	2019	Ar-filled hollow-core antiresonant fiber	2460 nm, 100 fs, 8 μJ	200–4000 nm	SPM, soliton self-compression, dispersive wave generation
Yu, M., B. Desiatov, Y. Okawachi, A. L. Gaeta, and M. Loncar	2019	Lithium-niobate waveguide	1506 nm, 160 fs, 185 pJ	400–2400 nm	SPM, SHG, SHG-XPM, sum frequency generation
Zhang, N., X. Peng, Y. Wang, S. Dai, Y. Yuan, J. Su, G. Li, P. Zhang, P. Yang, and X. Wang	2019	Te-based chalcogenide tapered fiber	5500 nm, 150 fs, 22 mW (1 kHz)	1700–12,700 nm	SPM, OWB
Saini, T. S., T. H. Tuan, T. Suzuki, and Y. Ohishi	2020	Tapered chalcogenide fiber	2600 nm, 200 fs, 10.12 kW (peak)	1600–3700 nm	SPM, OWB

materials was reviewed in this chapter. These latter two processes are closely related to each other and are described by Baldeck et al. (Chap. 4) and Agrawal (Chap. 3).

In the early beginning days of supercontinuum generation using an 8-ps laser at 530 nm, typical Stokes sweeps were 4400 cm^{-1} in a calcite crystal of length 4 cm, 3900 cm^{-1} in a quartz crystal of length 4.5 cm, 1100 cm^{-1} in extradense flint glass of length 7.55 cm, 3900 cm^{-1} in NaCl of length 4.7 cm, and 4200 cm^{-1} in both BK-7 and LBC-1 glasses of length 8.9 cm. Sweeps on the anti-Stokes side were typically 6100 cm^{-1} in calcite, 5500 cm^{-1} in quartz, 7300 cm^{-1} in NaCl, and 7400 cm^{-1} in BK-7 and LBC-1 glasses. An infrared supercontinuum spanning the range from 3 to 14 μm can be obtained by passing an intense laser pulse generated from a CO_2 laser through GaAs, AgBr, ZnSe, and CdS crystals. Near- and medium-infrared spectral sweeps of 3200 cm^{-1} on the Stokes side and 4900 cm^{-1} on the anti-Stokes side can be realized by passing a strong 1.06-μm pulse through a KBr crystal of length 10 cm. Sweeps on the order of 1000 cm^{-1} are observed to both the red and blue sides of 530 nm in liquid argon. Similar spectral sweeps are observed in liquid and solid krypton arising from electronic mechanism for SPM. Using a picosecond laser train of wavelength 530 nm, the spectra were broadened up to 3000 cm^{-1} to either side of the laser frequency in a 5-cm-long magnetic $KNiF_3$ single crystal. Production of SPM near electronic levels of PrF_3 crystal and enhancement of supercontinuum in water by addition of Zn^{2+} and K^+ cations have been also discussed. The temporal properties of supercontinuum pulses have been described. Higher-order effects on SPM arising from dispersion, self-focusing, self-steepening, and initial pulse chirping were briefly described.

SPM will continue to be an important nonlinear process in science and technology and has been one of the most important ultrafast nonlinear optical processes for more than 50 years since the advent of ultrashort laser pulses.

In most recent developments (Alfano et al., 2021a), ultrasupercontinuum (USC) broadening has been theoretically stimulated from the slow nonelectronic response to the fifth- and third-order susceptibilities under the influence of an extremely high-intensity femtosecond laser pulse to produce spectra broadening changes extending from extreme UV to DC. The theoretical results show that a high-intensity pulse as high as on the order of ~10^{16} W/m^2 can influence the fourth-order refractive index arising from fifth-order susceptibility large enough that the nonlinear $n_4 {I_0}^2$ term to overtakes the $n_2 I_0$ term to produce the ultrasupercontinuum broadening in liquids such as CS_2 and rare-gas liquids such as Argon. There has been experimental verification that the supercontinuum extends from X-rays, UV to MIR by many researchers using various states of matter.

In addition, an electronic cloud distortion model is also proposed (Alfano et al., 2021b) based on the optical cycle response of rare-gas molecules to explain the High-order Harmonic Generation (HHG) and supercontinuum generation from the interaction of high-intensity ultrafast pulses. The theory reveals the salient experimental features of HHG: three regimes based on electronic self-phase modulation (ESPM) from nonlinear Kerr index n_2, the cutoff frequency using the method of the stationary phase on ESPM, and spectral broadening about the N harmonics supporting the theoretical ansatz presented in this paper with prior supporting

experimental results. The outcome from ESPM is a supercontinuum background superimposed with the sharp HHG which was experimentally observed before. The model also shows that the odd higher harmonic modes can be coupled in phase by Kerr index change to generation the attosecond laser pulses.

The uses of supercontinuum as an enabler will be important for many applications to understand the fundamentals of the underlying physics in biology, chemistry, condensed matter, and medicine processes. In communication and computation, the bandwidths of supercontinuum will enhance by increasing the bits/sec to unheard of limits!

A.1 Appendix: Nonlinear Wave Equation with Group Velocity Dispersion

We start with Maxwell equations for the electric and magnetic fields E and H in Gaussian units

$$\begin{aligned} &\nabla \times \mathbf{E} = -\tfrac{1}{c}\tfrac{\partial \mathbf{B}}{\partial t}, \\ &\nabla \times \mathbf{H} = \tfrac{1}{c}\tfrac{\partial \mathbf{D}}{\partial t} + \tfrac{4\pi}{c}\mathbf{J}, \\ &\nabla \cdot \mathbf{D} = 4\pi\rho \\ &\nabla \cdot \mathbf{B} = 0. \end{aligned} \tag{A.1}$$

The helping equations are $\mathbf{D} = \varepsilon\mathbf{E}$ and $\mathbf{B} = \mu\mathbf{H}$, and $\mathbf{J}$ and ρ are the current and charge densities, respectively. For nonmagnetic material, $\mathbf{B} \approx \mathbf{H}$. The refractive index of an isotropic material possessing nonlinearity can be written as

$$n(\omega) = [\varepsilon(\omega)]^{1/2} = n_0(\omega) + n_2|\mathbf{E}|^2, \tag{A.2}$$

where $n_0(\omega)$ is the linear refractive index, and n_2 the nonlinear refractive index. In the absence of sources, from Maxwell equations, one can readily obtain the wave equation

$$\nabla^2\mathbf{E}(\mathbf{r}, t) - \frac{1}{c^2}\frac{\partial^2}{\partial t^2}\mathbf{D}_L(\mathbf{r}, t) = \frac{2n_0n_2}{c^2}\frac{\partial^2}{\partial t^2}\left(|\mathbf{E}|^2\mathbf{E}(\mathbf{r}, t)\right), \tag{A.3}$$

where $\mathbf{D}_\mathrm{L}(\mathbf{r}, t)$ is the linear electric displacement vector. In obtaining the equation, we have used $\nabla \times (\nabla \times \mathbf{E}) = \nabla(\nabla \cdot \mathbf{E}) - \nabla^2\mathbf{E} \approx -\nabla^2\mathbf{E}$ and neglected the $(n_2)^2$ term.

The electric field can be written as

$$\mathbf{E}(\mathbf{r}, t) = \Phi(x, y)\,\mathbf{E}(z, t), \tag{A.4}$$

where $\Phi(x, y)$ is the transverse distribution function. Substitute Eq. (A.4) into the wave equation, and averaging over transverse coordinates, we have

$$\frac{\partial^2}{\partial z^2}\mathbf{E}(z,t) - \frac{1}{c}\frac{\partial^2}{\partial t^2}\mathbf{D}_L(z,t) = \frac{2n_0\overline{n}_2}{c^2}\frac{\partial^2}{\partial t^2}|\mathbf{E}(z,t)|^2\mathbf{E}(z,t). \tag{A.5}$$

We have neglected the $\partial^2/\partial x^2$ and $\partial\ ^2/\partial y\ ^2$ terms. The effective nonlinear refractive index $\overline{n}_2$ is

$$\overline{n}_2 = \frac{\int n_2\Phi^2(x,y)\,dxdy}{\int \Phi^2(x,y)\,dxdy} \approx \frac{1}{2}n_2. \tag{A.6}$$

Using a plane wave approximation with $(k_0z - \omega_0t)$ representation, a linearly polarized electric field propagating along z direction can be written as

$$\mathbf{E}(z,t) = \hat{e}A(z,t)\exp\left[i\left(k_0z - \omega_0t\right)\right], \tag{A.7}$$

where $\hat{e}$ is the unit vector of polarization of electric field, ω_0 the carrier frequency, k_0 the carrier wave number, and $A(z, t)$ the pulse envelope function. The form of $\mathbf{D}_L$ (z, t) becomes

$$\mathbf{D}_L(z,t) = \int_{-\infty}^{+\infty} n_0^2(\omega)\,\tilde{E}(z,\omega)\exp(-i\omega t)\,d\omega, \tag{A.8}$$

where

$$\tilde{E}(z,\omega) = \frac{1}{2\pi}\int_{-\infty}^{+\infty} E(z,t)\exp(i\omega t)\,dt. \tag{A.9}$$

If the $(\omega_0t - k_0z)$ representation is used, one obtains sign changes in the final reduced wave equation.

Using the foregoing equations, we can write the linear polarization term on the left-hand side of the one-dimensional wave equation as

$$\begin{aligned} -\tfrac{1}{c^2}\tfrac{\partial^2}{\partial t^2}\mathbf{D}_L(z,t) &= -\tfrac{1}{c^2}\textstyle\int_{-\infty}^{+\infty}\left(-\omega^2\right)n_0^2(\omega)\,\tilde{E}(z,\omega)\exp(-i\omega t)\,d\omega \\ &= \tfrac{1}{2\pi}\textstyle\int_{-\infty}^{\infty}\int_{-\infty}^{\infty}k^2(\omega)\,A\left(z,t'\right)\exp\left[i\omega\left(t'-t\right)\right]\exp\left[i\left(k_0z-\omega_0t'\right)\right]d\omega dt'. \end{aligned} \tag{A.10}$$

The derivation of the wave equation then proceeds by expanding $k^2(\omega)$ about the carrier frequency ω_0 in the form:

$$k^2(\omega) \approx k_0^2 + 2k_0k_0^{(1)}(\omega-\omega_0) + k_0k_P^{(2)}(\omega-\omega_0)^2 + \cdots, \tag{A.11}$$

where $k_0 = k(\omega_0)$ is the propagation constant, $k_0^{(1)} = \frac{\partial k}{\partial \omega}\big|_{\omega=\omega_0}$ is the inverse of group velocity, and $k_0^{(2)} = \frac{\partial^2 k}{\partial \omega}\Big|_{\omega=\omega_0}$ is the inverse of group velocity of dispersion. It is then possible to evaluate the integral of Eq. (A.10) by using the convenient delta function identities

$$\frac{1}{2\pi}\int_{-\infty}^{\infty} \exp\left[i\left(\omega-\omega_0\right)\left(t'-t\right)\right]\ d\omega = \delta\left(t'-t\right) \tag{A.12}$$

as well as

$$\frac{1}{2\pi}\int_{-\infty}^{\infty} \left(\omega-\omega_0\right)\exp\left[i\left(\omega-\omega_0\right)\left(t'-t\right)\right]\ d\omega = i\delta^{(1)}\left(t'-t\right), \tag{A.13}$$

and

$$\frac{1}{2\pi}\int_{-\infty}^{\infty} \left(\omega-\omega_0\right)^2\exp\left[i\left(\omega-\omega_0\right)\left(t'-t\right)\right]\ d\omega = -\delta^{(2)}\left(t'-t\right). \tag{A.14}$$

In these relations, $\delta^{(n)}(t)$ is an nth-order derivative of the Dirac delta function, with the property that

$$\int_{-\infty}^{\infty} \delta^{(n)}\left(t-t_0\right) f(t)dt = \frac{d^n f(t)}{\partial t^n}\Big|_{t=t_0} \tag{A.15}$$

when applied to a function $f(t)$. Substitute Eq. (A.11) into Eq. (A.10) and use Eqs. (A.12) to (A.15), the second term on the left-hand side of Eq. (1.5) becomes

$$\begin{aligned}
-\tfrac{1}{c^2}\tfrac{\partial^2}{\partial t^2}\mathbf{D}_L(z,t) &= \tfrac{1}{2\pi}\textstyle\int_{-\infty}^{\infty}\int_{-\infty}^{\infty}\left[k_0^2 + 2k_0k_0^{(1)}\left(\omega-\omega_0\right) + k_0k_0^{(2)}(\omega-\omega_0)^2\right]A\left(z,t'\right)\\
&\quad\times\exp\left[i\omega\left(t'-t\right)\right]\exp\left[i\left(k_0z-\omega_0t\right)\right]d\omega dt'\\
&= \textstyle\int_{-\infty}^{\infty}\left[k_0^2\delta\left(t'-t\right) + i2k_0k_0^{(1)}\delta^{(1)}\left(t'-t\right) - k_0k_0^{(2)}\delta^{(2)}\left(t'-t\right)\right]A\left(z,t'\right)\\
&\quad\times\exp\left[i\left(k_0z-\omega_0t\right)\right]dt'\\
&= \left[k_0^2A + i2k_0k_0^{(2)}\tfrac{\partial A}{\partial t} - k_0k_0^{(2)}\tfrac{\partial^2 A}{\partial t^2}\right]\exp\left[i\left(k_0z-\omega_0t\right)\right].
\end{aligned} \tag{A.16}$$

Neglecting the second derivative of $A(z,t)$ with respect to z and $\frac{\partial^2}{\partial t^2}|A(z,t)|^2$. $A(z,t)$, the first term on the left-hand side and the term on the right-hand side of Eq. (1.5) are simply

$$\frac{\partial^2 E(z,t)}{\partial z^2} \approx \left[-k_0^2A(z,t) + i2k_0\frac{\partial A(z,t)}{\partial z}\right]\exp\left[i\left(k_0z-\omega_0t\right)\right], \tag{A.17}$$

and

$$\frac{2n_0\bar{n}_2}{c^2}\frac{\partial^2}{\partial t^2}|E|^2E \approx -\frac{n_0n_2\omega_0^2}{c^2}|A|^2A\exp\left[i\left(k_0z-\omega_0t\right)\right], \tag{A.18}$$

respectively.

Inserting Eqs. (A.16) to (A.18) into Eq. (1.5), the wave equation for electric field reduces to the wave equation for the pulse envelope

$$i\left(\frac{\partial A}{\partial z}+\frac{1}{v_g}\frac{\partial A}{\partial t}\right)-\frac{1}{2}k_0^{(2)}\frac{\partial^2A}{\partial t^2}+\frac{\omega_0}{2c}n_2|A|^2A=0, \tag{A.19}$$

where $v_g \equiv 1/k_0^{(1)}$ is the group velocity. In Eq. (A.19), the first two terms describe the envelope propagation at the group velocity v_g; the third term determines the temporal pulse broadening due to group velocity dispersion; the fourth characterizes the second order of the nonlinear polarization, which is responsible for the self-phase modulation effect and spectral broadening. Neglecting the group velocity dispersion term in Eq. (A.19), we obtain

$$\frac{\partial A}{\partial z}+\frac{1}{v_g}\frac{\partial A}{\partial t}=i\frac{\omega_0}{2c}n_2|A|^2A. \tag{A.20}$$

This is Eq. (2.2).

References

Adair, R., Chase, L. L., & Payne, S. A. (1989). Nonlinear refractive index of optical crystals. *Physical Review B, 39*, 3337–3350.

Adamu, A. I., Habib, M. S., Petersen, C. R., Lopez, J. E. A., Zhou, B., Schülzgen, A., Bache, M., Amezcua-Correa, R., Bang, O., & Markos, C. (2019). Deep-UV to mid-IR supercontinuum generation driven by mid-IR ultrashort pulses in a gas-filled hollow-core fiber. *Scientific Reports, 9*, 4446.

Agrawal, G. P., & Potasek, M. J. (1986). Nonlinear pulse distortion in single-mode optical fibers at the zero-dispersion wavelength. *Physical Review A, 33*, 1765–1776.

Akhemediev, N., & Karlsson, M. (1995). Cherenkov radiation emitted by solitons in optical fibers. *Physical Review A, 51*, 2602–2607.

Alfano, R. R. (1972). *Interaction of picosecond laser pulses with matter. GTE Technical Report TR 72–330*. Published as Ph.D. thesis at New York University.

Alfano, R. R. (1986). The ultrafast supercontinuum laser source. In *Proceeding of the international conference laser '85* (pp. 110–122). STS Press.

Alfano, R. R., & Shapiro, S. L. (1970a). Emission in the region 4000–7000 A via four-photon coupling in glass. Phys. Rev. Lett. 24, 584–587; Observation of self-phase modulation and small scale filaments in crystals and glasses. Phys. Rev. Lett. 24, 592–594; Direct distortion of electronic clouds of rare-gas atoms in intense electric fields. *Physical Review Letters, 24*, 1219–1222.

Alfano, R. R., & Shapiro, S. L. (1970b). Picosecond spectroscopy using the inverse Raman effect. *Chemical Physics Letters, 8*, 631–633.

Alfano, R. R., Gersten, J., Zawadzkas, G., & Tzoar, N. (1974). Self-phase-modulation near the electronic resonances of a crystal. *Physical Review A, 10*, 698–708.

Alfano, R. R., Ho, P. P., Fleury, P., & Guggeneheim, H. (1976). Nonlinear optical effects in antiferromagnetic $KNiF_3$. *Optics Communication, 19*, 261–264.

Alfano, R. R., Wang, Q. Z., Jimbo, T., & Ho, P. P. (1987). Induced spectral broadening about a second harmonic generated by an intense primary ultrashort laser pulse in ZnSe crystals. *Physical Review A, 35*, 459–462.

Alfano, R. R., Mazhar, S. F. B., Sharonov, M., & Shi, L. (2021a). Ultra-supercontinuum and enhanced ultra-supercontinuum broadening from fifth- and third-order susceptibility from self-phase modulation for isotropic media with extremely intense femtosecond pulses. *Submitted to Optical Letter*.

Alfano, R. R., Mazhar, S. F. B., Sharonov, M., & Shi, L. (2021b). Higher harmonic and supercontinuum generation arising from electronic self-phase modulation under extreme ultrafast laser pulses. *Submitted to Scientific Reports*.

Allen, M. G. (1998). Diode laser absorption sensors for gas-dynamic and combustionflows. *Measurement Science and Technology, 9*, 545–562.

Auston, D. H. (1977). In S. L. Shapiro (Ed.), *Ultrafast light pulses*. Springer.

Baldeck, P. L., Raccah, F., & Alfano, R. R. (1987a). Observation of self-focusing in optical fibers with picosecond pulses. *Optics Letters, 12*, 588–589.

Baldeck, P. L., Ho, P. P., & Alfano, R. R. (1987b). Effects of self-, induced-, and cross-phase modulations on the generation of ps and fs white light supercontinuum. *Revue de Physique Appliquée, 22*, 1877–1894.

Belli, F., Abdolvand, A., Chang, W., Travers, J. C., St, P., & Russell, J. (2015). Vacuum-ultraviolet to infrared supercontinuum in hydrogen-filled photonic crystal fiber. *Optica, 2*, 292–300.

Birks, T. A., Wadsworth, W. J., & Russell, P. S. J. (2000). Supercontinuum generation in tapered fibers. *Optics Letters, 25*, 1415–1417.

Boggio, J. M. C., Moñux, A. O., Modotto, D., Fremberg, T., Bodenmüller, D., Giannone, D., Roth, M. M., Hansson, T., Wabnitz, S., Silvestre, E., & Zimmermann, L. (2016). Dispersion-optimized multicladding silicon nitride waveguides for nonlinear frequency generation from ultraviolet to mid-infrared. *Journal of the Optical Society of America B: Optical Physics, 33*, 2402–2413.

Bokov, O. G. (1974). Theory of the nonlinear refractive index of liquids. *Soviet Physics – JETP, 40*, 923–928.

Boyle, L. L., Buckingham, A. D., Disch, R. L., & Dunmur, D. A. (1966). Higher polarizability of the helium atom. *The Journal of Chemical Physics, 45*, 1318–1323.

Bree, C., Demircan, A., & Steinmeyer, G. (2010). Method for computing the nonlinear refractive index via Keldysh theory. *IEEE Journal of Quantum Electronics, 46*, 433–437.

Brewer, R. G., & Lee, C. H. (1968). Self-trapping with picosecond light pulses. *Physical Review Letters, 21*, 267–270.

Buckingham, A. D. (1955). Theoretical studies of the Kerr effect II: The influence of pressure. *The Proceedings of the Physical Society. Section A, 68*, 910–919.

Buckingham, A. D., & Hibbard, P. G. (1968). Polarizability and hyperpolarizability of the helium atom. *Symposia of the Faraday Society, 2*, 41–47.

Busch, G. E., Jones, R. P., & Rentzepis, P. M. (1973). Picosecond spectroscopy using a picosecond continuum. *Chemical Physics Letters, 18*, 178–185.

Chinn, S. R., Zeiger, H., & O'Connor, J. (1971). Two-magnon Raman scattering and exchange interactions in antiferromagnetic $KNiF_3$ and K_2NiF_4 and ferrimagnetic $RbNiF_3$. *Physical Review B: Condensed Matter and Materials Physics, 3*, 1709–1735.

Coen, S., Chau, A. H. L., Leonhardt, R., Harvey, J. D., Knight, J. C., Wadsworth, W. J., & Russell, P. S. J. (2001). White-light supercontinuum generation with 60-ps pump pulses in a photonic crystal fiber. *Optics Letters, 26*, 1356–1358.

Colley, C. S., Hebden, J. C., & Delpy, D. T. (2007). Mid-infrared optical coherence tomography. *The Review of Scientific Instruments, 78*, 123108.

Corkum, P., Ho, P. P., Alfano, R. R., & Manassah, J. (1985). Generation of infrared supercontinuum covering 3–14 μm in dielectrics and semiconductors. *Optics Letters, 10*, 624–626.

DeMartini, F., Townes, C. H., Gustafson, T. K., & Kelly, P. L. (1967). Self-steepening of light pulses. *Physics Review, 164*, 312–322.

Domachuk, P., Wolchover, N. A., Cronin-Golomb, M., Wang, A., George, A. K., Cordeiro, C. M. B., Knight, J. C., & Omenetto, F. G. (2008). Over 4000 nm bandwidth of mid-IR supercontinuum generation in sub-centimeter segments of highly nonlinear tellurite PCFs. *Optics Express, 16*, 7161–7168.

Dorsinville, R., Delfyett, P., & Alfano, R. R. (1987). Generation of 3 ps pulses by spectral selection of the supercontinuum generated by a 30 ps second harmonic Nd: YAG laser pulse in a liquid. *Applied Optics, 27*, 16–18.

Dremetsika, E., Dlubak, B., Gorza, S.-P., Ciret, C., Martin, M.-B., Hofmann, S., Seneor, P., Dolfi, D., Massar, S., Emplit, P., & Kockaert, P. (2016). Measuring the nonlinear refractive index of graphene using the optical Kerr effect method. *Optics Letters, 41*, 3281–3284.

Dudley, J. M., Provino, L., Grossard, N., Maillotte, H., Windeler, R. S., Eggleton, B. J., & Coen, S. (2002). Supercontinuum generation in air-silica microstructured fibers with nanosecond and femtosecond pulse pumping. *Journal of the Optical Society of America B: Optical Physics, 19*, 765–771.

Dudley, J. M., Genty, G., & Coen, S. (2006). Supercontinuum generation in photonic crystal fiber. *Reviews of Modern Physics, 78*, 1135–1184.

Dunsby, C., Lanigan, P. M. P., McGinty, J., Elson, D. S., Requejo-Isidro, J., Munro, I., Galletly, N., McCann, F., Treanor, B., Onfelt, B., Davis, D. M., Neil, M. A. A., & French, P. M. W. (2004). An electronically tunable ultrafast laser source applied to fluorescence imaging and fluorescence lifetime imaging microscopy. *Journal of Physics D: Applied Physics, 37*, 3296–3303.

Eggleton, B. J., Luther-Davies, B., & Richardson, K. (2011). Chalcogenide photonics. *Nature Photonics, 5*, 141–148.

Epping, J. P., Hellwig, T., Hoekman, M., Mateman, R., Leinse, A., Heideman, R. G., van Rees, A., van der Slot, P. J. M., Lee, C. J., Fallnich, C., & Boller, K.-J. (2015). On-chip visible-to-infrared supercontinuum generation with more than 495 THz spectral bandwidth. *Optics Express, 23*, 19596–19604.

Ere-Tassou, M., Przygodzki, C., Fertein, E., & Delbarre, H. (2003). Femtosecond laser source for real-time atmospheric gas sensing in the UV – Visible. *Optics Communication, 220*, 215–221.

Fleury, P. A., Hayes, W., & Guggenheim, H. J. (1975). Magnetic scattering of light in $K(NiMg)F_3$. *Journal of Physics C, 8*, 2183–2189.

Fork, R. L., Shank, C. V., Hirliman, C., Yen, R., & Tomlinson, J. (1983). Femtosecond white-light continuum pulse. *Optics Letters, 8*, 1–3.

Fork, R. L., Brito Cruz, C. H., Becker, P. C., & Shank, C. V. (1987). Compression of optical pulses to six femtoseconds by using cubic phase compensation. *Optics Letters, 12*, 483–485.

Ganeev, R. A., Ryasnyansky, A. I., Tugushev, R. I., & Usmanov, T. (2003). Investigation of nonlinear refraction and nonlinear absorption of semiconductor nanoparticle solutions prepared by laser ablation. *Journal of Optics A: Pure and Applied Optics, 5*, 409–417.

Genty, G., Lehtonen, M., Ludvigsen, H., Broeng, J., & Kaivola, M. (2002). Spectral broadening of femtosecond pulses into continuum radiation in microstructured fibers. *Optics Express, 10*, 1083–1098.

Genty, G., Lehtonen, M., & Ludvigsen, H. (2004a). Effect of cross-phase modulation on supercontinuum generated in microstructured fibers with sub-30 fs pulses. *Optics Express, 12*, 4614–4624.

Genty, G., Lehtonen, M., Ludvigsen, H., & Kaivola, M. (2004b). Enhanced bandwidth of supercontinuum generated in microstructured fibers. *Optics Express, 12*, 3471–3480.

Gersten, J., Alfano, R., & Belic, M. (1980). Combined stimulated Raman scattering in fibers. *Physical Review A, 21*, 1222–1224.

Gomes, A. S. L., Gouveia-Neto, A. S., Taylor, J. R., Avramopoulos, H., & New, G. H. C. (1986). Optical pulse narrowing by the spectral windowing of self-phase modulated picosecond pulses. *Optics Communication, 59*, 399.

Hagan, C. L., Walewski, J. W., & Sanders, S. T. (2006). Generation of a continuum extending to the midinfrared by pumping ZBLAN fiber with an ultrafast 1550-nm source. *IEEE Photonics Technology Letters, 18*, 91–93.

Halir, R., Okawachi, Y., Levy, J. S., Foster, M. A., Lipson, M., & Gaeta, A. L. (2012). Ultrabroadband supercontinuum generation in a CMOS-compatible platform. *Optics Letters, 37*, 1685–1687.

Hartl, I., Li, X. D., Chudoba, C., Ghanta, R. K., Ko, T. H., Fujimoto, J. G., Ranka, J. K., & Windeler, R. S. (2001). Ultrahigh-resolution optical coherence tomography using continuum generation in an air–silica microstructure optical fiber. *Optics Letters, 26*, 608–610.

Heidt, A. M., Hartung, A., & Bartelt, H. (2010). Deep ultraviolet supercontinuum generation in optical nanofibers by femtosecond pulses at 400-nm wavelength. *Proceedings of SPIE, 7714*(771407), 1–9.

Hellwarth, R. W., Cherlow, J., & Yang, T. T. (1975). Origin and frequency dependence of nonlinear optical susceptibilities of glasses. *Physical Review B, 11*, 964–967.

Hilligsøe, K. M., Andersen, T. V., Paulsen, H. N., Nielsen, C. K., Mølmer, K., Keiding, S., Kristiansen, R., Hansen, K. P., & Larsen, J. J. (2004). Supercontinuum generation in a photonic crystal fiber with two zero dispersion wavelengths. *Optics Express, 12*, 1045–1054.

Ho, P. P., & Alfano, R. R. (1978). Coupled molecular reorientational relaxation kinetics in mixed binary liquids directly measured by picosecond laser techniques. *The Journal of Chemical Physics, 68*, 4551–4563.

Ho, P. P., & Alfano, R. R. (1979). Optical Kerr effect in liquids. *Physical Review A, 20*, 2170–4564.

Ho, P. P., Li, Q. X., Jimbo, T., Ku, Y. L., & Alfano, R. R. (1987). Supercontinuum pulse generation and propagation in a liquid carbon tetrachloride. *Applied Optics, 26*, 2700–2702.

Holzwarth, R., Udem, T., Hansch, T. W., Knight, J. C., Wadsworth, W. J., & Russell, P. S. J. (2000). Optical frequency synthesizer for precision spectroscopy. *Physical Review Letters, 85*, 2264–2267.

Hsiung, P.-L., Chen, Y., Ko, T. H., Fujimoto, J. G., de Matos, C. J. S., Popov, S. V., Taylor, J. R., & Gapontsev, V. P. (2004). Optical coherence tomography using a continuous-wave, high-power, Raman continuum light source. *Optics Express, 12*, 5287–5295.

Hundertmark, H., Kracht, D., Wandt, D., Fallnich, C., Kumar, V. V. R. K., George, A. K., Knight, J. C., St, P., & Russell, J. (2003). Supercontinuum generation with 200 pJ laser pulses in an extruded SF6 fiber at 1560 nm. *Optics Express, 11*, 3196–3201.

Hurlbut, W. C., Lee, Y.-S., Vodopyanov, K. L., Kuo, P. S., & Fejer, M. M. (2007). Multiphoton absorption and nonlinear refraction of GaAs in the mid-infrared. *Optics Letters, 32*, 668–670.

Husakou, A. V., & Herrmann, J. (2001). Supercontinuum generation of higher-order solitons by fission in photonic crystal fibers. *Physical Review Letters, 87*, 203901-1–203901-4.

Husakou, A. V., & Herrmann, J. (2002). Supercontinuum generation, four-wave mixing, and fission of higherorder solitons in photonic-crystal fibers. *Journal of the Optical Society of America B: Optical Physics, 19*, 2171–2182.

Husakou, A. V., & Herrmann, J. (2003). Supercontinuum generation in photonic crystal fibers made from highly nonlinear glasses. *Applied Physics B: Lasers and Optics, 77*, 227–234.

Jiang, X., Joly, N. Y., Finger, M. A., Babic, F., Wong, G. K. L., Travers, J. C., St, P., & Russell, J. (2015). Deep-ultraviolet to mid-infrared supercontinuum generated in solid-core ZBLAN photonic crystal fiber. *Nature Photonics, 9*, 133–139.

Jimbo, T., Caplan, V. L., Li, Q. X., Wang, Q. Z., Ho, P. P., & Alfano, R. R. (1987). Enhancement of ultrafast supercontinuum generation in water by addition of Zn^{2+} and K^{+} cations. *Optics Letters, 12*, 477–479.

Jones, D. J. (2000). Carrier-envelope phase control of femtosecond mode-locked lasers and direct optical frequency synthesis. *Science, 288*, 635–639.

Jones, W. J., & Stoicheff, B. P. (1964). Inverse Raman spectra: Induced absorption at optical frequencies. *Physical Review Letters, 13*, 657–659.

Kartashov, D., Ališauskas, S., Pugžlys, A., Voronin, A., Zheltikov, A., Petrarca, M., Béjot, P., Kasparian, J., Wolf, J.-P., & Baltuška, A. (2012). White light generation over three octaves by femtosecond filament at 3.9 μm in argon. *Optics Letters, 37*, 3456–3458.

Kerr, J. (1875). A new relation between electricity and light: Dielectrified media birefringent. *Philosophical Magazine, 50*, 337–348.

Klimczak, M., Siwicki, B., Skibiński, P., Pysz, D., Stępień, R., Heidt, A., Radzewicz, C., & Buczyński, R. (2014). Coherent supercontinuum generation up to 2.3 μm in all-solid soft-glass photonic crystal fibers with flat all-normal dispersion. *Optics Express, 28*, 18824–18832.

Knight, J. C., Birks, T. A., Russell, P. S. J., & Atkin, D. M. (1996). All-silica single-mode optical fiber with photonic crystal cladding. *Optics Letters, 21*, 1547–1549.

Knox, K., Shulman, R. G., & Sugano, S. (1963). Covalency effects in $KNiF_3$. II. Optical studies. *Physics Review, 130*, 512–516.

Kobayashi, T. (1979). Broadband picosecond light generation in phosphoric acid by a mode-locked laser. *Optics Communication, 28*, 147–149.

Lallemand, P. (1966). Temperature variation of the width of stimulated Raman lines in liquids. *Applied Physics Letters, 8*, 276–277.

Lehtonen, M., Genty, G., Ludvigsen, H., & Kaivola, M. (2003). Supercontinuum generation in a highly birefringent microstructured fiber. *Applied Physics Letters, 82*, 2197–2199.

Levenson, M. D., & Bloembergen, N. (1974). Dispersion of the nonlinear optical susceptibility tensor in centrosymmetric media. *Physical Review B, 10*, 4447–4463.

Li, Q. X., Jimbo, T., Ho, P. P., & Alfano, R. R. (1986). Temporal distribution of picosecond supercontinuum generated in a liquid measured by a streak camera. *Applied Optics, 25*, 1869–1871.

Lu, X., Liu, Q., Liu, Z., Sun, S., Ding, P., Ding, B., & Hu, B. (2012). Measurement of nonlinear refractive index coefficient using emission spectrum of filament induced by gigawatt-femtosecond pulse in BK7 glass. *Applied Optics, 51*, 2045–2050.

Magde, D., & Windsor, M. W. (1974). Picosecond flash photolysis and spectroscopy: 3,3′-diethyloxadicarbocyanine iodide (DODCI). *Chemical Physics Letters, 27*, 31–36.

Maker, P. D., & Terhune, R. W. (1965). Study of optical effects due to an induced polarization third order in the electric field strength. *Physics Review, 137*, A801–A818.

Maker, P. D., Terhune, R. W., & Savage, C. M. (1964). Intensity-dependent changes in the refractive index of liquids. *Physical Review Letters, 12*, 507–509.

Marcuse, D. (1980). Pulse distortion in single-mode optical fibers. *Applied Optics, 19*, 1653–1660.

McTague, J., Fleury, P., & DuPre, D. (1969). Intermolecular light scattering in liquids. *Physics Review, 188*, 303–308.

Milam, D., Webert, M. J., & Glass, A. J. (1977). Nonlinear refractive index of fluoride crystals, *Applied Physics Letters, 31*, 822–824.

Morioka, T., Mori, K., & Saruwatari, M. (1993). More than 100-wavelength-channel picosecond optical pulse generation from single laser source using supercontinuum in optical fibers. *Electronics Letters, 29*, 862–864.

Nakashima, N., & Mataga, N. (1975). Picosecond flash photolysis and transient spectral measurements over the entire visible, near ultraviolet and near infrared regions. *Chemical Physics Letters, 35*, 487–492.

Petersen, C. R., Møller, U., Kubat, I., Zhou, B., Dupont, S., Ramsay, J., Benson, T., Sujecki, S., Abdel-Moneim, N., Tang, Z., Furniss, D., Seddon, A., & Bang, O. (2014). Mid-infrared supercontinuum covering the 1.4–13.3 μm molecular fingerprint region using ultra-high NA chalcogenide step-index fibre. *Nature Photonics, 8*, 830–834.

Petersen, C. R., Moselund, P. M., Huot, L., Hooper, L., & Bang, O. (2018a). Towards a table-top synchrotron based on supercontinuum generation. *Infrared Physics & Technology, 91*, 182–186.

Petersen, C. R., Prtljaga, N., Farries, M., Ward, J., Napier, B., Lloyd, G. R., Nallala, J., Stone, N., & Bang, O. (2018b). Mid-infrared multispectral tissue imaging using a chalcogenide fiber supercontinuum source. *Optics Letters, 43*, 999–1002.

Popov, A. A., Sherstnev, V. V., Yakovlev, Y. P., Baranov, A. N., & Alibert, C. (1997). Powerful mid-infrared light emitting diodes for pollution monitoring. *Electronics Letters, 33*, 86–88.

Provino, L., Dudley, J. M., Maillotte, H., Grossard, N., Windeler, R. S., & Eggleton, B. J. (2001). Compact broadband continuum source based on microchip laser pumped microstructured fibre. *Electronics Letters, 37*, 558–560.

Qin, G., Yan, X., Kito, C., Liao, M., Chaudhari, C., Suzuki, T., & Ohishia, Y. (2009). Ultrabroadband supercontinuum generation from ultraviolet to 6.28 μm in a fluoride fiber. *Applied Physics Letters, 95*, 161103.

Ranka, J. K., Windeler, R. S., & Stentz, A. J. (2000). Visible continuum generation in air-silica microstructure optical fibers with anomalous dispersion at 800 nm. *Optics Letters, 25*, 25–27.

Rau, I., Kajzar, F., Luc, J., Sahraoui, B., & Boudebs, G. (2008). Comparison of Z-scan and THG derived nonlinear index of refraction in selected organic solvents. *Journal of the Optical Society of America B: Optical Physics, 25*, 1738–1747.

Riedle, E., Bradler, M., Wenninger, M., Sailer, C. F., & Pugliesi, I. (2013). Electronic transient spectroscopy from the deep UV to the NIR: Unambiguous disentanglement of complex processes. *Faraday Discussions, 163*, 139–158.

Russell, P. S. J., Knight, J. C., Birks, T. A., & Atkin, D. M. (1996). All-silica single-mode optical fiber with photonic crystal cladding. *Optics Letters, 21*, 1547–1549.

Russell, P. S. J., Birks, T. A., & Knight, J. C. (1997). Endlessly single-mode photonic crystal fiber. *Optics Letters, 22*, 961–963.

Safioui, J., Leo, F., Kuyken, B., Gorza, S.-P., Selvaraja, S. K., Baets, R., Emplit, P., Roelkens, G., & Massar, S. (2014). Supercontinuum generation in hydrogenated amorphous silicon waveguides at telecommunication wavelengths. *Optics Express, 22*, 3089–3097.

Saini, T. S., Tuan, T. H., Suzuki, T., & Ohishi, Y. (2020). Coherent Mid-IR supercontinuum generation using tapered chalcogenide step-index optical fiber: Experiment and modelling. *Scientific Reports, 10*, 2236.

Sanders, S. T. (2002). Wavelength-agile fiber laser using group-velocity dispersion of pulsed supercontinua and application to broadband absorption spectroscopy. *Applied Physics B, 75*, 799–802.

Schliesser, A., Picqué, N., & Hänsch, T. W. (2012). Mid-infrared frequency combs. *Nature Photonics, 6*, 440–449.

Schnatz, H., & Hollberg, L. W. (2003). Optical frequency combs: From frequency metrology to optical phase control. *The IEEE Journal of Selected Topics in Quantum Electronics, 9*, 1041–1058.

Seddon, A. B. (2011). A prospective for new mid-infrared medical endoscopy using chalcogenide glasses. *International Journal of Applied Glass Science, 2*, 177–191.

Shank, C. V., Fork, R. L., Yen, R., & Stolen, R. H. (1982). Compression of femtosecond optical pulses. *Applied Physics Letters, 40*, 761–763.

Sharma, D. K., Yid, R. W., Williams, D. F., Sugamori, S. E., & Bradley, L. L. T. (1976). Generation of an intense picosecond continuum in D_2O by a single picosecond 1.06 μ pulse. *Chemical Physics Letters, 41*, 460–465.

Shen, Y. R. (1984). *The principles of nonlinear optics*. Wiley.

Stark, S. P., Travers, J. C., St, P., & Russell, J. (2012). Extreme supercontinuum generation to the deep UV. *Optics Letters, 37*, 770–772.

Stokowski, S., & Vaez-Iravani, M. (1998). Wafer inspection technology challenges for ULSI manufacturing. In *AIP conference proceedings* (Vol. 449, pp. 405–415). AIP.

Stolen, R. H., & Lin, C. (1978). Self-phase modulation in silica optical fibers. *Physical Review A, 17*, 1448–1453.

Takara, H., Ohara, T., Mori, K., Sato, K., Yamada, E., Inoue, Y., Shibata, T., Abe, M., Morioka T., & Sato, K-I. (2005). More than 1000 channel optical frequency chain generation from single supercontinuum source with 12.5GHz channel spacing. *Electronics Letters, 36*, 2089–2090.

Topp, M. R., & Orner, G. C. (1975). Group velocity dispersion effects in picoseconds spectroscopy. *Optics Communication, 13*, 276.

Walrafen, G. E. (1972). Stimulated Raman scattering and the mixture model of water structure. *Advances in Molecular Relaxation Processes, 3*, 43–49.

Wang, Q. Z., Ji, D., Yang, L., Ho, P. P., & Alfano, R. R. (1989). Self-phase modulation in multimode optical fibers with modest high power. *Optics Letters, 14*(11), 578–580.

Wang, Q. Z., Liu, Q. D., Liu, D., Ho, P. P., & Alfano, R. R. (1994a). High-resolution spectra of self-phase modulation in optical fibers. *Journal of the Optical Society of America B: Optical Physics, 11*, 1084–1089.

Wang, Q. Z., Liu, Q. D., Ho, P. P., Walge, E. K., & Alfano, R. R. (1994b). High-resolution spectra of cross-phase modulation in optical fibers. *Optics Letters, 19*, 1636–1638.

Wang, D., Leng, Y., & Xu, Z. (2013). Measurement of nonlinear refractive index coefficient of inert gases with hollow-core fiber. *Applied Physics B: Lasers and Optics, 111*, 447–452.

Wang, N., Cai, J.-H., Qi, X., Chen, S.-P., Yang, L.-J., & Hou, J. (2018). Ultraviolet-enhanced supercontinuum generation with a mode-locked Yb-doped fiber laser operating in dissipative-solitonresonance region. *Optics Express, 26*, 1689–1696.

Wegener, J., Wilsonand, R. H., & Tapp, H. S. (1999). Mid-infrared spectroscopy for food analysis: Recent new applications and relevant developments in sample presentation methods. *Trends in Analytical Chemistry, 18*, 85–93.

Xiang, B., Ren, X., Ruan, S., Wang, L., Yan, P., Han, H., Wang, M., & Yin, J. (2016). Visible to near-infrared supercontinuum generation in yttrium orthosilicate bulk crystal and ion implanted planar waveguide. *Scientific Reports, 6*, 31612-1–31612-7.

Yang, G., & Shen, Y. R. (1984). Spectral broadening of ultrashort pulse in a nonlinear medium. *Optics Letters, 9*, 510–512.

Yariv, A. (1975). *Quantum electronics* (2nd ed.p. 499). Wiley.

Yu, W., Alfano, R. R., Sam, C. L., & Seymour, R. J. (1975). Spectral broadening of picosecond 1.06 mm pulse in KBr. *Optics Communication, 14*, 344.

Yu, M., Desiatov, B., Okawachi, Y., Gaeta, A. L., & Loncar, M. (2019). Coherent two-octave-spanning supercontinuum generation in lithium-niobate waveguides. *Optics Letters, 44*, 1222–1225.

Zhang, N., Peng, X., Wang, Y., Dai, S., Yuan, Y., Su, J., Li, G., Zhang, P., Yang, P., & Wang, X. (2019). Ultrabroadband and coherent mid-infrared supercontinuum generation in Te-based chalcogenide tapered fiber with all-normal dispersion. *Optics Express, 27*, 10311–10319.

Chapter 3
Ultrashort Pulse Propagation in Nonlinear Dispersive Fibers

Govind P. Agrawal

Abstract This chapter focuses on the evolution of short optical pulses inside optical fibers. After discussing the role of self-phase modulation and optical solitons, we discuss supercontinuum generation, occurring when femtosecond pulses are launched into an optical fiber. The extension of supercontinuum into the mid-infrared and ultraviolet regions is also covered.

Keywords Optical fiber · Group-velocity dispersion · Nonlinear length · Dispersion length · Frequency chirp · Self-phase modulation · Spectral broadening · Optical soliton · Self-steepening · Supercontinuum generation · Soliton fission · Raman scattering · Four-wave mixing · Mid-infrared radiation · Ultraviolet radiation

3.1 Introduction

Ultrashort optical pulses are often propagated through optical waveguides for a variety of applications including telecommunications and supercontinuum generation (Agrawal, 2019). Typically, the waveguide is in the form of an optical fiber, but it can also be a planar waveguide. The material used to make the waveguide is often silica glass, but other materials such as silicon or chalcogenides have also been used in recent years. What is common to all such materials is they exhibit chromatic dispersion as well as the Kerr nonlinearity. The former makes the refractive index frequency-dependent, whereas the latter makes it to depend on the intensity of light propagating through the medium (Maker et al., 1964). Both of these effects become more important as optical pulses become shorter and more intense. For pulses not too short (pulse widths $>$ 1 ns) and not too intense (peak powers $<$ 10 mW), the waveguide plays a passive role (except for small optical losses) and acts as

G. P. Agrawal (✉)
The Institute of Optics, University of Rochester, Rochester, NY, USA
e-mail: gpa@optics.rochester.edu

R. R. Alfano (ed.), *The Supercontinuum Laser Source*,
https://doi.org/10.1007/978-3-031-06197-4_3

a transporter of optical pulses from one place to another, without significantly affecting their shape or spectrum. However, as pulses become shorter and more intense, both the group-velocity dispersion (GVD) and the Kerr nonlinearity start to affect the shape and spectrum of an optical pulse during its propagation inside the waveguide. This chapter focuses on silica fibers, but similar results are expected for other waveguides made of different materials.

Silica fibers have found many interesting applications owing to their nonlinear dispersive nature. They are often used for pulse compression and pulses with durations as short as 6 fs were produced by 1987 (Fork et al., 1987). In the anomalous-GVD regime, fibers support formation of optical solitons, resulting from a balance between the dispersive and nonlinear effects (Hasegawa & Tappert, 1973; Mollenauer et al. 1980; Mollenauer & Stolen, 1984; Stolen 2008). More recently, new types of optical fibers have been developed and used for making a supercontinuum source (Ranka et al. 2000; Dudley et al. 2006; Genty et al. 2007; Dudley & Taylor, 2010). In this case, dispersive effects and several nonlinear phenomena, such as self-phase modulation (SPM), cross-phase modulation (XPM), four-wave mixing (FWM), and stimulated Raman scattering (SRS), work together to produce an extensive spectral broadening of the incident pulse, similar to that observed by Alfano and Shapiro in several 1970 experiments (Alfano & Shapiro, 1970a, 1970b, 1970c, 1971).

This chapter reviews how the nonlinear and dispersive effects in optical fibers influence the propagation of ultrashort pulses with widths in the femtosecond to picosecond range. The basic propagation equation satisfied by the slowly varying amplitude of the pulse envelope is presented in Sect. 3.2. Section 3.3 introduces the dispersive and nonlinear length scales and identifies various propagation regimes of optical pulses. Sections 3.4 and 3.5 then focus separately on the cases of normal- and anomalous-GVD regimes. The phenomenon of supercontinuum generation is studied in Sect. 3.6 in both the normal- and anomalous-GVD regimes of the optical fiber used for this purpose. Extension of the supercontinuum into the ultraviolet (UV) and mid-infrared (mid-IR) regions is covered in Sect. 3.7, as such sources are useful for many practical applications. Section 3.8 provides a summary of the main results and conclusions.

3.2 Basic Propagation Equation

As is the case for all electromagnetic phenomena, we need to solve Maxwell's equations inside a dispersive nonlinear medium. Since details are available elsewhere (Agrawal, 2019), only the main steps are summarized here. Consider the simplest situation in which a single input pulse, polarized linearly at the carrier frequency ω_0, is launched such that it excites a single mode of the fiber. If we assume that the pulse maintains its linear polarization along the x axis during its propagation along fiber's length (the z axis), the electric field can be written in the form

$$\mathbf{E}(\boldsymbol{r}, t) = \frac{1}{2\pi} \int_{-\infty}^{\infty} \hat{x} F(x, y, \omega) \tilde{a}(0, \omega) e^{i[\beta(\omega) z - \omega t]} d\omega, \tag{3.1}$$

where $\hat{x}$ is a unit vector along the x axis and $F(x, y, \omega)$ represents the spatial distribution of the fiber mode. The physical meaning of this equation is clear. Each spectral component of the input field with the amplitude $\tilde{a}(0, \omega)$ acquires a slightly different phase shift because of the frequency dependence of the propagation constant $\beta(\omega)$ associated with that fiber mode.

As an exact functional form of $\beta(\omega)$ is rarely known, it is useful to expand it in a Taylor series around the carrier frequency ω_0 as

$$\beta(\omega) = \beta_0 + (\omega - \omega_0)\beta_1 + \tfrac{1}{2}(\omega - \omega_0)^2 \beta_2 + \cdots, \tag{3.2}$$

where various dispersion parameters are defined as $\beta_m = (d^m \beta / d\omega^m)_{\omega=\omega_0}$. Depending on the pulse bandwidth, one can stop after the group-velocity dispersion (GVD) term containing β_2 or may need to include the third- and higher-order dispersion terms. Another common approximation replaces the mode profile $F(x, y, \omega)$ with its shape at the carrier frequency ω_0. It is also useful to remove the rapidly varying part of the optical field at this frequency and introduce a slowly varying pulse envelope $A(z, t)$ by writing Eq. (3.1) in the form

$$\mathbf{E}(\boldsymbol{r}, t) = \hat{x}\, F(x, y, \omega_0) A(z, t) e^{i(\beta_0 z - \omega_0 t)}. \tag{3.3}$$

Maxwell's equations are then used to derive an equation for $A(z, t)$, representing the slowly varying amplitude of the pulse envelope at distance z.

As outlined in the book by Agrawal (2019), if we include both the Kerr and Raman contributions to the nonlinear susceptibility, the slowly varying pulse envelope $A(z, t)$ satisfies the following time-domain propagation equation:

$$\frac{\partial A}{\partial z} + \frac{\alpha}{2} A = i \sum_{m=1}^{\infty} \frac{i^m \beta_m}{m!} \frac{\partial^m A}{\partial t^m} + i\gamma \left(1 + \frac{i}{\omega_0} \frac{\partial}{\partial t}\right) \times \left(\int_0^{\infty} R(t') |A(z, t - t')|^2 dt'\right) A(z, t), \tag{3.4}$$

where α accounts for fiber losses and the nonlinear parameter γ is defined as

$$\gamma = \frac{\omega_0 n_2(\omega_0)}{c A_{\text{eff}}}, \quad A_{\text{eff}} = \frac{[\iint |F(x, y, \omega_0)|^2 dx dy]^2}{\iint |F(x, y, \omega_0)|^4 dx dy}. \tag{3.5}$$

A_{eff} is known as the effective mode area of the fiber. In the case of supercontinuum generation, it may become necessary to account for the frequency dependence of both $n_2(\omega)$ and $F(x, y, \omega)$.

The nonlinear response function $R(t)$ in Eq. (3.4) includes both the electronic and nuclear (Raman) contributions and can be written as

$$R(t) = (1 - f_R)\delta(t) + f_R h_R(t). \tag{3.6}$$

Both the Raman response function $h_R(t)$ and its fractional contribution ($f_R \approx 0.18$) are known for silica (Stolen et al., 1989). Because of the amorphous nature of silica glasses, the Raman gain spectrum $g_R(\omega)$ of optical fibers, shown in Fig. 3.1a, extends over a frequency range exceeding 50 THz. Since $g_R(\omega)$ is related to the imaginary part of the Fourier transform of $h_R(t)$, it can be used to deduce the real part through the Kramers–Kronig relation. The inverse Fourier transform of $\tilde{h}_R(\omega)$ then provides the Raman response function $h_R(t)$ shown in Fig. 3.1b.

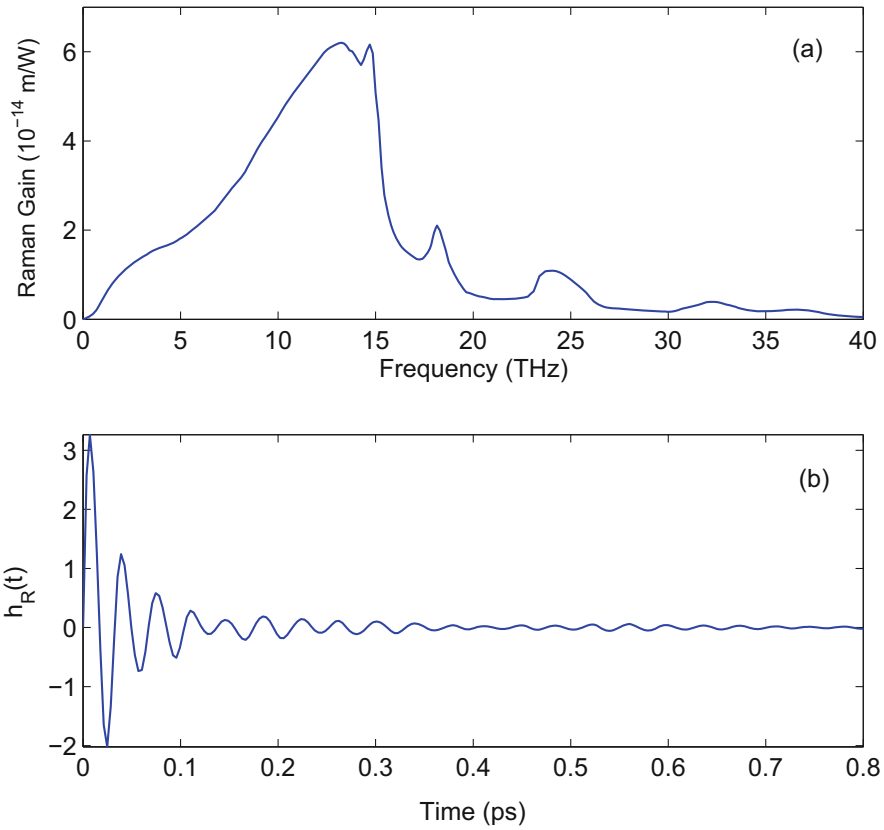

Fig. 3.1 (**a**) Measured Raman gain spectrum of silica fibers (Stolen et al., 1989); (**b**) temporal form of the Raman response function deduced from the gain data

3.3 Different Propagation Regimes

Although Eq. (3.4) must be solved for ultrashort optical pulses, it can be simplified considerably for picosecond pulses, a common situation in many applications. To understand why that is so, we note from Fig. 3.1 that $h_R(t)$ has an appreciable magnitude only for $t < 1$ ps. For pulses wider than 3–4 ps, $h_R(t)$ can be replaced with a delta function $\delta(t)$ with a reasonably good approximation. The derivative term containing ω_0 is also negligible for such pulses. At the same time, all dispersive effects higher than the third order can be ignored for such pulses. Using these three approximations, Eq. (3.4) is reduced to the following simpler equation:

$$\frac{\partial A}{\partial z} + \frac{\alpha}{2}A + \beta_1 \frac{\partial A}{\partial t} + \frac{i\beta_2}{2}\frac{\partial^2 A}{\partial t^2} - \frac{\beta_3}{6}\frac{\partial^2 A}{\partial t^2} = i\gamma |A|^2 A. \tag{3.7}$$

When $\alpha = 0$ and $\beta_3 = 0$, Eq. (3.7) is reduced to the nonlinear Schrödinger (NLS) equation that is well known in the filed of nonlinear optics (Agrawal, 2019). One can justify neglecting the loss term for fibers shorter than 1 km, especially in the wavelength region near 1550 nm where losses are the smallest. However, losses must be included for longer fibers.

Considerable insight can be gained by introducing normalized variables. For this purpose, we note that any input pulse launched into the fiber has its amplitude in the form $A(0, t) = \sqrt{P_0}\, S(t/T_0)$, where $S(t)$ is the shape function, P_0 is the peak power, and T_0 is a measure of the pulse width. For a fiber of length L, it is useful to define the normalized variables as

$$Z = z/L, \qquad \tau = (t - \beta_1 z)/T_0, \qquad A = \sqrt{P_0} e^{-\alpha z/2} U, \tag{3.8}$$

where τ is defined in a frame of reference moving with the pulse at the group velocity $v_g = 1/\beta_1$ (the so-called retarded frame). Note that the exponential decay of the amplitude has been included in the definition of the normalized amplitude U. The use of Eq. (3.8) in Eq. (3.7) leads to an equation in the form

$$\frac{\partial U}{\partial Z} + \frac{isL}{2L_D}\frac{\partial^2 U}{\partial \tau^2} - \frac{\beta_3 L}{6T_0^3}\frac{\partial^3 U}{\partial \tau^3} = \frac{iL}{L_{\mathrm{NL}}} e^{-\alpha z} |U|^2 U, \tag{3.9}$$

where $s = \mathrm{sgn}(\beta_2) = \pm 1$, and the dispersion and nonlinear lengths are defined as

$$L_D = \frac{T_0^2}{|\beta_2|}, \qquad L_{\mathrm{NL}} = \frac{1}{\gamma P_0}. \tag{3.10}$$

They provide two length scales over which the dispersive and nonlinear effects become important for the pulse evolution.

When fiber length L is such that $L \ll L_{\mathrm{NL}}$ and $L \ll L_D$, neither the dispersive nor the nonlinear effects play a significant role during pulse propagation. The fiber

plays a passive role in this regime and acts as a mere transporter of optical pulses (except for reducing the pulse energy because of fiber losses). At a wavelength near 1.5 μm, $\beta_2 \approx -20$ ps^2/km, and $\gamma \approx 2$ W^{-1}km^{-1} for standard telecommunication fibers. The use of these values in Eq. (3.10) shows that the dispersive and nonlinear effects are negligible for $L < 100$ km if $T_0 > 100$ ps and $P_0 < 1$ mW. However, L_D and $L_{\rm NL}$ become smaller as pulses become shorter and more intense. For example, L_D and $L_{\rm NL}$ are ∼0.1 km for $T_0 \sim 1$ ps and $P_0 \sim 1$ W. For such optical pulses, both the dispersive and nonlinear effects need to be included if fiber length exceeds 100 m. Depending on three relative magnitudes of these length scales, the propagation behavior can be classified in the following three regimes.

3.3.1 Dispersion-Dominant Regime

When the fiber length is such that $L \ll L_{\rm NL}$ but $L > L_D$, the last term in Eq. (3.9) is negligible compared to the other two. The dispersion-dominant regime is applicable whenever the fiber and pulse parameters are such that

$$N^2 = \frac{L_D}{L_{\rm NL}} = \frac{\gamma P_0 T_0^2}{|\beta_2|} \ll 1. \tag{3.11}$$

As a rough estimate, P_0 should be less than 10 mW for 10-ps pulses. The parameter N is later found to be related to the soliton order.

In the dispersion-dominant regime, the evolution of an optical pulse is governed by the GVD alone, and the nonlinear effects play a negligible role. The resulting linear equation,

$$\frac{\partial U}{\partial z} + \frac{is}{2L_D}\frac{\partial^2 U}{\partial \tau^2} - \frac{\beta_3}{6T_0^3}\frac{\partial^3 U}{\partial \tau^3} = 0, \tag{3.12}$$

can be solved with the Fourier transform method. Let $\tilde{U}(z, \omega)$ be the Fourier transform of $U(z, \tau)$ defined as

$$\tilde{U}(z, \omega) = \int_{-\infty}^{\infty} U(z, \tau) e^{i\omega\tau}\, d\tau. \tag{3.13}$$

In the Fourier domain, Eq. (3.12) becomes an ordinary differential equation and can be solved easily. Converting the result back to the time domain, we obtain the solution

$$U(z, \tau) = \frac{1}{2\pi}\int_{-\infty}^{\infty} \tilde{U}(0, \omega) \exp\left(\frac{is\omega^2 z}{2L_D} + \frac{i\beta_3\omega^3 z}{6T_0^3} - i\omega\tau\right) d\omega, \tag{3.14}$$

where $\tilde{U}(0, \omega)$ is the Fourier transform of the incident field at $z = 0$ and is obtained by setting $z = 0$ in Eq. (3.13). Equation (3.14) can be used for input pulses of arbitrary shapes. However, the integral can be evaluated in a closed form only for a few specific pulse shapes. In general, both the width and the phase of an optical pulse are expected to change as it propagates down the fiber. It should be stressed, however, that the GVD affects only the spectral phase and not the spectral intensity, i.e., the spectrum of any pulse remains unaltered during its propagation inside a linear dispersive medium.

As a simple example, consider the case of a Gaussian pulse, for which the incident field is of the form $U(0, \tau) = \exp(-\tau^2/2)$, and neglect the contribution of the β_3 term. The integration can be carried out analytically, and the final result is given by

$$U(z, \tau) = \left(1 - is\xi\right)^{-1/2} \exp\left[-\frac{\tau^2}{2(1 - is\xi)}\right], \tag{3.15}$$

where $\xi = z/L_D$ is the distance normalized to the dispersion length. This expression shows that a Gaussian pulse maintains its shape on propagation, but its width T_1 increases with the distance z as

$$T_1(\xi) = T_0(1 + \xi^2)^{1/2}. \tag{3.16}$$

At the same time, the pulse develops a time-dependent phase such that

$$\phi(\xi, \tau) = -\frac{s\xi\tau^2/2}{1 + \xi^2} + \frac{1}{2}\tan^{-1}(s\xi). \tag{3.17}$$

A time-dependent phase implies that the frequency of the electric-field oscillations changes with time, a feature referred to as the frequency chirp. This frequency change is related to the phase as

$$\delta\omega = \omega - \omega_0 = -\frac{\partial\phi}{\partial t} = \frac{s\xi\tau}{(1 + \xi^2)T_0}. \tag{3.18}$$

This relation shows that the frequency changes linearly across the pulse and its value depends on the sign of β_2. In the normal-GVD regime ($s = 1$), $\delta\omega$ is negative near the leading edge and increases linearly across the pulse. The opposite occurs in the anomalous-GVD regime ($s = -1$). As an example, Fig. 3.2 shows dispersion-induced broadening and chirping for a Gaussian pulse at $\xi = 2$ and 4 in the case of anomalous GVD ($s = -1$). As seen there, chirp imposed by GVD is perfectly linear for Gaussian pulses.

One may wonder what happens if the input pulse itself is chirped. In the case of linearly chirped Gaussian pulses, the incident field is of the form $U(0, \tau) = \exp[-(1 + iC)\tau^2/2]$, where C is a chirp parameter. It is common to refer to the chirp as being positive or negative, depending on whether C is positive or negative.

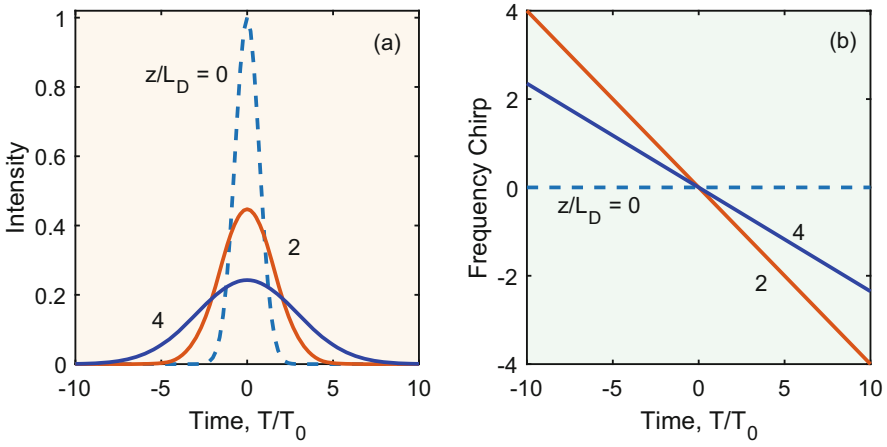

Fig. 3.2 Dispersion-induced broadening (**a**) and chirping (**b**) of a Gaussian pulse at distances of $2L_D$ and $4L_D$ in the case of anomalous GVD ($s = -1$). Dashed lines show the situation at $z = 0$

We can obtain $\tilde{U}(0, \omega)$ from Eq. (3.13) and use it in Eq. (3.14) to find $U(z, \tau)$. The integral can again be done analytically to obtain

$$U(z, \tau) = \frac{1}{\sqrt{Q}} \exp\left[-\frac{(1 + iC)\tau^2}{2Q(z)}\right], \tag{3.19}$$

where $Q = 1 - is\xi(1 + iC)$. Even a chirped Gaussian pulse maintains its shape on propagation, but its width and chirp change as

$$T_1(\xi) = \left[(1 + sC\xi^2)^2 + \xi^2)\right]^{1/2} T_0, \qquad C_1(z) = C + (1 + C^2)s\xi. \tag{3.20}$$

Figure 3.3 shows the broadening factor T_1/T_0 and the chirp parameter C_1 as a function of ξ in the case of anomalous GVD ($s = -1$). An unchirped pulse ($C = 0$) broadens monotonically by a factor of $(1 + \xi^2)^{1/2}$ and develops a negative chirp such that $C_1 = -\xi$ (the dotted curves). Chirped pulses, on the other hand, may broaden or compress depending on whether β_2 and C have the same or opposite signs. When $sC > 0$, a chirped Gaussian pulse broadens monotonically at a rate faster than that of the unchirped pulse (the dashed curves). The situation changes dramatically for $sC < 0$. In this case, the contribution of the dispersion-induced chirp is of a kind opposite to that of the input chirp. As seen from Eq. (3.20), C_1 becomes zero at a distance $\xi = |C|/(1 + C^2)$, and the pulse becomes unchirped. This is the reason why the pulse width initially decreases in Fig. 3.3 and becomes minimum at a specific distance. The minimum value of the pulse width depends on the input chirp parameter as $T_1^{\min} = T_0/\sqrt{1 + C^2}$.

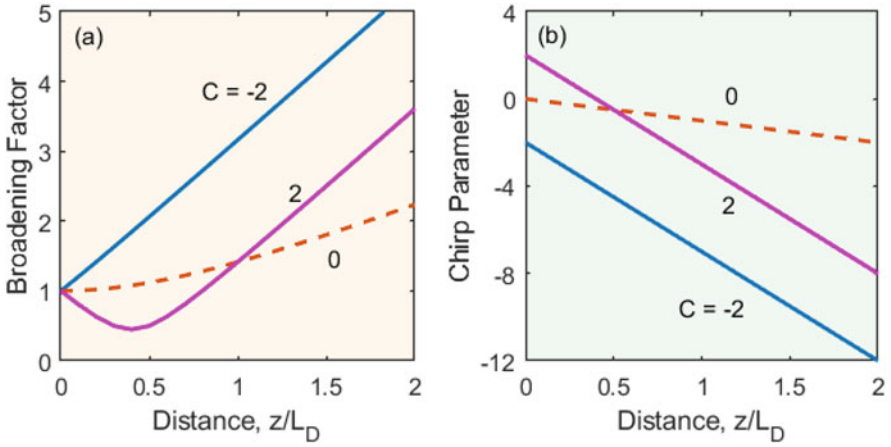

Fig. 3.3 Broadening factor (**a**) and chirp parameter (**b**) for chirped Gaussian input pulses propagating in the anomalous-GVD region of a fiber. Dashed curves show the case of an unchirped Gaussian pulse. The same curves are obtained for normal GVD if the sign of C is reversed

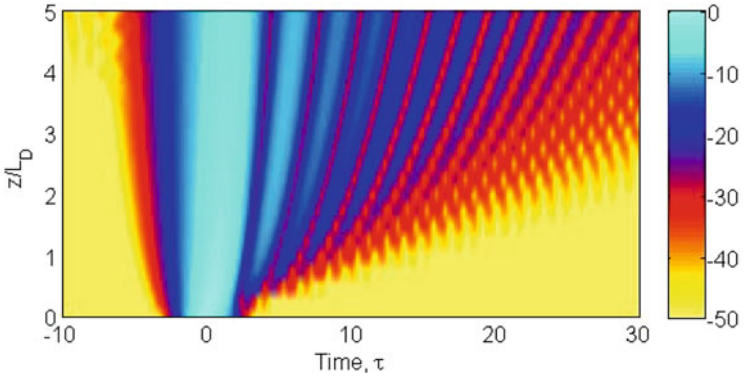

Fig. 3.4 Temporal evolution of an unchirped Gaussian input pulse propagating in the normal-GVD region of a fiber with non-negligible third-order dispersion ($\beta_3/(6T_0^3) = 0.2$)

We briefly consider the impact of third-order dispersion, which becomes important for short pulses propagating near the zero-dispersion wavelength (ZDWL) of the fiber. For a Gaussian input pulse, the integral can be done in a closed form in terms of an Airy function (Agrawal, 2019) but must be performed numerically for other pulse shapes. Figure 3.4 shows the evolution of a Gaussian pulse in the normal-GVD region ($s = 1$) over five dispersion lengths using $\beta_3 L_D/(6T_0^3) = 0.2$. The pulse develops an asymmetric shape with an oscillating structure in its trailing edge. A mirror image around $\tau = 0$ occurs for negative values of β_3 with an oscillating structure developing on the leading edge of the pulse. It will be seen later that the third-order dispersion plays an important role in the formation of a supercontinuum.

3.3.2 Nonlinearity-Dominant Regime

When the fiber length L is such that $L \ll L_D$ but $L > L_{\rm NL}$, the dispersion terms in Eq. (3.9) are negligible compared to the nonlinear term. In that case, pulse evolution in the fiber is governed by the SPM alone, which produces changes in the pulse spectrum but leaves the pulse shape intact. The nonlinearity-dominant regime is applicable only when $N \gg 1$. If we neglect the dispersion terms in Eq. (3.9), it can be solved analytically to obtain the general solution

$$U(L,\tau) = U(0,\tau)\exp[i\phi_{\rm NL}(L,\tau)], \tag{3.21}$$

where $\phi_{\rm NL}(L,\tau) = |U(0,\tau)|^2(L_{\rm eff}/L_{\rm NL})$. The effective length $L_{\rm eff}$ for a fiber of length L is defined as $L_{\rm eff} = [1-\exp(-\alpha L)]/\alpha$. It is smaller than L because of fiber losses. In the absence of fiber losses, $L_{\rm eff} = L$. Equation (3.21) shows that SPM gives rise to an intensity-dependent phase shift, but the pulse shape remains unaffected. The maximum phase shift $\phi_{\rm max}$ occurs at the pulse center located at $\tau = 0$. With U normalized such that $|U(0,0)| = 1$, it is given by

$$\phi_{\rm max} = L_{\rm eff}/L_{\rm NL} = \gamma P_0 L_{\rm eff}. \tag{3.22}$$

If we use $\gamma = 2\,{\rm W}^{-1}/{\rm km}$ and $L_{\rm eff} = 20\,{\rm km}$, $\phi_{\rm max} = 40$ at a power level $P_0 = 1\,{\rm W}$.

Spectral changes induced by SPM are a direct consequence of the time dependence of $\phi_{\rm NL}$. Recalling that a temporally varying phase implies that the pulse becomes chirped such that

$$\delta\omega(\tau) = -\frac{\partial\phi_{\rm NL}}{\partial t} = -\left(\frac{L_{\rm eff}}{L_{\rm NL}}\right)\frac{1}{T_0}\frac{\partial}{\partial\tau}|U(0,\tau)|^2. \tag{3.23}$$

The chirp induced by SPM increases in magnitude with the propagated distance. In other words, new frequency components are generated continuously as the pulse propagates down the fiber. These SPM-generated frequency components broaden the spectrum compared to its initial width at $z = 0$. The spectrum is obtained by taking the Fourier transform of Eq. (3.21). Figure 3.5 shows the spectrum $|\tilde{U}(L,\omega)|^2$ calculated for an unchirped Gaussian pulse using $\phi_{\rm max} = 40$. In this situation, the number of internal peaks increases linearly with the fiber length, and the dominant peaks occur near the spectral boundaries. These SPM-induced spectral features were first observed in optical fibers in a 1978 experiment (Stolen & Lin, 1978) and were used to estimate the nonlinear parameter n_2.

Since the nonlinear phase $\phi_{\rm NL}$ depends on the pulse intensity, its derivative needed in Eq. (3.23) is quite sensitive to the shape of the pulse. This feature makes the SPM-broadened spectrum to depend on the pulse shape. We can see this dependence by considering super-Gaussian pulses whose intensity varies with time as $|U(0,\tau)|^2 = \exp(-\tau^{2m})$, where $m > 1$ for super-Gaussian pulses. The pulse becomes nearly rectangular for $m > 5$. Figure 3.6 compares the evolution of

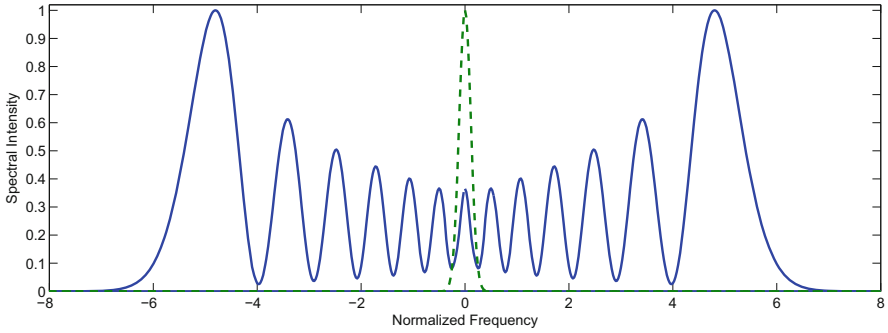

Fig. 3.5 SPM-induced spectral broadening of a Gaussian pulse for $\phi_{\max} = 40$. The dashed curve shows the input spectrum

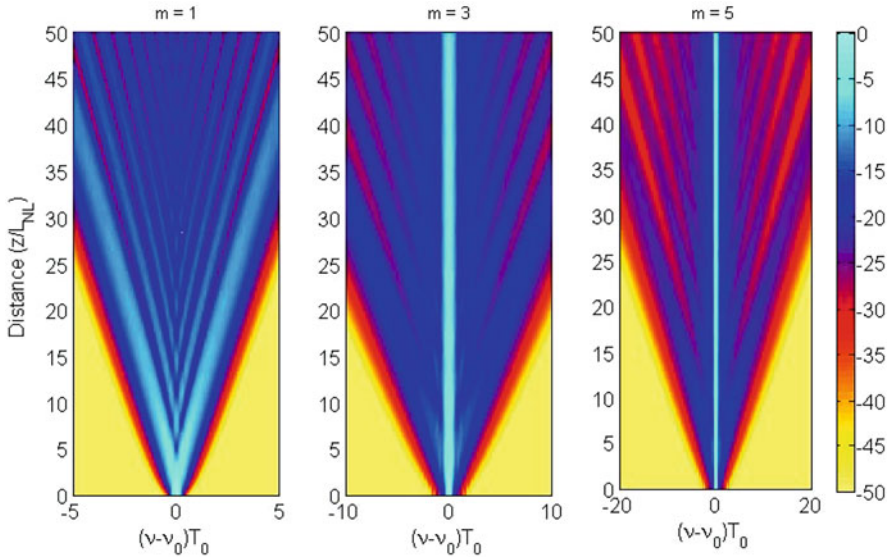

Fig. 3.6 Evolution of SPM-broadened spectra for fiber lengths in the range 0 to $50L_{\mathrm{NL}}$ for unchirped super-Gaussian pulses with $m = 1$, 3, and 5. A color bar shows the 50-dB range used for plotting the spectral density

pulse spectra for the Gaussian ($m = 1$) and super-Gaussian ($m = 3$ and 5) pulses over $50\,L_{\mathrm{NL}}$ using Eq. (3.22) in Eq. (3.21) and performing the Fourier transform numerically. In all cases, input pulses are assumed to be unchirped ($C = 0$), and fiber losses are ignored ($\alpha = 0$). The qualitative differences between the three spectra are quite noticeable. Even though all spectra in Fig. 3.6 exhibit multiple peaks, most of the energy remains in the central peak for a super-Gaussian pulse. This is so because the chirp is nearly zero over the central region for such a pulse, a consequence of the nearly uniform intensity of super-Gaussian pulses for

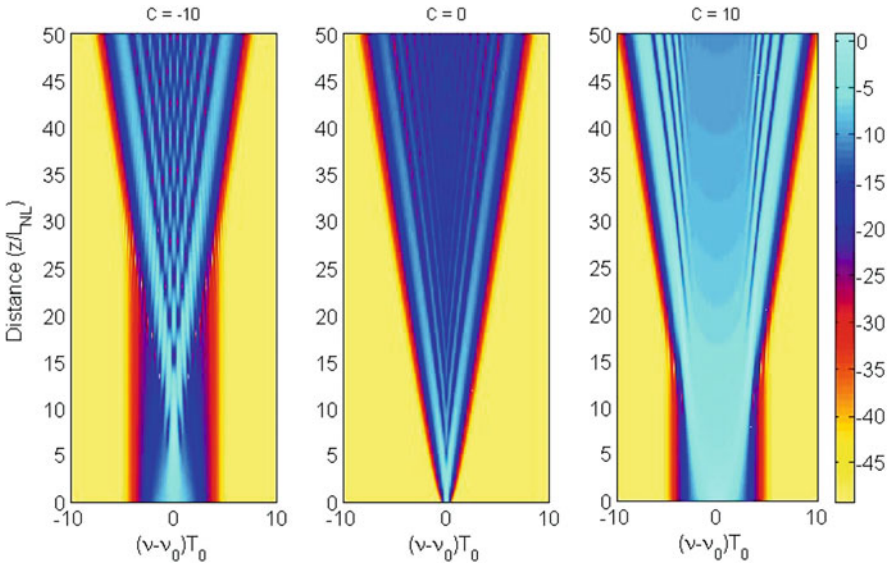

Fig. 3.7 Evolution of SPM-broadened spectra for fiber lengths in the range 0 to $50L_{\rm NL}$ for chirped Gaussian pulses with $C = -10$, 0, and 10. A color bar shows the 50-dB range used for plotting the spectral density

$|t| < T_0$. In contrast, most of the energy appears in the outermost spectral peaks for a Gaussian pulse. The spectral range becomes larger for super-Gaussian pulses because the maximum chirp becomes larger as m increases. A triangular shape of the spectral evolution in Fig. 3.6 indicates that the SPM-induced spectral broadening increases linearly with distance.

An initial frequency chirp on the input pulse can also lead to drastic changes in the SPM-broadened pulse spectrum. This is illustrated in Fig. 3.7, which compares the spectral evolution of a Gaussian pulse for $C = -10$, 0, and 10 under conditions identical to those used in Fig. 3.6. It is evident that the sign of the chirp parameter C plays a critical role. For $C > 0$, spectral broadening increases, and the oscillatory structure becomes less pronounced. However, a negatively chirped pulse undergoes a spectral narrowing phase before its spectrum begins to broaden and exhibit multiple peaks. This behavior can be understood from Eq. (3.23) by noting that the SPM-induced chirp is linear and positive (frequency increases with increasing time) over the central portion of a Gaussian pulse. Thus, it adds to the initial chirp for $C > 0$, resulting in a broader spectrum. In the case of $C < 0$, the two chirp contributions are of opposite signs (except near the pulse edges), and the pulse becomes less chirped. If we employ the approximation that $\phi_{\rm NL}(t) \approx \phi_{\max}(1 - t^2/T_0^2)$ near the pulse center for Gaussian pulses, the SPM-induced chirp is nearly canceled for $C = -2\phi_{\max}$. This relation provides a rough estimate of the distance at which which narrowest spectrum occurs for a given value of C.

3.3.3 Dispersive Nonlinear Regime

When the fiber length L is longer or comparable to both L_D and L_{NL}, dispersion and nonlinearity act together as the pulse propagates along the fiber. The interplay of the GVD and SPM effects can lead to a qualitatively different behavior compared with that expected from GVD or SPM alone. In the anomalous-GVD regime ($\beta_2 < 0$), the fiber can support solitons. Equation (3.9) is helpful in understanding pulse evolution in optical fibers when both the dispersive and nonlinear effects should be taken into account. It is a fundamental equation of nonlinear science and has been studied extensively in many different contexts. The β_3 term is often negligible in practice. The parameter β_2 can be positive or negative with values in the range 0.1–20 ps^2/km, depending on how close the pulse wavelength is to the ZDWL of the fiber. The nonlinear parameter γ is positive and has a value in the range of 1–10 W^{-1}/km for most silica fibers; its values can be increased to beyond 100 W^{-1}/km in narrow-core photonic crystal fibers; even values >1000 W^{-1}/km have been realized using non-silica glasses.

It is useful to normalize the distance as $\xi = z/L_D$ and write Eq. (3.9) in the form (assuming that the β_3 term is negligible)

$$\frac{\partial U}{\partial \xi} + \frac{is}{2}\frac{\partial^2 U}{\partial \tau^2} = N^2 e^{-\alpha z}|U|^2 U. \tag{3.24}$$

In the lossless case ($\alpha = 0$), Eq. (3.24) becomes the standard NLS equation. Its solutions depend on the nature of dispersion through $s = \pm 1$ and on the peak power of the input pulse through the parameter N. They also depend on the pulse shape. As an example, Fig. 3.8 shows the temporal and spectral evolution of an initially unchirped Gaussian-shape pulse launched in the anomalous-GVD regime ($s = -1$) with a peak power such that $N = 1$. The pulse broadens slightly, and its spectrum narrows a bit, but neither the temporal nor the spectral width of the pulse changes much after a dispersion length. The pulse also appears to lose some energy in the form of dispersive waves that form a low-intensity pedestal around the pulse.

This behavior can be understood by noting that the NLS equations have exact solutions in the form of solitons in the case of anomalous GVD. For an initial pulse shape $U(0, \tau) = \mathrm{sech}(\tau)$ and integer values of the parameter N, the solitons follow a periodic evolution pattern with the period $\xi_0 = \pi/2$. The fundamental soliton corresponds to $N = 1$ and propagates without change in its shape. The only reason that the pulse shape and spectrum change in Fig. 3.8 is that the initial pulse shape is Gaussian and does not correspond to a soliton. Indeed, if we repeat the calculation with a "sech" pulse shape, we find that both the shape and spectrum do not change with z. From Eq. (3.11), the peak power necessary to excite the fundamental soliton is given by $P_1 = |\beta_2|/\gamma T_0^2$. For a hyperbolic secant pulse, the pulse width is related to T_0 by $T_p \approx 1.76 T_0$. This relation should be used for comparison with experiments. As a rough estimate, for 1.55 μm solitons to form in silica fibers, $P_1 \sim 1$ W when $T_p = 1$ ps. In the next two sections, we consider the

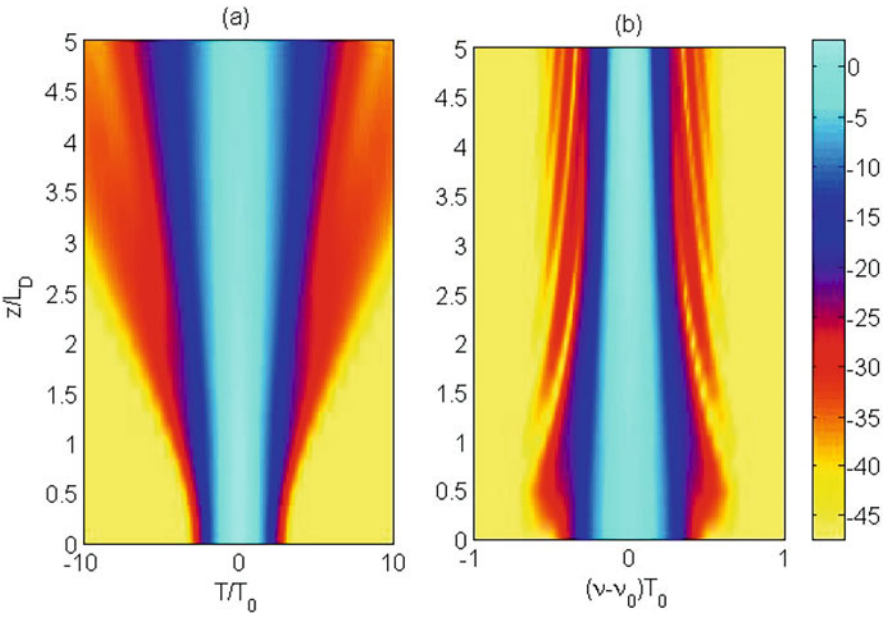

Fig. 3.8 Temporal and spectral evolution of an initially Gaussian-shape pulse launched in the anomalous-GVD region with a peak power such that $N = 1$. The color bar shows 50-dB range used for plotting the intensity

pulse propagation in the normal and anomalous GVD regimes by solving Eq. (3.24) numerically with the split-step Fourier method (Agrawal, 2019).

3.4 Normal Dispersion

In the normal-GVD region, the GVD parameter $\beta_2 > 0$ and $s = 1$ in Eq. (3.24). We set $\alpha = 0$ assuming that the fiber is short enough that losses are negligible. The parameter N can vary over a wide range depending on the widths and peak powers of input pulses. As an example, Fig. 3.9 shows the evolution of pulse shape and spectrum over one dispersion length for a sech-shape pulse launched with $N = 5$. Initially, the spectrum broadens because of SPM-induced chirping, while pulse shape remains almost unchanged. However, spectral broadening saturates at a distance of about $\xi = 0.3$, and beyond that the chirped pulse starts to broaden, and its shape changes drastically with a nearly flat central region.

An interesting phenomenon occurs for larger values of N. Figure 3.10 shows the evolution of an initially sech-shape pulse launched such that $N = 30$. As the pulse propagates, it broadens and develops a nearly rectangular profile with sharp leading and trailing edges. The combination of rapidly varying intensity and SPM in

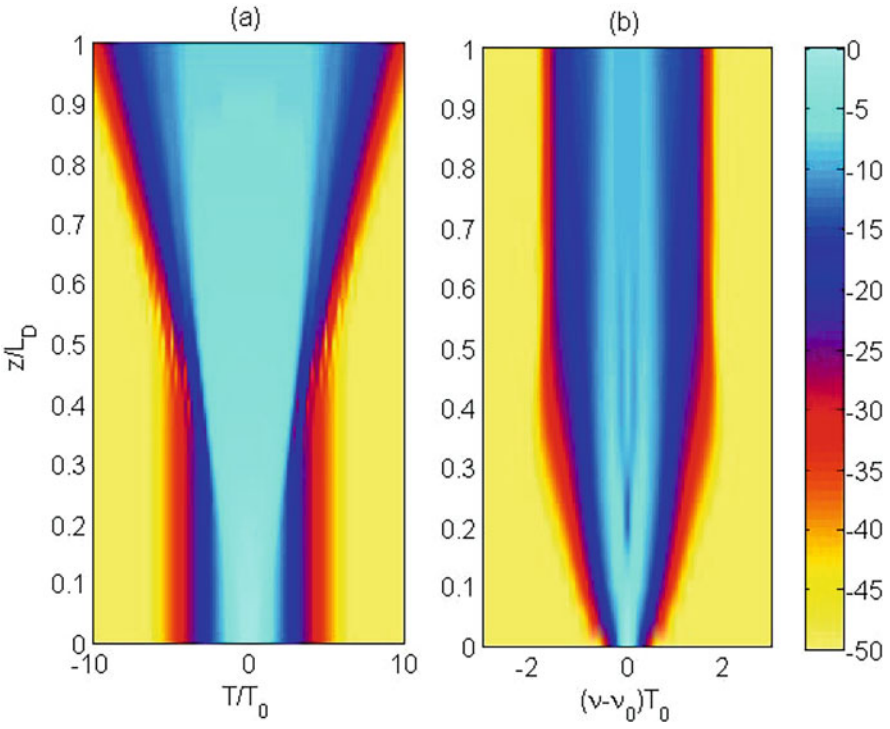

Fig. 3.9 Evolution of (**a**) pulse shape and (**b**) spectrum over one dispersion length in the normal-GVD region when a sech-shape pulse is launched with $N = 5$

these steep-slope regions broadens the pulse spectrum. Because the new frequency components are mainly generated near the edges, the pulse develops a nearly linear frequency chirp across its entire width. This linear chirp can be used to compress the pulse by passing it subsequently through a dispersive delay line such as a grating pair (Agrawal, 2020).

An interesting feature of Fig. 3.10 is the presence of rapid oscillations in the wings of the pulse. These can be more clearly in Fig. 3.11 where the pulse and spectrum are plotted at $\xi = 0.1$. In a 1985 paper, Tomlinson et al. (1985) interpreted such oscillations in terms of optical wave breaking, resulting from a mixing of the SPM-induced frequency-shifted components with the unshifted light in the wings. This phenomenon can also be understood as a FWM process. Indeed, one can clearly see two side bands in the pulse spectrum, as expected for a FWM process. The central structure in the spectrum is due to SPM (see Fig. 3.5). The results shown in Figs. 3.10 and 3.11 are for an initially unchirped pulse. If input pulses are chirped, they may follow a different evolution pattern than that shown in Fig. 3.10.

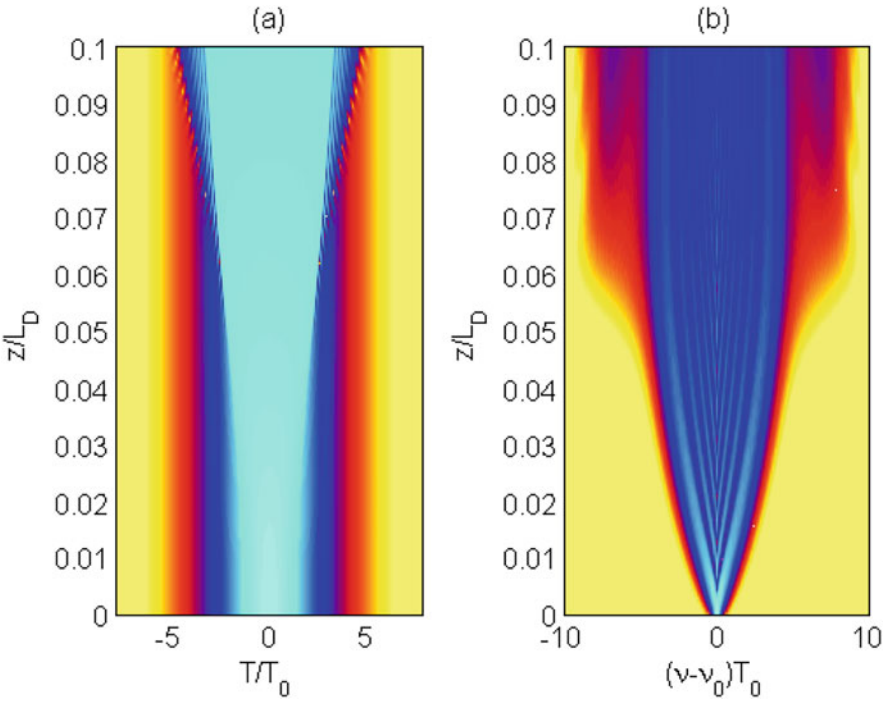

Fig. 3.10 Same as Fig. 3.9 except that the pulse is launched with $N = 30$. The color schemes are also identical in two figures

3.5 Anomalous Dispersion

In the anomalous-GVD regime, the GVD parameter $\beta_2 < 0$ and $s = -1$ in Eq. (3.24). For silica fibers, this is typically the situation in the spectral region near 1.55 μm that is of considerable interest for telecommunications. As mentioned earlier, a simple sign change leads to the formation of optical solitons. In particular, a sech-shape input pulse launched with $N = 1$ forms a fundamental soliton and propagates without any change in its shape. In the absence of fiber losses, the fundamental solitons can propagate undistorted for arbitrarily long distances (Hasegawa & Tappert, 1973). The soliton formation capacity of optical fibers has led to the development of the soliton laser (Mollenauer & Stolen, 1984). A piece of single-mode fiber inside the cavity was used to shape the intra-activity pulses, and the width of output pulses was controlled by adjusting the fiber length. Pulses as short as 50 fs have been generated directly from a soliton laser.

All higher-order solitons ($N > 1$) follow a periodic evolution pattern along the fiber with a period $z_0 = (\pi/2)L_D$. Figure 3.12 shows, as an example, the evolution pattern of the $N = 3$ soliton over one period, obtained by solving Eq. (3.24) with $U(0, \tau) = \text{sech}(t)$. The pulse initially narrows, develops a two-peak structure, and

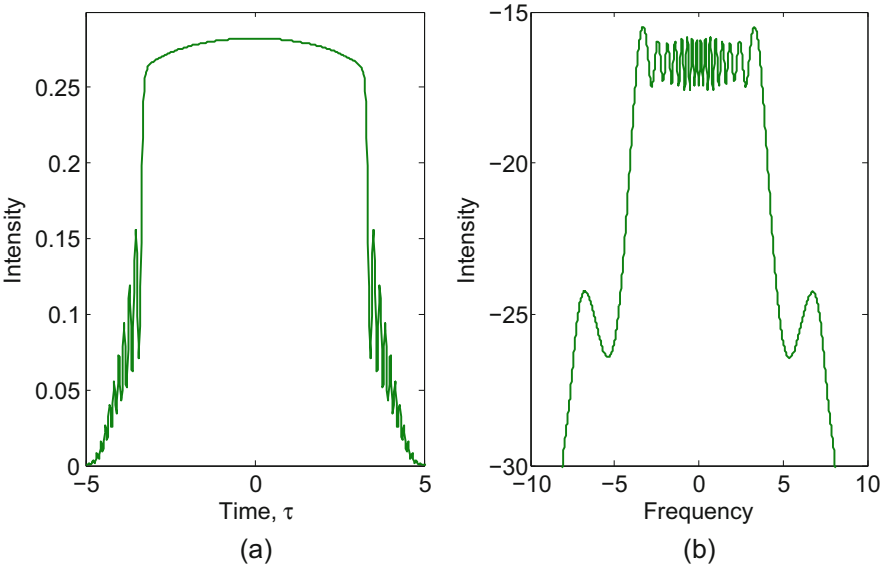

Fig. 3.11 (**a**) Pulse shape and (**b**) spectrum at $\xi = 0.1$ for $N = 30$. Two sidebands in the spectrum and temporal oscillations near the pulse edges are due to optical wave breaking

then reverses its propagation behavior beyond $z/L_D = \pi/4$ such that the original pulse is restored at $z/L_D = \pi/2$. Initial narrowing of the higher-order soliton can used to compress an optical pulse by suitably selecting its peak power and the fiber length (Agrawal, 2020).

3.5.1 Fission of High-Order Solitons

Equation (3.24) has proved to be very useful in understanding the propagation behavior in the anomalous-GVD regime of optical fibers. However, as discussed in Sect. 3.2, the NLS equation is not adequate for ultrashort pulses ($T_0 < 1$ ps), and its generalized version, Eq. (3.4), should be used in its place. It turns out that even the inclusion of third-order dispersion (TOD) affects the soliton dynamics considerably. As an example, Fig. 3.13 shows the evolution under conditions identical to those of Fig. 3.12 except that the TOD is included using $\delta_3 = \beta_3 L_D/6T_0^3 = 0.02$. The propagation distance was increased to $3L_D$ to identify all new features clearly. The TOD breaks up the third-order soliton into three fundamental solitons of different widths and peak powers, a phenomenon called soliton fission (Wai et al., 1986). A clear evidence of soliton fission is seen in the spectral evolution, where we see a sudden emergence of a new spectral peak at a distance of about $z = 0.4L_D$ on the high-frequency (blue) side of the pulse spectrum. This peak represents a dispersive

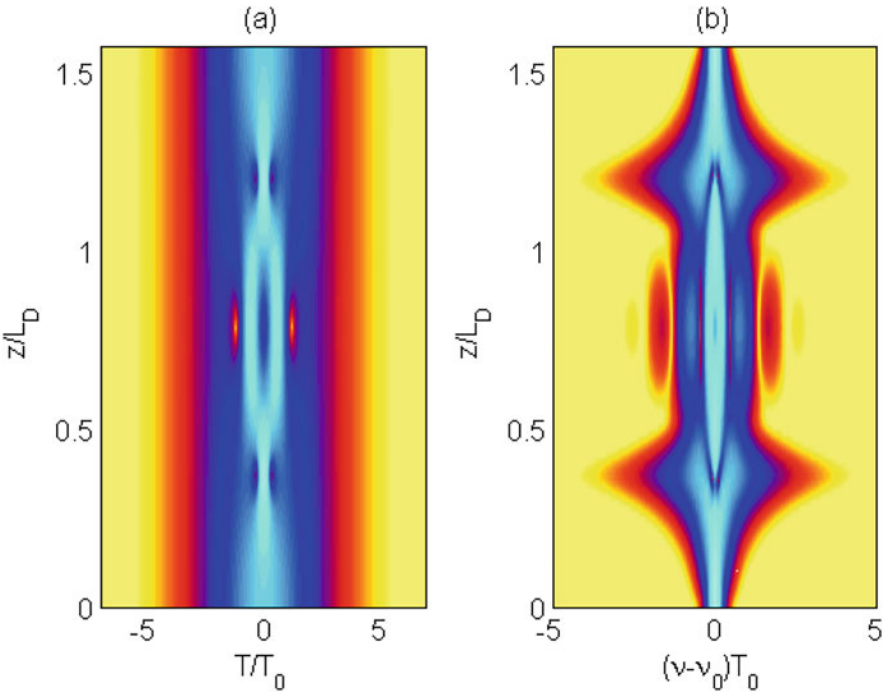

Fig. 3.12 Evolution of a third-order soliton from $\xi = 0$ to $\pi/2$; (**a**) pulse shape and (**b**) spectrum. The color bar is identical to that in Fig. 3.9

wave created after the fission through a Cherenkov-like phase-matching process (Akhmediev & Karlsson, 1995).

To understand the physics behind soliton fission, we need to realize that a high-order soliton, say of the order N, actually consists of N fundamental solitons that evolve, in the absence of TOD, as one entity in a periodic fashion because they move at the same speed inside the fiber. However, their speeds become slightly different when the TOD is not negligible. This feature destroys their periodic evolution, and individual fundamental solitons separate from each other as they travel inside the fiber. The inverse scattering method shows that the widths and peak powers of the individual fundamental solitons are related to the width T_0 and peak power P_0 of the input pulse as (Kodama & Hasegawa, 1987)

$$T_k = \frac{T_0}{2N+1-2k}, \qquad P_k = \frac{(2N+1-2k)^2}{N^2} P_0, \tag{3.25}$$

where k varies from 1 to N.

The TOD affects the dynamics of each fundamental soliton after the soliton fission because solitons can propagate unperturbed only in its absence. The TOD-induced perturbation forces each soliton to shed some energy in the form of a

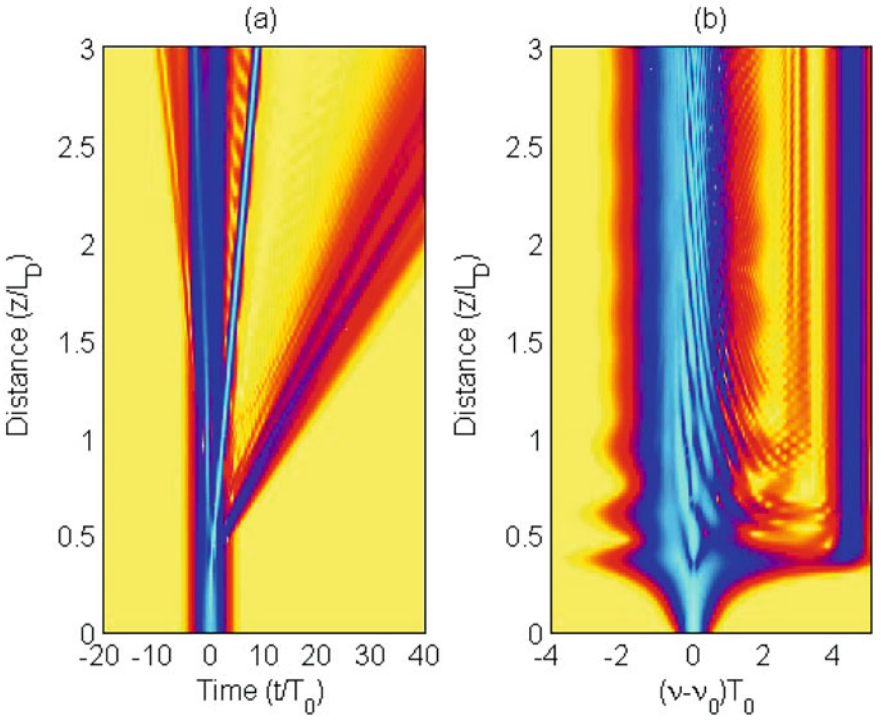

Fig. 3.13 Fission of a third-order soliton induced by TOD ($\delta_3 = 0.02$); (**a**) pulse shape (red tilted cone) and (**b**) spectrum (vertical blue line) show the signature of a blue-shifted dispersive wave. The color scheme is identical to that in Fig. 3.9

dispersive wave. Generation of dispersive waves through TOD attracted considerable attraction soon after this phenomenon was identified numerically (Wai et al., 1990; Gordon, 1992; Roy, 2009). Such radiation is also known as the Cherenkov radiation (Akhmediev & Karlsson, 1995). It is emitted at a frequency at which phase velocity of the dispersive wave matches that of the soliton. The frequency shift between the soliton and the dispersive wave is the temporal analog of the angle at which the Cherenkov radiation is emitted by charged particles in a bulk medium.

The frequency of the dispersive wave that grows because of radiation emitted by the perturbed soliton can be obtained by a simple phase-matching argument requiring that the dispersive wave at frequency ω propagates with the same phase velocity as that of the soliton at the frequency ω_s. The frequency shift $\Omega = \omega - \omega_s$ is found by the roots of a third-order polynomial (Akhmediev & Karlsson, 1995)

$$\beta_2 \Omega^2 + \frac{\beta_3}{3} \Omega^3 - \gamma P_s = 0, \tag{3.26}$$

where P_s is the peak power of the fundamental soliton formed after the fission process (and not that of the input pulse). Similarly, the dispersion parameters appearing in Eq. (3.26) are at the soliton central frequency ω_s. The only real solution of this polynomial is approximately given by

$$\Omega \approx -\frac{3\beta_2}{\beta_3} + \frac{\gamma P_s \beta_3}{3\beta_2^2}. \tag{3.27}$$

For solitons propagating in the anomalous-GVD region such that $\beta_2 < 0$ and $\beta_3 > 0$, the frequency shift of the dispersive wave is positive. As a result, the dispersive wave is emitted at a higher frequency (a blue shift) than that of the soliton. This was the case for the numerical results shown in Fig. 3.13. Indeed, the dispersive-wave frequency seen in this figure agrees well with the prediction of Eq. (3.27).

3.5.2 Intrapulse Raman Scattering

The Raman term appearing in Eq. (3.4) affects the fission process considerably through a phenomenon known as the soliton self-frequency shift. First observed in 1986, it manifests as a red shift of short optical pulses propagating as fundamental solitons (Mitschke & Mollenauer, 1986). Physically, the low-frequency components of the pulse are amplified from the Raman gain by the high-frequency components of the same pulse (Gordon, 1986). Since such an amplification is not restricted to solitons, the term Raman-induced frequency shift (RIFS) or intrapulse Raman scattering is also employed (Santhanam & Agrawal, 2003). Large values of the RIFS (>50 THz) were observed after 2000 with the advent of microstructured fibers (Liu et al., 2001).

In a 1987 experiment, 30-fs input pulses of different peak powers (resulting in different values of N) were launched into a 1-km-long fiber, and their spectra observed at its output end (Beaud et al., 1987). The fission process occurred at different distances within the fiber for different N values, but in all cases the spectrum of each fundamental soliton shifted toward longer wavelengths because of intrapulse Raman scattering, the shortest pulse exhibiting the largest shift. At the highest peak power of 530 W, three distinct spectral peaks appeared that corresponded to three fundamental solitons. The shortest soliton had a RIFS of nearly 200 nm.

For the sake of comparison, Fig. 3.14 shows the evolution of a third-order soliton under conditions identical to those of Fig. 3.13 except that, in addition to the TOD, intrapulse Raman scattering is also included by solving Eq. (3.4) numerically. In addition to the blue-shifted dispersive wave (appearing as a red cone on the left), one can see a considerable red shift of the shortest soliton that increases continuously with distance. In the time domain, this red shift leads to bending of the soliton trajectory because of a continuous slowing down of the red-shifted soliton owing to changes in its group velocity. It should be clear by now that the generalized

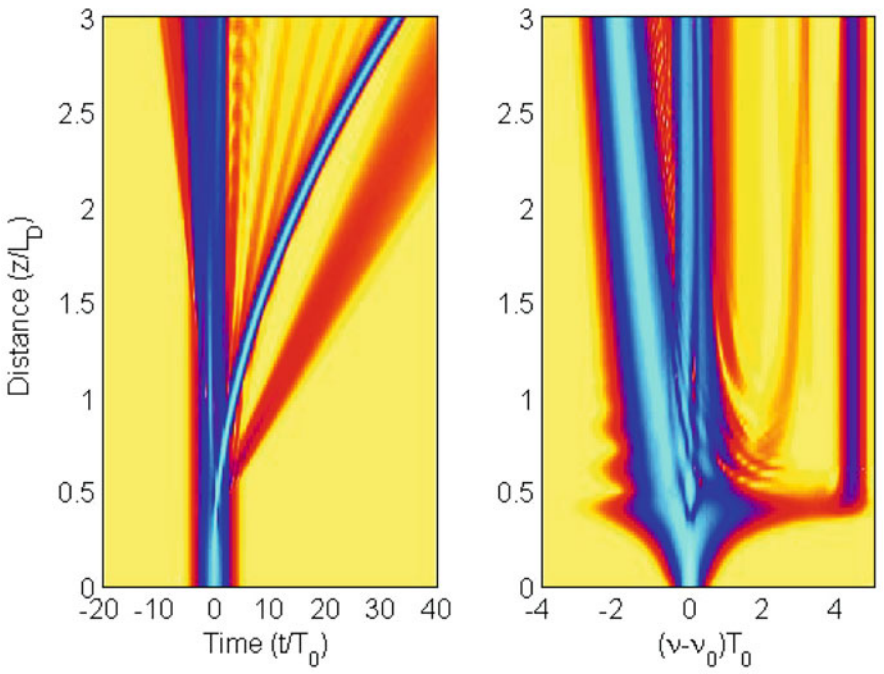

Fig. 3.14 Fission of a third-order soliton in the presence of TOD ($\delta_3 = 0.02$) and intrapulse Raman scattering. In addition to a blue-shifted dispersive wave, the shortest soliton slows down (light blue curve on the left). The color scheme is identical to that in Fig. 3.9

NLS equation, Eq. (3.4), should be used for a realistic description of the underlying physics when ultrashort pulses are propagated through optical fibers.

3.6 Supercontinuum Generation

As we saw in Sect. 3.5, when an optical pulse propagates through a nonlinear dispersive fiber, its temporal as well as spectral evolution is affected not only by a multitude of nonlinear effects but also by the dispersive properties of that fiber. It turns out that, for sufficiently intense pulses, the pulse spectrum becomes so broad that it often extends over a frequency range exceeding 50 THz. Such extreme spectral broadening is referred to as *supercontinuum generation*, a phenomenon first observed around 1970 in a glassy bulk nonlinear medium (Alfano & Shapiro, 1970a). In the context of optical fibers, a supercontinuum was first observed in 1976 using 10-ns pulses from a dye laser (Lin & Stolen, 1976). Although this topic attracted some attention during the decades of 1980s and 1990s, it was only after 2000, with the emergence of microstructured and photonic crystal fibers (PCFs), that

the use of optical fibers for supercontinuum generation became common (Dudley et al. 2006; Genty et al. 2007; Dudley & Taylor, 2010).

In a 2000 experiment, 100-fs pulses with 7-kW peak power at 790 nm were launched in the anomalous-GVD region of a microstructured fiber that was only 75 cm long (Ranka et al., 2000). Even for such a short fiber, the supercontinuum extended from 400 to 1600 nm; it was also relatively flat over the entire bandwidth (on a logarithmic power scale). Since then, similar features have been observed in many experiments using different types of fibers. In this section, we review the physical mechanisms behind the supercontinuum generation using optical fibers and discuss the progress realized since the year 2000.

3.6.1 Supercontinuum Generation Through Soliton Fission

The important question is what physical processes within an optical fiber are responsible for generating such a wide supercontinuum. The answer turned out to be the soliton fission in the case of femtosecond pulses. One can see a hint of this in Fig. 3.14 showing the evolution of a third-order soliton over three dispersion lengths. The pulse spectrum at $z = 3L_D$ has broadened considerably compared to its input shape and consists of multiple peaks. In addition to the central SPM-broadened structure and the leftmost dominant peak that corresponds to the shortest soliton created after the soliton fission, there is blue-shifted peak on the right belonging to a dispersive wave. Moreover, several other peaks have begun to appear as a result of XPM and FWM. The spectrum in Fig. 3.14 cannot yet be called a supercontinuum, but it is not difficult to imagine that a supercontinuum may form for solitons of much higher orders.

As an example, Fig. 3.15 shows the evolution of an eighth-order soliton ($N = 8$) over one dispersion length, obtained by solving Eq. (3.4) numerically in its following dimensionless form:

$$i\frac{\partial U}{\partial \xi} - \frac{s}{2}\frac{\partial^2 U}{\partial \tau^2} - is\delta_3\frac{\partial^3 U}{\partial \tau^3} + \delta_4\frac{\partial^4 U}{\partial \tau^4} = N^2\left(1 + if_s\frac{\partial}{\partial \tau}\right)\left(U(\xi,\tau)\int_0^\infty R(\tau')|U(\xi,\tau-\tau')|^2 d\tau'\right), \quad (3.28)$$

where $s = \pm 1$ and $f_s = (\omega_0 T_0)^{-1}$ is the self-steepening parameter. We have retained dispersion up to fourth order through

$$\delta_3 = \beta_3 L_D/(6T_0^3), \qquad \delta_4 = \beta_4 L_D/(24T_0^4). \quad (3.29)$$

In obtaining Fig. 3.15, we used $U(0,t) = \mathrm{sech}(t/T_0)$ with $T_0 = 50$ fs, neglected the self-steepening term by setting $f_s = 0$, and used the form of $h_R(t)$ suggested by Lin and Agrawal in a 2006 paper (Lin & Agrawal, 2006). The two dispersion

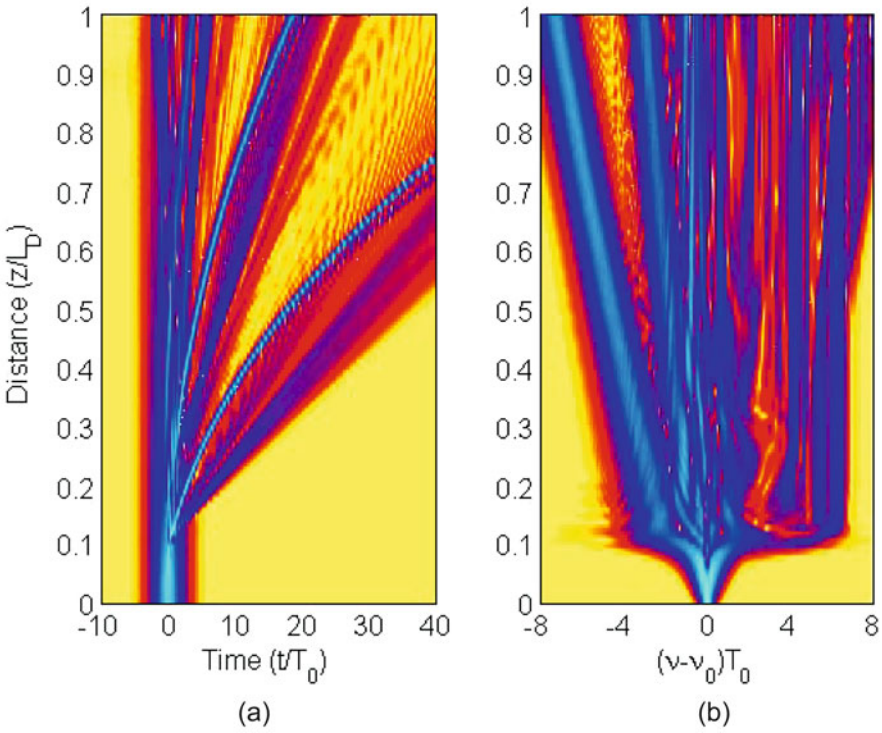

Fig. 3.15 Evolution of an $N = 8$ soliton from $\xi = 0$ to 1 using the parameter values given in the text; (**a**) pulse shape and (**b**) spectrum. The supercontinuum nature of the spectrum becomes apparent for such large values of N. The color scheme is identical to Fig. 3.9

parameters were chosen to be $\delta_3 = 0.02$ and $\delta_4 = 1 \times 10^{-4}$. It is clear from Fig. 3.15 that the pulse evolution becomes quite complex for an $N = 8$ soliton. In particular, the pulse spectrum begins to look like a supercontinuum that extends over a bandwidth that is more than 20 times larger compared to that of the input pulse.

To understand the role of self-steepening, Fig. 3.16 shows the pulse evolution under conditions identical to those used for Fig. 3.15 except that self-steepening is included assuming an input wavelength of 1550 nm; $f_s = 0.0163$ at this wavelength. Clearly, self-steepening affects both the temporal and spectral features. Although it reduces the total width of the supercontinuum, it also makes the supercontinuum more uniform compared to the one in Fig. 3.15. Figure 3.17 compares the input and output pulse spectra for the $N = 8$ soliton after one dispersion length.

Figure 3.16 shows how the pulse spectrum begins to broaden after the fission of an $N = 8$ soliton and how the pulse spreads rapidly in the time domain. However, it does not reveal which parts of the spectrum belong to which parts of the pulse. The mathematical tool for revealing this information is known as the short-time or

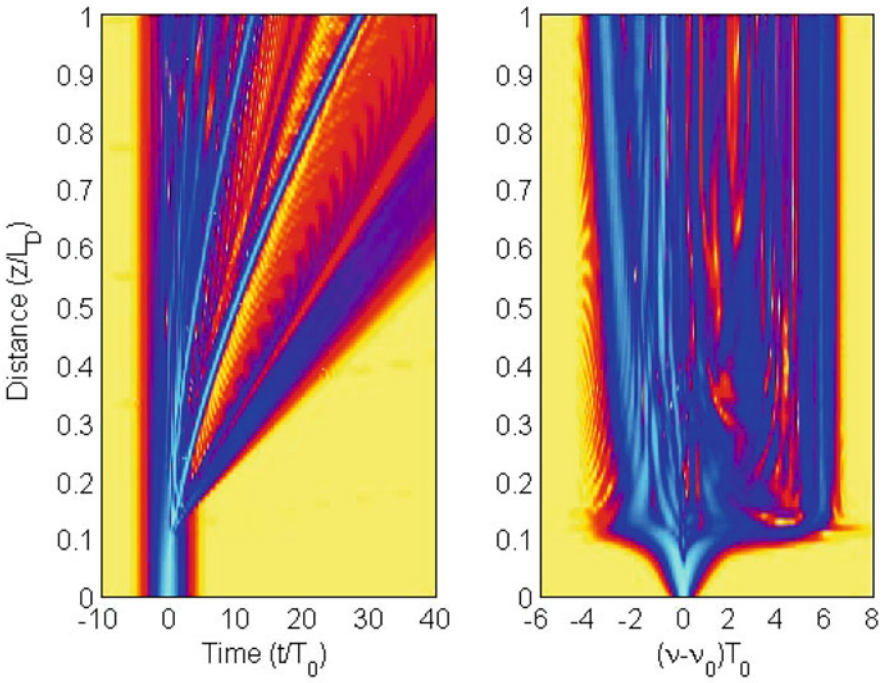

Fig. 3.16 Evolution of an $N = 8$ soliton from $\xi = 0$ to 1 under conditions identical to those used for Fig. 3.15 except that self-steepening is also included. The color scheme is identical to Fig. 3.9

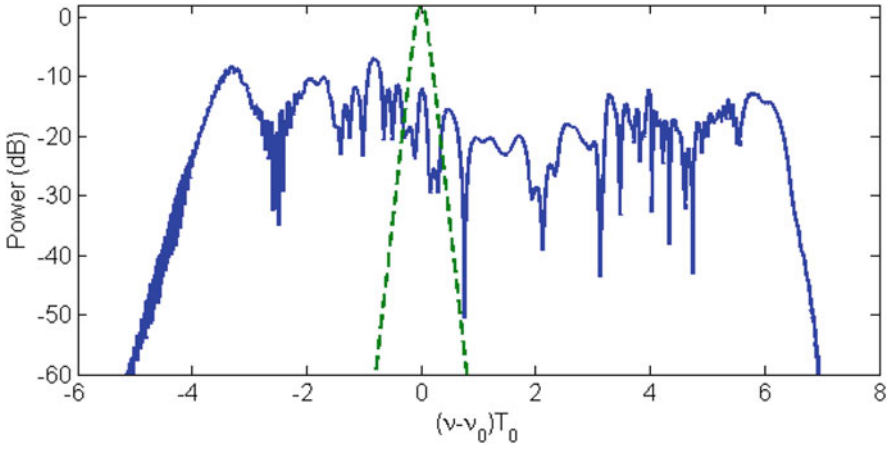

Fig. 3.17 Supercontinuum generated by launching an $N = 8$ soliton into a fiber of length $L = L_D$. The input spectrum is shown for comparison by a dashed green line

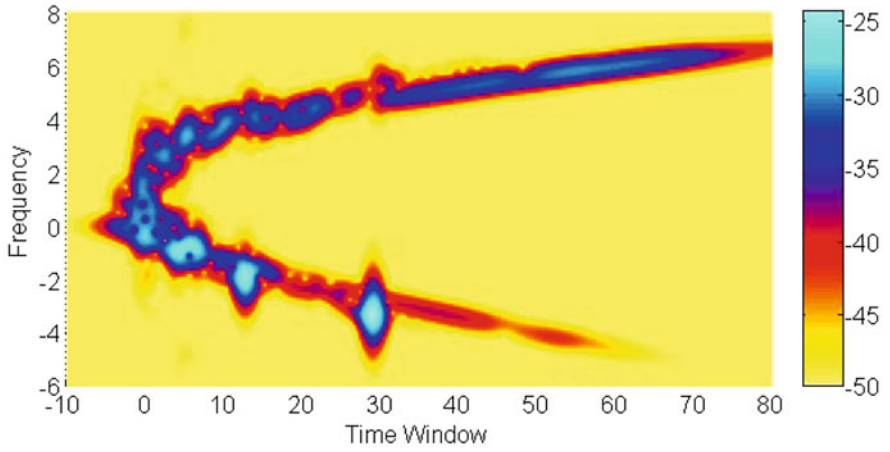

Fig. 3.18 Spectrogram generated numerically at a distance $L = L_D$ by launching an $N = 8$ soliton in a fiber with $L = L_D$. The input spectrum is also shown for comparison by a dashed line

windowed Fourier transform (WFT). In contrast with the optical spectrum, shown in Fig. 3.17 and obtained by taking the Fourier transform of $U(L, \tau)$ over the entire range of τ, the WFT employs a window function that selects $U(L, \tau)$ over a limited range of τ centered at a specific location T. Mathematically, the WFT is given by

$$S(T, \omega) = \left| \int_{-\infty}^{\infty} U(L, \tau) W(\tau - T) \exp(i\omega\tau)\, d\tau \right|^2, \tag{3.30}$$

where $W(\tau - T)$ is the window function centered at $\tau = T$. A Gaussian form is often used for the window function by choosing

$$W(\tau - T) = \frac{1}{\sqrt{2\pi}\sigma} \exp\left[-\frac{(\tau - T)^2}{2\sigma^2} \right], \tag{3.31}$$

where σ controls the window size. The WFT depends on both time and frequency and reveals which parts of the pulse contain which spectral contents. It is also called the spectrogram, a term borrowed from acoustics.

Figure 3.18 shows the spectrogram corresponding to the spectrum shown in Fig. 3.17 by choosing $\sigma = 1$. It shows the output at a distance of one dispersion length when an $N = 8$ soliton is launched into a fiber. The spectral features near $T = 0$ represent SPM-induced spectral broadening of the pulse before it undergoes soliton fission. Two bright spots near $T = 12$ and 28 represent two shortest solitons created after the fission. Their spectra are shifted toward the red side because of intrapulse Raman scattering, the shortest soliton undergoing the most red shift. The two blue-shifted cigar-like features extending over $T = 30$–75 belong to the dispersive waves created by these solitons. Depending on the dispersive properties

of the fiber, such dispersive waves are sometimes trapped by the red-shifted solitons through XPM if they happen to overlap in time.

Spectrograms can be constructed experimentally (Nishizawa & Goto, 2001) using an extension of the frequency resolved optical gating (FROG), a technique used commonly for measuring the width of ultrashort optical pulses (Trebino, 2002). It is referred to as the X-FROG technique, and it consists of performing cross-correlation of the output pulse with a narrow reference pulse whose peak can be shifted using an adjustable delay line. The two pulses overlap inside a nonlinear crystal that creates a signal through sum-frequency generation. Spectrogram is produced by recording a series of optical spectra at the crystal output with different delays between the two pulses.

3.6.2 Supercontinuum Generation Through Modulation Instability

The use of ultrashort optical pulses is not essential for supercontinuum generation. In a 2003 experiment, 42-ns pulses from a Q-switched Nd:YAG laser were launched into a 2-m-long microstructured fiber (with a random hole pattern) to produce a relatively wide supercontinuum at 10-kW peak-power levels (Town et al., 2003). Somewhat surprisingly, it turned out that even continuous-wave (CW) lasers can produce a supercontinuum at sufficiently high power levels. Indeed, CW lasers were used for this purpose as early as 2003, and, by now, such supercontinuum sources are being used for a variety of applications (Avdokhin et al., 2003; Nicholson et al., 2003; Abeeluck et al., 2004; Travers, 2010).

It should come as no surprise that the phenomenon of modulation instability is behind the CW or quasi-CW supercontinuum generation (Travers, 2010). It is well known that when a CW beam propagates in the anomalous-GVD region of an optical fiber, the phenomenon of modulation instability can create amplitude modulations that manifest spectrally as two sidebands at specific frequencies $\omega_0 \pm \Omega_{\max}$, where ω_0 is the frequency of the CW beam (Agrawal, 2019). The frequency shift $\Omega_{\max}$ depends on the input power P_0 and fiber's dispersion and nonlinear parameters as

$$\Omega_{\max} = \sqrt{\frac{2\gamma P_0}{|\beta_2|}}. \tag{3.32}$$

In the case of spontaneous modulation instability, the growth of these sidebands is initiated by intensity fluctuations within the CW beam. Their amplitudes grow initially with distance z exponentially. This growth manifests in the time domain as sinusoidal oscillations with the period $T_m = 2\pi/\Omega_{\max}$. The exponential growth continues as long as the fraction of the power in the two sidebands remains a small fraction of the total power (the so-called linear regime).

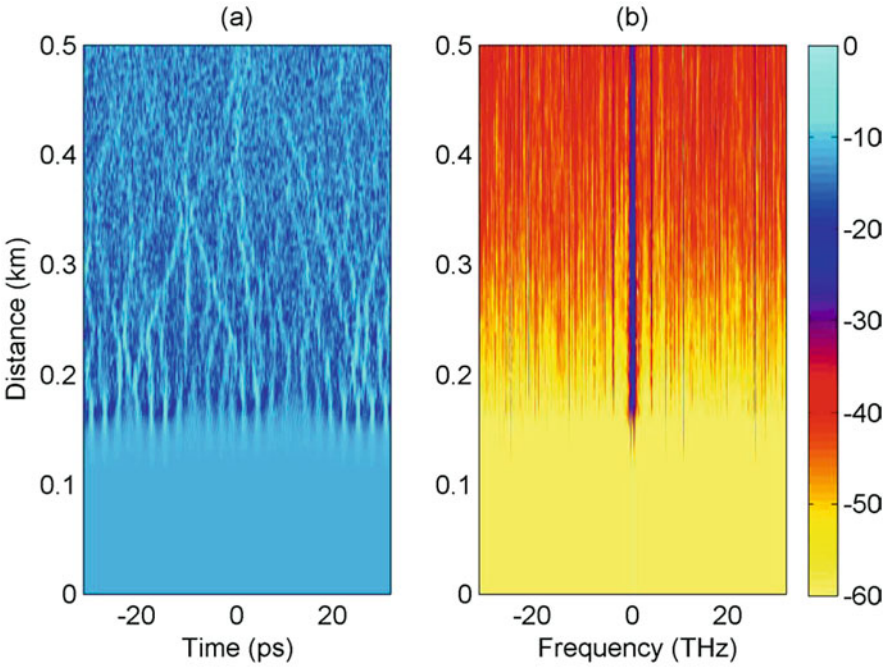

Fig. 3.19 Temporal and spectral evolutions of a noisy CW beam in the anomalous-GVD region of a fiber using parameter values given in the text

Once the modulation-instability process enters the nonlinear regime, evolution of the optical field can only be studied by solving the NLS equation (3.7) numerically with noise added to the input CW beam. Figure 3.19 shows, as an example, the temporal and spectral evolutions of a noisy CW beam assuming $\alpha = 0$, $\beta_2 = -20$ ps^2/km, and $L_{NL} = 10$ m. The TOD is included using $\beta_3 = 0.2$ ps^3/km, but intrapulse Raman scattering is not included in these simulations. The input spectrum is quite narrow in this case and nothing much happens until the onset of modulation instability begins to create spectral sidebands at a frequency predicted by Eq. (3.32), together with the corresponding temporal modulations on the CW beam. Both of these features are clearly apparent in Fig. 3.19 at a distance of about 150 m. With further propagation, temporal modulations become sharper and take the form of a train of short optical pulses of different widths and peak powers that propagate as fundamental solitons in the anomalous-GVD regime of the fiber. The reason why solitons have different widths is related to the noisy nature of spontaneous modulation instability. Indeed, when modulation instability is induced by launching a weak signal at the sideband frequency, all solitons within the pulse train are expected to have nearly the same width.

Even without the Raman effects, one can see supercontinuum formation as more and more spectral sidebands are created through FWM. In the presence of intrapulse

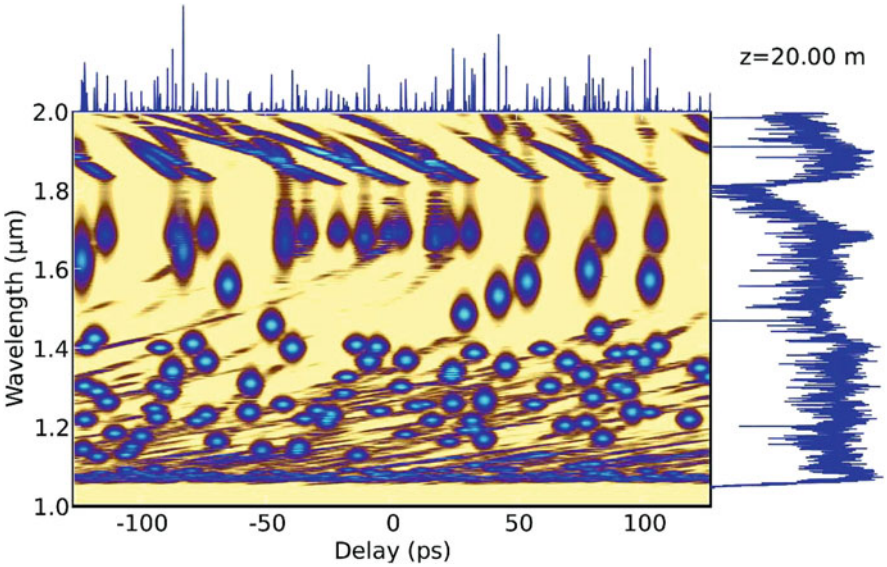

Fig. 3.20 X-FROG spectrogram calculated numerically when a CW beam with 44 W power is launched inside a 20-m-long PCF at a wavelength of 10570 nm. The output pulse train and spectrum are shown on the top and the right side, respectively (After Cumberland et al. (2008); ©2008 OSA.)

Raman scattering, the formation of a supercontinuum proceeds as follows. First, modulation instability converts the CW beam into a train of pulses of different widths and peak powers that propagate as fundamental solitons. Since the RIFS depends on the pulse width, different solitons shift their spectra by different amounts toward longer wavelengths. At the same time, blue-shifted radiation is generated in the form of dispersive waves because of perturbations of these solitons by third-order dispersion. As a soliton shifts its spectrum, it also slows down as long as it experiences anomalous GVD. As a result, solitons collide (overlap temporally) with neighboring solitons and dispersive waves and interact with them though XPM and FWM. It turns out that such a collision can transfer energy to the slowing soliton, which reduces its width further (to maintain the condition $N = 1$) and slows down even more, and its spectrum shifts even further toward longer wavelengths. Multiple soliton collisions eventually produce a supercontinuum that is extended mostly toward the red side of the input wavelength.

Figure 3.20 shows the numerically computed WFT spectrogram of a supercontinuum with parameters corresponding to a 2008 experiment in which a CW beam with 44 W power was launched inside a 20-m-long PCF ($\gamma = 43$ W^{-1}/km) at a wavelength of 1057 nm (Cumberland et al., 2008). The PCF exhibited two ZDWLs located near 810 and 1730 nm. As a result, dispersion was relatively large (65 ps/km/nm) at the pump wavelength of 1070 nm, but it decreased for longer wavelengths. One sees clearly the formation of solitons (round objects)

through modulation instability, together with their different spectral shifts and different speeds (leading to different delays). Collisions among these solitons are also apparent from their temporal overlap. Eventually, the spectrum of a short soliton approaches the ZDWL near 1730 nm, where it stops shifting because of the radiation pressure induced by the corresponding dispersive waves (cigar-like objects) emitted at wavelengths longer than 1730 nm. The interaction (collision) of solitons with these dispersive waves generates new spectral components through FWM in the wavelength region near 1900 nm. The spectrogram in Fig. 3.20 shows both the calculated spectrum and noisy pulse train in the time domain.

It is clear from the preceding description that the noisy nature of the input CW beam plays a critical role since it seeds the process of modulation instability. Even a CW laser beam is only partially coherent because of its finite spectral width resulting from intrinsic phase fluctuations. Any numerical modeling must include such fluctuations. The nonlinear propagation of a partially coherent CW beam inside single-mode optical fibers was investigated in several studies, revealing the physics behind CW supercontinuum generation (Mussot et al. 2004; Vanholsbeeck et al. 2005; Kobtsev & Smirnov, 2005; Cumberland et al. 2008).

The two most important ingredients for generating a CW supercontinuum are a high-power laser and a highly nonlinear fiber so that the product $\gamma P_0 L$ exceeds 30, where P_0 is the CW power launched into a fiber of length L. This condition can be satisfied for a 100-m-long fiber with $\gamma = 100\ \mathrm{W}^{-1}/\mathrm{km}$ at a pump–power level of a few watts. Such power levels are readily available from modern, high-power, Yb-doped fiber lasers. In the original 2003 experiment, a 100-m-long holey fiber was employed, and a Yb-fiber laser was used for CW pumping at 1065 nm (Avdokhin et al., 2003). The resulting supercontinuum extended from 1050 to 1380 nm when 8.7 W of CW power was coupled into the fiber. In a 2004 experiment, highly nonlinear fibers of lengths $\sim$ 1 km were used for supercontinuum generation by launching a CW beam at 1486 nm (Abeeluck et al., 2004). The ZDWL of the fibers was below 1480 nm, resulting in the anomalous GVD at the pump wavelength. Output spectra extended from 1200 to >1800 nm when pump power was close to 4 W. The spectrum was highly asymmetric with much more power on the long-wavelength side. This asymmetry was due to intrapulse Raman scattering that selectively extended the spectrum toward the long-wavelength side. The PCF used in a 2008 experiment exhibited two ZDWLs located near 810 and 1730 nm (Cumberland et al., 2008). When 44 W of CW power was launched into this fiber, the supercontinuum extended from 1050 to 1680 nm. More importantly, the output power was close to 29 W, and the spectral power density exceeded 50 mW/nm up to 1400 nm. These features are useful for applications of such a supercontinuum source for biomedical imaging.

The formation of CW supercontinuum in the visible region has also attracted attention (Cumberland et al., 2008a; Kudlinski et al., 2009, 2010). This is not easy to do because the most practical source of CW radiation is a high-power Yb-fiber laser emitting light near 1060 nm. When such a laser is used with a suitable PCF having its ZDWL near 1000 nm, the observed supercontinuum rarely extends below 900 nm. In a 2006 experiment, a tapered PCF whose core diameter decreased

along its length was employed for this purpose together with a quasi-CW source (a Nd:YAG microchip laser) emitting nanosecond pulse (Kudlinski et al., 2006). The observed supercontinuum extended from 350 to 1750 nm with a high spectral density when the taper length exceeded 5 m. The extension of the supercontinuum into the visible region was possible because of a monotonically decreasing $|\beta_2(z)|$ that allowed the FWM phase-matching condition to be satisfied for progressively shorter idler wavelengths.

In a 2009 experiment, the use of a PCF whose core was both tapered and doped with GeO_2 created a CW supercontinuum that extended toward wavelengths as short as 450 nm (Kudlinski et al., 2009). In the case of a uniform-core PCF pumped at 1075 nm with 70 W of CW power, the supercontinuum extended on the visible side only up to 550 nm and contained no light in the blue region. However, when a uniform-core section of 50 m was followed with a 130-m-long PCF section whose outer diameter decreased from 135 to 85 μm, the supercontinuum extended from 470 to >1750 nm when pumped with 40 W of CW power and thus covered the entire visible region. These results clearly show that an ultrabroad supercontinuum covering both the visible and near-infrared regions can be produced with 1060-nm pumping provided the PCF is suitably designed.

3.6.3 Supercontinuum Pumping in the Normal-GVD Region

From a practical perspective, coherence properties of a supercontinuum are important when it is employed as a broadband source of light for medical, metrological, or other applications. When optical pulses propagate inside a single-mode fiber with a fixed spatial profile, the output is clearly spatially coherent. However, its temporal coherence is affected by fluctuations in the energy, width, and arrival time of individual input pulses. As a result, spectral phase is also likely to fluctuate from pulse to pulse across the bandwidth of the supercontinuum (Dudley et al., 2006). Indeed, coherence measurements show that the spectral coherence of a supercontinuum is limited in practice when the process of soliton fission or modulation instability initiates its buildup (Kobtsev & Smirnov, 2006; Türke et al. 2007; Genty et al. 2010).

The origin of coherence degradation in both cases is related to a noisy process that is very sensitive to small variations in the widths and peak powers associated with the input pulses. It follows that the supercontinuum coherence should improve dramatically if input pulses are launched in the normal-GVD regime of a fiber where solitons cannot form. Indeed, this feature was predicted as early as 2005 in a PCF exhibiting two ZDWLs that was tapered along its length to ensure that optical pulses always experienced normal dispersion (Falk et al., 2005). However, the resulting supercontinuum was not very broad, and its bandwidth was limited to below 400 nm. The problem was solved by 2011, and broadband supercontinua were generated with normal-GVD pumping by using PCFs whose dispersion was suitably tailored (Heidt et al., 2011a; Hooper et al., 2011a; Heidt et al., 2011b).

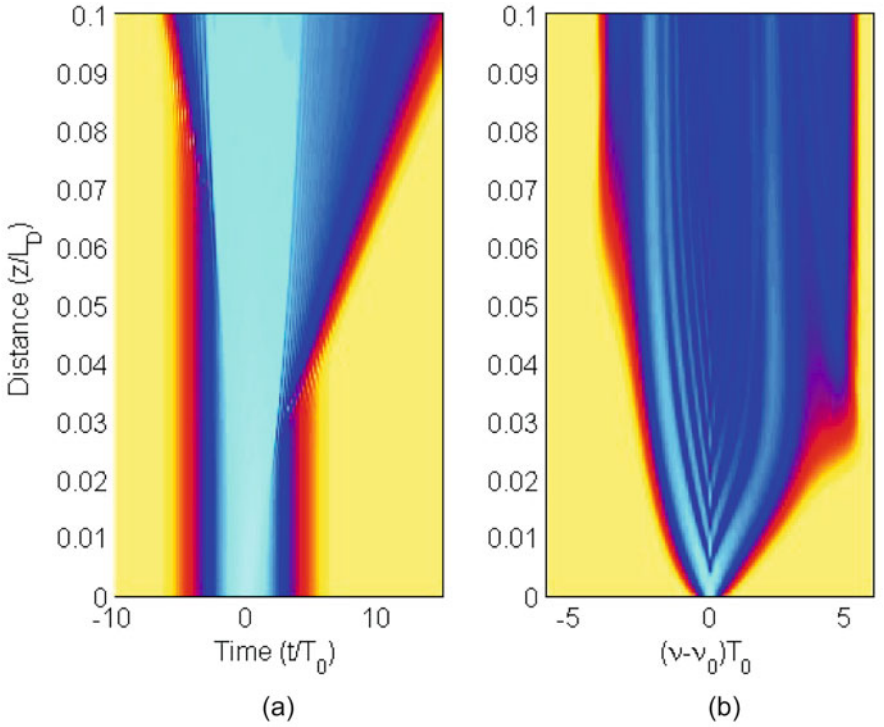

Fig. 3.21 Evolution of (**a**) pulse shape and (**b**) spectrum from $\xi = 0$ to 0.1 in the normal-GVD region when a sech-shape pulse is launched with $N = 30$

As an example, Fig. 3.21 shows the temporal and spectral evolutions of an intense sech-shape pulse launched in the normal-GVD region of a fiber with $N = 30$. The generalized NLS equation (3.4) was solved numerically with $s = 1$, $\delta_3 = 0$, and $\delta_4 = 0.001$ to ensure that the minimum dispersion occurs at the input wavelength of the pulse. It should be compared with Fig. 3.10, obtained for the same input pulse without including the higher-order nonlinear and dispersive effects. In both cases, the spectrum broadens mainly through the SPM but becomes asymmetric in the general case because of self-steepening and intrapulse Raman scattering. Two spectral sidebands are still generated because of optical wave breaking but their amplitudes are quite different. The supercontinuum formed at $z = 0.1L_D$ is relatively uniform over its entire bandwidth. Since soliton fission does not occur, it is also expected to be relatively coherent.

Experiments support the preceding numerical scenario. In a 2011 experiment, the PCF employed was designed such that it exhibited normal GVD over a wavelength region that extended from 400 to beyond 1500 nm (Heidt et al., 2011a). Figure 3.22a shows the broadband spectra observed at the output of a 50-cm-long PCF (fabricated with a 2.3 μm-diameter core) when it was pumped at 1050 nm with 50-fs pulses of

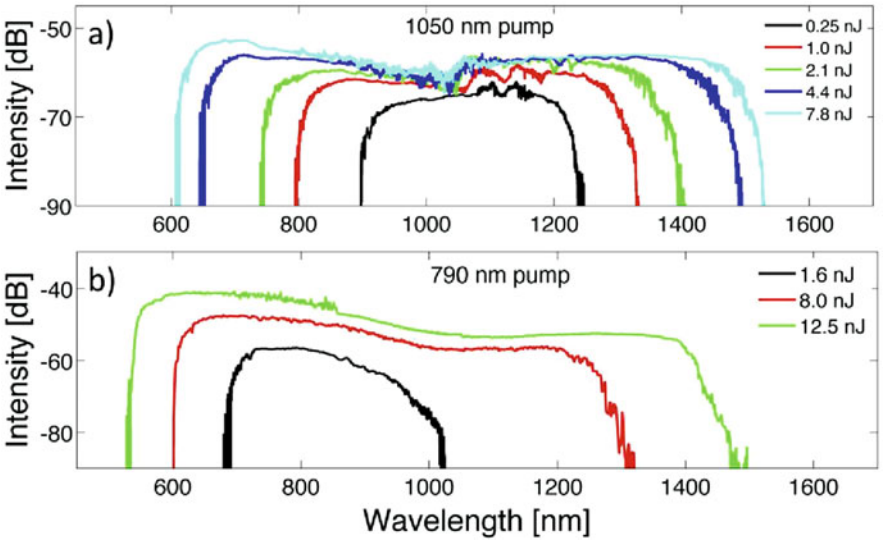

Fig. 3.22 (**a**) Optical spectra observed at the output of a 50-cm-long PCF when it was pumped at a wavelength of 1050 nm with 50-fs pulses of energies ranging from 0.25 to 7.8 nJ. (**b**) Output spectra when the same PCF was pumped at 790 nm (After Heidt et al. (2011a); ©2011 OSA.)

energies ranging from 0.25 to 7.8 nJ. Figure 3.22b shows the output spectra when the same PCF was pumped at 790 nm. In both cases, the supercontinua extend over an 800-nm bandwidth at the highest pulse energy and are relatively flat and smooth compared to those formed in the anomalous-GVD region.

A similar PCF design was used in another 2011 study (Hooper et al., 2011a). It exhibited normal dispersion over a wide wavelength region with a minimum occurring near 1064 nm, the wavelength at which 400-fs input pulses were launched. The output spectrum at the end of a 4-cm-long piece of such a fiber exhibited a shape that is typical of SPM (see Fig. 3.23). When fiber was 1 m long, the supercontinuum extended over 800 nm, and its shape was relatively flat and smooth. Moreover, the output was compressible to a duration of 26 fs and exhibited a high degree of coherence between its spectral components. The width of the compressed pulse was only 5 fs in another experiment (Heidt et al., 2011b) in which octave-spanning spectra were generated by launching 15-fs pulses with 1.7 nJ energy into a fiber that was only 1.7 mm long. Such a coherent supercontinuum is useful for a variety of applications including biomedical imaging. Chapter 6 by Heidt et al. describes in detail supercontinuum generation in the normal-GVD region of an optical fiber.

3.7 Mid-Infrared and Ultraviolet Regions

The experimental results seen in Fig. 3.22 clearly show that the nonlinear effects inside optical fibers can provide a coherent, wideband source of radiation covering the visible and near-infrared regions. An important question is whether a supercontinuum can be extended into the ultraviolet (UV) and mid-infrared (mid-IR) regions because such sources are useful for many practical applications. In this section, we focus first on the mid-IR region and then consider generation of UV radiation.

3.7.1 Supercontinuum in the Mid-Infrared Region

As early as 2000, experiments showed that the supercontinuum extended into the near-IR region up to 1600 nm when a PCF was pumped with short optical pulses at a wavelength near 800 nm (Ranka et al., 2000). Wavelengths beyond 1600 nm could be produced by pumping silica fibers at a wavelength near 1550 nm, but high losses of such fibers in the mid-IR region limited the use of such fibers. A fiber made with lead-silicate glass was used in a 2006 experiment, and it was found that the supercontinuum extended beyond 3 μm, even for a fiber that was only 6 mm long (Omenetto et al., 2006).

As coherent sources in the mid-IR region (wavelength range 3–10 μm) have many applications, the use of nonlinear fibers for producing such radiation became an important area of research after the year 2005. In a 2006 experiment, the supercontinuum was extended to 4500 nm by combining a silica fiber (length ∼1 m) with a few-meter-long fluoride fiber (Xia et al., 2006). Longer wavelengths could not be produced in this experiment because of strong absorption exhibited by fluoride fibers at wavelengths beyond 4500 nm. An ultrabroad supercontinuum was realized in 2009 when a 2-cm-long fluoride fiber was pumped with 180-fs pulses at a wavelength of 1450 nm (Qin et al., 2009). Figure 3.23a shows the output spectrum observed for pulses with 50 MW peak power; its 10 dB bandwidth extends from 565 to 5240 nm. The spectra in the mid-IR region are compared in part (b) for two fibers of different lengths. As seen there, almost the same bandwidth is obtained for the shorter 0.9-cm-long fiber. The drop in power at wavelengths beyond 5 μm is due to high losses of fluoride fibers. In a 2020 experiment (Li et al., 2020), a 60-cm-long fluorotellurite fiber generated a supercontinuum extending from 0.93 to 3.95 μm with a total power of 22.7 W and a high conversion efficiency of 57%.

Starting in 2010, chalcogenide fibers were used to extend the supercontinuum into the mid-IR region (Hudson et al., 2011; Rudy et al., 2013; Yu et al., 2015; Cheng et al., 2016; Karim et al., 2015, 2018; Lemière et al., 2019; Jiao et al., 2019; Yuan et al., 2020). Such fibers have low losses for wavelengths beyond 10 μm and can be made to provide large values of the nonlinear parameter γ. In a 2011 experiment, an As_2S_3 fiber was tapered such that its effective mode area was $< 1\ \mu m^2$, resulting in $\gamma = 12,400\ W^{-1}/km$ at the pump wavelength of 1.55 μm. When 250-fs pulses

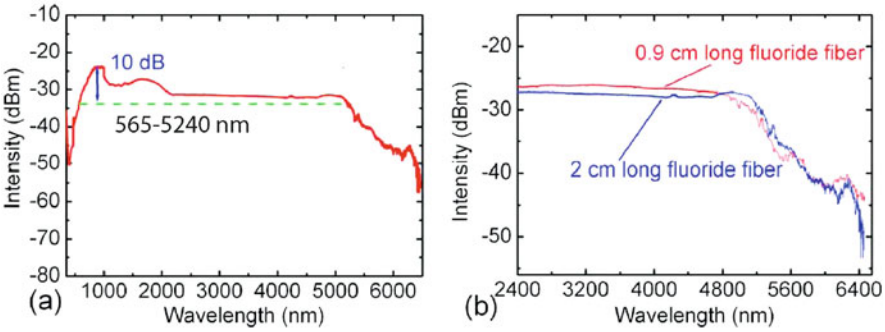

Fig. 3.23 (**a**) Supercontinuum observed at the output of a 2-cm-long fluoride fiber by pumping with 100-fs pulses with a peak power about 50 MW. Dashed line shows the 10-dB bandwidth. (**b**) Comparison of the mid-IR spectra for two fibers of different lengths (After Qin et al. (2009) ©2009 American Institute of Physics.)

were launched into such a 5-cm-long fiber, the supercontinuum extended from 0.97 to near 2 μm (Hudson et al., 2011). A later experiment employed a Tm-doped fiber laser operating at 2.04 μm to pump a 2.1-mm-long As_2S_3 fiber (Rudy et al., 2013). The resulting supercontinuum extended from 1 to 3.7 μm, clearly showing the potential of chalcogenide fibers for mid-IR generation.

This potential was realized in a 2015 experiment that pumped a 11-cm-long fiber with 330-fs pulses at a wavelength of 4.0 μm (Yu et al., 2015). The spectrum extended from 1.8 to 10 μm at the 40-mW average power, and this range was limited by fiber's losses. In a 2016 experiment, losses were reduced enough that the observed supercontinuum extended from 2 to 15 μm, when a 3-cm-long fiber was pumped with 170-fs pulses at a wavelength of 9.8 μm (Cheng et al., 2016). Figure 3.24 shows the measured and stimulated spectra for input pulses with 2.9 MW peak powers. A similar spectral range was realized by using chalcogenide fibers that avoided the use of toxic materials such as arsenic and antimony (Lemière et al., 2019). By 2020, a 16-cm-long microstructured chalcogenide fiber generated a coherent supercontinuum that extended from 2 to 13 μm, when pumped in the normal-GVD region of the fiber with 150-fs pulses at a wavelength of 5 μm (Yuan et al., 2020).

Dispersion engineering plays an important role for chalcogenide fibers used for mid-IR generation. In a 2015 study, three fibers with microstrucured air holes were analyzed for optimizing the fiber's design (Karim et al., 2015). Among these, equiangular spiral microstrucured fiber was found to be the most promising candidate for generating an ultrawide supercontinuum in the mid-IR region. In a later study, a triangular-core fiber was designed such that the predicted supercontinuum extended from 2.3 to 17 μm, when pumped with 100-fs pulses of 3-kW peak power at a wavelength of 4 μm (Karim et al., 2018).

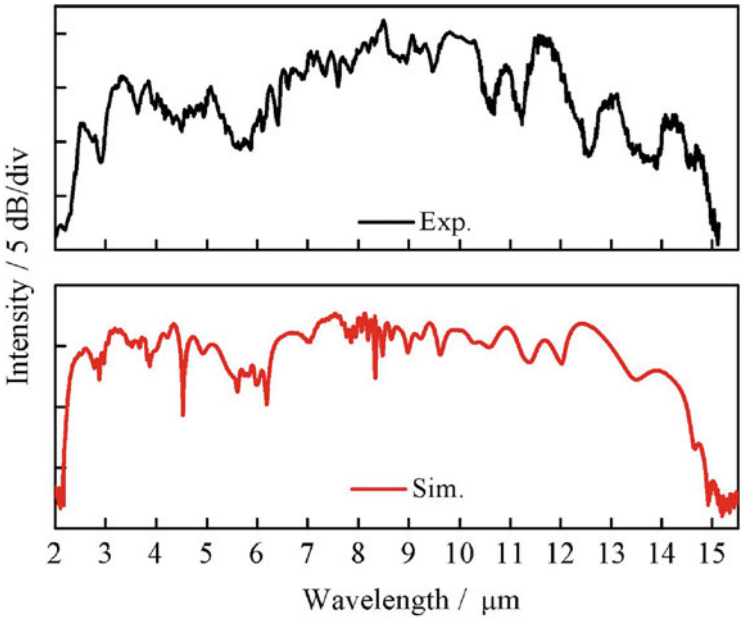

Fig. 3.24 Experimental (top) and simulated (bottom) supercontinuum at the output of a 3-cm-long chalcogenide fiber, pumped at 9.8 μm using 170-fs pulses with 2.9 MW peak power (After Cheng et al. (2016) ©2016 OSA.)

3.7.2 Sources of Ultraviolet Radiation

An important application of the supercontinuum process is to use it as a source of UV radiation. Extending supercontinuum into the UV region is not easy because optical fibers not only become lossy in this region, but their dispersive properties also become unsuitable. The ZDWL of standard silica fibers occurs at a wavelength near 1300 nm such that they provide anomalous GVD at longer wavelengths. The ZDWL can be moved closer to 800 nm by reducing the fiber's core diameter. In fact, the microstructured fiber used for the 2000 supercontinuum experiment (Ranka et al., 2000) had a core diameter close to 2 μm for this reason. For extension into the UV region, the ZDWL must be shifted below 400 nm.

In one approach, the core size of fibers is reduced to below 1 μm, resulting in the so-called nanofibers. As early as 2006, fibers with core diameters ranging from 0.2 to 1.2 μm were made (Gattass et al., 2006). They were used for extending the supercontinuum into the UV region by pumping the tapered fibers with femtosecond pulses at 800 nm. However, the UV radiation near 400 nm was observed only for the fiber with the 1.2-μm core diameter.

In a 2010 experiment, a 5-cm-long tapered PCF, having a core diameter of only 600 nm and exhibiting two ZDWLs at 509 and 640 nm, was employed for extending the supercontinuum into the UV region (Stark et al., 2010). The fiber was pumped

using femtosecond pulses (width <50 fs) whose peak powers could be as high as 4 kW. Input wavelength of 640 nm was near the second ZDWL of the fiber in this experiment. The soliton order N exceeded 200 at peak powers >3 kW. The observed supercontinuum covered the entire visible region and extended into the UV region. It should be noted that the fiber's GVD was anomalous only from 509 to 640 nm, the region between the two ZDWLs. The UV band was formed owing to the dispersive waves emitted by solitons, and it extended as far as 350 nm when the peak power of pulses was close to 4 kW. When the fiber was pumped at 523 nm, the UV band extended from 300 to 470 nm and was intense enough to be useful for practical applications.

It is clear that pumping a fiber at shorter wavelengths will help in producing the UV radiation. An extreme example of this approach was provided in an experiment in which a supercontinuum extending from 350 to 470 nm was produced by pumping a PCF with Q-switched pulses at 355 nm (Sylvestre et al., 2012). The PCF exhibited large normal GVD (β_2 nearly 2000 ps^2/km) and strong absorption in the UV region. It also supported several modes at the pump wavelength (core diameter close to 4 μm). Physical mechanisms behind supercontinuum generation were found to be cascaded SRS and intermodal FWM.

In another study, numerical simulations were used to show that nanofibers with core diameters < 1 μm can extend a supercontinuum into the UV region with pumping in the visible region (Hartung et al., 2012). The fibers were assumed to exhibit normal GVD in both the UV and visible regions. As discussed in Chap. 6, a coherent supercontinuum can be produced under such conditions, without making use of soliton fission or modulation instability. Indeed, the predicted spectra, for a fiber with 450-nm core diameter and pumped at 400 nm with 50-fs pulses, extended into the UV region near 220 nm at a peak power of 80 kW. A similar behavior occurs for suspended-core fibers.

In a different approach, hollow-core fibers are filled with a suitable gas before launching femtosecond pulses into them. In a 2013 study, a 10-cm-long, hollow-core, PCF was filled with different gases and pumped with 38-fs pulses at a wavelength of 805 nm (Mak et al., 2013). The output spectra depended considerably on pulse energy and gas pressure and extended into the UV region near 200 nm because of dispersive waves generated by the perturbed solitons. The same technique was used in a 2020 experiment where an anti-resonant hollow-core fiber was filled with argon gas and pumped with 30-fs pulses obtained from a fiber laser operating at 1030 nm. Figure 3.25 shows how the spectra of dispersive waves emitted in the UV region could be shifted over a range from 220 to 400 nm by varying the pressure of argon gas and the energy of pump pulses (Smith et al., 2020).

It has proved difficult to generate UV wavelengths shorter than 180 nm using gas-filled fibers. In a 2018 study, it was found numerically that wavelengths as short as 90 nm can be realized using a tapered, Ne-filled fiber (Habib et al., 2018). The fiber had a 12-cm-long uniform section that was followed by a 25-cm-long tapered section. It was pumped with 30-fs pulses at 800 nm with peak powers such that each pulse propagated as a fifth-order soliton ($N = 5$) inside the fiber. The higher-order soliton went through a compression phase in the uniform section (down to

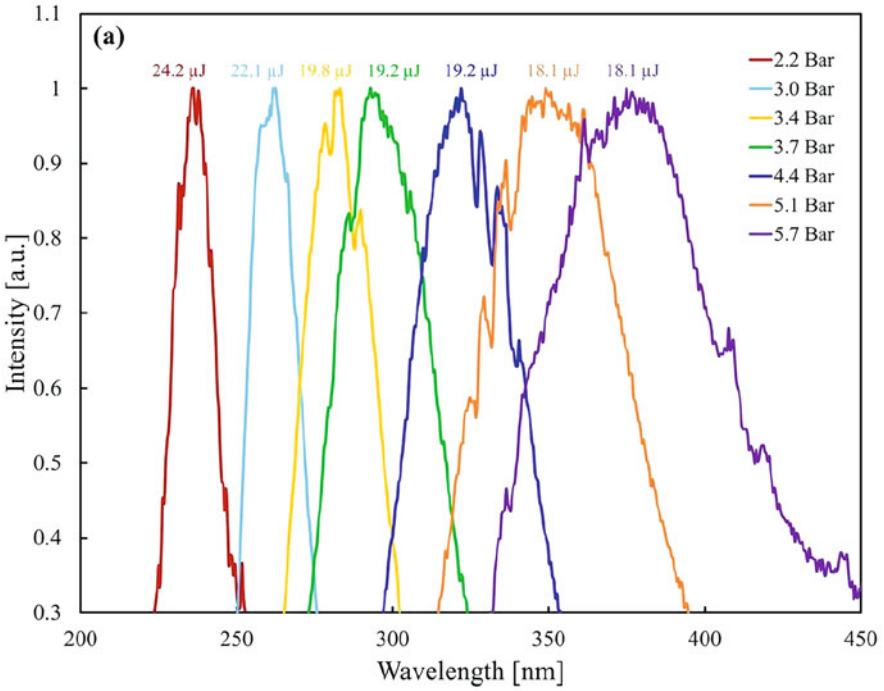

Fig. 3.25 Spectra of dispersive waves in the 220–400 nm range at different pressures of argon gas and energies of 30-fs pump pulses (at 1030 nm) from an argon-filled PCF (After Smith et al. (2020) ©2020 CC BY.)

$<$ 2 fs), which broadened its spectrum and increased its peak power so much that the neon gas was partially ionized. Fission of the compressed fifth-order soliton created multiple dispersive waves whose wavelengths were in the deep UV region. These results indicate that suitably designed, gas-filled fibers provide a practical route for generating the UV radiation.

One may wonder whether it is possible to extend the bandwidth of a supercontinuum so much that it extends from UV to IR regions. Considerable work has been done in recent years to realize such ultrawide spectra. In a 2015 experiment, a 15-cm-long, hollow-core PCF was filled with hydrogen gas. Figure 3.26 shows the ultrawide spectrum obtained when such a fiber was pumped at 805 nm using 30-fs pulses with 2.5-μJ energy (Belli et al., 2015). As seen there, the supercontinuum extended from 120 nm to $>$1000 nm with a relatively strong peak at 182 nm that could be attributed to a dispersive wave. Such a supercontinuum, extending over multiple octaves, is useful for a variety of applications.

It is possible to realize spectra that are even wider than the one in Fig. 3.26. The main issue is related to fiber's losses as it is hard to find a fiber exhibiting low losses over a very wide spectral range. In a 2015 study, a 4-cm-long, zirconium fluoride fiber (known as the ZBLAN fiber) was used because this glass exhibits relatively low

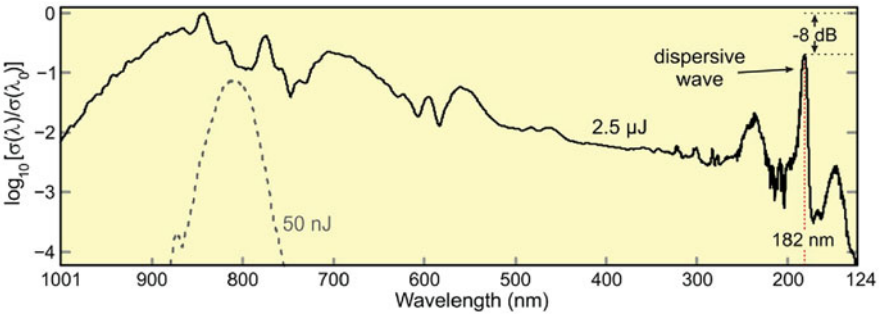

Fig. 3.26 Supercontinuum at the output of a 15-cm-long, H_2-filled, PCF pumped at 805 nm with 30-fs pulses of 2.5-μJ energy. Dashed curves show the low-energy spectrum for comparison (After Belli et al. (2015) ©2015 OSA.)

losses over a wavelength region extending from 0.2 to 6 μm (Jiang et al., 2015). The fiber was in the form of a PCF with a slightly elliptical core (average diameter 3 μm), and its ZDWL was near 1 μm. When it was pumped at a wavelength of 1.04 μm in the anomalous-GVD region with pulse energies of up to 1 nJ, the output spectrum extended from 0.2 to 2.5 μm. In a 2017 experiment, a gas-filled, hollow-core fiber was used containing a single ring of air holes in its cladding (Cassataro et al., 2017). This fiber structure was found to have relatively low losses (<5 dB/m) over a wide spectral range over which its GVD was also relatively flat. The 5-cm-long fiber was filled with the krypton gas at a pressure of 18 bar and pumped with 30-fs pulses of 10 μJ energy at a wavelength of 1.7 μm. Such a pulse formed a 13th-order soliton and produced a supercontinuum that extended from 270 nm to 3100 nm.

Even a wider supercontinuum was obtained in a 2019 experiment using a 30-cm-long, argon-filled, anti-resonant, hollow-core fiber (Adamu et al., 2019). It was realized by pumping the fiber at a wavelength near 2460 nm, where the fiber exhibited an anti-resonant transmission window. When 100-fs pulses with 8-μJ energies were launched into the fiber, the output was in the form of a supercontinuum that extended from 200 nm to 4000 nm. Moreover, the output was spectrally coherent over this entire range. Figure 3.27 shows both the measured ultrawide spectrum (top) and the degree of coherence (bottom). The numerically simulated spectrum is also shown for comparison. The physical mechanism behind the extreme spectral broadening is related to the soliton–plasma nonlinear dynamics that leads to efficient generation of dispersive wave (DW) in the deep UV region. This experiment clearly indicates that the nonlinear effects in suitably designed fibers can produce ultrabroad supercontinua, extending from deep UV to mid-IR regions, with a proper choice of the pump wavelength.

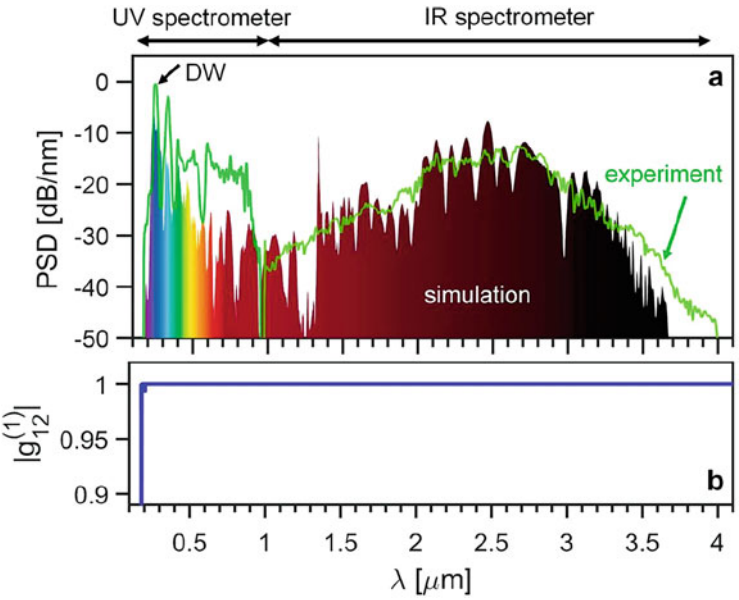

Fig. 3.27 Ultrawide supercontinuum extending from 200 to 4000 nm (top) from an argon-filled, hollow-core fiber pumped at 2460 nm with 100-fs pulses of 8-μJ energy. Simulated spectrum is also shown for comparison. The bottom curve shows measured degree of coherence (After Adamu et al. (2019) ©2019 CC BY.)

3.8 Summary

This chapter has reviewed the propagation characteristics of ultrashort optical pulses in single-mode fibers influenced by various dispersive and nonlinear effects. When pulse widths exceed a few picoseconds and only second-order dispersive effects dominate, the propagation behavior is modeled quite well by the NLS equation. New qualitative features arise depending on whether the propagation occurs in the normal or the anomalous dispersion regime. It is useful to introduce two length scales, L_D and $L_{\rm NL}$, referred to as the dispersion and nonlinear lengths, respectively. A dimensionless parameter defined as $N^2 = L_D/L_{\rm NL}$ plays a particularly important role. The nonlinear effects become important when N is close to or exceeds 1.

In the case of normal GVD, pulses broaden as they propagate and their shape becomes more rectangular. For $N > 10$, the pulse begins to exhibit optical wave breaking and develops a linear chirp across its entire width, a feature that is useful for compressing such pulses. In the case of anomalous GVD, the fiber supports optical solitons that are of fundamental interest and have also found important applications. In this case, the pulse preserves its shape and spectrum throughout its propagation when $N = 1$ and is referred to as the fundamental soliton. In contrast, the pulse evolves in a periodic fashion for other integer values of N.

Much more interesting effects occur for femtosecond pulses, for which one must include both the TOD of the fiber and the phenomenon of intrapulse Raman scattering. Mathematically, one must use a generalized version of the NLS equation. It shows that higher-order solitons undergo a fission process in which an Nth-order soliton is broken into N fundamental solitons of different widths and peak powers. At the same time, dispersive waves are generated through a Cherenkov-like process. For sufficiently large values of N, the onset of dispersive waves in combination with intrapulse Raman scattering, XPM, and FWM leads to the formation of a supercontinuum, whose spectral bandwidth can exceed 1000 nm under suitable conditions. Depending on the input wavelength of the optical pulses and the material used to make the fiber, a supercontinuum can be produced to cover the visible, near-IR, or the mid-IR spectral regions. With a proper choice of the pump wavelength, hollow-core fibers filled with gases can be used to obtain ultrawide supercontinua that extend from deep UV to mid-IR regions and are spectrally coherent over the entire wavelength range.

The use of optical fibers for supercontinuum generation has found a variety of applications, especially in the area of biomedical imaging. Indeed, fiber-based supercontinuum sources have been available commercially for more than a decade by now. Clearly, optical fibers provide an extremely versatile optical medium for studying nonlinear phenomena and for creating novel optical sources in different spectral regions. Such sources are already used and will continue to be used for a variety of applications in diverse areas of optics and photonics.

References

Abeeluck, A. K., Headley, C., & Jørgensen, C. G. (2004). High-power supercontinuum generation in highly nonlinear, dispersion-shifted fibers by use of a continuous-wave Raman fiber laser. *Optics Letters, 29*, 2163–2164.

Adamu, A. I., Habib, M. S., Petersen, C. R., Lopez, J. E. A., Zhou, B., Schülzgen, A., Bache, M., Amezcua-Correa, R., Bang, O., & Markos, C. (2019). Deep-UV to mid-IR supercontinuum generation driven by mid-IR ultrashort pulses in a gas-filled hollow-core fiber. *Scientific Reports, 9*, 4446.

Agrawal, G. P. (2019). *Nonlinear fiber optics* (6th ed.) New York: Academic.

Agrawal, G. P. (2020). *Applications of nonlinear fiber optics* (3rd ed.). New York: Academic.

Alfano, R. R., & Shapiro, S. L. (1970a). Emission in the region 4000 to 7000 Åvia four-photon coupling in glass. *Physical Review Letters, 24*, 584–587.

Alfano, R. R., & Shapiro, S. L. (1970b). Observation of self-phase modulation and small scale filaments in crystals and glasses. *Physical Review Letters, 24*, 592–594.

Alfano, R. R., & Shapiro, S. L. (1970c). Direct distortion of electronic clouds of rare gas atoms in intense electric fields. *Physical Review Letters, 24*, 1217–1220.

Alfano, R. R., & Shapiro, S. L. (1971). Picosecond spectroscopy using the inverse Raman effect. *Chemical Physics Letters, 8*, 631–633.

Akhmediev, N., & Karlsson, M. (1995). Cherenkov radiation emitted by solitons in optical fibers. *Physical Review A, 51*, 2602–2607.

Avdokhin, A. V., Popov, S. V., & Taylor, J. R. (2003). Continuous-wave, high-power, Raman continuum generation in holey fibers. *Optics Letters, 28*, 1353–1355.

Beaud, P., Hodel, W., Zysset, B., & Weber, H. P. (1987). Ultrashort pulse propagation, pulse breakup, and fundamental soliton formation in a single-mode optical fiber. *IEEE Journal of Quantum Electronics, 23*, 1938–1946.

Belli, F., Abdolvand, A., Chang, W., Travers, J. C., & Russell, P. St. J. (2015). Vacuum-ultraviolet to infrared supercontinuum in hydrogen-filled photonic crystal fiber. *Optica, 2*, 292–300.

Cassataro, M., Novoa, D., Günendi, M. C., Edavalath, N. N., Frosz, M. H., Travers, J. C., Russell, P. St. J. (2017). Generation of broadband mid-IR and UV light in gas-filled single-ring hollow-core PCF. *Optics Express, 25*, 7637–7644.

Cheng, T., Nagasaka, K., Tuan, T. H., Xue, X., Matsumoto, M., Tezuka, H., Suzuki, T., & Ohishi, Y. (2016). Mid-infrared supercontinuum generation spanning 2.0 to 15.1 μm in a chalcogenide step-index fiber. *Optics Letters, 41*, 2117–2120.

Cumberland, B. A., Travers, J. C., Popov, S. V., & Taylor, J. R. (2008). 29 W high power CW supercontinuum source. *Optics Express, 16*, 5954–5962.

Cumberland, B. A., Travers, J. C., Popov, S. V., & Taylor, J. R. (2008a). *Optics Letters, 33*, 2122.

J. M. Dudley & J. R. Taylor, (Eds.). (2010). *Supercontinuum generation in optical fibers* Cambridge: Cambridge University Press.

Dudley, J. M., Genty, G., & Coen, S. (2006). Supercontinuum generation in photonic crystal fiber. *Reviews of Modern Physics, 78*, 1135–1184.

Falk, P., Frosz, M. H., & Bang, O. (2005). Supercontinuum generation in a photonic crystal fiber with two zero-dispersion wavelengths tapered to normal dispersion at all wavelengths. *Optics Express, 13*, 7535–7540.

Fork, R. L., Brito Cruz, C. H., Becker, P. C., & Shank, C. V. (1987). Compression of optical pulses to six femtoseconds by using cubic phase compensation. *Optics Letters, 12*, 483–485.

Gattass, R. R., Svacha, G. T., Tong, L., & Mazur, E. (2006). Supercontinuum generation in submicrometer diameter silica fibers. *Optics Express, 14*, 9408–9414.

Genty, G., Coen, S., & Dudley, J. M. (2007). Fiber supercontinuum sources. *Journal of the Optical Society of America, 24*, 1771–1785.

Genty, G., Surakka, M., Turunen, J., & Friberg, A. T. (2010). Second-order coherence of supercontinuum light. *Optics Letters, 35*, 3057–3059.

Gordon, J. P. (1986). Theory of the soliton self-frequency shift. *Optics Letters, 11*, 662–664.

Gordon, J. P. (1992). Dispersive perturbations of solitons of the nonlinear Schrödinger equation. *Journal of the Optical Society of America B, 9*, 91–97.

Habib, M. S., Markos, C., Antonio-Lopez, J. E., Correa, R. A., Bang, O., & Bache, M. (2018). Multi-stage generation of extreme ultraviolet dispersive waves by tapering gas-filled hollow-core anti-resonant fibers. *Optics Express, 26*, 24357.

Hartung, A., Heidt, A. M., & Bartelt, H. (2012). Nanoscale all-normal dispersion optical fibers for coherent supercontinuum generation at ultraviolet wavelengths. *Optics Express, 20*, 13777–13788.

Hasegawa, A., & Tappert, F. (1973). Transmission of stationary nonlinear optical pulses in dispersive dielectric fibers: I. Anomalous dispersion. *Applied Physics Letters, 23*, 142–144.

Heidt, A. M., Hartung, A., Bosman, G. W., Krok, P., Rohwer, E. G., Schwoerer, H., & Bartelt, H. (2011a). Coherent octave spanning near-infrared and visible supercontinuum generation in all-normal dispersion photonic crystal fibers. *Optics Express, 19*, 3775–3787.

Heidt, A. M., Rothhardt, J., Hartung, A., Bartelt, H., Rohwer, E. G., Limpert, J., & Tünnermann, A. (2011b). High quality sub-two cycle pulses from compression of supercontinuum generated in all-normal dispersion photonic crystal fiber. *Optics Express, 19*, 13873–13879.

Hooper, L. E., Mosley, P. J., Muir, A. C., Wadsworth, W. J., & Knight, J. C. (2011a). Coherent supercontinuum generation in photonic crystal fiber with all-normal group velocity dispersion. *Optics Express, 19*, 4902–4907.

Hudson, D. D., Dekker, S. A., Mägi, E. C., Judge, A. C., Jackson, S. D., Li, E., Sanghera, J. S., Shaw, L. B., Aggarwal, I. D., & Eggleton, B. J. (2011). Octave spanning supercontinuum in an As_2S_3 taper using ultralow pump pulse energy. *Optics Letters, 36*, 1122.

Jiang, X., Joly, N. Y., Finger, M. A., Babic, F., Wong, G. K. L., Travers, J. C., & Russell, P. St. J. (2015). Deep-ultraviolet to mid-infrared supercontinuum generated in solid-core ZBLAN photonic crystal fibre. *Nature Photonics, 9*, 133.

Jiao, K., Yao, J., Zhao, Z., Wang, X., Si, N., Wang, X., Chen, P., Xue, Z., Tian, Y., Zhang, B., Zhang, P., Dai, S., Nie, Q., & Wang, R. (2019). Mid-infrared flattened supercontinuum generation in all-normal dispersion tellurium chalcogenide fiber. *Optics Express, 27*, 2036–2043.

Karim, M. R., Rahman, B. M. A., Azabi, Y. O., Agrawal, A., & Agrawal, G. P. (2015). Ultrabroadband mid-infrared supercontinuum generation through dispersion engineering of chalcogenide microstructured fibers. *Journal of the Optical Society of America B, 32*, 2343–2352.

Karim, M. R., Ahmad, H., & Rahman, B. M. A. (2018). Design and modeling of dispersion-engineered all-chalcogenide triangular-core fiber for mid-infrared-region supercontinuum generation. *Journal of the Optical Society of America B, 35*, 266–275.

Kobtsev, S. M., & Smirnov, S. V. (2005). Modelling of high-power supercontinuum generation in highly nonlinear, dispersion shifted fibers at CW pump. *Optics Express, 13*, 6912–8918.

Kobtsev, S. M., & Smirnov, S. V. (2006). Coherent properties of supercontinuum containing clearly defined solitons. *Optics Express, 14*, 3968–3980.

Kodama, Y., & Hasegawa, A. (1987). Nonlinear pulse propagation in a monomode dielectric guide. *IEEE Journal of Quantum Electronics, 23*, 510–524.

Kudlinski, A., George, A. K., Knight, J. C., Travers, J. C., Rulkov, A. B., Popov, S. V., & Taylor, J. R. (2006). Zero-dispersion wavelength decreasing photonic crystal fibers for ultraviolet-extended supercontinuum generation. *Optics Express, 14*, 5715–5722.

Kudlinski, A., Bouwmans, G., Vanvincq, O., Quiquempois, Y., Le Rouge, A., Bigot, L., Mélin, G., & Mussot, A. (2009). White-light CW-pumped supercontinuum generation in highly GeO_2-doped core photonic crystal fibers. *Optics Letters, 34*, 3631–3634.

Kudlinski, A., Barviau, B., Leray, A., Spriet, C., Héliot, L., & Mussot, A. (2010). Control of pulse-to-pulse fluctuations in visible supercontinuum. *Optics Express, 18*, 27445–27454.

Lemière, A., Désévédavy, F., Mathey, P., Froidevaux, P., Gadret, G., Jules, J.-C., Aquilina, C., Kibler, B., Béjot, P., Billard, F., Faucher, O., & Smektala, F. (2019). Mid-infrared supercontinuum generation from 2 to 14 μm in arsenic- and antimony-free chalcogenide glass fibers. *Journal of the Optical Society of America B, 36*, A183–A192.

Li, Z., Jia, Z., Yao, C., Zhao, Z., Li, N., Hu, M., Ohishi, Y., Qin, W., & Qin, G. (2020). 22.7 W mid-infrared supercontinuum generation in fluorotellurite fibers. *Optics Letters, 45*, 1882–1885.

Lin, Q., & Agrawal, G. P. (2006). Raman response function for silica fibers. *Optics Letters, 31*, 3086–3088.

Lin, C., & Stolen, R. H. (1976). New nanosecond continuum for excited-state spectroscopy. *Applied Physics Letters, 28*, 216–228.

Liu, X., Xu, C., Knox, W. H., Chandalia, J. K., Eggleton, B. J., Kosinski, S. G., & Windeler, R. S. (2001). Soliton self-frequency shift in a short tapered air–silica microstructure fiber. *Optics Letters, 26*, 358–360.

Mak, K. F., Travers, J. C., Hölzer, P., Joly, N. Y., & Russell, P. St. J. (2013). Tunable vacuum-UV to visible ultrafast pulse source based on gas-filled Kagome-PCF. *Optics Express, 21*, 10942–10953.

Maker, P. D., Terhune, R. W., & Savage, C. M. (1964). Intensity-dependent changes in the refractive index of liquids. *Physical Review Letters, 12*, 507–509 (1964).

Mitschke, F. M., & Mollenauer, L. F. (1986). Discovery of the soliton self-frequency shift. *Optics Letters, 11*, 659–661.

Mollenauer, L. F., & Stolen, R. H. (1984). The soliton laser. *Optics Letters, 9*, 13–15.

Mollenauer, L. F., Stolen, R. H., & Gordon, J. P. (1980). Experimental observation of picosecond pulse narrowing and solitons in optical fibers. *Physical Review Letters, 45*, 1095–1098.

Mussot, A., Lantz, E., Maillotte, H., Sylvestre, R., Finot, C., & Pitois, S. (2004). Spectral broadening of a partially coherent CW laser beam in single-mode optical fibers. *Optics Express, 12*, 2838–2843.

Nicholson, J. W., Abeeluck, A. K., Headley, C., Yan, M. F., & Jørgensen, C. G. (2003). Pulsed and continuous-wave supercontinuum generation in highly nonlinear, dispersion-shifted fibers. *Applied Physics B, 77*, 211–218.

Nishizawa, N., & Goto, T. (2001). Experimental analysis of ultrashort pulse propagation in optical fibers around zero-dispersion region using cross-correlation frequency resolved optical gating. *Optics Express, 8*, 328–334.

Omenetto, F. G., Wolchover, N. A., Wehner, M. R., Ross, M., Efimov, A., Taylor, A. J., Kumar, V. V. R. K., George, A. K., Knight, J. C., Joly, N. Y., & Russell, P. St. J. (2006). Spectrally smooth supercontinuum from 350 nm to 3 μm in sub-centimeter lengths of soft-glass photonic crystal fibers. *Optics Express, 14*, 4928–4934.

Qin, G., Yan, X., Kito, C., Liao, M., Chaudhari, C., Suzuki, T., & Ohishi, Y. (2009). Ultrabroadband supercontinuum generation from ultraviolet to 6.28 μm in a fluoride fiber. *Applied Physics Letters, 95*, 161103.

Ranka, J. K., Windeler, R. S., & Stentz, A. J. (2000). Visible continuum generation in air–silica microstructure optical fibers with anomalous dispersion at 800 nm. *Optics Letters, 25*, 25–27.

Roy, S., Bhadra, S. K., & Agrawal, G. P. (2009). Dispersive waves emitted by solitons perturbed by third-order dispersion inside optical fibers. *Physical Review A, 79*, 023824.

Rudy, C. W., Marandi, A., Vodopyanov, K. L., & Byer, R. L. (2013). Octave-spanning supercontinuum generation in in situ tapered As_2S_3 fiber pumped by a thulium-doped fiber laser. *Optics Letters, 38*, 2865–2868.

Santhanam, J., & Agrawal, G. P. (2003). Raman-induced spectral shifts in optical fibers: general theory based on the moment method. *Optics Communications, 222*, 413–420.

Smith, C. R., Moltke, A., Adamu, A. I., Michieletto, M., Bowen, P., Moselund, P. M., Markos, C., & Bang, O. (2020). Low-noise tunable deep-ultraviolet supercontinuum laser. *Scientific Reports, 10*, 18447.

Stark, S. P., Podlipensky, A., Joly, N. Y., & Russell, P. St. J. (2010). Ultraviolet-enhanced supercontinuum generation in tapered photonic crystal fiber. *Journal of the Optical Society of America B, 27*, 592–598.

Stolen, R. H. (2008). The early years of fiber nonlinear optics. *Journal of Lightwave Technology, 26*, 1021–1031.

Stolen, R. H., & Lin, C. (1978). Self-phase-modulation in silica optical fibers. *Physical Review A, 17*, 1448–1453.

Stolen, R. H., Gordon, J. P., Tomlinson, W. J., & Haus, H. A. (1989). Raman response function of silica-core fibers. *Journal of the Optical Society of America B, 6*, 1159–1166.

Sylvestre, T., Ragueh, A. R., Lee, M. W., Stiller, B., Fanjoux, G., Barviau, B., Mussot, A., & Kudlinski, A. (2012). Black-light continuum generation in a silica-core photonic crystal fiber. *Optics Letters, 37*, 130–132.

Tomlinson, W. J., Stolen, R. H., & Johnson, A. M. (1985). Optical wave breaking in nonlinear optical fibers. *Optics Letters, 10*, 457–459.

Town, G. E., Funaba, T., Ryan, T., & Lyytikainen, K. (2003). Optical supercontinuum generation from nanosecond pump pulses in an irregularly microstructured air-silica optical fiber. *Applied Physics B, 77*, 235–238.

Travers, J. C. (2010). Continuous wave supercontinuum generation. In J. M. Dudley & J. R. Taylor (Eds.) *Supercontinuum generation in optical fibers* (Chap. 8). Cambridge: Cambridge University Press.

Trebino, R. (2002). *Frequency-resolved optical gating: The measurement of ultrashort laser pulses*. New York: Springer.

Türke, D., Pricking, S., Husakou, A., Teipel, J., Herrmann, J., & Giessen, H. (2007). Coherence of subsequent supercontinuum pulses generated in tapered fibers in the femtosecond regime. *Optics Express, 15*, 2732–2741.

Vanholsbeeck, F., Martin-Lopez, S., González-Herráez, M., & Coen, S. (2005). The role of pump incoherence in continuous-wave supercontinuum generation. *Optics Express, 13*, 6615.

Wai, P. K. A., Menyuk, C. R., Lee, Y. C., & Chen, H. H. (1986). Nonlinear pulse propagation in the neighborhood of the zero-dispersion wavelength of monomode optical fibers. *Optics Letters, 11*, 464–488.

Wai, P. K. A., Chen, H. H., & Lee, Y. C. (1990). Radiations by solitons at the zero group-dispersion wavelength of single-mode optical fibers. *Physical Review A, 41*, 426–439.

Xia, C., Kumar, M., Kulkarni, O. P., Islam, M. N., Terry, F. L., Freeman, M. J., Poulain, M., & Mazé, G. (2006). Mid-infrared supercontinuum generation to 4.5 μm in ZBLAN fluoride fibers by nanosecond diode pumping. *Optics Letters, 31*, 2553–2556.

Yu, Y., Zhang, B., Gai, X., Zhai, C., Qi, S., Guo, W., Yang, Z., Wang, R., Choi, D.-Y., Madden, S., & Luther-Davies, B. (2015). 1.8–10 μm mid-infrared supercontinuum generated in a step-index chalcogenide fiber using low peak pump power. *Optics Letters, 40*, 1081–1084.

Yuan, Y., Yang, P., Peng, X., Cao, Z., Ding, S., Zhang, N., Liu, Z., Zhang, P.G., Wang, X., & Dai, S. (2020). Ultrabroadband and coherent mid-infrared supercontinuum generation in all-normal dispersion Te-based chalcogenide all-solid microstructured fiber. *Journal of the Optical Society of America B, 37*, 227–232.

Chapter 4
Cross-Phase Modulation: A New Technique for Controlling the Spectral, Temporal, and Spatial Properties of Ultrashort Pulses

P. L. Baldeck, P. P. Ho, and Robert R. Alfano

Abstract The chapter focus on self-phase modulation, cross-phase modulation (XPM)processes, white-light supercontinuum, modulation instability for SRS, SHG, and four-wave mixing properties of beams for different XPM applications for computation, defection, and coding of beams in communication for wide spectral from UV to THz.

Keywords Cross-phase modulation · Self-phase modulation · Continuum · Modulation instability · Normal dispersion · Group velocity · Pulse walk off · Optical fibers · THz · Polarization · Stimulated Raman scattering · 4 wave and · Second harmonic beams

4.1 Introduction

Self-phase modulation (SPM) is the principal mechanism responsible for the generation of picosecond and femtosecond white-light supercontinua. When an intense ultrashort pulse propagates through a medium, it distorts the atomic configuration of the material, which changes the refractive index. The pulse phase is time modulated, which causes the generation of new frequencies. This phase modulation

P. L. Baldeck (✉)
Laboratoire de chimie, UMR 5182, Ecole Normale Supérieure, CNRS, Lyon, France
e-mail: patrice.baldeck@ens-lyon.fr

P. P. Ho
Department of Electrical Engineering, The City College of the City University of New York, New York, USA
e-mail: pho@ccny.cuny.edu

R. R. Alfano
Department of Physics, The City College of the City University of New York, New York, USA
e-mail: ralfano@ccny.cuny.edu

R. R. Alfano (ed.), *The Supercontinuum Laser Source*,
https://doi.org/10.1007/978-3-031-06197-4_4

originates from the pulse itself (*self*-phase modulation). It can also be generated by a copropagating pulse (*cross*-phase modulation).

Several schemes of nonlinear interaction between optical pulses can lead to cross-phase modulation (XPM). For example, XPM is intrinsic to the generation processes of stimulated Raman scattering (SRS) pulses, second harmonic generation (SHG) pulses, and stimulated four-photon mixing (SFPM) pulses. More important, the XPM generated by pump pulses can be used to control, with femtosecond time response, the spectral, temporal, and spatial properties of ultrashort probe pulses.

Early studies on XPM characterized induced polarization effects (optical Kerr effect) Kimura et al. (1986), Kitayama et al. (1985b) and induced phase changes (Chraplyvy & Stone, 1984), but did not investigate spectral, temporal, and spatial effects on the properties of ultrashort pulses. In 1980, Gersten, Alfano, and Belic predicted that Raman spectra of ultrashort pulses would be broadened by XPM (Gersten et al., 1980). The first experimental observation of XPM spectral effects dates to early 1986, when it was reported that intense picosecond pulses could be used to enhance the spectral broadening of weaker pulses copropagating in bulk glasses (Alfano et al., 1986). Since then, several groups have been studying XPM effects generated by ultrashort pump pulses on copropagating Raman pulses (Schadt et al., 1986; Schadt & Jaskorzynska, 1987a; Islam et al., 1987a; Alfano et al., 1987b; Baldeck et al., 1987b, c, d; Manassah, 1987a, b; Hook et al., 1988), second harmonic pulses (Alfano et al., 1987a; Manassah, 1987c; Manassah and Cockings, 1987; Ho et al., 1988), stimulated four-photon mixing pulses (Baldeck & Alfano, 1987), and probe pulses (Manassah et al., 1985; Agrawal et al., 1989a; Baldeck et al., 1988a, c). Recently, it has been shown that XPM leads to the generation of modulation instability (Agrawal, 1987; Agrawal et al., 1989b; Schadt and Jaskorzynska, 1987b; Baldeck et al., 1988b, d; Gouveia-Neto et al., 1988a, b), solitary waves (Islam et al., 1987b; Trillo et al., 1988), and pulse compression (Jaskorzynska & Schadt, 1988; Manassah, 1988; Agrawal et al., 1988). Finally, XPM effects on ultrashort pulses have been proposed to tune the frequency of probe pulses (Baldeck et al., 1988a), to eliminate the soliton self-frequency shift effect (Schadt & Jaskorzynska, 1988), and to control the spatial distribution of light in large core optical fibers (Baldeck et al., 1987a).

This chapter reviews some of the key theoretical and experimental works that have predicted and described spectral, temporal, and spatial effects attributed to XPM. In Sect. 4.2, the basis of the XPM theory is outlined. The nonlinear polarizations, XPM phases, and spectral distributions of copropagating pulses are computed. The effects of pulse walk-off, input time delay, and group velocity dispersion broadening are particularly discussed. (Additional work on XPM and on SPM theories can be found in Manassah (Chap. 5) and Agrawal (Chap. 3).) Experimental evidence for spectral broadening enhancement, induced-frequency shift, and XPM-induced optical amplification is presented in Sect. 4.3. Sections 4.4, 4.5, and 4.6 consider the effects of XPM on Raman pulses, second harmonic pulses, and stimulated four-photon mixing pulses, respectively. Section 4.7 shows how induced focusing can be initiated by XPM in optical fibers. Section 4.8 presents measurements of modulation instability induced by cross-phase modulation in the

normal dispersion region of optical fibers. Section 4.9 describes XPM-based devices that could be developed for the optical processing of ultrashort pulses with terahertz repetition rates. Finally, Sect. 4.10 summarizes the chapter and highlights future trends.

4.2 Cross-Phase Modulation Theory

4.2.1 Coupled Nonlinear Equations of Copropagating Pulses

The methods of multiple scales and slowly varying amplitude (SVA) are the two independent approximations used to derive the coupled nonlinear equations of copropagating pulses. The multiple scale method, which has been used for the first theoretical study on induced-phase modulation, is described in Manassah (Chap. 5). The following derivation is based on the SVA approximation.

The optical electromagnetic field of two copropagating pulses must ultimately satisfy Maxwell's vector equation:

$$\nabla \times \nabla \times \mathbf{E} = -\mu_0 \frac{\partial \mathbf{D}}{\partial t} \tag{4.1a}$$

and

$$\mathbf{D} = \varepsilon\, \mathbf{E} + \mathbf{P}^{NL}, \tag{4.1b}$$

where ε is the medium permittivity at low intensity and $\mathbf{P}^{NL}$ is the nonlinear polarization vector.

Assuming a pulse duration much longer than the response time of the medium, an isotropic medium, the same linear polarization for the copropagating fields, and no frequency dependence for the nonlinear susceptibility $\chi^{(3)}$, the nonlinear polarization reduces to

$$P^{NL}(r, z, t) = \chi^{(3)} E^3(r, z, t), \tag{4.2}$$

where the transverse component of the total electric field can be approximated by

$$E(r, z, t) = \frac{1}{2}\left\{A_1(r, z, t)\, e^{i(\omega_1 t - \beta_1 z)} + A_2(r, z, t)\, e^{i(\omega_2 t - \beta_2 z)} + c.c.\right\}. \tag{4.3}$$

A_1 and A_2 refer to the envelopes of copropagating pulses of carrier frequencies ω_1 and ω_2, and β_1 and β_2 are the corresponding propagation constants, respectively.

Substituting Eq. (4.3) into Eq. (4.2) and keeping only the terms synchronized with ω_1 and ω_2, one obtains

$$P^{NL}(r, z, t) = P_1^{NL}(r, z, t) + P_2^{NL}(r, z, t), \tag{4.4a}$$

$$P_1^{NL}(r,z,t) = \frac{3}{8}\chi^{(3)}\left(|A_1|^2 + 2|A_2|^2\right)A_1 e^{i(w_1 t - \beta_1 z)}, \tag{4.4b}$$

$$P_2^{NL}(r,z,t) = \frac{3}{8}\chi^{(3)}\left(|A_2|^2 + 2|A_1|^2\right)A_2 e^{i(w_2 t - \beta_2 z)}, \tag{4.4c}$$

where P_1^{NL} and P_2^{NL} are the nonlinear polarizations at frequencies ω_1 and ω_2, respectively. The second terms in the right sides of Eqs. (4.4b) and (4.4c) are cross-phase modulations terms. Note the factor of 2.

Combining Eqs. (4.1a and 4.1b)–(4.4a, 4.4b and 4.4c) and using the slowly varying envelope approximation (at the first order for the nonlinearity), one obtains the coupled nonlinear wave equations:

$$\frac{\partial A_1}{\partial z} + \frac{1}{v_{g1}}\frac{\partial A_1}{\partial t} + \frac{i}{2}\beta_1^{(2)}\frac{\partial^2 A_1}{\partial t^2} = i\frac{\omega_1}{c}n_2\left[|A_1|^2 + 2|A_2|^2\right]A_1, \tag{4.5a}$$

$$\frac{\partial A_2}{\partial z} + \frac{1}{v_{g2}}\frac{\partial A_2}{\partial t} + \frac{i}{2}\beta_2^{(2)}\frac{\partial^2 A_2}{\partial t^2} = i\frac{\omega_2}{c}n_2\left[|A_2|^2 + 2|A_1|^2\right]A_2, \tag{4.5b}$$

where v_{gi} is the group velocity for the wave i, $\beta_i^{(2)}$ is the group velocity dispersion for the wave i, and $n_2 = 3\chi^{(3)}/8n$ is the nonlinear refractive index.

In the most general case, numerical methods are used to solve Eqs. (4.5a and 4.5b). However, they have analytical solutions when the group velocity dispersion temporal broadening can be neglected.

Denoting the amplitude and phase of the pulse envelope by a and α, that is,

$$A_1(\tau,z) = a_1(\tau,z)\,e^{i\alpha_1(\tau,z)} \quad \text{and} \quad A_2(\tau,z) = a_2(\tau,z)\,e^{i\alpha_2(\tau,z)}, \tag{4.6}$$

and assuming $\beta_1^{(2)} \approx \beta_2^{(2)} \approx 0$, Eqs. (4.5a) and (4.5b) reduce to

$$\frac{\partial a_1}{\partial z} = 0, \tag{4.7a}$$

$$\frac{\partial a_1}{\partial z} = i\frac{\omega_1}{c}n_2\left[a_1^2 + 2a_2^2\right], \tag{4.7b}$$

$$\frac{\partial a_2}{\partial z} + \left(\frac{1}{v_{g2}} - \frac{1}{v_{g1}}\right)\frac{\partial a_2}{\partial \tau} = 0, \tag{4.7c}$$

$$\frac{\partial \alpha_2}{\partial z} = i\frac{\omega_2}{c} n_2 \left[a_2^2 + 2a_1^2\right], \tag{4.7d}$$

where $\tau = (t - z/v_{g1})/T_0$ and T_0 is the $1/e$ pulse duration.

In addition, Gaussian pulses are chosen at $z = 0$:

$$A_1(\tau, z = 0) = \sqrt{\frac{P_1}{A_{\text{eff}}}}\ e^{-\tau^2/2}, \tag{4.8a}$$

$$A_2(\tau, z = 0) = \sqrt{\frac{P_2}{A_{\text{eff}}}}\ e^{-(\tau-\tau_d)^2/2}, \tag{4.8b}$$

where P is the pulse peak power, A_{eff} is the effective cross-sectional area, and $\tau_d = T_d/T_0$ is the normalized time delay between pulses at $z = 0$. With the initial conditions defined by Eqs. (4.8a and 4.8b), Eqs. (4.5a and 4.5b) have analytical solutions when temporal broadenings are neglected:

$$A_1(\tau, z) = \sqrt{\frac{P_1}{A_{\text{eff}}}} e^{-\tau^2/2} e^{i\alpha_1(t,z)}, \tag{4.9a}$$

$$A_2(\tau, z) = \sqrt{\frac{P_2}{A_{\text{eff}}}}\ e^{-(\tau-\tau_d-z/L_w)^2/2} e^{i\alpha_2(\tau,z)}, \tag{4.9b}$$

$$\begin{aligned}\alpha_1(\tau, z) = {} & \tfrac{\omega_1}{c} n_2 \tfrac{P_1}{A_{\text{eff}}} z e^{-\tau^2} \\ & + \sqrt{\pi}\tfrac{\omega_1}{c} n_2 \tfrac{P_2}{A_{\text{eff}}} L_w \left[\text{erf}(\tau - \tau_d) - \text{erf}\left(\tau - \tau_d - \tfrac{z}{L_w}\right)\right],\end{aligned} \tag{4.9c}$$

$$\begin{aligned}\alpha_2(\tau, z) = {} & \tfrac{\omega_2}{c} n_2 \tfrac{P_2}{A_{\text{eff}}} z e^{-(\tau-\tau_d-z/L_w)^2} \\ & + \sqrt{\pi}\tfrac{\omega_2}{c} n_2 \tfrac{P_1}{A_{\text{eff}}} L_w \left[\text{erf}(\tau) - \text{erf}\left(\tau - \tfrac{z}{L_w}\right)\right],\end{aligned} \tag{4.9d}$$

where $L_w = T_0/(1/v_{g\,1} - 1/v_{g\,2})$ is defined as the walk-off length.

Equations (4.9c) and (4.9d) show that the phases $\alpha_1(\tau, z)$ of copropagating pulses that overlap in a nonlinear Kerr medium are modified by a cross-phase modulation via the peak power $P_{j \neq i}$. In the case of ultrashort pulses, this cross-phase modulation gives rise to the generation of new frequencies, as does self-phase modulation.

The instantaneous XPM-induced frequency chirps are obtained by differentiating Eqs. (4.9c) and (4.9d) according to the instantaneous frequency formula $\Delta\omega = -\partial\alpha/\partial\tau$. These are

$$\Delta\omega_1(\tau, z) = 2\frac{\omega_1}{c}n_2\frac{P_1}{A_{\text{eff}}}\frac{z}{T_0}\tau e^{-\tau^2} 2\frac{\omega_1}{c}n_2\frac{P_2}{A_{\text{eff}}} \times \frac{L_w}{T_0}\left[e^{-(\tau-\tau_d-2/L_w)^2} - e^{-(\tau-\tau_d-z/L_w)^2}\right], \tag{4.10a}$$

$$\Delta\omega_2(\tau, z) = 2\frac{\omega_2}{c}n_2\frac{P_2}{A_{\text{eff}}}\frac{z}{T_0}(\tau - \tau_d - 2/L_w)\, e^{-(\tau-\tau_d-z/L_w)^2} + 2\frac{\omega_2}{c}n_2\frac{P_1}{A_{\text{eff}}}\frac{L_w}{T_0}\left[e^{-\tau^2} - e^{-(\tau-2/L_w)^2}\right], \tag{4.10b}$$

where $\Delta\omega_1 = \omega - \omega_1$ and $\Delta\omega_2 = \omega - \omega_2$. The first and second terms on the right sides of Eqs. (4.10a) and (4.10b) are contributions arising from SPM and XPM, respectively. It is interesting to notice in Eqs. (4.10a and 4.10b) than the maximum frequency chirp arising from XPM is inversely proportional to the group velocity mismatch $L_w/T_0 = 1/(1/v_{g1}-1/v_{g2})$ rather than the pump pulse time duration or distance traveled z as for ZPM. Therefore, the time duration of pump pulses does not have to be as short as the time duration of probe pulses for XPM applications.

More generally, spectral profiles affected by XPM can be studied by computing the Fourier transform:

$$S(\omega - \omega_0, z) = \frac{1}{2\pi}\int_{-\infty}^{+\infty} a(\tau, z)\, e^{i\alpha(\tau,z)} e^{i(\omega-\omega_0)\tau} d\tau, \tag{4.11}$$

where $|S(\omega - \omega_0, z)|^2$ represents the spectral intensity distribution of the pulse. Equation (4.10a and 4.10b) is readily evaluated numerically using fast Fourier transform algorithms.

Analytical results of Eqs. (4.9a, 4.9b, 4.9c, and 4.9d) take in account XPM, SPM, and group velocity mismatch. These results are used in Sect. 4.2.2 to isolate the specific spectral features arising from the nonlinear interaction of copropagating pulses. Higher-order effects due to group velocity dispersion broadening are discussed in Sect. 4.2.3.

4.2.2 Spectral Broadening Enhancement

The spectral evolution of ultrashort pulses interacting in a nonlinear Kerr medium is affected by the combined effects of XPM, SPM, and pulse walk-off.

For a negligible group velocity mismatch, XPM causes the pulse spectrum to broaden more than expected from SPM alone. The pulse phase of Eqs. (4.9c) and (4.9d) reduces to

$$\alpha_i(\tau, z) = \frac{\omega_i}{c} n_2 \frac{\left(P_i + 2P_j\right)}{A_{\text{eff}}} z e^{-\tau^2}. \tag{4.12}$$

The maximum spectral broadening of Gaussian pulses, computed using Eq. (4.12), is given by

$$\Delta\omega_i(z) \approx \frac{\omega_i}{c} n_2 \frac{\left(P_i + 2P_j\right)}{A_{\text{eff}}} \frac{z}{T_0}. \tag{4.13}$$

Thus, the spectral broadening enhancement arising from XPM is given by

$$\frac{\Delta\omega_{\text{iSPM+XPM}}}{\Delta\omega_{\text{iSPM}}} = 1 + \frac{2P_j}{P_i}. \tag{4.14}$$

Therefore, XPM can be used to control the spectral broadening of probe pulses using strong command pulses. This spectral control is important, for it is based on the electronic response of the interacting medium. It could be turned on and off in a few femtoseconds, which could lead to applications such as the pulse compression of weak probe pulses, frequency-based optical computation schemes, and the frequency multiplexing of ultrashort optical pulses with terahertz repetition rates.

The effect of pulse walk-off on XPM-induced spectral broadening can be neglected when wavelengths of pulses are in the low dispersion region of the nonlinear material, the wavelength difference, or/and the sample length are small, and the time duration of pulses is not too short. For other physical situations, the group velocity mismatch and initial time delay between pulses affect strongly the spectral shape of interacting pulses (Islam et al., 1987a; Manassah 1987a; Agrawal et al., 1988, 1989a; Baldeck et al., 1988a).

Figure 4.1 shows how the spectrum of a weak probe pulse can be affected by the XPM generated by a strong copropagating pulse. The wavelength of the pump pulse was chosen where the pump pulse travels faster than the probe pulse. Initial time delays between pulses at the entrance of the nonlinear medium were selected to display the most characteristic interaction schemes. Figure 4.1a, b are displayed for reference. They show the probe pulse spectrum without XPM interaction (Fig. 4.1a) and after the XPM interaction but for negligible group velocity mismatch (Fig. 4.1b). Figure 4.1c is for the case of no initial time delay and total walk-off. The probe spectrum is shifted and broadened by XPM. The anti-Stokes shift is characteristic of the probe and pump pulse walk-off. The probe pulse is blue shifted because it is modulated only by the back of the faster pump pulse. When the time delay is chosen such that the pump pulse enters the nonlinear medium after the probe and has just time to catch up with the probe pulse, one obtains a broadening similar to that in Fig. 4.1c but with a reverse Stokes shift (Fig. 4.1d). The XPM broadening becomes symmetrical when the input time delay allows the pump pulse not only to catch up with but also to pass partially through the probe pulse (Fig. 4.1e). However, if the

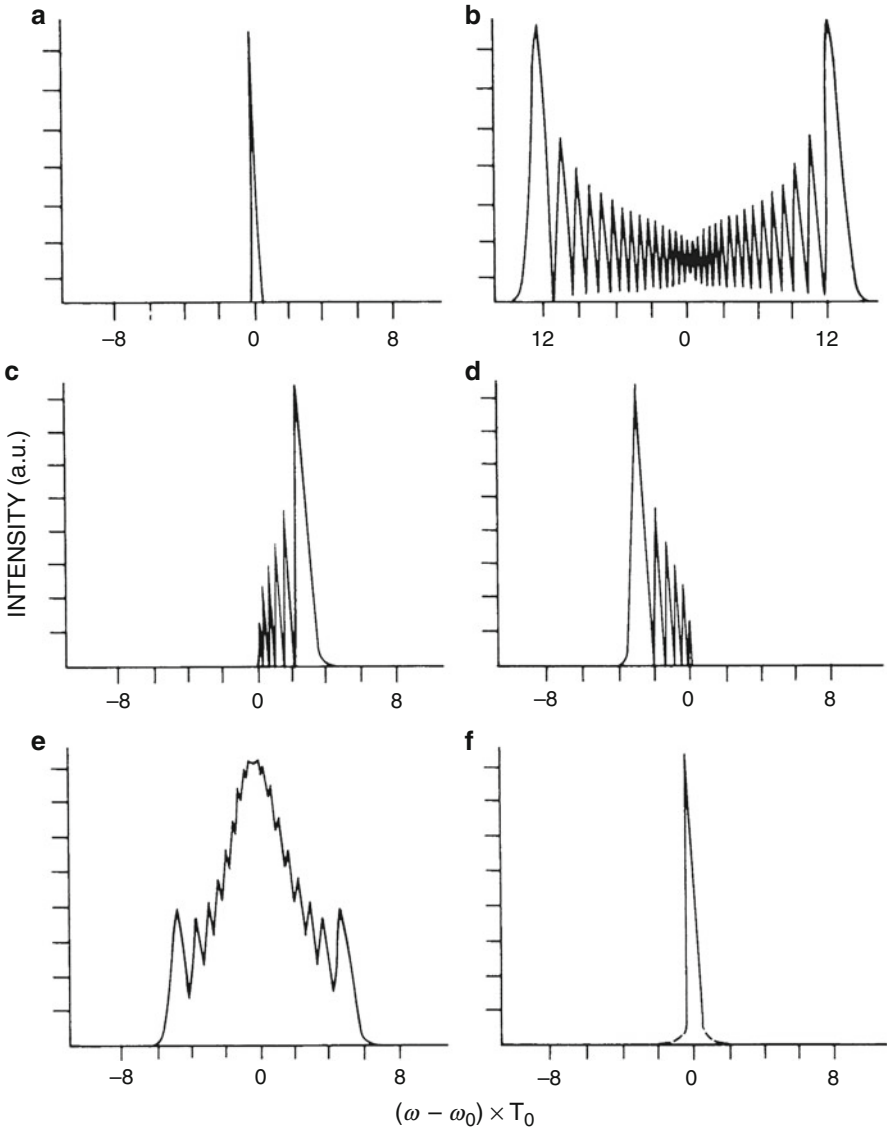

Fig. 4.1 Influence of cross-phase modulation, walk-off, and input time delay on the spectrum of a probe pulse from Eqs. (4.9a, 4.9b, 4.9c and 4.9d) and (4.11) with $P_1 \ll P_2$. $\phi = 2(\omega_1/c)n_2P_2L_w$, $\delta = z/L_w$, and τ_d are the XPM, walk-off, and input time delay parameters, respectively. (**a**) Reference spectrum with no XPM; i.e., $\phi = 0$. (**b**) XPM in the absence of walk-off; i.e., $\phi = 50$ and $\delta = 0$. (**c**) XPM, total walk-off, and no initial time delay; i.e., $\phi = 50$, $\delta = -5$, and $\tau_d = 0$. (**d**) XPM and initial time delay to compensate the walk-off; i.e., $\phi = 50$, $\delta = -5$, and $\tau_d = 5$. (**e**) XPM and symmetrical *partial* walk-off; i.e., $\phi = 50$, $\delta = -3$, and $\tau_d = 1.5$. (**f**) XPM and symmetrical *total* walk-off; i.e., $\phi = 50$, $\delta = -5$, and $\tau_d = 2.5$

interaction length is long enough to allow the pump pulse to completely overcome the probe pulse, there is no XPM-induced broadening (Fig. 4.1f).

The diversity of spectral features displayed in Fig. 4.1 can easily be understood by computing the phase and frequency chirp given by Eqs. (4.9a, 4.9b, 4.9c and 4.9d) and (4.10a and 4.10b) (Fig. 4.2). For reference, Fig. 4.2a shows the locations of the pump pulse (solid line) and the probe pulse (dotted line) at the output of the nonlinear sample (case of no initial delay and total walk-off). In this case, the XPM phase, which is integrated over the fiber length, has the characteristic shape of an error function whose maximum corresponds to neither the probe pulse maximum nor the pump pulse maximum (Fig. 4.2b). The probe pulse (dotted line in Fig. 4.2c) sees only the blue part of the frequency chirp (solid line in Fig. 4.2c) generated by the pump pulse. As a result, the probe spectrum is simultaneously broadened and shifted toward the highest frequencies (Fig. 4.1c). One should notice that opposite to the SPM frequency chirp, the XPM chirp in Fig. 4.2c is not monotonic. The pulse leading edge and trailing edge have a positive chirp and negative chirp, respectively. As a result, dispersive effects (GVD, grating pair, ...) are different for the pulse front and the pulse back. In the regime of normal dispersion ($\beta^{(2)} > 0$), the pulse front would be broadened by GVD, while the pulse back would be sharpened. Figure 4.2d, e show XPM-induced phase and frequency chirp for the mirror image case of Fig. 4.2b, c. The probe spectrum is now shifted toward the smallest frequencies. Its leading edge has a negative frequency chirp, while the trailing edge has a positive one. A positive GVD would compress the pulse front and broaden the pulse back. The case of a partial symmetrical walk-off is displayed in Fig. 4.2f, g. In first approximation, the time dependence of the XPM phase associated with the probe pulse energy is parabolic (Fig. 4.2f), and the frequency chirp is quasi-linear (4.2 g). This is the prime quality needed for the compression of a weak pulse by following the XPM interaction by a grating pair compressor (Manassah, 1988). Figure 4.2h, i show why there is almost no spectral broadening enhancement when the pump pulse passes completely through the probe pulse (Fig. 4.1f): The part of XPM associated with the probe pulse energy is constant (Fig. 4.2h). The probe pulse is phase modulated, but *the phase shift is time independent*. Therefore, there is neither frequency chirp (Fig. 4.2i) nor spectral broadening enhancement by XPM.

The combined effects of XPM and walk-off on the spectra of weak probe pulses (negligible SPM) have been shown in Figs. 4.1 and 4.2. When the group velocity mismatch is large, the spectral broadening is not significant, and the above spectral features reduce to a tunable induced-frequency shift of the probe pulse frequency (see Sect. 4.3.2). When strong probe pulses are used, the SPM contribution has to be included in the analysis. Figure 4.3 shows how the results of Fig. 4.1 are modified when the probe power is the same as the pump power, that is, the SPM has to be taken in account. Figure 4.3a shows the spectral broadening arising from the SPM alone. Combined effects of SPM and XPM are displayed in Figs. 4.3b–e with the same initial delays as in Fig. 4.1. The SPM contribution to the spectral broadening is larger than the XPM contribution because the XPM interaction length is limited by the walk-off between pump and probe pulses.

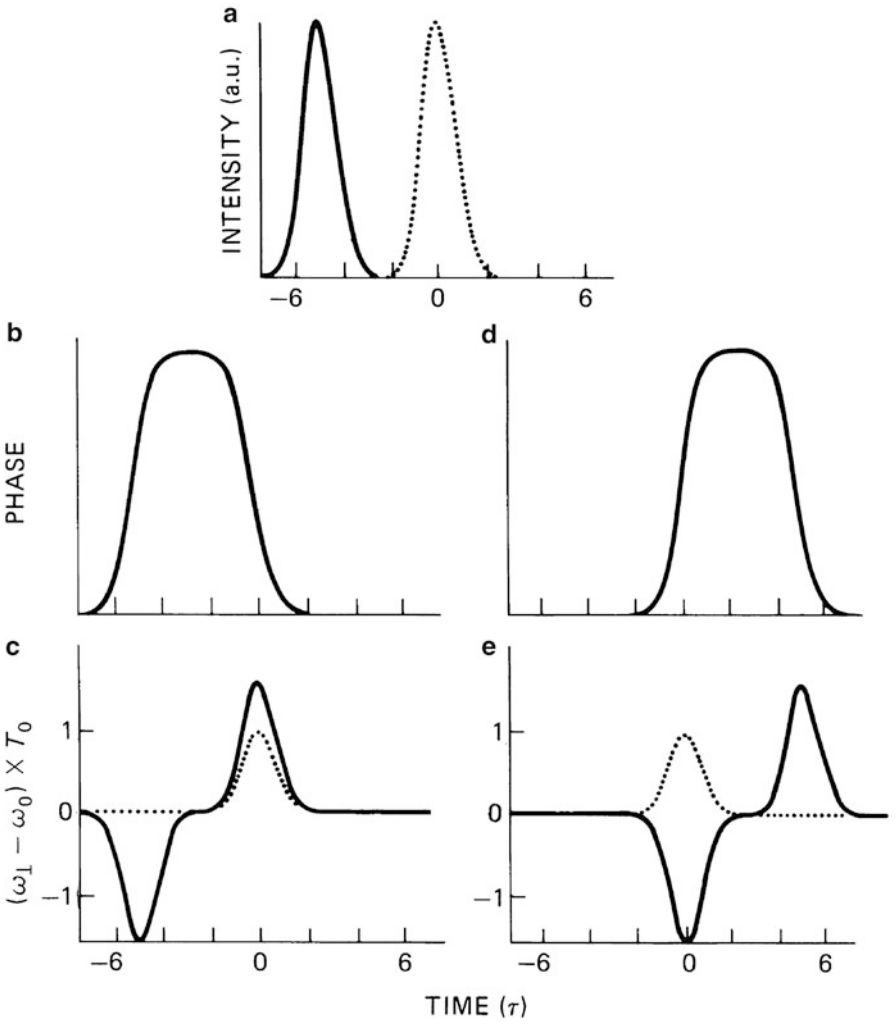

Fig. 4.2 Influence of cross-phase modulation, walk-off, and input time delay on the phase and frequency chirp of a probe pulse. (**a**) Locations of pump (solid line) and probe (dotted line) at the output of the nonlinear medium for total walk-off and no initial time-delay; i.e., $\delta = -5$ and $\tau_d = 0$. (**b**) XPM phase with a total walk-off and no initial time delay; i.e., $\phi = 50$, $\delta = -5$, and $\tau_d = 0$. (**c**) XPM-induced chirp (solid line) with total walk-off and no initial time delay. (Dotted line) Probe pulse intensity. (**d**) XPM phase with an initial time delay to compensate the walk-off; i.e., $\phi = 50$, $\delta = -5$, and $\tau_d = 5$. (**e**) XPM-induced chirp (solid line) with an initial time delay to compensate the walk-off. (Dotted line) Probe pulse intensity. (**f**) XPM phase and symmetrical *partial* walk-off; i.e., $\phi = 50$, $\delta = -3$, and $\tau_d = 1.5$. (**g**) XPM-induced chirp (solid line) and symmetrical *partial* walk-off. (Dotted line) Probe pulse intensity. (**h**) XPM phase and symmetrical *total* walk-off; i.e., $\phi = 50$, $\delta = -5$, and $\tau_d = 2.5$. (**i**) XPM-induced chirp (solid line) and symmetrical *total* walk-off. (Dotted line) Probe pulse intensity

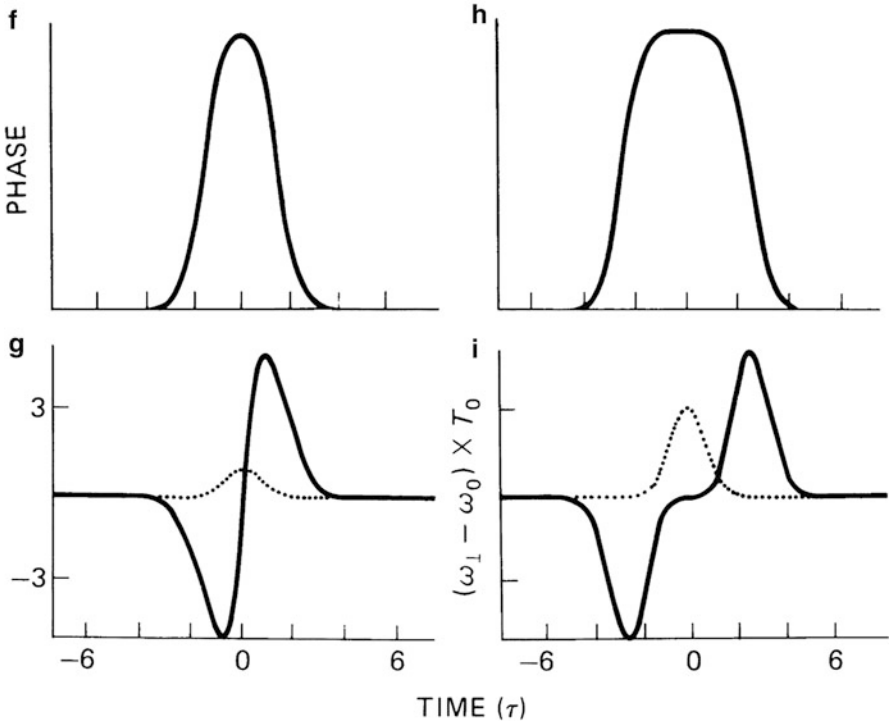

Fig. 4.2 (continued)

The XPM spectral features described in this section have been obtained using first-order approximation of the nonlinear polarization, propagation constant, and nonlinearity in the nonlinear wave equation (Eqs. 4.1a and 4.1b). Moreover, plane wave solutions and peak powers below the stimulated Raman scattering threshold have been assumed. For practical purposes, it is often necessary to include the effects of (1) first- and second-order group velocity dispersion broadening, $\beta^{(2)}$ and $\beta^{(3)}$, (2) induced- and self-steepening, (3) four-wave mixing occurring when pump and probe pulses are coupled through $\chi^{(3)}$, (4) stimulated Raman scattering generation, (5) the finite time response of the nonlinearity, and (6) the spatial distribution of interacting fields (i.e., induced- and self-focusing, diffraction, Gaussian profile of beams, . . .). In Sect. 4.2.3, the combined effect of XPM and group velocity dispersion broadening $\beta^{(2)}$ is shown to lead to new kinds of optical wave breaking and pulse compression. Some other effects that lead to additional spectral, temporal, and spatial features of XPM are discussed by Agrawal (Chap. 3) and Manassah (Chap. 5).

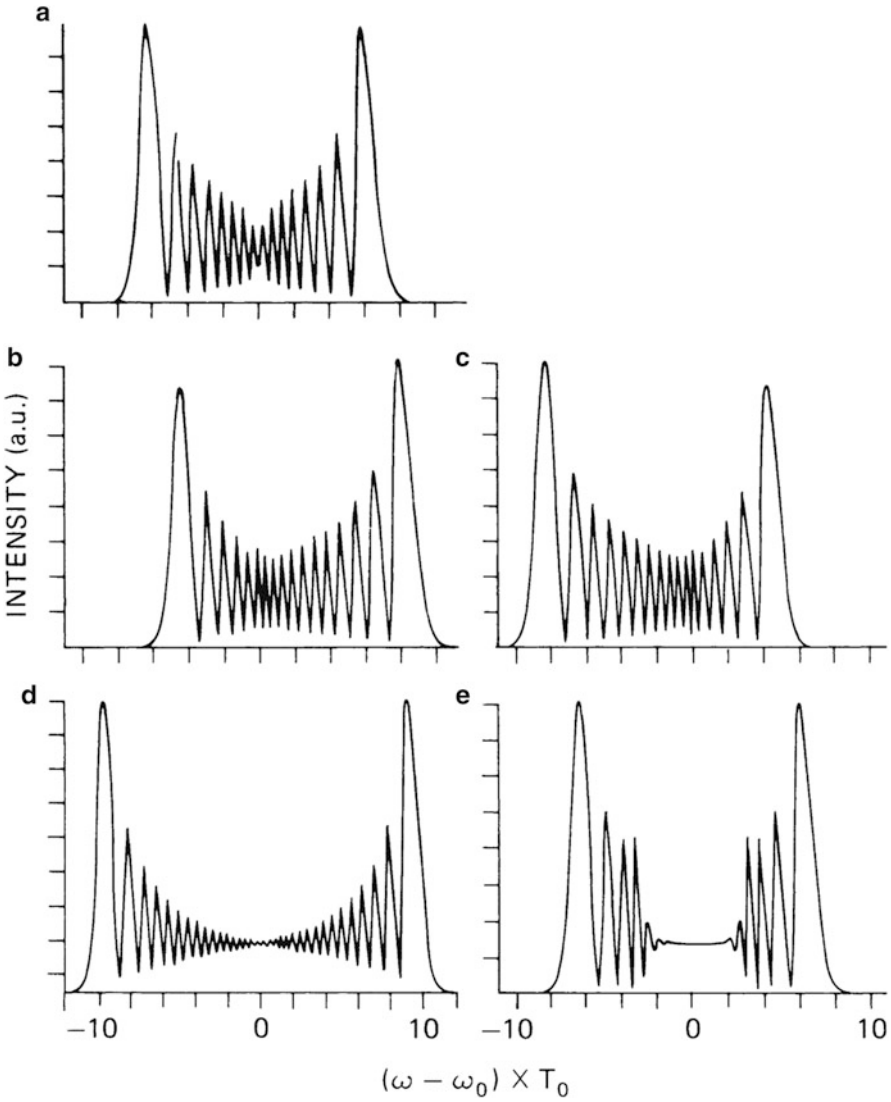

Fig. 4.3 Influence of self-phase modulation, cross-phase modulation, walk-off, and input time delay on the spectrum of a probe pulse from Eqs. (4.9a, 4.9b, 4.9c, 4.9d) and (4.11) with $P_1 = P_2$. The parameter values in Fig. 4.1 are used

4.2.3 Optical Wave Breaking and Pulse Compression Due to Cross-Phase Modulation in Optical Fibers

When an ultrashort light pulse propagates through an optical fiber, its shape and spectrum change considerably as a result of the combined effect of group velocity

dispersion $\beta^{(2)}$ and self-phase modulation. In the normal dispersion regime of the fiber ($\lambda \leq 1.3\ \mu$m), the pulse can develop rapid oscillations in the wings together with spectral sidelobes as a result of a phenomenon known as optical wave breaking (Tomlinson et al., 1985). In this section, it is shown that a similar phenomenon can lead to rapid oscillations near one edge of a weak pulse that copropagates with a strong pulse (Agrawal et al., 1988).

To isolate the effects of XPM from those of SPM, a pump-probe configuration is chosen ($P_2 \ll P_1$) so that pulse 1 plays the role of the pump pulse and propagates without being affected by the copropagating probe pulse. The probe pulse, however, interacts with the pump pulse through XPM. To study how XPM affects the probe evolution along the fiber, Eqs. (4.5a) and (4.5b) have been solved numerically using a generalization of the beam propagation or the split-step method (Agrawal & Potasek, 1986). The numerical results depend strongly on the relative magnitudes of the length scales L_d and L_w, where $L_d = T_0^2/|\beta_2|$ is the dispersion length and $L_w = v_{g1}v_{g2}T_0/|v_{g1} - v_{g2}|$ is the walk-off length. If $L_w \ll L_d$, the pulses walk off from each other before GVD has an opportunity to influence the pulse evolution. However, if L_w and L_d become comparable, XPM and GVD can act together and modify the pulse shape and spectra with new features.

To show these features as simply as possible, a specific case is considered in which $L_w/L_d = 0.1$ and $\lambda_1/\lambda_2 = 1.2$. Both pulses are assumed to propagate in the normal GVD regime with $\beta_1 = \beta_2 > 0$. It is assumed that the pump pulse goes faster than the probe pulse ($v_{g1} > v_{g2}$). At the fiber input both pulses are taken to be a Gaussian of the same width with an initial delay τ_d between them. First, the case $\tau_d = 0$ is considered, so the two pulses overlap completely at $z = 0$. Figure 4.4 shows the shapes and spectra of the pump and probe pulses at $z/L_d = 0.4$ obtained by solving Eqs. (4.5a) and (4.5b) numerically with $N = (\gamma_1 P_1 L_d)^{0.5} = 10$. For comparison, Fig. 4.5 shows the probe and pump spectra under identical conditions but without GVD effects ($\beta_1 = \beta_2 = 0$). The pulse shapes are not shown since they remain unchanged when the GVD effects are excluded.

From a comparison of Figs. 4.4 and 4.5, it is evident that GVD can substantially affect the evolution of features expected from SPM or XPM alone. Consider first the pump pulse for which XPM effects are absent. The expected from dispersive SPM for $N = 10$. With further propagation, the pump pulse eventually develops rapid oscillations in the wings as a result of conventional SPM-induced optical wave breaking. Consider now the probe pulse for which SPM effects are absent and probe pulse evolution is governed by dispersive XPM. In absence of GVD, the pulse shape would be a narrow Gaussian centered at $\tau = 4$ (the relative delay at the fiber output because of group velocity mismatch). The GVD effects not only broaden the pulse considerably but also induce rapid oscillations near the trailing edge of the probe pulse. These oscillations are due to XPM-induced optical wave breaking.

To understand the origin of XPM-induced optical wave breaking, it is useful to consider the frequency chirp imposed on the probe pulse by the copropagating pulse. As there is total walk-off and no initial delay, maximum chirp occurs at the center of the probe pulse. Since the chirp is positive, blue-shifted components are generated

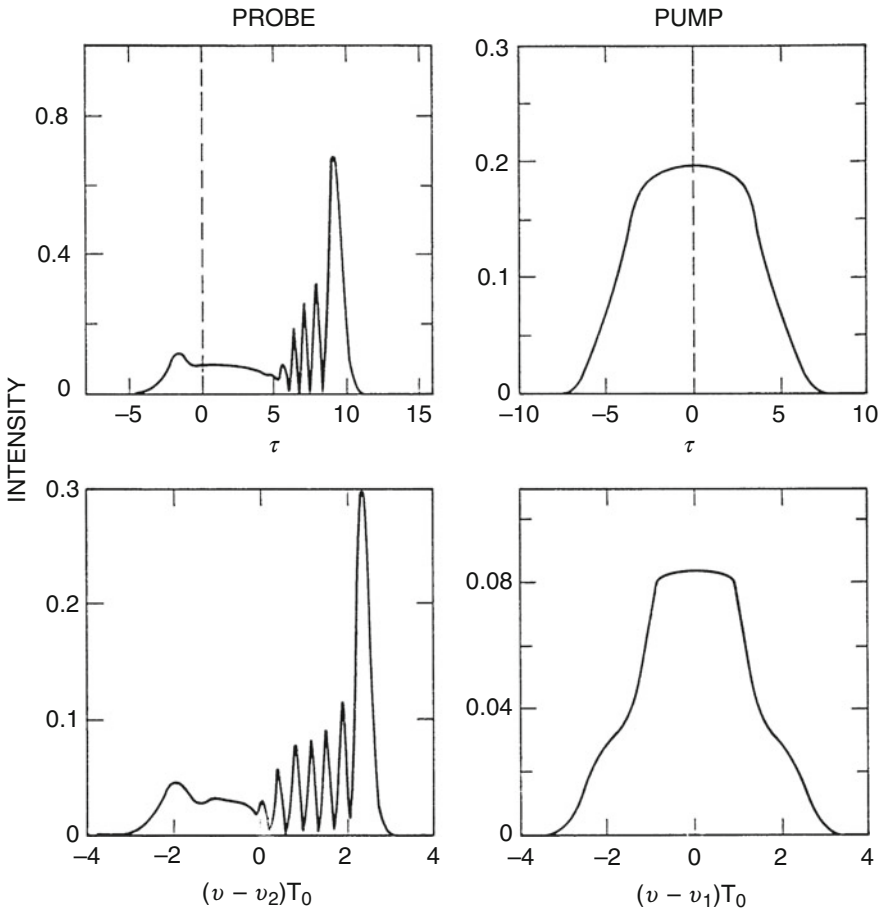

Fig. 4.4 Shape and spectrum of probe pulse (left) and pump pulse (right) at $z/L_d = 0.4$ when the two pulses copropagate in the normal dispersion regime of a single-mode fiber. The parameters are $N = 10$, $L_w/L_d = 0.1$, $\lambda_1/\lambda_2 = 1.2$, and $\tau_d = 0$. Oscillations near the trailing edge (positive time) of the probe pulse are due to XPM-induced optical wave breaking. (From Agrawal et al., 1988)

by XPM near the pulse center. As a result of the normal GVD, the peak of the probe pulse moves slower than its tails. Since the peak lags behind as the probe pulse propagates, it interferes with the trailing edge. Oscillations seen near the trailing edge of the probe pulse in Fig. 4.4 result from such an interference. Since the basic mechanism is analogous to the optical wave-breaking phenomenon occurring in the case of dispersive XPM, we call it XPM-induced optical wave breaking.

In spite of the identical nature of the underlying physical mechanism, optical wave breaking exhibits different qualitative features in the XPM case compared with the SPM case. The most striking difference is that the pulse shape is asymmetric with only one edge developing oscillations. For the case shown in Fig. 4.4,

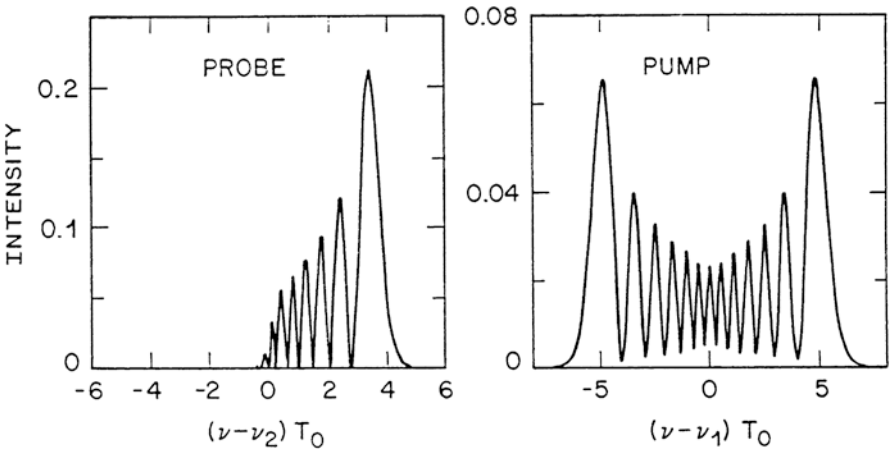

Fig. 4.5 Spectra of probe and pump pulses under conditions identical to those of Fig. 4.4 but without the GVD effects ($\beta_1 = \beta_2 = 0$). Pulse shapes are not shown as they remain unchanged. (From Agrawal et al., 1988)

oscillations occur near the trailing edge. If the probe and pump wavelengths were reversed so that the pump pulse moved slower than the probe pulse, oscillations would occur near the leading edge since the pump pulse would interact mainly with that edge. In fact, in that case, the shape and the spectrum of the probe pulse are just the mirror images of those shown in Figs. 4.4 and 4.5.

The effect of initial delay between probe and pump pulses is now investigated. The effect of initial delay on XPM-induced spectral broadening has been discussed in the dispersionless limit ($\beta_1 = \beta_2 = 0$) in Sect. 4.2.2. For example, if the pump pulse is delayed by the right amount so that it catches up with the probe pulse at the fiber output, the probe spectrum is just the mirror image of that shown in Fig. 4.4, exhibiting a red shift rather than a blue shift. Furthermore, if τ_d is adjusted such that the pump pulse catches up with the probe pulse halfway through the fiber, the probe spectrum is symmetrically broadened since the pump walks through the probe in a symmetric manner. Our numerical results show that the inclusion of GVD completely alters this behavior. Figure 4.6 shows the probe shape and spectrum under conditions identical to those of Fig. 4.4 except that the probe pulse is advanced ($\tau_d = -2$) such that the pump pulse would catch it halfway through the fiber in the absence of GVD effects. The lower row shows the expected behavior in the dispersionless limit, showing the symmetrical spectral broadening in this case of symmetrical walk-off. A direct comparison reveals how much the presence of GVD can affect the SPM effects on the pulse evolution. In particular, both the pulse shape and spectra are asymmetric. More interestingly, the probe pulse is compressed, in sharp contrast to the case of Fig. 4.4, where GVD led to a huge broadening. This can be understood qualitatively from Eqs. (4.10a and 4.10b). For the case shown in Fig. 4.6, the XPM-induced chirp is negative and nearly linear across the trailing part of

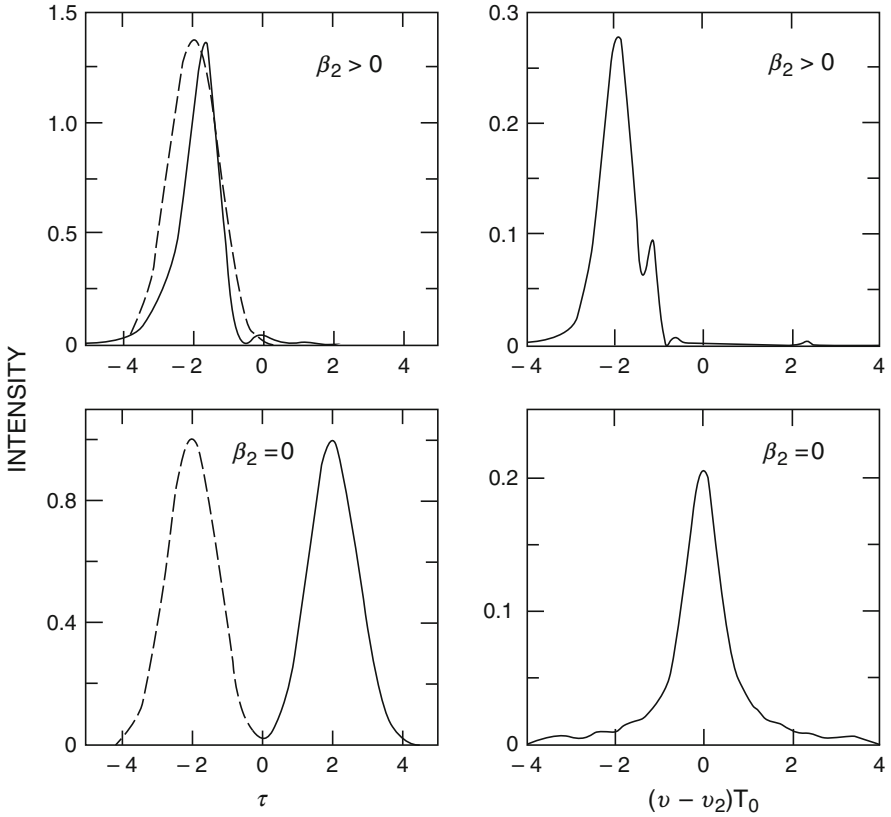

Fig. 4.6 Probe shape and spectrum with (top) and without (bottom) the GVD effects under conditions identical to those of Fig. 4.5 except that $\tau_d = -2$. Note the important effect on pulse evolution of the initial time delay between the pump and probe pulses. (From Agrawal et al., 1988)

the probe pulse. Because of this chirp, the traveling part is compressed as the probe pulse propagates inside the fiber.

Experimental observation of XPM-induced optical wave breaking would require the use of femtosecond pulses. This can be seen by noting that for picosecond pulses with $T_0 = 5$–10 ps, typically $L_d \approx 1$ km while $L_w \approx 1$ m even if the pump-probe wavelengths differ by as little as 10 nm. By contrast, if $T_0 = 100$ fs, both L_d and L_w become comparable (≈ 10 cm), and the temporal changes in the probe shape discussed here can occur in a fiber less than a meter long. Pulses much shorter than 100 f. should also not be used since higher-order nonlinear effects such as self-steepening and a delayed nonlinear response then become increasingly important. Although these effects are not expected to eliminate the phenomenon of XPM-induced optical wave breaking, they may interfere with the interpretation of experimental data.

4.3 Pump-Probe Cross-Phase Modulation Experiments

Cross-phase modulation is intrinsic to numerous schemes of ultrashort pulse interaction. The first observation of spectral effects arising from XPM was reported using a pump-probe scheme (Alfano et al., 1986). The phase modulation generated by the infrared pulse at the probe wavelength was referred to as an induced-phase modulation (PM). More recently, the induced-frequency shift and spectral broadening enhancement of picosecond probe pulses have been observed using optical fibers as nonlinear media (Baldeck et al., 1988a; Islam et al., 1987a, b). Pump-probe experiments on XPM are of prime importance for they could lead to applications for pulse compression, optical communication, and optical computation purposes. Results of the pump-probe experiments on XPM are discussed in this section.

4.3.1 Spectral Broadening Enhancement by Cross-Phase Modulation in BK-7 Glass

The possibility of enhancing the spectral broadening of a probe pulse using a copropagating pump pulse was first observed experimentally in early 1986 (Alfano et al., 1986). The spectral broadening of a weak 80-μJ picosecond 530-nm laser in BK-7 glass was enhanced over the entire spectral band by the presence of an intense millijoule picosecond 1060-nm laser pulse. The spectral distributions of the self-phase modulation and the cross-phase modulation signals were found to be similar. The dominant enhancement mechanism for the induced supercontinuum was determined to be a cross-phase modulation process, not stimulated four-photon scattering.

The experimental setup is shown in Fig. 4.7. A single 8-ps laser pulse at 1060 nm generated from a mode-locked glass laser system was used as the pump beam. Its second harmonic was used as the probe beam. These pulses at the primary 1060-nm and the second harmonic 530-nm wavelengths were weakly focused into a 9-cm-long BK-7 glass. A weak supercontinuum signal was observed when both 530- and 1060-nm laser pulses were sent through the sample at the same time. This signal could arise from the IPM process and/or stimulated four-photon parametric generation (FPPG).

In this induced supercontinuum experiment, the 530-nm laser pulse intensity was kept nearly constant with a pulse energy of about 80 μJ. The primary 1060-nm laser pulse energy was a controlled variable changing from 0 to 2 mJ. Filters were used to adjust the 1060-nm pump-laser pump intensity. The output beam was separated into three paths for diagnosis.

The output beam along path 1 was imaged onto the slit of a 0.5-m Jarrel-Ash spectrograph to separate the contributions from the possible different mechanisms for the supercontinuum by analyzing the spatial distribution of the spectrum from phase modulation and stimulated four-photon scattering processes. In this

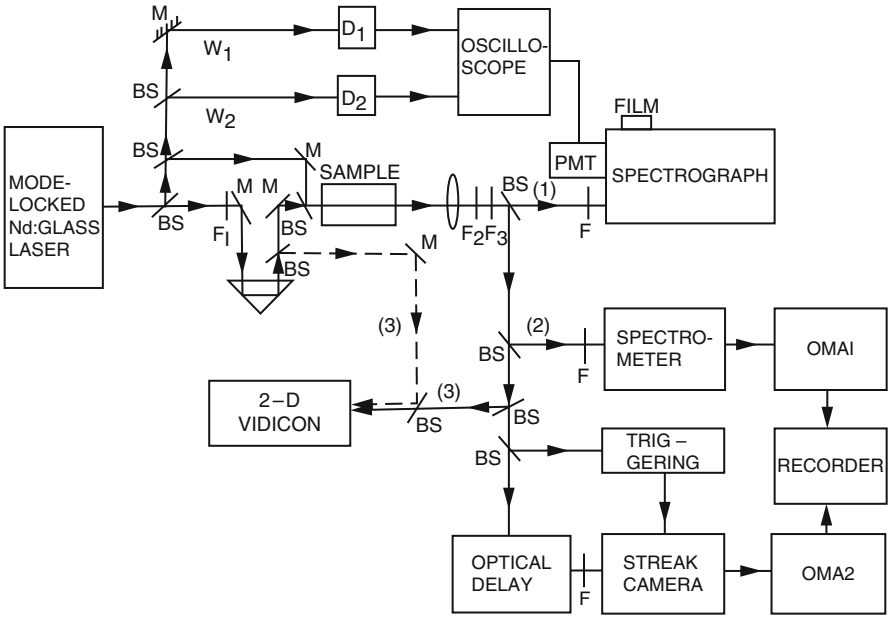

Fig. 4.7 Schematic diagram of the experimental arrangement for measuring the spectral broadening enhancement of probe pulses by induced-phase modulation. F_1: Hoya HA30 (0.03%), R72 (82%), Corning 1–75 (1%), 1–59 (15%), 0–51 (69%), 3–75 (80%). The numbers in parentheses correspond to the transmittivity at 1054 nm. All these color filters have about 82% transmittivity at 527 nm. F_2: 1–75 + 3–67 for Stokes side measurements; F_2: 1–75 + 2 (5–57) for anti-Stokes side measurements; F_3: neutral density filters; F: ND3 + 1–75; D1, D2; detectors; M: dielectric-coated mirror; BS: beam splitter. (From Alfano et al., 1986)

spectrograph measurement, films were used to measure the spatial distribution of the supercontinuum spectrum, and a photomultiplier tube was used to obtain quantitative reading. To distinguish different contributions from either phase modulation or stimulated four-photon scattering, geometric blocks were arranged in the path for the selection of a particular process. An aperture of 6-mm diameter was placed in front of the entrance slit of the spectrograph to measure the signal contributed phase modulation, while an aluminum plate of 7-mm width was placed in front of the spectrograph entrance slit to measure the $\lambda = 570$-nm contribution.

The beam along path 2 was directed into a spectrometer with an optical multichannel analyzer to measure the supercontinuum spectral intensity distribution. The spectrum was digitized, displayed, and stored in 500 channels as a function of wavelength. The beam along path 3 was delayed and directed into a Hamamatsu Model C1587 streak camera to measure the temporal distribution of the laser pulse and induced supercontinuum. The duration of the induced supercontinuum with a selected 10-nm bandwidth was measured to be about the same as the incident laser pulse duration.

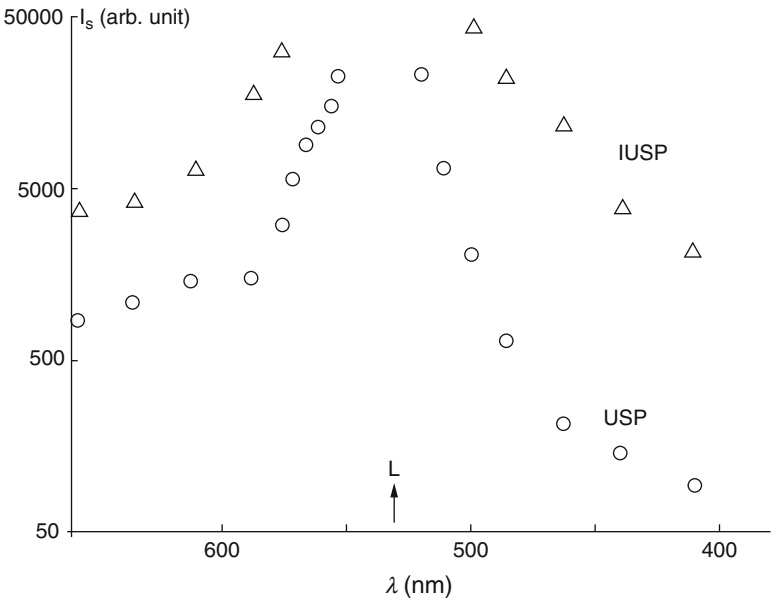

Fig. 4.8 Intensities of the induced ultrafast supercontinuum pulse (IUSP) and the ultrafast supercontinuum pulse (USP). Each data point was an average of about 20 laser shots and was corrected for the detector, filter, and spectrometer spectral sensitivity. (△) IUSP (F_1: 3–75); (○) USP from 527 nm (F_1: HA30). USP from 1054 nm, which is not shown here was ≈1% of the IUSP signal. The measured 527-nm probe pulse was about 5 × 10 counts on this arbitrary unit scale. The error bar of each data point is about ±20%. (From Alfano et al., 1986)

Experimental results for the spectral distribution of induced supercontinuum and supercontinuum are displayed in Fig. 4.8. More than 20 laser shots for each data point in each instance have been normalized and smoothed. The average gain of the induced supercontinuum in a BK-7 glass from 410- to 660-nm wavelength was about 11 times that of the supercontinuum. In this instance, both the 530- and 1060-nm laser pulse energies were maintained nearly constant: 80 μJ for 530 nm and 2 mJ for 1060 nm. In this experiment, the 530-nm laser pulse generated a weak supercontinuum and the intense 1060-nm laser pulse served as a catalyst to enhance the super-continuum in the 530-nm pulse. The supercontinuum generated by the 1060-nm pulse alone in this spectral region was less than 1% of the total induced supercontinuum. The spectral shapes of the induced supercontinuum pulse and the supercontinuum pulse in Fig. 4.8 are similar. Use of several liquid samples such as water, nitrobenzene, CS_2, and CCl_4 has also been attempted to obtain the induced supercontinuum. There was no significant (twofold) enhancement from all other samples that we tested.

A plot of the intensity dependence of the induced supercontinuum is displayed in Fig. 4.9 as a function of the 1060-nm pump pulse energy. The wavelengths plotted in Fig. 4.9 were $\lambda = 570$ nm for the Stokes side and $\lambda = 498$ nm for the

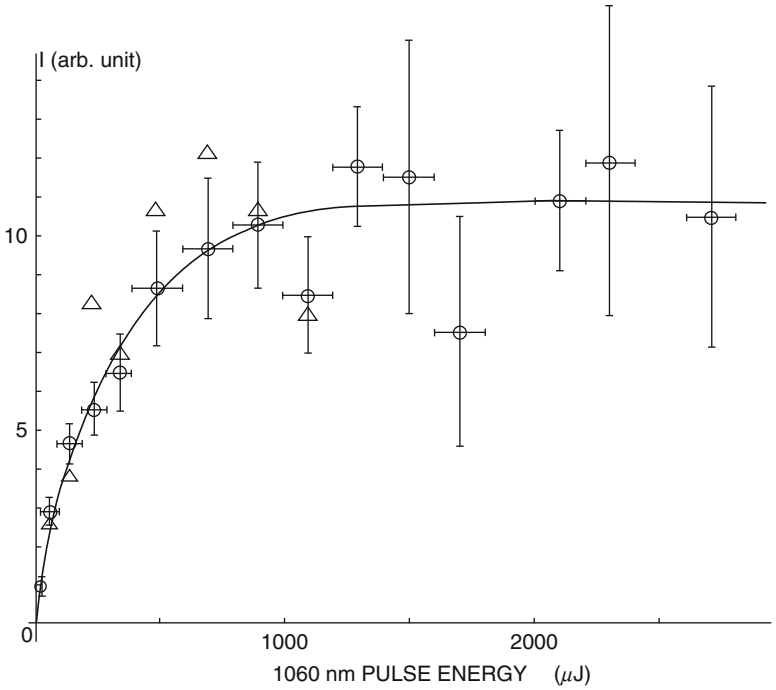

Fig. 4.9 Dependence of the IUSP signal on the intensity of the 1.06-μm pump pulse. (○) Stokes side at $\lambda = 570$ nm; (Δ) anti-Stokes side at $\lambda = 498$ nm. The error bars of the anti-Stokes side were similar to those of the Stokes side. The solid line is a guide for the eye. The vertical axis is the normalized $I_{\text{IUSP}}/I_{527\text{ nm}}$. (From Alfano et al., 1986)

anti-Stokes side. The 530-nm pulse energy was set at 80 ± 15 μJ. The induced supercontinuum increased linearly as the added 1060-nm laser pulse energy was increased from 0 to 200 μJ. When the 1060-nm pump pulse was over 1 mJ, the supercontinuum enhancement reached a plateau and saturated at a gain factor of about 11 times over the supercontinuum intensity generated by only the 530-nm pulse. This gain saturation may be due to the trailing edge of the pulse shape function being maximally distorted when the primary pulse intensity reaches a certain critical value. This implies a saturation of the PM spectral distribution intensity when the pumped primary pulse energy is above 1 mJ, as shown in Fig. 4.9.

Since the supercontinuum generation can be due to the phase modulation and/or the stimulated four-photon scattering processes, it is important to distinguish between these two different contributions to the induced supercontinuum signal. Spatial filtering of the signal was used to separate the two main contributions. The induced supercontinuum spectrum shows a spatial spectral distribution similar to that of the conventional supercontinuum. The collinear profile that is due to the phase modulation has nearly the same spatial distribution as the incident laser

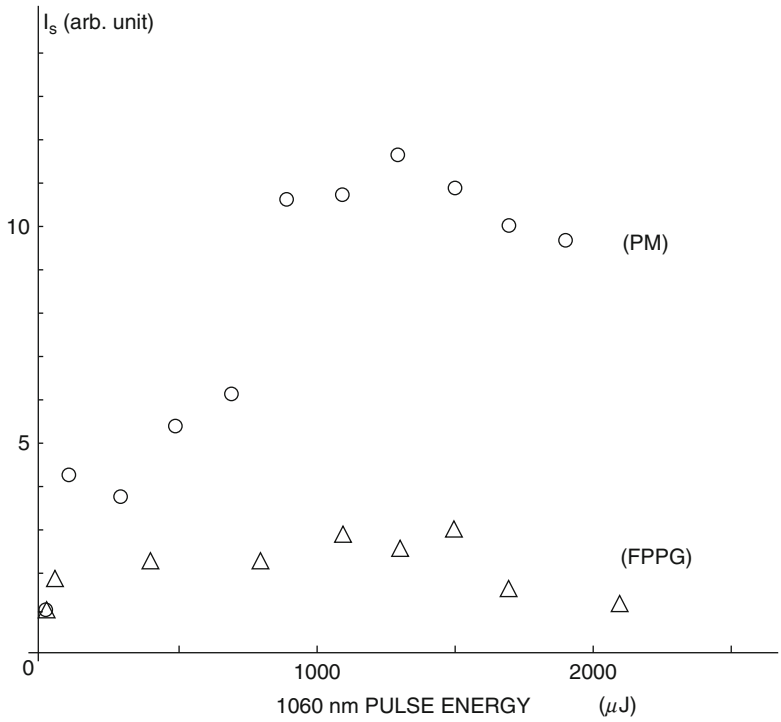

Fig. 4.10 Dependence of I_S (PM) and I_S (FPPG) at $\lambda = 570$ nm or the intensity of the 1054-nm pump laser pulse. (○) PM; (△) FPPG. The measured signal has been normalized with the incident 527-nm pulse energy. The error bar of each data point is about ±20% of the average value. (From Alfano et al., 1986)

pulse. Two emission wings at noncollinear angles correspond to the stimulated four-photon scattering continuum arising from the phase-matching condition of the generated wavelengths emitted at different angles from the incident laser beam direction. Using a photomultiplier system and spatial filtering, quantitative measurements of the induced supercontinuum contributions from the collinear PM and the noncollinear stimulated four-photon scattering parts were obtained (Fig. 4.10). These signals, measured at $\lambda = 570$ nm from the collinear PM and the noncollinear parts of the induced supercontinuum, are plotted as a function of the pump pulse energy. There was little gain from the contribution of the stimulated four-photon scattering process over the entire pulse-energy-dependent measurement as shown in Fig. 4.10. The main enhancement of the induced supercontinuum generation is consequently attributed to the PM mechanism, which corresponds to the collinear geometry. Another possible mechanism for the observed induced supercontinuum could be associated with the enhanced self-focusing of the second harmonic pulse induced by the primary pulse. There was no significant difference

in the spatial intensity distribution of the 530-nm probe beam with and without the added intense 1060-nm pulse.

In this experiment, the spectral broadening of 530-nm pulses was enhanced by nonlinear interaction with copropagating strong infrared pulses in a BK-7 glass sample. The spectral change has been found to arise from a phase modulation process rather than a stimulated four-photon mixing process. It is in good agreement with predictions of the induced-phase modulation theory. This experiment showed the first clear evidence of a cross-phase modulation spectral effect.

4.3.2 Induced-Frequency Shift of Copropagating Pulses

Optical fibers are convenient for the study of nonlinear optical processes. The optical energy is concentrated into small cross section (typically 10^{-7} cm^2) for long interaction lengths. Thus, large nonlinear effects are possible with moderate peak powers (10–10^4 W). Optical fibers appear to be an ideal medium in which to investigate XPM effects. The first pump probe experiment using picosecond pulses propagating in optical fibers demonstrated the importance of the pulse walk-off in XPM spectral effects (Baldeck et al., 1988a). It was shown that ultrashort pulses that overlap in a nonlinear and highly dispersive medium undergo a substantial shift of their carrier frequencies. This new coherent effect, which was referred to as an induced-frequency shift, resulted from the combined effect of cross-phase modulation and pulse walk-off. In the experiment, the induced-frequency shift was observed by using strong infrared pulses that shifted the frequency of weak picosecond green pulses copropagating in a 1-m-long single-mode optical fiber. Tunable red and blue shifts were obtained at the fiber output by changing the time delay between infrared and green pulses at the fiber input.

A schematic of the experimental setup is shown in Fig. 4.11. A mode-locked Nd: YAG laser with a second harmonic crystal was used to produce 33-ps infrared pulses and 25-ps green pulses. These pulses were separated using a Mach–Zehnder interferometer delay scheme with wavelength-selective mirrors. The infrared and green pulses propagated in different interferometer arms. The optical path of each pulse was controlled using variable optical delays. The energy of infrared pulses was adjusted with neutral density filters in the range 1–100 nJ, while the energy of green pulses was set to about 1 nJ. The nonlinear dispersive medium was a 1-m-long single-mode optical fiber (Corguide of Corning Glass). This length was chosen to allow for total walk-off without losing control of the pulse delay at the fiber output. The group velocity mismatch between 532- and 1064-nm pulses was calculated to be about 76 ps/m in fused silica. The spectrum of green pulses was measured using a grating spectrometer (1 meter, 1200 lines/mm) and an optical multichannel analyzer (OMA2).

The spectra of green pulses propagating with and without infrared pulses are plotted in Fig. 4.12. The dashed spectrum corresponds to the case of green pulses propagating alone. The blue-shifted and red-shifted spectra are those of green pulses

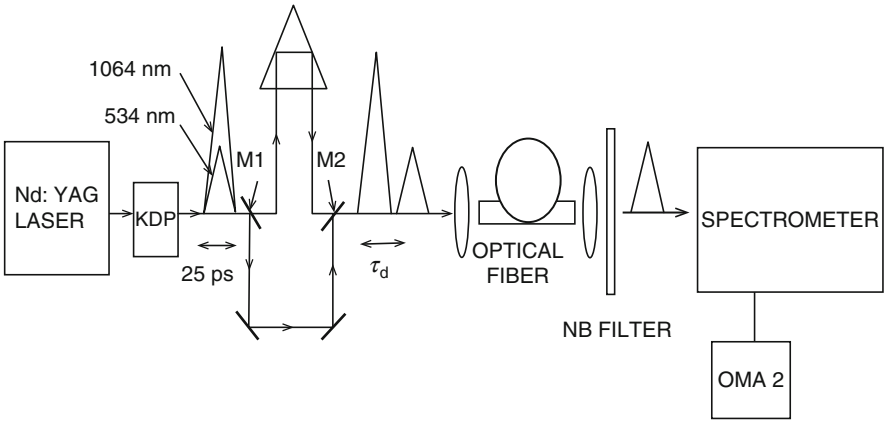

Fig. 4.11 Experimental setup used to measure the induced-frequency shift of 532-nm pulses as a function of the time delay between pump and probe pulses at the optical fiber input. Mirrors M_1 and M_2 are wavelength selective; i.e., they reflect 532-nm pulses and transmit 1064-nm pulses (From Baldeck et al., 1988a)

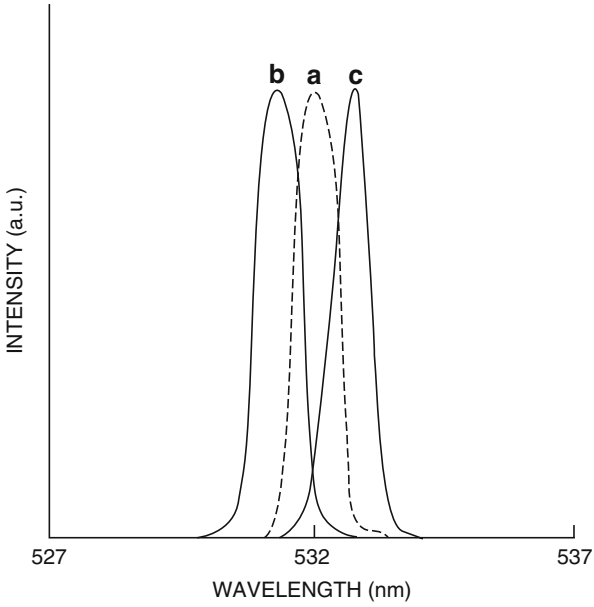

Fig. 4.12 Cross-phase modulation effects on spectra of green 532-nm pulses. (**a**) Reference spectrum (no copropagating infrared pulse). (**b**) Infrared and green pulses overlapped at the fiber input. (**c**) Infrared pulse delayed by 80 ps at the fiber input. (From Baldeck et al., 1988a)

copropagating with infrared pulses after the input delays were set at 0 and 80 ps, respectively. The main effect of the nonlinear interaction was to shift the carrier frequency of green pulses. The induced-wavelength shift versus the input delay between infrared and green pulses is plotted in Fig. 4.13. The maximum induced-wavelength shift increased linearly with the infrared pulse peak power (Fig. 4.14). Hence, the carrier wavelength of green pulses could be tuned up to 4 Å toward both

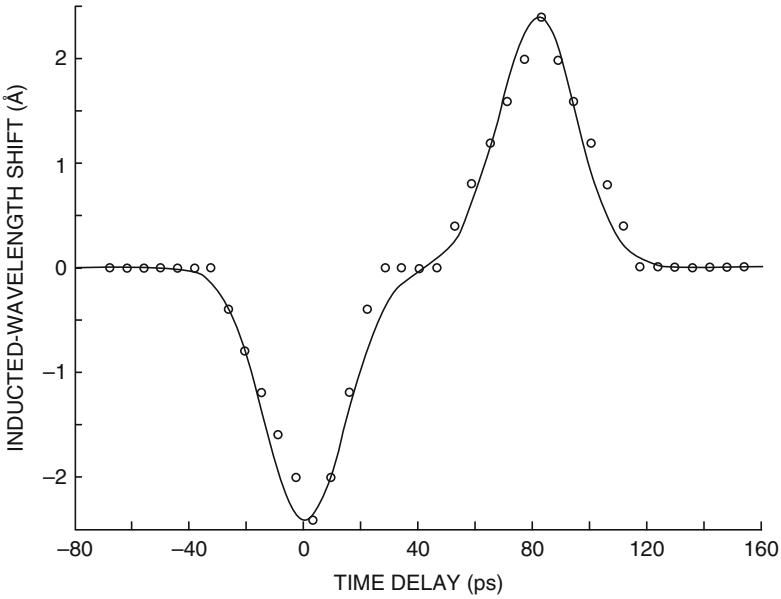

Fig. 4.13 Induced wavelength shift of green 532-nm pulses as a function of the input time delay between 532-nm pulses and infrared 1064-nm pulses at the input of a 1-m-long optical fiber, (○) Experimental points. The solid line is the theoretical prediction from Eq. (3.3). (From Baldeck et al., 1988a)

the red and blue sides by varying the time delay between infrared and green pulses at the fiber input. The solid curves in Figs. 4.13 and 4.14 are from theory.

When weak probe pulses are used, the SPM contribution can be neglected in Eqs. (4.9a, 4.9b, 4.9c, 4.9d) and (4.10a and 4.10b). Thus, nonlinear phase shifts and frequency chirps are given by

$$\alpha_1(\tau, z) \approx \sqrt{\pi}\frac{\omega_1}{c} n_2 \frac{P_2}{A_{\text{eff}}} L_w \left[\text{erf}(\tau - \tau_d) - \text{erf}\left(\tau - \tau_d + \frac{z}{L_w}\right)\right], \tag{4.15}$$

$$\delta\omega_1(\tau, z) \approx -2\frac{\omega_1}{c} n_2 \frac{P_2}{A_{\text{eff}}} \frac{L_w}{T_0}\left[e^{-(\tau-\tau_d)^2} - e^{-(\tau-\tau_d-z/L_w)^2}\right]. \tag{4.16}$$

When the pulses coincide at the fiber entrance ($t_d = 0$), the point of maximum phase is generated ahead of the green pulse peak because of the group velocity mismatch (Eq. 4.15). The green pulse sees only the trailing part of the XPM profile because it travels slower than the pump pulse. This leads to a blue induced-frequency shift (Eq. 4.16). Similarly, when the initial delay is set at 80 ps, the infrared pulse has just sufficient time to catch up with the green pulse. The green pulse sees only the leading part of the XPM phase shift, which gives rise to a red

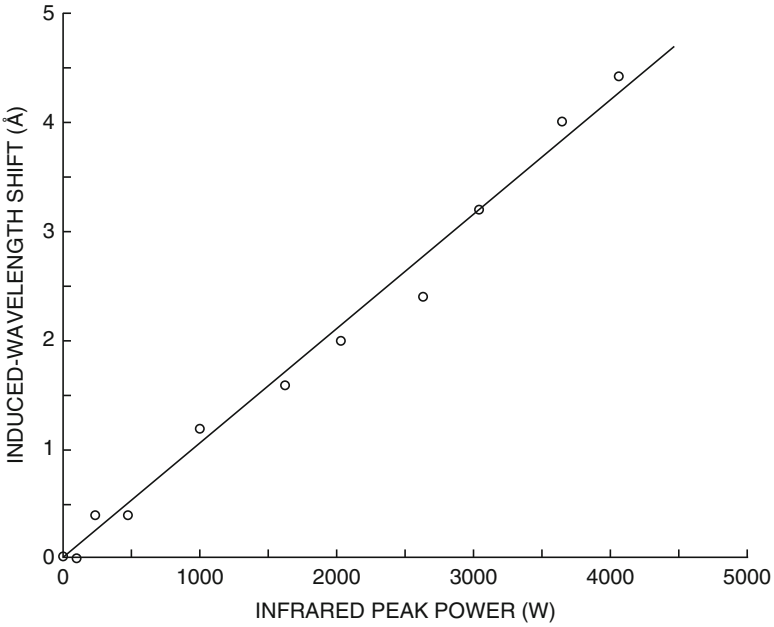

Fig. 4.14 Maximum induced wavelength shift of 532-nm pulses versus the peak power of infrared pump pulses, (○) Experimental points. The solid line is the theoretical prediction from Eq. (3.4). (From Baldeck et al., 1988a)

induced-frequency shift. When the initial delay is about 40 ps, the infrared pulse has time to pass entirely through the green pulse. The pulse envelope sees a constant dephasing, and there is no shift of the green spectrum (Fig. 4.13).

Equations (4.15) and (4.16) can be used to fit our experimental data shown in Figs. 4.13 and 4.14. Assuming that the central part of the pump pulses provides the dominant contribution to XPM, we set $t = 0$ in Eq. (4.16) and obtain

$$\delta\omega_1(\tau, z) \approx \frac{\omega_1}{c} n_2 \frac{P_2}{A_{\text{eff}}} \frac{L_w}{T_0} \left[e^{-(\tau-\tau_d)^2} - e^{-(\tau-\tau_d+z/L_w)^2} \right]. \tag{4.17}$$

The maximum induced-frequency shift occurs at $t_d = d = z/L_w$ and is given by

$$|\Delta\omega_{\max}| = \frac{\omega_1}{c} n_2 \frac{P_2}{A_{\text{eff}}} \frac{L_w}{T_0}. \tag{4.18}$$

Equations (4.17) and (4.18) are plotted in Figs. 4.13 and 4.14, respectively. There is very good agreement between this simple analytical model and experimental data. It should be noted that only a simple parameter (i.e., the infrared peak power at the maximum induced-frequency shift) has been adjusted to fit the data. Experimental parameters were $\lambda = 532$ nm, $T_0 = 19.8$ ps (33 ps FWHM), $L_w = 26$ cm, and $\delta = 4$.

We have shown experimentally and theoretically that ultrashort optical pulses that overlap in a nonlinear and highly dispersive medium can undergo a substantial shift of their carrier frequency. This induced-frequency shift has been demonstrated using strong infrared pulses to shift the frequency of copropagating green pulses. The results are well explained by an analytical model that includes the effect of cross-phase modulation and pulse walk-off. This experiment led to a conclusive observation of XPM spectral effects.

4.3.3 XPM-Induced Spectral Broadening and Optical Amplification in Optical Fibers

This section presents additional features that can arise from the XPM interaction between a pump pulse at 630 nm and a probe pulse at 532 nm. With this choice of wavelengths, the group velocity dispersion between the pump pulse and the probe pulse is reduced and the XPM interaction enhanced. The spectral width and the energy of the probe pulse were found to increase in the presence of the copropagating pump pulse (Baldeck et al., 1988c).

A schematic of the experimental setup is shown in Fig. 4.15. A mode-locked Nd: YAG laser with a second harmonic crystal was used to produce pulses of 25-ps duration at 532 nm. Pump pulses were obtained through stimulated Raman scattering by focusing 90% of the 532-nm pulse energy into a 1-cm cell filled with ethanol and using a narrowband filter centered at 630 nm. Resulting pump pulses at 630 nm were recombined with probe pulses and coupled into a 3-m-long single-mode optical fiber. Spectra of probe pulses were recorded for increasing pump intensities and varying input time delays between pump and probe pulses.

With negative delays (late pump at the optical fiber input), the spectrum of the probe pulse was red shifted as in the 1064 nm/532 nm experiment (Fig. 4.12). A new

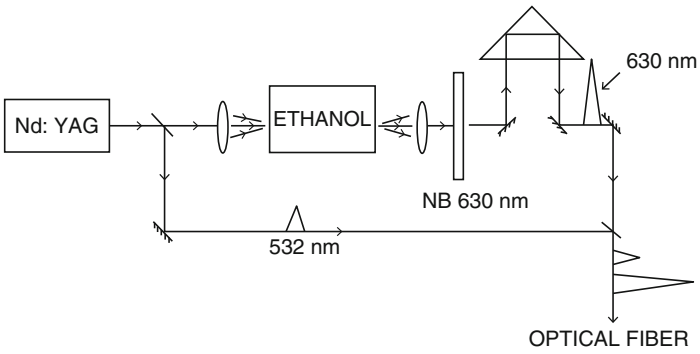

Fig. 4.15 Experimental setup for generating copropagating picosecond pulses at 630 and 532 nm. (From Baldeck et al., 1988c)

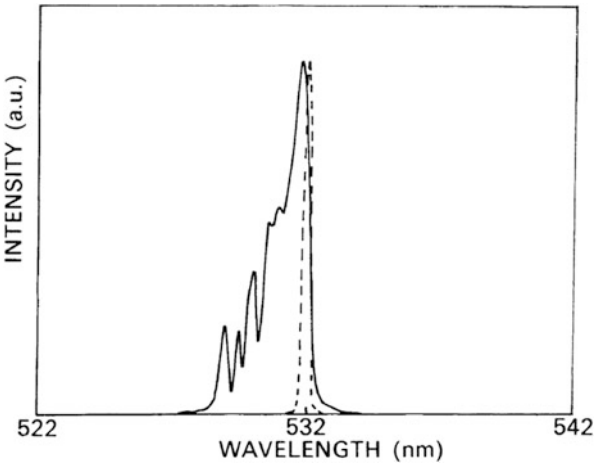

Fig. 4.16 Cross-phase modulation effects on the spectrum of a probe picosecond pulse. (Dashed line) Reference spectrum without XPM. (Solid line) With XPM and no time delay between pump and probe pulses at the optical fiber input. (From Baldeck et al., 1988c)

XPM effect was obtained when both pulses entered the fiber simultaneously. The spectrum of the probe pulse not only shifted toward blue frequencies as expected but also broadened (Fig. 4.16). An spectral broadening as wide as 10 nm could be induced, which was, surprisingly, at least one order of magnitude larger than predicted by the XPM theory. As shown in Fig. 4.16, the probe spectrum extended toward the blue-shifted frequencies with periodic resonant lines. These lines could be related to modulation instability sidelobes that have been predicted theoretically to occur with cross-phase modulation (see Sect. 4.8).

The optical amplification of the probe pulse is another new and unexpected feature arising from the XPM interaction. Pump power-dependent gain factors of 3 or 7 were measured using probe pulses at 532 nm and pump pulses at 630 or 1064 nm, respectively. Figure 4.17 shows the dependence of the XPM-induced gain for the probe pulse at 532 nm with the input time delay between the probe pulse and the pump pulse at 630 nm. The shape of the gain curve corresponds to the overlap function of pump and probe pulses. Figure 4.18 shows the dependence or the gain factor on the intensity of pump pulses at 1064 nm. This curve is typical of a parametric amplification with pump depletion. The physical origin of this XPM-induced gain is still under investigation. It could originate from an XPM-phase-matched four-wave mixing process.

The spectral distribution of probe pulses can be significantly affected by the XPM generated by a copropagating pulse. In real time, the probe pulse frequency can be tuned, its spectrum broadened, and its energy increased. XPM appears as a new technique for controlling the spectral properties and regenerating ultrashort optical pulses with terahertz repetition rates.

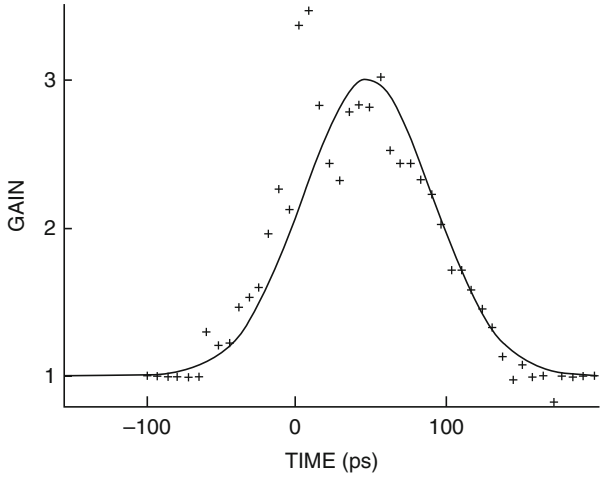

Fig. 4.17 XPM-induced optical gain $I_{532}(\text{out})/I_{532}(\text{in})$ versus input time delay between pump pulses at 630 nm and probe pulses at 532 nm. (Crosses) Experimental data; (solid line) fit obtained by taking the convolution of pump and probe pulses. (From Baldeck & Alfano, 1988c)

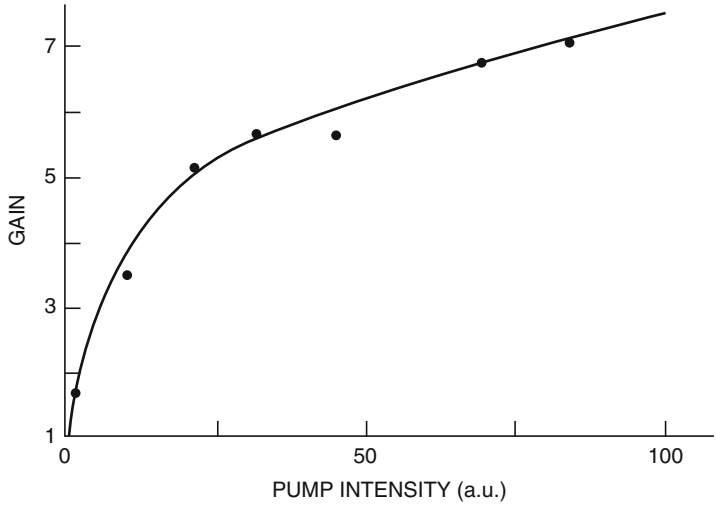

Fig. 4.18 XPM-induced optical gain $I_{532}(\text{out})/I_{532}(\text{in})$ versus intensity of pump pulses at 1064 nm. (From Baldeck et al., 1987c, d)

4.4 Cross-Phase Modulation with Stimulated Raman Scattering

When long samples are studied optically, stimulated Raman scattering (SRS) contributes to the formation of ultrafast supercontinua. In 1980, Gersten, Alfano,

and Belic predicted that ultrashort pulses should generate broad Raman lines due to the coupling among laser photons and vibrational phonons (Gersten et al., 1980). This phenomenon was called cross-pulse modulation (XPM). It characterized the phase modulation of the Raman pulse by the intense pump laser pulse. Cornelius and Harris (1981) stressed the role of SPM in SRS from more than one mode. Recently, a great deal of attention has been focused on the combined effects of SRS, SPM, and group velocity dispersion for the purposes of pulse compression and soliton generation (Dianov et al., 1984; Lu Hian-Hua et al., 1985; Stolen & Johnson, 1986; French et al., 1986;Nakashima et al., 1987; Johnson et al., 1986; Gomes et al., 1988; Weiner et al., 1986, 1988, to name a few). Schadt et al. numerically simulated the coupled wave equations describing the changes of pump and Stokes envelopes (Schadt et al., 1986) and the effect of XPM on pump and Stokes spectra (Schadt & Jaskorzynska, 1987a) in nonlinear and dispersive optical fibers. Manassah (1987a, b) obtained analytical solutions for the phase and shape of a weak Raman pulse amplified during the pump and Raman pulse walk-off. The spectral effects of XPM on picosecond Raman pulses propagating in optical fibers were measured and characterized (Islam et al., 1987a, b; Alfano et al., 1987b; Baldeck et al., 1987b, d). In this section, we review (1) Schadt and Jaskorzynska theoretical analysis of stimulated Raman scattering in optical fibers and (2) measurements of XPM and SPM effects on stimulated Raman scattering.

4.4.1 Theory of XPM with SRS

The following theoretical study of stimulated Raman scattering generation of picosecond pulses in optical fibers is from excerpts from Schadt et al. (1986) and Schadt and Jaskorzynska (1987a).

In the presence of copropagating Raman and pump pulses, the nonlinear polarization can be approximated in the same way as in Sect. 4.2.1 by

$$P^{NL}(r, z, t) = \chi^{(3)} E^3(r, z, t), \tag{4.19}$$

where the total electric field $E^3(r, z, t)$ is given by

$$E(r, z, t) = \frac{1}{2}\left\{A_p(r, z, t)\, e^{i(\omega_P t - \beta_P z)} + A_s(r, z, t)\, e^{i(\omega_S t - \beta_S z)} + c.c.\right\}. \tag{4.20}$$

In this case, $A_1 = A_p$ and $A_2 = A_s$.

The subscripts P and S refer to the pump and Stokes Raman pulses, respectively. The anti-Stokes Raman is neglected. Substituting Eq. (4.20) into Eq. (4.19) and keeping only terms synchronized with either pump or Stokes carrier frequency, the nonlinear polarization becomes

$$P_P^{NL}(z,t) = \frac{3}{8}\left\{i2\chi_R^{(3)}|A_S|^2 + \chi_{PM}^{(3)}\left[|A_P|^2 + 2|A_S|^2\right]\right\} A_P e^{i(\omega_P t - \beta_P z)} + c.c., \tag{4.21a}$$

$$P_S^{NL}(z,t) = \frac{3}{8}\left\{-i2\chi_R^{(3)}|A_P|^2 + \chi_{PM}^{(3)}\left[|A_S|^2 + 2|A_P|^2\right]\right\} A_S e^{i(\omega_S t - \beta_S z)} + c.c., \tag{4.21b}$$

where $\chi^{(3)} = \chi_{PM}^{(3)} + i\chi_R^{(3)}$, $\chi_R^{(3)}$ gives rise to the Raman gain (or depletion) of the probe (or pump), and $\chi_{PM}^{(3)}$ leads to self- and cross-phase modulations. Note the factor 2 associated with XPM.

As in the pump-probe case, the phase shift contribution of the nonlinear polarization at the pump (or Raman) frequency depends not only on the pump (or Raman) peak power but also on the Raman (or pump) peak power. This gives rise to cross-phase modulation during the Raman scattering process.

Using the expressions for P_P^{NL} and P_S^{NL} in the nonlinear wave equation leads to the coupled nonlinear dispersive equations for Raman and pump pulses:

$$\begin{aligned}\frac{\partial A_P}{\partial Z} + \frac{z_K}{z_W}\frac{\partial A_P}{\partial T} + \frac{i}{2}\frac{z_K}{z_D}\frac{\partial^2 A_P}{\partial T^2} = &-\frac{1}{2}\frac{\Omega_P}{\Omega_S}\frac{z_K}{z_A}|A_S|^2 A_P + \frac{i}{2}\left[|A_P|^2 + 2|A_S|^2\right]A_P \\ &-\frac{z_K}{z_L}A_P,\end{aligned} \tag{4.22a}$$

$$\begin{aligned}\frac{\partial A_S}{\partial Z} + \frac{i}{2}\frac{k_R''}{k_P''}\frac{z_K}{z_D}\frac{\partial^2 A_S}{\partial T^2} = &\frac{1}{2}\frac{z_K}{z_A}|A_P|^2 A_S + \frac{i}{2}\frac{\Omega_S}{\Omega_P}\left[|A_S|^2 + 2|A_P|^2\right]A_S \\ &-\frac{\Gamma_S}{\Gamma_P}\frac{z_K}{z_L}A_S,\end{aligned} \tag{4.22b}$$

where $A_1 = a_1/|a_{0P}|$ are the complex amplitudes a_1 normalized with respect to the initial peak amplitude $|a_{0P}|$ of the pump pulse. The index $1 = P$ refers to the pump, whereas $1 = S$ refers to the Stokes pulse. $Z = z/z_K$ and $T = (t - z/v_s)/\tau_0$ are the normalized propagation distance and the retarded time normalized with respect to the duration of the initial pump pulse. $\Omega = \omega/(1/\tau_0)$ is a normalized frequency. Moreover, the following quantities were introduced:

- $z_K = 1/\gamma_P |a_{0P}|^2 = 1/(|a_{0P}|^2 n_2 \omega_P/c)$ is the Kerr distance, with the PM coefficient γ_P, the Kerr coefficient n_2, and ω_P as the carrier frequency of the pump pulse; c is the velocity of light.
- $z_W = \tau_0/\left(v_p^{-1} - v_s^{-1}\right)$ is the walk-off distance; v_p and v_s are the group velocities at the pump and Stokes frequencies, respectively.
- $z_D = \tau_0^2/k_P''$ is the dispersion length; $k''_P = \partial^2 k_P/\partial\omega^2$, where k_P is the propagation constant of the pump.
- $z_D = 1/\alpha_S |a_{0P}|^2 = 1/\gamma|a_{0P}|^2$ is the amplification length, with g the Raman gain coefficient.

$z_L = 1/\Gamma_P$ is the pump loss distance, where Γ_P is the attenuation coefficient at the pump frequency.

The derivation of Eqs. (4.22a and 4.22b) assumes that a quasisteady-state approximation holds. Thus, it restricts the model to pulses much longer than the vibrational dephasing time (∼100 fs) of fused silica. The Raman gain or loss is assumed to be constant over the spectral regions occupied by the Stokes and pump pulses, respectively. Furthermore, the quasimonochromatic approximation is used, which is justified as long as the spectral widths of the pulses are much smaller than their carrier frequencies. As a consequence of these simplifications, the considered spectral broadening of the pulses is a result only of phase modulations and pulse reshaping. The direct transfer of the chirp from the pump to the Stokes pulse by SRS is not described by the model. The frequency dependence of the linear refractive index is included to a second-order term, so both the walk-off arising from a group velocity mismatch between the pump and Stokes pulses and the temporal broadening of the pulses are considered.

Using Eqs. (4.22a) and (4.22b), Schadt and Jaskorzynska numerically simulated the generation of picosecond Raman pulses in optical fibers. They particularly investigated the influence of walk-off on the symmetry properties of pulse spectra and temporal shapes and the contributions from SPM and XPM to the chirp of the pulses.

4.4.1.1 Influence of Walk-Off on the Symmetry Properties of the Pulse Spectra

Results obtained in absence of walk-off are shown in Fig. 4.19 (Schadt & Jaskorzynska, 1987a). The pump spectrum, broadened and modulated by SPM, is slightly depleted at its center due the energy transfer toward the Raman pulse (Fig. 4.19a). The Raman spectrum is almost as wide as the pump spectrum, but without modulations (Fig. 4.19b). The spectral broadening of the Raman spectrum arises mainly from XPM. The modulationless feature appears because the Raman pulse, being much shorter than the pump pulse, picks up only the linear part of the XPM-induced chirp. Such a linearly chirped Raman pulse could be efficiently compressed using a grating-pair pulse compressor.

The influence of the walk-off on the Raman process is displayed in Fig. 4.20. The pronounced asymmetry of the spectra in Fig. 4.20a, b is connected with the presence of the pulse walk-off in two different ways. When the Stokes pulse has grown strong enough to deplete the pump pulse visibly, it has also moved toward the leading edge of the pump (it is referred only to regions of normal dispersion). The leading edge has in the meantime been downshifted in frequency as a result of SPM. Consequently, the pump pulse loses energy from the lower-frequency side. On the other hand, the asymmetric depletion of the pump gives rise to the asymmetric depletion buildup of the frequency shift itself, as can be seen from Fig. 4.20c, d. Theoretical spectra in Fig. 4.20 agree very well with measured spectra (Gomes et al., 1986; Weiner et al., 1986; Zysset & Weber, 1986).

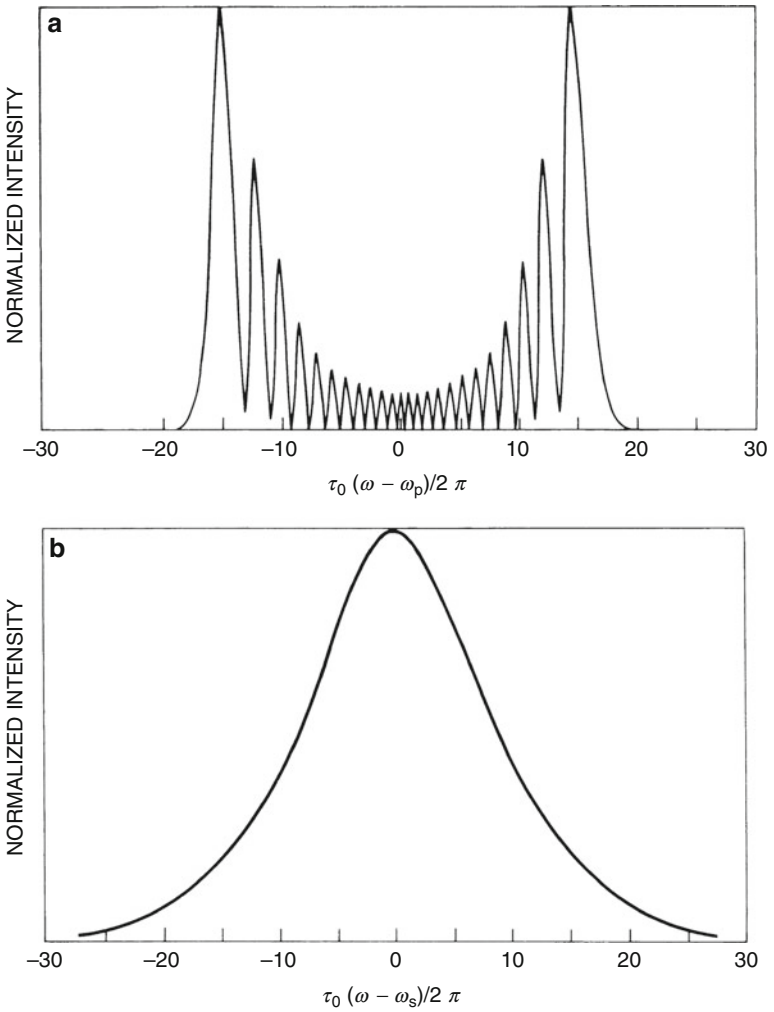

Fig. 4.19 Spectra of pump and Stokes Raman pulses in the absence of walk-off. (**a**) Spectrum of the pump pulse. (**b**) Spectral broadening of the Stokes pulse because of phase modulations. (From Schadt & Jaskorzynska, 1987a)

4.4.1.2 Contributions from Self-Phase Modulation and Cross-Phase Modulation to the Chirp of Pulses

The chirps of Raman and pump pulses originate from SPM and XPM. The contributions from SPM and XPM are independent as long as the effect of second-order dispersion is negligible. In Fig. 4.21 are plotted the contributions to the pump and Stokes chirps coming from either SPM only (Fig. 4.21a, b) or XPM only (Fig. 4.21c, d). The shapes of SPM contributions shown in Fig. 4.21a, b apparently reflect

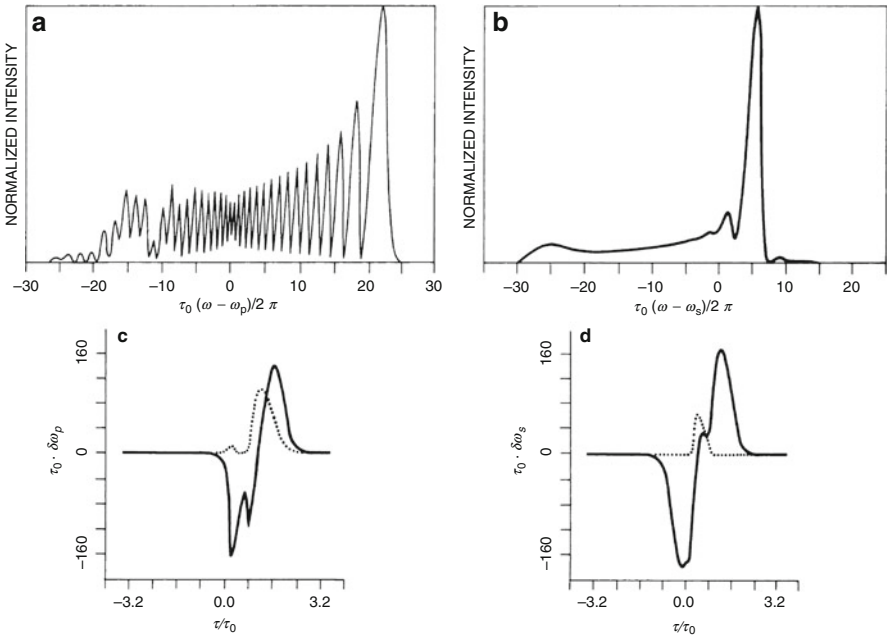

Fig. 4.20 Influence of walk-off on spectra and chirps of pump and Stokes Raman pulses, (**a**) Spectrum of the pump pulse, (**b**) Spectral broadening of the Stokes pulse because of phase modulations, (**c**) Chirp (solid line) and shape (dashed line) of the pump pulse, (**d**) Chirp (solid line) and shape (dashed line) of the Stokes pulse. (From Schadt & Jaskorzynska, 1987a)

the history of their buildup according to the changes of pulse shapes during the propagation. Their strong asymmetry is a result of an asymmetric development of the pulse shapes that is due to walk-off. The XPM affecting the pump pulse in the initial stage of the Raman process plays a lesser role as the pump depletion becomes larger. This constituent of the chirp, associated with the Stokes pulse is built up just in the region where most of the pump energy is scattered to the Stokes frequency if the Raman process goes fast enough. However, if for a fixed walk-off SRS is slow, as in the case illustrated by Fig. 4.21c, the leading part of the pump pulse will remain affected by the XPM.

The most characteristic feature of the XPM-induced part of the Stokes chirp, shown in Figure 4.21d, is a plateau on the central part of the Stokes pulse. In the case of the lower input power (Fig. 4.21d), this plateau can be attributed mainly to the effect of walk-off. Since pump depletion becomes considerable only close to the end of the propagation distance, it has little influence on the buildup of the chirp. For higher input powers, the range over which the chirp vanishes is wider. Consequently, after the walk-off distance, the effect of XPM on the Stokes chirp is negligible for a severely depleted pump, whereas in the case of insignificant pump depletion, the leading part of the Stokes pulse will remain influenced by XPM.

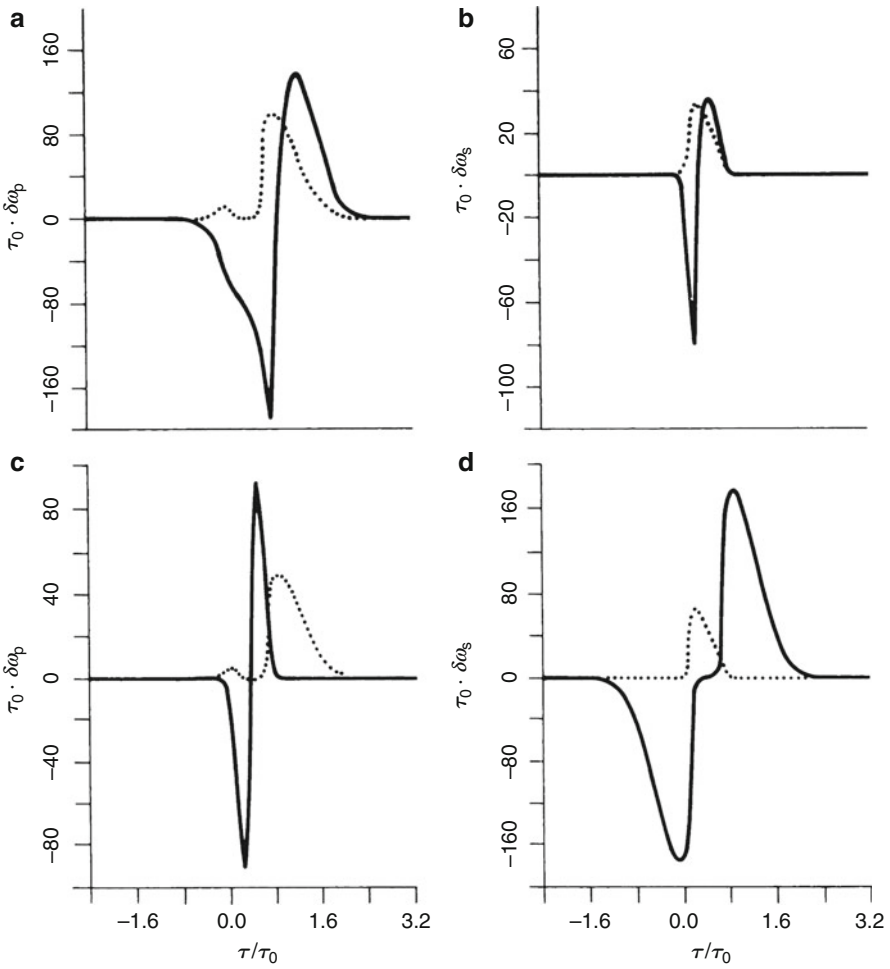

Fig. 4.21 Chirp components that are due to SPM and XPM for the case of walk-off. (**a**) Pump chirp due to SPM only. (**b**) Stokes chirp due to SPM only. (**c**) Pump chirp due to XPM only. (**d**) Stokes chirp due to XPM only. (From Schadt & Jaskorzynska, 1987a)

Schadt et al. have developed a numerical model to describe combined effects of SRS, SPM, XPM, and walk-off in single-mode optical fibers. They explained the influence of the above effects on pump and Stokes spectra and chirps. They separately studied the contributions of SPM and XPM to the chirps and found that both walk-off and pump depletion tend to cancel the effect of XPM on the chirp in the interesting pulse regions. However, for more conclusive results, an investigation of the direct transfer of the pump chirp and consideration of the finite width of the Raman gain curve are needed.

4.4.2 *Experiments*

In the late 1970s and early 1980s, numerous experimental studies investigated the possibility of using SRS to generate and amplify Raman pulses in optical fibers (Stolen, 1979). However, most of these studies involved "long" nanosecond pulses and/or neglected to evaluate SPM and XPM contributions to the pump and Raman spectral broadenings. It was not until 1987, after the success of the first spectral broadening enhancement experiment (Alfano et al., 1986), that measurements of XPM effects on Raman pulses were reported (Islam et al., 1987a; Alfano et al., 1987b). In this section, research work at AT&T Bell Laboratories and at the City College of New York is reported.

4.4.2.1 XPM Measurements with the Fiber Raman Amplification Soliton Laser

Islam et al. showed the effects of pulse walk-off on XPM experimentally in the Fiber Raman Amplification Soliton Laser (FRASL) (Islam et al., 1986). They proved that XPM prevents a fiber Raman laser from producing pedestal-free, transform limited pulses except under restrictive conditions (Islam et al., 1987b). The following simple picture of walk-off effects and experimental evidence is excerpted from reference (Islam et al., 1987a).

The spectral features and broadening resulting from XPM depend on the walk-off between the pump and signal pulses. These spectral features can be confusing and complicated, but Islam et al. show that they can be understood both qualitatively and quantitatively by concentrating on the phase change as a function of walk-off. XPM is most pronounced when the pump and signal are of comparable pulse widths and when they track each other. The phase change $\Delta\varphi$ induced on the signal is proportional to the pump intensity, and the signal spectrum (Fig. 4.22a) looks like that obtained from self-phase modulation (SPM).

The opposite extreme occurs when the phase shift is uniform over the width of the signal pulse. This may happen in the absence of pump depletion or spreading if the pump walks completely through the signal, or if the signal is much narrower than the pump and precisely tracks the pump. XPM is canceled in this limit, and the original spectral width of the signal (much narrower than any shown in Fig. 4.22) results.

A third simple limit exists when the pump and signal coincide at first, but then the pump walks off. This is most characteristic of stimulated amplification processes (i.e., starting from noise) and may occur also in synchronously-pumped systems such as the FRASL. The net phase change turns out to be proportional to the integral of the initial pump pulse, and, as Fig. 4.22b shows, the signal spectrum is asymmetric and has "wiggles." Figure 4.22c treats the intermediate case where the pump starts at the trailing edge of the signal, and in the fiber walks through to the leading edge. A symmetric spectrum results if the walk-off is symmetric.

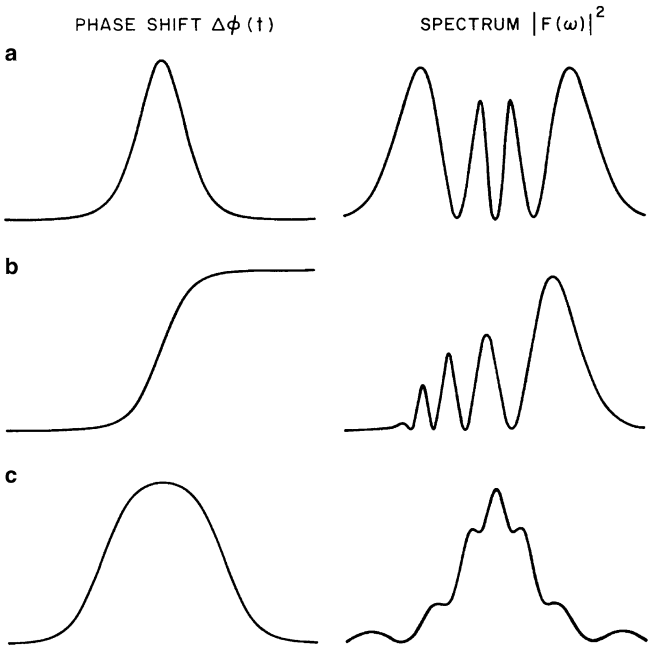

Fig. 4.22 Phase shifts and spectra corresponding to various degrees of walk-off between pump and signal pulses. (**a**) Perfect tracking case ($t_0 = \beta = 0$, $2A^2 l = 3.5\pi$, $\alpha = 1$); (**b**) pump and signal coincide initially, and then pump walks off ($t_0 = 0$, $\beta l = 4$, $2A^2/\beta = 3.5\pi$, $\alpha = 1$); and (**c**) pump walks from trailing edge of signal to the leading edge ($t_0 = -2$, $\beta l = 4$, $2A^2/\beta = 3.5\pi$, $\alpha = 1$). (From Islam et al., 1987a)

A FRASL consists of a optical fiber ring cavity that is synchronously pumped by picosecond pulses and designed to lase at the stimulated Raman scattering Stokes wavelength (Fig. 4.23). To obtain the generation of soliton Raman pulses, the pump wavelength is chosen in the positive group velocity dispersion region of the optical fiber, whereas the Raman wavelength is in the negative group velocity dispersion region. Inserting a narrowband tunable etalon in the resonant ring, Islam et al. turned their laser in a pump-probe configuration in which they could control the seed feedback into the fiber and observe the spectral broadening in a single pass. The effect of walk-off on XPM could be studied by changing the fiber length in the cavity. Output Raman signals were passed through a bandpass filter to eliminate the pump and then sent to a scanning Fabry-Perot and an autocorrelator.

When a 50-m fiber is used in the FRASL ($l < l_w$), the signal remains with the pump throughout the fiber. With no etalon in the cavity, the signal spectrum is wider than the 300-cm^{-1} free spectral range of the Fabry-Perot. Even with the narrow-passband etalon introduced into the cavity, the spectral width remains greater than 300 cm^{-1} (Fig. 4.24a). Therefore, more or less independent of the seed, the pump in a single pass severely broadens the signal spectrum. As expected from theory, the Raman spectrum is featureless.

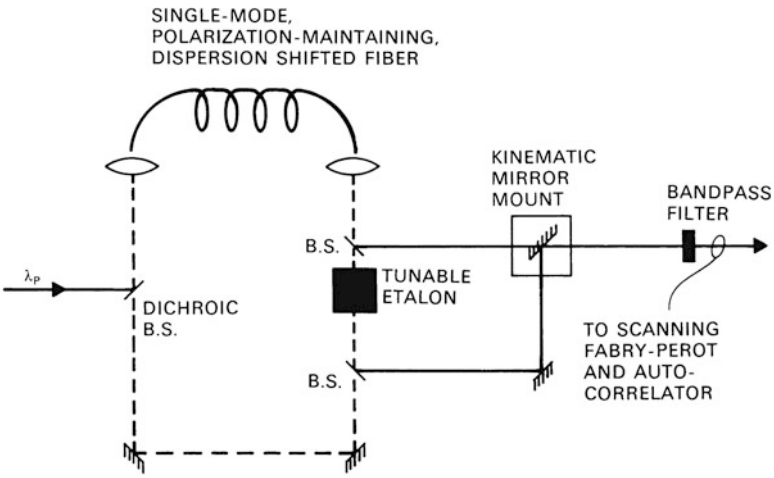

Fig. 4.23 Modified fiber Raman amplification soliton laser (FRASL). B.S., beam splitter. (From Islam et al., 1987a)

If the fiber length is increased to 100 m ($l \approx l_w$), there is partial walk-off between the pump and signal, and XPM again dominates the spectral features. Without an etalon in the FEASL cavity, the emerging spectrum is wide and has wiggles (Fig. 4.24b). By time dispersion tuning the FRASL, thus varying the amount of walk-off, the details of the spectrum can be changed as shown in Fig. 4.24c. Even after the etalon is inserted and the cavity length appropriately adjusted, the spectrum remained qualitatively the same (Fig. 4.24d).

When there is complete walk-off between pump and signal ($l = 400$ m $\gg l_w$), without an etalon, the spectrum is symmetric and secant-hyperboliclike, although still broad (Fig. 4.24e). The effects of XPM are reduced considerably, but they are not canceled completely because the walk-off is asymmetrized by pump depletion. As Fig. 4.24f shows, the addition of the etalon narrows the spectrum (the narrow peak mimics the seed spectrum). However, XPM still produces a broad spectral feature (at the base of the peak), which is comparable in width to the spectrum without the filter (Fig. 4.24e). In autocorrelation, it was found that the low-level wider feature corresponded to a $\tau \approx 250$ f. peak, while the narrow spectral peak results in a broader $\tau \approx 2.5$ ps pulse.

With these experimental results, Islam et al. have conclusively assessed the effects of walk-off on Raman XPM. It should be noted that, despite the long nonlinear interaction lengths, spectral broadenings were small and the SPM generated by the Raman pulse itself was negligible. Furthermore, measured spectral features were characteristic of XPM for the Raman amplification scheme, as expected for the injection of Raman seed pulses in the optical fiber loop.

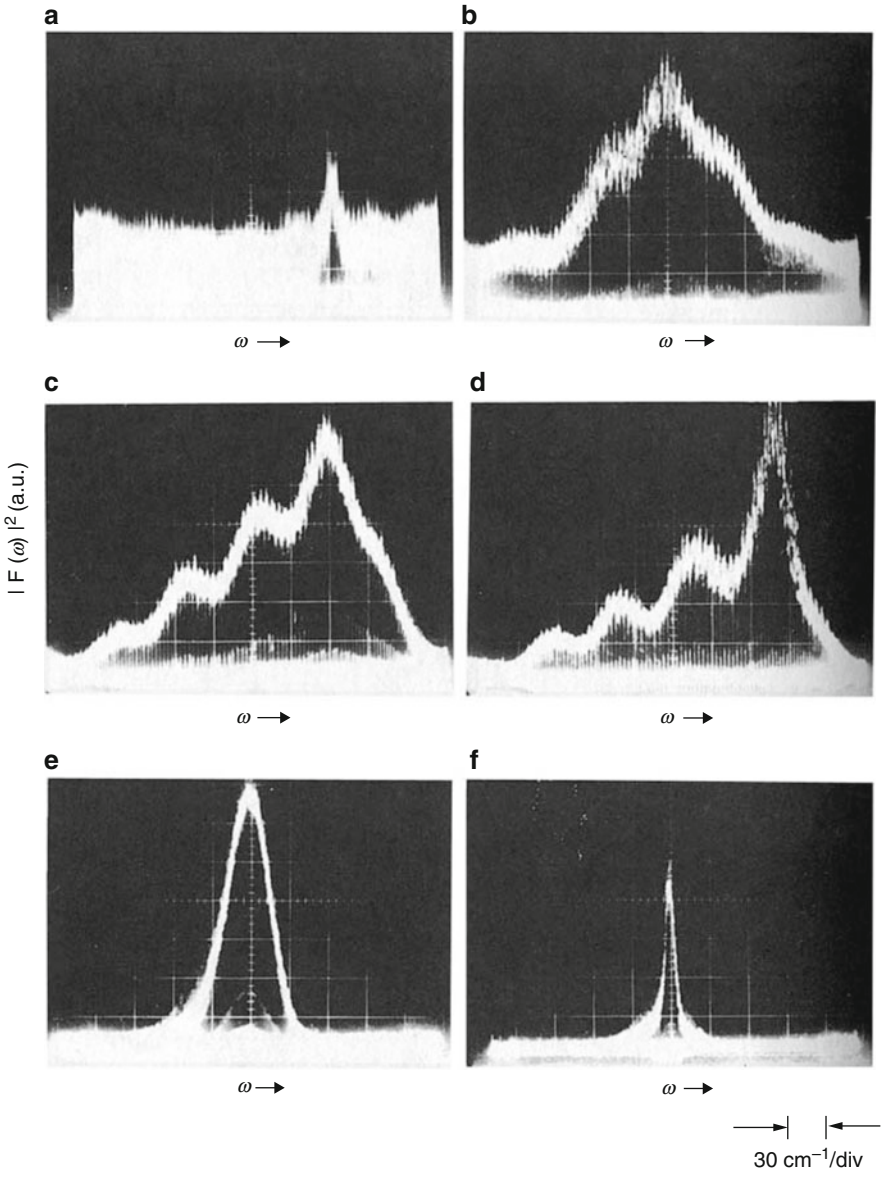

Fig. 4.24 Experimental spectra for various fiber lengths (l) with and without the tunable etalon in the FRASL cavity. (**a**) $l = 50$ m with etalon in cavity. (**b**) $l = 100$ m, no etalon. (**c**) $l = 100$ m, no etalon, but different FRASL cavity length than in (**b**). (**d**) Same as (**c**), except with etalon inserted. (**e**) $l = 400$ m, no etalon. (**f**) Same as (**e**), except with etalon inserted. Here, except for the wings, the spectrum is nearly that of the etalon. The vertical scales are in arbitrary units, and the signal strength increases for increasing fiber lengths. (From Islam et al., 1987a)

4.4.2.2 Generation of Picosecond Raman Pulses in Optical Fibers

Stimulated Raman scattering of ultrashort pulses in optical fibers attracts a great deal of interest because of its potential applications for tunable fiber lasers and all-optical amplifiers. XPM effects on weak Raman pulses propagating in long low-dispersive optical fibers were characterized in the preceding section. Temporal and spectral modifications of pump and Raman pulses are more complex to analyze when Raman pulses are generated in short lengths (i.e., high Raman threshold) of very dispersive optical fibers. In addition to XPM and walk-off, one has to take into account pump depletion, SPM of the Raman pulse, Raman-induced XPM of the pump pulse, group velocity dispersion broadening, higher-order SRS, and XPM-induced modulation instability. This section presents measurements of the generation of Raman picosecond pulses from the noise using short lengths of a single-mode optical fiber (Alfano et al., 1987b; Baldeck et al., 1987b–d).

A mode-locked Nd:YAG laser was used to generate 25-ps time duration pulses at $\lambda = 532$ nm with a repetition rate of 10 Hz. The optical fiber was custom-made by Corning Glass. It has a 3-μm core diameter, a 0.24% refractive index difference, and a single-mode cutoff at $\lambda = 462$ nm. Spectra of output pulses were measured using a grating spectrometer (1 m, 600 lines/mm) and recorded with an optical multichannel analyzer OMA2. Temporal profiles of pump and Raman pulses were measured using a 2-ps resolution Hamamatsu streak camera.

Spectra of pump and Raman pulses, which were measured for increasing pump energy at the output of short fiber lengths, are plotted in Fig. 4.25. The dashed line in Fig. 4.25a is the reference laser spectrum at low intensity. Figures 4.25a (solid line) and 4.25b show spectra measured at the Raman threshold at the output of 1- and 6-m-long optical fibers, respectively. The Raman line appears at $\lambda = 544.5$ nm (about 440 cm^{-1}). The laser line is broadened by SPM and shows XPM-induced sidebands, which are discussed in Sect. 4.8. For moderate pump intensities above the stimulated Raman scattering threshold, spectra of Raman pulses are broad, modulated, and symmetrical in both cases (Fig. 4.25c, d). For these pump intensities, the pulse walk-off (6 m corresponds to two walk-off lengths) does not lead to asymmetric spectral broadening. For higher pump intensities, Raman spectra become much wider (Fig. 4.25e, f). In addition, spectra of Raman pulses generated in the long fiber are highly asymmetric (Fig. 4.25f). The intensity-dependent features observed in Fig. 4.24 are characteristic of spectral broadenings arising from nonlinear phase modulations such as SPM and XPM as predicted by the theory (Sect. 4.4.1). At the lowest intensities XPM dominates, while at the highest intensities, the SPM generated by the Raman pulse itself is the most important. However, it should be noted that the widths of Raman spectra shown in Fig. 4.25 are one order of magnitude larger than expected from the theory. Modulation instability induced by pump pulses could explain such a discrepancy between measurements and theory (Sect. 4.8).

Temporal measurements of the generation process were performed to test whether the spectral asymmetry originated from the pump depletion reshaping as in the case of longer pulses (Schadt et al., 1986). Pump and Raman profiles were

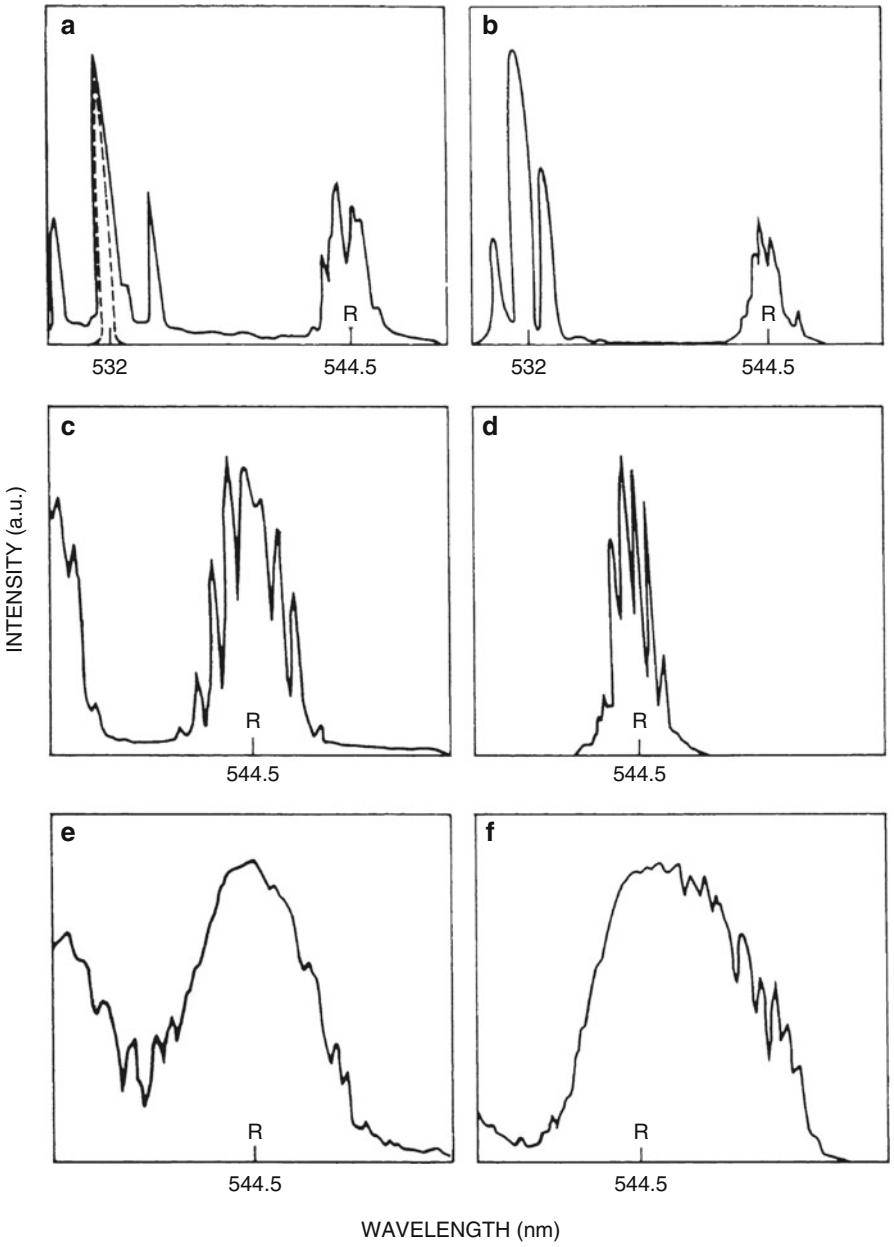

Fig. 4.25 Spectra of picosecond Raman pulses generated in short lengths of a single-mode optical fiber. The laser and Raman lines are at 532 and 544.5 nm, respectively. Results in the left column and right column were obtained with 1- and 6-m-long single-mode optical fibers, respectively. (**a** and **b**) Dashed line: referenced of laser spectrum at low intensity; solid line: pump and Raman lines near the stimulated Raman scattering threshold. Frequency sidebands about the laser line are XPM-induced modulation instability sidebands (see Sect. 4.8). (**c** and **d**) Raman spectra for moderate pump peak powers above threshold. (**e** and **f**) Raman spectra for higher pump peak powers. (From Baldeck et al., 1987c, d)

measured at the output of a 17-m-long fiber (Fig. 4.26). The dotted line is for a pump intensity at the SRS threshold and the solid line for a higher pump intensity. The leading edge of the pump pulse is partially "eaten" but is not completely emptied because of the quick walk-off between pump and Raman pulses. Thus, the leading edge of the pump pulse does not become very sharp, and the contribution of pump depletion effects to the spectral asymmetry of pump and Raman pulses does not seem to be significant.

Figure 4.26 shows a typical sequence of temporal profiles measured for input pump intensities strong enough to generate higher-order stimulated Raman scattering lines. The temporal peaks are the maxima of high-order SRS scatterings that satisfy the group velocity dispersion delay of 6 ps/m for each frequency shift of 440 cm^{-1}. These measurements show that (1) the Raman process clamps the peak power of pulses propagating into an optical fiber to a maximum value and (2) high-order stimulated Raman scatterings occur in cascade during the laser pulse propagation.

4.4.2.3 Generation of Femtosecond Raman Pulses in Ethanol

Nonlinear phenomena such as supercontinuum generation and stimulated Raman scattering were first produced in unstable self-focusing filaments generated by intense ultrashort pulses in many liquids and solids. Optical fibers are convenient media for studying such nonlinear phenomena without the catastrophic features of collapsing beams. However, optical fibers are not suitable for certain applications such as high-power experiments, the generation of larger Raman shifts (>1000 cm^{-1}), and Raman pulses having high peak powers (>1 MW). In this section, spectral measurements of SRS generation in ethanol are presented. Spectral shapes are shown to result from the combined effects of XPM, SPM, and walk-off.

Spectral measurements of SRS in ethanol have been performed using the output from a CPM ring dye amplifier system (Baldeck et al., 1987b). Pulses of 500 f duration at 625 nm were amplified to an energy of about 1 mJ at a repetition rate of 20 Hz. Pulses were weakly focused into a 20-cm-long cell filled with ethanol. Output pulses were imaged on the slit of a $\frac{1}{2}$-m Jarrell-Ash spectrometer, and spectra were recorded using an optical multichannel analyzer OMA2.

Ethanol has a Raman line shifted by 2928 cm^{-1}. Figure 4.27 shows how the Stokes spectrum of the Raman line changes as a function of the pump intensity. Results are comparable to those obtained using optical fibers. At low intensity, the Stokes spectrum is narrow and symmetrical (Fig. 4.27). As the pump intensity increases, the Raman spectrum broadens asymmetrically with a long tail pointing toward the longer wavelengths. Spectra of the anti-Stokes Raman line were also measured (Baldeck et al., 1987b). They were as wide as Stokes spectra but with tails pointing toward the shortest wavelengths, as predicted by the sign of the walk-off parameter.

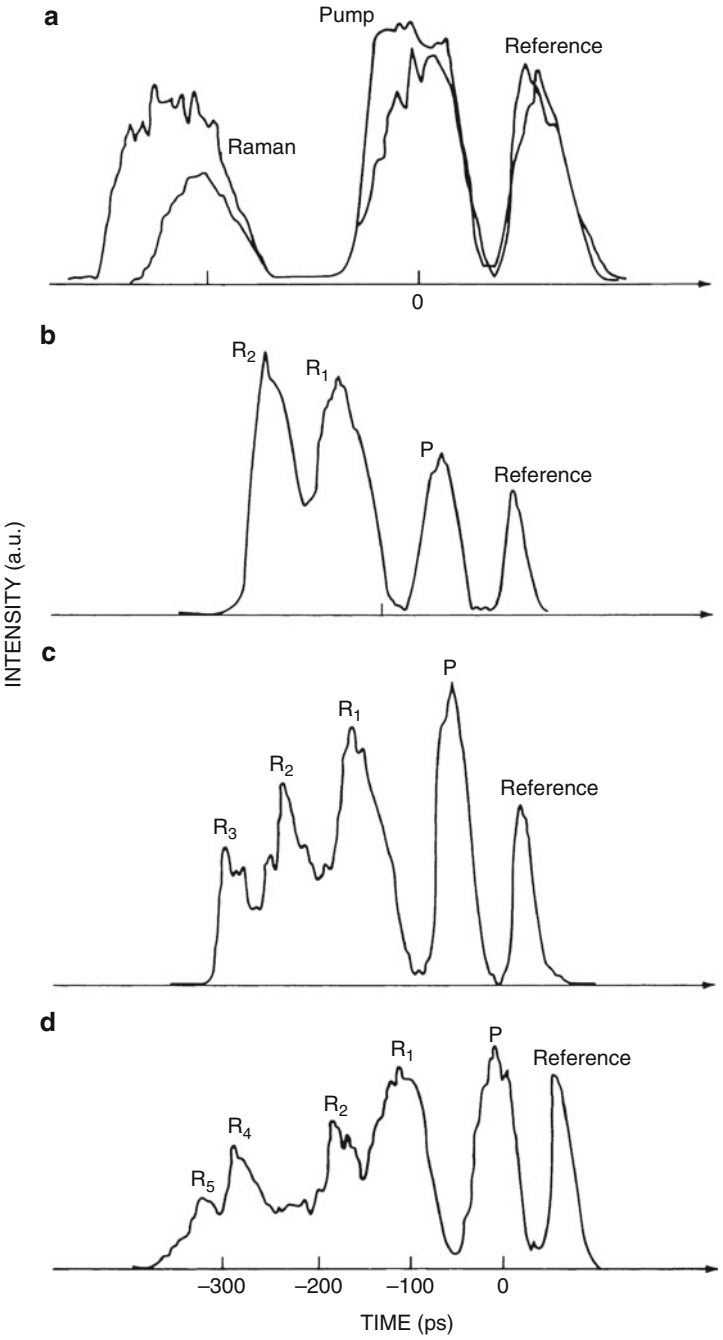

Fig. 4.26 Temporal shapes of reference pulse, pump pulse, and SRS pulses at the output of a 17-m-long single-mode optical fiber for increasing pump intensity. (**a**) First-order SRS for slightly different pump intensity near threshold. (**b**) First- and second-order SRS. (**c**) First- to third-order SRS. (**d**) First- to fifth-order SRS. (From Baldeck et al., 1987d)

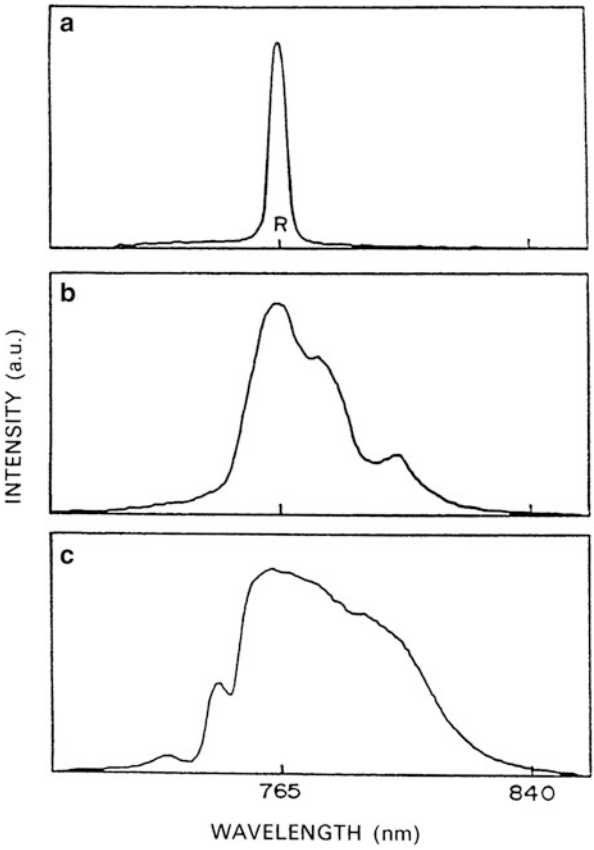

Fig. 4.27 Effects of cross- and self-phase modulations on the Stokes-shifted Raman line generated by 500-fs pulses in ethanol. (**a**–**c**) Increasing laser intensity. (From Baldeck et al., 1987b)

4.5 Harmonic Cross-Phase Modulation Generation in ZnSe

Like stimulated Raman scattering, the second harmonic generation (SHG) process involves the copropagation of a weak generated-from-the-noise pulse with an intense pump pulse. The SHG of ultrashort pulses occurs simultaneously with cross-phase modulation, which affects both the temporal and spectral properties of second harmonic pulses. In this section, measurements of XPM on the second harmonic generated by an intense primary picosecond pulse in ZnSe crystals are reported (Alfano et al., 1987a; Ho et al., 1988).

The laser system consisted of a mode-locked Nd:glass laser with single-pulse selector and amplifier. The output laser pulse had about 2 mJ energy and 8 ps duration at a wavelength of 1054 nm. The 1054-nm laser pulse was weakly focused into the sample. The spot size at the sample was about 1.5 mm in diameter. The second harmonic produced in this sample was about 10 nJ. The incident laser energy was controlled using neutral density filters. The output light was sent through a $\frac{1}{2}$-m Jarrell-Ash spectrometer to measure the spectral distribution of the signal light. The

1054-nm incident laser light was filtered out before detection. A 2-ps time resolution Hamamatsu streak camera system was used to measure the temporal characteristics of the signal pulse. Polycrystalline ZnSe samples 2, 5, 10, 22, and 50 mm thick were purchased from Janos, Inc., and a single crystal of ZnSe 16-mm thick was grown at Philips.

Typical spectra of nonphase-matched SHG pulses generated in a ZnSe crystal by 1054-nm laser pulses of various pulse energies are displayed in Fig. 4.28. The spectrum from a quartz sample is included in Fig. 4.28d for reference. The salient features of the ZnSe spectra indicate that the extent of the spectral broadening about the second harmonic line at 527 nm depends on the intensity of the 1054-nm laser pulse. When the incident laser pulse energy was 2 mJ, there was significant spectral broadening of about 1100 cm^{-1} on the Stokes side and 770 cm^{-1} on the anti-Stokes side (Fig. 4.29). There was no significant difference in the spectral broadening distribution measured in the single and polycrystalline materials. The spectral width of the SHG signal is plotted for the Stokes and anti-Stokes sides as a function of the incident pulse energy in Fig. 4.30. The salient feature of Fig. 4.30 is that the Stokes side of the spectrum is broader than the anti-Stokes side. When the incident pulse energy was less than 1 mJ, the spectral broadening was found to be monotonically increasing on the pulse energy of 1054 nm. The spectral broadening generated by sending an intense 80-μJ, 527-nm, 8-ps laser pulse alone through these ZnSe crystals was also measured for comparison with the $\pm$1000 cm^{-1} induced spectral broadening. The observed spectral broadening was only 200 cm^{-1} when the energy of the 527-nm pulse was over 0.2 mJ. This measurement suggests that the self-phase modulation process from the 10-nJ SHG pulse in ZnSe is too insignificant to explain the observed 1000 cm^{-1}. Most likely, the broad spectral width of the SHG signal arises from the XPM generated by the pump during the generation process.

The temporal profile and propagation time of the intense 1054-nm pump pulse and the second harmonic pulse propagating through a 22-mm ZnSe polycrystalline sample is shown in Fig. 4.31. A pulse delay of $\sim$189 ps at 1054 nm was observed (Fig. 4.31a) when an intense 1054-nm pulse passed through the crystal. The second harmonic signal, which spread from 500 to 570 nm, indicated a sharp spike at 189 ps and a long plateau from 189 to 249 ps (Fig. 4.31b). Using 10-nm bandwidth narrowband filters, pulses of selected wavelengths from the second harmonic signal were also measured. For example, time delays corresponding to the propagation of two pulses with wavelengths centered at 530 and 550 nm are displayed in Fig. 4.31c, d, respectively. All traces from Fig. 4.31 indicated that the induced spectrally broadened pulses have one major component emitted at nearly the same time as the incident pulse (Fig. 4.31a). The selected wavelength shifted 10 nm from the second harmonic wavelength has shown a dominant pulse distribution generated at the end of the crystal. Furthermore, when a weak 3-nJ, 527-nm calibration pulse propagated alone through the 22-mm ZnSe, a propagation time of about 249 ps was observed, as expected from the group velocity.

The difference in the propagation times of a weak 527-nm calibration pulse and a 1054-nm pump pulse through a ZnSe crystal can be predicted perfectly by the difference in group velocities. The measured group refractive indices of ZnSe can

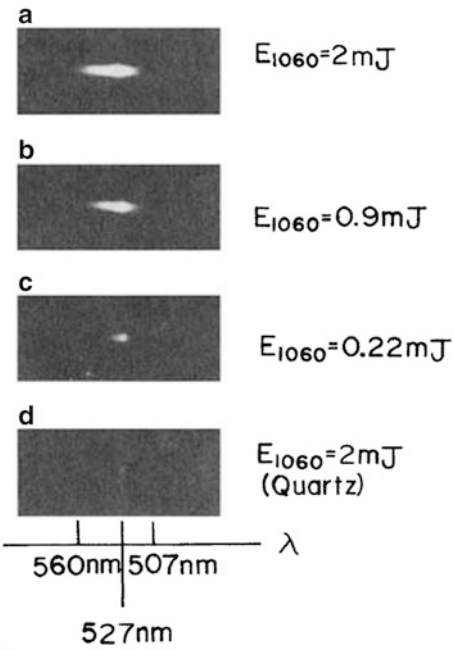

Fig. 4.28 Induced spectral broadening spectra in ZnSe crystal excited by an intense 1060-nm laser pump. In (d), the ZnSe crystal was replaced by a 3.7-cm-long quartz crystal. (From Alfano et al., 1987a)

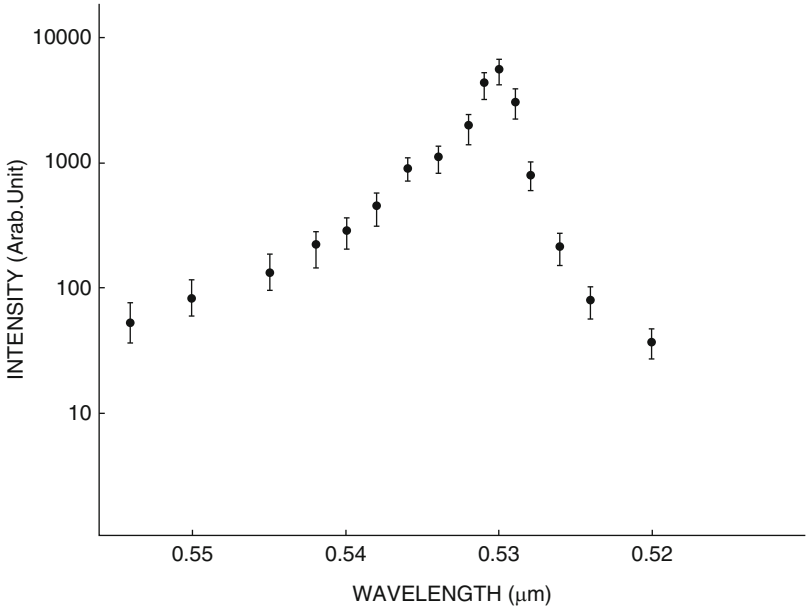

Fig. 4.29 Spectral measurement of the induced spectrally broadened pulse about $\lambda = 527$ nm by sending a 1054-nm pulse through 22-mm ZnSe. (From Alfano et al., 1988)

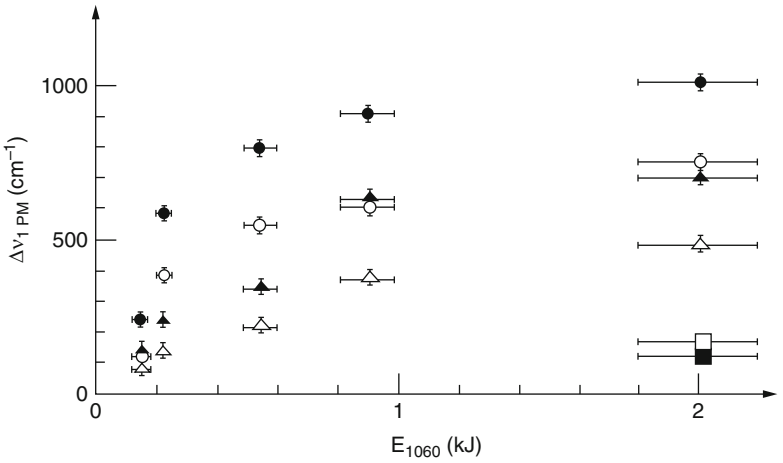

Fig. 4.30 Intensity dependence of induced spectral width about 530 nm in ZnSe pumped by a 1060-nm laser pulse. The horizontal axis is the incident laser pulse energy. (○) 2.2-cm-long polycrystalline ZnSe anti-Stokes broadening. (•) 2.2-cm-long polycrystalline ZnSe Stokes broadening. (▲) 1.6-cm-long single-crystal ZnSe anti-Stokes broadening. (△) 1.6-cm-long single-crystal ZnSe Stokes broadening. (□) 3.7-cm-long quartz crystal anti-Stokes broadening. (■) 3.7-cm-long quartz crystal Stokes broadening. The measured Δn is defined as the frequency spread from 527 nm to the farthest detectable wavelengths measured either photographically or by an optical multichannel analyzer. (From Alfano & Ho, 1988)

be fitted to $n_{g,1054} = 3.39$ and $n_{g,1054} = 2.57$, respectively. These values are in agreement with the calculated values.

The sharp spike and plateau of the second harmonic pulse can be explained using the XPM model of second harmonic generation (Ho et al., 1980). Because of lack of phase matching, i.e., destructive interferences, the energy of the second harmonic pulse cannot build up along the crystal length. As a result, most of the second harmonic power is generated at the exit face of the crystal, which explains the observed spike. However, since very intense pump pulses are involved, there is a partial phase matching due to the cross-phase modulation and two photon absorption effects at the second harmonic wavelength. Some second harmonic energy can build up between the entrance and exit faces of the sample, which explains the plateau feature.

4.6 Cross-Phase Modulation and Stimulated Four-Photon Mixing in Optical Fibers

Stimulated four-photon mixing (SFPM) is an ideal process for designing parametric optical amplifiers and frequency converters. SFPM is produced when two high-intensity pump photons are coupled by the third-order susceptibility $\chi^{(3)}$ to generate

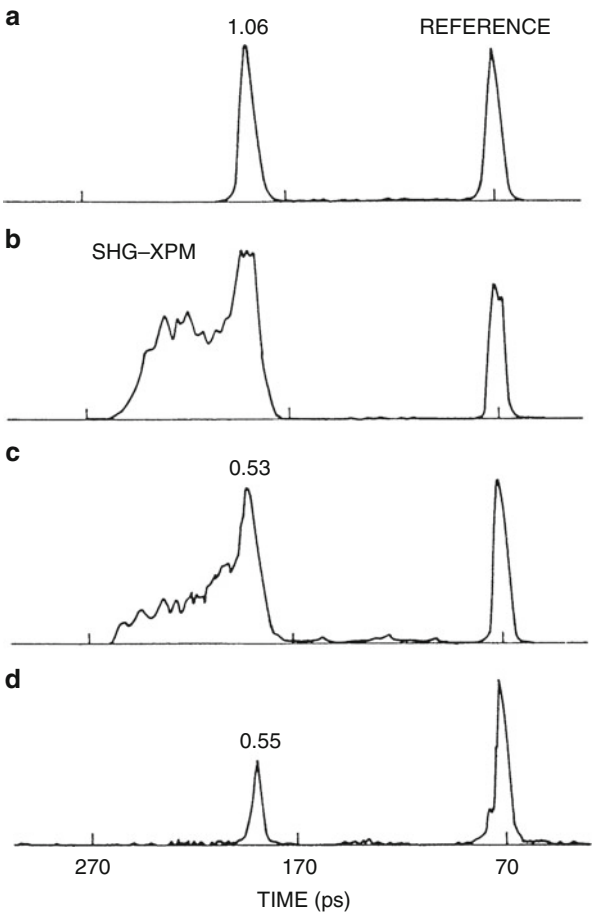

Fig. 4.31 Temporal profile and propagation delay time of (**a**) incident 1054 nm, (**b**) SHG-XPM signal of all visible spectra, and (**c**) selected 530 nm from SHG-XPM of a 22-nm-long ZnSe crystal measured by a 2-ps resolution streak camera system. (**d**) same as (**c**) for a signal selected at 550 nm. The reference time corresponds to a laser pulse traveling through air without the crystal. The right side of the time scale is the leading time. The vertical scale is an arbitrary intensity scale. (From Alfano & Ho, 1988)

a Stokes photon and an anti-Stokes photon. The frequency shifts of the SFPM waves are determined by the phase-matching conditions, which depend on the optical geometry. SFPM was produced in glass by Alfano and Shapiro (1970) using picosecond pulses. Later, SFPM was successfully demonstrated by a number of investigators in few mode, birefringent, and single-mode optical fibers (Stolen, 1975; Stolen et al., 1981; Washio et al., 1980). Most of the earlier experiments using optical fibers were performed with nanosecond pulses. Lin and Bosch (1981) obtained large-frequency shifts; however, the spectral dependence on the input intensity was not investigated. In the following, measurements of the intensity dependence of SFPM spectra generated by 25-ps pulses in an optical fiber are reported (Baldeck & Alfano, 1987). For such short pulses, spectra are influenced by the combined effects of SPM and XPM. The broadening of SFPM lines and the formation of frequency continua are investigated.

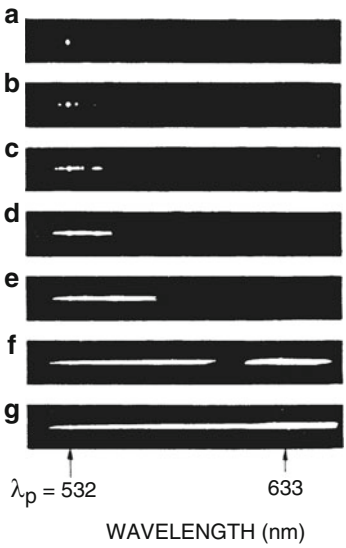

Fig. 4.32 Evolution of a stimulated four-photon spectrum with increasing pulse intensity. (**a**) $I < 10^8$ W/cm^2; (b and c) $I = 5 \times 10^8$ W/cm^2; (**d**) $I = 10 \times 10^8$ W/cm^2; (**e**) $I = 15 \times 10^8$ W/cm^2; (**f**) $I = 30 \times 10^8$ W/cm^2; (g) $I = 35 \times 10^8$ W/cm^2. (From Baldeck & Alfano, 1987)

The experimental method is as follows. A Quantel frequency-doubled mode-locked Nd: YAG laser produced 25-ps pulses. An X20 microscope lens was used to couple the laser beam into the optical fiber. The spectra of the output pulses were measured using a 1-m, 1200 lines/mm grating spectrometer. Spectra were recorded on photographic film and with an optical multichannel analyzer OMA2. Average powers coupled in the fiber were measured with a power meter at the optical fiber output. The 15-m-long optical fiber had a core diameter of 8 mm and a normalized frequency $V = 4.44$ at 532 nm. At this wavelength, the four first LP modes (LP_{01}, LP_{11}, LP_{21}, and LP_{02}) were allowed to propagate.

Typical intensity-dependent spectra are displayed in Figs. 4.32, 4.33, and 4.34. At low intensity, $I < 10^8$ W/cm^2, the output spectrum contains only the pump wavelength $\lambda = 532$ nm (Fig. 4.32a). At approximately 5×10^8 W/cm^2, three sets of symmetrical SFPM lines (at $\Omega = 50$, 160, and 210 cm^{-1}) and the first SRS Stokes line (at 440 cm^{-1}) appear (Fig. 4.32b, c). As the intensity increases, the SFPM and SRS lines broaden, and a Stokes frequency continuum is generated (Fig. 4.32d, e). Above an intensity threshold of 20×10^8 W/cm^2, new sets of SFPM lines appear on the Stokes and anti-Stokes sides with frequency ranging from 2700 to 3865 cm^{-1}. Finally, the large shifts merge (Fig. 4.32f) and contribute to the formation of a 4000 cm^{-1} frequency continuum (Fig. 4.32g). Figure 4.33 shows how the large Stokes shift SFPM lines are generated and broaden when the pump intensity increases from 20×10^8 to 30×10^8 W/cm^2. Figure 4.34 gives two examples of complete spectra including the large-shift anti-Stokes and Stokes lines. The measured SFPM shifts correspond well with the phase-matching condition of SFPM in optical fibers.

Figure 4.35 shows the development of a Stokes continuum from the combined effects of SFPM, SRS, SPM, and XPM. As the pump intensity is increased, the

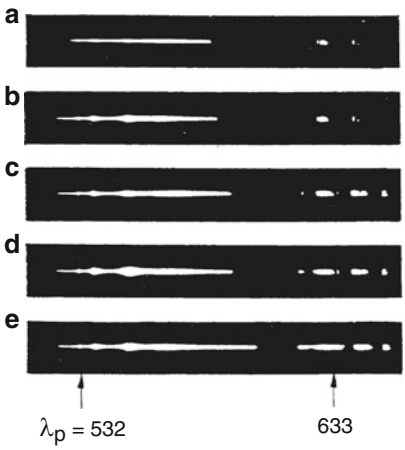

Fig. 4.33 (**a**–**e**) Sequence of the large-shift SFPM line broadening. The pulse peak intensity increases from $I = 20 \times 10^8$ W/cm^2 in (**a**) to $I = 30 \times 10^8$ W/cm^2 in (**e**) in steps of 2.5×10^8 W/cm^2 (From Baldeck & Alfano, 1987.)

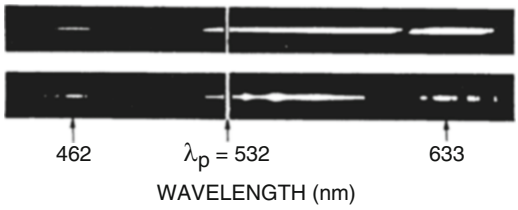

Fig. 4.34 Examples of large-shift Stokes lines with their corresponding anti-Stokes lines. Photographs of the Stokes and anti-Stokes regions were spliced together. (From Baldeck & Alfano, 1987)

pump, SFPM, and first SRS lines broaden and merge (Fig. 4.35a). For stronger pump intensities, the continuum is duplicated by stimulated Raman scattering, and the continuum expands toward the lowest optical frequencies (Fig. 4.35b). As shown, the maximum intensities of new frequencies are self-limited.

The broadening of the SFPM and SRS lines arises from self- and cross-phase modulation effects. It is established that spectral broadenings generated by SPM are inversely proportional to the pulse duration and linearly proportional to the pump intensity. In this experiment, SPM effects are important because of the pump pulse shortness (25 ps) and intensity (10^9 W/cm^2). Furthermore, the modulation that is seen in the continuum spectrum fits well with the spectrum modulation predicted by phase modulation theories.

Figure 4.36 shows the spectral broadening of the anti-Stokes SFPM line of $\lambda = 460$ nm ($\Omega = 2990$ cm^{-1}). This line is a large-shift SFPM anti-Stokes line generated simultaneously with the $\lambda = 633$ nm SFPM Stokes line by the laser pump of $\lambda = 532$ nm (see Fig. 4.34). The corresponding frequency shift and mode distribution are $W = 2990$ cm^{-1} and LP_{01} (pump)–LP_{11} (Stokes and anti-Stokes), respectively. From Figs. 4.36a–d, the peak intensity of the $\lambda = 460$ nm line increases

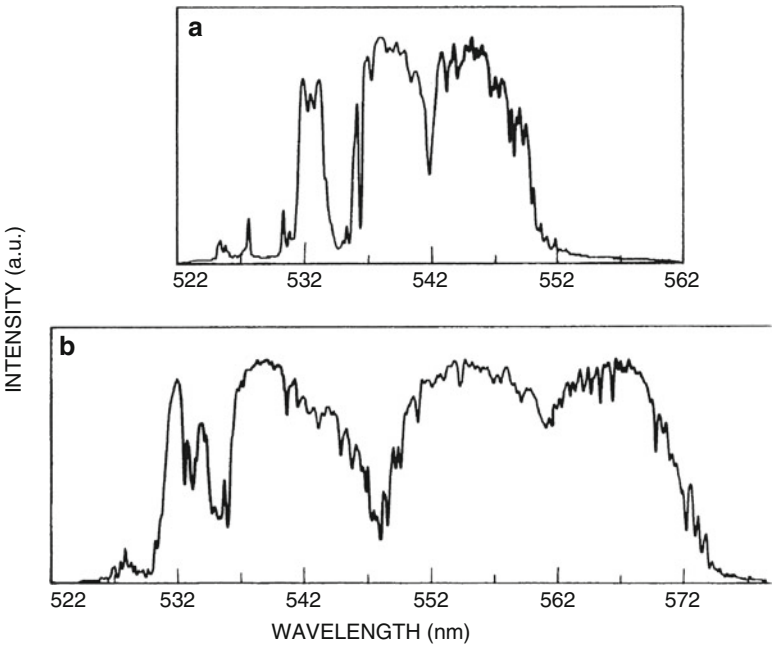

Fig. 4.35 Supercontinuum generation. (**a**) The pump, SFPM, and first SRS Stokes lines are broadened at $I = 10 \times 10^8$ W/cm^2. (**b**) The broadened second and third SRS Stokes lines appear and extend the spectrum toward the Stokes wavelengths at $I = 15 \times 10^8$ W/cm^2. (From Baldeck & Alfano, 1987)

from approximately 20×10^8 to 30×10^8 W/cm^2 in steps of 2.5×10^8 W/cm^2. In Fig. 4.36a, the spectrum contains only the 460-nm SFPM line generated by the laser pump ($\lambda = 532$ nm). In Fig. 4.36b, the line begins to broaden and two symmetrical lines appear with a frequency shift of 100 cm^{-1}. This set of lines could be a new set of small-shift SFPM lines generated by the 460-nm SFPM line acting as a new pump wavelength. Figure 4.36c, d show significant broadening, by a combined action of SFPM, SPM, and XPM, of the 460 nm into a frequency continuum. Similar effects were observed on the Stokes side as displayed in Fig. 4.33.

The intensity effects on SFPM spectra generated by 25-ps pulses propagating in optical fibers have been investigated experimentally. In contrast to SFPM lines generated by nanosecond pulses, spectra were broadened by self-phase modulation and cross-phase modulation. Intensity-saturated wide frequency continua covering the whole visible spectrum were generated for increasing intensities. Applications are for the design of wideband amplifiers, the generation of "white" picosecond pulses, and the generation by pulse compression of femtosecond pulses at new wavelengths.

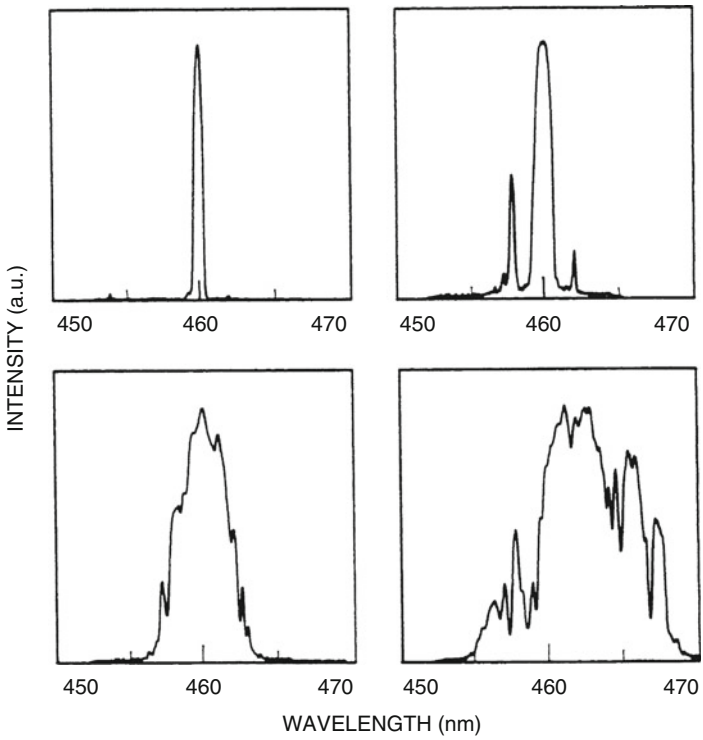

Fig. 4.36 (**a–d**) Spectral broadening of the anti-Stokes SFPM line generated at 460 nm. The pulse peak intensity increases from $I = 20 \times 10^8$ W/cm^2 in (**a**) to $I = 30 \times 10^8$ W/cm^2 in (**e**) in steps of 2.5×10^8 W/cm^2. (From Baldeck & Alfano, 1987)

4.7 Induced Focusing by Cross-Phase Modulation in Optical Fibers

Cross-phase modulation originates from the nonlinear refractive index $\Delta n\,(r, t) = 2n_2 E_p^2\,(r, t)$ generated by the pump pulse at the wavelength of the probe pulse. Consequently, XPM has not only temporal and spectral effects but also spatial effects. Induced focusing is a spatial effect of XPM on the probe beam diameter. Induced focusing is the focusing of a probe beam because of the radial change of the refractive index induced by a copropagating pump beam. Induced focusing is similar to the self-focusing (Kelley, 1965) of intense lasers beams that has been observed in many liquids and solids. Overviews and references on self-focusing in condensed media are given by Auston (1977) and Shen (1984).

In 1987, Baldeck, Raccah, and Alfano reported on experimental evidence for focusing of picosecond pulses propagating in an optical fiber (Baldeck et al., 1987a). Focusing occurred at Raman frequencies for which the spatial effect of the nonlinear refractive index was enhanced by cross-phase modulation. Results

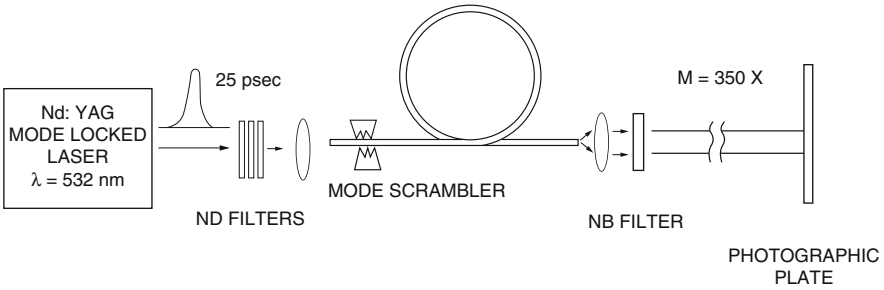

Fig. 4.37 Experimental setup for the observation of Raman focusing in a large-core optical fiber. (From Baldeck et al., 1987a, b, c, d)

of this experiment on induced focusing by cross-phase modulation in optical fibers are summarized in this section.

The experimental setup is shown in Fig. 4.37. A Quantel frequency-doubled mode-locked Nd: YAG laser produced 25-ps pulses at 532 nm. The laser beam was coupled into the optical fiber with a 10× microscope lens. A stable modal distribution was obtained with a Newport FM-1 mode scrambler. Images of the intensity distribution at the output face were magnified by 350× and recorded on photographic film. Narrowband (NB) filters were used to select frequencies of the output pulses. The optical fiber was a commercial multimode step-index fiber (Newport F-MLD). Its core diameter was 100 μm, its numerical aperture 0.3, and its length 7.5 m.

Several magnified images of the intensity distributions that were observed at the output face of the fiber for different input pulse energies are shown in Fig. 4.38. The intensity distribution obtained for low pulse energies ($E < 1$ nJ) is shown in Figure 4.38a. It consists of a disk profile with a speckle pattern. The intensity distribution of the disk covers the entire fiber core area. The disk diameter, measured by comparison with images of calibrated slits, is 100 μm, which corresponds to the core diameter. The characteristics of this fiber allow for the excitation of about 200,000 modes. The mode scrambler distributed the input energy to most of the different modes. The speckle pattern is due to the interference of these modes on the output face. Figure 4.37b shows the intensity distribution in the core for intense pulses ($E > 10$ nJ). At the center of the 100-mm-diameter disk image, there is an intense smaller (11-mm) ring of a Stokes-shifted frequency continuum of light. About 50% of the input energy propagated in this small-ring pattern. The corresponding intensities and nonlinear refractive indices are in the ranges of gigawatts per square centimeter and 10^{-6}, respectively. For such intensities, there is a combined effect of stimulated Raman scattering, self-phase modulation, and cross-phase modulation that generates the observed frequency continuum. In Fig. 4.37c, an NB filter selected the output light pattern at 550 nm. This clearly shows the ring distribution of the Stokes-shifted wavelengths. Such a ring distribution was observed

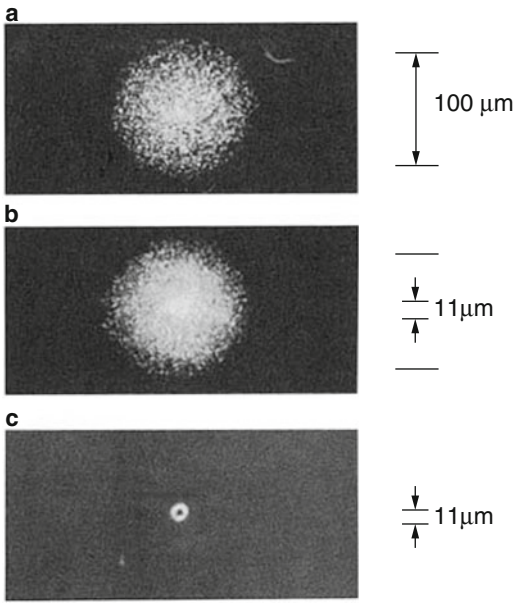

Fig. 4.38 Images of the intensity distributions at the optical fiber output: (**a**) input pulses of low energies ($E < 1$ nJ); (**b**) input pulses of high energies ($E > 10$nJ); (**c**) same as (**b**) with an additional narrowband filter centered at $\lambda = 550$ nm. ($M = 350\chi$). (From Baldeck et al., 1987a)

for a continuum of Stokes-shifted wavelengths up to 620 nm for the highest input energy before damage.

The small-ring intensity profile is a signature of induced focusing at the Raman wavelengths. First, the small ring is speckless, which is characteristic of single-mode propagation. This single-mode propagation means that the guiding properties of the fiber are dramatically changed by the incoming pulses. Second, SRS, SPM, and XPM occur only in the ring structure, i.e., where the maximum input energy has been concentrated. Our experimental results may be explained by an induced-gradient-index model for induced focusing. For high input energies, the Gaussian beam induces a radial change of the refractive index in the optical fiber core. The step-index fiber becomes a gradient-index fiber, which modifies its light-guiding properties. There is further enhancement of the nonlinear refractive index at Raman frequencies because of XPM. Thus, Stokes-shifted light propagates in a well-marked induced-gradient-index fiber. The ray propagation characteristics of a gradient-index fiber are shown schematically in Fig. 4.39 (Keiser, 1983). The cross-sectional view of a skew-ray trajectory in a graded-index fiber is shown. For a given mode u, there are two values for the radii, r_1 and r_2, between which the mode is guided. The path followed by the corresponding ray lies completely within the boundaries of two coaxial cylindrical surfaces that form a well-defined ring. These surfaces are known as the caustic surfaces. They have inner and outer radii r_1 and r_2, respectively. Hence, Fig. 4.39 shows that skew rays propagate in a ring structure comparable to the one shown in Fig. 4.38c. This seems to support the induced-gradient-index model for induced focusing in optical fibers.

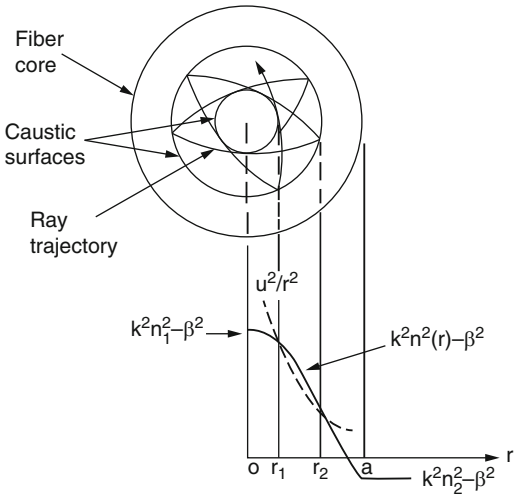

Fig. 4.39 Cross-sectional projection of a skew ray in a gradient-index fiber and the graphical representation of its mode solution from the WBK method. The field is oscillatory between the turning points r_1 and r_2 and is evanescent outside this region

Induced focusing of Raman picosecond pulses has been observed in optical fibers. Experimental results may be explained by an induced-gradient-index model of induced focusing. An immediate application of this observation could be the single-mode propagation of high-bit-rate optical signals in large-core optical fibers.

4.8 Modulation Instability Induced by Cross-Phase Modulation in Optical Fibers

Modulation instability refers to the sudden breakup in time of waves propagating in nonlinear dispersive media. It is a common nonlinear phenomenon studied in several branches of physics (an overview on modulation instability can be found in Hasegawa, 1975). Modulation instabilities occur when the steady state becomes unstable as a result of an interplay between the dispersive and nonlinear effects. Tai, Hasegawa, and Tomita have observed the modulation instability in the anomalous dispersion regime of silica fibers, i.e., for wavelengths greater than 1.3 μm (Tai et al., 1986). Most recently, Agrawal (1987) has suggested that a new kind of modulation instability can occur even in the normal dispersion regime when two copropagating fields interact with each other through the nonlinearity-induced cross-phase modulation. This section summarizes the first observation by Baldeck, Alfano, and Agrawal of such a modulation instability initiated by cross-phase modulation in the normal dispersion regime of silica optical fibers (Baldeck et al., 1988b; Baldeck & Alfano, 1989).

Optical pulses at 532 nm were generated by either a mode-locked Nd: YAG laser or a Q-switched Nd: YAG laser with widths of 25 ps or 10 ns, respectively. In both cases, the repetition rate of pulses was 10 Hz. Pulses were coupled into a single-

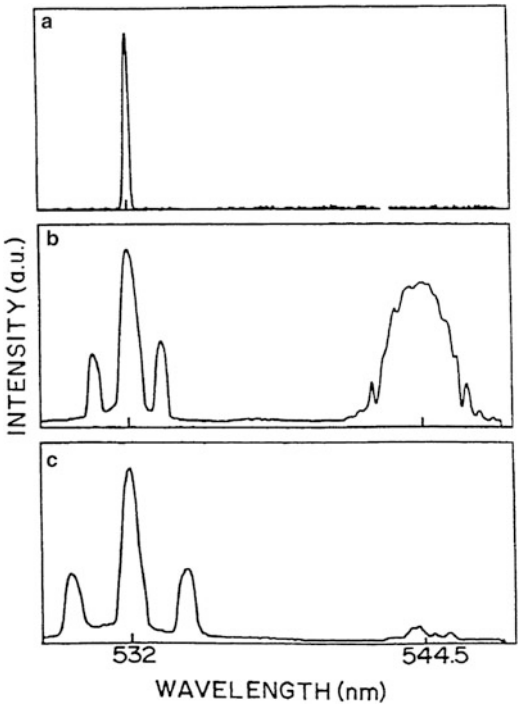

Fig. 4.40 Characteristic frequency sidebands of modulation instability resulting from cross-phase modulation induced by the simultaneously generated Raman pulses in lengths L of a single-mode optical fiber. The laser line is at $\lambda = 532$ nm and the Raman line at $\lambda = 544.5$ nm. The time duration of input pulses is 25 ps. (**a**) Reference spectrum at low intensity; (**b**) Spectrum at about the modulation instability threshold and $L = 3$ m; (**c**) same as (**b**) for $L = 0.8$ m. (From Baldeck et al., 1988d; Baldeck & Alfano, 1989)

mode optical fiber using a microscope lens with a magnification of 40. The peak power of pulses into the fiber could be adjusted in the range $1–10^4$ W by changing the coupling conditions and by using neutral density filters. The optical fiber was custom-made by Corning Glass. It has a 3-μm core diameter, a 0.24% refractive index difference, and a single-mode cutoff at $\lambda = 462$ nm. Spectra of output pulses were measured using a grating spectrometer (1 m, 600 lines/mm) and recorded with an optical multichannel analyzer OMA2.

Figures 4.40 and 4.41 show spectra of intense 25-ps pulses recorded for different peak powers and fiber lengths. Figure 4.40a is the reference spectrum of low-intensity pulses. Figures 4.40b, c show spectra measured at about the modulation instability threshold for fiber lengths of 3 and 0.8 m, respectively. They show modulation instability sidebands on both sides of the laser wavelength at 532 nm and the first-order stimulated Raman scattering line at 544.5 nm. Notice that the frequency shift of sidebands is larger for the shorter fiber. Secondary sidebands were also observed for pulse energy well above the modulation instability threshold and longer optical fibers as shown in Fig. 4.41.

Similar to spectra in the experiment of Tai et al., spectra shown in Figs. 4.40 and 4.41 are undoubtedly signatures of modulation instability. A major salient difference in the spectra in Figs. 4.40 and 4.41 is that they show modulation instability about 532 nm, a wavelength in the *normal dispersion regime* of the fiber. According to the theory, modulation instability at this wavelength is possible only if there is a cross-

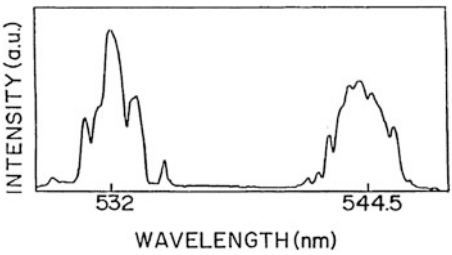

Fig. 4.41 Secondary sidebands observed for pulse energies well above the modulation instability threshold. (From Baldeck et al., 1988d; Baldeck & Alfano, 1989)

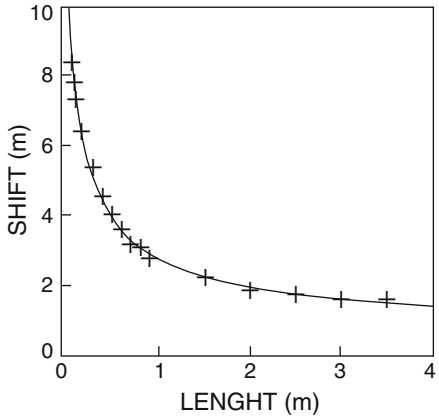

Fig. 4.42 Sideband shifts versus fiber length near the modulation instability threshold. The time duration of input pulses is 10 ns. Crosses are experimental points. The solid line is the theoretical fit from Eq. (4.25). (From Baldeck et al., 1988d; Baldeck & Alfano, 1989)

phase modulation interaction (Agrawal, 1987). As shown in Fig. 4.40, modulation instability sidebands were observed only in the presence of stimulated Raman scattering light. It has recently been demonstrated that cross-phase modulation is intrinsic to the stimulated Raman scattering process (see Sect. 4.4). Therefore, sideband features observed in Figs. 4.40 and 4.41 are conclusively a result of the cross-phase modulation induced by the simultaneously generated Raman pulses. To rule out the possibility of a multimode or single-mode stimulated four-photon mixing process as the origin of the sidebands, Baldeck et al. note that the fiber is truly single-mode (cutoff wavelength at 462 nm) and that the sideband separation changes with the fiber length.

The strengthen the conclusion that the sidebands are due to modulation instability induced by cross-phase modulation, Baldeck et al. measured and compared with theory the dependence of sideband shifts on the fiber lengths. For this measurement, they used 10-ns pulses from the Q-switched Nd:YAG laser to ensure quasi-CW operation. The spectra were similar to those obtained with 25-ps pulses (Fig. 4.40). As shown in Fig. 4.42, the side-lobe separation, defined as the half-distance between sideband maxima, varied from 1.5 to 8.5 nm for fiber lengths ranging from 4 to 0.1 m, respectively. The energy of input pulses was set at approximately the modulation instability threshold for each fiber length. The solid line in Fig. 4.42 corresponds to the theoretical fit. As discussed in Agrawal (1987), the maximum gain of modulation instability sidebands is given by $g_{\max} = k''\Omega_m^2$, where

$\Omega_m = 2\pi f_m$ is the sideband shift. Thus, the power of a sideband for an optical fiber length L is given by

$$P(\Omega_m, L) = P_{\text{noise}} \exp\left(k''\Omega_m^2 L\right), \tag{4.23}$$

where P_{noise} is the initial spontaneous noise, and $k'' = \partial(v_g) - {}^1/\partial\omega$ is the group velocity dispersion at the laser frequency.

For such amplified spontaneous emission, it is common to define a threshold gain g_{th} by

$$P_{\text{th}}(L) = P_{\text{noise}} \exp(g_{\text{th}}), \tag{4.24}$$

where P_{th} is the sideband power near threshold such that each sideband contains about 10% of the input energy. A typical value for g_{th} is 16 (Tai et al., 1986).

From Eqs. (4.23) and (4.24), the dependence of the sideband shift on the fiber length near threshold is given by

$$\Omega_m = \left(g_{\text{th}}/k''L\right)^{1/2}. \tag{4.25}$$

At $\lambda = 532$ nm, the group velocity dispersion in $k'' \approx 0.06$ ps^2/m. The theoretical fit shown in Fig. 4.42 (solid line) is obtained using this value and $g_{\text{th}} = 18.1$ in Eq. (4.25). The good agreement between the experimental data and the theory of modulation instability supports the belief of Baldeck et al. that they have observed cross-phase modulation-induced modulation instability, as predicted in Agrawal (1987).

Tai et al. have shown that modulation instability leads to the breakup of long quasi-CW pulses in trains of picosecond subpulses. The data in Fig. 4.42 show that the maximum sideband shift is $\Delta\lambda_{\text{max}} \approx 8.5$ nm or 8.5 THz, which corresponds to the generation of femtosecond subpulses within the envelope of the 10-ns input pulses with a repetition time of 120 fs. Even though autocorrelation measurements were not possible because of the low repetition rate (10 Hz) needed to generate pulses with kilowatt peak powers, Baldeck et al. believe they have generated for the first time modulation instability subpulses shorter than 100 fs.

Baldeck et al. (1988b) observed modulation instability in the normal dispersion regime of optical fibers. Modulation instability sidebands appear about the pump frequency as a result of cross-phase modulation induced by the simultaneously generated Raman pulses. Sideband frequency shifts were measured for many fiber lengths and found to be in good agreement with theory. In this experiment, cross-phase modulation originated from an optical wave generated inside the nonlinear medium, but similar results are expected when both waves are incident externally. Modulation instability induced by cross-phase modulation represents a new kind of modulation instability that not only occurs in normally dispersive materials but also,

most important, has the potential to be controlled in real time by switching on or off the copropagating pulse responsible for the cross-phase modulation. Using optical fibers, such modulation instabilities could lead to the design of a novel source of femtosecond pulses at visible wavelengths.

4.9 Applications of Cross-Phase Modulation for Ultrashort Pulse Technology

Over the last 20 years, picosecond and femtosecond laser sources have been developed. Researchers are now investigating new applications of the unique properties of these ultrashort pulses. The main efforts are toward the design of communication networks and optical computers with data streams in, eventually, the tens of terahertz. For these high repetition rates, electronic components are too slow and all-optical schemes are needed. The discovery of cross-phase modulation effects on ultrashort pulses appears to be a major breakthrough toward the real-time all-optical coding/decoding of such short pulses. As examples, this section describes the original schemes for a frequency shifter, a pulse compression switch, and a spatial light deflector. These all-optical devices are based on spectral, temporal, and spatial effects of cross-phase modulation on ultrashort pulses.

The first XPM-based technique to control ultrashort pulses was developed in the early 1970s. It is the well-known optical Kerr gate, which is shown in Fig. 4.43. A probe pulse can be transmitted through a pair of cross-polarizers only when a pump pulse induces the (cross-) phase (modulation) needed for the change of polarization of the probe pulse. The principle of the optical Kerr gate was demonstrated using nonlinear liquids (Shimizu & Stoicheff, 1969; Duguay & Hansen, 1969) and optical fibers (Stolen & Ashkin, 1972; Dziedzic et al., 1981; Ayral et al., 1984). In optical fibers, induced-phase effects can be generated with milliwatt peak powers because of their long interaction lengths and small cross

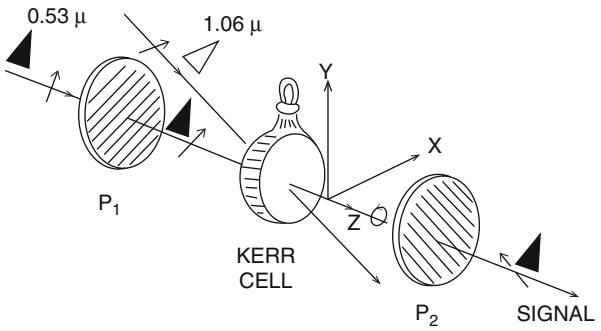

Fig. 4.43 Schematic diagram of an optical Kerr gate

sections (White et al., 1988). XPM effects in optical fibers have been shown to alter the transmission of frequency multiplexed signals (Chraplyvy et al., 1984) and also to allow quantum nondemolition measurements (Levenson et al., 1986; Imoto et al., 1987). In addition, phase effects arising from XPM have been used to make all-fiber logic gates (Kitayama et al., 1985a), ultrafast optical multi/demultiplexers (Morioka et al., 1987), and nonlinear interferometers (Monerie & Durteste, 1987).

The novelty of our most recent work was to show that XPM leads not only to phase effects but also to spectral, temporal, and spatial effects on ultrashort pulses. New schemes for XPM-based optical signal processors are proposed in Fig. 4.44. The design of an ultrafast frequency shifter is shown in Fig. 4.44a. It is based on spectral changes that occur when pulses copropagate in a nonlinear dispersive medium. In the absence of a pump pulse, the weak signal pulse passes undistorted through the nonlinear medium. When the signal pulse copropagates in the nonlinear medium with a pump pulse, its carrier wavelength can be changed by an amount $\Delta\lambda$ that is linearly proportional to the peak power of the pump pulse (see Sect. 4.3.2). Thus, in Fig. 4.44, the signal pulses S1 and S2 have their frequencies shifted by $\Delta\lambda_1$ and $\Delta\lambda_2$ by the pump pulses P1 and P2, while S3 is not affected by the stream of pump pulses.

The design of a pulse-compression switch is proposed in Fig. 4.44b. It is a modified version of the usual optical fiber/grating-pair pulse compression scheme (see Chap. 9 by Dorsinville et al. and Chap. 10 by Johnson and Shank). First, the probe pulse is spectrally broadened by a copropagating pump pulse in the nonlinear medium (case of negligible group velocity mismatch; see Sects. 4.2.2 and 4.3.1). Then, or simultaneously, it is compressed in time by a dispersive element. Thus, in the presence of the pump pulse, the signal pulse is compressed ("on" state), while in its absence, the signal pulse is widely broadened ("off" state) by the device.

An example of an all-optical spatial light deflector based on spatial effects of XPM is shown in Fig. 4.44c. In this scheme, the pump pulse profile leads to an induced focusing of the signal pulse through the induced nonlinear refractive index (Sect. 4.7). The key point in Fig. 4.43c is that half of the pump pulse profile is cut by a mask, which leads to an asymmetric induced-focusing effect and a spatial deflection of the signal pulse. This effect is very similar to the self-deflection of asymmetric optical beams (Swartlander & Kaplan, 1988). In the proposed device, pump pulses originate from either path P1 or path P2, which have, respectively, their left side or right side blocked. Thus, if a signal pulse copropagates with a pump pulse from P1 or P2, it is deflected on, respectively, the right or left side of the nondeflected signal pulse.

The prime property of future XPM-based optical devices will be their switching speed. They will be controlled by ultrashort pulses that will turn on or off the induced nonlinearity responsible for XPM effects. With short pulses, the nonlinearity originates from the fast electronic response of the interacting material. As an example, the time response of electronic nonlinearity in optical fibers is about 2–4 f (Grudinin et al., 1987). With such a response time, one can envision the optical processing of femtosecond pulses with repetition rates up to 100 THz.

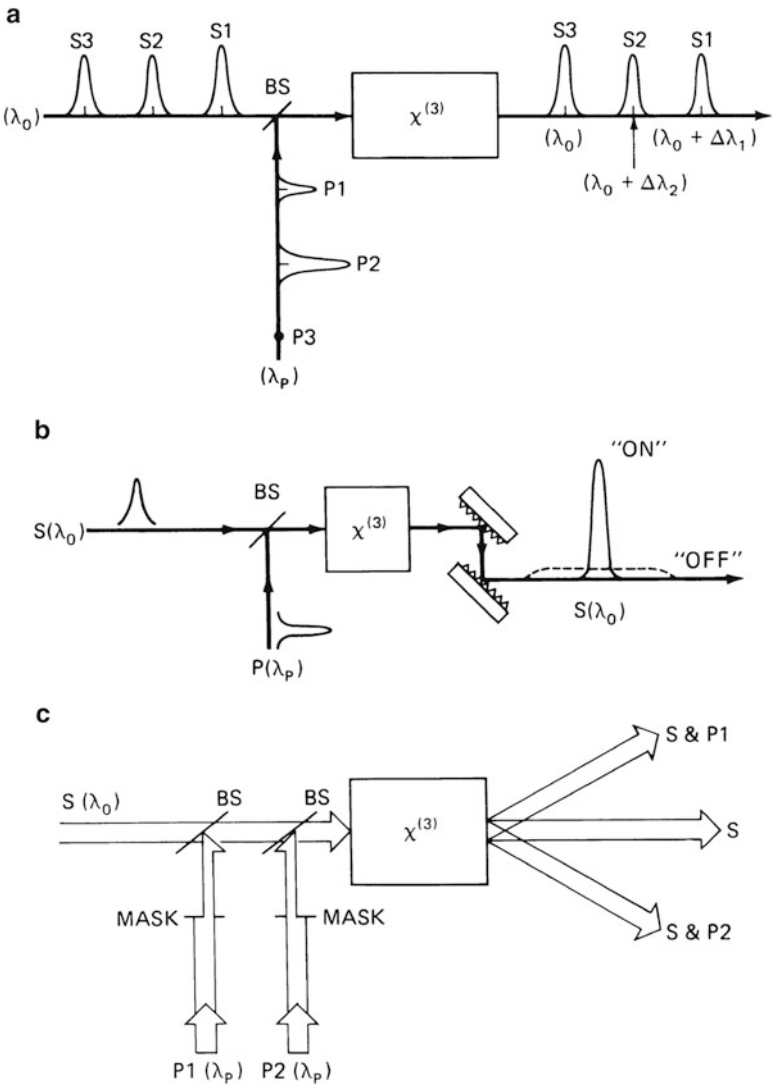

Fig. 4.44 Schematic diagrams of ultrafast optical processors based on cross-phase modulation effects. (**a**) Ultrafast frequency shifter; (**b**) all-optical pulse compression switch; (**c**) all-optical spatial light deflector

4.10 Conclusion

This chapter reviewed cross-phase modulation effects on ultrashort optical pulses. It presented XPM measurements that were obtained during the years 1986–1988. XPM is a newly identified physical phenomenon with important potential

applications based on the picosecond and femtosecond pulse technology. XPM is similar to SPM but corresponds to the phase modulation caused by the nonlinear refractive index *induced by a copropagating pulse*. As for SPM, the time and space dependences of XPM lead to spectral, temporal, and spatial changes of ultrashort pulses.

Experimental investigations of cross-phase modulation effects began in 1986, when the spectral broadening enhancement of a probe pulse was reported for the first time. Subsequently, spectra of Raman, second harmonic, and stimulated four-photon mixing picosecond pulses were found to broaden with increasing pump intensities. Moreover, it was demonstrated that the spectral shape of Raman pulses was affected by the pulse walk-off, that the frequency of copropagating pulses could be tuned by changing the input time delay between probe and pump pulses, and that modulation instability could be obtained in the normal dispersion regime of optical fibers. All these results are well understood in terms of the XPM theory. Furthermore, induced focusing of Raman pulses, which was recently observed in optical fibers, was explained as a spatial effect of XPM.

The research trends are now toward more quantitative comparisons between measurement and theory and the development of XPM-based applications. Future experiments should clarify the relative contributions of SPM, XPM, and modulation instability to the spectral broadening of Raman, second harmonic, and stimulated four-photon mixing pulses. XPM appears to be a new tool for controlling (with the fast femtosecond time response of electronic nonlinearities) the spectral, temporal, and spatial properties of ultrashort pulses. Applications could include the frequency tuning in real time of picosecond pulses, the compression of weak pulses, the generation of femtosecond pulse trains from CW beams by XPM-induced modulation instability, and the spatial scanning of ultrashort pulses. The unique controllability of XPM should open up a broad range of new applications for the supercontinuum laser source.

Experiments on induced- and cross-phase modulations have been performed by the authors in close collaboration with T. Jimbo, Z. Li, Q.Z. Wang, D. Ji, and F. Raccah. Theoretical studies were undertaken in collaboration with J. Gersten and Jamal Manassah of the City College of New York and, most recently, with Govind P. Agrawal of AT&T Bell Laboratories.

We gratefully acknowledge partial support from Hamamatsu Photonics K.K.

4.11 Addendum

This chapter was written during the spring of 1988. Since then, many more of new theoretical and experimental results on XPM effects have been or are being published by various research groups. The reference list in the introduction section of this chapter has been updated. The interested readers should refer themselves to original reports in the most recent issues of optics and applied physics publications.

References

Agrawal, G. P. (1987). Modulation instability induced by cross-phase modulation. *Physical Review Letters, 59*, 880–883.

Agrawal, G. P., & Potasek, M. J. (1986). Nonlinear pulse distortion in single-mode optical fibers at the zero-dispersion wavelength. *Physics Review, 3*, 1765–1776.

Agrawal, G. P., Baldeck, P. L., & Alfano, R. R. (1988). Optical wave breaking and pulse compression due to cross-phase modulation in optical fibers. Conference abstract #MW3, in Digest of the 1988 OSA annual meeting. Optical Society of America, Washington, D.C. *Optics Letters, 14*, 137–139. 1989.

Agrawal, G. P., Baldeck, P. L., & Alfano, R. R. (1989a). Temporal and spectral effects of cross-phase modulation on copropagating ultrashort pulses in optical fibers. *Physical Review A*.

Agrawal, G. P., Baldeck, P. L., & Alfano, R. R. (1989b, April). Modulation instability induced by cross-phase modulation in optical fibers. *Physical Review A*.

Alfano, R. R., & Ho, P. P. (1988). Self-, cross-, and induced-phase modulations of ultrashort laser pulse propagation. *IEEE Journal of Quantum Electronics, 24*, 351–364.

Alfano, R. R., & Shapiro, S. L. (1970). Emission in the region 4000–7000 Å via four-photon coupling in glass. Phys. Rev. Lett. 24, 584-587. Observation of self-phase modulation and small scale filaments in crystals and glasses. *Physical Review Letters, 24*, 592–594.

Alfano, R. R., Li, Q., Jimbo, T., Manassah, J. T., & Ho, P. P. (1986). Induced spectral broadening of a weak picosecond pulse in glass produced by an intense ps pulse. *Optics Letters, 11*, 626–628.

Alfano, R. R., Wang, Q. Z., Jimbo, T., & Ho, P. P. (1987a). Induced spectral broadening about a second harmonic generated by an intense primary ultrafast laser pulse in ZnSe crystals. *Physics Review, A35*, 459–462.

Alfano, R. R., Baldeck, P. L., Raccah, F., & Ho, P. P. (1987b). Cross-phase modulation measured in optical fibers. *Applied Optics, 26*, 3491–3492.

Alfano, R. R., Baldeck, P. L., & Ho, P. P. (1988). *Cross-phase modulation and induced-focusing of optical nonlinearities in optical fibers and bulk materials. Conference abstract #ThA3, In Digest of the OSA topical meeting on nonlinear optical properties of materials*. Optical Society of America.

Auston, D. H. (1977). In S. L. Shapiro (Ed.), *Ultrafast light pulses*. Springer-Verlag.

Ayral, J. L., Pochelle, J. P., Raffy, J., & Papuchon, M. (1984). Optical Kerr coefficient measurement at 1.15 μm in single-mode optical fivers. *Optics Communication, 49*, 405–408.

Baldeck, P. L., & Alfano, R. R. (1987). Intensity effects on the stimulated four-photon spectra generated by picosecond pulses in optical fibers. Conference abstract #FQ7, March meeting of the American Physical Society, New York, New York, 1987. *Journal of Lightwave Technology, T-5*, 1712–1715.

Baldeck, P. L., Raccah, F., & Alfano, R. R. (1987a). Observation of self-focusing in optical fibers with picosecond pulses. *Optics Letters, 12*, 588–589.

Baldeck, P. L., Ho, P. P., & Alfano, R. R. (1987b). Effects of self, induced-, and cross-phase modulations on the generation of picosecond and femtosecond white light supercontinua. *Physical Review Applied, 22*, 1677–1694.

Baldeck, P. L., Ho, P. P., & Alfano, R. R. (1987c). *Experimental evidences for cross-phase modulation, induced-phase modulation and self-focusing on picosecond pulses in optical fibers. Conference abstract #TuV4, in Digest of the 1987 OSA annual meeting*. Optical Society of America.

Baldeck, P. L., Raccah, F., Garuthara, R., & Alfano, R. R.. (1987d). *Spectral and temporal investigation of cross-phase modulation effects on picosecond pulses in singlemode optical fibers*. Proceeding paper #TuC4, International Laser Science conference ILS-III, Atlantic City, New Jersey, 1987.

Baldeck, P. L., Alfano, R. R., & Agrawal, G. P. (1988a). Induced-frequency shift of copropagating pulses. *Applied Physics Letters, 52*, 1939–1941.

Baldeck, P. L., Alfano, R. R., & Agrawal, G. P. (1988b). *Observation of modulation instability in the normal dispersion regime of optical fibers. Conference abstract #MBB7, in Digest of the 1988 OSA annual meeting*. Optical Society of America.

Baldeck, P. L., Alfano, R. R., & Agrawal, G. P.. (1988c). *Induced-frequency shift, induced spectral broadening and optical amplification of picosecond pulses in a single-mode optical fiber*. Proceeding paper #624, Electrochemical Society symposium on nonlinear optics and ultrafast phenomena, Chicago, Illinois, 1988.

Baldeck, P. L., Alfano, R. R., & Agrawal, G. P. (1988d). *Generation of sub-100-fsec pulses at 532 nm from modulation instability induced by cross-phase modulation in single-mode optical fibers. Proceeding paper #PD2, in Utrafast Phenomena* (p. 6). Springer-Verlag.

Baldeck, P. L., & Alfano, R. R.. (1989). *Cross-phase modulation: A new technique for controlling the spectral, temporal and spatial properties of ultrashort pulses*. SPIE Proceedings of the 1989 Optical Science Engineering conference, Paris, France.

Chraplyvy, A. R., & Stone, J. (1984). Measurement of cross-phase modulation in coherent wavelength-division multiplexing using injection lasers. *Electronics Letters, 20*, 996–997.

Chraplyvy, A. R., Marcuse, D., & Henry, P. S. (1984). Carrier-induced phase noise in angel-modulated optical-fiber systems. *Journal of Lightwave Technology, LT-2*, 6–10.

Cornelius, P., & Harris, L. (1981). Role of self-phase modulation in stimulated Raman scattering from more than one mode. *Optics Letters, 6*, 129–131.

Dianov, E. M., Karasik, A. Y., Mamyshev, P. V., Onishchukov, G. I., Prokhorov, A. M., & M.F. Stel'Marh, and A.A. Formichev. (1984). Picosecond structure of the pump pulse in stimulated Raman scattering in optical fibers. *Optical and Quantum Electronics, 17*, 187.

Duguay, M. A., & Hansen, J. W. (1969). An ultrafast light gate. *Applied Physics Letters, 15*, 192–194.

Dziedzic, J. M., Stolen, R. H., & Ashkin, A. (1981). Optical Kerr effect in ling fibers. *Applied Optics, 20*, 1403–1406.

French, P. M. W., Gomes, A. S. L., Gouveia-Neto, A. S., & Taylor, J. R. (1986). Picosecond stimulated Raman generation, pump pulse fragmentation, and fragment compression in single-mode optical fibers. *IEEE Journal of Quantum Electronics, QE-22*, 2230.

Gersten, J., Alfano, R. R., & Belic, M. (1980). Combined stimulated Raman scattering and continuum self-phase modulation. *Physics Review, A#21*, 1222–1224.

Gomes, A. S. L., Sibbet, W., & Taylor, J. R. (1986). Spectral and temporal study of picosecond-pulse propagation in a single-mode optical fibers. *Applied Physics, B#39*, 44–46.

Gomes, A. S. L., da Silva, V. L., & Taylor, J. R. (1988). Direct measurement of nonlinear frequency chirp of Raman radiation in single-mode optical fibers using a spectral window method. *Journal of the Optical Society of America, B#5*, 373–380.

Gouveia-Neto, A. S., Faldon, M. E., Sombra, A. S. B., Wigley, P. G. J., & Taylor, J. R. (1988a). Subpicosecond-pulse generation through cross-phase modulation-induced modulation instability in optical fibers. *Optics Letters, 12*, 901–906.

Gouveia-Neto, A. S., Faldon, M. E., & Taylor, J. R. (1988b). Raman amplification of modulation instability and solitary-wave formation. *Optics Letters, 12*, 1029–1031.

Grudinin, A. B., Dianov, E. M., Korobkin, D. V., Prokhorov, A. M., Serkinand, V. N., & Khaidarov, D. V. (1987). Decay of femtosecond pulses in single-mode optical fibers. *Pis'ma Zh. Eksp. Teor. Fiz, 46*, 175–177. [Sov. Phys. JETP Lett. 46, 221, 225.].

Hasegawa, A. (1975). *Plasma instabilities and nonlinear effects*. Springer-Verlag.

Ho, P. P., Wang, Q. Z., Ji, D., & Alfano, R. R. (1988). Propagation of harmonic cross-phase-modulation pulses in ZnSe. *Applied Physics Letters*, 111–113.

Hook, A. D., & Anderson, and M. Lisak. (1988). Soliton-like pulses in stimulated Raman scattering. *Optics Letters, 12*, 114–116.

Imoto, N., Watkins, S., & Sasaki, Y. (1987). A nonlinear optical-fiber interferometer for nondemolition measurement of photon number. *Optics Communications, 61*, 159–163.

Islam, M. N., Mollenauer, L. F., & Stolen, R. H. (1986). Fiber Raman amplification soliton laser. In *Ultrafast Phenomena 5*. Springer-Verlag.

Islam, M. N., Mollenauer, L. F., Stolen, R. H., Simson, J. R., & Shang, H. T. (1987a). Cross-phase modulation in optical fibers. *Optics Letters, 12*, 625–627.

Islam, M. N., Mollenauer, L. F., Stolen, R. H., Simson, J. R., & Shang, H. T. (1987b). Amplifier/compressor fiber Raman lasers. *Optics Letters, 12*, 814–816.

Jaskorzynska, B., & Schadt, D. (1988). All-fiber distributed compression of weak pulses in the regime of negative group-velocity dispersion. *IEEE Journal of Quantum Electronics, QE-24*, 2117–2120.

Johnson, A. M., Stolen, R. H., & Simpson, W. M. (1986). The observation of chirped stimulated Raman scattered light in fibers. In *Ultrafast Phenomena 5*. Springer-Verlag.

Keiser, G. (1983). *In optical Fiber communications*. McGraw-Hill.

Kelley, P. L. (1965). Self-focusing of optical beams. *Physical Review Letters, 15*, 1085.

Kimura, Y., Kitayama, K. I., Shibata, N., & Seikai, S. (1986). All-fibre-optic logic "AND" gate. *Electronics Letters, 22*, 277–278.

Kitayama, K. I., Kimura, Y., & Seikai, S. (1985a). Fiber-optic logic gate. *Applied Physics Letters, 46*, 317–319.

Kitayama, K. I., Kimura, Y., Okamoto, K., & Seikai, S. (1985b). Optical sampling using an all-fiber optical Kerr shutter. *Applied Physics Letters, 46*, 623–625.

Levenson, M. D., Shelby, R. M., Reid, M., & Walls, D. F. (1986). Quantum nondemolition detection of optical quadrature amplitudes. *Physical Review Letters, 57*, 2473–2476.

Lin, C., & Bosh, M. A. (1981). Large Stokes-shift stimulated four-photon mixing in optical fibers. *Applied Physics Letters, 38*, 479–481.

Hian-Hua, L., Li, Y.-L., & Jiang, J.-L. (1985). On combined self-phase modulation and stimulated Raman scattering in fibers. *Optical and Quantum Electronics, 17*, 187.

Manassah, J. T. (1987a). Induced phase modulation of the Raman pulse in optical fibers. *Applied Optics, 26*, 3747–3749.

Manassah, J. T. (1987b). Time-domain characteristics of a Raman pulse in the presence of a pump. *Applied Optics, 26*, 3750–3751.

Manassah, J. T. (1987c). Amplitude and phase of a pulsed second-harmonic signal. *Journal of the Optical Society of America, B#4*, 1235–1240.

Manassah, J. T. (1988). Pulse compression of an induced-phase modulated weak signal. *Optics Letters, 13*, 752–755.

Manassah, J. T., & Cockings, O. R. (1987). Induced phase modulation of a generated second-harmonic signal. *Optics Letters, 12*, 1005–1007.

Manassah, J. T., Mustafa, M., Alfano, R. R., & Ho, P. P. (1985). Induced supercontinuum and steepening of an ultrafast laser pulse. *Physics Letters, 113A*, 242–247.

Monerie, M., & Durteste, Y. (1987). Direct interferometric measurement of nonlinear refractive index of optical fibers by cross-phase modulation. *Electronics Letters, 23*, 961–962.

Morioka, T., Saruwatari, M., & Takada, A. (1987). Ultrafast optical multi/demultiplexer utilising optical Kerr effect in polarisation-maintaining single-mode optical fibers. *Electronics Letters, 23*, 453–454.

Nakashima, T., Nakazawa, M., Nishi, K., & Kubuta, H. (1987). Effect of stimulated Raman scattering on pulse-compression characteristics. *Optics Letters, 12*, 404–406.

Schadt, D., Jaskorzynska, B., & Osterberg, U. (1986). Numerical study on combined stimulated Raman scattering and self-phase modulation in optical fibers influenced by walk-off between pump and Stokes pulses. *Journal of the Optical Society of America, B#3*, 1257–1260.

Schadt, D., & Jaskorzynska, B. (1987a). Frequency chirp and spectra due to self-phase modulation and stimulated Raman scattering influenced by walk-off in optical fibers. *Journal of the Optical Society of America, B#4*, 856–862.

Schadt, D., & Jaskorzynska, B. (1987b). Generation of short pulses from CW light by influence of cross-phase modulation in optical fibers. *Electronics Letters, 23*, 1091–1092.

Schadt, D., & Jaskorzynska, B. (1988). Suppression of the Raman self-frequency shift by cross-phase modulation. *Journal of the Optical Society of America, B#5*, 2374–2378.

Shen, Y. R. (1984). *In the principles of nonlinear optics*. Wiley.

Shimizu, F., & Stoicheff, B. P. (1969). Study of the duration and birefringence of self-trapped filaments in CS_2. *IEEE Journal of Quantum Electronics, QE-5*, 544.

Stolen, R. H. (1975). Phase-matched stimulated four-photon mixing. *IEEE Journal of Quantum Electronics, QE-11*, 213–215.

Stolen, R. H. (1979). In S. E. Miller & A. G. Chynoweth (Eds.), *Nonlinear properties of optical fibers*. Academic Press. Chapter 5.

Stolen, R. H., & Ashkin, A. (1972). Optical Kerr effect in glass waveguide. *Applied Physics Letters, 22*, 294–296.

Stolen, R. H., Bosh, M. A., & Lin, C. (1981). Phase matching in birefringent fibers. *Optics Letters, 6*, 213–215.

Stolen, R. H., & Johnson, A. M. (1986). The effect of pulse walk-off on stimulated Raman scattering in optical fibers. *IEEE Journal of Quantum Electronics, QE-22*, 2230.

Swartzlander, G. A., Jr., & Kaplan, A. E. (1988). Self-deflection of laser beams in a thin nonlinear film. *Journal of the Optical Society of America, B5*, 765–768.

Tai, K., Hasegawa, A., & Tomita, A. (1986). Observation of modulation instability in optical fibers. *Physical Review Letters, 56*, 135–138.

Tomlinson, W. J., Stolen, R. H., & Johnson, A. M. (1985). Optical wave breaking of pulses in nonlinear optical fibers. *Optics Letters, 10*, 457–459.

Trillo, S., Wabnitz, S., Wright, E. M., & Stegeman, G. I. (1988). Optical solitary waves induced by cross-phase modulation. *Optics Letters, 13*, 871–873.

Wahio, K., Inoue, K., & Tanigawa, T. (1980). Efficient generation near-IR stimulated light scattering in optical fibers pumped in low-dispersion region at 1.3 mm. *Electronics Letters, 16*, 331–333.

Weiner, A. M., Heritage, J. P., & Stolen, R. H. (1986). Effect of stimulated Raman scattering and pulse walk-off on self-phase modulation in optical fibers. In *Digest of the conference on lasers and electro-optics* (p. 246). Optical Society of America.

Weiner, A. M., Heritage, J. P., & Stolen, R. H. (1988). Self-phase modulation and optical pulse compression influenced by stimulated Raman scattering in fibers. *Journal of the Optical Society of America, B5*, 364–372.

White, I. H., Penty, R. V., & Epworth, R. E. (1988). Demonstration of the optical Kerr effect in an all-fibre Mach-Zehnder interferometer at laser diode powers. *Electronics Letters, 24*, 172–173.

Zysset, B., & Weber, H. P. (1986). Temporal and spectral investigation of Nd: YAG pulse compression in optical fibers and its application to pulse compression. In *Digest of the conference on lasers and electro-optics* (p. 182). Optical Society of America.

Chapter 5
Fibre-Based Supercontinuum

J. C. Travers and J. R. Taylor

Abstract We comprehensively review the historical development, fundamental physical processes, numerical modelling, practical implementation and recent progress in supercontinuum generation in optical fibres.

Keywords Supercontinuum generation · Non-linear fibre optics · Modulational instability · Solitons · Photonic crystal fibre · Dispersive wave emission · Single-mode fibre · Pulse compression · Raman self-frequency shift · Frequency conversion · Pulse propagation

5.1 Introduction

As comprehensively described in the earlier chapters of this book, by 1970, Alfano and Shapiro had published three defining papers on supercontinuum generation in bulk materials (Alfano & Shapiro, 1970a, b, c), identifying some of the principal non-linear effects contributing to the observed spectral broadening, as well as recognising the importance of the source in transient absorption measurements, and publishing on the application to picosecond Raman absorption (Alfano & Shapiro, 1970d). By 1970 enormous progress was also being made on the development of low-loss silica glass fibres (Kapron et al., 1970) with the achievement of a loss of ~17 dB/km in a titanium-doped silica fibre by Maurer, Schultz and Keck at Corning Inc. that was driven by the promise of high-capacity broadband optical communications, as predicted by Kao and Hockham (1966), should such "low loss" be attainable. The availability of relatively low-loss single-mode or few-mode optical fibre was the catalyst for expanding the relatively new field of non-linear

J. C. Travers (✉)
School of Engineering and Physical Sciences, Heriot-Watt University, Edinburgh, UK
e-mail: j.travers@hw.ac.uk

J. R. Taylor
Physics Department, Imperial College, London, UK
e-mail: jr.taylor@ic.ac.uk

R. R. Alfano (ed.), *The Supercontinuum Laser Source*,
https://doi.org/10.1007/978-3-031-06197-4_5

optics to lower-power regimes. The discovery of the laser (Maiman, 1960) and the techniques of Q-switching (McClung & Helwarth, 1962) and mode locking of solid-state lasers (Mocker & Collins, 1965; De Maria et al., 1966) meant that even for pulses of relatively modest energy, power densities greater than a terawatt per square centimetre could be readily achieved at the focal spot of a convex lens, with corresponding field strengths exceeding a megavolt per centimetre. The consequential need to consider higher-order terms of the electric field in the description of the pump-induced polarisation provided the foundation of non-linear optics and the remarkably simple experimental expedient of simply focusing such pulsed laser outputs into bulk materials provided the early means to generate basic supercontinua.

Despite the fact that silica has one of the lowest non-linear coefficients, the advantage of deploying single-mode fibre over bulk material can be realised by considering the power-length factor associated with non-linear optical processes. With lens focusing in bulk, the effective interaction length is limited by the confocal parameter, and with a focal spot size of a few microns, a confocal parameter of only a few millimetres is possible. If, on the other hand, the light is focused into a single-mode fibre with a core diameter of a few microns, the interaction length is limited only by absorption. For modern fibres, exhibiting a loss of around 0.2 dB/km this gives rise to an effective length in excess of 10 km, although this is wavelength dependent. As a consequence, enhancement of the power-length factor by six or seven orders of magnitude compared to deployment in bulk material clearly demonstrates the potential for lower pump power requirements when undertaking studies of non-linear optics in optical fibre structures. In addition, the use of single-mode fibre permitted greater control over the non-linear processes through the elimination of self-focusing and filamentation, which often played a major role in supercontinuum generation in bulk materials but often led to pulse-to-pulse irreproducibility.

5.2 Non-linear Optics in Fibres

The first non-linear effect in optical fibre to be reported was stimulated Raman scattering in a 1-m-long, 12-μm-diameter, hollow-core fibre filled with carbon disulphide (Ippen, 1970), when pumped by a relatively low peak power (~5 W) pulsed Argon ion laser. Raman laser action was achieved by placing high reflectors at each end of the fibre assembly. The first reported non-linear effect to be characterised in a solid-core silica fibre was the stimulated Brillouin scattering of a pulsed Xenon laser at 535.5 nm with a measured threshold peak power of less than 1 W in a 20-m-long fibre (Ippen & Stolen, 1972). Self-phase modulation (SPM) was subsequently characterised (Ippen et al., 1974) in a 7-μm-diameter hollow-core fibre filled with carbon disulphide, when pumped by the pulses from a mode-locked dye laser. In solid-core fibres, SPM was characterised using the ~200-ps pulses from an actively mode-locked argon ion laser, and an independent measurement

of the non-linear refractive index of silica was determined (Stolen & Lin, 1978). Throughout the 1970s, all the non-linear effects that had been characterised in the previous decade using direct laser pumping of bulk materials were reinvestigated in single-mode fibres, taking advantage of the reduced power levels required as a result of the increased interaction lengths achievable in fibre. These included stimulated Raman scattering (Stolen et al., 1972), the optical Kerr effect (Stolen & Ashkin, 1973) and four-wave mixing (Stolen et al., 1974). Other effects such as second harmonic generation (Österberg & Margulis, 1986) and third harmonic generation (Gabriagues, 1983) in fibres have been characterised and exploited; however, these tend to play an insignificant role in the overall supercontinuum generation process. An excellent review of the early years of non-linear fibre optics is given by Stolen (2008) who pioneered and made an extensive contribution to the field in its formative years, while a comprehensive coverage of the field can be found in Agrawal's seminal text "Nonlinear Fiber Optics", presently in its fifth edition (Agrawal, 2012).

The first report of supercontinuum generation in fibre (Lin & Stolen, 1976) utilised nanosecond pulse excitation provided by several different nitrogen laser-pumped dye lasers operating in the visible spectral region. Pumping a 19.5-m-long, 7-μm core, silica fibre with kilowatt pulses generated a continuum extending from around 440 to 620 nm. Cascaded stimulated Raman scattering and self-phase modulation were identified as the principal broadening mechanisms, and the potential use of the source for excited state spectroscopy was identified by the authors. Subsequently, the use of a Q-switched Nd:YAG laser—capable of producing 150-kW, 20-ns pulses—enabled a cascaded Raman supercontinuum in the infrared to be achieved in a 315-m-long, 35-μm core diameter, relatively low-loss (less than 10 dB/km from 0.7 to 1.7 μm) multimode fibre (Lin et al., 1978). When a single-mode fibre was deployed, similar spectral behaviour was observed at substantially lower pump powers. That supercontinuum, which is shown in Fig. 5.1, exhibits all the classic features of cascaded Raman generation. With the pump in the normal dispersion regime at 1.06 μm, the first three distinct cascaded Raman orders at 1.12, 1.18 and 1.24 μm were observed. Beyond 1.3 μm an effective continuum was recorded apart from a large dip in the region around 1.38 μm as a result of the relatively large water loss associated with these early fibres. To the short-wavelength side of the pump, weak four-wave mixing (FWM) was observed. In Fig. 5.1 the intensity scale of the FWM has been expanded by an order of magnitude, since the efficiency of generation was low as a result of the pump being far away from the dispersion zero.

Similar performance had been achieved by Cohen and Lin (1977) using a Q-switched and mode-locked Nd:YAG laser system to provide a broadband source that was employed in the measurement of the dispersion of optical fibres using the pulse delay technique. The most interesting feature of these supercontinua is the broad continuous nature of the spectra in the anomalous dispersion regime at wavelengths above the dispersion zero, what is now generally referred to as the soliton-Raman continuum. Initially, it was solely attributed to broadening of the cascaded Raman components due to self-phase modulation (Cohen & Lin, 1978), and although

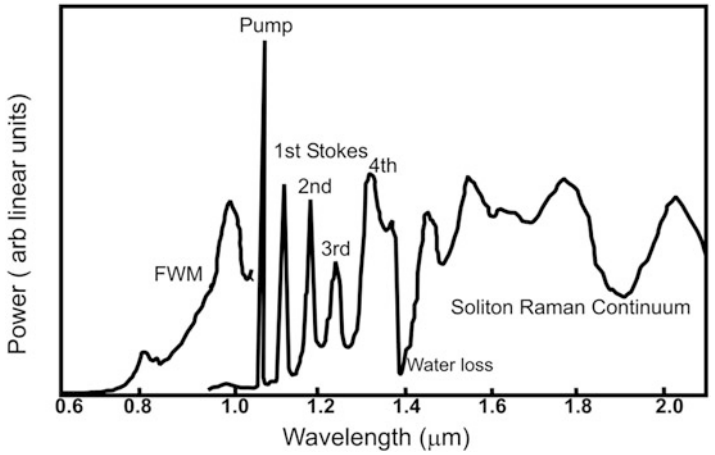

Fig. 5.1 Supercontinuum generated in 315 m of multimode Ge-doped silica fibre by 50-kW pulses from a Q-switched Nd:YAG laser. (After Lin et al., 1978)

time-resolved measurements were taken of the various spectral components of the supercontinuum, the temporal resolution of a few hundred picoseconds used in the pulse delay measurements was inadequate to resolve what most certainly would have been the femtosecond pulse structures of the Raman soliton supercontinuum; consequently the important role of solitons in the dynamics of the supercontinuum was only to be resolved much later.

The role of the pump laser and its location relative to the dispersion zero was qualitatively investigated by Washio et al. (1980) in various lengths of single-mode fibre with a dispersion zero, left unspecified, in the region of the pump wavelength. Using a Q-switched Nd:YAG laser operating at either ~1.32 or ~1.34 μm, the pump wavelength-dependent output spectra were investigated in relation to the fibre length. In short fibres pumped at 1.32 μm, distinct four-wave mixing was recorded, but with increased length the first Raman Stokes at 1.40 μm was generated and a continuum evolved essentially from this. In long-length fibres pumped at 1.34 μm, Washio et al. observed what was the signature of a modulational instability-initiated soliton-Raman supercontinuum, as a result of the long pump pulses operating directly in the anomalous dispersion regime. However, these results were taken in the very early days of soliton and modulational instability studies, and so these were not proposed as contributing mechanisms for the spectral broadening observed. In addition it would be several more years before the soliton-Raman mechanism would be purported (Vysloukh & Serkin, 1983).

5.3 Solitons, Modulational Instability and Pulse Compression

The formation of optical solitons through a balance of non-linear and linear effects—either spatially through self-focusing and diffraction, or temporally through the balance of self-phase modulation and dispersion—was first proposed theoretically by Zakharov and Shabat (1971); in fact they showed that any system described by the non-linear Schrödinger equation (NLSE) supported solitons. A few years later Hasegawa and Tappert (1973) proposed the use of optical fibres to achieve soliton propagation, which would enable both spatial and temporal pulse shape preservation. They derived an NLSE describing the propagation through a fibre of the complex optical pulse envelope $U(z,\tau)$ in a single fibre mode (normalised such that $|U(z,\tau)|^2 = P(z,\tau)$ where $P(z,\tau)$ is the instantaneous power in Watts, z is the fibre position and τ is a co-moving time frame). By defining the group velocity dispersion $\beta_2(\omega) = \partial^2_\omega \beta$ (where $\beta(\omega) = n_{\text{eff}}\omega/c$ is the axial wavenumber, n_{eff} is the effective modal refractive index, ω is the angular frequency and c the speed of light) and the non-linear coefficient $\gamma = n_2\omega/cA_{\text{eff}}$ (where n_2 is the non-linear refractive index, and A_{eff} is the effective modal area), the NLSE can be written as

$$\partial_z U = -i\frac{\beta_2}{2}\partial^2_\tau U + i\gamma|U|^2 U, \tag{5.1}$$

which has soliton solutions of the form

$$U(z,\tau) = \sqrt{P_0}\,\text{sech}\left(\frac{\tau}{\tau_0}\right)\exp\left(i\frac{\gamma P_0}{2}z\right), \tag{5.2}$$

where the soliton peak power $P_0 = |\beta_2|/\gamma\tau_0^2$ and τ_0 is the soliton duration. From Eq. (5.2) it is clear that the soliton pulse profile does not change upon propagation.

Although it can be argued that optical solitons were generated in the supercontinua of Cohen and Lin (1977, 1978) and Lin et al. (1978), no real physical characterisation of soliton behaviour was presented, and it was not until 1980 that Mollenauer et al. provided unequivocal experimental evidence of optical soliton generation and propagation.

Soliton dynamics plays a pivotal role in the physics of supercontinuum generation, and the early historical development of optical solitons and their properties have been comprehensively treated by Mollenauer and Gordon (2006). The long delay between the theoretical prediction of Hasegawa and Tappert and Mollenauer's experimental realisation was simply due to the lack of a suitable pulse source, while in addition, in 1973, long lengths of low-loss single-mode fibre in the spectral regions around 1.3 or 1.55 μm did not exist. The initial experiments required picosecond, transform-limited pulses in the anomalously dispersive spectral region, which for conventional silica fibres was above 1.3 μm. Mollenauer had, in fact, spent many years developing synchronously pumped mode-locked colour centre lasers to undertake what was to be a series of classic experiments on the characterisa-

tion of optical solitons in fibres, which apart from the first observation (Mollenauer et al., 1980) included soliton breathing and pulse restoration (Stolen et al., 1983), pulse compression (Mollenauer et al., 1983), the soliton laser (Mollenauer & Stolen, 1984), long-distance soliton propagation and Raman amplification (Mollenauer et al., 1985), soliton-soliton interaction (Mitschke & Mollenauer, 1987a) and ultrashort pulse generation (Mitschke & Mollenauer, 1987b). Soliton generation was expedited by Mollenauer using transform-limited picosecond pulses with the precise soliton power. We have seen above that solitons had previously been generated but had gone unrecognised in the early supercontinuum work, while Hasegawa and Kodama (1981) theoretically proposed that pulses of any reasonable shape could evolve into a soliton, with any excess energy of the launched pulse shed off as dispersive radiation. It has subsequently been experimentally demonstrated that optical solitons can evolve from noise bursts of sufficient power, again with the excess radiation shed as a dispersive wave (Gouveia-Neto & Taylor, 1989), and that the Raman amplification of noise bursts could give rise to ultrashort pulse, and consequently broadband, soliton generation (Gouveia-Neto et al., 1989a).

The spectral-temporal breathing of solitons and the extreme temporal narrowing initially observed by Mollenauer and colleagues are a result of the high-order soliton propagation that had been predicted by Satsuma and Yajima (1974). This occurs when instead of initial conditions corresponding to Eq. (5.2), a pulse with a higher peak power is launched: $U(0,\tau) = N\sqrt{P_0}\,\mathrm{sech}(\tau/\tau_0)$. For integer N the ideal Satsuma and Yajima high-order soliton dynamics result, but any $N > 0$ will result in at least initial breather dynamics. The ideal high-order solitons are simply a non-linear superposition of N fundamental solitons. Pulse narrowing results from the periodic non-linear interference between these solitons upon propagation, with a compression factor of $4.1N$ being theoretically possible (Dianov et al., 1986). Throughout the 1980s, high-order soliton decay was extensively investigated as a mechanism for ultrashort pulse generation, with associated ultrabroad spectral bandwidths. The technique was first demonstrated by Tai and Tomita (1986) using 2-ps pulses at 1.32 μm derived from a fibre-grating pair pulse compressor and launched into a fibre with a dispersion zero at 1.275 μm, with pulses as short as 90 fs being generated. On optimisation of the launch power and fibre length, pulses of only four optical cycles (~18 fs) were generated centred around 1.3 μm (Gouveia-Neto et al., 1988a). Figure 5.2 shows the spectrum of such a pulse with an intensity autocorrelation trace as the insert.

In the early to mid-1980s, pulses of the order of a few femtoseconds were generated using the optical fibre grating compressor configuration (Tomlinson et al., 1984). This technique utilised grating pairs to compensate the effects of spectral broadening through self-phase modulation and normal dispersion experienced by intense short pulses on propagation through single-mode fibres, enabling the generation of pulses on the order of the inverse of the bandwidth. Johnson and Shank (1989) provided a comprehensive treatment of the technique in the first edition of this book. As many of these systems were pumped by amplified, mode-locked dye lasers operating around 600 nm, the generated supercontinua seldom exceeded 100-nm bandwidth (Halbout & Grischkowsky, 1985; Palfrey & Grischkowsky, 1984;

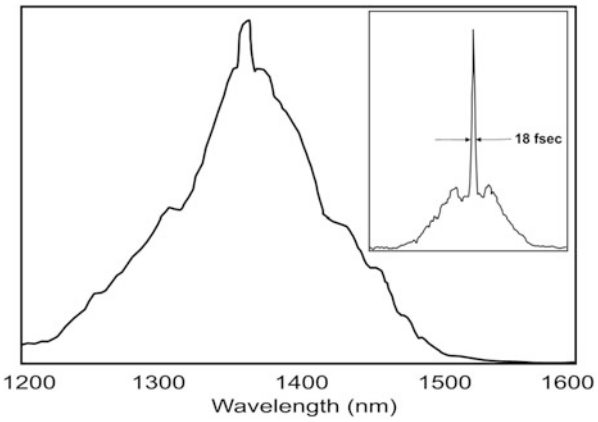

Fig. 5.2 Supercontinuum spectrum (on a linear scale) associated with high-order soliton compression to 18 fs (autocorrelation trace inset) in conventional optical fibre. (After Gouveia-Neto et al., 1988a)

Knox et al., 1985), while in the infrared, associated supercontinua of several hundred nanometres were achieved as represented by Fig. 5.2.

As first proposed by Hasegawa and Brinkman (1980), the process of modulational instability in single-mode fibres, which results from the interplay of nonlinearity and anomalous dispersion, is akin to soliton generation and leads to intense modulation of the steady state. Many non-linear equations exhibit modulational instabilities, and these had been predicted and observed in fluids and in plasmas (see Zakharov & Ostrovsky, 2009, for a review of the early works) prior to the first experimental observation in optical fibre by Tai et al. (1986a,b). In the mid-to-late 1980s, the unavailability of adequately powered continuous-wave (CW) sources operating in the anomalously dispersive regime and in the region of zero dispersion, as well as the difficulty in obtaining long lengths of low-loss fibres at the appropriate wavelength, restricted the initial observation of modulational instability to the quasi-CW regime, where the period of the modulation was substantially less than the duration of the pump pulse deployed. The initial report by Tai et al. used transform-limited 100-ps pulses from a mode-locked Nd:YAG laser operating at 1.319 μm and fibres of up to 2 km long, with typical dispersion of ~−3 ps/nm.km. In these conditions the modulation periods were ~2 ps, much shorter than the effectively CW 100-ps pump pulses. This process, supporting the growth of soliton-like structures, is essential for the initiation of supercontinuum generation in the "long" pulse pump regime. It can also degrade the coherence of the supercontinua generated through high-order soliton compression beyond the minimum compression point. True CW excitation of the modulational instability process was first reported by Itoh et al. (1989) using a 1.319-μm Nd:YAG laser to pump a small core, 5-km length of silica fibre with a fluoride-doped depressed cladding, which exhibited a −2.6-ps/nm.km

dispersion at the pump wavelength. Modulation frequencies in excess of 100 GHz were observed.

Modulational instability can be envisaged as four-wave mixing, where the Stokes and anti-Stokes sidebands exhibit an exponential growth at the expense of two photons from the pump. The process is generally self-starting and is noise seeded. For growth, the sideband frequency separation from the carrier should be less than a defined critical frequency given by $\sqrt{4\gamma P_0/\beta_2}$, where P_0 is the pump power. The maximum growth occurs at a frequency shift of $\sqrt{2\gamma P_0/\beta_2}$. It is possible to seed the process using an additional laser source provided the frequency separation from the carrier lies within the above frequency gain window. This technique was originally proposed by Hasegawa (1984) and experimentally realised by Tai et al. (1986a).

The modulational instability process plays a vitally important role in the initiation of the supercontinuum both in the CW and picosecond-pulsed pump regimes and indeed an equally important role in perturbing the coherence of supercontinua produced through the process of high-order soliton compression when the length scale of the generation process extends beyond the optimum compression length. Induced modulational instability does provide a mechanism to manipulate and enhance the supercontinuum generation process. This has been demonstrated by Gouveia-Neto et al. (1988b) in the quasi-CW pumping regime. Through seeding of the modulational instability sidebands, soliton generation can occur earlier in the fibre leading to significantly enhanced spectral coverage to the long-wavelength side of the generated spectra, for equivalent laser pump powers. The technique was reprised some 20 years later when Solli et al. (2008) actively seeded a modulational instability-initiated supercontinuum. The process allowed short pulse solitons once again to form earlier in the fibre.

5.4 Stimulated Raman Effect and Ultrashort Soliton Pulse Instabilities

As was remarked upon above, with reference to Fig. 5.1, for a pump pulse in the normally dispersive regime and for relatively long pump pulses, the stimulated Raman process cascades until the generated higher orders encroach the anomalously dispersive regime, beyond which a continuum is formed as a result of soliton effects. The stimulated Raman process was first proposed as a means of soliton generation by Vysloukh and Serkin (1983, 1984) and was first experimentally realised by Dianov et al. (1985). Also described in this paper was the first observation of the process of soliton self-Raman interaction, where, upon the evolution of ultrashort soliton structures, the associated bandwidth becomes large enough such that the short-wavelength component was capable of providing gain to the long-wavelength component, through the stimulated Raman process. As a consequence the generated solitons exhibited a long-wavelength shift of their central wavelength on propagation, which generally self-terminated through the increasing peak power

demands of the dispersion-dependent soliton power that increased with wavelength, or through the increased long-wavelength loss of the fibres used. This process was later termed the soliton self-frequency shift (Mitschke & Mollenauer, 1986) and was theoretically modelled by Gordon (1986), and it plays the major role in determining the long-wavelength extent in supercontinuum generation.

In the late 1980s, emphasis was placed upon studies of ultrashort pulse propagation in fibres primarily for pulse compression and femtosecond pulse generation, and although these did not highlight supercontinuum generation, they laid both the theoretical foundation and provided vital experimental discovery that would later underpin the description and realisation of the supercontinuum source. For the propagation of femtosecond pulses, self-effects and in particular self-Raman interaction were of principal interests (Golovchenko et al., 1985, 1987a, b, 1991). In order to achieve high-order solitons and correspondingly high compression ratios, pulses were launched in close proximity to the dispersion zero. This led to instability through the effect of higher-order dispersion and other self-effects such as Raman gain on the femtosecond soliton structures (Vysloukh, 1983; Wai et al., 1986a, 1986b) resulting in fragmentation into the numerous fundamental solitons constituting the high-order soliton, as had been theoretically predicted (Serkin, 1987a, 1987b). This fragmentation into coloured solitons which was renamed soliton fission (Herrmann et al., 2002) plays a dominant role in supercontinuum generation, with the consequently generated short pulse fragments experiencing self-Raman interaction and extending continuously into the longer-wavelength regions.

For a pulse of any arbitrary shape or intensity launched in the region of the dispersion minimum or extending across it, Wai et al. (1987) predicted solitons would emerge together with a dispersive wave component in the normal dispersion regime. They showed that with increasing amplitude at launch, the generated solitons would frequency down shift, as a result of the self-Raman interaction, and that the dispersive wave component would correspondingly frequency up shift. Using a tunable femtosecond pulse source, based upon a soliton self-frequency-shifted Nd:YAG laser source operating around 1.32 μm, Gouveia-Neto et al. (1988c) experimentally verified the predicted behaviour. Prior to that Zysset et al. (1987) and Beaud et al. (1987), by launching 800-fs, 1.341-μm pulses from a synchronously pumped dye laser into a single-mode fibre with a dispersion zero around the same wavelength, unequivocally demonstrated the group velocity matching between the spectrally shifting dispersive wave and the solitons, as the pump power was increased. It should be noted that these observations were made around the same time as Gordon's development of the theory of the soliton self-frequency shift (Gordon, 1986). Nishizawa and Goto (2002a, b) in a series of experiments further confirmed this process of the binding of the group velocity-matched soliton and dispersive wave which plays a pivotal role in the short-wavelength extension of the supercontinuum source.

5.5 Early Studies of Supercontinuum Generation in Fibres

Following the work of Lin et al. (1978) at the end of the 1970s and throughout the 1980s, most of the studies on supercontinuum generation employed mode-locked Nd:YAG lasers, lens coupled to differing fibre formats. Fuji et al. (1980) reported a smooth continuum extending from 300 to 2,100 nm, effectively the complete transmission window of silica, using 100-kW pulses from a Q-switched and mode-locked Nd:YAG coupled with 70% efficiency into comparatively short lengths (5–15 m) of both single-mode and multimode fibres. Although the main spectrum was not displayed, it was reported to be similar to the results of Lin et al. although only the first two cascaded Raman orders were apparent with the remainder of the spectrum being continuous and structureless. In the visible, because of the multimode nature of the fibres deployed, enhanced four-wave mixing through phase matching to higher-order modes was possible.

A Q-switched and mode-locked Nd:YAG laser operating at 1.338 μm was also used by Washio et al. (1980), demonstrating that through pumping in the region of the minimum dispersion of the fibre, the individual orders of the cascaded stimulated Raman signal were not observed, generating only a smooth continuum. When pumping a relatively long 150-m length of single-mode fibre, the clear signatures of both modulational instability and a soliton-Raman continuum are reported. However, the reported results predated the theoretical predictions of modulational instability (Hasegawa & Brinkman, 1980), the experimental realisation of optical solitons (Mollenauer et al., 1980) and the proposals for soliton-Raman generation (Vysloukh & Serkin, 1983), but the authors did clearly note the difference in spectral output through pumping around the dispersion zero.

It was also observed (Nakazawa & Tokuda, 1983) that the shape of the supercontinuum could be modified by using a dual-wavelength pump scheme in the region of low dispersion of a multimode fibre by pumping simultaneously at 1.32 and 1.34 μm from synchronised Q-switched Nd:YAG lasers. It was proposed that the 1.34-μm component along with the pump gave rise to four-wave mixing that enhanced the supercontinuum generation, whereas when only the 1.32-μm pump was deployed, only two cascaded Raman orders were observed.

These experiments were providing evidence that self-phase modulation and stimulated Raman scattering were not the sole contributions to the supercontinuum generation process. This had been realised by Grigoryants et al. (1982) who demonstrated that four-wave mixing was playing a vital role in the process when pumping a multimode fibre with a Q-switched YAG, as well as hinting that the increased peak power within the sub-nanosecond spikes of their Q-switched pump laser would enhance spectral coverage. They also pointed out that the role of noise was an important consideration in the overall generation process.

By the mid-1980s basic studies of supercontinuum generation in fibre were in decline, and although the source had been used in the dispersion characterisation of optical fibres, application was not particularly widespread despite the relative simplicity of the experimental configuration. On the other hand, there was consider-

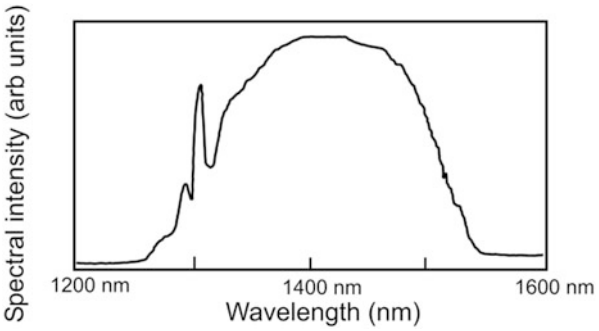

Fig. 5.3 High average power soliton-Raman supercontinuum on a linear intensity scale. (From Gouveia-Neto et al. 1987)

able interest in coherent broad bandwidth generation in optical fibre, primarily for ultrashort pulse generation. The techniques used were either self-phase modulation under normal dispersion, along with external grating pairs for phase compensation, or high-order soliton effects where pulses of only a few optical cycles had been generated, as described above.

Following the report of broadband generation as a result of high-order soliton compression and self-Raman interaction (Dianov et al., 1985), several laboratories worldwide were inspired to investigate Raman generation in the anomalous dispersion regime using a variety of laser sources and pump pulse durations as a means for short pulse generation and consequential broadband coverage in the near infrared (Gouveia-Neto et al., 1987; Vodop'yanov et al., 1987; Grudinin et al., 1987; Islam et al., 1989). These investigations used various pump wavelength and pump pulse durations. For pumps in the normal dispersion regime, the classic cascade of stimulated Raman orders was observed up to the region of zero dispersion beyond which a continuum developed. Gouveia-Neto et al. (1987) clearly demonstrated that modulational instability initiated the continuum generation process when deploying 100-ps pump pulses at 1.32 μm operating in the anomalously dispersive regime and close to the zero dispersion wavelength of the fibre. It was proposed too that the generated continuum spectrum contained many fundamental solitons randomly distributed in time, which gave rise to a pedestal on the measured autocorrelation/cross-correlations. Figure 5.3 shows a representative spectrum of a typical soliton-Raman supercontinuum, where the pump at 1.32 μm and modulational instability sidebands are clearly visible. It should also be noted that these were probably the first high average power supercontinuum sources, with average powers in the watt regime.

Islam et al. (1989) also noted the role of modulational instability in initiating the process, as well as that of the soliton self-frequency shift giving rise to the long-wavelength extension. They also pointed out the important role of soliton collisions in the presence of Raman gain as a wavelength extension mechanism. In the temporal and spectral domains, Gouveia-Neto et al. (1989b) investigated the evolution

from modulational instability to soliton-Raman continuum. It was also demonstrated that through seeding of the modulational instability sidebands, the continuum could be generated at substantially lower pump powers and that for equivalent total incident power, the seeded systems extended to longer wavelengths and the autocorrelation traces of the output soliton signals exhibited shorter durations and substantially reduced pedestal components (Gouveia-Neto et al., 1988b). Selection within the supercontinuum allowed the generation of a source of wavelength-tunable femtosecond pulses—although the process of evolution from noise to Raman solitons does prohibit application where low temporal jitter is required. Islam et al. (1989) demonstrated that there was no temporal correlation between widely separated wavelengths within the generated Raman supercontinuum.

As technological improvements allowed the scaling of average power levels in double-clad fibre laser configurations, soliton-Raman generation in a 2.8-km-long, 18% Ge-doped silica fibre for enhanced Raman gain allowed the first CW-pumped supercontinuum to be generated. Using a ring geometry pumped by a 1-W Yb:Er fibre laser at 1.55 μm, a spectrum extending nearly 400 nm was obtained (Persephonis et al., 1996). By the end of the 1990s, the further advances in fibre laser technology allowed the first all-fibre fully integrated supercontinuum source to be demonstrated by Chernikov et al. (1997). This was based upon a diode-pumped Yb fibre laser, directly fuse coupled to a length of single-mode fibre with an angled output facet. Rayleigh backscatter initiated laser action and spectral narrowing in the high gain device which consequently led to stimulated Brillouin scattering causing the laser to Q-switch. This produced pulses of about 2-ns duration at selectable repetition rates in the range 1–20 kHz and an average power of up to 1 W. With pulse energies of up to 50 μJ, peak powers in excess of 10 kW were generated in-fibre. Starting from the fundamental at 1.06 μm, the generated supercontinua exhibited the characteristic features of cascaded Raman orders up to the dispersion zero and a soliton-Raman continuum up to 2.3 μm. To the short-wavelength side, weak four-wave mixing was observed plus second and third harmonic generation of the pump and cascaded Raman orders. The peak power within the supercontinuum was also sufficient to also allow external frequency doubling in a crystal of the broad infrared supercontinuum spectrum allowing access to the complete visible. The completely integrated, compact nature of this source, with a footprint ~160 cm^2, made the source attractive for applications such as optical coherence tomography. Another application area that had been investigated was in the spectral selection of a continuum for channel allocation of synchronised pulse streams in dense wavelength division multiplexing in communications.

5.6 Supercontinuum Applications in Telecommunications

The concept of utilising a supercontinuum for the generation of multiple synchronised information channels was introduced by Morioka et al. (1993) using a mode-locked Nd:YLF laser operating at 1.314 μm, with the 7.6-ps, 100-W peak

power pulses used to pump a 450-m length of polarising maintaining fibre in the low anomalously dispersive regime (0.33 ps/nm.km). The generated spectrum extended nearly 200 nm, and a birefringent fibre filter was used to select 100 channels, each separated by about 1.9 nm. The spectral coverage requirements of the technique are quite modest needing only that the continuum coincides with the principal telecommunication amplifier windows, the second around 1.3 μm or the third around 1.5 μm. It also calls for the supercontinuum source to be relatively flat over its operational extent—although this can be achieved through passive filtering—and also that the noise-induced jitter on each channel should be less than the temporal window of the receiver. Consequently, the influence of noise on some soliton-based schemes, which can be significant, should be minimised.

To make the source more practical, by deploying an all-fibre, mode-locked Er-fibre laser–amplifier pump configuration, Morioka et al. (1994) demonstrated nearly penalty-free transmission of 6.3 Gbit/s over the spectral range 1535–1560 nm, although only a fraction of the 200-nm generated supercontinuum was effectively utilised. Further development in terms of capacity continued, with in excess of 1000 channels being generated over relatively modest spectral continua of around 100 nm (Collings et al., 2000; Takara et al., 2000). However, Kubota et al. (1999) did point out that coherence degradation occurred during soliton pulse compression and the associated supercontinuum generation through the interaction between amplified spontaneous emission and modulational instability. They numerically investigated techniques to negate or minimise this, proposing the use of normally dispersive fibre, consequently eliminating solitons, or through the use of dispersion-decreasing fibre or through spectral band filtering, and suggested that this should be considered when generating WDM channels from supercontinua.

Tapered fibres had been employed earlier (Lou et al., 1997; Mori et al., 1997; Okuno et al., 1998), with the fibres exhibiting a dispersion-decreasing characteristic along the length of the fibre and a dispersion-flattened profile. At input the dispersion was anomalous, changing to normal at the output. The relatively slow decreasing dispersion with transmission length gave rise to adiabatic pulse compression of the soliton input signals, which gave a corresponding spectral broadening, while at the normally dispersive output, self-phase modulation of the compressed pulses dominated the spectral broadening. However, on propagating through the region of zero dispersion, the evolution of very high-order solitons leads to severe temporal and spectral instability.

In a differing approach, adiabatic soliton compression in a 10-km-long distributed Raman amplifier also contributed to a supercontinuum extending over 100 nm centred around 1550 nm at 10 GHz generating up to 10 mW/nm (Lewis et al., 1998).

For potential telecommunications applications, increased stability was achieved through the simple expedient of operating in the normally dispersive regime, where broadening was simply dominated by self-phase modulation (Takushima et al., 1998). Using high-order soliton compression in two cascaded short fibres with a steplike decreasing dispersion profile, Nowak et al. (1999) generated a relatively

flat 210-nm broad continuum for potential application to communications, where spectral shaping was introduced using third-order dispersion effects.

Although total transmission rates of up to 1 Tbit/s were demonstrated (Morioka et al., 1996) with ten spectrally selected channels at 100 Gbit/s propagating over 40 km, the general technique was not investigated much further after the end of the century and was not deployed in the field; however, the techniques developed to minimise instability, such as the use of normal dispersion, short tapers, and short length, high-order soliton compression, were all successfully applied to the following generation of supercontinuum sources.

5.7 Modelling Broadband Pulse Propagation in Optical Fibres

The experimental demonstrations of dramatic soliton-effect pulse compression, soliton fission, coloured soliton generation and Raman self-frequency shift in the mid-1980s required the development of enhanced numerical modelling. The NLSE given by Eq. (5.1) was derived for narrowband pulses where the higher-order terms resulting in most of the supercontinuum dynamics are negligible, and were omitted. In the first numerical studies, the higher-order effects were considered individually: higher-order dispersion by Vysloukh (1983), Wai et al. (1986a, b) and Agrawal and Potasek (1986); self-steepening by Tzoar and Jain (1981) and Anderson and Lisak (1983); and the Raman effect by Vysloukh and Serkin (1983), Gordon (1986) and Stolen et al. (1989). Subsequently there emerged several seemingly independent papers describing comprehensive models which include all of the above effects, derived from first principles, by Golovchenko et al. (1987a), Beaud et al. (1987), Kodama and Hasegawa (1987), Blow and Wood (1989) and Mamyshev and Chernikov (1990). They all essentially reduce to what is now called the generalised non-linear Schrödinger equation (GNLSE), valid for optical pulses with just a few optical cycles. In the frequency domain, it takes the following form:

$$\partial_z \widetilde{U} = i\left(\beta(\omega) - \frac{\omega}{v_{ref}}\right)\widetilde{U} + i\frac{n_2\omega}{cA_{\text{eff}}}\mathcal{F}\left[\left(R * |U|^2\right)U\right], \tag{5.3}$$

where $\widetilde{U} = \mathcal{F}[U(z,\tau)]$, with $\mathcal{F}$ the Fourier transform, v_{ref} is a chosen reference velocity and $R(t)$ is the non-linear response function, which for glass takes the form $R(t) = (1 - f_r)\delta(t) + f_r h_R(t)$, i.e. there is an instantaneous Kerr part and a delayed Raman response described by h_{R} (Stolen et al., 1989). The GNLSE as presented in Eq. (5.3) includes the full modal dispersion, the Raman effect and—through the explicit ω prefix to the non-linear term—self-steepening (which leads to optical shock formation). It is often modified in a number of ways, for example, by using a truncated Taylor expansion of the dispersion operator, removing the phase velocity offset by subtracting $\beta(\omega_{\text{ref}})$ from the linear term and including the frequency

dependence of the effective area—though some care is required when doing this (Laegsgaard, 2007). It can also be further extended to include additional effects, such as adding a term describing third harmonic generation (Genty et al., 2007b), or non-linear effects arising from interactions with the conjugate of the envelope (i.e. negative frequencies) (Conforti et al., 2013). In the latter case, it is valid for arbitrary pulse durations—so long as the assumed material response remains valid (i.e. propagation far from resonances). The full GNLSE can also be generalised to the case of multimode propagation (Poletti & Horak, 2008), and tapered fibres (Mamyshev & Chernikov, 1990; Travers & Taylor, 2009; Laegsgaard, 2012).

Although the NLSE and GNLSE are widely used for supercontinuum simulations, and also are highly amenable to analysis, the ever-expanding bandwidth of supercontinuum sources makes the use of an envelope model more of a hindrance than a simplification. When dealing with multiple octave spectra—although the full GNLSE is still valid in that case—it can be much simpler to model the propagation of the real electric field, and this has become more prominent over the last decade (Husakou & Herrmann, 2001; Kolesik & Moloney, 2004; Kinsler, 2010; Chang et al., 2011). The field equivalent of Eq. (5.3), propagating the spectrum of the full real electric field $\widetilde{E} = \mathcal{F}[E(z,\tau)]$, is the so-called unidirectional pulse propagation equation (UPPE) given by

$$\partial_z \widetilde{E} = i\left(\beta(\omega) - \frac{\omega}{v_{ref}}\right)\widetilde{E} + i\frac{\chi^{(3)}\omega}{2cn_{\text{eff}}}\mathcal{F}\left[\left(R * E^2\right)E\right]. \tag{5.4}$$

This equation, while strikingly similar to Eq. (5.3), includes a full description of third harmonic generation, and is not restricted to positive frequencies. When modelling broadband supercontinua, it is also often more efficient. A multimode version of the UPPE has been recently introduced by Tani et al. (2014).

All of the propagation Eqs. (5.1), (5.3) and (5.4) can be straightforwardly and efficiently integrated using a variation of the split-step Fourier method introduced by Hardin and Tappert (1973), and further refined by Fisher and Bischel (1973, 1975), Blow and Wood (1989) and Hult (2007). Alternatively, through the transformation $\widetilde{E}' = \widetilde{E}\exp\left[-i\left(\beta(\omega) - \frac{\omega}{v_{\text{ref}}}\right)\right]$, Eq. (5.4) (and similarly Eqs. (5.1) and (5.3)) is cast as a system of ordinary differential equations, solvable with the usual techniques. A simple and complete implementation of Eq. (5.3) using this technique was provided by Travers et al. (2010).

For some parameter regimes, it is essential to include a realistic model of the noise inherent to the system to fully reproduce experimental results—especially when dealing with modulational instability-based dynamics. The most widespread treatment involves adding a representation of quantum noise fluctuations to the initial conditions, simply by adding a field with spectral power corresponding to one photon per mode with random phase (Drummond & Corney, 2001; Dudley et al., 2002; Corwin et al., 2003). Depending on the pump source conditions, the additional noise of the pump source may also need to be included (see, e.g. the CW Supercontinuum Modelling section below). Additionally, some works have included

a non-deterministic spontaneous Raman term in the GNLSE (Drummond & Corney, 2001; Corwin et al., 2003; Dudley et al., 2006), although this has a relatively minor effect.

As the basic models were complete by the late 1980s, several pioneering works numerically studied the generation and dynamics of what might be classed as supercontinua (Beaud et al., 1987; Golovchenko et al., 1987a; Islam et al., 1989; Blow & Wood, 1989; Dianov et al., 1989; Golovchenko et al., 1991; Gross & Manassah, 1992; Boyer, 1999). This effort was significantly reinvigorated when the next generation of experimental supercontinuum sources emerged at the turn of the last century (see below), and an explosion of modelling work began to understand the results (Karasawa et al., 2001; Husakou & Herrmann, 2001; Coen et al., 2001; Gaeta, 2002; Dudley & Coen, 2002; Dudley et al., 2002; Herrmann et al., 2002).

5.8 The New Generation of Supercontinuum Sources

Despite the enormous advances made in the understanding of the physical processes contributing to supercontinuum generation in fibres, up to 2000, apart from a few examples, the actual experimental configurations had changed very little since the first demonstrations by Alfano and Shapiro (1970a, b, c, d). Quite simply the bulk sample had been replaced by a single-mode fibre, yet the large frame, low repetition rate pump laser and lens coupling remained, making the schemes unstable, irreproducible and unsuitable for widespread application. The use of conventional fibre negated efficient generation in the visible spectral region, due to the unfavourable dispersion landscape, and most supercontinua exhibited the classic cascade of Raman orders followed by a soliton-generated continuum in the anomalously dispersive regime, if there was adequate pump power. Two factors were to then impact upon the scientific and commercial success of the supercontinuum. The first was the availability of high-power, fibre-based pulse sources in master oscillator power fibre amplifier configurations, which would allow pump formats from CW through to femtosecond pulses and permit complete fibre integration of the source. The second was the development of photonic crystal fibre, PCF (Knight et al., 1996; Knight, 2003; Russell, 2006) which—through design of the microstructure—allowed great control of the dispersion and the non-linearity, as well as endlessly single-mode operation over the complete supercontinuum spectrum (Birks et al., 1997). As a result soliton operation could be achieved with all of the readily available laser pump wavelengths (Wadsworth et al., 2000).

5.9 Femtosecond Pulse-Pumped Supercontinua

The result that probably had the greatest impact on supercontinuum generation in fibre and drove research and development into the first decade of the twenty-first

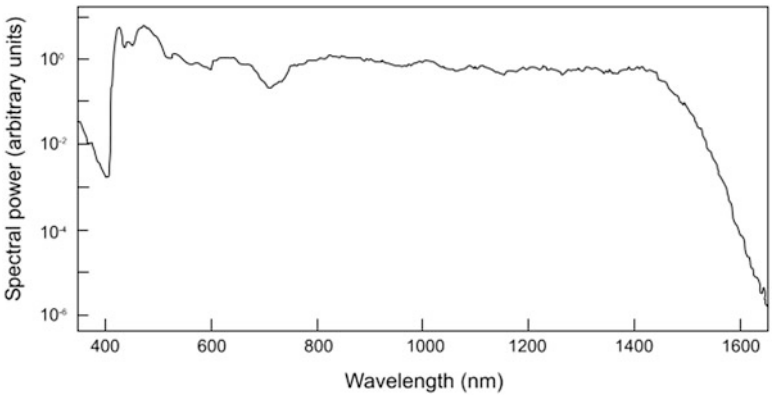

Fig. 5.4 Characteristic, time integrated, supercontinuum generated in a photonic crystal fibre with a zero dispersion around 770 nm pumped by 100-fs, 8-kW pulses at 795 nm. (After Ranka et al., 2000)

century was reported by Ranka et al. (2000). Using a mode-locked Ti-sapphire laser around 790 nm to pump a 75-cm length of PCF with a zero dispersion at 770 nm, the launch of 100-fs high-order solitons with a power of approximately 8 kW led to rapid pulse compression accompanied by spectral broadening, followed by pulse break-up or fission into numerous single solitons. As can be seen in Fig. 5.4, the generated supercontinuum extended from 400 to 1600 nm.

The striking features of the generated supercontinuum are its relative flatness (while remembering it is time integrated), the spectral coverage including the complete visible to the near infrared and saturation of the pump. No new non-linear processes were involved, yet the ability to manipulate the physical parameters of the PCF to allow control of the non-linearity and the dispersion zero to readily facilitate soliton generation of unamplified pulses from conventional femtosecond lasers created instant impact. Key to the generation process was the rapid pulse compression of the launched, high-order pump solitons to their minimum pulse width, over a length scale given approximately by $L_{\text{fiss}} = \tau_0^2/N\,|\beta_2|$. Beyond this length further propagation is affected by inherent system perturbation such as higher-order dispersion, self-Raman interaction and modulational instability, resulting in the temporal and spectral fragmentation into numerous fundamental solitonic and dispersive structures (Herrmann et al., 2002; Cristiani et al., 2004; Genty et al., 2007a). As a result of the noise-driven processes, the supercontinuum spectrum associated with each pump pulse is not identical, and the smooth profile recorded as in Fig. 5.4 is the result of the accumulation of ~10^8 spectra.

In situations where noise reduction and high stability are essential in application of the supercontinuum, such as in metrology, it is advisable to employ pump pulses with duration of 50 fs or less, such that for the peak pump powers launched, the fibre length corresponds to the length of maximum compression of the high-order soliton, with spectral extraction at that point. Alternatively, soliton effects can be negated by

solely operating in the normal dispersion regime such that self-phase modulation is the dominant process (Nowak et al., 1999; Heidt, 2010; Hooper et al., 2010).

For soliton-based spectra, if the bandwidth of a soliton extends beyond the zero dispersion and into the normally dispersive regime, dispersive waves can be emitted (Vysloukh, 1983; Wai et al., 1986a, b); usually the group velocity of these waves is lower than that of the solitons (as they are emitted further from the zero dispersion point), and hence they are delayed with respect to the main pulse. As the solitons then experience self-frequency shifting due to the Raman effect, they are decelerated to the point at which they overlap with the dispersive waves, which are subsequently blue-shifted due to cross-phase modulation from the trailing edge of the soliton. Thus, a cycle of soliton red shift and deceleration, dispersive wave blue shift and delay leads to the trapping of the dispersive waves, and is the main mechanism by which the short-wavelength edge of the supercontinuum is extended (Gorbach & Skyrabin, 2007). Experimentally this was originally reported by Beaud et al. (1987) and has been verified by many since (Nishizawa & Goto, 2002a, b; Cristiani et al., 2004; Genty et al., 2004).

Although photonic crystal fibres were instrumental in allowing solitons to be generated by common pump lasers, they were not essential. Innovative techniques were developed that allowed conventional telecommunications fibre to be used by employing controlled, tapered structures manufactured using a travelling flame and fibre stretching, with the zero group velocity dispersion of the taper shifting to shorter wavelengths with decreased taper diameters. Birks et al. (2000) demonstrated a continuum extending from 370 to 1545 nm pumped by an unamplified, 100-fs, mode-locked Ti-sapphire laser which allowed up to 0.25-mW/nm spectral density in the continuum. By cascading several tapers and pumping with a diode-pumped, picosecond, Nd:YVO_4 laser at 1064 nm, Teipel et al. (2005) generated supercontinua with 5.65-W average power. Manufacturing submicron diameter tapers, down to 200 nm, permitted Leon-Saval et al. (2004) to produce visible supercontinua using the low-power pump of a 532-nm frequency-doubled microchip laser delivering 1 kW, 600-ps pulses at 6.3 kHz.

This post-tapering process can also be applied to PCF, enabling the creation of extremely small isolated silica cores. The resulting very high non-linear coefficients and dispersion landscapes enable supercontinuum formation with extremely low peak powers, and this can be used to generate supercontinua from mode-locked frequency combs with very high repetition rate—Stark et al. (2011) demonstrated a stabilised 14-GHz repetition rate visible supercontinuum for applications to astronomy. Alternatively the dynamics in very short lengths of PCF tapers can enable deep-UV extended supercontinuum generation down to 280 nm (Stark et al., 2012a). These results were reviewed in Stark et al. (2012b).

Conventionally structured, highly non-linear fibres may also be used for femtosecond-pumped supercontinuum generation. A fibre with a γ of 8.5 W^{-1} km^{-1} was manufactured by Nicholson et al. (2003a, b) and pumped in an all-fibre configuration using a passively mode-locked Er fibre laser and amplifier delivering up to 50-mW pump power. The generated supercontinuum extended from about 1050 to 2400 nm. The system was later improved and power

scaled using a chirped pulse amplification scheme to generate 34-fs pump pulses at 1550 nm to enable a continuum that extended from around 850 to 2600 nm (Nicholson, Yablon, et al., 2004a). Er-doped femtosecond laser pumping of highly non-linear polarisation preserving (Takayanagi et al., 2005) and hybrid designs of cascaded dispersion shifted and highly non-linear fibres (Hori et al., 2004) have produced continua typically in the range of 1000–2400 nm, with the use of fibres with dispersion zeroes in the range of 1500 nm simply inhibiting visible wavelength generation. By utilising a cascaded hybrid of a highly non-linear conventional fibre, followed by a PCF with a zero dispersion at 753 nm, Nicholson et al. (2008) extended the short wavelength of an Er fibre laser-pumped supercontinuum to below 440 nm. An alternative technique to obtain visible generation with an Er pump is to simply frequency double to 780 nm and pump a PCF with a dispersion zero around 740 nm as was demonstrated by de Matos et al. (2005), generating a spectrum extending from about 400 to 1450 nm.

5.10 Modelling of Femtosecond-Pumped Supercontinua

With the increased understanding of the subtleties contributing to the overall spectral generation and with increased computing power, the modelling of supercontinuum generation exhibited remarkable agreement between experiment and theory (Husakou & Herrmann, 2001; Gaeta, 2002; Dudley & Coen, 2002; Dudley et al., 2002; Herrmann et al., 2002). Cross-correlation frequency-resolved optical gating traces were used to investigate the evolution of the spectral and temporal features of a 25-fs, Ti-sapphire-pumped continuum generated in a 16-cm-long PCF (Dudley et al., 2002). All the features of soliton fission, self-frequency shift, soliton-dispersive wave trapping and their relation to the supercontinuum were clearly identified.

Figure 5.5 shows modelling results, based on Eq. (5.3), for a 50-fs, 10-kW peak power pulse at 835 nm launched into a fibre with a zero dispersion wavelength of 780 nm and non-linear coefficient of 110 W^{-1} km^{-1}. The input soliton order is ~8.6. The lower part of Fig. 5.5b shows the initial soliton-effect self-compression, enhanced by self-steepening. The corresponding part of Fig. 5.5(c) shows the initial SPM-driven spectral broadening and blue asymmetry due to the self-steepening effect (DeMartini et al., 1967; Anderson & Lisak, 1983). When the pulse is sufficiently compressed, the blue edge extends into the normal dispersion region, and dispersive waves are emitted (Fig. 5.5b and c at $z = 6.8$ mm). This corresponds to the fission point in the time domain (Kodama & Hasegawa, 1987; Tai et al., 1988; Husakou & Herrmann, 2001). Subsequent propagation (upper parts of Fig. 5.5b and c) exhibits red soliton self-frequency shift and corresponding temporal delay. The blue edge of the supercontinuum is also extended. From the spectrogram plot in Fig. 5.5(a), we see that the most blue-shifted dispersive wave is trapped behind the most intense and red-shifted soliton (indicated by the dashed line), following the mechanism described above (Beaud et al., 1987; Nishizawa & Goto, 2002a, b; Genty et al., 2004; Gorbach & Skyrabin, 2007).

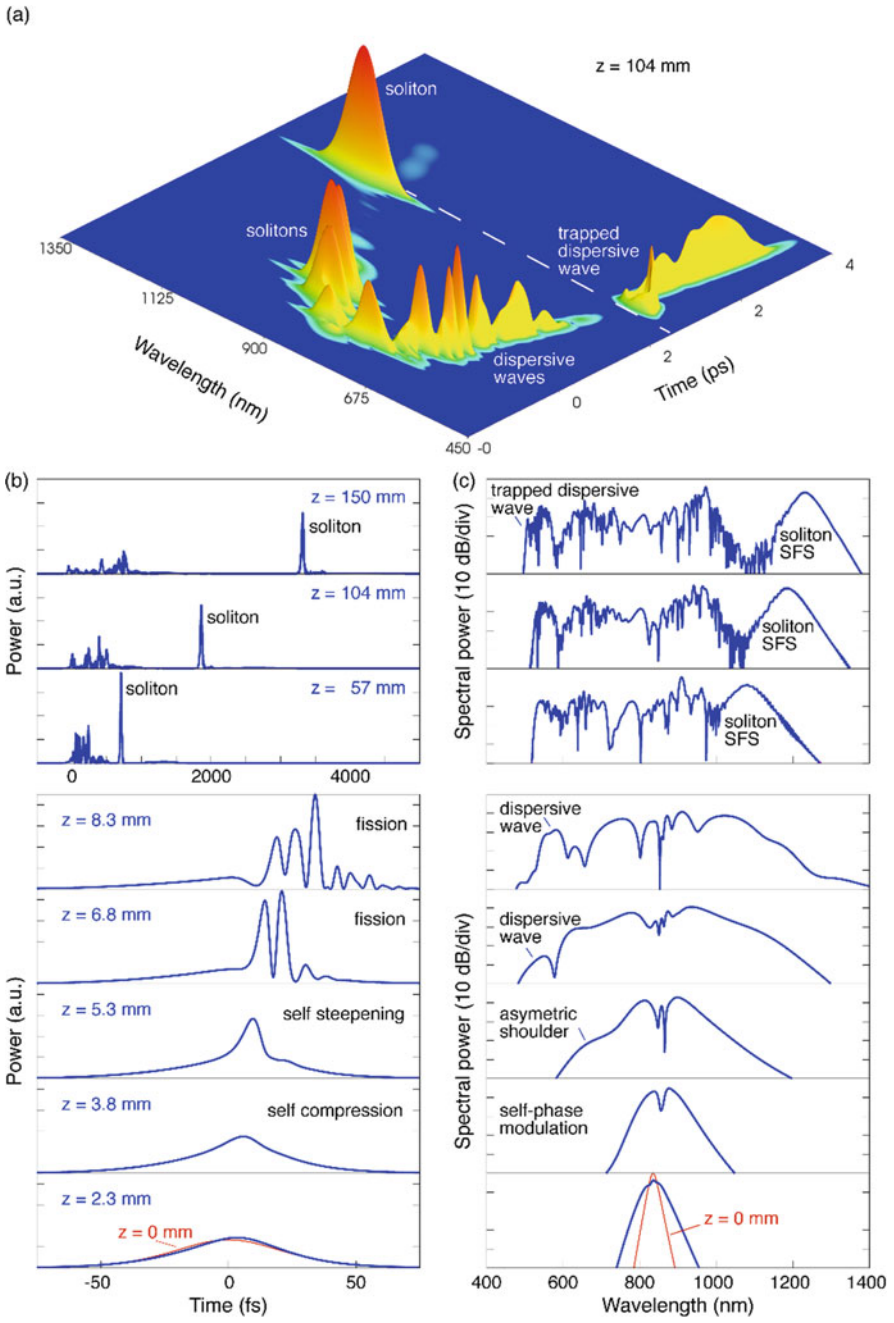

Fig. 5.5 Femtosecond-pumped supercontinuum from a 50-fs, 10-kW peak power pulse at 835 nm launched into a fibre with a zero dispersion wavelength of 780 nm, and non-linear coefficient of 110 W^{-1} km^{-1}. The input soliton order is ~8.6. (**a**) XFROG spectrogram at 104-mm propagation; (**b**) temporal slices through propagation; (**c**) corresponding spectral slices. The lower parts of (**b**, **c**) show details of the initial self-compression and soliton fission dynamics. The dashed line in (**a**) indicates the soliton-dispersive wave trapping

5.11 Picosecond Pulse-Pumped Supercontinua

Wide application of the supercontinuum source is based on the capability of extensive wavelength coverage, preferably covering the complete window of transmission of the fibre type used, which for silica is around 350–2400 nm. In addition, high spectral power densities, and consequently high average powers, lead also to ease of application. Although the fibre-integrated Er-pumped systems described above achieved power densities approaching 1 mW/nm, this occurred over a rather restricted spectral range. In addition, pumping at 1550 nm does not readily lead to operation in the visible through limitations of the soliton-dispersive wave interaction. Despite impressive spectral coverage using unamplified femtosecond Ti-sapphire pumping, the typical average power levels achievable were in the tens of milliwatts regime with corresponding spectral power densities in the few tens of microwatts per nanometre. Unlike the femtosecond regime, by operating in the picosecond regime, watts of average power can be extracted from oscillator–amplifier configurations without concerns of non-linearity. Initial reports on the application of 60-ps pump pulses from a krypton ion laser at 647 nm showed coverage from 400 nm to beyond 1000 nm (Coen et al., 2001), and a rather modestly average powered 800-ps, frequency-doubled microchip laser at 530-nm lens coupled into a PCF exhibited coverage from 450 to 800 nm and clearly identified the potential for construction of compact supercontinuum sources (Provino et al., 2001).

Increased average powers were achieved with picosecond (Seefeldt et al., 2003) and femtosecond (Schreiber et al., 2003) solid-state Nd-doped laser outputs, lens coupled to PCFs with up to 5-W average power, in the range of 500–1800 nm. The first, high-power, fully fibre-integrated supercontinuum source was reported by Rulkov et al. (2004a) and Rulkov et al. (2005). This used a master oscillator, power fibre amplifier configuration. The master oscillator was a normally dispersive, polarisation rotation mode-locked Yb fibre laser, generating chirped pulses, the duration of which was controlled through spectral filtering. The outputs were amplified, single pass, in a 1-m Yb preamp and a 1.5-m large mode area amplifier. The 60-kW peak power pulses at an average power of 8 W were launched into various lengths of PCF with a zero dispersion at 1040 nm. A typical spectral output is shown in Fig. 5.5 where spectral power densities in excess of 1 mW/nm were achieved over the spectral range 525–1800 nm.

The temporal behaviour of the spectral components of a similarly generated supercontinuum was investigated by Rusu et al. (2005), while over the years the power scaling has been undertaken (Chen et al., 2010; Hu et al. 2011a, b), with average power in the continuum reaching ~50 W.

High-order soliton dynamics do not play an important role in the formation of a supercontinuum using picosecond pumping, although the fundamental soliton power scales as the inverse square of the pulse duration, the fission length period scales as the square of the pulse duration and is also inversely proportional to the dispersion; consequently, the fission length tends to be substantially greater than the actual fibre lengths used. For these longer pulses, modulational instability and

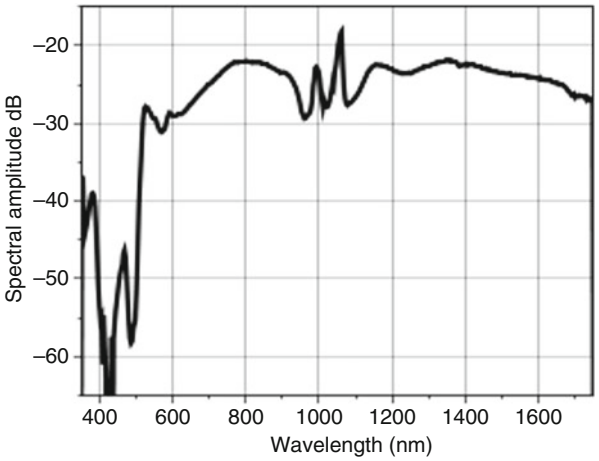

Fig. 5.6 High average power supercontinuum obtained in 35 m of photonic crystal fibre with a zero dispersion wavelength of 1040 nm pumped by a Yb MOPFA at 1 060 nm. (After Rulkov et al., 2005)

four-wave mixing are the processes that initiate the continuum generation, breaking the long input pulses into femtosecond scale sub-pulses that experience parametric and Raman gain (Coen et al., 2002), such that random femtosecond solitons evolve. These ultrashort pulse solitons subsequently experience the soliton self-frequency shift and collisions, leading to spectral broadening. In addition the previously discussed soliton-dispersive wave dynamic leads to short-wavelength extension of the spectral output.

It was observed, see, for example Fig. 5.6, that using 1060-nm pumping of anomalously dispersive fibres, in the region of the dispersion zero, that the short wavelength of the supercontinuum did not extend below 525 nm and that this also was independent both of pump power and fibre length. This was simply related to the observation made by Zysset et al. (1987) on the group velocity matching of the self-frequency shifting soliton and the coupled dispersive wave. Due to scattering and waveguiding, the losses of silica-based fibres begin to increase substantially above about 2000 nm. Consequently, self-shifting solitons approaching this wavelength will experience loss and subsequently broaden, and the process will be self-terminating. The short-wavelength extreme is thus limited to the spectral extent that is group velocity matched to this upper wavelength limit.

Several techniques were introduced to overcome the short-wavelength limit, and have been recently reviewed in Travers (2010c). The technique of cascading two photonic crystal fibres was introduced by Travers et al. (2005a, b), where the dispersion zero of the output fibre was less than that of the input fibre. In the first realisation of this, the input fibre generated a spectrum similar to that of Fig. 5.5 in a 0.7-m-long PCF with a dispersion zero at 1040 nm. The 10-m-long output fibre had a dispersion zero around 800 nm, and the supercontinuum generated in the input fibre

was used to pump the second fibre. Once the supercontinuum generated in the input fibre extended to around 750 nm, rapid extension of the output continuum to around 400 nm was observed. This was simply due to the fact that group velocity matching in the second fibre allowed shorter wavelength matching of the long wavelengths as a result of the lower dispersion zero point.

The concept of the concatenated, dispersion-decreasing fibre configuration was taken to its extreme in the form of a continuously dispersion-decreasing tapered PCF that was directly manufactured at the pulling tower through variation of the pull speed and manipulation of the environmental pressure to regulate hole size. In a 1-m-long taper, pumped by 3–4-ps pulses of up to 50-kW peak power at 1060 nm, the generated continuum effectively covered the complete transmission window of silica from 320 to 2300 nm at an average power of 3.5 W (Kudlinski et al., 2006; Travers et al., 2007). The use of a tapered fibre structure is also important in enhancing the soliton-dispersive wave interaction, leading to short-wavelength extension. For a PCF of constant pitch and air hole diameter, there is a single group velocity dispersion versus wavelength map. For a tapered fibre, this group velocity profile versus wavelength varies continuously along the length of the fibre, with the zero dispersion shifting to shorter wavelength as the dimensions compress. Consequently, for a given wavelength, the group velocity dispersion decreases continuously with wavelength. Even in the absence of the self-Raman effect, this GVD decrease with wavelength is equivalent to the soliton self-frequency shift, as the solitons will decelerate, experiencing a lower group velocity, leading to a trapping of the short-wavelength dispersive waves (Travers & Taylor, 2009). Consequently the taper process adds further enhancement to the short-wavelength continuum extension, which can be up to 300 nm as compared to equivalent operation in a fixed core fibre. Up to 2 mW/nm has been achieved in the UV region using tapered fibre technology (Kudlinski et al., 2006). Figure 5.7 shows a typical continuum generated in a 1.5-m taper, and the inset shows the detail of the short-wavelength extent of a continuum, down to 320 nm, generated in a similar taper (Travers et al., 2007). Several recent works have attempted to further optimise the long PCF tapers for picosecond pumping (Sørensen et al., 2012).

Stone and Knight (2008) proposed that through modifying the waveguide structure of their photonic crystal fibre in the infrared, by making it more like a strand of silica, i.e. by increasing the air fill fraction, they could decrease the group velocity in the IR, where the waveguide contribution is greatest, and so be able to match the group velocity on the short-wavelength side at a substantially shorter wavelength. Using 600-ps pulses from a 60-mW average power microchip laser at 1064 nm, they covered the spectral region 400–2450 nm in 10-m-long PCF. Other more complicated processes have been used to promote short-wavelength extension, such as the irradiation of highly non-linear fibres using UV light, which causes a UV-induced refractive index change such that the zero dispersion wavelength can shift by up to 100 nm, consequently allowing the short-wavelength limit of the generated supercontinuum to extend by up to 200 nm (Nicholson et al., 2004b; Westbrook et al., 2005).

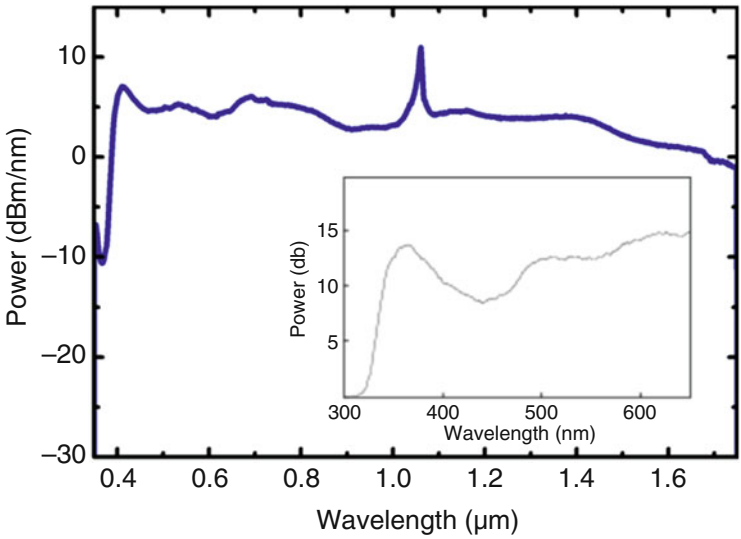

Fig. 5.7 3.5-W average power supercontinuum obtained in a 1.5-m tapered fibre pumped at 1,060 nm with an input zero dispersion at 1,040 nm (After Kudlinski et al., 2006). Inset shows the detail of the short-wavelength extent in a similar fibre. (After Travers et al., 2007)

Champert et al. (2004) used a long pulse, ~600 ps, dual-wavelength 1064-nm and 532-nm pumping scheme based on a frequency-doubled microchip laser. It was observed that when pumping a 4-m-long PCF with a zero dispersion at 870 nm with only the second harmonic signal, the classic cascade of up to seven Raman orders was observed, while on simultaneous excitation with both the fundamental and second harmonic pump signals, a smooth, featureless continuum was observed extending from just below 400 to 1700 nm, the upper limit of the detector. Although no explanation as to the mechanism was presented, it is highly likely that the cascaded Raman orders were trapped and broadened through cross-phase modulation and intra-pulse four-wave mixing from the solitonic infrared components derived from the pump pulse at 1064 nm.

As has been mentioned above, solitons can evolve from noise or from the amplification of noise, and noise seeding of modulational instability can influence signal evolution. Short pulse, noise-driven structures occurring in the early stages of soliton evolution experience self-Raman interaction earlier and consequently exhibit increased long-wavelength extent. This process underpins the observation of so-called rogue waves in supercontinua (Solli et al., 2007). Solli et al. undertook a novel dispersive Fourier transformation characterisation of the noise-based distribution of long-wavelength events. Further refinement in the technique has allowed single shot (Goda & Jalali, 2013) and the real-time measurements of spectral noise in the generation process (Wetzel et al., 2012; Godin et al., 2013). It should be noted that the understanding of what constitutes a rogue wave is now more nuanced, with soliton collisions, and generalised soliton solutions and breathers having been

identified as perhaps better rogue wave analogues than extreme solitons (Erkintalo et al., 2010; Ruban et al., 2010; Genty et al., 2010; Dudley et al., 2014).

5.12 Modelling of Picosecond-Pumped Supercontinua

Coen et al. (2001) were the first to model picosecond supercontinuum generation in PCF, using exactly the same equations as those for the femtosecond case, i.e. Eq. (5.3) or (5.4). It is important to include suitable noise conditions in the long pulse case, because, as described above, the dominant initial supercontinuum mechanism for long pulses is modulational instability (MI), which is noise seeded. Simulations of a 10-ps, 20-kW peak power pulses at 1060 nm propagating through a high air-filling fraction PCF, or silica strand, with a zero dispersion at 994 nm and nonlinear coefficient of 18 W^{-1} km^{-1}, are shown in Fig. 5.8. In the lower panel of Fig. 5.8b and c, the initial MI dynamics are exposed both in the emergence of a temporal ripple leading to >150-kW spikes in the time domain (starting from 20 kW) and corresponding multiple side-band growth in the spectral domain. In the upper panels of Fig. 5.8b and c, the whole temporal and spectral features of the emerging supercontinuum are exposed. The initial 10-ps pulse is completely broken up into many short structures. The MI side-band spectrum merges into a continuum that extends both to longer and shorter wavelengths upon propagation. Inspection of spectrogram traces, such as the one shown in Fig. 5.8a, reveals that, as proposed in the 1980s, the long-wavelength spectrum consists of many randomly separated, self-frequency red-shifting, solitons (notable by their clear sech^2 shape in both time and frequency and the fact that they do not chirp upon propagation), i.e. the so-called soliton-Raman continuum. The short-wavelength edge is less structured as the continuum is made up of dispersive waves. However, careful analysis of the evolution of the spectrograms reveals that, like in the femtosecond case, the shortest dispersive waves are associated with the most red-shifted solitons—merely this is repeated over many soliton-dispersive wave pairs. The averaging of randomly emerging solitons and dispersive waves is what leads to the very smooth continuum spectrum shown in Fig. 5.8c, as compared to the femtosecond pump case.

In the case of picosecond pump supercontinuum, many numerical studies have considered the shot-to-shot noise and rogue-wave formation resulting from the stochastic nature of the initial MI dynamics, simply by performing many numerical simulations and analysing the statistics of certain metrics of the supercontinuum fields (Erkintalo et al., 2010; Genty et al., 2010).

5.13 CW-Pumped Supercontinua

Despite the remarkable progress made in the power scaling of mid-infrared fibre lasers, at first it does appear quite anomalous that a CW laser producing an average

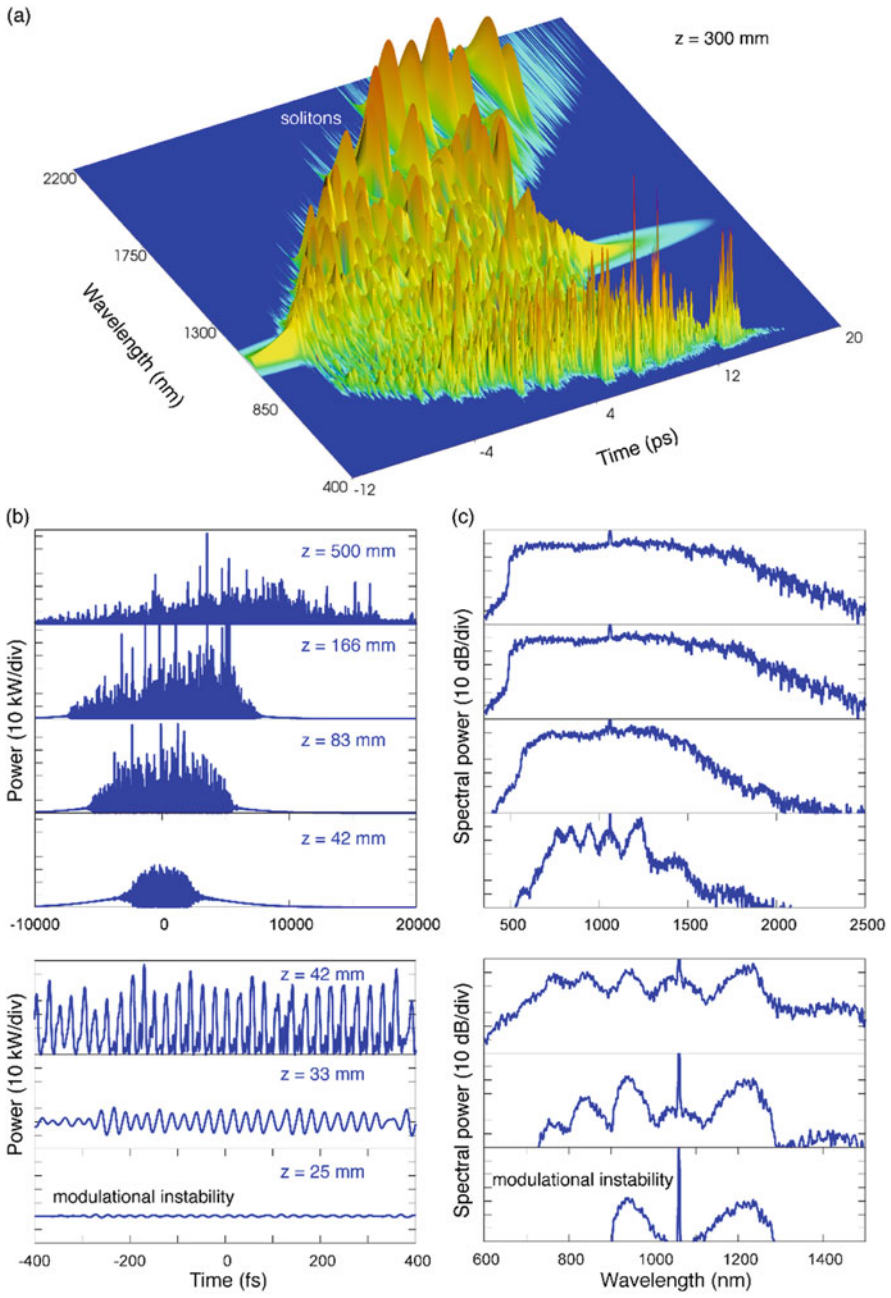

Fig. 5.8 Numerical simulations of supercontinuum generation by 10-ps, 20-kW peak power pulses at 1060 nm in a high air-filling fraction PCF with a zero dispersion at 994 nm and nonlinear coefficient of 18 W^{-1} km^{-1}. (**a**) XFROG spectrogram at 300-mm propagation; (**b**) temporal slices through propagation; (**c**) corresponding spectral slices. The lower parts of (**b**, **c**) show details of the initial MI dynamics

power of a few tens of watts should be capable of generating a supercontinuum in an optical fibre, when equivalent spectral coverage with a pulsed laser necessitates peak powers several orders of magnitude greater. Essential to the generation mechanism is the process of modulational instability, and the role it plays in CW supercontinuum generation has been comprehensively reviewed by Travers (2010a).

Although relatively high-power CW lasers had been used to observe modulational instability in 5-km lengths of small core anomalously dispersive fibre (Itoh et al., 1989) and broadband high-power operation had been observed from fibre Raman lasers pumped by a Yb:Er fibre laser at the watt level (Persephonis et al., 1996), the first report of high-power CW-pumped supercontinua in both conventional and photonic crystal fibres was made by Popov et al. (2002). In early reports using PCF water loss significantly affected the spectral extent. Avdokhin et al. (2003), using a CW Yb fibre laser pump at 1064 nm, reported a 3.8-W continuum in 100 m of a 2.3-μm cored PCF, where the long-wavelength operation terminated at 1380 nm as a result of strong water absorption at the hole-glass interfaces. Technological advance in manufacture enabled a reduction in the water loss by an order of magnitude and enabled long-wavelength extension to beyond 1550 nm, pumped at 1060 nm (Travers et al., 2005a).

The continuum generation process is initiated by modulational instability. This leads to the evolution of fundamental solitons, which experience adiabatic Raman gain and consequently temporally compress and subsequently experience self-Raman interaction and collisions, leading to long-wavelength shifting. The process terminates due to fibre loss, through increased dispersion placing too high power demands for soliton operation, or the presence of a second dispersion zero leading to normal dispersion terminating soliton operation. Soliton collisions in the presence of Raman gain provide an important contribution to the generated continuum (Frosz et al., 2006). The role of modulational instability was recognised by several researchers (González-Herráez et al., 2003; Nicholson et al., 2003b; Abeeluck et al., 2004). Using a high-power tunable fibre Raman laser, Rulkov et al. (2004b), pumping a highly non-linear conventionally structured fibre, showed that when the pump was in the normal dispersion regime that evolution of the continuum originated from the first Stokes component which was in the anomalously dispersive regime, but when the pump was tuned so that operation was just in the anomalously dispersive regime, the continuum evolved directly from the pump.

With the soliton-Raman process dominating CW-pumped supercontinuum generation, the spectra tend to be dominated by the long-wavelength component; however, significant short-wavelength excursion has been observed (Popov et al., 2002; Abeeluck & Headley, 2005). For short-wavelength generation, it is essential that the pump operates close to the dispersion zero and in the anomalously dispersive regime. Consequently, on evolution of soliton structures from modulational instability, there is sufficient spectral overlap of the solitons into the normally dispersive regime so that soliton-dispersive wave interaction occurs, as described previously for the picosecond and femtosecond cases. Low dispersion and high nonlinearity consequently enhance the process, and four-wave mixing can also make a significant contribution to the short-wavelength generation about the dispersion

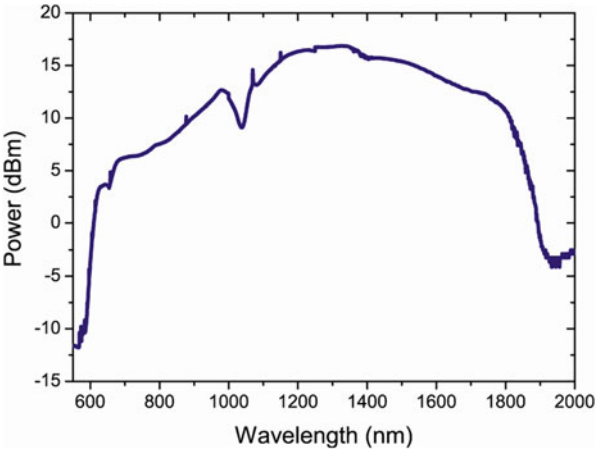

Fig. 5.9 CW-pumped supercontinuum in 50-m PCF with a zero dispersion at 1050 nm pumped by 230 W at 1060 nm. (After Travers et al., 2008)

zero (Cumberland et al., 2008b). Pumping far from the dispersion zero, but in the anomalously dispersive regime, can give high average power soliton-Raman-based supercontinua, up to 29 W, but the pump scheme inhibits short-wavelength generation (Cumberland et al., 2008a).

The continuum generation process using CW pumping is practically identical to that using long pulse picosecond pumping, although fibre length scales significantly increase as the peak powers are lower. Consequently, the soliton-dispersive wave interaction can be enhanced through similar fibre design considerations, specifically the use of long tapered structures and doping the core material (Kudlinski & Mussot, 2008; Mussot & Kudlinki, 2009; Kudlinski et al., 2009a,b; Labat et al., 2011). By employing GeO_2 doping, which allows an increased non-linear response, a 180-m fibre with a 130-m tapered end section supported spectral coverage from 470 to 1750 nm pumped by 40-W CW at 1060 nm; however, care should be taken in generating high power visible in Germania-doped fibres as photo-darkening and power roll-off can take place through colour centre generation. In a pure silica PCF, spectral extension down to 600 nm has been observed in a continuum extending to 1900 nm, with spectral power densities of ~3 mW/nm in the visible and up to 50 mW/nm in the infrared, by pumping a 50-m fibre with a zero dispersion at 1050 nm with a 400-W continuous-wave Yb fibre laser (Travers et al., 2008); Figure 5.9 shows a representative spectrum. In fibres that supported infrared generation only, through shifting the position of the dispersion zero to shorter wavelengths relative to the pump wavelength, up to 100 mW/nm in the IR was reported, using the same pumping scheme (Travers et al., 2008).

The role of noise on the pump has been recognised, and supercontinuum generation has been investigated using amplified low coherence diode pumps (Abeeluck & Headley, 2004), while de Matos et al. (2004) quantified the noise

performance when using either a fibre laser or high-power amplified spontaneous emission source. Martin-Lopez et al. (2006) experimentally studied the effect of Raman amplification of three signal sources of differing coherence using three fibre-based seed sources of spectral widths, 0.02, 0.22 nm and approximately 1 nm, and demonstrated that the intermediate bandwidth source acquired the greatest spectral broadening. Travers (2010a) proposed that there was an optimum degree of pump incoherence for supercontinuum formation based on the relative durations of the coherence time and modulational instability period. Kelleher et al. (2012a) undertook numerical simulations, and an experimental verification of the evolution of CW based supercontinuum from modulational instability and characterised the role of the pump source coherence through the use of an ASE-seeded amplifier pump scheme which incorporated a tunable wavelength, tunable bandwidth in line filter to control the pump coherence. A clear optimum bandwidth was demonstrated. This can be very simply understood in terms of the temporal characteristics of the noise signals associated with a given pump linewidth. A narrow linewidth would infer relatively long fluctuations in time. Consequently, the length scale for these temporal structures to evolve into solitons is long, and long pulse structures would be generated that would not efficiently self-frequency shift. At the other extreme, the inverse of exceedingly broad spectral pump bandwidths would infer ultrashort pulse durations, and the power requirement for soliton evolution would be exceedingly high. Empirically, it can be argued that an intermediate pump bandwidth would be optimum for maximum spectral broadening of a CW-pumped supercontinuum, as was theoretically proposed (Travers, 2010a) and experimentally verified by Kelleher et al. (2012a). It was subsequently understood that in the intermediate pump bandwidth regime (and hence intermediate coherence time), the individual temporal fluctuations can correspond to high-order solitons which undergo their own soliton fission dynamics (Kelleher et al. 2012b).

5.14 Modelling of CW-Pumped Supercontinua

The physics of CW supercontinuum generation is completely contained in the GNLE or UPPE (i.e. Eq. (5.3) or (5.4)); however, the issue arises of how to model what is essentially an infinite interaction between the CW pump source and the fibre. The solution adopted by all reports in the literature is simply to take a sufficiently long snapshot of the field and follow its propagation through the fibre. For most CW supercontinuum regimes, the MI dynamics occur on timescales less than 10 ps, and so snapshots of the order of 200 ps are common. In addition, averaging of an ensemble of simulations is required to obtain full agreement with experiment.

The generated continua under CW pumping exhibit a very smooth spectral profile, which results from the integration of numerous exceedingly noisy spectra. In the soliton-Raman process that plays a major role in the CW supercontinuum generation process, solitons are stochastically generated with a broad distribution of spectral and temporal parameters from phase and amplitude perturbations on the

pump. The usual CW pump sources are not single frequency, but instead have a finite bandwidth (of ~1 nm) and hence contain temporal and spectral phase and intensity fluctuations. Improvements in the modelling of noise both in the pump laser and in the continuum generation system have led to excellent agreement between theoretical prediction and experimental observation (Mussot et al., 2004, 2007, 2009; Vanholsbeeck et al., 2005; Kobtsev & Smirnov, 2005; Travers et al., 2008; Cumberland et al., 2008a, b; Travers, 2010a, b; Frosz et al., 2006; Frosz, 2010; Kelleher et al., 2012a). In what follows we use the technique described in Travers (2010a) and Kelleher et al. (2012a) to model a 50-W CW laser source with 1-nm spectral width. The initial spectral and temporal intensity are shown in the $z = 0$ m slice of the upper panels of Fig. 5.10b and c. The temporal intensity fluctuations on the scale of ~200 W are apparent.

The lower panels of Fig. 5.10b and c show how these intensity fluctuations break up due to MI, and the upper panels show the evolution towards a very flat and broad supercontinuum over 100 m of propagation. The spectrogram visualisation in Fig. 5.10a clearly shows how the red portion of the spectrum consists of a soliton-Raman continuum of randomly distributed solitons in both time and frequency—a phenomenon that has been described as a soliton gas (Travers, 2009). The short-wavelength part is much weaker in temporal intensity (but much more uniform, so time integration yields similar spectral power as seen in the upper panels of Fig. 5.10c), and consists of dispersive waves. Similar to the previous cases, some of the dispersive waves are temporally localised and are associated with intense solitons on the long-wavelength side, i.e. they are trapped and this enhances their blue shift. One particular soliton, individually visible in the upper panels of Fig. 5.10c, has very strongly red-shifted, and can be regarded as a rogue soliton under the original definition.

5.15 Extending Wavelength Operation

Since Lin and Stolen's first report (Lin & Stolen, 1976) of supercontinuum generation in an optical fibre, the source has been developed into a compact, highly efficient device that has been a commercial success, deployed in the laboratory and in the field in applications ranging from medical imaging to remote sensing. With a full understanding of the contributing processes and sophisticated numerical modelling, the operation of the source can be accurately predicted, exhibiting remarkable agreement between theory and experiment. However, the majority of commercial sources are based on silica fibres, consequently limiting spectral coverage from about 320 to 2400 nm. Over the past decade, numerous studies have been undertaken to extend this range. Beyond 2-μm germanium-based fibres exhibit lower loss than silica, and they also exhibit nearly an order of magnitude greater Raman gain coefficient. Consequently, as self-Raman gain shifting solitons provide the mechanism for long-wavelength extension, shorter fibre lengths can be deployed with good efficiency. Zhang et al. (2013) employed a compact, chirped

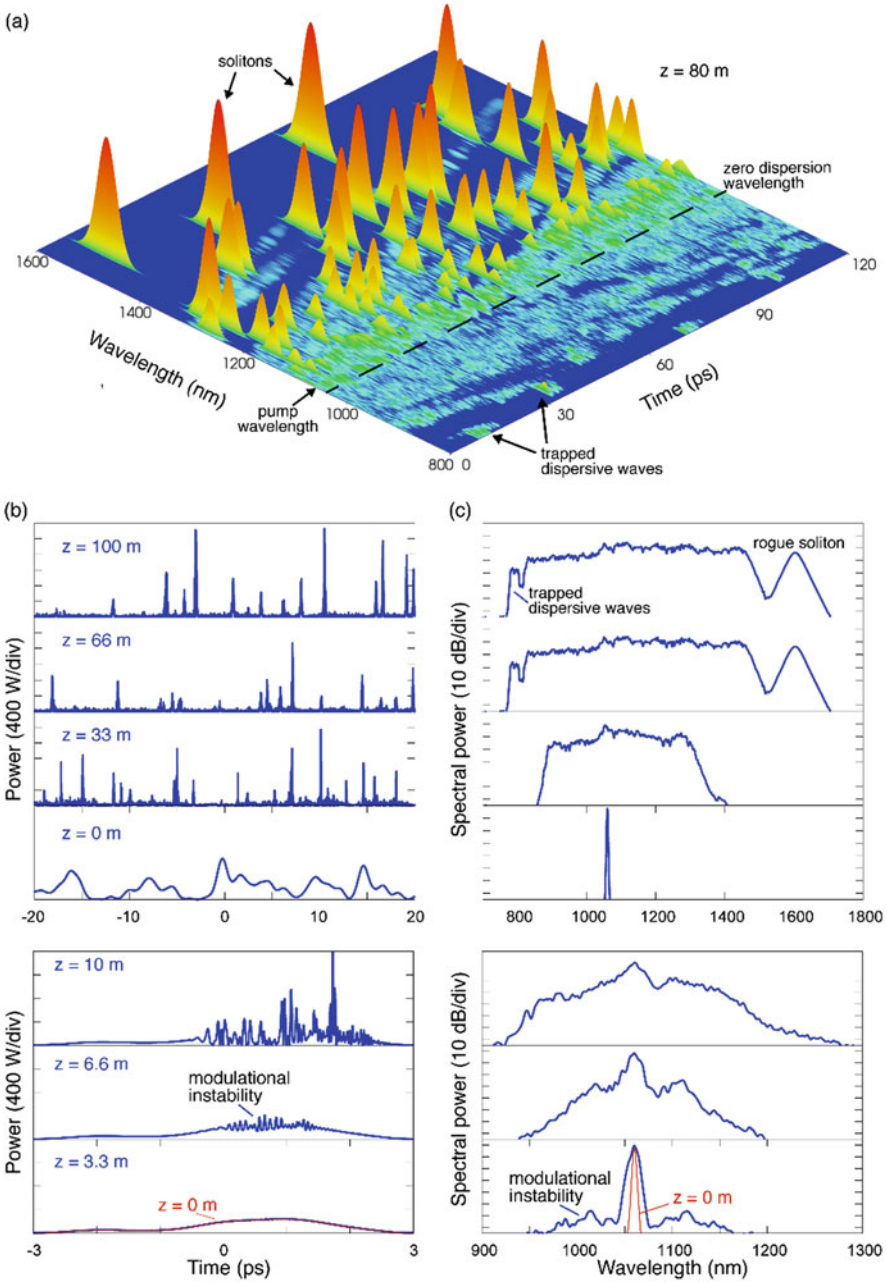

Fig. 5.10 Numerical simulation of supercontinuum generation when pumping a PCF with a zero dispersion wavelength at 1040 nm and a non-linear coefficient of 10 W^{-1} km^{-1} with a 50-W CW laser with 1-nm bandwidth. (**a**) XFROG spectrogram at 80-m propagation; (**b**) temporal slices through propagation; (**c**) corresponding spectral slices. The lower parts of (**b**, **c**) are zoomed in to show detailed modulational instability dynamics

pulse, amplified mode-locked Tm fibre laser system generating 850-fs, 1945-nm pulses with a peak power of 12 kW to generate a continuum from 1945 to 3000 nm in a 3.4-m-long highly germanium-doped silica fibre. However, to extend operation in the infrared, emphasis has been placed on the operation of new materials, primarily the soft glasses, while in the UV, sources have exploited gas-filled hollow-core photonic crystal fibres.

5.16 Infrared Supercontinuum Sources

Many of the non-silica glasses—although they currently have substantially lower-power handling capability, thus difficult to handle and may be hydroscopic—are attractive in that they exhibit substantially higher non-linear coefficients meaning that operational lengths can be shortened and pump power levels can be reduced while achieving extensive wavelength operation. In addition, the shorter lengths required often means that operational fibre lengths may be manufactured through extrusion (Kumar et al. (2002)), simplifying the overall manufacturing process. Mid-infrared supercontinuum generation in microstructured optical fibres constructed from an array of various glass types has been reviewed by Price et al. (2007).

A diode-pumped, passively mode-locked Yb fibre laser, generating 60-fs pulses with energies up to ~60 pJ in fibre at 1060 nm has been used unamplified, to pump a highly non-linear, 1.7-μm core SF6 glass PCF, 4 cm long to generate an octave spanning continuum from 600 to 1450 nm, clearly demonstrating the potential for compact, low-power supercontinuum operation (Hundertmark et al., 2009). In addition, a tellurite fibre, also manufactured by extrusion (Kumar et al., 2003) only 8 mm long, with a zero dispersion wavelength at 1380 nm, was pumped by the 100-fs, 1.9-nJ pulses from a Ti-sapphire-pumped optical parametric oscillator at 1550 nm to generate a continuum that extended from 789 to 4870 nm (Domachuk et al., 2008).

The manufacture of conventionally structured fluoride fibres is a relatively well-established technology. Despite the hydroscopic nature of the material, the broad material transmission window from 200 to 8000 nm makes ZBLAN-based fluoride an attractive fibre-based supercontinuum source for mid-infrared generation, although the waveguide loss contribution would contribute to a significant reduction on the long-wavelength edge. Initially pumped by a mode-locked Er fibre laser at 1550 nm, Hagen et al. (2006) reported a modest average power supercontinuum of 5 mW in the range of 1800–3400 nm, although the continuum did also extend down to 1400 nm. The technique was expanded upon by Xia et al. (2007, 2009) to achieve in excess of 10-W average power covering the range 800–4000 nm in a conventionally structured 7-m-long fluoride fibre, pumped by a pulsed 1542-nm semiconductor DFB laser-seeded Er-MOPFA system. Heidt et al. (2013) used a gain-switched 2-μm laser diode and a Tm fibre amplifier chain, generating 33-ps pulses with 3.5-μJ pulse energy to pump a 7-m-long step-index ZBLAN fibre,

to generate a continuum that extended from 750 to 4000 nm. Over three octaves generation was reported by Qin et al. (2009a, b), from 350 to 3850 nm in a 2.5-cm-long step-index fluoride fibre pumped by the 180-fs, 1-kHz, 20-mW average power pulses at 1450 nm from a Ti-sapphire-pumped OPO. Interestingly, a 2.5-cm silica fibre pumped by the same pulse source generated a continuum extending from approximately 360–3000 nm. In a similar experimental arrangement, using a 2-cm-long fluoride fibre sample and with peak pump powers of 50 MW, the supercontinuum covered the spectral range 350–6280 nm (Qin et al., 2009a, b). Recently, Jiang et al. (2013) have reported the successful fabrication of ZBLAN PCF with submicron features by fibre drawing, rather than by extrusion. Consequently, non-linear infrared generation is possible at substantially lower pump power in the submicron structures, and this was demonstrated by continuum generation from 400 to about 2400 nm in a 4.3-cm-long fibre, using nJ pumping of 140-fs pulses around 1040 nm.

Chalcogenide glass PCF structures have also been produced (Monro et al., 2000) for non-linear application in the 2–12-μm range. Using the 100-fs pulses at 2500 nm from an optical parametric amplifier pump system, Sanghera et al. (2009) have observed supercontinuum generation from 2000 to 3600 nm in conventionally structured 7-μm cored As-S fibre and from about 2000–3200 nm in a 10-μm cored selenide-based PCF. Arsenic selenide chalcogenide nanowires with non-linear coefficients up to 80,000 times that of standard single-mode silica-based fibre, with an effective mode area of 0.48 μm^2, have enabled low-threshold supercontinuum generation, pumped at a peak power of 7.8 W at 1550 nm and extending from about 1100–1750 m (Yeom et al., 2008). Using a suspended 3.5-μm core geometry AsSe fibre, 1.7 m long, with a zero dispersion at 3.15 μm, up to four cascaded Raman orders, which merged into a continuum extending to 2450 nm, were observed for a peak power of only 19 W from a gain-switched Tm fibre laser around 2 μm (Duhant et al., 2011). Møller et al. (2014) obtained a supercontinuum spanning from 2 to 6 μm in a 9-cm suspended core chalcogenide fibre by pumping close to the fibre zero dispersion wavelength at 3.5 μm with an OPA system. Extension to beyond 13 μm in a step-index chalcogenide fibre, pumped using a difference-frequency generation source, was recently realised by Petersen et al. (2014). The use of highly non-linear chalcogenide-based materials and submicron structures has enabled impressive spectral coverage through non-linear interaction at exceedingly low peak powers. The problem that arises in the handling and robustness of the submicron waveguides has been elegantly solved by Granzow et al. (2013) through the incorporation of arsenic trisulphide nano-spikes encapsulated in a fused silica cladding, providing a 2-mm-long uniform core of 1-μm diameter. When pumped by the 65-fs pulses from a Tm fibre laser with pulse energies as low as 18 pJ around 2 μm, the generated continuum extended to almost 4 μm. Such compact and highly efficient structures provide a clear route to the development of mid-infrared wavelength versatile sources.

5.17 Ultraviolet Supercontinuum Sources

Short-wavelength generation in silica PCF has been limited to 280 nm (Stark et al., 2012b), mainly due to glass damage and the large dispersion in the ultraviolet, prohibiting continued group velocity matching of the dispersive wave component of the supercontinuum spectra with the infrared soliton components. In one exceptional result, the use of recently realised ZBLAN PCF, pumped by a low-cost, 7-kW, 140-fs source at 1042 nm, enabled the generation of an extraordinary flat supercontinuum extending down to 200 nm, without any signs of glass degradation (Jiang et al., 2015).

An alternative way to expand spectral coverage beyond glass transmission windows (and damage thresholds) is to remove the glass from the core of the fibre. Two types of photonic crystal fibres have been particularly successful: those based on the use of a photonic band gap (Cregan et al., 1999) and those based on a kagomé-like anti-resonant structure (Benabid et al., 2002; Couny et al., 2006). While the former has been used for intense soliton propagation (Ouzounov et al., 2003; Fedotov et al., 2007), soliton-effect compression (Ouzounov et al., 2005) and soliton self-frequency shift (Gérôme et al., 2008), and also for many other non-linear optical experiments including stimulated Raman scattering (Benabid et al., 2004; Abdolvand et al., 2009), and experiments with alkali vapours (Ghosh et al., 2006), their limited guidance bandwidth and strong dispersion make them unsuitable for supercontinuum applications. In contrast, anti-resonant guiding PCF has broadband low-loss guidance, even with small hollow-core diameters (10–50 μm) (Benabid et al., 2002; Im et al., 2009), and the waveguide dispersion of these relatively small cores is anomalous with low dispersion slope, and can be readily balanced by the normal dispersion of a filling gas at pressures of a few atmospheres, enabling easy tuning of the zero dispersion wavelength (Im et al., 2009; Nold et al., 2010). The resulting fibre system can have weak anomalous dispersion in the visible spectral region, a zero dispersion in the near-UV, a high damage threshold and a non-linearity sufficient to create low-order optical solitons ($N = 1$–10) from ultrashort (~35 fs) μJ-scale pump pulses at 800 nm (Travers et al., 2011). Guidance in these types of fibres, or the very similar negative-curvature fibres, has been demonstrated from the mid-infrared (Yu & Knight, 2013) down to the VUV (Belli et al., 2015; Ermolov et al., 2015). A wide range of soliton and other non-linear dynamics have been observed in this system, and have been reviewed by Travers et al. (2011) and Russell et al. (2014). These include Raman frequency comb generation (Benabid et al., 2002; Abdolvand et al., 2012), UV dispersive wave emission (Joly et al., 2011; Mak et al., 2013a), soliton-plasma interactions (Hölzer et al., 2011), pulse compression (Mak et al., 2013b; Emaury et al., 2013), modulational instability (Tani et al., 2013) and non-linear multimode effects (Tani et al., 2014).

As described in the previous sections, pumping with high-order solitons in the anomalous dispersion region can lead to supercontinuum formation. Both long pump pulse, MI-driven supercontinuum dynamics, and short pulse soliton-fission-driven dynamics have been demonstrated in gas-filled kagomé PCF. Tani et al.

(2013) showed that by pumping an 18-μm-diameter kagomé PCF filled with 10-bar Xe with 5-μJ, 500-fs pulses at 800-nm, high-order solitons ($\sim N > 100$) are achievable, and the resulting modulational instability-based dynamics leads to the break-up of the pump pulse. A high-energy supercontinuum spanning from 320 to 1200 nm was observed after 20 cm.

Several routes to extending the supercontinuum to the vacuum UV have recently been demonstrated (Belli et al., 2015; Ermolov et al., 2015; Travers et al., 2014). In the first result, Belli et al. (2015) showed that 15 cm of 28-μm-diameter kagomé PCF filled with five bar of hydrogen broadened a 2.5-μJ, 35-fs pump pulse at 800 nm into a supercontinuum spanning from 124 to 1200 nm, through Kerr- and Raman-induced self-steepening and strong impulsive rotational and vibrational Raman scattering of dispersive waves. Subsequently, the use of 28-bar He in a similar fibre resulted in a supercontinuum spanning from 110 to over 200 nm with several hundred nanojoules of energy per shot (Ermolov et al., 2015). In that case, the primary mechanism was dispersive wave emission emerging from the fission of the self-compressed, high-order soliton pump pulse. The continuum was formed by repeated dispersive wave emission and broadening by ionisation-driven blue-shifting solitons.

5.18 Developments Since 2015

When the manuscript of this chapter in the third edition of *The Supercontinuum Laser Source* was originally prepared, if reference was made to an academic search engine to quantify the occurrences of the words "fibre supercontinuum" in the titles of published research papers, around 100–120 articles per year would have been recovered. Since publication, similarly identified titles have plateaued around this figure for the past 5 years. The supercontinuum source, based upon the relatively standard application of a solid-core, silica-based, photonic crystal fibre, pumped by either a bulk, solid-state laser or a fibre laser has become a considerable commercial success, with the latter format allowing the convenience and efficiency of all-fibre integration, while more than 20 companies offer devices with diverse specification in average power level, pulse repetition rate and spectral coverage. Typically in silica, commercial devices operating over a range of pulse formats cover the spectral range 400 nm–2400 nm with maximum average output power in the range of 5–10 W, with approximately 30% of the average power extending over the visible range.

As has been described above, the processes contributing to supercontinuum generation in fibre were very well established at the time of writing the third edition of this book, and the theoretical modelling and prediction of supercontinuum generation in fibre under the complete range of pump pulse conditions, from CW through to femtosecond, agreed exceptionally well with experimental measurement. In addition, the reported spectral coverage was that of the complete window of transmission of silica, consequently, leaving the average power in the supercontinuum as the only parameter potentially open to scaling in the interim period. In

2011a, b, Hu et al. had reported the generation of a supercontinuum covering the range from about 500 nm to 1700 nm with an average power of 49.8 W. An all-fibre MOPFA (master oscillator power fibre amplifier) integrated configuration had been used, incorporating a passively mode-locked Yb fibre laser generating 350-ps pulses at 4-MHz repetition rate at 1053.3 nm as a seed and a three-stage Yb fibre amplifier system which could deliver up to 100.3 W to pump a 5 m length of commercially available photonic crystal fibre with a nominal zero dispersion wavelength of 1040 nm. In a similar configuration, a 13-ps seed pulse at 1064 nm was amplified via a four-stage amplifier to an average power of 120 W (~19-kW peak power), with the all-fibre configuration terminated by a 2.6-m length of PCF with a mode field diameter of 6 μm and a zero dispersion wavelength at 1120 nm. Up to 92.5 W of average power was achieved in a supercontinuum extending from about 700 nm to over 1700 nm (Chen et al., 2013a), and the same authors subsequently reported breaking of the 100-W average power barrier (Chen et al., 2013b).

A combination of extreme average power and supercontinuum bandwidth has been achieved by combining the latest high-power pump laser configurations with tapered PCF (Zhang et al., 2021). A supercontinuum spanning from 390 nm to 2400 nm with over 314 W of output power was demonstrated by making use of a long-tapered PCF pumped with 75-ps pulses and 942-W average power. The spectral range up-converted from the pump, below 960 nm, contained over 36% of the output power, or 113.5 W, and exhibited a 16-dB spectral flatness.

With picosecond pulse seeds and extended multistage fibre amplifier lengths, extreme spectral broadening, caused by self-phase modulation, stimulated Raman scattering, soliton and associated soliton self-effects, can readily lead to supercontinuum generation in the final amplifier stages themselves, negating in some cases the need for any additional external fibre (Lewis et al., 1998). In an all-fibre-integrated scheme, using nanosecond seed pulses from a stretched pulse mode-locked fibre laser and a three-stage Yb-fibre amplifier configuration, with the final double-stage, double-clad Yb amplifier, 3 m long and with a core diameter of 30 microns, up to 70 W average power was observed in a soliton-Raman supercontinuum extending from the seed wavelength of 1060 nm to beyond 1700 nm (Song et al., 2012a). The authors subsequently power scaled the system to achieve an average power of 177.6 W in a similar supercontinuum (Song et al., 2012b). By reducing the restrictions of gain saturation through replacing the final stage amplifier with a 17-m-long, 25-μm core, 400-μm double-clad amplifier and with a final stage pump power of up to 360 W, a supercontinuum extending from 1000 nm to beyond 2200 nm was generated in this final stage with an average output power of 200 W (Song et al., 2013).

Average power scaling of all-fibre-integrated supercontinuum sources has primarily concentrated on the use of picosecond Yb-MOPFA configurations, where several stages of amplification incorporated final stage amplifiers with core diameters in the 10–30-μm range. Consequent mode matching problems have restricted achievable average powers and limited the coupling efficiency to the single, solid-core PCFs, which have typical diameters of the order of 5 μm, necessary to

have zero dispersions in the region of the Yb pump lasers and explaining also why continuum generation in the fibre amplifier themselves was attractive. With femtosecond pump schemes, however, it had been proposed that multicore PCFs because of their large effective mode area offered a very attractive solution to the power scaling question. Pumping with an average power of 16 W from a grating compressed, 80-fs, 49-MHz pulse source at 1038 nm, a supercontinuum extending from 500nm to 1700nm had been generated in a 5-cm length of seven-core PCF (Fang et al., 2012), where the fibre had a 2.62-μm pitch and an air hole size of 1.43 μm, enabling a zero dispersion around 1038 nm. With 160-picosecond pulse pumping at 1060 nm and an average power of 4.5 W from a gain-switched fibre laser scheme, a supercontinuum extending from 500 nm to 1700 mm was produced with an average output power of 2.44 W from a 35-m-long double-clad seven-core PCF (Huang et al., 2013). Power scaling subsequently took place, increasing the average output power to 42.3 W in a 720 nm–1700-nm continuum in a 20-m-long seven-core PCF with a zero dispersion at 1115 nm, where the process cascaded through the first Stokes generation from a 20-ps, fully fibre-integrated four-amplifier stage Yb MOPFA capable of delivering 56 W at 480 MHz (Wei et al., 2013). Following that, 104.2 W was recorded, from 750 nm to 1700 nm pumped by 141.6 W (Chen et al. 2014a) and 116 W, 800 nm–1650 nm at 1.9 GHz (Chen et al. 2014b).

With output powers from single small core PCFs reaching practical limits, the spatial combining of the outputs of several commercial supercontinuum sources was investigated by the commercial company Fianium (Hooper et al., 2015). The outputs from seven supercontinua from individual 20-W Yb lasers were combined into a single multimode fibre. The authors directed their efforts primarily to the visible range, and the combiner-filter configuration was designed to transmit only wavelengths below 950 nm. Up to 26-W average power was demonstrated over the range 450 nm–950 nm, with a peak spectral density of 75 mW/nm around 700 nm, dropping to about 50 mW/nm at 500 nm. The authors also proposed a moderately simple extension to the technique to allow scaling of the average power in the supercontinuum to the kilowatt level, which at time of writing has yet to be realised.

Power scaling of CW-pumped supercontinua has also been demonstrated by enhanced Raman gain through collecting back scattered Raman signals from two CW Yb fibre laser systems operating at 1070 nm and 1117 nm and relaunching it along with the pumps to enhance the Raman gain process (Arun et al., 2020). A continuum extending from 850 nm to 1900 nm was generated in a 1-km length of standard telecom fibre, with an average power of 72 W and a spectral power density of greater than 100 mW/nm from 1350 nm–1900 nm.

With seven-core PCF, researchers initially found it difficult to maintain the balance between an appropriate dispersion curve to allow spectral extension to the UV/blue and the in-phase supermode output. Through pumping at 800 nm, some relaxation was placed on the requirements, and by pumping with 80-fs pulses at 10-kHz repetition rate from a Ti-sapphire laser system and average powers of a few 10s of mW, operation down to 350 nm was observed; however, end face damage of the fibre was reported (Wang et al., 2018). Impressive power scaling in the visible spectral region, pumped by a Yb-amplified source at 1016 nm, was reported (Qi

et al., 2018). A 120-ps, 27-MHz source at 1016 nm was frequency quadrupled and amplified in a three-stage Yb fibre amplifier to an average power of 114 W, which was coupled into a seven-core PCF, designed to enhance visible generation, with an air hole pitch of 3.9 μm and an air hole diameter to pitch ratio of 0.85 μm. The zero dispersion wavelength of the in-phase supermode was at 991 nm, but quite intricate mode matching of the pump laser to PCF was required. However, up to 80-W average power extending from 350 nm to 2400 nm was reported, with up to 108 mW/nm at 580 nm recorded and over 50 mW/nm across the complete visible spectrum.

Pumping seven-core PCF in the visible has also been investigated as a mechanism to enhance generated visible supercontinua. A 1030-nm Yb fibre laser generating 2-ns pulses with 60-μJ pulse energy at 25 kHz was frequency doubled in LBO to give 20-μJ pulses, with the visible 515-nm radiation coupled into a seven-core, 6-m-long PCF. As the fibre exhibited a zero dispersion around 840 nm, supercontinuum generation proceeded through numerous cascaded orders of stimulated Raman scattering. The supercontinuum extended from 400 nm to 900 nm with an output energy of 4.2 μJ, beyond which, if the pump power was increased, facet damage to the PCF occurred. The authors also investigated generation in a tapered 7-core structure, and up to 15 orders of Raman scattering were observed (Bi et al., 2019).

As would be expected, numerical modelling of supercontinuum generation in seven-core PCF has shown that the generated spectra are very sensitive to the spacing between the cores, and it has been shown that larger core separations generally gave rise to broader spectra (Antikainen & Agrawal, 2019), with soliton formation playing the most important role in all cases. Soliton supermode transitions, inter-supermode four-wave mixing and inter-supermode dispersive wave generation were shown by the authors to be the key mechanisms in the overall supercontinuum generation process.

An alternative route to high average power or high pulse energy supercontinuum generation has been investigated through the use of multimode fibres and in particular graded index fibres. However, in the linear regime, mode beating and mixing give rise to speckled outputs, while output beam intensity profiles are also critically dependent on the launch condition. However, it has been shown that with increased intensity, the Kerr effect can negate the effects of linear mixing, and clean, multimode outputs with Gaussian-like profiles can be achieved, though the process which is termed Kerr self-cleaning (Krupa et al., 2016). Fortuitously, the Kerr self-cleaning process occurs at power levels that are more than an order of magnitude lower than the critical power for catastrophic self-focussing in graded index multimode fibres. Using an amplified 1064-nm Nd:YAG microchip laser with 900-ps pulses at 30 kHz and average in fibre powers at the watt level to pump various lengths of 52-μm core diameter graded index multimode fibre, supercontinua covering the range from about 500 nm to 2500 nm were generated, with Gaussian-like far-field profiles at the output. In a similar configuration, a 28.5-m-long graded index fibre with a 50-μm core diameter, pumped by 95-μJ, 400-ps pulses at 500-Hz repetition rate supported the generation of supercontinua extending from below 450 nm to 2400 nm, with high-quality mode profiles and the absence of speckle,

while spectral enhancement of regions of the spectra could be enabled through varying the launch condition (Lopez-Galmiche et al., 2016).

With the proliferation of commercial silica fibre-based supercontinuum sources, the reports of application have significantly increased over the past 5 years. One such area is that of optical coherence tomography (OCT), where white light interferometry is utilised to create 3-D images, primarily of biomedical specimens. As the axial resolution is inversely proportional to the bandwidth of the applied source, the high average power, fibre-based supercontinuum source, allowing central wavelength and bandwidth selectivity, was initially an attractive source; however, noise considerations also play a vitally important role in the applicability of these sources. It had long been realised that soliton Raman-based continua were inherently noisy (Gouveia-Neto et al., 1987, 1988; Keller et al., 1989). Since the vast majority of commercial supercontinuum sources are based upon the amplification of noise-like structures and non-linear soliton effects such as self-Raman interaction, the sources are inherently noisy and consequently can be problematic in application to OCT. Through avoiding soliton operation and operating in the normal dispersion regime, many of the effects can be mitigated (Heidt, 2010), and in recent years extended studies have been carried out on the amplification of such supercontinua and its application and impact on photonic applications (Sierro & Heidt, 2020; Heidt et al., 2020), while direct comparison of the noise performance of femtosecond-pumped supercontinua in the normal and the anomalous regimes has been undertaken (Klimczak et al., 2016) with two orders of magnitude signal to noise improvement experimentally reported through deploying the all-normal dispersion supercontinuum platform. All-normal dispersion photonic crystal fibres, with flattened and low dispersion in the region 1400 nm–1800 nm for pumping in the 1550-nm window with erbium fibre laser systems, have been realised for ultra-low noise supercontinuum generation (Rao et al., 2019). Polarisation noise, via polarisation modulational instability, however, has been predicted and demonstrated experimentally to decrease the pump pulse durations and the fibre lengths at which coherence in all-normal dispersion, femtosecond-pumped systems is degraded (Gonzalo et al., 2018). With longer fibre lengths and normally dispersive fibre, stimulated Raman scattering has also been shown to play an important role in degrading the coherence of continua, particularly with picosecond pumping (Gonzalo & Bang, 2018).

In the characterisation of the noise of supercontinuum sources for application in OCT, it was previously assumed that the source was thermal or pseudo-thermal. It has been shown (Jensen et al., 2019) that the excess photon noise cannot be generated by a modification of the established formula. They derived a general expression for the excess noise based on measurements of the noise and showed that it was superior in predicting OCT noise figures than the established method. They showed that the excess noise could be reduced by increasing the spectral integration time or by increasing the repetition rate of the supercontinuum source. Two pump schemes were investigated in a comparative study, one employing a commercial supercontinuum source and the other a bespoke all-normal dispersion supercontinuum source, with the latter demonstrating superior noise floor performance. It has

also been shown numerically that the relative intensity noise of a supercontinuum source pumped in the anomalous dispersion regime where multi-soliton effects are dominant and particular in picosecond-pumped systems can be reduced by more than a factor of two by so-called undertapering, where the host fibre is tapered to a diameter that is smaller than the diameter that leads to the shortest blue edge of the continuum. Such a process effectively limits the red spectral extent resulting from soliton self-interaction (the soliton self-frequency shift) with large numbers of solitons present effectively averaging (Engelsholm & Bang, 2019).

With the extensive commercialisation of silica-based supercontinuum sources and the relatively complete theoretical understanding of the supercontinuum generation processes under the extensive array of pump pulse formats together with significant power scaling and characterisation undertaken, in the past few years researchers have concentrated their efforts more to extending the sources into new spectral regions based on various glass hosts and investigate the power scaling of these in order to extend the applications palette and commercial potential.

In silica-based fibres, transmission loss effectively limits the upper extent of generated supercontinua to around 2200 nm–2400 nm. Above 2200-nm, germanium dioxide-based fibres exhibit a lower loss than silica and a phonon energy of around 820 cm^{-1}, while the non-linear coefficient of germania is about five times that of silica; consequently its exploitation as a host for supercontinuum generation above 2000 nm has been targeted. However, the increased refractive index of germania does lead to reduced core diameters and increased problems for integration with pump systems. Using a Er-Yb MOPFA, 1-ns pulsed pump source around 1550 nm, capable of delivering up to 34 W at 10 MHz, two germania-doped fibres of different doping level (74% and 56%) were investigated. Non-linearity in the Er-Yb amplifiers of the MOPFA extended the pump spectra to beyond 2200 nm and in a 0.9-m length of the 74% doped, 3.5-μm core diameter fibre the generated supercontinuum extended from around 700 nm–3200 nm at an average power of 1.44 W. With the larger core 9-μm-diameter fibre (56% doping), up to 4.9-W average power was achieved extending from 800 nm to 2700 nm (Jain et al., 2016). A supercontinuum source (1500 nm–2300 nm), derived from a Yb-Er MOPFA, was also used after amplification in a Tm fibre amplifier to provide a broadband pump source, ~1900 nm–2700 nm to pump a 3.5-μm pure germania-cored fibre, 12 cm long in a fully fibre-integrated configuration, to allow spectral coverage from 1900 nm to 3600 nm at a repetition rate of 2 MHz with an average power of 6.12 W (Yin et al., 2016). Up to 30 W average power was obtained by the same authors (Yin et al., 2018), in a supercontinuum extending from ~2000 nm to 3000 nm generated in a 8-μm pure Ge-cored fibre, 1 m long, pumped by chirped, several hundred picosecond pulses from a Tm MOPFA capable of delivering an average pump power of ~130 W.

For further spectral extension into the important MIR region, fluoride fibres such as ZBLAN have been widely investigated. Typically, the long-wavelength edge of generated supercontinua does not extend significantly beyond 4.3 μm (Yang et al., 2014), although up to 6.3 μm has been recorded by utilizing 2-cm fibre lengths pumped by 50-MW pulses at 1450 nm (Qin et al., 2009) and a maximum

average output power of 24.3 W has been reported (Liu et al., 2014). However, ZBLAN fibres can be quite difficult to work with. Because of their relatively low melting temperature, ZBLAN fibres can become distorted at high average power pump levels, misaligning in schemes where bulk optical coupling is involved or the ingression of OH- can ultimately lead to the damage of end facets, where high average power pumps are employed. Improved robustness has been achieved through an all-fibre fusion-spliced geometry with just over 10-W average power obtained in a supercontinuum that extended from around 1.9 μm to 4.1 μm (Zheng et al., 2016), where a picosecond Tm-MOPFA pump scheme was integrated with a 8-m-long single-mode ZBLAN passive fibre. In an alternative all-fibre-integrated approach, a nanosecond pulse from a distributed feedback laser was amplified in an Yb-Er MOPFA configuration, generating a soliton-Raman supercontinuum in a single-mode fibre, which was amplified in a high-power Tm amplifier, with the resulting pulses around 2.0 μm used to pump a 12-m length of 9-μm cored ZBLAN fibre. As expected, a relatively flat 15.2-W average power supercontinuum extending from 1.9 μm to 4.2 μm was achieved, with more than 8-W average power at wavelengths above 3 μm and 1 W average from 3.8 μm to 4.2 μm (Yin et al., 2017).

For supercontinuum generation at high average pump powers, photodegradation of ZBLAN fluoride fibres and chemical instability has resulted in alternative fluoride-based glasses being investigated as alternative host material in the spectral window 0.4 μm–5 μm. A 60-cm-long fluorotellurite fibre, with a 6.8-μm core diameter manufactured by the rod in tube technique, has been pumped by the 200-fs pulses from a Tm-amplified system and delivering an average power of 19.6 W at a 50-MHz repetition rate, generating a 10.4-W average power supercontinuum extending from 947 nm to 3,934 nm (Yao et al., 2018). Researchers from the same laboratory have recently used a multistage thulium fibre amplifier system to amplify the femtosecond pulses from a soliton Raman supercontinuum to a maximum average power of 46.7 W, with a broad spectrum extending from 1.93 to 2.5 μm at a 50-MHz repetition rate, which were used to pump a 0.6-m-long fluorotellurite fibre, with an 11-μm core, generating a supercontinuum extending from 0.93 μm to 3.95 μm at an average power of 22.7 W (Li et al., 2020).

With most practical fibre lengths, fluorozirconate (ZnF4)-based glass fibres like ZBLAN, the maximum wavelength extent of any generated supercontinuum is around 4.5 μm, although there are exceptions (see above, Qin et al., 2009a, b); consequently, in recent years interest has been increasingly directed towards fluoroindate (InF_3) glasses as a very competitive alternative. Fluoroindate is a low phonon energy glass (maximum frequency ~510 cm^{-1}), which allows high transparency to about 5 μm. In addition, fluoroindate glasses are relatively robust and environmentally stable. Researchers at Thorlabs (Salem et al., 2015) have reported on broadband generation in two lengths (30 cm and 55 cm) of step-index fluoroindate fibre, with a core diameter of 7 μm employing a novel femtosecond pump geometry. Commencing with a passively mode-locked, femtosecond Er-fibre laser at 1560-nm and 50-MHz repetition rate, the generated pulses were shifted in a highly non-linear fibre to 1960 nm using self-Raman interaction (the soliton self-

frequency shift) generating pulses with a 20-nm bandwidth at an average power of 30 mW. These were then amplified in a Tm fibre amplifier to an average power greater than 500 mW. As a result of self-frequency shifting in the amplifier, more than 90% of the output energy shifted to a spectral band around 2125 nm and a maximum average power of 570 mW in dispersion compensated pulses of about 100 fs. Lens coupling was used to excite the fluoroindate fibre. The generated supercontinua extended from about 1.25 μm to 4.6 μm, with -20 dB bandwidths of 2250 nm and 2980 nm in the 30- and 55-cm fibres, respectively.

Extension to beyond 5 μm was reported in a 15-m length of InF_3 fibre which was fusion coupled to a Er3+:ZrF4 amplifier which was seeded by picosecond pulses from an optical parametric generator operating at 2.75 μm (Gauthier et al., 2016). The seed pulses which were 400 ps long with an average power of 2 mW and a 2-kHz repetition rate were lens coupled into the 1.25-m-long, 16-μm core diameter double-clad amplifier and for a pump power of about 1 W, output ~20 mW, with the signal exhibiting significant spectral broadening (beyond 3 m) at the maximum pump power. The InF_3 fibre had a core diameter that varied over its 31-m length, from 12.5 μm to 14.5 μm. Optimal spectral coverage was achieved with a 15m long fibre, extending from 2.4 μm to 5.4 μm and an average power of 8.0 mW. As a result of the increasing material losses above about 5 μm, higher average power was obtained with shorter lengths of the fluoroindate fibre; however, the generated supercontinua did not extend beyond 4.7 μm.

Power scaling of infrared supercontinuum generation has been undertaken in a fluoroindate fibre through the use of a multistage Tm-based MOPFA system (Liang et al., 2018). The approximate 100-ps pulses from a 1-MHz repetition rate, gain-switched laser diode operating at 1953 nm with an average power of ~1 μW were amplified in a four-stage thulium fibre amplifier chain, which ultimately delivered a maximum average power of 10.34 W in pulses of 35 ps, corresponding to a peak power of 295 kW. These were lens coupled into a 10-m length of commercially available indium fluoride fibre, with a zero dispersion wavelength in the region of 1700 nm and with a loss of ~3 dB/m at 5.5 μm. A total average power of 1.76 W was recorded in a spectrum that extended from around 750 nm–5000 nm, with approximately 8% of the average power remaining in the pump signal. Above 2900 nm, the average power in the continuum was 0.56 W and with 0.33 W beyond 3500 nm.

Power scaling to the watt level was also reported using the gain-switched 50-ps pulses at 1 MHz from a 1.55-μm laser diode and amplifying them in a multistage Yb-Er amplifier configuration to generate a 1.2-μm–2.5-μm supercontinuum in silica fibre, which was then filtered and amplified in a dual-stage Tm amplifier to an average power of 2.3 W. The output from the Tm amplifier system was butt coupled to a 20-m length of InF_3 fibre with an efficiency of 56%, generating a watt level continuum that extended from around 1 μm to 5 μm (Théberge et al., 2018).

The increasing interest in mid-infrared has been driven by the technological need for simple, wavelength versatile sources for diverse application in spectroscopy and metrology to allow ease of diagnostics covering the function group region (2 μm–6 μm) and the so-called molecular fingerprint region (6 μm–20 μm). Of

the soft glasses that are transparent in these regions, the chalcogenides have been particularly attractive, because of their ultrawide transmission band and high non-linear coefficients, although power handing and damage have been major concerns with chalcogenides. At the time of writing the original chapter, probably the broad spectral coverage of the supercontinuum 1.4 μm–13.3 μm (Petersen et al., 2014) represented the benchmark for spectral extent. Since then, however, researchers have concentrated on simplifying the pump lasers, power scaling and spectrally extending the operational wavelength regime.

Long-wavelength extension was reported through the use of a custom-designed, triangular-core graded index, photonic crystal chalcogenide (As2Se3 based) fibre, designed to have an all-normal dispersion over the complete mid infrared range. A 5-mm length of fibre was pumped by 50-fs pulses, with a peak power of 3.5 kW at 4.1 μm, generating a continuum extending from 2 μm to 15 μm (Saini et al., 2015). Through co-doping chalcogenide glass with tellurium, the non-linear coefficient can be enhanced, and supercontinuum generation, from 1.5 μm to 14 μm, was reported in a 23-cm length of a 70-μm cored (Ge20As20Se15Te45) multimode step-index fibre, pumped by the 150-fs, 10-mW average power, 1-kHz repetition rate pulses at 4.5 μm derived through difference-frequency mixing of signal and idler sources generated by an amplified, mode-locked Ti:Sapphire laser pumped optical parametric amplifier (Zhao et al. 2016). A similar difference frequency generation technique was used to derive a 2.5–11 μm tunable source, although solely operated at 9.8 μm to pump a 3 cm long, hence reduced loss, step-index fibre based on As2Se3/AsSe2 with a 15-μm core diameter, that gave rise to a single zero dispersion wavelength around 5.5 μm and a dispersion-flattened profile. For an estimated in-fibre peak power of ~2.9 MW, the generated supercontinuum covered the range 2.0–15.1 μm (Cheng et al., 2016). As Te-based chalcogenide glass probably exhibits the highest non-linear refractive index of all glasses, as well as having potential transparency to 25 μm, a Ge-Te-AgI, 20-μm core fibre with a double-clad structure was designed and optimised for extended supercontinuum operation (Zhao et al., 2017). The fibre had a dispersion zero at 10.5 μm, and a 14-cm length was pumped at 7 μm by the 150-fs, 1-kHz repetition rate pulses from an optical parametric amplifier. The resultant supercontinuum covered the spectral range 2.0 μm–16 μm for an average pump power of 11.5 mW. To improve the potential coherence of the generated supercontinuum, a Ge-As-Se-Te, double-clad structured fibre was designed to have an all-normal dispersion, so as to remove soliton-like operation in the generation process (Jiao et al., 2019a). With a core diameter of 20 μm, the supported fundamental mode exhibited all-normal dispersion from 4 to 15 μm. Pumped at 5 μm from an OPA, producing 150-fs pulses at 1-kHz repetition rate and for 30-mW average power in a 22-cm length of fibre, a flatten spectrum covering 3.2 μm–12.1 μm at the -10-dB level and 2 μm–14 μm at the -30-dB mark.

Researchers have also endeavoured to simplify the experimental configurations for generation in chalcogenides and to lower the peak power requirements. A small, elliptical-core (4.1 × 4.6 μm), 11-cm fibre, pumped with the relatively low peak power of 3 kW from 330-fs pulses at 4 μm from an optical parametric amplifier, supported the generation of a continuum extending from 1.8 μm to 10 μm (Yu

et al., 2015). A compact source was reported using 400-ps pulses at 2.8 μm and 2-kHz repetition rate to seed an erbium-doped zirconium fluoride glass fibre amplifier giving rise to supercontinuum generation, which after filtering extended from around 3–4.2 μm and was used to pump a 3.5-m length of commercially available As2Se3 step-index fibre, which was single mode above ~5 μm. The generated supercontinuum covered the spectral range 3 μm–8 μm with an average output power of 1.5 mW at 2-kHz repetition rate (Robichaud et al., 2016). In a clear demonstration of potential simplification and in particular to reduce the need for large and expensive optical parametric oscillators/amplifiers/generators as pump sources, a mode-locked Holmium fibre laser was used as the pump for supercontinuum generation in a tapered As2Se3 fibre (Hudson et al., 2017). The Ho-Pr co-doped ZBLAN fibre laser was polarisation rotation mode locked to provide 230-fs pulses at 42-MHz repetition rate operating around 2.87 μm with an average output power of 140 mW. This was coupled into a 14-μm core diameter As2Se3 fibre, which was adiabatically tapered to provide a 5-cm-long, 3-μm-diameter, power density enhanced interaction zone. This novel and simple configuration allowed the generation of a continuum extending from 2 to 12 μm with an average output power of greater than 30 mW. A Kerr-lens mode-locked Cr:ZnSe laser oscillator, generating 38-fs pulses at 2.4 μm, and a 170-MHz cavity round-trip frequency, generating an average output power of 150 mW, has also been used to pump tapered suspended core AsSe fibres. Two tapers were investigated, a 10-mm interaction region with a 1.98-μm-core diameter and a 5-mm length with a 1.38-μm core diameter. For 90-mW average power launched into the taper, 35-mW average output power in a continuum extending from 1.4 μm to 4.2 μm was obtained in the 10-mm taper (Leonov et al., 2020). Another approach towards pump source simplification involved the amplification of the 440-fs pulses from an erbium-doped fluoride fibre laser, mode locked using non-linear polarisation rotation, to provide a peak power of about 9.5 kW at 2.8 μm at a 57.9-MHz repetition rate. These pulses were subsequently amplified in a 20-m-long Er-doped zirconium fluoride fibre amplifier. As a result of the gain and the short duration, the pulses exhibited a soliton self-frequency shift, which was lens coupled into various commercially available chalcogenide step-index fibres. Anti-reflection coatings were spluttered on to the facets of the chalcogenide fibres in order to maximise coupling efficiency and allowed an average power of 825 mW to be extracted from a continuum extending from 2.5 μm to 5.0 μm (Robichaud et al., 2020).

In order to allow extended mid-infrared coverage but pumping with more readily available fibre lasers and less demanding pulse durations, a cascaded supercontinuum all-fibre-integrated approach has been adopted (Martinez et al., 2018). The fundamental pump source was a Er-Yb MOPFA scheme, delivering 1.1-ns, 800-kHz repetition rate pulses at 1.553 μm, which on coupling into 10 m of standard telecom fibre generated a soliton Raman continuum, 1.5 μm–2.4 μm, with an average power of 3 W. This was subsequently amplified in a Tm fibre amplifier to an average power of 14 W covering the spectral range ~1.9 μm–2.5 μm. In cascade this pumped firstly a 6.5-m-long 7.5-μm core ZBLAN fibre extending the upper range of the continuum to ~4.5 μm, a 4 m, 9 μm core As2S3 fibre which

supported extension to ~6 μm and finally into a 4 m, length of 12-μm core As2Se3 fibre which delivered a continuum extending from ~1.6 μm to 11 μm at the -20-dB level, with an average power of 417 mW. It has been suggested that the cascade of As2S3 and As2Se3 fibres used above could be replaced by a single iodine-doped Ge10As22Se68 glass to produce a fibre with a zero dispersion in the region of 4.03 μm as compared to the ZDW of the host glass of ~7 μm (Jiao et al., 2019b). Characterisation and optimisation of this fibre was undertaken, and it was shown that a 12-cm length pumped by the 150 fs, 1 kHz repetition rate pulses from an optical parametric amplifier system at 4 μm, a 1.9 mW average power continuum ~1.5 μm–13 μm was obtained, and when pumped at 8 μm, the continuum extended from ~1.2 μm to 15.2 μm with and average power of ~0.8 mW.

The chalcogenides offer a versatile platform to extend the wavelength palette of the fibre-based supercontinuum source, and remarkable progress has been made since the first edition of this chapter. Various platforms have been investigated and optimised from conventional step-index profile fibres to suspended core (Møller et al., 2015), and microstructured fibres (Liu et al., 2016) or tapered fibre structures (Petersen et al., 2017) with all selectable all-normal dispersion (Zhang et al., 2019); however, there are many other equally important aspects that also require further addressing, such as the pump sources, the operational output power levels, the required coherence as well as host materials themselves, before impact on the commercial marketplace, although this has already commenced. Some of these parameters have been addressed in a recent review (Dai et al., 2018).

As addressed in the previous section, extension to the ultraviolet (UV) range is even more limited by material properties than the infrared. However, UV supercontinuum sources are of significant importance for applications (Poudel & Kaminski, 2019). Most solid-core fibre-based supercontinuum sources extend to the 350 nm–400-nm region, in the usual case, with carefully designed tapered fibres enabling further extension to around 280 nm (Stark et al., 2012b). These limits arise due to glass damage and the large dispersion in the UV, prohibiting continued group velocity matching of the dispersive wave component of the supercontinuum spectra with the infrared soliton components. Demonstrations of extension in solid-core fibres below 280 nm are limited to two exceptional results: generation down to 200 nm in ZBLAN as described previously (Jiang et al., 2015) and a brief report on UV supercontinuum generation to 200 nm in silica fibre by making use of higher-order modes (Wang et al., 2017), which unfortunately did not discuss any lifetime issues or elaborate significantly on the mechanism. Further extension to the UV region requires the use of gas-filled hollow fibres, as discussed in the previous section. Some notable new results in that context since 2015 include Hosseini et al. (2018), Smith et al. (2020) and Fu et al. (2021).

Many of these developments are discussed in further detail in the new chapters of the fourth edition of this book.

References

Abdolvand, A., Nazarkin, A., Chugreev, A. V., Kaminski, C. F., & Russell, P. S. J. (2009). Solitary pulse generation by backward Raman scattering in H_2-filled photonic crystal fibers. *Physical Review Letters, 103*(18), 183902.

Abdolvand, A., Walser, A. M., Ziemienczuk, M., Nguyen, T., & Russell, P. S. J. (2012). Generation of a phase-locked Raman frequency comb in gas-filled hollow-core photonic crystal fiber. *Optics Letters, 37*(21), 4362.

Abeeluck, A. K., & Headley, C. (2004). Supercontinuum growth in a highly nonlinear fiber with a low-coherence semiconductor laser. *Applied Physics Letters, 85*, 4863–4865.

Abeeluck, A. K., & Headley, C. (2005). Continuous-wave pumping in the anomalous-and normal-dispersion regimes of nonlinear fibers for supercontinuum generation. *Optics Letters, 30*, 61–63.

Abeeluck, A. K., Headley, C., & Jørgensen, C. G. (2004). High-power supercontinuum generation in highly nonlinear, dispersion-shifted fibers by use of a continuous-wave Raman fiber laser. *Optics Letters, 29*, 2163–2165.

Agrawal, G. P. (2012). *Nonlinear fiber optics* (5th ed.). Academic Press. ISBN 9780123970237.

Agrawal, G. P., & Potasek, M. J. (1986). Nonlinear pulse distortion in single-mode optical fibers at the zero-dispersion wavelength. *Physical Review A, 33*(3), 1765.

Alfano, R. R., & Shapiro, S. L. (1970a). Emission in region 4000 to 7000 Å via 4-photon coupling in glass. *Physical Review Letters, 24*, 584–587.

Alfano, R. R., & Shapiro, S. L. (1970b). Observation of self-phase modulation and small-scale filaments in crystals and glasses. *Physical Review Letters, 24*, 592–584.

Alfano, R. R., & Shapiro, S. L. (1970c). Direct distortion of electronic clouds of rare-gas atoms in intense electric fields. *Physical Review Letters, 24*, 1217–1220.

Alfano, R. R., & Shapiro, S. L. (1970d). Picosecond spectroscopy using the inverse Raman effect. *Chemical Physics Letters, 8*, 631–633.

Anderson, D., & Lisak, M. (1983). Nonlinear asymmetric self-phase modulation and self-steepening of pulses in long optical waveguides. *Physical Review A, 27*(3), 1393.

Avdokhin, A. V., Popov, S. V., & Taylor, J. R. (2003). Continuous-wave, high- power, Raman continuum generation in holey fibers. *Optics Letters, 28*, 1353–1355.

Beaud, P., Hodel, W., Zysset, B., & Weber, H. P. (1987). Ultrashort pulse propagation, pulse breakup and fundamental soliton formation in a single mode optical fiber. *IEEE Journal of Selected Topics in Quantum Electronics, 23*, 1938–1946.

Belli, F., Abdolvand, A., Chang, W., Travers, J. C., & Russell, P. S. J. (2015). Vacuum-ultraviolet to infrared supercontinuum in hydrogen-filled photonic crystal fiber. *Optica, 2*, 292–300.

Benabid, F., Knight, J. C., Antonopoulos, G., St, P., & Russell, J. (2002). Stimulated Raman scattering in hydrogen-filled hollow-core photonic crystal fiber. *Science, 298*(5592), 399–402.

Benabid, F., Bouwmans, G., Knight, J. C., St, P., Russell, J., & Couny, F. (2004). Ultrahigh efficiency laser wavelength conversion in a gas-filled hollow core photonic crystal fiber by pure stimulated rotational Raman scattering in molecular hydrogen. *Physical Review Letters, 93*(12), 123903.

Birks, T. A., Knight, J. C., & Russell, P. S. J. (1997). Endlessly single-mode photonic crystal fiber. *Optics Letters, 22*(13), 961–963.

Birks, T. A., Wadsworth, W. J., & Russell, P. S. J. (2000). Supercontinuum generation in tapered fibers. *Optics Letters, 25*, 1415–1417.

Blow, K. J., & Wood, D. (1989). Theoretical description of transient stimulated Raman scattering in optical fibers. *IEEE Journal of Quantum Electronics, 25*(12), 2665–2673.

Boyer, G. (1999). High-power femtosecond-pulse reshaping near the zero-dispersion wavelength of an optical fiber. *Optics Letters, 24*, 945–947.

Champert, P. A., Couderc, V., Leproux, P., Février, S., Tombelaine, V., Labonté, L., Roy, P., & Froehly, C. (2004). White-light supercontinuum generation in normally dispersive optical fiber using original multi-wavelength pumping system. *Optics Express, 12*, 4366–4371.

Chang, W., Nazarkin, A., Travers, J. C., Nold, J., Hölzer, P., Joly, N. Y., & Russell, P. S. J. (2011). Influence of ionization on ultrafast gas-based nonlinear fiber optics. *Optics Express, 19*(21), 21018–21027.

Chen, K. K., Alam, S.-u., Price, J. H. V., Hayes, J. R., Lin, D., Malinowski, A., Codemard, C., Ghosh, D., Pal, M., Bhadra, S. K., & Richardson, D. J. (2010). Picosecond fiber MOPA pumped supercontinuum source with 39 W output power. *Optics Express, 18*, 5426–5432.

Chernikov, S. V., Zhu, Y., Taylor, J. R., & Gapontsev, V. P. (1997). Supercontinuum self-Q switched ytterbium fiber laser. *Optics Letters, 22*, 298–300.

Coen, S., Chau, A. H. L., Leonhardt, R., Harvey, J. D., Knight, J. C., Wadsworth, W. J., & Russell, P. S. J. (2001). White light supercontinuum generation with 60 ps pump pulses in a photonic crystal fiber. *Optics Letters, 26*, 1356–1538.

Coen, S., Chau, A. H. L., Leonhardt, R., Harvey, J. D., Knight, J. C., Wadsworth, W. J., & Russell, P. S. J. (2002). Supercontinuum generation by stimulated Raman scattering and parametric four-wave mixing in photonic crystal fibers. *Journal of the Optical Society of America B: Optical Physics, 19*, 7533764.

Cohen, L. G., & Lin, C. (1977). Pulse delay measurements in the zero dispersion wavelength region for optical fibers. *Applied Optics, 16*, 3136–3139.

Cohen, L. G., & Lin, C. (1978). A universal fiber-optic (UFO) measurement system based upon a near-IR fiber Raman laser. *IEEE Journal of Quantum Electronics, QE14*, 855–859.

Collings, B. C., Mitchell, M. I., Brown, L., & Knox, W. H. (2000). A 1021 channel WDM system. *IEEE Photonics Technology Letters, 12*, 906–908.

Conforti, M., Marini, A., Tran, T. X., Faccio, D., & Biancalana, F. (2013). Interaction between optical fields and their conjugates in nonlinear media. *Optics Express, 21*(25), 31239–31252.

Corwin, K. L., Newbury, N. R., Dudley, J. M., Coen, S., Diddams, S. A., Weber, K., & Windeler, R. S. (2003). Fundamental noise limitations to supercontinuum generation in microstructure fiber. *Physical Review Letters, 90*(11), 113904.

Couny, F., Benabid, F., & Light, P. S. (2006). Large-pitch kagome-structured hollow-core photonic crystal fiber. *Optics Letters, 31*, 3574–3576.

Cregan, R. F., Mangan, B. J., Knight, J. C., Birks, T. A., Russell, P. S. J., Roberts, P. J., & Allan, D. C. (1999). Single mode photonic bandgap guidance of light in air. *Science, 285*, 1537–1539.

Cristiani, I., Tediosi, R., Tartara, L., & Degiorgio, V. (2004). Dispersive wave generation by solitons in microstructured optical fibers. *Optics Express, 12*, 124–135.

Cumberland, B. A., Travers, J. C., Popov, S. V., & Taylor, J. R. (2008a). 29 W High power CW supercontinuum source. *Optics Express, 16*, 5954–5962.

Cumberland, B. A., Travers, J. C., Popov, S. V., & Taylor, J. R. (2008b). Toward visible cw-pumped supercontinuua. *Optics Letters, 33*, 2122–2124.

De Maria, A. J., Ferrar, C. M., & Danielsonn, G. E. (1966). Mode locking of a Nd^{3+} doped glass laser. *Applied Physics Letters, 8*, 22–24.

de Matos, C. J. S., Popov, S. V., & Taylor, J. R. (2004). Temporal and noise characteristics of continuous-wave-pumped continuum generation in holey fibers around 1300 nm. *Applied Physics Letters, 85*, 2706–2707.

de Matos, C. J. S., Kennedy, R. E., Popov, S. V., & Taylor, J. R. (2005). 20-kW peak power all-fiber 1.57-μm source based on compression in air-core photonic bandgap fiber, its frequency doubling and broadband generation from 430 nm to 1450 nm. *Optics Letters, 30*, 436–438.

DeMartini, F., Townes, C. H., Gustafson, T. K., & Kelley, P. L. (1967). Self-steepening of light pulses. *Physical Review, 164*(2), 312.

Dianov, E. M., Karasik, A. Y., Mamyshev, P. V., Prokhorov, A. M., Serkin, V. N., Stelmakh, M. F., & Fomichev, A. A. (1985). Stimulated –Raman conversion of multisoliton pulses in quartz optical fibers. *JETP Letters, 41*, 294–297.

Dianov, E. M., Nikonova, Z. S., Prokhorov, A. M., Podshivalov, A. A., & Serkin, V. N. (1986). Optimal compression of multi-soliton pulses. *Soviet Technical Physics Letters (JETP), 12*, 311–313.

Dianov, E. M., Grudinin, A. B., Khaidarov, D. V., Korobkin, D. V., Prokhorov, A. M., & Serkin, V. N. (1989). Nonlinear dynamics of femtosecond pulse propagation through single mode optical fiber. *Fiber and Integrated Optics, 8*(1), 61–69.

Domachuk, P., Wolchover, N. A., Cronin-Colomb, M., Wang, A., George, A. K., Cordeiro, C. M. B., Knight, J. C., & Omenetto, F. G. (2008). Over 4000 nm bandwidth of mid-IR supercontinuum generation in sub-centimeter segments of highly nonlinear tellurite PCFs. *Optics Express, 16*, 7161–7168.

Drummond, P. D., & Corney, J. F. (2001). Quantum noise in optical fibers. I. Stochastic equations. *Journal of the Optical Society of America B, 18*(2), 139–152.

Dudley, J. M., & Coen, S. (2002). Coherence properties of supercontinuum spectra generated in photonic crystal and tapered optical fibers. *Optics Letters, 27*(13), 1180–1182.

Dudley, J. M., Gu, X., Xu, L., Kimmel, M., Zeek, E., O'Shea, P., Trebino, R., Coen, S., & Windeler, R. S. (2002). Cross-correlation frequency resolved optical gating analysis of broadband continuum generation in photonic crystal fiber: Simulations and experiments. *Optics Express, 10*, 1215–1221.

Dudley, J. M., Genty, G., & Coen, S. (2006). Supercontinuum generation in photonic crystal fiber. *Reviews of Modern Physics, 78*, 1135–1184.

Dudley, J. M., Dias, F., Erkintalo, M., & Genty, G. (2014). Instabilities, breathers and rogue waves in optics. *Nature Photonics, 8*, 755–764.

Duhant, M., Renard, W., Canat, G., Nguyen, T. N., Smektala, F., Troles, J., Coulombier, Q., Toupin, P., Brilland, L., Bourdon, P., & Renversez, G. (2011). Fourth-order cascaded Raman shift in AsSe chalcogenide suspended-core fiber pumped at 2 μm. *Optics Letters, 36*, 2859–2861.

Emaury, F., Dutin, C. F., Saraceno, C. J., Trant, M., Heckl, O. H., Wang, Y. Y., Schriber, C., et al. (2013). Beam delivery and pulse compression to sub-50 Fs of a modelocked thin-disk laser in a gas-filled Kagome-type HC-PCF fiber. *Optics Express, 21*(4), 4986–4994.

Erkintalo, M., Genty, G., & Dudley, J. M. (2010). On the statistical interpretation of optical rogue waves. *The European Physical Journal - Special Topics, 185*(1), 135–144.

Ermolov, A., Mak, K. F., Frosz, M. H., Travers, J. C., & Russell, P. S. J. (2015). Supercontinuum generation in the vacuum ultraviolet through dispersive-wave and soliton-plasma interaction in a noble-gas-filled hollow-core photonic crystal fiber. *Physical Review A, 92*, 033821.

Fedotov, A. B., Serebryannikov, E. E., & Zheltikov, A. M. (2007). Ionization-induced blueshift of high-peak-power guided-wave ultrashort laser pulses in hollow-core photonic-crystal fibers. *Physical Review A, 76*(5), 053811.

Fisher, R. A., & Bischel, W. (1973). The role of linear dispersion in plane-wave self-phase modulation. *Applied Physics Letters, 23*(12), 661–663.

Fisher, R. A., & Bischel, W. K. (1975). Numerical studies of the interplay between self-phase modulation and dispersion for intense plane-wave laser pulses. *Journal of Applied Physics, 46*(11), 4921–4934.

Frosz, M. H. (2010). Validation of input-noise model for simulations of supercontinuum generation and rogue waves. *Optics Express, 18*(14), 14778–14787.

Frosz, M. H., Bang, O., & Bjarklev, A. (2006). Soliton collisions and Raman gain regimes in continuous-wave pumped supercontinuum generation. *Optics Express, 14*, 9391–9407.

Fuji, Y., Kawasaki, B. S., Hill, K. O., & Johnson. (1980). Sum-frequency light generation in optical fibres. *Optics Letters, 5*, 48–50.

Gabriagues, J. M. (1983). Third-harmonic and three wave sum-frequency light generation in an elliptical-core optical fiber. *Optics Letters, 8*, 183–185.

Gaeta, A. L. (2002). Nonlinear propagation and continuum generation in microstructured optical fibers. *Optics Letters, 27*(11), 924–926.

Genty, G., Lehtonen, M., & Ludvigsen, H. (2004). Effect of cross-phase modulation on supercontinuum generated in microstructured fibers with sub-30 f. pulses. *Optics Express, 12*, 4614–4624.

Genty, G., Coen, S., & Dudley, J. M. (2007a). Fiber supercontinuum sources. *Journal of the Optical Society of America B: Optical Physics, 24*, 1771–1785.

Genty, G., Kinsler, P., Kibler, B., & Dudley, J. M. (2007b). Nonlinear envelope equation modeling of sub-cycle dynamics and harmonic generation in nonlinear waveguides. *Optics Express, 15*(9), 5382–5387.

Genty, G., de Sterke, C. M., Bang, O., Dias, F., Akhmediev, N., & Dudley, J. M. (2010). Collisions and turbulence in optical rogue wave formation. *Physics Letters A, 374*(7), 989–996.

Gérôme, F., Dupriez, P., Clowes, J., Knight, J. C., & Wadsworth, W. J. (2008). High power tunable femtosecond soliton source using hollow-core photonic bandgap fiber, and its use for frequency doubling. *Optics Express, 16*(4), 2381–2386.

Ghosh, S., Bhagwat, A. R., Renshaw, C. K., Goh, S., Gaeta, A. L., & Kirby, B. J. (2006). Low-light-level optical interactions with Rubidium vapor in a photonic band-gap fiber. *Physical Review Letters, 97*, 023603.

Goda, K., & Jalali, B. (2013). Dispersive Fourier transformation for fast continuous single-shot measurements. *Nature Photonics, 7*, 102–112.

Godin, T., Wetzel, B., Sylvestre, T., Larger, L., Kudlinski, A., Mussot, A., Ben Salem, A., Zghal, M., Genty, G., Dias, F., & Dudley, J. M. (2013). Real time noise and wavelength correlations in octave-spanning supercontinuum generation. *Optics Express, 21*, 18452–18460.

Golovchenko, E. A., Dianov, A. N., Prokhorov, A. M., & Serkin, V. N. (1985). Decay of optical solitons. *JETP Letters, 42*, 74–77.

Golovchenko, E. A., Dianov, E. M., Pilipetski, A. N., Prokhorov, A. M., & Serkin, V. N. (1987a). Self-effect and maximum contraction of optical femtosecond wave packets in a nonlinear dispersive medium. *JETP Letters, 45*, 91–95.

Golovchenko, E. A., Dianov, E. M., Karasik, A. Y., Pilipetski, A. N., & Prokhorov, A. M. (1987b). Stimulated Raman self-scattering of laser pulses. *Soviet Journal of Quantum Electronics, 19*, 391–392.

Golovchenko, E. A., Mamyshev, P. V., Pilipetski, A. N., & Dianov, E. M. (1991). Numerical analysis of the Raman spectrum evolution and soliton pulse generation in single mode fibers. *Journal of the Optical Society of America B: Optical Physics, 8*, 1626–1632.

González-Herráez, M., Martín-López, S., Corredera, P., Hernanz, M. L., & Horche, P. R. (2003). Supercontinuum generation using a continuous-wave Raman fiber laser. *Optics Communication, 226*, 323–328.

Gorbach, A. V., & Skyrabin, D. V. (2007). Theory of radiation trapping by accelerating solitons in optical fibers. *Physical Review A, 76*, 053803.

Gordon, J. P. (1986). Theory of the soliton self-frequency shift. *Optics Letters, 11*, 662–664.

Gouveia-Neto, A. S., & Taylor, J. R. (1989). Soliton evolution from noise bursts. *Electronics Letters, 25*, 736–737.

Gouveia-Neto, A. S., Gomes, A. S. L., & Taylor, J. R. (1987). High-efficiency single-pass solitonlike compression of Raman radiation in an optical fiber around 1.4 μm. *Optics Letters, 12*, 1035–1037.

Gouveia-Neto, A. S., Gomes, A. S. L., & Taylor, J. R. (1988a). Pulses of four optical cycles from an optimized optical fibre/grating pair/soliton pulse compressor. *Journal of Modern Optics, 35*, 7–10.

Gouveia-Neto, A. S., Faldon, M. E., & Taylor, J. R. (1988b). Raman amplification of modulational instability and solitary wave formation. *Optics Letters, 13*, 1029–1031.

Gouveia-Neto, A. S., Faldon, M. E., & Taylor, J. R. (1988c). Temporal and spectral evolution of femtosecond solitons in the region of the zero group velocity dispersion of a single mode optical fibre. *Optics Communication, 69*, 173–176.

Gouveia-Neto, A. S., Wigley, P. G. J., & Taylor, J. R. (1989a). Soliton generation through Raman amplification of noise bursts. *Optics Letters, 14*, 1122–1124.

Gouveia-Neto, A. S., Faldon, M. E., & Taylor, J. R. (1989b). Spectral and temporal study of the evolution from modulational instability to solitary wave. *Optics Communications, 69*, 325–328.

Granzow, N., Schmidt, M. A., Chang, W., Wang, L., Coulombier, Q., Troles, J., Toupin, P., Hartl, I., Lee, K. F., Fermann, M. E., Wondraczek, L., & Russell, P. S. J. (2013). Mid-infrared supercontinuum generation in As_2S_3-silica "nano spike" step index waveguide. *Optics Express, 21*, 10969–10977.

Grigoryants, E. E., Smirnov, V. I., & Chamorovski, Y. K. (1982). Generation of wide-band optical continuum in fiber waveguides. *Soviet Journal of Quantum Electronics, 12*, 841–847.

Gross, B., & Manassah, J. (1992). Supercontinuum in the anomalous group-velocity dispersion region. *Journal of the Optical Society of America B: Optical Physics, 9*, 1813–1818.

Grudinin, A. B., Dianov, E. M., Korobkin, D. V., Prokhorov, A. M., Serkin, V. N., & Kaidarov, D. V. (1987). Stimulated-Raman-scattering excitation of 18-fs pulses in 1.6-μm region during pumping of a single mode optical fiber by the beam from a Nd:YAG laser ($\lambda = 1.064$ μm). *JETP Letters, 45*, 260–263.

Hagen, C. L., Walewski, J. W., & Sanders, S. T. (2006). Generation of a continuum extending to the midinfrared by pumping ZBLAN fiber with an ultrafast 1550-nm source. *IEEE Photonics Technology Letters, 18*, 91–93.

Halbout, J.-M., & Grischkowsky, D. (1985). 12-fs ultrashort optical pulse compression at a high repetition rate. *Applied Physics Letters, 45*, 1281–1128.

Hardin, R. H., & Tappert, F. D. (1973). Applications of the split-step Fourier method to the numerical solution of nonlinear and variable coefficient wave equations. *SIAM Review (Chronicle), SIAM Review, 15*(2), 423.

Hasegawa, A. (1984). Generation of a train of soliton pulses by induced modulational instability in optical fibers. *Optics Letters, 9*, 288–290.

Hasegawa, A., & Brinkman, F. (1980). Tunable coherent IR and FIR sources utilizing modulational instability. *IEEE Journal of Quantum Electronics, QE16*, 694–699.

Hasegawa, A., & Kodama, Y. (1981). Signal transmission by optical solitons in monomode fiber. *Proceedings of the IEEE, 69*, 1145–1150.

Hasegawa, A., & Tappert, F. (1973). Transmission of stationary nonlinear optical pulses in dispersive dielectric fibers 1. Anomalous dispersion. *Applied Physics Letters, 23*, 142–144.

Heidt, A. M. (2010). Pulse preserving flat-top supercontinuum generation in all-normal dispersion photonic crystal fiber. *Journal of the Optical Society of America B: Optical Physics, 27*, 50–559.

Heidt, A. M., Price, J. H. V., Baskiotis, C., Feehan, J. S., Lii, Z., Alam, S. U., & Richardson, D. J. (2013). Mid-infra-red ZBLAN fiber supercontinuum source using picosecond didoe-pumping at 2 μm. *Optics Express, 21*, 24281–24287.

Herrmann, J., Greibner, U., Zhavoronkov, N., Husakou, A., Nickel, D., Knight, J. C., Wadsworth, W. J., Russell, P. S. J., & Korn, G. (2002). Experimental evidence for supercontinuum generation by fission of higher-order solitons in photonic fibers. *Physical Review Letters, 88*, 173901.

Hölzer, P., Chang, W., Travers, J. C., Nazarkin, A., Nold, J., Joly, N. Y., Saleh, M. F., Biancalana, F., & Russell, P. S. J. (2011). Femtosecond nonlinear fiber optics in the ionization regime. *Physical Review Letters, 107*(20), 203901.

Hooper, L. E., Mosley, P. J., Muir, A. C., Wadsworth, W. J., & Knight, J. C. (2010). Coherent supercontinuum generation in photonic crystal fiber with all-normal group velocity dispersion. *Optics Express, 19*, 4902–4907.

Hori, T., Takayanagi, J., Nishizawa, N., & Goto, T. (2004). Flatly broadened, wideband and low noise supercontinuum generation in highly nonlinear hybrid fiber. *Optics Express, 12*, 317–324.

Hu, X., Zhang, W., Yang, Z., Wang, Y., Zhao, W., Li, X., Wang, H., Li, C., & Shen, D. (2011a). *Optics Letters, 36*, 2659–2661.

Hult, J. (2007). A fourth-order Runge? Kutta in the interaction picture method for simulating supercontinuum generation in optical fibers. *Journal of Lightwave Technology, 25*(12), 3770–3775.

Hundertmark, H., Rammler, S., Wilken, T., Holzwarth, R., Hänsch, T. W., & Russell, P. S. J. (2009). Octave-spanning supercontinuum generated in SF6-glass PCF by a 1060 nm mode-locked fibre laser delivering 20 pJ per pulse. *Optics Express, 17*, 1919–1924.

Husakou, A. V., & Herrmann, J. (2001). Supercontinuum generation of high order solitons by fission in photonic crystal fibers. *Physical Review Letters, 87*, 203901.

Im, S.-J., Husakou, A., & Herrmann, J. (2009). Guiding properties and dispersion control of Kagome lattice hollow-core photonic crystal fibers. *Optics Express, 17*(15), 13050–13058.

Ippen, E. P. (1970). Low-power, Quasi-cw Raman oscillator. *Applied Physics Letters, 16*, 303–305.
Ippen, E. P., & Stolen, R. H. (1972). Stimulated-Brillouin scattering in optical fibers. *Applied Physics Letters, 21*, 539–541.
Ippen, E. P., Shank, C. V., & Gustafson, T. K. (1974). Self phase modulation of picosecond pulses in optical fibers. *Applied Physics Letters, 24*, 190–192.
Islam, M. N., Sucha, G., Bar-Joseph, I., Wegener, M., Gordon, J. P., & Chemla, D. S. (1989). Femtosecond distributed soliton spectrum in fibers. *Journal of the Optical Society of America B: Optical Physics, 6*, 1149–1158.
Itoh, H., Davis, G. M., & Sudo, S. (1989). Continuous-wave-pumped modulational instability in an optical fiber. *Optics Letters, 14*, 1368–1370.
Jiang, X., Joly, N. Y., Finger, M. A., Wong, G. K. L., Babic, F., Saad, M., & Russell, P. St. J. (2013). *Close to three-octave-spanning supercontinuum generated in ZBLAN photonic crystal fiber*. Paper JTh5A.6 Post deadline Advanced Solid State Lasers Congress.
Jiang, X., Joly, N. Y., Finger, M. A., Babic, F., Wong, G. K. L., Travers, J. C., & Russell, P. S. J. (2015). Deep-ultraviolet to mid-infrared supercontinuum generated in solid-core ZBLAN photonic crystal fibre. *Nature Photonics, 9*, 133–139.
Johnson, A. M., & Shank, C. V. (1989). Chapter 10: Pulse-compression in single-mode fibers – Picoseconds to femtoseconds. In R. R. Alfano (Ed.), *The Supercontinuum Laser Source*. Springer. ISBN 0-387-96946-2.
Joly, N. Y., Nold, J., Chang, W., Hölzer, P., Nazarkin, A., Wong, G. K. L., Biancalana, F., & Russell, P. S. J. (2011). Bright spatially coherent wavelength-tunable deep-UV laser source using an Ar-filled photonic crystal fiber. *Physical Review Letters, 106*(20), 203901.
Kao, K. C., & Hockham, G. A. (1966). Dielectric-fibre surface waveguides for optical frequencies. *Proceedings of the Institution of Electrical Engineers, 113*, 1151–1158.
Kapron, F. P., Keck, D. B., & Maurer, R. D. (1970). Radiation losses in glass optical waveguides. *Applied Physics Letters, 17*, 423–425.
Karasawa, N., Nakamura, S., Nakagawa, N., Shibata, M., Morita, R., Shigekawa, H., & Yamashita, M. (2001). Comparison between theory and experiment of nonlinear propagation for a-few-cycle and ultrabroadband optical pulses in a fused-silica fiber. *IEEE Journal of Quantum Electronics, 37*(3), 398–404.
Kelleher, E. J. R., Travers, J. C., Popov, S. V., & Taylor, J. R. (2012a). Role of pump coherence in the evolution of continuous-wave supercontinuum generation initiated by modulational instability. *Journal of the Optical Society of America B: Optical Physics, 29*, 502–512.
Kelleher, E. J. R., Erkintalo, M., & Travers, J. C. (2012b). Fission of solitons in continuous-wave supercontinuum. *Optics Letters, 37*(24), 5217–5219.
Kinsler, P. (2010). Optical pulse propagation with minimal approximations. *Physical Review A, 81*(1), 013819.
Knight, J. C. (2003). Photonic crystal fibers. *Nature, 424*, 847–851.
Knight, J. C., Birks, T. A., Russell, P. S. J., & Atkin, D. M. (1996). All-silica single-mode optical fiber with photonic crystal cladding. *Optics Letters, 21*, 1547–1549.
Knox, W. H., Fork, R. L., Downer, M. C., Stolen, R. H., & Shank, C. V. (1985). Optical pulse compression to 8 f. at a 5-kHz repetition rate. *Applied Physics Letters, 46*, 1220–1121.
Kobtsev, S. M., & Smirnov, S. V. (2005). Modelling of high-power supercontinuum generation in highly nonlinear, dispersion shifted fibers at CW pump. *Optics Express, 13*, 6912–6918.
Kodama, Y., & Hasegawa, A. (1987). Nonlinear pulse propagation in a monomode dielectric guide. *IEEE Journal of Quantum Electronics, 23*(5), 510–524.
Kolesik, M., & Moloney, J. V. (2004). Nonlinear optical pulse propagation simulation: From Maxwell's to unidirectional equations. *Physical Review E, 70*(3), 036604.
Kubota, H., Tamura, K. R., & Nakazawa, M. (1999). Analysis of coherence-maintained ultrashort optical pulse trains and supercontinuum, generation in the presence of soliton-amplified spontaneous-emission interaction. *Journal of the Optical Society of America B: Optical Physics, 16*, 2223–2232.
Kudlinski, A., & Mussot, A. (2008). Visible cw-pumped supercontinuum. *Optics Letters, 33*, 2407–2409.

Kudlinski, A., George, A. K., Knight, J. C., Travers, J. C., Rulkov, A. B., Popov, S. V., & Taylor, J. R. (2006). Zero-dispersion wavelength decreasing photonic crystal fibers for ultraviolet-extended supercontinuum generation. *Optics Express, 14*, 5715–5722.

Kudlinski, A., Bouwmans, G., Quiquempois, V., LeRouge, A., Bigot, L., Mélin, G., & Mussot, A. (2009a). Dispersion-engineered photonic crystal fibers for cw-pumped supercontinuum generation. *Journal of Lightwave Technology, 27*, 1556–1564.

Kudlinski, A., Bouwmans, G., Vanvincq, O., Quiquempois, V., LeRouge, A., Bigot, L., Mélin, G., & Mussot, A. (2009b). White-light cw-pumped supercontinuum generation in highly GeO_2 -doped-core photonic crystal fibers. *Optics Letters, 34*, 3621–3523.

Kumar, V. V. R. K., George, A. K., Reeves, W. H., Knight, J. C., Russell, P. S. J., Omenetto, F. G., & Taylor, A. J. (2002). Extruded soft glass photonic crystal fiber for ultrabroad supercontinuum generation. *Optics Express, 10*, 1520–1525.

Kumar, V. V. R. K., George, A. K., Knight, J. C., & Russell, P. S. J. (2003). Tellurite photonic crystal fiber. *Optics Express, 11*, 2641–2645.

Labat, D., Melin, G., Mussot, A., Fleureau, A., Galkovsky, L., Lempereur, S., & Kudlinski, A. (2011). Phosphorus-doped photonic crystal fibers for high-power (36 W) visible CW supercontinuum. *IEEE Photonics Journal, 3*(5), 815–820.

Laegsgaard, J. (2007). Mode profile dispersion in the generalised nonlinear Schrödinger equation. *Optics Express, 15*(24), 16110–16123.

Laegsgaard, J. (2012). Modeling of nonlinear propagation in fiber tapers. *Journal of the Optical Society of America B, 29*(11), 3183–3191.

Leon-Saval, S. G., Birks, T. A., Wadsworth, W. J., & Russell, P. S. J. (2004). Supercontinuum generation in submicron fibre waveguides. *Optics Express, 12*, 2864–2869.

Lewis, S. A. E., Chernikov, S. V., & Taylor, J. R. (1998). Ultra-broad-bandwidth spectral continuum generation in fibre Raman amplifier. *Electronics Letters, 34*, 2267–2268.

Lin, C., & Stolen, R. H. (1976). New nanosecond continuum for excited-state spectroscopy. *Applied Physics Letters, 28*, 216–218.

Lin, C., Nguyen, V. T., & French, W. G. (1978). Wideband near i.r. continuum (0.7–2.1 mm) generated in low-loss optical fibre. *Electronics Letters, 14*, 822–823.

Lou, J. W., Xia, T. J., Boyraz, O., Shi, C.-X., Nowak, G. A., & Islam, M. N. (1997). Broader and flatter supercontinuum spectra in dispersion-tailored fibers, paper TuH6. *Technical Digest Optical Fiber Communications*, 32–34.

Maiman, T. H. (1960). Stimulated optical radiation in ruby. *Nature, 187*, 493–494.

Mak, K. F., Travers, J. C., Hölzer, P., Joly, N. Y., & Russell, P. S. J. (2013a). Tunable vacuum-UV to visible ultrafast pulse source based on gas-filled kagome-PCF. *Optics Express, 21*(9), 10942–10953.

Mak, K. F., Travers, J. C., Joly, N. Y., Abdolvand, A., St, P., & Russell, J. (2013b). Two techniques for temporal pulse compression in gas-filled hollow-core kagomé photonic crystal fiber. *Optics Letters, 38*(18), 3592–3595.

Mamyshev, P. V., & Chernikov, S. V. (1990). Ultrashort-pulse propagation in optical fibers. *Optics Letters, 15*(19), 1076–1078.

Martin-Lopez, S., Carrasco-Sanz, A., Corredera, P., Abrardi, L., Hernanz, M. L., & Gonzalez-Herraez, M. (2006). Experimental investigation of the effect of pump incoherence on nonlinear pump spectral broadening and continuous-wave supercontinuum generation. *Optics Letters, 31*, 3477–3479.

Martinez, R. A., Plant, G., Guo, K., Janiszewski, B., Freeman, M. J., Maynard, R. L., Islam, M. N., Terry, F. L., Alvarez, O., Chenard, F., Bedford, R., Gibson, R., & Ifarraguerri, A. I. (2018). Mid-infrared supercontinuum generation from 1.6 to >11 μm using concatenated step-index fluoride and chalcogenide fibers. *Optics Letters 43*, 296–299.

McClung, F. J., & Helwarth, R. W. (1962). Giant optical pulsations from ruby. *Journal of Applied Physics, 33*, 828–829.

Mitschke, F. M., & Mollenauer, L. F. (1986). Discovery of the soliton self-frequency shift. *Optics Letters, 11*, 659–661.

Mitschke, F. M., & Mollenauer, L. F. (1987a). Experimental observation of interaction forces between solitons in optical fibers. *Optics Letters, 12*, 355–357.

Mitschke, F. M., & Mollenauer, L. F. (1987b). Ultrashort pulses from the soliton laser. *Optics Letters, 12*, 407–409.

Mocker, H. W., & Collins, R. J. (1965). Mode competition and self-locking effects in a Q-switched ruby laser. *Applied Physics Letters, 7*, 270–273.

Mollenauer, L. F., & Gordon, J. P. (2006). *Solitons in optical fibers*. Elsevier-Academic Press. ISBN 13: 978-0-12-504190-4.

Mollenauer, L. F., & Stolen, R. H. (1984). The soliton laser. *Optics Letters, 9*, 13–16.

Mollenauer, L. F., Stolen, R. H., & Gordon, J. P. (1980). Experimental observation of picosecond pulse narrowing and solitons in optical fibers. *Physical Review Letters, 45*, 1095–1098.

Mollenauer, L. F., Stolen, R. H., Gordon, J. P., & Tomlinson, W. J. (1983). Extreme picosecond pulse narrowing by means of soliton effect in single-mode optical fibers. *Optics Letters, 8*, 289–291.

Mollenauer, L. F., Stolen, R. H., & Islam, M. N. (1985). Experimental demostration of soliton propagation in long fibers: loss compensated by Raman gain. *Optics Letters, 10*, 229–231.

Møller, U., Yu, Y., Petersen, C. R., Kubat, I., Mechin, D., Brilland, L., Troles, J., Luther-Davies, B., & Bang, O. (2014). High average power mid-infrared supercontinuum generation in a suspended core chalcogenide fiber. In *Advanced Photonics, JM5A.54. OSA Technical Digest (online)*. Optical Society of America.

Monro, T. M., West, Y. D., Hewak, D. W., Broderick, N. C. R., & Richardson, D. J. (2000). Chalcogenide holey fibres. *Electronics Letters, 36*, 1998–2000.

Mori, K., Takara, H., Kawanishi, T., Saruwatari, M., & Morioka, T. (1997). Flatly broadened supercontinuum spectrum generated in a dispersion decreasing fibre with convex dispersion profile. *Electronics Letters, 33*, 1806–1808.

Morioka, T., Kawanishi, S., Mori, K., & Saruwatari, M. (1993). More than 100 wavelength channel picosecond optical pulse generation from single laser source using supercontinuum in optical fibres. *Electronics Letters, 29*, 862–863.

Morioka, T., Kawanishi, S., Mori, K., & Saruwatari, M. (1994). Nearly penalty free <4ps supercontinuum Gbits/s pulse generation over 1535–1560 nm. *Electronics Letters, 30*, 790–791.

Morioka, T., Takara, H., Kawanishi, S., Kamatani, O., Takiguchi, K., Uchiyama, K., Saruwatari, M., Takahashi, H., Yamada, M., Kanamori, T., & Ono, H. (1996). 1 Tbit/s (100Gbits/s x 10 channel) OTDM/WDM transmission using single supercontinuum WDM source. *Electronics Letters, 32*, 906–907.

Mussot, A., & Kudlinki, A. (2009). 19.5 W CW-pumped supercontinuum source from 0.65 to 1.38 μm. *Electronics Letters, 45*.

Mussot, A., Lantz, E., Maillotte, H., Sylvestre, T., Finot, C., & Pitois, S. (2004). Spectral broadening of a partially coherent CW laser beam in single-mode optical fibers. *Optics Express, 12*, 2838–2843.

Mussot, A., Beaugeois, M., Bouazaoui, M., & Sylvestre, T. (2007). Tailoring CW supercontinuum generation in microstructured fibers with two-zero dispersion wavelengths. *Optics Express, 15*, 11553–11563.

Mussot, A., Kudlinski, A., Kolobov, M., Louvergneaux, E., Douay, M., & Taki, M. (2009). Observation of extreme temporal events in CW-pumped supercontinuum. *Optics Express, 17*, 17101–17015.

Nakazawa, M., & Tokuda, M. (1983). Continuum spectrum generation in a multimode fiber using two pump beams at 1.3μm wavelength region. *Japanese Journal of Applied Physics, 22*, L239–L241.

Nicholson, J. W., Yan, M. F., Wisk, P., Fleming, J., DiMarcello, F., Monberg, E., Yablon, A., Jørgensen, C., & Veng, T. (2003a). All-fiber, octave-spanning supercontinuum. *Optics Letters, 28*, 643–645.

Nicholson, J. W., Abeluck, A. K., Headley, C., Yan, M. F., & Jørgensen, C. G. (2003b). Pulsed and continuous-wave supercontinuum generation in highly nonlinear, dispersion-shifted fibers. *Applied Physics B, 77*, 211–218.

Nicholson, J. W., Yablon, A. D., Westbrook, P. S., Feder, K. S., & Yan, M. F. (2004a). High power, single mode, all-fiber source of femtosecond pulses at 1550 nm and its use in supercontinuum generation. *Optics Express, 12*, 3025–3034.

Nicholson, J. W., Westbrook, P. S., Fedetr, K. S., & Yablon, A. D. (2004b). Supercontinuum generation in ultraviolet-irradiated fibers. *Optics Letters, 29*, 2363–2365.

Nicholson, J. W., Bise, R., Alonzo, J., Stockert, T., Trevor, D. J., Dimarcello, F., Monberg, E., Fini, J. M., Westbrook, P. S., Feder, K., & Grüner-Nielsen, L. (2008). Visible continuum generation using a femtosecond erbium-doped fiber laser and a silica nonlinear fiber. *Optics Letters, 33*, 28–30.

Nishizawa, N., & Goto, T. (2002a). Pulse trapping by ultrashort soliton pulses in optical fibers across zero-dispersion wavelength. *Optics Letters, 27*, 152–154.

Nishizawa, N., & Goto, T. (2002b). Characteristics of pulse trapping by use of ultrashort soliton pulses in optical fibers across the zero dispersion wavelength. *Optics Express, 10*, 1151–1159.

Nold, J., Hölzer, P., Joly, N. Y., Wong, G. K. L., Nazarkin, A., Podlipensky, A., Scharrer, M., & Russell, P. S. J. (2010). Pressure-controlled phase matching to third harmonic in Ar-filled hollow-core photonic crystal fiber. *Optics Letters, 35*(17), 2922–2924.

Nowak, G. A., Kim, J., & Islam, M. N. (1999). Stable supercontinuum generation in short lengths of conventional dispersion shifted fiber. *Applied Optics, 38*, 7364–7369.

Okuno, T., Onishi, M., & Nishimura, M. (1998). Generation of ultra-broad-band supercontinuum by dispersion-flattened and decreasing fiber. *IEEE Photonics Technology Letters, 10*, 72–74.

Österberg, U., & Margulis, W. (1986). Dye laser pumped by Nd:YAG laser pulses frequency doubled in a glass optical fiber. *Optics Letters, 11*, 516–518.

Ouzounov, D. G., Ahmad, F. R., Müller, D., Venkataraman, N., Gallagher, M. T., Thomas, M. G., Silcox, J., Koch, K. W., & Gaeta, A. L. (2003). Generation of megawatt optical solitons in hollow-core photonic band-gap fibers. *Science, 301*(5640), 1702–1704.

Ouzounov, D., Hensley, C., Gaeta, A., Venkateraman, N., Gallagher, M., & Koch, K. (2005). Soliton pulse compression in photonic band-gap fibers. *Optics Express, 13*(16), 6153–6159.

Palfrey, S. L., & Grischkowsky, D. (1984). Generation of 16-fsec frequency-tunable pulses by optical pulse compression. *Optics Letters, 10*, 562–564.

Persephonis, P., Chernikov, S. V., & Taylor, J. R. (1996). Cascaded CW fibre Raman laser source 1.6–1.9 μm. *Electronics Letters, 32*, 1486–1487.

Petersen, C. R., Møller, U., Kubat, I., Zhou, B., Dupont, S., Ramsay, J., Benson, T., Sujecki, S., Abdel-Moneim, N., Tang, Z., Furniss, D., Seddon, A., & Bang, O. (2014). Mid-infrared supercontinuum covering the 1.4–13.3 μm molecular fingerprint region using ultra-high NA chalcogenide step-index fibre. *Nature Photonics, 8*, 830–834.

Poletti, F., & Horak, P. (2008). Description of ultrashort pulse propagation in multimode optical fibers. *Journal of the Optical Society of America B, 25*(10), 1645–1654.

Popov, S. V., Champert, P. A., Solodyankin, M. A., & Taylor, J. R. (2002). *Seeded fibre amplifiers and multi-watt average power continuum generation in holety fibres*, Paper WKK2, Proceedings OSA Annual Meeting, 117.

Price, J. H. V., Monro, T. M., Ebendorff-Heidepriem, H., Poletti, F., Horak, P., Finazzi, V., Leong, J. Y. Y., Petropoulos, P., Flanagan, J. C., Brambilla, G., Feng, X., & Richardson, D. J. (2007). Mid-IR supercontinuum generation from nonsilica microstructured optical fibers. *IEEE Journal of Selected Topics in Quantum Electronics, 13*, 738–749.

Provino, L., Dudley, J. M., Maillotte, H., Grossard, N., Windeler, R. S., & Eggleton, B. J. (2001). Compact broadband continuum source based on microchip laser pumped microstructured fibre. *Electronics Letters, 37*, 558–559.

Qin, G., Yan, X., Kito, C., Liao, M., Chaudhari, C., Suzuki, T., & Ohishi, Y. (2009a). Supercontinuum generation spanning over three octaves from UV to 3.85 μm in a fluoride fiber. *Optics Letters, 34*, 2015–2017.

Qin, G., Yan, X., Kito, C., Liao, M., Chaudhari, C., Suzuki, T., & Ohishi, Y. (2009b). Ultrabroad supercontinuum generation from ultraviolet to 6.28 μm in a fluoride fiber. *Applied Physics Letters, 95*, 161103.

Ranka, J. K., Windeler, R. S., & Stentz, A. J. (2000). Visible continuum generation in air-silica microstructure optical fibers with anomalous dispersion at 800nm. *Optics Letters, 25*, 25–27.

Ruban, V., Kodama, Y., Ruderman, M., Dudley, J., Grimshaw, R., McClintock, P. V. E., Onorato, M., et al. (2010). Rogue waves – Towards a unifying concept?: Discussions and debates. *The European Physical Journal – Special Topics, 185*(1), 5–15.

Rulkov, A. B., Getman, A. G., Vyatkin, M. Y., Popov, S. V., Gapontsev, V. P., & Taylor, J. R. (2004a). *525–1800 nm, Watt level all-fibre picosecond source*, Paper CDPC7, Conference on Lasers and Electro-Optics, San Francisco.

Rulkov A. B., Popov S. V., & Taylor, J. R., (2004b). *1.5 – 2.0 μm, multi Watt white-light generation in CW format in highly nonlinear fibres*. Paper TuA6 OSA Conference, Advanced Solid State Photonics, Santa Fe, NM, USA.

Rulkov, A. B., Vyatkin, M. Y., Popov, S. V., Taylor, J. R., & Gapontsev, V. P. (2005). High brightness picosecond all-fiber generation in 525-1800 nm range with picosecond Yb pumping. *Optics Express, 13*, 377–381.

Russell, P. S. J. (2006). Photonic-crystal fibers. *Journal of Lightwave Technology, 24*, 4729–4749.

Russell, P. S. J., Hölzer, P., Chang, W., Abdolvand, A., & Travers, J. C. (2014). Hollow-core photonic crystal fibres for gas-based nonlinear optics. *Nature Photonics, 8*(4), 278–286.

Rusu, M., Grudinin, A. B., & Okhotnikov, O. G. (2005). Slicing the supercontinuum radiation generated in photonic crystal fiber using an all-fiber chirped-pulse amplification scheme. *Optics Express, 13*, 6390–6400.

Sanghera, J. S., Shaw, L. B., & Aggarwal, I. D. (2009). Chalcogenide glass-fiber-based mid-IR sources and applications. *IEEE Journal of Selected Topics in Quantum Electronics, 15*, 114–119.

Satsuma, J., & Yajima, N. (1974). Initial value problems of one-dimensional self-modulation of nonlinear waves in dispersive media. *Supplement, Progress Theoretical Physics, 55*, 284–306.

Schreiber, T., Limpert, J., Zellmer, H., Tünnermann, A., & Hansen, K. P. (2003). High average power supercontinuum generation in photonic crystal fibers. *Optics Communication, 228*, 71–78.

Seefeldt, M., Heuer, A., & Menzel, R. (2003). Compact white-light source with an average output power of 2.4W and 900 nm spectral bandwidth. *Optics Communication, 216*, 199–202.

Serkin, V. N. (1987a). Self compression and decay of femtosecond optical wavepackets in fiber light guides. *Soviet Physics/Lebedev Institute Reports, 6*, 49–53.

Serkin, V. N. (1987b). Colored envelope solitons in optical fibers. *Soviet Technical Physics Letters, 13*, 320–321.

Solli, D. R., Ropers, C., Koonath, P., & Jalali, B. (2007). Optical rogue waves. *Nature, 450*, 1054–1058.

Solli, D. R., Ropers, C., & Jalali, B. (2008). Active control of rogue waves for stimulated supercontinuum generation. *Physical Review Letters, 101*, 233902.

Sørensen, S. T., Møller, U., Larsen, C., Moselund, P. M., Jakobsen, C., Johansen, J., Andersen, T. V., Thomsen, C. L., & Bang, O. (2012). Deep-blue supercontinnum sources with optimum taper profiles ? Verification of GAM. *Optics Express, 20*(10), 10635–10645.

Stark, S. P., Steinmetz, T., Probst, R. A., Hundertmark, H., Wilken, T., Hänsch, T. W., Udem, T., Russell, P. S. J., & Holzwarth, R. (2011). 14 GHz visible supercontinuum generation: Calibration sources for astronomical spectrographs. *Optics Express, 19*(17), 15690–15695.

Stark, S., Travers, J. C., Joly, N. Y., & Russell, P. S. J. (2012a). Supercontinuum sources based on photonic crystal fiber. In O. G. Okhotnikov (Ed.), *Fiber lasers* (pp. 63–96). Wiley-VCH Verlag GmbH & Co.

Stark, S. P., Travers, J. C., & Russell, P. S. J. (2012b). Extreme supercontinuum generation to the deep UV. *Optics Letters, 37*(5), 770–772.

Stolen, R. H. (2008). The early years of fiber nonlinear optics. *IEEE Journal of Lightwave Technology, 26*, 1021–1031.

Stolen, R. H., & Ashkin, A. (1973). Optical Kerr effect in glass waveguides. *Applied Physics Letters, 22*, 294–296.

Stolen, R. H., & Lin, C. (1978). Self phase modulation in silica optical fibers. *Physical Review A, 17*, 1448–1453.

Stolen, R. H., Ippen, E. P., & Tynes, A. R. (1972). Raman oscillation in glass optical waveguides. *Applied Physics Letters, 20*, 62–64.

Stolen, R. H., Bjorkholm, J. E., & Ashkin, A. (1974). Phase matched three-wave mixing in silica fiber optical waveguides. *Applied Physics Letters, 24*, 308–310.

Stolen, R. H., Mollenauer, L. F., & Tomlinson, W. J. (1983). Observation of pulse restoration at the soliton period in optical fibers. *Optics Letters, 8*, 186–188.

Stolen, R. H., Gordon, J. P., Tomlinson, W. J., & Haus, H. A. (1989). Raman response function of silica-core fibers. *Journal of the Optical Society of America B, 6*(6), 1159–1166. https://doi.org/10.1364/JOSAB.6.001159

Stone, J. M., & Knight, J. C. (2008). Visibly "white" light generation in uniform photonic crystal fiber using a microchip laser. *Optics Express, 16*, 2670–2675.

Tai, K., & Tomita, A. (1986). 1100x optical fiber pulse compression using grating pair and soliton effect at 1.319 μm. *Applied Physics Letters, 48*, 1033–1035.

Tai, K., Hasegawa, A., & Tomita, A. (1986a). Observation of modulational instability in optical fibers. *Physical Review Letters, 56*, 135–138.

Tai, K., Tomita, A., Jewell, J. L., & Hasegawa, A. (1986b). generation of subpicosecond solitonlike optical pulses at 0.3 THz repetition rate by induced modulational instability. *Applied Physics Letters, 49*, 236–238.

Tai, K., Hasegawa, A., & Bekki, N. (1988). Fission of optical solitons induced by stimulated Raman effect. *Optics Letters, 13*(5), 392–394.

Takara, H., Ohara, T., Mori, K., Sato, K., Yamada, E., Inoue, Y., Shibata, T., Abe, M., Morioka, T., & Sato, K. I. (2000). More than 1000 channel optical frequency chain generation from single supercontinuum source with 12.5 GHz channel spacing. *Electronics Letters, 36*, 2089–2090.

Takayanagi, J., Nishizawa, N., Nagai, H., Yoshida, M., & Goto, T. (2005). Generation of high-power femtosecond pulse and octave-spanning ultrabroad supercontinuum using all-fiber system. *IEEE Photonics Technology Letters, 17*, 37–39.

Takushima, Y., Futami, F., & Kikuchi, K. (1998). Generation of over 140-nm-wide supercontinuum from a normal dispersion fiber by using a mode-locked-semiconductor laser source. *IEEE Photonics Technology Letters, 10*, 1560–1562.

Tani, F., Travers, J. C., & Russell, P. S. J. (2013). PHz-wide supercontinua of nondispersing subcycle pulses generated by extreme modulational instability. *Physical Review Letters, 111*(3), 033902.

Tani, F., Travers, J. C., & Russell, P. S. J. (2014). Multimode ultrafast nonlinear optics in optical waveguides: Numerical modeling and experiments in kagomé photonic-crystal fiber. *Journal of the Optical Society of America B, 31*(2), 311.

Teipel, J., Türke, D., & Giessen, H. (2005). Compact multi-watt picosecond coherent white light sources using multiple-taper fibers. *Optics Express, 13*, 1734–1742.

Tomlinson, W. J., Stolen, R. H., & Shank, C. V. (1984). Compression of optical pulses chirped by self-phase modulation in fibers. *Journal of the Optical Society of America B: Optical Physics, 1*, 139–149.

Travers, J. C. (2009). Blue solitary waves from infrared continuous wave pumping of optical fibers. *Optics Express, 17*(3), 1502–1507.

Travers, J. C. (2010a). Chapter 8: Continuous wave supercontinuum generation. In J. M. Dudley & J. R. Taylor (Eds.), *Supercontinuum generation in Optical Fibers*. Cambridge University Press. ISBN 978-0-521-51480-4.

Travers, J. C. (2010b). High average power supercontinuum sources. *Pramana-Journal of Physics, 75*, 769–785.

Travers, J. C. (2010c). Blue extension of optical fibre supercontinuum generation. *Journal of Optics, 12*(11), 113001.

Travers, J. C., & Taylor, J. R. (2009). Soliton trapping of dispersive waves in tapered optical fibers. *Optics Letters, 34*, 115–117.

Travers, J. C., Kennedy, R. E., Popov, S. V., Taylor, J. R., Sabert, H., & Mangan, B. (2005a). Extended continuous-wave supercontinuum generation in a low-water-loss holey fiber. *Optics Letters, 30*, 1938–1940.

Travers, J. C., Popov, S. V., & Taylor, J. R. (2005b). Extended blue supercontinuum generation in cascaded holey fibers. *Optics Letters, 30*, 3132–3134.

Travers, J. C., Rulkov, A. B., Popov, S. V., Taylor, J. R., Kudlinski, A., George, A. K., & Knight, J. C. (2007). Multi-watt supercontinuum generation from 0.3 to 2.4 μm in PCF tapers. In *Conference on lasers and electro-optics/quantum electronics and laser science conference and photonic applications systems technologies*, JTuB2. OSA Technical Digest (CD). Optical Society of America.

Travers, J. C., Rulkov, A. B., Cumberland, B. A., Popov, S. V., & Taylor, J. R. (2008). Visible supercontinuum generation in photonic crystal fibers with a 400 W continuous wave fiber laser. *Optics Express, 16*, 14435–14447.

Travers, J. C., Frosz, M. H., & Dudley, J. M. (2010). Chapter 3: Nonlinear fibre optics overview. In J. M. Dudley & J. R. Taylor (Eds.), *Supercontinuum generation in Optical Fibers*. Cambridge University Press. ISBN 978-0-521-51480-4.

Travers, J. C., Chang, W., Nold, J., Joly, N. Y., & Russell, P. S. J. (2011). Ultrafast nonlinear optics in gas-filled hollow-core photonic crystal fibers [Invited]. *Journal of the Optical Society of America B, 28*(12), A11–A26.

Travers, J. C., Ermolov, A., Belli, F., Mak, K. F., Frosz, M. H., Tani, F., Abdolvand, A., & Russell, P. S. J. (2014). Efficient broadband vacuum-ultraviolet generation in gas-filled hollow-core photonic crystal fibers. In *Frontiers in optics, FM4C.6. OSA Technical Digest (online)*. Optical Society of America.

Tzoar, N., & Jain, M. (1981). Self-phase modulation in long-geometry optical waveguides. *Physical Review A, 23*(3), 1266.

Vanholsbeeck, F., Martin-Lopez, S., González-Herráez, M., & Coen, S. (2005). The role of pump coherence in continuous-wave supercontinuum generation. *Optics Express, 13*, 6615–6625.

Vodop'yanov, K. L., Grudinin, A. B., Dianov, E. M., Kulevskii, L. A., Prokhorov, A. M., & Khaidarov, D. V. (1987). Generation of pulses of 100–200 f. duration by stimulated Raman scattering in a single-mode fiber waveguide at wavelengths 1.5–1.7 μm. *Sov. J. Quantum Elect., 17*, 1311–1313.

Vysloukh, V. A. (1983). Propagation of pulses in optical fibers in the region of a dispersion minimum. Role of nonlinearity and higher-order dispersion. *Soviet Journal of Quantum Electronics, 13*, 1113–1114.

Vysloukh, V. A., & Serkin, V. N. (1983). Generation of high-energy solitons of stimulated Raman radiation in fiber light guides. *JETP Letters, 38*, 199–202.

Vysloukh, V. A., & Serkin, V. N. (1984). Nonlinear transformation of solitons in fiber lightguides. *Bulletin of the Academy of Sciences of the USSR. Physical Series, 48*, 125–129.

Wadsworth, W. J., Knight, J. C., Ortigosa-Blanch, A., Arriaga, J., Silvestre, E., & Russell, P. S. J. (2000). Soliton effects in photonic crystal fibres at 850 nm. *Electronics Letters, 36*, 53–55.

Wai, P. K. A., Menyuk, C. R., Lee, Y. C., & Chen, H. H. (1986a). Nonlinear pulse propagation in the neighborhood of the zero-dispersion wavelength of monomode optical fibers. *Optics Letters, 11*(7), 464–466.

Wai, P. K. A., Menyuk, C. R., Lee, C., & Chen, H. H. (1986b). Nonlinear pulse propagation in the neighbourhood of the zero-dispersion wavelength of monomode optical fibers. *Optics Letters, 11*, 464–466.

Wai, P. K. A., Menyuk, C. R., Lee, C., & Chen, H. H. (1987). Soliton at the zero-group-velocity-dispersion wavelength of a single mode fiber. *Optics Letters, 12*, 628–630.

Washio, K., Inoue, K., & Tanigawa, T. (1980). Efficient generation of near-i.r. stimulated light scattering in optical fibres pumped in low-dispersion region at 1.3 μm. *Electronics Letters, 16*, 331–333.

Westbrook, P. S., Nicholson, J. W., Feder, K. S., & Yablon, A. D. (2005). Improved supercontinuum generation through UV processing of highly nonlinear fibers. *Journal of Lightwave Technology, 23*, 13–18.

Wetzel, B., Stefani, A., Larger, L., Lacourt, P. A., Merolla, J. M., Sylvestre, T., Kudlinski, A., Mussot, A., Genty, G., Dias, F., & Dudley, J. M. (2012). Real-time full bandwidth measurement of spectral noise in supercontinuum generation. *Scientific Reports, 2*(882), 1–7.

Xia, C., Kumar, M., Cheng, M. Y., Hegde, R. S., Islam, M. N., Galvanauskas, A., Winful, H. G., Terry, F. L., Jr., Freeman, M. J., Poulain, M., & Mazé, G. (2007). Power scalable mid-infrared supercontinuum generation in ZBLAN fluoride fibers with up to 1.3 watts time-averaged power. *Optics Express, 15*, 865–871.

Xia, C., Islam, M. N., Terry, F. L., Jr., Freeman, M. J., & Mauricio, J. (2009). 10.5 watts time-averaged power mid-infrared supercontinuum generation extending beyond 4 μm with direct pulse pattern modulation. *IEEE Journal of Selected Topics in Quantum Electronics, 15*, 422–434.

Yeom, D. I., Mägi, E. C., Lamont, M. R. E., Roelens, M. A. E., Fu, L., & Eggleton, B. J. (2008). Low-threshold supercontinuum generation in highly nonluinear chalcogenide nanowires. *Optics Letters, 33*, 660–662.

Yu, F., & Knight, J. C. (2013). Spectral attenuation limits of silica hollow core negative curvature fiber. *Optics Express, 21*(18), 21466–21471.

Zakharov, V. E., & Ostrovsky, L. A. (2009). Modulation instability: The beginning. *Physica D: Nonlinear Phenomena, 238*(5), 540–548.

Zakharov, V. E., & Shabat, A. B. (1971). Exact theory of two-dimensional self-focusing and one-dimensional self-modulation of waves in nonlinear media. *Zhurnal Eksperimental'noi i Teoreticheskoi Fiziki, 61*, 118–134.

Zhang, M., Kelleher, E. J. R., Runcorn, T. H., Mashinsky, V. M., Medvedkov, O. I., Dianov, E. M., Popa, D., Milana, S., Hasan, T., Sun, Z., Bonaccorso, F., Jiang, Z., Flahaut, E., Chapman, B. H., Ferrari, A. C., Popov, S. V., & Taylor, J. R. (2013). Mid-infrared Raman-soliton continuum pumped by a nanotube-mode-locked sub-picosecond Tm-doped MOPFA. *Optics Express, 21*, 23261–23271.

Zysset, B., Beaud, P., & Hodel, W. (1987). Generation of optical solitons in the wavelength region 1.37–1.49 μm. *Applied Physics Letters, 50*, 1027–1029.

New References Since 2015

Antikainen, A., & Agrawal, G. P. (2019). Supercontinuum generation in seven-core fibers. *Journal of the Optical Society of America B: Optical Physics, 36*, 2927–2937.

Arun, S., Choudhury, V., Balaswamy, V., & Supradeepa, V. R. (2020). Octave-spanning, continuous wave supercontinuum generation with record power using standard telecom fibers pumped with power-combined fiber lasers. *Optics Letters, 45*, 1172–1175.

Bi, W. J., Liu, Y. Y., Li, X., Liao, M. S., Hu, L. L., Ge, W. Q., He, F., Kuan, P. W., Yu, F., Wang, T. X., Wang, L. F., & Gao, W. Q. (2019). Micro-joule level visible supercontinuum generation in seven-core photonic crystal fibers pumped by a 5156 nm laser. *Optics Letters, 44*, 5041–5044.

Chen, H.-W., Chen, Z.-L., Chen, S.-P., Hou, J., & Lu, Q.-S. (2013a). Hundred-watt-level, all-fiber-integrated supercontinuum generation from photonic crystal fiber. *Applied Physics Express, 6*, 032702.

Chen, H.-W., Liang, G., Jin, A.-J., Chen, S.-P., Hou, J., & Lu, Q.-S. (2013b). Investigation of hundred-watt-level supercontinuum generation in photonic crystal fiber. *Acta Physica Sinica, 62*, 154207.

Chen, H. W., Wei, H. F., Liu, T., Zhou, X. F., Li, J., Tong, W. J., Chen, Z. L., Chen, S. P., Hou, J., & Lu, Q. S. (2014a). Hundred-watt-level supercontinuum generation in seven-core photonic crystal fiber. *Acta Physica Sinica, 63*, 044205.

Chen, H. W., Wei, H. F., Liu, T., Zhou, X. F., Yan, P. G., Chen, Z. L., Chen, S. P., Li, J., Hou, J., & Lu, Q. S. (2014b). All-fiber-integrated high-power supercontinuum sources based on multi-core photonic crystal fibers. *IEEE Journal of Selected Topics in Quantum Electronics, 20*, 0902008.

Cheng, T., Nagasaka, K., Tuan, T. H., Xue, X., Matsumoto, M., Tezuka, H., Suzuki, T., & Ohishi, Y. (2016). Mid-infrared supercontinuum generation spanning 2.0 to 15.1 μm in a chalcogenide step-index fiber. *Optics Letters, 41*, 2117–2120.

Dai, S., Wang, Y., Peng, X., Zhang, P., Wang, X., & Xu, Y. (2018). A review of mid-infrared supercontinuum generation in chalcogenide glass fibers. *Applied Sciences, 8*, 707.

Engelsholm, R. D., & Bang, O. (2019). Supercontinuum noise reduction by fiber undertapering. *Optics Express, 27*, 10320–10331.

Fang, H. H., Hu, M. L., Huang, L. L., Chai, L., Dai, N. L., Li, J. Y., Tashchilina, A. Y., Zheltikov, A. M., & Wang, C. Y. (2012). Multiwatt octave spanning supercontinuum generation in multicore photonic-crystal fiber. *Optics Letters, 37*, 2292–2294.

Fu, J., Chen, Y., Huang, Z., Yu, F., Wu, D., Pan, J., Zhang, C., Wang, D., Pang, M., & Leng, Y. (2021). Photoionization-induced broadband dispersive wave generated in an Ar-filled hollow-core photonic crystal fiber. *Crystals, 11*, 180.

Gauthier, J. C., Fortin, V., Carrée, J. Y., Poulain, S., Poulain, M., & Vallée and Bernier, M. (2016). Mid IR supercontinuum from 2.4 to 5.4 μm in a low-loss fluoroindate fiber. *Optics Letters, 41*, 1756–1759.

Gonzalo, I. B., & Bang, O. (2018). Role of the Raman gain in the noise dynamics of all-normal dispersion silica fiber supercontinuum generation. *Journal of the Optical Society of America B: Optical Physics, 35*, 2102–2110.

Gonzalo, I. B., Engelsholm, R. D., Sørensen, M. P., & Bang, O. (2018). Polarization noise places severe constraints on coherence of all-normal dispersion femtosecond supercontinuum generation. *Scientific Reports, 8*, 6579.

Gouveia-Neto, A. S., Gomes, A. S. L., & Taylor, J. R. (1988). Femtosecond soliton Raman generation. *IEEE Journal of Quantum Electronics, QE-24*, 332–340.

Heidt, A. M., Hodasi, J. M., Rampur, A., Spangenberg, D. M., Ryser, M., Klimczak, M., & Feurer, T. (2020). Low noise all-fiber amplification of a coherent supercontinuum at 2 μm and its limits imposed by polarization noise. *Scientific Reports, 10*, 16734.

Hooper, L., Kalita, M., Devine, A., Orec-Archer, A., & Clowes, J. (2015). White light 50W supercontinum – Roadmap to kW truly white lasers. *Proceedings of SPIE, 9344*, 93440X.

Hosseini, P., Ermolov, A., Tani, F., Novoa, D., & Russell, P. (2018). UV soliton dynamics and Raman-enhanced supercontinuum generation in photonic crystal fiber. *ACS Photonics, 5*, 2426–2430.

Hu, X., Zhang, W., Yang, Z., Wang, Y., Zhao, W., Wang, H., Li, C., & Shen, D. (2011b). High average power, strictly all-fiber supercontinuum source with good beam quality. *Optics Letters, 36*, 2659–2661.

Huang, S. S., Zhang, G. L., Wei, H. F., & Li, H. Q. (2013). Supercontinuum generation and mode analysis for double cladding seven-core photonic crystal fiber. *Chinese Journal of Lasers, 40*, 1105002.

Hudson, D. D., Antipov, S., Li, L., Alamgir, I., Hu, T., El-Amraoui, M., Messaddeo, Y., Rochette, M., Jackson, S. D., & Fuerbach, A. (2017). Toward all-fiber supercontinuum spanning the mid infrared. *Optica, 4*, 1163–1166.

Jain, D., Sidarthan, R., Moselund, P. M., Yoo, S., Ho, D., & Bang, O. (2016). Record power, ultra-broadband supercontinuum source based on highly GeO2 doped silica fiber. *Optics Express, 24*, 26667–26677.

Jensen, M., Gonzalo, T. B., Engelsholm, R. D., Maria, M., Israelsen, N. M., Podoleanu, A., & Bang, O. (2019). Noise of supercontinuum sources in spectral domain optical coherence tomography. *Journal of the Optical Society of America B: Optical Physics, 36*, A154–A160.

Jiao, K., Yao, J., Zhao, Z., Wang, X., Si, N., Wang, X., Chen, P., Xue, Z., Tian, Y., Zhang, B., Zhang, P., Dai, S., Nie, Q., & Wang, R. (2019a). Mid-infrared flattened supercontinuum generation in all-normal dispersion tellurium chalcogenide fiber. *Optics Express, 27*, 2036–2043.

Jiao, K., Yao, J., Wang, X. G., Wang, X., Zhao, Z., Zhang, B., Si, N., Liu, J., Shen, X., Zhang, P., Dai, S., Nie, Q., & Wang, R. (2019b). 1.2–15.2 μm supercontinuum generation in a low-loss chalcogenide fiber pumped at a deep anomalous-dispersion region. *Optics Letters, 44*, 5545–5548.

Keller, U., Li, K. D., Rodwell, M., & Bloom, D. M. (1989). Noise characterization of femtosecond fiber Raman soliton lasers. *IEEE Journal of Quantum Electronics, QE25*, 280–288.

Klimczak, M., Sobon, G., Kasztelanic, R., Abramski, K. M., & Buczynski, R. (2016). Direct comparison of shot-to shot noise performance of all normal dispersion and anomalous dispersion supercontinuum pumped with sub-picosecond pulse fiber-based laser. *Scientific Reports, 6*, 19284.

Krupa, K., Louot, C., Couderc, V., Fabert, M., Guenard, R., Shalaby, B. M., Tonello, A., Pagnoux, D., Leproux, P., Bendahmane, A., Dupiol, R., Millot, G., & Wabnitz, S. (2016). *Optics Letters, 41*, 5785–5788.

Leonov, S. O., Wang, Y., Shiryaev, V. S., Snopatin, G. E., Stepanov, B. S., Plotnichenko, V. G., Vicentini, E., Gambetta, A., Coluccelli, N., Svelto, C., Laporta, P., & Galzerano, G. (2020). Coherent mid-infrared supercontinuum generation in tapered suspended core As39Se61 fibers pumped by a few-optical-cycle Cr:ZnSe laser. *Optics Letters, 46*, 1346–1349.

Li, Z., Jia, Z., Yao, C., Zhao, Z., Li, N., Hu, M., Ohishi, Y., Qin, W., & Qin, G. (2020). 22.7 W mid-infrared supercontinuum generation in fluorotellurite fibers. *Optics Letters, 45*, 1882–1885.

Liang, S., Xu, L., Fu, Q., Jung, Y., Shepherd, D. P., Richardson, D. J., & Alam, S.-U. (2018). 295-kW peak power picosecond pul;ses from a thulium-doped-fiber MOPA and the generation of watt-level >2.5 octave supercontinuum extending up to 5 μm. *Optics Express, 26*, 6490–6498.

Liu, K., Liu, J., Shi, H., Tan, F., & Wang, P. (2014). *24.3 W mid-infrared supercontinuum generation from a single-mode ZBLAN fiber pumped by thullium-doped diber amplifier*. Paper AM3A.6 Advanced Solid State Lasers (ASSL).

Liu, L., Cheng, T., Nagasaka, K., Tong, H., Qin, G., Suzuki, T., & Ohishi, Y. (2016). Coherent mid-infrared supercontinuum generation in all-solid chalcogenide microstructured fibers with all-normal dispersion. *Optics Letters, 41*, 392–395.

Lopez-Galmiche, G., Eznaveh, Z. S., Eftekhar, M. A., Lopez, J. A., Wright, L. G., Wise, F., Christodoulides, D., & Correra, R. A. (2016). Visible supercontinuum generation in a graded index multimode fiber pumped at 1064 nm. *Optics Letters, 41*, 2553–2556.

Møller, U., Yu, Y., Kubat, I., Petersen, C. R., Gai, X., Brilland, L., Méchin, D., Caillaud, C., Troles, J., Luther-Davies, B., & Bang, O. (2015). Multi-milliwatt mid-infrared supercontinuum generation in a suspended core chalcogenide fiber. *Optics Express, 23*, 3282–3291.

Petersen, C. R., Engelsholm, R. D., Markos, C., Brilland, L., Caillaud, C., Troles, J., & Bang, O. (2017). Increased mid-infrared supercontinuum bandwidth and average power by tapering large-mode-area chalcogenide photonic crystal fibers. *Optics Express, 25*, 15336–15347.

Poudel, C., & Kaminski, C. (2019). Supercontinuum radiation in fluorescence microscopy and biomedical imaging applications. *Journal of the Optical Society of America B: Optical Physics, 36*, A139–A153.

Qi, X., Chen, S. P., Li, Z. H., Liu, T., Ou, Y., Wang, N., & Hou, J. (2018). High-Power visible-enhanced all-fiber supercontinuum generation in a seven-core photonic crystal fiber pumped at 1016 nm. *Optics Letters, 43*, 1019–1022.

Qin, G., Yan, X., Kito, C., Liao, M., Chaudhari, C., Suzuki, T., & Ohishi, Y. (2009). Ultrabroad supercontinuum generation from ultraviolet to 6.28 μm in a fluoride fiber. *Applied Physics Letters, 95*, 161103.

Rao, S., Engelsholm, R. D., Gonzalo, I. B., Zhou, B. B., Bowen, P., Moselund, P. M., Bang, O., & Bache, M. (2019). Ultra-low noise supercontinuum generation with a flat near-zero normal dispersion fiber. *Optics Letters, 44*, 2216–2219.

Robichaud, L.-R., Fortin, V., Gauthier, J.-C., Chatigny, S., Couillard, J.-F., Delarosbil, J.-L., Vallée, R., & Bernier, M. (2016). Compact 3-8 μm supercontinuum generation in a low loss As2Se3 step-index fiber. *Optics Letters, 41*, 4605–4608.

Robichaud, L.-R., Duval, S., Pleau, L. P., Fortin, V., Bah, S. T., Chatigny, S., Vallée, R., & Bernier, M. (2020). High-power supercontinuum generation in the mid-infrared pumped by a soliton self-frequency shifted source. *Optics Express, 28*, 107–115.

Saini, T. S., Kumar, A., & Sinah, R. K. (2015). Broadband mid-infrared supercontinuum spectra spanning 2-15 μm using As2Se3 chalcogenide glass triangular-core graded-index photonic crystal fiber. *Journal of Lightwave Technology, 33*, 3914–3920.

Salem, R., Jiang, Z., Liu, D., Pafchek, R., Gardner, D., Foy, P., Saad, M., Jenkins, D., Cable, A., & Fendel, P. (2015). mid-infrared supercontinuum generation spanning 1.8 octaves using step index indium fluoride fiber pumped by a femtosecond fiber laser near 2 μm. *Optics Express, 23*, 30592–30602.

Sierro, B., & Heidt, A. M. (2020). Noise amplification in all-normal dispersion fiber supercontinuum generation and its impact on ultrafast photonics applications. *OSA Continuum, 3*, 2347–2361.

Smith, C., Adamu, A., Michieletto, M., & Bang, O. (2020). Spectral broadening of ultraviolet dispersive waves in gas-filled hollow-core fiber using pump pulse modulation. *Optics Letters, 45*, 6744–6747.

Song, R., Hou, J., Chen, S.-P., Yang, W. Q., & Lu, Q.-S. (2012a). High power supercontinuum generation in a nonlinear ytterbium-doped fiber amplifier. *Optics Letters, 37*, 1529–1531.

Song, R., Hou, J., Chen, S.-P., Yang, W. Q., & Lu, Q.-S. (2012b). All-fiber 177.6 W supercontinuum source. *Acta Physica Sinica, 61*, 054217.

Song, R., Hou, J., Liu, T., Yang, W.-Q., & Lu, Q.-S. (2013). A hundreds of watt all-fiber near-infrared supercontinuum. *Laser Physics Letters, 10*, 065402.

Théberge, F., Bérubé, N., Poulain, S., Cozic, S., Robichaud, L.-R., Bernier, M., & Vallée, R. (2018). Watt-level and spectrally flat mid-infrared supercontinuum in fluoroindate fibers. *Photonics Research, 6*, 609–613.

Wang, X., Wang, D., Shen, X., Wu, Z., He, X., Yuan, J., Wang, X., & Yu, C. (2017). Supercontinuum generation from ultraviolet and visible wavelength based on the higher-order modes of photonic crystal fiber. *Optik, 140*, 423–426.

Wang, N., Chen, S. P., Qi, X., Yang, L. J., & Hou, J. (2018). Ultraviolet-extended flat supercontinuum generation in seven-core photonic crystal fiber. *Optical Engineering, 57*, 026110.

Wei, H. F., Chen, H. W., Chen, S. P., Yan, P. G., Liu, T., Guo, L., Lei, Y., Chen, Z. L., Li, J., Zhang, X. B., Zhang, G. L., Hou, J., Tong, W. J., Luo, J., Li, J. Y., & Chen, K. K. (2013). A compact seven-core photonics crystal fiber supercontinuum source with 42.3W output power. *Laser Physics Letters, 10*, 045101.

Yang, W., Zhang, B., Xue, G., Yin, K., & Hou, J. (2014). Thirteen watt all-fiber mid-infrared supercontinuum generation in a single mode ZBLAN fiber pumped by a 2 μm MOPA system. *Optics Letters, 39*, 1849–1852.

Yao, C., Jia, Z., Li, Z., Jia, S., Zhao, Z., Zhang, L., Feng, Y., Qin, G., Ohishi, Y., & Qin, W. (2018). High-power mid-infrared supercontinuum laser source using fluorotellurite fiber. *Optica, 5*, 1264–1270.

Yin, K., Zhang, B., Yao, J., Yang, L., Liu, G., & Hou, J. (2016). 1.9-3.6 μm supercontinuum generation in a very short highly nonlinear germania fiber with a high mid-infrared power ratio. *Optics Letters, 41*, 5067–5070.

Yin, K., Zhang, B., Yang, L., & Hou, J. (2017). 15.2 W spectrally flat all-fiber supercontinuum laser source with > 1 W power beyond 3.8 μm. *Optics Letters, 42*, 2334–2337.

Yin, K., Zhang, B., Yang, L., & Hou, J. (2018). 30W monolithic 2-3 μm supercontinuum laser. *Phot. Res., 6*, 123–126.

Yu, Y., Zhang, B., Gai, X., Zhai, C., Qi, S., Guo, W., Yang, Z., Wang, R., Choi, D. Y., Madden, S., & Luther-Davies, B. (2015). 1.8 -10 μm mid-infrared supercontinuum generated in a step index chalcogenide fiber using low peak pump power. *Optics Letters, 40*, 1081–1084.

Zhang, N., Peng, X., Wang, Y., Dai, S., Yuan, Y., Su, J., Li, G., Zhang, P., Yang, P., & Wang, X. (2019). Ultrabroadband and coherent mid-infrared supercontinuum generation in Te-based chalcogenide tapered fiber with all-normal dispersion. *Optics Express, 27*, 10311–10319.

Zhang, H., Li, F., Liao, R., Dong, K., Li, Y., Lin, H., Wang, J., & Jing, F. (2021). Supercontinuum generation of 314.7 W ranging from 390 to 2400 nm by tapered photonic crystal fiber. *Optics Express, 46*, 1429–1432.

Zhao, Z., Wang, X., Dai, S., Pan, Z., Liu, S., Sun, L., Zhang, P., Liu, Z., Nie, Q., Shen, X., & Wang, R. (2016). 1.5-14 μm midinfrared supercontinuum generation in a low loss Te-based chalcogenide step-index fiber. *Optics Letters, 41*, 5222–5225.

Zhao, Z., Wu, B., Wang, X., Pan, Z., Liu, Z., Zhang, P., Shen, X., Nie, Q., Dai, S., & Wang, R. (2017). Mid-infrared supercontinuum covering 2.0-16.0 μm in a low-loss telluride single-mode fiber. *Laser & Photonics Reviews, 11*, 1700005.

Zheng, Z., Ouyang, D., Zhao, J., Liu, M., Ruan, S., Yan, P., & Wang, J. (2016). Scaling all-fiber mid-infrared supercontinuum up to 10W-level based on thermal-spliced silica fiber and ZBLAN fiber. *Photonics Research, 4*, 135–139.

Chapter 6
All-Normal Dispersion Fiber Supercontinuum: Principles, Design, and Applications of a Unique White Light Source

Alexander M. Heidt, Dirk-Mathys Spangenberg, Anupamaa Rampur, Alexander Hartung, and Hartmut Bartelt

Abstract Ultrafast and low-noise supercontinuum (SC) sources based on all-normal dispersion (ANDi) fibers are emerging as key-enabling technology for new applications in spectroscopy, microscopy, and ultrafast photonics. In this chapter we review the fundamental physics, fiber designs, and applications of this unique white light source.

Keywords Supercontinuum · All-normal dispersion fibers · Ultrafast photonics · Photonic crystal fibers · Specialty optical fibers · Spectroscopy · Advanced microscopy · Biophotonics · Nonlinear pulse compression · Few-cycle pulses · Nonlinear fiber optics · Ultra-low noise lasers · Coherence

6.1 Introduction

Supercontinuum (SC) generation has become a scientific and commercial success story in the past decade driven by specialty optical fiber technology, in particular the invention of the photonic crystal fiber (PCF). From optical frequency metrology to biophotonic imaging—its unique spectral properties have revolutionized dozens of applications, many of which are described in this book. However, especially noise-sensitive or ultrafast photonics applications such as time-resolved spectroscopy and nonlinear pulse compression, which require not only a broad spectral bandwidth but also a coherent ultrashort pulse in the time domain, have struggled to incorporate fiber-based SC sources.

A. M. Heidt (✉) · D.-M. Spangenberg · A. Rampur
Institute of Applied Physics, University of Bern, Bern, Switzerland
e-mail: alexander.heidt@iap.unibe.ch

A. Hartung · H. Bartelt
Leibniz-Institute of Photonic Technology, Jena, Germany

R. R. Alfano (ed.), *The Supercontinuum Laser Source*,
https://doi.org/10.1007/978-3-031-06197-4_6

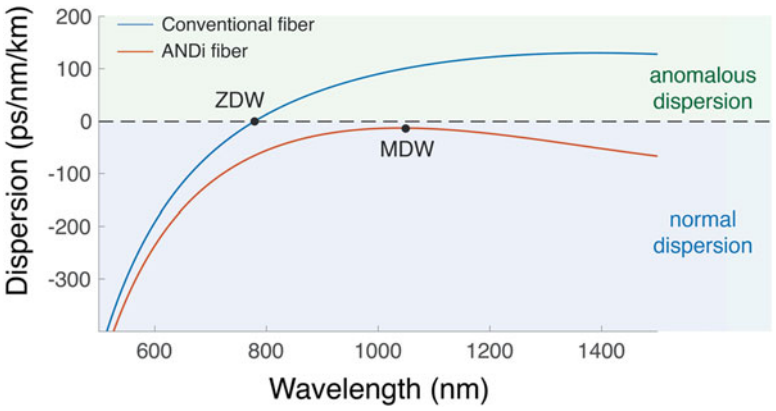

Fig. 6.1 Typical fiber dispersion profiles for two different concepts of SC generation. The "conventional" PCF has a single zero dispersion wavelength (ZDW) at 780 nm and is intended for anomalous dispersion pumping around 800 nm. The ANDi PCF has a minimum dispersion wavelength (MDW) at 1050 nm and is optimized for normal dispersion pumping in the vicinity of this MDW. Both fiber designs can be adapted for a large range of different pump wavelengths and can cover the spectral regions from the UV to the mid-IR

The reasons behind this initially surprising lack of adoption are the nonlinear dynamics in the most commonly used fiber design for SC generation when laser pulses with sub-picosecond durations are used for pumping. This "conventional" PCF design has a single zero dispersion wavelength (ZDW) closely matched to the central wavelength of the pump pulses, which are injected on the anomalous dispersion side and close to the ZDW. Figure 6.1 shows the group velocity dispersion (GVD) curve of such a fiber with ZDW at 780 nm. PCFs with similar dispersion designs are commercially available (e.g., NKT NL-PM-750) and frequently employed for pumping with Ti-sapphire femtosecond systems around 800 nm central wavelength. This anomalous dispersion pumping leads to rich soliton-driven nonlinear dynamics that maximize the obtainable bandwidth for a given pump source, but also cause the temporal breakup of the injected pump pulse and high sensitivity to noise (Dudley et al., 2006). Consequently, the generated SCs have highly complex temporal and spectral profiles that fluctuate from shot to shot under most pumping conditions, i.e., they have poor temporal coherence properties. This often plays a precision or resolution-limiting role, e.g., in applications that use the coherence as content in the acquired signal, such as coherent anti-Stokes Raman scattering (CARS) microscopy. Fiber-based SC sources using this conventional fiber design have therefore found only very limited use in ultrafast photonics and noise-sensitive applications.

It has long been known that temporal pulse breakup and noise amplification can largely be avoided when pumping occurs entirely in the normal dispersion regime. In fact, the first ever SC generation in 1970 was observed in the normal dispersion region of bulk glasses and crystals, as described by Alfano and Shapiro in their

three seminal papers (Alfano & Shapiro, 1970a, b, c). In their pioneering work, they reported the formation of filaments with micrometer diameters and centimeter lengths due to self-focusing of the optical pulse, and could link the spectral broadening to nonlinear electronic cloud distortion in these filaments leading to self-phase modulation and four-wave mixing, which are highly deterministic processes and conserve both coherence and temporal integrity of the input pulse. The filaments work as a short "natural fiber": they guide the light with extremely high intensity over extended lengths and therefore enhance the nonlinear interaction with the material. A review of SC generation in the normal dispersion region in a variety of condensed matter and gases can be found in Chaps. 1 and 2. After the realization of low-loss optical fibers, high intensity light pulses could be guided over much longer lengths than in bulk materials, which quickly led to the first fiber-based SC demonstrations (Lin & Stolen, 1976; Lin et al., 1978). In these cases pumping occurred also in the normal dispersion region, but long nanosecond pump pulse durations led to the occurrence of noise-seeded Raman scattering and resulted in the formation of incoherent SCs. When sub-picosecond pump pulses are employed, normal dispersion pumping of a fiber generates highly coherent SC pulses with properties very similar to the bulk case, but is associated with significantly reduced spectral bandwidths compared to anomalous dispersion pumping due to the steep slope of the dispersion curve and fast temporal broadening of the pump pulse. Hence, it has attracted only little attention after PCF technology was available.

This situation changed with the introduction of all-normal dispersion (ANDi) PCFs (Heidt, 2010). They are designed to have a flattened convex profile of normal GVD with a distinct point where the dispersion is closest to zero (minimum dispersion wavelength, MDW), but exhibit no ZDW in the region of interest. Figure 6.1 shows the dispersion curve of an ANDi PCF with MDW at 1050 nm. Similar to the ZDW in the conventional SC generation, the MDW should be located in the vicinity of the central pump wavelength to obtain maximum spectral broadening. The design shown here is therefore suited for pumping with ytterbium-doped fiber laser systems around 1 μm, and a commercial PCF with very similar dispersion profile is available, whose properties are discussed in more detail in Sect. 6.6.1. The low and flat dispersion minimizes temporal broadening of the input pulse and enables the generation of SCs with ultrabroad, more than octave-spanning bandwidths previously only known from anomalous dispersion pumping. At the same time, the SCs benefit from the typical characteristics of normal dispersion pumping, such as low-noise sensitivity, preservation of the injected ultrashort pump pulse, smooth and uniform spectral and temporal profiles, and the absence of spectral fine structure. Inspired by earlier work on PCFs with two closely spaced ZDWs (Hilligsøe et al., 2004; Falk et al., 2005) and solid circular fibers (Hori et al., 2004; Nishizawa & Takayanagi, 2007), the design of ANDi PCFs optimized for pumping at the emission wavelengths of the most commonly employed femtosecond pump sources and the first experimental demonstrations of octave-spanning coherent SC generation in these fibers was a breakthrough for the application of fiber-based SC sources in ultrafast photonics and noise-sensitive applications (Heidt, 2010; Heidt et al., 2011a; Hooper et al., 2011).

This chapter is dedicated to this relatively new concept of SC generation in optical fibers. We compare the characteristics of conventional, anomalously pumped SCs and ANDi SCs in detail using the fiber dispersion profiles of Fig. 6.1 as representative examples, explore the nonlinear dynamics of SC generation in the normal dispersion regime, examine the origins of noise in SC generation and how it can be suppressed by appropriate engineering of the fiber, give guidelines for the design of ANDi fibers for SC generation from the deep ultraviolet to the mid-infrared spectral regions, and review the most important experimental results and applications.

6.2 Brief Remarks About Numerical Modeling

The numerical simulations we use in this chapter are based on the generalized nonlinear Schrödinger equation (GNSLE) already introduced in Chap. 3 by Agrawal. In order to solve this equation, we use the Runge–Kutta in the interaction picture (RK4IP) integration method described by Hult (2008). We evaluate the GNLSE entirely in the frequency domain, because this approach was found to be numerically more accurate and efficient than the time-domain formulation (Rieznik et al., 2012). Additionally we employ an adaptive step size algorithm to improve computational speed and ensure sufficient accuracy as the pulse is propagated along the fiber (Heidt, 2009). A version of our simulation code that includes all these features in a MATLAB implementation is freely available for download under http://www.freeopticsproject.org.

In general, such pulse propagation models require the GVD and nonlinear characteristics of the fiber under investigation as input, which have to be obtained from the fiber's geometry and material properties. Commercial packages are available for this, but in the special case of PCFs with hexagonal lattice geometry, an analytical method has been formulated to obtain dispersion and effective mode field diameter of the fundamental mode (Koshiba & Saitoh, 2004; Saitoh & Koshiba, 2005). This can serve as a good starting point for any researcher wishing to simulate nonlinear pulse propagation in microstructured optical fibers.

We assume propagation in a single transversal mode and a single polarization axis, and exclude any coupling between the fundamental polarization modes. These conditions are usually fulfilled in highly birefringent fibers when the pump pulse polarization is aligned to one of the principle fiber polarization axes. For low-birefringence fibers or for off-axis pumping linear and nonlinear mode coupling, effects can introduce additional nonlinear processes with important consequences for the noise and coherence properties of the generated SC. The origin of noise in SC generation dynamics and its control by appropriate fiber engineering are discussed in Sect. 6.5.

6.3 Supercontinuum Generation: Conventional vs. ANDi PCF

The objective of this section is to give an overview of the most important differences between ANDi and conventional SC generation, using numerical simulations and the two fibers introduced in Sect. 6.1 as representative examples. We focus on the nonlinear dynamics and properties that are most relevant from an applications point of view. For a more detailed discussion of the nonlinear effects responsible for spectral broadening, we refer to Chaps. 3 and 5 by Agrawal and Taylor for conventional fibers and Sect. 6.4 in this chapter for ANDi fibers. Of course, this can only be a qualitative comparison as the exact properties and dynamics of SC generation are sensitively dependent on both fiber and pump source parameters, and the specialized literature and numerical simulations should be consulted to ensure that the SC properties generated from a specific system fulfill the requirements of any particular application of interest.

A good first impression of the major differences between the SCs generated in ANDi and conventional PCF can be obtained from Fig. 6.2, which illustrates the SC development in the spectral and temporal domain in our two example fibers from Fig. 6.1 under realistic pumping conditions. In the conventional case, these simulations correspond to pumping in the anomalous dispersion region with pump pulses of 50 fs duration (FWHM) and 10 kW peak power at 850 nm. For the ANDi fiber, we also consider 50 fs pump pulses, but with higher peak power of 90 kW and centered at 1050 nm, close to the MDW of the fiber.

When the pump pulses are injected into the anomalous dispersion region of the conventional PCF, they form solitons of order $N = (L_D/L_{NL})^{1/2} \gg 1$, where $L_D = T_0^2/|\beta_2|$ and $L_{NL} = (\gamma P_0)^{-1}$ are the dispersive and nonlinear lengths introduced in Chap. 3, respectively, γ and β_2 are nonlinear and second-order dispersive parameter of the fiber, and T_0 and P_0 are duration and peak power of the pump pulse. For our specific example, $N \approx 6.6$. Consequently, the initial dynamics of spectral broadening and temporal compression are very similar to the well-known high-order soliton evolution (Agrawal, 2007). However, the presence of higher-order dispersion and Raman scattering disturbs their ideal periodic evolution, and after approximately 1.5 cm, the pulses break up (Golovchenko et al., 1985). This process known as soliton fission is a crucial point in the nonlinear dynamics: the integrity of the input pulse is lost, and the temporal profile becomes extremely complex, consisting of a train of individual fundamental solitons and low-level dispersive waves (Herrmann et al., 2002). At the same time, the clean high-order soliton spectrum is transformed into a complex and highly structured SC as the solitons continuously self-frequency shift to longer wavelengths due to the Raman effect and transfer some of their energy to dispersive waves in the normal dispersion regime (Mitschke & Mollenauer, 1986; Gordon, 1986; Akhmediev & Karlsson, 1995; Gu et al., 2002). These dynamics are visualized in Fig. 6.2a, which highlight in particular the point of soliton fission, a spectrally and temporally shifting soliton and the dispersive waves. Of course, if the multi-pulse structure is undesirable in an application, it is possible to optimize the

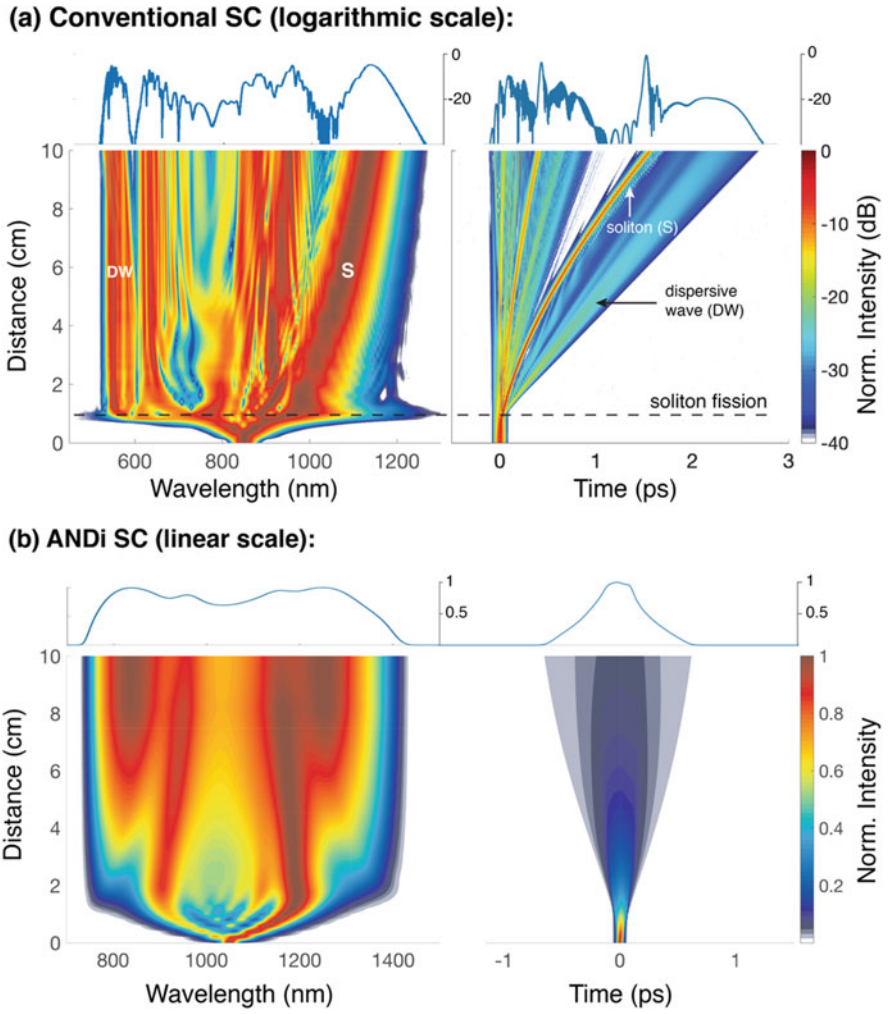

Fig. 6.2 Spectral and temporal evolution of the SC generation process in the PCFs of Fig. 6.1. (**a**) Conventional PCF, pumped at 850 nm with a 50 fs, 10 kW pulse. (**b**) ANDi PCF, pumped at 1050 nm with a 50 fs, 90 kW input pulse. Note the different scales (logarithmic vs. linear) used in these simulations, highlighting the superior flatness and smoothness of the ANDi SC

fiber length and interrupt the evolution just before soliton fission occurs. This has been studied in the context of soliton pulse compression, and a characteristic fission length could be determined that can be written approximately as (Chen & Kelley, 2002)

$$L_{\text{fiss}} \simeq L_D/N = T_0(\gamma P_0\,|\beta_2|)^{-1/2} \tag{6.1}$$

At this point the high-order soliton assumes its maximum spectral bandwidth and shortest pulse duration. However, the necessity of matching the fiber parameters exactly to the pump source and the quickly deteriorating quality of the compressed pulse with increasing N have limited the practical relevance of this technique for ultrafast photonics. Significant parts of spectral bandwidth and power density in the spectral wings are only generated after soliton fission occurs, and hence it is an integral part of the conventional SC generation dynamics.

In contrast, these soliton dynamics are completely suppressed in the ANDi fiber. As shown in Fig. 6.2b, during the SC evolution, a single ultrashort pulse is maintained at all times, which temporally broadens from its original duration of 50 fs to about 1 ps at the end of the investigated 10 cm propagation distance as it experiences normal dispersion along the fiber. After the initial formation of spectral side lobes, which identify SPM as the dominant spectral broadening process (Stolen & Lin, 1978), the spectrum smoothens very quickly and acquires an almost uniform rectangular shape with flat top and steep edges. The broadening is concluded after approximately 5 cm, which can be attributed to the decreasing peak power as the pulse spreads temporally. Both spectral and temporal profiles do not acquire any significant fine structure. In fact, the SC generation process occurs so quickly and smoothly that the logarithmic scale chosen for the conventional case is inadequate here, and even the linear scale used in the plots in Fig. 6.2b reveals very little about the broadening dynamics. We therefore investigate the SC development in more detail in Sect. 6.4 using projected axis spectrograms. Yet it is clear already from this initial comparison that the ANDi fiber delivers much cleaner, less complex, and more uniform SC pulses than would be possible in the conventional case. This is achieved at the cost of requiring higher peak powers than soliton-driven SC generation to achieve comparable, octave-spanning spectral bandwidths. However, the required peak powers are within easy reach of modern femtosecond oscillators and therefore do not limit the applicability of this type of SC.

6.3.1 Spectro-Temporal Characteristics

A more intuitive insight into the SC characteristics can be obtained from Fig. 6.3, which displays the time–wavelength correlations of the SCs investigated in the previous section in a projected axis spectrogram. This is arguably the most complete visualization of any ultrafast optical waveform (Cohen, 1989). These snapshots of the SC pulses are taken after a propagation distance of 15 cm in the conventional PCF and 6 cm in ANDi PCF, when the respective spectral broadening processes are essentially concluded. The pump pulse parameters are identical to the previous section. The figure visually contrasts the relative simplicity of the ANDi SC pulse against the full spectro-temporal complexity of the conventional SC, and can be used to deduct the major advantages of ANDi over conventional SCs.

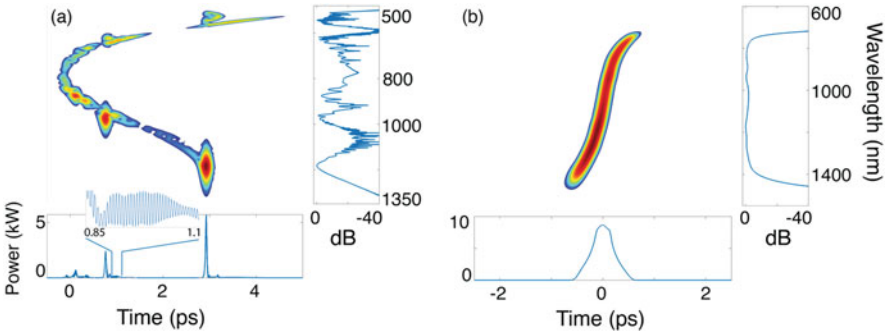

Fig. 6.3 Characteristic projected axis spectrograms of (**a**) conventional SC and (**b**) ANDi SC after the respective spectral broadening processes are concluded. Pump pulse parameters are identical to Fig. 6.2

Pulse Conservation We have already seen in the previous section that the SC generation process in ANDi fibers conserves a single ultrashort pulse in the time domain. In addition we can now deduce from the spectrogram that it also maintains a well-defined and relatively simple phase distribution. In the purely normal dispersion of the ANDi fiber, the group velocity strictly increases with wavelength, and hence the wavelength distribution within the SC pulse is also strictly increasing: from the slower short wavelengths at the trailing pulse edge to the faster long wavelengths at the front of the pulse. At the center of the pulse near the MDW, where the dispersion is minimal, the pulse has a nearly linear chirp, with increasing nonlinear contributions for wavelengths located in the pulse wings.

This is in sharp contrast to the significantly more complex temporal characteristics of the conventional SC. Here wavelength components at or near the ZDW are the first to arrive at any given position along the fiber. All other radiation experiences a higher group index and hence is delayed with respect to that at the ZDW (Knight & Wadsworth, 2010). Consequently, the spectrogram takes on a "U" shape with a normal (top) and anomalous (bottom) dispersion arm. Radiation in normal and anomalous dispersion arms can therefore temporally overlap and create interference structures and fast oscillations, as shown in the highlighted section between 0.8 and 1.1 ps. The individual solitons originating from the soliton fission process are readily identifiable as compact objects in the spectrogram, while the dispersive waves in the normal dispersion arm can be linked to low-level pedestals traveling in between the solitons and at the trailing edge of the pulse. The spectral phase follows the intrinsic fiber group index profile, but contains significant fine structure as well as distinct flat regions of wavelength-independent spectral phase across the fundamental solitons (Dudley & Coen, 2004).

Spectral Uniformity A large part of the fine structure in the conventional SC spectrum can be linked to the distinct spectral signatures of the individual solitons. Additionally, the overlapping bandwidths of the temporally separated solitons cause

spectral interference fringes in the central part of the spectrum (Gu et al., 2002). In the ANDi SC pulse, each wavelength component is located at a unique temporal position inside the pulse, such that spectral or temporal interference is avoided and both spectrum and temporal profile are free of any significant fine structure.

Compressibility The enormous bandwidths of supercontinua should allow the generation of very short, few-cycle (sub-5 fs) pulses using appropriate dispersive compression. Although it has been shown that it is indeed theoretically possible to compress the complex temporal structure of an octave-spanning conventional SC back into a single, few-cycle pulse by dispersively compensating its spectral phase (Dudley & Coen, 2004), in practice this could never be demonstrated owing to the significant fine structure present in spectrum and group delay (Schenkel et al., 2005). In contrast, the simple phase profile of the ANDi SC pulse is excellently suited for pulse compression, and in fact has led to the generation of high-quality, Fourier-limited pulses as short as 3.7 fs (Demmler et al., 2011). More details on the application of ANDi fibers in nonlinear pulse compression can be found in Sect. 6.7.1 of this chapter.

Coherence and Stability So far we have only considered the evolution of a *single* ultrashort pulse in the fiber. However, since there is always a certain level of quantum or technical noise on the input pulses, the evolution of subsequent pulses inside the fiber is not necessarily identical. The properties of the generated SC might change considerably from shot to shot if the nonlinear effects responsible for the spectral broadening are sensitive to this noise. Driven by the increased demand for ultra-low noise broadband coherent light sources in spectroscopy, microscopy, and ultrafast photonics, ANDi SCs are rapidly gaining popularity in these fields as it becomes increasingly apparent that the fiber design strongly suppresses the gain for noise-amplifying incoherent nonlinear dynamics (Heidt et al., 2017). In Sect. 6.5 we provide further details on the origin of SC noise and how to control it using specialty optical fiber design principles.

6.4 Nonlinear Dynamics in ANDi Fibers

In this section we have a closer look at the nonlinear dynamics in ANDi SC generation and identify the physical effects dominating the broadening process using numerical simulations. We focus on the coherent nonlinear processes that do not introduce any excess noise; pulse-to-pulse fluctuations and noise introduced by incoherent nonlinear processes are further discussed in Sect. 6.5.

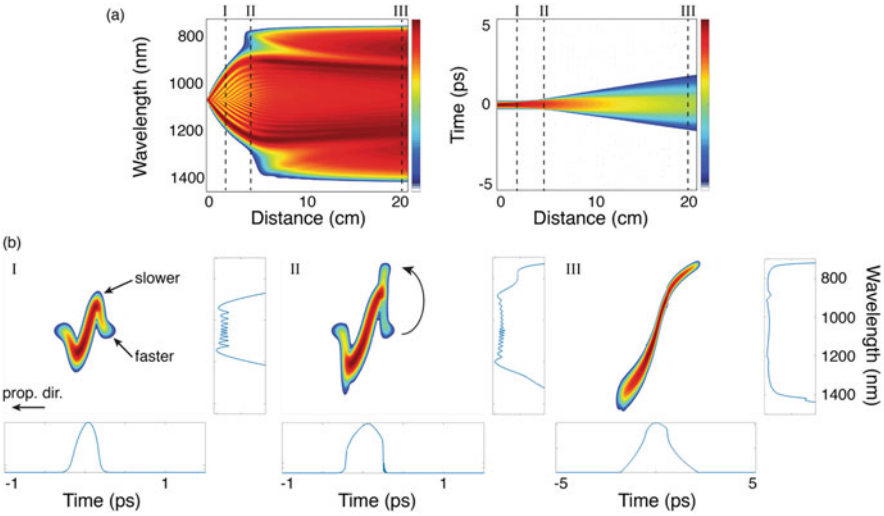

Fig. 6.4 (**a**) Simulated spectral and temporal evolution of the SC generation process in the ANDi PCF of Fig. 6.1, pumped with a 200 fs, 90 kW pulse at 1050 nm. (**b**) Projected axis spectrograms of the SC pulse at 2.0 cm, 3.7 cm, and 20 cm. *Arrows* indicate energy transfer process due to optical wave breaking

6.4.1 Spectrogram Analysis

A very convenient way to display the evolution of the pulse as it propagates along the fiber is the projected-axis spectrogram representation already introduced in Sect. 6.3.1. As representative example we chose again the ANDi PCF of Fig. 6.1, pumped at 1050 nm with a 90 kW peak power input pulse. However, we use a longer pump pulse duration of 200 fs since the nonlinear dynamics are slowed down for longer pulses and the physical effects can easier be identified. Fig. 6.4a shows the spectral and temporal evolution of the SC generation process over a propagation distance of 20 cm. Three distinctive positions along the fiber at 2.0 cm, 3.7 cm, and 20 cm are marked, and the spectrograms of the SC pulse at these positions are displayed in Fig. 6.4b.

For our input pulse and fiber parameters, L_D is >20 cm, i.e., much longer than L_{NL} (<1 mm). The dynamics are therefore initially dominated by nonlinear effects, in particular SPM-induced spectral broadening, which is discussed in more detail in Chaps. 1 and 2 of this book. The spectrogram of the SC pulse at 2.0 cm clearly shows the SPM-characteristic S shape, with spectral broadening toward longer wavelengths occurring at the leading edge of the pulse, while broadening toward shorter wavelengths is introduced at the trailing pulse edge. The spectrum also displays the typical oscillatory structure associated with SPM, which is created by spectral interference of identical spectral components being present at different temporal positions within the pulse.

With further propagation the dispersion profile of the fiber becomes the governing factor of the nonlinear dynamics: since the fiber exhibits normal dispersion at all wavelengths, the group velocity monotonically increases with wavelength. Hence, the pulse tail travels faster than the blue-shifted wavelength components created by SPM in the intermediate section of the pulse (marked in spectrogram (I) in Fig. 6.4b). The faster tail eventually overtakes the slower intermediate section, which leads to the steepening of the trailing pulse edge and the onset of optical wave breaking (OWB) (Anderson et al., 1992). The temporal overlap of the two pulse components with different instantaneous frequencies leads to the nonlinear generation of new frequency components at

$$\omega_{\mathrm{OWB}} = 2\omega_{\mathrm{SPM}} - \omega_0, \tag{6.2}$$

via a degenerate four-wave mixing (FWM) process (Agrawal, 2007; Finot et al., 2008), where ω_{SPM} is the angular frequency of the SPM components in the intermediate pulse section and ω_0 is the center frequency of the pulse. The energy transfer process from the center to the wing of the spectrum is clearly visible after 3.7 cm of propagation in spectrogram (II) in Fig. 6.4b and marked with an arrow. The overlap of SPM-generated components around 900 nm with the pulse tail at 1050 nm creates a new wavelength band around 750 nm. After further propagation, OWB also occurs on the leading pulse edge (not shown) and generates new wavelengths extending to >1400 nm. During the remaining part of the propagation, OWB continuously redistributes energy from the central frequency to the spectral wings until the original front and tail of the pulse at ω_0 are completely depleted. The corresponding spectrogram at the end of the 20 cm propagation distance is finally very similar to Fig. 6.3b, except for the longer temporal pulse duration. After OWB is concluded, no interference structures are present in neither temporal nor spectral profile as the OWB process assigns each wavelength to a unique temporal position within the pulse.

In summary, after an initial phase of SPM-dominated broadening OWB occurs on both leading and trailing edges of the pulse and is responsible for the generation of the extreme wavelengths on both sides of the spectrum as well as for the uniform temporal and spectral profiles of the final SC spectrum. As a consequence, a single ultrashort pulse with well-defined phase is available from the fiber after the SC generation process.

6.4.2 Influence of Fiber and Pump Pulse Parameters

The FWM energy transfer from the spectral center to the wings occurs only in the instant of their temporal overlap as they propagate with different group velocities. Hence, the OWB-induced FWM processes, which create the extreme wavelength components of the SC spectrum, are not phase-matched. Therefore, there is no restriction on the achievable bandwidth of the spectrum—it solely depends on the

amount of SPM-induced broadening before OWB occurs, according to Eq. (6.2). With this insight we can deduce some general dependencies of the generated SC bandwidth on fiber and input pulse parameters.

Since $L_{NL} \ll L_D$ in the first phase of the propagation, we can initially neglect dispersive effects and estimate the spectral broadening due to SPM as

$$|\omega_{\mathrm{SPM}}(z, t) - \omega_0| = \gamma P_0 \frac{\partial U(t)}{\partial t} z, \tag{6.3}$$

where $U(t)$ is the normalized intensity profile of the input pulse and z the propagation distance (Agrawal, 2007). In order to estimate the maximum broadening at the point of OWB, we estimate the maximum slope of the pump pulse as $\max(\partial U(t)/\partial t) \propto 1/T_0$, with the input pulse duration T_0 , and the expression for the OWB distance (Finot et al., 2008)

$$L_{\mathrm{OWB}} \simeq L_D/N = T_0(\gamma P_0 |\beta_2|)^{-1/2} \tag{6.4}$$

and obtain

$$|\omega_{\mathrm{SPM}}(L_{\mathrm{OWB}}) - \omega_0|_{\max} \propto \left(\frac{\gamma P_0}{\beta_2}\right)^{1/2} \tag{6.5}$$

In consequence, the spectral broadening in ANDi fibers can be enhanced by higher peak power of the input pulse, as well as higher nonlinearity or decreased and flattened dispersion of the fiber, which is a very intuitive result. However, there is usually a trade-off between spectral bandwidth and flatness. As the ratio of nonlinearity to dispersion is increased, the OWB process progressively depletes the central frequency such that a spectral "dip" with magnitude of >10 dB can form around the pump wavelength. This is especially an issue when the MDW approaches zero (Heidt, 2010). The spectral flatness can be improved by increasing the dispersion at the pump wavelength, but at the cost of decreased bandwidth (and vice versa).

Not quite so intuitive is the fact that the spectral bandwidth, and in extension also the coherence properties and temporal compressibility, is independent of the input pulse duration if the peak power remains constant. This has been verified by numerical simulations (Heidt et al., 2017), and is valid as long as incoherent nonlinear effects do not play a significant role, i.e., up to input pulse durations of about 1 ps (see also Sect. 6.5). However, since the wave breaking distance grows linearly with the pulse duration (Eq. (6.4)), the nonlinear dynamics are slowed down for longer pulses, and the fiber length needs to be increased accordingly. Therefore, the loss profile of the fiber may play a more significant role, particularly if technologically less mature non-silica glasses are used for fiber fabrication (Price et al., 2012).

Note also that the spectral broadening is only weakly dependent on β_2. It is therefore not a critical necessity to match the pump wavelength exactly to the MDW

of the fiber. If the dispersion profile is sufficiently flat, pump wavelengths several hundred nanometers on either side of the MDW can be acceptable and can still create more than octave-spanning SC spectra (Heidt et al., 2011a; see also Sect. 6.6.1). In this case, spectral broadening occurs preferentially toward the side where the MDW is located, i.e., toward wavelengths with low and flattened dispersion where the temporal broadening of the pulse is limited and continuously high peak powers are maintained during propagation. This can be effectively used to steer the SC generation process toward a desired spectral region (Price et al., 2012).

6.5 Noise Properties of Fiber Supercontinuum Sources

With every new edition of this book, a variety of new applications are emerging for the supercontinuum laser source, and as such these versatile broadband coherent light sources have become undispensable tools for spectroscopy, biomedical imaging, optical coherence tomography, advanced microscopy, and many more applications. However, due to the ever-increasing sensitivity and speed of spectroscopic detection and imaging techniques, the noise properties, shot-to-shot stability, and temporal characteristics of fiber-based SC sources are now becoming increasingly relevant.

Commercially available sources, often constructed from pico- or nanosecond pulsed lasers pumping an anomalous dispersion fiber, suffer from huge pulse-to-pulse fluctuations of spectral amplitude and phase that arise from nonlinear noise amplification processes dominating the SC generation dynamics. While the correspondingly large relative intensity noise (RIN) in the order of 50% or more can often be reduced by long-term averaging (Dupont et al., 2014), SC noise has become the predominant factor limiting the precision, speed, resolution, or sensitivity of many applications (Jensen et al., 2019).

In this section we explore the origin of this noise in more detail in an effort to identify strategies and fiber designs that can effectively suppress any nonlinear noise amplification during SC generation. While it is well-known that SC noise depends on input pulse duration and fiber length, only recent results have highlighted the fact that the noise characteristics of fiber-based SC sources can be effectively controlled both by the dispersion profile and the cross-sectional geometry of the nonlinear fiber. In particular, highly birefringent polarization-maintaining ANDi fibers are currently emerging as the key-enabling technology for the realization of the next generation of ultra-low noise SC sources.

6.5.1 Origin of Supercontinuum Noise

A typical fiber-based SC source operates at MHz repetition rates and thus emits millions of pulses per second. So far in this chapter, we have considered only the

evolution of a *single* ultrashort pulse and its transformation into a supercontinuum as it propagates along the fiber. However, since there is always a certain level of quantum or technical noise on the input pulses, the evolution of subsequent pulses inside the fiber is not necessarily identical. The properties of the generated SC might change considerably from shot to shot if the nonlinear effects responsible for the spectral broadening are sensitive to this noise.

We can investigate this sensitivity numerically by including quantum noise terms into the simulations, e.g., as described by Dudley et al. (2006), and comparing the results of multiple simulations obtained with different random noise seeds. It is common to characterize the shot-to-shot fluctuations using the spectrally resolved modulus of first-order coherence at zero path difference:

$$|g_{12}(\lambda)| = \left| \frac{\langle S_1^*(\lambda)\, S_2(\lambda) \rangle}{\sqrt{\langle |S_1(\lambda)|^2 \rangle \langle |S_2(\lambda)|^2 \rangle}} \right| \tag{6.6}$$

where angle brackets indicate an ensemble average over independently generated SC pairs $[S_1(\lambda), S_2(\lambda)]$ obtained from a large number of simulations. At each wavelength bin, this yields a positive number in the interval [0;1] with the value 1 representing perfect stability in amplitude and phase and the value 0 indicating completely uncorrelated fluctuations from pulse to pulse (Dudley & Coen, 2002).

In order to illustrate the origin of SC noise, we consider again our representative ANDi fiber from the previous sections, but increase the pump pulse duration to 5 ps and limit the peak power to 5 kW. Figure 6.5a shows the calculated evolution as well as the spectral fluctuations and coherence properties after 1 m of propagation through the fiber, extracted from 20 simulations with independent quantum noise seeds. In the central part of the spectrum, the coherent dynamics dominated by SPM/OWB discussed in Sect. 6.4 are at work, which are seeded by wavelength components within the pump pulse itself and, therefore, maintain high coherence. After about 40 cm of propagation, a broad peak starts to develop redshifted from the central spectrum by a frequency of around 13.2 THz, which corresponds to the peak frequency of the Raman gain in silica. Consequently, the origin of this peak is stimulated Raman scattering (SRS), which provides enormous exponential gain to any seed signal injected into its gain bandwidth. If the Raman gain remains unseeded, like in this case, then quantum noise serves as the seed and is amplified to become significant and even dominate the spectral broadening dynamics. The noise-seeded spectral components contained in the Raman peak exhibit random fluctuations in amplitude and phase from shot to shot and are thus incoherent with the pump. With further propagation cascaded Raman Stokes (redshifted) and anti-Stokes (blueshifted) peaks appear, which are also noise-seeded and show similarly large fluctuations and low coherence.

Raman anti-Stokes components are rarely observed in fibers, since neither SRS nor other nonlinear mechanisms such as parametric FWM are efficient enough to generate them by themselves—the ANDi profile excludes phase matching of Stokes and anti-Stokes Raman components with the pump wave. Instead, the presence

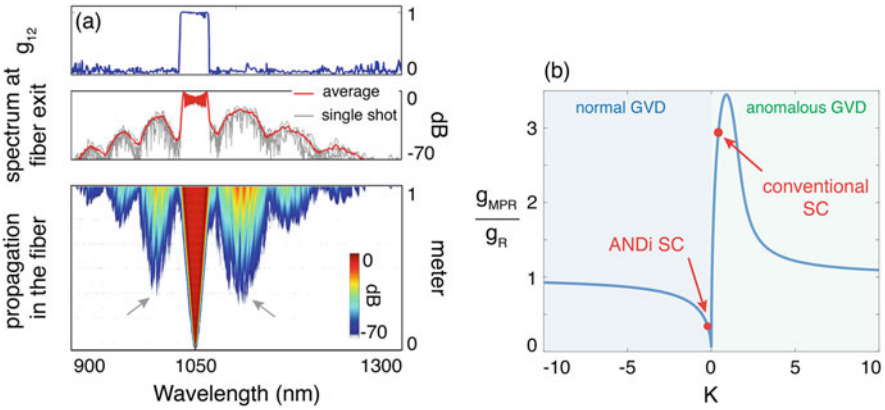

Fig. 6.5 (**a**) Origin of SC noise. Bottom: simulated spectral evolution of 5 ps, 5 kW pulses in the ANDi fiber from Fig. 6.1. Arrows indicate primary gain bands for amplification of quantum noise. Center: spectrum at the fiber exit. The mean spectrum is displayed in *red*, obtained from averaging 20 simulations with random noise seeds. *Gray* traces show single-shot spectra. Top: coherence calculated according to Eq. (6.6). (**b**) Mixed parametric Raman (MPR) gain g_{MPR}, normalized by the standard Raman gain g_R. We use the MPR gain to describe the dispersion dependence of noise-amplifying incoherent nonlinearities in SC generation dynamics. Typical conditions for octave-spanning SC generation for ANDi and conventional SC from Fig. 6.2 are indicated

of anti-Stokes peaks can only be explained by the combined action of SRS and FWM, which couple in a high peak power/low dispersion environment, i.e., exactly in conditions that are usually employed for SC generation (Bloembergen & Shen, 1964; Coen et al., 2002a). In single-mode fibers, this nonlinear coupling of SRS and FWM can be described by the mixed parametric Raman (MPR) gain (Coen et al., 2002b), which amplifies and distributes noise across the SC spectrum and can generally be regarded as the main noise-amplifying nonlinear effect responsible for incoherent spectral broadening (Heidt et al., 2017).

6.5.2 *Supercontinuum Noise Control by Fiber Dispersion Engineering*

Clearly, the noise properties of SC sources can be understood in terms of a competition between coherent and noise-amplifying incoherent nonlinear processes. While the coherent nonlinearities preserve the coherence and stability of the input pulses, the MPR gain builds up new spectral components from noise and quickly distributes it throughout the SC pulse. By comparing the strength of these two sets of nonlinearities and their dependence on input pulse and fiber design, we can develop strategies how to reduce noise amplification or even suppress it altogether.

As discussed in Sects. 6.3 and 6.4 of this chapter, the coherent dynamics are dominated by OWB in the normal dispersion and soliton fission in the anomalous dispersion regime. Interestingly, by comparing Eqs. (6.1) and (6.4), we note that the characteristic length scales of these two processes are virtually identical. In particular, for the low dispersion conditions employed for SC generation and for a given pump peak power, it is only weakly dependent on the fiber design and mainly proportional to the pump pulse duration.

In contrast, the MPR gain g_{MPR}, which we use here to describe the strength of noise-amplifying incoherent dynamics, is independent of the pump pulse duration, but highly dependent on the fiber dispersion. It is shown in Fig. 6.5b normalized to the standard peak Raman gain $g_R \simeq 0.5\gamma P_0$ in dependence of $K = -\beta_2\Omega_R^2/(2\gamma P_0)$, which is essentially the ratio of dispersion and nonlinearity (Vanholsbeeck et al., 2003). Here Ω_R is the angular frequency shift of the Raman gain peak. For large |K|, SRS and FWM decouple and $g_{MPR} \simeq g_R$. However, in the region $|K| < 1$ relevant to SC generation, the incoherent dynamics are strongly suppressed in the normal dispersion, while noise amplification is strongly amplified in the anomalous dispersion region. The peak of the MPR gain is located at $K \simeq 1 - f_R/2$, where f_R (~ 0.18 for silica) is the fractional contribution of the Raman effect to the nonlinear material response (see Chap. 3, Eq. (3.6)). At the peak, Stokes and anti-Stokes Raman sidebands are effectively amplified by FWM, a process that is also known as modulational instability (MI) and whose role in the coherence collapse of conventional SC has been investigated since the early days of fiber-based SC generation (Nakazawa et al., 1998; Corwin et al., 2003). Describing incoherent nonlinear dynamics in terms of the MPR gain therefore incorporates previous literature results, while providing a broader and more universal perspective on SC noise and the opportunities arising from its control via dispersion engineering.

Returning to our representative fiber designs and SC dynamics discussed in Sect. 6.3 pumped with high peak power femtosecond pulses for generating octave-spanning bandwidths, $K \simeq -0.02$ for the ANDi SC and $K \simeq +0.28$ for the conventional SC. The corresponding MPR gains are indicated in Fig. 6.5b. Hence, we find that the MPR gain and associated noise amplification can be decreased by over one order of magnitude by changing from the conventional to the ANDi fiber design. In fact, this order of magnitude difference in noise susceptibility is a recurrent factor found in many theoretical and experimental studies, as we detail below, and can be seen as the main reason behind the attraction of ANDi fibers for low-noise SC source development.

From this fundamental physics perspective, we expect ANDi SC to be significantly more stable than conventional SC for any given pump source. These analytical arguments are confirmed by the numerical simulations in Fig. 6.6 illustrating the significantly different noise amplification behavior of conventional and ANDi SC. Displayed are the calculated coherence properties and spectral fluctuations for various input pulse durations using our representative fiber designs.

The competition between the coherent and incoherent dynamics typically leads to a threshold pulse duration T_{crit} or threshold soliton number N_{crit} above which the nature of the SC changes from coherent to incoherent (Dudley et al., 2006; Genty et

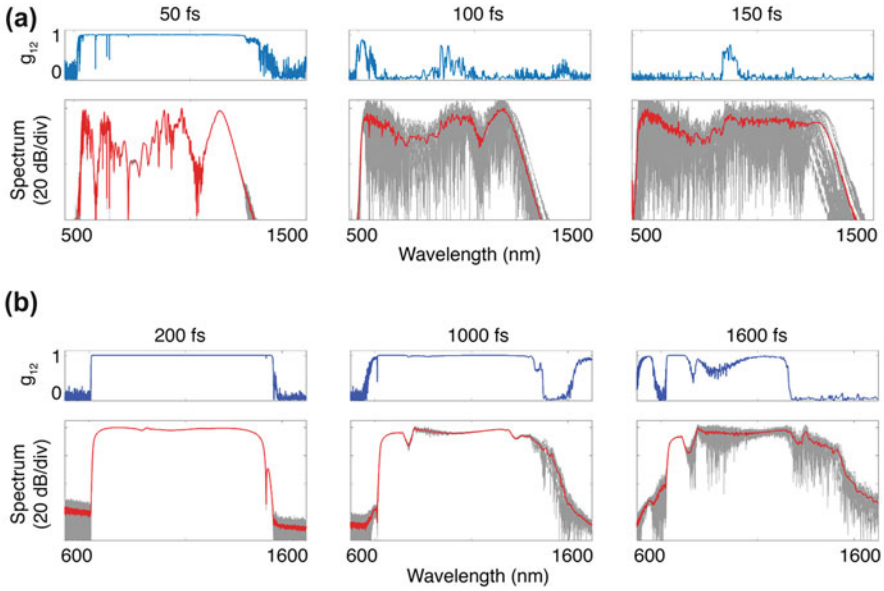

Fig. 6.6 Temporal coherence and stability calculations for (**a**) conventional SC and (**b**) ANDi SC in dependence of input pulse duration. Pump peak power and fiber lengths are fixed and values given in the text. The temporal coherence function $|g_{12}(\lambda)|$ (Eq. (6.6)) is displayed on top of each spectrum. The *gray* traces show spectra from 20 individual simulations including shot noise, while the mean spectrum appears in *red*

al., 2007). For the conventional SC, significant spectral shot-to-shot fluctuations and coherence degradation indicate the beginning dominance of incoherent dynamics governed by the MPR gain already for pump pulses as short as $T_{crit} \approx 100$ fs or $N_{crit} \approx 10$. Consequently, very short pump pulses, low pulse energies, and short fiber lengths are necessary to maintain coherence. In contrast, for ANDi fibers noise amplification becomes significant only for much longer pump pulse durations. At about 1000 fs, we observe first low-level fluctuations, especially at the long-wavelength edge, while the coherence function is still relatively unaffected. Only at pulse durations exceeding 1500 fs, incoherent dynamics become significant and the coherence function starts to collapse. In a comprehensive study on the coherence limits of ANDi SC, Heidt et al. (2017) clarified the role of the MPR gain in the decoherence of ANDi SC and revealed the complex interaction between coherent and incoherent dynamics in the long-pulse regime, which leads to novel mechanisms such as *incoherent cloud formation* and *incoherent optical wave breaking*. In ANDi fibers, coherent octave-spanning SC can be generated with pump pulse durations $T_{crit} > 1000$ fs and "soliton" orders of $N_{crit} \sim 600$, corresponding to an approximately 50 times increase of the coherent regime compared to conventional SC generation. Consequently, ANDi SCs allow for much higher pulse energies and power spectral densities in the order of mW/nm.

Since quantum noise amplified by the MPR gain grows exponentially with propagation distance (Smith, 1972), the coherence properties are also dependent on the fiber length. Shorter fibers generally yield better coherence, but might also result in narrower spectral bandwidths. In practice, balancing coherence and bandwidth with the correct choice of fiber length becomes more and more critical as the pump pulse duration is increased (Heidt et al., 2017).

The superior coherence and noise properties of ANDi SCs over conventional SCs were also experimentally verified, for example, by measurements of relative intensity noise (RIN), spectral coherence, dispersive Fourier transformation, and RF beating with stabilized laser diodes (Nishizawa & Takayanagi, 2007; Nishizawa et al., 2018; Klimczak et al., 2016). While initial results indicated a coherence collapse of ANDi SC when technical noise such as pump laser power fluctuations is considered (Genier et al., 2019), it was later shown that coherence is not a useful figure of merit to quantify SC stability in the presence of technical noise (Sierro & Heidt, 2020). In fact, ANDi SCs exhibit a remarkable resistance against technical noise (Sierro & Heidt, 2020, Eslami et al., 2020), and further studies have highlighted that the RIN of ANDi SC can actually be lower than the RIN of the pump laser in the central part of the spectrum (Genier et al., 2019; Rao et al., 2019). In contrast, in conventional SC technical noise is amplified by factors up to 20 dB, even in the regime where coherent dynamics dominate (Newbury et al., 2003).

6.5.3 Supercontinuum Noise Control by Designing Fiber Geometry and Birefringence

Although the above analysis suggests excellent stability of ANDi SC sources up to the picosecond regime, it assumes that the linear polarization state of the pulses remains unchanged during propagation in the fiber. In reality, every fiber exhibits a certain amount of birefringence that breaks the degeneracy of polarization states. This birefringence might be introduced, for example, by geometrical asymmetries of the fiber core and cross section, stresses introduced around air-hole microstructures, stresses due to different thermal expansion coefficients of multiple glass compositions, or twisting of the fiber during the drawing process. Consequently, linear and nonlinear mode coupling between the polarization modes leads to several nonlinear effects that, in addition to the MPR gain, have the potential to amplify quantum noise and results in unpredictable fluctuations of the polarization state. Table 6.1 provides an overview of the most relevant polarization-dependent noise-amplifying nonlinear processes in optical fibers. Polarization modulation instability (PMI) is especially relevant as it was shown to cause a significant degradation of coherence and stability of SC generated in low-birefringence ANDi fibers, even when the polarization of the pump pulses is aligned to one principal axes of the fiber (Gonzalo et al., 2018).

In general, the nonlinear noise amplification is a complex function of fiber birefringence and dispersion, as well as relative orientation of input pulse polarization

Table 6.1 Overview of the most relevant polarization-dependent nonlinear processes for (quantum) noise amplification in birefringent optical fibers, including the fiber or input pulse parameter that can be used for their control and suppression

Type	Description	Control parameter	Ref.
Polarization instability (PI)	Low-frequency polarization fluctuations Competition of fiber birefringence and nonlinear Kerr effect Onset above power threshold	Birefringence	Winful (1986), Domingue and Bartels (2013), and Tu et al. (2012b)
Polarization modulation instability (PMI)	Coherent (phase-dependent) coupling of polarization modes Weakly birefringent fibers Quantum noise amplification possible in two sidebands with orthogonal polarization to the pump Even for normal GVD and highly polarized beams along principal fiber axis	Birefringence	Wabnitz (1988), Liu et al. (2015), Gonzalo et al. (2018), and Loredo-Trejo et al. (2019)
Cross-phase modulation instability (XMI)	Incoherent (intensity-dependent) coupling of polarization modes Highly birefringent fibers Quantum noise amplification possible in one sideband created in each pol. axis In normal GVD: ceases above power threshold or for polarization close to principle fiber axis	Highly polarized beams Polarization alignment Peak power Dispersion design	Agrawal et al. (1989), Drummond et al. (1990), Rothenberg (1990), and Genier et al. (2020)
XPM-assisted Raman amplification	Transfer of MPR noise to a co-propagating signal in orthogonal polarization axis Occurs for both high and low birefringence Leads to chaotic polarization state once MPR dynamics dominate	Pump pulse duration	Feehan and Price (2020) and Feehan et al. (2020)

and fiber axes. This can be visualized by the high-resolution polarization-dependent RIN measurements shown in Fig. 6.7. For these measurements, pulses from an ultrafast Er-fiber laser (80 fs, 40 MHz, 0.05% RIN) were coupled into ANDi fibers with similar dispersion profiles, but very different geometries and birefringence, generating SC with comparable spectral bandwidths in the range 1.2–2.2 μm. A rotating half-wave plate in front of the fiber and a synchronized analyzer at the fiber exit control the plane of pump pulse and detection polarization with respect to the fiber geometry. Polarization-dependent RIN values are measured with an angular resolution of approximately 0.2° using a photodiode and electronic

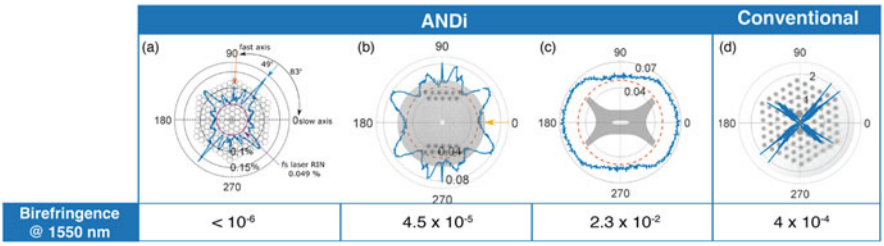

Fig. 6.7 Noise fingerprints of various ANDi SC (**a**–**c**) and conventional SC sources (**d**) pumped by an Er-fiber laser (80 fs, 40 MHz) at 1550 nm, generating comparable bandwidths in the range 1.2–2.2 μm. Shown are SC RIN values (in %) in a polar plot in dependence of pump pulse polarization orientation. The corresponding fiber geometry is shown in the background. The fiber's slow axis is aligned to zero degrees. The red-dotted line shows the RIN of the pump laser (0.05%). The birefringence at 1550 nm is given below each measurement. (**a**) Low-birefringence all-solid ANDi PCF with SF6 glass core (Klimczak et al., 2017). (**b**) Weakly polarization-maintaining (PM) air-hole microstructured PCF with Ge-doped silica core (Tarnowski et al., 2017). (**c**) Extremely birefringent nanohole suspended-core pure silica ANDi fiber (Hartung et al., 2019). (**d**) Commercial conventional fiber NKT PM-1550-01

spectrum analyzer and visualized in polar plots. These plots were found to be unique for each tested fiber and are therefore referred to as "noise fingerprints."

We observe a strong correlation between the noise fingerprints and the cross-sectional geometry of a particular fiber, which we attribute to the unique stress profile associated with each fiber structure. The ANDi fiber in Fig. 6.7a is designed as an all-solid microstructured PCF made from two different soft glasses forming the photonic lattice and inclusions (Klimczak et al., 2017). The structure causes a complex stress pattern due to different thermal expansion coefficients of the two glasses. Since there is no intentional stress axis defined in this design, the resulting birefringence is random, and the polarization axes are not well defined. This enables all of the nonlinear effects listed in Table 6.1 to occur at various angles; a more detailed analysis reveals PI as origin of the narrow noise spike around the fast axis, for example, while a combination of PMI and XMI is responsible for the noise peak at 49°.

Figure 6.7 also illustrates that birefringence is an effective control parameter to reduce polarization-dependent noise in ANDi SC generation. With increasing birefringence the noise fingerprints become more regular and environmentally stable. Near the slow axis of birefringent ANDi fibers, the noise of the SC is found to be virtually identical to the noise of the pump laser. Eventually, complete suppression of noise-amplifying nonlinear processes is observed ANDi fiber designs exhibiting extreme birefringence, such as the nanohole suspended-core fiber in Fig. 6.7c, even when the pump polarization is not aligned to one of the principal fiber axes. In contrast, the noise fingerprint of a comparable polarization-maintaining conventional SC source in Fig. 6.7d is significantly more complex, and shows noise amplification up to a factor of 40. In the test conditions, the soliton number is $N \simeq 6$, such that stable and coherent conventional SC is generated when the polarization of

the pump pulses is exactly aligned to a principal axis of the fiber. However, even slight misalignment of the polarization in the order of just 1° causes a significant rise of the SC noise.

These measurements highlight the importance of the cross-sectional fiber geometry and the homogeneity of the stress profile, in addition to dispersion engineering, for the realization of high-quality, low-noise SC sources. As we discuss in the following section, ANDi SC sources designed with these considerations in mind are currently emerging and provide further experimental evidence for the excellent quality and stability of these broadband coherent light sources.

6.6 Experimental Results and Fiber Designs for Various Spectral Regions

Based on the discussions in the previous sections, we can establish general fiber design guidelines for efficient SC generation in the normal dispersion region:

- The fiber should exhibit a convex and flattened all-normal dispersion profile. This ensures broadband uniform and smooth spectral and temporal profiles and suppresses soliton dynamics and MI gain entirely. The spectra can therefore be generally expected to be highly coherent if the MPR gain is negligible, i.e., for sub-picosecond pump pulses and 10s of cm fiber lengths.
- The fiber should have a birefringence in the order of 10^{-4} or higher in order to properly suppress polarization-dependent noise amplification processes, such as PMI. Alignment of the pump laser polarization to a principle fiber axis is generally recommended.
- For generating high-quality SC spectra, high-quality pump pulses are required. Nonideal pump pulse shapes containing satellite pulses or low-level pedestals lead to spectral and temporal fine structure (Rampur et al., 2020).
- The MDW should be close to the desired pump wavelength to ensure minimum temporal spreading of the input pulse and maximum generated SC bandwidth.
- For maximizing spectral bandwidth, the dispersion at the MDW should be close to zero and the dispersion profile as flat as possible. However, this can compromise spectral flatness and result in the formation of a depletion region around the MDW with a dip in spectral intensity larger than 10 dB.
- For maximizing spectral flatness, the dispersion at the MDW should be slightly normal to balance nonlinearity and dispersion and avoid the depletion region around the MDW. For typical input pulse parameters, the range -10 ps/(nm km) $\leq D \leq -30$ ps/(nm km) has led to good results.
- For asymmetric broadening toward a preferred wavelength region, the MDW should not be located at the pump wavelength, but further toward the preferred side of the spectrum.
- For a given fiber design, the generated spectral bandwidth is determined by the peak power and is independent of the input pulse duration (if MPR gain is

negligible). However, the fiber length should be chosen according to input pulse duration: longer pump pulses require longer fibers for the SC to fully develop. For pump pulses approaching the picosecond regime, careful adjustment of fiber length is required to maximize spectral bandwidth while maintaining coherence.

In the following paragraphs, we give examples of fiber designs that fulfill these guidelines and discuss important experimental results of SC generation pumped in the normal dispersion regime in different spectral bands.

6.6.1 Visible and Near-IR Spectral Region

In order to realize an all-normal GVD profile in the visible and near-IR spectral region, the material dispersion of silica, which has a single ZDW in the vicinity of 1300 nm, has to be substantially modified. In optical fibers, the geometry-dependent waveguide dispersion can counteract the material dispersion. This requires a high refractive index contrast between fiber core and cladding materials in combination with a small core diameter in the order of one wavelength. This can be realized using microstructured optical fiber technology, which enables the fabrication of fibers with small silica core surrounded by a photonic crystal cladding of air holes running longitudinally along the optical fiber (Knight, 2003). The structure of the photonic crystal cladding has a significant influence on the waveguide dispersion and hence allows the engineering of GVD profiles with large design freedom. Two kinds of microstructured optical fibers, PCF and suspended-core fibers (SCF), have been considered for the realization of ANDi fibers with MDW in the visible and near-IR region, and we discuss them here in more detail.

6.6.1.1 Photonic Crystal Fibers (PCFs)

Silica PCFs, in which the air-hole inclusions are arranged in a hexagonal lattice structure and a single lattice defect represents the guiding core, offer an enormous potential for dispersion engineering. By tuning the two design parameters, pitch Λ and relative air-hole diameter d/Λ, ANDi fibers with MDWs virtually anywhere between 500 and 1300 nm can be realized. Figure 6.8 demonstrates the full versatility of the concept, which is discussed in detail by Hartung et al. (2011a). The position of the MDW is predominantly determined by Λ, while d/Λ serves to reduce the GVD into the normal dispersion regime, accompanied by a slight decrease of the MDW. Consequently, small Λ and large d/Λ are required for the MDW to be located at visible wavelengths, while large Λ and small d/Λ shift the MDW further into the near-IR. Note that the absolute diameter d of the air holes stays almost constant at about 500 nm for every design.

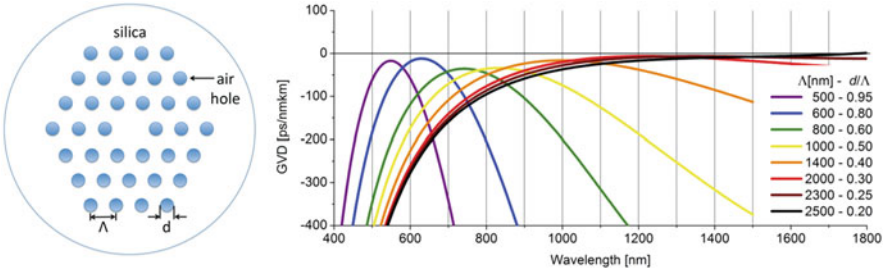

Fig. 6.8 Variety of possible ANDi PCF designs, optimized for various pump wavelengths in the visible and near-infrared spectral regions. The schematic cross section of the PCF illustrates the definition of the basic design parameters, pitch Λ and air-hole diameter d. (Adapted with permission from Hartung et al. (2011a). © The Optical Society)

Relative air-hole diameters near unity are approached for pumping at short wavelengths, which corresponds to a pure silica strand with submicron diameter suspended in air that can be fabricated simply by tapering of a standard single-mode fiber. Such nanofibers could therefore be an interesting approach for deep ultraviolet SC generation (see Sect. 6.6.2). On the long-wavelength side, the extremely flat profiles should result in ultra-broadband SC generation. However, the small d/Λ values result in large confinement losses and require a large number of rings in the photonic crystal cladding as counterbalance, which is challenging in fabrication. Additionally, a limit is imposed by the material dispersion of silica, and it is not possible to place the MDW further than around 1300 nm using the simple hexagonal PCF design considered here. However, using slightly modified PCF designs, the MDW can be shifted toward 1550 nm to create coherent and uniform spectra for telecommunications or optical coherence tomography (Hansen, 2003; Chow et al., 2006; Rao et al., 2019). In Sect. 6.6.3, we consider additional approaches how this limit can be overcome and discuss ANDi fiber designs for longer near-IR and mid-IR wavelengths.

ANDi PCF structures have usually been in-house fabricated, e.g., with MDWs around 650 nm (Heidt et al., 2011a), 800 nm (Humbert et al., 2006), and 1050 nm (Tse et al., 2006; Hooper et al., 2011). But the most extensively studied ANDi PCF to date is commercially available (NKT Photonics NL1050-NEG1) and optimized for pumping with femtosecond ytterbium fiber lasers at 1 μm, but also works well for pumping with widespread Ti-sapphire femtosecond systems around 800 nm. Figure 6.9 shows experimental ANDi SC generated in this fiber as well as in other selected low-birefringence PCF structures optimized for pump wavelengths in the visible and near-IR spectral regions.

The commercial NKT fiber has a dispersion profile very similar to our example fiber from Fig. 6.1 used in the numerical simulations in the previous sections. It has a core diameter of 2.3 μm and a photonic crystal cladding with design parameters $\Lambda \approx 1.46$ μm and $d/\Lambda \approx 0.39$, resulting in a peak dispersion parameter of $D \approx -11$ ps/(nm km) at a wavelength of 1020 nm. Since the ratio d/Λ is smaller than 0.4,

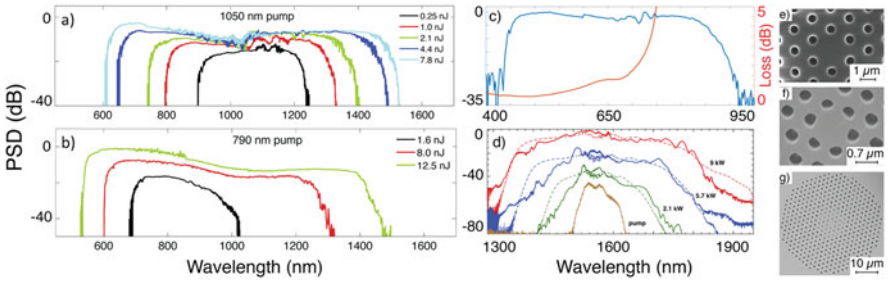

Fig. 6.9 Experimental SC generation results in low-birefringence ANDi PCF. Measured SC spectra in a commercially available ANDi PCF (NKT NL1050-NEG1) with MDW near 1020 nm using a central pump wavelength of (**a**) 1050 nm and (**b**) 790 nm in dependence of pump pulse energy. The pump pulse duration is 50 fs. The fiber cross section is shown in (**e**). (**c**) Visible ANDi SC generated in fiber (**f**) under 50 fs, 1.1 nJ, 650 nm pumping. (**d**) Near-IR ANDi SC generated in fiber (**g**) under 125 fs, 1550 nm pumping in dependence of peak power. (Adapted with permission from Heidt et al. (2011a) and Rao et al. (2019). © The Optical Society)

this fiber fulfills the criterion for endlessly single-mode guidance (Birks et al., 1997; Koshiba & Saitoh, 2004). Despite the relatively small core, input coupling efficiencies from free space in the order of 60% or more are achievable with properly sealed and cleaved or polished end facets. The SC spectra generated in this fiber exhibit the flatness and smoothness expected from the numerical simulations, and with a bandwidth of up to 1.5 octaves, they are among the broadest SC spectra generated in the normal dispersion regime of a silica optical fiber to date. These experiments demonstrate that a single fiber can consistently generate smooth, coherent, and broadband SC spectra with a variety of different pump sources if the dispersion curve is sufficiently flat. Note also the preferential broadening toward the side of the spectrum where the MDW is located in the case of 790 nm pumping. Experiments could also confirm the high temporal coherence of the SC and the conservation of single ultrashort pulses in the time domain (Heidt et al., 2011a), as well as their excellent compressibility (e.g., Heidt et al., 2011b; Demmler et al., 2011; Liu et al., 2012b).

Other experiments have demonstrated ANDi SC covering the entire visible spectral region (400–950 nm; Fig. 6.9c, f), where the small air-hole diameter (~400 nm) of the PCF structure leads to large confinement losses for longer wavelengths, which were minimized by using short pump pulses and fiber lengths (Heidt et al., 2011a). A different approach was chosen by Rao et al. (2019) for overcoming confinement losses of PCF structures above 1300 nm, highlighted in Fig. 6.9d, g. They fabricated a fiber with nonuniform design, where the air holes in the first three rings define the extremely flat dispersion according to the design criteria in Fig. 6.8, while rings 4–11 exhibit an increased diameter to reduce the losses. As a result, 9 kW pump peak power was sufficient to generate low-noise broadband ANDi SC in the 1300–1900 nm region with RIN as low as 0.5%.

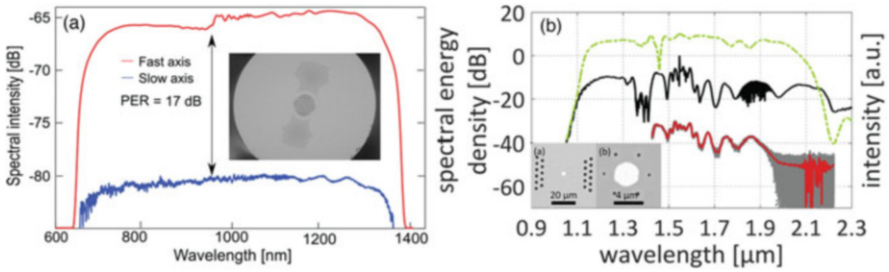

Fig. 6.10 Experimental SC generation results in high-birefringence, polarization-maintaining ANDi PCF. (**a**) Measured SC spectra and polarization extinction ratio (PER) in a PM-ANDi fiber (birefringence 4.7×10^{-4}) with MDW at 1040 nm pumped with 180 fs, 48 kW pulses at 1049 nm. The *inset* shows a microscope image of the fiber facet. Figure kindly provided by E. Genier, T. Sylvestre, Institut FEMTO-ST, Université de Franche-Comté (Genier et al., 2021). (b) Measured (black), simulated (green) SC spectra from an all-fiber ANDi SC source realized by splicing a PM-ANDi fiber (birefringence ~ 10^{-5}) with MDW at 1.7 µm directly to the output of an Er-fiber femtosecond laser. Dispersive Fourier transformation (individual traces, *gray*; mean, red) highlight the excellent shot-to-shot stability of the spectrum. *Insets* show microscope images of the fiber facet. Adapted from Tarnowski et al., 2019

A major advantage of ANDi SC is the extraordinarily good agreement of experimentally measured spectral intensity and phase with numerical simulations, which was shown by Tu et al. (2010, 2012a). So far, the same level of predictability has not been possible to achieve for conventional SC generation.

In Sect. 6.5.2 we stressed the critical importance of designing polarization-maintaining (PM) ANDi fibers with high birefringence and homogeneous stress profiles for avoiding quantum noise amplification via incoherent polarization-dependent nonlinear processes. Consequently, first prototypes of PM-ANDi fibers are now emerging. Figure 6.10 shows two recent examples of such fibers based on silica PCF, optimized for pumping at 1050 nm and 1550 nm, respectively. While Genier et al. (2021) demonstrated the extraordinary flatness, quality, and stability of their source, Tarnowski et al. (2019) realized an extremely simple and compact solution by splicing their PM-ANDi fiber directly to the output of a femtosecond Er-fiber laser. Both results impressively demonstrate the importance of highly birefringent ANDi fibers as the key-enabling technology for the next generation of ultra-low noise ultrafast SC sources. Nishizawa et al. (2004, 2007, 2018) describe multi-octaves for OCT and clocks.

6.6.1.2 Suspended-Core Fibers (SCF)

For the realization of silica fibers with ANDi profile, PCFs with a large number of closely spaced air holes in the cladding are necessary for reducing confinement losses, as seen in the previous section. SCF exhibit similar design freedom as PCF, but can be much simpler to fabricate (Hartung et al., 2011a). In these fibers, a core is

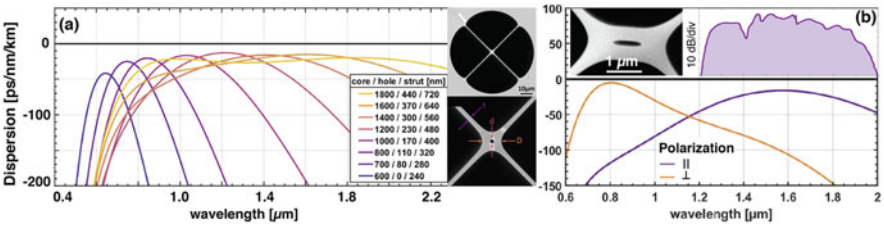

Fig. 6.11 (**a**) Calculated dispersion profiles of nanohole suspended-core fibers (SCF) with n = 3 struts in dependence of the core diameter, hole diameter, and strut width. Microscope image of SCF with n=4 struts are shown in the *insets*. (**b**) Dispersion characteristics of the fundamental polarization modes of highly birefringent nanohole SCF. Polarization direction is given with respect to the long core axis. The *insets* show microscope image and preliminary SC spectrum using an Er-fiber femtosecond pump laser. (Adapted with permission from Hartung et al. (2019). © The Optical Society)

suspended in air in the central section of a fiber, connected to the walls typically via three or more silica bridges. The dispersion parameters of such fibers depend on the core diameter d as well as on the number n of silica bridges and hence implicitly on the geometry of the core. Such structures have been exploited to generate ANDi SC in the visible range covering the spectral range 350–900 nm (Hartung et al., 2011b), but have not gained practical relevance to date.

An interesting new development in this area is the introduction of an additional degree of freedom into SCF design, achieved by including a nanohole into the center of the core with variable diameter (Hartung et al., 2019). As shown in Fig. 6.11a, this design facilitates ANDi fibers with MDWs between 500 nm and 1900 nm, but without the confinement loss challenges associated with PCF structures. By elongating one side of the core, extremely birefringent fibers with $\Delta n > 10^{-2}$ can be realized that exhibit very different dispersion characteristics of the two principal polarization modes. In one such design, shown in Fig. 6.11b, both principal polarization modes exhibit an ANDi profile, but with vastly different MDWs, 800 nm and 1600 nm, depending on the polarization direction with respect to the long core axis. Preliminary experiments using femtosecond pump pulses from an Er-fiber laser have confirmed highly polarized, high-quality ANDi SC generation in the region 1200–2000 nm. Such new fiber designs could in the future enable, for example, ultra-broadband ANDi SC by synchronized simultaneous pumping at different central wavelengths.

6.6.2 Deep-UV Spectral Region

A long-standing challenge in SC generation is the generation of significant power densities in the deep ultraviolet (UV) region at wavelengths below 350 nm. Especially applications in spectroscopy and fluorescence microscopy require light

sources in the UV, as many photo-induced processes are excited in this wavelength region (Prasad, 2003). Therefore, many studies have tried to extend the bandwidth of the conventional SC generation on the short wavelength edge (e.g., Kudlinski et al., 2006; Travers, 2010). However, it is difficult to generate significant spectral power densities below 350 nm wavelength, mainly due to the fact that many approaches rely on dispersive wave generation from soliton effects. This requires phase matching with the original soliton, which is difficult to achieve for short wavelengths.

In contrast, the generation of short wavelengths in ANDi fibers is extremely fast and independent of any phase-matching condition, and could therefore be an interesting approach to extend short wavelength edge of fiber-generated SCs deeper into the UV region. In addition, the coherence and temporal properties of the ANDi SC would be favorable, e.g., for broadband transient absorption spectroscopy at UV wavelengths. As discussed in the previous section, ANDi fibers with MDWs between 400 and 500 nm can be realized either with freestanding nanofibers or SCF with core diameters of approximately 500 nm, which can be easily obtained in taper configurations. However, SCF are generally the better choice as the tapered core is also protected by the surrounding silica cladding, which offers improved stability, ease of handling, and improved protection against surface contamination. Spectral broadening down to wavelengths of 250 nm can be expected when pumped with femtosecond pulses from frequency-doubled Ti-sapphire systems around 400 nm and peak powers of about 20–50 kW (Hartung et al., 2012). Although this approach is promising, it has not yet been verified experimentally.

Using a related technique exploiting nonlinear dynamics both in normal and anomalous dispersion regime of a tapered PCF, Stark et al. (2012) have succeeded to experimentally demonstrate deep-UV SC generation down to 280 nm—the current record for SC generation in solid-core silica fibers. In these experiments, summarized in Fig. 6.12, the pump pulses are launched in the normal dispersion regime at the input face of the fiber, but undergo soliton fission in the anomalous dispersion of the taper waist, where the nonlinearity is strongly enhanced. In order to achieve this, a PCF with high air-filling fraction ($d/\Lambda = 0.85$) and single ZDW at 1040 nm was tapered from an original core diameter of 5.4 μm down to ~620 nm using taper transition lengths of ~20 mm. The 130 fs, 50 kW peak power pump pulses are launched at 800 nm in the normal dispersion regime of the original fiber and experience SPM broadening. During propagation, the ZDW shifts toward shorter wavelengths as the fiber diameter decreases, and eventually sweeps across the pump pulse. The pulse, now experiencing anomalous dispersion and the high nonlinearity in the waist, undergoes a strong temporal compression to up to ten times higher peak power than the input pulse. Eventually soliton fission dynamics take place, generating the short wavelength components down to 280 nm. The energy conversion efficiency from the pump to UV (<400 nm) is about 20%.

The fundamental limit of the UV generation in solid-core silica fibers is ultimately given by both linear and nonlinear absorption in the material, defined by the relation

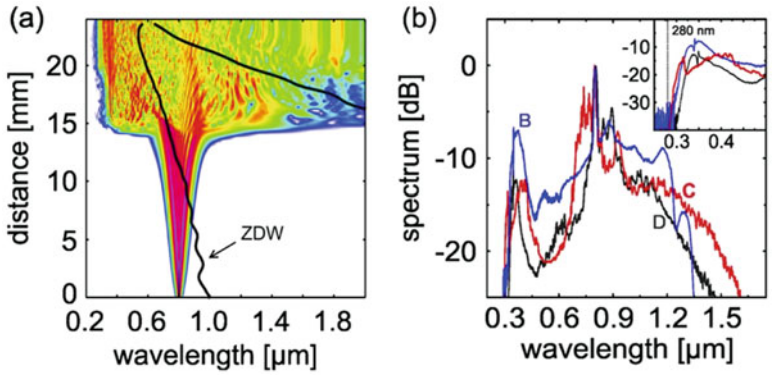

Fig. 6.12 (**a**) Simulated spectral evolution of SC generation in a 24-mm-long PCF taper, pumped by 110 fs, 50 kW pulses at 800 nm. The *black lines* show the evolution of ZDWs as the fiber core diameter decreases from 5.4 μm to 620 nm. (**b**) Experimental results from PCF tapers with different lengths. The lower spectral boundary is 280 nm. (Reproduced with permission from Stark et al. (2012). © The Optical Society)

$$-\frac{\partial I}{dz} = \alpha(\omega) I + \beta(\omega) I^2, \tag{6.7}$$

where $\alpha(\omega)$ and $\beta(\omega)$ are the frequency-dependent coefficients of linear and two-photon absorption (TPA), respectively, and I is the intensity. Although α rises sharply at UV wavelength in silica, it typically remains below 0.1 dB/cm and therefore almost negligible when considering a short taper as above. The TPA threshold, however, is reached at approximately 250 nm and causes an exponential increase in β (Brimacombe et al., 1989; Taylor et al., 1988). While the loss due to TPA depends on the intensity and hence the experimental conditions, Stark et al. (2012) estimated it to be as high as 100 dB/mm for their experiment described above. Such a strong attenuation would, of course, represent a hard barrier for any experiment, and therefore it seems hard to imagine a significant further UV extension of SC generation in solid-core silica fibers.

Further extension is possible in other fiber materials, and conventional SC spanning 200–2500 nm in ZBLAN PCF has been demonstrated (Jiang et al., 2015). However, hollow-core fibers filled with noble gases have emerged as the most successful approach for generating considerable spectral power density and powerful ultrashort pulses in the deep-UV hollow-core fibers filled with noble gases. Such fibers guide the light in the gas with minimal overlap with the silica cladding, avoiding the material-induced nonlinear absorption (Markos et al., 2017).

6.6.3 Mid-Infrared Spectral Region

We mentioned in Sect. 6.5.1 that the achievable bandwidth toward the mid-infrared (mid-IR) spectral region is limited with the traditional hexagonal silica PCF designs. For the extension of ANDi SCs toward the mid-infrared (mid-IR) spectral region, different fiber designs have to be considered. Since the material dispersion of silica is anomalous but fairly low and flat above 1300 nm, it can be compensated by modest waveguide dispersion and hence a relatively low refractive index step between core and cladding material, which can be realized also in standard solid silica fiber by doping a small diameter core with GeO_2, for instance. In their early work, Hori et al. (2004) and Nishizawa and Takayanagi (2007) could demonstrate broadband SC generation spanning up to 2.1 μm in such highly nonlinear fibers with extremely flat and low normal dispersion in most of the near-IR region, but pumping required more complex schemes and not much detail was given about fiber design and composition.

Ultimately, new fiber materials need to be introduced in order to realize ANDi fiber designs at wavelengths of 2 μm and beyond, where silica is intransparent. Soft glass materials offer low losses in the mid-IR and ZDWs between 1.6 μm for fluoride and 5 μm for chalcogenide glasses (Price et al., 2007). The variety of available soft glass materials provides a whole new dimension for the design of ANDi fibers at mid-IR wavelengths, because significant dispersion design flexibility is given not only by the inclusion of air-hole microstructures but also by combining glass materials with different characteristics in all-solid designs. An excellent example how this design freedom offered by soft glass materials can be exploited is given by the work of Klimczak et al. (2014), who realized ANDi SC generation in the range 900–2300 nm in an all-solid PCF combining commercial N-F2 glass used for the core and lattice structure with an in-house synthesized, thermally matched boron silicate glass used for lattice filling (Martynkien et al., 2014; Stepien et al., 2014). Of course, the SC has the typical excellent coherence and temporal properties associated with ANDi fibers, and the overlap with the amplification bandwidths of both thulium- and holmium-doped fiber amplifiers offers intriguing prospects for ultrafast coherent seeding and few-cycle pulse generation at wavelengths around 2 μm, which we discuss in Sect. 6.7.1. The design freedom offered by this approach is more comprehensively reviewed by Klimczak et al. (2017) as well as in Chap. 15 of this book.

Large freedom in dispersion design can not only be achieved in microstructured fibers but also in solid step-index fibers by combining core and cladding glasses with large refractive index difference and choosing an appropriate core size (Poletti et al., 2011). Chalcogenide glasses are good candidates for this approach as they exhibit extremely large refractive index variations depending on their composition, and additionally offer a transparency window covering the molecular fingerprint region up to 12 μm and above as well as orders of magnitude larger nonlinearity than silica (Price et al., 2007). A fiber design using these beneficial properties in an ANDi fiber context is shown in Fig. 6.13. It consists of Te-based chalcogenide

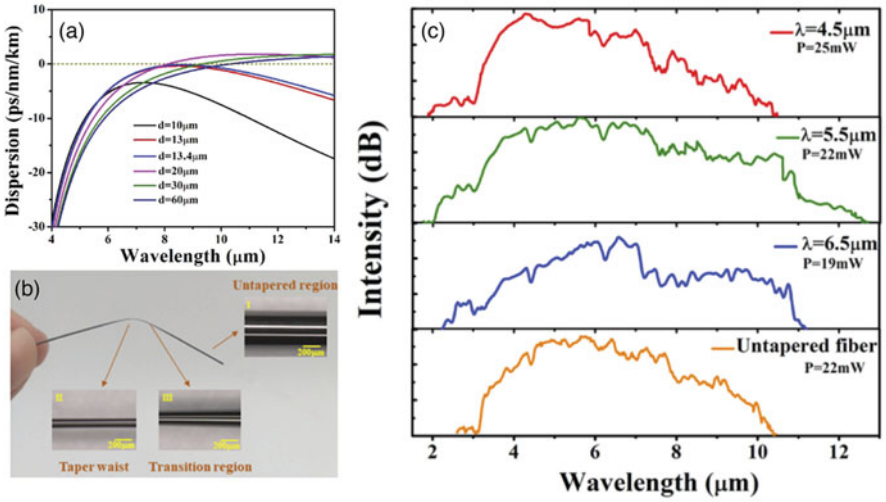

Fig. 6.13 (**a**) Dispersion profiles of a chalcogenide step-index fiber ($Ge_{20}As_{20}Se_{15}Te_{45}$ core, $Ge_{20}As_{20}Se_{20}Te_{40}$ cladding) in dependence of the core diameter. Effective dispersion control can be achieved by tapering the fiber to the desired size. (**b**) Robust handling of the tapers enabled by the polymer coating. *Insets* show microscope images of the taper in different regions. (**c**) Experimental measurement of the SC spectrum generated in a taper with 13.4 μm waist, pumped with pulses of about 150 fs duration at different central wavelengths. (Adapted with permission from Zhang et al. (2019). © The Optical Society)

core and cladding glasses with numerical aperture NA ≈ 0.4, embedded in a thermally matched polymer jacket (Zhang et al., 2019). The compatibility of thermal and mechanical properties of the three materials enables the tapering of this fiber in its entirety, i.e., without removing the polymer, which makes these devices mechanically extremely robust and in practice allows the precise control over the fiber dimensions via straightforward post-processing (Shabahang et al., 2013). By choosing an appropriate core diameter in the taper waist, ANDi profiles with MDWs between 7 and 8 μm can be realized, as illustrated in Fig. 6.13a. When pumped by 150 fs pulses with central wavelengths in the range 4.5–6.5 μm, SC spectra covering the range 2–12 μm were generated (Zhang et al., 2019) (Fig. 6.13c). Similar experimental results were obtained by Wang et al. (2017) in As-S-based chalcogenide fiber tapers, albeit with slightly narrower spectral bandwidth. Several other, more complex ANDi fiber designs have been proposed for increased flatness or other pump wavelengths (Baili et al., 2014; Ben Salem et al., 2016). In combination, these efforts represent important steps toward fiber-based broadband coherent and ultrafast photonics in the mid-IR, but the realization of birefringent fibers in this wavelength regime remains a challenge.

6.7 Selected Application Examples

It is clear that SCs generated in ANDi fibers will be particularly relevant for applications in which the spectral uniformity, the temporal profile, or the stability of the continuum is of importance and that have hence struggled to incorporate the noise-sensitive and complex conventional SCs. Two salient areas stand out and have received particular attention: ultrafast photonics and advanced imaging and spectroscopy. We therefore discuss them in more detail in this section.

6.7.1 Ultrafast Photonics

The generation and application of short laser pulses is at the heart of ultrafast optics, and the motto "shorter is better" usually applies. Today, laser pulses containing only a few or even just a single oscillation of the light field[1] enable the time-resolved study of fundamental processes in physics, chemistry, and biology (Kärtner, 2004), or drive the generation of coherent soft X-rays and attosecond pulses, which open up new frontiers in atomic spectroscopy (Krausz & Ivanov, 2009). Although Ti-sapphire oscillators are commercially available that can deliver few-cycle pulses directly in the near-IR, these systems are costly and sensitive to environmental changes, and the shortest pulses have relatively poor quality, i.e., are accompanied by pre- and post-pulses. Spectral broadening of longer femtosecond pulses in optical fibers with subsequent external compression has therefore long been considered as an inexpensive and robust alternative, and the extreme bandwidths of microstructured fiber SCs are particularly attractive. But although it is theoretically possible to compress octave-spanning conventional SCs to single-cycle pulses (Dudley & Coen, 2004), in practice the sub-two cycle regime could never be reached and the pulse duration remained above ~5.5 fs (Schenkel et al., 2005). Even when maximizing the coherence using very short 15 fs pump pulses and only a few millimeters of fiber, the noise sensitivity and the spectro-temporal fine structure are the main practical limitations to reach the predicted Fourier-limited pulse durations.

These fundamental limitations do not apply to ANDi SCs, and consequently numerous studies have investigated their compressibility. When considering nonlinear pulse compression based on solid-core optical fibers, the ANDi fiber design has enabled:

(i) *The highest compression ratio* to the sub-two optical cycle regime. Liu et al. (2012b) obtained a compression ratio of almost 30×, shortening 180 fs input pulses to high-quality, near transform-limited 6.4 fs (1.8 cycle) pulses after full phase compensation using a liquid crystal-based spatial light modulator (SLM). This is an impressive result, transforming a compact and reliable

[1] A single optical cycle has the duration λ_0/c, e.g., 2.7 fs at 800 nm central wavelength.

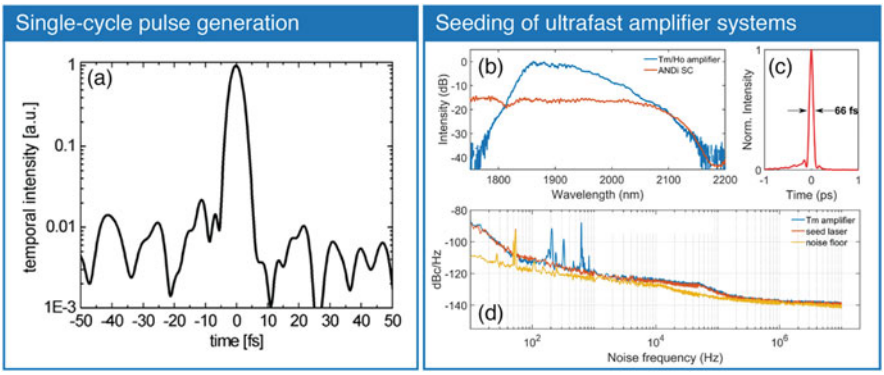

Fig. 6.14 Applications of ANDi SC sources in ultrafast photonics. (**a**) Generation of a single cycle of light via compression of an octave-spanning ANDi SC. Up to 19 dB pre- and post-pulse suppression (note the logarithmic scale!) and pulse durations as low as 3.7 fs (1.3 optical cycles) were measured. Adapted with permission from Demmler et al. (2011). © The Optical Society. (**b**) Measured spectrum of a Tm-/Ho-codoped chirped pulse fiber amplifier (CPFA) seeded by an ANDi SC, which is generated by an ultrafast Er-fiber laser at 1550 nm. (**c**) Measured pulse at the output of the all-fiber CPFA system. Adapted from Heidt et al. (2020). (**d**) Noise spectra of amplified pulses in an all-PM CPFA implementation in comparison with the Er-fiber seed laser. The integrated RIN of the ultra-low noise CPFA system is as low as 0.03% (10Hz–10 MHz). Adapted with permission from Rampur et al. (2019). © The Optical Society

commercial 180 fs oscillator into a sub-two cycle pulse source. Even when taking coupling efficiencies and losses in the compressor into account, the compressed pulses can have more than 10× higher peak power than the pulses available directly from the oscillator.

(ii) *The best pulse quality*. Demmler et al. (2011) demonstrated the compression of an octave-spanning SC to Fourier-limited, single-cycle pulses with a quality superior to any other technique. Almost 20 dB suppression of sub-pulses was achieved, as shown in Fig. 6.14a. Similarly high-quality sub-two cycle pulses could even be obtained using linear chirp compensation only, as Heidt et al. (2011b) could demonstrate using a static chirped mirror compressor and extremely short fiber lengths that limit the influence of higher-order dispersion.

(iii) *The shortest pulse duration*. Pulses as short as 3.67 fs (1.3 optical cycles) were measured by Demmler et al. (2011) by recompressing an octave-spanning ANDi SC using a SLM. This is the shortest pulse duration obtained from nonlinear pulse compression in solid-core fibers to date.

Such sub-two cycle, high-quality ultrashort ANDi SC pulses are the ideal seed source for ultra-broadband optical parametric chirped pulse amplification (OPCPA) systems, and have consequently facilitated the generation of carrier-envelope phase stable 5.0 fs pulses with up to 22 W average power at 1 MHz repetition rate (Rothhardt et al., 2012). Such high-power few-cycle laser systems have already enabled unique applications such as efficient generation of coherent soft X-ray

radiation and isolated attosecond pulses at up to 0.6 MHz repetition rate (Krebs et al., 2013). In the future, many more applications such as photoelectron spectroscopy and XUV microscopy might benefit from modern high-power few-cycle lasers based on amplified ANDi SC pulses (Rothhardt et al., 2017).

Low-noise ultrafast ANDi SC sources have recently also been considered as seed source for the next generation of ultra-low noise high-power ultrafast fiber amplifiers and frequency combs operating in the 2 μm spectral region. This waveband is particularly important as stepping stone for the exploration of the molecular fingerprint region in the mid-infrared via nonlinear frequency conversion. Pumped by robust, turnkey mode-locked Er-fiber systems with ultra-low amplitude and phase noise, ANDi fibers with MDW near 1550 nm were recently employed in proof-of-principle experiments for low-noise spectral broadening into the 2 μm region and subsequent coherent seeding of thulium (Tm)- or holmium (Ho)-doped fiber amplifiers (Rampur et al., 2019; Heidt et al., 2020). Figure 6.14b shows the spectrum of such an amplifier system with a -20 dB bandwidth of 320 nm and the comparison to the ANDi SC seed. High-quality 66 fs pulses with 70 kW peak power could be obtained at the output of the all-fiber system (Fig. 6.14c). When constructed with highly birefringent ANDi fibers in an all-PM architecture, the amplified pulses exhibit a RIN of only 0.03%, which is virtually identical to the Er-fiber seed laser (Fig. 6.14d). These excellent noise characteristics are enabled by the suppression of incoherent nonlinearities in the PM-ANDi fiber (as discussed in Sect. 6.5), as well as by the coherent seeding of the entire amplifier gain spectrum with the broadband ANDi SC, which effectively suppresses amplified spontaneous emission noise in the amplifier. These results represent an order of magnitude improvement of amplifier noise over comparable conventionally seeded implementations, overcoming the major challenge limiting the further development and power-scaling of frequency comb sources at 2 μm (Gaida et al., 2018).

Recent experiments also convincingly demonstrated the advantages of ANDi SC over conventional SC in the construction of stabilized frequency combs (Nishizawa et al., 2018). In combination with the progress of fiber amplifiers described above, these studies have laid the foundations for exciting opportunities arising from using ANDi SC seed sources for the next generation of ultra-low noise frequency combs and ultrafast fiber amplifiers operating in the 2 μm spectral region and beyond in the mid-IR.

6.7.2 Advanced Imaging and Spectroscopy

SC sources in the visible and near-IR have been commercially available for over a decade, and are the excitation source of choice for a range of advanced microscopy techniques, such as multiphoton- and stimulated emission depletion (STED) microscopy (Wildanger et al., 2008). In optical coherence tomography (OCT), SC sources facilitate high-speed, high-resolution 3D imaging across several medical specialities, including ophthalmology and cardiology (Moon & Kim 2006).

Pumped by high repetition-rate pico- or nanosecond pulsed lasers and equipped with the high beam quality of optical fibers, the brightness of these fiber-based SC sources is unparalleled. However, due to the stochastic nature of the nonlinear processes involved in spectral broadening, these SC sources provide spatially but not temporally coherent light and exhibit very large pulse-to-pulse fluctuations of spectral amplitude and phase. This SC noise has become the predominating factor limiting acquisition speed, sensitivity, and resolution in many applications (Jensen et al., 2019).

The adaptation of low-noise ultrafast ANDi SC sources has therefore started to push the boundaries in several spectroscopy and imaging modalities. Their recent implementation in hyperspectral stimulated Raman scattering microscopy for label-free, chemical-specific biomedical, and mineralogical imaging is particularly impressive, as source noise is critically important in this technique and has excluded the use of many other nonlinear spectral broadening schemes (Abdolghader et al., 2020). In high-resolution spectral-domain OCT, ANDi SC sources have enabled, for the first time, imaging limited by detection shot noise and not by SC source noise (Rao et al., 2020). ANDi SCs are also starting to replace white light generation in bulk media like YAG, sapphire, and CaF_2 in ultrafast spectroscopy, removing the need for expensive amplified laser systems (Kearns et al., 2019).

The combination of an ANDi SC source with a SLM-based pulse shaping device and subsequent imaging or spectroscopy system has proven to be an especially powerful and versatile tool in biophotonic imaging and spectroscopy (Fig. 6.15a) (Tu & Boppart, 2013). It offers full digital and programmable control over the spectro-temporal profile of the incident light field at the sample and allows the realization of numerous coherently controlled applications in a single setup. Conveniently, the incorporation of the pulse shaper facilitates the complete or partial compression of the SC pulses at the sample position via digital algorithms, such as multiphoton intrapulse interference phase scanning (MIIPS) and time-domain ptychography (Tu et al., 2011; Dwapanyin et al., 2020). Of course, an additional arbitrary spectral phase may be applied with the same pulse shaper to enable the desired coherently controlled applications.

Using such amplitude and phase shaping of an ANDi SC, alignment-free and programmable-contrast multimodal multiphoton microscopy of biological samples over a broad spectral range becomes possible (Liu et al. (2012a); Dwapanyin et al., 2020). Figure 6.15b illustrates such imaging of a human breast tumor. By carving different spectral slices out of the SC and compressing the resulting ultrashort pulses at the focus of a scanning microscope, selective and efficient nonlinear optical imaging using three different modalities (two-photon fluorescence, second-harmonic generation, and third-harmonic generation) was shown with a single beam and an easily tunable setup. The enhanced multiphoton signals enable the selective visualization of various intrinsic molecules and internal structures.

The full power of combining an ANDi SC source with a pulse shaper is revealed when implemented in a modality that requires full coherent control of the field incident on the sample, such as single-beam coherent anti-Stokes Raman scattering (CARS) spectroscopy (Fig. 6.15c). Due to the coherence and

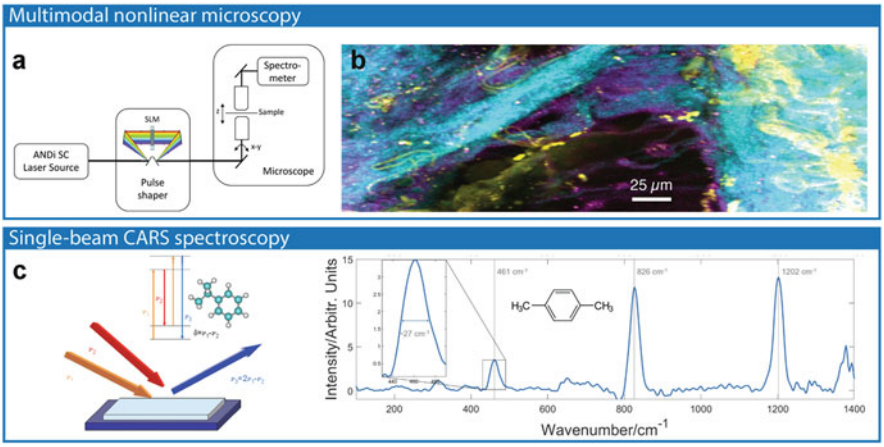

Fig. 6.15 (**a**) The combination of ANDi SC source, SLM-based pulse shaping device, and subsequent imaging or microspectroscopy system is a powerful setup in biophotonics. Multiple coherently controlled modalities can be realized, including label-free nonlinear microscopy with various contrast methods and single-beam CARS microspectroscopy. (**b**) Label-free multimodal multiphoton imaging of human mammary tumor using compressed pulses from the ANDi SC source. The image contains two-photon fluorescence (*yellow*), third-harmonic generation (*magenta*), and second-harmonic generation (*cyan*) signals used as contrast methods. Representative image data from the study detailed in Liu et al. (2012a), courtesy of Y. Liu, H. Tu, and S. Boppart, University of Illinois. (**c**) Schematic operational principle of CARS microspectroscopy and experimental single-beam CARS spectrum of para-xylene. (Adapted with permission from Viljoen et al. (2020). © The Optical Society)

ultrafast properties of the ANDi SC, pump, probe, and reference beam can be carved from a single SC pulse, and using the pulse shaper, it is possible to compress, stretch, and delay them independently as well as separating the coherent information from the incoherent background (Liu et al., 2013; Tu and Boppart, 2014; Viljoen et al., 2020). Ultimately, the combination of multiphoton microscopy and hyperspectral CARS imaging based on digitally programmable ANDi SC pulses has led to the development of an extremely versatile platform for optical alignment-free programmable-contrast imaging, offering the potential to translate stain-free molecular histopathology for disease diagnosis into routine clinical use (Tu et al., 2016). Even without the relatively expensive SLM device, broadband multimodal CARS and multiphoton imaging systems based on ANDi SC sources have been developed (Herdzik et al., 2020).

6.8 Conclusion

In this chapter, we provide a comprehensive review of SC generation in ANDi fibers, fiber design possibilities, and related applications. While coherent SC generation in normal dispersion fibers has been studied since the early beginnings of nonlinear

fiber optics, the emergence of the ANDi fiber design concept has pushed the obtainable bandwidths to magnitudes previously only known from anomalous dispersion pumping. In combination with their high stability, the conservation of an ultrashort compressible temporal pulse, and their uniform and flat spectral profiles, ANDi SCs are a truly unique "white light" source whose full potential is yet to be explored. The possibility to achieve these characteristics with relatively long pump pulses and the relaxation of previously demanding pump source requirements to maintain coherence increases availability and applicability of broadband coherent SC sources.

It should have become clear that the ANDi fibers are an important complement to the fibers with single ZDW conventionally used for SC generation, and both have their unique advantages and drawbacks. Ultimately, the choice of fiber design depends on the application demands. The ANDi design is preferable if coherence, stability, temporal profile, or spectral flatness is required, but for a given input peak power, the achievable spectral bandwidth is usually narrower in comparison with anomalous dispersion pumping. For applications in which stability and the presence of fine structure are less important, the classic approach of anomalous dispersion pumping close to the single ZDW still provides the broadest achievable spectral bandwidth and allows pump sources from the femtosecond to the CW regime. ANDi fibers do not offer the same flexibility in the choice of pump source; the high peak powers required for substantial spectral broadening put a practical limit on the pump pulse duration and imply a sub-picosecond pulse source.

Highly birefringent ANDi fibers are emerging as the key-enabling technology for the next generation of ultra-low noise ultrafast SC sources and are already beginning to push the boundaries in several spectroscopy and imaging applications. From our perspective this is really just the beginning of a movement that will see these versatile sources of broadband, low-noise, and ultrashort pulses being used in an increasing numbers of applications which so far were not able to use conventional fiber-based SC sources due to their noise or complex temporal pulse shapes. It will also be interesting to follow the further development of ANDi fibers made of soft glass materials like chalcogenides, which will enable the extension of coherent and ultrafast photonics based on optical fibers to the emerging mid-IR waveband.

Acknowledgments Funding by the Swiss National Science Foundation (SNSF) (PCEFP2_181222) and the Thuringian Ministry of Education, Science and Culture under the European EFRE program is gratefully acknowledged.

References

Abdolghader, P., Pegoraro, A. F., Joly, N. Y., Ridsdale, A., Lausten, R., Legare, F., & Stolow, A. (2020). All normal dispersion nonlinear fibre supercontinuum source characterization and application in hyperspectral stimulated raman scattering microscopy. *Optics Express, 28*, 35997.

Agrawal, G. (2007). *Nonlinear Fiber Optics*. Academic Press.

Agrawal, G. P., Baldeck, P., & Alfano, R. (1989). Modulation instability induced by cross-phase modulation in optical fibers. *Physical Review A, 39*, 3406.

Akhmediev, N., & Karlsson, M. (1995). Cherenkov radiation emitted by solitons in optical fibers. *Physical Review A, 51*, 2602.

Alfano, R. R., & Shapiro, S. L. (1970a). Emission in the region 4000 to 7000 Å via four-photon coupling in glass. *Physical Review Letters, 24*, 584.

Alfano, R. R., & Shapiro, S. L. (1970b). Observation of self-phase modulation and small scale filaments in crystals and glasses. *Physical Review Letters, 24*, 592.

Alfano, R. R., & Shapiro, S. L. (1970c). Direct distortion of electronic clouds of rare gas atoms in intense electric fields. *Physical Review Letters, 24*, 1217.

Anderson, D., Desaix, M., Lisak, M., & Quiroga-Teixeiro, M. L. (1992). Wave breaking in nonlinear-optical fibers. *Journal of the Optical Society of America B: Optical Physics, 9*, 1358.

Baili, A., Cherif, R., Heidt, A. M., & Zghal, M. (2014). Maximizing the band- width of coherent, mid-IR supercontinuum using highly nonlinear aperiodic nanofibers. *Journal of Modern Optics, 61*, 650.

Ben Salem, A., Diouf, M., Cherif, R., Wague, A., & Zghal, M. (2016). Ultraflat- top midinfrared coherent broadband supercontinuum using all normal As_2S_5-borosilicate hybrid photonic crystal fiber. *Optical Engineering, 55*, 066109.

Birks, T. A., Knight, J. C., & Russell, P. S. (1997). Endlessly single-mode photonic crystal fiber. *Optics Letters, 22*, 961.

Bloembergen, N., & Shen, Y. (1964). Coupling between vibrations and light waves in Raman laser media. *Physical Review Letters, 12*, 504.

Brimacombe, R. K., Taylor, R. S., & Leopold, K. E. (1989). Dependence of the nonlinear transmission properties of fused silica fibers on excimer laser wavelength. *Journal of Applied Physics, 66*, 4035.

Chen, C.-M., & Kelley, P. L. (2002). Nonlinear pulse compression in optical fibers: Scaling laws and numerical analysis. *Journal of the Optical Society of America B: Optical Physics, 19*, 1961.

Chow, K., Takushima, Y., Lin, C., Shu, C., & Bjarklev, A. (2006). Flat super-continuum generation based on normal dispersion nonlinear photonic crystal fibre. *Electronics Letters, 42*, 989.

Coen, S., Chau, A. H. L., Leonhardt, R., Harvey, J. D., Knight, J. C., Wadsworth, W. J., & Russell, P. S. J. (2002a). Supercontinuum generation by stimulated Raman scattering and parametric four-wave mixing in photonic crystal fibers. *Journal of the Optical Society of America B: Optical Physics, 19*, 753.

Coen, S., Wardle, D. A., & Harvey, J. D. (2002b). Observation of non-phase-matched parametric amplification in resonant nonlinear optics. *Physical Review Letters, 89*, 273901.

Cohen, L. (1989). Time-frequency distributions-a review. *Proceedings of the IEEE, 77*, 941.

Corwin, K. L., Newbury, N. R., Dudley, J. M., Coen, S., Diddams, S. A., Weber, K., & Windeler, R. S. (2003). Fundamental noise limitations to supercontinuum generation in microstructure fiber. *Physical Review Letters, 90*, 113904.

Demmler, S., Rothhardt, J., Heidt, A. M., Hartung, A., Rohwer, E. G., Bartelt, H., Limpert, J., & Tünnermann, A. (2011). Generation of high quality, 1.3 cycle pulses by active phase control of an octave spanning supercontinuum. *Optics Express, 19*, 20151.

Domingue, S. R., & Bartels, R. A. (2013). Overcoming temporal polarization instabilities from the latent birefringence in all-normal dispersion, wave- breaking-extended nonlinear fiber supercontinuum generation. *Optics Express, 21*, 13305.

Drummond, P., Kennedy, T., Dudley, J., Leonhardt, R., & Harvey, J. (1990). Cross-phase modulational instability in high-birefringence fibers. *Optics Communication, 78*, 137.

Dudley, J. M., & Coen, S. (2002). Coherence properties of supercontinuum spectra generated in photonic crystal and tapered optical fibers. *Optics Letters, 27*, 1180.

Dudley, J. M., & Coen, S. (2004). Fundamental limits to few-cycle pulse generation from compression of supercontinuum spectra generated in photonic crystal fiber. *Optics Express, 12*, 2423.

Dudley, J. M., Genty, G., & Coen, S. (2006). Supercontinuum generation in photonic crystal fiber. *Reviews of Modern Physics, 78*, 1135.

Dupont, S., Qu, Z., Kiwanuka, S.-S., Hooper, L. E., Knight, J. C., Keiding, S. R., & Kaminski, C. F. (2014). Ultra-high repetition rate absorption spectroscopy with low noise supercontinuum radiation generated in an all-normal dispersion fibre. *Laser Physics Letters, 11*, 075601.

Dwapanyin, G., Spangenberg, D., Heidt, A., Feurer, T., Bosman, G., Neethling, P., & Rohwer, E. (2020). Generalized spectral phase-only time-domain ptychographic phase reconstruction applied in nonlinear microscopy. *Journal of the Optical Society of America B: Optical Physics, 37*, A285.

Eslami, Z., Ryczkowski, P., Salmela, L., & Genty, G. (2020). Low-noise octave-spanning mid-infrared supercontinuum generation in a multimode chalcogenide fiber. *Optics Letters, 45*, 3103.

Falk, P., Frosz, M., & Bang, O. (2005). Supercontinuum generation in a photonic crystal fiber with two zero-dispersion wavelengths tapered to normal dispersion at all wavelengths. *Optics Express, 13*, 7535.

Feehan, J. S., & Price, J. H. (2020). Decoherence due to XPM-assisted Raman amplification for polarization or wavelength offset pulses in all-normal dispersion supercontinuum generation. *Journal of the Optical Society of America B: Optical Physics, 37*, 635.

Feehan, J. S., Brunetti, E., Yoffe, S., Li, W., Wiggins, S. M., Jaroszynski, D. A., & Price, J. H. (2020). Noise-related polarization dynamics for femto and picosecond pulses in normal dispersion fibers. *Optics Express, 28*, 21447.

Finot, C., Kibler, B., Provost, L., & Wabnitz, S. (2008). Beneficial impact of wave-breaking for coherent continuum formation in normally dispersive nonlinear fibers. *Journal of the Optical Society of America B: Optical Physics, 25*, 1938.

Gaida, C., Heuermann, T., Gebhardt, M., Shestaev, E., Butler, T. P., Gerz, D., Lilienfein, N., Sulzer, P., Fischer, M., Holzwarth, R., et al. (2018). High-power frequency comb at 2 μm wavelength emitted by a Tm-doped fiber laser system. *Optics Letters, 43*, 5178.

Genier, E., Bowen, P., Sylvestre, T., Dudley, J. M., Moselund, P., & Bang, O. (2019). Amplitude noise and coherence degradation of femtosecond supercontinuum generation in all-normal-dispersion fibers. *Journal of the Optical Society of America B: Optical Physics, 36*, A161.

Genier, E., Ghosh, A. N., Bobba, S., Bowen, P., Moselund, P. M., Bang, O., Dudley, J. M., & Sylvestre, T. (2020). Cross-phase modulation instability in PM ANDi fiber-based supercontinuum generation. *Optics Letters, 45*, 3545.

Genier, E., Grelet, S., Engelsholm, R. D., Bowen, P., Moselund, P. M., Bang, O., Dudley, J. M., & Sylvestre, T. (2021). An ultra-flat, low-noise and linearly polarized fiber supercontinuum source covering 670 nm-1390 nm. *Optics Letters, 46*, 1820.

Genty, G., Coen, S., & Dudley, J. M. (2007). Fiber supercontinuum sources (invited). *Journal of the Optical Society of America B: Optical Physics, 24*, 1771.

Golovchenko, E. A., Dianov, E. M., Prokhorov, A. M., & Serkin, V. N. (1985). Decay of optical solitons. *JETP Letters, 42*, 74.

Gonzalo, I. B., Engelsholm, R. D., Sørensen, M. P., & Bang, O. (2018). Polarization noise places severe constraints on coherence of all-normal dispersion femtosecond supercontinuum generation. *Scientific Reports, 8*, 6579.

Gordon, J. P. (1986). Theory of the soliton self-frequency shift. *Optics Letters, 11*, 662.

Gu, X., Xu, L., Kimmel, M., Zeek, E., O'Shea, P., Shreenath, A. P., Trebino, R., & Windeler, R. S. (2002). Frequency-resolved optical gating and single-shot spectral measurements reveal fine structure in microstructure-fiber continuum. *Optics Letters, 27*, 1174.

Hansen, K. (2003). Dispersion flattened hybrid-core nonlinear photonic crystal fiber. *Optics Express, 11*, 1503.

Hartung, A., Heidt, A. M., & Bartelt, H. (2011a). Design of all-normal dispersion microstructured optical fibers for pulse-preserving supercontinuum generation. *Optics Express, 19*, 7742.

Hartung, A., Heidt, A. M., & Bartelt, H. (2011b). Pulse-preserving broadband visible supercontinuum generation in all-normal dispersion tapered suspended-core optical fibers. *Optics Express, 19*, 12275.

Hartung, A., Heidt, A. M., & Bartelt, H. (2012). Nanoscale all-normal dispersion optical fibers for coherent supercontinuum generation at ultraviolet wavelengths. *Optics Express, 20*, 13777.

Hartung, A., Bierlich, J., Lorenz, A., Kobelke, J., & Jäger, M. (2019). Design and fabrication of all-normal dispersion nanohole suspended-core fibers. *Journal of the Optical Society of America B: Optical Physics, 36*, 3404.

Heidt, A. M. (2009). Efficient adaptive step size method for the simulation of supercontinuum generation in optical fibers. *Journal of Lightwave Technology, 27*, 3984.

Heidt, A. M. (2010). Pulse preserving flat-top supercontinuum generation in all-normal dispersion photonic crystal fibers. *Journal of the Optical Society of America B: Optical Physics, 27*, 550.

Heidt, A. M., Hartung, A., Bosman, G. W., Krok, P., Rohwer, E. G., Schwoerer, H., & Bartelt, H. (2011a). Coherent octave spanning near-infrared and visible supercontinuum generation in all-normal dispersion photonic crystal fibers. *Optics Express, 19*, 3775.

Heidt, A. M., Rothhardt, J., Hartung, A., Bartelt, H., Rohwer, E. G., Limpert, J., & Tünnermann, A. (2011b). High quality sub-two cycle pulses from compression of supercontinuum generated in all-normal dispersion photonic crystal fiber. *Optics Express, 19*, 13873.

Heidt, A. M., Feehan, J. S., Price, J. H. V., & Feurer, T. (2017). Limits of coherent supercontinuum generation in normal dispersion fibers. *Journal of the Optical Society of America B: Optical Physics, 34*, 764.

Heidt, A. M., Hodasi, J. M., Rampur, A., Spangenberg, D.-M., Ryser, M., Klimczak, M., & Feurer, T. (2020). Low noise all-fiber amplification of a coherent supercontinuum at 2 μm and its limits imposed by polarization noise. *Scientific Reports, 10*, 16734.

Herdzik, K. P., Bourdakos, K. N., Johnson, P. B., Lister, A. P., Pitera, A. P., Guo, C.-Y., Horak, P., Richardson, D. J., Price, J. H., & Mahajan, S. (2020). Multimodal spectral focusing CARS and SFG microscopy with a tailored coherent continuum from a microstructured fiber. *Applied Physics B: Lasers and Optics, 126*, 84.

Herrmann, J., Griebner, U., Zhavoronkov, N., Husakou, A., Nickel, D., Knight, J., Wadsworth, W., Russell, P. S. J., & Korn, G. (2002). Experimental evidence for supercontinuum generation by fission of higher-order solitons in photonic crystal fibers. *Physical Review Letters, 88*, 173901.

Hilligsøe, K. M., Andersen, T., Paulsen, H., Nielsen, C., Mølmer, K., Keiding, S., Kristiansen, R., Hansen, K., & Larsen, J. (2004). Supercontinuum generation in a photonic crystal fiber with two zero dispersion wavelengths. *Optics Express, 12*, 1045.

Hooper, L. E., Mosley, P. J., Muir, A. C., Wadsworth, W. J., & Knight, J. C. (2011). Coherent supercontinuum generation in photonic crystal fiber with all-normal group velocity dispersion. *Optics Express, 19*, 4902.

Hori, T., Takayanagi, J., Nishizawa, N., & Goto, T. (2004). Flatly broadened, wideband and low noise supercontinuum generation in highly nonlinear hybrid fiber. *Optics Express, 12*, 317.

Hult, J. (2008). A fourth-order runge–kutta in the interaction picture method for simulating supercontinuum generation in optical fibers. *Journal of Lightwave Technology, 25*, 3770.

Humbert, G., Wadsworth, W., Leon-Saval, S., Knight, J., Birks, T., Russell, P. S. J., Lederer, M., Kopf, D., Wiesauer, K., Breuer, E., & Stifter, D. (2006). Supercontinuum generation system for optical coherence tomography based on tapered photonic crystal fibre. *Optics Express, 14*, 1596.

Jensen, M., Gonzalo, I. B., Engelsholm, R. D., Maria, M., Israelsen, N. M., Podoleanu, A., & Bang, O. (2019). Noise of supercontinuum sources in spectral domain optical coherence tomography. *Journal of the Optical Society of America B: Optical Physics, 36*, A154.

Jiang, X., Joly, N. Y., Finger, M. A., Babic, F., Wong, G. K., Travers, J. C., & Russell, P. S. J. (2015). Deep-ultraviolet to mid-infrared supercontinuum generated in solid-core ZBLAN photonic crystal fibre. *Nature Photonics, 9*, 133.

Kärtner, F. X. (Ed.). (2004). *Few-Cycle Laser Pulse Generation and Its Applications*. Springer.

Kearns, N. M., Jones, A. C., Kunz, M. B., Allen, R. T., Flach, J. T., & Zanni, M. T. (2019). Two-dimensional white-light spectroscopy using supercontinuum from an all-normal dispersion photonic crystal fiber pumped by a 70 MHz Yb fiber oscillator. *The Journal of Physical Chemistry. A, 123*, 3046.

Klimczak, M., Siwicki, B., Skibinski, P., Pysz, D., Stepien, R., Heidt, A. M., Radzewicz, C., & Buczynski, R. (2014). Coherent supercontinuum generation up to 2.3 μm in all-solid soft-glass photonic crystal fibers with flat all-normal dispersion. *Optics Express, 22*, 18824–18832.

Klimczak, M., Sobon, G., Kasztelanic, R., Abramski, K. M., & Buczynski, R. (2016). Direct comparison of shot-to-shot noise performance of all normal dispersion and anomalous dispersion supercontinuum pumped with sub-picosecond pulse fiber-based laser. *Scientific Reports, 6*, 19284.

Klimczak, M., Siwicki, B., Heidt, A., & Buczynski, R. (2017). Coherent supercontinuum generation in soft glass photonic crystal fibers. *Photonics Research, 5*, 710.

Knight, J. C. (2003). Photonic crystal fibers. *Nature, 424*, 847.

Knight, J. C., & Wadsworth, W. J. (2010). Silica fibres for supercontinuum generation. In J. M. Dudley & J. R. Taylor (Eds.), *Supercontinuum generation in optical fibers*. Cambridge University Press.

Koshiba, M., & Saitoh, K. (2004). Applicability of classical optical fiber theories to holey fibers. *Optics Letters, 29*, 1739.

Krausz, F., & Ivanov, M. (2009). Attosecond physics. *Reviews of Modern Physics, 81*, 163.

Krebs, M., Hädrich, S., Demmler, S., Rothhardt, J., Zaïr, A., Chipperfield, L., Limpert, J., & Tünnermann, A. (2013). Towards isolated attosecond pulses at megahertz repetition rates. *Nature Photonics, 7*, 555.

Kudlinski, A., George, A. K., Knight, J. C., Travers, J. C., Rulkov, A. B., Popov, S. V., & Taylor, J. R. (2006). Zero-dispersion wavelength decreasing photonic crystal fibers for ultraviolet-extended supercontinuum generation. *Optics Express, 14*, 5715.

Lin, C., & Stolen, R. H. (1976). New nanosecond continuum for excited-state spectroscopy. *Applied Physics Letters, 28*, 216.

Lin, C., Nguyen, V., & French, W. (1978). Wideband near-i.r. continuum (0.7–2.1 μm) generated in low-loss optical fibres. *Electronics Letters, 14*, 822.

Liu, Y., Tu, H., Benalcazar, W. A., Chaney, E. J., & Boppart, S. A. (2012a). Multimodal nonlinear microscopy by shaping a fiber supercontinuum from 900 to 1160 nm. *IEEE Journal of Selected Topics in Quantum Electronics, 18*, 1209.

Liu, Y., Tu, H., & Boppart, S. A. (2012b). Wave-breaking-extended fiber supercontinuum generation for high compression ratio transform-limited pulse compression. *Optics Letters, 37*, 2172.

Liu, Y., King, M. D., Tu, H., Zhao, Y., & Boppart, S. A. (2013). Broadband nonlinear vibrational spectroscopy by shaping a coherent fiber supercontinuum. *Optics Express, 21*, 8269.

Liu, Y., Zhao, Y., Lyngso, J., You, S., Wilson, W. L., Tu, H., & Boppart, S. A. (2015). Suppressing short-term polarization noise and related spectral decoherence in all-normal dispersion fiber supercontinuum generation. *J. Lightwave Technol. 33*, 1814.

Loredo-Trejo, A., Lopez-Dieguez, Y., Velazquez-Ibarra, L., Diez, A., Silvestre, E., Estudillo-Ayala, J. M., & Andres, M. V. (2019). Polarization modulation instability in all-normal dispersion microstructured optical fibers with quasi-continuous pump. *IEEE Photonics Journal, 11*, 7104208.

Markos, C., Travers, J.C., Abdolvand, A., Eggleton, B.J., & Bang, O. (2017). Hybrid photonic-crystal fiber. *Reviews of Modern Physics 89*, 45003.

Martynkien, T., Pysz, D., Stepien, R., & Buczynski, R. (2014). All-solid microstructured fiber with flat normal chromatic dispersion. *Optics Letters, 39*, 2342.

Mitschke, F. M., & Mollenauer, L. F. (1986). Discovery of the soliton self-frequency shift. *Optics Letters, 11*, 659.

Moon, S., & Kim, D. Y. (2006). Ultra-high-speed optical coherence tomography with a stretched pulse supercontinuum source. *Optics Express, 14*, 11575.

Nakazawa, M., Tamura, K., Kubota, H., & Yoshida, E. (1998). Coherence degradation in the process of supercontinuum generation in an optical fiber. *Optical Fiber Technology, 4*, 215.

Newbury, N., Washburn, B., Corwin, K., & Windeler, R. (2003). Noise amplification during supercontinuum generation in microstructure fiber. *Optics Letters, 28*, 944.

Nishizawa, N., & Takayanagi, J. (2007). Octave spanning high-quality super-continuum generation in all-fiber system. *Journal of the Optical Society of America B: Optical Physics, 24*, 1786.

Nishizawa, N., Chen, Y., Hsiung, P., Ippen, E. P., & Fujimoto, J. G. (2004). Real-time, ultrahigh-resolution, optical coherence tomography with an all-fiber, femtosecond fiber laser continuum at 1.5 μm. *Optics Letters, 29*, 2846.

Nishizawa, N., Niinomi, T., Nomura, Y., Jin, L., & Ozeki, Y. (2018). Octave spanning coherent supercontinuum comb generation based on Er-doped fiber lasers and their characterization. *IEEE Journal of Selected Topics in Quantum Electronics, 24*, 5100409.

Poletti, F., Feng, X., Ponzo, G. M., Petrovich, M. N., Loh, W. H., & Richardson, D. J. (2011). All-solid highly nonlinear single mode fibers with a tailored dispersion profile. *Optics Express, 19*, 66.

Prasad, P. N. (2003). *Introduction to Biophotonics*. Wiley.

Price, J. H., Monro, T. M., Ebendorff-Heidepriem, H., Poletti, F., Horak, P., Finazzi, V., Leong, J. Y., Petropoulos, P., Flanagan, J. C., Brambilla, G., Feng, X., & Richardson, D. J. (2007). Mid-IR supercontinuum generation from nonsilica microstructured optical fibers. *IEEE Journal of Selected Topics in Quantum Electronics, 13*, 738.

Price, J. H., Feng, X., Heidt, A. M., Brambilla, G., Horak, P., Poletti, F., Ponzo, G., Petropoulos, P., Petrovich, M., Shi, J., Ibsen, M., Loh, W. H., Rutt, H. N., & Richardson, D. J. (2012). Supercontinuum generation in non-silica fibers. *Optical Fiber Technology, 18*, 327.

Rampur, A., Stepanenko, Y., Stepniewski, G., Kardas, T., Dobrakowski, D., Spangenberg, D.-M., Feurer, T., Heidt, A., & Klimczak, M. (2019). Ultra low-noise coherent supercontinuum amplification and compression below 100 fs in an all-fiber polarization-maintaining thulium fiber amplifier. *Optics Express, 27*, 35041.

Rampur, A., Spangenberg, D.-M., Stepniewski, G., Dobrakowski, D., Tarnowski, K., Stefanska, K., Pazdzior, A., Mergo, P., Martynkien, T., Feurer, T., et al. (2020). Temporal fine structure of all-normal dispersion fiber supercontinuum pulses caused by non-ideal pump pulse shapes. *Optics Express, 28*, 16579.

Rao, D. S. S., Engelsholm, R. D., Gonzalo, I. B., Zhou, B., Bowen, P., Moselund, P. M., Bang, O., & Bache, M. (2019). Ultra-low-noise supercontinuum generation with a flat near-zero normal dispersion fiber. *Optics Letters, 44*, 2216.

Rao, D. S. S., Jensen, M., Grüner-Nielsen, L., Olsen, J. T., Heiduschka, P., Kemper, B., Schnekenburger, J., Glud, M., Mogensen, M., Israelsen, N. M., & Bang, O. (2020). *Shot-noise limited, supercontinuum based optical coherence tomography*, arXiv preprint arXiv:2010.05226.

Rieznik, A. A., Heidt, A. M., Konig, P. G., Bettachini, V. A., & Grosz, D. F. (2012). Optimum integration procedures for supercontinuum simulation. *IEEE Photonics Journal, 4*, 552.

Rothenberg, J. E. (1990). Modulational instability for normal dispersion. *Physical Review A, 42*, 682.

Rothhardt, J., Demmler, S., Hädrich, S., Limpert, J., & Tünnermann, A. (2012). Octave-spanning OPCPA system delivering CEP-stable few-cycle pulses and 22 W of average power at 1 MHz repetition rate. *Optics Express, 20*, 10870.

Rothhardt, J., Hädrich, S., Delagnes, J., Cormier, E., & Limpert, J. (2017). High average power near-infrared few-cycle lasers. *Laser & Photonics Reviews, 11*, 1700043.

Saitoh, K., & Koshiba, M. (2005). Empirical relations for simple design of photonic crystal fibers. *Optics Express, 13*, 267.

Schenkel, B., Paschotta, R., & Keller, U. (2005). Pulse compression with super- continuum generation in microstructure fibers. *Journal of the Optical Society of America B: Optical Physics, 22*, 687.

Shabahang, S., Tao, G., Kaufman, J. J., & Abouraddy, A. F. (2013). Dispersion characterization of chalcogenide bulk glass, composite fibers, and robust nanotapers. *Journal of the Optical Society of America B: Optical Physics, 30*, 2498.

Sierro, B., & Heidt, A. M. (2020). Noise amplification in all-normal dispersion fiber supercontinuum generation and its impact on ultrafast photonics applications. *OSA Continuum, 3*, 2347.

Smith, R. G. (1972). Optical power handling capacity of low loss optical fibers as determined by stimulated Raman and Brillouin scattering. *Applied Optics, 11*, 2489.

Stark, S. P., Travers, J. C., & Russell, P. S. J. (2012). Extreme supercontinuum generation to the deep UV. *Optics Letters, 37*, 770.

Stepien, R., Cimek, J., Pysz, D., Kujawa, I., Klimczak, M., & Buczynski, R. (2014). Soft glasses for photonic crystal fibers and microstructured optical components. *Optical Engineering, 53*, 071815.

Stolen, R. H., & Lin, C. (1978). Self-phase-modulation in silica optical fibers. *Physical Review A, 17*, 1448.

Tarnowski, K., Martynkien, T., Mergo, P., Poturaj, K., Anuszkiewicz, A., Bejot, P., Billard, F., Faucher, O., Kibler, B., & Urbanczyk, W. (2017). Polarized all-normal dispersion supercontinuum reaching 2.5 μm generated in a birefringent microstructured silica fiber. *Optics Express, 25*, 27452.

Tarnowski, K., Martynkien, T., Mergo, P., Sotor, J., & Sobon, G. (2019). Compact all-fiber source of coherent linearly polarized octave-spanning supercontinuum based on normal dispersion silica fiber. *Scientific Reports, 9*, 12313.

Taylor, A. J., Gibson, R. B., & Roberts, J. P. (1988). Two-photon absorption at 248 nm in ultraviolet window materials. *Optics Letters, 13*, 814.

Travers, J. (2010). Blue extension of optical fibre supercontinuum generation. *Journal of Optics, 12*, 113001.

Tse, M.-L. V., Horak, P., Poletti, F., Broderick, N. G., Price, J. H., Hayes, J. R., & Richardson, D. J. (2006). Supercontinuum generation at 1.06 μm in holey fibers with dispersion flattened profiles. *Optics Express, 14*, 4445.

Tu, H., & Boppart, S. A. (2013). Coherent fiber supercontinuum for biophotonics. *Laser & Photonics Reviews, 7*, 628.

Tu, H., & Boppart, S. A. (2014). Coherent anti-Stokes Raman scattering microscopy: Overcoming technical barriers for clinical translation. *Journal of Biophotonics, 7*, 9.

Tu, H., Liu, Y., Lægsgaard, J., Sharma, U., Siegel, M., Kopf, D., & Boppart, S. A. (2010). Scalar generalized nonlinear Schrödinger equation-quantified continuum generation in an all-normal dispersion photonic crystal fiber for broadband coherent optical sources. *Optics Express, 18*, 27872.

Tu, H., Liu, Y., Turchinovich, D., & Boppart, S. A. (2011). Compression of fiber supercontinuum pulses to the Fourier-limit in a high-numerical-aperture focus. *Optics Letters, 36*, 2315.

Tu, H., Liu, Y., Lægsgaard, J., Turchinovich, D., Siegel, M., Kopf, D., Li, H., Gunaratne, T., & Boppart, S. (2012a). Cross-validation of theoretically quantified fiber continuum generation and absolute pulse measurement by MIIPS for a broadband coherently controlled optical source. *Applied Physics B: Lasers and Optics, 106*, 379.

Tu, H., Liu, Y., Liu, X., Turchinovich, D., Lægsgaard, J., & Boppart, S. A. (2012b). Nonlinear polarization dynamics in a weakly birefringent all-normal dispersion photonic crystal fiber: Toward a practical coherent fiber supercontinuum laser. *Optics Express, 20*, 1113.

Tu, H., Liu, Y., Turchinovich, D., Marjanovic, M., Lyngsø, J. K., Lægsgaard, J., Chaney, E. J., Zhao, Y., You, S., Wilson, W. L., et al. (2016). Stain-free histopathology by programmable supercontinuum pulses. *Nature Photonics, 10*, 534.

Vanholsbeeck, F., Emplit, P., & Coen, S. (2003). Complete experimental characterization of the influence of parametric four-wave mixing on stimulated Raman gain. *Optics Letters, 28*, 1960.

Viljoen, R., Neethling, P., Spangenberg, D., Heidt, A., Frey, H.-M., Feurer, T., & Rohwer, E. (2020). Implementation of temporal ptychography algorithm, i^2PIE, for improved single-beam coherent anti-Stokes Raman scattering measurements. *Journal of the Optical Society of America B: Optical Physics, 37*, A259.

Wabnitz, S. (1988). Modulational polarization instability of light in a nonlinear birefringent dispersive medium. *Physical Review A, 38*, 2018.

Wang, Y., Dai, S., Li, G., Xu, D., You, C., Han, X., Zhang, P., Wang, X., & Xu, P. (2017). 1.4–7.2 μm broadband supercontinuum generation in an As-S chalcogenide tapered fiber pumped in the normal dispersion regime. *Optics Letters, 42*, 3458.

Wildanger, D., Rittweger, E., Kastrup, L., & Hell, S. W. (2008). STED microscopy with a supercontinuum laser source. *Optics Express, 16*, 9614.

Winful, H. G. (1986). Polarization instabilities in birefringent nonlinear media: Application to fiber-optic devices. *Optics Letters, 11*, 33.

Zhang, N., Peng, X., Wang, Y., Dai, S., Yuan, Y., Su, J., Li, G., Zhang, P., Yang, P., & Wang, X. (2019). Ultrabroadband and coherent mid-infrared supercontinuum generation in Te-based chalcogenide tapered fiber with all-normal dispersion. *Opt Express 27*, 10311.

Chapter 7
Self-Focusing and Continuum Generation in Gases

Paul B. Corkum and Claude Rolland

Abstract The chapter focuses on nonlinear optics effects produced in gases; in particular, continuum generation with 100 femtoseconds for different pressures arising from gas ionization and n_2 in Xenon. At high pressures continuum generation, self-focusing, and conical emission occur similar to condense matter.

Keywords Gases · Nonlinear susceptibility · χ^3 · Kerr index · n_2 · fs · SPM · Pressure dependence · High pressures · Multiphoton · Ionization · Plasmas · Self-focusing · Xenon · Self-phase modulation · Continuum · Conical emission · 4 wave · Moving-focus model · n_2E^2

7.1 Introduction

This book attests to the fact continuum generation has become both technically and conceptually important. Discovered in 1970 (Alfano & Shapiro, 1970a, b), continuum generation is a ubiquitous response of transparent materials (liquids, solids, and gases) to high-power, ultrashort-pulse radiation. This chapter highlights some of these aspects while presenting the sometimes unique characteristics of continuum generation in gases. In addition, we introduce some related results that reflect on the light-atom interaction at high intensities.

Gases are ideal media in which to study nonlinear phenomena, such as continuum generation. The choice of low-density rare gases makes the nonlinearity simple since the susceptibility will be purely electronic in nature. Experimentally, the strength of the nonlinearity can be precisely controlled by varying the gas pressure. Gases are ideal in another way. There is a strong conceptual link between the

P. B. Corkum (✉)
Department of Physics, University of Ottawa, Ottawa, ON, Canada
e-mail: pcorkum@uOttawa.ca

C. Rolland
Division of Physics, National Research Council of Canada, Ottawa, ON, Canada

R. R. Alfano (ed.), *The Supercontinuum Laser Source*,
https://doi.org/10.1007/978-3-031-06197-4_7

susceptibility and the transition probability. Since there is a lot of emphasis, at present, on understanding multiphoton ionization in rare gases,[1] concepts being developed in this area can provide a framework for further advances of nonlinear optics in general and continuum generation in particular.

In gases, the lowest-order contribution to the nonlinear susceptibility is $\chi^{(3)}$. The magnitude of the nonresonant $\chi^{(3)}$ for the rare gases (Lehmeier et al., 1985) and for many molecular gases is well known. For xenon $n^2 = \left(3\chi^{(3)}_{1111}/n^0 = 2.4 \times 10^{-25}\ \mathrm{m^2/V^2\ atm}\right)$, where the refractive index n is given by $n = n_0 + n_2E^2 + \cdots$, E being the rms electric field. $\chi^{(3)}$ is proportional to the gas pressure.

This chapter is organized around the pressure-dependent strength of the nonlinearity. Much of the content originates from six experimental papers (Corkum et al., 1986a, b; Corkum & Rolland, 1987, 1988a, b; Chin et al., 1988) describing related work at the National Research Council of Canada.

Section 7.2 discusses the aspects of the experiment that are common to all parts of the chapter.

Section 7.3 describes the interaction of ultrashort pulses with very low-pressure gases. Low pressure ensures that nonlinear optics plays no role in the interaction (Corkum & Rolland, 1988a; Chin et al., 1988). This allows the ionization properties of xenon to be established. We will see that relatively high intensities are required to ionize gases with ultrashort pulses (~100 fs). In this way, we establish an upper intensity limit for the nonlinear interaction in a purely atomic system.

Section 7.3 also introduces the concept of transient resonances. Although transient resonances are a characteristic of the interaction of ultrashort pulses with matter in the intensity and wavelength range discussed in this chapter, their role in multiphoton ionization depends on the pulse duration.

As the gas pressure is increased, we enter the traditional realm of nonlinear optics. If the intensity for the production of significant plasma is not exceeded, changes to the spectrum of the pulse can be investigated under conditions where self-phase modulation is the dominant mechanism. We will see in Sect. 7.4 that high-order nonlinear terms must contribute to the spectral bandwidth if the laser intensity reaches 10^{13} W/cm^2 or higher (Corkum & Rolland, 1988b).

A qualitative explanation of why high-order terms must contribute to self-phase modulation is given in Sect. 7.5.

At still higher pressures, the region of continuum generation (Corkum et al., 1986a, b) and self-focusing (Corkum & Rolland, 1988b) is reached. Section 7.6.1 describes the spectral aspects of continua in gases. In particular, it shows that the spectra are similar for condensed media and for gases.

The spatial characteristics of continuum generation are particularly striking (Corkum & Rolland, 1988b). These are described in Sect. 7.6.2 with special

[1] See, for example, papers in *Multiphoton Ionization of Atoms* (S.L. Chin and P. Lambropoulos, eds.), Academic Press, New York (1984), and special issue on Multielectron Excitation of Atoms, J. Opt. Soc. Am. **B4**, no. 5 (1987).

emphasis on the role of self-focusing in continuum generation. There is a wide range of conditions over which continua are produced with virtually the same beam divergence as the incident diffraction-limited beam (Corkum & Rolland, 1987, 1988b). As the intensity or the gas pressure is increased, conical emission is observed.

7.2 Experimental Aspects

Pulses of three different durations (22, ~90, and ~900 fs full width at half maximum (FWHM)) were used in various parts of the experiment. This section discusses the experimental aspects that are common to all parts of the chapter. Each subsection includes experimental details of specific interest.

Laser pulses were produced by amplifying the output of either a spectrally filtered synchronously pumped dye laser (900 fs) or a colliding-pulse mode-locked dye laser (90 fs). The temporal, spatial, and spectral characteristics of the pulses have been fully described (Corkum & Rolland, 1988a; Rolland & Corkum, 1986). The wavelength of the 900-fs pulse was centered at 616 nm, and its bandwidth ($\Delta\nu$) was slightly greater than the transform limit ($\Delta t\ \Delta\nu = 0.52$; Δt is the FWHM pulse duration). The 90-fs pulse was centered at 625 nm and had $\Delta t\ \Delta\nu = 0.5$. The pulse durations were measured by autocorrelation and fit by a sech^2 (90 and 22 fs) or to a Gaussian (900 fs) pulse shape. After amplification the 90- and 900-fs pulses were spatially filtered to ensure diffraction-limited beam profiles.

The 22-fs pulses were created from the 90-fs pulses using large-aperture pulse compression techniques (Rolland & Corkum, 1988). The resulting 100-μJ pulses were diffraction limited with a signal-to-background power contrast ratio of approximately 30:1 (5:1 in energy). Compensation for the dispersion in all optical elements (lenses, windows, beam splitters, etc.) was accomplished by predispersing the pulse. Thus, the pulse measured 22 fs only in the target chamber and at the autocorrelation crystal. Since the 350-Å bandwidth of the 22-fs pulse gives rise to serious chromatic aberration in a single-element lens, an achromatic lens ($f = 14.3$ cm) was used to focus the pulses into the vacuum chamber (and onto the autocorrelation crystal).

All focal spot measurements were made by either scanning a pinhole (900 and 90 fs) through the focus or observing the portion of the energy transmitted through a pinhole (22 fs) of known diameter. Within the accuracy of the scans, the beam profiles were Gaussian.

7.3 Multiphoton Ionization

Some time ago it was proposed (Bloembergen, 1973) that ionization could play a major role in continuum generation though a time-dependent change in the plasma density. Plasma density changes impress a frequency chirp on a transmitted pulse.

However, to influence continuum generation (Corkum et al., 1986a, b) even to a small degree by plasma production, there is a price to pay in energy absorption and in the distortion of the spatial beam profile (Corkum & Rolland, 1988b). Since we will show that these signatures of plasma production are not observed, we can conclude that ionization plays no role in gaseous continuum generation. The absence of ionization can be used to establish a maximum intensity in the laser focus where the continuum is being generated and hence the maximum value of $\eta_2 E^2$.

Continuum experiments were the first to indicate that it is difficult to ionize xenon and krypton with ultrashort pulses (Corkum et al., 1986a, b) relative to extrapolations of 0.53-μm, 1.06-μm experiments (l'Huillier et al., 1983) (25 ps). Since the ionization threshold is a major uncertainty in continuum generation, we have performed two experiments (Corkum & Rolland, 1988a; Chin et al., 1988) whose specific aim was to study multiphoton ionization. The more recent and more quantitative of these is described in this section (Chin et al., 1988).

Femtosecond pulses were focused into a vacuum cell filled with $\sim 4 \times 10^{-6}$ torr of xenon. Ions were extracted with an ~80-V/cm static field into a time-of-flight mass spectrometer. Data were obtained using a microcomputer, coupled to a boxcar integrator that was programmed to accept only laser pulses within a narrow energy range (±2.5%). The computer recorded and averaged the associated ion signals. The intensity in the vacuum chamber was varied by rotating a λ/2 plate placed in front of a polarizer (reflection from a Brewster's angle germanium plate was used as a dispersion-free polarization selector for the 22-fs pulse).

Figure 7.1 is a graph of the number of ions as a function of the peak laser intensity for both rare gases and all three laser pulse durations. (Higher ionization states were observed but not plotted since they were too weak.) The solid curves were obtained from a modified Keldysh theory (Szöke, 1988). Although we did not measure the absolute number of ions, we estimate the threshold sensitivity (the lowest ion signals in Fig. 7.1) of our ion collector to be approximately 10 ions. The relative scaling between experimental and calculated ion signals for Xe (Fig. 7.1) is consistent with this estimate.

We performed this experiment to find the intensity at which ionization would need to be considered in nonlinear optics experiments. Not only does Fig. 7.1 answer this question qualitatively, but the agreement between theory and experiment allows us to make quantitative predictions. However, the agreement raises an important issue. How can a Keldysh theory, which assumes that resonances are unimportant, be consistent with electron spectral measurements (Freeman et al., 1987) which indicate that resonances play a major role in ionization? Because of the importance of this issue for nonlinear optics, we discuss it below with respect to ionization and, in Sect. 7.5, with respect to high-order nonlinear optics.

An important feature of the high-power light-atom interactions is the ac Stark shift. At $I = 10^{13}$ W/cm^2, the laser field exceeds the atomic field (of hydrogen) for all radii greater than $R = 4$ Å. At this radius the atomic potential is 3.8 eV below the ionization potential. For $R > 4$ Å, it is appropriate to consider the electron oscillating in the laser field as the lowest-order solution and the atomic field as a perturbation. Nearly all excited states, therefore, have an energy of oscillations (ac Stark shift)

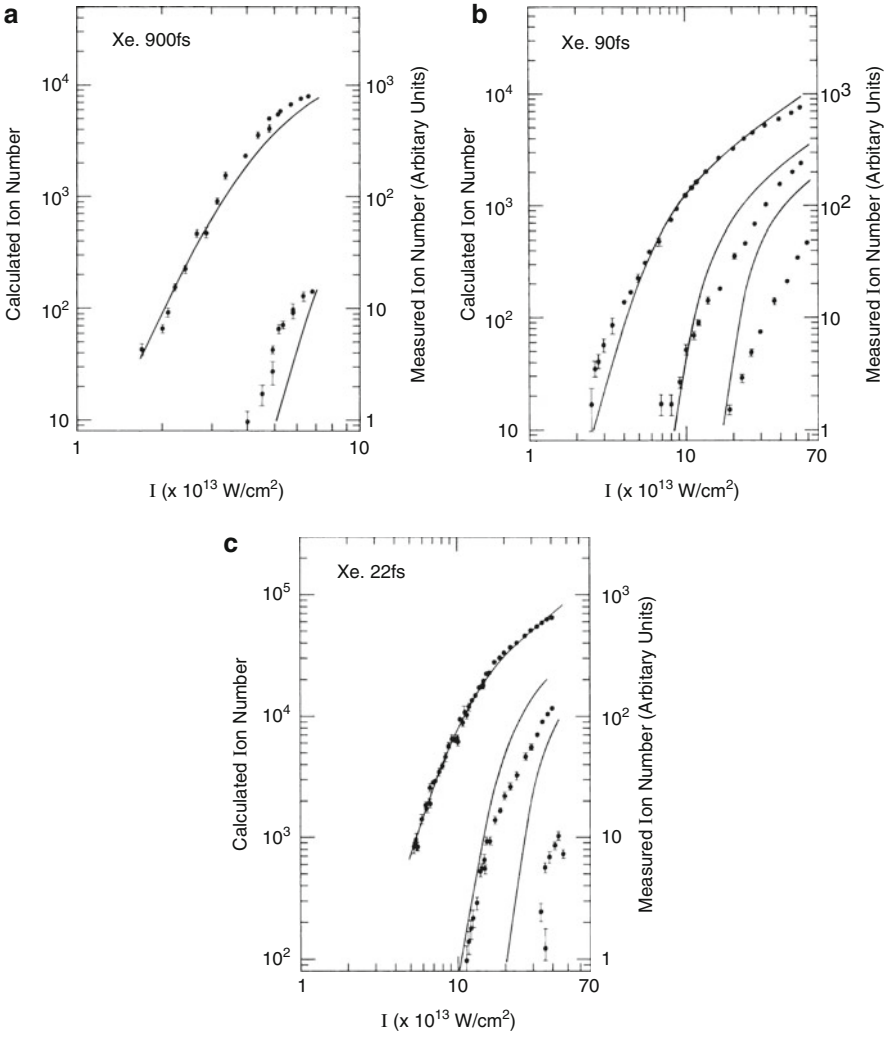

Fig. 7.1 Ion yield of Xe for 900-, 90-, and 22-fs pulses. The solid curves are calculated from a modified Keldysh theory (Szöke, 1988). The calculations give an absolute number of ions for the measured focal geometry and the neutral gas density. The experimental number of ions is plotted in relative units. The data have been positioned on the graph so as to emphasize the agreement between experiment and theory. The error bars show the standard error of the experimental data

approximately equal to the ponderomotive potential ($U_{\text{osc}} = (qE)^2/2m\omega^2$ where q is the electronic charge, ω is the laser angular frequency, and m is the electron mass). At 10^{13} W/cm^2 and 620 nm, the ponderomotive potential is approximately 0.4 eV. Thus, resonances are transiently produced, and resonant enhancement of high-order terms in the susceptibility will occur.

In view of the transient resonance induced in the medium, we might expect resonances always to be important. However, small deviations from Keldysh models appear only at relatively low intensities. Transient resonances appear to play a significant role in the overall ionization rate over, at most, a limited intensity/time range. (Note that detailed electron spectral measurements have so far been performed only in the 1–3 $\times$ 10^{13} W/cm^2 intensity range with ~500-fs pulses (Freeman et al., 1987).)

To understand why the contributions of transient resonances to ultrashort pulse ionization should be so small, consider just how transient these resonances can be. Assuming that all high-lying states move with the ponderomotive potential, we can write the maximum rate of change of the ponderomotive shift as $dU/dt)_{\max} = 2\sqrt{2}U_0\left(\ln(0.5)^{1/2}/\Delta t(0.5)\right)$ where U_0 is the maximum value of the ponderomotive shift during the pulse and a Gaussian pulse shape has been assumed. In the case of the 90-fs pulse with a characteristic peak intensity of 10^{14} W/cm^2, $dU/dt)_{\max} = 0.1$ eV/optical cycle. In the even more extreme case of the 22-fs pulse, the same peak intensity gives $dU/dt)_{\max} = 0.4$ eV/optical cycle.

The significance of such large ponderomotive shifts can be seen by considering a two-level system. For a two-level system, both the pulse duration dependence and the intensity dependence of the dephasing between the transition (transition frequency = ω_{ab}) and the near-resonant harmonic of the laser frequency can be estimated. For a constantly shifting transition, $\omega_{ab} + (dU/dt)t/h$, the dephasing time (T) is given by the condition that $\delta\phi \sim 2\pi$. That is, $T \sim (2\ h/dU/dt)^{1/2}$ where dU/dt is assumed constant. For a 90-fs pulse at 10^{14} W/cm^2, $T \sim 13$ fs. At the same intensity $T \sim 6$ fs for a 22-fs pulse. Resonances that last only a few cycles are hardly resonances at all and can be expected to have only minor effects on the overall ionization rate. Only for relatively small dU/dt can transient resonances play an important role. They may account for the deviations of the experimental and calculated curves observed in the 900-fs and low-power 90-fs xenon results.

The above discussion does not imply that transient resonances cannot lead to observable nonlinear optical consequences. In fact, nonlinear optics may provide one of the best methods of observing transient resonances.

In summary, these experiments show that ionization will be barely significant for 90-fs pulses at intensities of 10^{13} W/cm^2. In addition, the slopes of the ion curves in Fig. 7.1 indicate that a lowest-order perturbation expansion for the transition rate (and, therefore, the susceptibility) will be incomplete for intensities greater than ~3 $\times$ 10^{13} W/cm^2 for 0.6-μm light. This intensity can be used to estimate the maximum value of $\eta_2 E^2$ that is experimentally accessible with 90-fs pulses.

7.4 Self-Phase Modulation

One of the most studied nonlinear processes with ultrashort pulses is self-phase modulation. It is the basis of optical pulse compression, which is widely used in femtosecond technology. In many cases continuum generation is believed to

be an extreme version of self-phase modulation. Thus, it seems natural to adjust the strength of the nonlinearity by varying the gas pressure so that only modest self-phase modulation occurs. We can then follow the magnitude of the spectral broadening as the intensity or the nonlinearity is increased. Analogous experiments can be performed in fibers by increasing the length of the fiber.

Self-phase modulation is more complex in unbounded media than in fibers because, in unbounded media, self-phase modulation is inescapably related to self-focusing. (This relationship ensured that pulse compression based on self-phase modulation remained a curiosity until fiber compression became available.) It is possible to minimize the effects of self-focusing by keeping the medium shorter (Rolland & Corkum, 1988; Fork et al., 1983) than the self-focusing length. High-power pulse compression experiments use precisely this technique to control self-focusing (Rolland & Corkum, 1988). However, long before the self-phase modulation has become strong enough to generate continua, the beam propagation can no longer be controlled (Rolland & Corkum, 1988). In spite of this complexity, most continua are produced in long, unbounded media. Much of the remainder of the chapter addresses some of the physics issues associated with continuum production in this kind of medium.

The self-phase modulation experiment (Corkum & Rolland, 1988b) was performed with the 90-fs, 625-nm pulse with a maximum energy of ~500 μJ. A vacuum spatial filter with aperture diameter less than the diffraction limit of the incident beam produced an Airy pattern from which the central maximum was selected with an iris. The resulting diffraction-limited beam was focused into a gas cell that was filled to s maximum pressure of 40 atm. We report here mainly on the results obtained with xenon. However, where other gases have been investigated, we have found similar behavior.

As the gas pressure or laser power is increased, spectral broadening due to self-phase modulation is observed. In the η_2 limit (i.e., terms of higher order than $\eta_2 E^2$ are negligible) and neglecting dispersion, the spectral width depends only on the laser power:

$$\delta\lambda)_{\max} \sim \frac{8\sqrt{2}\eta_2 P_0}{c^2 \varepsilon_0 \tau \ \exp(0.5)} + \delta\lambda)_{\text{init}}, \tag{7.1}$$

where the power in the pulse is given by $P = P_0 e^{-(t/\tau)^2}$ and $\delta\lambda)_{\max}$ and $\delta\lambda)_{\text{init}}$ are the maximum and initial bandwidth of the pulse, respectively. All other symbols have their conventional meaning. The factor exp(0.5) arises because the maximum broadening for a Gaussian pulse occurs at $t = \tau/\sqrt{2}$. It will be present in Eq. (7.2) for the same reason. We can evaluate[2] $\delta\lambda)_{\max}$ for $\eta_2 = 2.4 \times 10^{-25}$ m^2/V^2 atm and obtain $\delta\lambda)_{\max} = 3.9 \times 10^{-7}$ Å/W atm. Equation (7.1) is valid only below the self-focusing threshold.

[2] η_2 of xenon at atmospheric pressure was erroneously reported to be $\eta_2 = 4 \times 10^{-26}$ m_2/V_2 in Corkum et al. (1986a, b).

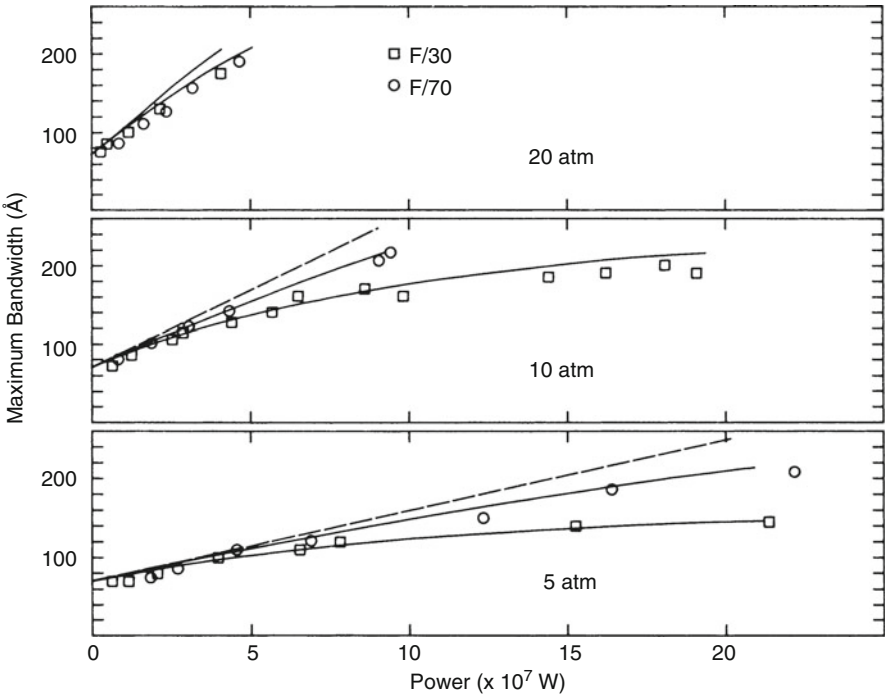

Fig. 7.2 Spectral width of the radiation transmitted through a cell filled with 5, 10, and 20 atm of xenon as a function of the peak laser power. The circles and squares represent data obtained with an *F*/70 and an *F*/30 lens, respectively. The solid curves are plots of Eq. (7.2) with a saturation intensity of 10^{13} W/cm^2 corresponding to 1.5×10^8 W for the *F*/30 lens ($\omega_0 = 21\ \mu$m)

Equation (7.1) shows that modifications of the nonlinearity can be observed through an intensity dependence of the spectral broadening. The results obtained with two different focusing lenses (*F*/70 and *F*/30) and a selection of pressures are presented in Fig. 7.2. In all cases, the power was maintained below the self-focusing threshold. The solid lines are a fit to the experimental data using Eq. (7.2) and a saturation intensity of $I_{\text{sat}} = 10^{13}$ W/cm^2:

$$\delta\lambda)_{\max} = \frac{8\sqrt{2}P_0}{(2.1)c^2\varepsilon_0\tau\exp(0.5)}\left[\frac{\eta_2}{1 + I/\left(I_{\text{sat}}\exp(0.5)\right)}\right] + \delta\lambda_{\text{init}}. \tag{7.2}$$

In Fig. 7.1, the saturation intensity of 10^{13} W/cm^2 corresponds to a power of 1.5×10^8 W for the *F*/30 and 8×10^8 W for the *F*/70 lens. The dashed lines are obtained using Eq. (7.2) and $I_{\text{sat}} = \infty$. Compared to Eq. (7.1), a factor of 2.1 is required in the denominator of Eq. (7.2) to fit the data. This factor is attributed to uncertainties in the input parameters such as the value of η_2, the pulse shape and

duration (measured by autocorrelation), and approximations made in deriving Eq. (7.1).

Saturation-like behavior of the nonlinearity could be caused by plasma produced by ionization (Corkum & Rolland, 1988b). There are four experimental reasons to believe that saturation is a fundamental phenomenon, not directly related to ionization:

1. At 10^{13} W/cm^2, sufficient ionization to modify the beam propagation by one diffraction-limited beam divergence, or to modify the spectrum measurably, would require ~25% of the beam energy. We measure an absorption of less than 3%.
2. Ionization would produce asymmetric self-phase modulation since the plasma would most affect the trailing region of the pulse. We observe a nearly symmetrical spectrum.
3. Figure 7.1 shows that insignificant plasma density is produced by $I < 3 \times 10^{13}$ W/cm^2.
4. Ionization would produce irreversible distortion of the transmitted beam profile. In fact, beam distortion is frequently used as a diagnostic of ionization (Corkum & Rolland, 1988a; Guha et al., 1985). We see little beam distortion.

7.5 Saturation of the Nonlinear Response in Gases

Since the nonlinear response is not modified by ionization, we must consider other explanations. For xenon and 0.6-μm light, the first excited state is 4.2 photon energies above the ground state. Any pulse duration or intensity-dependent changes must come from higher-order terms. In the absence of resonances, high-order terms should contribute to the nonlinear response approximately in the ratio $\chi^{(3)}E^2/\chi^{(1)}$. At 10^{13} W/cm^2, the ratio is ~0.04. To explain the observations in Fig. 7.2, resonant enhancement is required, and, as we have already indicated in Sect. 7.3, resonant enhancements are inevitable.

In discussing transient resonances, we have already pointed out that bound carriers in a high-lying resonant level respond as free electrons. It was just this fact that required that the ac Stark shift be equal to the ponderomotive potential. These bound electrons *must* reduce the refractive index as would truly free electrons. Since the high-lying states are only transiently resonant, they are only virtually occupied. Thus, aside from resonantly enhanced ionization, which is discussed below, the reduced refractive index need not be associated with net absorption from the beam. The change in refractive index due to bound electrons in high-lying levels is equivalent to $\eta_2 E^2$ when only 10^{-3} of the ground-state population is in these levels. (It is interesting to note that the connection between the ac Stark shift and the susceptibility, implicit in this description, can also be shown for a weakly driven two-level system (Delone & Krainov, 1985)).

It is essential to consider whether a transiently resonant population of 10^{-3} is consistent with low ionization levels, since transiently resonant states in xenon lie within one or two photon energies of the continuum. Resonantly enhanced ionization of xenon has been observed in multiphoton ionization experiments with ~500-fs pulses (Freeman et al., 1987). If we assign a cross section (Mainfray & Manus, 1980) of $\sigma = 10^{-19}$ (10^{-20}) cm^2 to the single-photon ionization from a near-resonant state, we can calculate the ratio of resonantly excited electrons (N_e) to free electrons (N_i) at an intensity of 10^{13} W/cm^2 ($N_e/N_i = \hbar\omega/\sigma I\tau$). The ratio for a 90-fs pulse is ~3(30). Note the pulse duration scaling. Thus, the resonant population can exceed the free-electron population for ultrashort pulses.

It may seem that the small cross section used above is in contrast to what would be calculated from Keldysh-type theories (Szöke, 1988; Keldysh, 1965) for 10^{13} W/cm^2, assuming an ionization potential of <1 eV. This apparent discrepancy is explained by the fact that a transiently resonant electron is only weakly bound. Since an unbound electron cannot absorb photons from a plane electromagnetic wave, as we cross the boundary between an unbound and a weakly bound electron, we should not expect the electron to absorb photons readily. (In the long-wavelength limit, this is no longer valid because of the Lorentz force contribution to ionization.)

Values for σ are very poorly known experimentally, especially for levels near the continuum. Recent UV measurements (Landen et al., 1987) for the krypton $4p5d$ and $4p4d$ levels (1 and 1.7 eV below the continuum) yielded values of $\sigma = 3 \times 10^{-18}$ and 8×10^{-18} cm^{-2}, respectively. These results satisfy the trend of decreasing σ as the continuum is approached.

It is useful to reexpress the above discussion in more general terms. Many high-order nonlinear terms will be enhanced by transient resonance due to the dense packing of levels at high energies. Our qualitative description of the plasmalike response of the electron is equivalent to summing a series of nonlinear terms. It should be emphasized that transient resonances will influence all nonlinear processes in this intensity range. Their effects could well exceed the nonresonant contributions to the susceptibility. Note that enhancement of the nonlinear response is also observed in partially ionized plasma due to excited state population (Gladkov et al., 1987).

7.6 Self-Focusing: $\chi^{(3)}$ Becomes Large

The modification to the nonlinear response of the medium that we have described has important consequences for self-focusing. In Fig. 7.2 the highest-intensity data points (for a given F-number and gas pressure) give approximately the threshold above which the nature of the spectral broadening changes nearly discontinuously. For F/70 optics this value is approximately a factor of 2 above the calculated self-focusing threshold. A factor of 2 discrepancy is consistent with the correction factor of 2.1 that we required to make Eq. (7.2) agree with experimental data. The critical power is clearly not a useful parameter if the intensity at the geometric focus exceeds 10^{13} W/cm^2.

To ensure that self-focusing will be initiated, all remaining results are taken with large F-number optics ($F/200$).

7.6.1 Spectral Characteristics of Gaseous Continua

When the beam intensity is increased above that plotted in Fig. 7.2, the wavelength scale of the spectral broadening increases dramatically. In Fig. 7.3 typical multishot spectra are plotted for the 70-fs and 2-ps pulses (with characteristics similar to the 90- and 900-fs pulses described previously) transmitted through a gas cell filled with various gases. Shown in Fig. 7.3a are spectra for 30 atm of xenon illuminated with 70-fs and 2-ps pulses, respectively. Figure 7.3b shows spectra for 40 atm of N_2 (2 ps) and 38 atm of H_2 (70 fs). The spectra in Fig. 7.3 are typical of spectra obtained with all gases that we have investigated, provided only that the laser intensity was sufficient to exceed the critical power for self-focusing.

The similarity in the blue spectral component for all the curves in Fig. 7.3 should be noted. In fact, the blue spectral component is nearly universal for all gases that produce continua regardless of the (above-threshold) intensity or pressure. (It is also typical of a chaotic spectrum (Ackerhalt et al., 1985).) The red component, however, varies with the laser and gas parameters. We have investigated the red cutoff only with CO_2 using femtosecond pulses. The maximum wavelength for 30 atm of CO_2 exceeded the 1.3-μm limit of our S1 photocathode. (Because of an orientational contribution to the nonlinearity, continua can be produced at a particularly low threshold intensity with picosecond pulses in CO_2.)

Figure 7.4 shows that spectral modulation is another characteristic of the spectrum of gaseous continua. Modulation has been noted previously on the single-shot spectra of gases (Glownia et al., 1986). Spectral modulation is a characteristic of continua from condensed media as well (Smith et al., 1977). Figure 7.4 illustrates the intensity and η_2 scaling of the spectral modulation of a xenon continuum as measured in the region of 450 nm. Figure 7.4a, b shows that the modulation frequency is reproducible from shot to shot. The modulation depth is not always as great as shown in Fig. 7.4. Figure 7.4c, d demonstrates that the modulation frequency varies with $\eta_2 E^2$ near the continuum threshold. However, in Fig. 7.4e–d, we see that the simple $\eta_2 E^2$ scaling is eventually lost at higher pressure-power products. In all cases, the modulation frequency increases further from the laser frequency. This behavior is in contrast with that expected for self-phase modulation (Smith et al., 1977).

The characteristics of gaseous continua described so far are similar to those of condensed-medium continua. However, the extra flexibility provided by pressure dependence of the nonlinearity allows issues like the $\eta_2 E^2$ dependence of the spectral modulation to be addressed. We will see that it also allows us to correlate self-focusing with continuum generation much more precisely than previously possible.

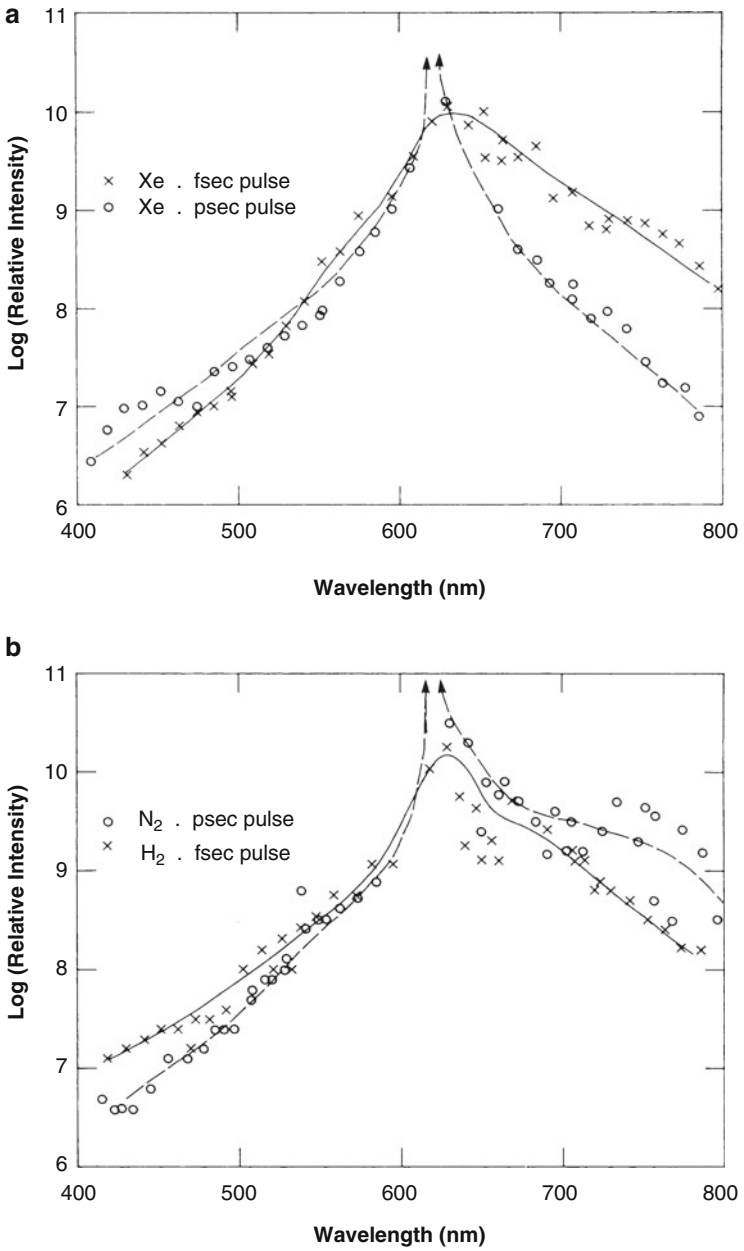

Fig. 7.3 Continuum spectra. (**a**) In xenon: $P = 30$ atm, $\Delta t = 70$ fs (crosses); $P = 15$ atm, $\Delta t = 2$ ps (circles). (**b**) In N_2, $P = 40$ atm; $\Delta t = 2$ ps (circles) in H_2, $P = 38$ atm; $\Delta t = 70$ fs (crosses)

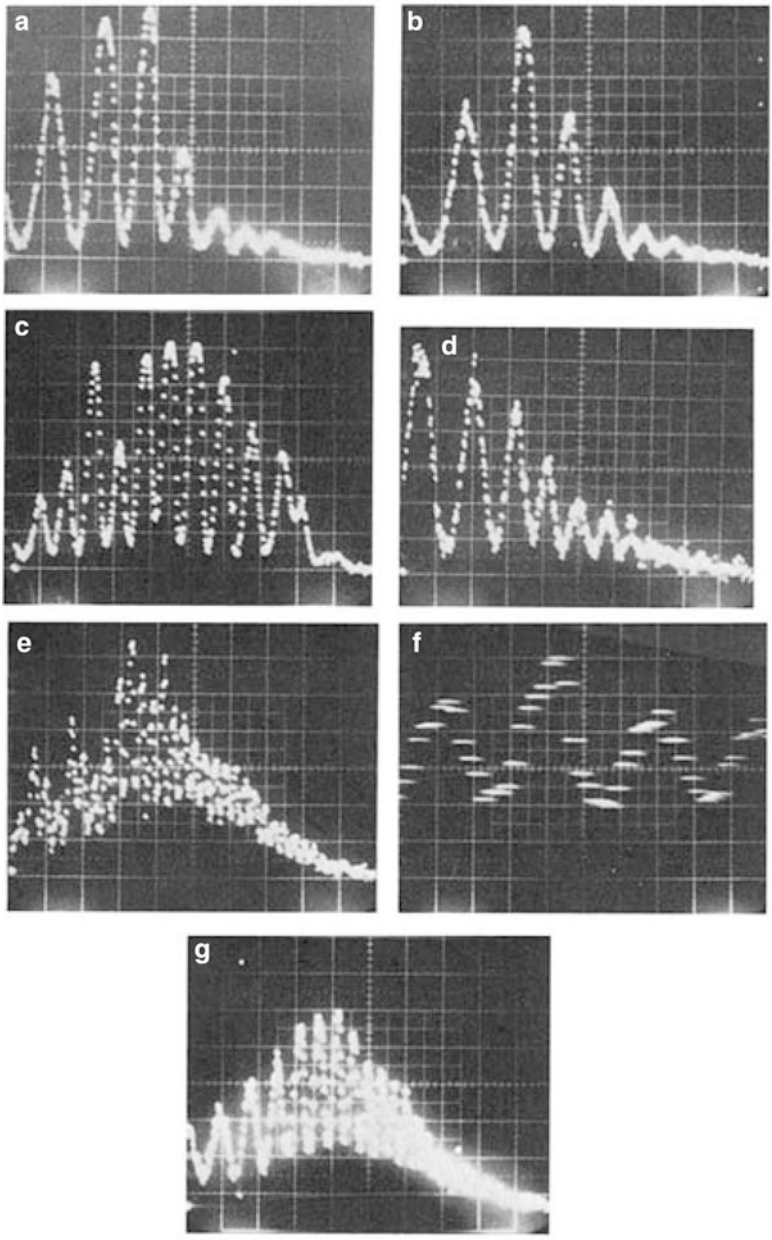

Fig. 7.4 Details of the single-shot continuum spectrum centered near $\lambda = 450$ nm illustrating the spectral modulation on the continuum. (The horizontal scale for all traces except (**f**) is 137 Å/div.) (**a**) and (**b**) (7 atm pressure of xenon) show the reproducibility of the spectral modulation. (**c**) and (**d**) (14 atm pressure of xenon) show the $\eta_2 E^2$ scaling of the spectral modulation. (**c**) was taken with the same laser power as (**a**) and (**b**). (**d**) was taken with one-half the laser power of (**a**)–(**c**). (**e**)–(**g**) (21 atm pressure of xenon) show that the $\eta_2 E^2$ scaling is not valid well above the continuum threshold. (**e**) and (**f**) were taken with the same laser power as (**a**)–(**c**). The wavelength scale in (**f**) has been expanded by a factor of 10. (**g**) was taken with one-third of the laser power of (**a**)–(**c**)

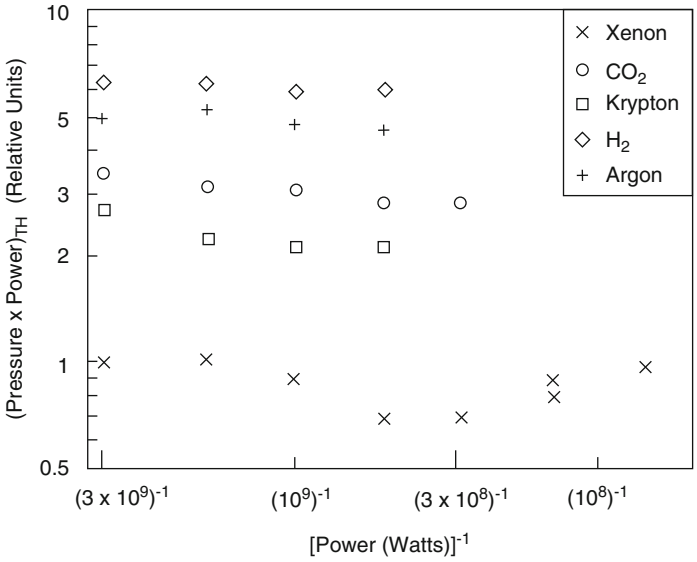

Fig. 7.5 Laser power multiplied by the gas pressure at the continuum threshold, plotted as a function of the inverse of the laser power for different gases

As already mentioned, continuum generation showed a sharp threshold, below which spectral broadening is described by Eq. (7.2) and above which full continua are produced. The threshold power for continuum generation equals the self-focusing threshold power to the accuracy to which the self-focusing threshold is known. The functional dependence of the continuum threshold on laser power, gas pressure, and the hyperpolarizability is also the same as that for self-focusing. This dependence is shown in Fig. 7.5, where the product of the gas pressure and the laser power at threshold for all gases investigated with the femtosecond pulse is plotted as a function of the laser power. Comparing the pressure-power products for each gas, we find that they are inversely proportional to the hyperpolarizabilites. Similar data were obtained (but are not plotted) with the picosecond pulse. For the rare gases and H_2, the picosecond data would fit on their respective lines in Fig. 7.5. Both N_2 and CO_2, however, have lower thresholds than would be indicated from their purely electronic nonlinearities. This is due to orientational effects that are important in both gases.

7.6.2 Spatial Characteristics of Gaseous Continua

One might expect that spatial changes in a beam that has experienced at least the onset of self-focusing would be severe. Considering that the spectrum of the

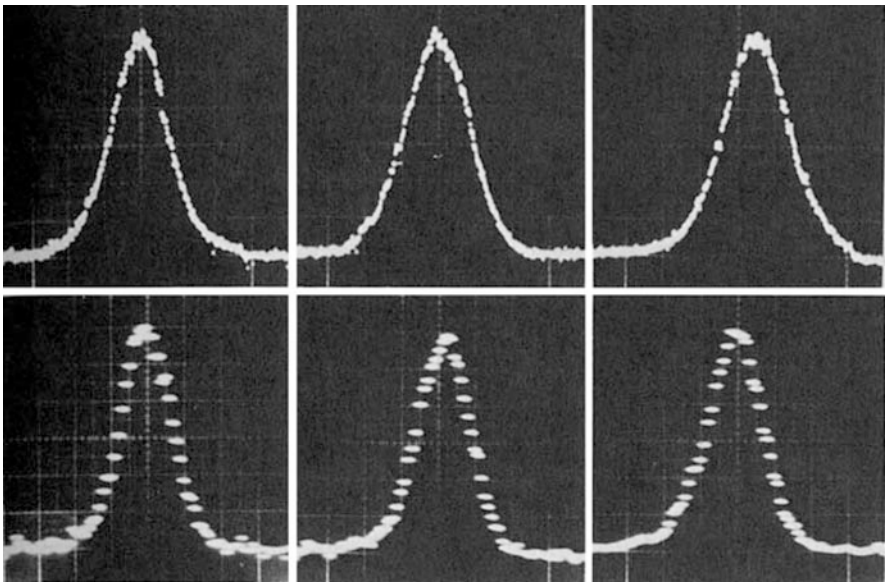

Fig. 7.6 Near-field (top row) and far-field (bottom row) distributions of the beam after passing through the gas cell. From left to right are shown the red spectral component ($\lambda > 650$ nm), the beam with the gas cell evacuated, and the blue spectral component ($\lambda < 525$ nm)

beam is catastrophically modified, can we expect anything but a severely distorted transmitted beam?

Figure 7.6 shows the near-field and far-field distributions of the beam after passing through the gas cell. The first row is composed of reproductions of Polaroid photos of the near-field spatial distribution as viewed through an ~0.5-mm-wide slit and recorded on an optical multichannel analyzer (OMA). The second row shows far-field distributions recorded in a similar manner. From left to right are distributions taken through a filter that blocks all wavelengths $\lambda < 650$ nm (left column), with the gas cell evacuated (middle column), and through a filter that blocks $\lambda > 525$ nm (right column). The left- and right-hand columns were obtained with the gas cell filled with sufficient pressure to ensure that the laser peak power exceeded the continuum threshold. On the basis of the spatial profile alone, it is virtually impossible (with large F-number optics) to distinguish between the presence and absence of self-focusing and continuum generation for powers near the self-focusing threshold.

As the laser power is increased to approximately four times the continuum threshold, conical emission is observed. At first the ring structure is simple, but it becomes increasingly complex at higher powers. Figure 7.7 shows the ring structure only slightly above the threshold for conical emission. Conical emission was previously observed in condensed-medium continuum generation (Smith et al., 1977; Alfano & Shapiro, 1970a).

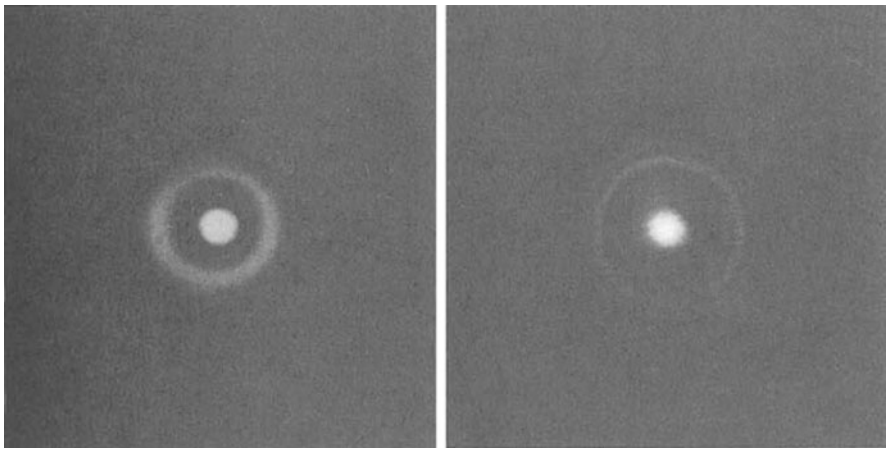

Fig. 7.7 Conical emission as observed in the near field through the red ($\lambda > 650$ nm, left image) and blue ($\lambda < 525$ nm, right image) filters

Figure 7.6 indicates that the transverse beam distribution is almost totally reconstructed after self-focusing. The spatial reconstruction of the beam stands in stark contrast to the catastrophic change in the initial spectrum. With such beam reconstruction, it is natural to reexamine whether self-focusing was ever initiated. Several reasons to associate continuum generation with self-focusing in gases are listed below:

1. Conceptually, self-focusing is just the free-space spatial manifestation of self-phase modulation. Since Eq. (7.1) is valid for large F-number optics, η_2 must be the dominant nonlinearity, rendering self-focusing inevitable. Of course, when the intensity approaches 10^{13} W/cm^2, η_2 is no longer dominant.
2. The continuum threshold has approximately the same magnitude as the calculated self-focusing threshold. It also has the same functional dependence on the gas pressure, laser power, and hyperpolarizability.
3. Conical emission has been predicted by the moving-focus model of self-focusing (Shen, 1975). It is also a characteristic of a saturating nonlinearity (Marburger, 1975) and high-order nonlinear mixing processes. With large F-number optics, all of these potential explanations of conical emission require self-focusing to increase the peak intensity.
4. We have projected conical emission to its source and find that it originates from the prefocal region. This origin can be graphically illustrated by placing a 3-mm-diameter opaque disk at the geometric focus. Significant conical emission escapes around its side.
5. The $\eta_2 E^2$ dependence of the spectral modulation implies that η_2 plays at least a limited role in continuum generation.
6. In no case have we been able to observe continuum generation without the laser power exceeding the calculated self-focusing power.

7.6.3 Discussion

It is not possible to consider gaseous continuum generation as if it were produced by self-phase modulation in the η_2 limit alone. The conceptual link between self-phase modulation and self-focusing makes this approach unrealistic. The very small value of $\eta_2 E^2$, even at the ionization threshold (Corkum et al., 1986a, b), gives additional evidence that continuum generation is not only an η_2 process.

There is a second conceptual problem. If plasma is not created (as we have shown experimentally), then high-order nonlinearities are required to stabilize self-focusing: consequently, η_2 is no longer the dominant nonlinear term. (It is interesting to note that nonlinear optics will be very different in the long-wavelength limit, where the Lorentz force severely limits the lifetime of most high-lying states.)

Out of this apparent complexity, however, very simple and near-universal behavior emerges. This simple behavior will have to be explained by continuum theories. In particular, theory will have to explain the periodicity of the modulation, the spatial properties of the beam, conical emission, and the universality of the blue spectral component of the continuum.

7.7 Conclusions

With the recent development of ultrashort pulses, it is now possible to perform nonlinear optics experiments in new limits of intensity and pulse duration. Due to the sweep of the focus, earlier self-focusing experiments may already have explored this region, although unwittingly.

This chapter has described experiments explicitly performed to investigate subpicosecond nonlinear optics. It described the first high-intensity experiments performed with pulses as short as 22 fs and showed that ionization cannot be described by perturbation theory for pulse durations shorter than 1 ps. It also discussed the role of transient resonances in multiphoton ionization and in high-intensity self-phase modulation experiments. For ultrashort pulses, these transient resonances dominate the nonlinear optical response of gases in much the same way that high-lying resonances dominate in partially ionized plasmas (Gladkov et al., 1987) (presumably, the same is true in condensed media near the multiphoton ionization threshold).

Continuum generation in gases (and indeed all nonlinear optical phenomena in this intensity and pulse duration range) will be understood only in the context of transient resonances and limited convergence of perturbation theory.

In conclusion, it should be emphasized that the observations in this chapter are very much in keeping with the condensed-medium results. The difference is only that gases show the properties of continua in such a dramatic form as to strongly challenge conventional ideas of continuum generation.

Acknowledgments The author acknowledges important contributions to this work by Dr. S.L. Chin, during a 5-month sabbatical at NRC. His experience with multiphoton ionization experiments was invaluable, as was his contribution to other concepts expressed in this chapter. Dr. T. Srinivasan-Rao's contributions are also acknowledged. Without her short visit to NRC, we would never have begun this set of experiments. D.A. Joines has cheerfully provided technical support throughout all of the experiments. Our rapid progress would not have been possible without him. Discussions with many colleagues at NRC are gratefully acknowledged.

References

Ackerhalt, J. R., Milonni, P. W., & Shih, M.-L. (1985). *Physics Reports, 128*, 207.
Alfano, R. R., & Shapiro, S. L. (1970a). *Physical Review Letters, 24*, 584.
Alfano, R. R., & Shapiro, S. L. (1970b). *Physical Review Letters, 24*, 592.
Bloembergen, N. (1973). *Optics Communication, 8*, 285.
Chin, S. L., Rolland, C., Corkum, P. B., & Kelly, P. (1988). *Physical Review Letters, 61*, 153.
Corkum, P. B., & Rolland, C. (1987). Summary of postdeadline papers, XV International Quantum Electron. Conference, April, Baltimore, Maryland, Paper PD-21.
Corkum, P. B., & Rolland, C. (1988a). In A. Bandrauk (Ed.), *In NATO ASI series – Physics B* (Vol. 171, p. 157). Plenum.
Corkum, P. B., & Rolland, C. (1988b). Unpublished.
Corkum, P. B., Rolland, C., & Srinivasan-Rao, T. (1986a). *Physical Review Letters, 57*, 2268.
Corkum, P. B., Rolland, C., & Srinivasan-Rao, T. (1986b). In G. R. Fleming & A. E. Siegman (Eds.), *Ultrafast phenomena V* (p. 149). Springer.
Delone, N. B., & Krainov, V. P. (1985). *Atoms in strong light fields* (p. 174). Springer.
Fork, R. L., Shank, C. V., Hirliman, C., Yen, R., & Tomlinson, W. J. (1983). *Optics Letters, 8*, 1.
Freeman, R. R., Bucksbaum, P. H., Milchberg, H., Darack, S., Schumacher, D., & Geusic, M. E. (1987). *Physical Review Letters, 59*, 1092.
Gladkov, S. M., Koroteev, N. I., Ruchev, M. V., & Fedorov, A. B. (1987). *Soviet Journal of Quantum Electronics, 17*, 687.
Glownia, J. H., Miswich, J., & Sorokin, P. P. (1986). *Journal of the Optical Society of America, B3*, 1573.
Guha, S., Van Stryland, E. W., & Soileau, M. J. (1985). *Optics Letters, 10*, 285.
Keldysh, L. V. (1965). *JETP, 20*, 1307.
l'Huillier, A, Lompre, L. A., Mainfray, G., & Manus, C. (1983). *Physics Review, A27*, 2503.
Landen, O. L., Perry, M. D., & Campbell, E. M. (1987). *Physical Review Letters, 59*, 2558.
Lehmeier, H. J., Leupacher, W., & Penzkofer, A. (1985). *Optics Communication, 56*, 67.
Mainfray, G., & Manus, C. (1980). *Applied Optics, 19*, 3934.
Marburger, J. H. (1975). *Progress in Quantum Electronics, 4*, 35.
Rolland, C., & Corkum, P. B. (1986). *Optics Communication, 59*, 64.
Rolland, C., & Corkum, P. B. (1988). *Journal of the Optical Society of America, B5*, 641.
Shen, Y. R. (1975). *Progress in Quantum Electronics, 4*, 1.
Smith, W. L., Liu, P., & Bloembergen, N. (1977). *Physics Review, A15*, 2396.
Szöke, A. (1988). In A. Bandrauk (Ed.), *NATO ASI series—Physics B* (Vol. 171, p. 207). Plenum.

Chapter 8
Attosecond Extreme Ultraviolet Supercontinuum

Qi Zhang, Kun Zhao, and Zenghu Chang

Abstract The chapter focus on a review of attosecond pulse generation and characterization toward single attosecond pulse toward achieving isolate 25 as pulses in gases. The mechanism toward HHG is discussed in terms of three-step model and cutoff frequency in a classical approach of tunneling followed by acceleration by driving laser electric field E(t) and electron return to parent ion with odd HHG of attosecond pulse in return to atom. The conversion to HHG is on order 10^{-6}. Several techniques are reviewed in XUV emission for HHG with discussions of double gating method and phase-retrieval algorithms.

Keywords Attoseconds · HHG · Cutoff frequency · Three-step model · Supercontinuum · 25 as pulses · Extreme ultraviolet · XUV · Gases · Multiphoton · Ionization · Plasmas · Coherent attosecond pulse · Laser pulse · Argon · Neon · Noble (inert) gas molecules · Double optical gating · Pressure up to 0.33 bars · 10^{-6} conversion

Q. Zhang
Coherent China, Beijing, China

Institute for the Frontier of Attosecond Science and Technology (iFAST), CREOL and Department of Physics, University of Central Florida, Orlando, FL, USA

K. Zhao
Institute of Physics, Chinese Academy of Sciences, Beijing, China

Institute for the Frontier of Attosecond Science and Technology (iFAST), CREOL and Department of Physics, University of Central Florida, Orlando, FL, USA

Z. Chang (✉)
Institute for the Frontier of Attosecond Science and Technology (iFAST), CREOL and Department of Physics, University of Central Florida, Orlando, FL, USA
e-mail: Zenghu.Chang@ucf.edu

R. R. Alfano (ed.), *The Supercontinuum Laser Source*,
https://doi.org/10.1007/978-3-031-06197-4_8

8.1 Introduction

The generation of attosecond laser pulses requires a spectrum that spans an ultrabroad range. One of the enabling methods in the generation of such attosecond pulses is to use the frequency comb composed of hundreds of beat notes of supercontinuum from rare gas medium irradiated by an intense laser pulse. It is found that when an intense ultrafast laser beam is focused into a gaseous target, hundreds of harmonic orders of the fundamental frequency of the driving laser can be generated, extending the spectrum to the extreme ultraviolet (XUV) region (Ferray et al., 1988; McPherson et al., 1987). This highly nonlinear process is termed high-order harmonic generation (HHG), and the broadband spectra generated from HHG can support a coherent light source with the pulse duration on the attosecond (as) time scale (Chang & Corkum, 2010; Chini et al., 2014). Since the high-order harmonic frequency comb is actually hundreds of beat notes of a series of supercontinuum spectra, there are a train of attosecond pulses in the time domain. If the train of the pulses can be truncated and only one single isolated attosecond pulse is produced, the corresponding spectrum is a real supercontinuum without any beat notes. We note here that, by the most restrictive definition, the attosecond pulse discussed here is not a *laser* pulse because there is no *amplification of stimulated emission of radiation* involved in the final generation process. However, the attosecond pulses produced by HHG are a kind of light radiation highly coherent in both space and time. In this sense, we refer to the *coherent* attosecond pulse as a *laser* pulse.

Since the first observation of attosecond pulses in 2001 (Hentschel et al., 2001; Paul et al., 2001), attosecond science has been a hot topic in the ultrafast community. Due to the unprecedented temporal resolution achievable by attosecond pulses in pump-probe spectroscopy, attosecond XUV pulses have been used to study fast electron dynamics in atomic, molecular, and condensed-matter systems (Baker et al., 2006; Cavalieri et al., 2007; Hentschel et al., 2001; Pfeifer et al., 2008; Sansone et al., 2010). High-order harmonics from a linearly polarized driving laser form a train of attosecond pulses. However, for studying electron dynamics, it is much more desirable to have a single attosecond pulse, which corresponds to a continuous spectrum in the frequency domain. The generation of a single attosecond pulse has attracted many significant interests (Feng et al., 2009; Gilbertson et al., 2010; Goulielmakis et al., 2008; Itatani et al., 2002; Kienberger et al., 2004; Mashiko et al., 2008; Sansone et al., 2006; Zhao et al., 2012). In 2001, a single attosecond pulse was first demonstrated. In 2008, 80 isolated attosecond pulses were realized (Goulielmakis et al., 2008). Most recently in 2012, a single 67 as pulse was generated, claiming the shortest optical pulse ever created (Zhao et al., 2012).

In this chapter, some of the most important advances in single attosecond pulse generation and characterization are reviewed. Section 8.2 introduces the basic concepts of HHG, which is the process for generating broadband spectra in the XUV region, and a semiclassical model for understanding the mechanics behind HHG. With this simple model, several characteristic parameters for HHG such as

the cutoff harmonic are calculated. In Sect. 8.3, several techniques for extracting single attosecond pulses from the pulse train are described. Among them, the Double Optical Gating (DOG) method is discussed in most detail. Section 8.4 focuses on two phase-retrieval algorithms for temporal characterization of an attosecond pulse. In Sect. 8.5, an experimental setup with a high-resolution electron energy spectrometer for attosecond streaking built at the Institute for the Frontiers of Attosecond Science and Technology (iFAST) is introduced, and simulations on the spectrometer resolution are compared with experimental results. In Sect. 8.6, some of the most recent progress toward the generation of isolated 25 as pulses is discussed. Finally in Sect. 8.7, a summary of the chapter is given, and paths for future work are brought up for consideration.

8.2 High-Order Harmonic Generation

High-order harmonic generation was first observed in late 1980s (Ferray et al., 1988). A 1067 nm, 50 ps laser was focused on an argon gas target, and a series of odd order harmonics of the driving laser was observed. This process has been understood through the so-called three-step model, a semiclassical picture involving an electron in an atom that is tunnel-ionized, accelerated, and finally recombined with the parent ion in a laser field (Corkum, 1993). The kinetic energy gained during the acceleration is released as the energy of a photon. A schematic drawing of this process is plotted in Fig. 8.1a. The recombination happens within a laser cycle, and repeats itself every half cycle. Therefore, only odd order harmonics can be observed. The generated spectra can cover up to thousands of harmonic orders, reaching keV photon energy (Popmintchev et al., 2012; Seres et al., 2005). A typical XUV spectrum from HHG is shown in Fig. 8.1b. A fast drop in signal strength is observed in the first few orders followed by a relatively flat plateau. After that, an abrupt drop is observed near the cutoff. This rather simplified model has been demonstrated to be particular useful, although a fully quantum-mechanical model should be used when accurate simulation of the HHG process is needed.

For a simple discussion, we consider a plane wave driving laser, linearly polarized in the x-direction, whose electric field at a given spatial point can be expressed by

$$\varepsilon(t) = E_0 \cos(\omega_0 t) . \tag{8.1}$$

In the first step, a ground-state electron tunnels through the potential barrier. We assume that the ionization happens instantaneously, and the initial position and velocity of the electron are both zero. We further assume in the second step that the Coulomb field of the atom is neglected for calculating the electron trajectory. The electron motion is treated classically

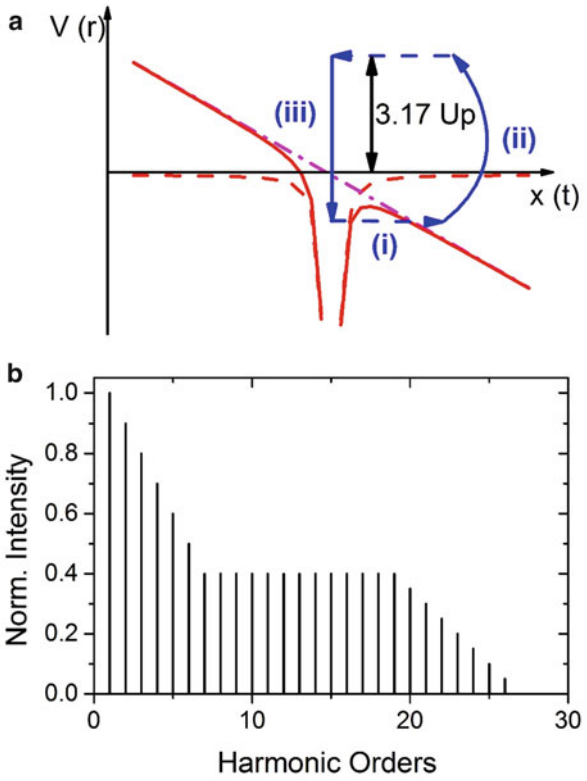

Fig. 8.1 (**a**) A schematic drawing illustrating the three-step model (i) Tunnel ionization. (ii) Acceleration by the driving field. (iii) Recombination with the parent ion. (**b**) A schematic plot of a typical intensity spectrum from high-order harmonic generation

$$\frac{d^2x}{dt^2} = -\frac{e}{m}\varepsilon(t) = -\frac{e}{m}E_0\cos(\omega_0 t)\,, \tag{8.2}$$

where e and m are the electron charge and mass, respectively.

We can hence solve the differential equation, finding that

$$v(t) = \frac{dx}{dt} = -\frac{eE_0}{m\omega_0}\left[\sin(\omega_0 t) - \sin(\omega_0 t_0)\right], \tag{8.3}$$

$$x(t) = \frac{eE_0}{m\omega_0^2}\left\{\left[\cos(\omega_0 t) - \cos(\omega_0 t_0)\right] + \omega_0 \sin(\omega_0 t_0)\,(t - t_0)\right\}. \tag{8.4}$$

Here, t_0 is the time that electron is freed. In the third step, the electron recombines with the parent ion at $x = 0$ and emits a photon, whose energy can be calculated by

$$\hbar\omega(t) = I_p + \frac{1}{2}mv^2(t) = I_p + 2U_p[\sin(\omega_0 t) + \sin(\omega_0 t_0)]^2, \tag{8.5}$$

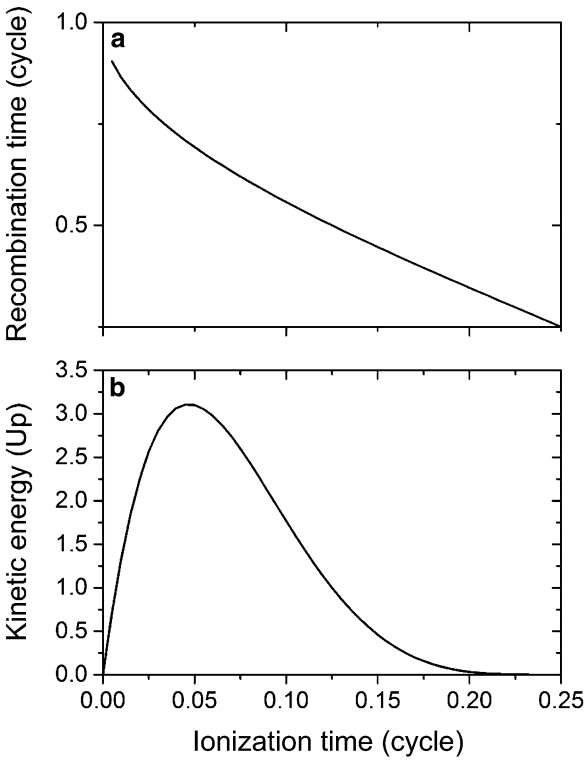

Fig. 8.2 (**a**) Numerically calculated recombination time as a function of the emission time for tunnel-ionized electron. (**b**) The kinetic energy of the returned electron before it recombines with the parent ion, as a function of the emission time

where I_p is the ionization potential of the atom and U_p is the ponderomotive energy defined by

$$U_p = \frac{(eE_0)^2}{4m\omega_0^2}. \tag{8.6}$$

If we set $x(t) = 0$ in Eq. (8.4), it can be seen that once we know the ionization time t_0, we are able to obtain the recombination time t. The relation between the recombination time and ionization time is plotted in Fig. 8.2a. The fact that the returning time spans over 0.75 laser cycle suggests that the emitted pulse may last for 2 fs for an 800 nm Ti-sapphire laser.

The kinetic energy of the returning electron can be calculated as

$$K = 2U_p[\sin(\omega_0 t) + \sin(\omega_0 t_0)]^2. \tag{8.7}$$

Plotting the kinetic energy vs. emission time in Fig. 8.2b shows that the maximum kinetic energy is $K_{\max} = 3.17U_p$, which is carried by the electron released at $\omega_0 t_0 = 0.05 \times 2\pi$ rad and returns at $\omega_0 t = 0.7 \times 2\pi$. Thus, the maximum photon energy emitted from HHG is

$$\hbar\omega_{\max} = I_p + 3.17U_p. \tag{8.8}$$

The ponderomotive energy U_p can be expressed as

$$U_p\,[eV] = 9.33 \times 10^{-14} I_0 \lambda_0^2, \tag{8.9}$$

in which I_0 is the peak intensity of the laser in W/cm^2 and λ_0 is the wavelength of the driving laser in μm. For example, for neon gas, $I_p = 21.6$ eV. The peak intensity from a Ti-sapphire laser can reach 10^{15} W/cm^2, and hence the corresponding cutoff photon energy can be 200 eV.

Moreover, from Fig. 8.2b, two important features of the HHG can be observed. First, each kinetic energy corresponds to two different ionization/recombination times, which means there are two trajectories contributing to the generation of a given harmonic. Electrons ionized before the critical time $\omega_0 t_0 = 0.05 \times 2\pi$ return later, so their trajectory is "long." In contrast, electrons emitted later will return earlier; therefore, the trajectory is "short." The existence of two trajectories further complicates the generation of isolated attosecond pulse. Fortunately, the long trajectory can be suppressed by phase matching, and the two trajectories can be separated by their different divergences so that the contribution of the long trajectory can be removed from the final HHG signal. Second, electrons with different energies recombine with parent ions at different times, causing the emitted XUV pulse carrying an intrinsic chirp. For photons generated from the short trajectory, this so-called attochirp is positive. In order to produce short attosecond pulses, the attochirp must be carefully compensated. More discussion can be found in Sect. 8.5.3.

The three-step model predicts that the tunneling, acceleration, and recombination processes occur once per half laser cycle, indicating that for a multi-cycle laser pulse, an attosecond pulse train is generated with a period of half of an optical cycle. A alternative model for HHG generation is given in Chap.17 based on electro magnetic model. While attosecond pulse trains are useful, an isolated pulse is more desirable for pump-probe experiments since contributions from pre- and post-pulses can excite or ionize the target, thereby modifying the time-resolved experimental results. In the next section, methods for generating isolated attosecond pulses are discussed.

8.3 Isolated Attosecond Pulse Generation with Gating Techniques

Ever since attosecond pulses were demonstrated for the first time in 2001, there have been many schemes proposed for single attosecond pulse generation, including amplitude gating (AG), polarization gating (PG), and double optical gating (DOG). AG takes advantage of the fact that only the field close to the envelope peak of a few-cycle laser contributes to the cutoff region. By filtering out all the low-

order harmonics, 80 as isolated pulses were generated (Goulielmakis et al., 2008). However, there are a few drawbacks to this technique. This gating method requires a few-cycle laser (3.5 fs used in the work (Goulielmakis et al., 2008)), which is difficult to achieve with high energy (>1 mJ). Besides that, since it filters out many low-order harmonics, only the cutoff region can contribute to the attosecond pulse. This condition significantly limits the achievable bandwidth for the supercontinuum, since the cutoff region is typically only a small portion of the total HH spectrum. On the other hand, PG and DOG loosen the requirement for the driving laser and can generate continuum spectra even in the plateau region. Therefore, in this section, more details are discussed about PG and DOG, especially DOG, which allows using longer driving pulses and has demonstrated the generation of single 67 as pulses (Zhao et al., 2012)—the shortest coherent optical pulse generated to date.

8.3.1 Polarization Gating

Polarization gating was first proposed by Corkum in 1994, and relies on the fact that high harmonic generation efficiency is strongly dependent on the ellipticity of the driving laser field (Corkum et al., 1994). In the original proposal, two laser pulses with different frequencies were used. In 1999, Platonenko and Strelkov suggested superimposing a left- and right-circularly polarized pulse for PG, which requires only one central frequency (Platonenko & Strelkov, 1999). In 2006, PG was experimentally demonstrated to generate single isolated attosecond pulses (Sansone et al., 2006).

The ellipticity dependence of the HHG can be understood by the three-step model. After the electron is ionized, it is accelerated by the laser field. A linearly polarized field drives the electron back to the parent ion. However, if the generating field is elliptically polarized, the electron can be steered away from the parent ion, resulting in no recombination and hence no XUV emission.

Experimentally, gating a single attosecond pulse from a pulse train is accomplished by changing a linearly polarized, few-cycle laser pulse into a pulse with time-varying polarization. By superimposing a right- and left-circularly polarized laser pulse with a certain delay T_d between them, a pulse that has circularly polarized leading and trailing edges and a linearly polarized central portion is created. This linearly polarized portion is where the gate opens, and the gate width can be made shorter than a half laser period by manipulating the delay T_d. For example, for a Ti-sapphire laser at a 780 nm center wavelength, the gate width should be narrower than 1.3 fs. In this scenario, only one single attosecond pulse can be generated, leading to a supercontinuum spectrum in the frequency domain.

Experimentally this can be achieved by two simple optical elements. At first, a linearly polarized driving laser is split into two perpendicularly polarized fields with a birefringent plate. A delay between those two pulses is introduced by the difference in the group velocities along the ordinary and extraordinary axes. The

two delayed pulses are then converted to circularly polarized pulses with a quarter-wave plate, resulting in a combined pulse with a time-dependent ellipticity.

Mathematically, the final pulse can be decomposed into two perpendicular components called the driving and gating fields, expressed as (Chang, 2004)

$$E_{\text{drive}}(t) = E_0 \left[e^{-2\ln(2)\left(\frac{t_- - T_d/2}{\tau_p}\right)^2} + e^{-2\ln(2)\left(\frac{t_+ - T_d/2}{\tau_p}\right)^2} \right] \cos\left(\omega_0 t + \varphi_{CE}\right), \tag{8.10}$$

$$E_{\text{gate}}(t) = E_0 \left[e^{-2\ln(2)\left(\frac{t_- - T_d/2}{\tau_p}\right)^2} - e^{-2\ln(2)\left(\frac{t_+ - T_d/2}{\tau_p}\right)^2} \right] \sin\left(\omega_0 t + \varphi_{CE}\right), \tag{8.11}$$

where E_0 is the amplitude of the circularly polarized laser field with carrier frequency ω_0, pulse duration τ_p, and CE phase φ_{CE}. Thus, the ellipticity is a function of time and can be expressed as

$$\xi(t) = \frac{1 - e^{-4\ln(2)\frac{T_d}{\tau_p^2}t}}{1 + e^{-4\ln(2)\frac{T_d}{\tau_p^2}t}} \tag{8.12}$$

Since we are only interested in the time range where the field is approximately linear, a Taylor expansion of Eq. (8.12) about the center of the pulse, or $t = 0$, keeping the first nontrivial term, yields:

$$\xi(t) = \left| 2\ln(2)\frac{T_d}{\tau_p^2}t \right| \tag{8.13}$$

Solving Eq. (8.13) for t and multiplying by 2 gives the gate width equation:

$$\delta t_G \approx \frac{\xi_{th}}{\ln(2)}\frac{\tau_p^2}{T_d}, \tag{8.14}$$

where ξ_{th} is the threshold ellipticity for harmonic generation. To generate a single attosecond pulse, the gate width must be less than half of the pump laser cycle. In the

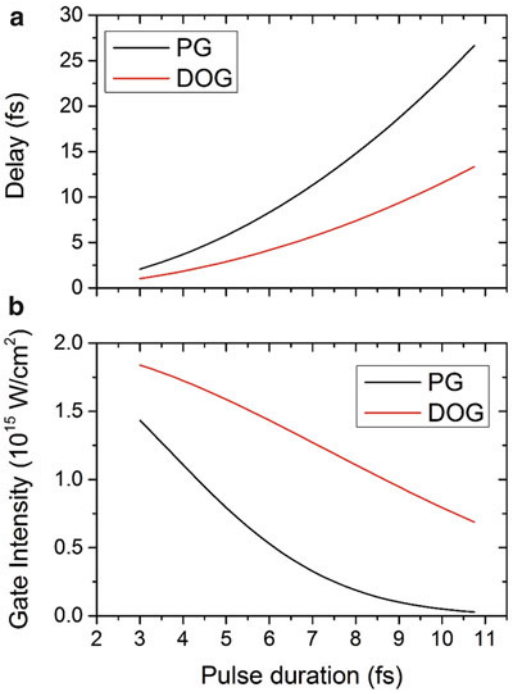

Fig. 8.3 (**a**) Delay of the first quartz plate required for generating single attosecond pulses as a function of the driving pulse duration. *Black*: PG. *Red*: DOG. (**b**) The peak intensity inside of the gate assuming the peak intensity of the linearly polarized input pulse is 2×10^{15} W/cm^2. Black: PG. Red: DOG

instance of a Ti-sapphire laser where the optical period T_0 is 2.5 fs and ξ_{th} is ~0.2, we can plot the required delay T_d as a function of the input laser pulse duration, as shown in Fig. 8.3a. Therefore, we can maintain a gate width of half the laser cycle—even with a very long pulse—if the delay is properly chosen. Moreover, it is also very important to know the peak intensity inside the gate, since this determines the HH spectral bandwidth and attochirp. Obviously, higher intensity is preferred to produce a broader bandwidth XUV source.

As shown in the black line in Fig. 8.3b, the maximum peak intensity inside the gate (determined by the half-cycle gate width) is plotted as a function of the pulse duration, assuming a linear peak intensity of 2×10^{15} W/cm^2. It is easy to see that shorter pulse duration requires less delay in the first quartz plate.

Besides the gate width, another necessary condition for HHG limiting the pulse duration and peak intensity is that the ground-state population of the atom responsible for attosecond light emission must not be zero. This means the electrons in the ground state of the atoms cannot be fully ionized before the gate. With the ADK model (Ammosov, Delone, and Krainov), we calculated the ionization probability of neon as a function of the peak intensity inside the gate, assuming PG is used with an input pulse duration of 7 fs (Ammosov et al., 1986). The result is shown in Fig. 8.3a. Obviously, the highest intensity achievable with neon gas for a driving field with 7 fs duration is 7×10^{14} W/cm^2, corresponding to a cutoff photon energy of 150 eV. Practically the measured bandwidth is usually

narrower due to phase matching, and PG has not demonstrated the ability to produce supercontinuum spectra with 150 eV or above. Alternatively, helium atoms can be used as the generation target for higher-intensity pulses due to a higher ionization potential. On the other hand, conversion efficiency of the harmonic generation is greatly sacrificed. Therefore, it is preferred to obtain higher peak intensity in the gate with neon atoms for higher photon flux.

8.3.2 Double Optical Gating

To reduce the leading edge ionization and still have an intense laser field inside the gate, the double optical gating (DOG) technique was developed (Chang, 2007; Gilbertson et al., 2008; Mashiko et al., 2008). The technique is a combination of the two-color gating and polarization gating, which means a second harmonic was applied in addition to the original polarization gating field. The second harmonic field breaks the symmetry of the system, and only one attosecond pulse is generated within one full optical cycle. A schematic plot of the driving and gating field of DOG is shown in Fig. 8.4, showing a similarity to PG except for the weak second harmonic field added to the driving field.

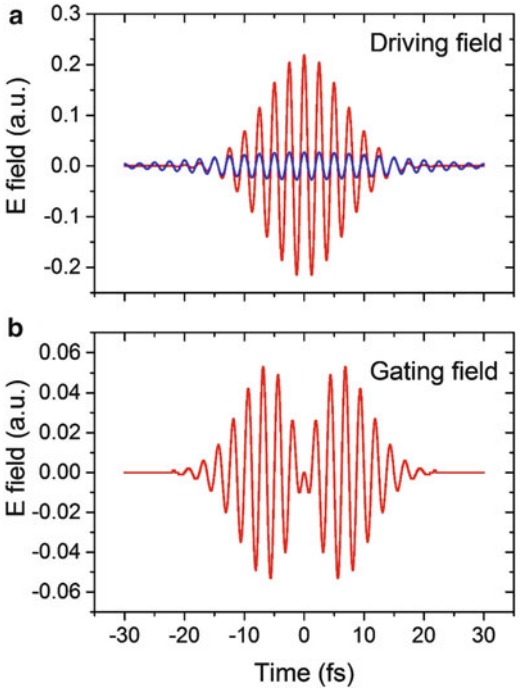

Fig. 8.4 Schematic drawings of the (**a**) driving and (**b**) gating field for double optical gating technique. The *blue line* in the (**a**) driving field is second harmonic of the gating field

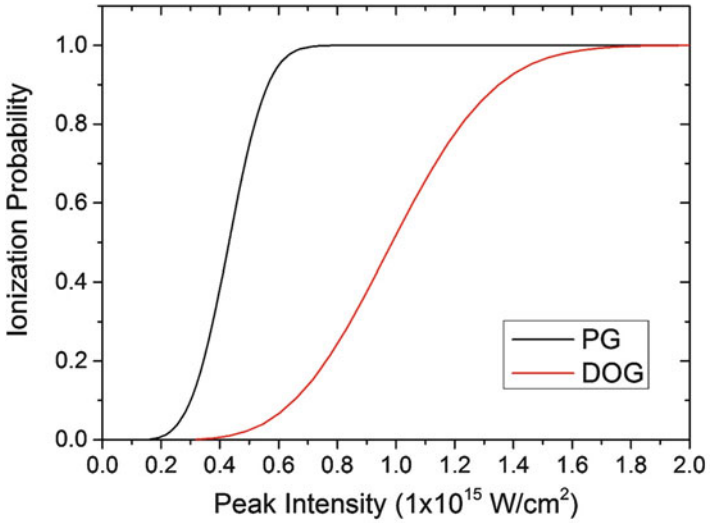

Fig. 8.5 The ionization probabilities of neon atom calculated from the ADK model as a function of the peak intensity inside the gate. The pulse duration is assumed to be 7 fs, and the gate width is calculated for PG and DOG to select a single attosecond pulse. *Black line*: PG. *Red line*: DOG

Compared to PG, one of the advantages of DOG is that much longer pulse durations can be used for isolated attosecond pulse generation due to the full-cycle gate width requirement, as shown in the red curve of Fig. 8.3a. Another advantage is that for equal pulse durations, DOG allows the use of less delay time T_d, hence increasing the peak intensity inside the gate with the same pulse energy, as shown in Fig. 8.3b with the red curve.

Most importantly, due to less delay time needed in the DOG, the ionization before the gate is significantly reduced under the same peak intensity, as calculated by ADK model and shown in the red curve of Fig. 8.5. In other words, this calculation shows that a higher peak intensity inside the gate can be used for DOG than PG, which is crucial for generating a broadband supercontinuum from HHG.

Experimentally it is simple to apply DOG (Gilbertson et al., 2008; Mashiko et al., 2008). In place of the quarter-wave plate in PG, a combination of a quartz plate and a β-BaB_2O_4 (BBO) crystal is used. The BBO generates a second harmonic from the fundamental beam and forms a zero-order quarter-wave plate with the second quartz plate.

8.4 Temporal Characterization of Attosecond Pulses

While the single attosecond pulse spectrum can be measured readily, determining the pulse duration remains a challenge. Since the photon spectrum can be measured

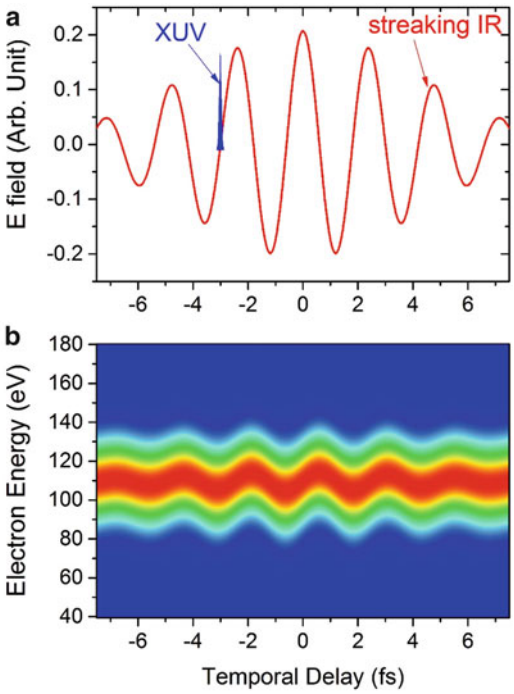

Fig. 8.6 (**a**) A schematic drawing illustrating the attosecond streaking by scanning the delay between the IR and the XUV pulses. (**b**) The streaking trace obtained by recording the XUV photoelectron spectra at each temporal delay. A single 60 as pulse and a 7 fs streaking IR field is assumed. The peak intensity for the streaking field is 5×10^{11}W/cm^2

by recording the corresponding photoelectron spectrum, only the phase information is needed for the complete characterization. In this section, the principle of the attosecond streaking technique for measuring the spectral phase is introduced, and two algorithms to retrieve the phase are discussed.

8.4.1 Principle of Attosecond Streaking

Traditional streak cameras have been used to image fast (femtosecond) electron pulses by applying a fast-varying high voltage perpendicular to the flying electrons. The electrons are then streaked depending on the time they experience in the fast-varying voltage. The basic idea of the attosecond streaking is also similar, which is to modify the momentum of the photoelectrons ionized by the XUV pulse by applying a phase-locked femtosecond laser field, which is called the "streaking pulse" (Itatani et al., 2002; Mairesse & Quéré, 2005). By scanning the delay between the XUV and the streaking field as shown in Fig. 8.6a, a spectrogram can be obtained, as plotted in Fig. 8.6b. This so-called streaking trace contains the complete information needed for temporal characterization. The phase can be retrieved through the reconstruction of the streaking spectrogram.

8.4.2 Complete Reconstruction of Attosecond Bursts

In a streaking experiment, the attosecond XUV pulse is focused into a gaseous target to generate a burst of photoelectrons. The photoelectrons are then streaked with a few-cycle intense IR laser field, giving a momentum shift to the electrons. When using a linearly polarized laser, the momentum change can be expressed as (Itatani et al., 2002; Mairesse & Quéré, 2005)

$$\Delta\ p(t) = \int_{t}^{\infty} e\varepsilon\left(t'\right) dt' = eA_L(t), \tag{8.15}$$

where $A_L\ (t)$ is the vector potential of the laser field. Then, the electron kinetic energy is modulated, which can be measured with a time-of-flight (TOF) electron spectrometer. As the temporal delay between the XUV and the streaking field is altered, the so-called streaking trace can be measured, which can be expressed in atomic unit as (Mairesse & Quéré, 2005)

$$S\left(W, \tau_D\right) \approx \left| \int_{-\infty}^{\infty} dt E_X\left(t-\tau\right) d\left[p + A_L(t)\right] e^{i\varphi(p,t)} e^{-i\left(W+I_p\right)t} \right|^2 \tag{8.16}$$

$$\varphi\left(p, t\right) = -\int_{t}^{\infty} dt' \left[pA_L\left(t'\right) \cos\theta + {A_L}^2\left(t'\right)/2 \right]. \tag{8.17}$$

where E_X is the complex field amplitude of the XUV pulse, τ is the delay between the XUV and streaking pulses, W is the kinetic energy of the photoelectron, and I_p is the ionization potential of the target gas.

In Eq. (8.15), the momentum shift of the classical electron can be understood as a phase modulation of the quantum electron wave packet by the laser field, which is expressed in Eq. (8.17). To understand the physical mechanisms of the phase modulation, we assume the momentum in (8.17) can be replaced by the central momentum p_0 and the dipole transition element $d(p)$ to be constant since the energy bandwidth of the ionized electrons is narrow compared to the central energy. This is called the central momentum approximation (CMA). Under the CMA, we obtain:

$$S\left(W, \tau_D\right) \propto \left| \int_{-\infty}^{\infty} dt E_X\left(t-\tau\right) G\ \ (t) e^{-i\left(W+I_p\right)t} \right|^2 \tag{8.18}$$

where the gating function $G(t)$ can be expressed as (assuming only electrons parallel to the streaking field are detected)

$$G(t) = \exp\left\{-i\int_{t}^{\infty} dt' \left[p_0 A_L\left(t'\right) + {A_L}^2\left(t'\right)/2\right]\right\}. \tag{8.19}$$

The key replacement here is using the central momentum p_0 instead of p from the Eq. (8.17), resulting in a phase modulation independent of the momentum of the electron. Under this approximation, the measured spectrogram has the same form as a frequency-resolved optical gating (FROG) trace for femtosecond laser pulse characterization. The phase modulation acts as a temporal phase gate in the FROG language, which can be retrieved by the well-known principal component generalized projections algorithm (PCGPA) (Trebino et al., 1997). This technique is known as the complete reconstruction of attosecond burst (CRAB) (Mairesse & Quéré, 2005).

The gate function here is a pure phase modulation, which can be written as $G(t) = e^{-i\varphi(t)}$, where the total phase $\varphi(t) = \varphi_1(t) + \varphi_2(t) + \varphi_3(t)$, with

$$\varphi_1(t) = \int_{t}^{\infty} dt U_p(t), \tag{8.20}$$

$$\varphi_2(t) = -\left(\sqrt{8WU_p(t)}/\omega_0\right)\cos\ (\omega_0 t)\,, \tag{8.21}$$

$$\varphi_3(t) = \left(U_p(t)/2\omega_0\right)\sin\left(2\omega_0 t\right), \tag{8.22}$$

and $U_p(t) = E_0^2(t)/4\omega_0^2$ is the ponderomotive potential. Apparently, the kinetic energy shift due to $\varphi_2(t)$ is

$$\Delta W(t) = \Delta\omega(t) = \frac{d\varphi_2(t)}{dt} = -\sqrt{8W_0U_p(t)}\sin\left(\omega_0 t\right), \tag{8.23}$$

where W_0 is the central energy. A very efficient algorithm, PCGPA, can be used to extract both $E_X\ (t)$ and $G(t)$ from the streaking trace. It is very robust against noise (Delong et al., 1994; Trebino et al., 1997; Wang et al., 2009). However, the CMA must be obeyed for CRAB to perform correctly. When generating isolated attosecond pulses with DOG, we can generate broadband continuous spectra at low energy, thereby violating the CMA.

8.4.3 Phase Retrieval by Omega Oscillation Filtering

The CRAB technique assumes that the bandwidth of the attosecond pulse is much smaller than the central energy of the photoelectrons. This central momentum

approximation is needed to apply the FROG phase-retrieval technique developed for measurement of femtosecond lasers, and it poses a limitation on the shortest attosecond pulses that can be characterized at a given central photon energy. Moreover, in the streaking model, high streaking laser intensity is needed for the FROG-CRAB to retrieve the phase correctly (Gagnon & Yakovlev, 2009; Itatani et al., 2002; Mairesse & Quéré, 2005). This intense streaking field can produce high-energy photoelectrons through above-threshold ionization of the target atoms, which would overlap with the XUV photoelectron spectrum, thereby preventing the phase from being correctly retrieved.

In phase retrieval by omega oscillation filtering (PROOF), the mechanism of phase encoding in the electron spectrogram and the method of phase retrieval are different (Chini et al., 2010). For low streaking intensities, one can interpret the streaking as the interference of electrons ionized through different pathways. As explained in Chini et al. (2010), the electron signal at a given energy may come from direct ionization from one XUV photon, one XUV plus one IR photon, and one XUV minus one IR photon. Therefore, when the component of oscillation with the dressing laser center frequency ω_L is extracted, the phase angle of the sinusoidal oscillation, $\alpha(v)$, is related to the spectral phases $\varphi(\omega_v - \omega_L)$, $\varphi(\omega_v)$, and $\varphi(\omega_v + \omega_L)$ of the three XUV frequency components separated by one laser photon energy and the intensities $I(\omega_v - \omega_L)$, $I(\omega_v + \omega_L)$:

$$\tan[\alpha(v)] = \frac{\sqrt{I(\omega_v + \omega_L)}\sin[\varphi(\omega_v) - \varphi(\omega_v + \omega_L)] - \sqrt{I(\omega_v - \omega_L)}\sin[\varphi(\omega_v - \omega_L) - \varphi(\omega_v)]}{\sqrt{I(\omega_v + \omega_L)}\cos[\varphi(\omega_v) - \varphi(\omega_v + \omega_L)] - \sqrt{I(\omega_v - \omega_L)}\cos[\varphi(\omega_v - \omega_L) - \varphi(\omega_v)]} \tag{8.24}$$

The equation can be understood as the interference between the single-photon (XUV only) and two-photon (XUV plus NIR) transitions from the atomic ground state to the continuum state $\omega_v - I_p$ (Fig. 8.7).

To retrieve the spectral phase difference, it is only needed to guess the spectral phase that matches the modulation amplitudes and phase angles of the sinusoidal oscillation. Then, retrieving the spectral phase from these oscillations reduces to a minimization problem (Chini et al., 2010). Unlike FROG-CRAB, this PROOF method does not use FROG phase-retrieval algorithms, and the central momentum approximation is not needed. Furthermore, observation of this oscillation does not require high streaking intensities, as only one NIR photon is needed to couple the continuum states.

Initially, the PROOF algorithm was written to minimize only the difference between the experimental phase angle and the guessed one. However, the robustness against many practical parameters was untested. In contrast, the PCGPA algorithm applied in the CRAB method has been demonstrated to be very robust against noise and other imperfections. Therefore, it would be ideal to use the PCGPA algorithm in the PROOF. In the limit of low streaking intensities, the streaking spectrogram is given by

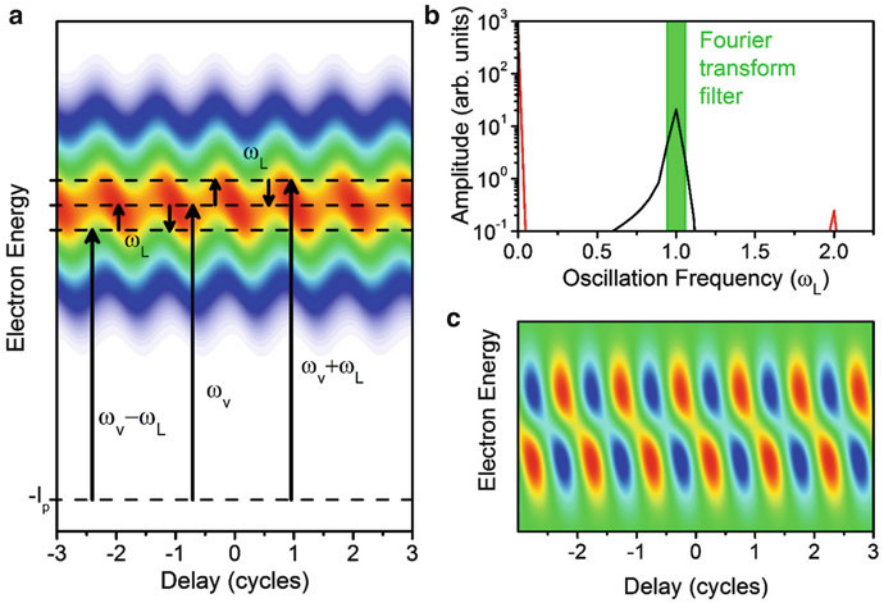

Fig. 8.7 The principle of PROOF. (**a**) The spectra of photoelectrons ionized by the single attosecond pulse are recorded as a function of delay. Any continuum state may come from three different quantum paths: ω_v, $\omega_v + \omega_L$, $\omega_v - \omega_L$. Therefore, the sinusoidal oscillation can be viewed as the interference between different quantum paths. (**b**) Fourier transform of the spectrogram from (a). The component with frequency ω_L is selected for filtering. (**c**) Spectrogram obtained by inverse Fourier transform of the filtered component. (Reproduced from Chini et al., 2010)

$$S'(v,\tau) \approx I_0(v) + I_{\omega_L}(v,\tau) + I_{2\omega_L}(v,\tau) \tag{8.25}$$

where $I_{\omega_L}(v,\tau)$ and $I_{2\omega_L}(v,\tau)$ are two spectrograms oscillating with the streaking laser frequency, ω_L, and twice the frequency, respectively (Chini et al., 2010). Since the spectrum and phase information is completely encoded in the modulation depth and phase angle of the component $I_{\omega_L}(v,\tau)$, we constrain the intensity of the retrieved spectrogram using $S'(v,\tau)$ only in the first iteration of the PCGPA. In subsequent iterations, the $I_0(v)$ and $I_{2\omega_L}(v,\tau)$ from the previous guess are fed back into the algorithm, along with the experimentally obtained $I_{\omega_L}(v,\tau)$. In this way, both the spectrum and phase of the XUV pulse can be simultaneously guessed to match the modulation depth and phase angle of $I_{\omega_L}(v,\tau)$, and comparison of the final guessed spectrum to that of an independent measurement can be used to check the accuracy of the retrieval. This method has been applied in retrieving the single 67 as pulse (Zhao et al., 2012).

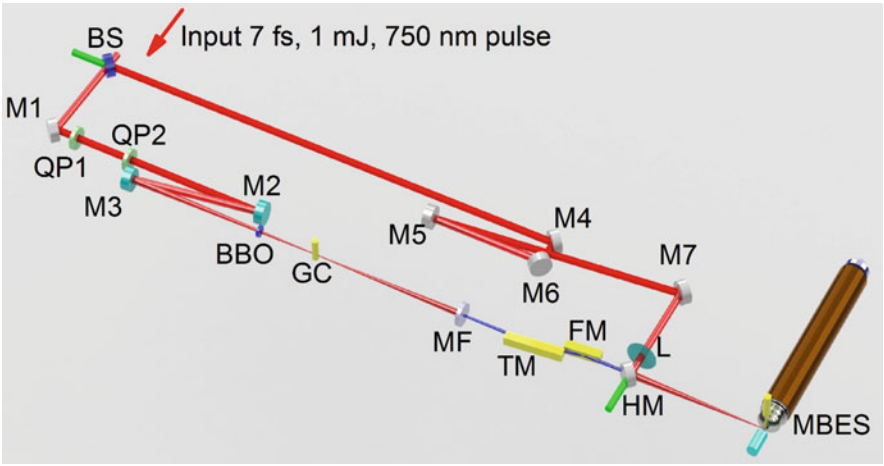

Fig. 8.8 Experimental configuration of the attosecond streak camera with a magnetic-bottle energy spectrometer (MBES). *BS* beam splitter, *QP* quartz plate, *M1–M7* silver mirror, *M2* and *M3* focusing mirrors, *GC* gas cell, *MF* metallic filter, *TM* toroidal mirror, *FM* flat mirror, *L* focus lens, *HM* hole mirror, *MBES* magnetic-bottle electron energy spectrometer

8.5 Experimental Configuration and Results

8.5.1 Magnetic-Bottle Electron Energy Spectrometer for Attosecond Streaking

The experimental setup at the authors' laboratory for attosecond streaking is shown in Fig. 8.8.

Laser pulse of about 25 fs duration and 2 mJ energy with central wavelength of 750 nm are produced at 1 kHz repetition rate by a home-built multi-pass Ti-sapphire amplifier. A hollow-core fiber filled with neon gas is used to expand the bandwidth by self-phase modulation, and six pairs of chirped mirrors compress the fiber output beam to around 7 fs duration. The beam is then split into two arms by a broadband beam splitter. The transmitted arm contains 90% of the total energy, and is sent through the DOG optics and focused to a neon gas target to produce isolated attosecond XUV pulses. The streaking arm (reflected, 10% of the total energy) is temporally locked relative to the generation arm and recombined with the XUV pulses by a hole-drilled mirror.

The laser field in the generation arm goes through two birefringent quartz plates for implementing DOG and is focused by a convex ($f = -150$ mm) and a concave mirror ($f = 250$ mm), whose effective focal length equals to 175 mm. Then, the focusing beam passes a BBO crystal with a thickness of 141 μm, which forms a zero-order quarter-wave plate with the second quartz plate. A neon gas cell with a

backing pressure of about 0.1 bar is positioned roughly 1 mm after the laser focal spot to promote good phase matching of the HHG.

The generated XUV pulses after the neon gas cell pass through a thin metal foil (hundreds of nanometers thick) to filter out the residual driving light and to compensate for the intrinsic XUV chirp. The XUV beam is then focused by a grazing-incidence gold-coated toroidal mirror (f = 250 mm) through the hole (diameter d = 2.5 mm) on a silver mirror to a neon gas jet located between the entrance of the flight tube and the tip of a strong permanent magnet. The generated photoelectrons are collected by a magnetic-bottle energy spectrometer (MBES). The streaking IR beam travels the same optical distance and is focused by a lens (f = 300 mm) to the same position as the XUV beam. The delay between the XUV and streaking field is controlled in the streaking optical path by a piezo-transducer (PZT) attached to one of the flat silver mirrors (M5). A 532 nm continuous-wave laser co-propagates through both arms and generates a temporal interference pattern once they recombine after the hole mirror, as indicated with green beams in Fig. 8.8. The interference fringes of the green light are detected by a CCD camera to stabilize the Mach-Zehnder interferometer to about 20 as RMS and to change the delay as well (Chini et al., 2009a).

The magnetic-bottle (MB) TOF spectrometer was chosen for two reasons. First, it has a high collection efficiency (Kruit and Read, 1983). The MB spectrometer can record electrons up to a 2π steradian solid angle and hence increase statistics of the experimental data significantly. As a comparison, for a half-meter-long field-free TOF with a 50-mm-diameter microchannel plate, the collecting solid angle is only 0.008 steradian. Second, it has a high resolution over a very broadband energy range. For a regular TOF spectrometer, increasing the flying distance reduces the collecting angle, hence limiting the longest flying distance in use, which results in a limitation on achievable energy resolution. In MBES, flying distance is independent of the collecting efficiency, giving a possibility of using a very long flying tube and thereby obtaining a high resolution (Kruit and Read, 1983).

8.5.2 MBES Resolution

The principle of the MB spectrometer has been explained in details in previous publications (Kruit & Read, 1983; Tsuboi et al., 1988). In our experimental configuration, a strong rare earth magnet (NdFeB) and a conical pole piece made of soft iron are used to create a bottle-shaped inhomogeneous magnetic field. The electrons with different flying angles can be parallelized by the strong magnetic field in about 100 mm. After that, a constant 10 G magnetic field from a solenoid guides the parallelized electrons until they reach the microchannel plate for detection. The flying tube after the parallelization is electronically isolated from the tube entrance, and retarding potential can be applied to the flying tube to improve the resolution.

To evaluate the energy resolution of the MBES, the electron trajectories and their flight times are traced by numerical simulations. As shown in Fig. 8.9a, for

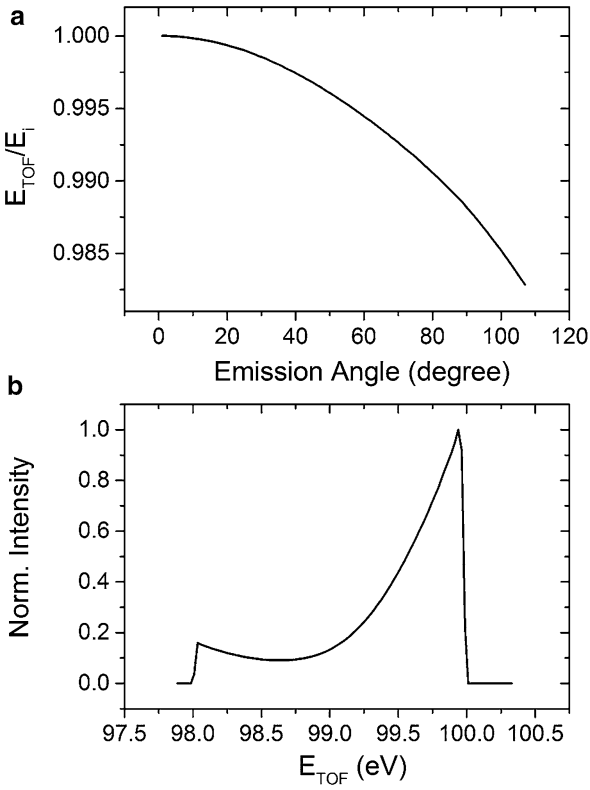

Fig. 8.9 (**a**) The calculated ratio between measured energy E_{TOF} and initial electron energy E_i as a function of emission angle of the photoelectron. (**b**) The calculated response function of 100 eV electrons with all possible emission angles

monochromatic 100 eV electrons, the kinetic energy calculated from the flight time depends on the emission angle of the photoelectrons relative to the axis of the flight tube. This energy is termed as the "TOF energy," to distinguish it from the true initial kinetic energy of the photoelectrons. Clearly, for electrons emitted with larger angles, the TOF energy is more deviated from the true value. For instance, the TOF energy of electrons emitted at 107°—the largest accepting angle of the current setup—is 1.8% smaller than the true value for a 3-m-long TOF.

The angular distribution of the photoelectrons for a given target atom can be expressed as

$$\frac{d\sigma}{d\Omega} \propto 1 + \frac{\beta}{2}\left[3\cos^2(\theta) - 1\right], \tag{8.26}$$

where dσ/dΩ is the differential photoionization cross section, θ is the emission angle, and β is the asymmetric parameter (Kennedy & Manson, 1972). Neon atoms are used in the simulations due to the large photoionization cross section and nearly constant β value for energies above 40 eV (Kennedy & Manson, 1972). Using the above equation and the results shown in Fig. 8.9a, we plot in Fig. 8.9b the TOF energy distribution of monochromatic 100 eV electrons with all emission angles

smaller than 107°, which is referred to as the "response function" of the MBES. The long tail in the lower energy part of the response function comes from the electrons with large emission angles. We note that with this unique distribution, it is not appropriate to define the energy resolution by the full width at half maximum (FWHM) since it does not reflect the contribution of the long tail.

Although experimentally it is difficult to measure the spectrometer resolution directly due to the lack of a narrowband light source, certain comparisons between experimental results and simulations can still be made, and good agreements between them are observed. A 25 fs pulse from the Ti-sapphire amplifier was used to drive HHG to produce narrow harmonic peaks. Then, a 30 V retarding potential was applied, as shown in Fig. 8.10a. For the harmonic peak around 33 eV, the measured spectrum should be the convolution of the response function of the MBES and the XUV harmonic peak. Since the latter one is unknown, we assumed a Gaussian spectrum in order to match the convoluted spectrum with the measurement performed with 30 V retarding potential, as shown in Fig. 8.10b. Then, the convolution can be done for the case of no retarding potential. The simulated and measured spectra are plotted in Fig. 8.10c for comparison, and reasonably good agreement was observed.

8.5.3 Generation of a Single 67 as Pulse

Up to now, we have presented the solution for generating broadband continua from HHG and characterizing single attosecond pulses. Before 2012, the shortest single attosecond pulses (with duration of 80 as) were generated from the cutoff region of the high harmonic spectrum using the AG technique (Goulielmakis et al., 2008). In our case, DOG allows the XUV continuum to cover both the plateau and cutoff region, extending the available bandwidth. If the attochirp, which is positive for photon emitted from the short trajectory, is properly compensated, even shorter attosecond pulses can be obtained (Zhao et al., 2012). From the three-step model, the attochirp is roughly a constant over the plateau region but increases rapidly at both the low- ($\omega_X < I_p$) and high-energy (approaching $I_p + 3.17U_p$) spectral regions (Chang, 2007). Here ω_X is the XUV photon angular frequency. Metallic filters are used to compensate the intrinsic chirp as well as to block the remaining driving IR laser. Within the transmission of many metallic filters, the group delay dispersion (GDD) is typically negative at low photon energies of the transmission window and gradually increases to positive at higher energies. Therefore, a metal filter usually provides good chirp compensation only in the low-energy part of its transmission window. Additional control over the spectrum and phase of the XUV continuum is therefore needed (Henke et al., 1993; Ko et al., 2012; López-Martens et al., 2005).

As shown in Fig. 8.11, the GDD of a 300 nm zirconium (Zr) filter (blue dash-dotted line) and the attochirp (red dashed line) calculated with a peak intensity of 1×10^{15} W/cm^2 are plotted. It is shown that the GDD of the filter is negative below 130 eV, which compensates the positive attochirp. However, above 130 eV,

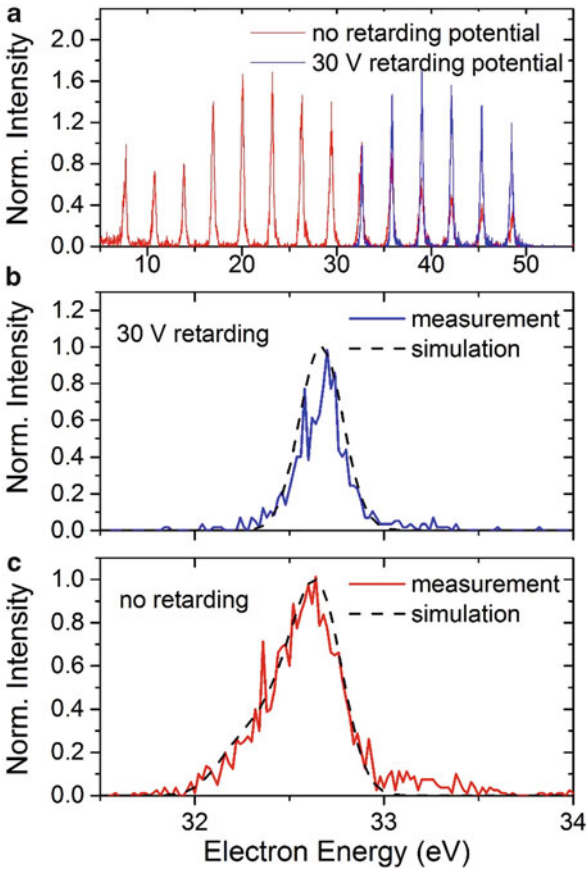

Fig. 8.10 (**a**) The narrow harmonic peaks from HHG driven by a 25 fs laser. *Red*: no retarding potential. *Blue*: 30 V retarding potential. (**b**) Harmonic peak around 33 eV with 30 V retarding potential. *Blue solid*: experiment result. *Black dash*: simulation. (**c**) Harmonic peak around 33 eV with no retarding potential. *Blue solid*: experiment result. *Black dash*: simulation

no compensation can be made. Therefore, the spectrum (black solid line) should be chosen to match the area where the attochirp is best compensated for generating the shortest attosecond pulses.

In high-order harmonic generation, the observable spectrum is determined not only by the response of individual atoms but also by the coherent buildup of the XUV photons. As a result, the macroscopic cutoff is $I_p + \alpha U_p$, with α smaller than 3.17 depending on the experimental phase-matching conditions. Utilizing phase mismatch, the single atom cutoff spectrum region with large attochirp that cannot be compensated by the filter can be removed. Experimentally the phase matching can be controlled by the gas pressure inside the gas target (Altucci et al., 1996; Huillier et al., 1993).

The photoelectron spectra generated with DOG recorded by the MBES are shown in Fig. 8.12. The driving peak intensity inside the gate is estimated to be 1×10^{15} W/cm^2. It can be seen that when the neon backing pressure in the gas cell was tuned from 0.03 to 0.33 bar, the cutoff photon energy was observed to decrease from 160 to 120 eV, corresponding to $I_p + 2.6U_p$ to $I_p + 1.8U_p$. It can be seen from Fig. 8.11,

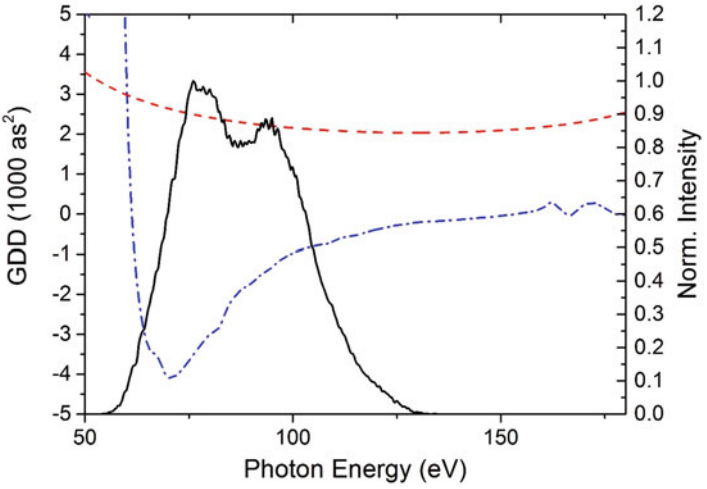

Fig. 8.11 Attosecond intrinsic chirp compensated by a 300 nm Zr filter. The spectrum is specially chosen to cover the area where the attochirp is best compensated. *Black solid line*: XUV spectrum taken with 300 nm Zr filter. *Red dashed line*: intrinsic chirp of the attosecond pulses. *Blue dash-dotted line*: GDD of 300 nm Zr filter

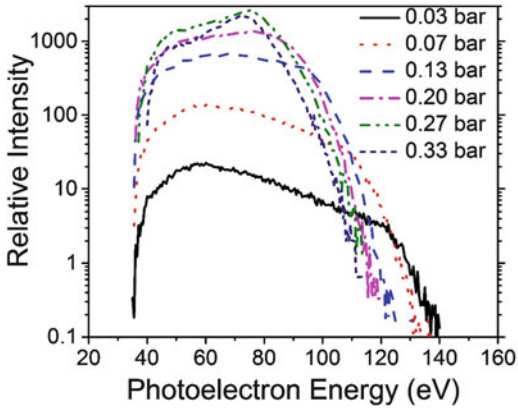

Fig. 8.12 XUV photoelectron spectrum generated by DOG in Ne gas with six different pressures. The length of the gas cell is 1 mm. The peak intensity at the center of the polarization gate is about 1×10^{15} W/cm^2. (Reproduced from Zhao et al., 2012)

the backing pressure of 0.2 bar should be used in the streaking experiment, since the spectrum under this condition matches well with the spectral range where the Zr filter can best compensate the attochirp. The streaking trace taken with this spectrum is shown in Fig. 8.13a, and retrieved spectrum and temporal phase are shown in Fig. 8.13c, d, respectively. Both CRAB and PROOF methods were applied to the experimental data, and the same results of single 67 as pulse were obtained. In Fig. 8.13b, the filtered streaking trace with one omega frequency $I_{\omega_L}(v, \tau)$ is compared with the retrieved one. The good agreement between those two indicates the validity of the retrieval.

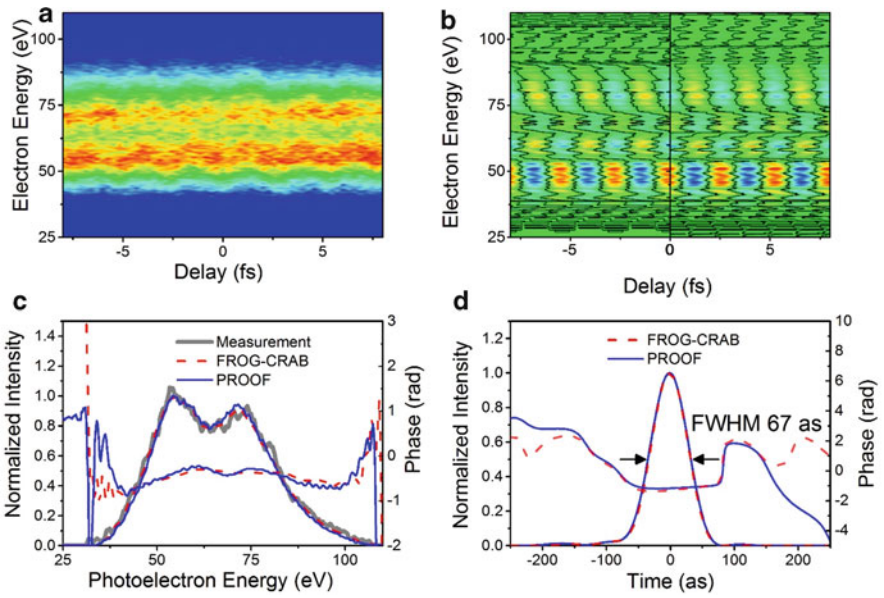

Fig. 8.13 Characterization of a 67 as XUV pulse. (**a**) Streaked photoelectron spectrogram obtained experimentally. (**b**) Filtered $I_{\omega L}$ trace (*left*) from the spectrogram in (**a**) and the retrieved $I_{\omega L}$ trace (*right*). (**c**) Photoelectron spectrum obtained experimentally (*thick gray solid*) and retrieved spectra and spectral phases from PROOF (*blue solid*) and FROG-CRAB (*red dashed*). (**d**) Retrieved temporal profiles and phases from PROOF (*blue solid*) and FROG-CRAB (red dashed). (Reproduced from Zhao et al., 2012)

8.5.4 Broadband Supercontinuum Generation with Lens Focusing

In order to generate an even broader-bandwidth attosecond continuum, higher intensity is needed inside the gate. The easiest way is to use a tighter focusing configuration for the input driving laser. However, due to space limitations, further shortening the focal length using the two-mirror configuration would introduce significant astigmatism. To reduce the astigmatism, lenses can provide a good alternative to mirrors if the input beam size and focal length are chosen properly and the material dispersion is compensated (Porras et al., 2012).

Calculations were done with the parameters for our experiment, assuming a transform-limited 7 fs input pulse and a 140 mm focal length lens. The beam waist on the lens surface is set at 3 mm (Fig. 8.14).

It can be seen that even when the beam size at the lens is 3 mm (which allows about 70% of the total power incident on the lens), the pulse duration and spectrum are not significantly changed at the focus when the dispersion is pre-compensated. Therefore, a lens can be used in generating supercontinuum spectra and single attosecond pulses. A spectrum using the lens focusing configuration and measured

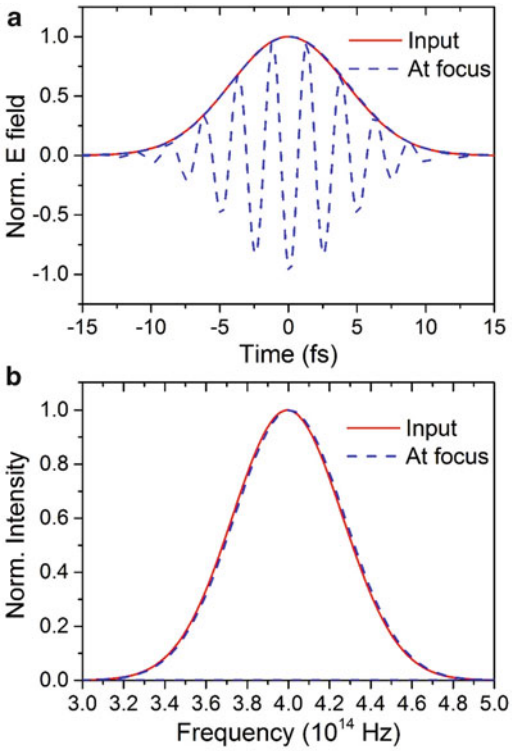

Fig. 8.14 Performance of the lens focusing a 7 fs TL input pulse, with 3 mm waist on the lens surface. (**a**) The electric field in the temporal domain. *Red solid line*: input field. *Blue dashed line*: electric field at the focus. (**b**) The laser spectra. *Red solid line*: input field. *Blue dashed line*: electric field at the focus

with our TOF spectrometer is shown in Fig. 8.15. The cutoff extends to 180 eV photon energy, which supports 40 as pulses.

8.6 Route to the Generation of Single 25 as Pulses

To generate 25 as pulses, which is about one atomic unit, significant challenges still remain. First of all, a transform-limited 25 as Gaussian pulse has a spectral FWHM of 75 eV, and its whole spectrum covers about 150 eV energy range. In order to detect such a broadband spectrum, the spectrometer resolution becomes a critical parameter. The imperfection of the spectrometer can smear out the small structures inside the XUV photoelectron spectra and therefore deteriorate the accuracy of the characterization. Second, to support 25 as pulses, ideally a photon spectrum covering I_p to 170 eV should be used. However, no metallic filters available are transparent within such a spectral window. Several filters can transmit over a 150 eV bandwidth only at the energy region near 500 eV or above, which is extremely difficult to achieve. In this section, important progress which has been made just recently at iFAST to address those two issues is discussed.

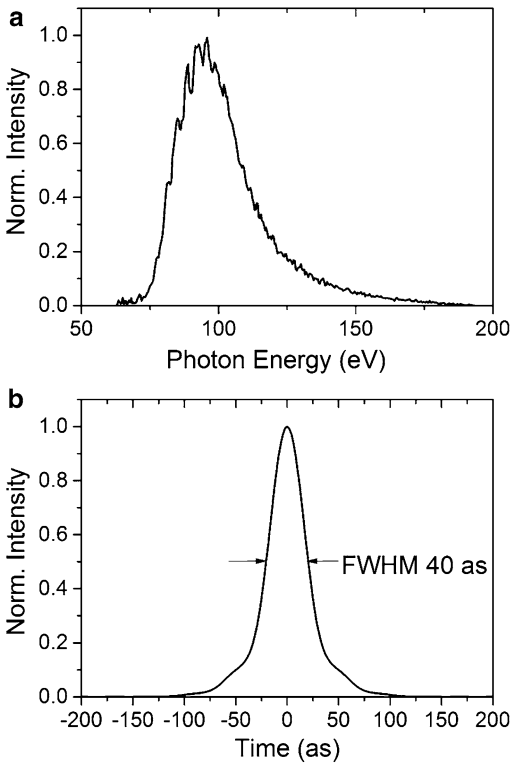

Fig. 8.15 (**a**) The supercontinuum spectrum measured with a 140 mm focal lens and a 300 nm molybdenum filter. The cutoff has extended to 180 eV photon energy. (**b**) The Fourier-transformed temporal spectrum assuming TL pulse for the spectrum in (**a**). The FWHM is 40 as

8.6.1 Characterizing the Contrast of 25 as Isolated Pulses

When an isolated attosecond pulse is generated from the HHG, the main pulse is always accompanied by pre- and post-pulses, usually referred to as satellite pulses, albeit one gating technique or another is employed (Chang, 2005; Chini et al., 2009b; Goulielmakis et al., 2008; Sansone et al., 2006). Usually the intensity of those satellite pulses should be less than 10% of the main pulse, to avoid disturbing the system under investigation by the attosecond pump-attosecond probe experiments. The contrast of the attosecond XUV pulses can be retrieved from attosecond streaking traces (Mairesse & Quéré, 2005). However, the effect of the spectrometer resolution on the characterization accuracy needs to be studied carefully, especially for 25 as pulse due to its ultrabroad spectral range.

To numerically study the retrieval effects, we considered the characterization of a 25 as transform-limited (TL) Gaussian pulse, with central energy at 151 eV. It has pre- and post-pulses with 1% intensity contrast to the main pulse. The satellite pulses have 50 as pulse duration and are 2500 as away from the main pulse, as depicted in Fig. 8.16a. The spacing equals to one optical period of the driving laser centered at 750 nm, which is typical for the double optical gating (Chang, 2007). The Fourier-transformed spectrum is shown in Fig. 8.16b, which extends from 30 eV to

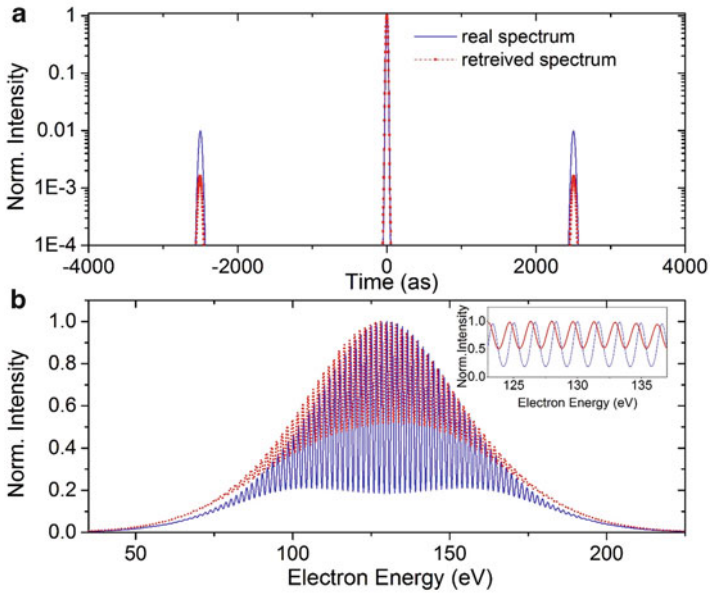

Fig. 8.16 Effects of the response function on characterizing satellite pulses (1% satellite pulse is assumed). (**a**) The *blue solid line* shows the input temporal pulse. The *red dashed line with dot* is the retrieved temporal pulse from the streaking trace. (**b**) The *blue solid line* shows the spectrum of the input pulse, and the *red dashed line* is the convoluted spectrum in a 3 m TOF. *Inset* shows the enlarged spectra from 120 to 140 eV

220 eV. The red dashed line in Fig. 8.16b represents the spectrum after convoluting the spectrum with the MBES response function calculated with 3 m flight tube. Since the response function is dependent on electron energy, the convolution is done by multiplying each element in the spectral spectrum by its corresponding response function, and then adding them together. Each response function has to be normalized to its area before the multiplication to ensure the equal weight for all energies. Immediately it can been seen that the interference depth is reduced, due to the convolution.

Next, a streaking spectrogram is generated with the XUV pulse and a 5 fs, 750 nm near-infrared (NIR) streaking pulse which has a peak intensity of 5×10^{11} W/cm^2. The spectrum at each delay in the streaking spectrogram is independently convoluted with the response function. Then, the spectrum phase is characterized by the CRAB technique, and the retrieved temporal intensity profile is plotted in Fig. 8.16a, as a comparison with the input pulse. It can be seen that the satellite pulse contrast retrieved from the convoluted spectrum is only 0.16%, much smaller than the 1% true value. The reason is the interference pattern between the satellite pulses, and the main pulse is greatly smeared out by the response function. Therefore, retrieval from the recorded spectrum significantly underestimates the satellite pulse contrast (best seen from the inset of Fig. 8.16b).

To improve the spectrometer resolution, one can increase the length of the flight tube of MBES. Our simulation shows that with an 8-m-long flight tube, the retrieved 1% satellite pulse is 0.36%. Even though the satellite pulse is retrieved more accurately than with the 3 m flight tube, it is still three times smaller than the real value.

Further increasing the flight tube could not significantly improve the energy resolution because the error introduced during the increased flight distance starts to play a role. Alternately, the response function of the TOF can be further improved by eliminating electrons with large emission angles. Actually, in the attosecond streaking experiment, electrons emitted with large angles are highly unwanted because the streaking effects decrease with emission angle. Electrons emitted with angles larger than 90° will be streaked to the opposite direction. Therefore, it would be ideal to block the large angle electrons for both the benefit of the streaking data quality and energy resolution. Given the fact that electrons with larger emission angle deviate transversely away from the axis of the flight tube more as they fly in the magnetic field, a pinhole can effectively block those electrons. Theoretically the pinhole can be put anywhere between the generation point of the photoelectrons and the electron detector. However, experimentally it is much easier to put it at the beginning of the electron trajectory. We plotted the relation between the pinhole size and the collection angle as shown in Fig. 8.17a, b. The pinhole size varies from 0.15 to 0.4 mm and is placed 2 mm away from the electron birth place. Then, the new response function with different pinhole size can be calculated from the revised collection angle. Particularly, the response functions of 180 eV electrons for 0.25 mm pinhole in 8 m TOF are shown in Fig. 8.18. Comparing with the response function without pinhole (red dashed line in Fig. 8.18), it can be seen that the long tail of the response function is eliminated and the FWHM is 0.19 eV for the 8 m TOF.

To study the effects of the pinhole size on the accuracy of satellite pulse contrast measurements, we simulated the streaking trace using the spectra convoluted with the new response functions and plotted the retrieved satellite pulse contrast as a function of pinhole size in Fig. 8.19. To compare, the real value is also plotted for satellite pulses with intensities of 1% of the main pulses. This figure shows that as pinhole size decreases, the satellite pulse characterization becomes more accurate, as expected. Particularly, a 0.25 mm pinhole in an 8 m TOF can be chosen to retrieve the satellite pulse ratio with less than 10% error. On the other hand, the collection efficiency is also reduced to 15%.

8.6.2 Driving Laser Suppression with Microchannel Plate Filters

In HHG, the driving IR pulse is converted to the XUV light source. However, the conversion efficiency of this process is typically on the order of 10^{-6}–10^{-5}. Therefore, the generated XUV coherent light has to be separated from the remaining

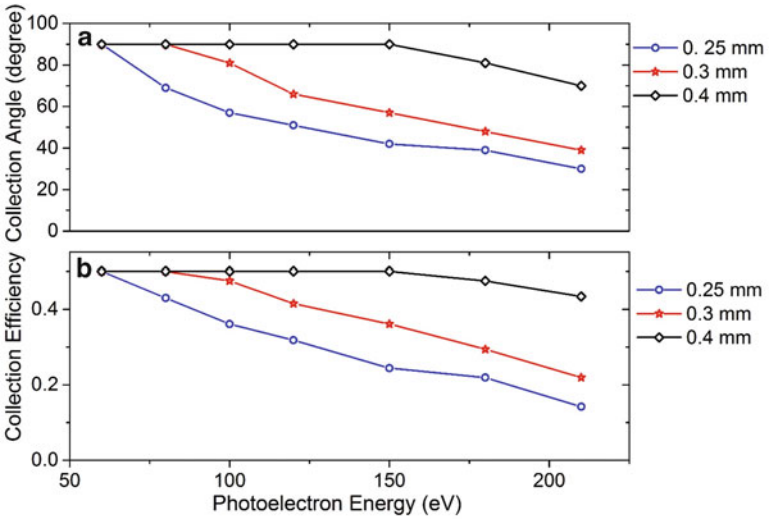

Fig. 8.17 (**a**) Collection angle and (**b**) collection efficiency as functions of the electron energy for different pinhole diameters

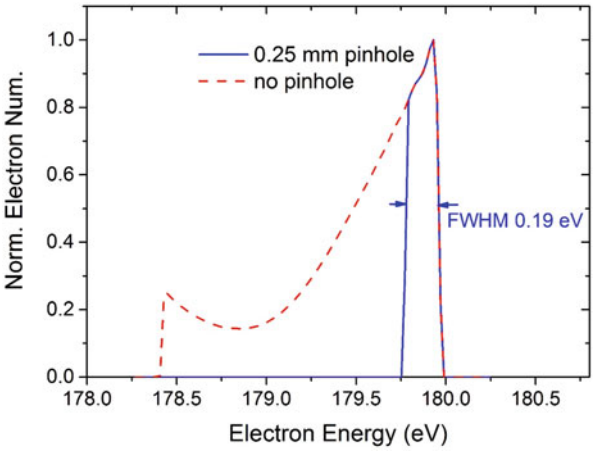

Fig. 8.18 Response function calculated with a 0.25 mm pinhole in the 8 m TOF, for 180 eV electrons (*blue solid line*). The response function without is plotted with red dashed line for comparison

driving laser for detection and characterization. This has been proven to be a technical challenge. Even though there are several methods for filtering out the XUV pulse, all of them lose certain portions of the spectral component, significantly limiting the spectral bandwidth available after the separation and hence ultimately limiting the shortest attosecond pulse achievable (Falcone & Bokor, 1983; Frassetto et al., 2008; Peatross et al., 1994; Takahashi et al., 2004). For example, a metallic filter with hundreds of nanometers thickness is often used to block the IR and transmit the XUV. However, the transmission window of the metallic filter is usually limited. A 300 nm zirconium filter can only transmit photon energies above 60 eV,

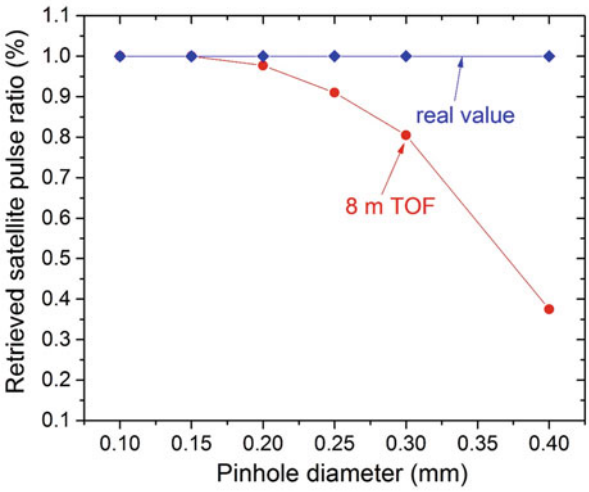

Fig. 8.19 Comparison of the retrieved satellite pulse contrast limited by MBES resolution with real values. The *red line with circles* shows the retrieved contrast with an 8 m TOF. The *blue line with diamonds* shows the real value of 1% contrast as a comparison

and the transmission drops significantly near 300 eV. Another technique is to use a specially designed dielectric mirror which reflects the XUV and transmit the IR. However, this type of dielectric mirror can only reflect XUV pulses with a relatively narrow bandwidth and a low reflectivity.

To address this issue, we proposed and demonstrated that a microchannel plate can be utilized as a short-wavelength-pass filter. It can effectively block the IR driving laser and transmit photons over a broad XUV and X-ray spectral region, leading to the full use of the bandwidth generated from the HHG.

An MCP is made of millions of parallel glass capillaries which lead from one surface to the other. The diameter of each channel is several micrometers, comparable to the wavelength of the IR laser but much larger than that of the XUV or soft X-ray. Therefore, the driving pulses propagating through the MCP are expected to be strongly diffracted, while the high harmonics should be relatively unperturbed after the MCP.

To demonstrate this scheme, the transmission of the MCP was measured at different wavelengths, as shown in Fig. 8.20. Three types of lasers with visible wavelength or longer were used in the measurement shown in Fig. 8.20b. The home-built Ti-sapphire laser has a central wavelength of 750 nm and pulse duration about 25 fs, which is commonly used as the driving pulse for HHG. The ultrafast Mid-IR laser is from a commercial TOPAS (Coherent, HE-TOPAS-Prime), with the central wavelength of 1.6 μm and pulse duration of 50 fs. This type of laser is capable of generating a much broader bandwidth supercontinuum from HHG due to the cutoff extension by the long wavelength (Shan & Chang, 2001). The 532 nm laser is a continuous laser with maximum output energy of 300 mW. The plot in Fig. 8.20 clearly shows that the zeroth-order transmission sensitively depends on the wavelength of the incident beam, varying from the lowest transmission of 0.4% for

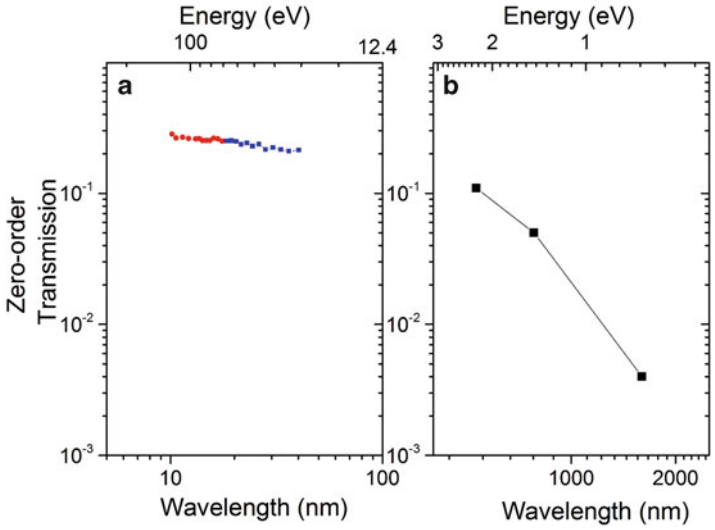

Fig. 8.20 The zeroth-order transmission of the MCP for (**a**) XUV photons and (**b**) visible or longer wavelengths. The *red line* in (**a**) is the transmission measured with 300 nm Zr filter and the *blue dotted line* is with 300 nm Al filter

1.6 μm to 11% for 532 nm wavelength. For the Ti-sapphire laser which is used for HHG in our current setup, the transmission is about 5%.

To separate the XUV and the driving pulse effectively, the transmission of the two through the MCP must be largely different. The total MCP transmission in the XUV spectral region has been measured to be as high as 60% for photon energy from 50 eV to 1.5 keV (Cao et al., 2013), reaching the upper limit set by the MCP opening ratio. For photons with even higher energy, the transmission should be the same due to their shorter wavelength. In our scenario, only the zeroth-order transmission should be used for studying ultrafast dynamics, and therefore the transmission should be evaluated carefully. Experimentally, we placed the filter in the same position as the metallic filter in our HHG beam line. Higher orders of the diffracted light were blocked by the hole mirror, and eventually only the zeroth-order transmission contributes to the photoelectron spectrum recorded by the MBES.

To obtain the zeroth-order transmission of the XUV photons over the MCP, photoelectron spectra with and without the MCP filter are measured under the same condition. An Al filter and a Zr filter were used to block the IR driving laser and to select different energy ranges. The results are shown in Fig. 8.20a. Within the measured energy range, the transmission is about 25%. From Fig. 8.20, it is clearly shown that the transmission is increasing for shorter wavelength, as expected. We believe that for an XUV signal with higher photon energies, the transmission should become larger and eventually reach the opening ratio of the MCP.

Even when the transmission of the MCP filter has been measured, it is still important to compare the photoelectron spectra with MCP filter and metallic filters.

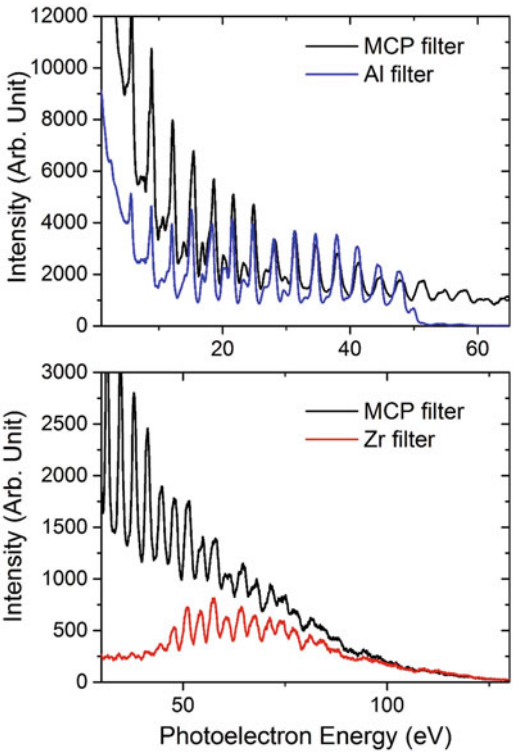

Fig. 8.21 The photoelectron spectra taken with MCP (black), Al filter (blue), and Zr filter (red) under the same condition. The relative intensities are adjusted to shown the comparison

As shown in Fig. 8.21, the spectra taken with MCP filter, 300 nm aluminum (Al) and 300 nm zirconium (Zr) filters under the same condition were plotted separately. The spectrum taken with the MCP filter has shown discrete harmonics clearly, and good agreement between the spectra with MCP and metallic filters can be observed. The remaining energy of the driving laser after passing through the MCP filter is less than 1 μJ due to the large diverging angle and does not noticeably affect the photoelectron spectrum. This means it is possible to characterize the attochirp with RABBITT or PROOF (Chini et al., 2010; Mairesse & Quéré, 2005).

This technique has greatly extended the bandwidth usable from the XUV supercontinuum generation and essentially paves the way for achieving an ultrabroadband coherent XUV light source.

8.7 Conclusion and Outlook

In summary, we have discussed the latest frontiers in the generation and characterization of a single attosecond pulse from high-order harmonic generation. The double optical gating method is developed to increase the intensity inside the gate and hence

to extend the bandwidth of the attosecond XUV source. To overcome the bandwidth limit set by previous phase-retrieving technique, the PROOF method is developed to retrieve phase information for the complete characterization of ultrabroadband attosecond XUV pulses. Experimentally, an electron energy spectrometer with high resolution and collection efficiency was built for attosecond streaking experiment. A 67 as isolated pulse was demonstrated in 2012. Finally, several important issues regarding the 25 as single pulse measurement have been discussed in detail. The spectrometer resolution is found to be greatly improved by placing a pinhole near the entrance of the MBES, enabling the accurate satellite pulse contrast retrieval. Additionally, an MCP filter was demonstrated for an ultrabroadband coherent light source.

To further shorten the attosecond pulse duration and to obtain broader bandwidth supercontinuum, few-cycle mid-infrared laser should be used for the extended HHG cutoff and reduced intrinsic chirp. Technologies which allows for compensating the HHG intrinsic chirp in a wide spectral range are still needed for generating isolated 25 as pulse.

Acknowledgments The authors acknowledge the contributions of Michael Chini for the PROOF algorithm development and Yi Wu and Eric Cunningham for maintaining the laser. The work is funded by the National Science Foundation under grant number 1068604, Army Research Office, and the DARPA PULSE program by a grant from AMRDEC.

References

Altucci, C., Starczewski, T., Mevel, E., Wahlström, C.-G., Carré, B., & L'Huillier, A. (1996). Influence of atomic density in high-order harmonic generation. *Journal of the Optical Society of America B, 13*(1), 148. https://doi.org/10.1364/JOSAB.13.000148

Ammosov, M. V., Delone, N. B., & Krainov, V. P. (1986). Tunnel ionization of complex atoms and of atomic ions in an alternating electromagnetic field. *Soviet Physics JETP, 64*, 1191.

Baker, S., Robinson, J. S., Haworth, C. A., Teng, H., Smith, R. A., Chirila, C. C., … Marangos, J. P. (2006). Probing proton dynamics in molecules on an attosecond time scale. *Science (New York, N.Y.), 312*(5772), 424–427. https://doi.org/10.1126/science.1123904

Cao, Z., Jin, F., Dong, J., Yang, Z., Zhan, X., Yuan, Z., … Ding, Y. (2013). Soft x-ray low-pass filter with a square-pore microchannel plate. *Optics Letters, 38*(9), 1509–1511.

Cavalieri, A. L., Müller, N., Uphues, T., Yakovlev, V. S., Baltuska, A., Horvath, B., … Heinzmann, U. (2007). Attosecond spectroscopy in condensed matter. *Nature, 449*(7165), 1029–1032. https://doi.org/10.1038/nature06229

Chang, Z. (2004). Single attosecond pulse and xuv supercontinuum in the high-order harmonic plateau. *Physical Review A, 70*, 43802.

Chang, Z. (2005). Chirp of the single attosecond pulse generated by a polarization gating. *Physical Review A, 71*(2), 023813. https://doi.org/10.1103/PhysRevA.71.023813

Chang, Z. (2007). Controlling attosecond pulse generation with a double optical gating. *Physical Review A, 76*, 051403(R).

Chang, Z., & Corkum, P. (2010). Attosecond photon sources: The first decade and beyond [Invited]. *Journal of the Optical Society of America B, 27*(11), B9. https://doi.org/10.1364/JOSAB.27.0000B9

Chini, M., Mashiko, H., Wang, H., Chen, S., Yun, C., Scott, S., ... Chang, Z. (2009a). Delay control in attosecond pump-probe experiments. *Optics Express, 17*, 21459.

Chini, M., Wang, H., Khan, S. D., Chen, S., & Chang, Z. (2009b). Retrieval of satellite pulses of single isolated attosecond pulses. *Applied Physics Letters, 94*(16), 161112. https://doi.org/10.1063/1.3125247

Chini, M., Gilbertson, S., Khan, S. D., & Chang, Z. (2010). Characterizing ultrabroadband attosecond lasers. *Optics Express, 18*(12), 13006–13016. https://doi.org/10.1364/OE.18.013006

Chini, M., Zhao, K., & Chang, Z. (2014). The generation, characterization and applications of broadband isolated attosecond pulses. *Nature Photonics, 8*(3), 178–186. https://doi.org/10.1038/nphoton.2013.362

Corkum, P. (1993). Plasma perspective on strong field multiphoton ionization. *Physical Review Letters, 71*(13), 1994–1997. https://doi.org/10.1103/PhysRevLett.71.1994

Corkum, P. B., Burnett, N. H., & Ivanov, M. Y. (1994). Subfemtosecond pulses. *Optics Letters, 19*(22), 1870. https://doi.org/10.1364/OL.19.001870

Delong, K. W., Fittinghoff, D. N., Trebino, R., Kohler, B., & Wilson, K. (1994). Pulse retrieval in frequency-resolved optical gating based on the method of generalized projections. *Optics Letters, 19*(24), 2152–2154.

Falcone, R. W., & Bokor, J. (1983). Dichroic beam splitter for extreme-ultraviolet and visible radiation. *Optics Letters, 8*(1), 21–23.

Feng, X., Gilbertson, S., Mashiko, H., Wang, H., Khan, S. D., Chini, M., ... Chang, Z. (2009). Generation of isolated attosecond Pulses with 20 to 28 Femtosecond Lasers. *Physical Review Letters, 103*, 183901.

Ferray, M., L'Huillier, A., Li, X. F., Lompre, L. A., Mainfray, G., & Manus, C. (1988). Multiple-harmonic conversion of 1064 nm radiation in rare gases. *Journal of Physics B, 21*, 31.

Frassetto, F., Villoresi, P., & Poletto, L. (2008). Beam separator for high-order harmonic radiation in the 3-10 nm spectral region. *Journal of the Optical Society of America. A, Optics, Image Science, and Vision, 25*(5), 1104–1114.

Gagnon, J., & Yakovlev, V. S. (2009). The robustness of attosecond streaking measurements. *Optics Express, 17*(20), 17678–17693.

Gilbertson, S., Mashiko, H., Li, C., Khan, S. D., Shakya, M. M., Moon, E., & Chang, Z. (2008). A low-loss, robust setup for double optical gating of high harmonic generation. *Applied Physics Letters, 92*, 71109.

Gilbertson, S., Wu, Y., Khan, S. D., Chini, M., Zhao, K., Feng, X., & Chang, Z. (2010). Isolated attosecond pulse generation using multicycle pulses directly from a laser amplifier. *Physical Review A, 81*, 43810.

Goulielmakis, E., Schultze, M., Hofstetter, M., Yakovlev, V. S., Gagnon, J., Uiberacker, M., ... Kleineberg, U. (2008). Single-cycle nonlinear optics. *Science, 320*, 1614.

Henke, B. L., Gullikson, E. M., & Davis, J. C. (1993). X-Ray interactions: Photoabsorption, scattering, transmission, and reflection at E = 50-30,000 eV, Z = 1-92. *Atomic Data and Nuclear Data Tables, 54*(2), 181–342. https://doi.org/10.1006/adnd.1993.1013

Hentschel, M., Kienberger, R., Spielmann, C., Reider, G. A., Milosevic, N., Brabec, T., ... Krausz, F. (2001). Attosecond metrology. *Nature, 414*(6863), 509–513. https://doi.org/10.1038/35107000

Huillier, A. L., Lewenstein, M., Salieres, P., & Balcou, P. (1993). High-order harmonic-generation cutoff. *Physical Review A, 48*(5), 69–72.

Itatani, J., Quéré, F., Yudin, G. L., Ivanov, M. Y., Krausz, F., & Corkum, P. B. (2002). Attosecond streak camera. *Physical Review Letters, 88*, 173903.

Kennedy, D., & Manson, S. (1972). Photoionization of the noble gases: Cross sections and angular distributions. *Physical Review A, 5*(1), 227–247. https://doi.org/10.1103/PhysRevA.5.227

Kienberger, R., Goulielmakis, E., Uiberacker, M., Baltuska, A., Yakovlev, V., Bammer, F., ... Krausz, F. (2004). Atomic transient recorder. *Nature, 427*, 817.

Ko, D. H., Kim, K. T., & Nam, C. H. (2012). Attosecond-chirp compensation with material dispersion to produce near transform-limited attosecond pulses. *Journal of Physics B:*

Atomic, Molecular and Optical Physics, 45(7), 074015. https://doi.org/10.1088/0953-4075/45/7/074015

Kruit, P., & Read, F. H. (1983). Magnetic field paralleliser for 2π electron-spectrometer and electron-image magnifier. *Journal of Physics E: Scientific Instruments, 16*, 313.

López-Martens, R., Varjú, K., Johnsson, P., Mauritsson, J., Mairesse, Y., Salières, P., … L'Huillier, A. (2005) Amplitude and phase control of attosecond light pulses. *Physical Review Letters, 94*(3), 033001. https://doi.org/10.1103/PhysRevLett.94.033001

Mairesse, Y., & Quéré, F. (2005). Frequency-resolved optical gating for complete reconstruction of attosecond bursts. *Physical Review A, 71*, 011401(R).

Mashiko, H., Gilbertson, S., Li, C., Khan, S. D., Shakya, M. M., Moon, E., & Chang, Z. (2008). Double optical gating of high-order harmonic generation with carrier-envelope phase stabilized lasers. *Physical Review Letters, 100*(10), 103906. https://doi.org/10.1103/PhysRevLett.100.103906

McPherson, A., Gibson, G., Jara, H., Johann, U., Luk, T. S., McIntyre, I. A., … Rhodes, C. K. (1987). Studies of multiphoton production of vacuum-ultraviolet radiation in the rare gases. *Journal of the Optical Society of America B, 4*(4), 595. https://doi.org/10.1364/JOSAB.4.000595

Paul, P. M., Toma, E. S., Breger, P., Mullot, G., Auge, F., Balcou, P., … Agostini, P. (2001). Observation of a train of attosecond pulses from high harmonic generation. *Science (New York, N.Y.), 292*(5522), 1689–1692. https://doi.org/10.1126/science.1059413

Peatross, J., Chaloupka, J. L., & Meyerhofer, D. D. (1994). High-order harmonic generation with an annular laser beam. *Optics Letters, 19*(13), 942–944. Retrieved from http://www.ncbi.nlm.nih.gov/pubmed/19844495

Pfeifer, T., Abel, M. J., Nagel, P. M., Jullien, A., Loh, Z.-H., Justine Bell, M., … Leone, S. R. (2008). Time-resolved spectroscopy of attosecond quantum dynamics. *Chemical Physics Letters, 463*(1–3), 11–24. https://doi.org/10.1016/j.cplett.2008.08.059

Platonenko, V. T., & Strelkov, V. V. (1999). Single attosecond soft-x-ray pulse generated with a limited laser beam. *Journal of the Optical Society of America B, 16*(3), 435. https://doi.org/10.1364/JOSAB.16.000435

Popmintchev, T., Chen, M.-C., Popmintchev, D., Arpin, P., Brown, S., Alisauskas, S., … Kapteyn, H. C. (2012). Bright coherent ultrahigh harmonics in the keV x-ray regime from mid-infrared femtosecond lasers. *Science (New York, N.Y.), 336*(6086), 1287–1291. https://doi.org/10.1126/science.1218497

Porras, M. A., Horvath, Z. L., & Major, B. (2012). On the use of lenses to focus few-cycle pulses with controlled carrier–envelope phase. *Applied Physics B, 108*(3), 521–531. https://doi.org/10.1007/s00340-012-5073-y

Sansone, G., Benedetti, E., Calegari, F., Vozzi, C., Avaldi, L., Flammini, R., & Nisoli, M. (2006). Isolated single-cycle attosecond pulses. *Science (New York, N.Y.), 314*(5798), 443–446. https://doi.org/10.1126/science.1132838

Sansone, G., Kelkensberg, F., Pérez-Torres, J. F., Morales, F., Kling, M. F., Siu, W., … Vrakking, M. J. J. (2010). Electron localization following attosecond molecular photoionization. *Nature, 465*, 763.

Seres, J., Seres, E., Verhoef, A. J., Tempea, G., Streli, C., Wobrauschek, P., … Krausz, F. (2005). Laser technology: Source of coherent kiloelectronvolt X-rays. *Nature, 433*(7026), 596. https://doi.org/10.1038/433596a

Shan, B., & Chang, Z. (2001). Dramatic extension of the high-order harmonic cutoff by using a long-wavelength driving field. *Physical Review A, 65*(1), 011804. https://doi.org/10.1103/PhysRevA.65.011804

Takahashi, E. J., Hasegawa, H., Nabekawa, Y., & Midorikawa, K. (2004). *Beam splitter for high-order harmonics in the extreme-ultraviolet region, 29*(5), 507–509.

Trebino, R., Delong, K. W., Fittinghoff, D. N., Sweetser, J. N., Richman, B. A., Krumbu, M. A., & Kane, D. J. (1997). *Review article measuring ultrashort laser pulses in the time-frequency domain using frequency-resolved optical gating, 68*(9), 3277–3295.

Tsuboi, T., Xu, E. Y., Bae, Y. K., & Gillen, K. T. (1988). Magnetic bottle electron spectrometer using permanent magnets. *Review of Scientific Instruments, 59*(8), 1357. https://doi.org/10.1063/1.1139722

Wang, H., Chini, M., Khan, S. D., Chen, S., Gilbertson, S., Feng, X., ... Chang, Z. (2009). Practical issues of retrieving isolated attosecond pulses. *Journal of Physics B: Atomic, Molecular and Optical Physics, 42*(13), 134007. https://doi.org/10.1088/0953-4075/42/13/134007

Zhao, K., Zhang, Q., Chini, M., Wu, Y., Wang, X., & Chang, Z. (2012). Tailoring a 67 attosecond pulse through advantageous phase-mismatch. *Optics Letters, 37*(18), 3891. https://doi.org/10.1364/OL.37.003891

Chapter 9
Supercontinuum in Telecom Applications

S. V. Smirnov, J. D. Ania-Castañón, S. Kobtsev, and S. K. Turitsyn

Abstract This chapter documents progress in the extensive area of supercontinuum (SC) generation research devoted to applications in telecommunications, including research into the different mechanisms of spectral broadening and their interplay, SC generation in various media and the most promising SC applications in fibre-based and free-space telecom.

Keywords Pump power · Optical fibre · Wavelength division multiplexing · Time division multiplexing · All-optical processing · Stimulate Raman scattering · Four-wave mixing · Photonic crystal fibre · Rogue wave · Orbital angular momentum

9.1 Introduction

Supercontinuum (SC) generation and spectral broadening of coherent or partially coherent light signals in optical fibres has captured much attention over the past couple of decades, fuelled by the advent of microstructured photonic crystal fibres (PCF) that can be designed for extremely high non-linear responses (Knight et al., 1996; Leong et al., 2005). Fibre-optic-based supercontinuum presents multiple practical applications both within and outside the field of optical communications (Holzwarth et al., 2000; Fedotov et al., 2000; He et al., 2002; Sanders, 2002; Hartl et al., 2001; Ivanov et al., 2001; Povazay et al., 2002; Wang et al., 2003a; Marks et al., 2002), and the interest in this phenomenon has led to an improved knowledge of the

S. V. Smirnov (✉) · S. Kobtsev
Novosibirsk State University, Novosibirsk, Russia
e-mail: smirnov@lab.nsu.ru

J. D. Ania-Castañón
Instituto de Óptica, CSIC, Madrid, Spain

S. K. Turitsyn
Aston Institute of Photonic Technologies, Birmingham, UK

R. R. Alfano (ed.), *The Supercontinuum Laser Source*,
https://doi.org/10.1007/978-3-031-06197-4_9

interplay between the different non-linear processes affecting high-power radiation evolution in optical fibre waveguides. By applying techniques such as frequency-resolved optical gating (FROG) (Kane & Trebino, 1993; Dudley et al., 2002a; Gu et al., 2002; Cao et al., 2003) and spectral-phase interferometry for direct electric-field reconstruction (SPIDER) (Iaconis & Walmsley, 1998, 1999; Anderson et al., 2000; Stibenz & Steinmeyer, 2004), researchers have been able to painstakingly analyse non-linearly broadened radiation, improve on the models used to describe the broadening process and increase our understanding of the phenomenon (Tamura et al., 2000; Appl. Phys. B **77**, No. 2–3 (2003) – Special Issue: Supercontinuum generation; Biancalana et al., 2003; Foster et al., 2004; Ranka & Gaeta, 1998; Dudley & Coen, 2002; Corwin et al., 2003a; Nikolov et al., 2003). From a purely practical point of view, the progress has also been impressive and has allowed, for example, for generation of high-power supercontinuum radiation (Cumberland et al., 2008; Chen et al., 2011; Chi et al., 2014) with spectra spanning more than one octave, and even reaching thousands of nm (Wadsworth et al., 2002; Nicholson et al., 2003a, 2004a; Takanayagi et al., 2005; Silva et al., 2012; Qin et al., 2009) in microstructured, tapered and highly non-linear fibres (HNLF). Broad supercontinua extending well into the mid-infrared region have been reported using ZBLAN HNLF fluoride fibres (Chenan et al., 2009), ZBLAN PCF (Jiang et al., 2015), chalcogenide tapered fibre (Petersen et al., 2014; Hudson et al., 2017), chalcogenide step-index fibre (Cheng et al., 2016) and silicon-on-sapphire nanowire (Singh et al., 2015).

Supercontinuum generation, first observed in 1970 by R.R. Alfano and S.L. Shapiro in bulk borosilicate glass (Alfano & Shapiro, 1970a), is an essentially non-linear phenomenon arising from synergic combination of several fundamental non-linear processes, most important of which are self-phase modulation (SPM), four-wave mixing (FWM) and stimulated Raman scattering (SRS). The interplay between different non-linear effects has a substantial impact on important SC properties such as homogeneity and coherence. These interactions between different non-linear processes are themselves determined by the pumps' spectral locations and powers and the non-linear and dispersive characteristics of the medium. In that regard, the development of PCFs offered interesting opportunities to control (to some extent) SC generation by using specially tailored fibre waveguides with desirable dispersive and non-linear properties (Reeves et al., 2003; Dudley et al., 2006). Large spectral broadening and SC in optical fibre at the telecom wavelengths was first demonstrated in (Nelson et al., 1983; Baldeck & Alfano, 1987), whereas the first application of photonic crystal fibre for SC generation was demonstrated in 1999 in (Ranka et al., 1999, 2000a).

Despite important recent advances in SC studies, and although the main mechanisms of SC generation are well understood, a number of fundamental problems are yet to be explored, and the complex interplay of intervening factors can be elusive. Hence, all-encompassing, universally valid, quantitatively precise numerical modelling for SC generation in optical fibre is yet to be fully realised. Important topics for basic research in this field have included the study of the noise and coherence properties (Dudley & Coen, 2002; Corwin et al., 2003a, b; Mori et al.,

1998; Nakazawa et al., 1998; Kubota et al., 1999; Washburn & Newbury, 2004; Kelleher et al., 2012) of SC, analysis of the effect of polarisation (Proulx et al., 2003; Lehtonen et al., 2003) in the non-linear broadening process, the observation of extreme temporal events such as rogue waves (Dudley et al., 2008) or formulation of a general theory of SC generation based on wave turbulence (Barviau et al., 2009; Swiderski & Michalska, 2013), to name a few.

From an application standpoint, a healthy fraction of the current research is focused on exploitation of fibre-optically generated spectrally broadened radiation, whether in bio-medical optics, where it allows for the improvement of longitudinal resolution in optical coherence tomography by more than an order of magnitude (Hartl et al., 2001; Povazay et al., 2002; Wang et al., 2003a, b; Marks et al., 2002; Drexler et al., 1999; Fercher et al., 2003; Drexler, 2004); in optical frequency metrology, where a revolutionary breakthrough has been achieved (Holzwarth et al., 2000, 2001; Fedotov et al., 2000; He et al., 2002; Sanders, 2002; Jones et al., 2000; Diddams et al., 2000a, b, 2001; Bellini & Hänsch, 2000); or in many other areas from material science (Wang et al., 2003c) to telecommunications. Note that in some telecom applications, in contrast to the technologies mentioned above, ultra-large broadening associated with SC generation is not a desirable feature at all, and many useful applications require moderate or even minimal spectral broadening of the signal or pumping wave. The aim of this manuscript is to provide the reader with a general overview of the recent development of spectral broadening applications and SC generation in the particular area of optical communications.

9.2 Basic Physics of Optical Spectral Broadening and SC Generation in Fibres

Light radiation propagating through a non-linear medium experiences spectral broadening that can be very substantial under certain conditions. SPM—an effect caused by dependence of the refractive index on the intensity of the transmitted light (Kerr non-linearity)—has been identified in the early works on continuum generation (CG) of 4-ps-long laser pulses propagated through bulk samples of different glasses and crystals (Alfano & Shapiro, 1970a, b) as the main mechanism responsible for generation of ~50-THz-wide spectra. In a medium with Kerr non-linearity, after propagation over the distance z, an optical pulse acquires an additional phase (due to non-linear part Δn of the refractive index) that can be estimated (Agrawal, 2001) as:

$$\varphi_{NL}(z,t) = \Delta n \cdot \frac{\omega}{c} z = n_2 I(t) \cdot \frac{\omega}{c} z \tag{9.1}$$

The corresponding frequency shift then is:

$$\delta\omega(z,t) = -\frac{d}{dt}\varphi_{NL}(z,t) = -n_2\frac{dI(t)}{dt}\cdot\frac{\omega}{c}z \tag{9.2}$$

where n_2 is the non-linear refractive index of the medium, ω the carrier frequency, c the light speed in vacuum and I the power flux density. It can be seen from (9.2) that, as the optical pulse propagates, the frequency at its leading edge decreases and that at the trailing edge, conversely, increases. Spectral broadening is proportional both to the energy flux and to the propagation distance; therefore, SPM can be amplified due to self-trapping, which was reported in (Alfano & Shapiro, 1970b). When the pump power is greater or about 10 TW/cm^2, which can be reached in light filaments, free-electron plasma formation can also occur, further strengthening the effect of SPM (Bloembergen, 1973).

One of the primary inherent disadvantages of CG schemes based on bulk media (also including those based on liquids (Werncke et al., 1972; Smith et al., 1977) and gases (Corkum et al., 1986; Corkum & Rolland, 1989; François et al., 1993) as non-linear media) is a requirement of high pump powers. Typical level of power density required is around several terawatts per cm^2, thus necessitating additional amplification of laser pulses at the risk of sample damage. It became possible to relax such high pump power requirements during the next phase of SC generation studies by using optical fibres as non-linear medium (Tamura et al., 2000; Lin & Stolen, 1976; Baldeck & Alfano, 1987; Morioka et al., 1993). The required pump power was lowered, on the one hand, due to a substantially longer path of interaction between light and matter and, on the other hand, thanks to a higher localisation of radiation. Thus, for example, dispersion length for 4-ps-long Gaussian pulses at 530 nm in standard SMF-28 is about 80 m, or 5.3×10^4 times larger than the length of light filaments observed in (Alfano & Shapiro, 1970b), which amounted to about 1.5 mm. The effective area of SMF-28 at 530 nm is about 50 μm^2, which is 30–60 times smaller than the area of power concentration estimated for 5–10 light filaments having diameter of 20 μm each as observed in (Alfano & Shapiro, 1970b). Correspondingly, generation of continuum covering a significant part of the visible spectrum became possible with a peak pump power of only 1 kW (Lin & Stolen, 1976), whereas the power used to induce CG in glasses was about 200 MW (Alfano & Shapiro, 1970b).

In early experiments using optical fibres (Lin & Stolen, 1976; Baldeck & Alfano, 1987), continuum was formed by broadening and merging of separate spectral lines, generated due to SRS and FWM. Phase matching conditions for the latter were met as a result of multi-mode propagation of light through the fibre. SPM could not contribute considerably to the spectrum broadening because of low power density and comparatively long pulses (within picosecond and nanosecond range), so that the value of dI/dt in (9.2) was small compared to those typical in bulk media experiments.

In the next generation of fibre experiments on SC generation, however, SPM plays a key role again, allowing one to obtain flat spectra with good noise parameters

in the normal dispersion regime. By using additional optical elements with negative second group velocity dispersion β_2, it is possible to achieve temporal compression of pump pulses as well (Fisher et al., 1969; Gouveia-Neto et al., 1987; Tomlinson et al., 1984). With this method, it was possible to generate pulses as short as 6-fs (Fork et al., 1987). Another physical mechanism of spectral broadening is based on adiabatic soliton compression in a fibre with decreasing dispersion (Tamura et al., 2000; Tamura & Nakazawa, 1998; Mori et al., 1997; Okuno et al., 1998). A relative disadvantage of this method is instability of higher-order solitons in the presence of noise, which imposes an upper limit on the pump power and, hence, on the resulting spectral width.

One can also combine these two approaches using specially designed fibres with dispersion smoothly changing along the fibre from positive to negative values (Mori et al., 1997, 2001; Okuno et al., 1998).

The most recent period of CG investigations is associated with the development of PCFs (Knight et al., 1996, 1997, 1998a, b, c; Birks et al., 1997; Broeng et al., 1998; Mogilevtsev et al., 1998; Silvestre et al., 1998). Essentially, they consist of quartz fibres sheathed in a conduit formed by two-dimensional (usually regular) array of air-filled capillaries (Zheltikov, 2000). It is pertinent to note that there are two different types of fibres called PCF. The first of them proposed in 1996 (Knight et al., 1996) has a quartz core with refractive index greater than the average refractive index of cladding formed by an array of air capillaries. The principle of light propagation in this type of fibre is similar to that in standard optical fibres where the condition $n_{core} > n_{cladding}$ is also met. Fibres of the second type introduced in 1999 (Cregan et al., 1999) have an air channel in the core, so that the inverse inequality holds: $n_{core} < n_{cladding}$. These fibres can be considered as two-dimensional crystals, and a single or several holes (capillaries) absent in the centre of the lattice can be treated as a defect. Light propagation along this type of fibre is possible due to the photon band-gap effect. One of the most important applications of the hollow-core PCF is in high-power lasers, since breakdown threshold in gases is much higher than in solids (Zheltikov, 2000), and thus special efforts are required to obtain intense SC in condensed media (Lu et al., 2014). In this paper, we will use the term PCF for fibres of the first type—guiding light through the effect of total internal reflection.

Compared to conventional optical fibres, PCF presents several significant advantages. First of all, this type of fibre gives a quite unique opportunity of dispersion control. This is possible because penetration of electro-magnetic field into the fibre cladding (and hence, its effective index of refraction) depends on the wavelength of radiation inside the fibre. As a result, the refractive index of the cladding at different wavelengths can be controlled by arranging capillaries in a certain way at the time of pulling. This technique was used to create fibres with flat dispersion profile (Ferrando et al., 1999, 2000, 2001; Reeves et al., 2002; Renversez et al., 2003; Saitoh et al., 2003; Poli et al., 2004; Saitoh & Koshiba, 2004), which allow generation of flat and wide SC spectra. In addition, one can shift the zero dispersion wavelength λ_{ZD} of PCF and produce anomalous dispersion in the visible spectral region (Knight et al., 2000; Ranka et al., 2000b). It is the latter feature that made

it possible to generate SC spanning more than two octaves (Ranka et al., 2000a). Another advantage is that PCF can be designed to support only one spatial mode in a wide spectral range (Birks et al., 1997; Mogilevtsev et al., 1998) having rather small effective area of the waveguide mode.

We note also a special type of PCF called free-strand or cobweb fibre (Wadsworth et al., 2002; Apolonski et al., 2002). The quartz core of such waveguides is attached to the cladding by a cobweb-like structure of thin bridges, from which the name of the fibres comes. Since the core of cobweb fibres is almost entirely surrounded by air, the structure of these waveguides is similar to that of air-clad tapered fibres (ACTF). Continuum spectra generated in these two types of fibres under the same conditions are nearly identical (Wadsworth et al., 2002). In particular, CG spanning two octaves was observed in ACTF (Birks et al., 2000; Akimov et al., 2002). Soliton self-frequency shift of several hundred nm was also demonstrated in ACTF (Kobtsev et al., 2004) and cobweb fibres (Kobtsev et al., 2005). ACTF have some advantages such as an easier fabrication process compared to PCF, as they can be made by pulling a heated conventional single-mode fibre. On the other hand, the design freedom is limited, since there is practically only one single parameter of ACTF that can be controlled—its waist diameter, which means there are limitations on the fabrication of ACTF with the required dispersion characteristics. Besides, it is quite complicated to make long ACTF due to fragility of very thin quartz strand.

Microstructured fibres can be designed within a huge range of possible dispersive characteristics and parameters, and their non-linearity can be rather large due to a small effective area. These remarkable features call into play a plethora of non-linear mechanisms of spectral broadening in PCF that may differ depending on waveguide dispersion profile, power, wavelength and duration of pumping pulses. For example, using femtosecond pump pulses within the anomalous dispersion region, most of the authors point out a key role of soliton effects in CG (Ortigosa-Blanch et al., 2002; Genty et al., 2002; Husakou & Herrmann, 2001; Herrmann et al., 2002). The red wing of the spectrum generated under these conditions is formed due to soliton self-frequency shift (Gordon, 1986; Mitschke & Mollenauer, 1986; Reid et al., 2002), while the blue one is a result of resonant energy transfer and soliton fission. In the case when a femtosecond pump falls within the normal dispersion region, CG develops in two stages. First, the spectrum of the pumping pulse is broadened to the point of zero dispersion due to SPM and SRS, upon which soliton effects come into play (Ortigosa-Blanch et al., 2002). Parametric processes and Raman scattering are also observed to contribute to CG under these circumstances (Genty et al., 2002).

When duration of pumping pulses is within the picosecond and nanosecond domain, SPM does not affect CG significantly. Spectral broadening is usually assumed to occur as a result of SRS giving rise to a series of spectral lines, each of which, once emerged, can act as a pump source for parametric processes. Phase matching conditions can be met in this case due to proximity of the zero dispersion wavelength (Dudley et al., 2002b; Coen et al., 2001, 2002). When energy is transferred into the region of anomalous dispersion, modulation instability (MI) and soliton effects come into operation and broaden the spectrum further (Knight et al., 1996; Coen et al., 2001).

Let us illustrate in more detail the spectral broadening of femtosecond pump pulses propagating in anomalous dispersion region, this case being the most frequent in CG studies. To do this we will examine the dynamics of spectrum broadening as a function of pump power. Figure 9.1 shows simulated spectra of chirp-free 60-fs-long sech^2 pulses after passing 10 cm through a 2.3-μm-diameter ACTF waist. Pump pulse power increases from 0.5 kW for the bottom graph (Fig. 9.1a) up to 20 kW for the top graph (Fig. 9.1f). The pump pulse spectrum is shown in the bottom of Fig. 9.1 with a dotted line. Our simulations are based on the generalised nonlinear Schrödinger equation (Agrawal, 2001) which is mostly used for theoretical modelling of CG when polarisation effects can be averaged out or neglected. Continuum spectra given in Fig. 9.1 are typical for the case of a femtosecond pump; similar results can be found in numerous published papers (Dudley et al., 2002a, b; Dudley & Coen, 2002). When $P_0 = 0.5$ kW (Fig. 9.1a), the pump pulse spectrum is broadened due to SPM. As the pump peak power reaches 2.5 kW (Fig. 9.1b), a peak at the long-wavelength side of the spectrum emerges. It corresponds to an optical soliton, which experiences an increased shift of its frequency farther into IR region as the pump power grows, thus leading to further spectral broadening. Besides, in this process, the number of solitons also increases, and their spectra begin overlapping and form the red wing of the continuum spectrum. As the pump power rises, the spectrum is also broadened toward shorter wavelengths. The position of the short-wavelength spectrum edge depends on the fibre dispersion and is governed by the equality of temporal delays for long- and short-wavelength components of continuum radiation, which agrees with the model of resonant energy transfer into the short-wavelength part of the spectrum mentioned above.

Reports on observation of spectral broadening in media or with light sources never used before with the purpose of CG constituted a significant part of early papers in this field, and they did not cease to appear till now. Among these are, for example, generation of broadband continuum directly in Ti/Sa laser (Morgner et al., 1999; Bartels & Kurz, 2002), CG in fibres with continuous wave pump (Nicholson et al., 2003b; González-Herráez et al., 2003; Avdokhin et al., 2003; Abeeluck et al., 2004) and CG in new types of fibres and waveguides (Phillips et al., 2011; Zhang et al., 2006; Hsieh et al., 2007; Liao et al., 2009; Hudson et al., 2011). However, at the present phase of CG studies, papers of another sort are more common. They are dedicated to investigation of different properties of continuum radiation, such as spectral shape and width (Wadsworth et al., 2002; Mori et al., 2001; Apolonski et al., 2002; Teipel et al., 2003; Tianprateep et al., 2004; Kobtsev et al., 2003), temporal structure (Dudley et al., 2002a; Dudley & Coen, 2002; Teipel et al., 2003; Kobtsev et al., 2003; Bagaev et al., 2004; Zeller et al., 2000), polarisation (Knight et al., 1996; Apolonski et al., 2002; Kobtsev et al., 2003), noise and coherence (Tamura et al., 2000; Dudley & Coen, 2002; Bellini & Hänsch, 2000; Apolonski et al., 2002; Kobtsev & Smirnov, 2006; Demircan & Bandelow, 2007; Heidt et al., 2017), as well as to research into dependence of these properties on conditions of CG. Aside from this, a considerable number of papers seek to understand the physical mechanisms of spectral broadening (Knight et al., 1996; Dudley et al., 2002a, b; Ortigosa-Blanch et al., 2002; Genty et al., 2002; Husakou & Herrmann,

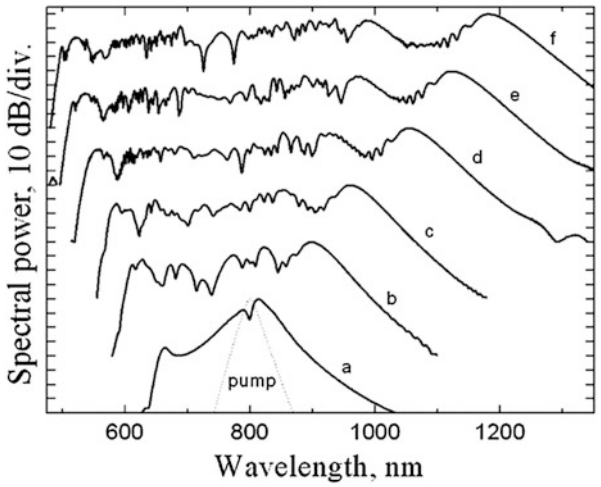

Fig. 9.1 Simulated spectra at the exit of 10-cm-long tapered fibre waist with diameter of 2.3 μm. We use 60-fs-long sech^2 pump pulses at $\lambda = 800$ nm. Pump peak power is 0.5 kW (for graph *a*), 2.5 kW (*b*), 5 kW (*c*), 10 kW (*d*), 15 kW (*e*) and 20 kW (*f*). The pump pulse spectrum is shown at the bottom with a dotted line

2001; Herrmann et al., 2002; Gaeta, 2002; Gorbach & Skryabin, 2007; Skryabin et al., 2003). The practical goal of most of these studies is to optimise continuum generation for diverse applications or even to make SC generators controllable (Kobtsev & Smirnov, 2008a; Genty et al., 2009; Cheung et al., 2011), since each application sets its own specific requirements to the SC properties. For instance, spectroscopic and some other applications require SC in different spectral areas, so that generation of mid- and near-IR SC in short waveguides of different types (Domachuk et al., 2008; Kurkov et al., 2011; Geng et al., 2012; Granzow et al., 2011; Lopez-Galmiche et al., 2016), producing ultra-broadband SC spectra (Silva et al., 2012; Qin et al., 2009), extending SC toward UV (Qin et al., 2009; Kudlinski et al., 2006; Belli et al., 2015; Jiang et al., 2015) and terahertz CG (Kim et al., 2008) and bandwidth maximising/restriction and spectral tailoring (Hu et al., 2010; Bétourné et al., 2009; Kudlinski et al., 2009) are of particular interest. Another example of contradictory requirements is related to the power level, so that both low-threshold (Hudson et al., 2011; Yeom et al., 2008) and high-power SC (Cumberland et al., 2008; Kudlinski & Mussot, 2008; Chen et al., 2010) are interesting for different applications.

As far as telecom applications are concerned, the spectral flatness and temporal parameters of continuum are of a prime importance in development of multiplexing schemes for fibre communication systems. Development of broadband Raman fibre amplifiers requires a high degree of spectral uniformity of the gain factor, and a continuum with a specific spectral profile $I(\lambda)$ can be used as a pump source to solve this problem in a cost-efficient way, avoiding multi-pump schemes.

Let's also note that optical fibre is obviously a very convenient optical medium for experimental investigations into SC generation as well as an appropriate basis for commercial SC generators. That's why the majority of recent studies deal with optical fibres, especially in what concerns telecom applications. However, there is another one very promising research area that is paid a constantly growing attention and that is expected to further gain research focus in the future, namely, on-chip (nano-photonics) SC generators. There have been a number of reports on broadband SC generation in different types of waveguides including silicon (Kuyken et al., 2011; Safioui et al., 2014; N. Singh et al., 2015, 2018; Ettabib et al., 2015), silicon nitride (Johnson et al., 2015; Epping et al., 2015) and others.

9.3 Application of Spectral Broadening and Continuum Generation in Telecom

In this section, we overview the main applications of the spectral broadening effect and SC generation in optical fibre communications. The idea of main SC applications is outlined, whereas in the next section, we will discuss preferable conditions of SC generation that should be met in order to better fulfil the requirements of SC applications in telecom.

9.3.1 Pulse Compression and Short Pulse Generation

Ultrashort optical pulses form the foundation of optical telecom systems. Information transmitted through telecom lines are encoded using amplitude and phase of such pulses. Therefore, it is essential for telecom to have reliable low-noise sources of high-quality ultrashort laser pulses, especially broadband or multi-wavelength sources. The latter can be used for simultaneous transmission of many information channels through a single optical fibre, known as wavelength division multiplexing (WDM) technology, which is the optical analogue of frequency-division multiplexing commonly used for radio transmission.

Islam et al. (1989) demonstrated application of non-linear broadening to generation of femtosecond pulses. When a fibre is pumped in the anomalous dispersion regime with a narrow-spectrum laser, modulation instability and the soliton self-frequency shift initiate a multi-soliton collision that generates a series of short, low-intensity solitons. On the other hand, non-linear temporal compression has been for a long time a well-known technique for generating ultrashort pulses (Tomlinson et al., 1984; Shank et al., 1982). In this technique, the spectrum of the signal is first non-linearly broadened, and the chirp is then eliminated by a dispersion-compensating element. Südmeyer et al. (2003) have recently demonstrated that the use of microstructured fibres, combined with a prism pair for chirp elimination,

would make it possible for this method to be applied at very high power levels, obtaining a train of 33 fs pulses with peak power of 12 MW, whereas Schenkel et al. (2003) employed gas-filled hollow fibres for the broadening, together with a spatial light modulator using SPIDER measurements as a feedback signal for adaptive pulse compression and generation 3.8-fs pulses with energies up to 15 μJ.

The fundamental limits on generation of few-cycle pulses by compression of SC spectra generated in microstructured fibres have been analysed by Dudley & Coen (2004), confirming that quality of compressed pulses was closely related to spectral coherence of the SC. According to their work, a median coherence of about 0.7 could be expected to be a good benchmark for the potential compressibility of SC down to few-cycle pulses, provided compressors with sufficiently high resolution to compensate for the fine structure in the SC group delay were made available in the future.

Conversely, high-power ultrashort pulse sources obtained with techniques such as the ones explained above can be used as the input to generate ultra-broadband octave-spanning SC radiation in optical fibres, as illustrated, for example, by the works of Takanayagi et al. (2005) and Nishizawa and Goto (2001). Stretched femtosecond pulses have been used by Nicholson et al. (2004b) in the development of a high-repetition-rate, swept-wavelength Raman pump source.

9.3.2 Pulse Train Generation at High Repetition Rates

Quite a simple and convenient technique for producing an ultrashort pulse train of high repetition rate was suggested by Hasegawa (1984) and for the first time was implemented by Tai et al. (1986) as early as 1986. This technique utilises the effect of induced modulation instability, i.e., growth of initial relatively small-intensity modulation amplitude of CW radiation due to modulation instability (MI). Such spectral sideband growth is an initial stage of spectral broadening and SC generation.

Since the first demonstration, a number of groups proposed different modifications and improvements of this method (see, for instance, Dianov et al., 1989; Chernikov et al., 1993, 1994; Tadakuma et al., 2000; Pitois et al., 2002). Specifically, using numerical modelling (Dianov et al., 1989) and experiment (Chernikov et al., 1993), it was demonstrated that application of optical fibres with adiabatically decreasing dispersion or optical amplifiers allows one to produce periodic trains of non-interacting solitons. Also it was shown that optical fibres with longitudinal step dispersion profile (Chernikov et al., 1994; Tadakuma et al., 2000) allow one to obtain periodic soliton trains. Paper Pitois et al. (2002) theoretically and experimentally demonstrated that generation of regular spectral-limited Gaussian pulses is possible in passive optical fibres with longitudinally constant dispersion provided the pumping wave has optimal power.

Various groups reported generation of ultrashort pulse (USP) trains with repetition frequency in the range between 60 GHz (Chernikov et al., 1994) and 340 GHz

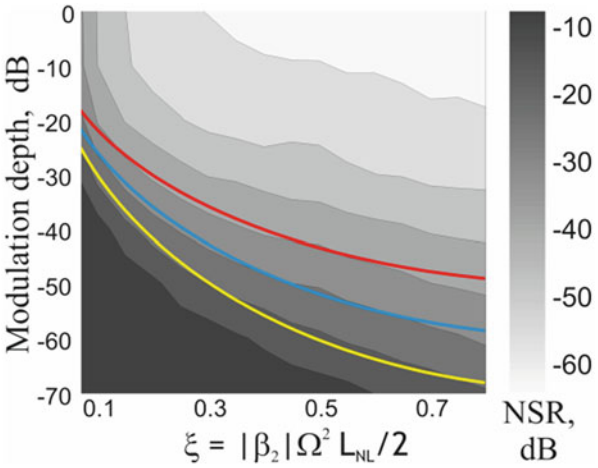

Fig. 9.2 Dependence of noise-to-signal ratio at the fibre exit on parameter ξ and modulation depth I_s/I_0

(Tai et al., 1986). Achieved relatively high USP repetition rates constrain substantially the application field of this technique, since most applications including telecom require post-processing of such pulse train by electronic means. This fact stimulates development of methods for changing and lowering pulse repetition rate attainable with this technique. For example, paper by Chernikov et al. (1993) reported pulse train generation with repetition rate of 80–120 GHz. In the past decade, USP generation with much wider range of repetition rates from 20 GHz up to 1 THz was produced (Fatome et al., 2006). As it has been shown recently (Kobtsev & Smirnov, 2008b), there is a fundamental problem preventing arbitrary low repetition frequencies with the use of induced MI, namely, noise amplification. It can be easily seen, if we consider initial modulation in terms of square of dimensionless frequency $\xi = -\beta_2 \Omega^2 L_{NL}/2 = (\Omega/\Omega_c)^2$, where $L_{NL} = (\gamma P)^{-1}$ stands for non-linear fibre length, γ is fibre non-linearity and P is power of CW pump, that Ω_c is the frequency scale introduced in (Agrawal, 2001). Figure 9.2 shows the results of NLSE-based full numerical modelling (Kobtsev & Smirnov, 2008b) for output pulse train noise-to-signal ratio (NSR) as a function of input modulation depth I_s/I_0 and modulation frequency square ξ. Note that the NSR reaches its minimum at large values of initial modulation depth (0.1 ... 1) and large values of ξ (minimum is reached at $\xi = 1$, whereas the plot shows the range $0.08 < \xi < 0.8$). As the modulation depth is reduced and/or ξ is decreased, NSR worsens and reaches unity (0 dB) in the lower left part of the area plotted in Fig. 9.2, which corresponds to completely "noisy" generation mode and irregular temporal structure of the formed pulse train. This result allows estimation of the minimal pulse repetition frequency for a given NSR and explains the problem of producing pulse frequencies lower than 1 GHz using induced MI (Kobtsev & Smirnov, 2008b).

9.3.3 Multi-wavelength Optical Sources

One of the most important applications of SC to the field of telecommunications is the design of multi-wavelength sources for ultra-broadband wavelength-division-multiplexed (WDM) systems based on spectral slicing of SC generated by a single laser. As it was mentioned in the previous section, a powerful short optical pulse can be non-linearly broadened into a SC spectrum. This spectrum can then be sliced with an array of filters to create a series of WDM channels. This was the approach originally adopted by Morioka et al. (1993) using short (few ps) pulses with GHz repetition rates in dispersion-decreasing fibre (DDF) to create WDM pulsed sources, and different variations have been implemented by multiple authors (Dudley et al., 2008; Morioka et al., 1996; Tamura et al., 1996; Sotobayashi et al., 2002a; Takara et al., 2000, 2003a; Yusoff et al., 2003; Mori et al., 2003; Takada et al., 2002; Miyagawa et al., 2006; Ohara et al., 2006) ever since. In particular, a long-haul data transfer was demonstrated, including distances over 1000 km (Takara et al., 2003a).

The ultimate limit for dense packing of WDM channels in a SC generated from a pulsed source is imposed by the spectral distance between cavity modes in the original mode-locked laser. In a medium with normal dispersion, cascaded non-linear processes used to broaden the spectrum preserve the structure of cavity modes (Alfano, 1989) present in the original laser output. This makes it possible to generate an optical frequency comb, in which the separation between peaks corresponds to the microwave mode-locking frequency of the source laser, with accuracy of the order of kHz (see Sect. 9.4.3 on frequency combs). Each peak can be considered as potential transmission channel. This property was used by Takara et al. (2000) to generate more than 1000 optical frequency channels with a channel spacing of 12.5 GHz between 1500 and 1600 nm. Out of those, between 600 and 700 were demonstrated to offer SNRs and Q-Factors sufficient for 2.5 Gbit/s multi-span transmission. Following the same principle, Takara et al. (2003b) recently reported 124 nm seamless transmission of 3.13 Tbit/s, over 160 km using 313 10 Gbit/s channels spaced at 50 GHz. In their experiment, they used Raman amplification in hybrid tellurite/silica fibre for improved gain flatness. In an even more recent experiment from the same group, Ohara et al. (2005) demonstrated transmission of over 1000 channels, with a 6.25 GHz spacing, using a SC multi-carrier source. In Ref. Takada et al. (2002), supercontinuum radiation within the 1460–1620 nm range was subdivided into 4200 channels spaced 5 GHz apart, and paper by Miyagawa et al. (2006) reports the highest channel count of 10,000 with individual channels spaced at 2.5 GHz within the range of 1460–1640 nm and per-channel data rate of 1.25 Gbit/s. The conservation of coherence properties was also successfully employed by Sotobayashi et al. (2002b) to create a 3.24 Tb/s (84 channels $\times$ 40 Gbit/s) WDM source of carrier-suppressed return-to-zero (CS-RZ) pulses. By generation of SC in a normal dispersion fibre, the relative phase between adjacent pulses is preserved in different channels, allowing for the multiplication of the CS-RZ structure. More recently, but following a related approach, multi-channel

coherent OFDM sources relying also on SC-generated optical frequency combs have allowed capacities of up to 32.5 Tbit/s (Hillerkuss et al., 2011, 2012).

SC WDM sources can be of great utility in more modest systems: Kartapoulos & Bouhiyate (2005), for example, studied the use of supercontinuum sources in coarse WDM applications with channel protection and concluded that in systems with a limited number of channels, the use of supercontinuum WDM sources can result in lower costs and increased reliability.

9.3.4 All-Optical Analogue-to-Digital Conversion

All-optical analogue-to-digital conversion, signal processing and switching are very promising technologies that open new horizons in ultra-high-speed data transmission by allowing one to overcome bit rate limits imposed by electronics.

In a series of recent papers (Oda et al., 2004; Oda & Maruta, 2004, 2005a), Oda et al. proposed and successfully demonstrated a novel quantisation scheme for all-optical analogue-to-digital conversion based on splicing of the non-linearly broadened spectrum of a train of short pulses by means of an arrayed waveguide grating (AWG).

By varying the power of the input pulses by means of an erbium-doped fibre amplifier (EDFA) prior to their launch into a section of dispersion-decreasing fibre (DDF), they were able to generate a series of non-linearly broadened quasi-symmetrical spectra, in which the degree of broadening was directly dependent on the amount of power injected into the fibre. The broadened spectra were then passed through an AWG providing a series of output ports set on the Stokes side of the initial signal. The number of ports that are "on" (i.e., the number of ports that transmit power above a certain threshold) for each spectrum depends on the amount of broadening and thus on the power of the input pulses. This imaginative solution, partially based on the work of Ho et al. (1997), still has to overcome some important problems, such as high average power requirements of the first prototype, but could open the door to a new generation of all-optical analogue-to-digital convertors. A later refinement (Oda & Maruta 2005b) uses a NOLM for coding of the signal after slicing. Since the proposed solution relies only on fibre non-linearity, and not on electronic devices, it can operate beyond 40 GHz.

9.3.5 TDM-to-WDM-to-TDM Conversion

Basically, there are two major approaches for combining low-speed data channels from different local networks into a single high-speed optical telecom line: multiplexing in wavelength and in time. The latter method known as time-division multiplexing (TDM) relies on synchronised switching of communication channels so that the signal from each channel is fed into the high-speed line only for a

fraction of time in an alternating pattern. In contrast, information from different WDM channels is transmitted simultaneously being separated spectrally rather than temporally. Both technologies are widely used to considerably (up to several orders of magnitude) improve the transmission capacity of telecom lines. WDM-to-TDM conversion is required between low-bit-rate WDM data stream and high-bit-rate TDM data stream and vice versa (e.g., at a gateway between local-, metropolitan- and wide-area networks). All-optical multiplexing/demultiplexing schemes allow one to go beyond the present limitations of electronic gateways and thus to further increase achievable bit rates.

Sotobayashi et al. (2001, 2002a) proposed and demonstrated the concept of a photonic gateway able to perform conversion from time-division-multiplexed (TDM) signals to WDM signals and vice versa by using SC generation. Their scheme is based on combining ultrafast photonic processing in both the time and the frequency domain, using optical gating and time shifting in the time domain, combined with non-linear broadening under normal dispersion and spectral slicing.

In order to convert from TDM to WDM, the signal is first amplified and then non-linearly broadened. The spectral properties of SC generated under normal dispersion (high coherence, flat spectrum, easily equalised channel power, similar pulse width in different frequencies and relative independence of the spectrum from the input pulse characteristics) make possible generation of a series of independent channels through spectral splicing, all of them carrying the same sequence of pulses as the original signal. By time-shifting different channels and using an optical time gate with the appropriate repetition rate, it is then possible to split the information between the newly created WDM channels, effectively switching from TDM to WDM.

For the opposite conversion, the process starts by differentially time-shifting the input WDM channels, so the bits transmitted at different frequencies are all in temporal sequence. Then, non-linear broadening effectively performs superposition of all the different channels, and spectral splicing selects a single channel at the central frequency, which now contains the complete bit sequence.

The solution, of course, is not without its drawbacks. Although quite robust with respect to input pulse quality and featuring good noise performance, its response is polarisation dependent (because of the time-gating devices), and its application is limited to the return-to-zero format. It is nevertheless an excellent illustration of the possibilities that non-linear broadening has opened in terms of adding flexibility to signal manipulation.

9.3.6 Optical Fibre Characterisation

Optical fibre plays crucial role in state-of-the-art telecom industry. Besides standard SMF fibres following ITU-T G.652 recommendations, such as SMF-28, used for long-haul data transmission, there is a plethora of types of optical fibres used for amplification, dispersion compensation, optical processing, etc. In order to

improve existing legacy telecom systems, new types of fibres are constantly invented with tailored dispersion and non-linearity. SC provides a convenient, quick and cost-effective way for characterisation of optical fibres in a wide spectral range. Measurements of wavelength-dependent attenuation can be made simultaneously over a wide bandwidth, and group-velocity-dispersion (GVD) measurements in conventional fibre with group delay resolutions of 0.01 ps/km in fibre lengths of up to 130 km over more than 600 nm, using SC white pulses as was demonstrated by Mori et al. (1995). GVD measurements can also be carried out in non-typical media such as tapered air-silica microstructure fibres by means of white-light interferometry with the help of broadband sources, as demonstrated by Ye et al. (2002). Spectral interferometry with a SC source was also used by Jasapara et al. (2003) to perform GVD measurements in photonic bandgap fibre. González-Herráez et al. (2003) showed that continuous-wave generated SC could be effectively used to perform accurate, long-range (>200 km) measurements of polarisation mode dispersion in fibres (see Sect. 9.4.4 for more information on CW-generated SC).

9.3.7 Frequency Combs

One of the most fascinating applications of SC generation, which has revolutionised optical frequency metrology and may potentially have impact on telecom, is frequency comb generation. An optical frequency comb is an optical spectrum showing spectral lines at fixed frequency spacing. A simple example would be the longitudinal mode structure at the output of a mode-locked cavity laser. By measuring frequency separation between laser radiation at a given frequency f and its second harmonic $2f$, the laser's absolute frequency can be determined. Hence, frequency combs can be used as "optical rulers" for high-precision spectroscopy and, by extension, for high-precision frequency or time-based metrology, achieving accuracies of one part in 10^{17} in the measurement of optical clocks (Newbury, 2011; Ye & Cundiff, 2005). In order for a frequency comb to be used for the purpose of determining absolute frequency, its spectrum must span at least a complete optical octave. The development of optical frequency combs earned Profs. John L. Hall and Theodor W. Hänsch one half of the Nobel Prize in Physics in 2005.

Non-linear broadening is the key for generation of at-least-octave-spanning optical frequency combs, and multiple different methods have been proposed and applied that go beyond the scope of this chapter. Let it be mentioned, as a typical example (Ye & Cundiff, 2005), that a stable (one allowing for multiple hours of continuous operation) frequency comb can be generated by non-linearly broadening a high-powered output pulse train from a mode-locked fs fibre laser in a single-mode HNLF. It is important that broadening in the HNLF takes place under controlled effective dispersion and that noise gain is kept sufficiently low not to spoil the spectral comb structure.

Potential applications of frequency combs in telecommunications can be grouped into two distinct groups: namely, those related to extremely precise transmission of signals and those related to transmission of high-speed optical data.

The former makes use of phase coherence and broad bandwidth of frequency combs and could theoretically and through the use of Doppler-compensated fibre links (Newbury, 2011) be used to couple optical clocks with uncertainties of one part in 10^{19}.

The latter application relies on the use of narrow-band, chip-scale frequency combs to enable highly parallel WDM or OFDM with tens or hundreds of channels, in which multi-Terabit/s rates can be achieved while symbol rates are kept low enough to stay compliant with electronics speed limitations (Hillerkuss et al., 2011, 2012; Levy et al., 2012). So far, frequency combs have been successfully applied in this type of Terabit/s optical interconnects to demonstrate 26.2 Tbit/s encoding-decoding with OFDM and up to 32.5 Tbit/s with Nyquist WDM, with net spectral efficiencies of 6.4 bits/Hz. These schemes have been demonstrated to be applicable to transmission of advanced coherent modulation formats (QPSK and dual-polarisation 16QAM signals with Nyquist pulse shaping). Gaeta et al. (2019) have overviewed recent developments and progress in the generation of the optical frequency comb in photonic-chip waveguides by using supercontinuum. The underlying physics of generating a frequency comb in microresonators exploiting Kerr effect is very similar to fibre systems. Therefore, a solid knowledge accumulated during the study of supercontinuum and solitons in nonlinear fibre-optics can be transferred to micro-resonator systems, enabling comb technology for a broad spectral range from the near-ultraviolet to the mid-infrared with numerous practical applications including and beyond telecom.

9.3.8 Orbital Angular Momentum Multiplexing

Although linear optics has a pretty long story, there is a concept that was discovered only several decades ago, namely, orbital angular momentum (OAM). Optical beams carrying OAM have a helical phase structure and attracted much attention last years. In contrast to spin angular momentum associated with photon spin that has only two possible values $\pm\hbar$ (what corresponds CW and CCW circular beam polarisations; here $\hbar$ is Planck's constant), OAM is theoretically unlimited and thus has a great potential for increasing the capacity of communication systems, either by using different OAM states as encoding basis or by employing OAM beams as information carriers for multiplexing (Gibson et al., 2004). Let's note that OAM multiplexing may be used in combination with other well-established techniques such as polarisation-division multiplexing (PDM), optical time-division multiplexing (OTDM), etc.

In particular, the group of Prof. Willner (Wang et al., 2012) reported proof-of-concept experiments demonstrating the multiplexing/demultiplexing of information-carrying OAM beams for terabit free-space data transmission, as well

as data exchange between OAM beams for efficient all-optical data processing. The authors used four polarisation-multiplexed OAM beams, each carrying a 42.8 × 4 Gbit/s (4 bits per symbol) quadrature amplitude modulation (16-QAM) signal, thereby achieving a capacity of 1369.6 (42.8 × 4 × 4 × 2) Gbit/s (4 bits per symbol for the 16-QAM, with 4 OAM beams and 2 polarisation states) with a spectral efficiency of 25.6 bit/s/Hz (50 GHz grid). Two years later, the Willner's group managed to improve their first results by almost two orders of magnitude: by utilising WDM along with OAM and polarisation multiplexion, they demonstrated 100 Tbit/s free space data link (Huang et al., 2014). Let's note that OAM-carrying supercontinuum for WDM and other applications can be generated by introducing helical phase wavefront either before (Prabhakar et al., 2019) or after spectral broadening (Sztul et al., 2006; Wright et al., 2008).

OAM multiplexing can be used also for data transfer through optical fibres, as a particular case of mode-division multiplexing, with much of the transmitter and receiver technology being similar to those used for free-space communications (Willner & Liu, 2020). However, in this case, special efforts should be made in order to mitigate significant modal cross-talk that takes place in conventional optical fibres (Bozinovic et al., 2013; Richardson et al., 2013; Ndagano et al., 2015; Brunet et al., 2014).

Finally it's worth noting that OAM multiplexing can be implemented not only in optics but also in other frequency bands of electromagnetic waves, in particular, in millimeter-wave communications (Yan et al., 2014; Willner et al., 2015; Ren et al., 2017), what makes this technique very promising for future generations of cellular data networks.

9.4 Different Regimes of SC Generation

A series of major SC applications in telecom were outlined above. In our treatment, we have so far focused on applications, not paying close attention to practically important questions about conditions that should be met in order to obtain required spectral broadening and properties of generated SC. In what follows, we perform briefly such analysis, namely, we discuss the main regimes of SC generation and properties of SC generated under different conditions (including peculiarities of temporal structure, noise and coherence) as well as applicability of different supercontinua in telecom.

9.4.1 Pulse-Pumped SC

Along with spectral properties such as bandwidth and spectral power uniformity, temporal structure of SC radiation may be critical for various applications including telecom, spectroscopy, sensing, ultrashort pulse generation and others. We continue

our discussion with an outline of peculiarities in temporal structure of SC radiation under different pumping conditions: pulse pumping in a fibre with normal dispersion, spectral broadening of relatively short (normally in the range of tens to hundreds of femtoseconds) and of long pulses in fibres with anomalous dispersion.

Spectral broadening of pumping pulses in the normal dispersion regime is caused mainly by the effect of self-phase modulation (SPM). Temporal radiation profile at the output from the optical fibre usually has the form of a train of isolated pulses with repetition rate equal that of the pumping pulse repetition rate (see typical results of numerical modelling (Kobtsev & Smirnov, 2007, 2008c) shown in Fig. 9.3, upper row). As a rule, such SC is highly coherent, which makes it preferable for noise-sensitive telecom applications. In most cases, such SC has comparatively narrow spectral width, usually not exceeding 100–200 nm in the telecom spectral range. However, in Ref. Heidt et al. (2011), authors managed to obtain an octave-spanning SC in all-normal dispersion PCF.

Efficiency of spectral broadening is usually considerably improved in the anomalous dispersion regime of the optical fibre due to soliton effects. In case of relatively short pumping pulses, soliton fission effect is the principal mechanism of spectral broadening during the initial stage of SC generation that leads to broadening of the pulse spectrum and its temporal decomposition into a train of sub-pulses (see Fig. 9.3, second row). This process can be regarded as the decay of a high-order soliton into a sequence of fundamental solitons. As they propagate further along the fibre, these fundamental solitons undergo a self-shift of their carrier frequency caused by the effect of stimulated Raman self-scattering, thus leading to widening of the SC spectrum. Since the multi-soliton pumping pulse decays into a train of fundamental solitons mostly because of SPM within a comparatively short stretch of fibre, noise amplification does not noticeably affect this process. As a result, the temporal profile of SC intensity in this case has the form of a regular sequence of wave packets, each of which, in its turn, consisting of a complicated non-periodic train of soliton sub-pulses with different intensity, energy and wavelength (Kobtsev & Smirnov 2004). Due to large spectral width achievable at moderate pump powers, this SC generation regime is attractive for a wide range of applications. However, for telecom tasks, the priority is not an extreme spectral width of SC (which in fact may be quite moderate, only covering data transmission bands) but perfect stability and reliability of light sources: low noise level, high coherence and spectral flatness, stable temporal profile of SC. From the viewpoint of these requirements, SC produced under pulsed pumping in normal dispersion is, as a rule, preferable for telecom applications.

A completely different picture can be seen when pumping with comparatively long (dozens of picoseconds and longer) pulses in the anomalous dispersion domain of the fibre (see Fig. 9.3, third row). Because the spectrum broadening rate caused by SPM is inversely proportional to pulse duration, soliton fission requires too long a fibre stretch, and therefore does not occur. Instead, modulation instability (MI) becomes the principal factor leading to noise amplification within two spectral bands located symmetrically with respect to the pumping line. By the time when the magnitude of amplified noise becomes comparable to that of the pumping pulse,

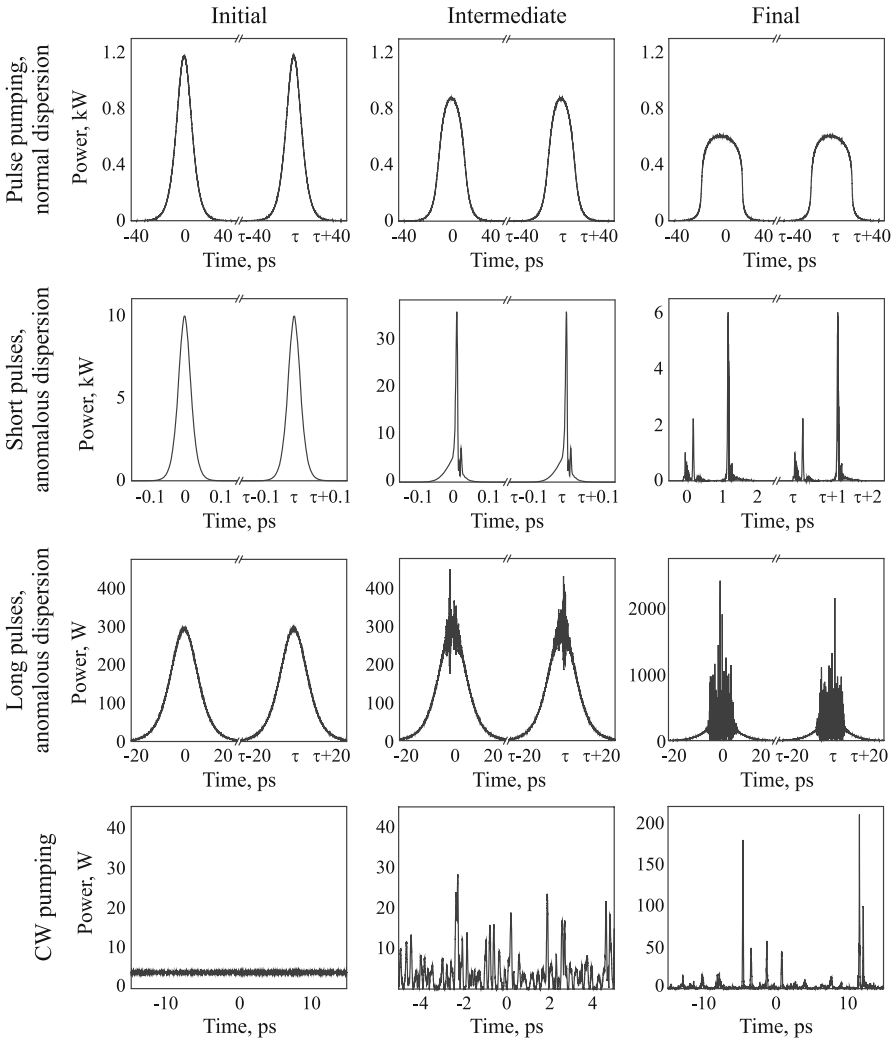

Fig. 9.3 Evolution of temporal structure of pumping radiation during SC generation under different conditions (Kobtsev & Smirnov, 2007, 2008c)

the pulse decays into a stochastic train of sub-pulses whose mean repetition rate is governed by the position of MI gain lines. Some of these sub-pulses form optical solitons experiencing self-shift of carrier frequency, thus giving rise to significant broadening of the SC spectrum. However, in contrast to the case of short pumping pulses discussed above, the energy and wavelength of these solitons are random values and exhibit considerable shot-to-shot fluctuations from one pumping pulse to another. Consequently, experimental SC spectra are much smoother and are often free from isolated soliton peaks, which happens because of averaging during data

acquisition over a large number of solitons with random parameters. The temporal structure of SC radiation is formed by a train of wave packets following one another with the pump pulse repetition rate, each of them consisting of a large number (several hundred or more) sub-pulses with essentially random parameters. Such SC has low pulse-to-pulse coherence and cannot be re-compressed to a single ultrashort pulse.

In an intermediate case of pulses with sub-picosecond and picosecond durations, partially coherent pulse trains (wave packets) are formed in the optical fibre due to interplay of soliton fission effect and modulation instability, which, the latter, creates a considerable level of amplified noise. As it has been shown previously (Kobtsev & Smirnov, 2006; Dudley & Coen, 2002), the pulse-to-pulse degree of coherence reaches its maximum in the limit of short pumping pulses, and in the opposite limit of very long pulses, it approaches zero, accordingly corresponding to generation of a regular or a stochastic wave packet sequence.

9.4.2 Spectral Broadening of CW Pump

As we have shown, non-linear broadening is usually achieved by transmitting short, high-power pulses through a strongly non-linear medium. The initial modulation may lead to an increased initial bandwidth and allows the effect of SPM to act on the transmitted signal from the beginning, usually increasing the efficiency of the broadening process. On occasion, however, it can be practical to generate a wide spectrum from a conventional high-power CW source (typically a fibre laser). This possibility was illustrated in 2000 by the work of Prabhu et al. (2000), who demonstrated generation of a 100 nm SC centred at 1483.4 nm with output power of over 1 W and a weak spectral modulation of 0.11 nm, from a 1064 nm CW 8.4 W ytterbium-doped fibre laser. The broadening medium consisted of a 700 m phosphorus-doped and a 500 m Flexcor-1060 single-mode fibre that, together with a series of gratings, formed a Raman and a Brillouin cavity. The whole setup worked as a hybrid Raman/Brillouin fibre laser that produced a broad output SC spectrum. Further work in this direction was carried out by Abeeluck et al. (Nicholson et al., 2003b; Abeeluck et al., 2003), who in 2003 demonstrated generation of a broad 247 nm SC by pumping a 4.5 km HNLF with a tuneable Raman fibre laser and clearly identified modulational instability (MI) as a fundamental effect in the generation of the SC. The same authors have recently reported much broader SC generation of more than 544 nm bandwidth, with output powers of up to 3.2 W (Abeeluck et al., 2004; Fermann et al., 2000). Other groups have made interesting contributions to the use of CW to generate SC for metrological applications (González-Herráez et al., 2003). In 2008, ultra-long cavity fibre lasers (Ania-Castañón et al., 2006) were used to obtain SC generation from CW in conventional (non-PCF) fibres with a flatness of <1 dB over 180 nm, with more than 40% energy conversion efficiency, thanks to partial confinement of the pumps within the laser cavity (El-Taher et al., 2009).

The spectral broadening of CW radiation may be considered in the limit as equivalent to the broadening of extremely long pulses, so similar physical mechanisms can be considered as responsible for CW SC generation and for the spectral broadening of quite long pulses in the anomalous dispersion regime. Thus, temporal distribution of SC intensity in this case takes the shape of a stochastic train of pulses (solitons) having different (random) parameters and propagating along the fibre at different velocities (see Fig. 9.3, the bottom row). When recording the spectra of such SC in the experiment, an average over an enormous number of "random" solitons is taken, giving, as a result, a smooth spectrum without any peaks corresponding to individual solitons (Vanholsbeeck et al., 2005; Kobtsev & Smirnov, 2005). For telecom applications, CW-pumped SC may be attractive due to its smooth and adjustable spectrum (El-Taher et al., 2009). Irregular temporal structure makes such SC inapplicable as a multi-wavelength source light source for data transmission; however, there are some other telecom applications that can use irregular temporal profile as well. Thus, for example, non-linear broadening of CW can be applied to the pumps of a Raman amplifier widely used in telecom, in order to reduce its gain ripple when amplifying over a large bandwidth. The gain ripple in broadband Raman amplification can also be minimised by using a large number of pumps, but this is not always a practical solution, since it implies an increase on the complexity of the system, reducing its adaptability and increasing its cost. A Raman pump can be initially modulated and then rapidly broadened through SPM, but a more interesting possibility is to use modulational instability in the fibre to provide the initial modulation, thus considerably simplifying the design of the amplifier by using continuous wave pump lasers. This was the approach originally taken by Ellingham et al. (2002) and later followed by Chestnut & Taylor (2003) to broaden the spectra of single pumps in different sets of fibre. In the original paper by Ellingham et al., broadening performance of several non-zero dispersion-shifted fibres was evaluated at different pump input powers, and a fivefold gain ripple reduction was predicted for future dual-pump implementations. In order to maximise the effect of modulational instability, the wavelengths of the pumps must be such that they propagate through the broadening fibre in a slightly anomalous regime, close to the zero-dispersion point. Other desirable properties of the fibre include a high non-linear coefficient and a small attenuation, in order to minimise the loss of the pump power. The non-linear-broadening method was finally applied to a multi-pump Raman amplifier by Ellingham et al. (2005), using Truewave™ fibre, and increasing the 0.1-dB gain ripple bandwidth from 5 to 19 nm in an amplifier designed to provide gain in the 1565–1595 nm region.

In general, using a pulsed pump in the normal dispersion regime is preferable for SC generation in telecom applications due to much better coherence and noise properties and preserved temporal pulse structure (Heidt, 2010; Hooper et al., 2011; Nishizawa & Takayanagi, 2007).

9.4.3 Rogue Waves

When discussing peculiarities of the temporal structure of spectrally broadened radiation, it is impossible to pass over an intriguing aspect of non-linear optical science involved in supercontinuum generation, which is related to the optical analogue of oceanic rogue waves—rare events with extremely large intensity fluctuations (Solli et al., 2007, 2008; Mussot et al., 2009; Dudley et al., 2009; Erkintalo et al., 2009; Lafargue et al., 2009; Akhmediev et al., 2013; Vergeles & Turitsyn, 2011). It was shown that supercontinuum generators can be used as a simple and convenient test bed for studying the optical analogue of oceanic freak waves, since non-linear optics provides a relatively large frequency of high-intensity fluctuations and presents an opportunity of experimental studies that can be carried out with just a table-top set of equipment offering a high degree of control and rapid data acquisition.

The appearance of rogue waves can be caused by MI, which is known to have high sensitivity to the initial conditions and to exhibit emergent behaviour (Solli et al., 2007; Mussot et al., 2009; Dudley et al., 2009). Extensive studies in this area were focused on different non-linear physical systems such as optical cavities, passively mode-locked lasers and EDFA (see review Akhmediev et al., 2013) and even in linear telecom data transmission lines (Vergeles & Turitsyn, 2011) due to pulse (bit) overlapping.

9.4.4 Noise and Coherence of SC Sources

Noise and coherence properties of light sources are extremely important in telecom. Coherence loss and excess noise potentially lead to deterioration of transmitted data. Thus, obtaining high coherence and low noise operation of SC generators are of primary importance for telecom applications. Let us note that there are several different types of coherence such as spatial, temporal, pulse-to-pulse and so on. Spatial coherence of SC is usually high enough, thanks to a small effective core area of single-mode fibres used for spectral broadening. Pulse-to-pulse coherence, on the other hand, will only be high in the case of SC generated from periodic pulse trains, in which the effects leading to non-linear broadening have preserved the correlation between the electric fields of different pulses. The noise limitations (Corwin et al., 2003a) and coherence properties (Dudley & Coen, 2002) of SC spectra generated in different kinds of fibre have been studied theoretically and experimentally by multiple groups with the goal of designing the best possible SC sources. The effect of pump fluctuations in the generation of SC pulses was first studied by Mori et al. (1998), who showed that pulses were more stable when generated in dispersion-flattened decreasing-dispersion fibre (DDF). Nakazawa et al. (1998) studied degradation of coherence during SC generation in DDF, concluding that FWM phase-matched by SPM and a small anomalous dispersion in the presence of

amplified spontaneous noise (i.e. modulational instability) was the main cause of the coherence loss. More recently, other studies appeared about the noise and coherence properties of SC generated in PCF and highly non-linear fibres (HNLF) (Washburn & Newbury, 2004; Gu et al., 2003). Corwin et al. (2003a, b) identified amplification of quantum-limited shot noise and spontaneous Raman scattering as the main causes of amplitude fluctuations in microstructured fibres and concluded that short input pulses were critical for generation of broad SC with low noise, whereas Dudley and Coen (2002) demonstrated that coherence degradation depended strongly on the input pulse duration and wavelength and that the effect of modulational instability in anomalous dispersion could be reduced by using short pulses.

9.5 Summary and Outlook

Research conducted over the past 20 or so years has convincingly demonstrated the possibility of efficient telecom applications relying on SC techniques, mostly in WDM and DWDM technologies using large numbers of channels (up to 10,000) with different wavelengths. However, despite this demonstration of efficiency over the entire telecommunication spectrum, these technologies have yet to be widely adopted in the industry. Most probably, the following considerations have played a role in delaying their acceptance by the industry:

1. Poor resilience. Failure of one master oscillator or an amplifier used in SC generation immediately causes interruption of data transfer in all generated channels. Separate diode lasers with different output wavelengths used to generate each channel generally provide better resilience of the data transfer system.
2. Difficulties in generation of SC with uniform radiation parameters over a broad spectral range. The output at different wavelengths may have different intensity, stability, different degree of coherence and so forth. In case of SC, not all of the channels may have identical data transmission parameters.

Still, improvements to the reliability of the components used in SC generators and the development of methods to better equalise SC radiation parameters within a broad spectral range might yet allow SC technologies to fully realise their potential and bring them into mainstream telecommunication applications. In this regard, it is worth pointing out recent advances in the generation of SC-based optical frequency combs, which have paved a promising way for applications in telecom.

Acknowledgments This work was supported by the Ministry of Science and Higher Education of the Russian Federation (FSUS-2020-0036); Russian Foundation for Basic Research (grant No. 18-29-20025). The work of S.K.T. was supported by the Russian Science Foundation (Grant No. 17-72-30006). The work of J.D.A.C. was supported by the Spanish Ministry of Science and Innovation (Grant RTI2018-097957-B-C33) and Comunidad de Madrid (Grant S2018/NMT-4326).

References

Abeeluck, A. K., Radic, S., Brar, K., Bouteiller, J.-C., & Headley, C. (2003). In *Optical Fiber Communication Conference (OFC) 2003, Postconference Digest, Vol. 86 of OSA trends in optics and photonics series* (pp. 561–562).

Abeeluck, A. K., Headley, C., & Jørgensen, C. G. (2004). High-power supercontinuum generation in highly nonlinear, dispersion-shifted fibers by use of a continuous-wave Raman fiber laser. *Optics Letters, 29*, 2163–2165.

Agrawal, G. P. (2001). *Nonlinear fiber optics*. Academic Press.

Akhmediev, N., Dudley, J. M., Solli, D. R., & Turitsyn, S. K. (2013). Recent progress in investigating optical rogue waves. *Journal of Optics, 15*(6), 060201.

Akimov, D. A., Ivanov, A. A., Alfimov, M. V., Bagayev, S. N., Birks, T. A., Wadsworth, W. J., Russell, P. S. J., Fedotov, A. B., Pivtsov, V. S., Podshivalov, A. A., & Zheltikov, A. M. (2002). Two-octave spectral broadening of subnanojoule Cr:forsterite femtosecond laser pulses in tapered fibers. *Applied Physics B, 74*, 307–311.

Alfano, R. R. (Ed.). (1989). *The super continuum laser sources*. Springer.

Alfano, R. R., & Shapiro, S. L. (1970a). Emission in the region 4000 to 7000 angstrom via four-photon coupling in glass. *Physical Review Letters, 24*, 584–587.

Alfano, R. R., & Shapiro, S. L. (1970b). Observation of self-phase modulation and small-scale filaments in crystals and glasses. *Physical Review Letters, 24*, 592–594.

Anderson, M. E., de Araujo, L. E. E., Kosik, E. M., & Walmsley, I. A. (2000). The effects of noise on ultrashortoptical-pulse measurement using SPIDER. *Applied Physics B, 70*, S85–S93.

Ania-Castañón, J. D., Ellingham, T. J., Ibbotson, R., Chen, X., Zhang, L., & Turitsyn, S. K. (2006). Ultralong Raman fiber lasers as virtually lossless optical media. *Physical Review Letters, 96*(2), 023902.

Apolonski, A., Povazay, B., Unterhuber, A., Drexler, W., Wadsworth, W. J., Knight, J. C., & Russell, P. S. J. (2002). Spectral shaping of supercontinuum in a cobweb photonic-crystal fiber with sub-20-fs pulses. *Journal of the Optical Society of America, 19*, 2165–2170.

Applied Physics B, 77(2–3) (2003) – Special issue: supercontinuum generation.

Avdokhin, A. V., Popov, S. V., & Taylor, J. R. (2003). Continuous-wave, high-power, Raman continuum generation in holey fibers. *Optics Letters, 28*, 1353–1355.

Bagaev, S. N., Denisov, V. I., Zakhar'yash, V. F., Klement'ev, V. M., Kobtsev, S. M., Kuznetsov, S. A., Kukarin, S. V., Pivtsov, V. S., Smirnov, S. V., & Fateev, N. V. (2004). Spectral and temporal characteristics of a supercontinuum in tapered optical fibres. *Quantum Electronics, 34*, 1107–1115.

Baldeck, P. L., & Alfano, R. R. (1987). Intensity effects on the stimulated four photon spectra generated by picosecond pulses in optical fibers. *Journal of Lightwave Technology, 5*, 1712–1715.

Bartels, A., & Kurz, H. (2002). Generation of a broadband continuum by a Ti:sapphire femtosecond oscillator with a 1-GHz repetition rate. *Optics Letters, 27*, 1839–1841.

Barviau, B., Kibler, B., & Picozzi, A. (2009). Wave-turbulence approach of supercontinuum generation: Influence of self-steepening and higher-order dispersion. *Physical Review A, 79*, 063840.

Belli, F., Abdolvand, A., Chang, W., Travers, J. C., & P. St. J. Russell. (2015). Vacuum-ultraviolet to infrared supercontinuum in hydrogen-filled photonic crystal fiber. *Optica, 2*(4), 292–300.

Bellini, M., & Hänsch, T. W. (2000). Phase-locked white-light continuum pulses: Toward a universal optical frequency-comb synthesizer. *Optics Letters, 25*, 1049–1051.

Bétourné, A., Kudlinski, A., Bouwmans, G., Vanvincq, O., Mussot, A., & Quiquempois, Y. (2009). Control of supercontinuum generation and soliton self-frequency shift in solid-core photonic bandgap fibers. *Optics Letters, 34*(20), 3083–3085.

Biancalana, F., Skryabin, D. V., & Russel, P. S. (2003). Four wave mixing instabilities in photonic-crystal and tapered fibers. *Physical Review E, 68*, 046631–046638.

Birks, T. A., Knight, J. C., & Russell, P. S. J. (1997). Endlessly single-mode photonic crystal fiber. *Optics Letters, 22*, 961–963.

Birks, T. A., Wadsworth, W. J., & Russell, P. S. J. (2000). Supercontinuum generation in tapered fibers. *Optics Letters, 25*, 1415–1417.

Bloembergen, N. (1973). The influence of electron plasma formation on superbroadening in light filaments. *Optics Communications, 8*, 285–288.

Bozinovic, N., Yue, Y., Ren, Y., Tur, M., Kristensen, P., Huang, H., Willner, A. E., & Ramachandran, S. (2013). Terabit-scale orbital angular momentum mode division multiplexing in fibers. *Science, 340*(6140), 1545–1548.

Broeng, J., Barkou, S. E., Bjarklev, A., Knight, J. C., Birks, T. A., & Russell, P. S. J. (1998). Highly increased photonic band gaps in silica/air structures. *Optics Communications, 156*, 240–244.

Brunet, C., Vaity, P., Messaddeq, Y., LaRochelle, S., & Rusch, L. A. (2014). Design, fabrication and validation of an OAM fiber supporting 36 states. *Optics Express, 22*(21), 26117–26127.

Cao, Q., Gu, X., Zeek, E., Kimmel, M., Trebino, R., Dudley, J., & Windeler, R. S. (2003). Measurement of the intensity and phase of supercontinuum from an 8-mm-long microstructure fiber. *Applied Physics B, 77*, 239–244.

Chen, K. K., Alam, S., Price, J. H. V., Hayes, J. R., Lin, D., Malinowski, A., Codemard, C., Ghosh, D., Pal, M., Bhadra, S. K., & Richardson, D. J. (2010). Picosecond fiber MOPA pumped supercontinuum source with 39 W output power. *Optics Express, 18*(6), 5426–5432.

Chen, H., Chen, S., Wang, J., Chen, Z., & Hou, J. (2011). 35W high power all fiber supercontinuum generation in PCF with picosecond MOPA laser. *Optics Communications, 284*(23), 5484–5487.

Chenan, X., Zhao, X., Islam, M. N., Terry, F. L., Freeman, M. J., Zakel, A., & Mauricio, J. (2009). 10.5 W time-averaged power mid-IR supercontinuum generation extending beyond 4 um with direct pulse pattern modulation. *Journal of Selected Topics in Quantum Electronics, 15*(2), 422–434.

Cheng, T., Nagasaka, K., Tuan, T. H., Xue, X., Matsumoto, M., Tezuka, H., Suzuki, T., & Ohishi, Y. (2016). Mid-infrared supercontinuum generation spanning 2.0 to 15.1 μm in a chalcogenide step-index fiber. *Optics Letters, 41*(9), 2117–2120.

Chernikov, S. V., Dianov, E. M., Richardson, D. J., Laming, R. I., & Payne, D. N. (1993). 114 Gbit/s soliton train generation through Raman self-scattering of a dual frequency beat signal in dispersion decreasing optical fiber. *Applied Physics Letters, 63*, 293–295.

Chernikov, S. V., Taylor, J. R., & Kashyap, R. (1994). Comblike dispersion-profiled fiber for soliton pulse train generation. *Optics Letters, 19*, 539–541.

Chestnut, D. A., & Taylor, J. R. (2003). Gain-flattened fiber Raman amplifiers with nonlinearity-broadened pumps. *Optics Letters, 153*, 2294–2296.

Cheung, K. K. Y., Zhang, C., Zhou, Y., Wong, K. K. Y., & Tsia, K. K. (2011). Manipulating supercontinuum generation by minute continuous wave. *Optics Letters, 36*(2), 160–162.

Chi, J.-J., Li, P.-X., Hu, H., Yao, Y.-F., Zhang, G.-J., Yang, C., & Zhao, Z.-Q. (2014). 120 W sub-nanosecond ytterbium-doped double clad fiber amplifier and its application in supercontinuum generation. *Laser Physics, 24*(8), 085103.

Coen, S., Chau, A. H. L., Leonhardt, R., Harvey, J. D., Knight, J. C., Wadsworth, W. J., & Russell, P. S. J. (2001). White-light supercontinuum generation with 60-ps pump pulses in a photonic crystal fiber. *Optics Letters, 26*, 1356–1358.

Coen, S., Chau, A. H. L., Leonhardt, R., Harvey, J. D., Knight, J. C., Wadsworth, W. J., & Russell, P. S. J. (2002). Supercontinuum generation by stimulated Raman scattering and parametric four-wave mixing in photonic crystal fibers. *Journal of the Optical Society of America B, 19*, 753–764.

Corkum, P. B., & Rolland, C. (1989). Femtosecond continua produced in gases. *Journal of Quantum Electronics, 25*, 2634–2639.

Corkum, P. B., Rolland, C., & Srinivasan-Rao, T. (1986). Supercontinuum generation in gases. *Physical Review Letters, 57*, 2268–2271.

Corwin, K. L., Newbury, N. R., Dudley, J. M., Coen, S., Diddams, S. A., Weber, K., & Windeler, R. S. (2003a). Fundamental noise limitations to supercontinuum generation in microstructure fiber. *Physical Review Letters, 90*, 113904.

Corwin, K. L., Newbury, N. R., Dudley, J. M., Coen, S., Diddams, S. A., Washburn, B. R., Weber, K., & Windeler, R. S. (2003b). Fundamental amplitude noise limitations to supercontinuum spectra generated in microstructure fiber. *Applied Physics B, 77*, 269–277.

Cregan, R. F., Mangan, B. J., & Knight, J. C. (1999). Single-mode photonic and gap guidance of light in air. *Science, 285*, 1537–1539.

Cumberland, B. A., Travers, J. C., Popov, S. V., & Taylor, J. R. (2008). 29 W High power CW supercontinuum source. *Optics Express, 16*(8), 5954–5962.

Demircan, A., & Bandelow, U. (2007). Analysis of the interplay between soliton fission and modulation instability in supercontinuum generation. *Applied Physics B, 86*(1), 31–39.

Dianov, E. M., Mamyshev, P. V., Prokhorov, A. M., & Chernikov, S. V. (1989). Generation of a train of fundamental solitons at a high repetition rate in optical fibers. *Optics Letters, 14*, 1008–1010.

Diddams, S. A., Jones, D. J., Ye, J., Cundiff, T., Hall, J. L., Ranka, J. K., Windeler, R. S., Holzwarth, R., Udem, T., & Hänsch, T. W. (2000a). Direct link between microwave and optical frequencies with a 300 THz femtosecond laser comb. *Physical Review Letters, 84*, 5102–5105.

Diddams, S. A., Jones, D. J., Ye, J., Fortier, T. M., Windeler, R. S., Cundiff, S. T., Hänsch, T. W., & Hall, J. L. (2000b). Towards the ultimate control of light: Optical frequency metrology and the phase control of femtosecond pulses. *Optics and Photonics News, 11*, 16–22.

Diddams, S. A., Jones, D. J., Ye, J., Cundiff, S. T., Hall, J. L., Ranka, J. K., & Windeler, R. S. (2001). Direct RF to optical frequency measurements with a femtosecond laser comb. *IEEE Transactions on Instrumentation and Measurement, 50*, 552–555.

Domachuk, P., Wolchover, N. A., Cronin-Golomb, M., Wang, A., George, A. K., Cordeiro, C. M. B., Knight, J. C., & Omenetto, F. G. (2008). Over 4000 nm bandwidth of mid-IR supercontinuum generation in sub-centimeter segments of highly nonlinear tellurite PCFs. *Optics Express, 16*(10), 7161–7168.

Drexler, W. (2004). Ultrahigh-resolution optical coherence tomography. *Journal of Biomedical Optics, 9*, 47–74.

Drexler, W., Morgner, U., Kärtner, F. X., Pitris, C., Boppart, S. A., Li, X. D., Ippen, E. P., & Fujimoto, J. G. (1999). In vivo ultrahigh-resolution optical coherence tomography. *Optics Letters, 24*, 1221–1224.

Dudley, J. M., & Coen, S. (2002). Coherence properties of supercontinuum spectra generated in photonic crystal and tapered optical fibers. *Optics Letters, 27*, 1180–1182.

Dudley, J. M., & Coen, S. (2004). Fundamental limits to few-cycle pulse generation from compression of supercontinuum spectra generated in photonic crystal fiber. *Optics Express, 12*, 2423–2428.

Dudley, J., Gu, X., Xu, L., Kimmel, M., Zeek, E., O'Shea, P., Trebino, R., Coen, S., & Windeler, R. (2002a). Cross-correlation frequency resolved optical gating analysis of broadband continuum generation in photonic crystal fiber: Simulations and experiments. *Optics Express, 10*, 1215–1221.

Dudley, J. M., Provino, L., Grossard, N., Maillotte, H., Windeler, R. S., Eggleton, B. J., & Coen, S. (2002b). Supercontinuum generation in air-silica microstructured fiber with nanosecond and femtosecond pulse pumping. *Journal of the Optical Society of America B, 19*, 765–771.

Dudley, J. M., Genty, G., & Coen, S. (2006). Supercontinuum generation in photonic crystal fibers. *Reviews of Modern Physics, 78*, 1135–1184.

Dudley, J. M., Genty, G., & Eggleton, B. J. (2008). Harnessing and control of optical rogue waves in supercontinuum generation. *Optics Express, 16*, 3644–3651.

Dudley, J. M., Genty, G., Dias, F., Kibler, B., & Akhmediev, N. (2009). Modulation instability, Akhmediev breathers and continuous wave supercontinuum generation. *Optics Express, 17*(24), 21497–21508.

Ellingham, T. J., Gleeson, L. M., & Doran, N. J. (2002). *Enhanced Raman amplifier performance using non-linear pump broadening*. In Proceedings ECOC 2002, 4.1.3.

Ellingham, T. J., Ania-Castañón, J. D., Turitsyn, S. K., Pustovskikh, A., Kobtsev, S., & Fedoruk, M. P. (2005). Dual-pump Raman amplification with increased flatness using modulation instability. *Optics Express, 13*, 1079–1084.

El-Taher, A. E., Ania-Castañón, J. D., Karalekas, V., & Harper, P. (2009). High efficiency supercontinuum generation using ultra-long Raman fiber cavities. *Optics Express, 17*, 17909–17915.

Epping, J. P., Hellwig, T., Hoekman, M., Mateman, R., Leinse, A., Heideman, R. G., van Rees, A., van der Slot, P. J. M., Lee, C. J., Fallnich, C., & Boller, K. J. (2015). On-chip visible-to-infrared supercontinuum generation with more than 495 THz spectral bandwidth. *Optics Express, 23*(15), 19596–19604.

Erkintalo, M., Genty, G., & Dudley, J. M. (2009). Rogue-wave-like characteristics in femtosecond supercontinuum generation. *Optics Letters, 34*(16), 2468–2470.

Ettabib, M. A., Xu, L., Bogris, A., Kapsalis, A., Belal, M., Lorent, E., Labeye, P., Nicoletti, S., Hammani, K., Syvridis, D., Shepherd, D. P., Price, J. H. V., Richardson, D. J., & Petropoulos, P. (2015). Broadband telecom to mid-infrared supercontinuum generation in a dispersion-engineered silicon germanium waveguide. *Optics Letters, 40*(15), 4118–4121.

Fatome, J., Pitois, S., & Millot, G. (2006). 20-GHz-to-1-THz repetition rate pulse sources based on multiple four-wave mixing in optical fiber. *IEEE Journal of Quantum Electronics, 42*, 1038–1046.

Fedotov, A. B., Zheltikov, A. M., Ivanov, A. A., Alfimov, M. V., Chorvat, D., Beloglazov, V. I., Melnikov, L. A., Skibina, N. B., Tarasevitch, A. P., & von der Linde, D. (2000). Supercontinuum-generating holey fibers as new broadband sources for spectroscopic applications. *Laser Physics, 10*, 723–726.

Fercher, A. F., Drexler, W., Hitzenberger, C. K., & Lasser, T. (2003). Optical coherence tomography – Principles and applications. *Reports on Progress in Physics, 66*, 239–303.

Fermann, M. E., Kruglov, V. I., Thomsen, B. C., Dudley, J. M., & Harvey, J. D. (2000). Self-similar propagation and amplification of parabolic pulses in optical fibers. *Physical Review Letters, 84*(26), 6010–6013.

Ferrando, A., Silvestre, E., Miret, J. J., Monsoriu, J. A., Andres, M. V., & Russell, P. S. J. (1999). Designing a photonic crystal fibre with flattened chromatic dispersion. *Electronics Letters, 35*, 325–327.

Ferrando, A., Silvestre, E., Miret, J. J., & Andres, P. (2000). Nearly zero ultraflattened dispersion in photonic crystal fibers. *Optics Letters, 25*, 790–792.

Ferrando, A., Silvestre, E., Andres, P., Miret, J. J., & Andres, M. V. (2001). Designing the properties of dispersion-flattened photonic crystal fibers. *Optics Express, 9*, 687–697.

Fisher, R. A., Kelley, P. L., & Gustafson, T. K. (1969). Subpicosecond pulse generation using the optical Kerr effect. *Applied Physics Letters, 14*, 140.

Fork, R. L., Brito Cruz, C. H., Becker, P. C., & Shank, C. V. (1987). Compression of optical pulses to six femtoseconds by using cubic phase compensation. *Optics Letters, 12*, 483–485.

Foster, M. A., Moll, K. D., & Gaeta, A. L. (2004). Optimal waveguide dimensions for nonlinear interactions. *Optics Express, 12*, 2880–2887.

François, V., Ilkov, F. A., & Chin, S. L. (1993). Experimental study of the supercontinuum spectral width evolution in CO2 gas. *Optics Communications, 99*, 241–246.

Gaeta, A. L. (2002). Nonlinear propagation and continuum generation in microstructured optical fibers. *Optics Letters, 27*, 924–926.

Gaeta, A. L., Lipson, M., & Kippenberg, T. J. (2019). Photonic-chip-based frequency combs. *Nature Photonics, 13*, 158–169.

Geng, J., Wang, Q., & Jiang, S. (2012). High-spectral-flatness mid-infrared supercontinuum generated from a Tm-doped fiber amplifier. *Applied Optics, 51*(7), 834–840.

Genty, G., Lehtonen, M., Ludvigsen, H., Broeng, J., & Kaivola, M. (2002). Spectral broadening of femtosecond pulses into continuum generation in microstructured fibers. *Optics Express, 10*, 1083–1098.

Genty, G., Dudley, J. M., & Eggleton, B. J. (2009). Modulation control and spectral shaping of optical fiber supercontinuum generation in the picosecond regime. *Applied Physics B, 94*(2), 187–194.

Gibson, G., Courtial, J., Padgett, M. J., Vasnetsov, M., Pas'ko, V., Barnett, S. M., & Franke-Arnold, S. (2004). Free-space information transfer using light beams carrying orbital angular momentum. *Optics Express, 12*(22), 5448–5456.

González-Herráez, M., Martín-López, S., Corredera, P., Hernanz, M. L., & Horche, P. R. (2003). Supercontinuum generation using a continuous-wave Raman fiber laser. *Optics Communications, 226*, 323–328.

Gorbach, A. V., & Skryabin, D. V. (2007). Light trapping in gravity-like potentials and expansion of supercontinuum spectra in photonic-crystal fibres. *Nature Photonics, 1*, 653–657.

Gordon, J. P. (1986). Theory of the soliton self-frequency shift. *Optics Letters, 11*, 662–664.

Gouveia-Neto, A. S., Gomes, A. S. L., & Taylor, J. R. (1987). Generation of 33-fsec pulses at 1.32 mcm through a high-order soliton effect in a single-mode optical fiber. *Optics Letters, 12*, 395–397.

Granzow, N., Stark, S. P., Schmidt, M. A., Tverjanovich, A. S., Wondraczek, L., & P. St. J. Russell. (2011). Supercontinuum generation in chalcogenide-silica step-index fibers. *Optics Express, 19*(21), 21003–21010.

Gu, X., Xu, L., Kimmel, M., Zeek, E., O'Shea, P., Shreenath, A. P., Trebino, R., & Windeler, R. S. (2002). Frequency-resolved optical gating and single-shot spectral measurements reveal fine structure in microstructure-fiber continuum. *Optics Letters, 27*, 1174.

Gu, X., Kimmel, M., Shreenath, A. P., Trebino, R., Dudley, J. M., Coen, S., & Windeler, R. S. (2003). Experimental studies of the coherence of microstructure-fiber supercontinuum. *Optics Express, 11*, 2697–2703.

Hartl, I., Li, X. D., Chudoba, C., Ghanta, R. K., Ko, T. H., Fujimoto, J. G., Ranka, J. K., & Windeler, R. S. (2001). Ultrahigh-resolution optical coherence tomography using continuum generation in an air-silica microstructure optical fiber. *Optics Letters, 26*, 608–610.

Hasegawa, A. (1984). Generation of a train of soliton pulses by induced modulational instability in optical fibers. *Optics Letters, 9*, 288–290.

He, G. S., Lin, T. C., & Prasad, P. N. (2002). New technique for degenerate two-photon absorption spectral measurements using femtosecond continuum generation. *Optics Express, 10*, 566–574.

Heidt, A. M. (2010). Pulse preserving flat-top supercontinuum generation in all-normal dispersion photonic crystal fibers. *Journal of the Optical Society of America B, 27*(3), 550–559.

Heidt, A. M., Hartung, A., Bosman, G. W., Krok, P., Rohwer, E. G., Schwoerer, H., & Bartelt, H. (2011). Coherent octave spanning near-infrared and visible supercontinuum generation in all-normal dispersion photonic crystal fibers. *Optics Express, 19*(4), 3775–3787.

Heidt, A. M., Feehan, J. S., Price, J. H. V., & Feurer, T. (2017). Limits of coherent supercontinuum generation in normal dispersion fibers. *Journal of the Optical Society of America B, 34*(4), 764–775.

Herrmann, J., Griebner, U., Zhavoronkov, N., Husakou, A., Nickel, D., Knight, J. C., Wadsworth, W. J., Russell, P. S. J., & Korn, G. (2002). Experimental evidence for supercontinuum generation by fission of higher-order solitons in photonic fibers. *Physical Review Letters, 88*, 173901.

Hillerkuss, D., Schmogrow, R., Schellinger, T., Jordan, M., Winter, M., Huber, G., Vallaitis, T., Bonk, R., Kleinow, P., Frey, F., Roeger, M., Koenig, S., Ludwig, A., Marculescu, A., Li, J., Hoh, M., Dreschmann, M., Meyer, J., Ben Ezra, S., et al. (2011). 26 Tbit/s line-rate super-channel transmission utilizing all-optical fast Fourier transform processing. *Nature Photonics, 5*, 364–371.

Hillerkuss, D., Schmogrow, R., Meyer, M., Wolf, S., Jordan, M., et al. (2012). Single-laser 32.5 Tbit/s Nyquist WDM transmission. *Journal of Optical Communications and Networking, 4*(10), 715–723.

Ho, P. P., Wang, Q. Z., Chen, J., Liu, Q. D., & Alfano, R. R. (1997). Ultrafast optical pulse digitization with unary spectrally encoded cross-phase modulation. *Applied Optics, 36*, 3425–3429.

Holzwarth, R., Udem, T., Hansch, T. W., Knight, J. C., Wadsworth, W. J., & Russell, P. S. J. (2000). Optical frequency synthesizer for precision spectroscopy. *Physical Review Letters, 85*, 2264–2267.

Holzwarth, R., Zimmermann, M., Udem, T., Hänsch, T. W., Nevsky, A., von Zanthier, J., Walther, H., Knight, J. C., Wadsworth, W. J., P. St. J. Russell, Skvortsov, M. N., & Bagayev, S. N. (2001). Absolute frequency measurement of iodine lines with a femtosecond optical synthesizer. *Applied Physics B, 73*, 269–271.

Hooper, L. E., Mosley, P. J., Muir, A. C., Wadsworth, W. J., & Knight, J. C. (2011). Coherent supercontinuum generation in photonic crystal fiber with all-normal group velocity dispersion. *Optics Express, 19*(6), 4902–4907.

Hsieh, I.-W., Chen, X., Liu, X., Dadap, J. I., Panoiu, N. C., Chou, C.-Y., Xia, F., Green, W. M., Vlasov, Y. A., & Osgood, R. M. (2007). Supercontinuum generation in silicon photonic wires. *Optics Express, 15*(23), 15242–15249.

Hu, J., Menyuk, C. R., Shaw, L. B., Sanghera, J. S., & Aggarwal, I. D. (2010). Maximizing the bandwidth of supercontinuum generation in As2Se3 chalcogenide fibers. *Optics Express, 18*(7), 6722–6739.

Huang, H., Xie, G., Yan, Y., Ahmed, N., Ren, Y., Yue, Y., Rogawski, D., Willner, M. J., Erkmen, B. I., Birnbaum, K. M., Dolinar, S. J., Lavery, M. P. J., Padgett, M. J., Tur, M., & Willner, A. E. (2014). 100 Tbit/s free-space data link enabled by three-dimensional multiplexing of orbital angular momentum, polarization, and wavelength. *Optics Letters, 39*(2), 197–200.

Hudson, D. D., Dekker, S. A., Mägi, E. C., Judge, A. C., Jackson, S. D., Li, E., Sanghera, J. S., Shaw, L. B., Aggarwal, I. D., & Eggleton, B. J. (2011). Octave spanning supercontinuum in an As2S3 taper using ultralow pump pulse energy. *Optics Letters, 36*(7), 1122–1124.

Hudson, D. D., Antipov, S., Li, L., Alamgir, I., Hu, T., El Amraoui, M., Messaddeq, Y., Rochette, M., Jackson, S. D., & Fuerbach, A. (2017). Toward all-fiber supercontinuum spanning the mid-infrared. *Optica, 4*(10), 1163–1166.

Husakou, A. V., & Herrmann, J. (2001). Supercontinuum generation of higher-order solitons by fission in photonic crystal fibers. *Physical Review Letters, 87*, 203901.

Iaconis, C., & Walmsley, I. A. (1998). Spectral phase interferometry for direct electric-field reconstruction of ultrashort optical pulses. *Optics Letters, 23*, 792–794.

Iaconis, C., & Walmsley, I. A. (1999). Self-referencing spectral interferometry for measuring ultrashort optical pulses. *IEEE Journal of Quantum Electronics, 35*, 501–509.

Islam, M. N., Sucha, G., Bar-Joseph, I., Wegener, M., Gordon, J. P., & Chemla, D. S. (1989). Femtosecond distributed soliton spectrum fibers. *Journal of the Optical Society of America B, 6*, 1149–1158.

Ivanov, A. A., Alfimov, M. V., Fedotov, A. B., Podshivalov, A. A., Chorvat, D., & Zheltikov, A. M. (2001). An all-solid-state sub-40-fs self-starting Cr4+: Forsterite laser with holey-fiber beam delivery and chirp control for coherence-domain and nonlinear-optical biomedical applications. *Laser Physics, 11*, 158–163.

Jasapara, J., Her, T. H., Bise, R., Windeler, R., & DiGiovanni, D. J. (2003). Group-velocity dispersion measurements in a photonic bandgap fiber. *Journal Optical Society of America B, 20*(8), 1611–1615.

Jiang, X., Joly, N. Y., Finger, M. A., Babic, F., Wong, G. K. L., Travers, J. C., & P. St. J. Russell. (2015). Deep-ultraviolet to mid-infrared supercontinuum generated in solid-core ZBLAN photonic crystal fibre. *Nature Photonics, 9*, 133–139.

Johnson, A. R., Mayer, A. S., Klenner, A., Luke, K., Lamb, E. S., Lamont, M. R. E., Joshi, C., Okawachi, Y., Wise, F. W., Lipson, M., Keller, U., & Gaeta, A. L. (2015). Octave-spanning coherent supercontinuum generation in a silicon nitride waveguide. *Optics Letters, 40*(21), 5117–5120.

Jones, D. A., Diddams, S. A., Ranka, J. K., Stentz, A., Windeler, R. S., Hall, J. L., & Cundiff, S. T. (2000). Carrier-envelope phase control of femtosecond mode-locked lasers and direct optical frequency synthesis. *Science, 288*, 635–639.

Kane, D. J., & Trebino, R. (1993). Single-shot measurement of the intensity and phase of an arbitrary ultrashort pulse by using frequency-resolved optical gating. *Optics Letters, 18*, 823–825.

Kartapoulos, S. V., & Bouhiyate, M. (2005). *Supercontinuum sources in CWDM applications with channel protection*. Proceedings of OFC 2005, NTuH4, Anaheim.

Kelleher, E. J. R., Travers, J. C., Popov, S. V., & Taylor, J. R. (2012). Role of pump coherence in the evolution of continuous-wave supercontinuum generation initiated by modulation instability. *Journal of the Optical Society of America B, 29*, 502–512.

Kim, K. Y., Taylor, A. J., Glownia, J. H., & Rodriguez, G. (2008). Coherent control of terahertz supercontinuum generation in ultrafast laser-gas interactions. *Nature Photonics, 2*, 605–609.

Knight, J. C., Birks, T. A., Russell, P. S. J., & Atkin, D. M. (1996). All-silica single-mode optical fiber with photonic crystal cladding. *Optics Letters, 21*(19), 1547–1549.

Knight, J. C., Birks, T. A., Russell, P. S. J., & Atkin, D. M. (1997). All-silica single-mode optical fiber with photonic crystal cladding: Errata. *Optics Letters, 22*, 484–485.

Knight, J. C., Birks, T. A., Russell, P. S. J., & de Sandro, J. P. (1998a). Properties of photonic crystal fiber and the effective index model. *Journal of the Optical Society of America A, 15*, 748–752.

Knight, J. C., Birks, T. A., Cregan, R. F., Russell, P. S. J., & de Sandro, J. P. (1998b). Large mode area photonic crystal fibre. *Electronics Letters, 34*, 1347–1348.

Knight, J. C., Broeng, J., Birks, T. A., & Russel, P. S. J. (1998c). Photonic band gap guidance in optical fibers. *Science, 282*, 1476–1478.

Knight, J. C., Arriaga, J., Birks, T. A., Ortigosa-Blanch, A., Wadsworth, W. J., & Russell, P. S. J. (2000). Anomalous dispersion in photonic crystal fiber. *IEEE Photonics Technology Letters, 12*, 807–809.

Kobtsev, S. M., & Smirnov, S. V. (2004). Optimization of temporal characteristics of supercontinuum generated in tapered air-clad fibers. *Laser Optics 2003: Diode Lasers and Telecommunication Systems, Proceedings SPIE, 5480*, 64–71.

Kobtsev, S., & Smirnov, S. (2005). Modelling of high-power supercontinuum generation in highly nonlinear, dispersion shifted fibers at CW pump. *Optics Express, 13*(18), 6912–6918.

Kobtsev, S. M., & Smirnov, S. V. (2006). Coherent properties of super-continuum containing clearly defined solitons. *Optics Express, 14*, 3968–3980.

Kobtsev, S. M., & Smirnov, S. V. (2007). Supercontinuum fiber sources under pulsed and CW pumping. *Laser Physics, 17*(11), 1303–1305.

Kobtsev, S. M., & Smirnov, S. V. (2008a). Fiber supercontinuum generators with dynamically controlled parameters. *Laser Physics, 18*(11), 1264–1267.

Kobtsev, S. M., & Smirnov, S. V. (2008b). Influence of noise amplification on generation of regular short pulse trains in optical fibre pumped by intensity-modulated CW radiation. *Optics Express, 16*(10), 7428–7434.

Kobtsev, S. M., & Smirnov, S. V. (2008c). Temporal structure of a supercontinuum generated under pulsed and CW pumping. *Laser Physics, 18*(11), 1260–1263.

Kobtsev, S. M., Kukarin, S. V., & Fateev, N. V. (2003). Generation of a polarised supercontinuum in small-diameter quasi-elliptic fibres. *Quantum Electronics, 33*, 1085–1088.

Kobtsev, S. M., Kukarin, S. V., Fateev, N. V., & Smirnov, S. V. (2004). Generation of self-frequency-shifted solitons in tapered fibers in the presence of femtosecond pumping. *Laser Physics, 14*, 748–751.

Kobtsev, S. M., Kukarin, S. V., Fateev, N. V., & Smirnov, S. V. (2005). Coherent, polarization and temporal properties of self-frequency shifted solitons generated in polarization-maintaining microstructured fibre. *Applied Physics B, 81*(2–3), 265–269.

Kubota, H., Tamura, K., & Nakazawa, M. (1999). Analyzes of coherence maintained ultrashort optical pulse trains and supercontinuum in the presence of soliton-amplified spontaneous-emission interaction. *Journal of the Optical Society of America, 16*, 2223–2232.

Kudlinski, A., & Mussot, A. (2008). Visible cw-pumped supercontinuum. *Optics Letters, 33*(20), 2407–2409.

Kudlinski, A., George, A. K., Knight, J. C., Travers, J. C., Rulkov, A. B., Popov, S. V., & Taylor, J. R. (2006). Zero-dispersion wavelength decreasing photonic crystal fibers for ultraviolet-extended supercontinuum generation. *Optics Express, 14*(12), 5715–5722.

Kudlinski, A., Bouwmans, G., Douay, M., Taki, M., & Mussot, A. (2009). Dispersion-engineered photonic crystal fibers for CW-pumped supercontinuum sources. *Journal of Lightwave Technology, 27*(11), 1556–1564.

Kurkov, A. S., Kamynin, V. A., Sholokhov, E. M., & Marakulin, A. V. (2011). Mid-IR supercontinuum generation in Ho-doped fiber amplifier. *Laser Physics Letters, 8*, 754.

Kuyken, B., Liu, X., Osgood, R. M., Jr., Baets, R., Roelkens, G., & Green, W. M. J. (2011). Mid-infrared to telecom-band supercontinuum generation in highly nonlinear silicon-on-insulator wire waveguides. *Optics Express, 19*(21), 20172–20181.

Lafargue, C., Bolger, J., Genty, G., Dias, F., Dudley, J. M., & Eggleton, B. J. (2009). Direct detection of optical rogue wave energy statistics in supercontinuum generation. *Electronics Letters, 45*(4), 217–219.

Lehtonen, M., Genty, G., Ludvigsen, H., & Kaivola, M. (2003). Supercontinuum generation in a highly birefringent microstructured fiber. *Applied Physics Letters, 82*, 2197–2199.

Leong, J. Y. Y., Petropoulos, P., Asimakis, S., Ebendorff-Heidepriem, H., Moore, R. C., Frampton, K., Finazzi, V., Feng, X., Price, J. H., Monro, T. M., & Richardson, D. J. (2005). *A lead silicate holey fiber with γ=1820 $W^{-1}km^{-1}$ at 1550 nm*. Proceedings of OFC 2005, Anaheim, PDP22.

Levy, J. S., Saha, K., Okawachi, Y., Foster, M. A., Gaeta, A. L., & Lipson, M. (2012). High-performance silicon-nitride-based multiple-wavelength source. *Photonics Technology Letters, 24*(16), 1375–1377.

Liao, M., Chaudhari, C., Qin, G., Yan, X., Suzuki, T., & Ohishi, Y. (2009). Tellurite microstructure fibers with small hexagonal core for supercontinuum generation. *Optics Express, 17*(14), 12174–12182.

Lin, C., & Stolen, R. H. (1976). New nanosecond continuum for excited-state spectroscopy. *Applied Physics Letters, 28*, 216–218.

Lopez-Galmiche, G., Sanjabi Eznaveh, Z., Eftekhar, M. A., Antonio Lopez, J., Wright, L. G., Wise, F., Christodoulides, D., & Amezcua Correa, R. (2016). Visible supercontinuum generation in a graded index multimode fiber pumped at 1064 nm. *Optics Letters, 41*(11), 2553–2556.

Lu, C. H., Tsou, Y. J., Chen, H. Y., Chen, B. H., Cheng, Y. C., Yang, S. D., Chen, M. C., Hsu, C. C., & Kung, A. H. (2014). Generation of intense supercontinuum in condensed media. *Optica, 1*(6), 400–406.

Marks, D. L., Oldenburg, A. L., Reynolds, J. J., & Boppart, S. A. (2002). Study of an ultrahigh-numerical-aperture fiber continuum generation source for optical coherence tomography. *Optics Letters, 27*, 2010–2012.

Mitschke, F. M., & Mollenauer, L. F. (1986). Discovery of the soliton self-frequency shift. *Optics Letters, 11*, 659–661.

Miyagawa, Y., Yamamoto, T., Masuda, H., Abe, M., Takahashi, H., & Takara, H. (2006). Over-10000-channel 2.5-GHz-spaced ultra-dense WDM light source. *Electronics Letters, 42*(11), 655–657.

Mogilevtsev, D., Birks, T. A., & Russell, P. S. J. (1998). Group-velocity dispersion in photonic crystal fibers. *Optics Letters, 23*, 1662–1664.

Morgner, U., Kärtner, F. X., Cho, S. H., Chen, Y., Haus, H. A., Fujimoto, J. G., Ippen, E. P., Scheuer, V., Angelow, G., & Tschudi, T. (1999). Sub-two-cycle pulses from a Kerr-lens mode-locked Ti:sapphire laser. *Optics Letters, 24*, 411–413.

Mori, K., Morioka, T., & Saruwatari, M. (1995). Ultrawide spectral range group velocity dispersion measurement utilizing supercontinuum in an optical fiber pumped by a 1.5 μm compact laser source. *IEEE Transactions on Instrumentation and Measurement, 44*, 712–715.

Mori, K., Takara, H., Kawanishi, S., Saruwatari, M., & Morioka, T. (1997). Flatly broadened supercontinuum generated in a dispersion decreasing fiber with convex dispersion profile. *Electronics Letters, 33*, 1806–1808.

Mori, K., Takara, K., & Kawanishi, S. (1998). The effect of pump fluctuation in supercontinuum pulse generation. *Nonlinear Guided Waves & Their Applications, OSA Tech Dig Ser, 5*, 276–278.

Mori, K., Takara, H., & Kawanishi, S. (2001). Analysis and design of supercontinuum pulse generation in a single-mode optical fiber. *Journal of the Optical Society of America B, 18*, 1780–1792.

Mori, K., Sato, K., Takara, H., & Ohara, T. (2003). Supercontinuum lightwave source generating 50 GHz spaced optical ITU grid seamlessly over S-, C-and L-bands. *Electronics Letters, 39*(6), 544.

Morioka, T., Mori, K., & Saruwatari, M. (1993). More than 100-wavelength-channel picosecond optical pulse generation from single laser source using supercontinuum in optical fibers. *Electronics Letters, 29*, 862–864.

Morioka, T., Takara, H., Kawanishi, S., Kamatani, O., Takiguchi, K., Uchiyama, K., Saruwatari, M., Takahashi, H., Yamada, M., Kanamori, T., & Ono, H. (1996). 1 Tbit/s 100 Gbit/s 10 channel OTDM-WDM transmission using a single supercontinuum WDM source. *Electronics Letters, 32*(10), 906.

Mussot, A., Kudlinski, A., Kolobov, M., Louvergneaux, E., Douay, M., & Taki, M. (2009). Observation of extreme temporal events in CW-pumped supercontinuum. *Optics Express, 17*(19), 17010–17015.

Nakazawa, M., Tamura, K., Kubota, H., & Yoshida, E. (1998). Coherence degradation in the process of supercontinuum generation in an optical fiber. *Optical Fiber Technology, 4*, 215–223.

Nelson, B. P., Cotter, D., Blow, K. J., & Doran, N. J. (1983). Large non-linear pulse broadening in long lengths of monomode fibre. *Optics Communications, 48*, 292–294.

Newbury, N. (2011). Searching for applications with a fine-tooth comb. *Nature Photonics, 5*, 186–188.

Ndagano, B., Brüning, R., McLaren, M., Duparré, M., & Forbes, A. (2015). Fiber propagation of vector modes. *Optics Express, 23*(13), 17330–17336.

Nicholson, J. W., Yan, M. F., Wisk, P., Fleming, J., DiMarcello, F., Monberg, E., Yablon, A., Jørgensen, C., & Veng, T. (2003a). All-fiber, octave-spanning supercontinuum. *Optics Letters, 28*, 643–645.

Nicholson, J. W., Abeeluck, A. K., Headley, C., Yan, M. F., & Jørgensen, C. G. (2003b). Pulsed and continuous-wave SC generation in highly nonlinear, dispersion-shifted fibers. *Applied Physics B, 77*, 211–218.

Nicholson, J. W., Westbrook, P. S., Feder, K. S., & Yablon, A. D. (2004a). Supercontinuum generation in ultraviolet-irradiated fibers. *Optics Letters, 29*, 2363–2365.

Nicholson, J. W., Fini, J. M., Bouteiller, J.-C., Bromage, J., & Brar, K. (2004b). Stretched ultrashort pulses for high repetition rate swept-wavelength Raman pumping. *Journal of Lightwave Technology, 22*(1), 71–78.

Nikolov, N. I., Sorensen, T., Bang, O., & Bjarklev, A. (2003). Improving efficiency of supercontinuum generation in photonic crystal fibers by direct degenerate four-wave-mixing. *Journal of the Optical Society America B, 11*, 2329–2337.

Nishizawa, N., & Goto, T. (2001). Widely broadened super continuum generation using highly nonlinear dispersion shifted fibers and femtosecond fiber laser. *Japanese Journal of Applied Physics, 40*, L365–L367.

Nishizawa, N., & Takayanagi, J. (2007). Octave spanning high-quality supercontinuum generation in all-fiber system. *Journal of the Optical Society of America B, 24*(8), 1786–1792.

Oda, S., & Maruta, A. (2004). *Experimental demonstration of optical quantizer based on slicing supercontinuum spectrum for all-optical analog-to-digital conversion*. In Conference Proceedings of ECOC 2004, Paper We4.P.084, Stockholm, Sweden.

Oda, S., & Maruta, A. (2005a). A novel quantization scheme by slicing supercontinuum spectrum for all-optical analog-to-digital conversion. *IEEE Photonics Technology Letters, 17*, 465–467.

Oda, S., & Maruta, A. (2005b). *All-optical analog-to-digital conversion by slicing supercontinuum spectrum and switching with nonlinear optical loop mirror*. Proceedings of OFC 2005, paper OThN3, Anaheim.

Oda, S., Okamoto, S., & Maruta, A. (2004). *A novel quantization scheme by slicing supercontinuum spectrum for all-optical analog-to-digital conversion*. In Conference Proceedings NLGW 2004, Toronto, Canada, Paper TuB3.

Ohara, T., Takara, H., Yamamoto, T., Masuda, H., Morioka, T., Abe, M., & Takahashi, H. (2005). *Over 1000 channel, 6.25 GHz-spaced ultra-DWDM transmission with supercontinuum multi-carrier source*. Proceedings of OFC 2005, OWA6, Anaheim.

Ohara, T., Takara, H., Yamamoto, T., Masuda, H., Morioka, T., Abe, M., & Takahashi, H. (2006). Over-1000-channel ultradense WDM transmission with supercontinuum multicarrier source. *Journal of Lightwave Technology, 24*(6), 2311–2317.

Okuno, T., Onishi, M., & Nishimura, M. (1998). Generation of ultra-broad-band supercontinuum by dispersion-flattened and decreasing fiber. *IEEE Photonics Technology Letters, 10*, 72–74.

Ortigosa-Blanch, A., Knight, J. C., & Russell, P. S. J. (2002). Pulse breaking and supercontinuum generation with 200-fs pump pulses in PCF. *Journal of the Optical Society of America B, 19*, 2567–2572.

Petersen, C. R., Møller, U., Kubat, I., Zhou, B., Dupont, S., Ramsay, J., Benson, T., Sujecki, S., Abdel-Moneim, N., Tang, Z., Furniss, D., Seddon, A., & Bang, O. (2014). Mid-infrared supercontinuum covering the 1.4–13.3 μm molecular fingerprint region using ultra-high NA chalcogenide step-index fibre. *Nature Photonics, 8*, 830–834.

Phillips, C. R., Langrock, C., Pelc, J. S., Fejer, M. M., Jiang, J., Fermann, M. E., & Hartl, I. (2011). Supercontinuum generation in quasi-phase-matched $LiNbO_3$ waveguide pumped by a Tm-doped fiber laser system. *Optics Letters, 36*(19), 3912–3914.

Pitois, S., Fatome, J., & Millot, G. (2002). Generation of a 160-GHz transform-limited pedestal-free pulse train through multiwave mixing compression of a dual-frequency beat signal. *Optics Letters, 27*, 1729–1731.

Poli, F., Cucinotta, A., Selleri, S., & Bouk, A. H. (2004). Tailoring of flattened dispersion in highly nonlinear photonic crystal fibers. *IEEE Photonics Technology Letters, 16*, 1065–1067.

Povazay, B., Bizheva, K., Unterhuber, A., Hermann, B., Sattmann, H., Fercher, A. F., Drexler, W., Apolonski, A., Wadsworth, W. J., Knight, J. C., Russell, P. S. J., Vetterlein, M., & Scherzer, E. (2002). Submicrometer axial resolution optical coherence tomography. *Optics Letters, 27*, 1800–1802.

Prabhakar, G., Gregg, P., Rishoj, L., Kristensen, P., & Ramachandran, S. (2019). Octave-wide supercontinuum generation of light-carrying orbital angular momentum. *Optics Express, 27*(8), 11547–11556.

Prabhu, M., Kim, N. S., & Ueda, K. (2000). Ultra-broadband CW supercontinuum generation centered at 1483.4 nm from Brillouin/Raman fiber laser. *Japanese Journal of Applied Physics, 39*, L291–L293.

Proulx, A., Ménard, J., Hô, N., Laniel, J. M., Vallée, R., & Paré, C. (2003). Intensity and polarization dependences of the supercontinuum generation in birefringent and highly nonlinear microstructured fibers. *Optics Express, 11*, 3338–3345.

Qin, G., Yan, X., Kito, C., Liao, M., Chaudhari, C., Suzuki, T., & Ohishi, Y. (2009). Ultrabroadband supercontinuum generation from ultraviolet to 6.28 um in a fluoride fiber. *Applied Physics Letters, 95*, 161103.

Ranka, J. K., & Gaeta, A. L. (1998). Breakdown of the slowly varying envelope approximation in the self-focusing of ultrashort pulses. *Optics Letters, 23*, 534–536.

Ranka, J. K., Windeler, R. S., & Stentz, A. J. (1999). *Efficient visible continuum generation in air-silica microstructure optical fibers with anomalous dispersion at 800 nm*. Conference on lasers and electro-optics CLEO '99 CPD8/1 -CPD8/2.

Ranka, J. K., Windeler, R. S., & Stentz, A. J. (2000a). Visible continuum generation in air-silica microstructure optical fibers with anomalous dispersion at 800 nm. *Optics Letters, 25*, 25–27.

Ranka, J. K., Windeler, R. S., & Stentz, A. J. (2000b). Optical properties of high-delta air-silica microstructure optical fibers. *Optics Letters, 25*, 796–798.

Reeves, W. H., Knight, J. C., Russell, P. S. J., & Roberts, P. J. (2002). Demonstration of ultra-flattened dispersion in photonic crystal fibers. *Optics Express, 10*, 609–613.

Reeves, W. H., Skryabin, D. V., Biancalana, F., Knight, J. C., Russell, P. S. J., Omenetto, F. G., Efimov, A., & Taylor, A. J. (2003). Transformation and control of ultra-short pulses in dispersion-engineered photonic crystal fibres. *Nature, 424*, 511–515.

Reid, D. T., Cormack, I. G., Wadsworth, W. J., Knight, J. C., & Russell, P. S. J. (2002). Soliton self-frequency shift effects in photonic crystal fibre. *Journal of Modern Optics, 49*, 757–767.

Ren, Y., Li, L., Xie, G., Yan, Y., Cao, Y., Huang, H., Ahmed, N., Zhao, Z., Liao, P., Zhang, C., Caire, G., Molisch, A., Tur, M., & Willner, A. E. (2017). Line-of-sight millimeter-wave communications using orbital angular momentum multiplexing combined with conventional spatial multiplexing. *IEEE Transactions on Wireless Communications, 16*(5), 3151–3161.

Renversez, G., Kuhlmey, B., & McPhedran, R. (2003). Dispersion management with microstructured optical fibers: Ultraflattened chromatic dispersion with low losses. *Optics Letters, 28*, 989–991.

Richardson, D. J., Fini, J. M., & Nelson, L. E. (2013). Space-division multiplexing in optical fibres. *Nature Photonics, 7*(5), 354–362.

Safioui, J., Leo, F., Kuyken, B., Gorza, S.-P., Selvaraja, S. K., Baets, R., Emplit, P., Roelkens, G., & Massar, S. (2014). Supercontinuum generation in hydrogenated amorphous silicon waveguides at telecommunication wavelengths. *Optics Express, 22*(3), 3089–3097.

Saitoh, K., & Koshiba, M. (2004). Highly nonlinear dispersion-flattened photonic crystal fibers for supercontinuum generation in a telecommunication window. *Optics Express, 12*, 2027–2032.

Saitoh, K., Koshiba, M., Hasegawa, T., & Sasaoka, E. (2003). Chromatic dispersion control in photonic crystal fibers: Application to ultra-flattened dispersion. *Optics Express, 11*, 843–852.

Sanders, S. T. (2002). Wavelength-agile fiber laser using group-velocity dispersion of pulsed supercontinua and application to broadband absorption spectroscopy. *Applied Physics B, 75*, 799–802.

Schenkel, B., Biegert, J., Keller, U., Vozzi, C., Nisoli, M., Sansone, G., Stagira, S., De Silvestri, S., & Svelto, O. (2003). Generation of 3.8-fs pulses from adaptive compression of a cascaded hollow fiber supercontinuum. *Optics Letters, 28*, 1987–1989.

Shank, C. V., Fork, R. L., Yen, R., & Stolen, R. H. (1982). Compression of femtosecond optical pulses. *Applied Physics Letters, 40*(9), 761.

Silva, F., Austin, D. R., Thai, A., Baudisch, M., Hemmer, M., Faccio, D., Couairon, A., & Biegert, J. (2012). Multi-octave supercontinuum generation from mid-infrared filamentation in a bulk crystal. *Nature Communications, 3*, 807.

Silvestre, E., Russell, P. S. J., Birks, T. A., & Knight, J. C. (1998). Analysis and design of an endlessly single-mode finned dielectric waveguide. *Journal of the Optical Society of America A, 15*, 3067–3075.

Singh, N., Hudson, D. D., Yu, Y., Grillet, C., Jackson, S. D., Casas-Bedoya, A., Read, A., Atanackovic, P., Duvall, S. G., Palomba, S., Luther-Davies, B., Madden, S., Moss, D. J., & Eggleton, B. J. (2015). Midinfrared supercontinuum generation from 2 to 6 μm in a silicon nanowire. *Optica, 2*(9), 797–802.

Singh, N., Xin, M., Vermeulen, D., Shtyrkova, K., Li, N., Callahan, P. T., Magden, E. S., Ruocco, A., Fahrenkopf, N., Baiocco, C., Kuo, B. P., Radic, S., Ippen, E., Kärtner, F. X., & Watts, M. R. (2018). Octave-spanning coherent supercontinuum generation in silicon on insulator from 1.06 μm to beyond 2.4 μm. *Light: Science & Applications, 7*, 17131.

Skryabin, D. V., Luan, F., Knight, J. C., & P. St. J. Russell. (2003). Soliton self-frequency shift cancellation in photonic crystal fibers. *Science, 301*(5640), 1705–1708.

Smith, W. L., Liu, P., & Bloembergen, N. (1977). Superbroadening in H_2O and D_2O by self-focused picosecond pulses from a YAlG:Nd laser. *Physical Review A, 15*, 2396–2403.

Solli, D. R., Ropers, C., Koonath, P., & Jalali, B. (2007). Optical rogue waves. *Nature, 450*, 1054–1057.

Solli, D. R., Ropers, C., & Jalali, B. (2008). Active control of rogue waves for stimulated supercontinuum generation. *Physical Review Letters, 101*, 233902.

Sotobayashi, H., Chujo, W., & Ozeki, T. (2001). *Bi-directional photonic conversion between 4×10 Gbit/s OTDM and WDM by optical time-gating wavelength interchange*. Proceeding of OFC 2001, paper WM5, Ahaneim.

Sotobayashi, H., Chujo, W., Konishi, A., & Ozeki, T. (2002a). Wavelength-band generation and transmission of 3.24-Tbit/s (81-channel WDMx40-Gbit/s) carrier-suppressed return-to-zero

format by use of a single supercontinuum source for frequency standardization. *Journal of the Optical Society of America B, 19*(11), 2803.

Sotobayashi, H., Chujo, W., & Kitayama, K. (2002b). Photonic gateway: TDM-to-WDM-to-TDM conversion and reconversion at 40 Gbit/s (4 channels x 10 Gbits/s). *Journal of the Optical Society of America B, 19*(11), 2810.

Stibenz, G., & Steinmeyer, G. (2004). High dynamic range characterization of ultrabroadband white-light continuum pulses. *Optics Express, 12*, 6319–6325.

Südmeyer, T., Brunner, F., Innerhofer, E., Paschotta, R., Furusawa, K., Baggett, J. C., Monro, T. M., Richardson, D. J., & Keller, U. (2003). Nonlinear femtosecond pulse compression at high average power levels by use of a large mode-area holey fiber. *Optics Letters, 28*, 1951–1953.

Swiderski, J., & Michalska, M. (2013). Over three-octave spanning supercontinuum generated in a fluoride fiber pumped by Er & Er:Yb-doped and Tm-doped fiber amplifiers. *Optics & Laser Technology, 52*, 75–80.

Sztul, H. I., Kartazayev, V., & Alfano, R. R. (2006). Laguerre–Gaussian supercontinuum. *Optics Letters, 31*(18), 2725–2727.

Tadakuma, M., Aso, O., & Namiki, S. (2000). *A 104 GHz 328 fs soliton pulse train generation through a comb-like dispersion profiled fiber using short high nonlinearity dispersion shifted fibers*. Presented at OFC 2000.

Tai, K., Tomita, A., Jewell, J. L., & Hasegawa, A. (1986). Generation of subpicosecond solitonlike optical pulses at 0.3 THz repetition rate by induced modulational instability. *Applied Physics Letters, 49*, 236–238.

Takada, K., Abe, M., Shibata, T., & Okamoto, K. (2002). 5 GHz-spaced 4200-channel two-stage tandem demultiplexer for ultra-multi-wavelength light source using supercontinuum generation. *Electronics Letters, 38*(12), 572–573.

Takanayagi, J., Nishizawa, N., Nagai, H., Yoshida, M., & Goto, T. (2005). Generation of high-power femtosecond pulse and octave-spanning ultrabroad supercontinuum using all-fiber system. *IEEE Photonics Technology Letters, 17*, 37–39.

Takara, T., Ohara, T., Mori, K., Sato, K., Yamada, E., Jinguji, K., Inoue, Y., Shibata, T., Morioka, T., & Sato, K.-I. (2000). More than 1000 channel optical frequency chain generation from a single supercontinuum source with 12.5 GHz channel spacing. *Electronics Letters, 36*, 2089–2090.

Takara, H., Ohara, T., & Sato, K. (2003a). Over 1000 km DWDM transmission with supercontinuum multi-carrier source. *Electronics Letters, 39*(14), 1078.

Takara, H., Masuda, H., Mori, K., Sato, K., Inoue, Y., Ohara, T., Mori, A., Kohtoku, M., Miyamoto, Y., Morioka, T., & Kawanishi, S. (2003b). 124 nm seamless bandwidth, 313x10 Gbit/s DWDM transmission. *Electronics Letters, 39*(382–383), 2003.

Tamura, K., & Nakazawa, M. (1998). Timing jitter of solitons compressed in dispersion-decreasing fibers. *Optics Letters, 23*, 1360–1362.

Tamura, K., Yoshida, E., & Nakazawa, M. (1996). Generation of 10 GHz pulse trains at 16 wavelengths by spectrally slicing a high power femtosecond source. *Electronics Letters, 32*(18), 1691.

Tamura, K., Kubota, H., & Nakazawa, M. (2000). Fundamentals of stable continuum generation at high repetition rates. *Journal of Quantum Electronics, 36*(7), 773–779.

Teipel, J., Franke, K., Turke, D., Warken, F., Meiser, D., Leuschner, M., & Giessen, H. (2003). Characteristics of supercontinuum generation in tapered fibers using femtosecond laser pulses. *Applied Physics B, 77*, 245–251.

Tianprateep, M., Tada, J., Yamazaki, T., & Kannari, F. (2004). Spectral-shape-controllable supercontinuum generation in microstructured fibers using adaptive pulse shaping technique. *Japanese Journal of Applied Physics, 43*, 8059–8063.

Tomlinson, W. J., Stolen, R. J., & Shank, C. V. (1984). Compression of optical pulses chirped by self-phase modulation in fibers. *Journal of the Optical Society of America B, 1*, 139–149.

Vanholsbeeck, F., Martin-Lopez, S., González-Herráez, M., & Coen, S. (2005). The role of pump incoherence in continuous-wave supercontinuum generation. *Optics Express, 13*(17), 6615–6625.

Vergeles, S., & Turitsyn, S. K. (2011). Optical rogue waves in telecommunication data streams. *Physical Review A, 83*, 061801.

Wadsworth, W. J., Ortigosa-Blanch, A., Knight, J. C., Birks, T. A., Man, T. P. M., & P. St. J. Russell. (2002). Supercontinuum generation in photonic crystal fibers and optical fiber tapers: A novel light source. *Journal of the Optical Society of America B, 19*, 2148–2155.

Wang, Y. M., Zhao, Y. H., Nelson, J. S., Chen, Z. P., & Windeler, R. S. (2003a). Ultrahigh-resolution optical coherence tomography by broadband continuum generation from a photonic crystal fiber. *Optics Letters, 28*, 182–184.

Wang, Y. M., Nelson, J. S., Chen, Z. P., Reiser, B. J., Chuck, R. S., & Windeler, R. S. (2003b). Optimal wavelength for ultrahigh-resolution optical coherence tomography. *Optics Express, 11*, 1411–1417.

Wang, D., Jiang, H., Wu, S., Yang, H., Gong, Q., Xiang, J., & Xu, G. (2003c). An investigation of solvent effects on the optical properties of dye IR-140 using the pump supercontinuum-probing technique. *Journal of Optics A: Pure and Applied Optics, 5*, 515–519.

Wang, J., Yang, J. Y., Fazal, I. M., Ahmed, N., Yan, Y., Huang, H., Ren, Y., Yue, Y., Dolinar, S., Tur, M., & Willner, A. E. (2012). Terabit free-space data transmission employing orbital angular momentum multiplexing. *Nature Photonics, 6*, 488–496.

Washburn, B. R., & Newbury, N. R. (2004). Phase, timing, and amplitude noise on supercontinua generated in microstructure fiber. *Optics Express, 12*, 2166–2175.

Werncke, W., Lau, A., Pfeiffer, M., Lenz, K., Weigmann, H.-J., & Thuy, C. D. (1972). An anomalous frequency broadening in water. *Optics Communications, 4*, 413–415.

Willner, A. E., & Liu, C. (2020). Perspective on using multiple orbital-angular-momentum beams for enhanced capacity in free-space optical communication links. *Nanophotonics, 10*(1), 225–233.

Willner, A. E., Huang, H., Yan, Y., Ren, Y., Ahmed, N., Xie, G., Bao, C., Li, L., Cao, Y., Zhao, Z., Wang, J., Lavery, M. P. J., Tur, M., Ramachandran, S., Molisch, A. F., Ashrafi, N., & Ashrafi, S. (2015). Optical communications using orbital angular momentum beams. *Advances in Optics and Photonics, 7*, 66–106.

Wright, A. J., Girkin, J. M., Gibson, G. M., Leach, J., & Padgett, M. J. (2008). Transfer of orbital angular momentum from a super-continuum, white-light beam. *Optics Express, 16*(13), 9495–9500.

Yan, Y., Xie, G., Lavery, M. P. J., Huang, H., Ahmed, N., Bao, C., Ren, Y., Cao, Y., Li, L., Zhao, Z., Molisch, A. F., Tur, M., Padgett, M. J., & Willner, A. E. (2014). High-capacity millimetre-wave communications with orbital angular momentum multiplexing. *Nature Communications, 5*, 4876.

Ye, J., & Cundiff, S. T. (Eds.). (2005). *Femtosecond optical frequency comb technology*. Springer.

Ye, Q., Xu, C., Liu, X., Knox, W. H., Yan, M. F., Windeler, R. S., & Eggleton, B. (2002). Dispersion measurement of tapered air–silica microstructure fiber by white-light interferometry. *Applied Optics, 41*, 4467–4470.

Yeom, D.-I., Mägi, E. C., Lamont, M. R. E., Roelens, M. A. F., Fu, L., & Eggleton, B. J. (2008). Low-threshold supercontinuum generation in highly nonlinear chalcogenide nanowires. *Optics Letters, 33*(7), 660–662.

Yusoff, Z., Petropoulos, P., Furusawa, K., Monro, T. M., & Richardson, D. J. (2003). A 36 channel x 10 GHz spectrally sliced pulse source based on supercontinuum generation in normally dispersive highly nonlinear holey fibre. *IEEE Photonics Technology Letters, 15*(12), 1689–1691.

Zeller, J., Jasapara, J., Rudolph, W., & Sheik-Bahae, M. (2000). Spectro-temporal characterization of a femtosecond white-light continuum generation by transient-grating diffraction. *Optics Communications, 185*, 133–137.

Zhang, R., Teipel, J., & Giessen, H. (2006). Theoretical design of a liquid-core photonic crystal fiber for supercontinuum generation. *Optics Express, 14*(15), 6800–6812.

Zheltikov, A. M. (2000). Holey fibers. *Uspekhi Fizicheskikh Nauk, Russian Academy of Sciences, 43*, 1125–1136.

Chapter 10
Twisted Light in Supercontinuum: From Self-Phase Modulation to Superfluidity in Kerr Medium

J. T. Mendonça

Abstract This chapter considers the influence of laser pulse topology on the formation of a supercontinuum. This occurs when the usual Gaussian laser pulses are replaced by twisted pulses, which carry a finite amount of orbital angular momentum (OAM). Generation of ring-shaped and of helical pulses with a broad spectrum is discussed. We also study the possible relation between self-phase modulation (SPM), which is at the origin of the supercontinuum, and the superfluidity of light. These two phenomena can occur in a Kerr medium. For short pulses and long propagation distances, SPM could modify the conditions for the observation of superfluid light.

Keywords Photon OAM · Self-phase modulation · Superfluidity · Kerr medium

10.1 Introduction

Self-phase modulation (SPM) of a short laser pulse, which is at the origin of the so-called supercontinuum, is presently well understood (Boyd, 1992; Alfano, 2016; Alfano & Shapiro, 1970). The supercontinuum arises from the nonlinear change in the refractive index which occurs in a Kerr medium. In a recent work Mendonça (2020), we have extended SPM to the case of twisted laser pulses from OAM, a topic which became popular in the modern literature (Secor et al., 2017; Yao & Padgett, 2011). It is well-known that twisted laser pulses carry a finite amount of orbital angular momentum and possess remarkable nonlinear properties (Mendonça et al., 2009; Zhu et al., 2018).

In this chapter, we review SPM and the supercontinuum of twisted laser pulses and discuss two different pulse configurations. One is that of a single twisted mode, characterized by a single topological charge l, and corresponds to a donut or

J. T. Mendonça (✉)
Instituto Superior Técnico, Universidade de Lisboa, Lisbon, Portugal
e-mail: titomend@tecnico.ulisboa.pt

R. R. Alfano (ed.), *The Supercontinuum Laser Source*,
https://doi.org/10.1007/978-3-031-06197-4_10

ring-shaped helical intensity distribution. The other is that of mode superposition, particularly that of light springs (Pariente and Quéré, 2015), which corresponds to a helical energy distribution, and contains two or more topological charges. Light springs are particularly important because they are able to accelerate helical electron beams (Vieira et al., 2018).

We also relate SPM with the superfluidity of light, another possible process in a nonlinear Kerr medium. The interest on superfluid light emerged in recent years, as an alternative experimental approach to condensed matter processes (Carusoto & Ciuti, 2013; Bolda et al., 2001; Chiao & Boyce, 1999). This effect is associated with the disappearance of diffraction produced by optical obstacles and can occur for sufficiently intense laser beams. Nonlinear inhibition of diffraction is the main signature of superfluidity, when light becomes insensitive to small optical obstacles. Several experimental arrangements have been proposed (Lerario et al., 2017; Michel et al., 2018; Silva et al., 2017; Rodrigues et al., 2020). The standard theoretical models of superfluid light usually ignore the influence of pulse duration. But, for short pulses, nonlinear frequency shifts associated with SPM could eventually interfere with superfluidity. In that case, SPM could modify the basic properties of the photon fluid and, as a result, introduce qualitative changes in the fluid-superfluid transition, due to its sensitivity to frequency and intensity space-time distributions.

10.2 Ring-Shaped Supercontinuum

We first consider SPM in a twisted beam of light with topological charge l. This charge represents the orbital angular momentum of light in the forward direction. The corresponding transverse field profile is given by a radial Laguerre-Gauss (LG) function, for unbounded beam propagation, or by a radial Bessel function for fiber mode propagation. Let us then describe the field mode as:

$$\mathbf{E}\left(\mathbf{r},t\right)=\mathbf{e}_{\mathrm{l}}E_{\mathrm{l}}\left(\mathbf{r}_{\perp},z,t\right)\ \exp\ \left(i\phi_{\mathrm{l}}\left(\mathbf{r},t\right)\right), \tag{10.1}$$

where $\mathbf{e}_{\mathrm{l}}$ is the unit polarization vector, $E_{\mathrm{l}}(\mathbf{r}_{\perp},z,t)$ is a slowly varying amplitude, and $\phi_{\mathrm{l}}(\mathbf{r}_{\perp},z,t)$ is the total phase. We can write them explicitly as:

$$E_{\mathrm{l}}\left(\mathbf{r}_{\perp},z,t\right)=u\left(z,t\right)\mid F_{\mathrm{lp}}\left(\mathbf{r}_{\perp}\right)\mid, \tag{10.2}$$

where $u(z,t)$ is the mode amplitude profile and (l,p) are pairs of quantum numbers specifying the different LG modes. The mode number p gives the number of zeros in the radial direction, and will be considered equal to zero in the numerical examples given here, for simplicity. Using polar coordinates $\mathbf{r}_{\perp}=(r,\theta)$, we can write the LG functions as:

$$F_{\mathrm{lp}}\left(\mathbf{r}\perp\right)=C_{\mathrm{lp}}\ X^{|l|/2}L^{|l|}\mathrm{p}(X)\ \exp\ \left(-X/2+il\theta\right), \tag{10.3}$$

where L_p^1 are the associated Laguerre polynomials with argument $X = r^2/w^2$ and w defines the laser beam waist. Note that this quantity is slowly varying along propagation but can be assumed nearly constant inside of the focal region, over a distance of the order of the Rayleigh length. This is valid for unbounded media. The normalization factors C_{lp} are used to satisfy the orthonormal relations between modes, as defined by:

$$\int_0^\infty r\, dr \int_0^{2\pi} d\Theta\, F_{lp}^*(r,\Theta)\, F_{l'p'}(r,\Theta) = \delta_{ll'}\delta_{pp'}. \tag{10.4}$$

A similar description can be used for optical fibers, but using radial Bessel functions, instead of the above LG functions. The field phase in Eq. (10.1) is given by:

$$\phi_l(\mathbf{r},t) = l\theta + (kz - \omega t), \tag{10.5}$$

where the frequency ω is related to the wavenumber by the nonlinear dispersion relation:

$$\omega = \frac{kc}{\sqrt{\epsilon(\omega)}}\left[1 - \alpha(\omega)|E|^2\right], \tag{10.6}$$

with:

$$\epsilon(\omega) = 1 + \chi^{(1)}(\omega), \qquad \alpha(\omega) = \frac{\omega\, v_k}{2kc^2}\chi^{(3)}, \tag{10.7}$$

where $\chi^{(1)}$ and $\chi^{(3)}$ are the linear and the Kerr susceptibilities, respectively. The resulting nonlinear dependence of the phase on the field intensity leads to a radially symmetric frequency shift, determined by the expression:

$$\omega(t) = \omega_0\left\{1 + \alpha\frac{t}{v_0}\left|F_{lp}(\boldsymbol{r}_\perp)\right|^2\frac{\partial}{\partial\eta}|u(\eta)|^2\right\}. \tag{10.8}$$

Here, $\omega_0 = \omega(t=0)$ is the initial pulse frequency, $\eta = (z - v_0 t)$ is the space variable in the pulse reference frame, and v_0 is the linear group velocity. SFM and the subsequent generation of the supercontinuum will therefore depend on the radial pulse profile, as determined by the new factor $|F_{lp}(\mathbf{r}_\perp)|^2$. Noting that the intensity profile is independent of the angular variable θ, this will lead to a donut or ring-shaped frequency shift, as illustrated in Fig. 10.1. Here, we have used a Gaussian envelope profile, as determined by $|u(\eta)| = u_0 \exp.(-\eta^2/2\sigma^2)$, where σ determines the pulse duration.

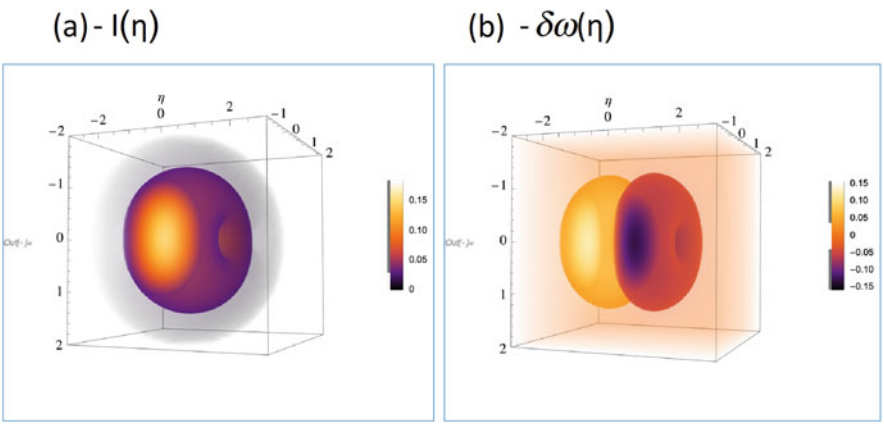

Fig. 10.1 Three-dimensional representation of a twisted laser beam, described by the LG mode (l = 1, p = 0): (**a**) laser pulse intensity I(η); (**b**) frequency shift $\delta\omega(\eta)$, due to SPM inside the pulse. This configuration can lead to the formation of a ring-shaped white light

10.3 Helical Supercontinuum

Let us now consider the superposition of two different twisted modes, characterized by two distinct topological charges, or angular momentum quantum numbers, l_1 and l_2. In this case, Eq. (10.1) is replaced by:

$$\boldsymbol{E}\left(\boldsymbol{r},t\right)=\sum_{j=1,2}\boldsymbol{e}_{j}E_{j}\left(\boldsymbol{r}_{\perp},\eta\right)\ \exp\left[i\phi_{j}\left(\boldsymbol{r},t\right)\right], \tag{10.9}$$

With:

$$E_{j}\left(\boldsymbol{r}_{\perp},\eta\right)=u_{j}\left(\eta\right)\left|F_{j}\left(\boldsymbol{r}_{\perp}\right)\right|,\phi_{j}\left(\boldsymbol{r},t\right)=l_{j}\theta+\left(k_{j}z-\omega_{j}t\right), \tag{10.10}$$

We assume $\mathbf{e}_{\mathrm{j}}=\mathbf{e}$ and ignore polarization effects. Let us introduce the relative amplitude $R=E_2/E_1$. In general, this quantity depends on both the axial and radial variables, $R\equiv R(\mathbf{r}_{\perp},\ \eta)$, but in some useful cases, its radial dependence is small and can be ignored. The resulting pulse intensity will then be proportional to the quantity:

$$\left|E\left(\mathbf{r}_{\perp},\eta\right)\right|^{2}=\left|E_{1}\right|^{2}\left\{\left(1+R^{2}\right)+2R\ \cos\left(\delta_{1}\theta-\delta k\ z-\delta\omega\ t\right)\right\}, \tag{10.11}$$

with $\delta_1=l_1-l_2$, $\delta k=k_1-k_2$, and $\delta\omega=\omega_1-\omega_2$. For $\delta\omega\neq0$, we get the so-called light springs. These configurations are particularly useful for laser acceleration schemes, because they lead to the formation of energetic helical electron beams

(Vieira et al., 2018). The simplest example of a light spring corresponds to $R \simeq 1$, and $\delta_1 = 1$. The above expression is reduced to:

$$|E(\mathbf{r}_\perp, \eta)|^2 \simeq 2|E_1|^2 \left\{ \left(1 + \cos(\theta - \delta k\, z - \delta\omega\, t) \right\}, \tag{10.12}$$

The other interesting example is that of two modes with the same frequency, such that $\delta k = \delta\omega = 0$, but dephased in time. We get the self-torque configurations, recently discussed in Rego et al. (2019). They can be described by:

$$|E(\mathbf{r}_\perp, \eta)|^2 \simeq |E_1|^2 \left[1 + R(\eta)^2 \right] + 2R(\eta)\ \cos(\delta_1 \theta), \tag{10.13}$$

The interest of this new example of two temporally dephased modes is that the angular momentum seems to vary continuously inside the pulse, from l_1 to $l_2 \neq l_1$, due to the variation of their relative amplitudes.

The frequency shift originating from the light spring configuration of Eq. (10.12) is given by:

$$\omega(t) = \omega_0 \{1 + \overline{\alpha}\, t \cos(\theta - \delta k\, z - \delta\omega\, t)\}, \tag{10.14}$$

with the nonlinear factor:

$$\overline{\alpha} = \sum_{j=1,2} \frac{\alpha_j}{v_j} \left| F_j(r_\perp) \right|^2 \frac{\partial}{\partial \eta} |u(\eta)|^2. \tag{10.15}$$

Here, the pulse envelope was assumed identical for the two modes, $u_j(\eta) = u(\eta)$. This leads to the formation of a supercontinuum with new topological properties. The frequency space-time distribution follows a helical shape, similar to that of the pulse intensity, and is fundamentally different from that of a single twisted mode, because it now depends on both the transverse and the angular coordinates. These new features are illustrated in Fig. 10.2. Of particular interest is the topological similarity between the acceleration of helical electron beams, demonstrated in Vieira et al. (2018), and the formation of the helical frequency shifts shown in this figure. Similarities between particle acceleration and photon frequency shifts were noted long ago in plasma physics and led to the concept of photon acceleration [see Mendonça, 2001 and references therein].

Finally, for the self-torque configurations of Eq. (10.13), the SPM frequency shifts are determined by an expression of the form:

$$\omega(t) = \omega_0 \{1 + \nu_0 t + [2\mathrm{R} + \cos(\delta_1 \theta)]\ \nu_1 t\}, \tag{10.16}$$

where $\nu_0 \simeq \bar{\alpha}$ and $\nu_1 \propto (\partial R/\partial \eta)$. Here, the frequency distribution not only loses the axial symmetry of the single twisted mode case, shown in Fig. 10.1b, but also

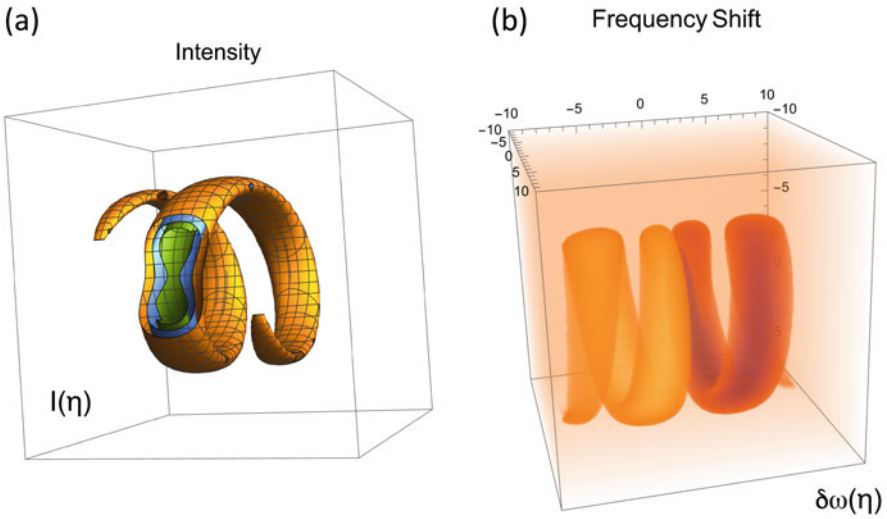

Fig. 10.2 Three-dimensional representation of a light spring, described by the superposition of two LG modes ($l = 6$, $p = 0$) and ($l = 7$, $p = 0$) with equal amplitude: (**a**) laser pulse intensity $I(\eta)$; (**b**) frequency shift $\delta\omega\ (\eta)$, due to SPM inside the spring

the helical property observed with light springs, shown in Fig. 10.2b. This lack of symmetry is due to the conditions ($\delta l \neq 0$, $\delta\omega = 0$), similar to those considered in Mendonça and Vieira (2014), and also to an additional contribution associated with v_1.

10.4 Superfluidity

We now briefly discuss the superfluidity of twisted laser pulses. It is well-known that pulse propagation in a Kerr medium satisfies a nonlinear equation of the form:

$$i\frac{\partial E}{\partial z} = -\left[\frac{1}{2k}\nabla_\perp^2 + \frac{k}{2\epsilon\,(\omega)}\chi^{(3)}|E|^2\right]E. \tag{10.17}$$

We should keep in mind that, for any given location inside the pulse, specified by η, the frequency will increase or decrease along propagation. But we are now more interested in the processes taking place in the perpendicular direction. Equation (10.17) is able to describe the evolution of perturbations in the perpendicular plane $\mathbf{r}_\perp$, during pulse propagation along the z direction. Noting that the center of the pulse moves with $\eta = 0$, or $z = v_0 t$, we can replace the axial variation along z by a temporal variation of the envelope. On the other hand, we can introduce a new

field function, $\psi(\mathbf{r}_\perp, t) = E(\mathbf{r}_\perp, z = \mathrm{v}_0 t)$, and reduce Eq. (10.17) to the standard nonlinear Schrödinger form:

$$i\hbar \frac{\partial}{\partial z}\psi = -\left[\frac{\hbar^2}{2m}\nabla_\perp^2 - g|\psi|^2\right]\psi. \tag{10.18}$$

The effective photon mass m, and coupling parameter g, appearing in this equation, are defined by:

$$m = \frac{\hbar k}{v_0}, \qquad g = -\frac{\hbar v_0}{c}\,\frac{\omega}{\sqrt{\epsilon\,(\omega)}}. \tag{10.19}$$

The Planck constant $\hbar$ was introduced for dimensional purposes. This is formally identical to the Gross-Pitaevskii equation used to describe Bose-Einstein condensates (Pethick and Smith, 2008), and we have chosen the sign of g according to the usual convention. The case of positive nonlinear susceptibility, $\chi^{(3)} > 0$, will correspond to condensates with attractive interactions, and the opposite case of a negative nonlinearity, $\chi^{(3)} < 0$, to repulsive condensates. At this point, it is useful to introduce a Madelung transformation, such that $\psi = \sqrt{n}\,\exp.\,(i\phi)$. This allows us to describe the laser pulse as a fluid, where the photon fluid density n and mean velocity $\mathbf{v}$ are defined as $n = |\psi|^2 = |E|^2$, and $\mathbf{v} = \nabla_\perp \phi$. From Eq. (10.18), we can then derive the corresponding fluid equations, similar to those of a condensate, as (Carusoto & Ciuti, 2013; Rodrigues et al., 2020):

$$\frac{\partial n}{\partial t} + \nabla_\perp\,(n\,\mathbf{v}) = 0, \quad \frac{\partial \mathbf{v}}{\partial t} + \mathbf{v}.\nabla_\perp\,\mathbf{v} = -\frac{g}{m}\,\nabla_\perp n + \frac{\hbar^2}{2m^2}\,\nabla_\perp\left(\frac{\nabla_\perp^2\sqrt{n}}{\sqrt{n}}\right), \tag{10.20}$$

Here, the laser pulse (or photon fluid) parameters m and g depend on the position η inside the laser pulse envelope. It should be noticed that the equilibrium values for the photon density and transverse velocity, n_0 and $\mathbf{v}_0$, are determined by the appropriate twisted mode structure. They will also depend on the frequency shifts associated with SPM, which result from the pulse propagation through the nonlinear medium. In that way, the fluid properties become dependent on the SPM process. For a single twisted mode, characterized by the topological charge l, these equilibrium values are:

$$n_0 = |u_l|^2\left|F_{lp}\,(r_\perp)\right|^2, \quad \mathrm{v}_0 = \nabla_\perp \phi = \frac{l}{r}\,e_\theta. \tag{10.21}$$

This equilibrium state corresponds to a concentric photon fluid ring, as represented in Fig. 10.1a, rotating with a finite polar velocity $\mathbf{v}_0 = \mathbf{v}_\theta$. The resulting transverse flow is proportional to the orbital angular momentum of the twisted beam, $\hbar\, l$, and vanishes for a purely Gaussian pulse.

Let us now assume some elementary perturbations inside these rotating rings of light, as defined by the perturbed quantities $\delta n = n - n_0$, and $\delta \mathbf{v} = \mathbf{v} - \mathbf{v}_0$. Assuming that these perturbed quantities are proportional to exp. $(i\mathbf{q}\cdot\mathbf{r}_\perp - i\Omega t)$, where $\mathbf{q}$ is the wave vector and Ω is the frequency, assumed very small with respect to the photon frequencies, $\Omega \ll \omega$, we can obtain after linearization of Eq. (10.20), a dispersion relation of the form:

$$(\Omega - \mathbf{v}_0.\mathbf{q})^2 = c_s^2 q^2 + \frac{\hbar^2 q^4}{4m^2}. \tag{10.22}$$

where $c_s = (g\ n_0/m)^{1/2}$ can be called the Bogoliubov speed of the photon fluid. Notice that this quantity depends parametrically on η, through the values of g and m, given by Eq. (10.19). It also depends on t, because the photon frequency $\omega(\eta)$ and wavenumber $k(\eta)$ evolve along propagation, and on the radial position as well, through the equilibrium density n_0. This shows that, even if this dispersion relation is formally identical to that of a moving Bose-Einstein condensate, its physical meaning is significantly different and that a more complex view of light superfluidity emerges when SPM is taken into account.

These elementary oscillations in the photon fluid reveal a possible transition to superfluidity, as shown next. Given the radial shape of this fluid, it is appropriate to consider purely poloidal oscillations, eventually relevant to experiments. In this case, we assume $\mathbf{q} = q_\theta \mathbf{e}_\theta$ and, due to the existence of periodic boundaries, we should also keep in mind that such oscillations typically evolve as $q_\theta \sim l'/w$, with $l' \gg l$. The dispersion relation (10.22) then becomes:

$$\left(\Omega - \frac{l q_\theta}{r}\right)^2 = \frac{g n_0\,(r_\perp)}{m}\, q_\theta^2 + \frac{\hbar^2 q_\theta^4}{4m^2}. \tag{10.23}$$

At this point, it is useful to invoke the Landau criterion (Pethick and Smith, 2008). It states that superfluidity will only occur if none of these acoustic type of oscillations can be excited. The photon flow in the poloidal direction will then become insensitive to any given obstacle. This is only possible when $v_\theta < c_s$, or in other terms, when the laser intensity $I \equiv n_0$ is larger than some critical value $I \geq I_c$, defined as:

$$I_c = \frac{l^2}{w^2}\,\frac{m}{g}. \tag{10.24}$$

It is clear that this quantity will depend on η and t, as well as on the radial position. This means that, sufficiently close to the optical axis, superfluidity will necessarily collapse, at a critical radius $r_c \leq l\ m/g$, thus creating a kind of moving horizon between the normal fluid and superfluid.

Let us now discuss the implications of our analysis to possible observation of superfluidity with SPM. For very long pulses, with duration $\Delta t = \sigma/v_0$, SPM can be ignored if the maximum frequency shift is smaller than the natural pulse width,

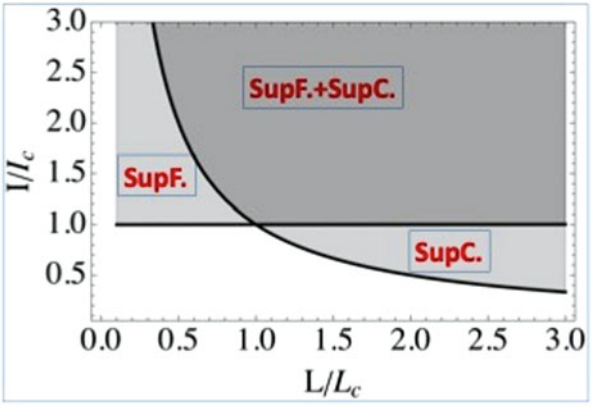

Fig. 10.3 Map of laser intensity versus propagation distance. Intensity is normalized to the critical intensity I_c for superfluidity; and distance is normalized to the critical distance L_c for supercontinuum. Three regions are identified for the observation of superfluidity alone, supercontinuum alone, and both

$\delta\omega_0 \simeq 1/\Delta t$. In this case, we can study superfluidity as an isolated phenomenon. This is no longer true for large propagation distances L, because the frequency shifts modify the value of this critical intensity, I_c. It is therefore useful to state a condition for the inclusion of SPM in the analysis of superfluid light. This can be approximately written as:

$$\Delta\omega \geq \alpha \frac{2\omega_0 \eta}{\sigma} n_0, \tag{10.25}$$

Assuming that maximum frequency shifts occur at a position $\eta \simeq \sigma$, we can establish a criterion for the occurrence of SPM in a superfluid experiment in terms of the propagation distance as $L \geq L_c$, where the critical distance is determined by:

$$L_c = \frac{v_0}{\alpha\omega_0 n_0}. \tag{10.26}$$

This means that, for sufficiently large laser pulse intensities $I \equiv n_0$, or alternatively, for sufficiently long distances L, the two effects of SPM and light superfluidity will eventually merge and will have to be considered simultaneously. However, for sufficiently long pulses, or sufficiently weak laser intensities, they can be observed separately, as it occurs in most experiments so far. The three possible experimental regions are illustrated in the (I, L) diagram of Fig. 10.3.

10.5 Conclusions

In this chapter, we have explored the new topological features of SPM and supercontinuum when twisted laser configurations are introduced, as well as their relations with the superfluid properties of light.

Twisted laser pulses carry a finite amount of orbital angular momentum, and the influence of their topological properties on the formation of a supercontinuum was discussed. Two main examples of twisted pulses were considered. One is that of simple twisted pulses, characterized by a single topological charge l. The other example corresponds to more complex pulses, such as those of light springs and self-torque configurations proposed in recent years. They result from the superposition of two (or more) twisted modes with different topological charges and frequencies. Simple twisted pulses lead to ring-shaped frequency profiles, whereas more complex pulses can lead to helical-shaped or to asymmetric frequency profiles. This opens the way to even more complex configurations, such as those of half-integer (or spin type of fermionic) configurations, described in Mendonça et al. (2018). The road to topological studies of the supercontinuum is therefore open for exploration.

We have also briefly discussed the possible observation of superfluid light, which is related with the inhibition of diffraction above some critical intensity. This property is related with the inhibition of poloidal perturbations in the transverse direction. It is particularly relevant for twisted laser pulses because, in contrast with purely Gaussian pulses, they possess a transverse photon flow velocity proportional to the topological charge. Superfluidity is adequately described by a nonlinear Schrödinger equation, generally valid in Kerr media, from where appropriate fluid equations can be derived.

Transition between a normal fluid and superfluid light can be established using the celebrated Landau criterion. When applied to the present problem, this criterion depends on the laser pulse intensity and frequency profiles and is modified by the occurrence of SPM. Based on the Landau criterion, an intensity-distance map was established, where three different experimental regimes could be identified. They correspond to the observation of SPM and supercontinuum alone, to the observation of superfluidity alone, or to a yet unexplored new regime where SPM modifies the Landau criterion and nonlinear effects along the propagation direction can influence those in the perpendicular direction. This could bring new challenges and opportunities for the experimental work and for future optical applications.

References

Alfano, R. R. (2016). *The supercontinuum laser source* (3rd ed.). Springer.
Alfano, R. R., & Shapiro, S. L. (1970). *Physical Review Letters, 24, 584, 592*, 1217.
Bolda, E. L., Chiao, R. Y., & Zurek, W. H. (2001). *Physical Review Letters, 86*, 416.
Boyd, R. W. (1992). *Nonlinear optics*. Academic Press.
Carusoto, I., & Ciuti, C. (2013). *Reviews of Modern Physics, 85*, 299.

Chiao, R. Y., & Boyce, J. (1999). *Physical Review A, 60*, 4114.
Lerario, G., Fieramosca, A., Barachati, F., Ballarini, D., Daskalakis, K. S., Dominici, L., De Giorgi, M., Maier, S. A., Gigli, G., Kéna-Cohen, S., & Sanvitto, D. (2017). *Nature Physics, 13*, 837.
Mendonça, J. T. (2001). *Theory of photon acceleration*. Institute of Physics Publishing.
Mendonça, J. T. (2020). *Europhysics Letters, 129*, 64004.
Mendonça, J. T., & Vieira, J. (2014). *Physics of Plasmas, 21*, 033107.
Mendonça, J. T., Thidé, B., & Then, H. (2009). *Physical Review Letters, 102*, 185005.
Mendonça, J. T., Serbeto, A., & Vieira, J. (2018). *Scientific Reports, 8*, 7817.
Michel, C., Boughdad, O., Alber, M., Larré, P.-E., & Bellec, M. (2018). *Nature Communications, 9*, 2108.
Pariente, G., & Quéré, F. (2015). *Optics Letters, 40*, 2037.
Pethick, C. J., & Smith, H. (2008). *Bose-Einstein condensates in dilute gases* (2nd ed.). Cambridge University Press.
Rego, L., Dorney, K. M., Brooks, N. J., Nguyen, Q. L., Liao, C.-T., San Román, J., Couch, D. E., Liu, A., Pisanty, E., Lewenstein, M., Plaja, L., Kapteyn, H. C., Murnane, M. M., & Hernández-García, C. (2019). *Science, 364*, 1253.
Rodrigues, J. D., Mendonça, J. T., & Terças, H. (2020). *Physical Review A, 101*, 043810.
Secor, J., Alfano, R., & Ashrafi, S. (2017). *Complex light*. Institute of Physics Publishing.
Silva, N. A., Mendonça, J. T., & Guerreiro, A. (2017). *JOSA B, 34*, 2220.
Vieira, J., Mendonça, J. T., & Quéré, F. (2018). *Physical Review Letters, 121*, 054801.
Yao, A. M., & Padgett, M. J. (2011). *Advances in Optics and Photonics, 3*, 161.
Zhu, Z.-H., Chen, P., Li, H.-W., Zhao, B., Zhou, Z.-Y., Hu, W., Gao, W., Lu, Y.-Q., & Shi, B. S. (2018). *Applied Physics Letters, 112*, 161103.

Chapter 11
Conical Emission Produced from Femtosecond Laser Pulses

Henry J. Meyer and Robert R. Alfano

Abstract Presented is a review of conical emission (CE) produced from femtosecond pulses in transparent solids, focusing on BK-7 glass. Conical emission is one of the most fundamental and colorful nonlinear optical effects. CE describes the radial emission of light due to four-wave mixing, producing a beautiful ring-like color pattern. The effect today is often modeled using the X-wave equation from 2006 but has been historically described using the Luther method from 1994 and the original model from CE's first recorded observation by Alfano and Shapiro in 1970. Often left out of modern literature is what is known as degenerate conical emission, which described the angular re-emission of light matching the source laser due to the influence of the nonlinear index of refraction (n_2). This type of emission was first observed in 1970 by Alfano and Shaprio and can yield important information into the transient nature of the nonlinear index induced by femtosecond pulses. A method of measuring degenerate CE and how it can be used as a new way for measuring the nonlinear index of material are described in this review.

Keywords Conical emission · Four-wave mixing · Nonlinear optics · Ultrafast optics · BK-7 glass · Phase matching · Nonlinear index · Transient nonlinear index · X-waves · Nonlinear Schrodinger equation

11.1 Introduction

Conical emission (CE) is one of the most fundamental and beautiful nonlinear effects. Its name refers to the cone-like shape of the emitted light. CE was first observed by Alfano and Shapiro in 1970 (Alfano & Shapiro, 1970), after being first modeled in 1966 (Shimoda, 1966a, b). The first observation of CE was done using 532 nm picosecond pulses focused into BK-7 glass. The glass sample emitted

H. J. Meyer (✉) · R. R. Alfano
Department of Physics, Institute for Ultrafast Spectroscopy and Lasers, The City College of the City University of New York, New York, NY, USA
e-mail: hmeyer@ccny.cuny.edu; ralfano@ccny.cuny.edu

R. R. Alfano (ed.), *The Supercontinuum Laser Source*,
https://doi.org/10.1007/978-3-031-06197-4_11

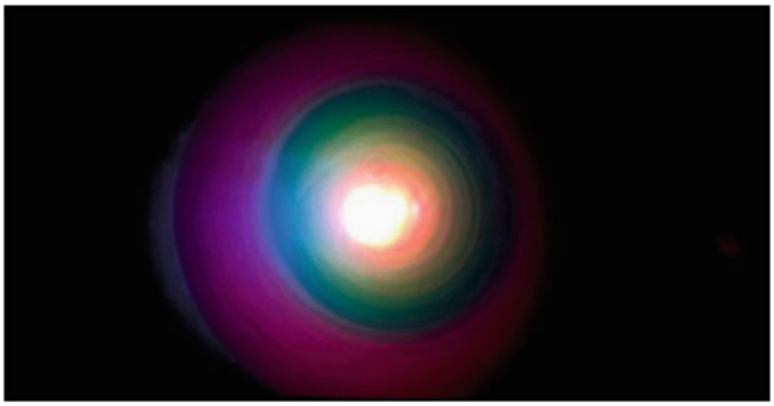

Fig. 11.1 Rings of anti-Stokes conical emission surrounding a white supercontinuum center. Image shows how colorful rings of red, orange, yellow green, blue, and violet spread out angularly from a central white light supercontinuum signal

supercontinuum white light surrounded by multicolored rings that were blue and red shifted from the input green laser. These rings spread out angularly in a cone-like structure as a function of the emitted photon's wavelength in both the Stokes and anti-Stokes directions. This creates an effect that in appearance looks similar to a circular rainbow or grating. In the case of an 800 nm light source, anti-Stokes CE can be seen in Fig. 11.1, in which the generated CE covers the entire visible spectrum (Meyer & Alfano, 2020).

Since CE was first theorized (Chiao & Kelley, 1966), ultrafast lasers have vastly improved. Current lasers can easily achieve pulse durations thousands of times smaller than what was possible in the 1970s putting them into femtosecond regime. This improvement has a dramatic impact on the response of a material's nonlinear index (n_2). The nonlinear index is transient in nature, as it is comprised of multiple different processes with different relaxation times (τ_R) (Shen, 1964; Shen & Yang, 2016; Ho & Alfano, 1979). Pulse durations in the femtosecond regime are often too short for many of nonlinear index's (n_2) components to ramp up and activate (Brewer & Lee, 1968; Hellwarth et al., 1971). For example, a laser pulse in the tens of femtoseconds would render the n_2 of material in its nearly pure electronic state. The laser pulse in this case is too short for the molecular contributions, which typically have picosecond relaxation times, to adequately express themselves. This can have a large effect on nonlinear optical process such as conical emission. So, it is important to note that it can be expected that a 50 fs laser would produce a very different angular spectrum in BK-7 glass than what was first measured using a picosecond laser in 1970.

11.2 Theory

Conical emission comes from the four-wave mixing (FWM) effect (Alfano & Shapiro, 1970). During nonlinear optical action, two photons (k_1 and k_2) can nonlinearly combine in a material and emit two new photons of new frequencies (k_3 and k_4), such that $k_1 + k_2 = k_3 + k_4$. In its original 1970 description, this interaction is entirely subject to the phase matching condition, which is where the process gets its angular dependence (ϕ) (Alfano & Shapiro, 1970). However, CE is now often described using solutions to the nonlinear Schrodinger equation, and this has given rise to new models of the effect such as the Luther model of 1994 (Luther et al., 1994) and the X-wave model of 2006 (Faccio et al., 2006). The X-wave model is currently the most popular model in use today. These three models all predict different emission angles, with the original 1970 model being the only one that predicts degenerate emission. Degenerate CE is a special case in which the material angular re-emits photons at source wavelength such that $k_1 = k_2 = k_3 = k_4$.

For the derivations of these models, we will consider the case of monochromic laser light source such that $k_L = k_1 = k_2$ that undergoes CE and emits a Stokes photon (k_S) with a loss of energy and an anti-Stokes photon (k_A) with a gain in energy compared to source laser giving the relationship $2k_L = k_A + k_S$. This condition is often represented by the linear phase matching triangle in Fig. 11.2a and the energy level diagram Fig. 11.2b.

11.2.1 The Alfano-Shapiro Model

The original 1970 model (Alfano & Shapiro, 1970) comes from the condition of phase mismatch (Δk_A) of the wavevectors, such that $\Delta k_A = k_A + k_S - 2k_L$. Following the work of Shimoda (1966a, b), this can be used to calculate the emitted

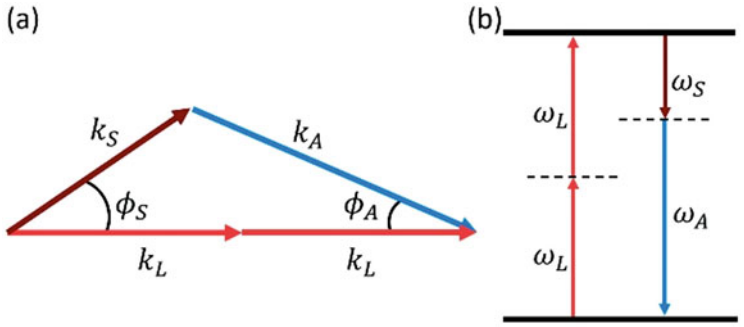

Fig. 11.2 The phase matching triangle (**a**) and the energy level diagram (**b**) of FWM. Here $k_{L,\,S,\,A}$ represents the wavevectors, and $\omega_{L,\,S,\,A}$ represents the input photon frequencies, Stokes, and anti-Stokes. ϕ_S and ϕ_A are the angles of conical emission

angle ϕ_A using the small angle approximation giving

$$\phi_{\mathrm{A}}^2 = \frac{2\Delta \mathrm{k_A}}{\mathrm{k_A}} + \frac{\mathrm{a}^2}{2\mathrm{l}^2} \tag{11.1}$$

The term Δk_A can be expanded using $\Delta k'_A = (k_A + 2\Delta k) + (k_S + 2\Delta k) - 2(k_L + \Delta k)$, to include the contribution of the nonlinear index n_2. This expansion allows for Eq. 11.1 to be rewritten as

$$\phi_A^2 = \frac{2\Delta k_A}{k_A} + \frac{4\Delta k}{k_A} + \frac{a^2}{2l^2}. \tag{11.2}$$

Here $\Delta k = \Delta n_L\, \omega_L/c$, with ω_L being the frequency of the laser and c the speed of light. The term Δn_L is the change in the index of refraction at the laser wavelength due to the nonlinear index of refraction n_2. The term Δn_L is derived from the first term in the equation of nonlinear polarization ($\mathrm{P^{NL}}$) of four-wave mixing (Alfano, 1972)

$$P^{NL} = \frac{\epsilon_2}{8\pi} \{I\,(E_L + 2E_S + 2E_A) + \ldots\}, \tag{11.3}$$

Combining this with the nonlinear polarization created by the charge in the dielectric constant

$$P^{NL} = \frac{\Delta\epsilon}{4\pi} E = \frac{2n\ \Delta n}{4\pi} E. \tag{11.4}$$

gives $\Delta n_L \cong \frac{1}{4}\,\epsilon_2\, I/n_L$ for the strong wave and $\Delta n_{S,A} = \frac{1}{2}\,\epsilon_2\, I/n_{S,A}$ for the weak waves (Alfano, 1972). The term ϵ_2 is the electronic Kerr coefficient $\epsilon_2 = 2\, n_L\, n_2$, with $\mathrm{n_2}$ representing the nonlinear index of the material. The variable I is the input intensity, and n_L and $n_{S,A}$ are the linear indexes of refraction at the input laser, Stokes and Anti-Stokes wavelengths. It is also important to note that the term $a^2/2l^2$ in Eq. 11.2 corresponds to the filament diameter and length and is very small in both Eqs. 11.1 and 11.2, making it negligible in most cases.

Importantly, Eq. 11.2 is nonzero when $\Delta k_A = 0$, and this occurs when $k_L = k_A = k_S$, or $\Delta\omega = 0$. This is a prediction of the angular re-emission of the source wavelength otherwise known as degenerate conical emission. Equation 11.2 in this case simplifies to

$$\phi^2\,(\Delta\omega = 0) = \frac{2n_2 I}{k_L} \tag{11.5}$$

This relationship directly ties the degenerate angular emission of CE to the Kerr nonlinear index n_2. Of the models reviewed in this chapter, only the Alfano-Shapiro model predicts this type of emission.

11.2.2 The Luther Model

The Luther and X-wave models come from the nonlinear Schrödinger equation of the form

$$\frac{dA}{dz} = \frac{i}{2k_L}\nabla_\perp^2 A - \frac{i\,k_L''}{2}\frac{d^2A}{dt^2} + i\,\frac{\omega_L\,n_2}{c}\,I\,A, \tag{11.6}$$

with $A = Exp(i\,k_\perp\,r - i\,\Omega\,t) \bullet Exp(i\,k_L\,z)$, $k_\perp = \sqrt{k_x^2 + k_y^2}$, $r = \sqrt{x^2 + y^2}$, and $\Omega = \omega_A - \omega_L$ (Silberberg, 1990; Liou et al., 1992).

Following Luther et al. (1994), CE occurs during the phase matching of maximum instability growth; mathematically, this occurs when the linear diffraction term and the dispersion term cancel each other out for both Stokes and anti-Stokes emission. Solving Eq. 11.6 for the perpendicular wavevector ($k_\perp$) in this condition gives the relationships

$$k_\perp = \sqrt{k_L k_L''}\;\Omega, \tag{11.7}$$

$$\phi_A = \frac{k_\perp}{k_L} = \sqrt{\frac{k_L''}{k_L}}\;\Omega, \tag{11.8}$$

The Luther model (Eq. 11.8) predicts an essentially linear relationship between the emitted angle and wavelength and doesn't account for degenerate emission and the influence on the nonlinear index. In modern comparative literature, this model underperforms; however, this model provided an important steppingstone to the formation of the X-wave model.

11.2.3 The X-Wave Model

The X-wave model, first proposed by D. Faccio et al., is described as the four-wave mixing and amplification of X-waves (Faccio et al., 2006), and it mathematically follows a similar calculation to the Luther model. Here the dispersion, diffraction,

and nonlinear term from Eq. 11.6 are taken to cancel to zero; solving for the perpendicular wavevector (Liou et al., 1992) gives

$$k_{\perp}^{2} = k_L \, k_L'' \, \Omega^2 - 2 \, \beta \, k_L, \tag{11.9}$$

where $\beta = \frac{\omega_L \, n_2}{c} \, I$. At $k_{\perp} = 0$ gives the relationships $k_L'' \Omega^2 / 2 = \beta$ and $\Omega_{k_{\perp}=0} = \sqrt{2\,\beta / k_L''}$. The perpendicular wavevector can also be written as

$$k_{\perp} = \sqrt{k(\omega)^2 - k_z^2}, \tag{11.10}$$

expanding the k_z term gives $k_z = k_L + k_L' \, \Omega + \frac{1}{2} k_L'' \Omega^2$. This can be rewritten as

$$k_z = k_L + \left(k_L' + \frac{\beta}{\Omega_{k_{\perp}=0}} \right) \Omega. \tag{11.11}$$

Combining Eqs. 11.9, 11.11, and 11.12 gives the X-wave model (Faccio et al., 2006, 2007, 2008)

$$\phi_A = \frac{k_{\perp}}{k_L} = \sqrt{1 - \left(\frac{k_L + \frac{\Omega}{vg}}{k\,(\omega)} \right)^2}, \tag{11.12}$$

The original derivation of the X-wave model omits predictions of CE in the near-degenerate state. In most literature published since its derivation, the X-wave model has been the most common model used for CE outside the degenerate range.

11.3 Measuring Conical Emission

Conical emission can be experimentally measured fairly simply. CE is naturally produced when focusing a high-intensity pulsed beam of light into a material, such as glass. However, the intensity threshold needed for noticeable generation can vary dramatically depending on nature and state of them sample. Transparent solid lattice structures like glass or calcite require significantly less intensity than air, for example. The angle of CE can be measured using a CCD camera, a spectrometer, simple lens trigonometry, and Snell's Law. An example of a CE measuring system can be seen in Fig. 11.3 (Meyer & Alfano, 2020).

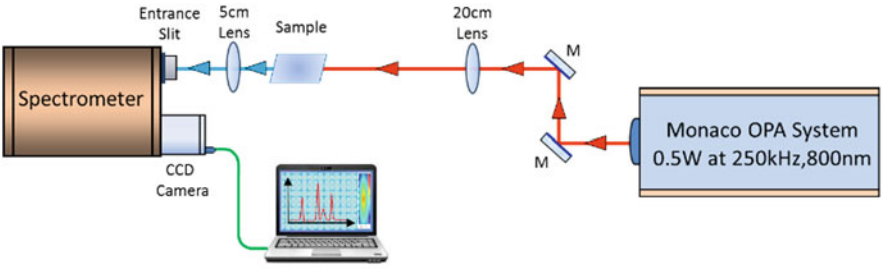

Fig. 11.3 Diagram of the system used to collect conical emission data. Spectrometer used a single grating with 600 line/mm blazed at 750 nm

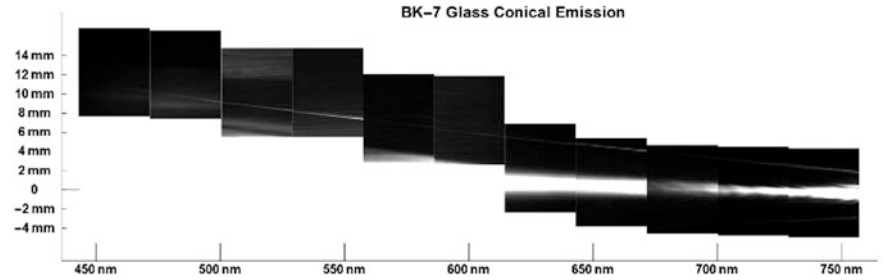

Fig. 11.4 Image of the angular growth of anti-Stokes conical emission. X-axis is the span of 450 nm to 750 nm and the Y-Axis is the height change at the slit entrance before converting into internal sample angle. The zero location is the center of the generated supercontinuum

11.3.1 Non-degenerate Emission

In this system, a 2uJ, 50 fs beam centered at 800 nm with a repetition rate of 250 kHz from a pulse compressed Monaco pumped Opera-F system is focused into a 7.5-cm-long sample of BK-7 glass using a 20 cm lens. Light emitted from the sample is collected through a 5 cm lens placed directly behind the sample and exactly 5 cm from the entrance slit of a single grating spectrometer. This configuration allows for the height of the signal at the entrance slit to be converted into the angle of the light leaving the sample using lens trigonometry. The angle can then be converted into the sample's internal emission angle using Snell's Law. A CCD camera can be placed at the end of the spectrometer and its x and y pixel axis calibrated to height at the slit and wavelength emitting from the grating. In the case of this experiment, the calibration was done using a HeNe laser with adjustable height. In this experiment, several images from the CCD camera were taken and spliced together to create Fig. 11.4 (Meyer & Alfano, 2020).

The image in Fig. 11.4 can be converted into a dataset allowing for calculation of the internal sample angle using lens trigonometry and Snell's law. This image when plotted gives Fig. 11.5, which shows the angle of the emitted anti-Stokes

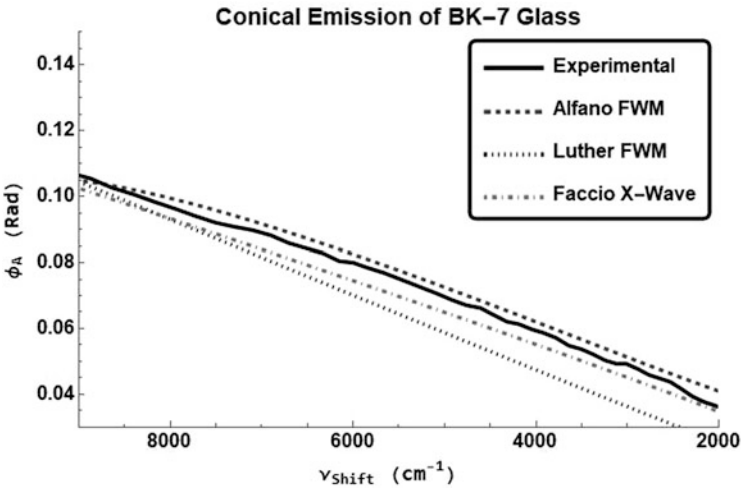

Fig. 11.5 Anti-Stokes conical emission produced from BK-7 glass, in the anti-Stokes span of 2000 to 9000 cm^{-1}

light compared to the three models discussed earlier in the energy change span of 2000 cm^{-1} to 9000 cm^{-1} from at 50 fs 800 nm source beam in BK-7 glass (Meyer & Alfano, 2020).

This image shows the angular spectrum of the emitted anti-Stokes light covering a span of +2000 to +9000 cm^{-1}. This span is approaching $\omega_A \rightarrow 2\omega_L$, which is the limit of the Alfano-Shapiro model as the reciprocal Stokes signal would be quickly approaching zero $\omega_S \rightarrow 0$. Omitted from this figure is the sub 2000 cm^{-1} range that covers the degenerate state and near-degenerate emission. The light in the spectral region is emitted at smaller angles and becomes obscured by the much stronger colinear signals, so it is rarely investigated.

11.3.2 Degenerate Emission

To measure CE emitted in the region at or near the degeneracy state, the system in Fig. 11.3 can be adapted by adding a small wire in front of the entrance focal distance (f) away from the collection lens. If the wire is sufficiently small, any angular emission should be able to go around it, while collinear signals such as supercontinuum and the remainder of the source laser are blocked. A diagram showing how this works can be seen in Fig. 11.6.

With the addition of the wire, all colinear signals are visibly absent from the spectrometer's output spectrum. Repeating the technique that gave Fig. 11.4 now gives Fig. 11.7.

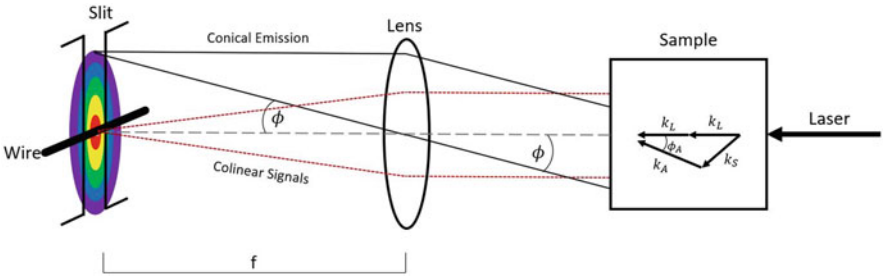

Fig. 11.6 A diagram showing how the degenerate conical emission can be measured using a wire and the same lens trigonometry discussed in the previous section. The wire blocks out any of the colinear light traveling along the dashes line while allowing CE at angle ϕ to travel around it. This figure is also relevant for measuring non-degenerate emission

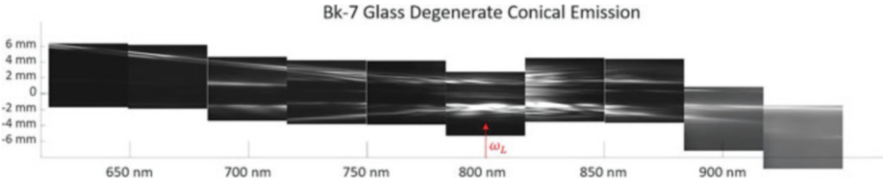

Fig. 11.7 Image of the angular growth of CE from Bk-7 glass before correcting for internal angle. In the span of $+3000$ to -2000 cm^{-1}. (Note that the wire is visibly blocking collinear signals, compared to Fig. 11.4)

Noticeably, in Fig. 11.7, the CE signal is nonzero at the source wavelength of 800 nm. The addition of the wire also makes it possible to view the Stokes emission produced in the range of the CCD camera. Plotting this figure after adjusting for internal angle gives Fig. 11.8.

The produced degenerate emission is nonzero and fits well with the value predicted by the Alfano-Shapiro model. As noted in Eq. 11.5, the degenerate angle is directly tied to the nonlinear index of refraction (n_2) of a material and its response time. This observation also implies that a term resembling Eq. 11.5 could be used to adapt the other models discussed to better fit in this region.

11.4 Concluding Remarks

In practice today, the X-wave model is the most commonly used. It has been shown to make accurate predictions of conical emission in air and fused silica (Maioli et al., 2009; Gong et al., 2016), allowing for it to become an important part of CE-derived technology such as optical parametric amplification (Li et al., 2019). However, omitted from its original derivation is the behavior of CE in the degenerate in near-degenerate spectral region. In this range, the nonlinear index has a pronounced

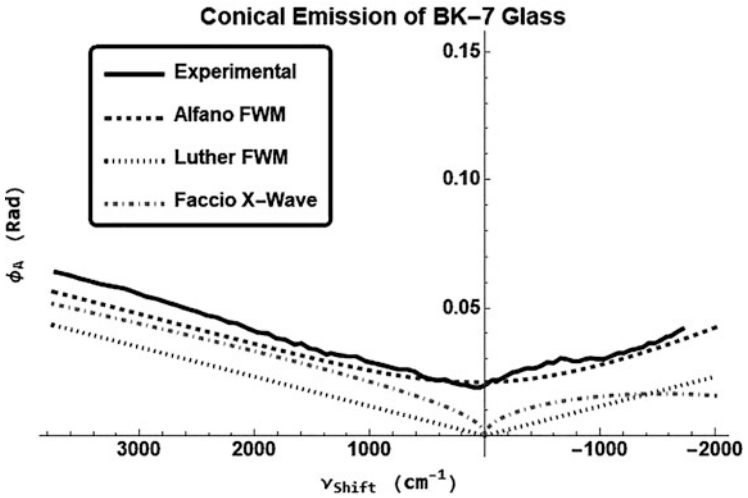

Fig. 11.8 Degenerate and near-degenerate CE produced from BK-7 glass in the Stokes and anti-Stokes span of $+3000$ to $-2000\ \mathrm{cm}^{-1}$

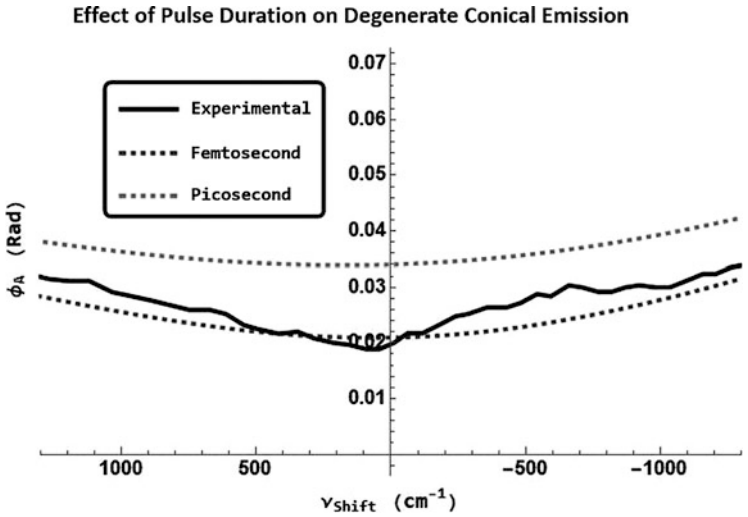

Fig. 11.9 Difference of the predicted degenerate CE when using the $3.18 \times 10^{-20}\mathrm{m}^2/\mathrm{W}$ nonlinear index of a femtosecond laser (Lu et al., 2012) and the $8.3 \times 10^{-20}\ \mathrm{m}^2/\mathrm{W}$ of a picosecond laser (Alfano & Shapiro, 1970)

contribution to the phase matching process of CE. This means that degenerate CE can provide new useful information about a materials expression of the nonlinear index. For example, effect of transience in the nonlinear index can be easily seen in Fig. 11.9.

Figure 11.9 shows how the predictions of degenerate emission by the Alfano model change depending on the transience of the nonlinear index. The nonlinear index of picosecond pulses in BK-7 of $8.3 \times 10^{-20} m^2/W$ used in the original 1970 paper (Alfano & Shapiro, 1970) missed the observed angle from a 50 fs laser by approximately 70%, while the 33 fs femtosecond nonlinear index of $3.18 \times 10^{-20} m^2/W$ calculated and measured by X. Lu et al. (2012) was accurate within less than 5%. This is because the pulse of a 50 fs femtosecond laser is significantly shorter than the relaxation times of many other components of the nonlinear index leaving only the ultrafast electronic response (Ho & Alfano, 1979). This means the n_2 of a BK-7 glass interacting with a femtosecond pulse is much smaller than when interacting with a picosecond pulse.

The relationship of degenerate conical emission angle and the accuracy of the described data suggest that this method of measuring degenerate CE could be used as a new means of measuring the nonlinear index of a material and cataloging n_2's transient responses. Degenerate conical emission could prove to be a useful tool in the field of nonlinear optics, working in conjunction with Z-scanning and other n_2 measuring tools.

References

Alfano, R. R. (1972). *Interaction of picosecond laser pulses with matter*. GTE Laboratories Inc (Technical Report 72–230.1 (1972); and NYU PhD thesis (1972), pp. 79–103).

Alfano, R. R., & Shapiro, S. L. (1970). Emission in the region 4000 to 7000 A via four-photon coupling in glass. *Physical Review Letters, 24*, 584.

Brewer, R. G., & Lee, C. H. (1968). Self-trapping with picosecond light pulses. *Physical Review Letters, 21*, 267.

Chiao, R. Y., & Kelley, P. L. (1966). Stimulated four-photon interaction and its influence on stimulated Rayleigh-wing scattering. *Physical Review Letters, 17*, 1158.

Faccio, D., Porras, M. A., Dubietis, A., Bragheri, F., Couairon, A., & Trapani, P. D. (2006). Conical emission, pulse splitting, and X-wave parametric amplification in nonlinear dynamics of ultrashort light pulses. *Physical Review Letters, 96*, 193901.

Faccio, D., Averchi, A., Couaron, A., Kolesik, M., Moloney, J. V., Dubietis, A., Tamosauskas, G., Polesana, P., Piskarskas, A., & Trapani, P. D. (2007). X wave generation by cross-phase-modulation induced spatio-temporal reshaping and amplification within optical filaments. *Optics Express, 15*, 13077.

Faccio, D., Averchi, A., Lotti, A., Trapani, P. D., Couairon, A., Papazoglou, D., & Tzortzakis, S. (2008). Ultrashort laser pulse filamentation from spontaneous X wave formation in air. *Optics Express, 16*, 1565.

Gong, C., Li, Z., Hua, L., Quan, W., & Liu, X. (2016). Angle-resolved conical emission spectra from filamentation in a solid with an Airy pattern and a Gaussian laser beam. *Optics Letters, 41*, 4305.

Hellwarth, R. W., Owyoung, A., & George, N. (1971). Origin of the nonlinear Refractive Index in Liquid CCL_4. *Physical Review A, 4*, 2342.

Ho, P. P., & Alfano, R. R. (1979). Optical Kerr effect in liquids. *Physical Review A, 20*, 2170.

Li, X., Wu, J., Xiong, S., Chen, M., Yan, H., Wang, Z., & Zhang, Y. (2019). Spatial and frequency multimode in the dressing parametric amplified multiwave mixing process. *Photonics Research, 7*, 1454.

Liou, L. W., Cao, X. D., McKinstrie, C. J., & Agrawal, G. P. (1992). Spatiotemporal instabilities in dispersive nonlinear media. *Physical Review A, 46*, 4202.

Lu, X., Liu, Q., Liu, Z., Sun, S., Ding, P., Ding, B., & Hu, B. (2012). Measurement of nonlinear refractive index coefficient using emission spectrum of filament induced by gigawatt-femtosecond pulse in BK7 glass. *Applied Optics, 51*, 2045.

Luther, G. G., Newell, A. C., Moloney, J. V., & Wright, E. M. (1994). Short-pulse conical emission and spectral broadening in normally dispersive media. *Optics Letters, 19*, 789.

Maioli, P., Salame, R., Lascoux, N., Salmon, E., Bejot, P., Kasparian, J., & Wolf, J. P. (2009). Ultraviolet-visible conical emission by multiple laser filaments. *Optics Express, 17*, 4726.

Meyer, H. J., & Alfano, R. R. (2020). Femtosecond anti-Stokes conical emission in BK-7 glass and O and E-wave calcite. *Optics Letters, 45*, 6222.

Shen, Y. R. (1964). *The principles of nonlinear optics*. Wiley.

Shen, Y. R., & Yang, G. (2016). Chapter 1- theory of self-phase modulation and spectral broadening. In *Supercontinuum laser source* (pp. 1–32). Springer edited by R. R. Alfano.

Shimoda, K. (1966a). Angular distribution of stimulated Raman radiation. *Japanese Journal of Applied Physics, 5*, 95.

Shimoda, K. (1966b). Gain, frequency shifts, and angular distribution of stimulated Raman radiations under multimode excitation. *Japanese Journal of Applied Physics, 5*, 615.

Silberberg, Y. (1990). Collapse of optical pulses. *Optics Letters, 15*, 1282.

Chapter 12
Supercontinuum in IR–MIR from Narrow Bandgap Bulk Solid-State Materials

Audrius Dubietis, Vytautas Jukna, and Arnaud Couairon

Abstract In this chapter, we present a brief summary on the state of the art of supercontinuum generation in wide-bandgap dielectric materials with near-infrared pumping and a more detailed overview of recent experimental developments along with representative examples of infrared supercontinuum generation employing narrow bandgap bulk solid-state materials: dielectric crystals, soft glasses, and semiconductors pumped by femtosecond pulses with carrier wavelengths located in the near- and mid-infrared.

Keywords Supercontinuum generation · Femtosecond filamentation · Nonlinear index of refraction · Pulse splitting · Pulse compression · Wide bandgap dielectrics · Narrow bandgap dielectrics · Soft glasses · Semiconductors · Polycrystalline materials · Zinc blende

12.1 Introduction

Since its discovery by Alfano and Shapiro in 1970 (Alfano & Shapiro, 1970a, 1970b), supercontinuum (SC) generation in bulk materials attracts a great deal of scientific and technological interest. The advent of ultrafast solid-state laser technology, which was initiated by the invention of the chirped pulse amplification (CPA) technique in 1985 (Strickland & Mourou, 1985) and the discovery of Kerr-lens mode locking a couple of years later (Spence et al., 1991), boosted an exciting experimental progress in SC generation. With femtosecond CPA Ti:sapphire lasers (Backus et al., 1998), SC generation in transparent dielectric materials became a robust, reliable, compact, and well-established technique for the generation of

A. Dubietis · V. Jukna
Laser Research Center, Vilnius University, Vilnius, Lithuania
e-mail: audrius.dubietis@ff.vu.lt; vytautas.jukna@ff.vu.lt

A. Couairon (✉)
CPHT, CNRS, Ecole Polytechnique, Institut Polytechnique de Paris, Palaiseau, France
e-mail: arnaud.couairon@polytechnique.edu

R. R. Alfano (ed.), *The Supercontinuum Laser Source*,
https://doi.org/10.1007/978-3-031-06197-4_12

spatially and temporally coherent and spectrally uniform broadband light sharing the distinctive properties of laser radiation. SC sources currently find numerous applications in diverse fields of modern ultrafast science.

Owing to simple experimental implementation, which guarantees stable and reproducible operation without optical degradation and damage of the nonlinear material, SC sources paved new ways in the development of a particular class of ultrafast laser sources, optical parametric amplifiers, which provide broad wavelength tunability by employing SC light as a broadband seed signal (Cerullo & De Silvestri, 2003). In that regard, SC generation became a backbone of few optical cycle technology, providing perfectly suited seed for noncollinear optical parametric amplification (Wilhelm et al., 1997), which affords extremely broad amplification bandwidths, and serves as a well-established technique for the generation of few optical cycle pulses, see, e.g., Brida et al. (2010). More recently, the average and peak powers of these pulses were boosted to unprecedented levels by the use of the optical parametric chirped pulse amplification (OPCPA) technique (Rigaud et al., 2016; Budriunas et al., 2017; Toth et al., 2020). On the other hand, SC generation-based extracavity compression allows generation of pulses with sub-TW peak power (He et al., 2017) and duration of a single optical cycle (Seo et al., 2020). Moreover, femtosecond SC sources serve as powerful tools in ultrafast electronic spectroscopy, performing pump and probe experiments with femtosecond time resolution, see, e.g., Aubock et al. (2012); Riedle et al. (2013).

In the meantime, the advent of Yb-doped laser systems (Fattahi et al., 2014) allowed the generation of femtosecond pulses at very high repetition rates, while subsequent frequency downconversion and pulse shaping techniques (Krogen et al., 2017), extracavity compression/self-compression in bulk materials (Hemmer et al., 2013; Shumakova et al., 2016), and more recent developments of ultrafast transition metal-doped chalcogenide lasers (Mirov et al., 2018) made high-power-femtosecond and few optical cycle pulses in the mid-infrared readily available. These developments in turn fostered the research on SC generation in this particular spectral range, which is of growing interest for spectroscopic studies in the molecular fingerprint region (Calabrese et al., 2012), experiments in strong field physics (Wolter et al., 2015), and attosecond science (Popmintchev et al., 2012), connected with further advancement of OPCPA technology (Voronin et al., 2016), and pulse compression techniques (Kurucz et al., 2020), potentially yielding extremely short pulses, with a duration approaching a single optical cycle and carrier wavelengths located in the far infrared.

However, the performance of standard, commonly used wide-bandgap dielectric materials in this spectral region is restricted first of all by their limited transmittance in the mid-infrared. In that regard, a broad class of solid-state materials: narrow bandgap dielectric crystals, soft glasses, and semiconductors, which possess considerably broader infrared transparency windows and much larger cubic nonlinearities, emerge as very promising and versatile nonlinear media for SC generation. Although these materials show just very modest spectral broadening or do not produce SC generation at all with visible and near-infrared pump wavelengths, they

have a great and yet not fully explored potential for ultrabroad SC generation with mid-infrared pumping.

12.2 Physics of Supercontinuum Generation

In simple terms, the optical properties of the material: energy bandgap, nonlinear index of refraction, chromatic dispersion, and laser wavelength are the relevant parameters, which define the basic features of the SC light, i.e., the extent of spectral broadening and attainable spectral blueshifts (Brodeur & Chin, 1998, 1999; Kolesik et al. 2003). However, the entire picture of SC generation in transparent dielectrics fully unveils in the framework of femtosecond filamentation (Couairon & Mysyrowicz, 2007), which explains spatial, temporal, and spectral features of the SC light in great detail.

Filamentation of femtosecond laser pulses in transparent materials with cubic nonlinearity is a very dynamic process that emerges from a complex interplay between nonlinear (self-focusing, self-phase modulation, multiphoton absorption, generation of a free electron plasma, and four-wave mixing) and linear (diffraction and dispersion processes), which take place simultaneously in space and time domains. Propagation features of a light filament (a narrow light beam that carries a broadband spectrum) such as the spatial localization of light could be well explained as a result of dynamic balance between self-focusing due to Kerr effect, diffraction, and defocusing due to free electron plasma created via multiphoton absorption and impact ionization. However, the temporal features of the pulse, which are responsible for large-scale spectral broadening, are more complex as they originate from space–time coupling and exhibit non-trivial dynamics.

In that regard, the sign of material group velocity dispersion (GVD) plays a central role in driving the temporal dynamics, suggesting two distinct temporal scenarios of SC generation. In a normally dispersive medium, the pulse spectrum gets broadened due to self-phase modulation that produces red (Stokes) and blue (anti-Stokes) shifts of the instantaneous frequency at the leading (ascending) and trailing (descending) fronts, respectively. At the same time, intensity continues increasing due to self-focusing of the beam, until the nonlinear absorption comes into play acting on the most intense part of the pulse and beam. The interplay between these nonlinear effects and chromatic dispersion, which tends to stretch the spectrally broadened pulse in time, results in pulse splitting at the nonlinear focus where intensity becomes the highest. As a result, two sub-pulses with redshifted (the leading pulse, which is faster) and blueshifted (the trailing pulse, which is slower) carrier frequencies are produced. These sub-pulses thereafter undergo independent self-steepening that arises from the velocity differences between their peaks and tails as a result of intensity-dependent refractive index. This induces sharp intensity gradients (optical shocks) in the temporal profiles of the sub-pulses, which facilitate explosive spectral broadening, i.e., SC generation (Gaeta, 2000, 2009). On the other hand, the scale of anti-Stokes spectral broadening is related to self-

steepening of the descending front of the trailing sub-pulse, which is defined by the phase matching condition derived from the effective three-wave mixing model that interprets generation of new frequency components as scattering of the incident optical field from material perturbation via the nonlinear polarization (Kolesik et al., 2003). In that way, small chromatic dispersion of the material allows fulfilment of the phase matching condition for a broader range of scattered spectral components, that is, supports a larger spectral broadening, while the opposite is true for materials with large chromatic dispersion. Note that the attainable redshifts of the SC spectra, which are associated with self-steepening of the ascending front of the trailing pulse, greatly depend on the pump focusing condition: longer filament that is produced at loose focusing of the pump beam favors enhanced, redshifted spectral broadening (Jukna et al., 2014).

A qualitatively different temporal scenario applies in a nonlinear material with anomalous GVD. Here the redshifted and blueshifted frequencies generated by self-phase modulation of the ascending (leading) and descending (trailing) fronts of the pulse, respectively, are pushed back to the peak of the pulse by material GVD, forcing the pulse to compress. In that way, the interplay between self-focusing, self-phase modulation, and anomalous GVD leads to a simultaneous compression in spatial and temporal dimensions and produces a robust self-compressed three-dimensional object, termed light bullet (Durand et al., 2013) that in turn favors production of ultrabroadband, multiple octave-spanning SC spectrum, see, e.g., Silva et al. (2012), Garejev et al. (2017), and Chekalin et al. (2019).

12.3 Wide-Bandgap Dielectrics

Wide-bandgap dielectrics serve as excellent and experimentally proven nonlinear materials for SC generation with pump wavelengths in the visible, near-, and mid-infrared (Dubietis et al. 2017; Dubietis & Couairon, 2019). In particular, ample experimental data are available for the near-infrared pump that is provided by amplified Ti:sapphire (around 800 nm) and Yb-doped lasers (around 1030 nm), where transparent materials possess normal GVD, so the pulse splitting-based SC generation scenario generally applies.

Figure 12.1 summarizes the experimental data representing the shortwave (blueshifted) SC cut-off wavelengths (defined at the $10^{-3} - 10^{-4}$ intensity level) reported using femtosecond fundamental harmonic pulses from Ti:sapphire lasers having a central wavelength of $\sim$ 800 nm for various solid-state dielectric materials: lithium fluoride (LiF) (Kohl et al., 2013), calcium fluoride (CaF_2), sapphire (Al_2O_3), yttrium aluminum garnet ($Y_3 3Al_5O_{12}$, YAG), potassium gadolinium tungstate ($KGd(WO_4)_2$, KGW), yttrium vanadate (YVO_4), and gadolinium vanadate ($GdVO_4$), all taken from Bradler et al. (2009), lithium strontium hexafluoroaluminate ($LiSrAlF_6$, LiSAF) (Suminiene et al., 2020), magnesium fluoride (MgF_2) (Tzankov et al., 2002), barium fluoride (BaF_2) (Dharmadhikari et al., 2014), fused silica (SiO_2) (Fang & Kobayashi, 2003), gadolinium orthosilicate

(Gd_2SiO_5, GSO), gallium gadolinium garnet ($Gd_3Ga_5O_{12}$, GGG), lithium tantalate ($LiTaO_3$, LTO), and lutetium vanadate ($LuVO_4$, LVO), all taken from Ryba et al. (2014), Macalik et al. (2018) and diamond (Kardas et al., 2013). Also data for popular dielectric crystals possessing second-order nonlinearity, potassium dihydrogen phosphate (KDP) (Srinivas et al., 2005), beta barium borate (BBO) (Suminas et al., 2017b), lithium niobate (LN) (Wang et al., 2013), and periodically poled lithium tantalate PPLT (Zhao et al., 2018), are presented. Figure 12.1a

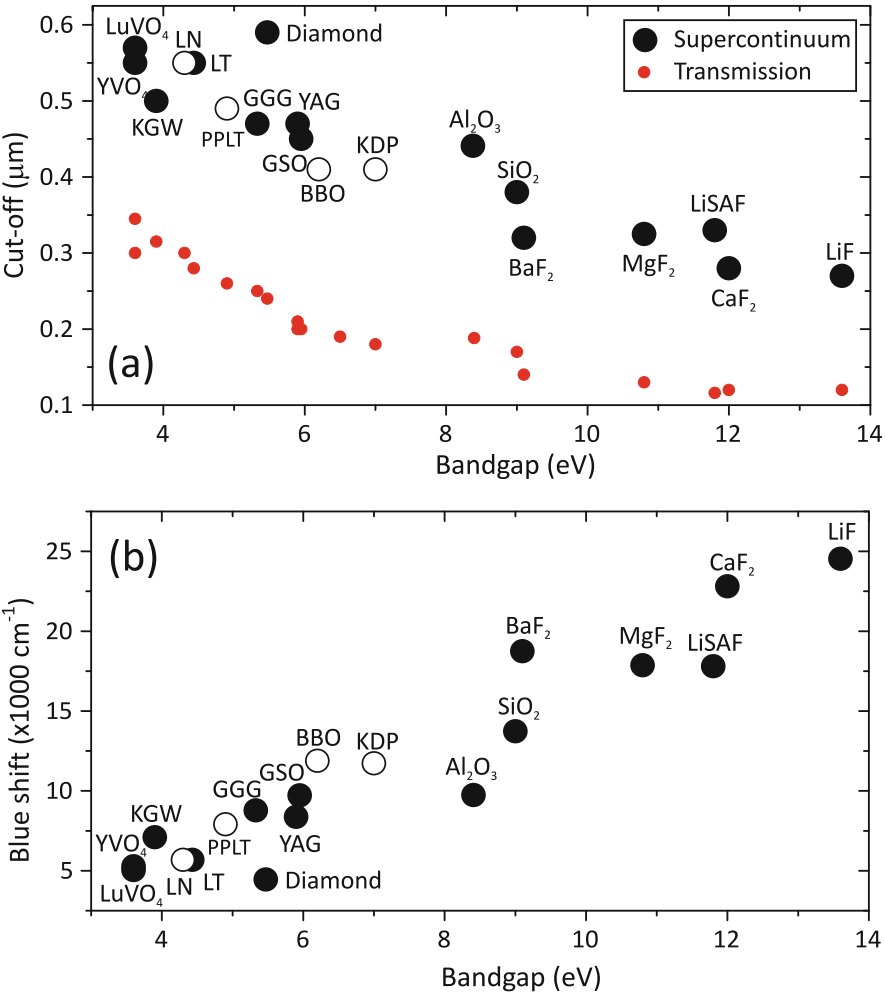

Fig. 12.1 (**a**) The bandgap dependence of the short-wavelength cut-off of supercontinuum spectra produced with a Ti:sapphire laser in various wide-bandgap solid-state materials. The red dots denote the shortwave absorption edge for a given material. Hollow circles stand for crystals possessing second-order nonlinearity. (**b**) The same dependence expressed in terms of the spectral blueshift

depicts the data in terms of cut-off wavelength, which is compared to the shortwave transparency edge of the material, while Fig. 12.1b illustrates the attained blueshifts in terms of wavenumbers.

The data presented in Fig. 12.1 nicely illustrates the universal trend of supercontinuum bandgap dependence, which suggests that the largest spectral broadening and the largest spectral blueshifts in particular are attained in dielectric materials with the largest energy bandgap (Brodeur & Chin, 1998). Note also how the trend of shortwave cut-off of SC spectrum follows the trend of shortwave absorption edge. Indeed, alkali metal fluorides, LiF, CaF_2, MgF_2, BaF_2, and LiSAF, whose transparency extends far into vacuum UV, produce SC spectra with cut-off wavelengths located in the UV. Alkali metal fluorides are also well suited for SC generation with shorter, visible, and UV pump wavelengths; however, these materials are prone to long-lived color center formation and heat accumulation and hence suffer from rapid optical degradation.

In contrast, materials with a moderate energy bandgap (< 8 eV) produce rather modest spectral blueshifts, with cut-off wavelengths in the visible part of the spectrum. Out of these, laser host crystals, sapphire and YAG, are recognized as most reliable nonlinear materials for SC generation in the visible and near-infrared spectral range (Bradler et al., 2009). Although the attainable spectral blueshifts in these materials are smaller than in alkali metal fluorides, spectral broadening is appreciable for many applications in ultrafast science. Moreover, sapphire and YAG exhibit durable performance even at very high pulse repetition rates (Grigutis et al., 2020). In particular, YAG crystal shows excellent performance with a variety of pump wavelengths, where SC generation mechanisms based on either pulse splitting (in the region of normal GVD) or pulse self-compression (in the region of anomalous GVD) take place. The SC spectra in a YAG crystal exhibit an almost constant cut-off wavelength (in the 470–490 nm range), regardless of the pumping wavelength, which converts into a dramatic increase of the spectral blueshift versus wavelength, as illustrated in Fig. 12.2. Here, the blueshift trend is compiled from the experimental data measured with pump wavelengths in the visible, at 515 nm (Bradler and Riedle, 2014), near-infrared: at, 775 nm, 1.3 μm and 1.6 μm (Bradler et al., 2009), 800 nm (Kudarauskas et al., 2018), 1035 nm (Grigutis et al., 2020) and mid-infrared: at 2.0 μm (Darginavicius et al., 2013), 2.15 μm (Fattahi et al., 2016), 2.3 μm (Garejev et al., 2017), and 3.1 μm (Silva et al., 2012).

12.4 Narrow-Bandgap Materials

The progress of femtosecond mid-infrared sources opens new perspectives in SC generation. First, mid-infrared wavelengths give an access to the region of anomalous GVD of wide-bandgap dielectric materials, where SC is produced via pulse self-compression, yielding simultaneous generation of ultrabroadband spectra and few optical cycle pulses. Second, a long carrier wavelength corresponds to a low photon energy, extending the nomenclature of nonlinear materials that are suitable

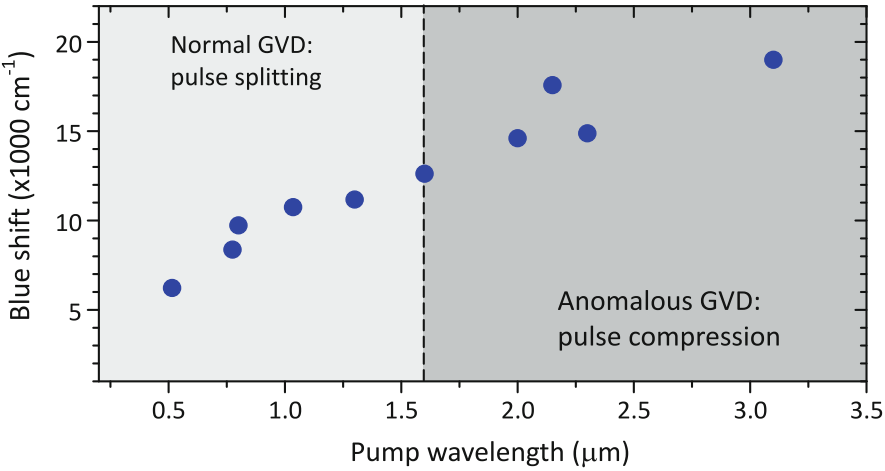

Fig. 12.2 Supercontinuum spectral blueshifts in a YAG crystal measured with various pump wavelengths that fall into regions of normal and anomalous GVD of the material. A zero GVD of the crystal at 1.6 μm is marked by a vertical dashed line

to achieve a considerable spectral broadening. In that regard, a variety of infrared bulk materials, dielectric crystals with narrow energy bandgap, soft glasses, and semiconductors, emerge as very attractive nonlinear media for SC generation. These materials exhibit considerably wider infrared transparency windows and large to huge cubic nonlinearities as compared to wide-bandgap dielectrics, as illustrated in Fig. 12.3, which in turn imply remarkably low threshold energies for beam filamentation and SC generation.

12.4.1 Soft Glasses

Non-silica glasses currently receive increasing attention as very promising nonlinear media for SC generation, especially aiming at spectral broadening in the mid-infrared spectral range. Spectral broadening from the visible up to 6 μm was reported in tellurite glass using femtosecond pump pulses with a central wavelength of 1.6 μm (Liao et al., 2013). Similar spectral broadening along with pulse compression was reported with pump pulses at 2.05 μm (Bejot et al., 2016). More recently, supercontinuum generation in tellurite glass was reported with picosecond laser pulses at 1.064 μm (Zheng et al., 2021). Recent results on spectral broadening in undoped and Pr-doped barium zinc borate oxyfluoride and bismuth zinc borate glasses, whose energy bandgaps vary in the 3.42–5.69 eV range, suggest that these materials are potentially interesting for SC generation (Neethish et al., 2021).

Due to broad transparency windows extending above 10 μm, a broad family of chalcogenide glasses holds a great potential for SC generation in the mid-infrared

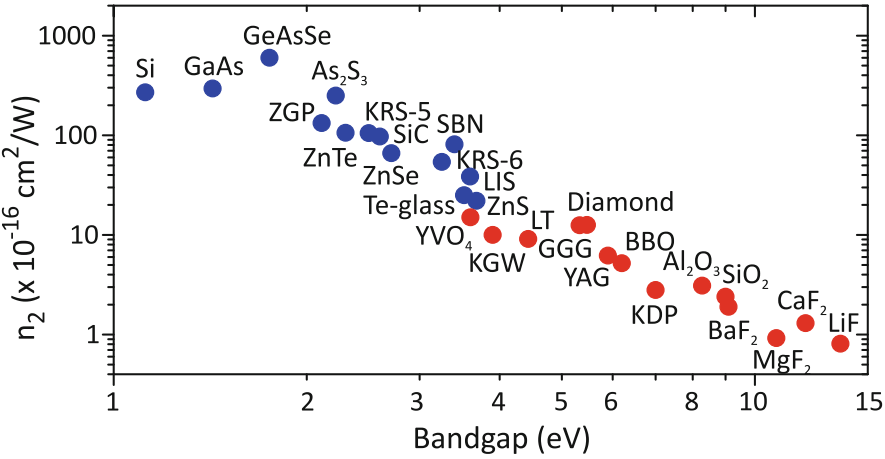

Fig. 12.3 Nonlinear index of refraction, n_2, versus the energy bandgap for various solid-state materials. Red dots denote the nonlinear index of refraction for wide-bandgap dielectrics at 800 nm, and blue dots show the nonlinear index of refraction for narrow bandgap materials in the wavelength range of 2–4 μm

spectral range. Notably, the linear and nonlinear refractive indexes, as well as resistance to optical damage of chalcogenide glasses, could be varied in broad confines by varying glass composition and exchanging the elemental materials (Wang et al., 2014). The potential of SC generation using femtosecond mid-infrared pulses in bulk chalcogenide glasses was first demonstrated almost a decade ago, reporting on spectral broadening in the 2.5–7.5 μm range using pump pulses with a central wavelength of 5.3 μm (Yu et al., 2013). SC spectra with remarkable mid-infrared coverage from 2.5 to ~11 μm were generated in As_2S_3 and GeS_3 samples with a pump wavelength of 4.8 μm nearly matching the zero GVD wavelengths of these materials (Mouawad et al., 2015), see Fig. 12.4. Very similar, flat and broadband infrared SC spectra were also reported in commercially available chalcogenide glass samples of various composition, using 3.75–5.0 μm tunable femtosecond pump pulses (Stingel et al., 2017). A more recent study demonstrated that a change of the composition of chalcogenide glasses by introducing more polarizable elements (Se instead of S and Te instead of S and Se) favorably modifies their optical properties by increasing nonlinearity, extending the transmission window into far infrared, and shifting the corresponding zero dispersion wavelengths farther into the infrared region (Mouawad et al., 2018). Using 65 fs pump pulses with a carrier wavelength of 4.5 μm, more than 2 octave-spanning SC spectra from 2.6 to 11 μm and 12 μm were generated in GeSSe and GeSe samples, respectively, effectively extending the transmission of these materials up to the far infrared region. Even broader SC spectra with remarkable broadening into the far infrared (up to 16 μm) were produced in TGG sample, using pump pulses with a carrier wavelength of 7.3 μm.

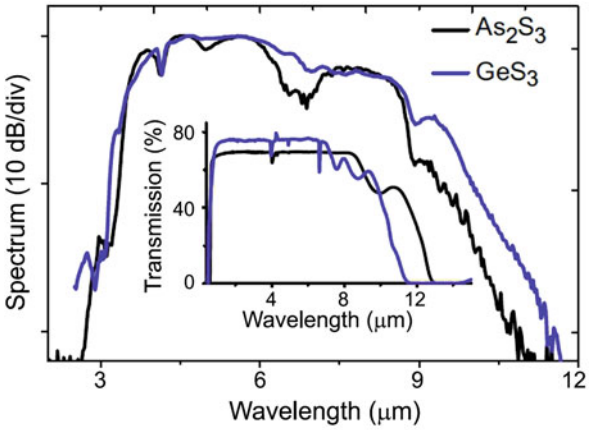

Fig. 12.4 Supercontinuum spectra produced by filamentation of 65 fs, 4.8 μm pulses in 3.3-mm-long samples of As_2S_3 and GeS_3. The inset shows measured spectral transmission of the samples. Reprinted from Mouawad et al. (2015) by permission from Springer Nature

12.4.2 Narrow Bandgap Dielectric Crystals

Narrow bandgap dielectric crystals with cubic symmetry, thallium bromoiodide (KRS-5) and thallium chlorobromide (KRS-6), possess an attractive combination of high nonlinearity and wide-infrared transparency range, which extends from the visible well into the far infrared, making these materials very attractive alternatives to soft glasses for SC generation in the mid-infrared spectral range. Almost two octave-wide supercontinuum spectra spanning wavelength range from 1.5 μm to more than 5.5 μm were produced in KRS-5 and KRS-6 samples of 6-mm thickness by filamentation of 60 fs pulses with central wavelengths of 3.1 μm and 3.6 μm (Marcinkeviciute et al., 2018). Long-term measurements revealed that KRS-5 is more resistant to optical degradation than KRS-6, showing excellent reproducibility of the SC spectrum for at least 2 hours at 1 kHz repetition rate. As the zero GVD wavelength of KRS-5 is at 6.6 μm, much larger SC spectral bandwidths are expected from filamentation of long-wavelength infrared pulses, whose wavelengths fall into the range of anomalous GVD of the crystal. To this end, more than three-octave supercontinuum spanning from 2 to 16 μm was generated by pumping KRS-5 crystal with two optical cycle (68 fs) pulses at 9.7 μm, produced by the technique of intrapulse difference frequency generation (Liu et al., 2019), see Fig. 12.5. More recently, SC spectra with very similar bandwidths were produced in a 5-mm-long KRS-5 sample with pulses from a LGS crystal-based OPCPA system, having a central wavelength of 9 μm, and yielding also more than three-fold self-compression of the pump pulses from 145 to 45 fs (Qu et al., 2020).

Generation of more than octave-spanning SC spectra was reported in unpoled polycrystalline strontium barium niobate ($Sr_{0.61}Ba_{0.39}Nb_2O_6$, SBN), which con-

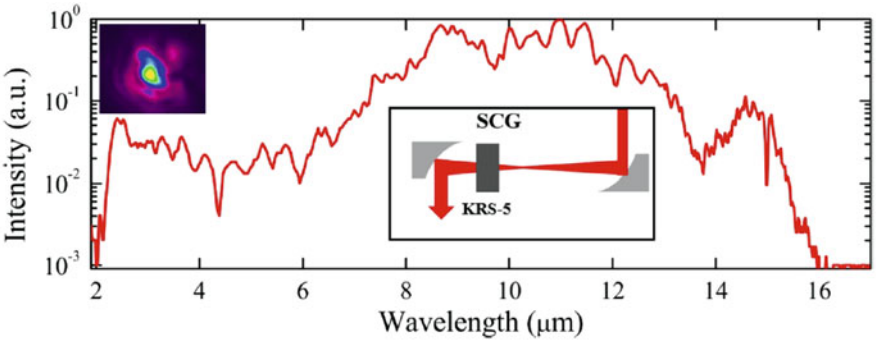

Fig. 12.5 The SC spectrum produced in KRS-5 crystal by filamentation of 2.4 μJ, 68 fs, 9.7 μm pulses. The insets show the corresponding SC beam profile and the setup of SC generation, respectively. Reprinted from Liu et al. (2019) by permission from the Optical Society of America

sists of birefringent needle-like randomly distributed ferroelectric domains, whose widths vary between a few nanometers and a few micrometers and whose lengths are of a few hundreds of micrometers, and has an energy bandgap of 3.4 eV. The SC spectrum in the wavelength range of 1.0–3.32 μm was produced with sub-100 nJ pump pulses having a central wavelength of 2.4 μm (Suminas et al., 2020). Simultaneously with SC generation, polycrystalline SBN emits planar second harmonic with an octave-spanning bandwidth due to non-zero second-order nonlinearity and random quasi-phase matching. However, spectral broadening in SBN to longer wavelengths is restricted by its infrared absorption edge at 5.5 μm.

12.4.3 Semiconductor Crystals

The feasibility of semiconductor materials for SC generation with picosecond laser pulses in the mid-infrared spectral region was first considered in the mid-90s, where spectral broadening of picosecond CO_2 laser pulses at 9.3 μm in gallium arsenide (GaAs), zinc selenide (ZnSe), and cadmium sulfide (CdS) crystals was experimentally demonstrated (Corkum et al., 1985). In the era of femtosecond solid-state lasers, the spectral broadening of 100 fs pulses having a central wavelength of 5 μm in the 3.5–7 μm range was demonstrated in GaAs crystal (Ashihara & Kawahara, 2009). Spectral broadening of a similar scale, in the 4–9 μm wavelength range, was reported with 4.2–6.8 μm tunable pulses, also demonstrating post-compression of spectrally broadened pulses at 6 μm down to sub-two optical cycle duration (Lanin et al., 2014). Further studies on SC generation in this particular material using pump wavelengths that fall into its anomalous GVD region (the zero GVD wavelength of GaAs is at 6 μm) reported impressive spectral broadening into the far infrared. The SC spectrum spanning the 2–20 μm range was produced in 67-mm-long GaAs slab using 2.5 ps, 9.3 μm pump pulses from a CO_2 laser (Pigeon

et al., 2014). The SC spectrum in the $3 - 18$ μm range was reported in a 5-mm-long GaAs plate pumped by femtosecond laser pulses with a central wavelength of 7.9 μm (Lanin et al., 2015). A simultaneous pulse self-compression from 150 fs to 45 fs, corresponding to only 1.2 cycles of the field at 7.9 μm, was measured (Lanin et al., 2015).

Since GaAs possesses second-order nonlinearity, in these experiments the crystal orientation and pump beam polarization were intentionally chosen to suppress the generation of second harmonic. In contrast, several other experiments make use of Kerr-like nonlinearities arising from second-order cascading due to phase-mismatched second harmonic generation. SC spectra covering the 1.6–7.0 μm wavelength range and exceeding two octaves were measured in lithium thioindate crystal ($LiInS_2$, LIS) using 85 fs pump pulses with a central wavelength of 3.86 μm that is slightly above the zero GVD point (3.5 μm) of the crystal and making use of cascading-induced self-defocusing (Zhou & Bache, 2016). A similar approach was exploited in chalcopyrite ($ZnGeP_2$, ZGP) crystal, where 2.6–8.8 μm spanning SC spectrum featuring a broad second harmonic peak was generated by pumping 2-mm-long crystal with 140-fs pulses having a central wavelength of 4.1 μm (Seidel et al., 2018).

Low-threshold SC generation was recently reported in crystalline silicon (Si). Octave-spanning infrared SC spectra were produced by filamentation of femtosecond mid-infrared pulses with carrier wavelengths in the range of 3.25–4.7 μm in an undoped 6.4-mm-thick silicon sample (Marcinkeviciute et al., 2019). More specifically, the broadest SC spectrum extending from 2.5 to 5.8 μm was recorded with 106 fs, 4.7 μm pump pulses undergoing filamentation and a SC generation threshold as low as 110 nJ was measured. Moreover, the recorded spatiotemporal intensity distributions of SC-producing filaments clearly demonstrated pulse splitting after the nonlinear focus, thereby confirming the universality of the SC generation scenario based on pulse splitting in normally dispersive nonlinear media. Finally, the results also confirmed the general assumption that propagation of very short, femtosecond pulses in silicon is much less affected by the presence of free carriers.

As compared to silicon, silicon carbide (SiC) has a larger energy bandgap (2.6 eV), hence the reduced nonlinear absorption in the near and mid-infrared. More recently, smooth, more than octave-spanning supercontinuum spectra with fairly stable short-wavelength cut-offs around 0.9 μm were produced in a 5-mm-thick 6H-SiC sample with 1.2–2.4 μm tunable femtosecond pulses (Suminiene et al., 2021). Figure 12.6a shows the SC spectra generated by filamentation of pulses with central wavelengths of 1.7, 2.0, and 2.4 μm, which fall into the regions of normal, near zero, and anomalous GVD of the crystal, respectively. Figure 12.6b shows the dynamics of spectral broadening versus the pump pulse energy recorded with pump pulses at 2.4 μm in more detail. In particular, an explosive spectral broadening at 150 nJ marks the threshold energy for SC generation, while a second burst of spectral broadening at 225 nJ indicates the refocusing of the filament, which is accompanied by well-pronounced spectral modulation. Below the SC generation threshold, a faint but clearly distinguishable signal with a center wavelength of 1.2 μm is attributed to

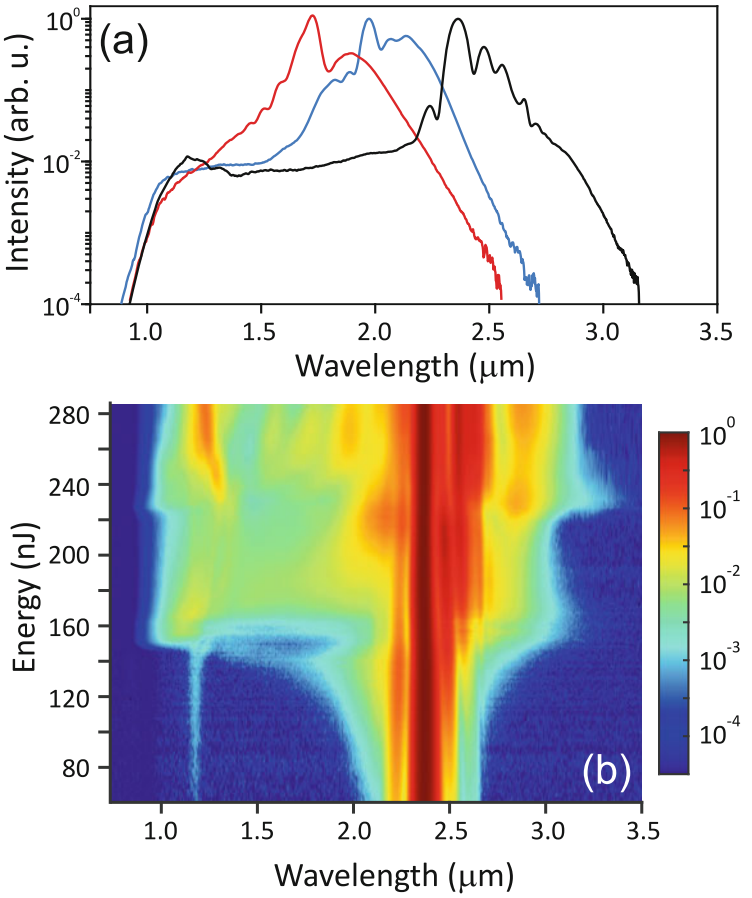

Fig. 12.6 (**a**) Supercontinuum spectra produced by filamentation of 90 fs pulses with central wavelengths of 1.7 μm (red), 2.0 μm (blue), and 2.4 μm (black) in a 5-mm-long 6H-SiC sample. (**b**) Spectral dynamics versus the pump pulse energy measured with pump pulses at 2.4 μm. Reprinted from Suminiene et al. (2021) by permission from the Optical Society of America

phase-mismatched second harmonic generation, due to non-vanishing second-order nonlinearity of the crystal.

12.4.4 Zinc-Blende Semiconductors

A particularly interesting case of SC generation in narrow bandgap materials refers to filamentation in zinc-blende semiconductors, such as zinc sulfide (ZnS) and zinc selenide (ZnSe), which are transparent from the visible to the far infrared and exhibit large cubic nonlinearities and relatively high optical damage thresholds. The

first experiments reported on ultrabroadband, multioctave, visible to mid-infrared-spanning SC spectra in ZnS (Liang et al., 2015) and ZnSe (Mouawad et al., 2016) crystals using few optical cycle pump pulses with carrier wavelengths of 2.1 and 5 μm, respectively.

However, the most intriguing features concerning nonlinear frequency conversion in these materials arise from the combination of their polycrystalline structure and large second-order nonlinearities owing to $\bar{4}3m$ symmetry. Random quasi-phase matching, stemming from the orientation disorder of tens-of-microns sized crystallites, enables efficient frequency conversion via simultaneous second-order nonlinear interactions (second harmonic, sum and difference frequency generation) within very wide spectral range, which is essentially limited only by the material transmittance window. The state of the art of modern growth technology allows for adjustment of the average sizes and size distributions of crystallites in a desired way to enhance frequency conversion of three-wave interactions (Chen & Gaume, 2019).

To this end, the generation of multiple even and odd harmonics was demonstrated to efficiently accompany spectral broadening and SC generation produced by filamentation of mid-infrared pulses in polycrystalline ZnSe (Archipovaite et al., 2017; Suminas et al., 2017a, 2019; Werner et al., 2019; Marble et al., 2019) and ZnS (Suminas et al., 2019) yielding remarkable spectral blueshifts that are limited only by the short-wavelength absorption edge of the crystals: 0.5 μm in ZnSe and 0.4 μm in ZnS. Figure 12.7 shows even and odd harmonics-enhanced SC spectra produced by filamentation of 3.6 μm, 60 fs pulses in polycrystalline ZnSe and ZnS samples. In shorter samples of 2-mm thickness (gray dashed curves), the overall spectrum is composed of a broadened spectrum around the carrier wavelength and multiple broadband peaks that correspond to the individual harmonics. With increased propagation length (longer samples, black solid curves), all the harmonics spectra merge into a broadband and almost spectrally uniform SC radiation, whose width corresponds to 3.3 optical octaves in ZnSe and 3.6 optical octaves in ZnS. An even larger number of harmonics was detected using longer wavelength pump pulses: even and odd harmonics up to the 10th order were measured in ZnS with pump pulses at 4.6 μm (Suminas et al., 2019) and up to the 12th order in ZnSe with pump pulses having a central wavelength of 7 μm (Marble et al., 2019). In contrast, only very modest spectral broadening with just few generated harmonics was observed in single ZnSe (Werner et al., 2019) and ZnTe (Suminas et al., 2019) crystals.

The high efficiency of broadband frequency conversion in polycrystalline zinc-blende materials, the effects of grain size, polarization and coherence properties as well as the pulse temporal structure were investigated using realistic numerical models (Kawamori et al., 2019; Gu et al., 2020, 2021). The numerical results provide a comprehensive understanding of the properties of the upconverted light, which is necessary for optimization of SC generation and pulse-compression setups that employ polycrystalline materials. Numerical simulations also predicted that light bullet formation via self-compression in filamentation regime down to a single optical cycle and even less due to favorable interplay between self-phase modulation and anomalous GVD and extreme self-steepening is feasible for pulses with central

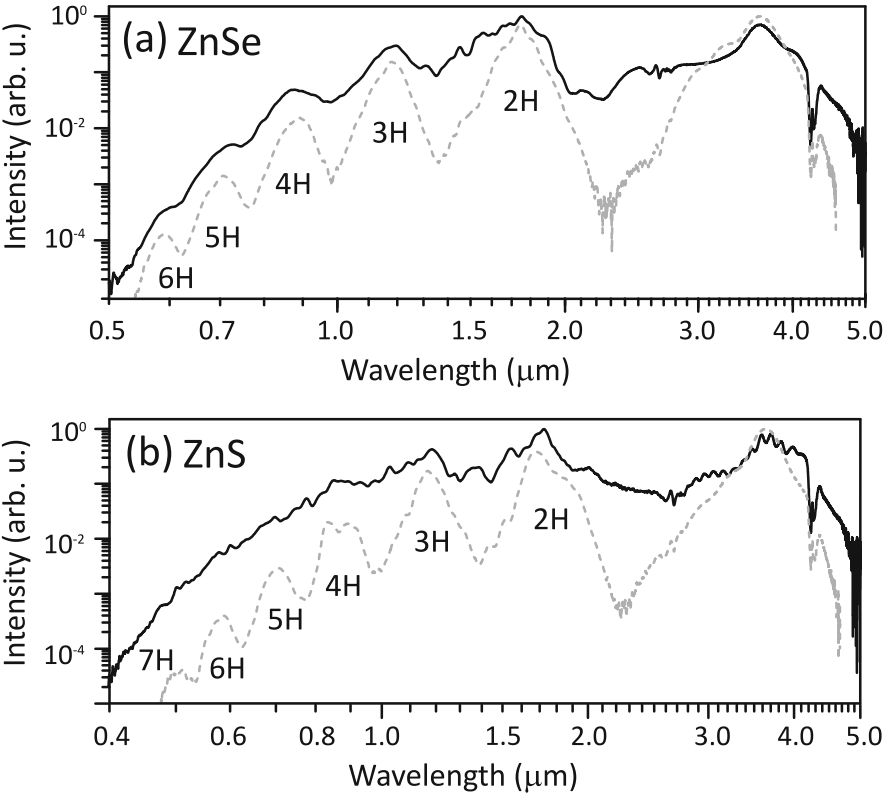

Fig. 12.7 Supercontinuum spectra in polycrystalline (**a**) ZnSe and (**b**) ZnS samples, produced by filamentation of 60 fs, 3.6 μm pulses with an energy of 0.73 μJ. Dashed curves depict the SC spectra in 2-mm-thick samples, while solid curves show SC spectra generated in 3-mm-thick ZnSe and 4-mm-thick ZnS samples, respectively. Reprinted from Suminas et al. (2019) by permission from the Optical Society of America

wavelengths in the ranges of 5–7 μm in ZnS (Li et al., 2017) and 6–10 μm in ZnSe (Grynko et al., 2018). These impressive self-compression factors are yet to be demonstrated in real experimental settings. To date, self-compression of 9 μm, 145 fs pulses down to 69 fs was experimentally achieved in ZnSe crystal (Qu et al., 2020).

Finally, polycrystalline gain elements (Cr:ZnS and Cr:ZnSe) usefully combine ultrafast laser capabilities with high nonlinearity and polycrystalline microstructure, yielding efficient nonlinear frequency conversion and spectral broadening directly in the ultrafast mid-infrared oscillators and amplifiers (Vasilyev et al., 2017). In that regard, a more recent study demonstrated efficient polycrystalline Cr:ZnS amplifier configured for simultaneous amplification, spectral broadening, generation of harmonics, and compression of few optical cycle pulses (Vasilyev et al., 2019).

12.5 Concluding Remarks

Figure 12.8 provides a graphical summary that illustrates the bandgap dependence of SC generation in narrow bandgap solid-state materials, showing less regular trend, which nevertheless preserves very similar character of dependence as wide-bandgap dielectrics, shown in Fig. 12.1. A much larger scattering of data points in the present case is in part due to scatter of pump wavelengths at which the

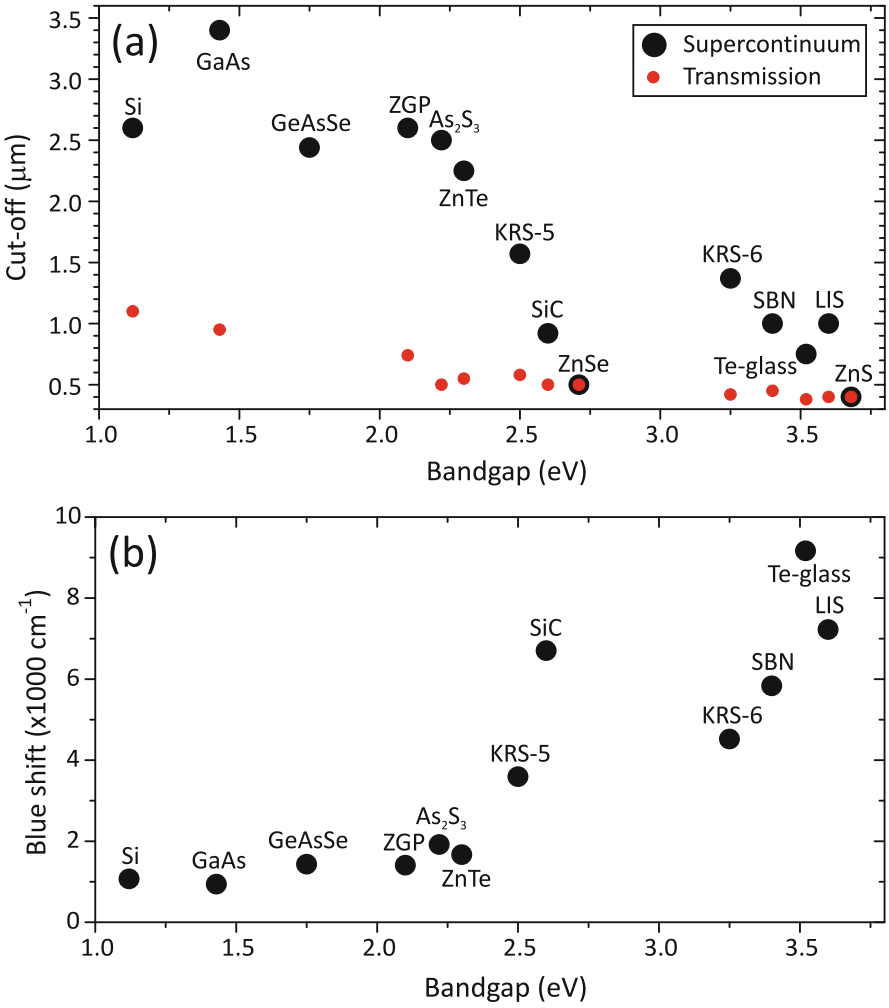

Fig. 12.8 (**a**) The bandgap dependence of supercontinuum short-wavelength cut-off in various narrow bandgap solid-state materials assuming pump wavelengths in the 2.4–5 μm range. The red dots denote the shortwave absorption edge for a given material. (**b**) The same dependence expressed in terms of the spectral blueshift

particular experiments were performed. More specifically, the SC spectra in Te-glass (Bejot et al., 2016), SBN (Suminas et al., 2020), and SiC (Suminiene et al., 2021) were produced using the pump wavelength of 2.4 μm, the measurements in KRS-5, KRS-6 (Marcinkeviciute et al., 2018), ZnS, ZnSe, ZnTe (Suminas et al., 2019), Si (Marcinkeviciute et al., 2019), and LIS (Zhou & Bache, 2016) were performed with the pump wavelength of 3.6 μm, while the SC spectra in the remaining materials, GeAsSe (Stingel et al., 2017), ZGP (Seidel et al., 2018), As_2S_3 (Mouawad et al., 2015), and GaAs (Ashihara & Kawahara, 2009) were measured with pump wavelengths of 3.75, 4.1, 4.8, and 5 μm, respectively. Note that polycrystalline ZnS and ZnSe are the exceptions, clearly falling out of this general trend, since these materials produce very broad even and odd harmonics-enhanced SC spectra due to random quasi-phase matching, whose short-wavelength cut-offs coincide with their transmission cut-off wavelengths, yielding huge spectral blueshifts ($>$ 22000 and $>$ 17000 cm^{-1}, respectively), which are outside the margins of Fig. 12.8b.

Summarizing the above results, narrow bandgap solid-state materials serve as efficient nonlinear media for the generation of more than octave-spanning SC spectra with near- and mid-IR driving wavelengths. Spectral broadening on the short-wavelength side in narrow bandgap solid-state materials follows the general trend of bandgap dependence, and the SC spectra produced in these materials are entirely confined to infrared wavelengths, showing remarkable redshifted spectral broadenings reaching the far infrared. Moreover, these materials possess very large values of nonlinear refractive indexes that in turn impose very low filamentation and SC generation thresholds with mid-IR driving wavelengths despite λ^2 scaling of the critical power for self-focusing.

References

Alfano, R. R., & Shapiro, L. (1970a). Emission in the region 4000 to 7000 Å via four photon coupling in glass. *Physical Review Letters, 24*, 584–587.

Alfano, R. R., & Shapiro, L. (1970b). Observation of self-phase modulation and small-scale filaments in crystals and glasses. *Physical Review Letters, 24*, 592–594.

Archipovaite, G. M., Petit, S., Delagnes, J.-C., & Cormier, E. (2017). 100 kHz Yb-fiber laser pumped 3 μm optical parametric amplifier for probing solid-state systems in the strong field regime. *Optics Letters, 42*, 891–894.

Ashihara, S., & Kawahara, Y. (2009). Spectral broadening of mid-infrared femtosecond pulses in GaAs. *Optics Letters, 34*, 3839–3841

Auböck, G., Consani, C., Monni, R., Cannizzo, A., Van Mourik, F., & Chergui, M. (2012). Femtosecond pump/supercontinuum probe setup with 20 kHz repetition rate. *Review of Scientific Instruments, 83*, 093105.

Backus, S., Durfee, C. G., Murnane, M. M., & Kapteyn, H. C. (1998). High power ultrafast lasers. *Review of Scientific Instruments, 69*, 1207–1223.

Béjot, P., Billard, F., Peureux, C., Diard, T., Picot-Clémente, J., Strutynski, C., Mathey, P., Mouawad, O., Faucher, O., Nagasaka, K., Ohishi, Y., & Smektala, F. (2016). Filamentation-induced spectral broadening and pulse shortening of infrared pulses in Tellurite glass. *Optics Communications, 380*, 245–249.

Bradler, M., Baum, P., & Riedle, E. (2009). Femtosecond continuum generation in bulk laser host materials with sub-μJ pump pulses. *Applied Physics B, 97*, 561–574.

Bradler M., & Riedle, E. (2014). Sub-20 fs μJ-energy pulses tunable down to the near-UV from a 1 MHz Yb-fiber laser system. *Optics Letters, 39*, 2588–2591.

Brida, D., Manzoni, C., Cirmi, G., Marangoni, M., Bonora, S., Villoresi, P., De Silvestri, S., & Cerullo, G. (2010). Few-optical-cycle pulses tunable from the visible to the mid-infrared by optical parametric amplifiers. *Journal of Optics, 12*, 013001.

Brodeur, A., & Chin, S. L. (1998). Band-gap dependence of the ultrafast white-light continuum. *Physical Review Letters, 80*, 4406–4409.

Brodeur, A., & Chin, S. L. (1999). Ultrafast white-light continuum generation and self-focusing in transparent condensed media. *Journal of the Optical Society of America B, 16*, 637–650.

Budriūnas, R., Stanislauskas, T., Adamonis, J., Aleknavičius, A., Veitas, G., Gadonas, D., Balickas, S., Michailovas, A., & Varanavičius, A. (2017). 53 W average power CEP-stabilized OPCPA system delivering 5.5 TW few cycle pulses at 1 kHz repetition rate. *Optics Express, 25*, 5797–5806.

Calabrese, C., Stingel, A. M., Shen, L., & Petersen, P. B. (2012). Ultrafast continuum mid-infrared spectroscopy: Probing the entire vibrational spectrum in a single laser shot with femtosecond time resolution. *Optics Letters, 37*, 2265–2267.

Cerullo, G., & De Silvestri, S. (2003). Ultrafast optical parametric amplifiers. *Review of Scientific Instruments, 74*, 1–18.

Chekalin, S. V., Dormidonov, A. E., Kompanets, V. O., Zaloznaya, E. D., & Kandidov, V. P. (2019). Light bullet supercontinuum. *Journal of the Optical Society of America B, 36*, A43–A53.

Chen X., & Gaume, R. (2019). Non-stoichiometric grain-growth in ZnSe ceramics for $\chi^{(2)}$ interaction. *Optical Materials Express, 9*, 400–409.

Corkum, P. B., Ho, P. P., Alfano, R. R., & Manassah, J. T. (1985). Generation of infrared supercontinuum covering 3–14 μm in dielectrics and semiconductors. *Optics Letters, 10*, 624–626.

Couairon, A., & Mysyrowicz, A. (2007). Femtosecond filamentation in transparent media. *Physics Reports, 441*, 47–190.

Darginavičius, J., Majus, D., Jukna, V., Garejev, N., Valiulis, G., Couairon, A., & Dubietis, A. (2013). Ultrabroadband supercontinuum and third-harmonic generation in bulk solids with two optical-cycle carrier-envelope phase-stable pulses at 2 μm. *Optics Express, 21*, 25210–25220.

Dharmadhikari, J. A., Deshpande, R. A., Nath, A., Dota, K., Mathur, D., & Dharmadhikari, A. K. (2014). Effect of group velocity dispersion on supercontinuum generation and filamentation in transparent solids. *Applied Physics B, 117*, 471–479.

Dubietis, A., Tamošauskas, G., Šuminas, R., Jukna, V., & Couairon, A. (2017). Ultrafast supercontinuum generation in bulk condensed media. *Lithuanian Journal of Physics, 57*, 113–157.

Dubietis A., & Couairon, A. (2019). *Ultrafast Supercontinuum Generation in Transparent Solid State Media*. Cham: Springer Nature.

Durand, M., Jarnac, A., Houard, A., Liu, Y., Grabielle, S., Forget, N., Durécu, A., Couairon, A., & Mysyrowicz, A. (2013). Self-guided propagation of ultrashort laser pulses in the anomalous dispersion region of transparent solids: a new regime of filamentation. *Physical Review Letters, 110*, 115003.

Fang, X.-J., & Kobayashi, T. (2003). Evolution of a super-broadened spectrum in a filament generated by an ultrashort intense laser pulse in fused silica. *Applied Physics B, 77*, 167–170.

Fattahi, H., Barros, H. G., Gorjan, M., Nubbemeyer, T., Alsaif, B., Teisset, C. Y., Schultze, M., Prinz, S., Haefner, M., Ueffing, M., Alismail, A., Vámos, L., Schwarz, A., Pronin, O., Brons, J., Geng, X. T., Arisholm, G., Ciappina, M., Yakovlev, V. S., Kim, D.-E., Azzeer, A. M., Karpowicz, N., Sutter, D., Major, Z., Metzger, T., & Krausz, F. (2014). Third-generation femtosecond technology. *Optica, 1*, 45–63.

Fattahi, H., Wang, H., Alismail, A., Arisholm, G., Pervak, V., Azzeer, A. M., & Krausz, F. (2016). Near-PHz-bandwidth, phase-stable continua generated from a Yb:YAG thin-disk amplifier. *Optics Express, 24*, 24337–24346.

Gaeta, A. L. (2000). Catastrophic collapse of ultrashort pulses. *Physical Review Letters, 84*, 3582–3585.

Gaeta, A. L. (2009). Spatial and temporal dynamics of collapsing ultrashort laser pulses. *Topics in Applied Physics, 114*, 399–412.

Garejev, N., Tamošauskas, G., & Dubietis, A. (2017). Comparative study of multioctave supercontinuum generation in fused silica, YAG, and LiF in the range of anomalous group velocity dispersion. *Journal of the Optical Society of America, 34*, 88–94.

Grigutis, R., Tamošauskas, G., Jukna, V., Risos, A., & Dubietis, A. (2020). Supercontinuum generation and optical damage of sapphire and YAG at high repetition rates. *Optics Letters, 45*, 4507–4510.

Grynko, R. I., Nagar, G. C., & Shim, B. (2018). Wavelength-scaled laser filamentation in solids and plasma-assisted subcycle light-bullet generation in the long-wavelength infrared. *Physical Review A, 98*, 023844.

Gu, J., Hastings, M. G., & Kolesik, M. (2020). Simulation of harmonic and supercontinuum generation in polycrystalline media. *Journal of the Optical Society of America B, 37*, 1510–1517.

Gu, J., Schweinsberg, A., Vanderhoef, L., Tripepi, M., Valenzuela, A., Wolfe, C., Ensley, T.R., Chowdhury, E., & Kolesik, M. (2021). Random quasi-phase-matching in polycrystalline media and its effects on pulse coherence properties. *Optics Express, 29*, 7479–7493.

He, P., Liu, Y., Zhao, K., Teng, H., He, X., Huang, P., Huang, H., Zhong, S., Jiang, Y., Fang, S., Hou, X., & Wei, Z. (2017). High-efficiency supercontinuum generation in solid thin plates at 0.1 TW level. *Optics Letters, 42*, 474–477.

Hemmer, M., Baudisch, M., Thai, A., Couairon, A., & Biegert, J. (2013). Self-compression to sub-3-cycle duration of mid-infrared optical pulses in dielectrics. *Optics Express, 21*, 28095–28102.

Jukna, V., Galinis, J., Tamošauskas, G., Majus, D., & Dubietis, A. (2014). Infrared extension of femtosecond supercontinuum generated by filamentation in solid-state media. *Applied Physics B, 116*, 477–483.

Kardaś, T. M., Ratajska-Gadomska, B., Gadomski, W., Lapini, A., & Righini, R. (2013). The role of stimulated Raman scattering in supercontinuum generation in bulk diamond. *Optics Express, 21*, 24201–24209.

Kawamori, T., Ru, Q., & Vodopyanov, K. L. (2019). Comprehensive model for randomly phase-matched frequency conversion in zinc-blende polycrystals and experimental results for ZnSe. *Physical Review Applied, 11*, 054015.

Kohl-Landgraf, J., Nimsch, J.-E., & Wachtveitl, J. (2013). LiF, an underestimated supercontinuum source in femtosecond transient absorption spectroscopy. *Optics Express, 21*, 17060–17065.

Kolesik, M., Katona, G., Moloney, J. V., & Wright, E. M. (2003). Physical factors limiting the spectral extent and band gap dependence of supercontinuum generation. *Physical Review Letters, 91*, 043905.

Krogen, P., Suchowski, H., Liang, H., Flemens, N., Hong, K.-H., Kärtner, F. X., & Moses, J. (2017). Generation and multi-octave shaping of mid-infrared intense single-cycle pulses. *Nature Photonics, 11*, 222–226.

Kudarauskas, D., Tamošauskas, G., Vengris, M., & Dubietis, A. (2018). Filament-induced luminescence and supercontinuum generation in undoped, Yb-doped, and Nd-doped YAG crystals. *Applied Physics Letters, 112*, 041103.

Kurucz, M., Flender, R., Haizer, L., Nagymihaly, R. S., Cho, W., Kim, K. T., Toth, S., Cormier, E., & Kiss, B. (2020). 2.3-cycle mid-infrared pulses from hybrid thin-plate post-compression at 7 W average power. *Optics Communications, 472*, 126035.

Lanin, A. A., Voronin, A. A., Stepanov, E. A., Fedotov, A. B., & Zheltikov, A. M. (2014). Frequency tunable sub-two-cycle 60-MW-peak-power free space waveforms in the mid-infrared. *Optics Letters, 39*, 6430–6433.

Lanin, A. A., Voronin, A. A., Stepanov, E. A., Fedotov, A. B., Zheltikov, A. M. (2015). Multioctave, 3–18 μm sub-two-cycle supercontinua from self-compressing, self-focusing soliton transients in a solid. *Optics Letters, 40*, 974–977.

Li, W., Li, Y., Xu, Y., Guo, X., Lu, J., Wang, P., & Leng, Y. (2017). Design and simulation of a single-cycle source tunable from 2 to 10 micrometers. *Optics Express, 25*, 7101–7111.

Liang, H., Krogen, P., Grynko, R., Novak, O., Chang, C.-L., Stein, G. J., Weerawarne, D., Shim, B., Kärtner, F. X., & Hong, K.-H. (2015). Three-octave-spanning supercontinuum generation and sub two-cycle self-compression of mid-infrared filaments in dielectrics. *Optics Letters, 40*, 1069–1072.

Liao, M., Gao, W., Cheng, T., Duan, Z., Xue, X., Kawashima, H., Suzuki, T., & Ohishi, Y. (2013). Ultrabroad supercontinuum generation through filamentation in tellurite glass. *Laser Physics Letters, 10*, 036002.

Liu, K., Liang, H., Qu, S., Li, W., Zou, X., Zhang, Y., & Wang, Q. J. (2019). High-energy mid-infrared intrapulse difference-frequency generation with 5.3% conversion efficiency driven at 3 μm. *Optics Express, 27*, 37706–37713.

Macalik, B., Kowalski, R. M., & Ryba-Romanowski, W. (2018). Spectral features of the Stokes part of supercontinuum generated by femtosecond light pulses in selected oxide crystals: a comparative study. *Optical Materials, 78*, 396–401.

Marble, C. B., O'Connor, S. P., Nodurft, D. T., Wharmby, A. W., & Yakovlev, V. V. (2019). Eye safety implications of high harmonic generation in zinc selenide. *Optics Express, 27*, 2828–2836.

Marcinkevičiūtė, A., Tamošauskas, G., & Dubietis, A. (2018). Supercontinuum generation in mixed thallous halides KRS-5 and KRS-6. *Optical Materials, 78*, 339–344.

Marcinkevičiūtė, A., Jukna, V., Šuminas, R., Garejev, N., Tamošauskas, G., & Dubietis, A. (2019). Femtosecond filamentation and supercontinuum generation in bulk silicon. *Optics Letters, 44*, 1343–1346.

Mirov, S.B., Moskalev, I.S., Vasilyev, S., Smolski, V., Fedorov, V. V., Martyshkin, D., Peppers, J., Mirov, M., Dergachev, A., & Gapontsev, V. (2018). Frontiers of mid-IR lasers based on transition metal doped chalcogenides. *IEEE Journal of Selected Topics in Quantum Electronics, 24*, 1601829.

Mouawad, O., Béjot, P., Billard, F., Mathey, P., Kibler, B., Désévédavy, F., Gadret, G., Jules, J.-C., Faucher, O., & Smektala, F. (2015). Mid-infrared filamentation-induced supercontinuum in As-S and an As-free Ge-S counterpart chalcogenide glasses. *Applied Physics B, 121*, 433–438.

Mouawad, O., Béjot, P., Billard, F., Mathey, P., Kibler, B., Désévédavy, F., Gadret, G., Jules, J.-C., Faucher, O., & Smektala, F. (2016). Filament induced visible-to-mid-IR supercontinuum in a ZnSe crystal: toward multi-octave supercontinuum absorption spectroscopy. *Optical Materials, 60*, 355–358.

Mouawad, O., Béjot, P., Mathey, P., Froidevaux, P., Lemière, A., Billard, F., Kibler, B., Désévédavy, F., Gadret, G., Jules, J.-C., Faucher, O., & Smektala, F. (2018). Expanding up to far-infrared filamentation-induced supercontinuum spanning in chalcogenide glasses. *Applied Physics B, 124*, 182.

Neethish, M. M., Kumar, V. V. R. K., Nalam, S. A., Harsha, S. S., & Kiran, P. P. (2021). Supercontinuum generation from Zinc Borate glasses: Bandgap vs Rare-earth doping. *Optics Letters, 46*, 1201–1204.

Pigeon, J. J., Tochitsky, S. Ya., Gong, C., & Joshi, C. (2014). Supercontinuum generation from 2 to 20 μm in GaAs pumped by picosecond CO_2 laser pulses. *Optics Letters, 39*, 3246–3249.

Popmintchev, T., Chen, M.-C., Popmintchev, D., Arpin, P., Brown, S., Ališauskas, S., Andriukaitis, G., Balčiunas, T., Mücke, O. D., Pugžlys, A., Baltuška, A., Shim, B., Schrauth, S.E., Gaeta, A., Hernández-Garcia, C., Plaja, L., Becker, A., Jaron-Becker, A., Murnane, M. M., & Kapteyn, H. C. (2012). Bright coherent ultrahigh harmonics in the keV X-ray regime from mid-infrared femtosecond lasers. *Science, 336*, 1287–1291.

Qu, S., Nagar, G. C., Li, W., Liu, K., Zou, X., Luen, S. H., Dempsey, D., Hong, K.-H., Wang, Q. J., Zhang, Y., Shim, B., & Liang, H. (2020). Long-wavelength-infrared laser filamentation in solids in the near-single-cycle regime. *Optics Letters, 45*, 2175–2178.

Riedle, E., Bradler, M., Wenninger, M., Sailer, C. F., & Pugliesi, I. (2013). Electronic transient spectroscopy from the deep UV to the NIR: unambiguous disentanglement of complex processes. *Faraday Discussions, 163*, 139–158.

Rigaud, P., Van de Walle, A., Hanna, M., Forget, N., Guichard, F., Zaouter, Y., Guesmi, K., Druon, F., & Georges, P. (2016). Supercontinuum-seeded few-cycle mid-infrared OPCPA system. *Optics Express, 24*, 26494–26502.

Ryba-Romanowski, W., Macalik, B., Strzęp, A., Lisiecki, R., Solarz, P., & Kowalski, R. M. (2014). Spectral transformation of infrared ultrashort pulses in laser crystals. *Optical Materials, 36*, 1745–1748.

Seidel, M., Xiao, X., Hussain, S. A., Arisholm, G., Hartung, A., Zawilski, K. T., Schunemann, P. G., Habel, F., Trubetskov, M., Pervak, V., Pronin, O., & Krausz, F. (2018). Multi-watt, multi-octave, mid-infrared femtosecond source. *Science Advances, 4*, eaaq1526.

Seo, M., Tsendsuren, K., Mitra, S., Kling, M., & Kim, D. (2020). High-contrast, intense single-cycle pulses from an all thin-solid-plate setup. *Optics Letters, 45*, 367–370.

Shumakova, V., Malevich, P., Ališauskas, S., Voronin, A., Zheltikov, A.M., Faccio, D., Kartashov, D., Baltuška, A., & Pugžlys, A. (2016). Multi-millijoule few-cycle mid-infrared pulses through nonlinear self-compression in bulk. *Nature Communications, 7*, 12877.

Silva, F., Austin, D. R., Thai, A., Baudisch, M., Hemmer, M., Faccio, D., Couairon, A., & Biegert, J. (2012). Multi-octave supercontinuum generation from mid-infrared filamentation in a bulk crystal. *Nature Communications, 3*, 807.

Spence, D. E., Kean, P. N., & Sibbett, W. (1991). 60-fsec pulse generation from a self-mode-locked Ti:sapphire laser. *Optics Letters, 16*, 42–44.

Srinivas, N. K. M. N., Harsha, S. S., & Rao, D. N. (2005). Femtosecond supercontinuum generation in a quadratic nonlinear medium (KDP). *Optics Express, 13*, 3224–3229.

Stingel, A. M., Vanselous, H., & Petersen, P. B. (2017). Covering the vibrational spectrum with microjoule mid-infrared supercontinuum pulses in nonlinear optical applications. *Journal of the Optical Society of America B, 34*, 1163–1168.

Strickland, D., & Mourou, G. (1985). Compression of amplified chirped optical pulses. *Optics Communications, 56*, 219–221.

Šuminas, R., Tamošauskas, G., Valiulis, G., Jukna, V., Couairon, A., & Dubietis, A. (2017a). Multi-octave spanning nonlinear interactions induced by femtosecond filamentation in polycrystalline ZnSe. *Applied Physics Letters, 110*, 241106.

Šuminas, R., Tamošauskas, G., Jukna, V., Couairon, A., & Dubietis, A. (2017b): Second-order cascading-assisted filamentation and controllable supercontinuum generation in birefringent crystals. *Optics Express, 25*, 6746–6756.

Šuminas, R., Marcinkevičiūtė, A., Tamošauskas, G., & Dubietis, A. (2019). Even and odd harmonics-enhanced supercontinuum generation in polycrystalline zinc-blende semiconductors. *Journal of the Optical Society of America B, 36*, A22–A27.

Šuminas, R., Garejev, N., Šuminiene, A., Jukna, V., Tamošauskas, G., & Dubietis, A. (2020). Femtosecond filamentation, supercontinuum generation, and determination of n_2 in polycrystalline SBN. *Journal of the Optical Society of America B, 37*, 1530–1534.

Šuminienė, A., Jukna, V., Šuminas, R., Tamošauskas, G., Vengris, M., & Dubietis, A. (2020). LiSAF: An efficient and durable nonlinear material for supercontinuum generation in the ultraviolet. *Lithuanian Journal of Physics, 60*, 217–224.

Šuminiene, A., Jukna, V., Šuminas, R., Tamošauskas, G., & Dubietis, A. (2021). Femtosecond infrared supercontinuum generation in 6H-SiC crystal. *OSA Continuum, 7*, 911–917.

Toth, S., Stanislauskas, T., Balciunas, I., Budriunas, R., Adamonis, J., Danilevicius, R., Viskontas, K., Lengvinas, D., Veitas, G., Gadonas, D., Varanavičius, A., Csontos, J., Somoskoi, T., Toth, L., Borzsonyi, A., & Osvay, K. (2020). SYLOS lasers – the frontier of few-cycle, multi-TW, kHz lasers for ultrafast applications at extreme light infrastructure attosecond light pulse source. *Journal of Physics: Photonics, 2*, 045003.

Tzankov, P., Buchvarov, I., & Fiebig, T. (2002). Broadband optical parametric amplification in the near UV-VIS. *Optics Communications, 203*, 107–113.

Vasilyev, S., Moskalev, I., Mirov, M., Smolski, V., Mirov, S., & Gapontsev, V. (2017). Ultrafast middle-IR lasers and amplifiers based on polycrystalline Cr:ZnS and Cr:ZnSe. *Optical Materials Express, 7*, 2636–2650.

Vasilyev, S., Moskalev, I., Smolski, V., Peppers, J., Mirov, M., Fedorov, V., Martyshkin, D., Mirov, S., & Gapontsev, V. (2019). Octave-spanning Cr:ZnS femtosecond laser with intrinsic nonlinear interferometry. *Optica, 6*, 126–127.

Voronin, A. A., Lanin, A. A., & Zheltikov, A. M. (2016). Modeling high-peak-power few-cycle field waveform generation by optical parametric amplification in the long-wavelength infrared. *Optics Express, 24*, 23207–23220.

Wang, Y., Ni, H., Zhan, W., Yuan, J., & Wang, R. (2013). Supercontinuum and THz generation from Ni implanted $LiNbO_3$ under 800 nm laser excitation. *Optics Communications, 291*, 334–336.

Wang, T., Gai, X., Wei, W., Wang, R., Yang, Z., Shen, X., Madden, S., & Luther-Davies, B. (2014). Systematic z-scan measurements of the third order nonlinearity of chalcogenide glasses. *Optical Materials Express, 4*, 1011–1022.

Werner, K., Hastings, M. G., Schweinsberg, A., Wilmer, B. L., Austin, D., Wolfe, C. M., Kolesik, M., Ensley, T. R., Vanderhoef, L., Valenzuela, A., & Chowdhury, E. (2019). Ultrafast mid-infrared high harmonic and supercontinuum generation with n_2 characterization in zinc selenide. *Optics Express, 27*, 2867–2885.

Wilhelm, T., Piel, J., & Riedle, E. (1997). Sub-20-fs pulses tunable across the visible from a blue-pumped single pass noncollinear parametric converter. *Optics Letters, 22*, 1494–1496.

Wolter, B., Pullen, M. G., Baudisch, M., Sclafani, M., Hemmer, M., Senftleben, A., Schröter, C. D., Ullrich, J., Moshammer, R., & Biegert, J. (2015). Strong-field physics with Mid-IR fields. *Physical Review X, 5*, 021034.

Yu, Y., Gai, X., Wang, T., Ma, P.,Wang, R., Yang, Z., Choi, D.-Y., Madden, S., & Luther-Davies, B. (2013). Mid-infrared supercontinuum generation in chalcogenides. *Optical Materials Express, 3*, 1075–1086.

Zhao, L., Zeng, X., Tong, L., Gao, Y., Liu, J., Ren, Y., Zhao, Y., & Li, J. (2018). Femtosecond supercontinuum generation and Čerenkov conical emission in periodically poled $LiTaO_3$. *Optik, 156*, 333–337.

Zheng, J., Jiang, J., Chen, H., Zheng, R., Shen, X., Yu, K., & Wei, W. (2021). Optical nonlinearity and supercontinuum generation of tellurite glass at 1.064 μm. *Optics & Laser Technology, 138*, 106832.

Zhou B., & Bache, M. (2016). Multiple-octave spanning mid-IR supercontinuum generation in bulk quadratic nonlinear crystals. *APL Photonics, 1*, 050802.

Chapter 13
Chalcogenide Glass Fibers for Mid-IR Supercontinuum Generation

Jonathan Hu and Curtis R. Menyuk

Abstract Chalcogenide fibers are natural candidates for infrared supercontinuum sources. In this chapter, we describe mid-IR supercontinuum generation using step-index fibers, tapered fibers, suspended-core fibers, and photonic crystal fibers, double-clad fibers, polarization-maintaining fibers, and cascaded fibers. We also discuss how computer simulations contribute to our understanding of mid-IR supercontinuum generation. We describe the impact of nonlinearity and dispersion, loss, materials, damage threshold, fabrication, and output power on chalcogenide fibers that are used for mid-IR supercontinuum generation. It is the combination of wide transmission range, strong nonlinear properties, high optical damage threshold, and environmental stability that makes chalcogenide fibers an excellent system for fiber-based mid-IR supercontinuum laser sources.

Keywords Chalcogenide glass · Glass materials · Mid-IR supercontinuum generation · Spectral bandwidth · Step-index fibers · Tapered fibers · Suspended-core fibers · Photonic crystal fibers · Double-clad fibers · Polarization-maintaining fibers · Cascaded fibers · Numerical simulation · Damage threshold · Fabrication

13.1 Introduction

Supercontinuum generation light sources using dispersion and nonlinear effects in silica optical fibers have many applications in fluorescence, microscopy, and spectroscopy (Dudley et al., 2006). However, the upper wavelength that can be obtained from supercontinuum generation using silica fibers is limited because silica

J. Hu (✉)
Baylor University, Waco, TX, USA
e-mail: Jonathan_Hu@baylor.edu

C. R. Menyuk
University of Maryland Baltimore County, Baltimore, MD, USA
e-mail: menyuk@umbc.edu

R. R. Alfano (ed.), *The Supercontinuum Laser Source*,
https://doi.org/10.1007/978-3-031-06197-4_13

fibers have high material loss above 2.4 μm, which limits the spectral generation into the mid-infrared (IR). The mid-IR spectral region is particularly important, because the fundamental molecular vibrational absorption bands exist in the mid-IR region. The supercontinuum generation at mid-IR wavelengths requires fibers with a transmission window in the mid-IR region. For this reason, the pursuit of suitable host materials for generating light sources in the mid-IR spectral region has been a research focus in recent years. Several non-silica glasses have attracted growing interest as host materials for mid-IR fibers, including tellurite (Domachuk et al., 2008; Liao et al., 2009), fluoride (Xia et al., 2006, 2009), and chalcogenide (Eggleton et al., 2011) glasses. Among these candidates, chalcogenide glasses are natural candidates for infrared supercontinuum sources due to their long wavelength multiphoton absorption edge. Hence, they can transmit light out to 20 μm, compared to a transmission window of less than 5 μm for both fluoride and tellurite (Eggleton et al., 2011; Shiryaev & Churbanov, 2013). Chalcogenide glasses contain chalcogen elements sulfur (S), selenium (Se), and tellurium (Te) in combination with other metalloid elements such as arsenic (As), antimony (sb), and germanium (Ge). Figure 13.1 (Tao et al., 2015) shows typical infrared transmission spectra for S, Se, and Te chalcogenide, millimeter-thick bulk samples. Chalcogenide glasses also have strong optical nonlinearities up to tens or hundreds of times greater than those of fluoride and tellurite glasses, making them promising candidates for mid-IR supercontinuum generation (Slusher et al., 2004; Petit et al., 2006; Sanghera et al., 2008).

The first supercontinuum generation in bulk borosilicate glass was reported by Alfano and Shapiro in 1970 with a spectrum from 400 nm to 700 nm (Alfano & Shapiro, 1970b, c). Later in 1970, they also observed supercontinuum generation in liquid argon and solid krypton (Alfano & Shapiro, 1970a). In 1976, Lin and Stolen reported the first supercontinuum generation in silica fiber (Lin & Stolen,

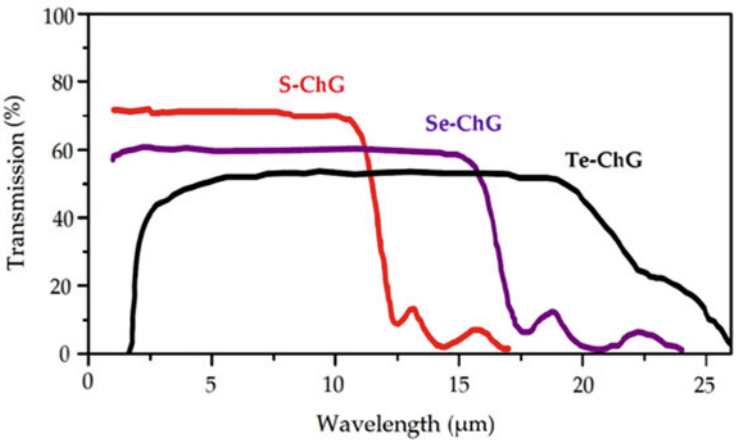

Fig. 13.1 Typical infrared transmission spectra of S, Se, and Te chalcogenide millimeter-thick bulk samples. (Reproduced with permission from Tao et al., 2015)

1976). They injected kilowatt-peak-power pulses from a nanosecond dye laser into 19.5 m of standard silica optical fiber to generate a supercontinuum over a spectral range of 434–614 nm. The supercontinuum mechanism was attributed to cascaded stimulated Raman scattering and self-phase modulation. In 1985, Corkum et al. observed supercontinua spanning the range from 3 to 14 μm when CO_2 laser light was passed into GaAs, AgBr, ZnSe, and CdS crystals (Corkum et al., 1985). In 2005, Shaw et al. demonstrated the first supercontinuum generation in chalcogenide fiber (Shaw et al., 2005). They coupled laser light with a wavelength of 2.5 μm and a pulse width of 100 fs into 1 meter of As-Se photonic crystal fiber with one air-hole ring, which led to a supercontinuum spectrum that ranged from 2.1 μm to 3.2 μm. Magi et al. demonstrated the first tapered chalcogenide fiber in 2007 (Magi et al., 2007). The nonlinearity was estimated to be 62,000 times larger than in standard silica single-mode fiber, owing to the 500 times larger nonlinear coefficient n_2 and almost 125 times smaller effective mode area (Magi et al., 2007). El-Amraoui et al. demonstrated the first chalcogenide suspended-core fiber in 2010 (El-Amraoui et al., 2010a). Since the initial investigations of mid-IR supercontinuum generation, researchers have made extensive efforts to reduce fiber loss, design fibers with near-zero flattened dispersion, shift the pump wavelength to the long wavelength region, and decrease the fiber length to reduce the loss. Numerical simulations have also demonstrated the potential of chalcogenide fibers for broad mid-IR supercontinuum generation (Cheng et al., 2016a; Saini et al., 2015a; Kubat et al., 2014a, b; Yuan, 2013). Supercontinuum generation has since been the subject of numerous investigations in a wide variety of fibers and waveguides. Due to the strong interest, there are several review papers on this topic (Dai et al., 2018; Wu et al., 2018b; Eggleton et al., 2011; Zhou et al., 2021). Chalcogenide glass waveguides are covered in another book chapter (Yeom et al., 2010). This chapter will focus the mid-IR supercontinuum generation using chalcogenide glass fibers.

This chapter is organized as follows. Section 13.2 discusses supercontinuum generation using different types of fibers, including step-index fibers, tapered fibers, suspended-core fibers, photonic crystal fibers, double-clad fibers, polarization-maintaining fibers, and cascaded fibers. Section 13.3 discusses theoretical work on mid-IR supercontinuum generation. Section 13.4 discusses different aspects of mid-IR supercontinuum generation including the impact of nonlinearity and dispersion, loss, the choice of materials, the damage threshold, fabrication methods, and the output power. Section 13.5 discusses future prospects.

13.2 Mid-IR Supercontinuum Generation in Chalcogenide Fibers

Supercontinuum generation using chalcogenide fibers with a large bandwidth, high brightness, and high degree of coherence has applications in spectroscopy, sensing, biology, metrology, biomedical diagnostics, and spectral imaging (Wu et al., 2018b).

Using chalcogenide glass increases the nonlinearity by up to three orders of magnitude relative to silica tapered fiber, which reduces the power requirement for supercontinuum generation (Hudson et al., 2012). This section discusses different fiber types that are used for supercontinuum generation in the mid-IR region. Figure 13.2 shows the output spectral range and the power as a function of the publication year. The limits of the output spectrum are 20 dB from the peak of the spectrum unless otherwise specified. We only show experiments for which the output spectrum includes wavelengths that are higher than 2 μm. In Fig. 13.2b, we use open circles to indicate the average output power of the supercontinuum generation. Some publications only show the average input power. In this case, we use solid dots to indicate the average input power. In some cases, we estimated the average power using the pulse duration, peak power, and laser repetition rate that are reported in the publication. We include different types of fibers, including step-index fibers (Petersen et al., 2014; Zhang et al., 2015, 2016, 2019a; Eslami et al., 2020; Wang et al., 2018a, 2019; Lemiere et al., 2019; Yao et al., 2016a, b; Luo et al., 2017; Yu et al., 2015; Cheng et al., 2016a; Zhao et al., 2016; Kedenburg et al., 2015; Granzow et al., 2011, 2013; Deng et al., 2016; Lemiere et al., 2021), tapered fibers (Wang et al., 2017, 2018b; Rudy et al., 2013; Sun et al., 2015; Petersen et al., 2017; Al-kadry et al., 2013; Shabahang et al., 2012), suspended-core fibers (Mouawad et al., 2016; Yuan et al., 2019; Gao et al., 2011, 2013, 2014; Han et al., 2017; El-Amraoui et al., 2010b; Wu et al., 2018a; Mouawad et al., 2014b; Moller et al., 2015; Cheng et al., 2015, 2014, 2016b; Savelii et al., 2012), photonic crystal fibers (Shaw et al., 2005; Petersen et al., 2018, 2019; Nguyen et al., 2020), double-clad fibers (Jiao et al., 2019; Zhao et al., 2017; Nagasaka et al., 2017b, c; Xiao et al., 2020), polarization-maintaining fibers (Ghosh et al., 2019; Ren et al., 2019; Jayasuriya et al., 2019), and cascaded fibers (Gattass et al., 2012; Hudson et al., 2017; Petersen et al., 2016; Yin et al., 2017b; Robichaud et al., 2016; Martinez et al., 2018; Woyessa et al., 2021). Most of the experiments reported in Fig. 13.2 with a broad bandwidth and a high output power used step-index fibers and cascaded fibers, which have relatively large power handling capabilities. We now describe in more detail the different fiber types for the mid-IR supercontinuum generation.

The subscript in the chalcogenide glass $As_{40}S_{60}$ and $As_{40}Se_{60}$ indicates the molar percentage of the As, S, and Se elements (Zhang et al., 2020; Qiao et al., 2011). Alternatively, As_2S_3 and As_2Se_3 have often been used to represent the same ratio or percentage of the elements. Alternatively, As-S and As-Se have also been used without the information regarding the percentages of the elements. In this chapter, we will follow the original references that we cite in denoting the chalcogenide glasses.

13.2.1 Step-Index Fibers

Step-index fibers have the simplest structure among the different types of fibers and are well reported in Fig. 13.2. Their main advantage is that they have higher coupling

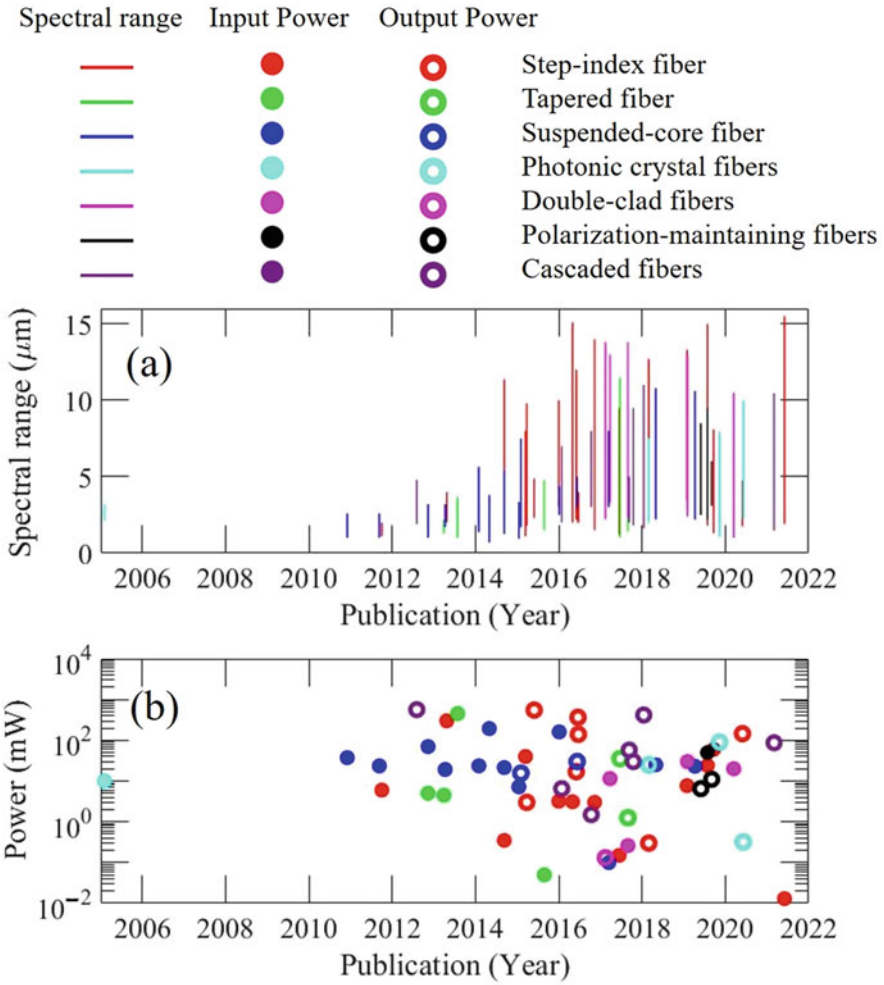

Fig. 13.2 Experimental output spectral range (**a**) and average input or output power (**b**) vs. the reported publication year. In (**b**), we use open circles to show the output average power of the supercontinuum generation, and we use solid dots to show the input average power of the supercontinuum generation if the output power is not stated in the publication. We include different types of fibers, including step-index fibers, tapered fibers, suspended-core fibers, photonic crystal fibers, double-clad fibers, polarization-maintaining fibers, and cascaded fibers

efficiency and lower fiber loss compared to other fiber types, like suspended-core fibers or photonic crystal fibers. The optical attenuation in step-index fibers can be much lower than 10 dB/km (Shiryaev & Churbanov, 2017; Churbanov et al., 2011). The zero-dispersion wavelengths (ZDWs) for the As_2S_3 and As_2Se_3 material dispersion are 5 μm and 7.4 μm, respectively (Petersen et al., 2014; Ebendorff-Heidepriem, 2014; Dantanarayana et al., 2014). When the waveguide dispersion

is increased by using a smaller core size, the ZDW including both materials and waveguide dispersion shifts to a lower wavelength. However, further decreasing the core size leads to two ZDWs. Red-shifted solitons are then limited to wavelengths below the second ZDW region, due to cancellation of the self-frequency shift (Skryabin et al., 2003; Cheng et al., 2016a). It is difficult to match the ZDW of the fiber to the operating wavelength of existing fiber lasers. Hence, it is common to use the output light sources in the mid-IR region from optical parametric amplifiers and oscillators, which serve as an input pump source for the supercontinuum generation.

Instead of using chalcogenide glasses for both the core and cladding in a step-index fiber, it is possible to use the pressure-filling technique to fill capillary fibers with chalcogenide glass to form chalcogenide-silica step-index fibers (Granzow et al., 2011). The index difference between the chalcogenide and silica leads to highly nonlinear devices with strong optical confinement. The silica cladding provides a robust sheath for the mechanically less stable chalcogenide glass and protects it from atmospheric degradation (Granzow et al., 2011). The ZDW lies close to 1550 nm (Granzow et al., 2011), which is a useful pump wavelength for erbium-doped fiber lasers. The drawback is that the supercontinuum generation is mainly limited to short wavelengths near 2 μm.

13.2.2 Tapered Fibers

Tapered fibers have been used in many applications, such as frequency conversion, chemical sensing, and supercontinuum generation (Birks et al., 2000; Korposh et al., 2019). The bandwidth of supercontinuum generation can be enhanced by tapering a fiber to a small diameter. A smaller fiber diameter produces a smaller effective area, which leads to a higher nonlinearity (Hudson et al., 2011). Additionally, it is possible to tailor the dispersion along the fiber so that it changes from normal to anomalous at the pump wavelength. Hence, it is possible to use a tapered fiber with a shorter ZDW and a shorter pump wavelength than a standard fiber with a longer ZDW since it is difficult to generate a high-power laser source at mid-IR wavelengths. Due to the high nonlinearity, strong self-phase modulation usually leads to a coherent supercontinuum spectrum (Saini et al., 2020; Marandi et al., 2012). Highly coherent broadband supercontinuum generation from 1.5 to 8.3 μm in tapered As-S chalcogenide fibers has been obtained using a 15-cm-long fiber with a waist core diameter of 4.8 μm (Li et al., 2019).

Much research has been aimed at extending the supercontinuum spectrum into the mid-IR region power by using chalcogenide tapered fibers (Li et al., 2019; Wang et al., 2017). The energy loss in the transition region of tapered fibers due to the decrease in fiber core size plays an important role in the effectiveness of the supercontinuum generation. When the transition length is increased, a higher transmission efficiency of light leads to a higher output power and a larger spectral width (Wang et al., 2017). Figure 13.3a presents the measured output spectra from tapered fibers with length of tapered region being 6.7, 7.6, 8.4, 9.2, and 10.5 mm

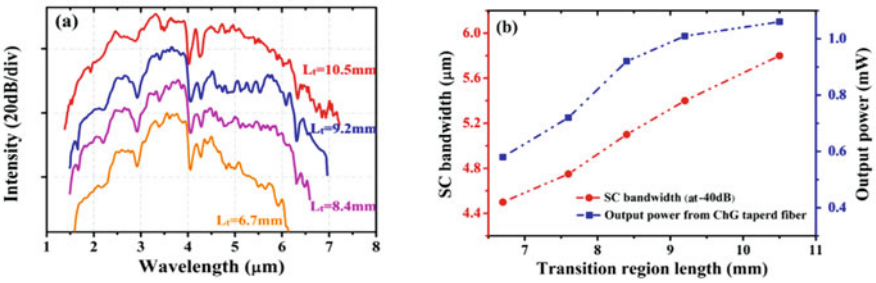

Fig. 13.3 (**a**) The supercontinuum spectra that are generated using 12-cm-long As-S chalcogenide tapered fibers when the length of the transition region varies from 6.7 to 10.5 mm. (**b**) Bandwidth of the generated supercontinuum spectrum at 40 dB from the peak and the corresponding output power as a function of the length of the transition region. (Reproduced with permission from Wang et al., 2017)

(Wang et al., 2017). As the tapered region increases, a broader supercontinuum spectrum is obtained. An ultrabroad and relatively flattened supercontinuum spectrum spanning from 1.4 to 7.2 μm at 40 dB from the peak has been obtained with a tapered fiber length of 10.5 mm (Wang et al., 2017). The spectral broadening in these tapered fibers was primarily attributable to the mutual interaction of self-phase modulation, optical wave breaking, and four-wave mixing. Figure 13.3b shows the bandwidth of the generated supercontinuum spectrum at 40 dB from the peak and the corresponding output power as a function of the length of the transition region. The output power increased from 0.6 to 1.1 mW, and the supercontinuum bandwidth increased from 4.5 to 5.8 μm, as the length of transition region increased.

Fibers can be tapered down to a few micrometers or even nanometers. Hence, tapered fibers usually have low mechanical strength in practical applications, and polymer jackets have often been used to coat chalcogenide fibers for convenient handing (Al-Kadry et al., 2015). A thick built-in polymer jacket improves the fiber mechanical properties relative to bare chalcogenide fibers. The thermal compatibility between the chalcogenide and the polymer makes it possible to taper a fiber without first removing the polymer jacket, resulting in robust tapers that can be more easily handled and manipulated (Shabahang et al., 2014).

13.2.3 Suspended-Core Fibers

Suspended-core fibers have the advantages that their dispersion can be adjusted over a wide range and they can have large nonlinearity due to the variable core sizes with a high index contrast between chalcogenide glass and air. Detailed theoretical research has been carried out to study the dispersion with different core diameters and bridge widths (Coscelli et al., 2015; Mi et al., 2017; Karim et al., 2018). Figure 13.4a shows the cross-section of Ge-Sb-Se suspended-core fibers that are fabricated

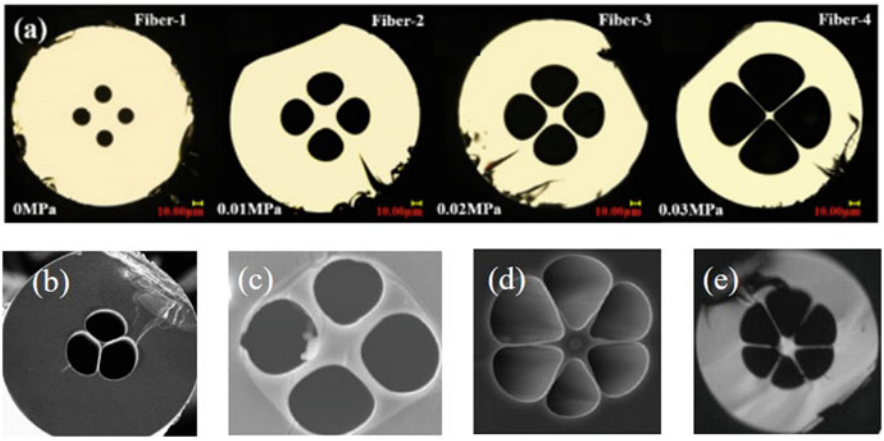

Fig. 13.4 (**a**) Cross-section of $Ge_{15}Sb_{15}Se_{70}$ suspended-core fibers that were fabricated with varying gas pressure (Yuan et al., 2019). (**b**) The first reported chalcogenide suspended-core fiber (El-Amraoui et al., 2010a). (**c**) $AsSe_2$ fiber with a glass core with four holes and an As_2S_5 cladding (Cheng et al., 2014). (**d**) A fiber with a chalcogenide solid core with six holes and a tellurite cladding (Cheng et al., 2015; Petersen et al., 2014). (**e**) A chalcogenide suspended-core fiber with a loss of 0.05 dB/m at 3.7 μm (Troles et al., 2010). (Reproduced with permission from Cheng et al., 2014, 2015; El-Amraoui et al., 2010a; Troles et al., 2010; Yuan et al., 2019)

with different gas pressures and which have estimated ZDWs that vary from 3.3 to 5.6 μm (Yuan et al., 2019). The principal drawback of suspended-core fibers for supercontinuum generation is their low power coupling efficiency, which limits the output power from supercontinuum generation. In addition, the longitudinal variation of the fiber leads to a relatively large loss due to the high index contrast between chalcogenide glass and air. A typical loss is on the order of 1 dB/m or 0.1 dB/m in suspended-core fibers (Troles et al., 2010; Cheng et al., 2014, 2015; Yuan et al., 2019; Fatome et al., 2011).

Figure 13.4b shows the first chalcogenide suspended-core fiber, which was reported in 2010 (El-Amraoui et al., 2010a). It is also possible to combine the concept of a suspended-core fiber and a step-index fiber. In one reported case, the core was made from $AsSe_2$ glass with four holes, and the cladding glass was made from As_2S_5 glass, as shown in Fig. 13.4c (Cheng et al., 2014). Efficient chromatic dispersion control was achieved. The ZDW of the fiber was 3380 nm. Broadband mid-IR supercontinuum generation with the spectrum from 1256 to 5400 nm was obtained with a peak power of 1337 kW at the wavelength of 3389 nm (Cheng et al., 2014). Alternatively, a chalcogenide-tellurite hybrid suspended-core fiber was designed and fabricated by the rod-in-tube drawing technique, as shown in Fig. 13.4d (Cheng et al., 2015). The solid core was made of chalcogenide glass with a composition of Ge-Ga-Sb-S, and the cladding was made of tellurite glass with a composition of $78TeO_2$-5ZnO-$12Li_2O$-$5Bi_2O_3$ (mol%, TZLB) with six holes. The ZDW of the fiber was shifted down to 2.37 μm due to the suspended-core

fiber structure. Using 1-cm-long fiber, flattened and broadband supercontinuum generation from 0.95 to 3.35 μm with the intensity fluctuation of only 6 dB was obtained (Cheng et al., 2015). Figure 13.4e shows a chalcogenide suspended-core fiber with a low loss of 0.05 dB/m at 3.7 μm (Troles et al., 2010).

Another consideration is the impact of optical aging in suspended-core fibers or photonic crystal fibers on supercontinuum generation for long-term applications in non-controlled atmosphere conditions (Mouawad et al., 2014a, c; Toupin et al., 2014). A 2012 study (Gris-Sanchez & Knight, 2012) monitored the changes in spectral attenuation over 16 weeks of exposure to a laboratory environment in silica suspended-core fibers. Increased spectral attenuation was observed at 1364 nm and at 1384 nm, which corresponds to O-H absorption bands in silica (Gris-Sanchez & Knight, 2012). This increased spectral attenuation was attributed to the diffusion of contaminants (i.e., O-H) interacted with the glass (Gris-Sanchez & Knight, 2012). Another study (Mouawad et al., 2016) using As_2S_3 suspended-core fibers directly discussed the impact of aging on supercontinuum generation. When the fibers were new, this study found that the mid-IR supercontinuum spectrum covered the 2 μm spectral range from 3 to 5 μm. After aging several months, the supercontinuum spectrum only covered a 1.2 μm spectral range from 3.2 to 4.4 μm.

13.2.4 Photonic Crystal Fiber

In order to obtain a broad mid-IR supercontinuum spectral output from a chalcogenide glass fiber, it is necessary to design the fiber with a blue-shifted ZDW and a small mode field area. Chalcogenide photonic crystal fibers (PCFs) (Ghosh et al., 2019; Troles et al., 2010) are good candidates for supercontinuum generation since they offer the possibility to significantly enhance the nonlinearity by making a small effective mode area and the ability to tailor the material dispersion by adjusting the waveguide dispersion design. The design flexibility has led to a large amount of computational work to design chalcogenide PCFs for mid-IR supercontinuum generation using triangular arrangements (Karim et al., 2017; Huang et al., 2020; Saini et al., 2015b; Medjouri & Abed, 2019b; Ali et al., 2016; Khalifa et al., 2017; Saghaei et al., 2015, 2016) and square arrangements (Chauhan et al., 2018, 2020) of the holes. Experimental work that is based on these designs has also been carried out (Petersen et al., 2019; Ghosh et al., 2019). Figure 13.5a shows a fabricated chalcogenide PCF with two extra-large holes with a larger birefringence (Ghosh et al., 2019). Figure 13.5b, c shows a tapered fiber at the input and waist, respectively, with the same magnification (Petersen et al., 2017). The tapered PCF was able to confine the light in a small mode area, generating a high nonlinearity and leading to a supercontinuum spectrum between 1.0 and 11.5 μm (Petersen et al., 2017). Due to the fabrication complexity, there are fewer experimental publications using chalcogenide PCFs, compared to chalcogenide step-index fibers, tapered fibers, or suspended-core fibers, as shown in Fig. 13.2.

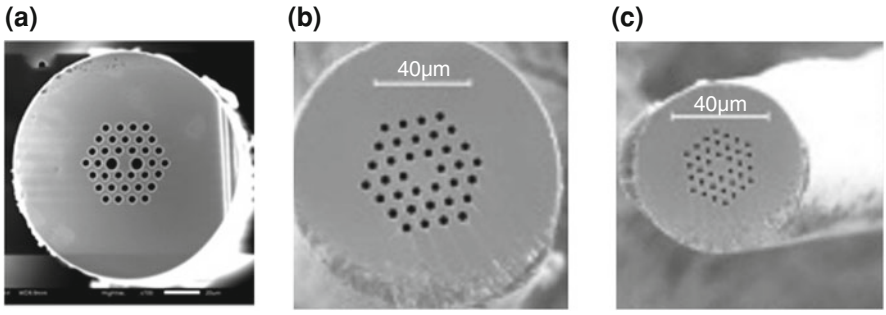

Fig. 13.5 (**a**) A polarization-maintaining PCF (Ghosh et al., 2019). A tapered PCF at the input (**b**) and waist (**c**) with the same magnification (Petersen et al., 2017). (Reproduced with permission from Ghosh et al., 2019; Petersen et al., 2017)

Using PCF with a single material compared to step-index fiber with a high numerical aperture can alleviate the thermomechanical compatibility issue of different glasses during taper fabrication, which avoids the problem of a thermal expansion coefficient mismatch at the core/cladding interface. A comparison between simulation and experiments shows that no significant hole collapse occurred during tapering (Petersen et al., 2017).

13.2.5 Double-Clad Fibers

Double-clad fibers or W-type fibers have also been used for mid-IR supercontinuum generation (Nagasaka et al., 2017a, b; Jiao et al., 2019; Saini et al., 2018; Singh et al. 2020; Khamis et al., 2018). The dispersion can be better controlled than in step-index fibers because of the additional structural flexibility that is added by the additional layer (Wang et al., 2020). Additionally, double-clad fibers are easier to make using the rod-in-tube method than is the case for other PCFs. Double-clad fibers with As_2Se_3, $AsSe_2$, and As_2S_5 glasses have been used to demonstrate mid-IR supercontinuum from 2.3 to 13.8 μm (Nagasaka et al., 2017b) and 2.2 to 13.8 μm (Nagasaka et al., 2017c). Glasses using different concentrations of Ge-As-Se-Te with different indices have been used in the core, inner cladding, and outer cladding, which leads to a supercontinuum spectrum from 1.0 to 10.5 μm (Xiao et al., 2020).

13.2.6 Polarization-Maintaining Fibers

Mid-IR supercontinuum generation was studied computationally in chalcogenide fibers, taking into account both polarizations and the higher-order modes (Chen et al., 2018; Khalifa et al., 2017). When coupling of the fundamental mode to the other

modes occurs, the modeling indicates that the supercontinuum bandwidth in which only a single polarization is taken into account appears substantially larger than the supercontinuum bandwidth when both polarizations are taken into account (Kubat & Bang, 2016).

Experimental studies of polarization-preserving supercontinuum generation in the mid-IR region have also been carried out using a polarization-maintaining chalcogenide PCF with two larger holes near the fiber core, as also shown in Fig. 13.5c (Petersen et al., 2017). Supercontinuum generation from 3.10 to 6.02 μm has been demonstrated using a chalcogenide PCF with a high birefringence of 6.5×10^{-4} at 4.6 μm (Ghosh et al., 2019). A chalcogenide step-index fiber with an elliptical core has also been fabricated with a birefringence of 2×10^{-2} at 11.5 μm, which leads to a supercontinuum spectrum that ranges from 2.5 to 8.5 μm (Jayasuriya et al., 2019). Additionally, tuning the input polarization angle with respect to the fiber axes affects the supercontinuum bandwidth, which has also been confirmed by numerical simulations that use the coupled nonlinear Schrödinger equation (Ghosh et al., 2019). Chalcogenide glass fibers with a rectangular core have been used to generate a polarized mid-IR supercontinuum spectrum from 2.2 to 9.5 μm (Ren et al., 2019). Numerical analysis of this fiber indicates a high birefringence of 8×10^{-3} at 4 μm.

13.2.7 Cascading Fibers

Most of the experimental work that we describe in this chapter has employed free-space systems that use complex and expensive optical parametric amplifiers and optical parametric oscillators as the pump systems. These systems are generally unsuitable for practical applications due to their large size and sensitivity to environmental vibration. Therefore, it is important in practical settings to use alignment-free cascaded fiber systems to generate broadband supercontinuum sources with high-power spectral densities. All fiber-based supercontinuum generation using optical amplifiers or lasers has the advantages of having a much smaller size, a higher beam quality, a lower weight, a low power consumption, and a more rugged packaging (Gattass et al., 2012). Hence, all-fiber broadband mid-IR laser sources have the potential to offer robust, compact, and low-cost solutions.

A typical all-fiber system has a seed laser, which is amplified in multiple stages to produce a high-power mid-IR frequency source. Supercontinuum generation using chalcogenide fibers is then used in the last stage. Mid-IR lasers can usually be obtained from non-silica fibers that are doped with rare-earth ions. By doping with Er^{3+}, Ho^{3+}, Pr^{3+}, or Dy^{3+} ions, laser transitions in the mid-IR region have been produced (Hu et al., 2015; Sanghera et al., 2009; Shaw et al., 2001, 2011; Sojka et al., 2012). The output of ultrafast Ho^{3+}-doped fiber laser operating at 2.9 μm has been launched into an As_2Se_3/As_2S_3 tapered fiber, which generated a supercontinuum spectrum spanning from 1.8 to 9.5 μm with an average power of more than 30 mW (Hudson et al., 2017). A high output of 565 mW has also

been report using an all-fiber based supercontinuum source with emission covering the wavelength range from 1.9 to 4.8 μm (Gattass et al., 2012; Shaw et al., 2011). The laser source was based on a combination of silica commercial off-the-shelf components and a chalcogenide-based nonlinear optical fiber. The output power can also be increased by scaling the repetition rate (Gattass et al., 2012). Alternatively, one can use a seed laser, which is Raman-shifted in highly nonlinear fibers to filter a source in the mid-IR range (Yao et al., 2016a).

It is also possible to cascade supercontinuum sources, so that the fiber-based supercontinuum from an initial stage serves as the pump source in the following stage to further extend the spectral coverage. This cascading approach requires that the first supercontinuum spectrum is in the anomalous dispersion region and contains many solitons with femtosecond pulse duration and high peak powers. The second fiber should have a high nonlinearity and a ZDW below the long wavelength edge on the supercontinuum spectrum that is generated by the first fiber, so that the solitons can continue their redshift and thus further increase the bandwidth and wavelength edge of the supercontinuum generation. This cascading approach was first proposed in a numerical simulation that used a cascaded ZBLAN and chalcogenide fibers (Kubat et al., 2014b). The first stage using a ZBLAN fiber generated a supercontinuum spectrum from 0.9 to 4.1 μm, which was further broadened to supercontinuum from 0.9 to 9 μm in the second stage that used an As_2Se_3 suspended-core fiber with a core diameter of 5 μm. The ZBLAN fiber was chosen as the first fiber because of its high damage threshold, its ability to generate supercontinuum radiation around 4 μm, and high output powers of tens of watts (Yin et al., 2017a; Yang et al., 2014; Liu et al., 2014). After the initial proposal in 2014 (Kubat et al., 2014b), cascaded supercontinuum spectrum was experimentally demonstrated in 2016 (Petersen et al., 2016). The first stage that consisted of a 5-m-long ZBLAN fiber produced a long wavelength edge of 4.4 μm with a power of 51.4 mW. The second stage that consisted of an $As_{38}Se_{62}$ suspended-core fiber with a 4 μm core extended the supercontinuum spectrum to 7 μm with an output power of 6.5 mW. In 2016, cascaded fibers were also demonstrated, in which the first stage consisted of a 1-m-long ZrF_4 fiber that was pumped with an Er-doped ZrF_4 fiber amplifier to generate a supercontinuum spectrum covering the range from 3.0 to 4.2 μm, which was then used to excite a low-loss As_2Se_3 step-index fiber, whose output spectrum that range from 3 to 8 μm with an output power of 1.5 mW (Robichaud et al., 2016). Later in 2017, a thulium-doped fiber amplifier was used to generate a supercontinuum spectrum from 2.0 to 4.2 μm in a 12-m-long ZBLAN fiber, which was then used to excite an As_2S_3 step-index fiber, when they generated supercontinuum spectrum from 2.0 to 5.0 μm that spectrally flat within 10 dB with an output power of 57.6 mW (Yin et al., 2017b). In 2018, a supercontinuum spectrum that was generated using three cascaded ZBLAN, As_2S_3, and As_2Se_3 fibers was demonstrated, as shown in Fig. 13.6a (Guo et al., 2018; Martinez et al., 2018). The As_2S_3 fiber played an important role in the middle stage because of its high-power handling capability. When the repetition rate of the pump was scaled up to 800 kHz, the output of the cascaded fibers spanned a broadband spectrum that ranged from 1.6 to 11 μm, as shown in Fig. 13.6b. The output power was 417

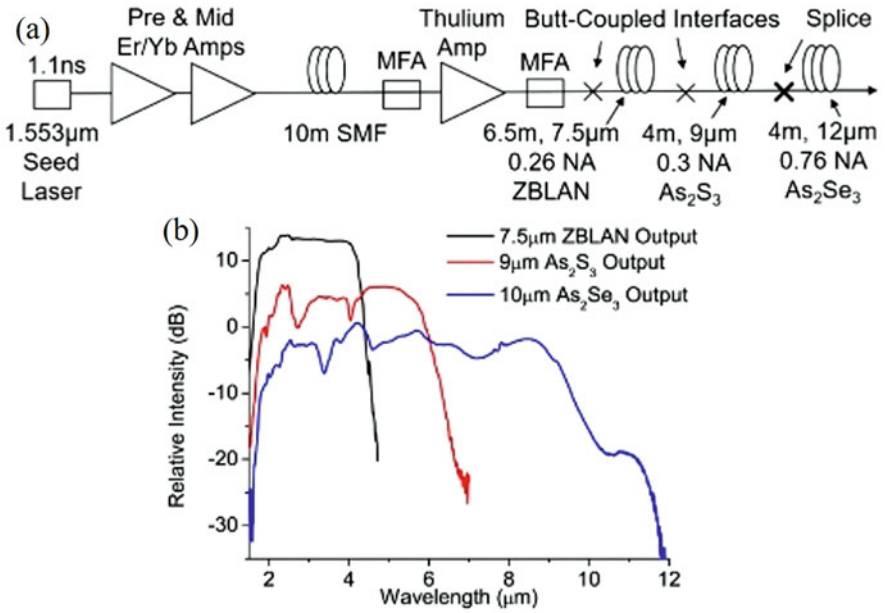

Fig. 13.6 (**a**) Setup of the cascading scheme for all-fiber supercontinuum generation. (**b**) Measured supercontinuum spectra using ZBLAN (black), AS_2S_3 (red), and As_2Se_3 (blue) fibers. (Reproduced with permission from Martinez et al., 2018)

mW. The wide spectral range and high average power will be important for practical applications. In 2021, three cascaded ZBLAN, As_2S_3, and As_2Se_3 fibers were used to demonstrate a simple and power stable supercontinuum generation span from 1.5 to 10.5 μm (Woyessa et al., 2021). Stability measurements for 7 days with 8–9 h of operation daily revealed an average power of 86.6 mW with a maximum fluctuation from the average power that is within 1 mW, which underlines their suitability as stable sources for industrial and field applications.

13.3 Theoretical Work

Supercontinuum generation uses the Kerr effect and the Raman effect, in combination with dispersion in optical fibers, to broaden the bandwidth of an optical signal. In order to maximize the bandwidth of mid-IR supercontinuum generation in the chalcogenide glass fibers, theoretical investigations have studied the physics behind it by modeling the spectral broadening in nonlinear fibers. In simulations, the generalized nonlinear Schrödinger equation (GNLS) (Hu et al., 2010b; Price et al., 2007; Dudley et al., 2006) is used to model nonlinear pulse propagation in an optical fiber

$$\begin{aligned}\frac{\partial A(z,t)}{\partial z}+\frac{a}{2}A-i\mathrm{IFT}\left\{\left[\beta\left(\omega_0+\Omega\right)-\beta\left(\omega_0\right)-\Omega\beta_1\left(\omega_0\right)\right]\tilde{A}\left(z,\Omega\right)\right\}\\ =i\gamma\left(1+\frac{i}{\omega_0}\frac{\partial}{\partial t}\right)\left[A\left(z,t\right)\int_{-\infty}^{t}R\left(t-t'\right)\left|A\left(z,t'\right)\right|^2dt'\right]\end{aligned} \tag{13.1}$$

where z is the distance along the fiber, t is the recorded time, and A is the electric field envelope normalized so that $|A|^2$ has units of power. We use IFT to indicate the inverse Fourier transform, where Ω is the transform variable and the tilde indicates the Fourier transform. The parameter ω_0 is angular carrier frequency, $\beta(\omega_0)$ is the corresponding propagation constant, and a is the fiber loss. The quantity $\beta_1(\omega_0)$ is the first derivative of $\beta(\omega_0)$. While one often writes the GNLS with a Taylor series, this calculation is usually done in practice using the inverse Fourier transform, as shown in Eq. (13.1), unless the Taylor expansion only has two or three terms (Dudley et al., 2006). The right-hand side accounts for the nonlinear generation (Hu et al., 2010b). The parameter $\gamma = n_2\omega_0/(cA_{\mathrm{eff}})$ is the Kerr coefficient, where n_2 is the nonlinear refractive index, c is the speed of light, and A_{eff} is the fiber's effective area. The nonlinear response function, $R(t) = (1-f_R)\,\delta(t) + f_R\,h_R(t)$, includes both the Kerr (instantaneous) contribution proportional to $\delta(t)$ and the Raman (delayed) contribution proportional to $h_R(t)$, where $\int h_R(t) = 1$. The split-step Fourier method is typically used to solve Eq. (13.1) (Sinkin et al., 2003). The refractive indices for chalcogenide glasses can be obtained using a Sellmeier equation (Petersen et al., 2017; Ma et al., 2013; Rodney et al., 1958; Coscelli et al., 2015; Dantanarayana et al., 2014; Chaudhari et al., 2009). Raman response $h_R(t)$, fiber loss a, the material-dependent parameter n_2 and f_R, and the geometry parameter A_{eff} must be determined experimentally (Hu et al., 2010b; Slusher et al., 2004). Most of the parameters are well known. Due to the measurement uncertainty, different values of f_R have been found in different literature. The values of 0.148 (Nagasaka et al., 2017a; Cheng et al., 2016a, b), 0.1 (Hu et al., 2010b; Zhao et al., 2018; Ung & Skorobogatiy, 2010; Ghosh et al., 2019), or 0.03 (Kubat et al., 2014a; Kohoutek et al., 2011) have been used in the simulation for the parameter f_R.

Simulations can be a great asset in support of experimental work. In particular, simulations can determine the optimum fiber length. The spectral broadening typically reaches a maximum shortly after reaching the waist section of the taper (Petersen et al., 2017), after which the supercontinuum bandwidth and output power are continuously diminished by fiber loss. Hence, one should choose a fiber length that corresponds to this maximum. Numerical simulations with and without the loss peaks due to impurities can also determine the impact of those loss peaks (Savelii et al., 2012; Kubat et al., 2014a) and the benefits that can be obtained by removing impurities and decreasing loss peaks. Simulations can also indicate the degree of spectral coherence that can be obtained. Chalcogenide fibers with all-normal dispersion have been studied to generate a mid-IR supercontinuum spectrum with high coherence (Diouf et al., 2017; Karim et al., 2017; Liu et al., 2016a; Medjouri & Abed, 2019a; Nguyen et al., 2020). In a 2016 work, coherence was found to be sensitive to the modelled noise, polarization orientation, and the actual tapering profile (Liu et al., 2016b). Experimental work using all-normal dispersion

fiber has been done in which high coherence has been demonstrated (Yuan et al., 2020; Zhang et al., 2019c; Jiao et al., 2019; Xing et al., 2018).

In many cases, simulations proposed new ideas that were later confirmed by experiments. As previously described, cascaded supercontinuum generation was first proposed in simulations (Kubat et al., 2014b). Follow-up experiments confirmed this idea just 2–3 years later (Petersen et al., 2016; Yin et al., 2017b; Robichaud et al., 2016). Simulations also studied mid-IR supercontinuum that is produced by using a picosecond pulse as a pump in the anomalous region of As_2Se_3 chalcogenide PCF, along with an additional weak CW trigger that had 0.1% of the pump power. The simulation showed that the bandwidth could be broadened when the CW input is near the Raman gain peak. The strong Raman gain along with the pump leads to four-wave mixing components that broaden the spectrum (Huang et al., 2020). Corresponding experimental work has not yet been carried out.

The repetition rate of the input pulse source in many experiments is much greater than the sampling rate of the optical spectrum analyzer. Hence, the output supercontinuum spectrum actually consists of an ensemble average over many pulse realizations in which the pump pulses that generate this ensemble can vary significantly in their pulse durations, peak power, and noise-induced fluctuation levels. Because supercontinuum generation is extremely sensitive to any changes in the input pulse when the input pulse energy is large, a single-shot numerical simulation will not yield an accurate representation of the experimental supercontinuum spectrum, and it is necessary to use an ensemble average (Weiblen et al., 2010). It has been shown that an ensemble with 5000 or fewer realizations is sufficient to reproduce the experimentally expected spectral power density and bandwidth (Weiblen et al., 2014). Smaller ensembles with 100 individual simulations and random noise have also been used in the simulations (Zhao et al., 2018; Huang et al., 2020; Liu et al., 2016b).

Due to the multiple design parameters including different hole diameters in different layers, the potential of a wide variety of chalcogenide PCFs to generate a broadband supercontinuum spectrum in the mid-IR region has been studied numerically (Cheshmberah et al., 2020; Saghaei et al., 2015, 2016; Diouf et al., 2019a, b; Chaitanya et al., 2016; Karim et al., 2015; Hu et al., 2010a; Li et al., 2014). Computational work shows that an As_2Se_3-based chalcogenide-glass triangular-core graded-index PCF can generate an ultra-broadband mid-IR spectrum spanning a range from 2 to 15 μm (Saini et al., 2015a, b). Additional numerical results show that using 3 μm laser pulse with 0.6 nJ energy and 50 fs duration in a Ge-Sb-Se chalcogenide PCF with normal dispersion generates a highly coherent, ultra-flat, and broadband supercontinuum spanning 1.86 to 5.35 μm with a spectral variation that is less than 3 dB (Medjouri & Abed, 2019b). Borosilicate and As_2S_3 multimaterial fibers have been proposed to yield a flat dispersion that extends from 1.8 to 8.0 μm (Kalra et al., 2018). A silica PCF with an As_2S_3 chalcogenide core region and with a large nonlinear coefficient has been studied. This fiber was reported to have a very low ZDW, and with a pump at 1.55 μm, it can generate a supercontinuum spectrum from 1.0 to 3.1 μm (Ali et al., 2016). A highly nonlinear rectangular core chalcogenide PCF has also been proposed (Chauhan et al., 2018, 2020).

13.4 General Aspects of Mid-IR Supercontinuum Generation

There are many aspects of supercontinuum generation that are common to all fiber types. In this section, we will discuss the impact of nonlinearity and dispersion, loss, the choice of materials, the damage threshold, fabrication methods, and the output power.

13.4.1 Nonlinearity and Dispersion

The process of supercontinuum generation is complicated, and it involves self-phase modulation, cross-phase modulation, four-wave mixing, stimulated Raman scattering, the modulational instability, and dispersive wave generation. Efficient and broadband supercontinuum generation is obtained by pumping in the anomalous dispersion regime close to the ZDW of the fiber (Petersen et al., 2014; Wang et al., 2019). The impact of pump wavelength has been demonstrated by using a low-loss 18-cm-long suspended-core $As_{38}Se_{62}$ fiber with a ZDW of 3.5 μm. When the pump is at 3.3 μm in the normal dispersion region, the supercontinuum spectrum ranges from 1.5 to 6.3 μm. When the pump is 4.7 μm in the anomalous dispersion region, the supercontinuum spectrum range from 1.7 to 7.5 μm (Moller et al., 2015).

When the input pulse is in the anomalous dispersion region of the fiber, a high-intensity input pulse undergoes soliton fission, and the solitons then experience a redshift due to the soliton self-frequency shift (SSFS). In addition, four-wave mixing process can generate shorter or longer wavelengths, which can also generate additional solitons, which then undergo a further SSFS (Hu et al., 2010b). It is advantageous for the Stokes wavelength that is generated in the initial stage to be as large as possible so that the final bandwidth is larger. Meanwhile, dispersive waves are created at shorter wavelengths. As the solitons that are created shift to longer wavelengths via the Raman effect, the dispersive waves at shorter wavelengths maintain their positions relative to individual solitons due to soliton trapping (Travers & Taylor, 2009; Gorbach & Skryabin, 2007a, b). The trapping of the dispersive waves by the soliton leads to a continuous shift toward shorter wavelengths. Trapping of dispersive waves by solitons is significantly enhanced in tapered optical fibers as compared to untapered fibers (Travers & Taylor, 2009). Consequently, the supercontinuum spectrum can be larger on both the long and short wavelength sides of the pump. As the soliton power decreases while propagating in the fiber, the SSFS effects weaken. A tapered fiber can be used to increase the nonlinearity during the propagation (Hu et al., 2006, 2013).

A small core in chalcogenide glass fibers can lead to two ZDWs, which in turn leads to the possibility that red-shifted solitons are limited by the second ZDW (Cheng et al., 2016a; Hu et al., 2010b). However, when two ZDWs are present, dispersive waves can be generated beyond the second ZDW (Petersen et al., 2017), which further broadens the spectrum. In a 2014 work, the second ZDW actually

allows for formation of mid-IR dispersive waves that were able to push the long wavelength edge of spectrum out to 12.5 μm (Kubat et al., 2014a). On the other hand, in a fiber with only one ZDW, the long wavelength edge of the spectrum was limited to 10.7 μm (Kubat et al., 2014a).

It is usually difficult to fabricate a fiber with a smaller core and high waveguide dispersion, which can lead to a higher transmission loss and a high insertion loss. Power scaling and power handling with small-core structures are usually problematic, especially with suspended-core fibers where the core is in effect thermally isolated from the cladding by an air layer. Hence, the bulk of the reported work has been done on fibers that have a larger core size and use a pump wavelength at normal dispersion (Gattass et al., 2012). The process of supercontinuum generation in a normal dispersion fiber relies on self-phase modulation, which leads to a symmetric broadening of the spectrum. After propagation through some distance, the spectrum can extend beyond the ZDW (Petersen et al., 2017), which then initiates soliton formation and fission followed by the SSFS, similar to supercontinuum generation when the dispersion is anomalous. Multiple stages of Raman gain in chalcogenide fiber can also lead to a broadband supercontinuum spectrum (Gattass et al., 2012; Kubat et al., 2014a). Each of the Raman peaks further experiences broadening with parametric four-wave mixing, self-phase modulation, and cross-phase modulation, which lead to smooth broad spectrum (Gattass et al., 2012; Yao et al., 2016a; Coen et al., 2002). The Raman-induced broadening is then gradually overtaken by soliton-based broadening. A 2020 study of the noise in supercontinuum generation showed that the normal pumping scheme is also a promising approach to generate a high-power broadband supercontinuum source for noise-sensitive applications such as sensing (Eslami et al., 2020).

13.4.2 Loss

Supercontinuum generation is a nonlinear effect, which diminishes in effectiveness as the optical power decreases. Hence, propagation loss has a negative impact on the supercontinuum generation. There are several absorption bands from 2 to 20 μm, which correspond to residual O-H, As-O, Se-O, Ge-O, S-H, Se-H, and S-O impurities in the glass (Cheng et al., 2016a; Savelii et al., 2012; Gattass et al., 2012; Churbanov et al. 2011; Wang et al., 2018a; Theberge et al., 2014). Numerical simulations with and without the loss peaks due to the impurities can determine the impact of the loss peaks on the final supercontinuum spectrum. In a 2012 experiment, supercontinuum generation using low-loss, highly nonlinear, As_2S_3 chalcogenide fibers led to a supercontinuum spectrum that ranged from 1.0 to 3.2 μm. Corresponding numerical simulations showed that the supercontinuum generation without O-H and S-H absorption peaks could be extended to 5.5 μm, thus confirming the dramatic limitation imposed by the O-H and S-H peaks (Savelii et al., 2012). In another 2012 experiment, the large absorption peak around 4.1 μm due to ppm-level hydrogen impurities that formed H-S bonds in the fiber impacted the

experimental work when the pump wavelength was shorter than the H-S absorption band (Gattass et al., 2012).

On the other hand, supercontinuum generation usually only uses fiber lengths of a few centimeters, and the nonlinearity often occurs at a relatively short distance with high peak power. With enough power below the wavelength of the absorption peak, a Raman scattering can lead to energy leap-frogging over an absorption band, so that the supercontinuum spectrum can continue to broaden. This power-dependent "leap" over the absorption band is clearly seen in the power evolution of the supercontinuum with different powers in (Gattass et al., 2012; Petersen et al., 2014). The light can almost immediately be shifted away from the pump wavelength and is therefore not affected by the loss peak (Petersen et al., 2014). In a 2014 work, a comparison of simulation results with different loss profiles shows that the loss profiles make a negligible difference (Kubat et al., 2014a). Hence, the O-H and H_2O absorption bands at 2.9 and 6.3 μm lead to a negligible degradation of the supercontinuum spectrum.

13.4.3 Materials

Chalcogenide glasses are commonly based on S and Se associated with high phonon energies. Different chalcogenide compositions such as Ge-As-Se, Ge-Sb-Se, and Ge-As have exhibited ultra-broadband supercontinuum generation from 2 to 12 μm (Petersen et al., 2014; Zhang et al., 2016; Yu et al., 2015). Different material compositions can increase the linear and nonlinear refractive index of chalcogenide glass. The nonlinear refractive index of Ge-Sb-Se has been shown to increase with the concentration of Sb (Chen et al., 2015) as well as Se (El-Amraoui et al., 2010a). The multicomponent bulk GAP-Se chalcogenide glasses exhibit high values of linear and nonlinear refractive indices while maintaining high, broadband transparency and low optical losses at all infrared wavelengths (Goncalves et al., 2018).

On the other hand, Te glasses have high linear and nonlinearity indices and have lower phonon energies and result in wider optical windows compared to S and Se (Danto et al., 2006; Zhao et al., 2016; Wilhelm et al., 2007; Yang et al., 2010). An increase in the concentration of Te in Ge-As-Se-Te glasses has been shown to increase glass nonlinearity (Cherukulappurath et al., 2004; Wang et al., 2019; Mouawad et al., 2018). However, the metallic character of Te leads to a greater tendency for crystallite formation, which prevents the production of low-loss optical fibers due to scattering effects (Yang et al., 2010). This drawback can be alleviated by substituting a small amount of Te with Se, which lowers the conductivity and dramatically increases the resistance to crystallization while retaining a wide optical window at long wavelengths, leading to Ge-As-Te-Se glass with a transmission window between 5 and 12 μm (Yang et al., 2010). Te-based chalcogenide step-index fiber has been fabricated and used for supercontinuum generation from 1.5 to 14 μm (Zhao et al., 2016).

The replacement of highly toxic arsenic (As) with antimony (Sb) makes the glasses more environmentally friendly, and Ge-Sb-Se glasses exhibit higher thermal and mechanical durability (Ou et al., 2016). Furthermore, the optical nonlinearity of Ge-Sb-Se glass is greater than that of Ge-As-Se because of the replacement of As by the more metallic Sb (Dai et al., 2015). More importantly, the visible damage occurs at a beam intensity of 3674 GW/cm^2 for the Ge-Sb-Se glass, which is much higher than the beam intensity of 1524 GW/cm^2 for As_2Se_3 glass (Ou et al., 2016). Additionally, an environment-friendly chalcogenide glass fiber with a Ge-Sb-Se core and a Ge-Se cladding has been fabricated that generates a supercontinuum spectrum from 2.2 to 12 μm with an output average power of 17 mW (Ghosh et al., 2019).

It has also been shown that the nonlinearity of chalcogenide glasses can be enhanced with copper (Cu) or silver (Ag) doping (Ogusu & Shinkawa, 2009). A broad supercontinuum spectrum from 2.0 to 16.0 μm was successfully achieved using a Ge-Te-AgI fiber with a double-clad fiber (Zhao et al., 2017).

13.4.4 Damage Threshold

Mid-IR laser-induced damage of chalcogenide glass is first initiated by the accumulation of electrons and subsequently driven by thermal accumulation (You et al., 2017). When Ge-As-S glasses were exposed to 216 fs pulses with repetition rates of kilohertz to megahertz at 1030 nm, the laser damage threshold decreases with the increasing repetition rate of the irradiation pulses (Zhang et al., 2019b). Tables of damage threshold with different compositions can also be found in (Zhang et al., 2017; 2019a). For example, an incident peak intensity at the fiber front face of 4.5 GW/cm^2 can be used with a repetition rate of 10 MHz (Granzow et al., 2011). With a lower repetition rate of 560 kHz, an incident peak intensity of 12 GW/cm^2 can be used (Shaw et al., 2011). In addition, the experimental demonstration of an input power density of 1.07 GW/cm^2 without fiber damage for $\leq 1.5 \times 10^7$ pulses was close to the predicted threshold of about 3.0 GW/cm^2 due to dielectric breakdown at the surface (Sanghera & Aggarwal, 1999).

Glass with a higher average bond energy tends to have a higher damage threshold, so that S-based chalcogenide glasses generally have a higher damage threshold than do Se- and Te-based glasses (You et al., 2017). As Se is progressively replaced by S, the damage threshold rises (Wang & Luther-Davies, 2013; You et al., 2017). The optical damage thresholds of As_2S_3 and As_2Se_3 fibers were 2.9 and 2.8 GW/cm^2, respectively, for 2 ns pulses at a wavelength of 1.9 μm (Zhang et al., 2017). Among sulfide glasses, those containing Ge have superior laser damage resistance because of the relatively strong bond strength of Ge-S (Zhang et al., 2017, 2019a; Zhu et al., 2018). The Ge-As-Se glass composition has superior damage threshold over the more nonlinear As_2Se_3 glass due to its stability during fabrication, resistance to crystallization, and higher transition temperature (Toupin et al., 2012; Petersen et al., 2017).

13.4.5 Fabrication

The stack and draw technique is the most common method for manufacturing silica PCFs and has also been used to fabricate chalcogenide PCFs (Monro et al., 2000). Small tubes are elongated into capillaries, which are then stacked in a hexagonal lattice around a glass rod of an identical diameter. The stack is then introduced in a jacket tube to be drawn into a PCF with a solid core. The diameters of the holes can be adjusted by applying pressure in the holes.

The molding method to prepare chalcogenide PCFs uses a casting process (Coulombier et al., 2010). A purified glass rod is heated until it is nearly liquid. Then, the glass flows in a structured silica mold, which is quenched in air and annealed. The silica mold can be removed with hydrofluoric acid. The chalcogenide-glass preform is then drawn in a fiber-drawing tower. It is easier to prepare preforms with different cross-section structures using the molding method than is the case for the stack and draw method. However, the molding method cannot prepare PCFs with different core and cladding compositions.

The drilling method refers to a mechanical drilling process, which is used for preform fabrication, allowing the design of a wide range of microstructured optical fibers (El-Amraoui et al., 2010b). The advantage of the drilling method is that it can be used to prepare PCFs with complicated structures. However, the drilling method can only be used to prepare short fiber preforms. In addition, the surface of the drilled hole is very rough, leading to a high fiber loss.

Extrusion is the shaping of a glass melt under high temperature and high pressure through a mold with simple or complex geometry (Seddon et al., 1998). The extrusion method is the preferred method for preparing ultra-low-loss chalcogenide PCFs with the advantages of reducing the manufacturing processing and enabling the extrusion of a variety of structures. The hole surface is smoother than is possible with the drilling method.

13.4.6 Output Power

It has been shown that using a pump wavelength in the mid-IR region generally leads to a wider spectrum than when the pump wavelength is shorter. The output power of supercontinuum generation is typically on the order of milliwatts or even microwatts, due to the low repetition rate of the pump. Besides simply increasing the peak power of the pump pulses, effort has been paid to increase the output power by increasing the repetition rate of the pump, which in one case has led to 550 mW of the output power (Kedenburg et al., 2015). The increase of the repetition rate with the same peak power may reduce the risk of optical damage. On the other hand, one can also increase the pulse duration to a nanosecond with a relatively low repetition rate of 100 kHz, which leads to an output power of 143 mW (Yao et al., 2016b). The

combination of these two techniques with a long pulse duration of 40 ps and a large repetition rate of 10 MHz led to a power of 565 mW (Gattass et al., 2012).

Overcoming the trade-off between the spectral bandwidth and average output power from chalcogenide fiber-based mid-IR supercontinuum sources is one of the major roadblocks toward practical application of the technology. Tapering of large-mode-area chalcogenide PCFs has been used to study this trade-off (Petersen et al., 2017). By pumping the tapered fibers at 4 μm using a megahertz optical parametric generation source and choosing different lengths of the untapered fiber segments, the output could be tailored for either a broadest spectrum that ranges from 1.0 to 11.5 μm with an average output power of 35.4 mW or a high output power of 57.3 mW with a spectrum that ranges from 1.0 to 8.0 μm (Petersen et al., 2017).

13.5 Future Perspectives

Despite over 15 years of effort on mid-IR supercontinuum generation and the achievement of hundreds of milliwatts of output power in current experimental work, the output powers of supercontinuum sources generated from chalcogenide fibers still must be improved to reach one watt. Generally, efficient and broadband supercontinuum generation was obtained by pumping in the anomalous dispersion regime close to the ZDW of the fiber. Because bulk As_2Se_3 and As_2S_3 glasses have a ZDW of ~7.4 μm and 5 μm, respectively, it is challenging to fabricate fibers with a ZDW that matches commercially available high-peak-power lasers or building new high-peak-power lasers that match the ZDW of chalcogenide fiber. Currently, no commercial fiber lasers can generate ultra-short pulses at wavelengths beyond 4 μm. The development of fiber lasers (Hu et al., 2015; Shaw et al., 2001; Sojka et al., 2012) at longer wavelengths has the potential to increase the output power of supercontinuum generation.

PCFs have played an important role in supercontinuum generation at mid-IR wavelengths. However, a major disadvantage of using PCFs with air capillaries is the large diffusion surface of the glass, leading to an accumulation of O-H defects from atmospheric water vapor. One approach to avoid this difficulty is to seal the fiber with a solid endcap immediately after drawing (Petersen et al., 2017), which has the added benefit of allowing the post-processing of the end facets with anti-reflection coatings or nanoimprinted motheye structures to further improve the damage threshold and output power. The maximum total transmission of a nano-imprinted uniform fiber was increased by 27.9% relative to the non-imprinted fiber, and the average power above 3.5 μm was increased by up to 60.2% (Petersen et al., 2019).

Impurities have limited the bandwidth of supercontinuum generation (Gattass et al., 2012). While it is possible to boost the power to overcome the limit of the bandwidth set by impurities (Gattass et al., 2012), reducing the losses by reducing the impurities is a preferred long-term solution. There are known processes for reducing the level of impurities in chalcogenide fibers with low attenuation

loss (Nguyen et al., 2002; Shiryaev & Churbanov, 2014, 2017; Churbanov, 1992; Churbanov et al., 2011). A combination of increased power and better purification should significantly improve the bandwidth of supercontinuum generation.

All-fiber mid-IR supercontinuum generation based on chalcogenide fibers appears promising for many industrial and environmental applications. On one hand, it is necessary to increase the average pump power that is injected into chalcogenide fibers by adjusting the repetition rate and pulse duration of the seed sources. On the other hand, the propagation losses of the all-fiber systems need to be further reduced. A large portion of the system loss are still from the high Fresnel reflection at the end faces of chalcogenide fibers, due to lens focusing, butt-coupling, and splicing (Dai et al., 2018). However, fusion splicing of silica with ZBLAN fibers or chalcogenide fibers for the purpose of all-fiber supercontinuum generation has been successfully demonstrated to significantly reduce the losses (Okamoto et al., 2011; Thapa et al., 2015; Yin et al., 2016, 2017a). All-fiber approaches for supercontinuum sources with high average output powers have great potential to increase the robustness and reliability mid-IR supercontinuum sources for applications.

References

Alfano, R. R., & Shapiro, S. L. (1970a). Direct distortion of electronic clouds of rare-gas atoms in intense electric fields. *Physical Review Letters, 24*, 1217–1220.

Alfano, R. R., & Shapiro, S. L. (1970b). Emission in Region 4000 to 7000 a Via Four-Photon Coupling in Glass. *Physical Review Letters, 24*, 584–587.

Alfano, R. R., & Shapiro, S. L. (1970c). Observation of self-phase modulation and small-scale filaments in crystals and glasses. *Physical Review Letters, 24*, 592–594.

Ali, R. A. H., Hameed, M. F. O., & Obayya, S. S. A. (2016). Ultrabroadband supercontinuum generation through photonic crystal fiber with As2S3 chalcogenide core. *Journal of Lightwave Technology, 34*, 5423–5430.

Al-kadry, A., Baker, C., El Amraoui, M., Messaddeq, Y., & Rochette, M. (2013). Broadband supercontinuum generation in As2Se3 chalcogenide wires by avoiding the two-photon absorption effects. *Optics Letters, 38*, 1185–1187.

Al-Kadry, A., Li, L. Z., El Amraoui, M., North, T., Messaddeq, Y., & Rochette, M. (2015). Broadband supercontinuum generation in all-normal dispersion chalcogenide microwires. *Optics Letters, 40*, 4687–4690.

Birks, T. A., Wadsworth, W. J., & Russell, P. S. (2000). Supercontinuum generation in tapered fibers. *Opt. Lett., 25*, 1415–1417.

Chaitanya, A. G. N., Saini, T. S., Kumar, A., & Sinha, R. K. (2016). Ultra broadband mid-IR supercontinuum generation in Ge11.5As24Se64.5 based chalcogenide graded-index photonic crystal fiber: design and analysis. *Applied Optics, 55*, 10138–10145.

Chaudhari, C., Suzuki, T., & Ohishi, Y. (2009). Design of zero chromatic dispersion chalcogenide As2S3 glass nanofibers. *Journal of Lightwave Technology, 27*, 2095–2099.

Chauhan, P., Kumar, A., & Kalra, Y. (2018). Mid-infrared broadband supercontinuum generation in a highly nonlinear rectangular core chalcogenide photonic crystal fiber. *Optical Fiber Technology, 46*, 174–178.

Chauhan, P., Kumar, A., & Kalra, Y. (2020). Numerical exploration of coherent supercontinuum generation in multicomponent GeSe2-As2Se3-PbSe chalcogenide based photonic crystal fiber. *Optical Fiber Technology, 54*, 102110.

Chen, L. Y., Chen, F. F., Dai, S. X., Tao, G. M., Yan, L. H., Shen, X., Ma, H. L., Zhang, X. H., & Xu, Y. S. (2015). Third-order nonlinearity in Ge-Sb-Se glasses at mid-infrared wavelengths. *Materials Research Bulletin, 70*, 204–208.

Chen, L., Gao, W. Q., Chen, L., Wang, P., Ni, C. Q., Chen, X. C., Zhou, Y., Zhang, W., Hu, J. G., Liao, M. S., Suzuki, T., & Ohishi, Y. (2018). Numerical study on supercontinuum generation by different optical modes in AsSe2-As2S5 chalcogenide microstructured fiber. *Applied Optics, 57*, 382–390.

Cheng, T. L., Kanou, Y., Xue, X. J., Deng, D. H., Matsumoto, M., Misumi, T., Suzuki, T., & Ohishi, Y. (2014). Mid-infrared supercontinuum generation in a novel AsSe2-As2S5 hybrid microstructured optical fiber. *Optics Express, 22*, 23019–23025.

Cheng, T. L., Kawashima, H., Xue, X. J., Deng, D. H., Matsumoto, M., Misumi, T., Suzuki, T., & Ohishi, Y. (2015). Fabrication of a chalcogenide-tellurite hybrid microstructured optical fiber for flattened and broadband supercontinuum generation. *Journal of Lightwave Technology, 33*, 333–338.

Cheng, T. L., Nagasaka, K., Tuan, T. H., Xue, X. J., Matsumoto, M., Tezuka, H., Suzuki, T., & Ohishi, Y. (2016a). Mid-infrared supercontinuum generation spanning 2.0 to 15.1 μm in a chalcogenide step-index fiber. *Optics Letters, 41*, 2117–2120.

Cheng, T. L., Tuan, T. H., Liu, L., Xue, X. J., Matsumoto, M., Tezuka, H., Suzuki, T., & Ohishi, Y. (2016b). Fabrication of all-solid AsSe2-As2S5 microstructured optical fiber with two zero-dispersion wavelengths for generation of mid-infrared dispersive waves. *Applied Physics Express, 9*, 022502.

Cherukulappurath, S., Guignard, M., Marchand, C., Smektala, F., & Boudebs, G. (2004). Linear and nonlinear optical characterization of tellurium based chalcogenide glasses. *Optics Communications, 242*, 313–319.

Cheshmberah, A., Seifouri, M., & Olyaee, S. (2020). Supercontinuum generation in PCF with As2S3/Ge20Sb15Se65 Chalcogenide core pumped at third telecommunication wavelengths for WDM. *Optical and Quantum Electronics, 52*, 509.

Churbanov, M. F. (1992). Recent advances in preparation of high-purity chalcogenide glasses in the USSR. *Journal of Non-Crystalline Solids, 140*, 324–330.

Churbanov, M. F., Snopatin, G. E., Shiryaev, V. S., Plotnichenko, V. G., & Dianov, E. M. (2011). Recent advances in preparation of high-purity glasses based on arsenic chalcogenides for fiber optics. *Journal of Non-Crystalline Solids, 357*, 2352–2357.

Coen, S., Chau, A. H. L., Leonhardt, R., Harvey, J. D., Knight, J. C., Wadsworth, W. J., & Russell, P. S. J. (2002). Supercontinuum generation by stimulated Raman scattering and parametric four-wave mixing in photonic crystal fibers. *J. Opt. Soc. Am. B, 19*, 753–764.

Corkum, P. B., Ho, P. P., Alfano, R. R., & Manassah, J. T. (1985). Generation of infrared supercontinuum covering 3-14 μm in dielectrics and semiconductors. *Optics Letters, 10*, 624–626.

Coscelli, E., Poli, F., Li, J. F., Cucinotta, A., & Selleri, S. (2015). *Chalcogenide suspended-core fibers for supercontinuum generation in the mid-infrared* (p. 9347). *Materials, Devices, and Applications Xiv*.

Coulombier, Q., Brilland, L., Houizot, P., Chartier, T., N'Guyen, T. N., Smektala, F., Renversez, G., Monteville, A., Mechin, D., Pain, T., Orain, H., Sangleboeuf, J. C., & Troles, J. (2010). Casting method for producing low-loss chalcogenide microstructured optical fibers. *Optics Express, 18*, 9107–9112.

Dai, S. X., Chen, F. F., Xu, Y. S., Xu, Z., Shen, X., Xu, T. F., Wang, R. P., & Ji, W. (2015). Mid-infrared optical nonlinearities of chalcogenide glasses in Ge-Sb-Se ternary system. *Optics Express, 23*, 1300–1307.

Dai, S. X., Wang, Y. Y., Peng, X. F., Zhang, P. Q., Wang, X. S., & Xu, Y. S. (2018). A review of mid-infrared supercontinuum generation in chalcogenide glass fibers. *Applied Sciences, 8*, 707.

Dantanarayana, H. G., Abdel-Moneim, N., Tang, Z. Q., Sojka, L., Sujecki, S., Furniss, D., Seddon, A. B., Kubat, I., Bang, O., & Benson, T. M. (2014). Refractive index dispersion of chalcogenide glasses for ultra-high numerical-aperture fiber for mid-infrared supercontinuum generation. *Optical Materials Express, 4*, 1444–1455.

Danto, S., Houizot, P., Boussard-Pledel, C., Zhang, X. H., Smektala, F., & Lucas, J. (2006). A family of far-infrared-transmitting glasses in the Ga-Ge-Te system for space applications. *Advanced Functional Materials, 16*, 1847–1852.

Deng, D. H., Liu, L., Tuan, T. H., Kanou, Y., Matsumoto, M., Tezuka, H., Suzuki, T., & Ohishi, Y. (2016). Mid-infrared supercontinuum covering 3–10 μm using a As2Se3 core and As2S5 cladding step-index chalcogenide fiber. *Journal of the Ceramic Society of Japan, 124*, 103–105.

Diouf, M., Ben Salem, A., Cherif, R., Saghaei, H., & Wague, A. (2017). Super-flat coherent supercontinuum source in As38.8Se61.2 chalcogenide photonic crystal fiber with all-normal dispersion engineering at a very low input energy. *Applied Optics, 56*, 163–169.

Diouf, M., Mandeng, L. M., Tchawoua, C., & Zghal, M. (2019a). Numerical Investigation of Supercontinuum Generation Through AsSe2As2S5 Chalcogenide Photonic Crystal Fibres and Rib Structures. *Journal of Lightwave Technology, 37*, 5692–5698.

Diouf, M., Wague, A., & Zghal, M. (2019b). Numerical investigation of an ultra-broadband coherent mid-infrared supercontinuum in a chalcogenide AsSe2-As2S5 multimaterial photonic crystal fiber. *Journal of the Optical Society of America B-Optical Physics, 36*, A8–A14.

Domachuk, P., Wolchover, N. A., Cronin-Golomb, M., Wang, A., George, A. K., Cordeiro, C. M. B., Knight, J. C., & Omenetto, F. G. (2008). Over 4000 nm bandwidth of mid-IR supercontinuum generation in sub-centimeter segments of highly nonlinear tellurite PCFs. *Optics Express, 16*, 7161–7168.

Dudley, J. M., Genty, G., & Coen, S. (2006). Supercontinuum generation in photonic crystal fiber. *Rev. Mod. Phys., 78*, 1135–1184.

Ebendorff-Heidepriem, H. (2014). Non-silica microstructured optical fibers for infrared applications. In *2014 Optoelectronics and communications conference and Australian conference on optical fibre technology (Oecc/Acoft 2014)* (pp. 627–629).

Eggleton, B. J., Luther-Davies, B., & Richardson, K. (2011). Chalcogenide photonics. *Nature Photonics, 5*, 141–148.

El-Amraoui, M., Fatome, J., Jules, J. C., Kibler, B., Gadret, G., Fortier, C., Smektala, F., Skripatchev, I., Polacchini, C. F., Messaddeq, Y., Troles, J., Brilland, L., Szpulak, M., & Renversez, G. (2010a). Strong infrared spectral broadening in low-loss As-S chalcogenide suspended core microstructured optical fibers. *Optics Express, 18*, 4547–4556.

El-Amraoui, M., Gadret, G., Jules, J. C., Fatome, J., Fortier, C., Desevedavy, F., Skripatchev, I., Messaddeq, Y., Troles, J., Brilland, L., Gao, W., Suzuki, T., Ohishi, Y., & Smektala, F. (2010b). Microstructured chalcogenide optical fibers from As2S3 glass: towards new IR broadband sources. *Optics Express, 18*, 26655–26665.

Eslami, Z., Ryczkowski, P., Salmela, L., & Genty, G. (2020). Low-noise octave-spanning mid-infrared supercontinuum generation in a multimode chalcogenide fiber. *Optics Letters, 45*, 3103–3106.

Fatome, J., Kibler, B., El-Amraoui, M., Jules, J. C., Gadret, G., Desevedavy, F., & Smektala, F. (2011). Mid-infrared extension of supercontinuum in chalcogenide suspended core fibre through soliton gas pumping. *Electronics Letters, 47*, 398–399.

Gao, W. Q., Liao, M. S., Yan, X., Kito, C., Kohoutek, T., Suzuki, T., El-Amraoui, M., Jules, J. C., Gadret, G., Desevedavy, F., Smektala, F., & Ohishi, Y. (2011). Visible light generation and its influence on supercontinuum in chalcogenide As2S3 microstructured optical fiber. *Applied Physics Express, 4*, 102601.

Gao, W. Q., El Amraoui, M., Liao, M. S., Kawashima, H., Duan, Z. C., Deng, D. H., Cheng, T. L., Suzuki, T., Messaddeq, Y., & Ohishi, Y. (2013). Mid-infrared supercontinuum generation in a suspended-core As2S3 chalcogenide microstructured optical fiber. *Optics Express, 21*, 9573–9583.

Gao, W. Q., Duan, Z. C., Asano, K., Cheng, T. L., Deng, D. H., Matsumoto, M., Misumi, T., Suzuki, T., & Ohishi, Y. (2014). Mid-infrared supercontinuum generation in a four-hole As2S5

chalcogenide microstructured optical fiber. *Applied Physics B-Lasers and Optics, 116*, 847–853.

Gattass, R. R., Shaw, L. B., Nguyen, V. Q., Pureza, P. C., Aggarwal, I. D., & Sanghera, J. S. (2012). All-fiber chalcogenide-based mid-infrared supercontinuum source. *Optical Fiber Technology, 18*, 345–348.

Ghosh, A. N., Meneghetti, M., Petersen, C. R., Bang, O., Brilland, L., Venck, S., Troles, J., Dudley, J. M., & Sylvestre, T. (2019). Chalcogenide-glass polarization-maintaining photonic crystal fiber for mid-infrared supercontinuum generation. *Journal of Physics-Photonics, 1*, 044003.

Goncalves, C., Kang, M., Sohn, B. U., Yin, G. F., Hu, J. J., Tan, D. T. H., & Richardson, K. (2018). New candidate multicomponent chalcogenide glasses for supercontinuum generation. *Applied Sciences, 8*, 2082.

Gorbach, A. V., & Skryabin, D. V. (2007a). Light trapping in gravity-like potentials and expansion of supercontinuum spectra in photonic-crystal fibres. *Nature Photonics, 1*, 653–657.

Gorbach, A. V., & Skryabin, D. V. (2007b). Theory of radiation trapping by the accelerating solitons in optical fibers. *Physical Review A, 76*, 053803.

Granzow, N., Stark, S. P., Schmidt, M. A., Tverjanovich, A. S., Wondraczek, L., & Russell, P. S. J. (2011). Supercontinuum generation in chalcogenide-silica step-index fibers. *Optics Express, 19*, 21003–21010.

Granzow, N., Schmidt, M. A., Chang, W., Wang, L., Coulombier, Q., Troles, J., Toupin, P., Hartl, I., Lee, K. F., Fermann, M. E., Wondraczek, L., & Russell, P. S. (2013). Mid-infrared supercontinuum generation in As2S3-silica "nano-spike" step-index waveguide. *Optics Express, 21*, 10969–10977.

Gris-Sanchez, I., & Knight, J. C. (2012). Time-dependent degradation of photonic crystal fiber attenuation around OH absorption wavelengths. *Journal of Lightwave Technology, 30*, 3597–3602.

Guo, K. W., Martinez, R. A., Plant, G., Maksymiuk, L., Janiszewski, B., Freeman, M. J., Maynard, R. L., Islam, M. N., Terry, F. L., Bedford, R., Gibson, R., Chenard, F., Chatigny, S., & Ifarraguerri, A. I. (2018). Generation of near-diffraction-limited, high-power supercontinuum from 1.57 μm to 12 μm with cascaded fluoride and chalcogenide fibers. *Applied Optics, 57*, 2519–2532.

Han, X., You, C. Y., Dai, S. X., Zhang, P. Q., Wang, Y. Y., Guo, F. X., Xu, D., Luo, B. H., Xu, P. P., & Wang, X. S. (2017). Mid-infrared supercontinuum generation in a three-hole Ge20Sb15Se65 chalcogenide suspended-core fiber. *Optical Fiber Technology, 34*, 74–79.

Hu, J., Marks, B. S., Menyuk, C. R., Kim, J., Carruthers, T. F., Wright, B. M., Taunay, T. F., & Friebele, E. J. (2006). Pulse compression using a tapered microstructure optical fiber. *Optics Express, 14*, 4026–4036.

Hu, J., Menyuk, C. R., Shaw, L. B., Sanghera, J. S., & Aggarwal, I. D. (2010a). Computational study of 3–5 μm source created by using supercontinuum generation in As2S3 chalcogenide fibers with a pump at 2 μm. *Optics Letters, 35*, 2907–2909.

Hu, J., Menyuk, C. R., Shaw, L. B., Sanghera, J. S., & Aggarwal, I. D. (2010b). Maximizing the bandwidth of supercontinuum generation in As2Se3 chalcogenide fibers. *Optics Express, 18*, 6722–6739.

Hu, J., Menyuk, C. R., Shaw, L. B., Sanghera, J. S., & Aggarwal, I. D. (2013). A mid-IR source with increased bandwidth using tapered As2S3 chalcogenide photonic crystal fibers. *Optics Communications, 293*, 116–118.

Hu, J., Menyuk, C. R., Wei, C. L., Shaw, L. B., Sanghera, J. S., & Aggarwal, I. D. (2015). Highly efficient cascaded amplification using Pr3+-doped mid-infrared chalcogenide fiber amplifiers. *Optics Letters, 40*, 3687–3690.

Huang, R. L., Zhou, R. L., & Li, Q. (2020). Mid-infrared supercontinuum generation in chalcogenide photonic crystal fibers with a weak CW trigger. *Journal of Lightwave Technology, 38*, 1522–1528.

Hudson, D. D., Dekker, S. A., Maegi, E. C., Judge, A. C., Jackson, S. D., Li, E. B., Sanghera, J. S., Shaw, L. B., Aggarwal, I. D., & Eggleton, B. J. (2011). Octave spanning supercontinuum in an As2S3 taper using ultralow pump pulse energy. *Optics Letters, 36*, 1122–1124.

Hudson, D. D., Magi, E. C., Judge, A. C., Dekker, S. A., & Eggleton, B. J. (2012). Highly nonlinear chalcogenide glass micro/nanofiber devices: Design, theory, and octave-spanning spectral generation. *Optics Communications, 285*, 4660–4669.

Hudson, D. D., Antipov, S., Li, L. Z., Alamgir, I., Hu, T., Amraoui, M., Messaddeq, Y., Rochette, M., Jackson, S. D., & Fuerbach, A. (2017). Toward all-fiber supercontinuum spanning the mid-infrared. *Optica, 4*, 1163–1166.

Jayasuriya, D., Petersen, C. R., Furniss, D., Markos, C., Tang, Z., Habib, M. S., Bang, O., Benson, T. M., & Seddon, A. B. (2019). Mid-IR supercontinuum generation in birefringent, low loss, ultra-high numerical aperture Ge-As-Se-Te chalcogenide step-index fiber. *Optical Materials Express, 9*, 2617–2629.

Jiao, K., Yao, J. M., Zhao, Z. M., Wang, X. G., Si, N., Wang, X. S., Chen, P., Xue, Z. G., Tian, Y. M., Zhang, B., Zhang, P. Q., Dai, S. X., Nie, Q. H., & Wang, R. P. (2019). Mid-infrared flattened supercontinuum generation in all-normal dispersion tellurium chalcogenide fiber. *Optics Express, 27*, 2036–2043.

Kalra, S., Vyas, S., Tiwari, M., Buryy, O., & Singh, G. (2018). Highly nonlinear multi-material chalcogenide spiral photonic crystal fiber for supercontinuum generation. *Acta Physica Polonica A, 133*, 1000–1002.

Karim, M. R., Rahman, B. M. A., Azabi, Y. O., Agrawal, A., & Agrawal, G. P. (2015). Ultrabroadband mid-infrared supercontinuum generation through dispersion engineering of chalcogenide microstructured fibers. *Journal of the Optical Society of America B-Optical Physics, 32*, 2343–2351.

Karim, M. R., Ahmad, H., & Rahman, B. M. A. (2017). All-normal dispersion chalcogenide PCF for ultraflat mid-infrared supercontinuum generation. *IEEE Photonics Technology Letters, 29*, 1792–1795.

Karim, M. R., Ahmad, H., & Rahman, B. M. A. (2018). Design and modeling of dispersion-engineered all-chalcogenide triangular-core fiber for mid-infrared-region supercontinuum generation. *Journal of the Optical Society of America B-Optical Physics, 35*, 266–275.

Kedenburg, S., Steinle, T., Morz, F., Steinmann, A., & Giessen, H. (2015). High-power mid-infrared high repetition-rate supercontinuum source based on a chalcogenide step-index fiber. *Optics Letters, 40*, 2668–2671.

Khalifa, A. B., Salem, A. B., & Cherif, R. (2017). Mid-infrared supercontinuum generation in multimode As-2 Se-3 chalcogenide photonic crystal fiber. *Applied Optics, 56*, 4319–4324.

Khamis, M. A., Sevilla, R., & Ennser, K. (2018). Design of W-type index chalcogenide fiber for highly coherent mid-IR supercontinuum generation. *Journal of Lightwave Technology, 36*, 5388–5394.

Kohoutek, T., Yan, X., Shiosaka, T. W., Yannopoulos, S. N., Chrissanthopoulos, A., Suzuki, T., & Ohishi, Y. (2011). Enhanced Raman gain of Ge-Ga-Sb-S chalcogenide glass for highly nonlinear microstructured optical fibers. *Journal of the Optical Society of America B-Optical Physics, 28*, 2284–2290.

Korposh, S., James, S. W., Lee, S. W., & Tatam, R. P. (2019). Tapered optical fibre sensors: Current trends and future perspectives. *Sensors, 19*, 2294.

Kubat, I., & Bang, O. (2016). Multimode supercontinuum generation in chalcogenide glass fibres. *Optics Express, 24*, 2513–2526.

Kubat, I., Agger, C. S., Moller, U., Seddon, A. B., Tang, Z. Q., Sujecki, S., Benson, T. M., Furniss, D., Lamrini, S., Scholle, K., Fuhrberg, P., Napier, B., Farries, M., Ward, J., Moselund, P. M., & Bang, O. (2014a). Mid-infrared supercontinuum generation to 12.5 μm in large NA chalcogenide step-index fibres pumped at 4.5 μm. *Optics Express, 22*, 19169–19182.

Kubat, I., Petersen, C. R., Moller, U. V., Seddon, A., Benson, T., Brilland, L., Mechin, D., Moselund, P. M., & Bang, O. (2014b). Thulium pumped mid-infrared 0.9–9 μm supercontinuum generation in concatenated fluoride and chalcogenide glass fibers. *Optics Express, 22*, 3959–3967.

Lemiere, A., Desevedavy, F., Mathey, P., Froidevaux, P., Gadret, G., Jules, J. C., Aquilina, C., Kibler, B., Bejot, P., Billard, F., Faucher, O., & Smektala, F. (2019). Mid-infrared

supercontinuum generation from 2 to 14 μm in arsenic- and antimony-free chalcogenide glass fibers. *Journal of the Optical Society of America B-Optical Physics, 36*, A183–AA92.

Lemiere, A., Bizot, R., Desevedavy, F., Gadret, G., Jules, J. C., Mathey, P., Aquilina, C., Bejot, P., Billard, F., Faucher, O., Kibler, B., & Smektala, F. (2021). 1.7–18 μm mid-infrared supercontinuum generation in a dispersion-engineered step-index chalcogenide fiber. *Results in Physics, 26*, 104397.

Li, X., Chen, W., Xue, T. F., Gao, J. J., Gao, W. Q., Hu, L. L., & Liao, M. S. (2014). Low threshold mid-infrared supercontinuum generation in short fluoride-chalcogenide multimaterial fibers. *Optics Express, 22*, 24179–24191.

Li, G. T., Peng, X. F., Dai, S. X., Wang, Y. Y., Xie, M., Yang, L., Yang, C. F., Wei, W. Y., & Zhang, P. Q. (2019). Highly Coherent 1.5–8.3 μm Broadband Supercontinuum Generation in Tapered As-S Chalcogenide Fibers. *Journal of Lightwave Technology, 37*, 1847–1852.

Liao, M. S., Chaudhari, C., Qin, G. S., Yan, X., Suzuki, T., & Ohishi, Y. (2009). Tellurite microstructure fibers with small hexagonal core for supercontinuum generation. *Optics Express, 17*, 12174–12182.

Lin, C., & Stolen, R. H. (1976). New nanosecond continuum for excited-state spectroscopy. *Applied Physics Letters, 28*, 216–218.

Liu, K., Liu, J., Shi, H. X., Tan, F. Z., & Wang, P. (2014). High power mid-infrared supercontinuum generation in a single-mode ZBLAN fiber with up to 21.8 W average output power. *Optics Express, 22*, 24384–24391.

Liu, L., Cheng, T. L., Nagasaka, K., Tong, H. T., Qin, G. S., Suzuki, T., & Ohishi, Y. (2016a). Coherent mid-infrared supercontinuum generation in all-solid chalcogenide microstructured fibers with all-normal dispersion. *Optics Letters, 41*, 392–395.

Liu, L., Nagasaka, K., Qin, G. S., Suzuki, T., & Ohishi, Y. (2016b). Coherence property of mid-infrared supercontinuum generation in tapered chalcogenide fibers with different structures. *Applied Physics Letters, 108*, 011101.

Luo, B. H., Wang, Y. Y., Dai, S. X., Sun, Y. N., Zhang, P. Q., Wang, X. S., & Chen, F. F. (2017). Midinfrared supercontinuum generation in As2Se3-As2S3 chalcogenide glass fiber with high NA. *Journal of Lightwave Technology, 35*, 2464–2469.

Ma, P., Choi, D. Y., Yu, Y., Gai, X., Yang, Z., Debbarma, S., Madden, S., & Luther-Davies, B. (2013). Low-loss chalcogenide waveguides for chemical sensing in the mid-infrared. *Optics Express, 21*, 29927–29937.

Magi, E. C., Fu, L. B., Nguyen, H. C., Lamont, M. R. E., Yeom, D. I., & Eggleton, B. J. (2007). Enhanced Kerr nonlinearity in sub-wavelength diameter As2Se3 chalcogenide fiber tapers. *Optics Express, 15*, 10324–10329.

Marandi, A., Rudy, C. W., Plotnichenko, V. G., Dianov, E. M., Vodopyanov, K. L., & Byer, R. L. (2012). Mid-infrared supercontinuum generation in tapered chalcogenide fiber for producing octave-spanning frequency comb around 3 μm. *Optics Express, 20*, 24218–24225.

Martinez, R. A., Plant, G., Guo, K. W., Janiszewski, B., Freeman, M. J., Maynard, R. L., Islam, M. N., Terry, F. L., Alvarez, O., Chenard, F., Bedford, R., Gibson, R., & Ifarraguerri, A. I. (2018). Mid-infrared supercontinuum generation from 1.6 to > 11 μm using concatenated step-index fluoride and chalcogenide fibers. *Optics Letters, 43*, 296–299.

Medjouri, A., & Abed, D. (2019a). Design and modelling of all-normal dispersion As39Se61 chalcogenide photonic crystal fiber for flat-top coherent mid-infrared supercontinuum generation. *Optical Fiber Technology, 50*, 154–164.

Medjouri, A., & Abed, D. (2019b). Mid-infrared broadband ultraflat-top supercontinuum generation in dispersion engineered Ge-Sb-Se chalcogenide photonic crystal fiber. *Optical Materials, 97*, 109391.

Mi, N., Wu, B., Jiang, L., Sun, L. H., Zhao, Z. M., Wang, X. S., Zhang, P. Q., Pan, Z. H., Liu, Z. J., Dai, S. X., & Nie, Q. H. (2017). Structure design and numerical evaluation of highly nonlinear suspended-core chalcogenide fibers. *Journal of Non-Crystalline Solids, 464*, 44–50.

Moller, U., Yu, Y., Kubat, I., Petersen, C. R., Gai, X., Brilland, L., Mechin, D., Caillaud, C., Troles, J., Luther-Davies, B., & Bang, O. (2015). Multi-milliwatt mid-infrared supercontinuum generation in a suspended core chalcogenide fiber. *Optics Express, 23*, 3282–3291.

Monro, T. M., West, Y. D., Hewak, D. W., Broderick, N. G. R., & Richardson, D. J. (2000). Chalcogenide holey fibres. *Electronics Letters, 36*, 1998–2000.

Mouawad, O., Amrani, F., Kibler, B., Picot-Clemente, J., Strutynski, C., Fatome, J., Desevedavy, F., Gadret, G., Jules, J. C., Heintz, O., Lesniewska, E., & Smektala, F. (2014a). Impact of optical and structural aging in As2S3 microstructured optical fibers on mid-infrared supercontinuum generation. *Optics Express, 22*, 23912–23919.

Mouawad, O., Picot-Clemente, J., Amrani, F., Strutynski, C., Fatome, J., Kibler, B., Desevedavy, F., Gadret, G., Jules, J. C., Deng, D., Ohishi, Y., & Smektala, F. (2014b). Multioctave midinfrared supercontinuum generation in suspended-core chalcogenide fibers. *Optics Letters, 39*, 2684–2687.

Mouawad, O., Strutynski, C., Picot-Clemente, J., Desevedavy, F., Gadret, G., Jules, J. C., & Smektala, F. (2014c). Optical aging behaviour naturally induced on As2S3 microstructured optical fibres. *Optical Materials Express, 4*, 2190–2203.

Mouawad, O., Kedenburg, S., Steinle, T., Steinmann, A., Kibler, B., Desevedavy, F., Gadret, G., Jules, J. C., Giessen, H., & Smektala, F. (2016). Experimental long-term survey of mid-infrared supercontinuum source based on As2S3 suspended-core fibers. *Applied Physics B-Lasers and Optics, 122*, 177.

Mouawad, O., Bejot, P., Mathey, P., Froidevaux, P., Lemiere, A., Billard, F., Kibler, B., Desevedavy, F., Gadret, G., Jules, J. C., Faucher, O., & Smektala, F. (2018). Expanding up to far-infrared filamentation-induced supercontinuum spanning in chalcogenide glasses. *Applied Physics B-Lasers and Optics, 124*, 182.

Nagasaka, K., Liu, L., Tuan, T. H., Cheng, T. L., Matsumoto, M., Tezuka, H., Suzuki, T., & Ohishi, Y. (2017a). Numerical investigation of highly coherent mid-infrared supercontinuum generation in chalcogenide double-clad fiber. *Optical Fiber Technology, 36*, 82–91.

Nagasaka, K., Liu, L., Tuan, T. H., Cheng, T. L., Matsumoto, M., Tezuka, H., Suzuki, T., & Ohishi, Y. (2017b). Supercontinuum generation in chalcogenide double-clad fiber with near zero-flattened normal dispersion profile. *Journal of Optics, 19*, 095502.

Nagasaka, K., Tuan, T. H., Cheng, T. L., Matsumoto, M., Tezuka, H., Suzuki, T., & Ohishi, Y. (2017c). Supercontinuum generation in the normal dispersion regime using chalcogenide double-clad fiber. *Applied Physics Express, 10*, 032103.

Nguyen, V. Q., Sanghera, J. S., Cole, B., Pureza, P., Kung, F. H., & Aggarwal, I. D. (2002). Fabrication of arsenic sulfide optical fiber with low hydrogen impurities. *Journal of the American Ceramic Society, 85*, 2056–2058.

Nguyen, H. P. T., Tuan, T. H., Xing, L., Matsumoto, M., Sakai, G., Suzuki, T., & Ohishi, Y. (2020). Supercontinuum generation in a chalcogenide all-solid hybrid microstructured optical fiber. *Optics Express, 28*, 17539–17555.

Ogusu, K., & Shinkawa, K. (2009). Optical nonlinearities in As2Se3 chalcogenide glasses doped with Cu and Ag for pulse durations on the order of nanoseconds. *Optics Express, 17*, 8165–8172.

Okamoto, H., Kasuga, K., & Kubota, Y. (2011). Efficient 521 nm all-fiber laser: Splicing Pr3+-doped ZBLAN fiber to end-coated silica fiber. *Optics Letters, 36*, 1470–1472.

Ou, H. Y., Dai, S. X., Zhang, P. Q., Liu, Z. J., Wang, X. S., Chen, F. F., Xu, H., Luo, B. H., Huang, Y. C., & Wang, R. P. (2016). Ultrabroad supercontinuum generated from a highly nonlinear Ge-Sb-Se fiber. *Optics Letters, 41*, 3201–3204.

Petersen, C. R., Moller, U., Kubat, I., Zhou, B. B., Dupont, S., Ramsay, J., Benson, T., Sujecki, S., Abdel-Moneim, N., Tang, Z. Q., Furniss, D., Seddon, A., & Bang, O. (2014). Mid-infrared supercontinuum covering the 1.4–13.3 μm molecular fingerprint region using ultra-high NA chalcogenide step-index fibre. *Nature Photonics, 8*, 830–834.

Petersen, C. R., Moselund, P. M., Petersen, C., Moller, U., & Bang, O. (2016). Spectral-temporal composition matters when cascading supercontinua into the mid-infrared. *Optics Express, 24*, 749–758.

Petersen, C. R., Engelsholm, R. D., Markos, C., Brilland, L., Caillaud, C., Troles, J., & Bang, O. (2017). Increased mid-infrared supercontinuum bandwidth and average power by tapering large-mode-area chalcogenide photonic crystal fibers. *Optics Express, 25*, 15336–15347.

Petersen, C. R., Prtljaga, N., Farries, M., Ward, J., Napier, B., Lloyd, G. R., Nallala, J., Stone, N., & Bang, O. (2018). Mid-infrared multispectral tissue imaging using a chalcogenide fiber supercontinuum source. *Optics Letters, 43*, 999–1002.

Petersen, C. R., Lotz, M. B., Woyessa, G., Ghosh, A. N., Sylvestre, T., Brilland, L., Troles, J., Jakobsen, M. H., Taboryski, R., & Bang, O. (2019). Nanoimprinting and tapering of chalcogenide photonic crystal fibers for cascaded supercontinuum generation. *Optics Letters, 44*, 5505–5508.

Petit, L., Carlie, N., Richardson, K., Humeau, A., Cherukulappurath, S., & Boudebs, G. (2006). Nonlinear optical properties of glasses in the system Ge/Ga-Sb-S/Se. *Optics Letters, 31*, 1495–1497.

Price, J. H. V., Monro, T. M., Ebendorff-Heidepriem, H., Poletti, F., Horak, P., Finazzi, V., Leong, J. Y. Y., Petropoulos, P., Flanagan, J. C., Brambilla, G., Feng, M., & Richardson, D. J. (2007). Mid-IR supercontinuum generation from nonsilica microstructured optical fibers. *IEEE Journal of Selected Topics in Quantum Electronics, 13*, 738–749.

Qiao, H. A., Anheier, N. C., Musgraves, J. D., Richardson, K., & Hewak, D. W. (2011). Measurement of chalcogenide glass optical dispersion using a mid-infrared prism coupler. In *Window and dome technologies and materials XII* (p. 8016). SPIE.

Ren, H., Yu, Y., Zhai, C. C., Zhang, B., Yang, A. P., Tian, K. Z., Feng, X., Yang, Z. Y., Wang, P. F., & Luther-Davies, B. (2019). Chalcogenide glass fibers with a rectangular core for polarized mid-infrared supercontinuum generation. *Journal of Non-Crystalline Solids, 517*, 57–60.

Robichaud, L. R., Fortin, V., Gauthier, J. C., Chatigny, S., Couillard, J. F., Delarosbil, J. L., Vallee, R., & Bernier, M. (2016). Compact 3–8 μm supercontinuum generation in a low-loss As2Se3 step-index fiber. *Optics Letters, 41*, 4605–4608.

Rodney, W. S., Malitson, I. H., & King, T. A. (1958). Refractive index of arsenic trisulfide. *Journal of the Optical Society of America, 48*, 633–636.

Rudy, C. W., Marandi, A., Vodopyanov, K. L., & Byer, R. L. (2013). Octave-spanning supercontinuum generation in in situ tapered As2S3 fiber pumped by a thulium-doped fiber laser. *Optics Letters, 38*, 2865–2868.

Saghaei, H., Ebnali-Heidari, M., & Moravvej-Farshi, M. K. (2015). Midinfrared supercontinuum generation via As2Se3 chalcogenide photonic crystal fibers. *Applied Optics, 54*, 2072–2079.

Saghaei, H., Moravvej-Farshi, M. K., Ebnali-Heidari, M., & Moghadasi, M. N. (2016). Ultrawide mid-infrared supercontinuum generation in As40Se60 chalcogenide fibers: solid core PCF versus SIF. *IEEE Journal of Selected Topics in Quantum Electronics, 22*, 279–286.

Saini, T. S., Kumar, A., & Sinha, R. K. (2015a). Broadband mid-Infrared supercontinuum spectra spanning 2–15 μm using As2Se3 chalcogenide glass triangular-core graded-index photonic crystal fiber. *Journal of Lightwave Technology, 33*, 3914–3920.

Saini, T. S., Kumar, A., & Sinha, R. K. (2015b). Broadband mid-IR supercontinuum generation in As2Se3 based chalcogenide photonic crystal fiber: A new design and analysis. *Optics Communications, 347*, 13–19.

Saini, T. S., Hoa, N. P. T., Xing, L., Tuan, T. H., Suzuki, T., & Ohishi, Y. (2018). Chalcogenide W-type co-axial optical fiber for broadband highly coherent mid-IR supercontinuum generation. *Journal of Applied Physics, 124*, 213101.

Saini, T. S., Tuan, T. H., Suzuki, T., & Ohishi, Y. (2020). Coherent mid-IR supercontinuum generation using tapered chalcogenide step-index optical fiber: Experiment and modelling. *Scientific Reports, 10*, 2236.

Sanghera, J. S., & Aggarwal, I. D. (1999). Active and passive chalcogenide glass optical fibers for IR applications: A review. *Journal of Non-Crystalline Solids, 256*, 6–16.

Sanghera, J. S., Florea, C. M., Shaw, L. B., Pureza, P., Nguyen, V. Q., Bashkansky, M., Dutton, Z., & Aggarwal, I. D. (2008). Non-linear properties of chalcogenide glasses and fibers. *Journal of Non-Crystalline Solids, 354*, 462–467.

Sanghera, J. S., Shaw, L. B., & Aggarwal, I. D. (2009). Chalcogenide glass-fiber-based mid-IR sources and applications. *IEEE Journal of Selected Topics in Quantum Electronics, 15*, 114–119.

Savelii, I., Mouawad, O., Fatome, J., Kibler, B., Desevedavy, F., Gadret, G., Jules, J. C., Bony, P. Y., Kawashima, H., Gao, W., Kohoutek, T., Suzuki, T., Ohishi, Y., & Smektala, F. (2012). Mid-infrared 2000-nm bandwidth supercontinuum generation in suspended-core microstructured Sulfide and Tellurite optical fibers. *Optics Express, 20*, 27083–27093.

Seddon, A. B., Furniss, D., & Motesharei, A. (1998). Extrusion method for making fibreoptic preforms of special glasses. *Infrared Glass Optical Fibers and Their Applications, 3416*, 32–42.

Shabahang, S., Marquez, M. P., Tao, G. M., Piracha, M. U., Nguyen, D., Delfyett, P. J., & Abouraddy, A. F. (2012). Octave-spanning infrared supercontinuum generation in robust chalcogenide nanotapers using picosecond pulses. *Optics Letters, 37*, 4639–4641.

Shabahang, S., Tao, G. M., Marquez, M. P., Hu, H. H., Ensley, T. R., Delfyett, P. J., & Abouraddy, A. F. (2014). Nonlinear characterization of robust multimaterial chalcogenide nanotapers for infrared supercontinuum generation. *Journal of the Optical Society of America B-Optical Physics, 31*, 450–457.

Shaw, L. B., Cole, B., Thielen, P. A., Sanghera, J. S., & Aggarwal, I. D. (2001). Mid-wave IR and long-wave IR laser potential of rare-earth doped chalcogenide glass fiber. *Ieee Journal of Quantum Electronics, 37*, 1127–1137.

Shaw, L. B., Thielen, P. A., Kung, F. H., Nguyen, V. Q., Sanghera, J. S., & Aggarwal, I. D. (2005). IR supercontinuum generation in As-Se photonic crystal fiber. In *Advanced solid-State photonics (TOPS)* (*OSA Trends in Optics and Photonics*). Optical Society of America.

Shaw, L. B., Gattass, R. R., Sanghera, J., & Aggarwal, I. (2011). All-fiber mid-IR supercontinuum source from 1.5 to 5 μm. In *Fiber lasers Viii: Technology, systems, and applications* (p. 7914). SPIE.

Shiryaev, V. S., & Churbanov, M. F. (2013). Trends and prospects for development of chalcogenide fibers for mid-infrared transmission. *Journal of Non-Crystalline Solids, 377*, 225–230.

Shiryaev, V. S., & Churbanov, M. F. (2014). Preparation of high-purity chalcogenide glasses. In *Chalcogenide glasses: Preparation, properties and applications* (pp. 3–35). Woodhead Publishing.

Shiryaev, V. S., & Churbanov, M. F. (2017). Recent advances in preparation of high-purity chalcogenide glasses for mid-IR photonics. *Journal of Non-Crystalline Solids, 475*, 1–9.

Singh, S. P., Kaur, J., Modi, K. S., Tiwari, U., & Sinha, R. K. (2020). Temperature-assisted broadly unable supercontinuum generation in chalcogenide-glass-based capillary optical fiber. *Journal of the Optical Society of America B-Optical Physics, 37*, 1133–1139.

Sinkin, O. V., Holzlohner, R., Zweck, J., & Menyuk, C. R. (2003). Optimization of the split-step Fourier method in modeling optical-fiber communications systems. *Journal of Lightwave Technology, 21*, 61–68.

Skryabin, D. V., Luan, F., Knight, J. C., & Russell, P. S. (2003). Soliton self-frequency shift cancellation in photonic crystal fibers. *Science, 301*, 1705–1708.

Slusher, R. E., Lenz, G., Hodelin, J., Sanghera, J., Shaw, L. B., & Aggarwal, I. D. (2004). Large Raman gain and nonlinear phase shifts in high-purity As2Se3 chalcogenide fibers. *Journal of the Optical Society of America B-Optical Physics, 21*, 1146–1155.

Sojka, L., Tang, Z., Zhu, H., Beres-Pawlik, E., Furniss, D., Seddon, A. B., Benson, T. M., & Sujecki, S. (2012). Study of mid-infrared laser action in chalcogenide rare earth doped glass with Dy3+, Pr3+ and Tb3+. *Optical Materials Express, 2*, 1632–1640.

Sun, Y. A., Dai, S. X., Zhang, P. Q., Wang, X. S., Xu, Y. S., Liu, Z. J., Chen, F. F., Wu, Y. A., Zhang, Y. J., Wang, R. P., & Tao, G. M. (2015). Fabrication and characterization of multimaterial chalcogenide glass fiber tapers with high numerical apertures. *Optics Express, 23*, 23472–23483.

Tao, G. M., Ebendorff-Heidepriem, H., Stolyarov, A. M., Danto, S., Badding, J. V., Fink, Y., Ballato, J., & Abouraddy, A. F. (2015). Infrared fibers. *Advances in Optics and Photonics, 7*, 379–458.

Thapa, R., Gattass, R. R., Nguyen, V., Chin, G., Gibson, D., Kim, W., Shaw, L. B., & Sanghera, J. S. (2015). Low-loss, robust fusion splicing of silica to chalcogenide fiber for integrated mid-infrared laser technology development. *Optics Letters, 40*, 5074–5077.

Theberge, F., Thire, N., Daigle, J. F., Mathieu, P., Schmidt, B. E., Messaddeq, Y., Vallee, R., & Legare, F. (2014). Multioctave infrared supercontinuum generation in large-core As2S3 fibers. *Optics Letters, 39*, 6474–6477.

Toupin, P., Brilland, L., Troles, J., & Adam, J. L. (2012). Small core Ge-As-Se microstructured optical fiber with single-mode propagation and low optical losses. *Optical Materials Express, 2*, 1359–1366.

Toupin, P., Brilland, L., Mechin, D., Adam, J. L., & Troles, J. (2014). Optical aging of chalcogenide microstructured optical fibers. *Journal of Lightwave Technology, 32*, 2428–2432.

Travers, J. C., & Taylor, J. R. (2009). Soliton trapping of dispersive waves in tapered optical fibers. *Optics Letters, 34*, 115–117.

Troles, J., Coulombier, Q., Canat, G., Duhant, M., Renard, W., Toupin, P., Calvez, L., Renversez, G., Smektala, F., El Amraoui, M., Adam, J. L., Chartier, T., Mechin, D., & Brilland, L. (2010). Low loss microstructured chalcogenide fibers for large nonlinear effects at 1995 nm. *Optics Express, 18*, 26647–26654.

Ung, B., & Skorobogatiy, M. (2010). Chalcogenide microporous fibers for linear and nonlinear applications in the mid-infrared. *Optics Express, 18*, 8647–8659.

Wang, R. P., & Luther-Davies, B. (2013). Structural and physical properties of GexAsySe1-x-y glasses. In *Amorphous chalcogenides: Advances and applications* (pp. 97–141). Pan Stanford Publishing.

Wang, Y. Y., Dai, S. X., Li, G. T., Xu, D., You, C. Y., Han, X., Zhang, P. Q., Wang, X. S., & Xu, P. P. (2017). 1.4–7.2 μm broadband supercontinuum generation in an As-S chalcogenide tapered fiber pumped in the normal dispersion regime. *Optics Letters, 42*, 3458–3461.

Wang, Y. Y., Dai, S. X., Han, X., Zhang, P. Q., Liu, Y. X., Wang, X. S., & Sun, S. C. (2018a). Broadband mid-infrared supercontinuum generation in novel As2Se3-As2Se2S step-index fibers. *Optics Communications, 410*, 410–415.

Wang, Y. Y., Dai, S. X., Peng, X. F., Zhang, P. Q., Wang, X. S., & You, C. Y. (2018b). Mid-infrared supercontinuum generation spanning from 1.9 to 5.7 μm in a chalcogenide fiber taper with ultra-high NA. *Infrared Physics & Technology, 88*, 102–105.

Wang, X. G., Zhao, Z. M., Wang, X. S., Jiao, K., Xue, Z. G., Tian, Y. M., Zhang, P. Q., Shen, X., Dai, S. X., & Wang, R. P. (2019). Mid-infrared supercontinuum generation in low-loss single-mode Te-rich chalcogenide fiber. *Optical Materials Express, 9*, 3487–3493.

Wang, J. J., Feng, Z., Wang, J., Wu, G. L., Liang, X. L., Xiao, J., Xu, T. S., Zhong, M. H., Liu, J., Wang, X. S., Zhao, Z. M., Zhang, P. Q., Nie, Q. H., & Wang, R. P. (2020). Dispersion tuning and supercontinuum generating in novel W-typed chalcogenide fiber. *Infrared Physics & Technology, 111*, 103538.

Weiblen, R. J., Docherty, A., Hu, J., & Menyuk, C. R. (2010). Calculation of the expected bandwidth for a mid-infrared supercontinuum source based on As2S3 chalcogenide photonic crystal fibers. *Optics Express, 18*, 26666–26674.

Weiblen, R. J., Docherty, A., Menyuk, C. R., Shaw, L. B., Sanghera, J. S., & Aggarwal, I. D. (2014). Calculation of the expected output spectrum for a mid-infrared supercontinuum source based on As2S3 chalcogenide photonic crystal fibers. *Optics Express, 22*, 22220–22231.

Wilhelm, A. A., Boussard-Pledel, C., Coulombier, Q., Lucas, J., Bureau, B., & Lucas, P. (2007). Development of far-infrared-transmitting te based glasses suitable for carbon dioxide detection and space optics. *Advanced Materials, 19*, 3796–3800.

Woyessa, G., Kwarkye, K., Dasa, M. K., Petersen, C. R., Sidharthan, R., Chen, S. X., Yoo, S., & Bang, O. (2021). Power stable 1.5–10.5 μm cascaded mid-infrared supercontinuum laser without thulium amplifier. *Optics Letters, 46*, 1129–1132.

Wu, B., Zhao, Z. M., Wang, X. S., Tian, Y. M., Mi, N., Chen, P., Xue, Z. G., Liu, Z. J., Zhang, P. Q., Shen, X., Nie, Q. H., Dai, S. X., & Wang, R. P. (2018a). Mid-infrared supercontinuum generation in a suspended-core tellurium-based chalcogenide fiber. *Optical Materials Express, 8*, 1341–1348.

Wu, Y. M., Meneghetti, M., Troles, J., & Adam, J. L. (2018b). Chalcogenide microstructured optical fibers for mid-infrared supercontinuum generation: Interest, fabrication, and applications. *Applied Sciences, 8*, 1637.

Xia, C. A., Kumar, M., Kulkarni, O. R., Islam, M. N., Terry, F. L., & Freeman, M. J. (2006). Mid-infrared supercontinuum generation to 4.5 μm in ZBLAN fluoride fibers by nanosecond diode pumping. *Optics Letters, 31*, 2553–2555.

Xia, C. N., Xu, Z., Islam, M. N., Terry, F. L., Freeman, M. J., Zakel, A., & Mauricio, J. (2009). 10.5 W time-averaged power mid-IR supercontinuum generation extending beyond 4 μm with direct pulse pattern modulation. *Ieee Journal of Selected Topics in Quantum Electronics, 15*, 422–434.

Xiao, J., Tian, Y. M., Zhao, Z. M., Yao, J. M., Wang, X. S., Chen, P., Xue, Z. G., Peng, X. F., Zhang, P. Q., Shen, X., Nie, Q. H., & Wang, R. P. (2020). Investigation of tellurium-based chalcogenide double-clad fiber for coherent mid-infrared supercontinuum generation. *Optical Fiber Technology, 55*, 102114.

Xing, S. D., Kharitonov, S., Hu, J. Q., & Bres, C. S. (2018). Linearly chirped mid-infrared supercontinuum in all-normal-dispersion chalcogenide photonic crystal fibers. *Optics Express, 26*, 19627–19636.

Yang, Z. Y., Luo, T., Jiang, S. B., Geng, J. H., & Lucas, P. (2010). Single-mode low-loss optical fibers for long-wave infrared transmission. *Optics Letters, 35*, 3360–3362.

Yang, W., Zhang, B., Xue, G., Yin, K., & Hou, J. (2014). Thirteen watt all-fiber mid-infrared supercontinuum generation in a single mode ZBLAN fiber pumped by a 2 μm MOPA system. *Optics Letters, 39*, 1849–1852.

Yao, J. M., Zhang, B., Yin, K., Yang, L. Y., Hou, J., & Lu, Q. S. (2016a). Mid-infrared supercontinuum generation based on cascaded Raman scattering in a few-mode As2S3 fiber pumped by a thulium-doped fiber laser. *Optics Express, 24*, 14717–14724.

Yao, J. M., Zhang, B., Yin, K., Yang, L. Y., Hou, J., & Lu, Q. S. (2016b). Mid-infrared supercontinuum generation in step-index As2S3 fibers pumped by a nanosecond shortwave-infrared supercontinuum pump source. *Optics Express, 24*, 15093–15100.

Yeom, D.-I., Lamont, M., Davies, B. L., & Eggleton, B. J. (2010). Supercontinuum generation in chalcogenide glass waveguides. In J. M. Dudley & J. R. Taylor (Eds.), *Supercontinuum generation in optical fibers*. Cambridge University Press.

Yin, K., Zhang, B., Yao, J. M., Yang, L. Y., Chen, S. P., & Hou, J. (2016). Highly stable, monolithic, single-mode mid-infrared supercontinuum source based on low-loss fusion spliced silica and fluoride fibers. *Optics Letters, 41*, 946–949.

Yin, K., Zhang, B., Yang, L. Y., & Hou, J. (2017a). 15.2 W spectrally flat all-fiber supercontinuum laser source with > 1 W power beyond 3.8 μm. *Optics Letters, 42*, 2334–2337.

Yin, K., Zhang, B., Yao, J. M., Cai, Z., Liu, G. C., & Hou, J. (2017b). Toward high-power all-fiber 2–5 μm aupercontinuum generation in chalcogenide step-index fiber. *Journal of Lightwave Technology, 35*, 4535–4539.

You, C. Y., Dai, S. X., Zhang, P. Q., Xu, Y. S., Wang, Y. Y., Xu, D., & Wang, R. P. (2017). Mid-infrared femtosecond laser-induced damages in As2S3 and As2Se3 chalcogenide glasses. *Scientific Reports, 7*, 6497.

Yu, Y., Zhang, B., Gai, X., Zhai, C. C., Qi, S. S., Guo, W., Yang, Z. Y., Wang, R. P., Choi, D. Y., Madden, S., & Luther-Davies, B. (2015). 1.8–10 μm mid-infrared supercontinuum generated in a step-index chalcogenide fiber using low peak pump power. *Optics Letters, 40*, 1081–1084.

Yuan, W. (2013). 2–10 μm mid-infrared supercontinuum generation in As2Se3 photonic crystal fiber. *Laser Physics Letters, 10*, 095107.

Yuan, Y., Xia, K. L., Wang, Y. Y., Liu, Z. J., Zhang, N., Su, J. X., Jiang, L., Zhang, P. Q., & Dai, S. X. (2019). Precision fabrication of a four-hole Ge15Sb15Se70 chalcogenide suspended-core fiber for generation of a 1.5–12 μm ultrabroad mid-infrared supercontinuum. *Optical Materials Express, 9*, 2196–2205.

Yuan, Y., Yang, P. L., Peng, X. F., Cao, Z. F., Ding, S. J., Zhang, N., Liu, Z. J., Zhang, P. Q., Wang, X. S., & Dai, S. X. (2020). Ultrabroadband and coherent mid-infrared supercontinuum generation in all-normal dispersion Te-based chalcogenide all-solid microstructured fiber. *Journal of the Optical Society of America B-Optical Physics, 37*, 227–232.

Zhang, B., Guo, W., Yu, Y., Zhai, C. C., Qi, S. S., Yang, A. P., Li, L., Yang, Z. Y., Wang, R. P., Tang, D. Y., Tao, G. M., & Luther-Davies, B. (2015). Low Loss, high NA chalcogenide glass fibers for

broadband mid-infrared supercontinuum generation. *Journal of the American Ceramic Society, 98*, 1389–1392.

Zhang, B., Yu, Y., Zhai, C. C., Qi, S. S., Wang, Y. W., Yang, A. P., Gai, X., Wang, R. P., Yang, Z. Y., & Luther-Davies, B. (2016). High brightness 2.2–12 μm mid-infrared supercontinuum generation in a nontoxic chalcogenide step-index fiber. *Journal of the American Ceramic Society, 99*, 2565–2568.

Zhang, Y., Xu, Y. S., You, C. Y., Xu, D., Tang, J. Z., Zhang, P. Q., & Dai, S. X. (2017). Raman gain and femtosecond laser induced damage of Ge-As-S chalcogenide glasses. *Optics Express, 25*, 8886–8895.

Zhang, M. J., Li, L., Li, T. T., Wang, F., Tian, K. Z., Tao, H. Z., Feng, X., Yang, A. P., & Yang, Z. Y. (2019a). Mid-infrared supercontinuum generation in chalcogenide fibers with high laser damage threshold. *Optics Express, 27*, 29286–29295.

Zhang, M. J., Li, T. T., Yang, Y., Tao, H. Z., Zhang, X., Yuan, X., & Yang, Z. Y. (2019b). Femtosecond laser induced damage on Ge-As-S chalcogenide glasses. *Optical Materials Express, 9*, 555–561.

Zhang, N., Peng, X. F., Wang, Y. Y., Dai, S. X., Yuan, Y., Su, J. X., Li, G. T., Zhang, P. Q., Yang, P. L., & Wang, X. S. (2019c). Ultrabroadband and coherent mid-infrared supercontinuum generation in Te-based chalcogenide tapered fiber with all-normal dispersion. *Optics Express, 27*, 10311–10319.

Zhang, J., Li, Y., Zhang, C., Chen, F. F., Zhang, X. H., & Ji, W. (2020). Glass forming region and optical properties of chalcogenide glasses within a gallium-tin-selenium ternary system. *Journal of Non-Crystalline Solids, 545*, 120240.

Zhao, Z. M., Wang, X. S., Dai, S. X., Pan, Z. H., Liu, S., Sun, L. H., Zhang, P., Liu, Z. J., Nie, Q. H., Shen, X., & Wang, R. (2016). 1.5–14 μm midinfrared supercontinuum generation in a low-loss Te-based chalcogenide step-index fiber. *Optics Letters, 41*, 5222–5225.

Zhao, Z. M., Wu, B., Wang, X. S., Pan, Z. H., Liu, Z. J., Zhang, P. Q., Shen, X., Nie, Q. H., Dai, S. X., & Wang, R. P. (2017). Mid-infrared supercontinuum covering 2.0–16 μm in a low-loss telluride single-mode fiber. *Laser & Photonics Reviews, 11*, 1700005.

Zhao, S. L., Yang, H., & Xiao, Y. Z. (2018). Effects of a seed pulse on rogue-wave formation for midinfrared supercontinuum generation in chalcogenide photonic crystal fibers. *Physical Review A, 98*, 043817.

Zhou, X. L., Zhang, X. L., Tao, P. C., Wang, S., Yang, H., Peng, W., & Yu, Q. X.. (2021). Mid-infrared supercontinuum generation in chalcogenide photonic crystal fibers: A Brief Review. In *Seventh symposium on novel photoelectronic detection technology and applications*, 11763.

Zhu, L., Yang, D. D., Wang, L. L., Zeng, J. H., Zhang, Q., Xie, M., Zhang, P. Q., & Dai, S. X. (2018). Optical and thermal stability of Ge-as-Se chalcogenide glasses for femtosecond laser writing. *Optical Materials, 85*, 220–225.

Chapter 14
Quantum Mechanical Theory and Treatment of NLS Equations for Supercontinuum Generation

M. A. Bolorizadeh and A. Safaei Bezgabadi

Abstract The supercontinuum light generated in an appropriate dielectric such as a highly nonlinear dispersive fiber is described quantum mechanically. A Lagrangian is introduced to describe the propagation of light in an inhomogeneous, dispersive, and anisotropic dielectric. Proper creation and annihilation operators are introduced to define the linear part of the Hamiltonian, while the nonlinear term(s) of the Hamiltonian are defined in terms of these operators. As an example, the devised quantum theory is applied to the pulse propagation through an optical fiber. A coupled stochastic nonlinear Schrödinger equation (NLSE) type is obtained via the coherent positive-P representation in order to describe pulse propagation through the optical fiber. This approach is finally applied to the pulse propagation along a photonic crystal fiber when the response function of the medium is taken into account. The coupled stochastic generalized NLSE provided the quantum treatment of the supercontinuum light source. In addition to the coupling form of the equations and the stochastic terms, the main difference between the coupled stochastic equations and its classical form (i.e., GNLSE) is an additional term which has no counterpart in classical form. This additional term is brought about by commutation relations, which holds for creation and annihilation operators. This coupled quantum stochastic equation predicts squeezing in the region of anomalous dispersion, and the fluctuation can be reduced in the vicinity of the formed solitons in the supercontinuum generation process. Also, these equations can be used to study the soliton self-frequency shift quantum mechanically. Here, the coupled equation is

M. A. Bolorizadeh (✉)
Department of Photonics, Faculty of Sciences and Modern Technologies, Graduate University of Advanced Technology, Kerman, Iran
e-mail: mabolori@uk.ac.ir

A. Safaei Bezgabadi
Department of Nanotechnology, Faculty of Sciences and Modern Technologies, Graduate University of Advanced Technology, Kerman, Iran
e-mail: a.safaei@kgut.ac.ir

R. R. Alfano (ed.), *The Supercontinuum Laser Source*,
https://doi.org/10.1007/978-3-031-06197-4_14

simulated in the mean case. The quantum treatment of supercontinuum generation is essential for the high-intensity short-width pulses which are best described as photons.

Keywords Supercontinuum generation · Third-order dispersion · Ostrogradsky's theorem · Generalized nonlinear Schrödinger equation (GNLSE) · Stochastic GNLSE · Quantum soliton · Soliton fission · Fluctuation · Stochastic field · Stochastic variable

14.1 Introduction

Supercontinuum light sources have influenced the advancement of science and technology due to their widespread applications (Agrawal, 2012; Alfano, 2016; Alfano & Shapiro, 1970; Cumberland et al., 2008; Dudley & Genty, 2013; Dudley & Taylor, 2010; Fujimoto, 2003; Li et al., 2021; Venck et al., 2020, Vengris et al., 2019). However, a supercontinuum source exhibits unstable spectrum which affects their common use. The supercontinuum sources exhibit up to 50% fluctuation in their time-dependent profile depending on the initial photon intensity (Corwin et al., 2003; Dudley & Genty, 2013; Gonzalo et al., 2018; Wetzel et al., 2012). This fluctuation is partially dependent on the imperfect structure of fiber or dielectric media. Nonetheless, the fluctuation in the supercontinuum generation, SCG, has quantum origin as well (Corwin et al., 2003; Dudley & Genty, 2013; Gonzalo et al., 2018; Wetzel et al., 2012; Safaei Bezgabadi & Bolorizadeh, 2022). The quantum fluctuation in supercontinuum was studied semi-classically by Corwin et al. (2003), who introduced methodologically an additional term to the classical nonlinear Schrödinger equation. Controlling the supercontinuum source fluctuation is an important issue, yet. However, many researchers are working on different aspects of this fluctuation.

The main goal of this chapter is to describe the supercontinuum generation in a dielectric, such as an optical fiber, quantum mechanically. Here, initially, a Lagrangian is defined for the nonlinear propagation of light in an inhomogeneous, dispersive, and anisotropic dielectric, specifically an optical fiber. Then, the propagating fields are quantized by imposing the standard commutation relations. In the next step, the Hamiltonian is written in terms of creation and annihilation operators. As an example, the present theory is applied for pulse propagation through a simple optical fiber. Making use of the obtained Hamiltonian and the positive-P representation (Drummond & Gardiner, 1980; Drummond et al., 1981), the coupled stochastic nonlinear Schrödinger equation (NLSE) is obtained to describe the pulse propagation along the fiber. In addition, the quantum noise present in this process could be treated by these coupled equations (Drummond & Hillery, 2014). Also, by using these coupled equations, the equations for noise in the vicinity of the input soliton are obtained which they describe soliton squeezing. Finally, this approach is used for pulse propagation along a photonic crystal fiber when the retarded response

function of the medium is considered, and a coupled stochastic generalized NLSE is presented for quantum treatment of the SCG process. The obtained results for the quantum model are simulated in the mean case. The simulation results for quantum model are compared with the simulation results of the classical model. As a methodological standpoint in order to verify the presented quantum model, the simulation results for quantum model are compared with the experimental ones.

14.2 Quantum Theory for Pulse Propagation in a Dielectric

The quantum treatment of field propagation inside a dielectric becomes more important when the electromagnetic field should be described as photons, specifically for quantum photonics technologies (Dechoum et al., 2016; Drummond, 1990; Drummond & Corney, 2001; Drummond & Hillery, 2014; Drummond & Opanchuk, 2020; Drummond et al., 1993; Carter, 1995; Corona et al., 2011; Grangier et al., 1998; Sun et al., 2019; Yao, 1997). In this section, a detailed study of quantum field propagation through a dielectric is presented when dispersion is included up to the third order. The third-order dispersion coefficient was neglected in earlier quantum treatments of the pulse propagation through a dielectric in the literature. Due to the critical role of the third-order dispersion coefficient (Alfano, 2016) on optical phenomena, especially when the second-order dispersion coefficient is zero or infinitesimal, it is essential to include the third-order dispersion coefficient.

Firstly, a proper canonical Lagrangian is introduced which results in Maxwell's equations and the classical energy. Secondly, a constrained quantization approach (Faddeev & Jackiw, 1988; Gitman & Tyutin, 1990) is applied by using Ostrogradsky's theorem (Woodard, 2007) for higher-order field derivatives in the Lagrangian. Finally, a Hamiltonian is derived in terms of properly defined annihilation and creation operators. The resulted annihilation and creation operators are used to obtain the quantum fields that describe electromagnetic waves propagation inside a chosen dielectric in this work. The number operator defines the number of photon-polariton pairs in the dielectric. Additionally, the creation and annihilation operators were used to describe the nonlinearity of pulse propagation in a medium by adding the proper perturbation terms. In the next section, the present quantum theory will be applied to a simple optical fiber when a light signal is propagating along it. This theory has the ability to add the higher-order dispersions and higher nonlinear terms into the governing equations, e.g., to describe supercontinuum generation process.

14.2.1 Classical Energy and the Equation of Motion

It is necessary to define an appropriate canonical Lagrangian to establish a theory for quantization of the pulse propagation along a dielectric. The resulted Hamiltonian and the equations of motion should, respectively, be equal to the classical energy and

Maxwell's equations for the propagation of light in a dielectric when the dispersion terms up to the third-order dispersion are included. The usual definitions that have also been implemented by Drummond and Hillery (Drummond, 1990; Drummond & Hillery, 2014; Hillery, 2009) are used here. One can write the energy density for electromagnetic radiation as:

$$\mathrm{H} = \int_{-\infty}^{t} \left[\mathbf{E}\left(t', \mathbf{x}\right) \cdot \frac{\partial \mathbf{D}\left(t', \mathbf{x}\right)}{\partial t'} + \mathbf{H}\left(t', \mathbf{x}\right) \cdot \frac{\partial \mathbf{B}\left(t', \mathbf{x}\right)}{\partial t'} \right] dt' = \mathrm{H_e} + \mathrm{H_m} \tag{14.1}$$

where $\mathrm{H_e}$ and $\mathrm{H_m}$ are, respectively, the energy density due to the electric and the magnetic fields. The Fourier transform of the fields (e.g., electric field):

$$\mathbf{E}\left(t, \mathbf{x}\right) = \int_{-\infty}^{\infty} \mathbf{e}^{i\omega t} \mathbf{E}\left(\omega, \mathbf{x}\right) d\omega, \tag{14.2}$$

could be replaced in Eq. (14.1). The conditions:

$$\mathbf{E}\left(t, \mathbf{x}\right) = \mathbf{E}^{*}\left(t, \mathbf{x}\right), \tag{14.3a}$$

$$\mathbf{E}\left(-\omega, \mathbf{x}\right) = \mathbf{E}^{*}\left(\omega, \mathbf{x}\right) \tag{14.3b}$$

and

$$\boldsymbol{\varepsilon}\left(-\omega, \mathbf{x}\right) = \boldsymbol{\varepsilon}^{*}\left(\omega, \mathbf{x}\right) \tag{14.3c}$$

hold as the fields are real. One can rewrite $\mathbf{E}(t, \mathbf{x}) \cdot \partial \mathbf{D}(t, \mathbf{x})/\partial t$ in terms of the product of two Fourier integrals as:

$$\mathbf{E}\left(t, \mathbf{x}\right) \cdot \frac{\partial \mathbf{D}\left(t, \mathbf{x}\right)}{\partial t} = i \int_{-\infty}^{\infty} d\omega' \int_{-\infty}^{\infty} d\omega e^{i\left(\omega - \omega'\right)t} \omega \mathbf{E}^{*}\left(\omega', \mathbf{x}\right) \cdot \boldsymbol{\varepsilon}\left(\omega\right) \vdots \mathbf{E}\left(\omega, \mathbf{x}\right). \tag{14.4}$$

A similar argument can be applied to the magnetic part of the energy, which results in:

$$\mathbf{H}\left(t, \mathbf{x}\right) \cdot \frac{\partial \mathbf{B}\left(t, \mathbf{x}\right)}{\partial t} = \frac{i}{\mu} \int_{-\infty}^{\infty} d\omega' \int_{-\infty}^{\infty} d\omega e^{i\left(\omega - \omega'\right)t} \omega \mathbf{B}^{*}\left(\omega', \mathbf{x}\right) \cdot \mathbf{B}\left(\omega, \mathbf{x}\right). \tag{14.5}$$

Note that the difference between the electric filed energy, Eq. (14.4), and the corresponding relation for the magnetic field, Eq. (14.5), is that the magnetic permeability is assumed to be independent of frequency, while the electric permeability is frequency dependent. The frequency integral of Eq. (14.4) is split into two equal

terms, and $-\omega$ is substituted for ω in one of the terms. Then, Eq. (14.4) and Eq. (14.5) are substituted into Eq. (14.1). Finally, by integrating the resulting Eq. (14.1) over time and assuming all the local fields and stored energies are initially zero at $t = -\infty$, one finds the energy density as:

$$\mathrm{H} = \int_{-\infty}^{\infty} d\omega' \int_{-\infty}^{\infty} d\omega e^{i(\omega-\omega')t} \left\{ \mathbf{E}^*\left(\omega', \mathbf{x}\right) \cdot \frac{\left[\omega\boldsymbol{\varepsilon}\left(\omega, \mathbf{x}\right) - \omega'\boldsymbol{\varepsilon}\left(\omega', \mathbf{x}\right)\right]}{2\left(\omega - \omega'\right)} \dot{:}\mathbf{E}\left(\omega, \mathbf{x}\right) + \frac{1}{\mu}\omega\mathbf{B}^*\left(\omega', \mathbf{x}\right) \cdot \mathbf{B}\left(\omega, \mathbf{x}\right) \right\}. \tag{14.6}$$

Assuming a narrowband field at frequency, ω_0, there are significant contributions to the integral, Eq. (14.6), at $\omega = \omega' + \delta\omega \approx \pm\omega_0$. Note that for small values of $\delta\omega$, the relation:

$$\frac{\left[\omega\boldsymbol{\varepsilon}\left(\omega, \mathbf{x}\right) - \omega'\boldsymbol{\varepsilon}(\omega', \mathbf{x})\right]}{(\omega - \omega')} \approx \frac{\partial}{\partial\omega}\left(\omega\boldsymbol{\varepsilon}\left(\omega, \mathbf{x}\right)\right)\Big|_{\omega\simeq\omega'} \tag{14.7}$$

holds. If $\partial(\omega\boldsymbol{\varepsilon}(\omega, \mathbf{x}))/\partial\omega$ varies slowly over the field bandwidth, the time-averaged "linear energy" for the monochromatic pulse propagation at frequency ω through a dielectric is obtained as:

$$H_L = \int d^3\mathbf{x} \left[\frac{1}{2}\mathbf{E}^*\left(t, \mathbf{x}\right) \cdot \left(\frac{\partial\left(\omega\boldsymbol{\varepsilon}\left(\omega, \mathbf{x}\right)\right)}{\partial\omega} \right)_{\sim\text{constant}} \dot{:}\mathbf{E}\Big(t, \mathbf{x}\Big) + \frac{1}{2\mu}|\mathbf{B}\left(t, \mathbf{x}\right)|^2 \right] \tag{14.8}$$

which can be written in terms of displacement fields as:

$$H_L = \int d^3\mathbf{x} \left[\frac{1}{2}\mathbf{D}^*\big(t, \mathbf{x}\big) \cdot \left(\boldsymbol{\eta}\left(\omega, \mathbf{x}\right) - \omega\frac{\partial}{\partial\omega}\boldsymbol{\eta}\left(\omega, \mathbf{x}\right) \right)_{\sim\text{constant}} \dot{:}\mathbf{D}\big(t, \mathbf{x}\big) + \frac{1}{2\mu}|\mathbf{B}\left(t, \mathbf{x}\right)|^2 \right] \tag{14.9}$$

for:

$$\boldsymbol{\eta}\left(\omega, \mathbf{x}\right) = \left(\boldsymbol{\varepsilon}\left(\omega, \mathbf{x}\right)\right)^{-1}. \tag{14.10}$$

Detailed derivation of Equation (14.9) from (14.8) is given in the Appendix.

For a charge free media, one can make use of a dual potential function (Drummond & Hillery, 2014; Drummond, 1990; Hillery, 2009), $\boldsymbol{\Lambda}$, to define the electric displacement and magnetic fields, respectively, as:

$$\mathbf{D}\left(t, \mathbf{x}\right) = \nabla \times \boldsymbol{\Lambda}\left(t, \mathbf{x}\right) \tag{14.11}$$

and:

$$\mathbf{B}\left(t,\mathbf{x}\right)=\mu\dot{\mathbf{\Lambda}}\left(t,\mathbf{x}\right) \tag{14.12}$$

for:

$$\mathbf{\Lambda}\left(t,\mathbf{x}\right)=\sum_{\nu=-N}^{\nu=N}\mathbf{\Lambda}^{\nu}\left(t,\mathbf{x}\right) \tag{14.13}$$

where $2N+1$ narrowband field numbers (mode numbers), ν, are included in the field. The gauge used, here, is different from the usual Coulomb gauge as the dual potential, $\mathbf{\Lambda}(t,\mathbf{x})$ or $\mathbf{\Lambda}^{\nu}(t,\mathbf{x})$, is different from the vector potential. Note that the condition $[\mathbf{\Lambda}^{\nu}(t,\mathbf{x})]^{*}=\mathbf{\Lambda}^{-\nu}(t,\mathbf{x})$ should hold to have real dual function. Expansion of $\boldsymbol{\eta}(\omega,\mathbf{x})$ up to the third order in the Taylor series near the narrow-field frequency, ω^{ν}, leads to:

$$\begin{aligned}\boldsymbol{\eta}\left(\omega,\mathbf{x}\right)\approx{}&\boldsymbol{\eta}_{\nu}\left(\omega^{\nu},\mathbf{x}\right)+\left(\omega-\omega^{\nu}\right)\boldsymbol{\eta}_{\nu}^{(1)}\left(\omega^{\nu},\mathbf{x}\right)+\tfrac{1}{2}(\omega-\omega^{\nu})^{2}\boldsymbol{\eta}_{\nu}^{(2)}\left(\omega^{\nu},\mathbf{x}\right)\\&+\tfrac{1}{6}(\omega-\omega^{\nu})^{3}\boldsymbol{\eta}_{\nu}^{(3)}\left(\omega^{\nu},\mathbf{x}\right)+O\left((\omega-\omega^{\nu})^{4}\right)\end{aligned} \tag{14.14}$$

where:

$$\boldsymbol{\eta}_{\nu}^{(i)}\left(\omega^{\nu},\mathbf{x}\right)=\frac{d^{i}}{d\omega^{i}}\boldsymbol{\eta}_{\nu}\Big(\omega,\mathbf{x}\Big)\Big|_{\omega=\omega^{\nu}}. \tag{14.15}$$

Rewriting Eq. (14.14) as:

$$\boldsymbol{\eta}\left(\omega,\mathbf{x}\right)\approx\boldsymbol{\eta}_{\nu}\left(\mathbf{x}\right)+\omega\boldsymbol{\eta}_{\nu}^{\prime}\left(\mathbf{x}\right)+\frac{1}{2}\omega^{2}\boldsymbol{\eta}_{\nu}^{\prime\prime}\left(\mathbf{x}\right)+\frac{1}{6}\omega^{3}\boldsymbol{\eta}_{\nu}^{\prime\prime\prime}\left(\mathbf{x}\right)+O\left(\left(\omega-\omega^{\nu}\right)^{4}\right) \tag{14.16}$$

where $\boldsymbol{\eta}_{\nu}(\mathbf{x})$, $\boldsymbol{\eta}_{\nu}^{\prime}(\mathbf{x})$, $\boldsymbol{\eta}_{\nu}^{\prime\prime}(\mathbf{x})$ and $\boldsymbol{\eta}_{\nu}^{\prime\prime\prime}(\mathbf{x})$ are, respectively, defined as:

$$\boldsymbol{\eta}_{\nu}\left(\mathbf{x}\right)=\boldsymbol{\eta}_{\nu}\left(\omega^{\nu},\mathbf{x}\right)-\omega^{\nu}\boldsymbol{\eta}_{\nu}^{(1)}\left(\omega^{\nu},\mathbf{x}\right)+\frac{1}{2}\left(\omega^{\nu}\right)^{2}\boldsymbol{\eta}_{\nu}^{(2)}\left(\omega^{\nu},\mathbf{x}\right)-\frac{1}{6}\left(\omega^{\nu}\right)^{3}\boldsymbol{\eta}_{\nu}^{(3)}\left(\omega^{\nu},\mathbf{x}\right), \tag{14.17a}$$

$$\boldsymbol{\eta}_{\nu}^{\prime}\left(\mathbf{x}\right)=\boldsymbol{\eta}_{\nu}^{(1)}\left(\omega^{\nu},\mathbf{x}\right)-\omega^{\nu}\boldsymbol{\eta}_{\nu}^{(2)}\left(\omega^{\nu},\mathbf{x}\right)+\frac{1}{2}\left(\omega^{\nu}\right)^{2}\boldsymbol{\eta}_{\nu}^{(3)}\left(\omega^{\nu},\mathbf{x}\right), \tag{14.17b}$$

$$\boldsymbol{\eta}_{\nu}^{\prime\prime}\left(\mathbf{x}\right)=\boldsymbol{\eta}_{\nu}^{(2)}\left(\omega^{\nu},\mathbf{x}\right)-\omega^{\nu}\boldsymbol{\eta}_{\nu}^{(3)}\left(\omega^{\nu},\mathbf{x}\right) \tag{14.17c}$$

and:

$$\boldsymbol{\eta}_{\nu}^{\prime\prime\prime}\left(\mathbf{x}\right)=\boldsymbol{\eta}_{\nu}^{(3)}\left(\omega^{\nu},\mathbf{x}\right). \tag{14.17d}$$

Note that the quantities $\boldsymbol{\eta}_\nu(\mathbf{x})$, $\boldsymbol{\eta}'_\nu(\mathbf{x})$, $\boldsymbol{\eta}''_\nu(\mathbf{x})$, and $\boldsymbol{\eta}'''_\nu(\mathbf{x})$ are not derivatives of one another. Substituting $\boldsymbol{\eta}(\omega, \mathbf{x})$ from Eq. (14.16) into Eq. (14.9), the time averaged "linear energy" takes the form of:

$$H_L = \int d^3\mathbf{x} \left\{ \frac{1}{2}\mathbf{D}^*(t,\mathbf{x}) \cdot \left(\boldsymbol{\eta}_\nu(\mathbf{x}) - \frac{1}{2}\omega^2 \boldsymbol{\eta}''_\nu(\mathbf{x}) - \frac{1}{3}\omega^3 \boldsymbol{\eta}'''_\nu(\mathbf{x}) \right) \dot{:} \mathbf{D}(t,\mathbf{x}) + \frac{1}{2\mu}|\mathbf{B}(t,\mathbf{x})|^2 \right\}. \tag{14.18}$$

The higher-order terms of expansion (14.14) are neglected with respect to the second-order (if nonzero) and the third-order terms in many applications of optical fibers. Hence, expansion (14.18) is valid for nearly all applications which is free from term $\boldsymbol{\eta}'_\nu(\mathbf{x})$.

Inserting definitions 14.11, 14.12, and 14.13 into Eq. (14.18), one arrives at:

$$\begin{aligned} H_L = \tfrac{1}{12} \sum_{\nu'=-N}^{N} \sum_{\nu=-N}^{N} \int d^3\mathbf{x} \Big\{ \left(\nabla \times \boldsymbol{\Lambda}^{-\nu'}(t,\mathbf{x}) \right) \cdot \big(6\boldsymbol{\eta}_\nu(\mathbf{x}) - 3\omega^2 \boldsymbol{\eta}''_\nu(\mathbf{x}) \\ -2\omega^3 \boldsymbol{\eta}'''_\nu(\mathbf{x}) \big) \dot{:} \left(\nabla \times \boldsymbol{\Lambda}^{\nu}(t,\mathbf{x}) \right) + 6\mu \left(\dot{\boldsymbol{\Lambda}}^{-\nu'}(t,\mathbf{x}) \cdot \dot{\boldsymbol{\Lambda}}^{\nu}(t,\mathbf{x}) \right) \Big\}. \end{aligned} \tag{14.19}$$

Then, taking Fourier transform of Eq. (14.19) and assuming a narrow pulse of frequencies ω^ν, one has:

$$\begin{aligned} H_L = \tfrac{1}{12} \sum_{\nu'=-N}^{N} \sum_{\nu=-N}^{N} \int d^3\mathbf{x} \int d\omega^{\nu'} \int d\omega^{\nu} \Big\{ \Big[6 \left(\nabla \times \boldsymbol{\Lambda}^{-\nu'} \right) \cdot \boldsymbol{\eta}_\nu(\mathbf{x}) \dot{:} \left(\nabla \times \boldsymbol{\Lambda}^{\nu} \right) \\ -3 \left(\nabla \times \boldsymbol{\Lambda}^{-\nu'} \right) \cdot (\omega^\nu)^2 \boldsymbol{\eta}''_\nu(\mathbf{x}) \dot{:} \left(\nabla \times \boldsymbol{\Lambda}^{\nu} \right) - 2 \left(\nabla \times \boldsymbol{\Lambda}^{-\nu'} \right) \cdot (\omega^\nu)^3 \boldsymbol{\eta}'''_\nu(\mathbf{x}) \dot{:} \left(\nabla \times \boldsymbol{\Lambda}^{\nu} \right) \Big] \\ +6\mu \left(\dot{\boldsymbol{\Lambda}}^{-\nu'} \cdot \dot{\boldsymbol{\Lambda}}^{\nu} \right) \Big\} e^{i\left(\omega^\nu - \omega^{\nu'}\right)t} \end{aligned} \tag{14.20}$$

where the frequency and the position vector dependence of the dual potential function are omitted to shorten Eq. (14.20). Applying the superposition principle and the slowly varying envelope approximation (Drummond, 1990; Drummond & Hillery, 2014; Hillery, 2009) over narrowband field numbers -*N* to *N*, the average linear energy for a wideband field could be expressed in terms of the local fields and their time derivatives at the frequency ω^ν. Substituting $\pm i\dot{\boldsymbol{\Lambda}}^{\pm\nu}$ for $\omega^\nu \boldsymbol{\Lambda}^{\pm\nu}$, keeping the symmetry in terms of the field vector derivatives and orthogonality of modes, the inverse Fourier transform of Eq. (14.20) will result in:

$$\begin{aligned} H_L = \tfrac{1}{12} \sum_{\nu=-N}^{N} \int d^3\mathbf{x} \Big\{ \Big[6(\nabla \times \boldsymbol{\Lambda}^{-\nu}) \cdot \boldsymbol{\eta}_\nu(\mathbf{x}) \dot{:} (\nabla \times \boldsymbol{\Lambda}^{\nu}) - 3(\nabla \times \dot{\boldsymbol{\Lambda}}^{-\nu}) \cdot \boldsymbol{\eta}''_\nu(\mathbf{x}) \dot{:} (\nabla \times \dot{\boldsymbol{\Lambda}}^{\nu}) \\ + \mathrm{i}(\nabla \times \dot{\boldsymbol{\Lambda}}^{-\nu}) \cdot \boldsymbol{\eta}'''_\nu(\mathbf{x}) \dot{:} (\nabla \times \ddot{\boldsymbol{\Lambda}}^{\nu}) - \mathrm{i}(\nabla \times \ddot{\boldsymbol{\Lambda}}^{-\nu}) \cdot \boldsymbol{\eta}'''_\nu(\mathbf{x}) \dot{:} (\nabla \times \dot{\boldsymbol{\Lambda}}^{\nu}) \Big] + 6\mu (\dot{\boldsymbol{\Lambda}}^{-\nu} \cdot \dot{\boldsymbol{\Lambda}}^{\nu}) \Big\}. \end{aligned} \tag{14.21}$$

The nonlinear features of pulse propagation in dielectrics are included in the nonlinear part of the energy as perturbations (Drummond, 1990; Drummond & Hillery, 2014). In practice, the medium's response functions are frequency dependent (Alfano, 2016; Boyd, 2008). However, when the response time is relatively fast, the frequency dependence of the medium's nonlinear response function is neglected. In the supercontinuum generation process, the medium's response function is retarded (Agrawal, 2012; Dudley & Taylor, 2010).

Here, Maxwell's equations are the equations of motion for the pulse propagation through a dielectric. $\nabla \cdot \mathbf{D} = 0$ and $\nabla \times \mathbf{H} = \partial \mathbf{D}/\partial t$ are satisfied by definitions (14.11) and (14.12), respectively. Also, it is understood that the dual potential must be a transverse field as $\nabla \cdot \mathbf{B} = 0$. So the main equation of motion is:

$$\nabla \times \mathbf{E}\left(t, \mathbf{x}\right) = -\partial \mathbf{B}\left(t, \mathbf{x}\right)/\partial t, \tag{14.22a}$$

where $\mathbf{E}$ could be generally given by (Alfano, 2016; Boyd, 2008; Drummond & Hillery, 2014):

$$\mathbf{E}\left(t, \mathbf{x}\right) = \sum_{n>0} \left[\int_0^\infty \boldsymbol{\eta}_n \left(\tau_1, \ldots, \tau_n, \mathbf{x}\right) \vdots \left(\mathbf{D}\left(t-\tau_1, \mathbf{x}\right) \otimes \cdots \otimes \mathbf{D}\left(t-\tau_n, \mathbf{x}\right)\right) d\tau_1 \cdots d\tau_n \right] \tag{14.22b}$$

and $\boldsymbol{\eta}_n$ is the nth-order nonlinear response of the medium. It should be noted that $\boldsymbol{\eta}$ in Eq. (14.14) is the linear response of the medium, and, therefore, it is equal to $\boldsymbol{\eta}_1$. However, the quantities $\boldsymbol{\eta}_n$ are assumed to be independent of frequency when $n > 1$.

By implementing Hillery's method (2009) and using the nonlinear polarization term in Maxwell's equations (Alfano, 2016; Boyd, 2008), the nonlinear part of energy is obtained as:

$$H_{NL} = \sum_{n>1} \frac{1}{n+1} \int \mathbf{D}\left(t, \mathbf{x}\right) \cdot \boldsymbol{\eta}_n \left(\mathbf{x}\right) \vdots \mathbf{D}\left(t, \mathbf{x}\right) \otimes \cdots \otimes \mathbf{D}\left(t, \mathbf{x}\right) d^3\mathbf{x}, \tag{14.23}$$

where in terms of the dual functions, it is written as:

$$H_{NL} = \sum_{n>1} \sum_{\nu=-N}^{N} \sum_{\nu_1, \cdots, \nu_n} \frac{1}{n+1} \int \nabla \times \boldsymbol{\Lambda}^{-\nu}\left(t, \mathbf{x}\right) \cdot \boldsymbol{\eta}_n \left(\mathbf{x}\right) \vdots \left(\nabla \times \boldsymbol{\Lambda}^{\nu_1}\left(t, \mathbf{x}\right)\right) \otimes \cdots \otimes \left(\nabla \times \boldsymbol{\Lambda}^{\nu_n}\left(t, \mathbf{x}\right)\right) d^3\mathbf{x}. \tag{14.24}$$

Finally, the total energy can be written as:

$$H = H_L + H_{NL}. \tag{14.25}$$

The equation of motion (14.22a) for the present system is written in terms of dual potential for a mode number, ν, as:

$$-\mu\ddot{\mathbf{\Lambda}}^{\nu}(t,\mathbf{x}) = \nabla\times\left\{\boldsymbol{\eta}_{\nu}(\mathbf{x})\vdots\left[\nabla\times\mathbf{\Lambda}^{\nu}(t,\mathbf{x})\right]+i\boldsymbol{\eta}'_{\nu}(\mathbf{x})\vdots\left[\nabla\times\dot{\mathbf{\Lambda}}^{\nu}(t,\mathbf{x})\right]\right.$$
$$-\tfrac{1}{2}\boldsymbol{\eta}''_{\nu}(\mathbf{x})\vdots\left[\nabla\times\ddot{\mathbf{\Lambda}}^{\nu}(t,\mathbf{x})\right]-\tfrac{i}{6}\boldsymbol{\eta}'''_{\nu}(\mathbf{x})\vdots\left[\nabla\times\dddot{\mathbf{\Lambda}}^{\nu}(t,\mathbf{x})\right]$$
$$\left.+\sum_{n>1}\sum_{\nu;\nu_1,\cdots,\nu_n}\boldsymbol{\eta}_{n}(\mathbf{x})\vdots\left[\left(\nabla\times\mathbf{\Lambda}^{\nu_1}(t,\mathbf{x})\right)\otimes\cdots\otimes\left(\nabla\times\mathbf{\Lambda}^{\nu_n}(t,\mathbf{x})\right)\right]\right\} \tag{14.26}$$

by applying the slowly varying envelope approximation which is demonstrated in the Appendix. Here, the slowly varying envelope approximation requires that $e^{-i\omega^{\nu}\tau}\mathbf{\Lambda}^{\nu}(t-\tau,\mathbf{x})$ is treated as a slowly varying envelope function of τ, and it can be expanded in a Taylor series near $\tau=0$. Generally, a term proportional to $\boldsymbol{\eta}'_{\nu}(\mathbf{x})$ does not appear in the linear dispersive energy, i.e., Eq. (14.18). However, a term proportional to $\boldsymbol{\eta}'_{\nu}(\mathbf{x})$ appears in the wave equation as a result of changes in phase velocity due to dispersion. Note that when the terms proportional to $\boldsymbol{\eta}'''_{\nu}(\mathbf{x})$ are neglected, Eqs. (14.18, 14.19, 14.20, 14.21, 14.22a, 14.22b, 14.23, 14.24, 14.25, and 14.26) are similar to the corresponding equations in reference (Drummond, 1990).

14.2.2 Canonical Lagrangian and Hamiltonian Functions

To establish a quantum theory for the pulse propagation through a nonlinear dispersive dielectric in the presence of third-order dispersion (Drummond, 1990; Drummond & Hillery, 2014), a canonical Lagrangian leading to the equation of motion (14.26) and the classical energy (14.25) should be defined based on Ostrogradsky's theorem (Woodard, 2007). Due to the presence of third-order dispersion, the defined Lagrangian contains higher-order time derivatives. For the pulse propagation through a dielectric when the third-order dispersion is included, the Euler-Lagrange equation for the jth component of the dual potential, $\mathbf{\Lambda}^{\nu}$, is written as:

$$\frac{\partial\mathscr{L}}{\partial\Lambda_j^{\nu}}-\partial_t\left(\frac{\partial\mathscr{L}}{\partial\dot{\Lambda}_j^{\nu}}\right)-\partial_k\left(\frac{\partial\mathscr{L}}{\partial\left(\partial_k\Lambda_j^{\nu}\right)}\right)+\partial_t\partial_k\left(\frac{\partial\mathscr{L}}{\partial\left(\partial_k\dot{\Lambda}_j^{\nu}\right)}\right)-\partial_t\partial_t\partial_k\left(\frac{\partial\mathscr{L}}{\partial\left(\partial_k\ddot{\Lambda}_j^{\nu}\right)}\right)=0 \tag{14.27}$$

where $\mathscr{L}$ is Lagrangian density and k represents the space coordinates x, y, or z. Note that the summation rule is applied to k. For the present system, a proper form for the linear and nonlinear parts of the Lagrangian density will be:

$$\mathcal{L}_L = \frac{1}{2}\sum_{\nu=-N}^{\nu=N}\Bigg[-\left(\nabla\times\mathbf{\Lambda}^{-\nu}\right)\cdot\boldsymbol{\eta}_\nu(\mathbf{x})\vdots\left(\nabla\times\mathbf{\Lambda}^{\nu}\right)-\frac{1}{2}\left(\nabla\times\dot{\mathbf{\Lambda}}^{-\nu}\right)\cdot\boldsymbol{\eta}_\nu''(\mathbf{x})\vdots\left(\nabla\times\dot{\mathbf{\Lambda}}^{\nu}\right)$$
$$-\frac{i}{2}\left(\left(\nabla\times\mathbf{\Lambda}^{-\nu}\right)\cdot\boldsymbol{\eta}_\nu'(\mathbf{x})\vdots\left(\nabla\times\dot{\mathbf{\Lambda}}^{\nu}\right)-\left(\nabla\times\mathbf{\Lambda}^{\nu}\right)\cdot\boldsymbol{\eta}_\nu'(\mathbf{x})\vdots\left(\nabla\times\dot{\mathbf{\Lambda}}^{-\nu}\right)\right)$$
$$+\frac{i}{6}\left(\left(\nabla\times\ddot{\mathbf{\Lambda}}^{-\nu}\right)\cdot\boldsymbol{\eta}_\nu'''(\mathbf{x})\vdots\left(\nabla\times\dot{\mathbf{\Lambda}}^{\nu}\right)-\left(\nabla\times\ddot{\mathbf{\Lambda}}^{\nu}\right)\cdot\boldsymbol{\eta}_\nu'''(\mathbf{x})\vdots\left(\nabla\times\dot{\mathbf{\Lambda}}^{-\nu}\right)\right)+\mu\left(\dot{\mathbf{\Lambda}}^{-\nu}\cdot\dot{\mathbf{\Lambda}}^{\nu}\right)\Bigg] \tag{14.28}$$

and:

$$\mathcal{L}_{NL}=-\sum_{n>1}\sum_{\nu;\nu_1,\cdots,\nu_n}\frac{1}{n+1}\left(\nabla\times\mathbf{\Lambda}^{-\nu}(t,\mathbf{x})\right)\cdot\boldsymbol{\eta}_n(\mathbf{x})\vdots\left[\left(\nabla\times\mathbf{\Lambda}^{\nu_1}(t,\mathbf{x})\right)\otimes\cdots\otimes\left(\nabla\times\mathbf{\Lambda}^{\nu_n}(t,\mathbf{x})\right)\right] \tag{14.29}$$

where the total Lagrangian can be written as:

$$L=\int\left(\mathcal{L}_L+\mathcal{L}_{NL}\right)d^3\mathbf{x}. \tag{14.30}$$

Detailed derivation of the resulted equation of motion and the Hamiltonian, which are, respectively, equal to Equation (14.26) and Equation (14.25), are described in the Appendix. The linear part of the Lagrangian density, Eq. (14.28), is implemented to quantize the propagation of electromagnetic field through a nonlinear dispersive dielectric. As the Lagrangian density (14.28) is a function of higher-order time derivatives of the field, one should implement Ostrogradsky's theorem (Woodard, 2007) for higher-order scalar fields. Here, according to Ostrogradsky's theorem, there are two canonical coordinates $\mathbf{q}^\nu$ and $\mathbf{Q}^\nu$ corresponding to $\mathbf{\Lambda}^\nu$ and $\dot{\mathbf{\Lambda}}^\nu$. These canonical coordinates and their canonical momenta construct a canonical space. The canonical momenta:

$$\mathbf{\Pi}^\nu=\frac{1}{2}\left[\nabla\times\left(-\frac{i}{2}\left(\nabla\times\mathbf{\Lambda}^{-\nu}\right)\cdot\boldsymbol{\eta}_\nu'(\mathbf{x})-\frac{1}{2}\left(\nabla\times\dot{\mathbf{\Lambda}}^{-\nu}\right)\cdot\boldsymbol{\eta}_\nu''(\mathbf{x})+\frac{i}{6}\left(\nabla\times\ddot{\mathbf{\Lambda}}^{-\nu}\right)\cdot\boldsymbol{\eta}_\nu'''(\mathbf{x})\right)+\mu\dot{\mathbf{\Lambda}}^{-\nu}\right] \tag{14.31}$$

and:

$$\mathbf{\Sigma}^\nu=-\frac{i}{12}\nabla\times\left(\left(\nabla\times\ddot{\mathbf{\Lambda}}^{-\nu}\right)\cdot\boldsymbol{\eta}_\nu'''(\mathbf{x})\right) \tag{14.32}$$

correspond respectively to canonical coordinates $\mathbf{q}^\nu$ and $\mathbf{Q}^\nu$ or $\mathbf{\Lambda}^\nu$ and $\dot{\mathbf{\Lambda}}^\nu$. By neglecting the third-order dispersion term, $\boldsymbol{\eta}_\nu'''(\mathbf{x})$, the linear Lagrangian agrees with Eq. (3.117) in reference (Drummond & Hillery, 2014).

In summary, the results obtained by implementing the total Lagrangian agree in both dynamics and energy with the results obtained from Maxwell's equations and Poynting's theorem for slowly varying envelope functions. So, the total Lagrangian, describing the field propagation through a medium with a combination of dispersion, nonlinearity, and inhomogeneity, is unique as one can derive the correct equation of

motion and the Hamiltonian. Additionally, the linear Lagrangian density (14.28) describes the system in the framework of a local field theory of a linear dispersive medium. The first and the last terms of the linear Lagrangian density and the linear Hamiltonian resemble a massless boson, while the remaining terms indicate dispersive correction.

14.2.3 Field Quantization

For the present system, Dirac's commutation relations for the components of vector operators $\mathbf{\Lambda}^{\nu}$and $\mathbf{\Pi}^{\nu}$ are:

$$\left[\Lambda_j^{\nu}\left(t,\mathbf{x}\right),\Pi_{j'}^{\nu}\left(t,\mathbf{x}'\right)\right]=i\hbar\delta_{j,j'}\delta_{\perp}\left(\mathbf{x}-\mathbf{x}'\right). \tag{14.33}$$

Similar commutation relations hold between $\dot{\mathbf{\Lambda}}^{\nu}$ and $\mathbf{\Sigma}^{\nu}$. Since the dual potentials and their canonical momenta are transverse, the commutation relations (14.33) are transverse. Equation (14.33) expresses that the present system is a constrained system (Faddeev & Jackiw, 1988; Gitman & Tyutin, 1990) because no standard commutation relation holds. To extend the common approach of quantization to this constrained quantization, it is necessary to construct the appropriate form of the Dirac commutation relations for new coordinates. Thus, the dual potential functions are expanded in terms of spatial modes as:

$$\mathbf{\Lambda}^{\nu}\left(t,\mathbf{x}\right)=\frac{1}{\sqrt{V}}\sum_{\mathbf{k},\alpha}\lambda_{\mathbf{k},\alpha}^{\nu}(t)\,\hat{\mathbf{e}}_{\mathbf{k},\alpha}\,e^{i\mathbf{k}\cdot\mathbf{x}} \tag{14.34}$$

to rephrase the constraint, where the expansion coefficients are the new coordinates, $\lambda_{\mathbf{k},\alpha}^{\nu}$. By inserting expansion (14.34) into Eq. (14.28), the linear part of Lagrangian is obtained as:

$$\begin{aligned}L_L=\tfrac{1}{2}\sum_{\nu=-N}^{\nu=N}\sum_{\mathbf{k}',\alpha'}\sum_{\mathbf{k},\alpha}\Big\{&-\left(\lambda_{\mathbf{k}',\alpha'}^{\nu}\right)^{*}M_{(\mathbf{k}',\alpha')(\mathbf{k},\alpha)}^{(1)\nu}\lambda_{\mathbf{k},\alpha}^{\nu}-i\Big[\left(\lambda_{\mathbf{k}',\alpha'}^{\nu}\right)^{*}M_{(\mathbf{k}',\alpha')(\mathbf{k},\alpha)}^{(2)\nu}\dot{\lambda}_{\mathbf{k},\alpha}^{\nu}\\&-\left(\dot{\lambda}_{\mathbf{k}',\alpha'}^{\nu}\right)^{*}M_{(\mathbf{k}',\alpha')(\mathbf{k},\alpha)}^{(2)\nu}\lambda_{\mathbf{k},\alpha}^{\nu}\Big]+\left(\dot{\lambda}_{\mathbf{k}',\alpha'}^{\nu}\right)^{*}M_{(\mathbf{k}',\alpha')(\mathbf{k},\alpha)}^{(3)\nu}\dot{\lambda}_{\mathbf{k},\alpha}^{\nu}\\&+i\Big[\left(\ddot{\lambda}_{\mathbf{k}',\alpha'}^{\nu}\right)^{*}M_{(\mathbf{k}',\alpha')(\mathbf{k},\alpha)}^{(4)\nu}\dot{\lambda}_{\mathbf{k},\alpha}^{\nu}-\left(\dot{\lambda}_{\mathbf{k}',\alpha'}^{\nu}\right)^{*}M_{(\mathbf{k}',\alpha')(\mathbf{k},\alpha)}^{(4)\nu}\ddot{\lambda}_{\mathbf{k},\alpha}^{\nu}\Big]\Big\}\end{aligned} \tag{14.35}$$

where:

$$M_{(\mathbf{k}',\alpha')(\mathbf{k},\alpha)}^{(1)\nu}=\frac{1}{V}\int d^3\mathbf{x}\left(\mathbf{k}'\times\hat{\mathbf{e}}_{\mathbf{k}',\alpha'}^{*}\right)\cdot\boldsymbol{\eta}_{\nu}\left(\mathbf{x}\right)\vdots\left(\mathbf{k}\times\hat{\mathbf{e}}_{\mathbf{k},\alpha}\right)e^{i\left(\mathbf{k}-\mathbf{k}'\right)\cdot\mathbf{x}}, \tag{14.36a}$$

$$M_{(\mathbf{k}',\alpha')(\mathbf{k},\alpha)}^{(2)\nu}=\frac{1}{2V}\int d^3\mathbf{x}\left(\mathbf{k}'\times\hat{\mathbf{e}}_{\mathbf{k}',\alpha'}^{*}\right)\cdot\boldsymbol{\eta}_{\nu}'\left(\mathbf{x}\right)\vdots\left(\mathbf{k}\times\hat{\mathbf{e}}_{\mathbf{k},\alpha}\right)e^{i\left(\mathbf{k}-\mathbf{k}'\right)\cdot\mathbf{x}}, \tag{14.36b}$$

$$M^{(3)\nu}_{(\mathbf{k}',\alpha')(\mathbf{k},\alpha)} = \left[\mu \hat{\mathbf{e}}^{*}_{\mathbf{k}',\alpha'} \cdot \hat{\mathbf{e}}_{\mathbf{k},\alpha}\delta_{\mathbf{k}',\mathbf{k}} - \frac{1}{2\mathrm{V}}\int d^3\mathbf{x}\left(\mathbf{k}' \times \hat{\mathbf{e}}^{*}_{\mathbf{k}',\alpha'}\right) \cdot \boldsymbol{\eta}''_{\nu}(\mathbf{x}) \vdots \left(\mathbf{k} \times \hat{\mathbf{e}}_{\mathbf{k},\alpha}\right) e^{i(\mathbf{k}-\mathbf{k}')\cdot\mathbf{x}}\right] \tag{14.36c}$$

and:

$$M^{(4)\nu}_{(\mathbf{k}',\alpha')(\mathbf{k},\alpha)} = \frac{1}{6\mathrm{V}}\int d^3\mathbf{x}\left(\mathbf{k}' \times \hat{\mathbf{e}}^{*}_{\mathbf{k}',\alpha'}\right) \cdot \boldsymbol{\eta}'''_{\nu}(\mathbf{x}) \vdots \left(\mathbf{k} \times \hat{\mathbf{e}}_{\mathbf{k},\alpha}\right) e^{i(\mathbf{k}-\mathbf{k}')\cdot\mathbf{x}}. \tag{14.36d}$$

See the detailed derivation of Equation (14.35) and the coming results, Equation 14.37, in the Appendix. It is important to note that when the medium exhibits losses due to scattering or absorption, they appear as complex values in elements of $\boldsymbol{\eta}_{\nu}(\mathbf{x})$. In turn, these losses appear in matrices M. The M matrices will be diagonal when the response tensor of the medium is isotropic and homogeneous. The linear Lagrangian (14.35) is re-written as:

$$\begin{aligned}\mathrm{L_L} = \sum_{\nu=0}^{\nu=N}\Big\{&-(\lambda^{\nu})^{\dagger}M^{(1)\nu}\lambda^{\nu} - i\left[(\lambda^{\nu})^{\dagger}M^{(2)\nu}\dot{\lambda}^{\nu} - \left(\dot{\lambda}^{\nu}\right)^{\dagger}M^{(2)\nu}\lambda^{\nu}\right]\\ &+\left(\dot{\lambda}^{\nu}\right)^{\dagger}M^{(3)\nu}\dot{\lambda}^{\nu} + i\left[\left(\ddot{\lambda}^{\nu}\right)^{\dagger}M^{(4)\nu}\dot{\lambda}^{\nu} - \left(\dot{\lambda}^{\nu}\right)^{\dagger}M^{(4)\nu}\ddot{\lambda}^{\nu}\right]\Big\}\end{aligned} \tag{14.37}$$

by omitting the summations over (**k**, α, **k'**, α') and the corresponding indices for simplicity. In order to rephrase the constraint and obtain standard commutation relations, the new canonical momenta corresponding to the new set of coordinates are derived as:

$$\pi^{\nu} = \frac{\partial L_L}{\partial\dot{\lambda}^{\nu}} - \frac{\partial L_L}{\partial\ddot{\lambda}^{\nu}} = \left[-i\left(\lambda^{\nu}\right)^{\dagger}M^{(2)\nu} + \left(\dot{\lambda}^{\nu}\right)^{\dagger}M^{(3)\nu} + 2i\left(\ddot{\lambda}^{\nu}\right)^{\dagger}M^{(4)\nu}\right], \tag{14.38a}$$

$$\left(\pi^{\nu}\right)^{\dagger} = iM^{(2)\nu}\lambda^{\nu} + M^{(3)\nu}\dot{\lambda}^{\nu} - 2iM^{(4)\nu}\ddot{\lambda}^{\nu}, \tag{14.38b}$$

$$\sigma^{\nu} = \frac{\partial L_L}{\partial\ddot{\lambda}^{\nu}} = -i\left(\dot{\lambda}^{\nu}\right)^{\dagger}M^{(4)\nu} \tag{14.38c}$$

and:

$$\left(\sigma^{\nu}\right)^{\dagger} = \sigma^{\nu\dagger} = iM^{(4)\nu}\dot{\lambda}^{\nu}. \tag{14.38d}$$

Here, Ostrogradsky's theorem is applied again in order to obtain canonical momenta (14.38) from the Lagrangian density (14.28) where the Ostrogradsky choices for canonical coordinates are $\lambda^{\nu} \equiv q^{\nu}$ and $\dot{\lambda}^{\nu} \equiv Q^{\nu}$. One must impose the standard commutation relations between the canonical coordinates and momenta,

to quantize the fields for the current problem. These relations no longer have transversality restrictions as compared with the operators $\mathbf{\Lambda}^{\nu}$ and $\mathbf{\Pi}^{\nu}$ (or $\dot{\mathbf{\Lambda}}^{\nu}$ and $\mathbf{\Sigma}^{\nu}$). The commutation relations between coordinates and momenta can be simply written as:

$$\left[q^{\nu}_{\mathbf{k},\alpha}, \pi^{\nu}_{\mathbf{k}',\alpha'}\right] = i\hbar\delta_{\mathbf{k},\mathbf{k}'}\delta_{\alpha,\alpha'} \tag{14.39a}$$

and:

$$\left[Q^{\nu}_{\mathbf{k},\alpha}, \sigma^{\nu}_{\mathbf{k}',\alpha'}\right] = i\hbar\delta_{\mathbf{k},\mathbf{k}'}\delta_{\alpha,\alpha'}. \tag{14.39b}$$

It is straightforward to find the linear part of the Hamiltonian in terms of the new canonical coordinates and momenta as:

$$H_L = \sum_{\nu=0}^{N}\left(q^{\nu\dagger}M^{(1)\nu}q^{\nu} + \pi^{\nu}Q^{\nu} + Q^{\nu\dagger}\pi^{\nu\dagger} - Q^{\nu\dagger}M^{(3)^{\nu}}Q^{\nu} + iq^{\nu\dagger}M^{(2)\nu}Q^{\nu} - iQ^{\nu\dagger}M^{(2)\nu}q^{\nu}\right). \tag{14.40}$$

New canonical coordinate:

$$\tilde{q}^{\nu} = A^{\nu}\cdot q^{\nu} + B^{\nu}\cdot Q^{\nu} + C^{\nu}\cdot\pi^{\nu\dagger} + D^{\nu}\cdot\sigma^{\nu\dagger}, \tag{14.41a}$$

and momentum:

$$\tilde{p}^{\nu} = q^{\nu\dagger}\cdot E^{\nu} + Q^{\nu\dagger}\cdot F^{\nu} + \pi^{\nu}\cdot G^{\nu} + \sigma^{\nu}\cdot K^{\nu}, \tag{14.41b}$$

are defined to write the Hamiltonian (14.40) in a simpler form, where A^{ν} to K^{ν} (i.e.; A^{ν}, B^{ν}, C^{ν}, D^{ν}, E^{ν}, F^{ν}, G^{ν} and K^{ν}) are arbitrary invertible complex matrices. The coordinate and momentum, (14.41), obey the standard commutation relation. Thus, the conditions:

$$A^{\nu}\cdot C^{\nu\dagger} + B^{\nu}\cdot D^{\nu\dagger} = C^{\nu}\cdot A^{\nu\dagger} + D^{\nu}\cdot B^{\nu\dagger}, \tag{14.42a}$$

$$E^{\nu\dagger}\cdot G^{\nu} + F^{\nu\dagger}\cdot K^{\nu} = G^{\nu\dagger}\cdot E^{\nu} + K^{\nu\dagger}\cdot F^{\nu} \tag{14.42b}$$

and:

$$A^{\nu}\cdot G^{\nu} + B^{\nu}\cdot K^{\nu} - C^{\nu}\cdot E^{\nu} - D^{\nu}\cdot F^{\nu} = \mathbf{1} \tag{14.42c}$$

hold for the coefficients defined by Eqs. (14.41). Nonetheless, the Hamiltonian (14.40) is written in terms of the defined coordinate and momentum operators as:

$$H_L = \sum_{\nu=0}^{N} \left(\tilde{q}^{\nu\dagger} \cdot \Theta^{\nu} \cdot \tilde{q}^{\nu} + \tilde{p}^{\nu} \cdot \Upsilon^{\nu} \cdot \tilde{p}^{\nu\dagger} + i\, \tilde{q}^{\nu\dagger} \cdot \Delta^{\nu} \cdot \tilde{p}^{\nu\dagger} - i\, \tilde{p}^{\nu} \cdot \left(\Delta^{\nu}\right)^{\dagger} \cdot \tilde{q}^{\nu} \right), \tag{14.43}$$

where Θ^{ν}, Υ^{ν}, and Δ^{ν} are the frequency matrices. Equating the two forms of the Hamiltonian, (14.40) and (14.43), six equations in addition to equations (14.42) relating the frequency matrices and the arbitrary invertible complex matrices A^{ν} to K^{ν} are derived. Therefore, the unknown matrices (the frequency matrices and the matrices A^{ν} to K^{ν}) can be determined. The reader is referred to Appendix for the details of derivation of relations for the matrices A^{ν} to K^{ν}.

Using boson creation and annihilation operators, the linear part of the Hamiltonian is re-expanded. The operators $\mathbf{a}^{\nu}$ and $\mathbf{b}^{\nu}$ are defined as annihilation operators, while $(\mathbf{a}^{\nu})^{\dagger}$ and $(\mathbf{b}^{\nu})^{\dagger}$ are creation operators. These operators are defined as column vectors:

$$\mathbf{a}^{\nu} = \frac{1}{\sqrt{2\hbar}} \left\{ W^{\nu} \cdot \tilde{q}^{\nu} + i \left[\left(W^{\nu}\right)^{\dagger} \right]^{-1} \cdot \left(\tilde{p}^{\nu}\right)^{\dagger} \right\} \tag{14.44}$$

and:

$$\left(\mathbf{b}^{\nu}\right)^{\dagger} = \frac{1}{\sqrt{2\hbar}} \left\{ W^{\nu} \cdot \tilde{q}^{\nu} - i \left[\left(W^{\nu}\right)^{\dagger} \right]^{-1} \cdot \left(\tilde{p}^{\nu}\right)^{\dagger} \right\} \tag{14.45}$$

where the transformation matrix W^{ν} is an invertible complex matrix to be defined. Commutation relations for elements of these operators are:

$$\left[\mathbf{a}_i^{\nu}, \left(\mathbf{a}_j^{\nu}\right)^{\dagger} \right] = \left[\mathbf{b}_i^{\nu}, \left(\mathbf{b}_j^{\nu}\right)^{\dagger} \right] = \delta_{ij} \tag{14.46}$$

and:

$$\left[\mathbf{a}_i^{\nu}, \mathbf{a}_j^{\nu} \right] = \left[\mathbf{b}_i^{\nu}, \mathbf{b}_j^{\nu} \right] = \left[\mathbf{a}_i^{\nu}, \left(\mathbf{b}_j^{\nu}\right)^{\dagger} \right] = \left[\left(\mathbf{a}_i^{\nu}\right)^{\dagger}, \mathbf{b}_j^{\nu} \right] = 0. \tag{14.47}$$

Now, the Hamiltonian (14.43) is written in terms of the creation and the annihilation operators as:

$$H_L = \hbar \sum_{\nu=0}^{N} \left(\mathbf{a}^{\nu}\right)^{\dagger} \cdot \Omega^{\nu} \cdot \mathbf{a}^{\nu} + \hbar \sum_{\nu=1}^{N} \left(\mathbf{b}^{\nu}\right)^{\dagger} \cdot \Omega^{-\nu} \cdot \mathbf{b}^{\nu} \tag{14.48}$$

where $\Omega^{\pm\nu}$ is defined as frequency matrices and the relations:

$$\frac{1}{2} \left(W^{\nu}\right)^{-1} \cdot \left(\Omega^{+\nu} + \Omega^{-\nu}\right) \cdot \left(\left(W^{\nu}\right)^{\dagger} \right)^{-1} = \Upsilon^{\nu}, \tag{14.49a}$$

$$\frac{1}{2} \left(W^{\nu}\right)^{\dagger} \cdot \left(\Omega^{+\nu} - \Omega^{-\nu}\right) \cdot \left(\left(W^{\nu}\right)^{\dagger} \right)^{-1} = \Delta^{\nu} \tag{14.49b}$$

and:

$$\frac{1}{2}\left(W^{\nu}\right)^{\dagger}\cdot\left(\Omega^{+\nu}+\Omega^{-\nu}\right)\cdot W^{\nu}=\Theta^{\nu} \tag{14.49c}$$

hold by equating the two forms of the Hamiltonians (14.43) and (14.48) while neglecting zero-point energy. The relation:

$$\Theta^{\nu}=\left(W^{\nu}\right)^{\dagger}\cdot\left(W^{\nu}\right)\cdot\Upsilon^{\nu}\cdot\left(W^{\nu}\right)^{\dagger}\cdot\left(W^{\nu}\right) \tag{14.50}$$

holds for the matrices W^{ν} by eliminating $\Omega^{\pm\nu}$ in Eqs. (14.49). It could be shown that Eq. (14.48) holds when W^{ν} is the solution to the matrix Eq. (14.50). The corresponding frequency matrices are found as:

$$\Omega^{\pm\nu}=\left[W^{\nu}\cdot\Upsilon^{\nu}\pm\left(\left(W^{\nu}\right)^{\dagger}\right)^{-1}\cdot\Delta^{\nu}\right]\cdot\left(W^{\nu}\right)^{\dagger}. \tag{14.51}$$

In general, the resultant Hamiltonian is not diagonal as the $M^{(1)\nu}$ to $M^{(4)\nu}$ matrices are not diagonal. The matrices $\Omega^{\pm\nu}$ are diagonalized to obtain the frequency bands as:

$$\left[U^{\nu}\cdot\Omega^{\pm\nu}\cdot\left(U^{\nu}\right)^{-1}\right]_{nm}=\omega_{n}^{\pm\nu}\delta_{nm}. \tag{14.52}$$

The final form of the Hamiltonian is:

$$H_{L}=\hbar\sum_{\nu=0}^{N}\sum_{n=0}\omega_{n}^{+\nu}\left(\tilde{\mathbf{a}}_{n}^{\nu}\right)^{\dagger}\cdot\tilde{\mathbf{a}}_{n}^{\nu}+\hbar\sum_{\nu=1}^{N}\sum_{n=0}\omega_{n}^{-\nu}\left(\tilde{\mathbf{b}}_{n}^{\nu}\right)^{\dagger}\cdot\tilde{\mathbf{b}}_{n}^{\nu}, \tag{14.53}$$

where:

$$\tilde{\mathbf{a}}_{n}^{\nu}=U^{\nu}\cdot\mathbf{a}_{n}^{\nu} \tag{14.54}$$

and:

$$\tilde{\mathbf{b}}_{n}^{\nu}=U^{\nu}\cdot\mathbf{b}_{n}^{\nu}. \tag{14.55}$$

The Hamiltonian (14.53) is diagonal operator leading to normal and anomalous modes corresponding to operators $\tilde{\mathbf{a}}^{\nu}$ and $\tilde{\mathbf{b}}^{\nu}$. The operators in Eq. (14.53) indicate the number of photon-polariton pairs of the system. Note that the quantities $M^{(1)\nu}$ to $M^{(3)\nu}$, defined by Eqs. (14.36), change when the third-order dispersion is absent and $M^{(4)\nu}$ is zero.

The nonlinear term in the total Hamiltonian is:

$$H_{NL} = \frac{1}{4}\int \mathbf{D}\,(t,\mathbf{x})\cdot\boldsymbol{\eta}_3\,(\mathbf{x})\,\vdots\mathbf{D}\,(t,\mathbf{x})\,\mathbf{D}\,(t,\mathbf{x})\,\mathbf{D}\,(t,\mathbf{x})\;\;d^3\mathbf{x} \tag{14.56}$$

when only the third-order nonlinear term of Eq. (14.24) is taken into account. This nonlinear part of the Hamiltonian is found in terms of annihilation and creation operators where displacement field is written in terms of these two operators. The theory developed here could properly quantize the electromagnetic radiation in a three-dimensional dielectric, where the third-order nonlinear term is effective. When an optical soliton propagates along a dielectric waveguide, there are fluctuations in the vicinity of the soliton (Drummond & Hillery, 2014; Safaei Bezgabadi et al., 2019, 2020a and 2020b) depending on the intensity of the soliton.

The present quantization scheme is a fundamental basis for squeezing the soliton fluctuations. Drummond applied a model to squeeze the fluctuations for soliton propagation along an optical fiber when the dispersion is expanded up to the second order. In a more realistic view, the third-order dispersion has a vital role for pulse propagation along optical fibers. Therefore, this section provides a basic theory for pulse propagation when the third-order dispersion is included. The method devised here is capable of being extended to higher-order dispersions and also enables one to study quantum aspects of noise in dielectrics, especially fibers (Drummond & Hillery; 2014; Safaei Bezgabadi et al., 2018, 2020a). Generally, quantum treatment of pulse propagation through dielectric waveguides is essential for light propagation along photonic chips used in quantum simulations, quantum sensing, and quantum communications experiments.

14.3 Application of the Present Quantum Theory to an Optical Fiber

In this section, the field propagation along an optical fiber, i.e., a cylindrical optical waveguide, is presented making use of the theory established in the previous section. This field is assumed to be a polarized single-frequency plane wave, i.e. a single transverse mode ν, while the longitudinal mode components have discrete wave numbers k ranging from $-k_{\min}$ to $k_{\max}$. For an optical fiber, it is assumed a cylindrical waveguide whose axis lies along the z-axis. Making use of the dual potential as described by Eq. (14.13) and the Maxwell's equation (14.22a) for the usual case of $\eta(\omega,\mathbf{x}) \equiv \eta(\omega)$, one could derive the wave equation. The wave equation for the dual potential is:

$$\nabla^2\boldsymbol{\Lambda}^{\nu}\,(\omega,\mathbf{x}) + \mu\tilde{\varepsilon}\omega^2\boldsymbol{\Lambda}^{\nu}\,(\omega,\mathbf{x}) = 0 \tag{14.57}$$

where $\tilde{\varepsilon}$ is the permittivity of the medium and the relation:

$$\mu\tilde{\boldsymbol{\varepsilon}}\omega^2 \equiv \mu \begin{pmatrix} \varepsilon_1 & 0 & 0 \\ 0 & \varepsilon_2 & 0 \\ 0 & 0 & \varepsilon_3 \end{pmatrix} \omega^2 = \kappa^2 \mathbf{1}, \tag{14.58}$$

holds. It is also assumed that the three εs are equal. The polarized dual potential is defined as:

$$\boldsymbol{\Lambda}^{\nu}(t, \mathbf{x}) = \boldsymbol{\Gamma}_{\perp}^{\nu} e^{in\varphi} \Lambda^{\nu}(t, z) \tag{14.59}$$

where:

$$\boldsymbol{\Gamma}_{\perp}^{\nu} = \hat{\boldsymbol{\rho}} g^{\nu}(\rho) + \hat{\boldsymbol{\varphi}} f^{\nu}(\rho). \tag{14.60}$$

One can show that the functions $f^{\nu}(\rho)$ and $g^{\nu}(\rho)$ are Bessel functions satisfying the differential equation:

$$\frac{1}{\rho}\frac{d}{d\rho}\left(\rho \frac{dF\left(k_{\rho}\rho\right)}{d\rho}\right) + \left(k_{\rho}^2 - \frac{n^2}{\rho^2}\right) F\left(k_{\rho}\rho\right) = 0 \tag{14.61}$$

where $\kappa^2 = k_{\rho}^2 + k^2$. The boundary conditions lead to the quantized values for k_{ρ}, $k_{\rho}^{(m)}$. Each transverse mode, ν, stands for n and m, and mode -ν corresponds to -n and m.

The displacement vector and the magnetic fields, respectively, are:

$$\mathbf{D}^{\nu}(t, \mathbf{x}) = e^{in\varphi}\partial_z \Lambda^{\nu}(t, z)\, \boldsymbol{\Gamma}_{\perp}^{\nu} \times \hat{\mathbf{z}} + \alpha^{\nu} e^{in\varphi} \Lambda^{\nu}(t, z)\, \hat{\mathbf{z}} = e^{in\varphi}\left(\partial_z \Lambda^{\nu}(t, z)\, g^{\nu}(\rho)\, \hat{\boldsymbol{\varphi}}\right.$$
$$\left. -\partial_z \Lambda^{\nu}\Big(t, z\Big) f^{\nu}(\rho)\, \hat{\boldsymbol{\rho}} + \alpha^{\nu}(\rho)\, \Lambda^{\nu}\Big(t, z\Big)\hat{\mathbf{z}}\right). \tag{14.62}$$

and:

$$\mathbf{B}^{\nu}(t, \mathbf{x}) = \mu \dot{\boldsymbol{\Lambda}}^{\nu}(t, \mathbf{x}) = \mu\left(\hat{\boldsymbol{\rho}} g^{\nu}(\rho) + \hat{\boldsymbol{\varphi}} f^{\nu}(\rho)\right) e^{in\varphi} \dot{\Lambda}^{\nu}(t, z). \tag{14.63}$$

where:

$$\alpha^{\nu}(\rho) = \frac{1}{\rho}\left[\partial_{\rho}\rho f^{\nu}(\rho) - ing^{\nu}(\rho)\right]. \tag{14.64}$$

One could assume the solution to $g^{\nu}(\rho)$ to be:

$$g^{\nu}(\rho) = \frac{1}{\sqrt{\mathscr{N}^{\nu}}} J_{\mathrm{n}}(k_{\rho}^{\mathrm{m}}\rho), \tag{14.65}$$

where $\mathscr{N}^{\nu}$ is a normalization factor.

The gauge condition, $\nabla \cdot \boldsymbol{\Lambda}(t, \mathbf{x}) = 0$, for the dual potential, leads to:

$$\rho \frac{dg^{\nu}(\rho)}{d\rho} + g^{\nu}(\rho) + inf^{\nu}(\rho) = 0 \tag{14.66}$$

where the final form for $f^{\nu}(\rho)$ is:

$$f^{\nu}(\rho) = i\left(\frac{n+1}{n\sqrt{\mathscr{A}^{\nu}}}\right)\mathrm{J}_n(k_{\rho}^{m}\rho) - \frac{i}{n\sqrt{\mathscr{A}^{\nu}}}\mathrm{J}_{n+1}(k_{\rho}^{m}\rho)\ . \tag{14.67}$$

In order to find $\mathscr{A}^{\nu}$, the condition:

$$\int_0^{\infty} d\rho \int_0^{2\pi} d\varphi\rho \left(f^{-\nu}(\rho)\, f^{\nu}(\rho) + g^{-\nu}(\rho)\, g^{\nu}(\rho)\right) = 1. \tag{14.68}$$

should be satisfied.

It is assumed that the response tensor for the medium is homogeneous and isotropic ($\eta_{\nu}(\mathbf{x}) = \eta_{\nu}$) and that the first nonzero nonlinear term corresponds to η_3 (centro-symmetric media). The linear part of the Lagrangian density (Eq. (14.28)) and the Hamiltonian (Eq. (14.21)) can be, respectively, simplified to:

$$\begin{aligned} L_L = \tfrac{1}{2}\sum_{\nu=-N}^{\nu=N} \int \{ & \left[-\eta_{\nu}\left[\partial_z \Lambda^{-\nu}(t,z)\partial_z \Lambda^{\nu}(t,z) + Y^{\nu}\Lambda^{-\nu}(t,z)\Lambda^{\nu}(t,z)\right]\right. \\ & - \tfrac{i}{2}\eta'_{\nu}\left[\partial_z \Lambda^{-\nu}(t,z)\partial_z \dot{\Lambda}^{\nu}(t,z) + Y^{\nu}\Lambda^{-\nu}(t,z)\dot{\Lambda}^{\nu}(t,z) - \partial_z \Lambda^{\nu}(t,z)\partial_z \dot{\Lambda}^{-\nu}(t,z) - Y^{\nu}\Lambda^{\nu}(t,z)\dot{\Lambda}^{-\nu}(t,z)\right] \\ & + \tfrac{i}{6}\eta'''_{\nu}\left[\partial_z \ddot{\Lambda}^{-\nu}(t,z)\partial_z \dot{\Lambda}^{\nu}(t,z) + Y^{\nu}\ddot{\Lambda}^{-\nu}(t,z)\dot{\Lambda}^{\nu}(t,z) - \partial_z \ddot{\Lambda}^{\nu}(t,z)\partial_z \dot{\Lambda}^{-\nu}(t,z) - Y^{\nu}\ddot{\Lambda}^{\nu}(t,z)\dot{\Lambda}^{-\nu}(t,z)\right] \\ & \left. - \tfrac{1}{2}\eta''_{\nu}\left[\partial_z \dot{\Lambda}^{-\nu}(t,z)\partial_z \dot{\Lambda}^{\nu}(t,z) + Y^{\nu}\dot{\Lambda}^{-\nu}(t,z)\dot{\Lambda}^{\nu}(t,z)\right]\right] + \mu\left(\dot{\Lambda}^{-\nu}(t,z)\dot{\Lambda}^{\nu}(t,z)\right)\Big\}\, dz \end{aligned} \tag{14.69}$$

and:

$$\begin{aligned} H_L = \tfrac{1}{2}\sum_{\nu=-N}^{\nu=N} \int \{ & \left[\eta_{\nu}\left(\partial_z \Lambda^{-\nu}(t,z)\partial_z \Lambda^{\nu}(t,z) + Y^{\nu}\Lambda^{-\nu}(t,z)\Lambda^{\nu}(t,z)\right)\right. \\ & + \tfrac{i}{6}\eta'''_{\nu}\left[\partial_z \ddot{\Lambda}^{-\nu}(t,z)\partial_z \dot{\Lambda}^{\nu}(t,z) + Y^{\nu}\ddot{\Lambda}^{-\nu}(t,z)\dot{\Lambda}^{\nu}(t,z) - \partial_z \ddot{\Lambda}^{\nu}(t,z)\partial_z \dot{\Lambda}^{-\nu}(t,z) - Y^{\nu}\ddot{\Lambda}^{\nu}(t,z)\dot{\Lambda}^{-\nu}(t,z)\right] \\ & \left. - \tfrac{1}{2}\eta''_{\nu}\left[\partial_z \dot{\Lambda}^{-\nu}(t,z)\partial_z \dot{\Lambda}^{\nu}(t,z) + Y^{\nu}\dot{\Lambda}^{-\nu}(t,z)\dot{\Lambda}^{\nu}(t,z)\right]\right] + \mu\left(\dot{\Lambda}^{-\nu}(t,z)\dot{\Lambda}^{\nu}(t,z)\right)\Big\}\, dz \end{aligned} \tag{14.70}$$

where:

$$Y^{\nu} = 2\pi \int_0^{\infty} \left[\frac{1}{\rho}\left(\left(d\rho f^{\nu}/d\rho\right)\left(d\rho f^{-\nu}/d\rho\right) + n^2 g^{\nu} g^{-\nu} + ing^{-\nu}\left(d\rho f^{\nu}/d\rho\right) - ing^{\nu}\left(d\rho f^{-\nu}/d\rho\right)\right)\right] d\rho. \tag{14.71}$$

Similar to the definition (14.34), the scalar field $\Lambda^{\nu}(t,z)$ is defined in terms of the canonical coordinates $\lambda_k^{\nu}(t)$ as:

$$\Lambda^{\nu}(t,z) = \left(1/\sqrt{L}\right)\sum\nolimits_k \lambda_k^{\nu}(t) e^{ikz}. \tag{14.72}$$

where L is the length of the optical fiber. Therefore, the linear part of the Lagrangian for the field propagation along the optical fiber can be written as:

$$L_L = \frac{1}{2}\sum_{\nu=-N}^{\nu=N}\sum_k \mathscr{C}_k^{\nu}\left[-\lambda_{-k}^{-\nu}\lambda_k^{\nu}\eta_{\nu} - \frac{i}{2}\left(\lambda_{-k}^{-\nu}\dot{\lambda}_k^{\nu} - \dot{\lambda}_{-k}^{-\nu}\lambda_k^{\nu}\right)\eta'_{\nu} + \mathscr{M}_k^{\nu}\dot{\lambda}_{-k}^{-\nu}\dot{\lambda}_k^{\nu} + \frac{i}{6}\left(\ddot{\lambda}_{-k}^{-\nu}\dot{\lambda}_k^{\nu} - \dot{\lambda}_{-k}^{-\nu}\ddot{\lambda}_k^{\nu}\right)\eta'''_{\nu}\right] \tag{14.73a}$$

where $\mathcal{C}_k^{\nu} = (k^2 + \Upsilon^{\nu})$ and $\mathcal{M}_k^{\nu} = \mu(\mathcal{C}_k^{\nu})^{-1} - \eta_{\nu}''/2$, making use of Equation (14.28). The Lagrangian (14.73a) will be:

$$L_L = \frac{1}{2}\sum_{\nu=0}^{\nu=N}\sum_k \mathcal{C}_k^{\nu}\left[-(\lambda_k^{\nu})^{\dagger}\lambda_k^{\nu}\eta_{\nu} - \frac{i}{2}\left((\lambda_k^{\nu})^{\dagger}\dot{\lambda}_k^{\nu} - \left(\dot{\lambda}_k^{\nu}\right)^{\dagger}\lambda_k^{\nu}\right)\eta_{\nu}' + \mathcal{M}_k^{\nu}\left(\lambda_k^{\nu}\right)^{\dagger}\lambda_k^{\nu} + \frac{i}{6}\left(\left(\ddot{\lambda}_k^{\nu}\right)^{\dagger}\dot{\lambda}_k^{\nu} - \left(\dot{\lambda}_k^{\nu}\right)^{\dagger}\ddot{\lambda}_k^{\nu}\right)\eta_{\nu}'''\right] \tag{14.73b}$$

where $\lambda_{-k}^{-\nu} \equiv \left(\lambda_k^{\nu}\right)^{\dagger}$, $\dot{\lambda}_{-k}^{-\nu} \equiv \left(\dot{\lambda}_k^{\nu}\right)^{\dagger}$ and $\ddot{\lambda}_{-k}^{-\nu} \equiv \left(\ddot{\lambda}_k^{\nu}\right)^{\dagger}$. It is assumed earlier that a single transverse mode ν for mode numbers n and m are considered, so the summation over ν in Eq. (14.73b) is dropped for the rest of this section.

The canonical momenta associated with $\lambda_k \equiv \lambda_k^{\nu}$, $\lambda_k^{\dagger} \equiv \left(\lambda_k^{\nu}\right)^{\dagger}$, $\dot{\lambda}_k \equiv \dot{\lambda}_k^{\nu}$ and $\dot{\lambda}_k^{\dagger} \equiv \left(\dot{\lambda}_k^{\nu}\right)^{\dagger}$ are:

$$\pi_k \equiv \pi_k^{\nu} = \frac{\partial L_L}{\partial \dot{\lambda}_k^{\nu}} - \frac{\partial L_L}{\partial \ddot{\lambda}_k^{\nu}} = \left[-\frac{i}{2}\eta_{\nu}'\lambda_k^{\dagger} + \mathcal{M}_k^{\nu}\dot{\lambda}_k^{\dagger} + \frac{i}{3}\eta_{\nu}'''\ddot{\lambda}_k^{\dagger}\right]\mathcal{C}_k^{\nu} \tag{14.74}$$

$$\pi_k^{\dagger} = \left[\frac{i}{2}\eta_{\nu}'\lambda_k + \mathcal{M}_k^{\nu}\dot{\lambda}_k - \frac{i}{3}\eta_{\nu}'''\ddot{\lambda}_k\right]\mathcal{C}_k^{\nu}, \tag{14.75}$$

$$\sigma_k \equiv \sigma_k^{\nu} = \frac{\partial L_L}{\partial \ddot{\lambda}_k^{\nu}} = -\frac{i}{6}\mathcal{C}_k^{\nu}\eta_{\nu}'''\dot{\lambda}_k^{\dagger} \tag{14.76}$$

and:

$$\sigma_k^{\dagger} = \frac{i}{6}\mathcal{C}_k^{\nu}\eta_{\nu}'''\dot{\lambda}_k, \tag{14.77}$$

respectively, when Ostrogradsky's theorem (Woodard, 2007) is implemented. The canonical coordinates are q_k, $q_k^{\dagger}$, Q_k, and $Q_k^{\dagger}$ which are equal to λ_k, $\lambda_k^{\dagger}$, $\dot{\lambda}_k$, and $\dot{\lambda}_k^{\dagger}$, respectively. Similarly, the linear part of the Hamiltonian, H_L, for field propagation along optical fibers is written as Eq. (14.40). Here, the M matrices defined by Equations (14.36) are diagonal, and they are obtained as:

$$M_{k',k}^{(1)\nu} = \mathcal{C}_k^{\nu}\eta_{\nu}\delta_{k',k}, \tag{14.78a}$$

$$M_{k',k}^{(2)\nu} = \frac{1}{2}\mathcal{C}_k^{\nu}\eta_{\nu}'\delta_{k',k}, \tag{14.78b}$$

$$M_{k',k}^{(3)\nu} = \left[\mu - \frac{1}{2}\mathcal{C}_k^{\nu}\eta_{\nu_0}''\right]\delta_{k',k} \tag{14.78c}$$

and:

$$M_{k',k}^{(4)\nu} = \frac{1}{6}\mathcal{C}_k^{\nu}\eta_{\nu}'''\delta_{k',k}. \tag{14.78d}$$

Note should be added that a careful comparison between the dual potential defined by Eq. (14.34) and the dual potential of a system with discrete modes, similar to our example, is needed to find the correct M matrices.

In order to use the Hamiltonian (14.43), the frequency matrices (Θ^{ν}, Υ^{ν}, and Δ^{ν}) and the arbitrary invertible complex matrices A^{ν} to K^{ν} must be determined. For the present simple example, these matrices are reduced to complex numbers. By using the six obtained relations and conditions (14.42), these complex numbers can be obtained.

Similar to operators given by Eqs. (14.41), new canonical coordinates, $\tilde{q}_k^{\nu}$, and momenta, $\tilde{p}_k^{\nu}$, are defined as:

$$\tilde{q}_k^{\nu} = A_k^{\nu} \cdot q_k^{\nu} + B_k^{\nu} \cdot Q_k^{\nu} + C_k^{\nu} \cdot \pi_k^{\nu\dagger} + D_k^{\nu} \cdot \sigma_k^{\nu\dagger} \tag{14.79}$$

and:

$$\tilde{p}_k^{\nu} = q_k^{\nu\dagger} \cdot E_k^{\nu} + Q_k^{\nu\dagger} \cdot F_k^{\nu} + \pi_k^{\nu} \cdot G_k^{\nu} + \sigma_k^{\nu} \cdot K_k^{\nu}. \tag{14.80}$$

In this one-dimensional example, the field is quantized when operators $\tilde{q}_k^{\nu}$ and $\tilde{p}_k^{\nu}$ obey the commutation relation:

$$\left[\tilde{q}_k^{\nu}, \tilde{p}_{k'}^{\nu}\right] = i\hbar\delta_{k,k'}. \tag{14.81}$$

Operators defined by Eqs. (14.44) and (14.45) are, respectively, given as:

$$a_k^{\nu} = \frac{1}{\sqrt{2\hbar}} \left\{ W_k^{\nu} \cdot \tilde{q}_k^{\nu} + i\left[\left(W_k^{\nu}\right)^*\right]^{-1} \cdot \left(\tilde{p}_k^{\nu}\right)^{\dagger} \right\} \tag{14.82}$$

and:

$$\left(b_k^{\nu}\right)^{\dagger} = \frac{1}{\sqrt{2\hbar}} \left\{ W_k^{\nu} \cdot \tilde{q}_k^{\nu} - i\left[\left(W_k^{\nu}\right)^*\right]^{-1} \cdot \left(\tilde{p}_k^{\nu}\right)^{\dagger} \right\} \tag{14.83}$$

where W_k^{ν} is generally a complex number. The creation operator $\left(a_k^{\nu}\right)^{\dagger}$ and the annihilation operator b_k^{ν} are likewise defined. Therefore, the linear part of Hamiltonian is:

$$H_L = \hbar \sum_k \omega^{+\nu}(k) \left(a_k^{\nu}\right)^{\dagger} a_k^{\nu} + \hbar \sum_k \omega^{-\nu}(k) \left(b_k^{\nu}\right)^{\dagger} b_k^{\nu} \tag{14.84}$$

while $\omega(k)$ is the solution to equations:

$$\omega^{\pm\nu}(k) = \left|W_k^{\nu}\right|^2 \Upsilon^{\nu} \pm \Delta^{\nu} \tag{14.85}$$

where W_k^{ν} is given as:

$$\left|W_k^{\nu}\right|^4 = \frac{\Theta^{\nu}}{\Upsilon^{\nu}}. \tag{14.86}$$

In order to calculate the nonlinear parts of the Hamiltonian, Eq. (14.56), it is essential to obtain Λ_k^ν (or equivalently λ_k^ν). It is straightforward to find the equation of motion as:

$$\vartheta_k^\nu \dot{\lambda}_k^\nu + \upsilon_k^\nu \lambda_k^\nu = \sqrt{\frac{\hbar}{2}} \varsigma_k^\nu a_k^\nu(t) + \sqrt{\frac{\hbar}{2}} \xi_k^\nu \left(b_k^\nu(t)\right)^\dagger \tag{14.87}$$

where:

$$\varsigma_k^\nu = \left[\left(G_k^\nu\right)^* \left(W_k^\nu\right)^{-1} + i C_k^\nu \left(W_k^\nu\right)^* \right], \tag{14.88}$$

$$\xi_k^\nu = \left[\left(G_k^\nu\right)^* \left(W_k^\nu\right)^{-1} - i C_k^\nu \left(W_k^\nu\right)^* \right], \tag{14.89}$$

$$\upsilon_k^\nu = A_k^\nu \left(G_k^\nu\right)^* - C_k^\nu \left(E_k^\nu\right)^* \tag{14.90}$$

and:

$$\vartheta_k^\nu = \left[B_k^\nu \left(G_k^\nu\right)^* + i D_k^\nu \left(G_k^\nu\right)^* M^{(4)\nu} - C_k^\nu \left(F_k^\nu\right)^* - i C_k^\nu \left(K_k^\nu\right)^* M^{(4)\nu} \right]. \tag{14.91}$$

Note that the Ostrogradsky's choices for canonical coordinates are $q^\nu \equiv \lambda^\nu$ and $Q^\nu \equiv \dot{\lambda}^\nu$.

According to the Heisenberg equation of motion, the operators $a_k^\nu(t)$ and $\left(b_k^\nu(t)\right)^\dagger$ evolve as $a_k^\nu(t) = a_k^\nu(0) e^{-i\,\omega^{+\nu}(k)t}$ and $\left(b_k^\nu(t)\right)^\dagger = \left(b_k^\nu(0)\right)^\dagger e^{i\,\omega^{-\nu}(k)t}$, respectively. The solution to Eq. (14.87) can be straightforwardly given as:

$$\lambda_k^\nu(t) = \left(\lambda_k^\nu(0) - C_2 - C_3\right) e^{-C_1\, t} + C_2 e^{-i\,\omega^{+\nu}(k)t} + C_3 e^{i\,\omega^{-\nu}(k)t} \tag{14.92}$$

where:

$$C_1 = \frac{\upsilon_k^\nu}{\vartheta_k^\nu}, \tag{14.93}$$

$$C_2 = \frac{\sqrt{\hbar/2}\varsigma_k^\nu}{\left[\upsilon_k^\nu - i\,\omega^{+\nu}(k)\vartheta_k^\nu\right]} a_k^\nu(0) \tag{14.94}$$

and:

$$C_3 = \frac{\sqrt{\hbar/2}\xi_k^\nu}{\left[\upsilon_k^\nu + i\,\omega^{-\nu}(k)\vartheta_k^\nu\right]} \left(b_k^\nu(0)\right)^\dagger. \tag{14.95}$$

In most optical waveguides, especially those used for SCG, C_1 is a relatively large positive number as $C_1 \propto \left|\eta_\nu''/\eta_\nu'''\right|$, so that the first term in the right side of Eq. (14.92) can be neglected compared with other terms. In addition, the third term

should be dropped as it corresponds to the anomalous modes (non-physical modes) defined by the operators b_k^{ν} and $\left(b_k^{\nu}\right)^{\dagger}$. The reader is referred to (Drummond, 1990) for detailed discussion on the anomalous modes. Therefore, Eq. (14.92) will be:

$$\lambda_k^{\nu}(t) \approx \frac{\sqrt{\hbar/2}\varsigma_k^{\nu}}{\left[\upsilon_k^{\nu} - i\ \omega^{+\nu}(k)\vartheta_k^{\nu}\right]} a_k^{\nu}(0) e^{-i\ \omega^{+\nu}(k)t}. \tag{14.96}$$

Making use of the scalar field, $\Lambda^{\nu}(t,z)$, defined by Eq. (14.72), one can rewrite it for the mode ν in terms of the annihilation operator a_k^{ν}:

$$\Lambda^{\nu}(t,z) = \frac{1}{\sqrt{L}} \sum\nolimits_k \frac{\sqrt{\hbar/2}}{\mathcal{N}_k^{\nu}} a_k^{\nu}(t) e^{ikz} \tag{14.97a}$$

where:

$$\mathcal{N}_k^{\nu} = \frac{\upsilon_k^{\nu} - i\,\omega^{+\nu}(k)\vartheta_k^{\nu}}{\varsigma_k^{\nu}}. \tag{14.97b}$$

It is assumed a single transverse mode ν; thus, the displacement vector is:

$$\mathbf{D}(\mathbf{x},t) = \mathbf{D}^{\nu}(\mathbf{x},t) + \mathbf{D}^{-\nu}(\mathbf{x},t). \tag{14.98}$$

Making use of Eqs. (14.97a) and (14.62), one has:

$$\mathbf{D}^{\nu}(t,\mathbf{x}) = \frac{1}{\sqrt{L}} \sum_k \frac{\sqrt{\hbar/2}\mathbf{Z}_k^{\nu}}{\mathcal{N}_k^{\nu}} a_k^{\nu}(t) e^{in\varphi} e^{ikz} \tag{14.99}$$

where:

$$\mathbf{Z}_k^{\nu} = ik\left[-\hat{\boldsymbol{\rho}} f^{\nu}(\rho) + g^{\nu}(\rho)\,\hat{\boldsymbol{\varphi}}\right] + \alpha^{\nu}(\rho)\,\hat{\mathbf{z}}. \tag{14.100}$$

The formalism introduced in this section can describe the propagation of quantum fields in nonlinear dispersive optical fibers. Assuming the field wavenumber and frequency to be near k_0 and $\omega = \omega(k_0)$, respectively, the slowly varying quantum photon-polariton field is defined as (Drummond & Hillery, 2014; Safaei et al., 2018):

$$\psi(z,t) = \frac{1}{\sqrt{L}} \sum_k e^{i(k-k_0)z} a_k(t) \tag{14.101}$$

to describe the field propagation along an optical fiber with nonlinearity η_3.

Ignoring the smearing effect for all practical purposes, the commutation relation for these fields can be expressed as:

$$\left[\psi(z,t), \psi^{\dagger}\left(z',t'\right)\right] = \delta\left(z-z'\right)\delta\left(t-t'\right), \tag{14.102}$$

which is applicable for temporally ultrashort fields. Inverting the relation between a_k and $\psi(z,t)$ yields:

$$a_k(t) = \frac{1}{\sqrt{L}} \int \psi\,(z,t)\, e^{-i(k-k_0)z} dz. \tag{14.103}$$

One can insert Eq. (14.103) into Eq. (14.84) to express the Hamiltonian in terms of $\psi(z,t)$. Here, the first term of Eq. (14.84), i.e., normal solution, is taken into account. Thus, the linear part of Hamiltonian can be written as:

$$H_L = \hbar \sum_k \omega(k) \mathrm{a}_k^\dagger \mathrm{a}_k = \frac{\hbar}{\mathrm{L}} \int dz \int dz' \left(\sum_k \omega(k) e^{i(k-k_0)(z-z')} \right) \psi^\dagger\,(z,t)\, \psi\,(z',t)\,. \tag{14.104}$$

Expanding $\omega(k)$ near k_0 as:

$$\omega(k) = \omega\,(k_0) + (k-k_0)\,\omega' + \frac{1}{2}(k-k_0)^2\omega'' + \frac{1}{6}(k-k_0)^3\omega''' + \ldots, \tag{14.105}$$

where $\omega'\left(=d\omega/dk|_{k=k_0}\right)$, $\omega''\left(=d^2\omega/dk^2|_{k=k_0}\right)$, and $\omega'''\left(=d^3\omega/dk^3|_{k=k_0}\right)$ are the group velocity and the first and second derivatives of group velocity, respectively. The expression in the parenthesis in Eq. (14.104) becomes:

$$\frac{1}{L}\sum_k \omega(k) e^{i(k-k_0)(z-z')} \cong \frac{1}{L}\sum_k \left[\omega\,(k_0) + \omega'\,(k-k_0) + \frac{1}{2}\omega''(k-k_0)^2 + \frac{1}{6}\omega'''(k-k_0)^3 \right] e^{i(k-k_0)(z-z')} \tag{14.106}$$

where the operator form is written as:

$$\begin{aligned} \tfrac{1}{L}\textstyle\sum_k \omega(k) e^{i(k-k_0)(z-z')} &\cong \tfrac{1}{L}\textstyle\sum_k \left[\omega\,(k_0) + \tfrac{i}{2}\omega'\left(\partial_{z'} - \partial_z\right) + \tfrac{1}{2}\omega''\partial_z\partial_{z'} + \tfrac{i}{12}\omega'''\left(\partial_z\left(\partial_{z'}\right)^2 - (\partial_z)^2\partial_{z'}\right)\right] e^{i(k-k_0)(z-z')} \\ &\cong \left[\omega\,(k_0) + \tfrac{i}{2}\omega'\left(\partial_{z'} - \partial_z\right) + \tfrac{1}{2}\omega''\partial_z\partial_{z'} + \tfrac{i}{12}\omega'''\left(\partial_z\left(\partial_{z'}\right)^2 - (\partial_z)^2\partial_{z'}\right)\right] \delta\,(z-z')\,. \end{aligned} \tag{14.107}$$

The linear part of Hamiltonian is, therefore, given by:

$$H_L = \hbar \int \left[\omega\,(k_0)\,\psi^\dagger\psi + \frac{i}{2}\omega' \left(\psi^\dagger \frac{\partial\psi}{\partial z} - \hat{\psi}\frac{\partial\psi^\dagger}{\partial z} \right) + \frac{1}{2}\omega'' \frac{\partial\psi^\dagger}{\partial z}\frac{\partial\psi}{\partial z} + \frac{i}{12}\omega''' \left(\frac{\partial\psi^\dagger}{\partial z}\left(\frac{\partial^2\psi}{\partial z^2}\right) - \left(\frac{\partial^2\psi^\dagger}{\partial z^2}\right)\frac{\partial\psi}{\partial z} \right) \right] dz, \tag{14.108}$$

where the argument of the photon-polariton field has been eliminated for simplicity. The nonlinear part of the Hamiltonian is given by:

$$\mathrm{H}_{NL} = \frac{1}{4}\int d^3\mathbf{x}\ \eta_3 \cdot (\mathbf{D}(t,\mathbf{x}))^4, \tag{14.109}$$

for:

$$\mathbf{D}^{\nu}(t,\mathbf{x}) = \frac{1}{L^2}\sum_k \frac{\sqrt{\hbar/2}\mathbf{Z}_k^{\nu}}{\mathscr{D}_k^{\nu}} e^{in\varphi}\int \mathrm{d}z'\left(e^{ik(z-z')+ik_0z'}\psi(z')\right). \tag{14.110}$$

Therefore, the nonlinear part of the Hamiltonian can be approximated as:

$$\mathrm{H}_{NL} \cong \frac{\eta_3\hbar^2}{16}\int \rho d\rho d\varphi dz\left[\frac{\mathbf{Z}_k^{\nu}}{\mathscr{D}_k^{\nu}} e^{i(n\varphi+k_0z)}\psi + \left(\frac{\mathbf{Z}_k^{\nu}}{\mathscr{D}_k^{\nu}}\right)^* e^{-i(n\varphi+k_0z)}\psi^{\dagger}\right]^4. \tag{14.111}$$

Hence, keeping the slowly varying terms, one obtains:

$$\mathrm{H}_{NL} \cong \frac{3\hbar^2\eta_3}{8}\left|\frac{1}{\mathscr{D}_k^{\nu}}\right|^4 \theta^{\nu}\int dz\left(\psi^{\dagger}\right)^2\psi^2, \tag{14.112}$$

where:

$$\theta^{\nu} = \int_0^{r_0}\int_0^{2\pi}\left[\frac{1}{3}\left(\alpha^{\nu}\alpha^{\nu} - k_0^2\mathbf{\Gamma}_{\perp}^{\nu}\cdot\mathbf{\Gamma}_{\perp}^{\nu}\right)\left(\alpha^{-\nu}\alpha^{-\nu} - k_0^2\mathbf{\Gamma}_{\perp}^{-\nu}\cdot\mathbf{\Gamma}_{\perp}^{-\nu}\right) + \frac{2}{3}\left(k_0^2\mathbf{\Gamma}_{\perp}^{\nu}\cdot\mathbf{\Gamma}_{\perp}^{-\nu} + \alpha^{\nu}\alpha^{-\nu}\right)^2\right]\rho d\rho d\varphi. \tag{14.113}$$

There are terms proportional to $\psi^{\dagger}\psi$, $\psi^{\dagger}$, and/or ψ in the nonlinear part of the Hamiltonian (Eq. (14.112)), which is usually called simple terms as they could be interpreted similar to the term of the linear Hamiltonian (Eq. (14.108)). Therefore, they do not show any nonlinear effect.

The total Hamiltonian and field operator is expressed in the interaction picture as:

$$\mathrm{H}_I = e^{-iht/\hbar}\mathrm{H}e^{iht/\hbar} \tag{14.114}$$

and:

$$\psi_I = e^{-iht/\hbar}\psi e^{iht/\hbar} \tag{14.115}$$

where h is defined as:

$$h = \hbar\int dz\ \omega(k_0)\ \psi^{\dagger}\psi. \tag{14.116}$$

A new frame is defined that moves at the group velocity ($Z = z - \omega' t$). One obtains the following equation of motion in this frame from the interaction Hamiltonian:

$$i\frac{\partial\psi_I}{\partial t} = -\frac{\omega''}{2}\frac{\partial^2\psi_I}{\partial Z^2} - i\frac{\omega'''}{6}\frac{\partial^3\psi_I}{\partial Z^3} + g\psi_I^{\dagger}\psi_I^2, \tag{14.117}$$

where $g = (3\hbar^2 k^4 \eta_3/4)(\theta^v)^2 \left|1/(\bar{\omega}_k^v)\right|^4$. Equation (14.117) is an operator form of the nonlinear Schrödinger equation taking the third-order dispersion term into account. There is another operator equation, the equation of motion for $\psi_I^\dagger$, which is coupled to Eq. (14.117) by transforming $\psi_I \to \psi_I^\dagger$ and $i \to -i$.

Depending on the optical fiber characteristics, the signs of g (nonlinear parameter) and ω'' (group velocity dispersion) can be positive or negative. Taking into account their signs, one can form the quantum solitons and study their interactions in the presence of the third-order dispersion term. Note that the terms proportional to $(\psi^\dagger)^2\psi^2$ in Eq. (14.111) lead to the last term in Eq. (14.117). The terms of the order $\psi^\dagger\psi$ in Eq. (14.111), which have been omitted, would lead to a linear term and have no nonlinear effect on the operator form of the nonlinear Schrödinger equation, Eq. (14.117) or equivalently Eq. (14.118). These terms just change $\omega(k_0)$ in the first term of Eq. (14.108), so the nonlinear term of Equations (14.117) and (14.118) is not affected by them.

To solve the coupled operator equation, Eq. (14.117) is written as common partial differential equations. The positive-P representation method is followed here (Drummond & Gardiner, 1980; Drummond & Hillery, 2014). The Glauber-Sudarshan P representation (Glauber, 1963; Sudarshan, 1963) is not used here, as it leads to a Fokker-Planck equation with non-positive definite diffusion coefficients. By using the positive-P representation in the master equation, one can arrive at the coupled stochastic partial differential equation (Carter, 1995; Drummond & Gardiner, 1980; Drummond & Hillery, 2014; Drummond & Corney, 2001; Drummond & Carter, 1987):

$$\frac{\partial}{\partial z}\Psi_I(T,z) = \left(-\frac{i\omega''}{2\omega'^3}\frac{\partial^2}{\partial T^2} + \frac{\omega'''}{6\omega'^4}\frac{\partial^3}{\partial T^3}\right)\Psi_I(T,z) - i\left(g/\omega'\right)\Psi_I{}^+(T,z)\,\Psi_I{}^2(T,z) + \left(ig/\omega'\right)^{1/2}\zeta(T,z)\,\Psi_I(T,z) \tag{14.118a}$$

and:

$$\frac{\partial}{\partial z}\Psi_I{}^+(T,z) = \left(\frac{i\omega''}{2\omega'^3}\frac{\partial^2}{\partial T^2} + \frac{\omega'''}{6\omega'^4}\frac{\partial^3}{\partial T^3}\right)\Psi_I{}^+(T,z) + i\left(g/\omega'\right)\Psi_I(T,z)\,\Psi_I{}^{+2}(T,z) + \left(-ig/\omega'\right)^{1/2}\zeta^+(T,z)\,\Psi_I{}^+(T,z) \tag{14.118b}$$

for the functions $\Psi_I(T,z)$ and $\Psi_I{}^+(T,z)$, respectively, which are related to the creation and annihilation operators. The fields $\zeta(T,z)$ and $\zeta^+(T,z)$ are Gaussian stochastic fields with correlation relations:

$$\left\langle \zeta(T_1,z_1)\,\zeta\left(T_2,z_2\right)\right\rangle = \delta(z_1-z_2)\,\delta(T_1-T_2), \tag{14.119}$$

$$\left\langle \zeta^+(T_1,z_1)\,\zeta^+\left(T_2,z_2\right)\right\rangle = \delta(z_1-z_2)\,\delta(T_1-T_2), \tag{14.120}$$

and:

$$\left\langle \zeta\left(T_1, z_1\right) \zeta^{+}\left(T_2, z_2\right)\right\rangle = 0. \tag{14.121}$$

The origin of stochastic partial differential equations (14.118) for the functions $\Psi_I(T, z)$ and $\Psi_I^{+}(T, z)$ comes from the positive-P representation. Making use of the positive-P representation, the Fokker-Planck equation with positive semi-definite diffusion coefficients amounts to an equivalent Ito stochastic differential equation, Equations (14.118) (Carter, 1995; Drummond & Corney, 2001; Drummond & Carter, 1987, Koleden & Platen, 1992; Sauer, 2013). $\Psi_I(T, z)$ and $\Psi_I^{+}(T, z)$ are not complex conjugates of one another except in the mean case (Koleden & Platen, 1992; Sauer, 2013).

Equations (14.118) govern the quantum treatment of pulse propagation in an optical fiber in the presence of the third-order dispersion term ($\beta_3 = \omega'''/\omega'^4$). To increase the bit rate in optical communication systems, a light source (a laser) is usually employed close to the zero dispersion wavelength (ZDW) of optical fibers, $\left(\beta_2 = \omega''/\omega'^3\Big|_{\omega_0} = 0 \text{ i.e. } \omega'' = 0\right)$, where β_3 plays an important role (Agrawal, 2012). Thus, Equations (14.118) provide the quantum treatment of pulse propagation in this situation.

The quantum noise near the propagating solitons is simulated using the linearized fluctuation equation (Drummond & Carter, 1987) for the propagating soliton as:

$$\begin{aligned}\frac{\partial}{\partial z}\delta\Psi\left(T, z\right) = &\left(-\frac{i\omega''}{2\omega'^3}\frac{\partial^2}{\partial T^2} + \frac{\omega'''}{6\omega'^4}\frac{\partial^3}{\partial T^3} + 4ig\psi_0^2(T)\right)\delta\Psi\left(T, z\right) \\ &+ 2ig\psi_0^2(T)\delta\Psi^{+}\left(T, z\right) + (ig)^{1/2}\psi_0(T)\zeta\left(T, z\right)\end{aligned} \tag{14.122}$$

where $\Psi(T, z) = \psi_0(T, z) + \delta\Psi(T, z)$ and $\psi_0(T, z) = \langle\Psi(T, z)\rangle$. Recall that Eq. (14.122) together with the equation obtained by using the transformation $\Psi \rightarrow \Psi^{+}$, $i \rightarrow -i$, and $\zeta \rightarrow \zeta^{+}$ forms a set of coupled equations.

Here, ψ_0 is the classical solution to the generalized first-order approximation of the nonlinear Schrödinger equation. The function ψ_0 corresponds to a classical coherent input state at $z = 0$, which has a form of $\psi_0\left(T, z = 0\right) = \sqrt{P_0}\,\mathrm{sech}\left(T/T_0\right)$, where P_0 and T_0 are, respectively, the peak power and width of the input pulse launched into an optical fiber.

To find the solutions to Eqs. 14.118 and 14.122, numerical algorithms can be applied to solve these stochastic partial differential equations (Sauer, 2013; Dennis et al., 2013). One could assume that the input solitonic pulse $\psi_0(T, 0)$ is launched into an optical fiber in which the dispersion length $\left(L_D = T_0^2/|\beta_2|\right)$, third-order dispersion length ($L_D' = T_0^3/|\beta_3|$), and nonlinear length ($L_{NL} = \omega'/gP_0$) are approximately equal, $L_D \approx L_D' \approx L_{NL}$. Figure 14.1 shows the evolution of the intensity of the travelling solitonic pulse along the optical fiber. The soliton intensity evolution and the soliton amplitude fluctuations at the center are shown in Figs. 14.2 and 14.3, respectively. The central intensity evolution of the propagated soliton

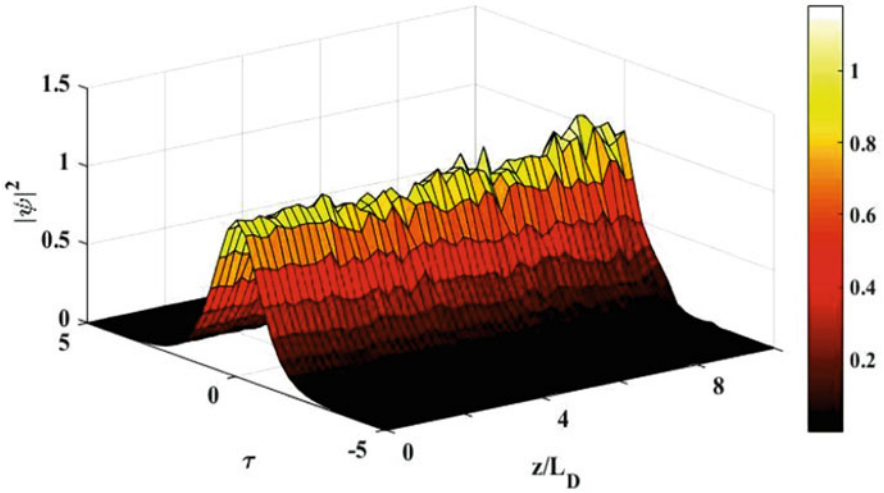

Fig. 14.1 The normalized intensity of the propagated soliton along the optical fiber (Noted that normalized time, τ, is $\tau = T/T_0$)

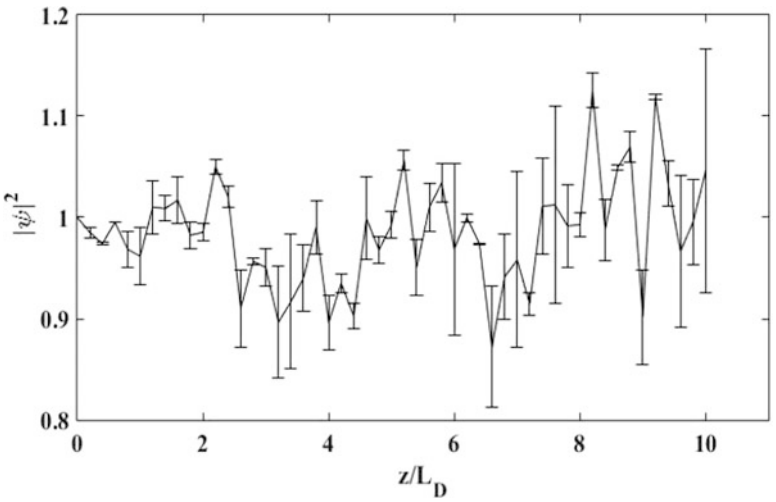

Fig. 14.2 The intensity evolution of the propagated soliton at center ($\tau = 0$) versus the length of the optical fiber

has been obtained from Eq. 14.118, while the soliton's amplitude fluctuation at its central peak is deduced from Eq. 14.122. Due to the present simulation results, it is understood that the propagated soliton suffers from quantum noise, and there are fluctuations in the vicinity of the soliton. These fluctuations should be taken into consideration in the future quantum technologies (Vinh et al., 2021).

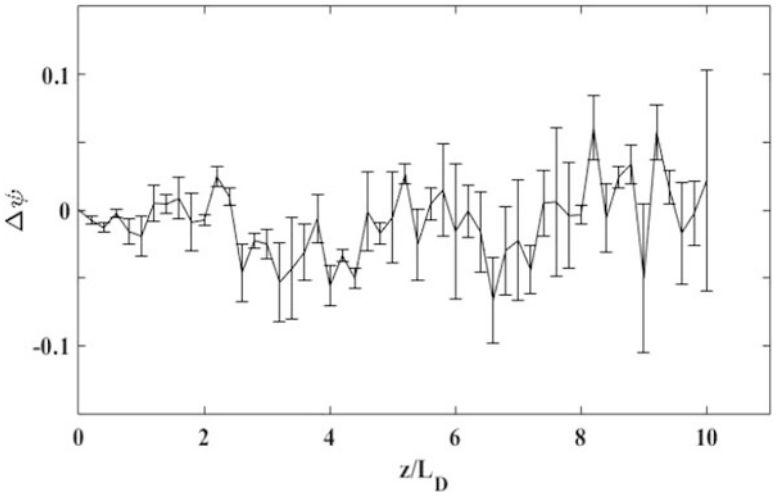

Fig. 14.3 Soliton amplitude noise at the center ($\tau = 0$) as a function of the optical fiber's length

14.4 Quantum Model for Supercontinuum Generation Process

In Sect. 14.2, the propagation of electromagnetic field was quantized when the third-order dispersion term was present. The method discussed in Sect. 14.2 was applied to an optical fiber, when the electromagnetic field was travelling along it in Sect. 14.3. The method introduced could be applied to higher dispersive terms if needed. The process by which a high-intensity light pulse is launched into a dispersive dielectric; the extreme frequency broadening is observed due to dispersive and nonlinear effects, known as supercontinuum generation. Both experimental and theoretical studies performed by several groups indicate the formation of the supercontinuum light in a dielectric, e.g., optical fiber. A comprehensive study of this process was published by Dudley et al. (2006) based on classical models. In this section, the quantum treatment of SCG by pulse propagation in the presence of the higher-order dispersion terms, retarded response of the medium, and the third-order susceptibility is focused (Safaei Bezgabadi & Bolorizadeh, 2022).

Generation of noise in a dielectric used to generate supercontinuum light source is the main cause of instability in it and, therefore, reducing its applicability in industry. Depending on the parameters of the input pulse, the generated supercontinuum noise could cause up to 50% fluctuation in the temporal intensity profile of output pulse (Corwin et al., 2003; Dudley & Genty, 2013; Gonzalo et al., 2018; Wetzel et al., 2012). The fundamental part of this noise has its root in quantum noise, which is inherent in the nonlinear process leading to the generated continuum light. Corwin and coworkers measured the noise and provided a model describing it (Corwin et

al., 2003). Their model, which is called a semi-classical model, adds a noise term into the generalized nonlinear Schrödinger equation (GNLSE). The term added to GNLSE, by Corwin and coworkers (2003), is a quantum noise, which has been phenomenologically a sound term to be added to the classical GNLSE. Real-time measurements of optical noise showed long-tailed statistics in the spectral intensity of a generated supercontinuum light (Wetzel et al., 2012; Närhi et al., 2016). Gonzalo and coworkers (2018) were able to reduce noise fluctuation in all-normal dispersion supercontinuum sources. However, the instability of the supercontinuum light due to the noise is still an open question.

It is intended to devise a quantum mechanical model to treat the SCG in a dielectric using the positive-P representation (Safaei Bezgabadi & Bolorizadeh, 2022). This model describes the soliton self-frequency shift, nonetheless, and the noise associated with solitons in a dielectric. The quantum treatment of supercontinuum is essential for the development of quantum communication, quantum computers, and spectroscopy. The higher-order solitons split into lower order and fundamental ones due to the soliton interactions, the third order dispersion effect, the Raman effect, and the self-steepening phenomenon. A powerful quantum theory is needed to explain all these effects.

The usual model for a centrosymmetric fiber (photonic crystal fiber (PCF)) is chosen where the first nonlinear term to be included is the third-order nonlinear susceptibility, which is not instantaneous in all practical applications (for details, see Ref. (Alfano, 2016; Agrawal, 2012)). The proper canonical Lagrangian leading to the correct Hamiltonian and to the Maxwell's equations as the Hamilton's equation of motion was devised earlier. The Hamiltonian is:

$$H = \sum_k \hbar\omega(k)\mathrm{a}_k^\dagger \mathrm{a}_k - \frac{\eta_3}{4}\int\left(D^2(t,\mathbf{x})\int_{-\infty}^{t} R(t')\ D^2(t-t',\mathbf{x})\ dt'\right)d^3\mathbf{x} \tag{14.123}$$

where $R(t)$, a_k, D, and η_3 are, respectively, the response function of the medium, the mode operators, the electric displacement operator, and the third-order nonlinear response of the medium. The first term in Eq. (14.123) was derived earlier, by the approach presented in the previous sections, which included the higher-order dispersion terms. The interaction picture is assumed, Eq. (14.114), and the spatial dependence is discretized making use of the expansion (14.105) near k_0.

Due to the discrete nature of the longitudinal mode spacing ($\Delta k = 2\pi/L$) in an optical fiber of length L, the local operators are defined as (Drummond & Carter, 1987):

$$\alpha_\ell \triangleq \left(2N'+1\right)^{-1/2}\sum\nolimits_{n=-N'}^{n=N'} a_n\ \exp\left(2\pi n i\ell/\left(2N'+1\right)\right), \tag{14.124}$$

where spatial z-dependence, ($z \equiv \ell\Delta z$), is discrete and the steps of $\Delta z = L/(2N' + 1)$ are arranged along the optical fiber from $\ell = -N'$ to $+N'$. The local operators satisfy the harmonic oscillator commutation relations (Drummond & Carter, 1987).

As discussed earlier, the quantum mechanical treatment of the SCG process is done making use of the positive-P representation, the method developed by Drummond (Drummond & Hillery, 2014; Drummond & Carter, 1987). The definition (Drummond & Hillery, 2014; Drummond & Carter, 1987):

$$|\theta(t)\rangle\langle\theta(t)| = \int P\left(t;\boldsymbol{\alpha},\boldsymbol{\alpha}^{+}\right)\frac{|\boldsymbol{\alpha}\rangle\left\langle\left(\boldsymbol{\alpha}^{+}\right)^{*}\right|}{\left\langle\left(\boldsymbol{\alpha}^{+}\right)^{*}|\boldsymbol{\alpha}\right\rangle}\,d^{2}\boldsymbol{\alpha}d^{2}\boldsymbol{\alpha}^{\dagger} \tag{14.125}$$

is the starting point where $|\boldsymbol{\alpha}\rangle$ and α_ℓ are the coherent state of total field and the eigenvalue for the local operator α_ℓ, respectively. In addition, $|\theta(t)\rangle$ is the total wave function for the interaction Hamiltonian, while $P(t;\boldsymbol{\alpha},\boldsymbol{\alpha}^{+})$ develops in time according to a Fokker-Planck equation with positive semi-definite diffusion coefficient. The Fokker-Planck equation amounts to an equivalent equation of motion for appropriate stochastic variables $\boldsymbol{\alpha}(t)$ and $\boldsymbol{\alpha}^{+}(t)$:

$$\begin{aligned}\frac{\partial\alpha_\ell}{\partial t} = i\Bigg(&\chi_\alpha\alpha_\ell\left[\int_{-\infty}^{t}R\left(t'\right)\,\alpha_\ell{}^{+}\left(t-t'\right)\alpha_\ell\left(t-t'\right)\,dt'\right]\\&+\chi_\alpha\alpha_\ell{}^{+}\alpha_\ell\left[\int_{-\infty}^{t}R\left(t'\right)\,\alpha_\ell\left(t-t'\right)\,dt'\right]-\sum_{\ell'}\omega_{\ell\ell'}\alpha_{\ell'}\Bigg)+(2i\chi_\alpha)^{1/2}\alpha_\ell\,\xi_\ell(t)\end{aligned} \tag{14.126a}$$

and:

$$\begin{aligned}\frac{\partial\alpha_\ell{}^{+}}{\partial t} = -i\Bigg(&\chi_\alpha\alpha_\ell{}^{+}\left[\int_{-\infty}^{t}R\left(t'\right)\,\alpha_\ell{}^{+}\left(t-t'\right)\alpha_\ell\left(t-t'\right)\,dt'\right]\\&+\chi_\alpha\alpha_\ell{}^{+}\alpha_\ell\left[\int_{-\infty}^{t}R\left(t'\right)\,\alpha_\ell{}^{+}\left(t-t'\right)\,dt'\right]-\sum_{\ell'}\omega_{\ell\ell'}\alpha_{\ell'}{}^{+}\Bigg)+(-2i\chi_\alpha)^{1/2}\alpha_\ell{}^{+}\,\xi_\ell{}^{+}(t)\end{aligned} \tag{14.126b}$$

where:

$$\begin{aligned}\omega_{\ell\ell'} =&\Delta\omega\delta_{\ell\ell'}+\sum_{n}\left(2N'+1\right)^{-1}\left[(n\Delta k)\,\omega'+\frac{1}{2}(n\Delta k)^{2}\omega''+\frac{1}{6}(n\Delta k)^{3}\omega'''\right]\\&\times\exp\left[\frac{2\pi ni}{2N'+1}\left(\ell-\ell'\right)\right]\end{aligned} \tag{14.127}$$

and:

$$\chi_\alpha = \frac{3\varepsilon_0\hbar\left(\omega' k_0\right)^{2}}{8\varepsilon^{2}\Delta V}\,\chi^{(3)}. \tag{14.128}$$

Here, $\xi_\ell(t)$ and $\xi_\ell^{+}(t)$ are real Gaussian stochastic functions. The correlation relations $\left\langle\xi_\ell\left(t_1\right)\xi_{\ell'}^{+}\left(t_2\right)\right\rangle = 0$ and $\left\langle\xi_\ell\left(t_1\right)\xi_{\ell'}\left(t_2\right)\right\rangle = \left\langle\xi_\ell^{+}\left(t_1\right)\xi_{\ell'}^{+}\left(t_2\right)\right\rangle = \delta_{\ell\ell'}\delta\left(t_1-t_2\right)$ are valid for the functions $\xi_\ell(t)$ and $\xi_\ell^{+}(t)$. Note, firstly that the rotating wave

approximation is used to calculate the integral term of the Hamiltonian (14.123) and secondly α_ℓ and α_ℓ^+ are not exactly complex conjugate to each other as the positive-P representation is used. The stochastic field, Φ, is defined as (Drummond & Carter, 1987):

$$\Phi(z) \cong \lim_{\Delta z \to 0} (\alpha_\ell) \left(\frac{\omega'}{\Delta z}\right)^{1/2} \tag{14.129}$$

in the limit $\Delta z \to 0$, at the location $z = \ell \Delta z$. As the continuum representation is now used, the discrete stochastic terms are replaced by Gaussian stochastic fields $\xi(T, z)$ and $\xi^+(T, z)$, with correlation relations similar to Eq. (14.119) to Eq. (14.121).

In addition to the quantum noise, one may include additional fluctuations due to variations in the refractive index, which would result in a set of correlation relation different from those of Eq. (14.119) to Eq. (14.121). However, these fluctuations are ignored for the ideal photonic system or the photonic crystal fibers. Making use of the transformation ($T = t - z/\omega^{'}$), the problem is solved in a new frame moving at a velocity equal to the group velocity. Now, a wavenumber dependent nonlinear parameter, χ_Φ, is defined which is similar to χ_α. For all practical cases, it can be expanded as:

$$\chi_\Phi = \chi_\Phi(k_0) + (k - k_0)\, \chi'_\Phi + \cdots, \tag{14.130}$$

where $\chi'_\Phi = d\chi_\Phi/dk|_{k=k_0}$.

Finally, the full stochastic equation governing the SCG for the field $\Phi(T,z)$ is obtained as:

$$\begin{aligned}\frac{\partial}{\partial z}\Phi(T,z) = &\left(-\frac{i\omega''}{2\omega'^3}\frac{\partial^2}{\partial T^2} + \frac{\omega'''}{6\omega'^4}\frac{\partial^3}{\partial T^3} + \cdots\right)\Phi(T,z) + i\left(\chi_\Phi + i\chi'_\Phi\frac{\partial}{\partial T}\right)\Psi(T,z)\\ &+ (i\chi_\Phi)^{1/2}\overline{\xi}(T,z)\,\Phi(T,z),\end{aligned} \tag{14.131}$$

where:

$$\begin{aligned}\Psi(T,z) = &\Phi(T,z)\left[\int_{-\infty}^{T} R(T')\ \Phi^+(T-T',z)\,\Phi(T-T',z)\,dT'\right]\\ &+ \Phi^+(T,z)\,\Phi(T,z)\left[\int_{-\infty}^{T} R(T')\ \Phi(T-T',z)\,dT'\right].\end{aligned} \tag{14.132}$$

There is also a coupled equation to Eq. (14.131) by transforming $\Phi \to \Phi^+$, $i \to -i$ and $\overline{\xi} \to \overline{\xi}^+$, which in the mean case it is the complex conjugate of Eq. (14.131). Equation (14.131) can be regarded as the fundamental result of the present work. Equation (14.131) and its coupled equation for $\Phi^+(T,z)$ form a set of coupled generalized nonlinear Schrödinger equations for the quantum treatment of the SCG in fibers (e.g., PCF). Here, the stochastic terms introduce fluctuations originated

from quantum noise. In addition to the coupling form of the two equations, the main difference between the coupled quantum-stochastic equations and its classical form is the term proportional to $\int_{-\infty}^{T} R\left(T'\right) \Phi\left(T-T', z\right) dT'$ in Eq. (14.131) which has no counterpart in classical form. This additional term is brought about by commutation relations, which holds for creation and annihilation operators. Indeed, this term appears when one obtains the Fokker-Planck equation (from master equation) by using Hamiltonian (14.123). Also, note that the quantity χ_{Φ} introduced here for the quantum case is half its value for the classical form.

In the instantaneous medium response limit, $R(T)$ is replaced by delta function where the quantity defined by Eq. (14.132) takes the form:

$$\Psi(T, z) = 2\Phi^{+}(T, z)\ \Phi^{2}(T, z). \tag{14.133}$$

Therefore, the coupled quantum-stochastic equation leads to the well-known coupled stochastic nonlinear Schrödinger equation (Drummond & Hillery, 2014; Drummond & Carter, 1987) which resulted from the Fokker-Planck equation (Drummond & Hillery, 2014) or the results of the previous section (Eq. 14.118). Hence, Eq. (14.131) gives a rigorous basis for earlier results (Drummond & Carter, 1987) for instantaneous medium response. Also, if one does not apply the nature of the commutation relation, the resulted equation of motion (master equation) from Hamiltonian (14.123) leads to the classical generalized nonlinear Schrödinger equation (Alfano, 2016; Dudley et al., 2006; Dudley & Taylor, 2010). There are self-phase modulation and cross-phase modulation, which are the side effect of Kerr effect and four wave mixing due to nonzero value for the χ_{Φ}. Also, the stimulated Raman scattering and self-steepening are discussed assuming the retarded response function, $R(T)$, and the dispersive nature of χ_{Φ}.

The coupled quantum-stochastic equations will have soliton solutions, called quantum solitons. There are many works in the literature to study quantum solitons (Drummond & Hillery, 2014; Drummond et al., 1993; Yao, 1997; Vinh et al., 2021), but these solitons have not studied in SCG process, and in these works, the higher-order dispersion coefficients were not included. If these solitons are not a fundamental one, they split into the lower order and fundamental ones after propagating inside the optical fiber, which is known as soliton fission. In some applications of the supercontinuum generation (e.g., quantitative experiments), it is necessary to squeeze the quantum noise in the vicinity of these solitons. The linearized fluctuation equation to study quantum noise will be:

$$\begin{aligned}
\tfrac{\partial}{\partial z}\delta\Phi(T, z) = &\left(-\tfrac{i\omega''}{2\omega'^{3}}\tfrac{\partial^{2}}{\partial T^{2}} + \tfrac{\omega'''}{6\omega'^{4}}\tfrac{\partial^{3}}{\partial T^{3}}\right)\delta\Phi(T, z) + i\chi_{\Phi}\left(\int_{-\infty}^{T} R\left(T'\right)\phi_{0}^{2}\left(T-T'\right)dT'\right)\delta\Phi(T, z) \\
&+ i\chi_{\Phi}\phi_{0}(T)\left(\int_{-\infty}^{T} R\left(T'\right)\phi_{0}\left(T-T'\right)dT'\right)\delta\Phi(T, z) + i\chi_{\Phi}\phi_{0}^{2}(T)\int_{-\infty}^{T} R\left(T'\right)\delta\Phi\left(T-T', z\right)dT' \\
&+ i\chi_{\Phi}\phi_{0}(T)\int_{-\infty}^{T} R\left(T'\right)\phi_{0}\left(T-T'\right)\delta\Phi\left(T-T', z\right)dT' + i\chi_{\Phi}\phi_{0}(T)\delta\Phi^{+}(T, z)\int_{-\infty}^{T} R\left(T'\right) \\
&\phi_{0}\left(T-T'\right)dT' + i\chi_{\Phi}\phi_{0}(T)\int_{-\infty}^{T} R\left(T'\right)\phi_{0}\left(T-T'\right)\delta\Phi^{+}\left(T-T', z\right)dT' + (i\chi_{\Phi})^{1/2}\phi_{0}(T)\overline{\xi}(T, z).
\end{aligned} \tag{14.134}$$

where $\phi_0(T,z) = \langle \Phi(T,z) \rangle$ and $\Phi(T,z) = \phi_0(T,z) + \delta\Phi(T,z)$. Equation (14.134) together with the equation obtained by transforming $\Phi \to \Phi^+$, $i \to -i$, and $\overline{\xi} \to \overline{\xi}^+$ forms a new set of coupled equations to be called the coupled quantum-stochastic noise equations.

Here, ϕ_0 can be considered as a mean case solution to the coupled generalized nonlinear Schrödinger equations for the quantum treatment of SCG (Eq. 14.131). The function ϕ_0 at $z = 0$ corresponds to a classical coherent input state, which, in resemblance to the classical case, can be treated as $\phi_0(T, z = 0) = \sqrt{P_0}\,\mathrm{sech}\,(T/T_0)$, where P_0 and T_0 are, respectively, peak power and width of the input pulse which is launched into the photonic crystal fiber.

In summary, a quantum description of SCG of highly nonlinear pulse propagation in an optical fiber is established. This theory leads to a coupled quantum-stochastic generalized nonlinear Schrödinger equation. In addition to the coupling term, the second term in Eq. (14.132) is not present in the classical generalized nonlinear Schrödinger equation for the description of SCG. The reason behind this difference is the commutation relation that holds for the stochastic fields of the master equation, leading to the Fokker-Planck equation.

Making use of a stochastic field, the quantum noise source was included in the governing equation. Subsequently, the coupled linearized fluctuation equation is obtained by implementing the proper definition for squeezed quantum solitons (Drummond & Carter, 1987). One argues that the resultant squeezing for the normal dispersion regime is different from the resultant squeezing for the anomalous dispersion regime. In order to arrive at this prediction, it is necessary to solve the coupled linearized fluctuation equation numerically. The equations, obtained here, could be used to study non-optical systems involving the retarded response, when the Hamiltonian (14.123) holds.

Applying the fourth-order Runge-Kutta algorithm and employing the quantum formalism, Eq. (14.131), the supercontinuum generation in photonic crystal fibers under the mean case can be studied where Φ and Φ^+ are complex conjugates to each other. Note that the expectation value of the last term in Eq. (14.131) is zero under mean case (Drummond & Hillery, 2014; Drummond & Carter, 1987). A PCF and incoming light parameters assumed by Dudley et al. (2006) were used in the experimental results of Corwin and coworkers (2003) which is compared with the results of the present quantum mechanical model as shown in Fig. 14.4. A pulse of a 0.9 nJ energy at ultrashort width was used to measure the supercontinuum spectrum between 400 and 1400 nm as shown in Fig. 14.4 (Corwin et al., 2003). The present quantum model for the generation of SCG is plotted in Fig. 14.4 for comparison with the experimental results, where the two agree. The peak of solitons in the experimental results agrees with the quantum mechanical model. The results of the quantum and classical models for the retarded nonlinear response condition are shown in Fig. 14.5. The input pulse of 10 kW peak power and 28.4 fs width at 835 nm was chosen in this work. Due to the additional term in Eq. (14.131), which is absent in the classical GNLSE, there are differences between the two results for the SCG. Note that the higher dispersion terms and retarded response of the medium were not included in the work reported in 2016 (Safaei Bezgabadi & Bolorizadeh,

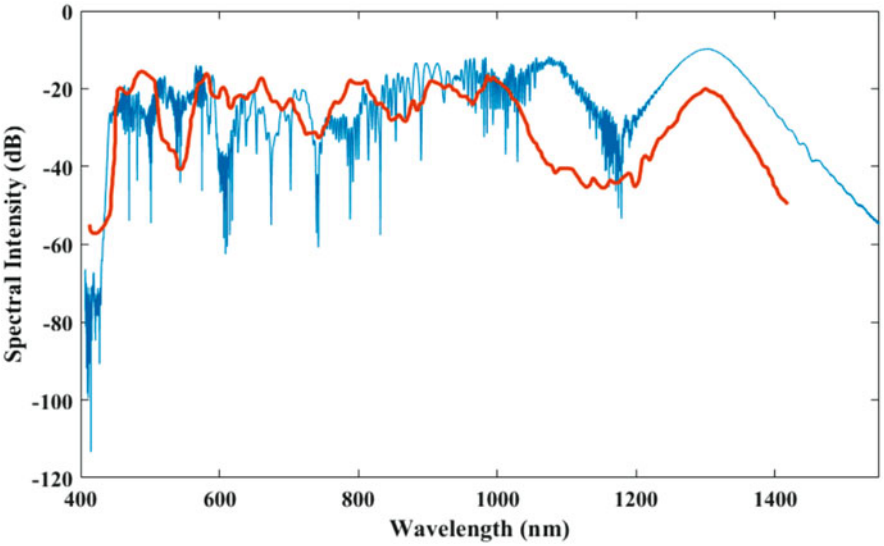

Fig. 14.4 A comparison between the present simulation of SCG (the blue line) in the fiber and the experimental results of Corwin et al. (2003) (the red line)

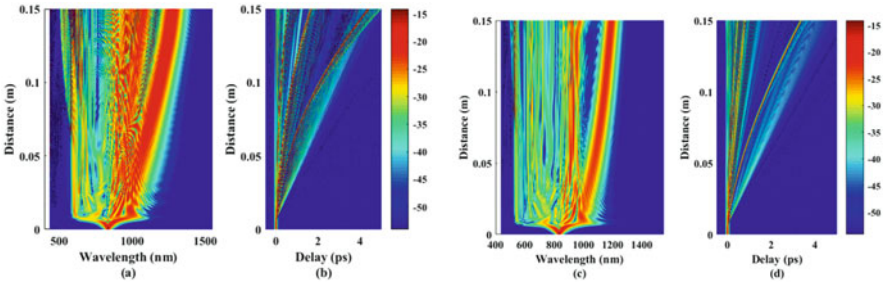

Fig. 14.5 Simulation results for the quantum mechanical (**a** and **b**) and classical treatment (**c** and **d**) of SCG along the first 15 cm of a PCF fiber. Photons generated at wavelengths from 400 nm (**a**) to 1450 nm in a quantum treatment and (**c**) to 1350 nm in a classical treatment of SCG. Time development of the input pulse is shown in (**b**) and (**d**) with respect to the delayed pulse in a quantum and classical models, respectively

2016), and therefore the results do not show the soliton self-frequency shift and soliton fission present in this work as shown in Fig. 14.5. The resulting simulation of the SCG is shown by Fig. 14.5a, b for the quantum model, while similar data is provided in Fig. 14.5c, d for the classical model. The difference between the two results, classical and quantum treatments, arises due to the presence of the additional term. One can compare the spectral broadening of a pulse inside the optical fiber by the two methods as shown in Fig. 14.6. Comparing the results of the classical treatment of the SCG in a specific PCF shown by Figs. 14.5c, d and 14.6b and the quantum results presented in Figs. 14.5a, b and 14.6a show that not only the spectral

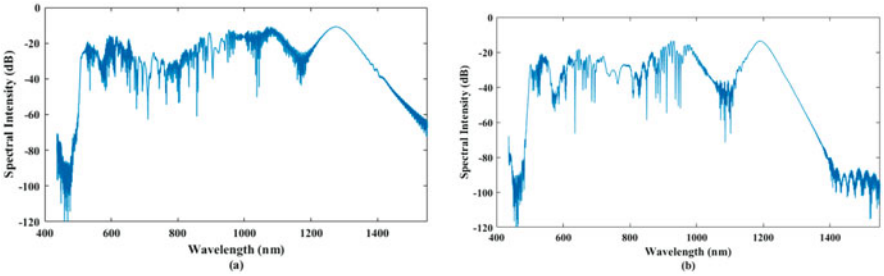

Fig. 14.6 The generated wavelengths at the output of a 15 cm PCF in (**a**) quantum mechanical and (**b**) classical calculations for the input pulse of 10 kW power and 28.4 fs pulse width at 835nm

broadening increases in the quantum treatment but also that the generated frequency combs are closer and richer. In Fig. 14.5b, the quantum mechanical model predicts longer delay for the formed soliton as compared with the classical result of Fig. 14.5d. However, the two models predict the soliton fission to occur at about the same travel distance of the pulse along the optical fiber. Figure 14.6a indicates that the peak intensity of soliton pulse calculated by the present quantum model is at 1300 nm which fits well with the experimental results of Corwin and coworkers (2003) shown in Fig. 14.4, while the classical result, Fig. 14.6b, shows that the peak of soliton pulse is at 1220 nm. As shown in Fig. 14.6b, the simulation of the supercontinuum spectrum in the classical model reaches the background level at wavelengths 1400 nm, while both experimental data and quantum results extend beyond this wavelength.

As described earlier, the additional term in Eq. (14.132) originated from the non-commutative nature of the creation and the annihilation operators defined in obtaining the Fokker-Planck equation. This term changes the evolution of the optical pulse inside an optical fiber, which causes the difference in the simulation results between the two treatments. In reality, this term alters how the nonlinear part would affect the broadening of the pulse and generation of new frequencies. As an example, the soliton evolves according to the interplay between the third-order dispersion term, the Raman scattering term, and the self-steepening term. Thus, the evolution of solitons is predicted differently in the quantum treatment as compared with the classical model.

In an experimental work, the resolution of the spectrometer should be less than 1 nm, in order to be able to show deeper details of the SCG. We therefore suggest a more detailed and precise experimental work needed in this field to be able to understand the deeper physics behind the nonlinear effects in dielectrics and, especially, fibers. This is essential in order to understand and to reduce the noise and, most important, the quantum noise.

In the following, the quantum mechanical treatment results are compared with the classical ones for different peak powers and pulse widths. Figure 14.7 indicates that when the peak power is low, such as 1 kW, and the pulse width is large, 10 ps, the two models lead, approximately, to similar results. Note that the quantum

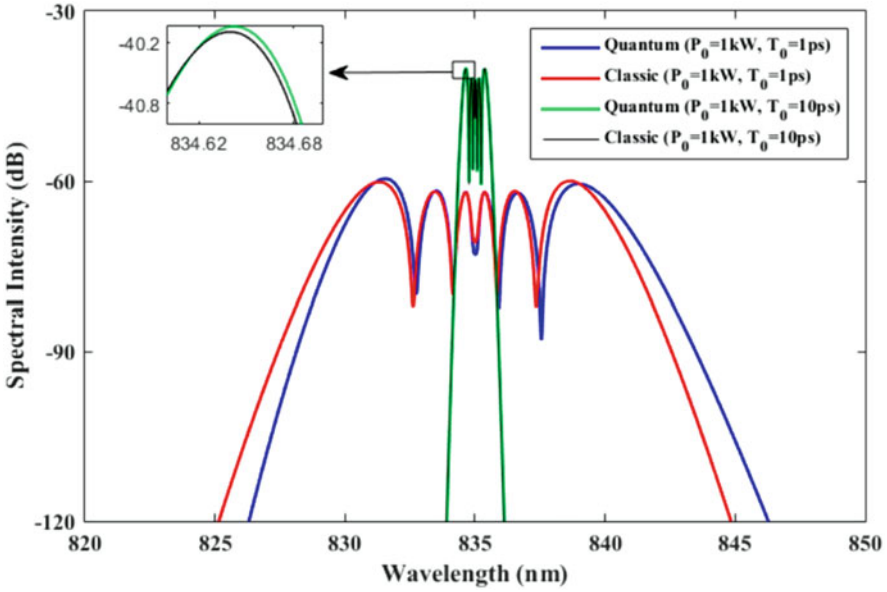

Fig. 14.7 The propagation of light pulses at 1 kW, low power, and large width of 1 ps and 10 ps are compared for both classical and quantum mechanical models. Inset shows details of the spectrum in a region of the spectrum

mechanical description of wave and particles is the same and leads to the wave packet descriptions of both. When the width of a light pulse is small, it represents a small particle which makes the quantum treatment essential. It is interesting that the two results, classical and quantum models, deviate as the width of input pulse changes from 10 ps to 1 ps. The classical results are closer to the quantum mechanical model at the pulse width of 10 ps as compared with the 1 ps ones. This study shows how important is the quantum nature of pulse for short width. In practice, the nonlinear terms do not have significant contributions on the generation of pulses of new wavelengths at such peak powers and pulse widths. However, the quantum mechanical treatment of the pulse propagation along dielectrics or optical fibers is still indispensable, because this approach is applicable to study quantum solitons and to reduce the fluctuations in the vicinity of these solitons. From a quantum mechanical point of view, a soliton is considered as a collection of particles traveling together in a medium.

14.5 Conclusion

In summary, a higher-order Lagrangian has been introduced for the field propagation in an inhomogeneous, dispersive, and anisotropic dielectric in Sect. 14.2, specifically an optical fiber. By establishing a quantum theory, the propagating fields are

quantized by imposing the Dirac commutation relations. The Hamiltonian is then written in terms of proper creation and annihilation operators. In Sect. 14.3, the quantum theory is applied to study pulse propagation inside a conventional optical fiber where the coupled stochastic NLSE is resulted as the governing equation. By using this coupled stochastic NLSE, propagation of quantum soliton in the presence of higher-order dispersion can be described, and the quantum noise in the vicinity of the soliton can be reduced.

As it is essential to study SCG quantum mechanically, this approach is applied for ultrashort pulse propagation along a nonlinear media when the retarded response function of the medium should be taken into account. Here, the quantum theory for the SCG process is presented, and it has included the terms with the significant contributions involved in the supercontinuum generation a nonlinear media, specifically the PCFs. Besides the obtained coupled stochastic equation for the quantum treatment of the SCG, the source of significant difference is the additional term which has no classical resemblance and roots in the non-commutative nature of the creation and the annihilation operators defined in obtaining the Fokker-Planck equation. The result of the quantum treatment, as compared with the experimental results, indicates conformity between theory and experiment (Corwin et al., 2003). The generated supercontinuum spectrums for the quantum mechanical and the classical treatments are studied for different peak powers and widths of the input pulse. It is concluded that the pulses of fs width behave as particles and described best by quantum models. In conclusion, the quantum theoretical treatments of light pulses passing through a nonlinear media describes the supercontinuum generation process closer to the experimental data as compared with classical models.

There are different types of noise involved in supercontinuum light, or generally in the propagation of electromagnetic waves in a nonlinear media, which are related to absorption, gain, Raman effects, and the quantum mechanical noise that could be described by stochastic equations. The noise involved in Raman effects has quantum origin, and it is present in a vacuum state (Corwin et al., 2003) due to spontaneous Raman effects. A semi-classical model of noise, due to the propagation of light pulses in fibers devised by Corwin and coworkers (2003), is based on adding this kind of noise to the GNLSE. However, the second-order nonlinear term was not included which is the source of the Raman noise. Nonetheless, this noise exists and should be included in the quantum theory of the field propagation in dielectric media (Corwin et al., 2003). In the present work, in order to reduce the fluctuations near solitons, one has to make use of Eq. (14.134) instead of Eq. (14.131), a process that is referred to as linearization (Safaei et al., 2018). However, it should be noted that the linearization is handled for squeezed photons, and, therefore, Eq. (14.134) is not valid for long-distance travel of light pulses even for an instantaneous nonlinear response. It is important to add the quantum noise involved in Raman effects to Eq. (14.131), to correctly reduce the quantum noises in the vicinity of the solitons, which were formed during the SCG process. New experimental work based on real-time measurement, similar to those of Närhi and coworkers (2016) and Wetzel and coworkers (2012) at 1550 nm pulses, is needed to study the SCG and all noises involved. Detailed understanding of the physics of ultrashort light pulses needs more

experimental works and their comparison with the present quantum theory of pulse propagation, specifically in fiber applications. Nonetheless, the medium response function and/or the parameters involved in it (such as Raman parameters and Raman delayed factor) could be different when a light pulse should be modeled quantum mechanically.

Appendix

Derivation of Eqs. (14.9) from (14.8) in this Chapter
Starting with the definition of displacement vector and its relation with the electric field as:

$$\mathbf{D}\left(t,\mathbf{x}\right)=\boldsymbol{\varepsilon}\left(\omega,\mathbf{x}\right)\dot{:}\mathbf{E}\left(t,\mathbf{x}\right), \tag{A.1}$$

one can rewrite it as:

$$\mathbf{E}\left(t,\mathbf{x}\right)=\boldsymbol{\eta}\left(\omega,\mathbf{x}\right)\dot{:}\mathbf{D}\left(t,\mathbf{x}\right), \tag{A.2}$$

where $\boldsymbol{\eta}^{-1}(\omega,\mathbf{x})=\boldsymbol{\varepsilon}(\omega,\mathbf{x})$. Therefore, Eq. (14.8) is rewritten as:

$$H_L=\int d^3\mathbf{x}\left[\frac{1}{2}\mathbf{D}^*\left(t,\mathbf{x}\right)\dot{:}\boldsymbol{\eta}\left(\omega,\mathbf{x}\right)\cdot\left(\frac{\partial\left(\omega\boldsymbol{\eta}^{-1}\left(\omega,\mathbf{x}\right)\right)}{\partial\omega}\right)_{\sim\text{constant}}\cdot\boldsymbol{\eta}\left(\omega,\mathbf{x}\right)\dot{:}\mathbf{D}\left(t,\mathbf{x}\right)+\frac{1}{2\mu}|\mathbf{B}\left(t,\mathbf{x}\right)|^2\right]. \tag{A.3}$$

One can simplify the frequency dependent factor of the first term in the integrand of equation (A.3) as:

$$\boldsymbol{\eta}\left(\omega,\mathbf{x}\right)\cdot\left(\frac{\partial\left(\omega\boldsymbol{\eta}^{-1}\left(\omega,\mathbf{x}\right)\right)}{\partial\omega}\right)_{\sim\text{constant}}\cdot\boldsymbol{\eta}\left(\omega,\mathbf{x}\right)=\boldsymbol{\eta}\left(\omega,\mathbf{x}\right)-\omega\frac{\partial}{\partial\omega}\boldsymbol{\eta}\left(\omega,\mathbf{x}\right), \tag{A.4}$$

which results in Eq. (14.9) in the chapter.

Derivation of Eq. 14.26, Starting from Maxwell's Equations
Let's start with the Maxwell equation (14.22a) from the manuscript. Substituting the dual potential for magnetic field from Equation (14.12), one arrives at:

$$-\mu\ddot{\boldsymbol{\Lambda}}\left(t,\mathbf{x}\right)=\nabla\times\mathbf{E}\left(t,\mathbf{x}\right). \tag{A.5}$$

Rewriting Equation (14.22b) for the electric field as:

$$\mathbf{E}(t,\mathbf{x}) = \int_0^\infty \boldsymbol{\eta}_1(\tau,\mathbf{x}) \dot{:} \dot{\mathbf{D}}(t-\tau,\mathbf{x})\, d\tau + \sum_{n>1}\left[\int_0^\infty \boldsymbol{\eta}_n(\tau_1,\ldots,\tau_n,\mathbf{x}) \dot{:} \dot{\mathbf{D}}(t-\tau_1,\mathbf{x}) \otimes \cdots \otimes \mathbf{D}(t-\tau_n,\mathbf{x})\, d\tau_1 \ldots d\tau_n\right]. \tag{A.6}$$

and substituting into (A.5), one concludes:

$$-\mu \ddot{\boldsymbol{\Lambda}}(t,\mathbf{x}) = \nabla \times \left[\int_0^\infty \boldsymbol{\eta}_1(\tau,\mathbf{x}) \dot{:} \dot{\mathbf{D}}(t-\tau,\mathbf{x})\, d\tau\right] + \nabla \times \left[\sum_{n>1}\int_0^\infty \boldsymbol{\eta}_n(\tau_1,\ldots,\tau_n,\mathbf{x}) \dot{:} \dot{\mathbf{D}}(t-\tau_1,\mathbf{x}) \otimes \cdots \otimes \mathbf{D}(t-\tau_n,\mathbf{x})\, d\tau_1 \ldots d\tau_n\right] \tag{A.7}$$

for the equation of motion. Making use of the dual potential for displacement vector, Eq. (14.12) in the chapter, Eq. (A.7) could be written as:

$$-\mu \ddot{\boldsymbol{\Lambda}}(t,\mathbf{x}) = \nabla \times \int_0^\infty \boldsymbol{\eta}_1(\tau,\mathbf{x}) \dot{:} \nabla \times \boldsymbol{\Lambda}(t-\tau,\mathbf{x})\, d\tau + \sum_{n>1} \nabla \times \int_0^\infty \boldsymbol{\eta}_n(\mathbf{x}) \dot{:} \nabla \times \boldsymbol{\Lambda}(t,\mathbf{x}) \otimes \cdots \otimes \nabla \times \boldsymbol{\Lambda}(t,\mathbf{x})\, d\tau_1 \ldots d\tau_n, \tag{A.8}$$

where it is assumed that $\boldsymbol{\eta}_n(\mathbf{x})$ for $n > 1$ to be independent of frequency. Substituting expansion (14.13) for the dual potential into Eq. (A.8), one arrives at:

$$-\mu \sum_{\nu=-N}^{\nu=N} \ddot{\boldsymbol{\Lambda}}^{\nu}(t,\mathbf{x}) = \sum_{\nu=-N}^{\nu=N} \nabla \times \int_0^\infty \boldsymbol{\eta}_1(\tau_1,\mathbf{x}) \dot{:} \nabla \times \boldsymbol{\Lambda}^{\nu}(t-\tau_1,\mathbf{x})\, d\tau_1 + \sum_{n>1} \sum_{\nu;\nu_1,\cdots,\nu_n} \nabla \times \left(\boldsymbol{\eta}_n(\mathbf{x}) \dot{:} \nabla \times \boldsymbol{\Lambda}^{\nu_1}(t,\mathbf{x}) \otimes \cdots \otimes \nabla \times \boldsymbol{\Lambda}^{\nu_n}(t,\mathbf{x})\right) \tag{A.9a}$$

where the equation of motion for mode ν is:

$$-\mu \ddot{\boldsymbol{\Lambda}}^{\nu}(t,\mathbf{x}) = \nabla \times \int_0^\infty \boldsymbol{\eta}_1(\tau,\mathbf{x}) \dot{:} \nabla \times \boldsymbol{\Lambda}^{\nu}(t-\tau,\mathbf{x})\, d\tau + \sum_{n>1} \sum_{\nu;\nu_1,\nu_2,\cdots,\nu_n} \nabla \times \left(\boldsymbol{\eta}_n(\mathbf{x}) \dot{:} \nabla \times \boldsymbol{\Lambda}^{\nu_1}(t,\mathbf{x}) \otimes \cdots \otimes \nabla \times \boldsymbol{\Lambda}^{\nu_n}(t,\mathbf{x})\right). \tag{A.9b}$$

Note the parameters of summation $\sum_{\nu;\nu_1,\nu_2,\cdots,\nu_n}$ stands for summation over all frequency modes other than mode ν. Additionally, the quantity $\boldsymbol{\eta}_1(\tau,\mathbf{x})$ will be written as $\boldsymbol{\eta}_\nu(\tau,\mathbf{x})$. Inserting $e^{i\omega^\nu\tau}e^{-i\omega^\nu\tau}=1$ into the integrand of Eq. (A.9b), one has:

$$-\mu\ddot{\boldsymbol{\Lambda}}^\nu(t,\mathbf{x}) = \nabla\times\left\{\int_0^\infty \boldsymbol{\eta}_\nu(\tau,\mathbf{x})\,e^{i\omega^\nu\tau}\vdots\left[\nabla\times e^{-i\omega^\nu\tau}\boldsymbol{\Lambda}^\nu(\mathbf{x},t-\tau)\right]d\tau + \sum_{n>1}\sum_{\nu_1,\cdots,\nu_n(\nu)}\boldsymbol{\eta}_n(\mathbf{x})\vdots\nabla\times\boldsymbol{\Lambda}^{\nu_1}(t,\mathbf{x})\otimes\cdots\otimes\nabla\times\boldsymbol{\Lambda}^{\nu_n}(t,\mathbf{x})\right\}. \tag{A.10}$$

The quantity $e^{-i\omega^\nu\tau}\boldsymbol{\Lambda}^\nu(\mathbf{x},t-\tau)$ is expanded into a Taylor series in terms of τ up to the third order as:

$$e^{-i\omega^\nu\tau}\boldsymbol{\Lambda}^\nu(\mathbf{x},t-\tau)\approx\boldsymbol{\Lambda}^\nu(\mathbf{x},t)-\tau\left[\dot{\boldsymbol{\Lambda}}^\nu(\mathbf{x},t)+i\omega^\nu\boldsymbol{\Lambda}^\nu\Big(\mathbf{x},t\Big)\right] + \tfrac{1}{2}\tau^2\left[\ddot{\boldsymbol{\Lambda}}^\nu(\mathbf{x},t)+2i\omega^\nu\dot{\boldsymbol{\Lambda}}^\nu\Big(\mathbf{x},t\Big)-(\omega^\nu)^2\boldsymbol{\Lambda}^\nu\Big(\mathbf{x},t\Big)\right]+\tfrac{1}{6}\tau^3[\cdots], \tag{A.11}$$

where slowly varying envelope approximation is applied. Equation (A.11) is rewritten as:

$$e^{-i\omega^\nu\tau}\boldsymbol{\Lambda}^\nu(\mathbf{x},t-\tau)\approx\boldsymbol{\Lambda}^\nu(\mathbf{x},t)\left[1-i\omega^\nu\tau-\tfrac{1}{2}\tau^2(\omega^\nu)^2+\cdots\right] + \dot{\boldsymbol{\Lambda}}^\nu(\mathbf{x},t)\left[-\tau+i\tau^2\omega^\nu+\cdots\right]+\ddot{\boldsymbol{\Lambda}}^\nu(\mathbf{x},t)\left[\tfrac{1}{2}\tau^2+\cdots\right]+\dddot{\boldsymbol{\Lambda}}^\nu(\mathbf{x},t)[\cdots]. \tag{A.12}$$

Now, Eq. (A.12) is replaced into the first term in the relation (A.10), and integrated over τ, the result will be:

$$\nabla\times\left\{\int_0^\infty d\tau\left[1-i\omega^\nu\tau-\frac{1}{2}\tau^2(\omega^\nu)^2+\cdots\right]e^{i\omega^\nu\tau}\boldsymbol{\eta}_\nu(\mathbf{x},\tau)\vdots\left[\nabla\times\boldsymbol{\Lambda}^\nu(t)\right]\right\} = \nabla\times\left[\boldsymbol{\eta}_\nu(\mathbf{x})\vdots\left(\nabla\times\boldsymbol{\Lambda}^\nu(\mathbf{x},t)\right)\right]. \tag{A.13a}$$

Similar arguments could be used for other terms of Eq. (A.11b), where one gets:

$$\nabla\times\left\{\int_0^\infty d\tau\left[-\tau-i\tau^2\omega^\nu+\cdots\right]e^{i\omega^\nu\tau}\boldsymbol{\eta}_\nu(\mathbf{x},\tau)\vdots\left[\nabla\times\dot{\boldsymbol{\Lambda}}^\nu(t)\right]\right\}=\nabla\times\left[i\boldsymbol{\eta}'_\nu(\mathbf{x})\vdots\left[\nabla\times\ddot{\boldsymbol{\Lambda}}^\nu(\mathbf{x},t)\right]\right] \tag{A.13b}$$

and:

$$\nabla \times \left\{ \int_0^\infty d\tau \left[\frac{1}{2}\tau^2 + \cdots \right] e^{i\omega^\nu \tau} \boldsymbol{\eta}_\nu (\mathbf{x}, \tau) \vdots \left[\nabla \times \dot{\boldsymbol{\Lambda}}^\nu (t) \right] \right\} = \nabla \times \left[-\frac{1}{2} \boldsymbol{\eta}_\nu'' (\mathbf{x}) \vdots \left[\nabla \times \dot{\boldsymbol{\Lambda}}^\nu (\mathbf{x}, t) \right] \right]. \tag{A.13c}$$

Therefore, by substituting results (A.13) into Eq. (A.10), the equation of motion will be:

$$\begin{aligned} -\mu \ddot{\boldsymbol{\Lambda}}^\nu (t, \mathbf{x}) = \nabla \times \Bigg\{ & \boldsymbol{\eta}_\nu (\mathbf{x}) \vdots \left[\nabla \times \boldsymbol{\Lambda}^\nu (\mathbf{x}, t) \right] + i \boldsymbol{\eta}_\nu' (\mathbf{x}) \vdots \left[\nabla \times \dot{\boldsymbol{\Lambda}}^\nu (\mathbf{x}, t) \right] - \tfrac{1}{2} \boldsymbol{\eta}_\nu'' (\mathbf{x}) \vdots \left[\nabla \times \ddot{\boldsymbol{\Lambda}}^\nu (\mathbf{x}, t) \right] \\ & - \tfrac{i}{6} \boldsymbol{\eta}_\nu''' (\mathbf{x}) \vdots \left[\nabla \times \dddot{\boldsymbol{\Lambda}}^\nu (\mathbf{x}, t) \right] + \sum_{n>1} \sum_{\nu; \nu_1, \cdots, \nu_n} \boldsymbol{\eta}_n (\mathbf{x}) \vdots (\nabla \times \boldsymbol{\Lambda}^{\nu_1} (\mathbf{x}, t)) \otimes \cdots \otimes (\nabla \times \boldsymbol{\Lambda}^{\nu_n} (\mathbf{x}, t)) \Bigg\}. \end{aligned} \tag{A.14}$$

Lagrangian Method to Derive Eqs. 14.25 and 14.26

Here, the equation of motion and the Hamiltonian will be derived making use of the Lagrangian density (14.28), which will, respectively, be equal to Equation (14.26) and Equation (14.25). When the Lagrangian density $\mathcal{L}$ is a function of $\boldsymbol{\Lambda}^\nu$, $\dot{\boldsymbol{\Lambda}}^\nu$, and $\ddot{\boldsymbol{\Lambda}}^\nu$, the Euler-Lagrange equation is:

$$\begin{aligned} & \frac{\partial \mathcal{L}}{\partial \Lambda_j^\nu} - \partial_t \left(\frac{\partial \mathcal{L}}{\partial \dot{\Lambda}_j^\nu} \right) - \partial_k \left(\frac{\partial \mathcal{L}}{\partial \left(\partial_k \Lambda_j^\nu \right)} \right) + \partial_t \partial_k \left(\frac{\partial \mathcal{L}}{\partial \left(\partial_k \dot{\Lambda}_j^\nu \right)} \right) \\ & \quad - \partial_t \partial_t \partial_k \left(\frac{\partial \mathcal{L}}{\partial \left(\partial_k \ddot{\Lambda}_j^\nu \right)} \right) = 0 \end{aligned} \tag{A.15}$$

where k represents the space coordinates x, y, and z and double k means summation over it. For an arbitrary vector $\mathbf{w}$, the transverse derivatives with respect to the components of vector $\boldsymbol{\Lambda}$ have the property:

$$\partial_k \frac{\partial}{\partial \partial_k \Lambda_x} (\nabla \times \boldsymbol{\Lambda}) \cdot \mathbf{w} = -(\nabla \times \mathbf{w})_x. \tag{A.16}$$

It is assumed that in Eq. (A.16), the vector $\boldsymbol{\Lambda}$ stands for either $\boldsymbol{\Lambda}^\nu$ or $\boldsymbol{\Lambda}^{-\nu}$ or their time derivative. For the present system, a general form of the Lagrangian density is defined as:

$$\begin{aligned}\mathcal{L} = \frac{1}{2}\sum_{\nu=-N}^{\nu=N}\Big[& a\left(\nabla\times\mathbf{\Lambda}^{-\nu}(t,\mathbf{x})\right)\cdot\boldsymbol{\eta}_{\nu}(\mathbf{x})\vdots\left(\nabla\times\mathbf{\Lambda}^{\nu}(t,\mathbf{x})\right) + b\left(\nabla\times\mathbf{\Lambda}^{-\nu}(t,\mathbf{x})\right)\cdot\boldsymbol{\eta}'_{\nu}(\mathbf{x})\vdots\left(\nabla\times\dot{\mathbf{\Lambda}}^{\nu}(t,\mathbf{x})\right)\\ & + c\left(\nabla\times\dot{\mathbf{\Lambda}}^{-\nu}(t,\mathbf{x})\right)\cdot\boldsymbol{\eta}'_{\nu}(\mathbf{x})\vdots\left(\nabla\times\mathbf{\Lambda}^{\nu}(t,\mathbf{x})\right) + d\left(\nabla\times\dot{\mathbf{\Lambda}}^{-\nu}(t,\mathbf{x})\right)\cdot\boldsymbol{\eta}''_{\nu}(\mathbf{x})\vdots\left(\nabla\times\dot{\mathbf{\Lambda}}^{\nu}(t,\mathbf{x})\right)\\ & + e\left(\nabla\times\ddot{\mathbf{\Lambda}}^{-\nu}(t,\mathbf{x})\right)\cdot\boldsymbol{\eta}'''_{\nu}(\mathbf{x})\vdots\left(\nabla\times\dot{\mathbf{\Lambda}}^{\nu}(t,\mathbf{x})\right) + f\left(\nabla\times\dot{\mathbf{\Lambda}}^{-\nu}(t,\mathbf{x})\right)\cdot\boldsymbol{\eta}'''_{\nu}(\mathbf{x})\vdots\left(\nabla\times\ddot{\mathbf{\Lambda}}^{\nu}(t,\mathbf{x})\right)\\ & + \mu\left(\dot{\mathbf{\Lambda}}^{-\nu}(t,\mathbf{x})\cdot\dot{\mathbf{\Lambda}}^{\nu}\left(t,\mathbf{x}\right)\right) + 2g\sum_{n>1}\sum_{\nu_1,\ldots,\nu_n}\frac{1}{n+1}\left(\nabla\times\mathbf{\Lambda}^{-\nu}(t,\mathbf{x})\right)\cdot\boldsymbol{\eta}_{n}(\mathbf{x})\\ & \vdots\left[\left(\nabla\times\mathbf{\Lambda}^{\nu_1}(\mathbf{x},t)\right)\cdots\left(\nabla\times\mathbf{\Lambda}^{\nu_n}(\mathbf{x},t)\right)\right]\end{aligned} \tag{A.17}$$

where coefficients a to g are to be determined by comparing the equation of motion and the Hamiltonian resulting from the Lagrangian density, Equation (A.17), with Equations 14.26 and 14.25 forming the chapter, respectively. Making use of Equation (A.16), the terms in Equation (A.15) are written as:

$$\frac{\partial\mathcal{L}}{\partial\Lambda_j^{-\nu}} = 0, \tag{A.18}$$

$$-\left(\frac{\partial\mathcal{L}}{\partial\dot{\Lambda}_j^{-\nu}}\right) = -\frac{1}{2}\mu\dot{\mathbf{\Lambda}}_j^{\nu}(t,\mathbf{x}), \tag{A.19}$$

$$\begin{aligned}-\partial_k\left(\frac{\partial\mathcal{L}}{\partial\left(\partial_k\dot{\Lambda}_j^{-\nu}\right)}\right) = {} & \frac{1}{2}a\left\{\nabla\times\left[\boldsymbol{\eta}_{\nu}(\mathbf{x})\vdots\left(\nabla\times\mathbf{\Lambda}^{\nu}(t,\mathbf{x})\right)\right]\right\}_j + \frac{1}{2}b\left\{\nabla\times\left[\boldsymbol{\eta}'_{\nu}(\mathbf{x})\vdots\left(\nabla\times\dot{\mathbf{\Lambda}}^{\nu}(t,\mathbf{x})\right)\right]\right\}_j\\ & + \left\{g\sum_{n>1}\sum_{\nu;\nu_1,\cdots,\nu_n}\nabla\times\left[\boldsymbol{\eta}_{n}(\mathbf{x})\vdots\left(\nabla\times\mathbf{\Lambda}^{\nu_1}(\mathbf{x},t)\right)\ldots\left(\nabla\times\mathbf{\Lambda}^{\nu_n}(\mathbf{x},t)\right)\right]\right\}_j,\end{aligned} \tag{A.20}$$

$$\begin{aligned}\partial_k\left(\frac{\partial\mathcal{L}}{\partial\left(\partial_k\ddot{\Lambda}_j^{-\nu}\right)}\right) = {} & -\frac{1}{2}c\left\{\nabla\times\left[\boldsymbol{\eta}'_{\nu}(\mathbf{x})\vdots\left(\nabla\times\mathbf{\Lambda}^{\nu}(t,\mathbf{x})\right)\right]\right\}_j\\ & - \frac{1}{2}d\left\{\nabla\times\left[\boldsymbol{\eta}''_{\nu}(\mathbf{x})\vdots\left(\nabla\times\dot{\mathbf{\Lambda}}^{\nu}(t,\mathbf{x})\right)\right]\right\}_j - \frac{1}{2}f\left\{\nabla\times\left[\boldsymbol{\eta}'''_{\nu}(\mathbf{x})\vdots\left(\nabla\times\ddot{\mathbf{\Lambda}}^{\nu}(t,\mathbf{x})\right)\right]\right\}_j\end{aligned} \tag{A.21}$$

and:

$$-\partial_k\left(\frac{\partial\mathcal{L}}{\partial\left(\partial_k\dddot{\Lambda}_j^{-\nu}\right)}\right) = \frac{1}{2}e\left\{\nabla\times\left[\boldsymbol{\eta}'''_{\nu}(\mathbf{x})\vdots\left(\nabla\times\dot{\mathbf{\Lambda}}^{\nu}(t,\mathbf{x})\right)\right]\right\}_j. \tag{A.22}$$

Substituting the results (A.18, A.19, A.20, A.21, and A.22) into Euler-Lagrange equation, Eq. (A.15), each component of the equation of motion will be:

$$-\mu\ddot{\mathbf{\Lambda}}_j^{\nu}(t,\mathbf{x}) = (c-b)\left\{\nabla\times\left[\boldsymbol{\eta}_{\nu}'(\mathbf{x})\vdots\left(\nabla\times\dot{\mathbf{\Lambda}}^{\nu}(t,\mathbf{x})\right)\right]\right\}_j - a\left\{\nabla\times\left[\boldsymbol{\eta}_{\nu}(\mathbf{x})\vdots\left(\nabla\times\mathbf{\Lambda}^{\nu}(t,\mathbf{x})\right)\right]\right\}_j$$
$$+ d\left\{\nabla\times\left[\boldsymbol{\eta}_{\nu}''(\mathbf{x})\vdots\left(\nabla\times\ddot{\mathbf{\Lambda}}^{\nu}(t,\mathbf{x})\right)\right]\right\}_j + (e-f)\left\{\nabla\times\left[\boldsymbol{\eta}_{\nu}'''(\mathbf{x})\vdots\left(\nabla\times\dddot{\mathbf{\Lambda}}^{\nu}(t,\mathbf{x})\right)\right]\right\}_j$$
$$-\left\{g\sum_{n>1}\sum_{\nu;\nu_1,\cdots,\nu_n}\nabla\times\left[\boldsymbol{\eta}_n(\mathbf{x})\vdots\left(\nabla\times\mathbf{\Lambda}^{\nu_1}(\mathbf{x},t)\right)\ldots\left(\nabla\times\mathbf{\Lambda}^{\nu_n}(\mathbf{x},t)\right)\right]\right\}_j \tag{A.23}$$

where the equation of motion will be:

$$-\mu\ddot{\mathbf{\Lambda}}^{\nu}(t,\mathbf{x}) = \nabla\times\left\{-a\boldsymbol{\eta}_{\nu}(\mathbf{x})\vdots\left[\nabla\times\mathbf{\Lambda}^{\nu}(t,\mathbf{x})\right] + (c-b)\,\boldsymbol{\eta}_{\nu}'(\mathbf{x})\vdots\left[\nabla\times\dot{\mathbf{\Lambda}}^{\nu}(t,\mathbf{x})\right] + d\boldsymbol{\eta}_{\nu}''(\mathbf{x})\vdots\left[\nabla\times\ddot{\mathbf{\Lambda}}^{\nu}(t,\mathbf{x})\right]\right.$$
$$\left. + (e-f)\,\boldsymbol{\eta}_{\nu}'''(\mathbf{x})\vdots\left[\nabla\times\dddot{\mathbf{\Lambda}}^{\nu}(t,\mathbf{x})\right] - g\sum_{n>1}\sum_{\nu;\nu_1,\cdots,\nu_n}\boldsymbol{\eta}_n(\mathbf{x})\vdots\left[\left(\nabla\times\mathbf{\Lambda}^{\nu_1}(t,\mathbf{x})\right)\otimes\cdots\otimes\left(\nabla\times\mathbf{\Lambda}^{\nu_n}(t,\mathbf{x})\right)\right]\right\}. \tag{A.24}$$

Comparing (A.24) with Eq. (14.26) in the chapter, the relations:

$$a=-1,\quad e-f=-\frac{i}{6},\quad c-b=i,\quad d=-\frac{1}{2}\ \ and\ \ g=-1 \tag{A.25}$$

are found for the parameters a to g in Eq. (A.17).

According to Ostrogradsky's theorem, when the Lagrangian density is a function of $\mathbf{\Lambda}^{\nu}$, $\dot{\mathbf{\Lambda}}^{\nu}$, $\ddot{\mathbf{\Lambda}}^{\nu}$, $\mathbf{\Lambda}^{-\nu}$, $\dot{\mathbf{\Lambda}}^{-\nu}$, and $\ddot{\mathbf{\Lambda}}^{-\nu}$, there are four canonical coordinates and momenta. Therefore, the canonical momenta are obtained by the definitions:

$$\Pi_j^{-\nu} = \left(\frac{\partial\boldsymbol{\mathcal{L}}}{\partial\dot{\Lambda}_j^{-\nu}}\right) - \partial_k\left(\frac{\partial\boldsymbol{\mathcal{L}}}{\partial\left(\partial_k\dot{\Lambda}_j^{-\nu}\right)}\right) + \partial_t\partial_k\left(\frac{\partial\boldsymbol{\mathcal{L}}}{\partial\left(\partial_k\ddot{\Lambda}_j^{-\nu}\right)}\right) \tag{A.26}$$

and:

$$\Sigma_j^{-\nu} = -\partial_k\left(\frac{\partial\boldsymbol{\mathcal{L}}}{\partial\left(\partial_k\ddot{\Lambda}_j^{-\nu}\right)}\right). \tag{A.27}$$

Substituting relations (A.19), (A.21), and (A.22) into definitions (A.26) and (A.27), the components of canonical momenta for the canonical coordinates $\mathbf{\Lambda}^{-\nu}$ and $\dot{\mathbf{\Lambda}}^{-\nu}$ are found as:

$$\Pi_j^{-\nu} = \tfrac{1}{2}\mu\dot{\mathbf{\Lambda}}_j^{\nu}(t,\mathbf{x}) + \tfrac{1}{2}c\left\{\nabla\times\left[\boldsymbol{\eta}_{\nu}'(\mathbf{x})\vdots\left(\nabla\times\mathbf{\Lambda}^{\nu}(t,\mathbf{x})\right)\right]\right\}_j$$
$$+\tfrac{1}{2}d\left\{\nabla\times\left[\boldsymbol{\eta}_{\nu}''(\mathbf{x})\vdots\left(\nabla\times\dot{\mathbf{\Lambda}}^{\nu}(t,\mathbf{x})\right)\right]\right\}_j + \tfrac{1}{2}(f-e)\left\{\nabla\times\left[\boldsymbol{\eta}_{\nu}'''(\mathbf{x})\vdots\left(\nabla\times\ddot{\mathbf{\Lambda}}^{\nu}(t,\mathbf{x})\right)\right]\right\}_j \tag{A.28}$$

and:

$$\Sigma_j^{-\nu} = \frac{1}{2} e \left\{ \nabla \times \left[\boldsymbol{\eta}_\nu''' (\mathbf{x}) \vdots \left(\nabla \times \dot{\boldsymbol{\Lambda}}^{\nu} (t, \mathbf{x}) \right) \right] \right\}_j . \tag{A.29}$$

Therefore, the canonical momenta associated with the canonical coordinates $\boldsymbol{\Lambda}^{-\nu}$, $\dot{\boldsymbol{\Lambda}}^{-\nu}$, $\boldsymbol{\Lambda}^{\nu}$, and $\dot{\boldsymbol{\Lambda}}^{\nu}$ are:

$$\begin{aligned} \boldsymbol{\Pi}^{-\nu} = \sum_j \Pi_j^{-\nu} \hat{\mathbf{e}}_j = \tfrac{1}{2} \mu \dot{\boldsymbol{\Lambda}}^{\nu} (t, \mathbf{x}) + \tfrac{1}{2} c \nabla \times \Big[& \boldsymbol{\eta}_\nu' (\mathbf{x}) \vdots (\nabla \times \boldsymbol{\Lambda}^{\nu} (t, \mathbf{x})) \\ & + \tfrac{1}{2} d \ \boldsymbol{\eta}_\nu'' (\mathbf{x}) \vdots \left(\nabla \times \dot{\boldsymbol{\Lambda}}^{\nu} (t, \mathbf{x}) \right) + \tfrac{1}{2} (f - e) \ \boldsymbol{\eta}_\nu''' (\mathbf{x}) \vdots \left(\nabla \times \ddot{\boldsymbol{\Lambda}}^{\nu} (t, \mathbf{x}) \right) \Big], \end{aligned} \tag{A.30}$$

$$\boldsymbol{\Sigma}^{-\nu} = \sum_j \Sigma_j^{-\nu} \hat{\mathbf{e}}_j = \frac{1}{2} \nabla \times \left[e \boldsymbol{\eta}_\nu''' (\mathbf{x}) \vdots \left(\nabla \times \dot{\boldsymbol{\Lambda}}^{\nu} (t, \mathbf{x}) \right) \right], \tag{A.31}$$

$$\begin{aligned} \boldsymbol{\Pi}^{\nu} = \sum_j \Pi_j^{\nu} \hat{\mathbf{e}}_j = \tfrac{1}{2} \mu \dot{\boldsymbol{\Lambda}}^{-\nu} (t, \mathbf{x}) + \tfrac{1}{2} \nabla \times \Big[& b \ \left(\nabla \times \boldsymbol{\Lambda}^{-\nu} (t, \mathbf{x}) \right) \cdot \boldsymbol{\eta}_\nu' (\mathbf{x}) \\ & + d \ \left(\nabla \times \dot{\boldsymbol{\Lambda}}^{-\nu} (t, \mathbf{x}) \right) \cdot \boldsymbol{\eta}_\nu'' (\mathbf{x}) + (e - f) \ \left(\nabla \times \ddot{\boldsymbol{\Lambda}}^{-\nu} (t, \mathbf{x}) \right) \cdot \boldsymbol{\eta}_\nu''' (\mathbf{x}) \Big] \end{aligned} \tag{A.32}$$

and:

$$\boldsymbol{\Sigma}^{\nu} = \sum_j \Sigma_j^{\nu} \hat{\mathbf{e}}_j = \frac{1}{2} \nabla \times \left[f \left(\nabla \times \dot{\boldsymbol{\Lambda}}^{-\nu} (t, \mathbf{x}) \right) \cdot \boldsymbol{\eta}_\nu''' (\mathbf{x}) \right], \tag{A.33}$$

respectively.

Making use of the definition for Hamiltonian as:

$$H = \left[\sum_{\nu=-N}^{\nu=N} \int d^3\mathbf{x} \left(\boldsymbol{\Pi}^{\nu} \cdot \dot{\boldsymbol{\Lambda}}^{\nu} + \boldsymbol{\Pi}^{-\nu} \cdot \dot{\boldsymbol{\Lambda}}^{-\nu} + \boldsymbol{\Sigma}^{\nu} \cdot \ddot{\boldsymbol{\Lambda}}^{\nu} + \boldsymbol{\Sigma}^{-\nu} \cdot \ddot{\boldsymbol{\Lambda}}^{-\nu} \right) \right] - \int d^3\mathbf{x} \, \mathcal{L} \tag{A.34}$$

in the Euler-Lagrange formalism, integrating some of the terms by parts as:

$$\int d^3\mathbf{x} \, \mathbf{V}_1 \cdot (\nabla \times \mathbf{V}_2) = \int d^3\mathbf{x} \, \mathbf{V}_2 \cdot (\nabla \times \mathbf{V}_1) \tag{A.35}$$

with the fact that the fields vanish at infinity, one finds the Hamiltonian to be:

$$H=\frac{1}{2}\sum_{\nu=-N}^{\nu=N}\int\left\{\left[-a\left(\nabla\times\mathbf{\Lambda}^{-\nu}(t,\mathbf{x})\right)\cdot\boldsymbol{\eta}_{\nu}(\mathbf{x})\vdots\left(\nabla\times\mathbf{\Lambda}^{\nu}(t,\mathbf{x})\right)+d\left(\nabla\times\dot{\mathbf{\Lambda}}^{-\nu}(t,\mathbf{x})\right)\cdot\boldsymbol{\eta}_{\nu}''(\mathbf{x})\vdots\left(\nabla\times\dot{\mathbf{\Lambda}}^{\nu}(t,\mathbf{x})\right)\right.\right.$$
$$+(e-f)\left(\nabla\times\ddot{\mathbf{\Lambda}}^{-\nu}(t,\mathbf{x})\right)\cdot\boldsymbol{\eta}_{\nu}'''(\mathbf{x})\vdots\left(\nabla\times\dot{\mathbf{\Lambda}}^{\nu}(t,\mathbf{x})\right)+(f-e)\left(\nabla\times\dot{\mathbf{\Lambda}}^{-\nu}(t,\mathbf{x})\right)\cdot\boldsymbol{\eta}_{\nu}'''(\mathbf{x})\vdots\left(\nabla\times\ddot{\mathbf{\Lambda}}^{\nu}(t,\mathbf{x})\right)\Big]$$
$$+\mu\left(\dot{\mathbf{\Lambda}}^{-\nu}(t,\mathbf{x})\cdot\dot{\mathbf{\Lambda}}^{\nu}\left(t,\mathbf{x}\right)\right)-2g\sum_{n>1}\sum_{\nu_1,\ldots,\nu_n}\frac{1}{n+1}\left(\nabla\times\mathbf{\Lambda}^{\nu}(t,\mathbf{x})\right)\cdot\boldsymbol{\eta}_{n}(\mathbf{x})$$
$$\left.\left.\vdots\left[\left(\nabla\times\mathbf{\Lambda}^{\nu_1}(\mathbf{x},t)\right)\cdots\left(\nabla\times\mathbf{\Lambda}^{\nu_n}(\mathbf{x},t)\right)\right]\right\}d^3\mathbf{x}. \tag{A.36}$$

Again, comparing the parameters in (A.36) with the Hamiltonian (14.25) in the chapter which are similar to the parameters (A.25) and assuming the symmetry in the Lagrangian density, the final parameters will be:

$$a=-1,\ \ b=-\frac{i}{2},\ \ c=\frac{i}{2},\ \ d=-\frac{1}{2},\ \ e=-\frac{i}{12},\ \ f=\frac{i}{12},\ \ and\ \ g=-1. \tag{A.37}$$

In summary, the results obtained implementing the Lagrangian density A.17 agree both in dynamics and energy with the results obtained from Maxwell equations and Poynting's theorem for slowly varying envelope functions. Thus, the Lagrangian density (A.17) describes the system in the framework of a local field theory of a nonlinear dispersive medium. By using the scaler coefficients, A.37, and separating the Lagrangian density A.17 into the linear and nonlinear parts, Eqs. 14.28 and 14.29 of the chapter are yielded. In addition, Eqs. 14.25, 14.26, 14.31, and 14.32 are also obtained by implementing the coefficients A.37 into A.36, A.24, A.32, and A.33, respectively.

Derivation of Eqs. 14.35, 14.36, and 14.37

Starting with Equation 14.34 from the manuscript and the fact that $(\mathbf{\Lambda}^{\nu}(t,\mathbf{x}))^{*}=\mathbf{\Lambda}^{-\nu}(t,\mathbf{x})$, it is concluded that:

$$\left(\lambda_{\mathbf{k},\alpha}^{\nu}(t)\right)^{*}\hat{\mathbf{e}}_{\mathbf{k},\alpha}^{*}=\lambda_{\text{-}\mathbf{k},\alpha}^{-\nu}(t)\hat{\mathbf{e}}_{\text{-}\mathbf{k},\alpha}. \tag{A.38a}$$

Thus:

$$\left(\lambda_{\mathbf{k},\alpha}^{\nu}(t)\right)^{*}=-(-1)^{\alpha}\lambda_{\text{-}\mathbf{k},\alpha}^{-\nu}(t) \tag{A.38b}$$

and:

$$\hat{\mathbf{e}}_{\mathbf{k},\alpha}^{*}=-(-1)^{\alpha}\hat{\mathbf{e}}_{\text{-}\mathbf{k},\alpha}. \tag{A.39}$$

By simple algebra, it can be shown that:

$$\nabla \times \mathbf{\Lambda}^{\nu}(t,\mathbf{x}) = \frac{i}{\sqrt{\mathrm{V}}} \sum_{\mathbf{k},\alpha} \lambda^{\nu}_{\mathbf{k},\alpha}(t) e^{i\mathbf{k}\cdot\mathbf{x}} \mathbf{k} \times \hat{\mathbf{e}}_{\mathbf{k},\alpha} \tag{A.40}$$

and:

$$\nabla \times \mathbf{\Lambda}^{-\nu}(t,\mathbf{x}) = \frac{-i}{\sqrt{\mathrm{V}}} \sum_{\mathbf{k},\alpha} \left(\lambda^{\nu}_{\mathbf{k},\alpha}(t)\right)^{*} e^{-i\mathbf{k}\cdot\mathbf{x}} \mathbf{k} \times \hat{\mathbf{e}}^{*}_{\mathbf{k},\alpha}. \tag{A.41}$$

Substituting (A.40) and (A.41) into the linear part of Lagrangian density (14.28) in the chapter, one arrives at the linear part of the Lagrangian as:

$$\begin{aligned} L_L = \tfrac{1}{2V} \sum_{\nu=-N}^{\nu=N} \sum_{\mathbf{k}',\alpha'} \sum_{\mathbf{k},\alpha} \int d^3\mathbf{x} \Bigg\{ \Bigg[& -\left(\lambda^{\nu}_{\mathbf{k}',\alpha'}(t)\right)^{*} \left(\mathbf{k}' \times \hat{\mathbf{e}}^{*}_{\mathbf{k}',\alpha'}\right) \cdot \boldsymbol{\eta}_{\nu}(\mathbf{x}) \vdots \left(\mathbf{k} \times \hat{\mathbf{e}}_{\mathbf{k},\alpha}\right) \lambda^{\nu}_{\mathbf{k},\alpha}(t) + \tfrac{i}{2} \left(\dot{\lambda}^{\nu}_{\mathbf{k}',\alpha'}(t)\right)^{*} \\ & \left(\mathbf{k} \times \hat{\mathbf{e}}_{\mathbf{k},\alpha}\right) \cdot \boldsymbol{\eta}'_{\nu}(\mathbf{x}) \vdots \left(\mathbf{k}' \times \hat{\mathbf{e}}^{*}_{\mathbf{k}',\alpha'}\right) \lambda^{\nu}_{\mathbf{k},\alpha}(t) - \tfrac{i}{2} \left(\lambda^{\nu}_{\mathbf{k}',\alpha'}(t)\right)^{*} \left(\mathbf{k}' \times \hat{\mathbf{e}}^{*}_{\mathbf{k}',\alpha'}\right) \cdot \boldsymbol{\eta}'_{\nu}(\mathbf{x}) \vdots \left(\mathbf{k} \times \hat{\mathbf{e}}_{\mathbf{k},\alpha}\right) \dot{\lambda}^{\nu}_{\mathbf{k},\alpha}(t) \\ & + \tfrac{i}{6} \left(\ddot{\lambda}^{\nu}_{\mathbf{k}',\alpha'}(t)\right)^{*} \left(\mathbf{k}' \times \hat{\mathbf{e}}^{*}_{\mathbf{k}',\alpha'}\right) \cdot \boldsymbol{\eta}'''_{\nu}(\mathbf{x}) \vdots \left(\mathbf{k} \times \hat{\mathbf{e}}_{\mathbf{k},\alpha}\right) \dot{\lambda}^{\nu}_{\mathbf{k},\alpha}(t) - \tfrac{i}{6} \left(\dot{\lambda}^{\nu}_{\mathbf{k}',\alpha'}(t)\right)^{*} \left(\mathbf{k} \times \hat{\mathbf{e}}_{\mathbf{k},\alpha}\right) \cdot \boldsymbol{\eta}'''_{\nu}(\mathbf{x}) \vdots \\ & \left(\mathbf{k}' \times \hat{\mathbf{e}}^{*}_{\mathbf{k}',\alpha'}\right) \ddot{\lambda}^{\nu}_{\mathbf{k},\alpha}(t) + \mu \left(\dot{\lambda}^{\nu}_{\mathbf{k}',\alpha'}(t)\right)^{*} \hat{\mathbf{e}}^{*}_{\mathbf{k}',\alpha'} \cdot \hat{\mathbf{e}}_{\mathbf{k},\alpha} \dot{\lambda}^{\nu}_{\mathbf{k},\alpha}(t) - \tfrac{1}{2} \left(\dot{\lambda}^{\nu}_{\mathbf{k}',\alpha'}(t)\right)^{*} \left(\mathbf{k}' \times \hat{\mathbf{e}}^{*}_{\mathbf{k}',\alpha'}\right) \\ & \cdot \boldsymbol{\eta}''_{\nu}(\mathbf{x}) \vdots \left(\mathbf{k} \times \hat{\mathbf{e}}_{\mathbf{k},\alpha}\right) \dot{\lambda}^{\nu}_{\mathbf{k},\alpha}(t) \Bigg] e^{i(\mathbf{k}-\mathbf{k}')\cdot\mathbf{x}} \Bigg\}. \end{aligned} \tag{A.42}$$

Defining the quantities:

$$M^{(1)\nu}_{(\mathbf{k}',\alpha')(\mathbf{k},\alpha)} = \frac{1}{\mathrm{V}} \int d^3\mathbf{x} \left(\mathbf{k}' \times \hat{\mathbf{e}}^{*}_{\mathbf{k}',\alpha'}\right) \cdot \boldsymbol{\eta}_{\nu}(\mathbf{x}) \vdots \left(\mathbf{k} \times \hat{\mathbf{e}}_{\mathbf{k},\alpha}\right) e^{i(\mathbf{k}-\mathbf{k}')\cdot\mathbf{x}}, \tag{A.43}$$

$$M^{(2)\nu}_{(\mathbf{k}',\alpha')(\mathbf{k},\alpha)} = \frac{1}{2\mathrm{V}} \int d^3\mathbf{x} \left(\mathbf{k}' \times \hat{\mathbf{e}}^{*}_{\mathbf{k}',\alpha'}\right) \cdot \boldsymbol{\eta}'_{\nu}(\mathbf{x}) \vdots \left(\mathbf{k} \times \hat{\mathbf{e}}_{\mathbf{k},\alpha}\right) e^{i(\mathbf{k}-\mathbf{k}')\cdot\mathbf{x}}, \tag{A.44}$$

$$M^{(2')\nu}_{(\mathbf{k},\alpha)(\mathbf{k}',\alpha')} = \frac{1}{2\mathrm{V}} \int d^3\mathbf{x} \left(\mathbf{k} \times \hat{\mathbf{e}}_{\mathbf{k},\alpha}\right) \cdot \boldsymbol{\eta}'_{\nu}(\mathbf{x}) \vdots \left(\mathbf{k}' \times \hat{\mathbf{e}}^{*}_{\mathbf{k}',\alpha'}\right) e^{i(\mathbf{k}-\mathbf{k}')\cdot\mathbf{x}} = M^{(2)\nu *}_{(\mathbf{k},\alpha)(\mathbf{k}',\alpha')}, \tag{A.45}$$

$$\begin{aligned} M^{(3)\nu}_{(\mathbf{k}',\alpha')(\mathbf{k},\alpha)} &= \tfrac{1}{\mathrm{V}} \int d^3\mathbf{x} \left\{ \mu \hat{\mathbf{e}}^{*}_{\mathbf{k}',\alpha'} \cdot \hat{\mathbf{e}}_{\mathbf{k},\alpha} - \tfrac{1}{2} \left(\mathbf{k}' \times \hat{\mathbf{e}}^{*}_{\mathbf{k}',\alpha'}\right) \cdot \boldsymbol{\eta}''_{\nu}(\mathbf{x}) \cdot \left(\mathbf{k} \times \hat{\mathbf{e}}_{\mathbf{k},\alpha}\right) \right\} e^{i(\mathbf{k}-\mathbf{k}')\cdot\mathbf{x}} \\ &= \left[\mu \hat{\mathbf{e}}^{*}_{\mathbf{k}',\alpha'} \cdot \hat{\mathbf{e}}_{\mathbf{k},\alpha} \delta_{\mathbf{k}',\mathbf{k}} - \tfrac{1}{2\mathrm{V}} \int d^3\mathbf{x} \left(\mathbf{k}' \times \hat{\mathbf{e}}^{*}_{\mathbf{k}',\alpha'}\right) \cdot \boldsymbol{\eta}''_{\nu}(\mathbf{x}) \vdots \left(\mathbf{k} \times \hat{\mathbf{e}}_{\mathbf{k},\alpha}\right) e^{i(\mathbf{k}-\mathbf{k}')\cdot\mathbf{x}} \right], \end{aligned} \tag{A.46}$$

$$M^{(4)\nu}_{(\mathbf{k}',\alpha')(\mathbf{k},\alpha)} = \frac{1}{6\mathrm{V}} \int d^3\mathbf{x} \left(\mathbf{k}' \times \hat{\mathbf{e}}^{*}_{\mathbf{k}',\alpha'}\right) \cdot \boldsymbol{\eta}'''_{\nu}(\mathbf{x}) \vdots \left(\mathbf{k} \times \hat{\mathbf{e}}_{\mathbf{k},\alpha}\right) e^{i(\mathbf{k}-\mathbf{k}')\cdot\mathbf{x}} \tag{A.47}$$

and:

$$M^{(4')\nu}_{(\mathbf{k},\alpha)(\mathbf{k}',\alpha')} = \frac{1}{6\mathrm{V}} \int d^3\mathbf{x} \left(\mathbf{k} \times \hat{\mathbf{e}}_{\mathbf{k},\alpha}\right) \cdot \boldsymbol{\eta}'''_{\nu}(\mathbf{x}) \vdots \left(\mathbf{k}' \times \hat{\mathbf{e}}^{*}_{\mathbf{k}',\alpha'}\right) e^{i(\mathbf{k}-\mathbf{k}')\cdot\mathbf{x}} = M^{(4)\nu *}_{(\mathbf{k}',\alpha')(\mathbf{k},\alpha)}, \tag{A.48}$$

the Lagrangian (A.42) will be simplified as:

$$\begin{aligned} L_L = \tfrac{1}{2} \sum_{\nu=-N}^{\nu=N} \sum_{\mathbf{k}',\alpha'} \sum_{\mathbf{k},\alpha} \Big[& -\left(\lambda^{\nu}_{\mathbf{k}',\alpha'}(t)\right)^{*} M^{(1)\nu}_{(\mathbf{k}',\alpha')(\mathbf{k},\alpha)} \lambda^{\nu}_{\mathbf{k},\alpha}(t) - i\left(\lambda^{\nu}_{\mathbf{k}',\alpha'}(t)\right)^{*} M^{(2)\nu}_{(\mathbf{k}',\alpha')(\mathbf{k},\alpha)} \dot{\lambda}^{\nu}_{\mathbf{k},\alpha}(t) \\ & + i\left(\dot{\lambda}^{\nu}_{\mathbf{k}',\alpha'}(t)\right)^{*} M^{(2')\nu}_{(\mathbf{k},\alpha)(\mathbf{k}',\alpha')} \lambda^{\nu}_{\mathbf{k},\alpha}(t) + \left(\dot{\lambda}^{\nu}_{\mathbf{k}',\alpha'}(t)\right)^{*} M^{(3)\nu}_{(\mathbf{k}',\alpha')(\mathbf{k},\alpha)} \dot{\lambda}^{\nu}_{\mathbf{k},\alpha}(t) \\ & + i\left(\ddot{\lambda}^{\nu}_{\mathbf{k}',\alpha'}(t)\right)^{*} M^{(4)\nu}_{(\mathbf{k}',\alpha')(\mathbf{k},\alpha)} \dot{\lambda}^{\nu}_{\mathbf{k},\alpha}(t) \;\; -i\left(\dot{\lambda}^{\nu}_{\mathbf{k}',\alpha'}(t)\right)^{*} M^{(4')\nu}_{(\mathbf{k},\alpha)(\mathbf{k}',\alpha')} \ddot{\lambda}^{\nu}_{\mathbf{k},\alpha}(t) \Big]. \end{aligned} \tag{A.49}$$

It is necessary to discuss the quantities M, specifically for definitions (A.47) and (A.48). Starting with Eq. (A.48), one arrives at:

$$\begin{aligned} M^{(4')\nu}_{(\mathbf{k},\alpha)(\mathbf{k}',\alpha')} &\to \tfrac{1}{6\mathrm{V}} \int d^3\mathbf{x} \left(-\mathbf{k} \times \hat{\mathbf{e}}_{-\mathbf{k},\alpha}\right) \cdot \boldsymbol{\eta}'''_{\nu}(\mathbf{x}) \vdots \left(-\mathbf{k}' \times \hat{\mathbf{e}}^{*}_{-\mathbf{k}',\alpha'}\right) e^{-i(\mathbf{k}-\mathbf{k}')\cdot\mathbf{x}} \\ &= \tfrac{1}{6\mathrm{V}} \int d^3\mathbf{x} \left(\mathbf{k} \times \hat{\mathbf{e}}_{-\mathbf{k},\alpha}\right) \cdot \boldsymbol{\eta}'''_{\nu}(\mathbf{x}) \vdots \left(\mathbf{k}' \times \hat{\mathbf{e}}^{*}_{-\mathbf{k}',\alpha'}\right) e^{-i(\mathbf{k}-\mathbf{k}')\cdot\mathbf{x}}. \end{aligned} \tag{A.50}$$

where **k** and **k'** are changed into $-\mathbf{k}$ and $-\mathbf{k}'$, respectively. Now making use of the relation (A.39), one concludes that:

$$M^{(4')\nu}_{(\mathbf{k},\alpha)(\mathbf{k}',\alpha')} \to \frac{1}{6\mathrm{V}} \int d^3\mathbf{x} \left(\mathbf{k} \times \hat{\mathbf{e}}^{*}_{\mathbf{k},\alpha}\right) \cdot \boldsymbol{\eta}'''_{\nu}(\mathbf{x}) \vdots \left(\mathbf{k}' \times \hat{\mathbf{e}}_{\mathbf{k}',\alpha'}\right) e^{-i(\mathbf{k}-\mathbf{k}')\cdot\mathbf{x}}. \tag{A.51}$$

Another change into Eq. (A.51), i.e., interchanging **k** with **k'**, leads to:

$$M^{(4')\nu}_{(\mathbf{k},\alpha)(\mathbf{k}',\alpha')} \overset{(\mathbf{k},\alpha)\leftrightarrow(\mathbf{k}',\alpha')}{\to} \frac{1}{6\mathrm{V}} \int d^3\mathbf{x} \left(\mathbf{k}' \times \hat{\mathbf{e}}^{*}_{\mathbf{k}',\alpha'}\right) \cdot \boldsymbol{\eta}'''_{\nu}(\mathbf{x}) \vdots \left(\mathbf{k} \times \hat{\mathbf{e}}_{\mathbf{k},\alpha}\right) e^{i(\mathbf{k}-\mathbf{k}')\cdot\mathbf{x}} = M^{(4)\nu}_{(\mathbf{k}',\alpha')(\mathbf{k},\alpha)}. \tag{A.52}$$

A similar argument holds for definition (A.44), which results in:

$$M^{(2')\nu}_{(\mathbf{k},\alpha)(\mathbf{k}',\alpha')} \to M^{(2)\nu}_{(\mathbf{k}',\alpha')(\mathbf{k},\alpha)}. \tag{A.53}$$

Therefore, the Lagrangian will be simplified as:

$$L_L = \frac{1}{2}\sum_{\nu=-N}^{\nu=N}\sum_{\mathbf{k}',\alpha'}\sum_{\mathbf{k},\alpha}\left\{-\left(\lambda^{\nu}_{\mathbf{k}',\alpha'}\right)^{*}M^{(1)\nu}_{(\mathbf{k}',\alpha')(\mathbf{k},\alpha)}\lambda^{\nu}_{\mathbf{k},\alpha} - i\left[\left(\lambda^{\nu}_{\mathbf{k}',\alpha'}\right)^{*}M^{(2)\nu}_{(\mathbf{k}',\alpha')(\mathbf{k},\alpha)}\dot{\lambda}^{\nu}_{\mathbf{k},\alpha}\right.\right.$$
$$\left.-\left(\dot{\lambda}^{\nu}_{\mathbf{k}',\alpha'}\right)^{*}M^{(2)\nu}_{(\mathbf{k}',\alpha')(\mathbf{k},\alpha)}\lambda^{\nu}_{\mathbf{k},\alpha}\right] + \left(\dot{\lambda}^{\nu}_{\mathbf{k}',\alpha'}\right)^{*}M^{(3)\nu}_{(\mathbf{k}',\alpha')(\mathbf{k},\alpha)}\dot{\lambda}^{\nu}_{\mathbf{k},\alpha}$$
$$\left.+i\left[\left(\ddot{\lambda}^{\nu}_{\mathbf{k}',\alpha'}\right)^{*}M^{(4)\nu}_{(\mathbf{k}',\alpha')(\mathbf{k},\alpha)}\dot{\lambda}^{\nu}_{\mathbf{k},\alpha} - \left(\dot{\lambda}^{\nu}_{\mathbf{k}',\alpha'}\right)^{*}M^{(4)\nu}_{(\mathbf{k}',\alpha')(\mathbf{k},\alpha)}\ddot{\lambda}^{\nu}_{\mathbf{k},\alpha}\right]\right\}$$

which is the same as Eq. 14.35 in the chapter. Eq. 14.37 in the chapter is resulted by removing the indices $\mathbf{k}$, $\mathbf{k}^{'}$, α, and $\alpha^{'}$ for simplicity. Additionally, the limits of ν have changed from $-N$ to N to 0 to N. It should be noted that the negative values of ν are taken into account by removing the factor ½ into $1/(1+\delta_{\nu,0})$. However, the factor $1/(1+\delta_{\nu,0})$ has been neglected for the simplicity of the equations as it affects only the first term.

Derivation of Relations Between the Parameters in Equations (14.41)

In order to find the Hamiltonian (14.40) for the optical fiber, new set of canonical coordinates and momenta are defined by Equations (14.41) in the chapter. In order to quantize the system, standard Dirac's commutation relations:

$$\left[\tilde{q}^{\nu}, \tilde{q}^{\nu'\dagger}\right] = 0, \tag{A.54}$$

$$\left[\tilde{p}^{\nu\dagger}, \tilde{p}^{\nu'}\right] = 0 \tag{A.55}$$

and:

$$\left[\tilde{q}^{\nu}, \tilde{p}^{\nu'}\right] = i\hbar\mathbf{1}\delta_{\nu,\nu'}. \tag{A.56}$$

should hold between the new canonical coordinates $\tilde{q}^{\nu}$ and $\tilde{p}^{\nu}$ to arrive at the relations (14.42a), (14.42b), and (14.42c), respectively. Note that the commutation relations for quantities X and Y are related to the Poisson's bracket as:

$$[X, Y] = i\hbar\sum_{i=1}\left\{\frac{\partial X}{\partial q_i}\frac{\partial Y}{\partial p_i} - \frac{\partial X}{\partial p_i}\frac{\partial Y}{\partial q_i}\right\} \tag{A.57}$$

where q_i and p_i are also coordinates q^{ν}, Q^{ν}, $q^{\nu\dagger}$, and $Q^{\nu\dagger}$ and their corresponding momenta.

Substituting Equations (14.41) for the canonical coordinates and momenta in Equation 14.43 and comparing it with the Hamiltonian 14.40, following six equations:

$$A^{\nu\dagger}\cdot\Theta^{\nu}\cdot A^{\nu} + E^{\nu}\cdot\Upsilon^{\nu}\cdot E^{\nu\dagger} + iA^{\nu\dagger}\cdot\Delta^{\nu}\cdot E^{\nu\dagger} - iE^{\nu}\cdot\Delta^{\nu\dagger}\cdot A^{\nu} = M^{(1)\nu} \tag{A.58}$$

$$\left[A^{\nu\dagger}\cdot\Theta^{\nu}-iE^{\nu}\cdot\Delta^{\nu\dagger}\right]\cdot\left[B^{\nu}+iD^{\nu}\cdot M^{(4)\nu}\right]+\left[E^{\nu}\cdot\Upsilon^{\nu}+iA^{\nu\dagger}\cdot\Delta^{\nu}\right]\cdot\left[F^{\nu\dagger}+iK^{\nu\dagger}\cdot M^{(4)\nu}\right]=iM^{(2)\nu}, \tag{A.59}$$

$$A^{\nu\dagger}\cdot\Theta^{\nu}\cdot C^{\nu}+E^{\nu}\cdot\Upsilon^{\nu}\cdot G^{\nu\dagger}+iA^{\nu\dagger}\cdot\Delta^{\nu}\cdot G^{\nu\dagger}-iE^{\nu}\cdot\Delta^{\nu\dagger}\cdot C^{\nu}=\mathbf{0}, \tag{A.60}$$

$$\left[B^{\nu\dagger}-iM^{(4)\nu}\cdot D^{\nu\dagger}\right]\cdot\left[\Theta^{\nu}\cdot B^{\nu}+i\Theta^{\nu}\cdot D^{\nu}\cdot M^{(4)\nu}+i\Delta^{\nu}\cdot F^{\nu\dagger}-\Delta^{\nu}\cdot K^{\nu\dagger}\cdot M^{(4)\nu}\right]+\left[F^{\nu}-iM^{(4)\nu}\cdot K^{\nu}\right]\cdot\left[\Upsilon^{\nu}\cdot F^{\nu\dagger}+i\Upsilon^{\nu}\cdot K^{\nu\dagger}\cdot M^{(4)\nu}-i\Delta^{\nu\dagger}\cdot B^{\nu}+\Delta^{\nu\dagger}\cdot D^{\nu}\cdot M^{(4)\nu}\right]=-M^{(3)\nu} \tag{A.61}$$

$$\left[B^{\nu\dagger}-iM^{(4)\nu}\cdot D^{\nu\dagger}\right]\cdot\left[\Theta^{\nu}\cdot C^{\nu}+i\Delta^{\nu}\cdot G^{\nu\dagger}\right]+\left[F^{\nu}-iM^{(4)\nu}\cdot K^{\nu}\right]\cdot\left[\Upsilon^{\nu}\cdot G^{\nu\dagger}-i\Delta^{\nu\dagger}\cdot C^{\nu}\right]=\mathbf{1} \tag{A.62}$$

and:

$$C^{\nu\dagger}\cdot\Theta^{\nu}\cdot C^{\nu}+G^{\nu}\cdot\Upsilon^{\nu}\cdot G^{\nu\dagger}+iC^{\nu\dagger}\cdot\Delta^{\nu}\cdot G^{\nu\dagger}-iG^{\nu}\cdot\Delta^{\nu\dagger}\cdot C^{\nu}=\mathbf{0}. \tag{A.63}$$

will be resulted. These six relations in addition to the relations (14.42) are used to find the frequency matrices and the matrix parameters A^{ν} to K^{ν}, which are needed to define coordinates $\tilde{q}^{\nu}$ and $\tilde{p}^{\nu}$.

References

Agrawal, G. P. (2012). *Nonlinear fiber optics*. 5th Ed. Academic Press.

Alfano, R. R. (2016). *The supercontinuum laser source: The ultimate white light*. Springer.

Alfano, R. R., & Shapiro, S. L. (1970). Emission in the region 4000–7000 A via four-photon coupling in glass; Observation of self-phase modulation and small scale filaments in crystals and glasses; Direct distortion of electronic clouds of rare-gas atoms in intense electric fields. *Physical Review Letters, 24*, 584, 592, 1217.

Boyd, R. W. (2008). *Nonlinear optics*. Academic.

Carter, S. J. (1995). Quantum theory of nonlinear fiber optics phase-space representations. *Physical Review A, 51*, 3274.

Corona, M., Palmett, K. G., & U'Ren, A. B. (2011). Third order spontaneous parametric down conversion in thin optical fiber as a photon triplet sources. *Physical Review A, 84*, 033823.

Corwin, K., Newbury, N., Dudley, J. M., Coen, S., Diddams, S. A., Weber, K., & Windeler, R. (2003). Fundamental noise limitations to supercontinuum generation in microstructure fiber. *Physical Review Letters, 90*, 113904.

Cumberland, B. A., Travers, J. C., Popov, S. V., & Taylor, J. R. (2008). 29 W High power CW supercontinuum source. *Optics Express, 16*, 5954.

Dechoum, K., Rosales-Zárate, L., & Drummond, P. D. (2016). Critical fluctuations in an optical parametric oscillator: When light behaves like magnetism. *Journal of the Optical Society of America B: Optical Physics, 33*, 871.

Dennis, G. R., Hope, J. J., & Johnson, M. T. (2013). XMDS2: Fast, scalable simulation of coupled stochastic partial differential equations. *Computer Physics Communications, 184*, 201.

Drummond, P. D. (1990). Electromagnetic quantization in dispersive inhomogeneous nonlinear dielectrics. *Physical Review A, 42*, 6845.

Drummond, P. D., & Carter, S. J. (1987). Quantum field theory of squeezing in solitons. *Journal of the Optical Society of America B: Optical Physics, 4*, 1565.

Drummond, P. D., & Corney, J. F. (2001). Quantum noise in optical fibers: I. Stochastic equations. *Journal of the Optical Society of America B: Optical Physics, 18*, 139.

Drummond, P. D., & Gardiner, C. W. (1980). Generalized P-representations in quantum optics. *Journal of Physics A, 13*, 2353.

Drummond, P. D., & Hillery, M. (2014). *The quantum theory of nonlinear optics*. Cambridge University Press.

Drummond, P. D., & Opanchuk, B. (2020). Initial states for quantum field simulations in phase space. *Physical Review Research, 2*, 033304.

Drummond, P. D., Gardiner, C. W., & Walls, D. F. (1981). Quasiprobability methods for nonlinear chemical and optical systems. *Physical Review A,**24***, 914.

Drummond, P. D., Shelby, R. M., Friberg, S. R., & Yamamoto, Y. (1993). Quantum solitons in optical fibres. *Nature, 365*, 307.

Dudley, J. M., & Genty, G. (2013). Supercontinuum light. *Physics Today, 66*, 29.

Dudley, J. M., & Taylor, J. R. (2010). *Supercontinuum generation in optical fibers*. Cambridge University Press.

Dudley, J. M., Genty, G., & Coen, S. (2006). Supercontinuum generation is photonic crystal fiber. *Reviews of Modern Physics 78*, 1135–1184.

Faddeev, L., & Jackiw, R. (1988). Hamiltonian reduction of unconstrained and constrained systems. *Physical Review Letters, 60*, 1692.

Fujimoto, J. G. (2003). Optical coherence tomography for ultrahigh resolution in vivo imaging. *Nature Biotechnology, 21*, 1361.

Gitman, F. D. M., & Tyutin, I. V. (1990). *Quantization of fields with constraints*. Springer.

Glauber, R. J. (1963). Coherent and incoherent states of the radiation field. *Physics Review, 131*, 2766.

Gonzalo, I. B., Engelsholm, R. D., & Bang, O. (2018). Noise study of all-normal dispersion supercontinuum sources for potential application in optical coherence tomography. *Proceedings of SPIE, 10591*, 105910C.

Grangier, P., Levenson, J. A., & Poizat, J. P. (1998). Quantum nondemolition measurements in optics. *Nature, 396*, 537.

Hillery, M. (2009). An introduction to the quantum theory of nonlinear optics. *Acta Physica Slovaca, 59*, 1.

Koleden, P. E., & Platen, E. (1992). *Numerical solution of stochastic differential equations*. Springer.

Li, J., Tan, W., Si, J., Kang, Z., & Hou, X. (2021). Generation of ultrabroad and intense supercontinuum in mixed multiple thin plates. *Photonics, 8*, 311.

Närhi, M., Turunen, J., Friberg, A. T., & Genty, G. (2016). Experimental Measurement of the Second-Order Coherence of Supercontinuum. *Physical Review Letters, 116*, 243901.

Safaei Bezgabadi, A., & Bolorizadeh, M. A. (2016). Quantum mechanical treatment of the third order nonlinear term in NLS equation and the supercontinuum generation. *Proceedings of SPIE, 9958*, 995803.

Safaei Bezgabadi, A., Borhani Zarandi, M., Bolorizadeh, M., & Bolorizadeh, M. A. (2019). Quantum noise for the propagating solitons in an optical fiber in presence of the third order dispersion coefficient. *Proceedings of SPIE, 11123*, 111230S.

Safaei Bezgabadi, A., Borhani Zarandi, M., & Bolorizadeh, M. A. (2020a). A quantum approach to electromagnetic wave propagation inside a dielectric. *European Physical Journal Plus, 135*, 650.

Safaei Bezgabadi, A., Borhani Zarandi, M., & Bolorizadeh, M. A. (2020b). Quantizing the propagated field through a dielectric including general class of permutation symmetries for nonlinear susceptibility tensors. *Results in Physics, 19*, 103622.

Safaei Bezgabadi, A., & Bolorizadeh, M. A. (2022). Quantum model for supercontinuum generation process. *Scientific Reports, 12*, 9666.

Safaei, A., Bassi, A., & Bolorizadeh, M. A. (2018). Quantum treatment of field propagation in a fiber near the zero dispersion wavelength. *Journal of Optics, 20*, 055402.

Sauer, T. (2013). Computational solution of stochastic differential equations WIREs. *Computational Statistics,**5***, 362.

Sudarshan E. C. G. (1963). Equivalence of semiclassical and quantum mechanical descriptions of statistical light beams. *Physical Review Letters,**10***, 277.

Sun, F.-X., He, Q., Gong, Q., Teh, R. Y., Reid, M. D., & Drummond, P. D. (2019). Schrödinger cat states and steady states in subharmonic generation with Kerr nonlinearities. *Physical Review A, 100*, 033827.

Venck, S., et al. (2020). 2–10 μm mid-infrared fiber- based supercontinuum laser source: Experiment and simulation. *Laser & Photonics Reviews,**14***, 2000011.

Vengris, M., et al. (2019). Supercontinuum generation by co-filamentation of two color femtosecond laser pulses. *Scientific Reports,**9***, 9011.

Vinh, N. T., Tsarev, D. V., & Alodjants, A. P. (2021). Coupled solitons for quantum communication and metrology in the presence of particle dissipation. *Journal of Russian Laser Research,**42***, 523.

Wetzel, B., et al. (2012). Real-time full bandwidth measurement of spectral noise in supercontinuum generation. *Scientific Reports,**2***, 882.

Woodard, R. (2007). Avoiding dark energy with 1/R modifications of gravity. In L. Papantonopoulos (Ed.), *The invisible universe: Dark matter and dark energy* (Lecture Notes in Physics, vol 720). Springer.

Yao, D. (1997). Schrödinger-cat-like states for quantum fundamental solitons in optical fibers. *Physical Review A, 55*, 3184.

Chapter 15
All-Solid Soft Glass Photonic Crystal Fibers for Coherent Supercontinuum Generation

Mariusz Klimczak, Dariusz Pysz, Ryszard Stępień, and Ryszard Buczyński

Abstract Material dispersion of soft glasses simplifies fiber designing for compatibility with femtosecond fiber lasers, while their high nonlinearity facilitates efficient broadening. We review fiber dispersion and birefringence engineering using the all-solid glass approach and relate different physical fiber geometries to supercontinuum spectro-temporal characteristics recorded using cross-correlation frequency-resolved optical gating.

Keywords Supercontinuum · Soft glasses · All-solid glass microstructured fibers · Silicate fibers · Tellurite fibers · Chromatic dispersion engineering · All-normal dispersion · Birefringence · Noise · Coherence · Spectrograms · Frequency-resolved optical gating · Cross-correlation frequency-resolved optical gating

15.1 Introduction

The photonic crystal fiber has reigned supreme in the field of supercontinuum generation since its first demonstration in this application by Ranka et al. (2000). The critical advantage, which this type of fiber provided to nonlinear optics over the classic, step-index fibers, is that by changing the arrangement of micron-scale air-holes surrounding the solid glass core, the chromatic dispersion profile could be designed to match the pumping laser wavelength (Reeves et al., 2003). This

M. Klimczak
Faculty of Physics, University of Warsaw, Warsaw, Poland

D. Pysz · R. Stępień
Łukasiewicz Research Network – Institute of Microelectronics and Photonics, Warsaw, Poland

R. Buczyński (✉)
FacultyofPhysics, UniversityofWarsaw, Warsaw, Poland

Łukasiewicz Research Network – Institute of Microelectronics and Photonics, Warsaw, Poland
e-mail: ryszard.buczynski@fuw.edu.pl

R. R. Alfano (ed.), *The Supercontinuum Laser Source*,
https://doi.org/10.1007/978-3-031-06197-4_15

opened much broader dispersion design flexibility, that the mature chemical vapor deposition technology for step-index fiber preforms fabrication.

The first supercontinuum generation experiments involved green picosecond pump pulses and bulk glasses and crystals, in which spectral broadening has been attributed to four-wave mixing and self-phase modulation (Alfano & Shapiro, 1970a, b). Currently, the most widespread scenario, which has found its way to commercial supercontinuum devices as well, is the one where a positively sloped chromatic dispersion profile crosses zero at a wavelength slightly blue-shifted from the central pump laser wavelength – thus the pumping occurs at a wavelength of anomalous chromatic dispersion of the fiber, where soliton propagation is supported (Agrawal, 2007). Depending on the pump pulse time duration, the nonlinear dynamics of supercontinuum formation begin with soliton fission and self-phase modulation, in the case of femtosecond pump pulses, or from modulation instability breakup of the injected laser pulses in the case of picosecond-scale and longer pump pulses (Dudley et al., 2006). Supercontinuum spectral coverage achievable by commercial state-of-the-art apparatus is limited practically by the effective transmission window of the silica glass, but at the cost of significant decoherence due to amplification of noise (Dudley & Coen, 2002). Notwithstanding, under specific conditions, including the initial pulse durations well below 50 fs and a specially designed chromatic dispersion profile, coherence is maintained in soliton-driven supercontinuum generation enabling single-cycle pulse synthesis (Krauss et al., 2010; Sell et al., 2009).

An entirely alternative approach in designing fibers for nonlinear optics applications involves exclusion of soliton dynamics altogether by engineering the chromatic dispersion profile in such a way that it maintains normal values over all wavelengths of interest (Heidt, 2010). Suppression of soliton dynamics in all-normal dispersion supercontinuum generation increases the threshold for modulation instability-driven decoherence by a factor of 50 (Heidt et al., 2017), but it comes at a price. Octave-spanning bandwidths require femtosecond pump pulse durations at reasonable peak power levels in the tens of kW range. Chap. 6 provides an in-depth overview of the self-phase modulation and optical wave-breaking dynamics, coherence preservation, and noise performance of all-normal dispersion supercontinuum in photonic crystal fibers based on the silica glass technology. Material dispersion of fused silica provides very convenient means to designing of normally dispersive photonic crystal fibers compatible with femtosecond lasers exploiting, e.g., the Ti/sapphire technology and especially the robust Yb^{3+}-doped fiber lasers, which means all-normal dispersion fibers designed for pumping with laser pulses centered around wavelengths of 800 nm or 1030 nm. Compensation of silica material dispersion in an air-hole lattice design of a microstructured fiber over longer wavelengths in the near-infrared, and specifically for the fiber's compatibility with mode-locked Er^{3+}-fiber lasers, is challenging (although not impossible, as shown in Chap. 6). Another drawback of silica glass is its transmission window limitation, which excludes extending of supercontinuum spectral coverage into mid-infrared wavelengths. These reasons prompted the dynamic development of non-silica, soft glass fibers for nonlinear optics (Price et al., 2012). Importantly,

some soft glass compositions, e.g., tellurite or fluoride glasses, combine mid-infrared transmission with the compatibility with pumping at wavelengths available from robust lasers. This enabled multioctave supercontinuum generation extending into the mid-infrared, under near-infrared pumping centered either at c.a. 1.5 μm or 2.0 μm (Domachuk et al., 2008; Nguyen et al., 2020; Qin et al., 2009; Xia et al., 2006). Chalcogenide glass fibers very often do not share this conveniency, requiring mid-infrared laser pumping, but the achievable supercontinuum spectral coverage can be spectacular, reaching out into the mid-infrared well in excess of 10 μm (Petersen et al., 2014). The relative difficulty in the development of microstructured fluoride glass fibers and thus in their dispersion shaping held back the exploiting of their excellent short-wavelength transmission for supercontinuum generation. In the recent years, microstructured fluoride fibers have been achieved either by the extrusion or by stack-and-draw techniques, and in particular, the latter enabled fiber supercontinuum generation in the ultraviolet (Ebendorff-Heidepriem et al., 2008; Jiang et al., 2015).

Among other advantages of different soft glasses is the feasibility of designing all-normal chromatic dispersion profiles in photonic crystal fibers, e.g., using various heavy-metal oxide soft glasses, such as the lead-silicate, boron silicate, or tellurite glasses (Cimek et al., 2016). Additionally, the nonlinear refractive index of most of these materials is one or two orders of magnitude higher than that of silica or even more in the case of chalcogenide glasses (Cimek et al., 2017). Their usually low melting point, compared to silica, excludes direct fusion splicing with silica fibers, which is admittedly a disadvantage, however not impossible to work around as demonstrated by different concatenation approaches in cascaded supercontinuum sources (Venck et al., 2020). The strength of soft glass fiber technology is within its feasibility of rapid fiber prototyping. Even more important is that soft glass properties, both optical and thermomechanical, can be adjusted by modification of their chemical composition, i.e., doping, quite straightforwardly and significantly simpler than in the case of silica glass.

In this chapter, we provide an overview on the development and supercontinuum generation performance of heavy-metal oxide-based soft glass fibers with engineered, all-normal dispersion profiles. The wavelength range of interest in our discussion is the long-wave near-infrared, including the gain bands of modern Er^{3+}- and Tm^{3+}-doped ultrafast fiber lasers and amplifiers.

The main advantage – as well as a limitation in a way – of the air-hole lattice photonic crystal fiber designing – is that the glass material dispersion is compensated by waveguide dispersion related to the arrangement of air-holes in the photonic cladding. An extension of this concept has been proposed by Feng and coauthors who used two thermally matched soft glasses with a refractive index contrast, in what can be called an all-solid glass photonic crystal fiber (Feng et al., 2013). In Sect. 15.2 of this chapter, we describe application of this approach to the designing of flattened, all-normal dispersion characteristics in various all-solid soft glass photonic crystal fibers developed for operation specifically with mode-locked Er^{3+}-doped fiber lasers. The discussion encompasses shaping of linear characteristics and goes on to the selection of soft glasses in context of their nonlinear response, and in Sect. 15.3 it continues to the demonstration of supercontinuum generation

performance in context of trade-offs between the flatness of the dispersion profile and the nonlinearity strength.

Section 15.4 is devoted to introduction of intentional birefringence aimed at providing polarization holding functionality in the discussed fibers. Two variants of the all-solid lattice modifications are explored, and the achievable birefringence, supercontinuum generation performance, and its polarization extinction ratio are compared. An alternative in the form of an air-hole lattice, highly nonlinear, and birefringent tellurite glass photonic crystal fiber is described as a possible future, as well.

Section 15.5 of this chapter focuses on spectro-temporal characterization of supercontinuum pulses generated in the discussed soft glass fibers. While the nonlinear dynamics, coherence properties, and performance of coherent supercontinuum generation in normally dispersive waveguides have been well described, data obtained in physical measurements of actual pulse shapes of this supercontinuum is rare. Our discussion includes results on recording of octave-spanning, near-infrared group delay profiles of coherent, all-normal dispersion supercontinuum using cross-correlation frequency-resolved optical gating (Trebino, 2012). Obtained data is reconstructed numerically using nonlinear propagation simulations, in which the input condition is not limited solely to ideal, Gaussian models of mode-locked pump laser pulses. Simulations where the pump pulse idealization is assumed at input are confronted with numerical results obtained for input condition comprising full-field information on the physical pulses of a femtosecond Er^{3+}-fiber laser used in the experiments. The spectral and temporal fine structures in physical supercontinuum pulses are reproduced in this way with remarkable accuracy. This enables tracing back specific features of the supercontinuum pulses in the spectral and time domains to distortions of the pump pulse, as well as to specific characteristics of the fiber designs, such as birefringence. These results provide a new perspective on the shaping of coherent supercontinuum generation in fiber-based systems, from the point of view of both the fiber design and the laser system used for pumping.

15.2 Chromatic Dispersion Engineering in All-Solid Soft Glass Structured Fibers

Supercontinuum light pulses with multioctave-spanning spectra are routinely obtained in fibers with a zero-dispersion wavelength, but the usual soliton-driven dynamics are prone to modulation instability decoherence. An all-normal chromatic dispersion fiber under femtosecond laser pumping can be used to deliver coherent and full-octave-spanning supercontinuum pulses, as discussed in Chap. 6. Ideally, this requires engineered, flattened chromatic dispersion profile of the fiber, which is challenging to achieve due to material properties of glasses at near-infrared wavelengths, at which robust mode-locked fiber-based lasers operate. It is the material dispersion of the fiber glass which has to be compensated by the waveguide dispersion in a fiber design, regardless if the fiber layout is a classic step-index

fiber or an air-hole lattice microstructured fiber, because material dispersion of air can be reasonably assumed as wavelength-independent. Introduction of gasses or liquids into the photonic lattice air-holes partly solves the challenge of dispersion engineering, but at a significant cost of handling convenience and robustness (Cassataro et al., 2017; Kedenburg et al., 2015). Another solution is possible, and it involves making use of the all-solid glass photonic crystal fiber design, in which the air-holes in the photonic lattice are filled with a thermally matched glass with a different refractive index, than the lattice glass. Compared to the "classic" air-hole photonic crystal fibers, the all-solid glass ones can be shaped with extended dispersion engineering freedom, by enabling not only manipulation of the waveguide contribution into the chromatic dispersion but also to influence it through the material dispersion of the employed glasses, analogically to the gas- or liquid-filled air-hole lattice fibers. At the same time, an all-solid glass microstructured fiber not only does not sacrifice robustness but gains the advantage in mechanical sturdiness with its structure devoid of air-holes. A photonic crystal fiber with an all-solid glass layout has been demonstrated for the first time by Feng and coauthors (Feng et al., 2013). Design and development of an all-solid structured fiber requires at least two glasses with different refractive indices. However, the thermal properties of both these materials should be matched as close as possible. It is critical to assure similar values of the thermal expansion coefficients and the characteristic temperatures. Fibers, drawn using the all-solid glass approach and designed specifically for coherent, pulse-preserving supercontinuum generation, were first reported by Buczyński et al. (2012; Martynkien et al., 2014), and this was followed by demonstration of supercontinuum generation in a later work (Klimczak et al., 2014, 2016a). The fibers had a solid, high refractive index glass core surrounded by a honeycomb lattice made of the same glass and with its air-holes filled with inclusions made of a low refractive index glass. Typical scanning electron microscope images of the developed fiber structures are shown in Fig. 15.1.

The initial implementation of this type of fiber, shown in Fig. 15.1a – fiber series label used in literature: "NL21" (Klimczak et al., 2014, 2016a) – involved use of a lead oxide glass with the vendor label F2 (Schott) and an in-house developed boron-silicate glass labeled NC21a. The latter glass composition is SiO_2, 56.84; B_2O_3, 23.19; Al_2O_3, 0.61; Li_2O, 6.23; Na_2O, 9.51; and K_2O, 3.63. Refractive index values measured for each of the glasses at a wavelength of 1550 nm are $n = 1.59487$ in the case of Schott F2 glass and $n = 1.51130$ for the boron-silicate NC21a glass; thus, the fiber made from these materials can support total internal reflection guiding if the core is composed of F2 glass. Glass transition temperatures for these glasses are $T_g = 434$ °C and T_g NC21a = 492 °C, respectively, for the lead oxide F2 glass and the boron-silicate NC21a glass. Thermal expansion coefficients are $\alpha_{+20/+300°C} = 9.2 \times 10^{-6}$/K for the F2 and $\alpha_{+20/+300°C} = 8.7 \times 10^{-6}$/K for the NC21a. This set of parameters is sufficiently matched to enable joint thermal processing, i.e., drawing into an optical fiber from stacked glass canes and capillaries. The hexagonal shape of the structure is acquired during drawing at a fiber drawing tower. Nonlinear refractive indices, measured at a wavelength of 1064 nm using the z-scan method are, $n_2 = 2.9 \times 10^{-20}$ m^2/W for the F2 glass and $n_2 = 1.1 \times 10^{-20}$ m^2/W for the NC21a glass (Lorenc et al., 2008), which is

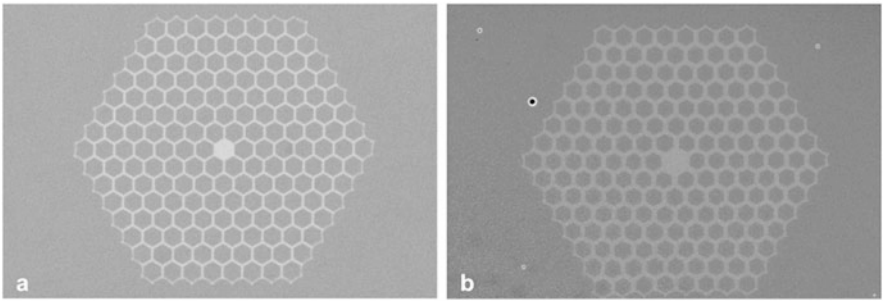

Fig. 15.1 Scanning electron microscope images of all-solid soft glass microstructured fibers with engineered normal chromatic dispersion: (**a**) the NL21 series fiber – core and hexagonal lattice (light color) is made of Schott F2 glass, and lattice inclusions and the surrounding tube are an in-house boron-silicate glass; (**b**) the NL38 series fibers – Schott SF6 in the core and lattice, Schott F2 in the inclusions and the surrounding tube. (Adapted with permission from Klimczak et al. (2016a) ©The Optical Society)

comparable to the value obtained earlier for fused silica, $n_2 = 2.7 \times 10^{-20}$ m^2/W at 1550 nm (Kato et al., 1995). The nonlinear response of the fiber can be further improved from the material side, by replacing the F2 glass with a different lead oxide glass under the vendor label SF6 (Schott). The nonlinear refractive index measured at a wavelength of 1550 nm for this glass is $n_2 = 21.0 \times 10^{-20}$ m^2/W (Kalashnikov et al., 2007). The SF6 has glass transition temperature of $T_g = 423$ °C, and its thermal expansion coefficient is $\alpha_{+20/+300°C} = 9.0 \times 10^{-6}$/K making it almost a perfect match for F2 for fiber drawing. Linear refractive index of the SF6 glass, measured at 1550 nm wavelength, is $n = 1.764133$. This also determines total internal reflection as the guiding mechanism in a fiber geometry shown in Fig. 15.1b, where SF6 glass forms the core and the cladding honeycomb lattice, while F2 fills the lattice inclusions and surrounds the entire photonic lattice structure. In the literature, a label "NL38" is used for this fiber (Klimczak et al., 2016a, 2017).

Designing of these fiber structures involves establishing geometric parameters, such as the core diameter (i.e., diameter of a circle inscribed in the center, high-index glass hexagon of the photonic lattice), as well as the inclusion size d and the lattice constant Λ, which are used together to define the relative inclusion size d/Λ. Aim of the designing is the normal chromatic dispersion characteristic over the wavelengths of interest, which would specifically cover the three major fiber-based amplifier systems, beginning with Yb^{3+}-doped fibers, through Er^{3+}-doped fibers, up to Tm^{3+}-doped fibers. Since optical fibers commonly have strong normal chromatic dispersion at visible and short-wave near-infrared wavelengths, the challenge is assuring normal dispersion at wavelengths where standard step-index fibers have anomalous dispersion, especially at the Tm^{3+}/Ho^{3+} gain bands of 1800–2200 nm. Typical chromatic dispersion profiles computed for geometric parameters of the photonic lattice, which are technologically feasible, are shown

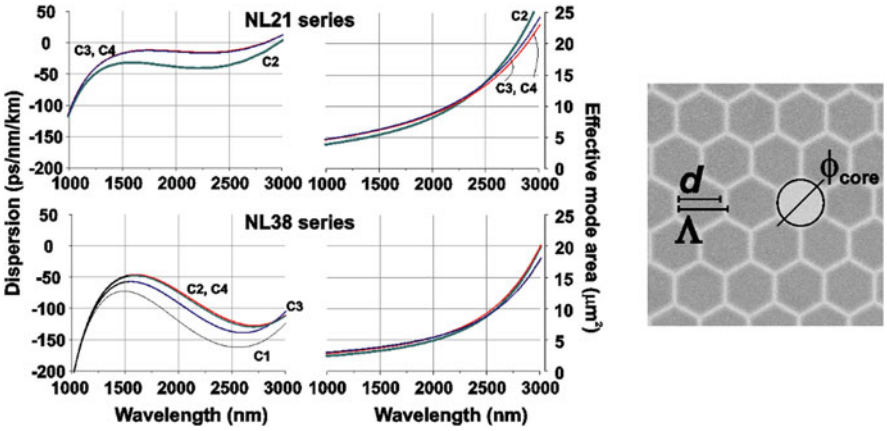

Fig. 15.2 Chromatic dispersion profiles and effective mode areas computed using numerical simulations for the all-solid soft glass microstructured fibers of NL21 and NL38 series and geometric parameters set in the fiber designing. (Adapted with permission from Klimczak et al. (2017) ©CLP Publishing)

Table 15.1 Geometric parameters of all-solid soft glass microstructured fibers designed for normal chromatic dispersion profile in the long-wave near-infrared

	Outer diameter (μm)	Core size (μm)	Inclusion size *d* (μm)	Relative inclusion size d/Λ
NL21 series				
C2	155.0	2.46	2.3	0.90
C3	148.4	2.46	2.2	0.90
C4	142.8	2.46	2.16	0.89
NL38 series				
C1	126.0	2.36	1.30	0.79
C2	132.5	2.53	1.39	0.77
C3	132.6	2.49	1.33	0.77
C4	135.4	2.44	1.38	0.77

in Fig. 15.2, and the corresponding fiber dimensions assumed in calculations are gathered in Table 15.1.

The main feature of all-normal chromatic dispersion characteristics feasible with the all-solid soft glass photonic lattice approach is the flattened "saddle" section extending roughly from the wavelength of 1000 nm to 2800 nm. It is to be noted that the long-wavelength edge of this range is conventional and related to the glass transmission cutoff. The short-wavelength edge is critically related to the blue-shifted edge of spectrum in femtosecond supercontinuum generation (as explained in Chap. 6 as well as in the following section of this chapter). Shape of the "saddle" section and specifically its flatness, for both used glass pair combinations, depends on parameters of the lattice: the larger the core diameter and lattice inclusion relative size, the flatter is the "saddle." For example, for the NL21C2 fiber, it is

within ±10 ps/nm/km over wavelengths from 1500 nm to around 2000 nm. The "saddle" flatness facilitates high efficiency of the optical wave breaking forming the spectral wings of the normal-dispersion supercontinuum, due to low time offset of the four-wave mixing components, but it is to be noted that this fiber's effective mode area at a wavelength of 2200 nm already exceeds 10 μm^2. Because of the nonlinear coefficient of the fiber γ scales with the reciprocal of the effective mode area, there is a trade-off between the dispersion characteristic flatness and the effective nonlinearity in case of all fibers summarized in Table 15.1. In other words, increasing the core diameter flatness spectrally extends the dispersion "saddle," but it also increases the effective mode area, which decreases nonlinearity. This is shown in Fig. 15.2, where effective mode area for the NL21 series fibers at a wavelength of 2000 nm is around 8 μm^2, while for the NL38 series, it is around 5 μm^2 at the same wavelength. At the same time, the flatness of the dispersion characteristic of the NL38 series fibers is ±25 ps/nm/km over 1500 nm to 2000 nm wavelengths. The following section discusses how these parameters correspond to coherent supercontinuum generation performance under pumping with different femtosecond laser systems.

15.3 Supercontinuum Generation in All-Solid Soft Glass Structured Fibers

Technological processes of fiber drawing confirmed the feasibility of obtaining broadband, flattened chromatic dispersion profiles in fibers designed and fabricated using the all-solid glass photonic lattice approach, as well as of the applicability of these structures in efficient coherent supercontinuum generation. Literature on supercontinuum generation in these fibers includes results obtained under femtosecond pumping centered around wavelengths of 1560 nm (Klimczak et al., 2014) and around 2000 nm (Klimczak et al., 2016a, 2019), as well as on detailed characterization using dispersive Fourier transformation (Klimczak et al., 2016b) or, later, using cross-correlation frequency-resolved optical gating (Rampur et al., 2020) as well. The initial fiber series for these experiments was directly based on the NL21 design discussed in the preceding section. A family of five fibers has been drawn within a range of geometrical parameters including varied core diameter, photonic cladding size and its pitch, and relative inclusion size. These parameters are listed in Table 15.2. Chromatic dispersion of the fibers has been verified over a range of wavelengths from around 900 nm up to 1700 nm, and obtained spectral characteristics are shown in Fig. 15.3. Confronting of the geometrical parameters in Table 15.2 with these dispersion profiles reveals that decreasing of the overall lattice size results in increment of the absolute value of dispersion, i.e., brings the "saddle" plateau closer to the zero dispersion, and it red-shifts the local maximum of the dispersion profile (Martynkien et al., 2014). Supercontinuum generation spectra obtained with these fibers pumped from an optical parametric chirped-pulse

Table 15.2 Geometric parameters of the NL21 series fibers used for octave-spanning all-normal dispersion supercontinuum generation

NL21 series fiber no.	Outer diam. (μm)	Lattice diagonal (μm)	Core diam. (μm)	Inclusion size d (μm)	d/Λ
B1	143.0	35.61	2.43	2.15	0.91
B2	140.3	35.06	2.40	2.13	0.91
B3	136.6	34.65	2.37	2.11	0.91
B4	131.0	33.33	2.25	1.99	0.91
B5	128.8	31.55	2.13	1.93	0.91

Source: Klimczak et al. (2014)

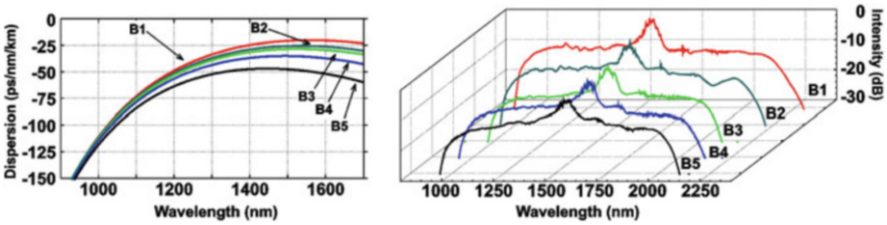

Fig. 15.3 Measured chromatic dispersion profiles in a series of NL21-type all-solid soft glass, all-normal dispersion photonic crystal fibers and supercontinuum generation spectra obtained in these fibers under femtosecond pumping from a chirped-pulse optical parametric amplifier, pump pulses centered around 1560 nm, pulse duration was 50 fs. (Adapted with permission from Klimczak et al. (2014). ©The Optical Society)

amplifier tuned to a center wavelength of 1560 nm and delivering around 50 fs pulses are shown in Fig. 15.3. The widest of the spectra spans from 900 nm up to 2300 nm, effectively covering the amplification bands of all three major fiber amplifiers, i.e., the Yb^{3+}-doped, Er^{3+}-doped, and Tm^{3+}-doped fiber amplifiers. The spectra have been achieved in up to a dozen of cm long fiber samples, a length which already had been a convenience of handling, rather than necessity at such short pump pulse durations. Nearly tabletop flat shape of the spectra is disturbed only by a peak around the center pump wavelength, which is related to the residual of the pump radiation propagating in the photonic cladding. This part of pump energy does not contribute directly to the nonlinear broadening process but has been related to decoherence mechanisms under longer pump pulse durations (Klimczak et al., 2016b).

The fiber designs based on the all-solid silicate soft glass compositions have the advantage of being in principle compatible with either 1560 nm pumping or the 2000 nm pumping. This is because the numerically predicted zero-dispersion wavelength falls well beyond the wavelength of 2800 nm, which is the practical transmission limit of these soft glasses. In contrast to that, pumping around the wavelength of 1000 nm or shorter is impractical with these structures, due to strong and sloped normal dispersion in this spectral range – thus in context of pumping at wavelengths characteristic to Yb^{3+}-doped systems, these fibers are uncompetitive

to pure silica designs discussed in detail in Chap. 6. The 2000 nm wavelength is interesting, because for once it is available from the emerging Tm^{3+} and Ho^{3+} doped fiber-based mode-locked lasers and amplifiers and, secondly, it provides the opportunity to demonstrate and validate the role of dispersion of nonlinearity in specialty photonic crystal fiber designs for supercontinuum generation (Kibler et al., 2005). With this specifically in mind, the NL21 and NL38 series fibers have been used in supercontinuum generation experiments with an optical parametric chirped-pulse amplifier as pump source (Klimczak, Siwicki, et al., 2016a). Central pump wavelength was tuned to 2160 nm and pulse duration was 60 fs. Both fibers enabled spectral broadening in excess of an octave, but the recorded spectra exhibited noticeable differences in width and reach of their sidebands, shown in Fig. 15.4. Most significantly, the NL21 series fibers provided favorable conditions for development of the blue-shifted spectral wing, with virtually no broadening on the red-shifted side of the central pump wavelength. Supercontinuum generation at the red-shifted side of the pump wavelength continued in the NL38 fiber up to its transmission cutoff around 2800 nm. The NL38 series fiber also proved more resistant to optical power damage and was pumped stronger than the NL21 series fiber (average pump powers shown in Fig. 15.4 for each supercontinuum trace), but comparable results as those shown for the NL38 fiber were obtainable

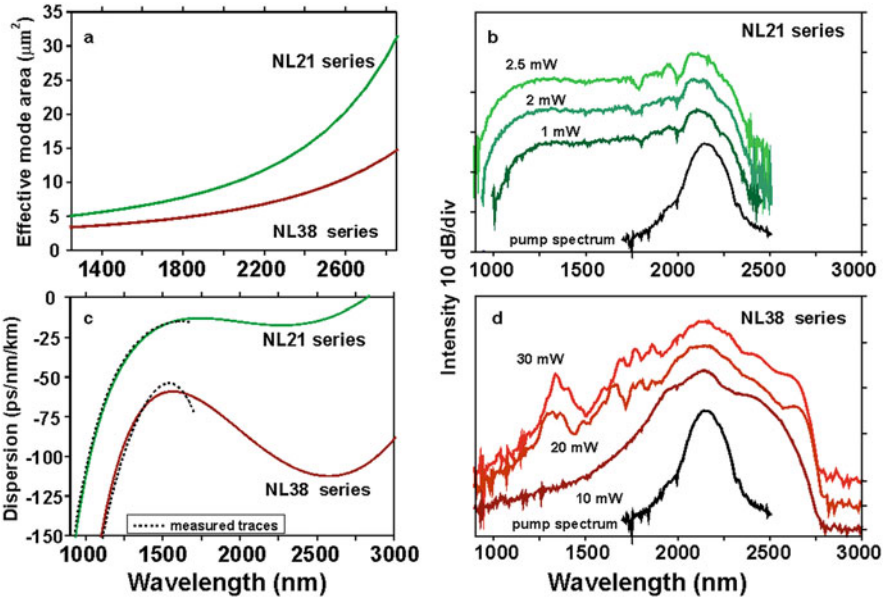

Fig. 15.4 (**a**) Calculated wavelength-dependent effective mode area profiles and (**b**) measured and computed chromatic dispersion characteristic of NL21 and NL38 series all-solid soft glass photonic crystal fibers; (**c**–**d**) measured supercontinuum spectra in both fiber series under femtosecond pumping centered around 2000 nm; average pump powers shown above respective traces. (Adapted with permission from Klimczak et al., 2016a. ©The Optical Society)

at incident average power levels shown for the NL21 fiber. These differences in supercontinuum generation efficiency can be explained directly in relation to the trade-off between the dispersion flatness, assured by the NL21 structure, and the nonlinearity advantage of the NL38 fiber – standing out especially in the spectral broadening results obtained over the 2000–2800 nm wavelengths in both fibers. Fiber attenuation was ruled out as a sole decisive factor (Klimczak et al., 2016a). Figure 15.4 again shows the computed effective mode areas and chromatic dispersion profiles of the two types of fibers. The refractive index difference between the glasses of the NL38 fiber ($\Delta n = 0.169263$ at the wavelength of 1550 nm) is two times higher than between the glasses in the NL21 lattice ($\Delta n = 0.08357$ at 1550 nm), and the NL38 fiber has just above half of the effective mode area of the NL21 fiber at a wavelength of 2000 nm. The stronger mode confinement in the NL38 fiber, compared to NL21 fiber, provides for continuously strong nonlinear response and thus spectral broadening up to the transmission limit of the fiber. The flatter chromatic dispersion profiles at the blue-shifted edge of supercontinuum spectra in the NL21 fiber (compared to the NL38 fiber), on the other hand, contribute to favorable optical wave-breaking conditions at the short-wavelength part of spectrum, where mode confinement in both fibers is comparable. Thus, moderately better blue-shifted broadening performance was recorded in the NL21 fiber, compared to NL38.

An important context of the nonlinear performance in these specialty fibers, as of yet omitted in the discussion here, is the optical pumping conditions. Results discussed to this point were obtained with powerful and complex pump systems, delivering MW-range peak powers and 50–60 fs pulses, albeit at kHz repetition rate. This is a critical parameter – and a disadvantage for ultrafast photonics applications where the coherent, broadband pulses are delivered as seed signals in fiber amplifiers. For once, the demonstrated supercontinuum signals combine many advantageous properties – they originate from a single mode-locked laser source; thus, when used to seed, for example, two amplifiers simultaneously, no extra synchronization electronics would be necessary. Furthermore, simultaneous coverage of the Yb^{3+}-doped fiber and Tm^{3+}-doped fiber gain bands (which are separated by roughly an octave) in an ultrafast system opens potentially disrupting opportunities for all-fiber few-cycle laser pulse synthesis. The downside is that using a powerful but complex optical parametric chirped-pulse amplifier system as a pump source defeats the fiber robustness advantage to begin with, and even for a feasibility study, the kHz repetition rate is not enough to seed an ultrafast fiber amplifier, which is normally continuous-wave pumped. Compact, chirped-pulse amplification, fiber-based lasers and amplifiers, delivering roughly 100 fs pulses at MHz repetition rates, would be a handy substitute, but their robustness and relative simplicity come at the cost of peak power, which in the cases of the available Er^{3+} or Tm^{3+} systems is in the kW range, and pulse energies are often few to a dozen nJ. Supercontinuum generation performance with these lasers as pumps to the fibers discussed in this chapter cannot be directly compared to scenarios, where a complex, MW peak power system is used for pumping. The primary difference is that the strongly sloped chromatic dispersion at the blue-shifted edge of supercontinuum spectra around

900–1000 nm wavelengths becomes a bottleneck, which cannot be compensated neither by the limited kW peak power nor by the nJ pulse energy available from a fiber-based mode-locked pump laser. All-normal dispersion supercontinuum spectra, recorded for the NL21 series or the NL38 series fibers, reach at the short-wavelength side as far as 1100 nm, which is insufficient to cover the Yb^{3+} fiber amplifier gain band simultaneously with the Er^{3+} or Tm^{3+} amplifiers. Moreover, nonlinear response of the NL21 series fibers is not strong enough to enable an optical wave-breaking sideband broad enough to cover the entire Tm^{3+} amplifier gain band under such pumping conditions. If we compare the nonlinear coefficients of the two fiber series, i.e., the NL21 and NL38, we note that there is a factor of around 16 difference between them, as shown in Table 15.3, for the center pump wavelength of 1560 nm. With such an advantage, despite the less favorable dispersion profile of the NL38 (stronger, sloped normal dispersion compared to the NL21), it is the NL38 series fiber which enabled spectral broadening up to almost 2200 nm using a robust, fiber-based femtosecond laser delivering pump pulses just below 100 fs with just 3.5 nJ energy. This supercontinuum signal has been successfully applied as seed in an ultrafast fiber amplifier system implementing a Tm^{3+}+Ho^{3+} co-doped fiber under continuous-wave pumping (Heidt et al., 2020). This implementation allowed recompression of amplified output pulses down to 66 fs with excellent relative intensity noise characteristics.

Results with silicate soft glass fibers discussed using the two examples in this chapter are by no means exhaustive in terms of how much broadening can be achieved from low-energy, 100-fs-long driving pulses centered around the Er^{3+} or Tm^{3+} wavelengths. However, the simple confrontation between a fiber with modest nonlinearity and nearly tabletop flat dispersion profile (NL21 series) with one that sacrifices dispersion flatness for the "raw power" of nonlinear response (NL38 series) provides some clues on what the next step could be in extending supercontinuum spectrum toward the mid-infrared wavelengths. Data in Table 15.3 and supercontinuum spectra, generated using Er^{3+}-doped fiber-based femtosecond laser (3.5 nJ, 90-fs-long pulses), include yet another fiber, which follows the direction of scaling nonlinearity. The design, labeled in literature as NL47 (Klimczak et al., 2019), was drawn using a highly nonlinear tellurite glass. Chemical composition of this particular glass was $65TeO_2$ $28WO_3$ $7(Na_2O + Nb_2O_5)$, (Stępień et al., 2011) and its nonlinear refractive index, measured at a wavelength of 1064 nm, is 51.0×10^{-20} m^2/W (Cimek et al., 2017). This glass has twice as high nonlinear refractive index as that of the SF6 glass (Table 15.3). The fiber geometry features a regular air-hole lattice with two rings of air-holes with different diameters. Variation of air-hole diameters in the lattice's subsequent rings extends dispersion engineering freedom significantly. This particular designing approach has been proposed and demonstrated with silica photonic crystal fibers by Saitoh et al. (2003). The disadvantage of its application to tellurite glasses is related to maintaining of a regular lattice comprising various air-hole diameters across many rings of a structure stacked from a technologically challenging material. In addition to that, the air-hole structure suffers from somewhat inferior heat dissipation than an all-solid glass microstructured fiber. This makes the NL47 design susceptible to laser damage.

Table 15.3 Comparison of nonlinear optical properties of selected heavy-metal oxide soft glass all-normal dispersion microstructured fibers

Fiber series	Nonlinear refractive index of glass in the core	Effective mode area calculated at $\lambda = 1560$ nm	Nonlinear coefficient $\gamma\lambda = 1560$ nm	Ref.
NL47 series, air-hole lattice, tellurite glass	51.0×10^{-20} m^2/W	3.5 μm^2	582.6 W^{-1} km^{-1}	Klimczak et al. (2019)
NL38 series, all-solid lead-silicate glasses	21.0×10^{-20} m^2/W	4.0 μm^2	213.7 W^{-1} km^{-1}	Klimczak et al. (2016a)
NL21 series all-solid lead-silicate and boron-silicate glasses	2.9×10^{-20} m^2/W	6.2 μm^2	13.6 W^{-1} km^{-1}	Klimczak et al. (2014)

Notwithstanding, the benefit of high nonlinearity and the potential of extending the fiber's transmission toward the mid-infrared part of spectrum, due to the application of the mid-infrared capable tellurite glass, have driven continuous research yielding demonstrations of microstructured fibers made of highly nonlinear tellurite glasses using the all-glassy lattice, as well (Nguyen et al., 2020). The important advantage of these implementations is that they enable reaching the mid-infrared wavelengths, while at the same time their chromatic dispersion profiles can still be engineered for compatibility with near-infrared wavelength pumping.

The final question on further improvement of the soft glass microstructured fiber relates to modifications of the designs in such ways, as to introduce intentional birefringence in order to determine – ideally – linear polarization state of the generated coherent supercontinuum light. This context of soft glass photonic crystal fiber engineering is discussed in the following section of this chapter.

15.4 Introduction of Birefringence

Unintentional form birefringence of about 10^{-5} in an optical fiber, caused, e.g., by built-in stresses or external factors (i.e., bending), already facilitates nonlinear as well as linear coupling of the polarization mode components, which in turn amplify quantum noise and can lead to decoherence of ultrashort laser pulses. Polarization modulation instability is one example of the nonlinear processes, which have been related to decoherence in all-normal dispersion supercontinuum generation (Liu et al., 2015). In contrast to that, intentional birefringence in a nonlinear microstructured fiber, combined with aligning of the input femtosecond laser pulse polarization to one of the fiber's principal axes, allowed for suppression of these noise-amplifying nonlinear processes. Later work explored the concept of supercontinuum noise control by microstructure design and specifically by birefringence control in nonlinear photonic crystal fibers in detail, as discussed in Chap. 6. Introduction of birefringence to nonlinear structured fibers with engineered normal dispersion is crucial in fiber-based ultrafast fiber amplifiers. Not only does it facilitate noise suppression but contributes to simplification of the entire setup, because a determined state of polarization of a broadband, coherent supercontinuum seed signal in such an amplifier eliminates polarization controllers (Heidt et al., 2020; Rampur et al., 2019).

Soft glass structured fiber engineering allows for rapid fiber prototyping. The possibility of manipulation of optical and thermal properties of glasses by changes of their chemical compositions is a special advantage in context of developing structures with unique characteristics. The two designs of all-solid soft glass fibers with all-normal chromatic dispersion profiles, discussed in the previous sections in this chapter, can be redesigned into birefringent variants without scarifying their advantages for efficient, coherent femtosecond supercontinuum generation.

In this type of hexagonal photonic lattice, birefringence can be introduced in two ways. Stress areas can be designed in the fiber layout resembling the

classic Panda or bow-tie fibers. In the context of microstructured fibers and the fibers designed specifically for coherent supercontinuum generation, this approach has been exploited in fibers compatible with 1030 nm femtosecond pumping (Liu et al., 2015). The stress zones facilitate change of the refractive index in the structure's transverse plane. In an alternative way, high birefringence can be achieved by introducing air-holes on each side of the fiber core. Thus, the guided mode experiences defined optical axes with dramatically different refractive indices (Anuszkiewicz et al., 2013). This particular design is however somewhat impractical with the type of structures discussed so far, because of the intricate role of the hexagonal all-solid glass lattice in shaping of the chromatic dispersion (Martynkien et al., 2014). An elliptical deformation of the fiber structure, for example a lateral squeeze along one of the axes, can be considered as an alternative means of inducing birefringence in these fibers.

The two realized intentionally birefringent variants of the all-solid soft glass microstructured fibers discussed in the previous sections are shown in SEM images in Fig. 15.6. The NL46 series fiber features an elliptical deformation of the photonic lattice, while the NL48 series fiber is modified mainly by introduction of a bow-tie stress areas around the lattice. Both fiber types were designed using silicate glasses F2 and SF6, analogically to the NL38 series fibers described earlier.

In contrast to the NL38 series though, the modified fiber lattices have reduced number of lattice rings in the photonic cladding, in order to increase the impact of index-modifying structure alterations on the fiber core. In case of the NL46 fiber, the number of lattice rings is reduced to 5. The lateral squeeze in the final fiber was obtained by stacking two large tubes, with inner diameter comparable to the diagonal of the photonic lattice stack, along one of the diagonals of the lattice, just outside of its perimeter. During fiber drawing, these air-holes were subsequently collapsed resulting in ellipticity of the fiber microstructure. The final fiber dimensions are 2.7 μm $\times$ 1.9 μm of the elliptical core and 25.8 μm $\times$ 16.3 μm of the squeezed-lattice diagonals, and its lattice constant is $\Lambda = 2$ μm.

The bow-tie NL48 series fiber variant had less intrusive modification of the lattice, in which the number of rings was reduced from 7 to 6, compared to the initial NL38 design. Core size in this fiber had dimensions of 2.5 μm $\times$ 2.0 μm, and the cladding lattice diagonals (excluding the stress zones) were 25 μm $\times$ 19 μm. The lattice constant was $\Lambda = 1.7$ μm. In addition to the F2 and SF6 glasses, used here in the same roles as in the NL38 and NL46 series fibers, this design included a third glass type used for the bow-tie stress elements. At the structural preform level, these areas were stacked from individual rods made of a custom lead-silicate glass. Its chemical composition was (compound, mol.%) SiO_2, 70.17; PbO, 15.55; Na_2O, 8.08; K_2O, 6.07; and As_2O_3, 0.13 and was designed to obtain significantly higher thermal expansion coefficient compared to the F2 and SF6 glasses (Dobrakowski et al., 2019). The relevant parameters, such as the glass transition temperatures and thermal expansion coefficients of the glasses comprising the NL48 fiber microstructure, are compared in Table 15.4.

Both fiber series were characterized for their chromatic dispersion, birefringence, and supercontinuum generation performance under pumping in similar conditions

Table 15.4 Glass transition temperatures and thermal expansion coefficients of soft glasses in the NL48 series fiber microstructure

Glass	Glass transition temperature T_g (°C)	Thermal expansion coefficient $\alpha_{20,\,300°C}$ (1/K)
Schott SF6	423	$9.0{\cdot}10^{-6}$
Schott F2	431	$9.2{\cdot}10^{-6}$
Stress zones glass for NL48 series fiber	417	$10.5{\cdot}10^{-6}$ Dobrakowski et al. (2019)

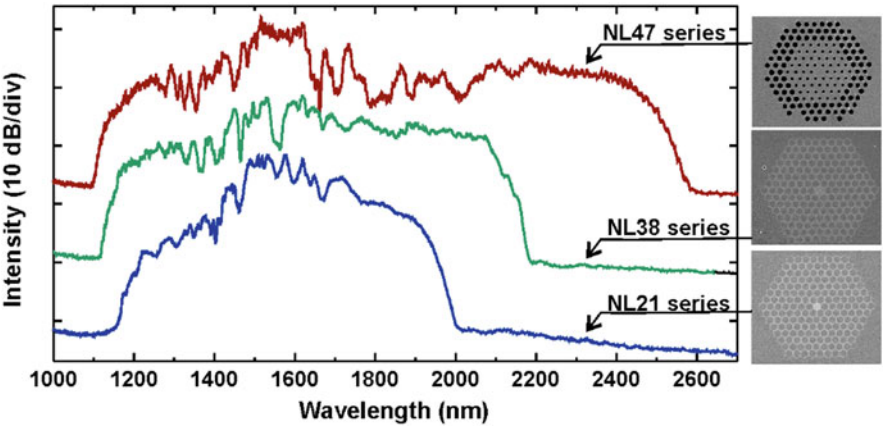

Fig. 15.5 Femtosecond supercontinuum generation in three series of all-solid glass and air-hole regular lattice soft glass fibers under pumping with a compact, mode-locked fiber-based laser – center wavelength 1560 nm, pump pulse energy 3.5 nJ, pulse duration 90 fs, 100 MHz repetition rate. (Adapted with permission from Klimczak et al. (2019) ©The Optical Society)

as in the case of the NL21, NL38, and NL47 fiber comparison, shown in the previous section in Fig. 15.5. Dispersion characteristics, measured for each of the polarization axes of the birefringent fiber variants using an unbalanced Mach-Zehnder interferometer, have easily sloped concave profiles in the normal range of values – a zero-dispersion wavelength can be theoretically established, e.g., using a finite element method-based mode solver, but it would be located well outside of the fiber's physical transmission window in the mid-infrared. Dispersion profiles measured for physical fibers are shown in Fig. 15.6. While differences between the two orthogonally polarized components of the fundamental mode in any given fiber are negligible from supercontinuum generation point of view, it is not as much so when dispersion profiles are compared between the two fiber variants. The squeezed-lattice NL46 fiber has dispersion with lower absolute values, and peak of the normal dispersion profile plateau red-shifted in comparison with the NL48 series, bow-tie fiber variant. Measured group birefringence characteristics (obtained using the standard crossed polarizer method) for each of the fibers, shown in Fig. 15.6 as well, are very similar and, importantly, reach reasonable level between

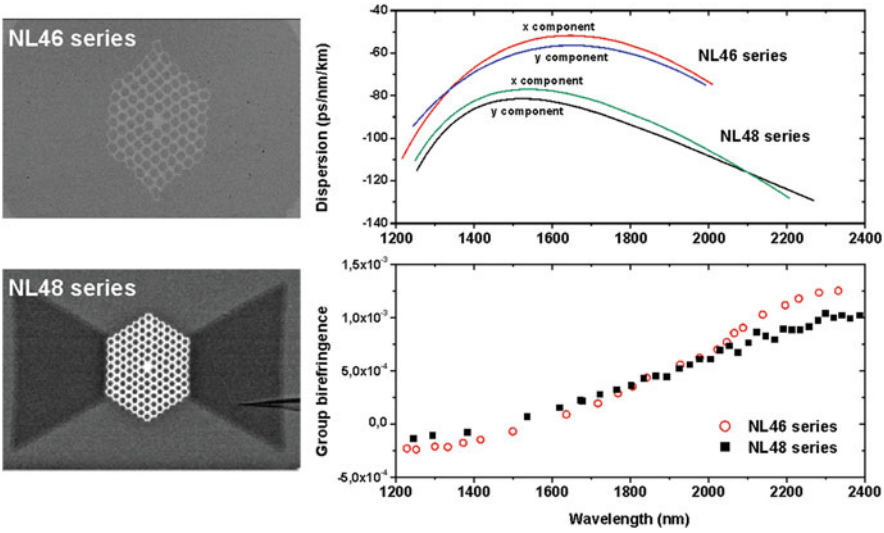

Fig. 15.6 Scanning electron microscope images of all-solid soft glass, all-normal dispersion, birefringent microstructured fibers of the NL46 and NL48 series. Measured chromatic dispersion profiles and group birefringence characteristics. (Adapted with permission from Dobrakowski et al. (2019) ©IOP Publishing)

5×10^{-4} and 10×10^{-4} over much of the Tm^{3+} gain band in the wavelength range around 1900–2200 nm. At wavelengths around 1400 nm and shorter, birefringence takes very low values, consequences of which are discussed in the following section. With comparable mode fields, it can be concluded that the benefit of the lower absolute dispersion favors the NL46 series fiber in context of supercontinuum generation performance. This finds confirmation in supercontinuum generation experiments, in which each of the fibers (10-cm-long samples) was used along with 3.5 nJ mode-locked laser pumping (less than 100-fs-long pulses), centered at a wavelength of 1560 nm, from an Er-doped fiber-based system, the same as the one used to obtain results shown in Fig. 15.5. The broadened output spectrum, shown in Fig. 15.7, obtained under such moderate pump levels, reaches out to roughly 2200 nm in case of the NL46 series fiber, inheriting the width and flatness of an all-normal dispersion supercontinuum demonstrated earlier with the all-solid glass NL38 photonic crystal fiber shown in Fig. 15.5. The NL46 birefringent fiber adds the advantage of a 10 dB polarization extinction ratio (PER), which is impossible with the original NL38 series fiber. The squeezed-lattice NL46 fiber variant has been successfully implemented as seed signal source in an ultralow noise Tm^{3+} fiber amplifier. This system enabled amplification of 100-fs-long pulses with exceptionally low relative intensity noise (RIN) of 0.047% over a bandwidth from 10 Hz to 10 MHz, which was practically unchanged from the RIN level of the Er^{3+}-doped fiber-based femtosecond laser driving the coherent supercontinuum generation in the NL46 fiber (Rampur et al., 2019). The NL48 bow-tie series fiber

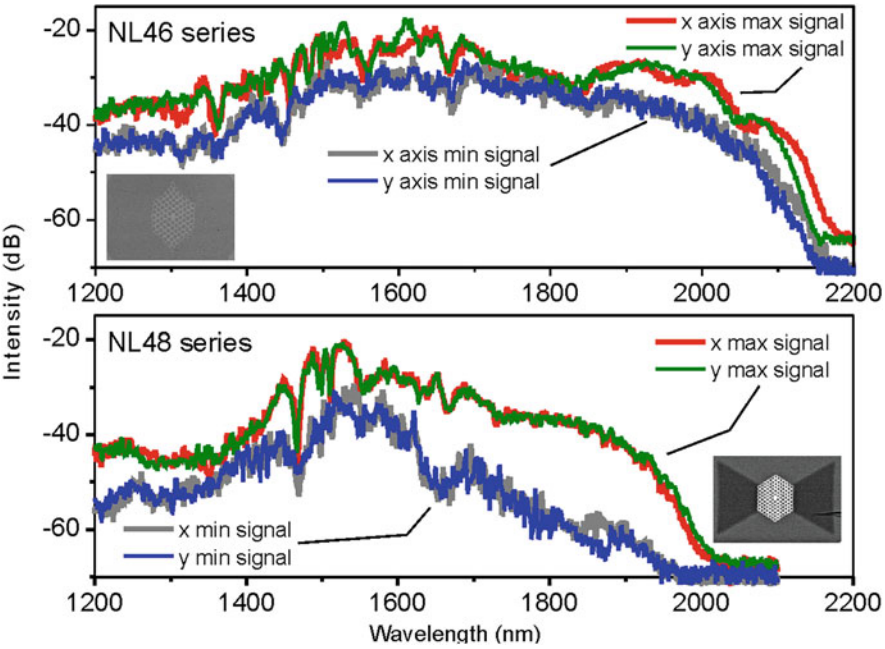

Fig. 15.7 Measured supercontinuum spectra in two types of birefringent, all-solid soft glass, all-normal dispersion microstructured fibers of the NL46 and NL48 series

underperformed in supercontinuum generation compared to the squeezed-lattice NL46, with the supercontinuum extending up to the wavelength of around 2000 nm. This also proved insufficient to effectively seed the ultrafast Tm-fiber amplifier system in the experiment described by authors in Ref. (Rampur et al., 2019). The direct reason behind the inferior supercontinuum performance of the bow-tie is that the stronger normal dispersion – with comparable nonlinearity to the NL46 variant – is explained by less favorable supercontinuum generation conditions due to shorter temporal overlaps between the central, self-phase modulation components and the trailing and leading parts of the normal-dispersion broadened pulse (Heidt, 2010).

Further improvement of the discussed results, in terms of both polarized supercontinuum bandwidth obtainable with a robust mode-locked laser pump and the achievable PER, is possible with the soft glass platform. As in the previous section, an interesting alternative can be found using tellurite glasses and a hexagonal, air-hole dual-ring lattice design. Physically realized fiber is shown in Fig. 15.8, along with measured chromatic dispersion profiles and group birefringence characteristics (Shreesha et al., 2020). The design is a variant of the NL47 fiber discussed in the previous section, drawn from a tellurite glass of identical composition and with very similar geometric dimensions: the core diameter (inscribed circle) is 2.3 μm, the photonic cladding diameter (inscribed circle) is 20 μm, and the air-hole diameters are 0.5 μm and 1.0 μm in the inner and outer rings, respectively. The NL47 design

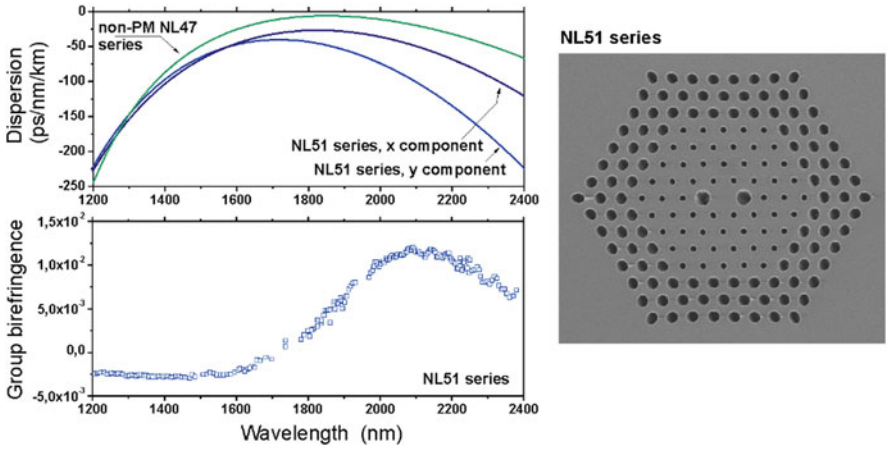

Fig. 15.8 Scanning electron microscope image of air-hole lattice all-normal dispersion, birefringent microstructured fiber of the NL51 series – highly nonlinear tellurite glass design. Measured chromatic dispersion profiles and group birefringence characteristics of the fiber

was modified by introducing two larger air-holes, around 1.7 μm in diameter, on each side of the core. The measured group birefringence, shown in Fig. 15.8, crosses zero around the wavelength of 1700 nm, but across the Tm^{3+} gain band between 1800 nm and 2100 nm, it is between 5×10^{-3} and 10×10^{-3}, an order of magnitude more than in the NL46 and NL47 silicate glass fiber designs. Chromatic dispersion profiles (Fig. 15.8) have stronger absolute values across the Er^{3+} and Tm^{3+} active ion gain bands, compared to the base, regular lattice tellurite glass fiber design labeled NL47, and also vary strongly between the two orthogonally polarized mode components. Combined with high nonlinearity of the glass, the fiber enabled efficient normal-dispersion supercontinuum generation (pump conditions identical to all previously discussed fiber designs and recorded spectral characteristics are shown in Fig. 15.9). As consequence of the stronger normal dispersion of one of the polarization components, the supercontinuum widths vary, and only one of the polarization components reaches near to the wavelength of 2300 nm with the red-shifted supercontinuum edge. PER at 20 dB level was also recorded across the entire red-shifted wing of the supercontinuum spectrum, completely covering both the Tm^{3+} and Tm^{3+}+Ho^{3+} co-doped gain bands, which makes this fiber an attractive seed signal source alternative for a system reported, e.g., by authors in (Heidt et al., 2020). It is very worth noting that the field of tellurite glass structured fibers, although undeniably more challenging technologically than the silicate soft glass fibers or silica fibers, is gaining momentum in ultrafast and nonlinear fiber optics for their compatibility with efficient and robust erbium and thulium fiber-based mode-locked lasers, as well as for their potential of extending transmission and supercontinuum spectrum into the mid-infrared (Nguyen et al., 2020). Despite the technological hurdles related to fabrication of these fibers, the

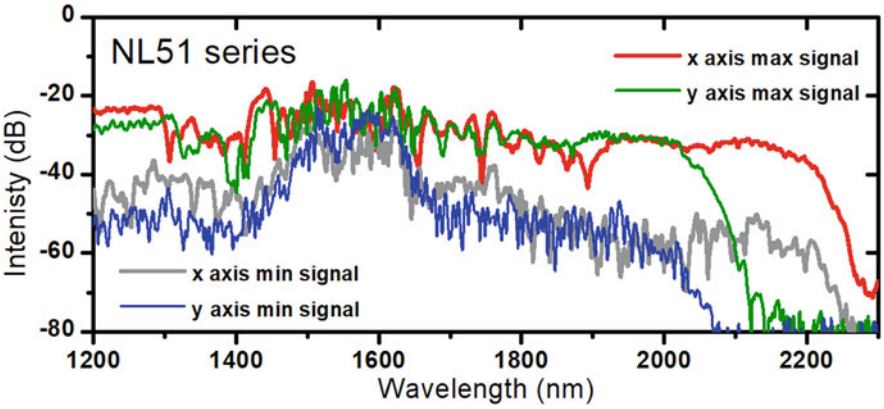

Fig. 15.9 Coherent supercontinuum generation for linearly polarized seed signals for 2 μm ultrafast fiber amplifiers, spectra obtained in NL51 series fibers under pumping with 100 fs, 3.5 nJ pulses centered around the wavelength of 1560 nm from a fiber-based, 100 MHz ultrafast laser

discussed examples prove its fabrication feasibility even in the case of complex cladding lattice designs. Yet another advantage is the multicomponent composition of the glass itself. It offers inhomogeneous ligand surrounding for the optically active dopants, including especially the Tm^{3+} ions, which contributes to wide broadening of the gain band. This enabled, e.g., "two color" operation of Tm^{3+}-doped tellurite glass fiber amplifiers, as demonstrated by authors in (Muravyev et al., 2018). Combining this with the high Kerr nonlinearity and the potential for transparency across the visible, near- and mid-infrared wavelengths sums up to an array of properties very promising for future applications.

15.5 Temporal Structure of Coherent Supercontinuum in Soft Glass Microstructured Fibers

Coherent supercontinuum generation in all-normal dispersion fibers is thoroughly described in literature including contexts like mechanics of the involved nonlinear processes, coherence, and noise performance (Finot et al., 2008; Genier et al., 2019; Heidt et al., 2017). This is in contrast to availability of experimental data on spectro-temporal characteristics of coherent supercontinuum generation in all-normal chromatic dispersion fibers, which is generally scarce (Okamura et al., 2015; Szczepanek et al., 2016). Mathematical models of nonlinear propagation in fibers, based on the generalized nonlinear Schrödinger equation (GNLSE), are known for accurate reconstruction of the basic dynamics, spectral width, and the shape of spectral envelope of supercontinuum pulses obtained in such conditions. These numerical reconstructions are in majority based on the assumption of an ideal Gaussian or hyperbolic secant pulse shape of the pump pulses used for

supercontinuum generation. In contrast to that, femtosecond pulses emitted by mode-locked lasers most often exhibit complex spectro-temporal structures, which are far from their mathematical idealizations. It should be underlined that analysis of experimental data from spectro-temporal measurements in ultrafast optics has served to broaden understanding of solitonic supercontinuum formation and has been exploited in very diverse settings, including, for example, coherent anti-Stokes Raman scattering spectroscopy (Dudley et al., 2002; Shen et al., 2018).

The ultrashort durations in the single picosecond range of all-normal dispersion broadened supercontinuum pulses, readily obtainable from nonlinear propagation simulations, are well below the rise and fall times of the fastest analog-to-digital converters, which makes direct measurements impractical. Second, harmonic frequency-resolved optical gating (FORG) and its cross-correlation variant (XFROG) enable overcoming of this limitation (Gu et al., 2002; Trebino, 2012). Both techniques are routinely applied in extending of characterization of supercontinuum pulses over to the time domain (Dudley et al., 2002; Okamura et al., 2015; Szczepanek et al., 2016). Since both FROG and XFROG are essentially measurements of intensity, the phase information is lost and obtaining of the full-field information requires application of a phase-retrieval algorithm, for example, the generalized projections, which is very suitable for use with pulses from mode-locked lasers (DeLong & Trebino, 1994; Trebino, 2012). Results of FROG characterization and full-field information retrieval performed this way for laser pulses used to pump supercontinuum generation in fibers discussed in this chapter are shown in Fig. 15.10. Retrieved pulse duration is around 75 fs, and spectral full width at half maximum is around 90 nm. The retrieved spectrogram reproduces experimental data with error less than 2×10^{-3}. The pulse profile shows pre- and post-pulses at an intensity level of around 10% of the central part of the pulse, as well as a pedestal extending over ± 500 ps around the pulse peak.

Reconstruction of supercontinuum pulses can be executed in a similar way but is more demanding due to their even greater complexity compared to the driving laser pulses. Implementation of the time-domain ptychography for recording and analysis of such pulses comes as an alternative (Spangenberg et al., 2015). It brings a powerful advantage by resolving supercontinuum pulse fine structure on timescales significantly shorter than the femtosecond laser pump pulse duration and can be considered a general recommendation for complex pulse retrieval (Heidt et al., 2016; Rampur et al., 2020).

All-normal dispersion femtosecond fiber supercontinuum is recognized for its spectral flatness and uniform pulse shape, which stems from its self-phase modulation and optical wave-breaking dynamics, dominating under a broad range of modern mode-locked laser operational parameters (Heidt et al., 2017). Somewhat in contrast to this common presumption, the XFROG measurements reveal their significant fine structuring, not only in the straightforwardly accessible spectral domain but in the timescale as well, which is shown in Fig. 15.11a. The particular example concerns supercontinuum obtained in the squeezed-lattice, birefringent NL46 series fiber. The supercontinuum was driven by pulses shown in Fig. 15.10. The pulse profiles shown have been recorded for a Menlo C-fiber HP mode-locked laser

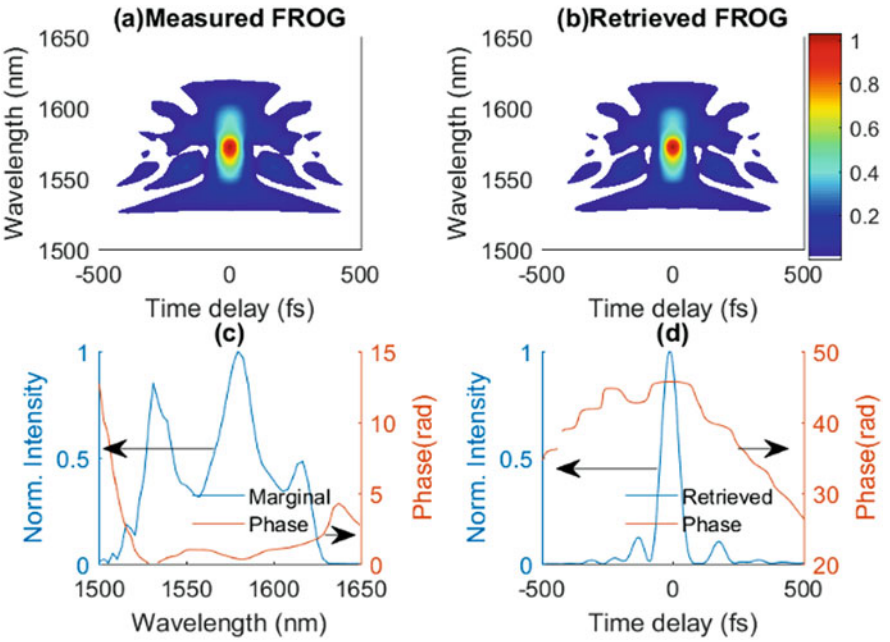

Fig. 15.10 Frequency-resolved optical gating measurements of spectro-temporal structure of femtosecond laser pulses from a mode-locked Er^{3+}-doped fiber-based laser (3.5 nJ, centered at 1560 nm, 100 MHz pulse repetition): (**a**) measured group delay profile, (**b**) pulse retrieval result obtained using a general projections algorithm, (**c**, **d**) retrieved pulse spectrum and temporal profile along with phase profiles. (Adapted with permission from Rampur et al. (2020). ©The Optical Society)

operating at a central wavelength of around 1560 nm (Menlo Systems, Germany). The shape of recorded group delay profile confirms nonlinear broadening dynamics typical to the all-normal dispersion fibers under these pumping conditions, i.e., a central self-phase modulation range accompanied by two optical wave-breaking sidebands. The temporal integrity of the pulse is preserved during broadening. Pulse duration at the output of a 10-cm-long fiber sample is around 4 ps. It can further be observed that the chirp of the pulses is positive and practically linear over wavelengths from around 1300 nm to 2100 nm.

The spectrum and the time profile are both substantially modulated, and the origin of these experimentally observed structures can be explained with the use of numerical simulations based on the GNLSE. A scalar (single mode) version of the equation can be employed, because the NL46 series fiber is polarization-maintaining and reasonable accuracy can be expected if only a single polarization component of the generated supercontinuum pulses is considered. Importantly, the computational part of the analysis has to be performed in two ways. Firstly, the full-field information on the complex pump pulse amplitude is input as the GNLSE starting condition. Simulation result for this scenario is shown in Fig.

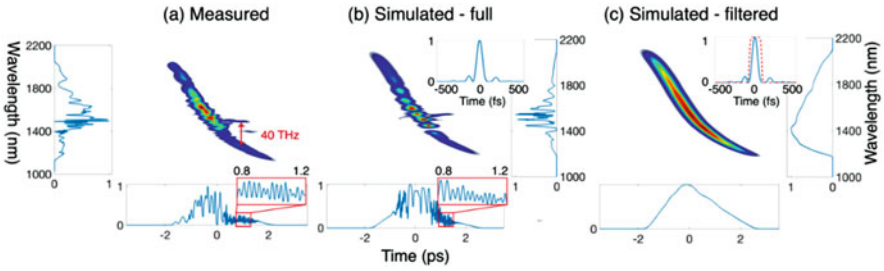

Fig. 15.11 Group delay profiles of supercontinuum pulses obtained in a short sample of NL46 series fiber: (**a**) measured profile, (**b**) simulated profile taking full amplitude and phase of the measured femtosecond pump pulse (75 fs, 3.5 nJ, centered at 1560 nm), and (**c**) simulated profile taking a temporally filtered pump pulse without side peaks or pedestal. The projected axes show the retrieved or simulated pulse spectra and temporal profiles in linear scale. The insets in (**b**) and (**c**) show the pump pulse shapes taken in the simulations. (Adapted with permission from Rampur et al. (2020). ©The Optical Society)

15.11b, and what is striking is the remarkable accuracy of this reconstruction of the measured data on physical supercontinuum pulses. For example, the shortest temporal features in both measured and simulated data sets are located at time delays of roughly 1 ps, which is expanded in the insets in Fig. 15.11a and in Fig. 15.11b. These beating oscillations are caused by temporally overlapping supercontinuum spectral components with a long and spectrally narrow spike around a wavelength of 1530 nm. The GNLSE simulation including the full-field information on the pump pulse allows tracking it back to the unconverted low-level pedestal of the pump pulse (Rampur et al., 2020). This is supported by the beat frequency of this oscillation, which can be determined from the group delay trace in Fig. 15.11 and is equal to 40 THz.

The second part of the numerical simulations should take an ideal Gaussian pump pulse as the starting condition. Here it was simply the pump pulse profile retrieved from the FROG data in Fig. 15.10, with the side peaks and the pedestal filtered out, as shown in the inset in Fig. 15.11c. While the general shape of the spectrogram, i.e., its curvature and spectral and temporal extent, is similar to the physical data, all the fine spectro-temporal structuring is missing. Confrontation of simulation results in Fig. 15.11b – with the full-field information on the initial pulse – and in Fig. 15.11c, where the initial pulse was ideally Gaussian, provides clear evidence that the nonideal pulse shapes of femtosecond lasers are traceable to fine temporal and spectral structuring of coherent supercontinuum pulses.

Interestingly, a feature negligible at first, which is located in the XFROG measured trace around the wavelength of 1400 nm and stretched between the first and the second picosecond of delay behind the pulse center, has not been reproduced by the GNLSE simulation including full-field data of the driving laser pulse. This feature is however repeatable in measurement and was reproducible with time-domain ptychography (Rampur et al., 2020). Explanation of its origin is aided by XFROG characterization of the remaining all-normal dispersion microstructured fibers in the

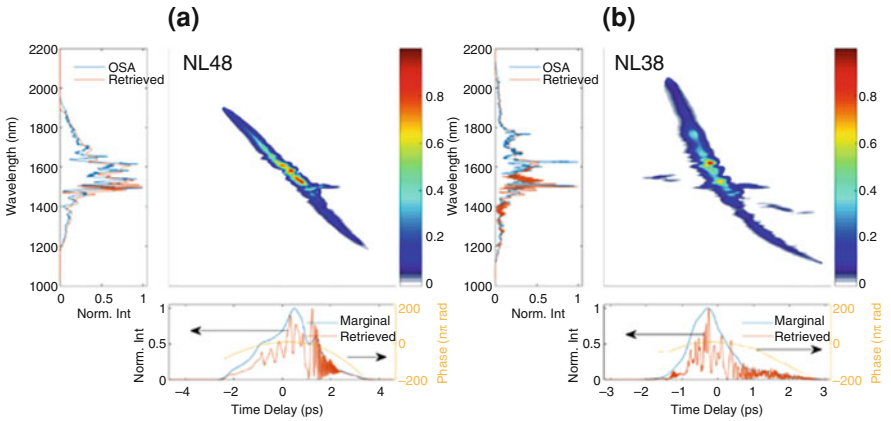

Fig. 15.12 Measured group delay profiles of supercontinuum pulses obtained in short samples of (**a**) NL48 series polarization-maintaining fiber and (**b**) NL38 series non-polarization-maintaining fiber; the spectral projection displays the spectrum retrieved by the e-PIE compared to an independent OSA measurement in linear scale. The temporal projection displays the marginal of the group delays and the intensity and retrieved phase. Pump: 75 fs, 3.5 nJ, centered at 1560 nm. (Adapted with permission from Rampur et al. (2020). ©The Optical Society)

lead-silicate soft glass family, including specifically the bow-tie birefringent variant NL48 and the non-polarization-maintaining base structure NL38. Corresponding group delay traces measured for supercontinuum pulses from these fibers with XFROG are shown in Fig. 15.12. The pumping conditions were identical to the analysis performed with the squeezed-lattice NL46 series fiber.

In the case of the polarization-maintaining NL48 series fiber, the group delay profile is characterized with a nearly perfect linear chirp, which is generally attractive for ultrafast amplifier seeding. The pulse extends in the time domain over around 6 ps, compared with 4 ps obtained for the same sample length (10 cm) of the NL46 series fiber. This is explained by the stronger normal dispersion of the bow-tie NL48 series fiber, in comparison with the squeezed-lattice NL46 series fiber. Both the modulation and temporal beating effects related to the pump pulse structure are clearly visible.

Group delay profile of supercontinuum generated in the non-polarization-maintaining NL38 series fiber shows several important differences. Partial similarities to the birefringent fiber variants include however nearly linear chirp, excluding the blue-shifted sideband, which slopes with increasing delay due to the shape of the fiber dispersion profile. Spectral and temporal structuring is also present. As opposed to clearly defined spectrograms obtained for supercontinuum from the two birefringent fibers, here the edges of the spectrogram are blurred and exhibit noisy contours. The main pulse is accompanied by weak features around the wavelengths of 1400 nm and 1600 nm at delays of -2 ps and $+$ 2 ps, respectively. The noisy contour and the features separated from the main pulse are not readily observable in the spectrograms recorded for the two birefringent fiber

variants, which delivered polarized supercontinuum pulses. Unintentional, weak birefringence has been assigned to onset of polarization modulational instability (PMI) decoherence in all-normal dispersion supercontinuum generation and to amplification of quantum noise during the process (Gonzalo et al., 2018; Millot et al., 1998). Finally, in order to explain the appearance of a similar feature around the 1400 nm wavelength in the spectrogram of the polarization-maintaining NL46 fiber, one has to recall the fiber's birefringence characteristic, shown in Fig. 15.6 in the preceding section. Birefringence around this wavelength nears zero, and for this reason, the nonlinear dynamics are prone to PMI. Notably, a similar low-level feature around the 1600 nm wavelength and at +2 ps delay, recorded for the NL38 fiber, is missing in the spectrogram of the NL46, where its birefringence reaches 2.5×10^{-4}. This further supports assignment of these separated features to the onset of PMI.

15.6 Conclusions

The highlight of the chapter is that the all-normal dispersion, coherent supercontinuum generation concept can benefit from broad design flexibility offered by soft glasses, when its spectral extension into the long-wave near-infrared is considered. The key advantage of multicomponent soft glasses – the easy adaptation of chemical composition for designed thermal, mechanical, and optical properties enables matching of glass transition temperatures down to $\Delta T_g = 11$ °C and thermal expansion coefficient down to $\Delta\alpha_{+20/+300°C} = 0.2 \times 10^{-6}$/K at the same time providing a refractive index contrast of $\Delta n = 0.169263$ – opens a route to designing highly nonlinear fibers with flattened normal dispersion profiles over their entire transmission windows. Currently, soft glasses allowing these design specifications are commercially available (Schott F2 and SF6), while the all-solid glass microstructure greatly simplifies fiber drawing procedure and facilitates reproducibility. Using this approach, all-normal dispersion photonic crystal fibers with nonlinear coefficients exceeding 200 W^{-1} km^{-1} are readily achievable. This is sufficient for generation of an octave-spanning supercontinuum with pumping from mode-locked Er-fiber lasers delivering 100 fs pulses with peak power below 50 kW and less than 5 nJ of energy. Spectral coverage of such coherent, broadband pulses is wide enough to simultaneously seed Er^{3+} and Tm^{3+} or Tm^{3+}+Ho^{3+} ultrafast fiber amplifiers for intriguing prospects of high-quality, ultrashort pulse synthesis using fully fiberized platforms. The long-wavelength arm of such a hypothetical system has already been demonstrated with a Tm^{3+}+Ho^{3+} co-doped fiber amplifier system (Heidt et al., 2020), seeded by coherent supercontinuum obtained from the NL38 series fibers described in this chapter. The Tm^{3+}+Ho^{3+} co-doped systems are attractive, because they have the broadest gain band out of all the mature fiber amplifiers containing the Yb^{3+}, Er^{3+}, or Tm^{3+} dopant ions and can be recompressed close to the transform limit using single mode fibers. Furthermore the 2 μm wavelength band is very attractive for ultrashort pulse amplification,

for its spectral closeness to the mid-infrared wavelength band and its biochemical sensing applications, as well as for a factor of 4 higher intensity threshold for detrimental transverse mode instability phenomena compared to the Yb^{3+}-doped systems (Gaida et al., 2018).

This particular application of the non-polarization-maintaining fiber of the NL38 series has revealed the first clues to polarization modulational instabilities limiting the already excellent noise performance of the reported Tm^{3+}+Ho^{3+} fiber amplifier (Heidt et al., 2020). This called for overcoming of the PMI-related decoherence, onset of which took place during the broadening in a non-polarization-maintaining soft glass fiber and was subsequently amplified in the Tm^{3+}+Ho^{3+} amplifier. The fast prototyping inherent to the soft glass platform and straightforward introduction of fiber preform modifications of the all-solid glass photonic crystal fiber supports the development of intentionally birefringent fiber variants. Polarization extinction ratio of 10 dB in the generated supercontinuum has proven sufficient for further limiting of relative intensity noise in a Tm^{3+} ultrafast fiber amplifier seeded by this supercontinuum signal, down to levels observed for the state-of-the-art femtosecond Er-fiber laser front-end (Rampur et al., 2019). Such performance characteristics are a promising perspective for the work on fiber-based wavelength-division multiplexed ultrashort pulse amplification systems. Worth noting is that this track record does not exhaust the potential of heavy-metal oxide soft glasses for specialty fiber optics. In each of the fiber variants, i.e., non-polarization-maintaining NL38 series and the two intentionally birefringent versions, an air-hole lattice photonic crystal fiber drawn from a highly nonlinear tellurite glass was discussed as a potential alternative (Klimczak et al., 2019; Shreesha et al., 2020). While admittedly lacking the advantage of straightforward fabrication and mechanical sturdiness of their all-solid glass counterparts, these two tellurite fibers exceeded the silicate designs in nonlinearity and birefringence (the NL51 series fiber) and consequently outperformed them in supercontinuum bandwidth and polarization extinction ratio (the birefringent variant NL51). Additionally, tellurite glasses possess the potential for access to the mid-infrared wavelengths. Thus, it would be very interesting to see the future dynamics of development and the contribution of this fiber technology in the field of ultrafast fiberized lasers and amplifiers.

In concluding remarks, it is fitting to point out that measurements using advanced ultrashort pulse diagnostics, applied to characterization of supercontinuum pulses from the discussed fibers, confirmed all of the earlier numerical predictions of coherent supercontinuum pulse profiles. What is however of special value is that the combination of XFROG measurements, ptychography pulse retrieval algorithms, and nonlinear propagation simulations based on the full-field information on the pump pulses offered a much deeper perspective on the coherent supercontinuum generation in fibers than the basic simulations assuming purely Gaussian (or hyperbolic secant) pump pulse idealizations. Comparison of minutiae features observed in spectrograms measured for pulses from polarization-maintaining and non-polarization-maintaining fiber variants, such as pulse contour details and trailing or leading features separated from the main, preserved supercontinuum pulse, enabled identification of noise amplification related to polarization modulational

instability. This demonstrated with clarity the advantage of the birefringent fiber designs in generation of coherent supercontinuum. In addition to that, confrontation of nonlinear propagation simulations assuming either physical, full-field data on the initial pulses or pulses with the technical distortions filtered out (pre- and post-pulses and a pedestal) provided the evidence necessary for tracing back the complex spectral and temporal structuring of the supercontinuum pulses to the femtosecond laser pulses used for pumping. These analyses are indeed of curiosity-driven value but are not without a practical dimension in the future development of light sources with unprecedented stability and pulse quality.

Acknowledgments The authors acknowledge funding from Foundation for Polish Science, grants POIG TEAM/2012-9/1; POIR.04.04.00-00-1C74/16; and POIR.04.04.00-00-1D64/16.

References

Agrawal, G. (2007). *Nonlinear fiber optics*. Academic Press.

Alfano, R. R., & Shapiro, S. L. (1970a). Emission in region 4000 to 7000 Å via 4-photon coupling in glass. *Physical Review Letters, 24*, 584.

Alfano, R. R., & Shapiro, S. L. (1970b). Observation of self-phase modulation and small-scale filaments in crystals and glasses. *Physical Review Letters, 24*, 592.

Anuszkiewicz, A., Martynkien, T., Mergo, P., Makara, M., & Urbanczyk, W. (2013). Sensing and transmission characteristics of a rocking filter fabricated in a side-hole fiber with zero group birefringence. *Optics Express, 21*, 12657.

Buczyński, R., Pniewski, J., Pysz, D., Stępień, R., Kasztelanic, R., Kujawa, I., Filipkowski, A., Waddie, A. J., & Taghizadeh, M. R. (2012). Dispersion management in soft glass all-solid photonic crystal fibres. *Optoelectronic Review, 20*, 207.

Cassataro, M., Novoa, D., Günendi, M. C., Edavalath, N. N., Frosz, M. H., Travers, J. C., St, P., & Russell, J. (2017). Generation of broadband mid-IR and UV light in gas-filled single-ring hollow-core PCF. *Optics Express, 25*, 7637.

Cimek, J., Stępień, R., Stępniewski, G., Siwicki, B., Stafiej, P., Klimczak, M., Pysz, D., & Buczyński, R. (2016). High contrast glasses for all-solid fibers fabrication. *Optical Materials, 62*, 159.

Cimek, J., Liaros, N., Couris, S., Stępień, R., Klimczak, M., & Buczyński, R. (2017). Experimental investigation of the nonlinear refractive index of various soft glasses dedicated for development of nonlinear photonic crystal fibers. *Optical Materials Express, 7*, 3471.

DeLong, K. W., & Trebino, R. (1994). Improved ultrashort pulse-retrieval algorithm for frequency-resolved optical gating. *Journal of the Optical Society of America. A, 11*, 2429.

Dobrakowski, D., Rampur, A., Stępniewski, G., Anuszkiewicz, A., Lisowska, J., Pysz, D., Kasztelanic, R., & Klimczak, M. (2019). Development of highly nonlinear polarization maintaining fibers with normal dispersion across entire transmission window. *Journal of Optics, 21*, 015504.

Domachuk, P., Wolchover, N. A., Cronin-Golomb, M., Wang, A., George, A. K., Cordeiro, C. M. B., Knight, J. C., & Omenetto, F. G. (2008). Over 4000 nm bandwidth of mid-IR supercontinuum generation in sub-centimeter segments of highly nonlinear tellurite PCFs. *Optics Express, 16*, 7161.

Dudley, J. M., & Coen, S. (2002). Coherence properties of supercontinuum spectra generated in photonic crystal and tapered optical fibers. *Optics Letters, 27*, 1180.

Dudley, J. M., Gu, X., Xu, L., Kimmel, M., Zeek, E., O'Shea, P., Trebino, R., Coen, S., & Windeler, R. S. (2002). Cross-correlation frequency resolved optical gating analysis of

broadband continuum generation in photonic crystal fiber: Simulations and experiments. *Optics Express, 10*, 1215.

Dudley, J. M., Genty, G., & Coen, S. (2006). Supercontinuum generation in photonic crystal fiber. *Reviews of Modern Physics, 78*, 1135.

Ebendorff-Heidepriem, H., Foo, T.-C., Moore, R. C., Zhang, W., Li, Y., Monro, T. M., Hemming, A., & Lancaster, D. G. (2008). Fluoride glass microstructured optical fiber with large mode area and mid-infrared transmission. *Optics Letters, 33*, 2861.

Feng, X., Monro, T. M., Petropoulos, P., Finazzi, V., & Hewak, D. (2013). Solid microstructured optical fiber. *Optics Express, 11*, 2225.

Finot, C., Kibler, B., Provost, L., & Wabnitz, S. (2008). Beneficial impact of wave-breaking for coherent continuum formation in normally dispersive nonlinear fibers. *Journal of the Optical Society of America B: Optical Physics, 25*, 1938–1948.

Gaida, C., Gebhardt, M., Heuermann, T., Stutzki, F., Jauregui, C., & Limpert, J. (2018). Ultrafast thulium fiber laser system emitting more than 1 kW of average power. *Optics Letters, 43*, 5853.

Genier E., P. Bowen, T. Sylvestre, J. M. Dudley, P. Moselund, and O. Bang (2019) Amplitude noise and coherence degradation of femtosecond supercontinuum generation in all-normal-dispersion fibers," Journal of the Optical Society of America B: Optical Physics 36, A161.

Gonzalo, I. B., Engelsholm, R. D., Sørensen, M. P., & Bang, O. (2018). Polarization noise places severe constraints on coherence of all-normal dispersion femtosecond supercontinuum generation. *Scientific Reports, 8*, 6579.

Gu, X., Xu, L., Kimmel, M., Zeek, E., O'Shea, P., Shreenath, A. P., Trebino, R., & Windeler, R. S. (2002). Frequency-resolved optical gating and single-shot spectral measurements reveal fine structure in microstructure-fiber continuum. *Optics Letters, 27*, 1174.

Heidt, A. M. (2010). Pulse preserving flat-top supercontinuum generation in all-normal dispersion photonic crystal fibers. *Journal of the Optical Society of America B: Optical Physics, 27*, 550.

Heidt, A. M., Spangenberg, D., Brügmann, M., Rohwer, E. G., & Feurer, T. (2016). Improved retrieval of complex supercontinuum pulses from XFROG traces using a ptychographic algorithm. *Optics Letters, 41*, 4903.

Heidt, A. M., Feehan, J. S., Price, J. H. V., & Feurer, T. (2017). Limits of coherent supercontinuum generation in normal dispersion fibers. *Journal of the Optical Society of America B: Optical Physics, 34*, 764.

Heidt, A. M., Hodasi, J. M., Rampur, A., Spangenberg, D. M., Ryser, M., Klimczak, M., & Feurer, T. (2020). Low noise all-fiber amplification of a coherent supercontinuum at 2 μm and its limits imposed by polarization noise. *Scientific Reports, 10*, 16734.

Jiang, X., Joly, N. Y., Finger, M. A., Babic, F., Wong, G. K. L., Travers, J. C., & Russell, P. S. J. (2015). Deep-ultraviolet to mid-infrared supercontinuum generated in solid-core ZBLAN photonic crystal fibre. *Nature Photonics, 9*, 133.

Kalashnikov, V. L., Sorokin, E., & Sorokina, I. T. (2007). Raman effects in the infrared supercontinuum generation in soft-glass PCFs. *Applied Physics B: Lasers and Optics, 87*, 37.

Kato, T., Suetsugu, Y., & Nishimura, M. (1995). Estimation of nonlinear refractive index in various silica-based glasses for optical fibers. *Optics Letters, 20*, 2279.

Kedenburg, S., Gissibl, T., Steinle, T., Steinmann, A., & Giessen, H. (2015). Towards integration of a liquid-filled fiber capillary for supercontinuum generation in the 1.2–2.4 μm range. *Optics Express,**23***, 8281.

Kibler, B., Dudley, J. M., & Coen, S. (2005). Supercontinuum generation and nonlinear pulse propagation in photonic crystal fiber: Influence of the frequency-dependent effective mode area. *Applied Physics B: Lasers and Optics, 81*, 337.

Klimczak, M., Siwicki, B., Skibiński, P., Pysz, D., Stçpień, R., Heidt, A., Radzewicz, C., & Buczyński, R. (2014). Coherent supercontinuum generation up to 2.3μm in all-solid soft-glass photonic crystal fibers with flat all-normal dispersion. *Optics Express,**22***, 18824.

Klimczak, M., Siwicki, B., Zhou, B., Bache, M., Pysz, D., Bang, O., & Buczyński, R. (2016a). Coherent supercontinuum bandwidth limitations under femtosecond pumping at 2 μm in all-solid soft glass photonic crystal fibers. *Optics Express, 24*, 29406.

Klimczak, M., Soboń, G., Kasztelanic, R., Abramski, K. M., & Buczyński, R. (2016b). Direct comparison of shot-to-shot noise performance of all normal dispersion and anomalous dispersion supercontinuum pumped with sub-picosecond pulse fiber-based laser. *Scientific Reports, 5*, 19284.

Klimczak, M., Siwicki, B., Heidt, A. M., & Buczyński, R. (2017). Coherent supercontinuum generation in soft glass photonic crystal fibers. *Photonics Research, 5*, 710.

Klimczak, M., Michalik, D., Stępniewski, G., Karpate, T., Cimek, J., Forestier, X., Kasztelanic, R., Pysz, D., Stępień, R., & Buczyński, R. (2019). Coherent supercontinuum generation in tellurite glass regular lattice photonic crystal fibers. *Journal of the Optical Society of America, 36*, A112.

Krauss, G., Lohss, S., Hanke, T., Sell, A., Eggert, S., Huber, R., & Leitenstorfer, A. (2010). Synthesis of a single cycle of light with compact erbium-doped fibre technology. *Nature Photonics, 4*, 33.

Liu, Y., Zhao, Y., Lyngsø, J., You, S., Wilson, W. L., Tu, H., & Boppart, S. A. (2015). Suppressing short-term polarization noise and related spectral decoherence in all-normal dispersion fiber supercontinuum generation. *Journal of Lightwave Technology, 33*, 1814.

Lorenc, D., Aranyosiova, M., Buczynski, R., Stępień, R., Bugar, I., Vincze, A., & Velic, D. (2008). Nonlinear refractive index of multicomponent glasses designed for fabrication of photonic crystal fibers. *Applied Physics B: Lasers and Optics, 93*, 531.

Martynkien, T., Pysz, D., Stępień, R., & Buczyński, R. (2014). All-solid microstructured fiber with flat normal chromatic dispersion. *Optics Letters, 39*, 2342.

Millot, G., Seve, E., Wabnitz, S., & Haelterman, M. (1998). Observation of induced modulational polarization instabilities and pulse-train generation in the normal-dispersion regime of a birefringent optical fiber. *Journal of the Optical Society of America B: Optical Physics, 15*, 1266.

Muravyev, S. V., Anashkina, E. A., Andrianov, A. V., Dorofeev, V. V., Motorin, S. E., Koptev, M. Y., & Kim, A. V. (2018). Dual-band Tm^{3+}-doped tellurite fiber amplifier and laser at 1.9 μm and 2.3 μm. *Scientific Reports,**8***, 16164.

Nguyen, H. P. T., Tuan, T. H., Matsumoto, M., Sakai, G., Suzuki, T., & Ohishi, Y. (2020). Mid-infrared supercontinuum generation with high spectral flatness in dispersion flattened tellurite all-solid hybrid microstructured optical fibers. *Japanese Journal of Applied Physics, 59*, 042002.

Okamura, A., Sakakibara, Y., Omoda, E., Kataura, H., & Nishizawa, N. (2015). Experimental analysis of coherent supercontinuum generation and ultrashort pulse generation using cross-correlation frequency resolved optical gating (X-FROG). *Journal of the Optical Society of America B: Optical Physics, 32*, 400.

Petersen Ch, R., Møller, U., Kubat, I., Zhou, B., Dupont, S., Ramsay, J., Benson, T., Sujecki, S., Abdel-Moneim, N., Tang, Z., Furniss, D., Seddon, A., & Bang, O. (2014). Mid-infrared supercontinuum covering the 1.4–13.3 μm molecular fingerprint region using ultra-high NA chalcogenide step-index fibre. *Nature Photonics,**8***, 830.

Price, J. H. V., Feng, X., Heidt, A. M., Brambilla, G., Horak, P., Poletti, F., Ponzo, G., Petropoulos, P., Petrovich, M., Shi, J., Ibsen, M., Loh, W. H., Rutt, H. N., & Richardson, D. J. (2012). Supercontinuum generation in non-silica fibers. *Optical Fiber Technology, 18*, 327.

Qin, G., Yan, X., Kito, C., Liao, M., Chaudhari, C., Suzuki, T., & Ohishi, Y. (2009). Ultrabroadband supercontinuum generation from ultraviolet to 6.28 μm in a fluoride fiber. *Applied Physics Letters,**95***, 161103.

Rampur, A., Stepanenko, Y., Stępniewski, G., Kardaś, T., Dobrakowski, D., Spangenberg, D.-M., Feurer, T., Heidt, A., & Klimczak, M. (2019). Ultra low-noise coherent supercontinuum amplification and compression below 100 fs in an all-fiber polarization-maintaining thulium fiber amplifier. *Optics Express, 27*, 35041.

Rampur, A., Spangenberg, D.-M., Stępniewski, G., Dobrakowski, D., Tarnowski, K., Stefańska, K., Paździor, A., Mergo, P., Martynkien, T., Feurer, T., Klimczak, M., & Heidt, A. M. (2020). Temporal fine structure of all-normal dispersion fiber supercontinuum pulses caused by non-ideal pump pulse shapes. *Optics Express, 28*, 16579.

Ranka, J. K., Windeler, R. S., & Stentz, A. J. (2000). Visible continuum generation in air-silica microstructure optical fibers with anomalous dispersion at 800 nm. *Optics Letters, 25*, 25.

Reeves, W. H., Skryabin, D. V., Biancalana, F., Knight, J. C., Russell, P. S. J., Omenetto, F. G., Efimov, A., & Taylor, A. J. (2003). Transformation and control of ultra-short pulses in dispersion-engineered photonic crystal fibres. *Nature, 424*, 511.

Saitoh, K., Koshiba, M., Hasegawa, T., & Sasaoka, E. (2003). Chromatic dispersion control in photonic crystal fibers: Application to ultra-flattened dispersion. *Optics Express, 11*, 843.

Sell, A., Krauss, G., Scheu, R., Huber, R., & Leitenstorfer, A. (2009). 8-fs pulses from a compact Er:Fiber system: Quantitative modeling and experimental implementation. *Optics Express, 17*, 1070.

Shen, Y., Voronin, A. A., Zheltikov, A. M., O'Connor, S. P., Yakovlev, V. V., Sokolov, A. V., & Scully, M. O. (2018). Picosecond supercontinuum generation in large mode area photonic crystal fibers for coherent anti-stokes Raman scattering microspectroscopy. *Scientific Reports, 8*, 9526.

Shreesha, R. D. S., Karpate, T., Ghosh, A. N., Klimczak, M., Pysz, D., Buczynski, R., Billet, C., Bang, O., Dudley, J. M., & Sylvestre, T. (2020). *Real-time noise measurement in supercontinuum generation in PM and non-PM ANDi tellurite fibers*. Conference on Lasers and Electro-Optics OSA Technical Digest (Optical Society of America, 2020), paper STh3P.4.

Siwicki, B., Kasztelanic, R., Klimczak, M., Cimek, J., Pysz, D., Stępień, R., & Buczyński, R. (2016). Extending of flat normal dispersion profile in all-solid soft glass nonlinear photonic crystal fibres. *Journal of Optics, 18*, 065102.

Spangenberg, D., Neethling, P., Rohwer, E., Brügmann, M. H., & Feurer, T. (2015). Time-domain ptychography. *Physical Review A, 91*, 21803.

Stępień, R., Buczynski, R., Pysz, D., Kujawa, I., Filipkowski, A., Mirkowska, M., & Diduszko, R. (2011). Development of thermally stable tellurite glasses designed for fabrication of microstructured optical fibers. *Journal of Non-Crystalline Solids, 357*, 873.

Szczepanek, J., Kardaś, T. M., & Stepanenko, Y. (2016). Group delay measurements of ultra-broadband pulses generated in highly nonlinear fibers. *Photonics Letters of Poland, 8*, 107.

Trebino, R. (2012). *Frequency-resolved optical gating: The measurement of ultrashort laser pulses*. Springer Science & Business Media.

Venck, S., St-Hilaire, F., Brilland, L., Ghosh, A. N., Chahal, R., Caillaud, C., Meneghetti, M., Troles, J., Joulain, F., Cozic, S., Poulain, S., Huss, G., Rochette, M., Dudley, J. M., & Sylvestre, T. (2020). 2–10 μm mid-infrared fiber-based supercontinuum laser source: Experiment and simulation. *Laser & Photonics Reviews, 14*, 2000011.

Xia, C., Kumar, M., Kulkarni, O. P., Islam, M. N., Terry, F. L., Jr., Freeman, M. J., Poulain, M., & Mazé, G. (2006). Mid-infrared supercontinuum generation to 4.5 μm in ZBLAN fluoride fibers by nanosecond diode pumping. *Optics Letters, 31*, 2553.

Chapter 16
Supercontinuum Generation in Birefringent All Normal Dispersion Fibers

Geng Wang, Stephen A. Boppart, and Haohua Tu

Abstract Supercontinuum generation using ultrafast pulses and nonlinear optical fibers has produced numerous broadband sources and enabled disparate applications. To ensure high spectral coherence, investigators have taken the advantage of birefringent all normal fibers and/or operating regimes that the supercontinuum is exclusively generated in a normal dispersion regime of birefringent fibers. (For additional information on all normal dispersion effects for supercontinuum generation, see Chap. 6 by Alexander M. Heidt).

Keywords Supercontinuum generation · Spectral coherence · Photonic crystal fibers · Normal dispersion · Birefringence · Polarization-maintaining · Relative intensity noise · Pulse compression · Wave-breaking

16.1 Introduction

Alfano and Shapiro discovered the supercontinuum generation in bulk materials (Alfano & Shapiro, 1970). White-light generation by the combination of a photonic crystal fiber (PCF) and an oscillator-type ultrafast laser was reported later (Ranka et al., 2000) and has since initiated the so-called supercontinuum (SC) revolution (Dudley & Taylor, 2009). Before this revolution, SC was typically generated in a conventional fiber with its full bandwidth falling into a normal dispersion regime of the fiber, so that the fiber functioned like an all normal dispersion (ANDi) fiber.

G. Wang
Beckman Institute for Advanced Science and Technology, University of Illinois Urbana-Champaign, Urbana, IL, USA

S. A. Boppart · H. Tu (✉)
Beckman Institute for Advanced Science and Technology, University of Illinois Urbana-Champaign, Urbana, IL, USA

Department of Electrical and Computer Engineering, University of Illinois Urbana-Champaign, Urbana, IL, USA
e-mail: htu@illinois.edu

R. R. Alfano (ed.), *The Supercontinuum Laser Source*,
https://doi.org/10.1007/978-3-031-06197-4_16

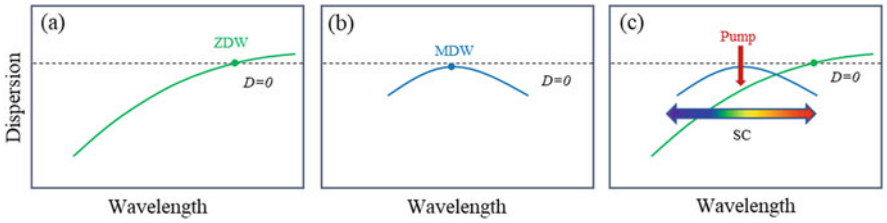

Fig. 16.1 (**a**) Dispersion engineering of typical ZDW PCFs. (**b**) Dispersion engineering of DFDD-ANDi-PCFs. (**c**) Comparison of supercontinuum generation in a DFDD-ANDi-PCF and a ZDW PCF

This was a natural condition dictated by the available laser sources and nonlinear fibers. Although pulse compression down to 6 fs (i.e., broad coherent bandwidth) was attained (Fork et al., 1987), the complicated source laser (low repetition-rate amplifier) limited the widespread application of the resulting SC.

After the revolution, SC was typically generated in a zero-dispersion wavelength (ZDW) PCF with its bandwidth falling into both normal and anomalous regimes of the fiber (i.e., ZDW lies within SC spectrum). The powerful dispersion engineering of PCFs [Fig. 16.1a] shifts the ZDW of the fiber close to the wavelength of a standard mode-locked (femtosecond or picosecond) source laser, leading to this widely accessible SC dominated by soliton dynamics. Unfortunately, the pulse compressibility (or coherence) of the SC is generally poor due to the intrinsic noise of the soliton dynamics (Dudley et al., 2006). The nonlinear frequency generation of a PCF having a ZDW of λ_{ZDW} can be broadly classified into three operating regimes:

(1) $\lambda_{ZDW} << \lambda_{pump}$, soliton-Cherenkov-radiation regime. In this regime, the pump pulses transfer their energy into discrete bands of solitons and Cherenkov radiation(s), so that no spectrally uniform SC is generated (Tu & Boppart, 2009).
(2) $\lambda_{ZDW} \approx \lambda_{pump}$, incoherent SC generation regime. This regime has generated the broadest SC via soliton excitation and has received the most attention. However, the coherence of the SC is often suboptimal (Dudley et al., 2006).
(3) $\lambda_{ZDW} >> \lambda_{pump}$, coherent SC generation regime. This regime produces relatively narrow bandwidth SC mainly through self-phase modulation (SPM). However, the generated SC has full coherence (Dudley et al., 2006), which has been demonstrated by pulse compression (Südmeyer et al., 2003; McConnell & Riis, 2004).

Then, the concept of dispersion engineering of PCFs [Fig. 16.1b] (Chow et al., 2006; Heidt, 2010; Tu et al., 2010; Hooper et al., 2011), which was suggested by earlier studies on conventional circular fibers (Mori et al., 1997; Nishizawa & Takayanagi, 2007) and the PCFs with two closely spaced ZDWs (Falk et al., 2005; Tse et al., 2006; Hartung et al., 2011), was considered as a method to generate soliton-free coherent SC. The engineered PCF has a flattened convex profile of

normal dispersion with a distinct minimum-dispersion wavelength (MDW) but no ZDW. It was therefore termed as a dispersion-flattened dispersion-decreased all normal dispersion (DFDD-ANDi) fiber (Tu & Boppart, 2013). The interest in DFDD-ANDi-PCFs was driven by the need of a practical fiber SC source with full coherence across all the frequency components of the SC. Broadband coherent sources are indispensable in coherent nonlinear microscopy (Silberberg, 2009; Marks & Boppart, 2004), frequency metrology (Udem et al., 2002), nonlinear frequency conversion/amplification, ultrashort pulse generation, and other coherently controlled applications. This trend reflected a shift of focus for dispersion engineering from pursuing the broadest SC generation to preserving the coherence of SC generation.

Because only the SC generation in a normal dispersion region of the fiber is guaranteed to be coherent, it is fair to compare the performance of the optimized DFDD-ANDi-PCF with that of the ZDW PCF operated in the third regime ($\lambda_{ZDW} >> \lambda_p$) [Fig. 16.1c]. Due to the sloped dispersion profile of the ZDW PCF, the λ_{ZDW} of the fiber must be placed at a longer wavelength than the red edge of the intended SC. Thus, an undesirably large dispersion occurs at λ_{pump} to adversely influence the spectral broadening [Fig. 16.1c]. This observation clearly illustrates the advantage of the DFDD-ANDi-PCF over the conventional ZDW PCF in broadband coherent SC generation.

Despite the progress along this line of research, the noticeable effect of the birefringence of the DFDD-ANDi-PCFs on the SC generation (Tu et al., 2010; Wang et al., 2007) was completely ignored. This birefringence is widely present in nonlinear non-polarization-maintaining fibers with a typical core size of 2 μm, presumably due to the structural symmetry breaks introduced in the fiber drawing process (Tu et al., 2012). The intrinsic form-birefringence was found to be on the order of 10^{-5} and to profoundly affect the SC generation in a wide variety of nonlinear PCFs (Tu et al., 2012). The weak unintentional birefringence not only negatively affects the controllability and long-term stability of the ANDi fiber SC generation (Tu et al., 2012; Domingue & Bartels, 2013) but also fundamentally limits the application of this technology when full spectral coherence or a low-noise polarized source is required. Fortunately, this hidden intrinsic noise and the accompanied spectral decoherence can be effectively suppressed by using a polarization-maintaining (PM) ANDi fiber with a large intentional birefringence ($>10^{-4}$).

16.2 Quantified Supercontinuum Generation in Birefringent All Normal Fibers

Theoretically, the scalar generalized nonlinear Schrödinger eq. (S-GNLSE) is used to quantitatively predict the spectral-temporal properties of fiber continuum pulses under a non-depolarization condition (Agrawal, 2001; Hori et al., 2004; Dudley

et al., 2006; Hult, 2007; Heidt, 2009; Tu et al., 2010; Liu et al., 2016), i.e., with polarized fiber output from polarized pump input. However, due to the weak unintentional form-birefringence ($B = 1 \times 10^{-6} - 5 \times 10^{-5}$) intrinsic in these nonlinear fibers, a complete understanding of the corresponding SC generation must rely on the coupled generalized nonlinear Schrödinger eq. (C-GNLSE) that takes account of the birefringence (Agrawal, 2001; Coen et al., 2002; Zhu & Brown, 2004; Tianprateep et al., 2005; Tu et al., 2012), rather than the S-GNLSE that ignores this effect. Conventional simulations based on the S-GNLSE fail to reproduce the prominent observed features of the SC generation in a short piece of DFDD-ANDi-PCF, but these features can be qualitatively or semiquantitatively understood by the C-GNLSE (Tu, 2012). The nonlinear polarization effects induced by the birefringence significantly distort the otherwise simple spectrotemporal field of the SC pulses. Also, the local random variation of the linear and circular birefringence may further complicate the rigorous theoretical modeling to guide the pulse compression and may be responsible for the discrepancy between the observed SC spectra and the simulated spectra (Tu et al., 2012).

Experiments have been consistent with theoretical predictions. Under a wide range of fiber lengths and incident powers, the spectrum of SC generated from non-birefringent or weakly birefringent PCFs was found to depend sensitively on the polarization of the incident laser pulses (Tu et al., 2010). Changing the polarization direction of the incident laser beam did not change the power of the continuum but noticeably varied the spectrum of the continuum, particularly at high incident powers. Also, the continuum was rather unpolarized, particularly at long fiber lengths and high incident powers.

The birefringence of the fiber can be measured by a cutback method (Tu et al., 2010), which can quantify the periodicity of the polarization pattern of the fiber output, i.e., the beat length. To evaluate the extent of possible polarization-mode depolarization, the polarizer can be oriented along the same principal axis at the exit end of the fiber to measure the output power $P_{\parallel}$ and along its orthogonal axis to measure the output power $P_{\perp}$. The extent of the depolarization is then represented by $P_{\perp} / (P_{\perp} + P_{\parallel})$. The experiment indicated the beneficial effect of a large linear birefringence to delay the nonlinear polarization-mode depolarization onset (Tu et al., 2010).

Because the nonlinear polarization-mode depolarization will limit the bandwidth of the broadband coherent optical source, the most straightforward method to implement a coherent broadband source should avoid the non-birefringent DFDD-ANDiF with a guiding core of circular, hexagonal, or other types of high-order rotational symmetry (Steel et al., 2001). Rather, a certain degree of asymmetry should be intentionally introduced to the DFDD-ANDi-PCF to attain a linear modal birefringence of $>2 \times 10^{-5}$. Therefore, a PM DFDD-ANDi-PCF is one promising candidate to develop a practical coherent fiber SC laser with a highly polarized output. In addition, the smooth spectral phase of SC pulses permits simple transform-limited pulse compression based on noniterative pulse compression by applying a phase mask to theoretically quantified SCs (Tu et al., 2012).

16.3 Polarization Noise and Related Spectral Decoherence in All Normal Dispersion Fiber Supercontinuum Generation

The SC generated exclusively in the normal dispersion regime of a nonlinear fiber is widely believed to possess low optical noise and high spectral coherence (Liu et al., 2015). The DFDD-ANDi fibers have been motivated by this belief to construct a general-purpose broadband coherent optical source. However, a large short-term polarization noise is identified in this type of SC generation that has been masked by the total-intensity measurement in the past. This short-term noise will affect the generation of coherent SC. It can be easily detected by filtering the SC with a linear polarizer (Liu et al., 2015) before polarized relative intensity noise (RIN) measurements (Nishizawa & Takayanagi, 2007) [Fig. 16.2]. Also, the spectral decoherence can be measured by pulse compressibility assessment (Hooper et al., 2011; Tu et al., 2012). Importantly, the observed short-term (>1 MHz) RIN noise (Nishizawa & Takayanagi, 2007) can be discriminated against long-term (<100 Hz) instability (Domingue & Bartels, 2013), because the former corresponds to the intrinsic (quantum) broadband noise component due to input shot noise and spontaneous Raman scattering, whereas the latter corresponds to the large-amplitude noise component at low frequencies arising from technical noise (Dudley et al., 2006).

For the DFDD-ANDi fiber SC generation, the existence of the short-term polarization noise redistributes the SC pulse energy pulse-by-pulse along the slow and fast axes but conserves the total pulse energy. However, a more complex situation is encountered in the depolarized hybrid anomalous-normal dispersion (HANDi) fiber SC generation, wherein the observed noise is a mixture of the total-intensity noise and polarization noise while the total pulse energy is not conserved. The total-intensity noise is specific to the HANDi fiber SC generation and can

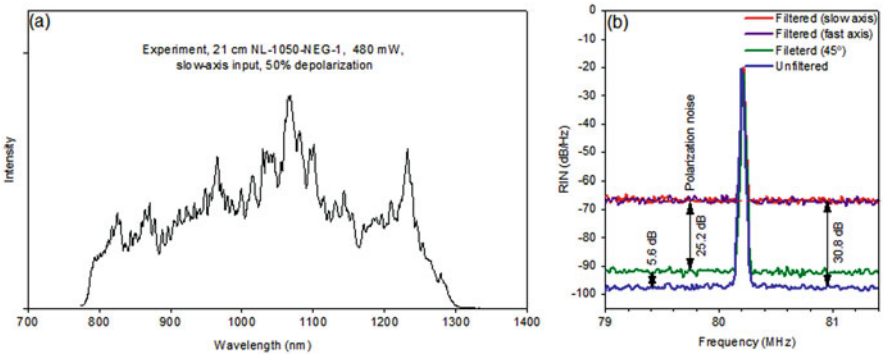

Fig. 16.2 (**a**) Spectrum of SC generation in a non-PM DFDD-ANDi-PCF. (**b**) Observed polarization noise of this SC either filtered by linear polarization or without the filtering

be simply explained through rogue-wavelike characteristics (Liu et al., 2015). Specifically, a generated SC pulse is mostly "median" so that its long-wavelength edge solitons undergo average redshifts, resulting in a normal energy loss to the pulse. This pulse-to-pulse energy fluctuation is more pronounced in a longer fiber where the disparity of the redshifts is enlarged (Dudley et al., 2008), leading to the observed buildup of total-intensity noise along the fiber.

The polarization noise may arise from the amplification of the input shot noise that distributes photons along two orthonormal polarizations, since the simulated SC generation above an output power threshold is sensitive to (instable against) the input polarization (Tu et al., 2012). Fortunately, this hidden intrinsic noise and the accompanied spectral decoherence can be effectively suppressed by using a PM ANDi fiber (Liu et al., 2015). In order to build a broadband coherent fiber SC laser, the combination of a laser with ANDi fiber SC generation from a PM fiber seems to be the optimal strategy. The coherence-disrupting total-intensity noise is avoided by the ANDi fiber SC generation free of the rogue behavior, and the coherence-disrupting polarization noise can be eliminated by the PM fiber with large intentional linear birefringence. It has been shown experimentally that the PM ANDi fiber significantly improves the coherent bandwidth (780–1300 nm) and output spectral power (~1 mW/nm) over its non-PM predecessor (Liu et al., 2015).

A later study (Gonzalo et al., 2018) employed the C-GNLSE to investigate the coherence and noise of the SC generated in a standard ANDi fiber and explained the mechanism of polarization noise in the weakly birefringent fiber pumped with femtosecond pulses. The result further verified that a well-controlled input polarization would be required for coherent SC generation from PM ANDi fibers. Also, they tested the maximum pump pulse length for low-noise SC operation in which optical wave-breaking (see below) is fully used to generate the broadest possible spectrum.

16.4 Wave-Breaking-Extended Fiber Supercontinuum Generation

Optical wave-breaking (WB) is a well-documented effect that dramatically distorts the temporal and spectral properties of a short optical pulse propagating along a normally dispersive optical fiber (Anderson et al., 1992; Rothenberg & Grischkowsky, 1989; Tomlinson et al., 1985). It can be equivalently induced by increasing the coupling power of the input pulses or the fiber length of pulse propagation (Finot et al., 2008).

Because the SPM spectral fringes are asymmetrically broadened toward the high frequency, this effect produces an optical shock that precedes WB, evidenced by the temporal oscillations immediately following the trailing edge. These oscillations reflect the interference between the short-wavelength components of the pulse, leading to the short-wavelength tail in the pulse spectrum through four-wave mixing

(Anderson et al., 1992; Rothenberg & Grischkowsky, 1989; Tomlinson et al., 1985). At elevated coupling powers, the oscillations following the trailing edge strengthen so that the short-wavelength tail develops into an intense sidelobe. By a similar mechanism, WB occurs on the steepened leading edge of the pulse to produce the long-wavelength tail in the pulse spectrum. In general, WB is responsible for the emerging spectral tail at the short- or long-wavelength end of the SC, while the self-steepening (Agrawal, 2011) is responsible for the earlier onset of the short-wavelength tail and the biased spectral extension of WB toward the high-frequency (short-wavelength) end (Liu et al., 2012).

This effect has conventionally been avoided (Anderson et al., 1993) in fiber SC-based pulse compression because the accumulated frequency chirp of the output pulse cannot be fully compensated by a standard prism (or grating) pair (Tomlinson et al., 1984, 1985). However, this limitation is not intrinsic if a 4*f* pulse shaper (Tomlinson et al., 1984) is employed to remove both the linear and nonlinear chirps of the SC pulse (Metzger et al., 2011; Tu et al., 2012; Demmler et al., 2011). When the SC is generated beyond the WB limit by using a larger input pulse energy and/or a longer fiber length (Finot et al., 2008), the spectral edges of the SPM-extended SC are further extended by WB through four-wave mixing (Anderson et al., 1992; Heidt, 2010; Heidt et al., 2011; Rothenberg & Grischkowsky, 1989; Tomlinson et al., 1985). Thus, the resulting WB-extended SC (i.e., above the WB limit) may lead to a shorter pulse at a higher compression ratio (Heidt, 2010; Heidt et al., 2011) by avoiding the limiting factor of nonlinear depolarization (Tu et al., 2012).

By using the 4*f* pulse shaper and operating under fully developed WB, a short compressed pulse width (6.4 fs) and a high compression ratio (28×) were simultaneously achieved (Liu et al., 2012), which greatly improves the performance (9.6 fs at a compression ratio of 24×) reported in a similar study operated in a WB-free regime (Tu et al., 2010, 2012). Therefore, WB is not an intrinsic barrier for high-quality pulse compression, and the SC generation beyond the WB limit is beneficial for pulse compression, with both a short pulse width and a high compression ratio. A later study (Castelló-Lurbe & Silvestre, 2015) numerically obtained coherent octave-spanning mid-infrared SC generation at telecommunication wavelengths from a silicon waveguide in a normal dispersion regime. The large spectral broadening relied on nonlinear processes beyond WB and departed from common SC produced in a solitonic regime.

16.5 Recent Progress and Application of Supercontinuum in Birefringent All Normal Fibers

By coupling pulses (1041 nm, 220 fs, 80 MHz) from a Yb:KYW laser (femtoTRAIN IC model-Z, High Q Laser) into a 21 cm custom-made PM PCF (NL-1050-NEG-PM-FUD, NKT Photonics, Mode field diameter @1064 nm: 2.2 ± 0.5 μm) along the slow axis of the fiber, Tu et al. (2016) generated a broadband SC spectrum (780–

1320 nm) that enabled high-quality multiphoton imaging of unstained biological samples. To suppress the variation of the spectrum due to environmental changes, the linear birefringence of the fiber was designed to be approximately 4.2×10^{-4}, ensuring small (<0.5%) nonlinear depolarization along the fast axis of the fiber. Throughout a 1-year test period, this spectrum and the corresponding spectral phase were reproducibly measured in daily operations. The results demonstrated reliable spectral phase stability of this source and reproducible output power and polarization without either the short-term quantum-noise instability or the long-term birefringence-induced instability. In order to compress broad-bandwidth SC pulses generated in an ANDi-PCF, Dwapanyin et al. demonstrated the improved efficiency of i^2PIE over MIIPS based on time-domain ptychography (Dwapanyin et al., 2020). In this work, a tunable femtosecond titanium-sapphire laser (Spectra-Physics Tsunami) with a 13 nm bandwidth centered at 800 nm with 12.5 nJ energy pulses (80 MHz) was used to pump an experimental PM ANDi-PCF (NL-1050-PM-NEG, NKT Photonics) to create a broadband SC spanning from 720 to 840 nm.

High peak-power coherent SC generation has been the focus for some studies. Using a low-nonlinearity fiber and pulses from a nonlinear fiber amplifier seeded by a mode-locked Yb-doped fiber oscillator, S. R. Domingue and R. A. Bartels (2015) generated 19-fs pulses centered at 1065 nm with 11.5 nJ of pulse energy (700 mW average power) based on a high-efficiency pulse shaper and a Plössl lens with up to 80% transmission efficiency. Because small-core PM nonlinear fibers (solid core and cladding) are limited in availability and have a low damage threshold, this study employed a widely available, all normal dispersion, polarization-maintaining fiber with a 10-μm core and a short fiber length (<15 cm) to minimize deleterious nonlinear effects and to eliminate fiber damage while still producing pulse bandwidths well beyond the Yb gain bandwidth limit. Anomalous dispersion fibers were not used because they limit the pulse energy to soliton numbers of ~10 (<1 nJ pulses) for coherent SC generation. By using a large mode-area fiber (PM-LMA-15, NKT Photonics, Denmark, Mode field diameter @1064 nm: 12.6 ± 1.5 μm) to avoid photodamage to the fiber itself and an industrial laser (10.2 MHz, femtoTrain, Spectra-Physics, Santa Clara, USA), You and Tu et al. (2018) generated a coherent broadband SC (865–1210 nm) with high peak power. The 1110 ± 30 nm band of the SC was selected by amplitude shaping in the pulse shaper for multiphoton imaging, and the average power of this band after the pulse shaper was able to reach 100 mW.

To expand the spectral coverage of coherent SC generation, Tarnowski et al. (2017) demonstrated a polarized all normal dispersion SC spanning beyond 2.5 μm based on 70 fs pump pulses and a birefringent silica microstructured fiber with a germanium doped core and very small air channels in the microstructured cladding. The output reached the furthest ever generated into the mid-infrared wavelengths in all normal dispersion silica fibers. This study also identified the asymmetry between propagation in both polarization axes and showed that pumping along a slow fiber axis is beneficial for a higher degree of polarization. In addition, the numerical simulations based on C-GNLSE showed good agreement with experimental spectra and addressed the long-wavelength limit of the silica all normal dispersion SC. Another study (Dobrakowski et al., 2018) used relatively sturdy silicate soft glasses

to develop a weakly birefringent (10^{-4}) PM ANDi-PCF with normal dispersion across its entire transmission window, which was compatible with 1560 nm femtosecond lasers.

A long-standing issue in coherent SC generation is the difficulty in generating a SC robustly maintained in one polarization state across its entire spectrum. Because the polarization state of SC generated in straight PCFs varies over its spectrum due to random fluctuations in weak linear birefringence, coupling between orthogonally polarized components is induced by modulational instability and the vectoral nature of soliton fission. Using a helically twisted, circularly birefringent (10^{-6}), solid-core PCF created by spinning a linearly birefringent fiber preform during the draw, Sopalla et al. (2019) experimentally generated a broadband circularly polarized SC (350–1750 nm) across its entire spectrum. The SC shared the same polarization state as the pump and showed no sign of depolarization. A numerical study of the polarization properties of the SC generated in twisted and untwisted PCFs was also carried out based on C-GNLSE, yielding results that were in good agreement with the experimental results.

The spectral coherence is intrinsically linked to polarization noise. Using the polarization-resolved vector extension of the generalized nonlinear Schrödinger equation, Feehan et al. (2020) conducted a further numerical investigation on the noise-related polarization dynamics in normal dispersion fibers and found that the pulse coherence starting from its leading edge was degraded when the influence of Raman amplification surpassed that of the coherent self-phase modulation and optical WB processes, i.e., when dispersion was high or when a long fiber or pump pulse duration was used. Moreover, this process was found to have no power threshold for a given polarization group velocity mismatch and is maximized when the weaker polarization component has a higher group velocity. In addition, the polarization noise is reduced (but not fully prevented) when the high energy component propagates along the low index axis of the fiber. This effect is different from other birefringence-dependent effects (Tu et al., 2012) which also lead to decoherence and destabilization of the polarization in ANDi SC generation (Liu et al., 2015).

16.6 Conclusion and Outlook

The development of supercontinuum generation in birefringent all normal dispersion fibers parallels its counterpart in non-birefringent and/or anomalous dispersion fibers. The underlying mechanisms have been revealed by numerous studies over the last few decades, and a relatively comprehensive understanding of the related nonlinear optical effects has been gained. Future studies are expected to balance various trade-offs in coherent supercontinuum generation, such as broad spectral coverage, high spectral coherence or low optical noise across all wavelengths, high average and/or peak power, good single-mode spatial profile of the fiber, and the

absence of long-term photodamage to the fiber. It is possible that the optimal combination of these aspects would depend on a given application (e.g., multiphoton microscopy). With more efforts on specialty fiber fabrication and laser source engineering, it is reasonable to assume that high peak-power broadband coherent supercontinuum sources will be available commercially for specific biological and biomedical applications.

Acknowledgments This work was partially supported by grants from the National Institutes of Health, US Department of Health and Human Services (R01 CA241618, R43 MH119979, and R41 GM139528 to H. Tu and S. A. Boppart).

References

Agrawal, G. P. (2001). *Nonlinear fiber optics*. Academic Press.

Agrawal, G. P. (2011). Nonlinear fiber optics: Its history and recent progress. *JOSA B, 28*(12), A1–A10.

Alfano, R. R., & Shapiro, S. L. (1970). Observation of self-phase modulation and small-scale filaments in crystals and glasses. *Physical Review Letters, 24*, 592.

Anderson, D., Desaix, M., Karlsson, M., Lisak, M., & Quiroga-Teixeiro, M. L. (1993). Wave-breaking-free pulses in nonlinear-optical fibers. *JOSA B, 10*(7), 1185–1190.

Anderson, D., Desaix, M., Lisak, M., & Quiroga-Teixeiro, M. L. (1992). Wave breaking in nonlinear-optical fibers. *JOSA B, 9*(8), 1358–1361.

Castelló-Lurbe, D., & Silvestre, E. (2015). Supercontinuum generation in silicon waveguides relying on wave-breaking. *Optics Express, 23*(20), 25462–25473.

Chow, K. K., Takushima, Y., Lin, C., Shu, C., & Bjarklev, A. (2006). Flat super-continuum generation based on normal dispersion nonlinear photonic crystal fibre. *Electronics Letters, 42*(17), 989–991.

Coen, S., Chau, A. H. L., Leonhardt, R., Harvey, J. D., Knight, J. C., Wadsworth, W. J., & Russell, P. S. J. (2002). Supercontinuum generation by stimulated Raman scattering and parametric four-wave mixing in photonic crystal fibers. *JOSA B, 19*(4), 753–764.

Demmler, S., Rothhardt, J., Heidt, A. M., Hartung, A., Rohwer, E. G., Bartelt, H., ... Tünnermann, A. (2011). Generation of high quality, 1.3 cycle pulses by active phase control of an octave spanning supercontinuum. *Optics Express, 19*(21), 20151–20158.

Dobrakowski, D., Rampur, A., Stępniewski, G., Anuszkiewicz, A., Lisowska, J., Pysz, D., ... Klimczak, M. (2018). Development of highly nonlinear polarization-maintaining fibers with normal dispersion across entire transmission window. *Journal of Optics, 21*(1), 015504.

Domingue, S. R., & Bartels, R. A. (2013). Overcoming temporal polarization instabilities from the latent birefringence in all normal dispersion, wave-breaking-extended nonlinear fiber supercontinuum generation. *Optics Express, 21*(11), 13305–13321.

Domingue, S. R., & Bartels, R. A. (2015). Nearly transform-limited sub-20-fs pulses at 1065 nm and >10 nJ enabled by a flat field ultrafast pulse shaper. *Optics Letters, 40*(2), 253–256.

Dudley, J. M., & Taylor, J. R. (2009). Ten years of nonlinear optics in photonic crystal fibre. *Nature Photonics, 3*(2), 85–90.

Dudley, J. M., Genty, G., & Coen, S. (2006). Supercontinuum generation in photonic crystal fiber. *Reviews of Modern Physics, 78*(4), 1135.

Dudley, J. M., Genty, G., & Eggleton, B. J. (2008). Harnessing and control of optical rogue waves in supercontinuum generation. *Optics Express, 16*(6), 3644–3651.

Dwapanyin, G., Spangenberg, D., Heidt, A., Feurer, T., Bosman, G., Neethling, P., & Rohwer, E. (2020). Generalized spectral phase-only time-domain ptychographic phase reconstruction applied in nonlinear microscopy. *JOSA B, 37*(11), A285–A292.

Falk, P., Frosz, M. H., & Bang, O. (2005). Supercontinuum generation in a photonic crystal fiber with two zero-dispersion wavelengths tapered to normal dispersion at all wavelengths. *Optics Express, 13*(19), 7535–7540.

Feehan, J. S., Brunetti, E., Yoffe, S., Li, W., Wiggins, S. M., Jaroszynski, D. A., & Price, J. H. (2020). Noise-related polarization dynamics for femto and picosecond pulses in normal dispersion fibers. *Optics Express, 28*(15), 21447–21463.

Finot, C., Kibler, B., Provost, L., & Wabnitz, S. (2008). Beneficial impact of wave-breaking for coherent continuum formation in normally dispersive nonlinear fibers. *JOSA B, 25*(11), 1938–1948.

Fork, R. L., Cruz, C. B., Becker, P. C., & Shank, C. V. (1987). Compression of optical pulses to six femtoseconds by using cubic phase compensation. *Optics Letters, 12*(7), 483–485.

Gonzalo, I. B., Engelsholm, R. D., Sørensen, M. P., & Bang, O. (2018). Polarization noise places severe constraints on coherence of all normal dispersion femtosecond supercontinuum generation. *Scientific Reports, 8*(1), 1–13.

Hartung, A., Heidt, A. M., & Bartelt, H. (2011). Design of all normal dispersion microstructured optical fibers for pulse-preserving supercontinuum generation. *Optics Express, 19*(8), 7742–7749.

Heidt, A. M. (2009). Efficient adaptive step size method for the simulation of supercontinuum generation in optical fibers. *Journal of Lightwave Technology, 27*(18), 3984–3991.

Heidt, A. M. (2010). Pulse preserving flat-top supercontinuum generation in all normal dispersion photonic crystal fibers. *JOSA B, 27*(3), 550–559.

Heidt, A. M., Hartung, A., Bosman, G. W., Krok, P., Rohwer, E. G., Schwoerer, H., & Bartelt, H. (2011). Coherent octave spanning near-infrared and visible supercontinuum generation in all normal dispersion photonic crystal fibers. *Optics Express, 19*(4), 3775–3787.

Hooper, L. E., Mosley, P. J., Muir, A. C., Wadsworth, W. J., & Knight, J. C. (2011). Coherent supercontinuum generation in photonic crystal fiber with all normal group velocity dispersion. *Optics Express, 19*(6), 4902–4907.

Hori, T., Nishizawa, N., Goto, T., & Yoshida, M. (2004). Experimental and numerical analysis of widely broadened supercontinuum generation in highly nonlinear dispersion-shifted fiber with a femtosecond pulse. *JOSA B, 21*(11), 1969–1980.

Hult, J. (2007). A fourth-order Runge–Kutta in the interaction picture method for simulating supercontinuum generation in optical fibers. *Journal of Lightwave Technology, 25*(12), 3770–3775.

Liu, W., Li, C., Zhang, Z., Kärtner, F. X., & Chang, G. (2016). Self-phase modulation enabled, wavelength-tunable ultrafast fiber laser sources: An energy scalable approach. *Optics Express, 24*(14), 15328–15340.

Liu, Y., Tu, H., & Boppart, S. A. (2012). Wave-breaking-extended fiber supercontinuum generation for high compression ratio transform-limited pulse compression. *Optics Letters, 37*(12), 2172–2174.

Liu, Y., Zhao, Y., Lyngsø, J., You, S., Wilson, W. L., Tu, H., & Boppart, S. A. (2015). Suppressing short-term polarization noise and related spectral decoherence in all normal dispersion fiber supercontinuum generation. *Journal of Lightwave Technology, 33*(9), 1814–1820.

Marks, D. L., & Boppart, S. A. (2004). Nonlinear interferometric vibrational imaging. *Physical Review Letters, 92*(12), 123905.

McConnell, G., & Riis, E. (2004). Ultra-short pulse compression using photonic crystal fibre. *Applied Physics B, 78*(5), 557–563.

Metzger, B., Steinmann, A., & Giessen, H. (2011). High-power widely tunable sub-20fs Gaussian laser pulses for ultrafast nonlinear spectroscopy. *Optics Express, 19*(24), 24354–24360.

Mori, K., Takara, H., Kawanishi, S., Saruwatari, M., & Morioka, T. J. E. L. (1997). Flatly broadened supercontinuum spectrum generated in a dispersion decreasing fibre with convex dispersion profile. *Electronics Letters, 33*(21), 1806–1808.

Nishizawa, N., & Takayanagi, J. (2007). Octave spanning high-quality supercontinuum generation in all-fiber system. *JOSA B, 24*(8), 1786–1792.

Ranka, J. K., Windeler, R. S., & Stentz, A. J. (2000). Visible continuum generation in air–silica microstructure optical fibers with anomalous dispersion at 800 nm. *Optics Letters, 25*(1), 25–27.

Rothenberg, J. E., & Grischkowsky, D. (1989). Observation of the formation of an optical intensity shock and wave breaking in the nonlinear propagation of pulses in optical fibers. *Physical Review Letters, 62*(5), 531.

Silberberg, Y. (2009). Quantum coherent control for nonlinear spectroscopy and microscopy. *Annual Review of Physical Chemistry, 60*, 277–292.

Sopalla, R. P., Wong, G. K., Joly, N. Y., Frosz, M. H., Jiang, X., Ahmed, G., & Russell, P. S. J. (2019). Generation of broadband circularly polarized supercontinuum light in twisted photonic crystal fibers. *Optics Letters, 44*(16), 3964–3967.

Steel, M. J., White, T. P., De Sterke, C. M., McPhedran, R. C., & Botten, L. C. (2001). Symmetry and degeneracy in microstructured optical fibers. *Optics Letters, 26*(8), 488–490.

Südmeyer, T., Brunner, F., Innerhofer, E., Paschotta, R., Furusawa, K., Baggett, J. C., … Keller, U. (2003). Nonlinear femtosecond pulse compression at high average power levels by use of a large-mode-area holey fiber. *Optics Letters, 28*(20), 1951–1953.

Tarnowski, K., Martynkien, T., Mergo, P., Poturaj, K., Anuszkiewicz, A., Béjot, P., … Urbanczyk, W. (2017). Polarized all normal dispersion supercontinuum reaching 2.5 μm generated in a birefringent microstructured silica fiber. *Optics Express, 25*(22), 27452–27463.

Tianprateep, M., Tada, J., & Kannari, F. (2005). Influence of polarization and pulse shape of femtosecond initial laser pulses on spectral broadening in microstructure fibers. *Optical Review, 12*(3), 179–189.

Tomlinson, W. J., Stolen, R. H., & Johnson, A. M. (1985). Optical wave breaking of pulses in nonlinear optical fibers. *Optics Letters, 10*(9), 457–459.

Tomlinson, W. J., Stolen, R. H., & Shank, C. V. (1984). Compression of optical pulses chirped by self-phase modulation in fibers. *JOSA B, 1*(2), 139–149.

Tse, M. L. V., Horak, P., Poletti, F., Broderick, N. G., Price, J. H., Hayes, J. R., & Richardson, D. J. (2006). Supercontinuum generation at 1.06 μm in holey fibers with dispersion flattened profiles. *Optics Express, 14*(10), 4445–4451.

Tu, H., & Boppart, S. A. (2009). Optical frequency up-conversion by supercontinuum-free widely-tunable fiber-optic Cherenkov radiation. *Optics Express, 17*(12), 9858–9872.

Tu, H., & Boppart, S. A. (2013). Coherent fiber supercontinuum for biophotonics. *Laser & Photonics Reviews, 7*(5), 628–645.

Tu, H., Liu, Y., Lægsgaard, J., Sharma, U., Siegel, M., Kopf, D., & Boppart, S. A. (2010). Scalar generalized nonlinear Schrödinger equation-quantified continuum generation in an all normal dispersion photonic crystal fiber for broadband coherent optical sources. *Optics Express, 18*(26), 27872–27884.

Tu, H., Liu, Y., Lægsgaard, J., Turchinovich, D., Siegel, M., Kopf, D., … Boppart, S. A. (2012a). Cross-validation of theoretically quantified fiber continuum generation and absolute pulse measurement by MIIPS for a broadband coherently controlled optical source. *Applied Physics B, 106*(2), 379–384.

Tu, H., Liu, Y., Liu, X., Turchinovich, D., Lægsgaard, J., & Boppart, S. A. (2012b). Nonlinear polarization dynamics in a weakly birefringent all normal dispersion photonic crystal fiber: Toward a practical coherent fiber supercontinuum laser. *Optics Express, 20*(2), 1113–1128.

Tu, H., Liu, Y., Turchinovich, D., Marjanovic, M., Lyngsø, J. K., Lægsgaard, J., … Boppart, S. A. (2016). Stain-free histopathology by programmable supercontinuum pulses. *Nature Photonics, 10*(8), 534–540.

Udem, T., Holzwarth, R., & Hänsch, T. W. (2002). Optical frequency metrology. *Nature, 416*(6877), 233–237.

Wang, H., Fleming, C. P., & Rollins, A. M. (2007). Ultrahigh-resolution optical coherence tomography at 1.15 μm using photonic crystal fiber with no zero-dispersion wavelengths. *Optics Express, 15*(6), 3085–3092.

You, S., Tu, H., Chaney, E. J., Sun, Y., Zhao, Y., Bower, A. J., & Boppart, S. A. (2018). Intravital imaging by simultaneous label-free autofluorescence-multiharmonic microscopy. *Nature Communications, 9*(1), 1–9.

Zhu, Z., & Brown, T. G. (2004). Polarization properties of supercontinuum spectra generated in birefringent photonic crystal fibers. *JOSA B, 21*(2), 249–257.

Chapter 17
Ultra-Supercontinuum Generation and Higher Harmonic Generation from Intense Ultrafast Laser Pulses in Various States of Matter

Shah Faisal Mazhar and Robert R. Alfano

Abstract In this chapter, we discuss the generation of coherent ultrawide spectral bands from DC to XUV and X-ray beams using intense femtosecond pulses in various states of matter for various applications such as microscopes. The mechanisms responsible for the ultra-supercontinuum (USC) and higher harmonic generation (HHG) arise from the temporal response of the nonlinear susceptibilities produced from the Kerr effect from various types of motion such as electron cloud distortion, molecular redistribution, ionization, plasma formation, rotation, and vibration of molecules in solids, liquids, and gases.

The slower molecular response to n_2 and n_4 from molecular and orientation motion which follows the envelope of the optical field of the laser gives rise to extreme broadening without HHG. The resulting spectra extend symmetrically on both the Stokes and anti-Stokes sides resulting in ultrawide supercontinuum from XUV on the anti-Stokes to the IR, RF, to DC on the Stokes side covering most of the electromagnetic spectrum.

The instantaneous fast response of n_2 and n_4 at the optical laser frequency of carrier-envelope phase at ω_0 results in odd HHG and spectral broadening about each harmonic on the anti-Stokes side of the pump pulse. CS_2 and the rare noble gas material are used to simulate USC and HHG spectra and compared with existing experimental spectra. The cutoff frequencies and attosecond pulse produced from HHG are explained from the fast Kerr n_2 model.

The theoretical simulations presented in this chapter on SC, USC, and HHG are generated from SPM and ESPM using the Kerr index n_2 and are compared with the existing experimental work performed and to be untaken in solids, liquids, and gases.

S. F. Mazhar (✉) · R. R. Alfano
Institute for Ultrafast Spectroscopy and Lasers, City College of New York, City University of New York, New York, NY, USA
e-mail: smazhar@gradcenter.cuny.edu; ralfano@ccny.cuny.edu

R. R. Alfano (ed.), *The Supercontinuum Laser Source*,
https://doi.org/10.1007/978-3-031-06197-4_17

Keywords Pulse envelope · Carrier-envelope phase · Self-phase modulation · Kerr effect · Nonlinear refractive index · n_2 · Spectral broadening · White-light generation · Ultra-supercontinuum · Higher harmonic generation · Femtosecond laser · Extreme intensity · Material response times · Electron cloud distortion · Ionization · Plasma formation · Molecular redistribution · Rotational motion · Vibrational motion

17.1 Introduction

Significant advances in understanding the underlying properties of materials in the fields of physics, chemistry, biology, and material sciences have been made since the development of the laser in the early 1960s. Over the years, the duration of the laser pulses became shorter initially from nanosecond to picosecond, followed by femtoseconds, and now entering the regime of attoseconds (see the Chap. 8 by Chang) and soon into the zeptosecond era and even more extremely intense beams toward 10^{22} W/m^2 as described recently by Mourou (2021). The use of these intense ultrafast laser pulses has opened a new era of optical science and nonlinear optics where phenomena of altering the frequencies of the laser sources have produced numerous light sources for a variety of applications in areas like metrology, imaging, time-resolved spectroscopy, computing, and communications.

Compared to the electrons and quasiparticles, light offers salient properties of coherence, polarization, wavefront, and wavelength. James Clark Maxwell's electromagnetic theory is based on combining fundamental laws of electricity and magnetism in 1847 which are still in use to describe electromagnetic waves. The fundamental equation describing an electromagnetic wave can be described by:

$$E(t) = \boldsymbol{E_0}(t)\, e\hat{\mathbf{c}}\mathbf{os}\ (\omega_L t - kz + \varphi(t)) \tag{17.1}$$

where the electric field envelope amplitude is $\boldsymbol{E_0(t)} = \boldsymbol{E_0} e^{-\frac{t^2}{T^2}}$, the polarization is $\hat{\mathbf{e}}$, the propagation constant is $\boldsymbol{k} = \frac{\mathbf{n}\omega_\mathbf{L}}{\mathbf{c}}$, $\boldsymbol{T}$ is the exponential time, and the pump angular frequency is denoted as $\omega_L = \omega_0$. The carrier-envelope phase (CEP) $\boldsymbol{\phi(t)}$is given by:

$$\phi(t) = \omega_L t - \frac{n\omega_L}{c} z + \varphi(t) \tag{17.2}$$

where $\varphi(t)$ is the phase offset. The intensity of the laser pulse is given by:

$$I(t) = I_0 e^{-4\ln 2 t^2/\tau_p{}^2}, \tag{17.3}$$

where $\tau_p$is the FWHM of the pulse,

$$\tau_p = T\sqrt{2\ln 2}, \tag{17.4}$$

and $\Delta\upsilon\ \tau_p = \mathbf{0.441}$ for a Gaussian beam without chirp.

The key part of the phase of $E(t)$ is the time-dependent index of refraction $n(t)$ of the materials. The Kerr index n_2 depends on several underlying mechanisms (see Shen, Y. Chap. 1 and Alfano, 1970a) arising from electronic and molecular motions (Alfano & Shapiro, 1973). The index becomes:

$$n_2 = \sum\nolimits_i n_{2i}, \tag{17.5}$$

where i arises from various motions:

$$n_{2i} = (electronic\ cloud) + (molecular\ redistribution) + (ionization) + (plasma\ formation) + (rotation) + (vibration) + \ldots. \tag{17.6}$$

These fall into temporal classes of ultrafast, fast, slow, and very slow where:

$$n_2 = n_2\,(ultrafast; \sim \mathbf{50}\ as) + n_2\left(fast; \sim \mathbf{10^{-13}}s\right) + n_2\,(slow; \sim \mathbf{1-10}\ ps) + n_2\,(very\ slow; > \mathbf{100}\ ps)\,. \tag{17.7}$$

The underlying processes associated with Kerr index n_2 can be revealed and studied in two ways: in angular frequency $n_2(\omega)$ and temporal $n_2(t)$ domains by way of Rayleigh wing light scattering $I(\omega)$ in ω space and the temporal domain from the optical Kerr effect, nonlinear optical polarization of $I(t)$, and the generation of new frequencies in conical emission. These processes are connected by Fourier transformations.

The light can be modulated in amplitude (amplitude modulation, AM) and phase (frequency modulation, FM). The electric field E(t) for the laser pulse is depicted in Fig. 17.1 for the envelope of bell shape and carrier phase in time with the offset $\varphi = \mathbf{0}$ for CEP. These two properties can give rise to modulations from the envelope and from the phase which will lead to changes in the index of refraction from Kerr processes in materials to produce spectral broadening depending on the response time of the Kerr index n_2.

James Kerr in 1875 first observed the Kerr effect using the DC electric field (Kerr, 1875) to change the index of refraction via n_2. Later in 1956, Buckingham proposed a higher frequency AC Kerr effect. He suggested an optical Kerr effect using intense polarized light traveling through an optical isotropic medium in the material, and the material becomes temporally anisotropic (Buckingham, 1956). Buckingham was limited to using the electric field of lamps which had an electric field on the order of 27.5 V/cm and suggested if only he had a high light source on the order of 10^5 W/cm^2 to produce an optical Kerr effect. Four years later, the laser appeared but was not utilized until 1969 when Duguay demonstrated optical Kerr effect using picosecond pulses in CS_2 (Duguay, 1969).

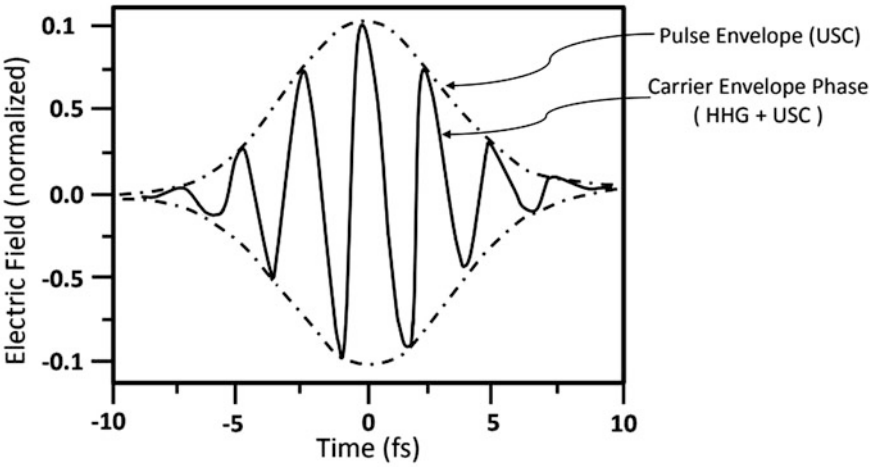

Fig. 17.1 Cosine-like electric field of light pulse from Eq. 17.1 for 5 fs for phase offset = 0. USC is generated primarily from the pulse envelope and slow n_2, and HHG and SC are primarily generated from the pulse envelope and carrier-envelope phase from the fast n_2

Buckingham extended the DC Kerr's idea to instantaneous response $n(t)$ of the Kerr index of the molecules from the applied electric field in terms of the modulating refractive index over time. He introduced the optical Kerr effect as an analog to DC and AC Kerr gate from the change in refractive index, n from E, as:

$$\boldsymbol{n = n_0 + n_2 E^2}. \tag{17.8}$$

The response time of the Kerr effect (τ_r) can be instantaneous following the optical cycles arising from the direct distortion of electron cloud response time about 50 attoseconds and from averaging the slower molecular motion $<n(t)>$ which follows the envelope of the optical field. A slower response from other mechanisms can alter the index of refraction. Here the key mechanism to give rise to the ultra-spectral broadening and higher harmonic generation (HHG) occurs from the electronic and molecular fast motions (see Eqs. 17.5, 17.6, and 17.7).

For a slow response, $\boldsymbol{n(t) = <n(t)>}$ can be taken as an average over many cycles so that $\boldsymbol{\cos^2\phi\,(t) = \frac{1}{2}}$. The response time of the materials will determine the type of modulation from the optical cycles and envelope. The index of refraction n can be altered by the temporal response of the electric field which was first introduced by Buckingham. For an ultrafast temporal response to the optical cycles of the material on the order of sub-femtoseconds, the Kerr index of refraction becomes instantaneous.

The response time of the material gives rise to the type of nonlinearity from the Kerr effect. Using a picosecond laser developed in late 1967, a major advance occurred when Duguay in 1969 realized this experimentally by extending the traditional DC/AC Kerr and theoretically proposed optical Kerr effect (Duguay,

1969) processes into the optical regime where E is the optical field on the order of about 10^7 V/cm from a 10 ps laser pulse, and it now is called the optical Kerr gate using CS_2 liquid which has a large n_2 and $n_4$with a slow optical response time of 1.8 ps from rotation and fast response of 160 fs (Kalpouzos, 1987).

Bloembergen and Shen expanded nonlinear polarization in 1964 (Bloembergen & Shen, 1964) in terms of a Taylor power series of nonlinear susceptibilities χ^n in laser electric field which is given by:

$$P = \chi^1 E + \chi^2 E^2 + \chi^3 E^3 + \chi^4 E^4 + \chi^5 E^5 + \ldots. \tag{17.9}$$

For isotropic media such as liquid, gases, glasses, and rare gas atoms, $\chi^2 = \chi^4 = 0$, where $\chi^1 \rightarrow n_0$, $\chi^2 \rightarrow n_1$, $\chi^3 \rightarrow n_2$, $\chi^5 \rightarrow n_4$. For materials at extreme laser intensity, higher order terms such as n_4 become active with n_2 for spectral broadening. Besse (2015) showed the relationship among $\chi^{(3)}$ and $\chi^{(5)}$ on n_2 and n_4 for CS_2 which are given by:

$$n_2 = \frac{3}{4}\frac{\chi^{(3)}(\omega)}{n_0{}^2 \varepsilon_0 c}, \tag{17.10}$$

$$n_4 = \frac{1}{(2n_0\varepsilon_0 c)^2}\left(\frac{5\chi^{(5)}(\omega)}{n_0} - \frac{9\left[\chi^{(3)}(\omega)\right]^2}{8n_0{}^3}\right). \tag{17.11}$$

where c is the speed of light and ε_0 is the vacuum permittivity. For CS_2, n_4 is positive for wavelengths of 532 nm and 1064 nm and negative for wavelengths of 800 nm and 920 nm due to the difference between $\chi^{(3)}$ and $\chi^{(5)}$. At $3w_L$ resonance, $(\chi^3)^2 > \chi^5$ charging sign of n_4 to be negative from Eq. 17.11.

One of the most startling and colorful nonlinear phenomena was discovered by Alfano and Shapiro in 1970 using 532 nm 5 ps ultrafast laser pulses to generate the white-light generation spanning the entire visible spectrum over 10,000 cm^{-1}. It is now called the supercontinuum. The mechanism has been attributed to self-phase modulation (SPM) and self-focusing from the Kerr index n_2 on various crystals, liquids, and glasses, including liquefied and solidified rare gases (Alfano & Shapiro, 1970a, b, c; 1972). They showed that the electronic mechanism for SPM is important in all materials and dominates all other processes in some materials, e.g., even in rare noble liquid argon and liquid and solid krypton. To fit the experimental observation of the white-light continuum, one needed sub-picosecond pulses within a 5 ps pulse. Depending on the pulse duration and the material, one can get a full conversion or partial conversion of the laser pulse on the order of 0.01 to the white-light continuum.

This chapter focuses on the simulation of the generation of two nonlinear processes based on the response time of the medium with extremely intense femtosecond laser pulses. One is the slow picosecond and fast femtosecond response following only the envelope of the laser's electric field which leads to

the supercontinuum generation without HHG, and the other is the ultrafast response following both the envelope and the carrier-envelope phase of the laser's electric field which leads to the HHG with spectral broadening around each of the harmonic. The attosecond pulses can arise from Kerr model locking, and cutoff frequencies can be determined below 500 eV to depend directly on the pump optical frequency of the intense fs laser.

The index of refraction $n(t)$ has two forms:

1. For the slow response, the index becomes:

$$\langle \boldsymbol{n} \rangle = \boldsymbol{n_0} + \frac{\mathbf{1}}{\mathbf{2}} \boldsymbol{n_2} [\boldsymbol{E_0}\,(\boldsymbol{t})]^{\mathbf{2}}, \tag{17.12}$$

which causes self-phase modulation (SPM) for slow temporal response to $E_0(t)$ – the envelope's temporal shape such as Gaussian and other symmetrical and distorted pulse shapes.

2. For the instantaneous response following the electric field envelope and the optical cycle of the phase $\boldsymbol{\phi(t)}$, the index becomes:

$$\boldsymbol{n}\,(\boldsymbol{t}) = \boldsymbol{n_0} + \boldsymbol{n_2} \left[\boldsymbol{E_0} \boldsymbol{e}^{-\frac{t^2}{T^2}} \boldsymbol{cos\phi}\,(\boldsymbol{t}) \right]^{\mathbf{2}}, \tag{17.13}$$

which causes electronic self-phase modulation (ESPM) for fast electron cloud temporal response and molecular redistribution temporal response to $E(t)$.

One of the highest n_2 materials, CS_2 liquid was selected with its large nonlinear index and fast molecular response time of 1.8 ps for rotational and 160 fs for molecular redistribution as compared to the electron cloud distortion part to demonstrate the ultra-supercontinuum broadening with an extreme laser beam with n_2 and n_4. Materials with ultrafast electronic response time are the rare gas atoms from their spherical shape in the gaseous, liquid, and solid forms and other solid materials like ZnO, MgO, GaSe, GaAs, sapphire (Al_2O_3) crystal, MgO, and MoS_2 to produce supercontinuum and HHG from ESPM. A faster-condensed matter sample is the different glasses such as silica and chalcogenides with the response time in the femtosecond scale. The underlying mechanism of the nonlinear index of refraction can arise from electronic, rotation, libration, and vibration motions. CS_2 demonstrates the largest nonlinear index from the rotation mechanism, and high index n_0. $\boldsymbol{\chi^5}$ arises for dispersion-less semiconductor media in six photon processes.

Both a slow pulse in the picosecond and a fast pulse in femtosecond following the envelope (SPM) result in total symmetrical conversion to spectral broadening from the laser from a Gaussian pulse. For example, a slow pulse of 4 ps could have a full conversion of the pulse from self-phase modulation (SPM) with a smaller spectral bandwidth of the order of a few 100 cm^{-1}. A faster pulse-like 100 fs or bursts of sub-

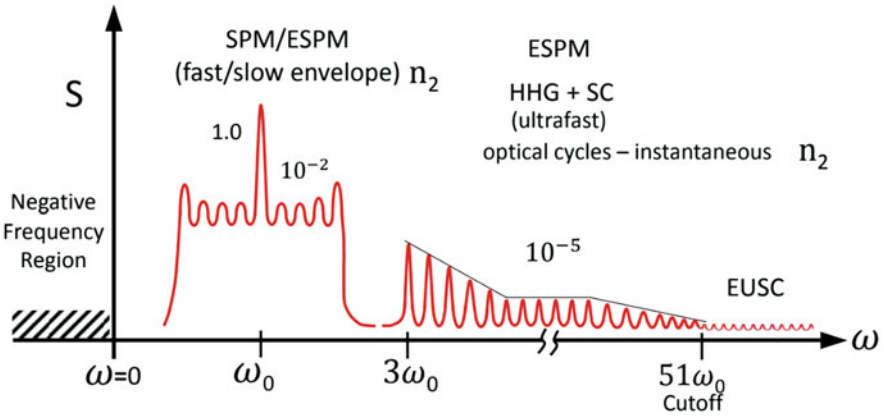

Fig. 17.2 Schematic mode for intensity of ESPM and HHG from envelope and phase of electric field $E(t)$ from temporal response to Kerr index n_2 for fs intense laser pulses

ps pulses could have a full conversion with a much wider bandwidth of 10,000 cm^{-1} for the supercontinuum. On the other hand, when the nonlinear index n(t) follows both envelope and phase from the electronic self-phase modulation (ESPM) for a fast fs pulse of 100 fs or ps pulses, the laser is not fully converted to the continuum by about a factor of 10^{-2}. The spectrum shows a large laser spike at ω_0 with a lower supercontinuum about 10^{-2} conversion efficiency surrounding the laser beam followed by the generation of higher harmonics about 10^{-5} conversion efficiency (see Fig. 17.2).

The conversion to HHG is presented by Comby (2019) for HHG in argon gas where they showed for a 50 W pulses at 1030 nm with 135 fs pulse duration from ytterbium-doped fiber amplifiers (YDFA), and the HHG conversion efficiency ranged from about 10^{-8} from the pump laser resulting 0.5 μW of HHG (see Fig. 17.5 from Comby, 2019) and higher conversion for the third harmonic of 1030 nm for 10^{-4} conversion efficiency up to a few mW of HHG. For plasma generation from n_2 mechanism, the broadening is not symmetrical having more anti-Stokes from the ionization process (Bloembergen, 1973).

$$\text{ESPM} \rightarrow n(t) \rightarrow \text{HHG} + \text{SC}, \text{ where } n(t) \text{ is instantaneous index of refraction.}$$

$$\text{SPM} \rightarrow < n(t) > \rightarrow \text{SC} + \text{USC}, \text{ where } < n(t) > \text{ is the average index of refraction over several optical cycle.}$$

17.2 Details on USC and HHG from SPM and ESPM

The remaining part of this chapter will describe the spectral broadening and HHG based on the response time of the nonlinear index of refraction given by Eqs. 17.12 and 17.13.

We have divided this section into two parts: **part 1** describes SPM from the envelope producing extreme spectral broadening called the ultra-supercontinuum (USC), and **part 2** describes ESPM from both carrier phase and envelope which results in higher harmonic generation (HHG).

17.2.1 Part 1: Ultra-Supercontinuum (USC) from the Average Response of the n_2

In part 1, we discuss the spectral broadening caused by the slow response to the envelope at extreme intensities which will include both the first nonlinear index n_2 followed by the additional term caused by higher intensity to activate the effect of n_4.

The outcome of the spectral broadening from the envelope due to n_2 and n_4 causes ultra-spectral broadening which can span the entire electromagnetic spectrum from X-rays, XUV, UV, visible, and NIR to THz with electronic and vibrational spectral lines from gases and condensed matter. The Kerr nonlinear index of refraction in the slow varying approximation (SVA) for the envelope of the ps and fs laser pulses arises from n_2I and n_4I^2 at extremely high laser pulse intensity $\geq 2\times10^{14}$ W/m^2 to produce ultra-supercontinuum (USC). For a Gaussian beam, SPM is symmetrical to the laser frequency which will be simulated, discussed, and analyzed in a later section (see Figs. 17.3, 17.4, 17.5, 17.6, 17.7, and 17.8).

The spectral broadening caused by the average index of refraction $<n(t)>$ following the envelope of the electric field including n_2 and n_4 reveals the ultra-supercontinuum without HHG. The average refractive index follows the slowly varying envelope including n_2 and n_4 part where the index of refraction is averaged over many optical cycles and becomes:

$$< n\,(t) >= n_0 + n_2 I + n_4 I^2, \tag{17.14}$$

where $I = E_0(t)^2$ which follows the envelope to produce ultra-super broadening. The phase from Eq. 17.2 becomes:

$$\phi\,(t) = \omega_L t - \frac{\left(n_0 + n_2 I + n_4 I^2\right)\omega_L}{c} z, \tag{17.15}$$

which becomes modulated by its own light intensity $I(t)$ via n_2 and n_4. The new frequency is:

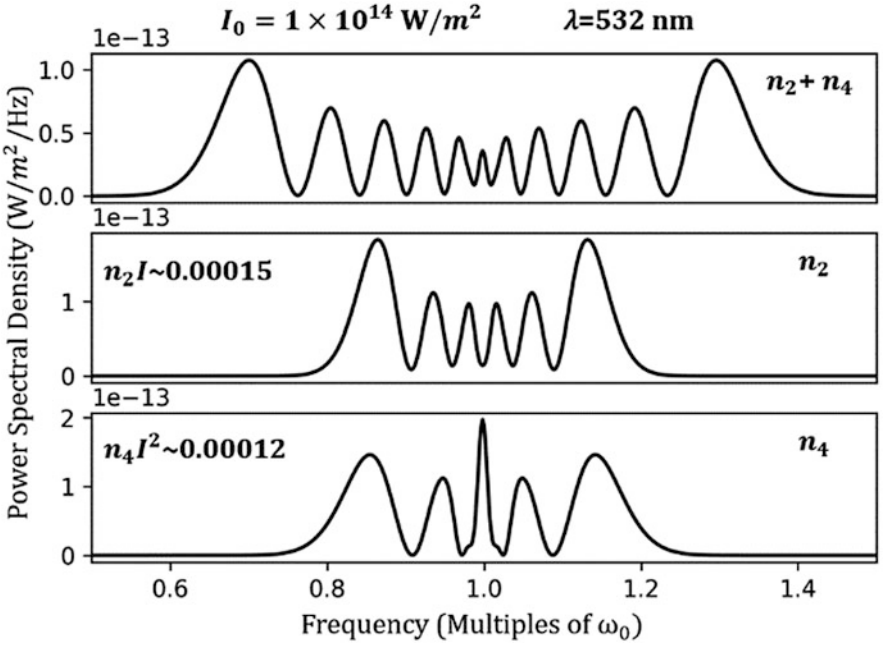

Fig. 17.3 CS_2 spectrum of SPM at $I_0 = 1 \times 10^{14}$ W/m^2 with central wavelength at 532 nm

$$\boldsymbol{\Omega}(t) = \frac{d\boldsymbol{\phi}(\mathbf{t})}{dt} = \boldsymbol{\omega}_{\mathbf{L}} - \left(\mathbf{0} + \mathbf{n_2}\frac{dI}{dt} + \mathbf{n_4}\frac{dI^2}{dt}\right)\frac{\boldsymbol{\omega}_{\mathbf{L}} z}{\mathbf{c}}. \tag{17.16}$$

The outgoing electric field becomes modulated as:

$$\boldsymbol{E}(t) = \boldsymbol{E_0} e^{-\frac{t^2}{T^2}} e^{-i\left(\omega_L t - \frac{<n(t)>\omega_L}{c} z\right)} + \boldsymbol{c.c.} \tag{17.17}$$

To produce SPM induced spectra via n_2 and n_4, Eqs. 17.14 and 17.15 are used and using fast Fourier transform (FFT) of $E(t)$ (into Eq. 17.17) are transformed to obtain $E(\omega)$ and power spectra $\boldsymbol{S}(\boldsymbol{\omega}) = \frac{c}{4\pi}|\boldsymbol{E}(\boldsymbol{\omega})|^2$.

The simulated ultra-supercontinuum (USC) spectra from the envelope approximation are shown in Figs. 17.3, 17.4, 17.5, and 17.6 for intensities from 10^{14} to 10^{15} W/m^2, n_2, and n_4 for CS_2. The SPM spectra are simulated using the laser beam of 532 nm for 50 fs pulse where $n_0 = 1.64$, $n_2 = 1.5 \times 10^{-18}$ m^2/W, and $n_4 = 1.2 \times 10^{-32}$ m^4/W^2 traveling through $z = 1$ cm distance of CS_2 in Figs. 17.3 and 17.4 with the different initial intensity of $I_0 = 1 \times 10^{14}$ W/m^2 (see Fig. 17.3) and $I_0 = 2 \times 10^{15}$ W/m^2 (see Fig. 17.4). Each graph of Figs. 17.3, 17.4, 17.5, and 17.6 shows the SPM spectrum with the combined combination of n_2 and n_4 at the top, contribution of the only n_2 at the middle, and contribution of the only n_4 at the

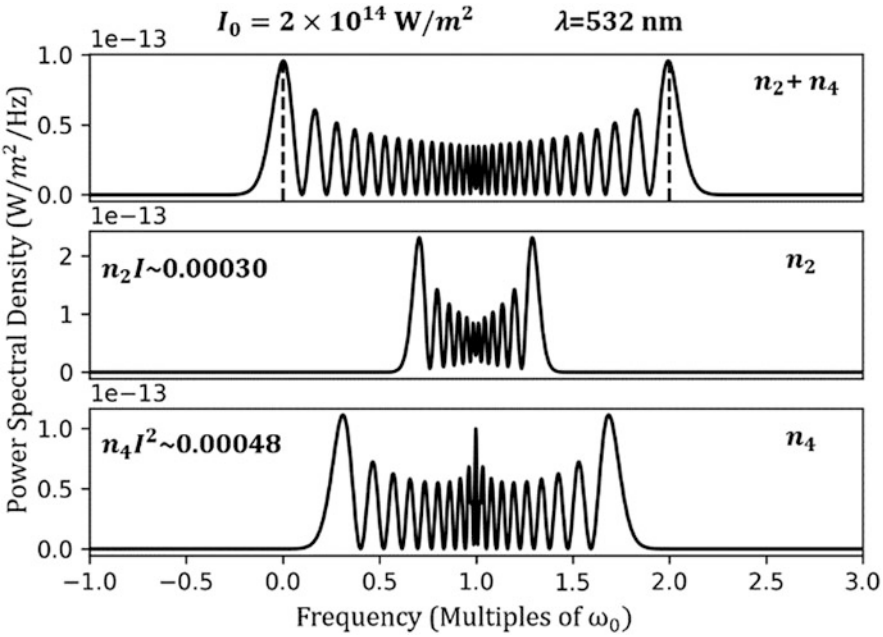

Fig. 17.4 CS_2 spectrum of SPM at $I_0 = 2 \times 10^{14}$ W/m^2 with central wavelength at 532 nm

bottom. The frequencies in Figs. 17.3, 17.4, 17.5, 17.6, 17.7 and 17.8 are presented as the multiples of the initial frequency (ω_0) as $\frac{\omega}{\omega_0}$.

Figure 17.3 shows symmetrical and completely converted spectral broadening around ω_0 for the Stokes and anti-Stokes frequencies going from $0.6\omega_0$ to $1.4\omega_0$ for the intensity of 10^{14} W/m^2. The salient spectral feature displayed in Fig. 17.4 shows the frequency extends from $2\omega_0$ to 0 for higher intensity of 2×10^{14} W/m^2 spanning from DC to $2\omega_0$. For higher intensity, the spectrum extends to the negative frequencies which are discussed in detail by Alfano et al. (2022).

The nonlinear refractive index n_4 becomes negative in CS_2 at 800 nm due to the χ^3 resonance. Kong (2009) experimentally measured $n_2 = 2.1 \times 10^{-19}$ m^2/W and $n_4 = -2 \times 10^{-35}$ m^4/W^2 for 800 nm at the intensity $I_0 = 1.36 \times 10^{15}$ W/m^2 (or 1.36 GW/cm^{-2}). To demonstrate the effect of the negative refractive index of SC, a spectrum is produced using Kong's measurements (see Fig. 17.5), and another spectrum is produced for 532 nm at $I_0 = 2 \times 10^{14}$ W/m^2 with the negative n_4 (see Fig. 17.6) to compare with the effect of positive n_4 in Fig. 17.3. From Besse (2015), n_4 is positive at 532 nm and 1064 nm and negative at 800 nm due to the χ^3 resonance. The negative n_4 refractive index in both Figs. 17.5 and 17.6 shows the interference between the positive n_2 and the negative n_4. Because of the interference, the combined SPM spectrum span becomes much smaller than the other spectra. At 800 nm, the contribution of the negative n_4 is much smaller and affects much less on the contribution of n_2 to produce the whole SPM spectrum (see Fig. 17.5). To see

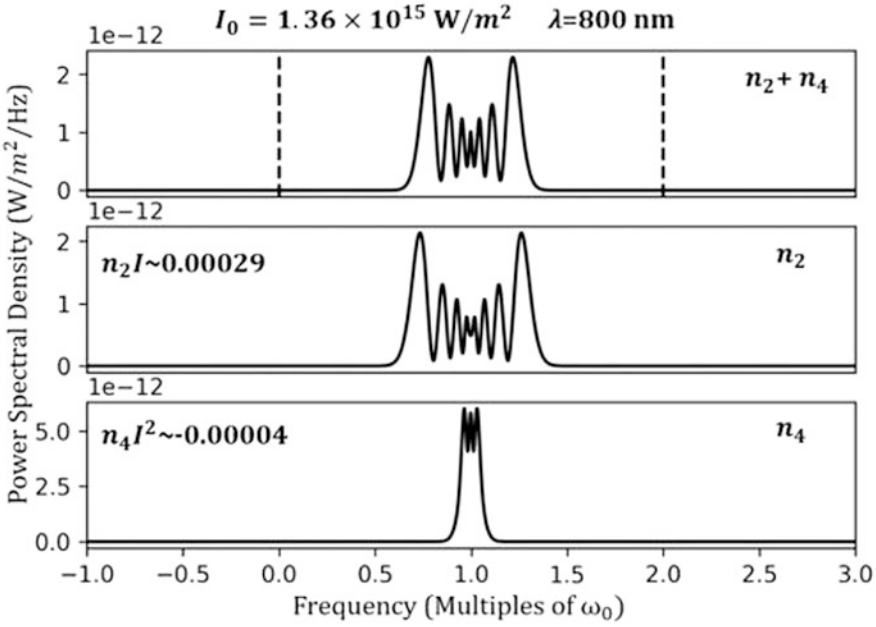

Fig. 17.5 CS_2 spectrum of SPM at $I_0 = 1.36 \times 10^{15}$ W/m^2 with central wavelength at 800 nm (with negative n_4)

the side-by-side comparison, an imaginary spectrum is produced assuming the n_4 is negative at 532 nm while keeping all values the same (see Fig. 17.6). The negative n_4 produces the interference with the positive n_2 and produces a much smaller SPM spectrum compared to the counterpart (see Fig. 17.4).

As the pump intensity I_0 becomes larger, the contribution of the nonlinear index from n_4 ($n_4|I_0|^2$ ~ 0.012 for $I_0 = 1 \times 10^{15}$ W/m^2) becomes larger than $n_2 I_0$ term, and n_4 term dominates on the production of the SPM (see Figs. 17.3 and 17.4 top and bottom). For higher intensities such as in Figs. 17.7 and 17.8, the SPM structure goes beyond $2\omega_0$ resulting in an enhanced broadening that can be described as the "enhanced ultra-supercontinuum" (EUSC). Figure 17.7 stimulated SC extends from zero direct current (DC) region – near zero to 50 eV into extreme ultraviolet (EUV). It is possible to enter the X-ray and Gama regions with higher intensities on order 10^{21} W/m^2 (with a laser beam of 5 mJ with 50 fs at 1KHz repetition rate to spot size of 10 μm to about 10^{17} W/cm^2). The electronic resonances do not affect the frequency broadening, but the absorptions curve holes in the spectrum (Alfano, 1974). More extensive simulations are given in the recent study on ultra-supercontinuum and enhanced ultra-supercontinuum by Alfano (2022).

Figures 17.7 and 17.8 show the energy of the photons showing the positive frequency portion of SC frequency extending from the DC region at $\omega_0 = 0$ to extreme ultraviolet (EUV) region (1–100 nm) covering most of EM spectrum. For $I_0 = 1 \times 10^{15}$ W/m^2 (see Fig. 17.7), the USC extends up to 25 nm/49.6 eV (~20

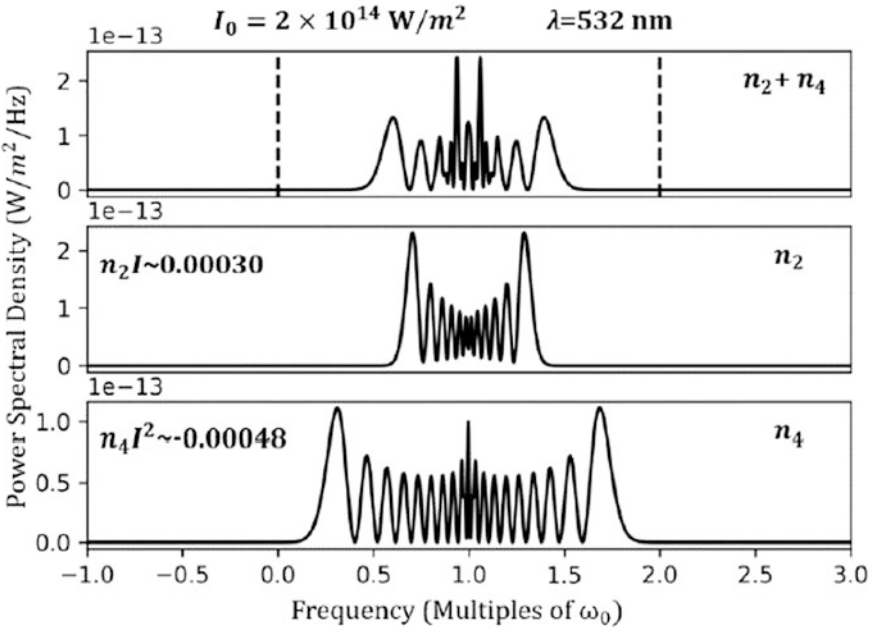

Fig. 17.6 CS_2 spectrum of SPM at $I_0 = 2 \times 10^{14}$ W/m^2 with central wavelength at 532 nm (with negative n_4)

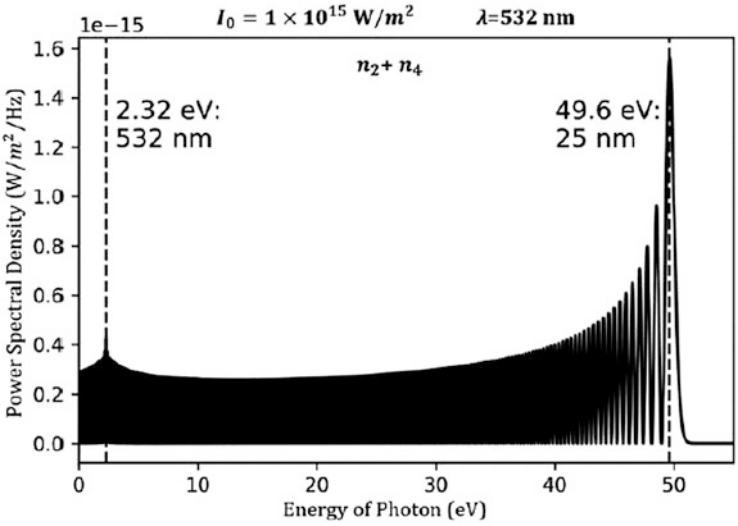

Fig. 17.7 CS_2 spectrum of SPM in terms of photon energy in eV from DC frequency to EUV at $I_0 = 1 \times 10^{15}$ W/m^2 with central wavelength at 532 nm

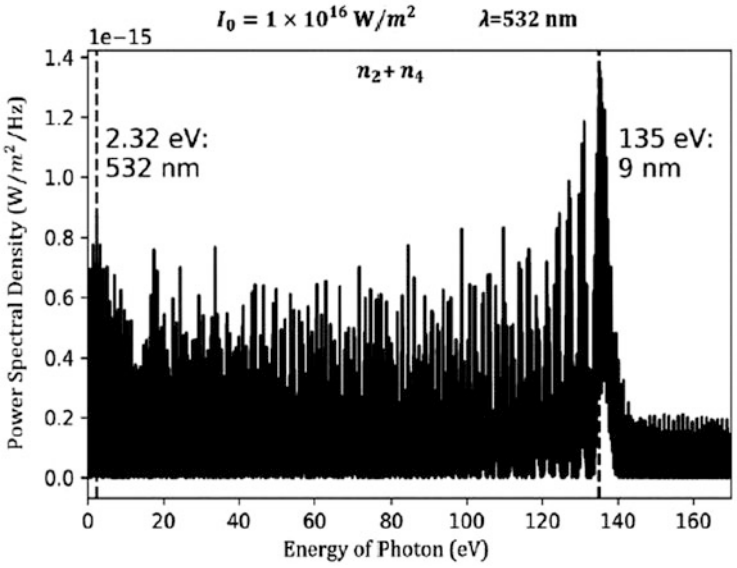

Fig. 17.8 CS_2 spectrum of SPM in terms of photon energy in eV from DC frequency to EUV at $I_0 = 1 \times 10^{16}$ W/m^2 with central wavelength at 532 nm

ω_0). A very interesting USC spectrum can be observed when the effect of n_4 comes close to n_0 (1.2 ~ 1.4) for higher intensity, $I_0 = 1 \times 10^{16}$ W/m^2 (see Fig. 17.8). For such spectrum, the EUSC extends up to 9 nm/135 eV (~ 60 ω_0), and after a 9 nm peak, a trail of low-intensity peaks continues beyond 2000 eV into the soft X-ray region. These low-intensity peaks might be hard to detect by the detector while detecting EUSC peaks. Such EUSC generation up to the EUV is both predicted in helium atoms and observed in argon atoms.

17.2.2 Part 2: Higher Harmonic Generation (HHG) and Supercontinuum (SC) Due to the Instantaneous Response of the n_2

In part 2, we will discuss HHG with spectral broadening caused by the instantaneous response to the phase and the envelope at extreme intensities arising from ESPM in which we included only n_2. In this part, we simulate the spectra and compare them with experimental data using the ansatz in which the index of refraction n(t) follows the instantaneous temporal response of the nonlinear index from both the optical phase and the envelope which causes HHG and spectral broadening. In this model, the simulated HHG shows the characteristic fingerprints (decreasing harmonics generation followed by a plateau to descending HHG signals

to the cutoff frequency using the method of the stationary phase on ESPM) of HHG observed experimentally and is driven coherently by the primary laser beam.

Over the past 29 years, there has been extensive experimental observation, from pioneers like Corkum (1993) and others, on generating the odd harmonics spectra into the XUV and the production of attosecond pulse from rare gases using extreme ultrafast laser beams. Theoretical models have been explained based on the three-step semiclassical and quantum-mechanical theoretical model (Lewenstein, 1994). Not to be too critical, this model relies on tunneling, acceleration, and return to the parent ion in the generation of HHG. As stated by Prof. Kjeld Eikema from Witte at ARCNL, Advanced Research Center for Nanolithography (ARCNL) focuses on fundamental physics and chemistry (Johnson, 2022) "despite the brutal process where an electron is 'ripped off' an atom and then slammed back to generate new light. Because the whole process is tightly linked to the phase of the fundamental wave, both spatially and temporally, you get really nice laser-like beams out of it, and incredible timing precision of the generated new electromagnetic waves. It's really a wonderful tool that enables things like precision spectroscopy, attosecond science, and imaging at extreme-ultraviolet wavelengths" (Johnson, 2022). The HHG produced attosecond pulse has been used for the applications like probing, and the notion of generating attosecond pulses using Fourier synthesis has been speculated by implementing high harmonic generation to mimic the mode-locked laser mechanism.

We introduce an ansatz that the index n follows the optical cycle of the phase, not the envelope (Alfano, 2021). This electronic self-phase modulation (ESPM) model (Alfano, 1970a, 1972, 2022) is more fundamental than the slow varying envelope approximation (SVEA) of nonlinear approximation and nonlinear Schrödinger equation (NLSE) from Maxwell equation where the envelope is followed. These approximations break down for electron cloud response of n_2 where the response time is to the carrier-envelope phase (CEP) on the optical cycle response. We have extended the pioneering research of John Kerr (1875) and Buckingham (1956) on the traditional DC and AC electronic voltage switching device to modulate and alter the polarization of light based on the rapid response of organic liquids to the applied electric field E to pair of electrodes. The original Kerr gates are based on the index of refraction that becomes electric field E dependent:

$$\boldsymbol{n}\,(\boldsymbol{t}) = \boldsymbol{n_0} + \boldsymbol{n_2}\{\boldsymbol{E}\,(\boldsymbol{t})\}^{\mathbf{2}}, \tag{17.18}$$

where n_0 is the index of refraction, n_2 is the nonlinear index, and E is the electric field (can be DC or AC). The index of refraction n arises from the underlying electronic state transition from among all states available from virtual and real as per quantum processes. So, the ansatz assumption given for n and nonlinear counterpart is more fundamental than that derived from a wave equation approximation.

In the Kerr effect, the material behaves optically as though it were a uniaxial crystal in which the electric field of the laser acts as an optic axis. The major mechanisms responsible for inducing birefringence can arise from distortion of electron clouds, rotations of molecules, and disturbance of molecular motion. The optical Kerr gate has been used extensively as an ultrafast optical gate. While propagating, an intense optical pulse changes the index of refraction by causing

the direct distortion of the electron cloud and the molecular motion. The change in index leads to spectral broadening from self-phase modulation (SPM).

The electronic distortion mechanism (Alfano & Shapiro, 1970a) arises from quantum transitions and is present in all condensed and gas material, a fact consistent with the experimental observation of SPM spectra in all samples studied under intense ultrafast laser excitation.

Two main theories were expounded to explain the HHG process: a complex phenomenological nonmathematical explanation for high ultrafast pulse interaction proposed by Corkum (1993) first followed by many other semiclassically by a three-step model and a quantum-mechanically Schrodinger dipole E.r approximation approach by Lewenstein (1994). The cutoff energy of HHG was related to $I_P + 3U_P$, the ionization (I_P), and potential (U_P) energy to remove electrons for a single electron model. This model has been explained as follows: ionization of electron, the high-intensity laser field (10^{14} to 10^{16} W/cm^2); the electron tunnels through the electric potential barrier; acceleration of the free electron, the free electron generated by tunneling with a zero initial velocity is accelerated away from the parent ion by the driven field; then finally, the electron is driven back to the parent ion. These explain the three regions of odd high harmonics (HH): decreasing harmonics, plateau, and cutoff. However, this process lacks basic physical insight for new materials, and a better mathematical and theoretical explanation is needed. So, the ansatz based on the ESPM model was developed from a nonlinear index arising from intense ultrafast E-field, and this index responds to the optical cycles of the carrier-envelope phase (CEP). Such instantaneous response is quantum-mechanical because n_2 for noble gases responds from the electron cloud, which is faster than 150 attoseconds, the Bohr orbital time to about 30 attoseconds.

An alternative ansatz theoretical model to Lewenstein's is presented in support of the ESPM direct-electron cloud distortion model of SPM for n_2 from χ^3 to give rise to odd HH. The HHG modes generation leads to locking in-phase of these N modes to generate attosecond pulses by Kerr mode-locking in rare noble gas atoms, like argon (Ar), krypton (Kr), nitrogen (N_2), and oxygen (O_2) in gaseous, liquid, and condensed states of matter. These materials can be placed in a hollow microfiber to enhance the interaction length.

After an intense light beam propagates a distance z into the material, the electric field is distorted in the CEP and has the form:

$$\boldsymbol{E}(t) = \boldsymbol{E_0} e^{-\frac{t^2}{T^2}} \cos[\boldsymbol{\phi}(t)], \tag{17.19}$$

where $T = \frac{\tau_p}{\sqrt{2ln2}}$, τ_p is the full width half maximum (FWHM) of the pulse, and the modulated instantaneous phase of CEP under the envelope is given by:

$$\boldsymbol{\phi}(t) = \boldsymbol{\omega_0}\left\{t - \frac{\boldsymbol{n}(t)\, z}{\boldsymbol{c}}\right\} + \boldsymbol{\varphi}, \tag{17.20}$$

where ω_0 is the central angular frequency of the laser, $n(t)$ is the refractive index, z is the propagating distance, and φ is the offset phase. The offset CEP phase is set to be zero for the cosine-like pulse which drives HHG modes. Following Alfano (1970a, 1972) and Buckingham (1956) without averaging over cycles, the general form for the Kerr effect (Eq. 17.18) is given by the nonlinear refractive index with quadratic field dependence and the response time τ which is:

$$n(t) = n_0 + \int_{-\infty}^{t}\int_{-\infty}^{t} f\left(t', t''\right) E\left(t - t'\right) E\left(t - t''\right) dt' dt'', \tag{17.21}$$

where n_0 is the ordinary index, E the electric field and,

$$f\left(t', t''\right) = \left(\frac{n_2}{\tau}\right) e^{-\frac{t'}{\tau}}\, \delta\left(t - t''\right), \tag{17.22}$$

where n_2 is the nonlinear index. Equation 17.21 may be simplified to:

$$n(t) = n_0 + \left(\frac{n_2}{\tau}\right) \int_{-\infty}^{t} e^{-\frac{(t-t')}{\tau}} E^2\left(t'\right) dt'. \tag{17.23}$$

The pure electronic mechanism of n_2 for rare noble gases like Ar, Kr, and Ne involves no translation of nuclei or rotation of atomic cluster and is expected to have relaxation response time much less than the optical period ($<< \frac{1}{\omega_0}$), faster than 150 attoseconds on the order of zeptosecond scale. For this case, the index $n(t)$ responses to $E(t)$ at optical frequencies. Hence the weighting function $(\frac{1}{\tau})e^{-\frac{(t-t')}{\tau}}$ may be replaced by $\delta(t - t')$. Following Eq. 17.18 for the Kerr effect, the electronic response of the nonlinear index becomes:

$$n(t) = n_0 + n_2\left[E_0 e^{-\frac{t^2}{T^2}} cos\phi\,(t)\right]^2, \tag{17.24}$$

which represents the instantaneous response of the index of refraction. Equation 17.24 is the ansatz that has been used before in the form of n by luminaries like Kerr and Buckingham. The ansatz $n(t)$ follows the modulation optical cycles of the phase of E. The instantaneous response is used to follow the optical cycle rather than the envelope of the CEP without time averaging.

This ansatz is a good assumption since the outcome as shown in the electronic SPM leads to experimentally observed three regimes of HHG, and cutoff frequency can be calculated based on this ansatz using the method of stationary phase for noble rare molecules like argon and krypton. The fact that n follows the optical cycle of the phase, not the envelope, is more fundamental than slow varying envelope approximation (SVEA) of nonlinear approximation and nonlinear Schrödinger equation NLSE from Maxwell equation where the envelope is followed. These

approximations break down for electronic response of n_2 where the response to optical cycle modulation.

Substituting Eq. 17.24 into Eqs. 17.19 and 17.20, the electric field $E(t)$ becomes electronic self-phase modulated at z and is given by:

$$\boldsymbol{E}(t) = \boldsymbol{E_0} e^{-\frac{t^2}{T^2}} \cos\left[\omega_0\left(t - \frac{n_0 z}{c}\right) - \beta e^{-\frac{2t^2}{T^2}} \cos^2\left(\omega_0\left(t - \frac{n_0 z}{c}\right)\right)\right], \tag{17.25}$$

where $\beta = n_2 {E_0}^2 \left(\frac{\omega_0 z}{c}\right)$. From Eq. 17.25, $E(t)$ results in Bessel function expansion resulting in odd harmonics and spectral broadening. In addition, from Eq. 17.25, the electronic self-phase modulated spectral $E(\omega)$ is obtained by the fast Fourier transform (FFT) technique resulting in odd harmonics from the cosine of a cosine squared function. The spectral density of the phase-modulated light is:

$$\boldsymbol{S}(\omega) = \frac{c}{4\pi} |\boldsymbol{E}(\omega)|^2, \tag{17.26}$$

where $E(\omega)$ is the Fourier transform of $E(t)$ which is shown in Figs. 17.9 and 17.10 showing the three characteristic features of the odd HHG with the cutoff frequency.

Figures 17.9 and 17.10 show the spectral amplitude vs. wavenumber with the higher harmonic modes and the first HHG mode for different pulse energies, respectively. The spectra consist of a set of odd higher harmonics, and each of them is broadened because of the self-phase modulation of each harmonic. The outcome from ESPM is a supercontinuum background superimposed with the sharp HHG which was experimentally observed.

Figure 17.10 shows HHG after doubling the incident beam energy of Fig. 17.9. The same result can be achieved by doubling the propagation distance as well. The electronic SPM n_2 model shows the three regions observed in HHG. Both figures show the same HHG structure of three phases with the plateau and cutoff regions like that has been experimentally observed in solid argon, krypton, and others.

A self-phase modulation about ω_0 is shown in Figs. 17.9 and 17.10 for a 500 nm, 80 fs input beam with the pulse energy of 6.5 mJ and 13 mJ, respectively, with a beam radius of 20 μm. The spectra calculated for argon ($n_0 = 1$ and $n_2 = 2.5 \times 10^{-19}$ cm^2/W) from Eqs. 17.25 and 17.26 show odd harmonic peaks up to N (see Figs. 17.9 and 17.10) arising from electronic self-phase n_2. The N harmonic peaks are separated by $2\omega_0$.

17.2.2.1 Attosecond Pulses from HHG from Kerr Mode-Locking

These N HHG pulses can be coherently driven by an optical pump field via the Kerr effect by an aperture. Several odd N for the Fourier transform bandwidth pulse τ_p from a 500 nm and 50 fs beam gives more than 31 HH peaks (see Figs. 17.9 and 17.10). These odd HHG appears like a mode-locked laser train except the modes are

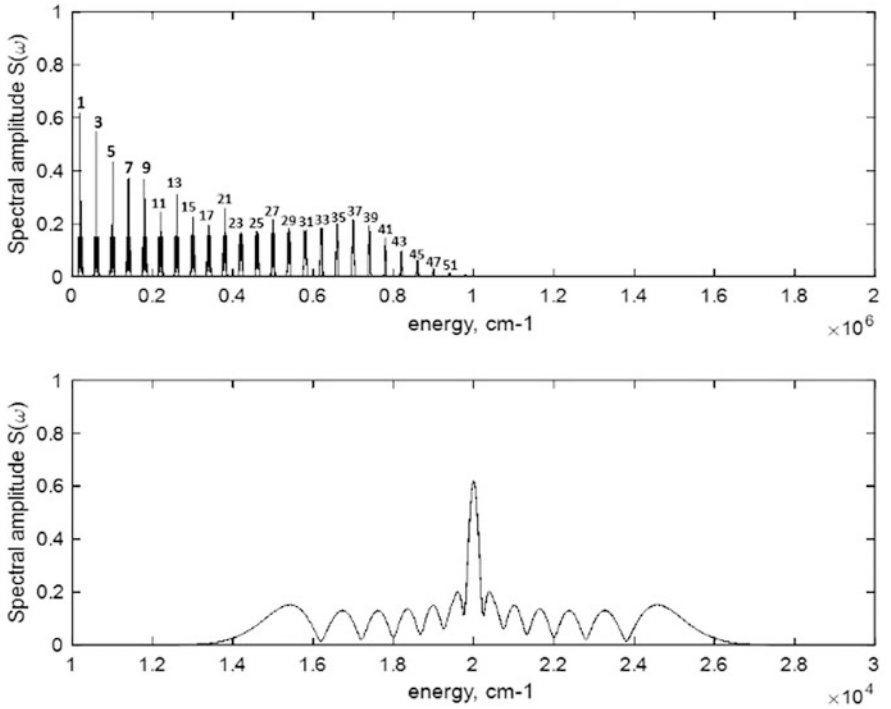

Fig. 17.9 Spectral amplitudes of electric filed after propagation of 6.5 mJ pulse through 0.5 mm thickness of argon gas. The bottom plot shows the spectral amplitude of the first harmonics (zoomed area of the upper plot)

not separated by $\frac{c}{2L}$ but by $2\omega_0$ and using the relation:

$$\boldsymbol{E}\,(\boldsymbol{\omega}) = \sum_{\boldsymbol{n=0}}^{\boldsymbol{N}} \boldsymbol{\delta}\,(\boldsymbol{\omega} - \boldsymbol{\omega_{2n+1}})\, \boldsymbol{e}^{-\boldsymbol{i}\,(\boldsymbol{\omega_{2n+1}}\boldsymbol{t}+\boldsymbol{\phi})}; \tag{17.27}$$

summing over odd n from 1 to N, where ϕ is an arbitrary number. The Kerr mode-locking occurs from these deltas like HHG peak which is driven by an intense laser pulse. The phases are locked by the Kerr index n_2 with the aperture and/or beam confinement to give attosecond pulse from the transform limited of Gaussian relation:

$$\boldsymbol{\tau}_{\boldsymbol{p}} = \frac{\mathbf{0.4}}{\boldsymbol{N}\,(\mathbf{2}\boldsymbol{\omega_0})}, \tag{17.28}$$

for N = 31 coupled modes driven by the intense pump beam, and the Kerr mode-locking from n_2 gives τ_p of 20 attoseconds.

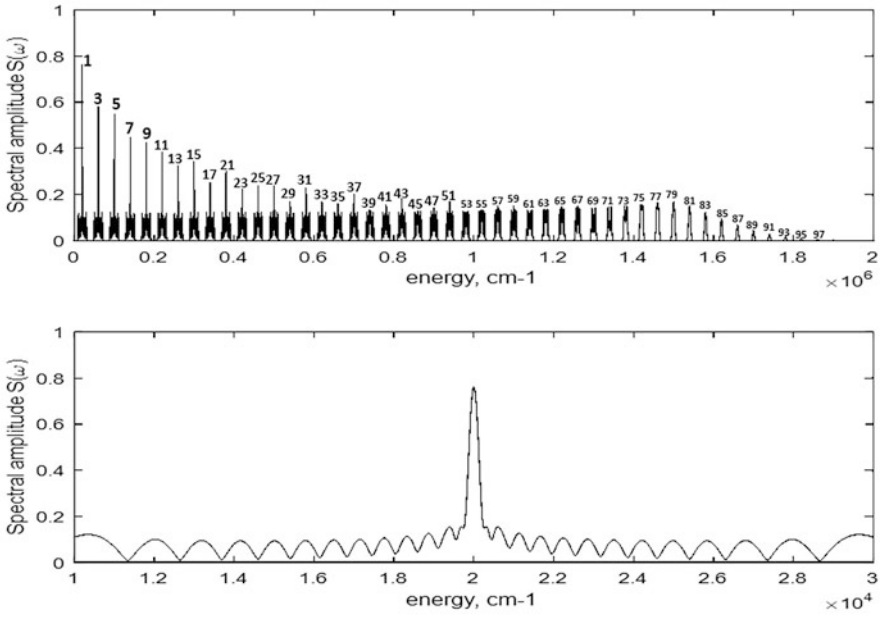

Fig. 17.10 Spectral amplitudes of electric filed after propagation of 13 mJ pulse through 0.5 mm thickness of argon gas. The bottom plot shows the spectral amplitude of the first harmonics (zoomed area of the upper plot). The same plot can be obtained with a pulse energy of 6.5 mJ and double propagation distance (1 mm)

In the case of the rare gas molecule that possesses spherical symmetry, a pure electronic mechanism for the nonlinear index n_2 involves no translation of nuclei, libration, or rotation of atomic clusters and is expected to have a relaxation time much less than the optical period. Buckingham and coworkers elaborate on induced dipole moment from nonlinear hyperpolarization arising from electronic distortion of the inert atom which occurs from intense electric fields.

Figure 17.11 shows the fifth harmonic pattern like Figs. 17.9 and 17.10. Compared to the first harmonic, the central frequency of the fifth harmonic has almost one-fourth of the intensity. Although both have a similar spectral SPM broad sideband structure with spectral oscillations about the fifth harmonic, these spectral patterns about HH should be observed as the fingerprint of electronic n_2 SPM.

We give an example of the HHG in different materials supporting the ESPM model. Figure 17.12 compares the simulated plots of S(ω) using Eqs. 17.25 and 17.26 for HHG in solid argon and krypton with experimental values using adjustable parameters. Figure 17.12 shows the comparison between the experimental result of HHG found by Ndabashimiye's group (2016; see Fig. 17.12a) and the theoretical spectrum obtained from the ESPM model for solid argon (Ar) (see Fig. 17.12b) and solid krypton (Kr) (see Fig. 17.12c) using the same parameters. Only the intensity is optimized to fit the theoretical spectrum with the experimental result. Figure 17.12

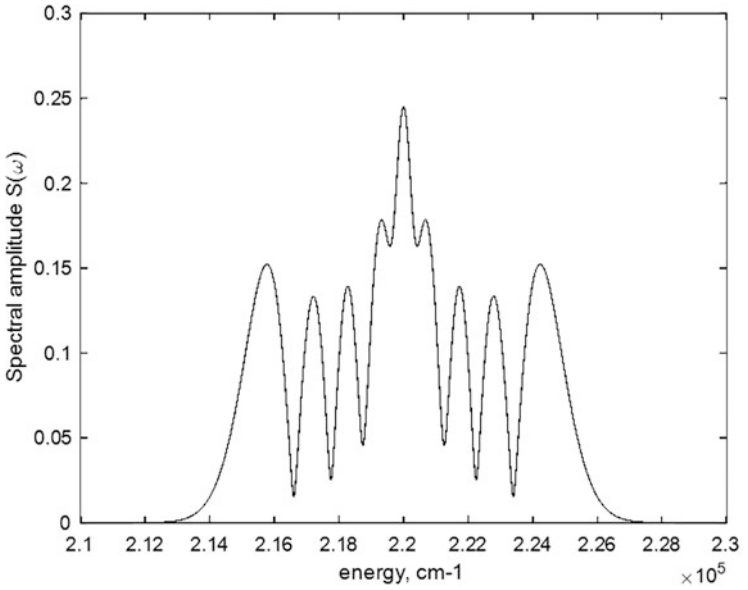

Fig. 17.11 Spectral amplitude of fifth harmonic ($\omega = 11\omega_0$)

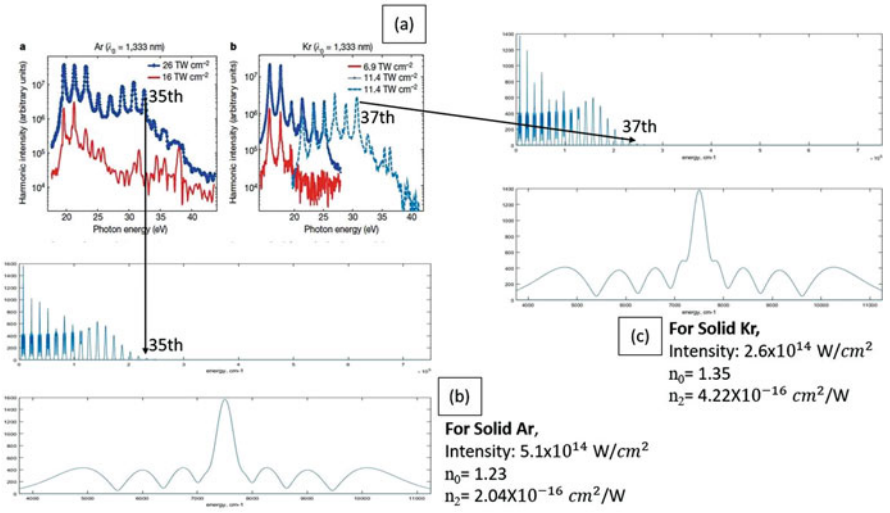

Fig. 17.12 Comparison between (**a**) the experimental result of HHG in solid Ar and solid Kr (Ndabashimiye, 2016) where the red spectrum is from 16 TWcm^{-2} and the blue spectrum is from 26 TWcm^{-2} and (**b**) the theoretical prediction (Alfano, 2021) of HHG from the ESPM model in (**b**) solid Ar and (**c**) solid Kr after fitting the beam intensity

shows the simulated HHG (see Figs. 17.12b, c) from ESPM with the same HHG structure with decreasing harmonics, the plateau, and cutoff regions which have been experimentally observed in solid argon and krypton (see Fig. 17.12a).

17.2.2.2 Cutoff Frequency ω_c of HHG

To find the cutoff frequency ω_{max} for HHG according to the ESPM theory, we use the method of stationary phase. The frequency spectrum of the beam propagating through a medium with the spherical atoms/molecules like rare gas molecules of Ar and Kr that give the electronic response to the optical cycle the propagating $E(t)$ beam can be described by Fourier transform as:

$$E(\omega) = \frac{\mathbf{Re}}{2\pi}\int_{-\infty}^{+\infty} E_0(t)\, e^{-i\left(\omega_L t - \frac{\omega_L n z}{c}\right)} e^{i\omega t} dt, \tag{17.29}$$

where z is the propagating distance into the medium, ω_L is the laser angular frequency, and $E_0(t)$ is the time-dependent envelope of the propagating electronic field of the beam, and the refractive index n can be found from Eq. 17.24. Combining Eq. 17.29 with Eq. 17.24 will give:

$$E(\omega) = \frac{\mathbf{Re}}{2\pi} e^{\frac{i n_0 \omega_L z}{c}} \int_{-\infty}^{+\infty} E_0(t)\, e^{i\left((\omega-\omega_L)t + \frac{\omega_L z}{c}\left[n_2\left(E_0 e^{-\frac{t^2}{T^2}}\cos\omega_L t\right)^2\right]\right)} dt. \tag{17.30}$$

The integral at Eq. 17.30 is the like integral used by the method of stationary phase (Kelvin, 1887) as:

$$f(x) = \int_{\alpha}^{\beta} g(t)\, e^{ixh(t)} dt, \tag{17.31}$$

which can be approximately evaluated by the method of stationary phase for $h(t)$. Equations 17.30 and 17.31 will give:

$$h(t) = (\omega - \omega_L)\, t + \frac{\omega_L z}{c}\left[n_2\left(E_0 e^{-\frac{t^2}{T^2}}\cos\omega_L t\right)^2\right]. \tag{17.32}$$

The first derivation of $h(t)$ is given by:

$$h'(t) = (\omega - \omega_L) + \frac{\omega_L z}{c} n_2 I_0 \left[e^{-\frac{2t^2}{T^2}}\left(-\frac{4t}{T^2}\right)\cos^2\omega_L t + e^{-\frac{2t^2}{T^2}}\,(2\cos\omega_L t)\,(-\omega_L \sin\omega_L t)\right]. \tag{17.33}$$

For method of stationary phase, $\dot{h}(t) = 0$ will yield the frequency extend in time:

$$(\omega - \omega_L) = \frac{\omega_L z}{c} n_2 I_0 e^{-\frac{2t^2}{T^2}} \left[\left(\frac{4t}{T^2} \right) \cos^2 \omega_L t + \omega_L \sin 2\omega_L t \right]. \tag{17.34}$$

At maximum values, $\cos^2\omega_L t = 1$ and $\sin 2\omega_L t = 1$, putting such values at maximum in Eq. 17.34 will give:

$$(\omega - \omega_L)_{max} = \frac{\omega_L z}{c} n_2 I_0 e^{-\frac{2t^2}{T^2}} \left[\frac{4t}{T^2} + \omega_L \right]. \tag{17.35}$$

At the critical point $t = 0$, Eq. 17.35 for maximum HHG extent becomes:

$$(\omega - \omega_L)_{max} = \left[\frac{\omega_L}{c} n_2 I_0 z \right] \omega_L \propto I_0 {\omega_L}^2. \tag{17.36}$$

Using $\frac{\omega_L}{c} = \frac{2\pi}{\lambda}$, where c = speed of light in vacuum, Eq. 17.36 can be written as:

$$(\omega - \omega_L)_{max} = \left[\frac{2\pi}{\lambda} n_2 I_0 z \right] \omega_L. \tag{17.37}$$

The cutoff frequency of the HHG $(\omega - \omega_L)_{max}$ depends on n_2, the intensity I_0, z, and ${\omega_L}^2$.

For example, when a 500 nm beam with the pulse energy of 6.5 mJ goes through 0.5 mm in argon ($n_0 = 1$, $n_2 = 2.5 \times 10^{-19}$ cm^2/W, $I_0 = 2.6 \times 10^{16}$ W/cm^2) gas, the cutoff frequency of the higher harmonics from Eq. 17.37 would be:

$$(\omega - \omega_L)_{max} \approx 41\, \omega_L. \tag{17.38}$$

Thus, a simple equation for the cutoff frequency for HHG generation can be analytically produced from ESPM theory using the method of the stationary phase. It depends on physical n_2, ω_L, z, and peak intensity rather than I_P and U_P.

Figure 17.13 shows the energy S(ω) example of HHG using FFT of $E(t)$ for argon with parameters above showing the cutoff. We have developed a simple maximum HHG cutoff frequency for material using electronic nonlinear index n_2 and physical properties and parameters of laser intensity, angular frequency, and thickness of material z.

The cutoff frequency above contradicts the common HHG cutoff energy shown in the past approximately as $I_P + 2U_P$ where I_p is the ionization energy and U_p is ponderomotive energy (varies as $\frac{I_L}{{\omega_L}^2}$) which is related to the kinetic energy of the electron. Extending the kinetic energy term given by Corkum and others, one finds that the $2U_P \frac{{\omega_L}^2 z^2}{{v_e}^2}$ (v_e is the velocity of the electron) is eliminating the ${\omega_L}^2$ in U_P term. So, the classical theory does not have a λ^2 dependency unless the higher terms are considered. In fact, the semiclassical theory of Corkum (1993) and the quantum-mechanical theory of Lewenstein (1994) do not take a nonlinear optical response

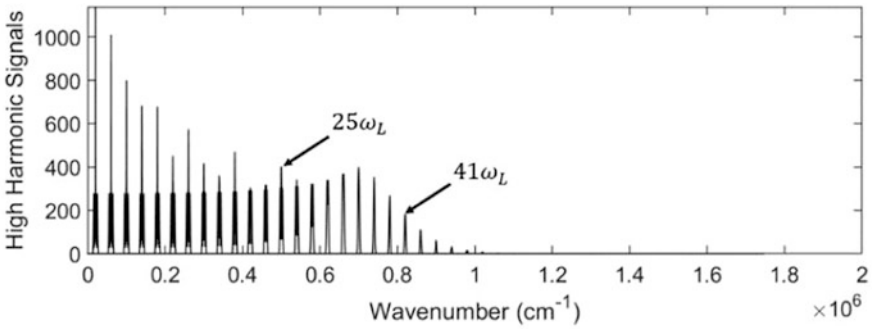

Fig. 17.13 Argon spectrum from ESPM at $I_0 = 2.6 \times 10^{16}$ W/cm^2 with central wavelength at 500 nm

(n_2) of the media and the parameters of the carrier-envelope phase of the electric field of the pulse into account.

Notice the cutoff energy from the method of steepest descent for ESPM generating the HHG spectrum varies with frequency and inversely on the pump wavelength. This result is in contrast with the three-step quantum-mechanical model for HHG. Our results are consistent with Gordon and Kartner for cutoff HHG energy below 500 eV. For HHG beyond 2 keV, the reverse happens for the optical pump frequency for HHG continua toward gamma rays (Gordon, 2005).

17.3 Applications of the Supercontinuum with USC and HHG

Currently, supercontinuum has been used as enabling technology in diverse applications in chemistry and biology in time-resolved spectroscopy, accurate frequency comb clocks, nonlinear optical spectroscopy, biomedical imaging, communications, computation, and microscopy using the visible and NIR range. With the advent of the USC and HHG, supercontinuum enters a new era spanning the entire Maxwell electromagnetic spectrum and offers a new paradigm in the development of compact UV to X-ray microscope to study the nanoscale science and the development of new computer chips.

USC and HHG in the UV X-ray microscope system can be used to explore biological for biomedical applications to image genes, the nucleus of cell components, nucleotides, and proteins to understand the most fundamental process in bio and nature by imaging on sub-nm and nm scale.

17.4 Conclusion

The generation of a coherent ultrawide spectral band from DC to XUV and X-ray beams using intense optical femtosecond pulses in various states of matter was simulated using two different temporal responses for the nonlinear Kerr index: slow (fs and ps) and ultrafast (as and fs).

In the simulation, we find that for the slow nonlinear index of refraction ($<n(t)>$), the envelope of the optical pulse gives rise to wide spectral broadening from SPM (noted as the SC, USC, and EUSC) which can span from DC to X-rays at extreme intensities ($>10^{14}$ W/m^2). For the ultrafast nonlinear index of refraction (n(t)), following both envelope and phase of the optical laser pulse gives rise to spectral broadening and HHG spanning from the visible range to X-rays for extreme intensities ($>10^{15}$ W/cm^2). The underlying temporal mechanisms for the Kerr effect arise from various types of motion: electron cloud distortion, molecular redistribution, ionization, plasma formation, rotation, and vibration of molecules in solids, liquids, and gases. CS_2 and the rare gas material are used to simulate USC and HHG spectra and compared with existing experimental spectra. These SPM and ESPM models will hold for Kerr media in different states of matter in particular solids. The cutoff frequencies of HHG varying as ω_0 and attosecond pulse produced from HHG are explained from the fast Kerr n_2 model.

Further research may take the effect of chirp and different CEP (carrier-envelope phase) offsets of the pulse such as sine-like pulse where $\varphi = \frac{\pi}{2}$ into account and can be expanded to include both fast electronics ($\boldsymbol{n_{2,F}}$) and slow molecular ($\boldsymbol{n_{2,S}}$) responses. The USC and HHG will be at the heart of a future compact UV X-ray microscope.

Acknowledgments We thank Dr. Daniel Nolan and Corning, Inc. for partially supporting ongoing advance optical research in science at CCNY IUSL. We also thank Prof. Lingyan Shi from UCSD for early interactions and suggestions, Henry Meyer and Sandra Mamani for discussions and Dr. Mikhail Sharonov for the calculation of the spectra of SC and HHG, and Mr. Yury Budansky for the drawings of this chapter.

References

Alfano, R. R. (1972). *Interactions of picosecond laser pulses with matter, GTE Laboratories Inc*. Technical Report, TR 72–230.1 (April 1972) and NYU PhD Thesis in Physics.

Alfano, R. R., & Shapiro, S. L. (1970a). Direct distortion of electronic clouds of rare-gas atoms in intense electric fields. *Physical Review Letters, 24*(22), 1217–1220.

Alfano, R. R., & Shapiro, S. L. (1970b). Observation of self-phase modulation and small-scale filaments in crystals and glasses. *Physical Review Letters, 24*(11), 592–594.

Alfano, R. R., & Shapiro, S. L. (1970c). Emission in the region 4000 to 7000 Å via four-photon coupling in glass. *Physical Review Letters, 24*(11), 584–587.

Alfano, R. R., & Shapiro, S. L. (1973). Ultrafast phenomena in liquids and solids. *Scientific American, 228*, 42–60.

Alfano, R. R., Hope, L. L., & Shapiro, S. L. (1972). Electronic mechanism for production of self-phase modulation. *Physical Review A, 6*(1), 433–438.

Alfano, R. R., Gersten, J. I., Zawadzkas, G. A., & Tzoar, N. (1974). Self-phase-modulation near electronic resonances of a crystal. *Physical Review A, 10*(2), 698–708.

Alfano, R. R., Mazhar, S. F. B., & Shi, L. (2021). Higher harmonic and supercontinuum generation arising from electronic self-phase modulation under ultrafast laser pulses for various states of matter. *Optik, 247*, 168208.

Alfano, R. R., Mazhar, S. F. B., Sharonov, M., & Shi, L. (2022). Ultra-supercontinuum generation with high intense femtosecond pulses. *Optik, 249*, 167872.

Besse, V., Levlond, H., & Boudebs, G. (2015). Fifth-order nonlinear susceptibility: Effect of third-order resonances in a classical theory. *Physical Review A, 92*, 013818.

Bloembergen, N. (1973). The influence of electron plasma formation on superbroadening of light filament. *Optics Communication, 8*(4), 285–288.

Bloembergen, N., & Shen, Y. R. (1964). Quantum- theoretical comparison of nonlinear susceptibilities in parametric media, lasers, and Raman lasers. *Physics Review, 133*(1A), A37–A49.

Buckingham, A. D. (1956). Birefringence resulting from the application of an intense beam of light to an isotropic medium. *Proceedings of the Physical Society, B69*, 344–349.

Comby, A., Descamps, D., Beauvarlet, S., Gonzalez, A., Guichard, F., Petit, S., Zaouter, Y., and Mairesse, Y. (2019). Cascaded harmonic generation from a fiber laser: a milliwatt XUV source, *Optics Express, 27*(15), 20383–20396.

Corkum, P. B. (1993). Plasma perspective on strong field multiphoton ionization. *Physical Review Letters, 71*(13), 1994–1997.

Duguay, M. A., & Hansen, J. W. (1969). An ultrafast light gate. *Applied Physics Letters, 15*(6), 192–194.

Gordon, A., & Kartner, F. X. (2005). Scaling of keV HHG photon yield with drive wavelength. *Optics Express, 13*(8), 2941–2947.

Johnson, S. C. (2022). *'High-harmonic generation sources enable extreme ultraviolet lensless imaging', Lasers & Sources*. Laser Focus World.

Kalpouzos, C., Lotshaw, W. T., McMorrow, D., & Kenney-Wallace, G. A. (1987). Femtosecond laser-induced Kerr responses in liquid CS_2. *The Journal of Physical Chemistry, 91*, 2028–2030.

Kelvin, L., & Thomson, W. (1887). On the waves produced by a single impulse in water of any depth, or in a dispersive medium. *Philosophical Magazine, 23*(142), 252–255.

Kerr, J. (1875). A new relation between electricity and light: Dielectrified media birefringent. *Philosophical Magazine, 4*(50), 337–348.

Kong, D. G., Chang, Q., Yu, H. A., Gao, Y. C., Wang, Y. X., Zhang, X. R., Yang, K., Wu, W. Z., & Song, Y. L. (2009). The fifth-order nonlinearity of CS_2. *Journal of Physics B: Atomic, Molecular and Optical Physics, 42*, 065401.

Lewenstein, M. (1994). Theory of high-harmonic generation by low-frequency laser fields. *Physical Review A, 49*(3), 2117–2132.

Mourou, G. A. (2021). *A Passion for extreme light*, Proc. SPIE 11664, Solid State Lasers XXX: Technology and Devices, 1166403 (Presented at SPIE LASE: March 08, 2021; Published: 8 March 2021).

Ndabashimiye, G., Ghimire, S., Mengxi, W., Browne, D. A., Schafer, K. J., Gaarde, M. B., & Reis, D. A. (2016). Solid-state harmonics beyond the atomic limit. *Nature, 534*, 520–523.

Index

R. R. Alfano (ed.), *The Supercontinuum Laser Source*,
https://doi.org/10.1007/978-3-031-06197-4